Kumari Namrata
Neeraj Priyadarshi
Ramesh C. Bansal
Jitendra Kumar   *Editors*

Smart Energy and Advancement in Power Technologies

Select Proceedings of ICSEAPT 2021, Volume 2

Springer

Lecture Notes in Electrical Engineering

Volume 927

The book series *Lecture Notes in Electrical Engineering* (LNEE) publishes the latest developments in Electrical Engineering—quickly, informally and in high quality. While original research reported in proceedings and monographs has traditionally formed the core of LNEE, we also encourage authors to submit books devoted to supporting student education and professional training in the various fields and applications areas of electrical engineering. The series cover classical and emerging topics concerning:

- Communication Engineering, Information Theory and Networks
- Electronics Engineering and Microelectronics
- Signal, Image and Speech Processing
- Wireless and Mobile Communication
- Circuits and Systems
- Energy Systems, Power Electronics and Electrical Machines
- Electro-optical Engineering
- Instrumentation Engineering
- Avionics Engineering
- Control Systems
- Internet-of-Things and Cybersecurity
- Biomedical Devices, MEMS and NEMS

For general information about this book series, comments or suggestions, please contact leontina.dicecco@springer.com.

To submit a proposal or request further information, please contact the Publishing Editor in your country:

China

Jasmine Dou, Editor (jasmine.dou@springer.com)

India, Japan, Rest of Asia

Swati Meherishi, Editorial Director (Swati.Meherishi@springer.com)

Southeast Asia, Australia, New Zealand

Ramesh Nath Premnath, Editor (ramesh.premnath@springernature.com)

USA, Canada:

Michael Luby, Senior Editor (michael.luby@springer.com)

All other Countries:

Leontina Di Cecco, Senior Editor (leontina.dicecco@springer.com)

** This series is indexed by EI Compendex and Scopus databases. **

Kumari Namrata · Neeraj Priyadarshi ·
Ramesh C. Bansal · Jitendra Kumar
Editors

Smart Energy and Advancement in Power Technologies

Select Proceedings of ICSEAPT 2021, Volume 2

Springer

Editors
Kumari Namrata
Department of Electrical Engineering
National Institute of Technology
Jamshedpur
Jamshedpur, Jharkhand, India

Ramesh C. Bansal
Department of Electrical Engineering
University of Sharjah
Sharjah, UAE

Department of Electrical, Electronic
and Computer Engineering
University of Pretoria
Pretoria, South Africa

Neeraj Priyadarshi
Department of Energy Technology
Aalborg University
Esbjerg, Denmark

Jitendra Kumar
Department of Electrical Engineering
National Institute of Technology
Jamshedpur
Jamshedpur, Jharkhand, India

Contents

Power Quality Improvement with Harmonic Reduction Using P-Q Theory-Based Shunt Active Power Filter

Kiran Yadav, Gitanjali Mehta, and Vinod Kumar Yadav

Abstract The penetration of nonlinear loads is responsible for load-side harmonic current. Customer awareness about power quality issues has made it indispensable to analyze the effect of nonlinear and linear loads. The active filter has shown a number of advantages against passive filter due to impractical solutions and size problems associated with the passive filter. In this paper, Shunt Active Power Filter (SAPF) has been implemented with a P-Q theory-based control scheme. A compensating current is calculated by the controller which is fed to the shunt active filter. SAPF can be widely implemented in industrial applications. The objective is to eliminate unrequited harmonics so as to improve the voltage profile in the system. Simulation on MATLAB has been carried out to corroborate the results, and Total Harmonic Distortion (THD) is compared for varying loads.

Keywords Power quality · Shunt active power filter · P-Q theory · Harmonics · Total harmonic distortion

1 Introduction

For the past decades, electronics-based equipment has proliferated the consumer market. The most prominent of them is adjustable speed drives (ASDs) providing efficient output to the industry. However, it produces a significant change in the sinusoidal nature of voltage and current. Hence, attempts have been made to meet the challenge of using drives by a reduction in distortion [1, 2]. When an ASD is connected to the system, it is responsible for producing harmonic distortion. These ASDs draw non-sinusoidal current from the supply filled with harmonics which in turn flows into the system and distorts voltage and current waveform. This was noted

K. Yadav · G. Mehta (✉)
Electrical Engineering Department, Galgotias University, G. Noida, India
e-mail: gitanjali.iitr@gmail.com

V. K. Yadav
Electrical Engineering Department, Delhi Technological University, Delhi, India

not only for ASDs but also for converter circuits, UPS and other AC-DC and DC-AC conversion systems. Thus, deviation of a waveform to non-sinusoidal is attributed to harmonics and distortion [3, 4]. Conditioning of load and conditioning of line are the two ways to address harmonic related issues. The latter comprises passive and active filter methodology. Resonance and distinct filter for each frequency limit the implementation of the passive filter. Therefore, active filters paved the way for cutting-edge solutions for voltage and current-related disturbances [5–7]. Control techniques employed in the system make it most suitable and in-demand industrial solution. Hence, active filter accomplishes harmonic limitation and reactive power compensation [8–12].

2   Active Power Filters

Conventionally, passive filters were used with the combination of inductor and capacitor [5]. Although they were low in cost and less complex in design, they were more prone to impact resonance and hence active filters were designed. Active filters generally employ IGBT or MOSFET to provide switching circuits [6]. Figures 1, 2 and 3 depict the general active filter mechanism in use. The controller is shown with only one gate signal. In all the cases, an internal goto signal is used in MATLAB to provide current information which is used to generate a compensating current in the system.
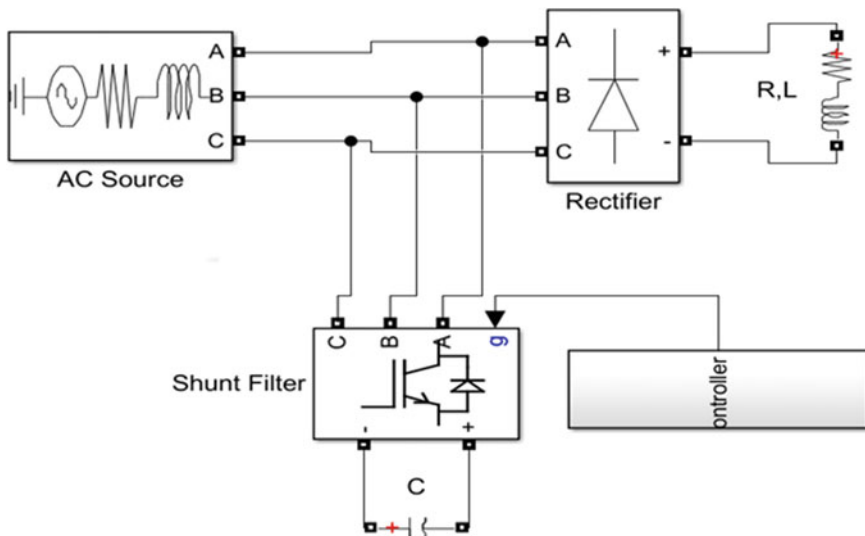
Fig. 1   SAPF circuit diagram
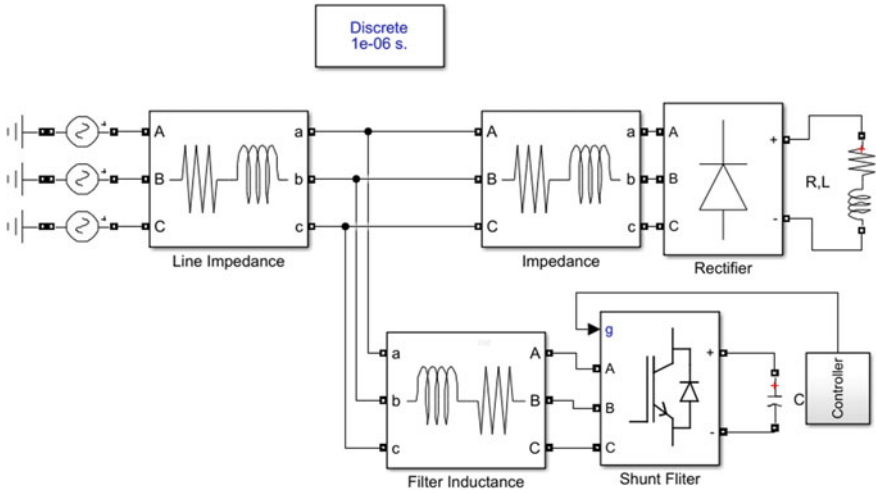
Fig. 2 SAPF being used as voltage source
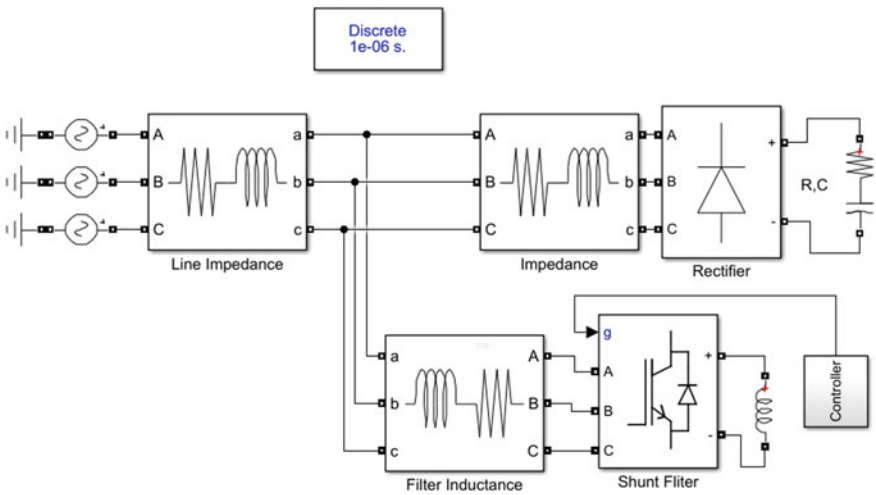
Fig. 3 SAPF being used as current source

In this, a rectifier is connected across linear or nonlinear load which converts AC-DC and hence harmonic generation from the load side. A parallel active filter is connected which gives compensating current based on controller and therefore prevents harmonic current to reach AC source. In this way, the harmonic current is prevented to distort the source voltage. Active filters are dynamic in nature. They can be used as a current source and voltage source. Figure 2 shows when a filter is used as a voltage source connected with a capacitor and Fig. 3 depicts when a filter
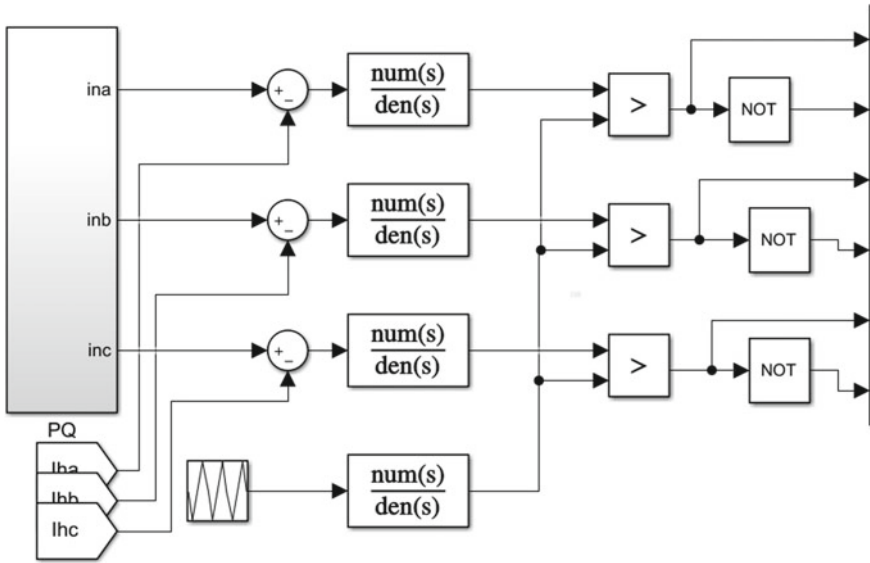
Fig. 4 Control scheme based on P-Q theory

is used as a current source connected with an inductor. Passive filter topologies are shunt LC and shunt low pass filter. Active filter topologies are series, shunt and a combination of series-shunt called hybrid [7]. Active filter offers the convenience of configuration for over current in system and can result in less harmonics with an increase in frequency component. Figure 4 shows the control scheme based on instantaneous P-Q theory.

3 Instantaneous P-Q Power Theory

The P-Q theory also referred to as instantaneous power theory is based on Clarke and Parke transformations. In Clarke transformation, voltages and current for a three-phase system are reconstructed in terms of α and β [8].

$$i_{\alpha\beta o} = \sqrt{2/3} \begin{bmatrix} 1 & -1/2 & -1/2 \\ 0 & \sqrt{3}/2 & -\sqrt{3}/2 \\ 1/\sqrt{2} & 1/\sqrt{2} & 1/\sqrt{2} \end{bmatrix} i_{abc} \tag{1}$$

$$v_{\alpha\beta o} = \sqrt{2/3} \begin{bmatrix} 1 & -1/2 & -1/2 \\ 0 & \sqrt{3}/2 & -\sqrt{3}/2 \\ 1/\sqrt{2} & 1/\sqrt{2} & 1/\sqrt{2} \end{bmatrix} v_{abc} \tag{2}$$

Here, i_{abc} is the three-phase source current and v_{abc} is the three-phase source voltage of the system. Similarly, active and reactive power components are represented. Equation 3 represents instantaneous real power and Eq. 4 represents instantaneous imaginary power where voltage and current are represented in terms of a-b-c coordinates and α-β coordinates.

$$p = v_\alpha i_\alpha + v_\beta i_\beta \tag{3}$$

$$q = v_\alpha i_\beta - v_\beta i_\alpha \tag{4}$$

In matrix form, the above equation is represented as

$$\begin{bmatrix} p \\ q \end{bmatrix} = \begin{bmatrix} v_\alpha & v_\beta \\ -v_\beta & v_\alpha \end{bmatrix} \begin{bmatrix} i_\alpha \\ i_\beta \end{bmatrix} \tag{5}$$

Then, active and reactive power is divided into AC and DC components. A low pass filter is connected across the circuit to obtain the DC component of both active and reactive power.

$$p = \overline{p} + \tilde{q} \tag{6}$$

$$q = \overline{q} + \tilde{p} \tag{7}$$

The P-Q theory states that the DC component of active power is represented in terms of α and β reference current as

$$i_{\alpha\beta}^* = \frac{1}{v_\alpha^2 + v_\beta^2} \begin{bmatrix} v_\alpha & v_\beta \\ -v_\beta & v_\alpha \end{bmatrix} \begin{bmatrix} p \\ q \end{bmatrix} \tag{8}$$

And thus, the reference current is given as

$$i_{\alpha\beta}^* = \sqrt{2/3} \begin{bmatrix} 1 & 0 \\ -1/2 & \sqrt{3}/2 \\ -1/\sqrt{2} & -\sqrt{3}/2 \end{bmatrix} i_{\alpha\beta}^* \tag{9}$$

4   Simulation Results and Discussion

Shunt active power filter circuit for simulation is shown in Fig. 5. Figure 6 shows the P-Q controller for shunt APF simulation. The authors have calculated THD under three different load conditions. In the first case, RL load is considered connected

to the DC side of the rectifier. Figures 7, 8, 9, 10, 11 and 12 depict waveforms for rectifier with RL load. In Fig. 7, source voltage of all three phases is depicted. In Fig. 8, source current is depicted in phase-a. In Fig. 9 load current is depicted. In Fig. 10 compensating current is depicted. In Fig. 11 THD for load current is depicted which is 24.49%. In Fig. 12, THD for source current is depicted which comes out to be 5.44%. In the second case, RC load is connected to the DC side of the rectifier. THD in source current for this came out to be 6.44%. Figures 13, 14, 15 and 16 show waveforms for rectifiers with RC load. Figure 13 shows the source current and in Fig. 14 load current is shown. In Fig. 15, THD for load current is depicted which is 22.49%. In Fig. 16, THD for source current is depicted which is 6.44%. And, in the third case R load is connected to the DC side of the rectifier. THD of source current comes out to be 10.27%. Waveforms from Figs. 17, 18, 19 and 20 are shown for rectifier with R load. In Fig. 17 source current is depicted. In Fig. 18 load current is shown. In Fig. 19, THD for load current is depicted which is 21.64%, and in Fig. 20 THD for source current is depicted which is 10.27%. Table 1 shows the parameters and their values. Table 2 shows order-wise source current harmonics with rectifier R-L load using SAPF. Table 3 shows the THD values of load current and source currents for different types of rectifier loads (Fig. 21).

5 Conclusion

Shunt active filter is implemented using a P-Q theory-based controller in this paper. SAPF has been able to mitigate harmonic components present in the source current due to the rectifier which is a nonlinear load. A control mechanism is used to provide compensating current in the system so as to maintain the source current sinusoidal. THDs obtained through FFT analysis for different loads conclude that THD in source current is considerably reduced for all three loads. MATLAB simulation has been carried out in order to inspect the waveforms and their THD components associated with them. Tabular representation is also provided for different loads to analyze its effect.
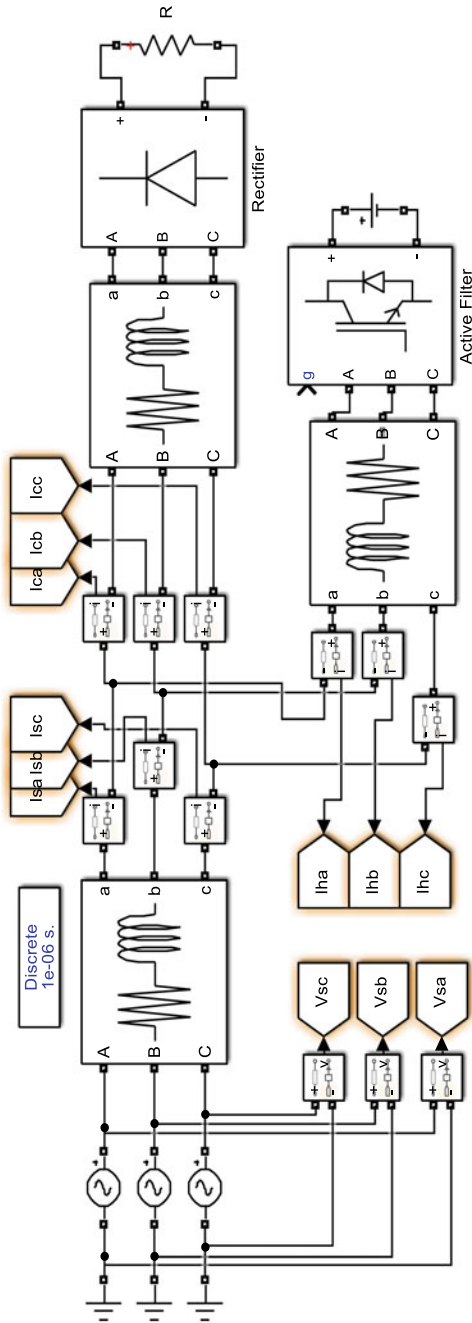
Fig. 5 Shunt APF showing Rectifier with *R* load
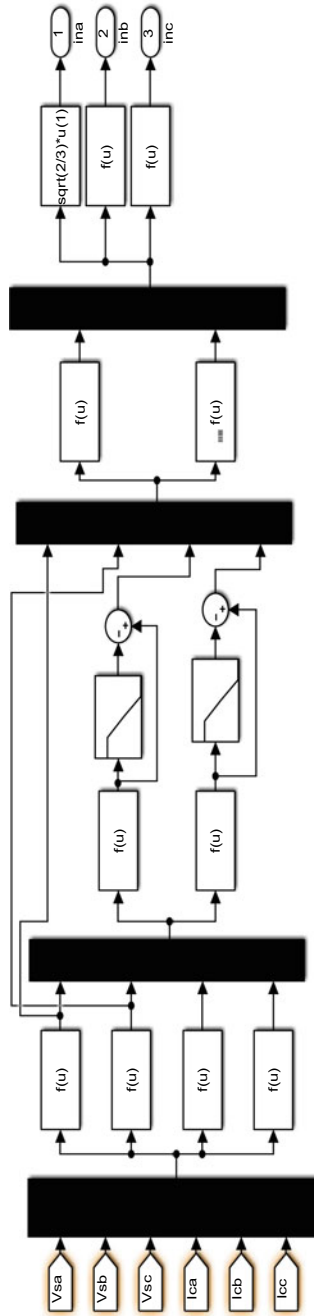
Fig. 6 P-Q controller for Shunt APF
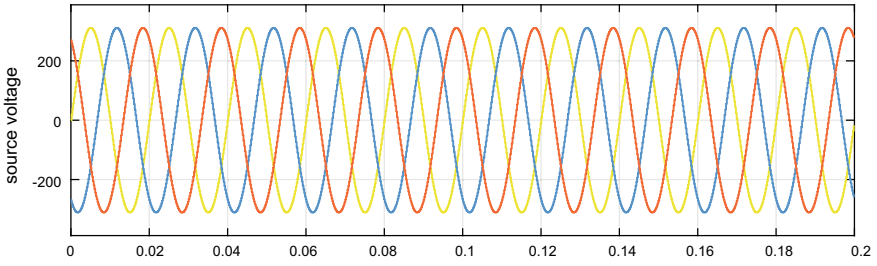
Fig. 7 Three-phase source voltage for RL load
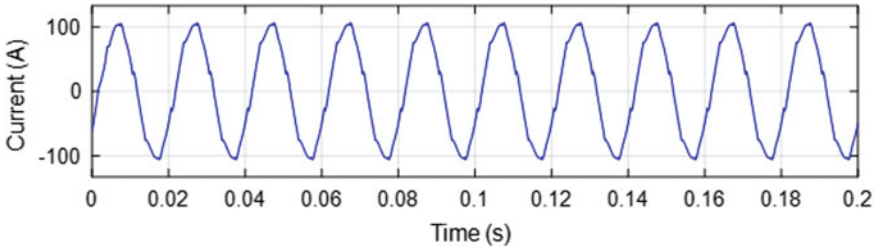
Fig. 8 Source current for RL load
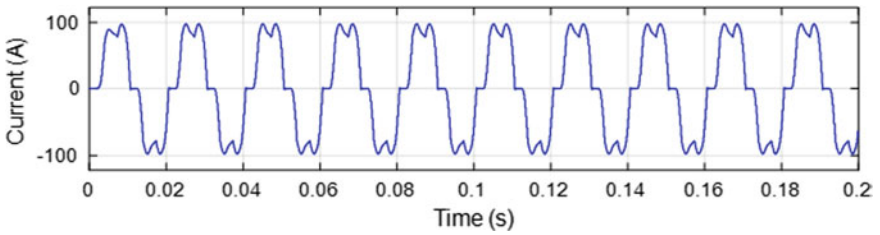
Fig. 9 Load current for RL load
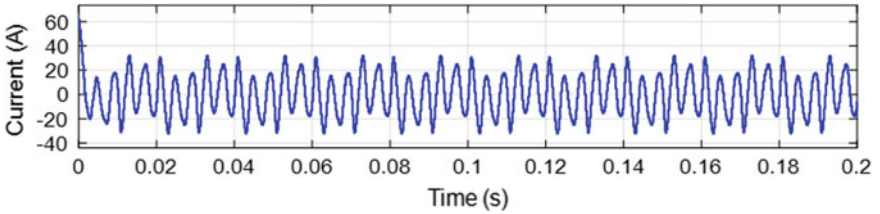
Fig. 10 Compensating current for RL load

Fig. 11 THD for load
current with RL load
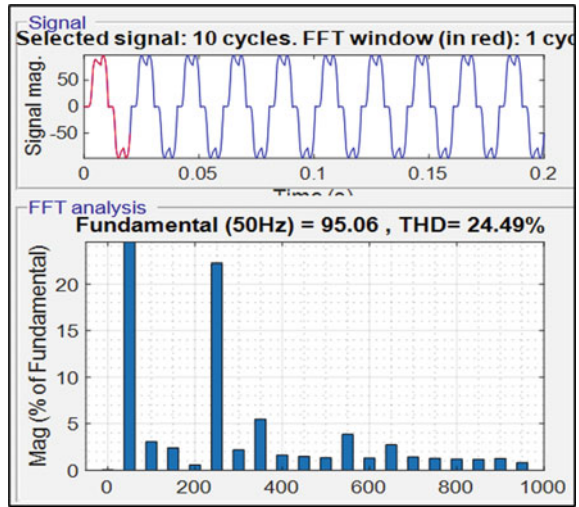
Fig. 12 THD for source
current with RL load
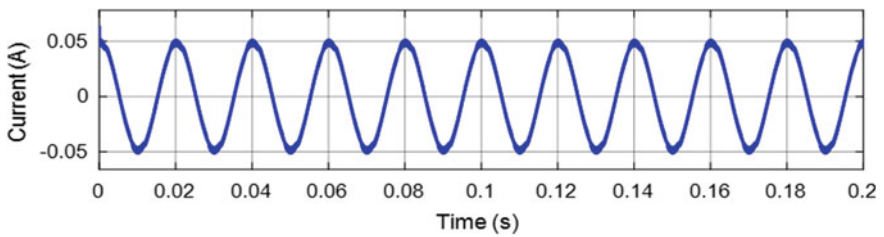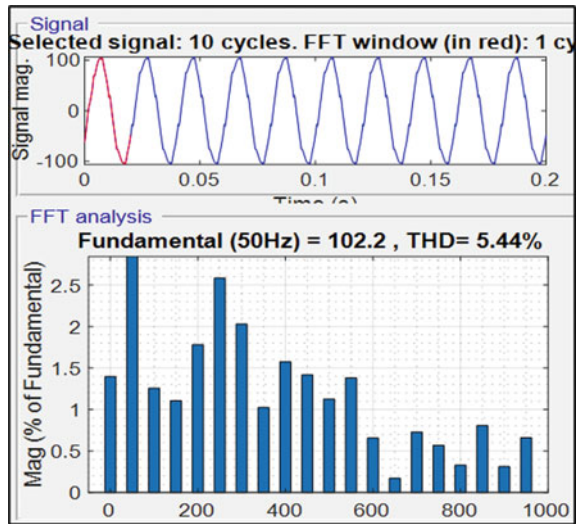
Fig. 13 Source current for RC load
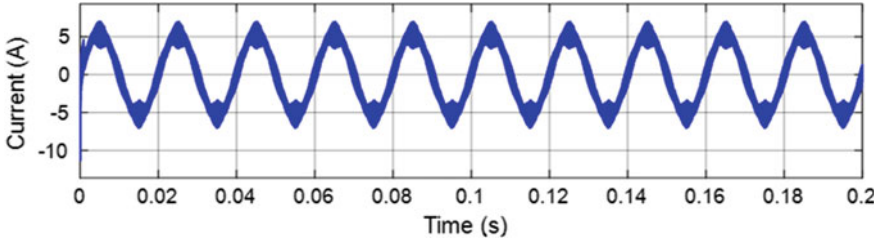
Fig. 14 Load current for RC load

Fig. 15 THD for load current with RC load
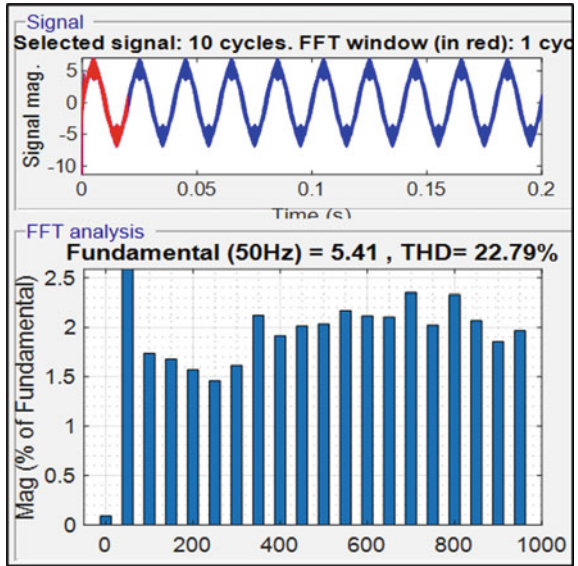
Fig. 16 THD for source
current with RC load
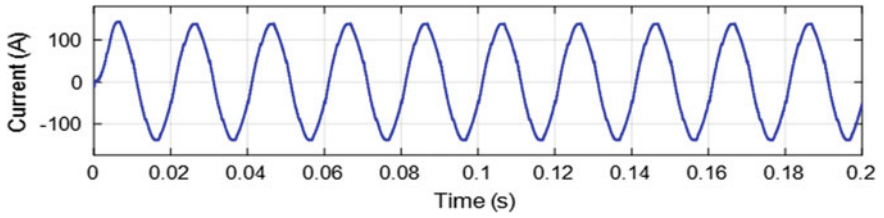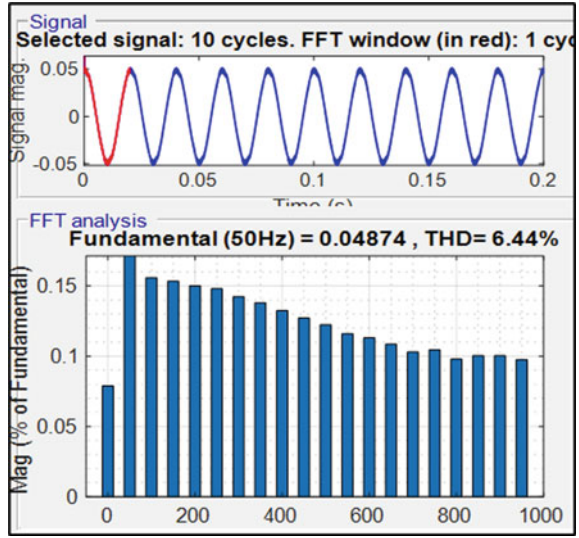
Fig. 17 Source current for R load
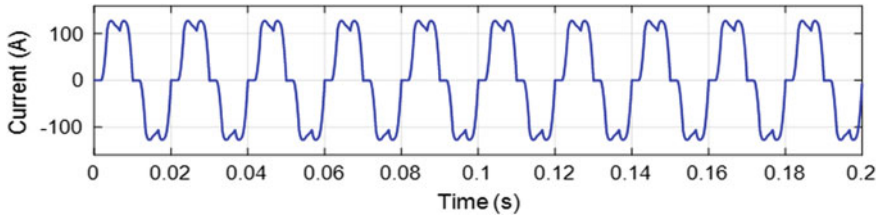
Fig. 18 Load current for R load
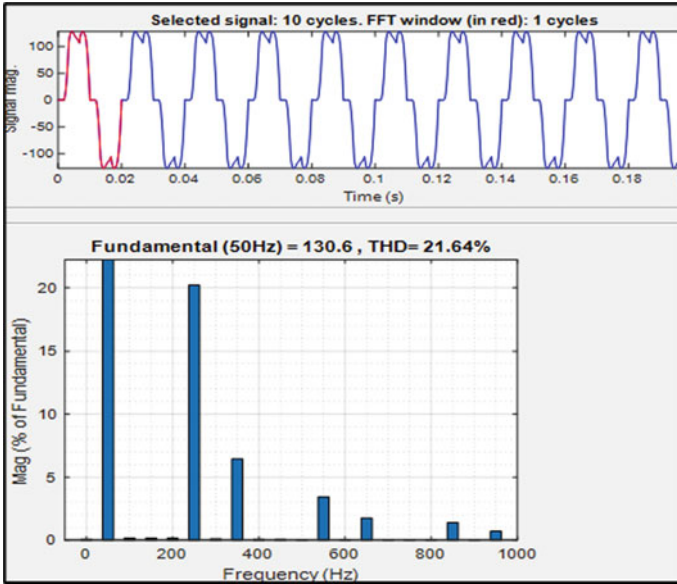
Fig. 19 THD for load current with R load
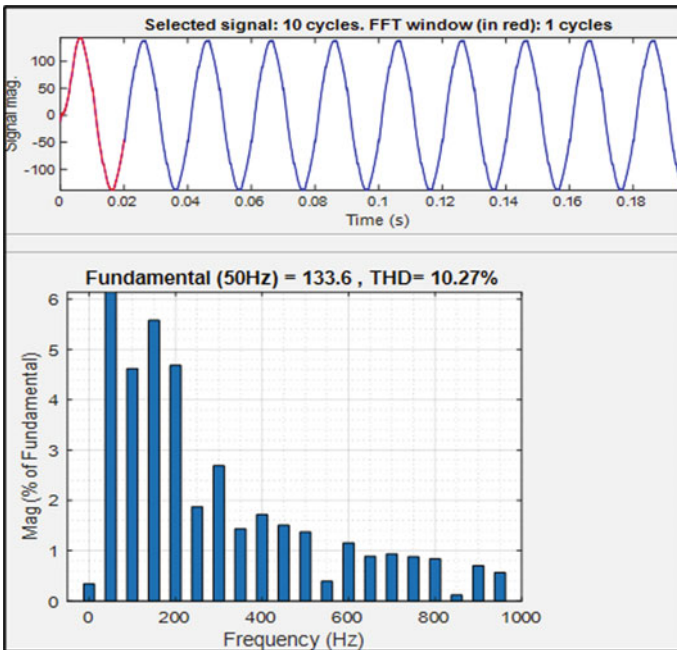
Fig. 20 THD for source current with R load

Table 1 Parameter values

Parameter	Value
Source voltage, frequency	310 V, 50 Hz
Source impedance	$R = 0.2\ \Omega\ L = 0.16$ mH
DC link voltage V_{dc}	840 V
Filter inductor L_c	3 mH
RL load	$R = 6.2\ \Omega L = 20$ mH
R load	$R = 6.2\ \Omega$
RC load	$R = 15\ \Omega\ C = 8\ \mu$F

Table 2 Harmonic components in source current for Rectifier RL load

Harmonic order	% Value
3rd	3.82
5th	1.1
7th	0.6
9th	0.43
11th	0.40
13th	0.3
15th	0.1
17th	0.3
19th	0.2
THD %	5.44

Table 3 Computation of THD

Load	Source current (%)	Load current (%)
Rectifier with R, L load	24.49	5.44
Rectifier with R load	21.64	10.27
Rectifier with R, C load	22.49	6.44

Fig. 21 THD for source current with R load harmonic order
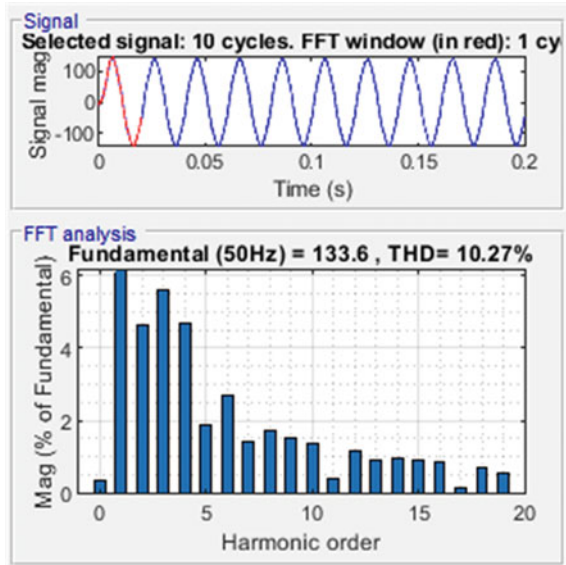
References

1. Bhattacharya S, Frank TM, Divan DM, Banerjee B (1998) Active filter system implementation. IEEE Ind Appl Mag 4(5):47–63
2. Hoevenaars T, LeDoux K, Colosino M (2003) Interpreting IEEE STD 519 and meeting its harmonic limits in VFD applications. In: IEEE industry applications society 50th annual petroleum and chemical industry conference, Houston, TX, USA, pp 145–150
3. Mehta G, Singh SP (2013) Power quality improvement through grid integration of renewable energy sources. IETE J Res 59(3):210–218
4. Mehta G, Singh SP (2013) Improvement of power quality at PCC through grid interfacing photovoltaic system. In: Proceedings of the sixth IASTED Asian conference on power and energy systems AsiaPES, Phuket, Thailand
5. Mehta G, Singh SP, Patidar RD (2013) Fuel cell based distributed generation system with power flow and power quality control. Int J Power Energy Conversion 4(1):73–94
6. Nie X, Liu J (2019) Current reference control for shunt active power filters under unbalanced and distorted supply voltage conditions. IEEE Access 7:177048–177055
7. Mehta G, Patidar RD, Singh SP (2011) Design, analysis and implementation of DSP based single-phase shunt active filter controller. In: Proceedings of IEEE international conference on emerging trends in electrical and computer technology, India, pp 166–173
8. Lada MY, Bugis I, Talib MHN (2010) Simulation a shunt active power filter using MATLAB/Simulink. In: International power engineering and optimization conference, Shah Alam, pp 371–375
9. Yadav VK, Mehta G, Kumari R, Patidar RD (2016) Power quality improvement using D-STATCOM and DVR. In: Proceedings of 2nd international conference on advances in steel, power and construction technology, O. P. Jindal University, Raigarh, Chhattisgarh, India
10. Amerise A, Mengoni M, Rizzoli G, Zarri L, Tani A, Casadei D (2020) Comparison of three voltage saturation algorithms in shunt active power filters with selective harmonic control. IEEE Trans Ind Appl 56(3):2762–2772

11. Meloni LFJ, Tofoli FL, Rezek AJJ, Ribeiro ER (2019) Modeling and experimental validation of a single-phase series active power filter for harmonic voltage reduction. IEEE Access 7:151971–151984
12. Devassy S, Singh B (2019) Implementation of solar photovoltaic system with universal active filtering capability. IEEE Trans Ind Appl 55(4):3926–3934

Industrial Automation Using ATmega328p-Based Programmable Logic Controller

Vishal Chauhan and Atma Ram Gupta

Abstract This paper explains how to use microcontroller-based programmable logic control devices to switch industrial loads in the sequential nature of works. This operation is generally required for the repetitive type of industrial work. Programmable Logic Controllers which are being used in the industries are quite expensive to operate and also have a high initial cost to operate on the sequential switching type of simple operations. Through this project only we are demonstrating the working of this general load switching operation having a low cost microcontroller belonging to Atmel (ATmega328p). The implementation of this project required program configuration using input switches. There are several tasks in the industries which are based on different orders and intervals according to the manufacturing requirements. Considering the automotive industry in which different machines operate for a different time and need to be switched after a fixed interval, microcontroller (ATmega328p) is programmed accordingly so that it can operate in different modes according to user needs. In this project, we are demonstrating only three modes of operation that are mainly used in the sequential switching of load. Set mode and Auto mode are used for time selection and automation of tasks, respectively. Eventually in the Manual Mode loads get ON/OFF as per the user's needs and requirements using the load buttons, respectively. Selection of different Modes and working status of the loads displayed on the (16 * 2) LCD. Hence, now the task performed by costly PLC can be achieved by using the low-cost microcontroller. This project can be advanced by adding a GSM module or Bluetooth module to control its functioning remotely.

Keywords Embedded system · ATmega328p · Arduino compiler · Relays · PCB

1 Introduction

This project highlights the concepts, working, implementation in real life, and application of programmable logic controllers in industries. It explains how the

V. Chauhan (✉) · A. R. Gupta
Electrical Engineering Department, National Institute of Technology Kurukshetra, Haryana, India
e-mail: vishal9580ch@gmail.com

microcontroller-based PLC can be useful in industrial applications in the repetitive nature of work [1]. This operation is generally required in industries where there is the need for sequential switching of the load for different time intervals and different nature of work using embedded system-based or microcontroller-based concept. It used the microcontroller from the Atmel family which works on the 8-bit architecture [2].

This project is going to work in three different modes: Manual mode, Set mode, and Auto mode. In the Set mode of operation, it gives us the flexibility to set the time after which it is going to switch the load in Auto mode; it allows us to set the required time for different loads according to our needs [3]. In the Auto mode, it operates a different load as per the time set in Set mode; after the time is over for a particular load, it automatically switches OFF that particular load and switches ON the next load in the queue [4]. And in the Manual mode, it operates the different loads and gets input from the user manually as per his need and flexibility [5]. Practically using this project helps us to reduce the cost of operation performed by costly PLCs as compared to the microcontroller-based PLCs [6]. Further, this project can be made technically advanced and more automated by introducing the GSM-based remote-control system [7], so that by merely using our mobile phones we can control our microcontroller-based PLC [8].

The programmable logic controller which is currently used in the industries is very expensive to use for such small operations like sequential switching of the load, so here we have tried to introduce the microcontroller-based small PLC which can similarly come at a lower initial cost and cost of operation [9]. It consists of an ATmega328p microcontroller and other components under the practical implementation. It can be programmed [10] in such a way so it can operate in three different modes, Manual mode, Set mode, and Auto mode, so that it can meet all the operational requirements needed for the successful completion of sequential switching types of works [11].

2   Components of Microcontroller PLC

The different components used in the project are as follows.

(1) **ATmega328p:** It is a low-power microcontroller that is based on the 8-bit AVR enhanced RISC architecture. It has 32 KB of flash program memory and 20MIPS of CPU speed. It takes only one clock cycle for the execution of the complex instruction, so it can work with a throughput speed of 1MIPS which enables the manufacturer to optimize the power consumption as per the processing speed of the microcontroller [12].

It has 32 general-purpose registers which are directly connected to Arithmetic Logic Unit (ALU) which enables the microcontroller to access the two different registers in a single clock cycle that makes it more code efficient and enhances the processing speed as compared to regular CISC architecture.

ATmega328p can be programmed in Arduino IDE and C or C++ language. In this project, I have used the Arduino IDE to code the microcontroller to work as the PLC. It needs to convert the Arduino file to a hex file for uploading it to the microcontroller. The microcontroller saved the code and start working as a processor to do the process without any error [13] (Table 1).

(2) **Center Tapped Transformer (9-0-9 V)**: It is the static device that is used to transfer the electrical energy from one part of the circuit to another. The transformer works on the principle of mutual induction (Faraday's law of electromagnetic induction) in which primary and secondary windings are electrically isolated. Voltage in the secondary is produced due to the induction of flux produced in the primary windings. In the center tap transformer (Fig. 1), secondary has tapped the middle of the secondary winding so that the extreme terminal produced full voltage and tapped terminal to any terminal produced half of the extreme voltage [14].

This transformer uses to power the PLC circuit. The 220 V AC supply was directly given to the transformer then it produced the 9 V output between any extreme and

Table 1 Pin description of ATmega328p

Types of pins	Name of pins
Interrupt pins	PD2, PD3
UART communication pins	PD0, PD1
SPI communication pins	PB2, PB3, PB4, PB5
I2C communication pins	PC4, PC5
Timers pins System clock pins Comparator pins PWM pins ADC pins AREF pin Reset pin Power pins Oscillator pins	PD4, PD5, PB6, PB7 PB0 PD6, PD7 PD5, PD6, PB1, PB1, PB2, PB3, PD3 PC0, PC1, PC2, PC3, PC4, PC5, AVCC PC6 VCC, GND PB6, PB7

Fig. 1 Center tap transformer
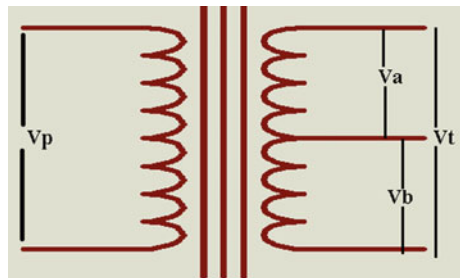
center tap terminal. The 9 V output is fed to the bridge rectifier that converts 9 V AC to 9 V DC so that it can be used to power the microcontroller and other circuit elements.

(3) **VOLTAGE REGULATOR (7805)**: It is used to control and keep the voltage constant to a particular level. Whenever it required a constant and steady voltage supply to power the electronics circuit or any circuit, a voltage regulator (Fig. 2) is used. It is also used when it needs to have the constant voltage from the pulsating DC output. It helps to protect the low-power circuit by maintaining the constant voltage with varying input and load conditions. It is a device that contains the feed-forward circuit and negative feedback control loops which help in the regulation purpose. Two types of voltage regulators are widely used in electronics devices: Linear and Switching voltage regulators [15].

In this project, it is used to obtain the stable 5 V DC output from the 9 V pulsating dc which is obtained from the (9-0-9) V center tap transformer. As we know, ATmega328p and all the components used in this project operate on a 5 V dc supply.

(4) **CRYSTAL OSCILLATOR (16 MHz)**: A crystal oscillator (electronic oscillator) contains the circuit that works on the principle of mechanical resonance to produce the oscillation of constant frequency. It is called the crystal oscillator because it contains the vibrating crystal (piezoelectric material) that produced the electrical oscillation of constant frequency as shown in an equivalent circuit (Fig. 3). Mostly, quartz crystals are used in the crystal oscillator that can produce the oscillation of frequency ranging from 10 kilohertz to 100 megahertz [16].

Mostly, crystal work is used to represent the oscillator, but piezoelectric devices or piezoelectric materials are more precise to represent the crystal oscillator. The vibrating crystal present in the crystal oscillator is a ceramic crystal or wafer of the quartz crystal.

(5) **LIQUID CRYSTAL DISPLAY (16*2)**: Liquid Crystal Display (LCD) is an electronic display that is widely used in small electronics for displaying the working state of the devices. A 16 × 2 LCD is a simple electronic module which contains 16 columns and 2 rows (Fig. 4) to display characters. These LCD

Fig. 2 7805 voltage regulator
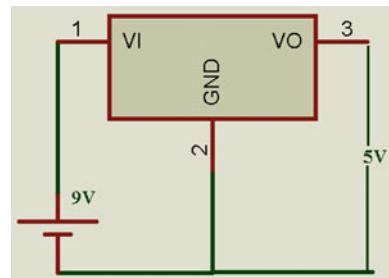
Fig. 3 Equivalent circuit of crystal oscillator
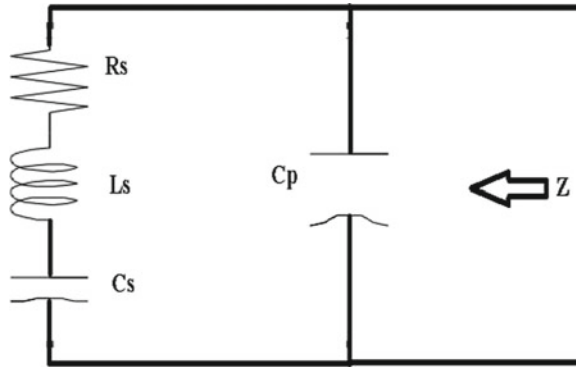
16 * 2 modules are very commonly used as compared to other display and multi-segment LEDs because LCDs are more economical and easily programmable [17]. It also doesn't have any limitation of displaying any special and custom characters (unlike in seven segments).

It is used to display the different states of loads such that "ON", "OFF", and "mode of selection".

(6) **RELAYS (12 V)**: Relay is an electromagnetic switch that is used for switching operations in the circuit where we need to control the devices automatically using a low-voltage supply. It is a low–high voltage switch used in the automated system. Here, low to high voltage switch represents the output of relays generally connected to the 220 V ac supply and a comparatively dc voltage of 6 V or 12 V is required to turn ON/OFF the relay [18].

In this project, it is used to automate the system using ATmega328p where the 5 V output of the microcontroller is used to turn ON/OFF the loads automatically which are connected to the relay (Table 2).

Fig. 4 (16*2) LCD display
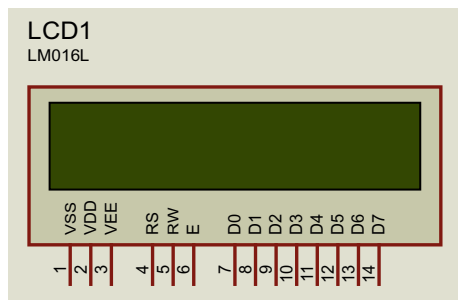
Table 2 Rating and description of components

Components	Rating and description
ATmega328p	Operating voltage: +1.8 V to +5.5 V External oscillator: 0–20 MHz @4.5 V to 5.5 V Internal oscillator: 8 MHz CPU speed: 1MIPS for 1 MHz Operating temperature: −40 °C to + 105 °C
Center tap transformer	Input voltage: 230 V AC Output voltage: 9 V, 9 V, or 18 V Output current: 500 mA
Voltage regulator	Input voltage: 7 V to 25 V (Unregulated) Operating current: 5 mA Output voltage: 5 V (Regulated) Maximum junction temperature: 125 °C
Crystal oscillator	Output frequency: 16 MHz Tolerance: 30% Operating temperature range: −10 °C to +60 °C
Liquid crystal display Relay	Operating voltage: 4.7 V to 5.3 V Current rating: 1 mA (without backlight) Current rating: 7A Voltage rating: 240 V AC Switching voltage: 12 V

3 Block Diagram

The block diagram in (Fig. 5) and the proteus circuit in (Fig. 6) show all the important components which are used to build my project. (9-0-9) V center tap transformer is used to convert the 220 V AC into the 9 V ac voltage, then the bridge rectifier is used to convert the 9 V ac output to 9 V dc output to power the circuit. A bridge rectifier can be formed using the diode connected in antiparallel. Since the 9 V dc output can't be used to power the circuit as it operates on 3.3 V to 5 V, by using a 7805 voltage regulator it gets converted into 5 V dc voltage. Then the 5v output is used to power the ATmega328p and other components of the microcontroller PLC. Loads switches and mode switches get connected to the microcontroller to operate in different modes. The programs for the working of the microcontroller can be written using the Arduino IDE and can be uploaded to the microcontroller PLC (Fig. 7) using the Arduino board. To verify the working of your code we can use the proteus software using its simulation features. Hex file of the programs can be uploaded to proteus for its verification of the programs. Relays are used to switch the loads after

a fixed time interval using the low 5 v output from the microcontroller. Input to the relays can be given in the form of 220 V ac.
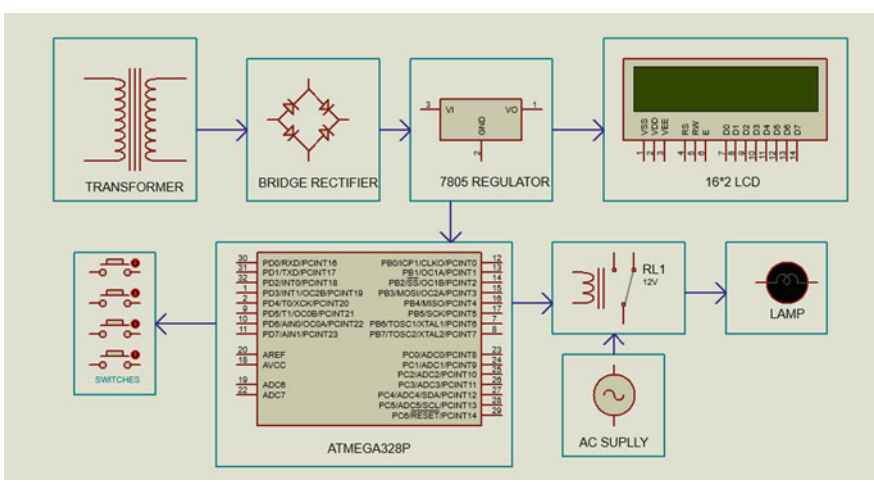
Fig. 5 Block diagram of project
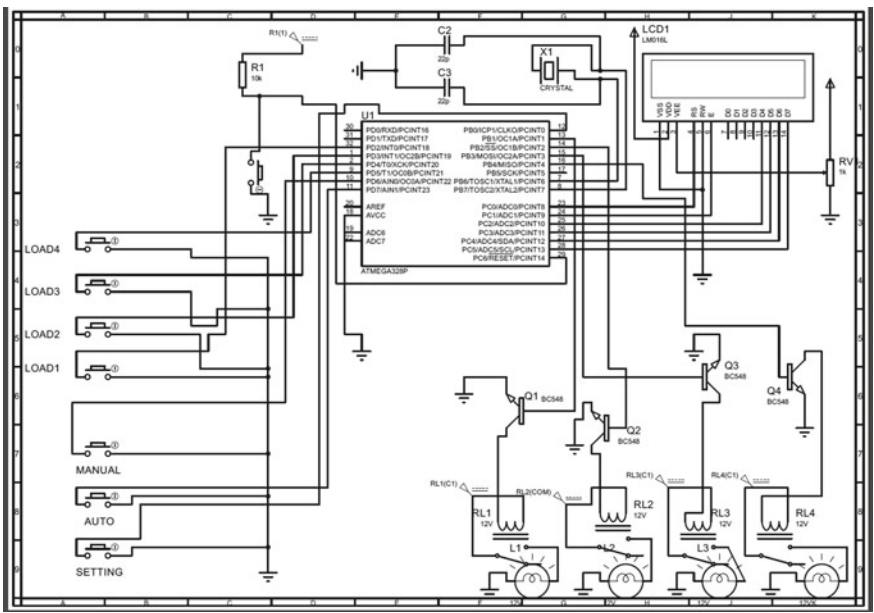
Fig. 6 Circuit diagram of project
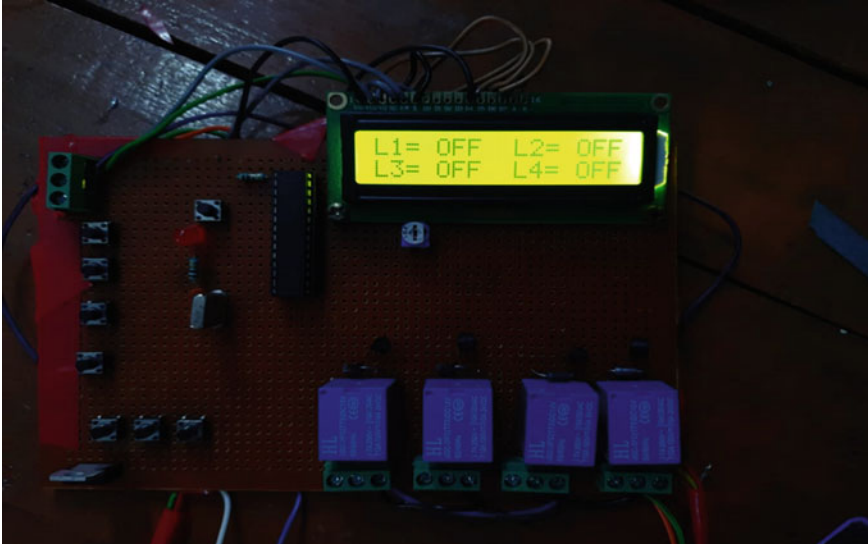
Fig. 7 Microcontroller PLC

4 Working of Project

Following are the working steps of the Project:

1. Switching on the power supply, the LCD shows "Programmable Logic Controller", which represents that circuit is perfectly working and PLC has got the supply from the source.
2. On pressing the set mode button, we can set the time interval of operation for the different loads using the load buttons provided on the microcontroller PLC board.
3. On pressing the auto mode button, the different loads get switched after a fixed time interval which is set in the set mode for different loads.
4. On pressing the manual mode button, different loads can be switched ON/OFF manually as per the manufacturer's needs and requirements using the load buttons for respective loads.
5. All the working processes: different modes of selection, setting of the time interval for different loads, the status of different loads which are ON or OFF, and time interval of operation remaining for different loads in the auto mode of operation would be shown on the LCD screen.

5 Innovation in the Proposed Project

This is a microcontroller-based project to perform simple operations like sequential switching of load. It is easy to operate because it displays each of the three modes of operation selection; time gets set for each load, for which of the load is ON or OFF, and remaining in the auto mode for each load.

Some important aspects of the project are the following:

1. **Initial cost**: As it is a simple microcontroller-based PLC, it has less initial cost as compared to bulky PLCs.
2. **Cost of operation**: The main component of the project is ATmega328p IC and it operates on only 5 V so it has less cost of operation too.
3. **Easy to program**: We can use simple Arduino IDE or C language to program our microcontroller according to our needs and flexibility.

6 Features

Some of the important features of our projects are the following:

1. It provides us with the flexibility of setting time for different operations according to our needs.
2. It can work in auto mode so there is no need to shift the load manually.
3. It can work in Manual mode so we also switch ON or OFF and shift the load manually.
4. It displays all the work of operation on the LCD that makes it easier to operates.
5. It can implement with less initial cost and also can operate at a lower cost of operation as compared to current PLCs.

7 Conclusion

This project is based on practical application; it can be used in industries with very less investment, and also it is user friendly; with little guidance, it can be operated easily. With the little advancement, it can be more automated; also, we can add some safety measures with an alarm system so it beeps the alarm whenever it shifts the loads so that user can get to know which machinery is currently working in the product. So, we can say that it can perfectly replace the bulky PLCs and with time it can be improved to meet the other requirements of the industries.

References

1. Dixit A, Mendiratta R, Kumari N (1998) Introduction to programmable logic controllers
2. ATMega328P Microcontroller Pinout, Pin Configuration, Features & Datasheet (n.d.) Components101. https://components101.com/microcontrollers/atmega328p-pinout-features-datasheet
3. Phad BV (2018) Industry process automation using programmable switching. Phad. Int J Res. https://journals.pen2print.org/index.php/ijr/article/view/13820
4. http://sersc.org/journals/index.php/IJCA/article/view/35149
5. Batista EA et al (2008) IEEE1451-based multi-interface module (I2M) for industrial processes automation. IEEE Sens Appl Symp 2008:220–224. https://doi.org/10.1109/SAS13374.2008.4472974
6. Blumenthal MS (1985) Programmable automation and the workplace. IEEE Technol Soc Mag 4(1):10–15. https://doi.org/10.1109/MTAS.1985.5009915
7. Zurawski R (2008) Networked embedded systems in industrial automation. In: 2008 6th IEEE international conference on industrial informatics, pp 3–8. https://doi.org/10.1109/INDIN.2008.4618051
8. Basile F, Chiacchio P, Gerbasio D (2013) On the implementation of industrial automation systems based on PLC. IEEE Trans Autom Sci Eng 10(4):990–1003. https://doi.org/10.1109/TASE.2012.2226578
9. Gayathri KCAKTSR (2020) Industry process automation using programmable switching. Int J Control Autom
10. Nitzan, Rosen (1976) Programmable industrial automation. IEEE Trans Comput C-25(12):1259–1270. https://doi.org/10.1109/TC.1976.1674593
11. Sanver U, Yavuz E, Eyupoglu C, Uzun T (2018) Design and implementation of a programmable logic controller using PIC18F4580. IEEE Conf Russian Young Res Electr Electron Eng (EIConRus) 2018:231–235. https://doi.org/10.1109/EIConRus.2018.8317072
12. https://www.seeedstudio.com/blog/2019/10/22/atmega328p-the-one-microcontroller-you-should-start-with/
13. Dey C, Sen SK (2020) Programmable logic controller (plc). Ind Autom Technol 15–82. https://doi.org/10.1201/9780429299346-2
14. https://www.electronicscomp.com/9-0-9-5amp-center-tapped-step-down-transformer
15. https://www.electronicshub.org/understanding-7805-ic-voltage-regulator/
16. https://www.nxp.com/docs/en/application-note/AN2500.pdf
17. https://www.elprocus.com/lcd-16x2-pin-configuration-and-its-working/
18. https://components101.com/switches/12v-relay

A New Asymmetric 23-Level Inverter Topology with Nearest Level and Unipolar Phase Disposition Control Techniques

Rajakumar Sakile, A. Bhanuchandar, Marco Rivera, Bandela Supriya, Kowstubha Palle, and Dongari Vamshy

Abstract In this paper, a new 23-level inverter topology has been proposed with two different modulation schemes, viz., Nearest Level Control (NLC) and Unipolar Phase Disposition (UPD) techniques. It comprises six unidirectional switches, three bidirectional switches, and five DC sources. A backend H-bridge is not needed to produce negative voltage levels because all levels are naturally produced. The main advantage of this topology is that in every state, only three switches are in conduction mode, and the rest are in the OFF state. Here, switching losses are significantly reduced due to the NLC technique's fundamental switching frequency, which is also particularly appropriate for a wide range of levels. Similarly, the UPD technique is a high switching frequency technique and because of absolute function, the number of carrier count can be reduced by half as compared with the conventional In-Phase Disposition (IPD) technique. Finally, with a step-change in input dc voltage, the proposed topology has been tested with two different control schemes and validated through MATLAB/Simulink platform.

Keywords Multilevel DC link inverter · Nearest level control · Unipolar phase disposition

R. Sakile (✉)
Electrical Engineering Department, NIT Jamshedpur, Jharkhand, India
e-mail: 2018rsee006@nitjsr.ac.in

A. Bhanuchandar
Electrical Engineering Department, NIT Warangal, Telangana, India

M. Rivera
Faculty of Engineering, Universidad de Talca, Talca, Chile

B. Supriya · K. Palle
EEE Department, CBIT (A), Gandipet, Hyderabad, Telangana, India

D. Vamshy
EEE Department, Mahatma Gandhi Institute of Technology, Hyderabad, India
e-mail: dongarivamshy_eee@mgit.ac.in

27

1 Introduction

Multilevel inverters (MLI) are playing a vital role in the DC–AC conversion of industrial applications and renewable energy systems. Solar energy is one of the most popular kind of renewable energy in the world. To meet the power quality requirements, proper power converter devices are required [1, 2]. Normally, photovoltaic cells generate the DC output, and the DC output can be converted to AC with the help of an inverter. The converted AC output had harmonic content and couldn't inject into the grid. Without any filters, the harmonics are reduced with the help of multilevel inverters [3]. The benefits of MLIs are lower order harmonics, less switching losses, draws input current with fewer distortions, lower dv/dt stress, higher fault-tolerant capability, and higher redundancy [4].

The conventional multilevel inverters are classified into diode clamped multilevel inverters, flying capacitor multilevel inverters, and cascaded H-bridge multilevel inverters. The cascaded H-bridge multilevel inverters have given better performance as compared to the remaining MLIs. The flying capacitor MLI and diode clamped MLIs are applicable only for 5-level output, whereas cascaded H-bridge MLI is suitable for higher-level output schemes and it also has higher modularity [5–7]. Two forms of cascaded H-bridge MLIs are distinguished: symmetrical and asymmetrical structures. A symmetrical configuration consists of equal values of DC voltage magnitude sources, whereas an asymmetrical configuration consists of different DC voltage magnitudes for achieving the higher-level output. Cascaded H-bridge MLIs can produce higher-level output, but they require a greater number of semiconductor devices. Each semiconductor device consists of one protection circuit, gate drive circuit, and heat sink [8–11]. Therefore, the number of switches or semiconductor devices are increasing then automatically the initial cost of the system is enhanced. To reduce the number of switches, a new multilevel DC link (MLDCL) inverter is introduced, for the generation of level, conventional methods required 2 × (P-1) active switches, whereas the MLDCL inverter topology required only (P + 3) active switches [12, 13]. Therefore, the MLDCL inverter consists of a smaller number of switches, and therefore, it is also called as reduced switch count or reduced device count method. Due to the smaller number of switch count, the switching losses are reduced, achieve faster response, and also cost is very less [14–17].

2 Circuit Diagram and Its Operation

The proposed 23-level inverter consists of five DC sources (V_1, V_2, V_3, V_4, and V_5), six unidirectional switches (S_1, S_2, S_{11}, S_{22}, T_1, and T_2), and three bidirectional switches (S_3, T_{11}, and T_{22}). The DC voltage magnitudes are considered to be different values such as $V_1 = V_2 = V_{dc}$, $V_3 = 3V_{dc}$ and $V_4 = V_5 = 6V_{dc}$. By selecting these values, the proposed circuit generates the 23-level output and the circuit behaves as an asymmetrical structure [18]. Therefore, this circuit is known as asymmetric

Fig. 1 Proposed topology—new 23-level inverter
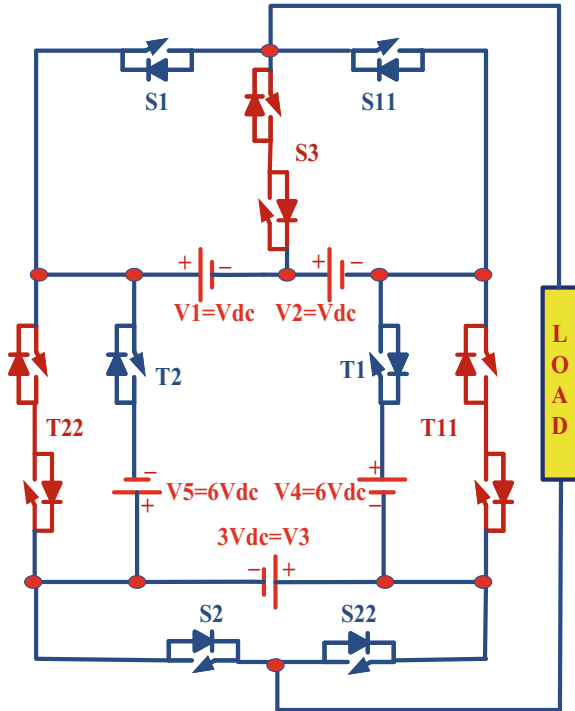
23-level inverter topology, the circuit is shown in Fig. 1. If all the DC voltage source values are considered to be equal, then the nine-level output can be achieved, whereas if the DC voltage source values are considered to be unequal, then the higher levels are going to be achievable (Table 1).

The switching table represents the conduction of switches for different output voltage levels. The main advantage of this topology is that, in every state, only three switches are in conduction mode, and the rest are in the OFF state.

3 Proposed Control Scheme Techniques

3.1 NLC Technique (CS-1)

The Nearest Level Control (NLC) scheme can produce the required switching pulses for the operation of power switches and it mainly depends on the round function. It is simple to compare the NLC scheme with other lower switching frequency systems because it operates at the fundamental frequency. In this technique, firstly, select the reference voltage (sine waveform or cosine waveform) to the closest voltage level, the reference waveform cuts the rising edges of MLI output voltage at exactly half of

Table 1 Switching table

On state switches	Level output
S1-S2-T1	11 V_{dc}
S2-S3-T1	10 V_{dc}
S2-T1-S11	9 V_{dc}
S1-T1-S22	8 V_{dc}
S3-T1-S22	7 V_{dc}
S11-T1-S22	6 V_{dc}
S1-T11-S2	5 V_{dc}
S3-T11-S2	4 V_{dc}
S11-T11-S2	3 V_{dc}
S1-T11-S22	2 V_{dc}
S3-T11-S22	V_{dc}
S1-T22-S2	0
S3-T22-S2	-1 V_{dc}
S11-T22-S2	-2 V_{dc}
S1-T22-S22	-3 V_{dc}
S3-T22-S22	-4 V_{dc}
S11-T22-S22	-5 V_{dc}
S1-T2-S2	-6 V_{dc}
S3-T2-S2	-7 V_{dc}
S11-T2-S2	-8 V_{dc}
S1-T2-S22	-9 V_{dc}
S3-T2-S22	-10 V_{dc}
S11-T2-S22	-11 V_{dc}

its magnitude voltage; shown in Fig. 2. To generate the switching pulses, the closest voltage level is compared with the inverter output voltage. The formulae of closest or nearest voltage level are represented as

$$\text{Nearest voltage level} = \frac{1}{V_{dc}} \times \text{round}(V_{ref}) \tag{1}$$

where V_{dc} represented the voltage difference between two levels, this scheme is applied nearest to the MLI output voltage at 0 0.5, it is known as the nearest level control scheme, the control diagram is shown in Fig. 2. It is operated at lower switching frequency; therefore, switching losses greatly reduces as compared with high switching frequency methods. Generally, by using PSIM software, it is possible to calculate switching and conduction losses directly with the involvement of respective data sheet values.
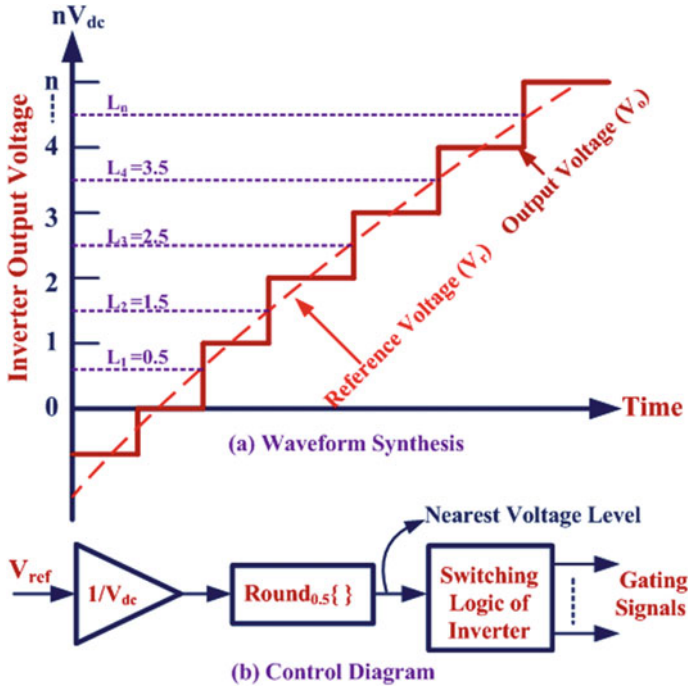
Fig. 2 Control scheme-1: NLC technique (non-carrier method)

3.2 UPD Technique (CS-2)

To generate P-level output, Phase Disposition (PD) technique requires (P-1) carriers. Whereas the Proposed Unipolar Phase Disposition (UPD) control scheme requires (P-1)/2 carriers only. Due to the absolute function, the number of carrier counts has been reduced. Therefore, the proposed control scheme reduces the carriers by half, due to the fewer carriers, the burden on the processor and complexity decreases.

To produce the 23-level output, the PD control scheme is used to generate 22 carriers, whereas the UPD control scheme required 11 carriers only. The unipolar phase disposition PWM scheme is shown in Fig. 3. The UPD control scheme operates at the higher switching frequency, i.e., 3 kHz.
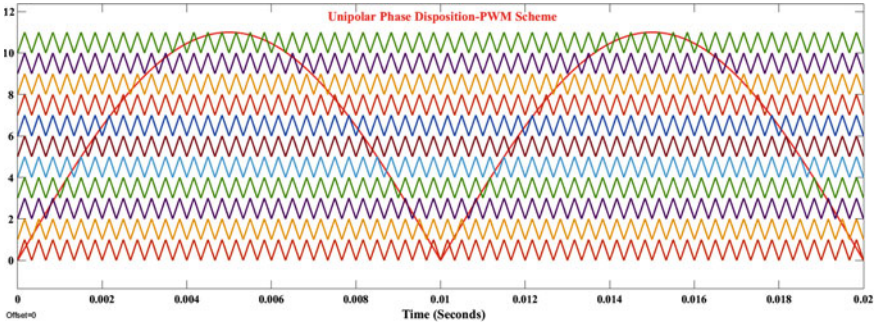
Fig. 3 Control scheme-2: UPD technique

4 Simulation Results and Discussion

4.1 Result Analysis Using NLC Scheme

In this control scheme, the 23-level output voltage is obtained even the step-change in input dc voltage is applied to the main circuit and operated at the fundamental frequency. Normally applied the $V_{dc} = 10$ V, the NLC scheme can generate 23-level output voltage and the peak value is obtained at the fundamental frequency is 110.3 V. whereas, if apply the sudden change in the input voltage $V_{dc} = 20$ V at $t = 0.05$ s, then this control scheme can generate 23-level output, but the peak value is obtained at the fundamental frequency is 220.6 V. Figure 4 shows the simulation result with step-change in input dc voltage and Fig. 5 represents the harmonic spectrum of the inverter output voltage at $V_{dc} = 10$ V. The Total Harmonic Distortion (THD) of this topology is achieved at 3.55%. Figure 6 shows that the harmonic spectrum of the inverter output voltage at $V_{dc} = 20$ V, the Total Harmonic Distortion (THD) of this topology is achieved at 3.55% and the peak value at the fundamental frequency is 220.6 V.
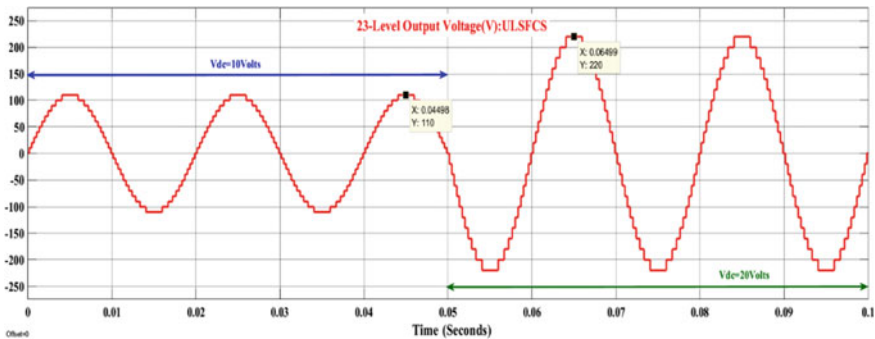
Fig. 4 Step change in input dc voltage: CS-1

Fundamental (50Hz) = 110.3 , THD= 3.55%

ULSFCS: Vdc=10Volts
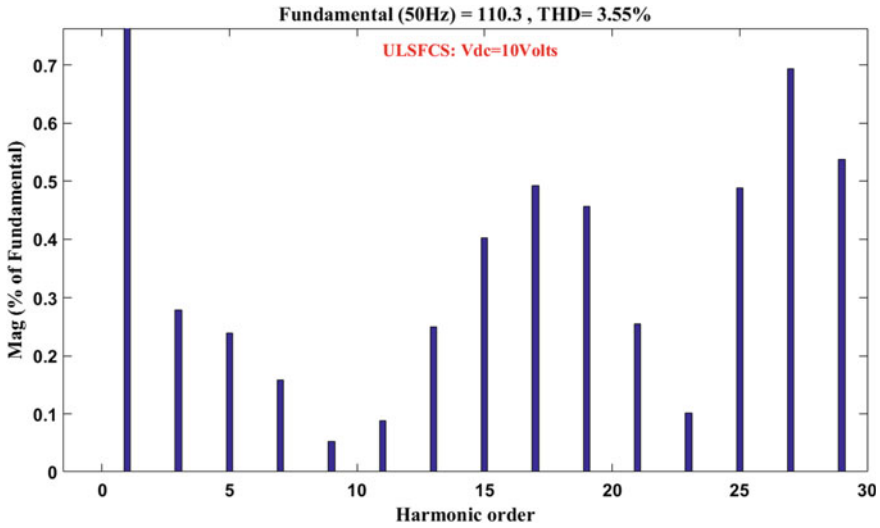
Fig. 5 Harmonic spectrum of inverter output voltage with $V_{dc} = 10$ V: CS-1

Fundamental (50Hz) = 220.6 , THD= 3.55%

ULSFCS:Vdc=20Volts
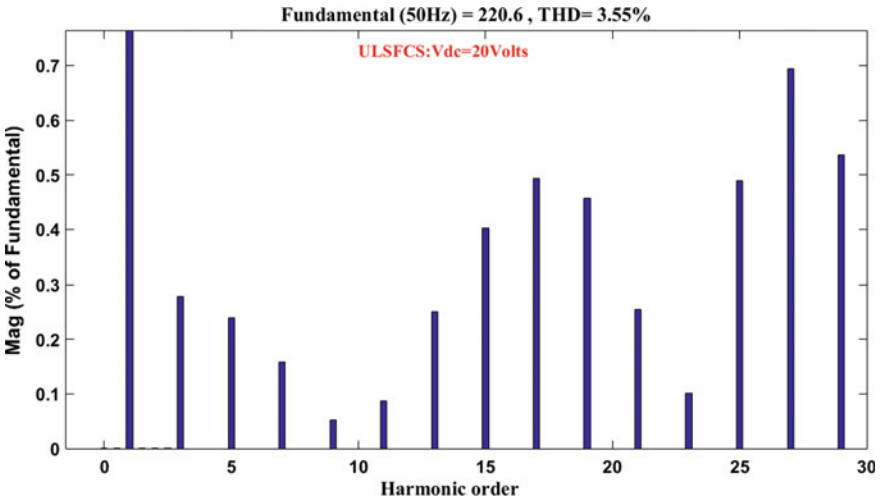
Fig. 6 Harmonic spectrum of inverter output voltage with $V_{dc} = 20$ V: CS-1

4.2 Result Analysis Using UPD Control Scheme

In this control scheme, the 23-level output voltage is obtained even the step-change in input dc voltage is applied to the main circuit and operated at a higher switching frequency. Normally apply the $V_{dc} = 10$ V, the UPD control scheme can generate 23-level output voltage and the peak value is obtained at the fundamental frequency

is 110.3 V. whereas, if apply a sudden change in the input voltage $V_{dc} = 20$ V at $t = 0.05$ s, then this control scheme can generate 23-level output, but the peak value at the fundamental frequency is 220.6 V. Figure 7 shows the step-change in input dc voltage and Fig. 8 represents the harmonic spectrum of the inverter output voltage at $V_{dc} = 10$ V. The Total Harmonic Distortion (THD) of this topology is achieved at 5.46%. Figure 9 shows that the harmonic spectrum of the inverter output voltage at $V_{dc} = 20$ V, the Total Harmonic Distortion (THD) of this control scheme is achieved at 5.47% and the peak value at the fundamental frequency is 220.5 V.

If five dc voltage sources are operated at symmetrical mode, i.e., $1V_{dc} = 2V_{dc} = 3V_{dc} = 4V_{dc} = 5V_{dc} = V_{dc}$, then each control scheme is able to generate 9-level
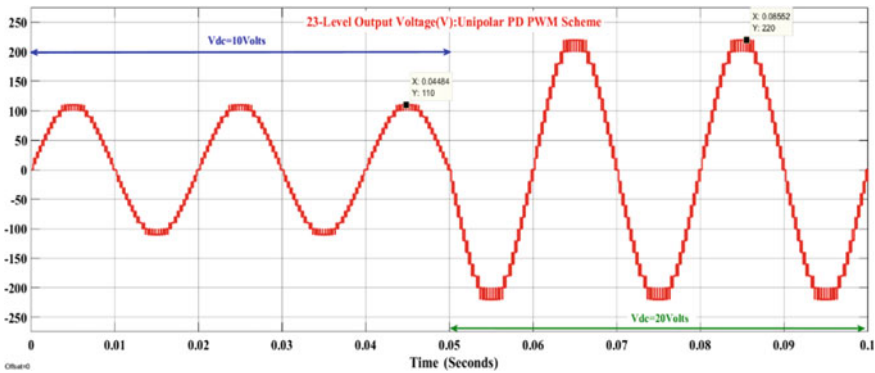
Fig. 7 Step change in input dc voltage: CS-2
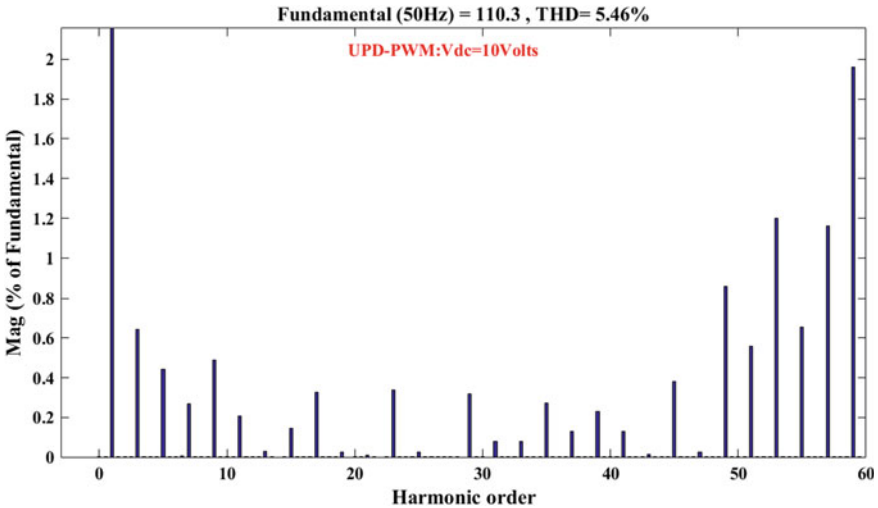
Fig. 8 Harmonic spectrum of inverter output voltage with $V_{dc} = 10$ V: CS-2
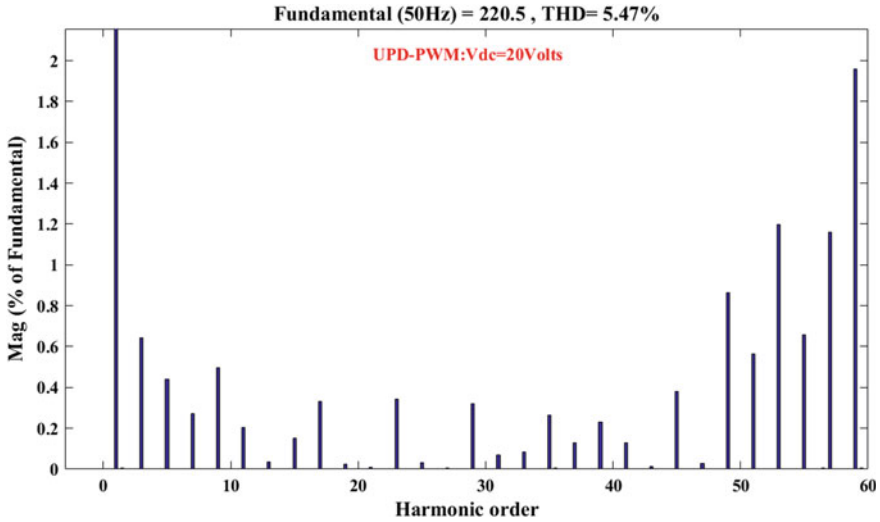
Fig. 9 Harmonic spectrum of inverter output voltage with $V_{dc} = 20$ V: CS-2

output only. Figure 10 shows the 9-level output for the NLC scheme and Fig. 11 shows the 9-level output for the UPD control scheme.

Both control schemes have their advantages and disadvantages, the NLC scheme is operated at the fundamental frequency, hence the switching losses of the NLC scheme are very less. The UPD control scheme is operated at a higher switching frequency at 3 kHz and this control scheme has more switching losses as compared with the NLC scheme. Due to the absolute function, the number of carrier counts can
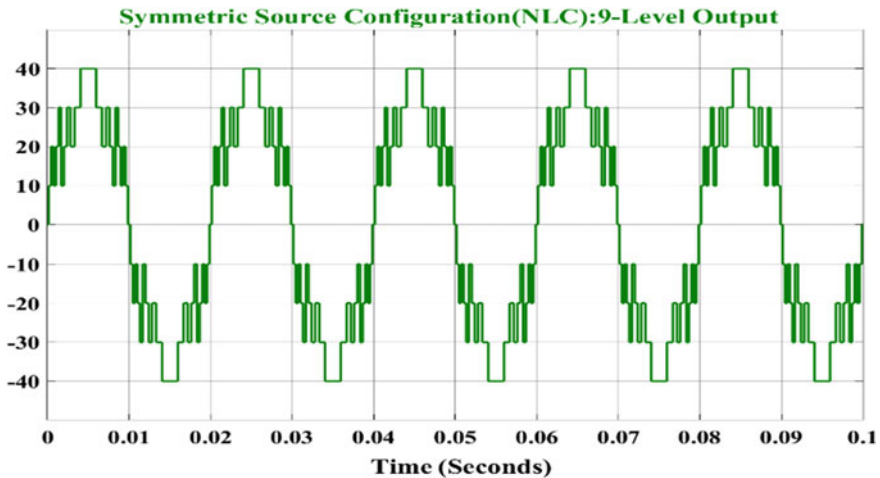
Fig. 10 Symmetric source configuration 9-level output voltage for NLC scheme
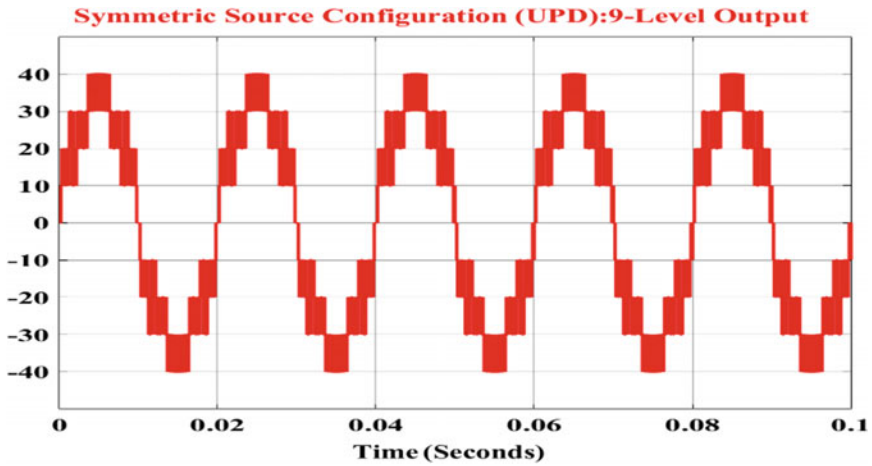
Fig. 11 Symmetric source configuration 9-level output voltage for UPD control scheme

be reduced by half as compared with the conventional In-Phase Disposition (IPD) technique. According to the comparative assessment of THD, The NLC scheme has a lesser value as compared to the UPD control scheme. The comparative assessment of %THD values is established in Table 2. As per the IEEE standard, the THD value is lesser than 5%. The proposed NLC scheme achieved lesser than 5% of THD even applying the small change in the input dc voltage. The switch component of the proposed circuit is very less as compared to the conventional topologies listed in Table 3. Normally, if the number of switches is more, it requires more gate drive circuits, protection circuits, control units, and heat sinks, therefore, if the switch component reduces, then the cost and complexity of the system can also reduce drastically (Table 4).

Table 2 Comparative assessment-%THD Value

S. No	Vdc	CS-1 (NLC)		CS-2 (UPD)	
		%THD	Peak value at 50 Hz	%THD	Peak value at 50 Hz
1	10 V	3.55	110.3 V	5.46	110.3 V
2	20 V	3.55	220.6 V	5.47	220.5 V

Table 3 Comparative study with basic conventional topologies

S. No	Components	NPC	FC	CHB	MLDCL	SSPS	RV	SCSS	Proposed
1	Main switches	44	44	44	26	26	26	26	12
2	Anti-parallel diodes	44	44	44	26	26	26	26	12
3	Clamping diodes	462	0	0	0	0	0	0	0
4	DC bus capacitors	22	22	11	11	11	11	11	5
5	Flying capacitors	0	231	0	0	0	0	0	0

Table 4 Simulation parameters

Simulation parameters
1. $V_{dc} = 10$ V, 20 V
2. Switching frequency = 3 kHz
3. Output frequency = 50 Hz
4. $R = 50\Omega$
5. $L = 0.197$H
6. TSV$_{pu} = 7.18$

5 Conclusion

In this paper, A New Asymmetric 23-Level Inverter Topology with Nearest Level and Unipolar Phase Disposition Control Techniques have been discussed. The NLC scheme operated at the lower switching frequency, thereby reducing the switching losses drastically as compared with the UPD technique since the involvement of high switching frequency carriers and is best suitable for a large number of levels. As compared to the UPD control technique, the NLC scheme has a lesser value of THD even after a sudden change in the input dc source magnitude value. A UPD control scheme is operated at a higher switching operation, and because of absolute function, the number of carrier counts can be reduced by half as compared with the conventional Phase Disposition technique. Generally, this UPD technique is most suitable for grid-connected applications. The proposed topology reduces the switch component as compared to the conventional topologies, which makes the proposed structure more practical but it requires a greater number of isolated dc sources.

References

1. Omer P, Kumar J, Surjan BS (2020) A review on reduced switch count multilwevel inverter topologies. IEEE Access 8:22281–22302. https://doi.org/10.1109/ACCESS.2020.2969551
2. Gupta KK, Ranjan A, Bhatnagar P, Sahu LK, Jain S (2016) Multilevel inverter topologies with reduced device count: a review. IEEE Trans Power Electron 31(1):135–151. https://doi.org/10.1109/TPEL.2015.2405012
3. Su G-J (2005) Multilevel DC-link inverter. IEEE Trans Ind Appl 41(3):848–854. https://doi.org/10.1109/TIA.2005.847306
4. Rodriguez J, Lai J-S, Peng FZ (2002) Multilevel inverters: a survey of topologies, controls, and applications. IEEE Trans Industr Electron 49(4):724–738. https://doi.org/10.1109/TIE.2002.801052
5. Sorto-Ventura K-R, Abarzadeh M, Al-Haddad K, Dessaint LA (2020) 23-level single DC source hybrid PUC (H-PUC) converter topology with reduced number of components: real-time implementation with model predictive control. IEEE Open J Ind Electron Soc 1:127–137. https://doi.org/10.1109/OJIES.2020.3007989
6. Sunitha T, Udhayakumar K, Annamalai t, Gopinath C (2018) A new 23 level cascaded multi-level ınverter with optimum structure. In: 2018 4th International Conference on Electrical Energy Systems (ICEES), pp 320–327. https://doi.org/10.1109/ICEES.2018.8443220
7. Nabae A, Takahashi I, Akagi H (1981) A new neutral-point-clamped PWM inverter. IEEE Trans Ind Appl IA-17(5):518–523. https://doi.org/10.1109/TIA.1981.4503992
8. Antonio-Ferreira A, Collados-Rodriguez C, Gomis-Bellmunt O (2018) Modulation techniques applied to medium voltage modular multilevel converters for renewable energy integration: a review. Electric Power Syst Res 155:21–39. https://doi.org/10.1016/j.epsr.2017.08.015
9. Bhanuchandar A, Murthy BK (2021) Single phase nine level switched capacitor based grid connected inverter with LCL filter. In: 2020 3rd international conference on energy, power and environment: towards clean energy technologies, pp 1–5. https://doi.org/10.1109/ICEPE50861.2021.9404491
10. Kumar KB, Bhanuchandar A, Mahesh C (2021) A novel control scheme for symmetric seven level reduced device count Multi-Level DC Link (MLDCL) inverter. Int Conf Sustain Energy Future Electric Transp (SEFET) 2021:1–4. https://doi.org/10.1109/SeFet48154.2021.9375714
11. Rao N, Kumar DVA, Babu CS (2013) New multilevel inverter topology with reduced number of switches using advanced modulation strategies. In: 2013 International Conference on Power, Energy and Control (ICPEC), Sri Rangalatchum Dindigul, pp 693–699. https://doi.org/10.1109/ICPEC.2013.6527745
12. Zeb K, Khan I, Uddin W, Khan MA, Sathishkumar P, Busarello TDC, Ahmad I, Kim HJ (2018) A review on recent advances and future trends of transformer less inverter structures for single-phase grid-connected photovoltaic systems. Energies
13. Barzegarkhoo R, Kojabadi HM, Zamiry E et al (2016) Generalized structure for a single phase switched-capacitor multilevel inverter using a new multiple DC link producer with reduced number of switches. In: 2016 IEEE, vol 31, issue 8
14. Kumawat RK, Palwalia DK. A comprehensive analysis of reduced switch count multilevel inverter. Austral J Electrical Electron Eng. https://doi.org/10.1080/1448837X.2019.1693884
15. Belekar RA, Nakade RP et al (2013) Single phase 9 level MLDCL ınverter with half bridge cell topology: performance analysis. In: 2013 International Conference on Power, Energy and Control (ICPEC)
16. Sakile RK, Kumar P, Sinha UK (2021) Modelling of lithium-ıon battery using MATLAB/simulink for electric vehicle applications. In: Recent advances in power electronics and drives. Springer, Singapore, pp 291–299

17. Thamizharasan S, Baskaran J (2014) FPGA implementation of a new hybrid modulation strategy for a modified dual bridge multilevel dc-link inverter topology. In: 2014 International Conference on Computation of Power, Energy, Information and Communication (ICCPEIC)
18. Hosseinzadeh MA, Sarbanzadeh M, Sarbanzadeh E, Rivera M, Wheeler P (2018) New asymmetric cascaded multi-level converter with reduced components. In: 2018 IEEE International Conference on Electrical Systems for Aircraft, Railway, Ship Propulsion and Road Vehicles & International Transportation Electrification Conference (ESARS-ITEC), pp 1–6. https://doi.org/10.1109/ESARS-ITEC.2018.8607383

Single Phase Five Level T-type Grid Connected Inverter with LCL Filter

Aratipamula Bhanuchandar and Bhagwan K. Murthy

Abstract In this paper, a Reduced Switch Count (RSC) single phase five level T-type grid connected multilevel inverter (MLI) with LCL filter has been presented. It possesses two stiff DC sources and six switches. In this topology, there is a uniformity in the standing voltage across all switches. Before going to grid connection, the performance of the topology has been reported with three different Pulse Width Modulation (PWM) schemes, viz., reduced carrier in alternative approach with single unipolar reference, reduced carrier In-Phase Disposition (IPD) approach with single unipolar reference, and Nearest Level Control (NLC). The comparative study has also been discussed in terms of the harmonic spectrum of load voltage. For higher ripple attenuation purpose, the LCL filter has been integrated with the grid. To inject active and reactive power into the grid, d-axis and q-axis current control strategies have been used, respectively. The operation and control schemes of the entire system with both resistive-inductive load and grid-connected cases have been validated by using the MATLAB/Simulink platform.

Keywords Reduced switch count · Nearest level control · In-phase disposition · Multilevel inverter · Pulse width modulation

1 Introduction

The concept of MLIs plays a very important role to imitate sine wave in terms of multiple stair levels with less total harmonic distortion (THD) [1, 2]. Conventionally, there are three different types (Cascaded H-Bridge, Flying capacitor (FC), and Neutral Point Clamped (NPC)) of MLI topologies that are widely used in industrial

A. Bhanuchandar (✉) · B. K. Murthy
National Institute of Technology Warangal, Telangana, India
e-mail: 202chandar@gmail.com

B. K. Murthy
e-mail: bhagwan_murthy@yahoo.com

41

applications with various control schemes like Sinusoidal PWM, Space Vector Modulation (SVM), and Selective Harmonic Elimination (SHE-Low switching frequency technique) [3–8]. In any MLI topology, the SPWM is the most and easiest implementation technique for generating switching pulses. This technique is further classified into Phase Shifted PWM (PSPWM) and Level Shifted PWM (LSPWM-Phase Disposition (PD), Alternative Phase Opposition Disposition (APOD) and Phase Opposition Disposition (POD)). In LSPWM technique, the number of carrier counts will depend on the number of levels. In this technique, at moderate switching frequencies, PD gives better line THD as compared with POD and APOD. At higher switching frequencies, all LSPWM schemes give approximately the same line THD value [9]. In RSC topologies, the T-type configuration is one of the important configurations in the mean of cost reduction as compared to traditional topologies [10–12]. Conventional SPWM technique in RSC topologies generates faulty effects on the respective switching states [13, 14]. By using logical operators, different multi-carrier PWM schemes are reported in a few RSC MLI topologies [15]. For grid-connected systems with multi reference PWM scheme, seven level T-type topology was reported in [16, 17]. This scheme is widely accepted because of the normalized nature of control [18–21]. But this scheme has high line THD as compared with the traditional LSPWM technique. Generally, the SHE method is suitable only for standalone systems. However, if going to higher levels, it takes more memory for solving the transcendental equations [22]. The design of the LCL filter has been reported in [23, 24]. However, careful design is required while considering grid stability.

Finally, from the literature review, it is observed that most of the conventional control schemes give high THD values, and to alleviate these problems, three different modulation schemes have been reported for 5L T-type topology with RL load case. And also to alleviate resonant peak problems in LCL filter, careful design of LCL filter has been reported in this paper without disturbing the grid stability. The structure of this paper is organized as follows. In Sect. 2, the operation of 5L T-type MLI topology and the design of LCL filter have been discussed. In Sect. 3, proposed control schemes with RL load and grid-connected cases have been explained. In Sect. 4, simulation results and a comparative study have been discussed. And finally, in Sect. 5, a conclusion has been reported.

2 Operation of 5L T-Type Topology and Design of LCL Filter

2.1 Operation of 5L T-type Topology

Figure 1 shows a 5L T-type inverter topology with RL load. This topology is composed of two stiff DC sources and six switches. In that, the S5 switch acts as a bidirectional switch which is the combination of two IGBTs. The advantage of the bidirectional switch is that it has both properties like bidirectional voltage blocking

Fig. 1 Five level T-type
inverter topology with RL
load
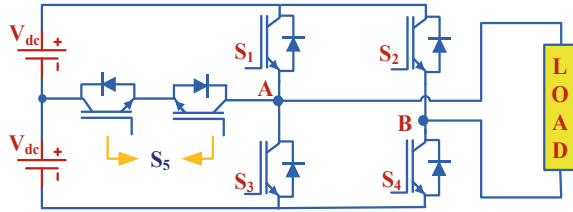
Table 1 Switching table for
T-type five level inverter
topology

S. No	[S1 to S5]	Output levels
1	[1 1 0 0 0]	0Vdc
2	[0 0 0 1 1]	1Vdc
3	[1 0 0 1 0]	2Vdc
4	[0 1 0 0 1]	−1Vdc
5	[0 1 1 0 0]	−2Vdc

capability and bidirectional current conducting capability. Here, S5 requires only
one gate driver circuit since it is operating in a common emitter configuration mode.
Generally, these stiff DC sources are obtained from either photovoltaic with boost
converter or fuel cell with a boost converter. Table 1 shows the switching table for
T-type five level inverter topology. From this table, the observation is that only two
switches are conducted at every state. In a general scenario, if 'm' is the level number
in phase voltage, then $(2m − 1)$ levels are present in the line voltage and the number
of switches per phase is equal to $4 + (m − 3)$, here '4' indicates the number of
switches in H-bridge circuit and $(m − 3)$ indicates the number of additional switches
to form one bidirectional switch. The concept of total standing is important criteria
in the cost requirement of devices. For this topology, the TSV becomes 10 Vdc and
voltage gain is equal to one.

$$\text{TSV}_{\text{pu}} = \frac{\text{TSV}}{V_{0,\text{peak}}} = 5 \, \text{p.u} \tag{1}$$

$$G = \frac{V_{0,\text{peak}}}{\text{Sum of stiff DC sources}} = 1 \tag{2}$$

2.2 Design of LCL Filter

Figure 2 shows single phase grid connected T-type five level inverter topology with
LCL filter. Once five level inverter output voltage is obtained based on the proper

Fig. 2 Single phase grid connected T-type five level inverter topology with LCL filter
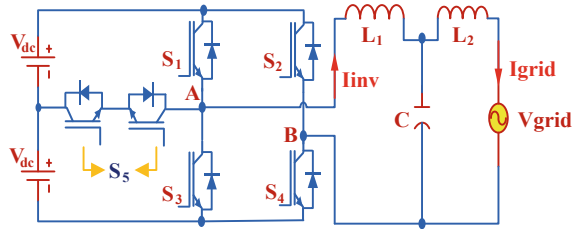
PWM scheme, it then needs to concentrate on the proper design of LCL filter for the grid connection.

Generally, as compared with L and LC filters, LCL filter has higher roll of rate that is -60dB/decade with third order in the transfer function. And also this filter has a higher ripple attenuation capability. However, there is an instability problem due to resonance of the filter. To tackle the resonance problem in a better way, the active damping method has been preferred. The advantage of this method is that there are no additional power losses present as compared with passive damping. However, it leads to more complexity and must be designed carefully to keep the system in stable mode [23]. Generally, inverter and grid side filter values can be decided based on the current ripple and the filter capacitor is designed based on the reactive power produced by the capacitor at fundamental frequency and resonance frequency. Based on references [24, 25], LCL filter values are calculated and applied to grid-connected system depicted in Fig. 2.

3 Proposed Control Schemes

3.1 With RL Load Case

The performance of the T-type topology with RL load has been verified with three different PWM schemes as mentioned below:

a. Method-1: Reduced carrier in alternative approach with single unipolar reference
b. Method-2:Reduced carrier in-phase disposition approach with a single un ipolar reference
c. Method-3: Nearest Level Control Scheme (NLC)—low switching frequency technique

In Method-1 and 2, the number of requirements of carriers is $(m - 1)/2 = 2$. For method-3, there is no need for the requirement of carriers. By using rounding function, it is possible to generate the required nearest voltage level and advantage of this method is, all switches are operating with fundamental frequency only thereby switching losses are greatly reduces [26]. Both method-1 and 2 are operated with a

high switching frequency. The PWM schemes of all methods are depicted in Figs. 4, 5, and 6, respectively.

3.2 With Grid-Connected Case

Figure 3 shows the complete control block diagram of a single phase five level T-type-based grid-connected inverter with LCL filter. As the first step generates V_α and V_β components from grid voltage ($V_{\text{grid}} = V_\beta$) and by using $\alpha\beta$ to dq transformation, V_d and V_q components have been generated. For grid synchronization and to generate reference variables, phase locked loop has been implemented by taking V_q (ref) as zero. In the second step, Iα and Iβ components are generated from inverter current (I_{inv} = I_β), and for controlling grid current, inverter current can be used as a feedback system. And by using $\alpha\beta$ to *dq* transformation, Id and Iq components have been generated. Here, Id (ref) is used to inject active power into the grid, and similarly, Iq (ref) is used to inject reactive power into the grid. In the third step, this Id (ref) and Id are compared and then fed to the PI controller, and similarly, Iq (ref) and Iq are compared and then fed to the PI controller. Finally, the PI controller reduces the steady state error and the obtained output is given to the decoupling controller then by using dq to $\alpha\beta$ transformation, the β-component has been generated. Here, P_G indicates the proper gain value to generate a desired modulating signal. According to level count, the Repeating Table Generation (RTG) has been developed. By taking the absolute function, it is possible to reduce the number of carrier counts by half as compared with LSPWM. After comparison of Abs and RTG, the output signals are to be added. And this output signal is fed to Proper Gain (P_G) gives to generate accumulated/aggregated signal will acts as desired control signal. Here, the Switching Table Generation (STG) as taken from the switching arrangement as mention in Table 1 and it will acts as data signal. Finally, both ASG and STG signals are pass through corresponding to the truncated value of ASG then it generates desired Gate Pulses (GP) according to reference peak value of injected grid current. By taking Iq (ref) as zero, it is possible to obtain unity power factor operation (UPF) at the grid side.

4 Simulation Results

Figures 4, 5, and 6 show simulation results with RL load using method-1, 2, and 3, respectively (Tables 2 and 3).

From the above table, it is concluded that method-3 gives less THD, and DC bus utilization also increases as compared to method-1 and 2. However, from the observation of all harmonic spectrums, lower order harmonics appear very nearer to the fundamental component. So, method-3 is mostly applicable for higher levels. Generally, the peak value of load current mainly depends on R and L values.
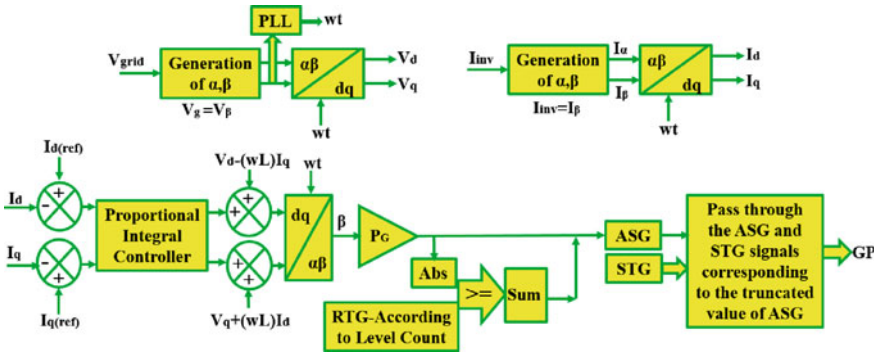
Fig. 3 Control scheme of single phase five level T-type-based grid-connected inverter
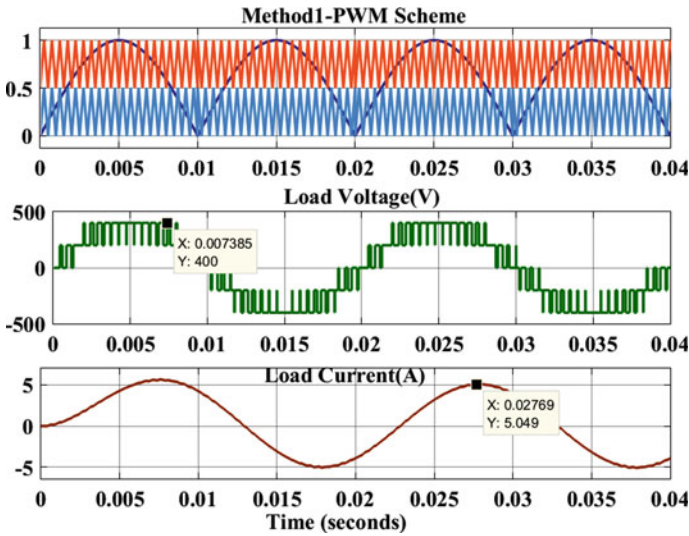
Fig. 4 Simulation results—Method-1

Figure 7 shows simulation results for grid-connected case with id (ref) and iq (ref) = 0. In this case, both grid voltage and grid current maintains UPF operation. Figure 8 shows the harmonic spectrum of inverter output voltage in grid-connected case. Similarly, Fig. 9 shows the harmonic spectrum of grid current waveform with peak value 9.91 A at 50 Hz and THD = 2.61%.
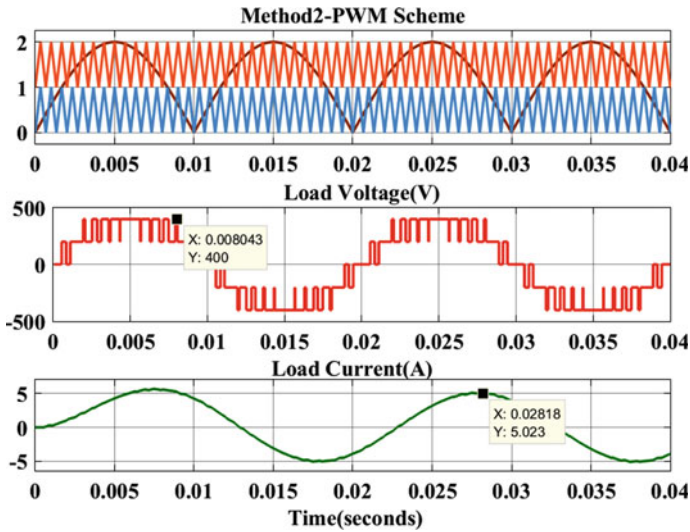
Fig. 5 Simulation results—Method-2
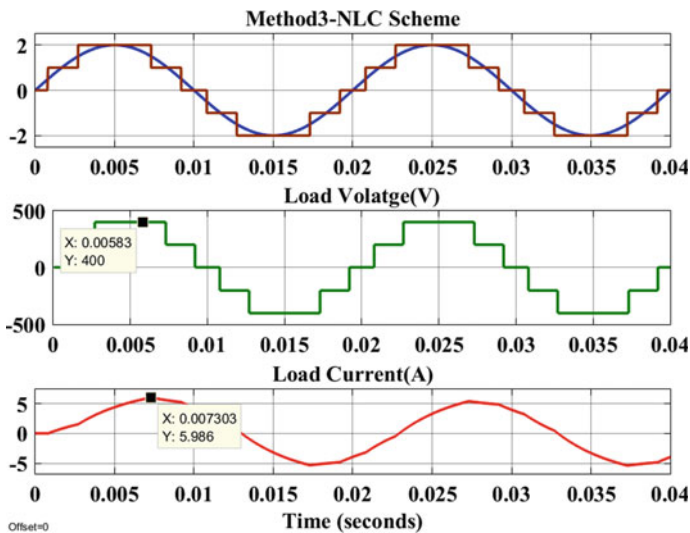
Fig. 6 Simulation results—Method-3

5 Conclusion

In this paper, the operation of 5L T-type inverter topology with RL load and grid-connected cases has been explained. In this topology, each switch possess uniform standing voltage of $2V_{dc}$ and finally, it has TSV_{pu} is equal to five. The performance

Table 2 Simulation parameters

S. No	With RL load case	With grid connected case
1	Vdc = 200 V $R = 50\ \Omega,\ L = 0.197$H Modulation index = 1.0 $F_{sw} = 1500$ Hz (Methods-1,2) $F_{sw} = 50$ Hz (Method-3)	Vdc = 200 V $L_1 = 4$ mH, $L_2 = 4.3$ mH and $C = 6\ \mu$F $V_{grid} = 230$ V(RMS) Switching frequency = 10 kHz Grid frequency = 50 Hz

Table 3 Comparative study

S. No	Control scheme-methods	Load voltage (RL load)-peak value at 50 Hz	%THD
0	Method-1	400 V	26.92
0	Method-2	401.3 V	26.20
0	Method-3	415 V	17.60
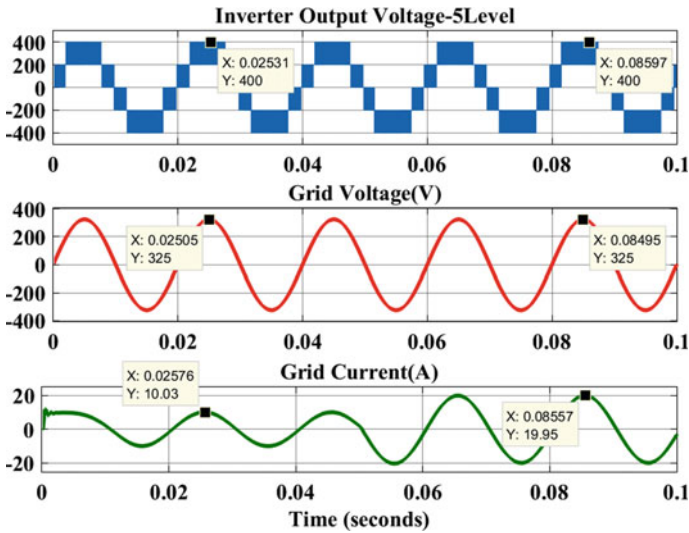
Fig. 7 Simulation results with step change at 0.05 s in reference direct axis current-10–20 A

of this topology with RL load has been reported with three different PWM methods, viz., reduced carrier in alternative approach with single unipolar reference, reduced carrier in-phase disposition (IPD) approach with single unipolar reference, and NLC schemes. Moreover, the same topology with LCL filter in single phase grid connected case has been explained through the dq-frame current control strategy. Here, the LCL filter has been designed carefully while considering grid stability and resonant peak problems. By using proposed control strategy, both grid voltage and grid current
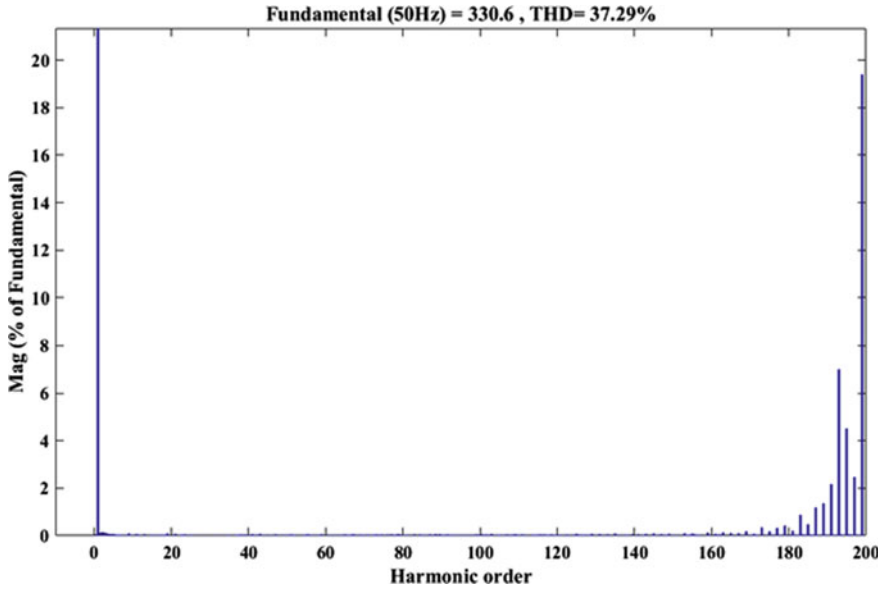
Fig. 8 Harmonic spectrum (grid connected case)—inverter output voltage (Volts)
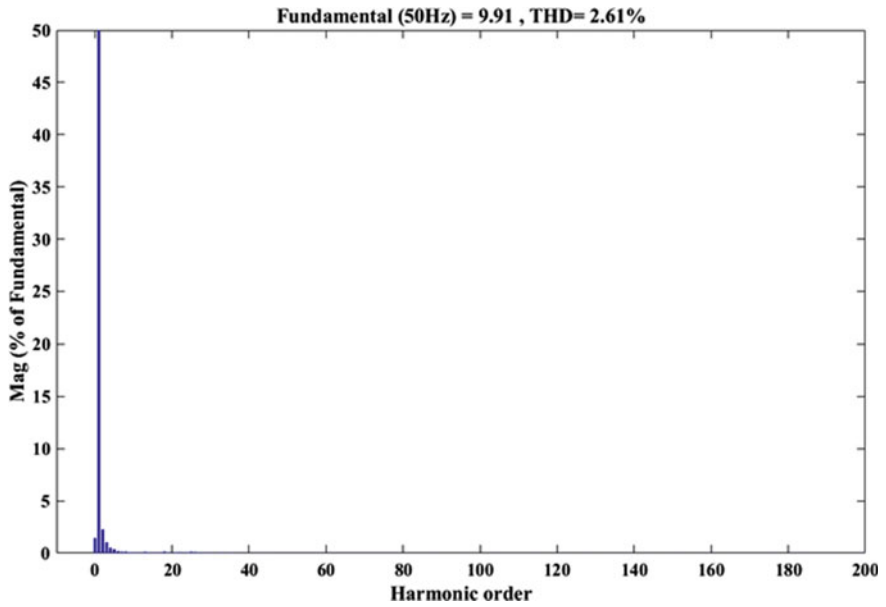
Fig. 9 Harmonic spectrum—grid current (Id_ref = 10 A)

have been attained UPF operation according to reference direct axis current with iq (ref) as zero. Finally, this topology is well suitable for renewable energy sources applications along with bipolar DC grid.

References

1. Vemuganti HP, Dharmavarapu S, Ganjikunta SK, Suryawanshi HM, Abu Rub H. A survey on reduced switch count multilevel inverters. IEEE Open J Ind Electronics Soc. https://doi.org/10.1109/OJIES.2021.3050214

2. Franquelo LG, Rodriguez J, Leon JI, Kouro S, Portillo R, Prats MAM (2008) The age of multilevel converters arrives. IEEE Ind Electron Mag 2(2):28–39. https://doi.org/10.1109/MIE.2008.923519

3. Kouro S et al (2010) Recent advances and industrial applications of multilevel converters. IEEE Trans Industr Electron 57(8):2553–2580. https://doi.org/10.1109/TIE.2010.2049719

4. Rodriguez J, Lai J-S, Peng FZ (2002) Multilevel inverters: a survey of topologies, controls, and applications. IEEE Trans Ind Electronics 49(4):724–738. https://doi.org/10.1109/TIE.2002.801052

5. McGrath BP, Holmes DG (2002) Multicarrier PWM strategies for multilevel inverters. IEEE Trans Industr Electron 49(4):858–867. https://doi.org/10.1109/TIE.2002.801073

6. Sreenivasarao D, Agarwal P, Das B (2014) Performance evaluation of carrier rotation strategy in level-shifted pulse-width modulation technique. IET Power Electronics 7:667–680. https://doi.org/10.1049/iet-pel.2013.0109

7. Dahidah MSA, Agelidis VG (2008) Selective harmonic elimination PWM control for cascaded multilevel voltage source converters: a generalized formula. IEEE Trans Power Electron 23(4):1620–1630. https://doi.org/10.1109/TPEL.2008.925179

8. Ahmed I, Borghate VB (2014) Simplified space vector modulation technique for seven-level cascaded H-bridge inverter. IET Power Electronics 7:604–613. https://doi.org/10.1049/iet-pel.2013.0135

9. Carrara G, Gardella S, Marchesoni M, Salutari R, Sciutto G (1990) A new multilevel PWM method: a theoretical analysis. In: 21st Annual IEEE conference on power electronics specialists, San Antonio, TX, USA, pp 363–371. https://doi.org/10.1109/PESC.1990.131211

10. Gupta KK, Ranjan A, Bhatnagar P, Sahu LK, Jain S (2016) Multilevel inverter topologies with reduced device count: a review. IEEE Trans Power Electron 31(1):135–151. https://doi.org/10.1109/TPEL.2015.2405012

11. Gupta KK, Jain S (2014) Comprehensive review of a recently proposed multilevel inverter. IET Power Electronics 7:467–479. https://doi.org/10.1049/iet-pel.2012.0438

12. Ceglia G, Guzman V, Sanchez C, Ibanez F, Walter J, Gimenez MI (2006) A new simplified multilevel inverter topology for DC–AC conversion. IEEE Trans Power Electron 21(5):1311–1319. https://doi.org/10.1109/TPEL.2006.880303

13. Babaei E, Laali S, Bayat Z (2015) A single-phase cascaded multilevel inverter based on a new basic unit with reduced number of power switches. IEEE Trans Industr Electron 62(2):922–929. https://doi.org/10.1109/TIE.2014.2336601

14. Gupta KK, Jain S (2014) A novel multilevel inverter based on switched DC sources. IEEE Trans Industr Electron 61(7):3269–3278. https://doi.org/10.1109/TIE.2013.2282606

15. Park S-J, Kang F-S, Lee MH, Kim C-U (2003) A new single-phase five-level PWM inverter employing a deadbeat control scheme. IEEE Trans Power Electronics 18(3):831–843. https://doi.org/10.1109/TPEL.2003.810837

16. Rahim NA, Chaniago K, Selvaraj J (2011) Single-phase seven-level grid-connected inverter for photovoltaic system. IEEE Trans Industr Electron 58(6):2435–2443. https://doi.org/10.1109/TIE.2010.2064278

17. Charles Ikechukwu Odeh (2014) A cascaded multi-level inverter topology with improved modulation scheme. Electric Power Components Syst 42(7):768–777. https://doi.org/10.1080/15325008.2014.890974
18. Rahim NA, Selvaraj J (2010) Multistring five-level inverter with novel PWM control scheme for PV application. IEEE Trans Industr Electron 57(6):2111–2123. https://doi.org/10.1109/TIE.2009.2034683
19. Selvaraj J, Rahim NA (2009) Multilevel inverter for grid-connected PV system employing digital PI controller. IEEE Trans Industr Electron 56(1):149–158. https://doi.org/10.1109/TIE.2008.928116
20. Choi J, Kang F (2015) Seven-level PWM inverter employing series-connected capacitors paralleled to a single DC voltage source. IEEE Trans Industr Electron 62(6):3448–3459. https://doi.org/10.1109/TIE.2014.2370948
21. Chadli H, Jebroni Z, Chadli S, Tahani A, Aziz A (2017) Design and implementation of a novel five-level inverter topology. In: 2017 international conference on Wireless Technologies, Embedded and Intelligent Systems (WITS), pp 1–6. https://doi.org/10.1109/WITS.2017.7934641
22. Rodriguez J et al (2009) Multilevel converters: an enabling technology for high-power applications. Proc IEEE 97(11):1786–1817. https://doi.org/10.1109/JPROC.2009.2030235
23. Zhang N, Tang H, Yao C (2014) A systematic method for designing a PR controller and active damping of the LCL filter for single-phase grid-connected PV inverters. Energies 7:3934–3954
24. Ali A, Shanmugham P, Somkun S (2017) Single-phase grid-connected voltage source converter for LCL filter with grid-current feedback. In: 2017 International Electrical Engineering Congress (iEECON), Pattaya, pp 1–6. https://doi.org/10.1109/IEECON.2017.8075720
25. Bhanuchandar A, Murthy BK (2021) Single phase nine level switched capacitor based grid connected inverter with LCL filter. In: 2020 3rd international conference on energy, power and environment: towards clean energy technologies, pp 1–5. https://doi.org/10.1109/ICEPE50861.2021.9404491
26. Kouro S, Bernal R, Silva C, Rodriguez J, Pontt J (2006) High performance torque and flux control for multilevel inverter fed induction motors. In: IECON 2006—32nd annual conference on IEEE industrial electronics, Paris, pp 805–810. https://doi.org/10.1109/IECON.2006.347906

The Review Paper on Different Topologies of LNA

Reeya Agrawal

Abstract This paper describes the different topologies of low-noise amplifiers from the last twenty years. Furthermore, each topology has been described with its diagram. Apart from it, all the topologies have been compared in the form of a table and a conclusion arises that a low-noise amplifier without an inductor is more suitable than others, and also in place of resistance a metal oxide semiconductor field-effect transistor can be used. Apart from it, the table has been compared on different parameters such as Gain, Power Consumption, Power supply, Noise Figure, S11, and IIP3. Apart from it, all the technologies have been compared.

Keywords Complementary common gate (CCG) · Common source (CS) · Noise figure (NF) · Low noise amplifier (LNA) · Complementary metal–oxide–semiconductor (CMOS) · Ultra-low voltage (ULV) · Ultra-low power (ULP)

1 Introduction

The wireless sensor networks (WSNs), including healthcare, environmental control, production environments, and agriculture, are commonly available in different applications. WSNs are widely used. The architecture of these programmers puts significant restrictions on the WSN node's power consumption. To optimize battery life and operate energy from the atmosphere, the Ultra-Low Power (ULP) radio frequency (RF) circuits are required. As the size of the feature is reduced in standard CMOS technology, the maximum permissible voltage is also reduced. The maximum power voltage of this function is reduced at the same time. While low voltage supply operations help to reduce conversion losses into energy collected systems, they also reduce the number of circuit topologies available and their operating speed. This makes circuits very important and thoroughly explored at very low input voltages. As an architectural issue and as a result of the inconvenience of the nano-scale CMOS

R. Agrawal (✉)
GLA University, Mathura, India
e-mail: Agrawalreeya0304@gmail.com

technologies such as higher performance, speed saturation and mobility degradation, low-power RF circuits with high bandwidth can be substituted for energy consumption in the short-chain CMOS technology with high-frequency f_T. In [1–3], a low-performance RF architecture metric is introduced, this compromise was initially demonstrated. While useful, this bias measurement does not affect the inherent increase of the output conductivity, g_{ds}, and V_{ds} drain voltage, all of which become particularly important in ULV and ULP designs. This paper provides a comprehensive biasing measure for the solution of certain ULV and ULP design noise-efficient issues and demonstrates their applicability with the development of an extremely broadband LNA ULP amplifier [4, 5]. The first component of the receiver front-end configuration relies on the low-noise amplifier (LNA), which is a low-noise amplifier (LNA). This is the first amplification block at the front end. Since there is a very small antenna signal, ~ 1μVp is present. The first step is LNA, which raises the antenna's weak input signal. The optimal design of their modules becomes an important function when the wireless network industry is at a high point. The noise production of receiver circuits and amplification has significant implications [6]. As a result, we get a meaningful signal without noise [7]. From a topological point of view, LNA is very plain. In architecture, all of the components on a single chip are combined with the NMOS transistor for industrial purposes. This decreased the expense of the computer and increased its efficiency. In the MOS VLSI process, the scaling channel length decreased to nanometers and induced a gigahertz increase in transit frequency.

It also led to lower power consumption (mill watts). The complexities exist and motivate exploring RF architectures, as seen in Fig. 1. The LNA should provide adequate transconductance gain, particularly in portable handheld applications, for sufficient nearness and power consumption to allow for long battery life [8]. There are also some trade-offs between gain, NF, linearity, and stability in design optimization. The first ingredient in the front end of the recipient is LNA, which is usually referred to as one of the hunger blocks [9]. The high-power consumption allows an LNA to be simultaneously broadband, high gain, low noise, and high linearity, both with high power and high voltages of supply. These mixed specifications have been a challenging topic of research in the creation of UWB LNAs, which have low power and low voltage [10]. There are several renowned techniques in this article for designing LNAs for broadband. But there is a trade between the input and the LNA NF, typically leading to increased energy usage simultaneously. New circuit design techniques to minimize energy consumption are, therefore, necessary. In terms of NF, IIP3, gain, s-parameters, and energy consumption, the efficiencies of the LNA [11–13] are considered.

Usually, LNA is the first active block in the receiving direction for transceivers. To ensure the integrity of the signal, the amount of noise entered by the amplifier should be minimum [14]. Therefore, the gain and noise efficiency of any LNA are two main characteristics. Input return loss, reliability, operating frequency, and linearity on certain devices are the major parameters of the specification. There are different interactions between these parameters of performance that complicate the design of an LNA, similar to any analog circuit. There are two forms of LNA for the matching network [15]. One is LNA broadband and the other is LNA smaller band. Two kinds
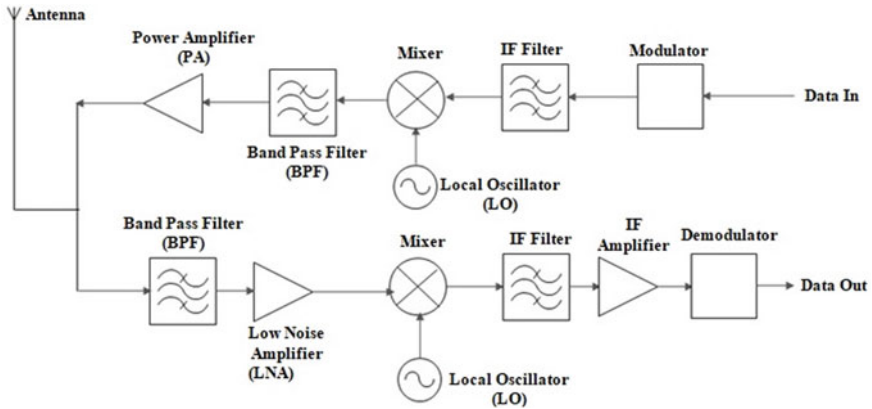
Fig. 1 Basic diagram of low noise amplifier

of LNA are available. The disadvantage of broadband ANL is excessive demands of complex nature as far as power hunger is concerned. The rhythm of the noise is bad as well. The narrowband LNA system, on the other hand, is better than the broadband LNA system, but there are other problems with the narrowband LNA system. Low NF, solid linearity, high gain, and low power should be the standard slim band LNA [16].

2 Literature Review

Initially, Ginzton suggested distributed topology. A modern extension of distributed circuit topologies for a better NF and higher power gain is used for the LNA system distributed. Input/output wideband matching can be achieved by distributed circuits. This feature is important for the UBW LNA design. However, the main problem in distributed topologies compared with lumped circuits is greater power dissipation and a wider chip region. Due to the downside of linearity and stability, another topology, named common gate topology, was invented. Due to the main concern of the wide chip region, a circuit is built free of an inductor, which is called an inductor less LNA [17]. Inside multi-standard radio, implementations of between 100 MHz and 6 GHz LNA without induction are proposed for the active balun. The combination of a CG and a CS stage with the replica partitioning implements a balanced process while simultaneously canceling the CG stage noise and distortion. This allows for the acoustic NF to be around or below 3 dB while the CS stage can be smoothly optimized with good linearity [18].

The literature contains a lot of circuit topologies, each having its strengths and drawbacks. The NF of the CG topology is less than the topology of the SC, although it provides high linearity and stability (Zhuo et al. 2005). The LNA methodology

employs a standard source with a form of topology for inducible degeneration to provide high linearity. It is highly complicated to maintain the linearity of this system in a poor inversion region so that the system can run in the area of saturation. If a value above a certain current is controlled by the system, the V_{dsat} overdrive voltage should be retained, by the law. The increase of feedback strength and the simultaneous satisfaction of input matching is one of the most powerful ways of increasing the amplifier's noise efficiency. That is why another topology is called the topology of shunt feedback [6, 19]. To reinforce IP_2, another topology has been developed called differential LNA.

Differential LNAs can achieve high IP_2, as symmetrical circuits are not responsible for distortions of order. Of course, some (random) asymmetry is affecting real circuits, leading to a finite, but still strong IP_2. In short, CG LNA differentials absorb four times the capacity of a single-ended stage [20] as shown in Fig. 2. Noise factor has also needed to be enhanced with the increase in linearity, stability, and IP_2's because of this purpose; researchers implemented a next technique called noise cancelation technique [21].

Two noise cancelation characteristics are obvious:

- The absolute value of the original R_s source (e.g., Impedance is seen looking in the finished coaxial cable) is the basis for noise cancelation.
- Cancelation is independent of the alpha of the source impedance and its consistency. The explanation is that each change in gm has an equal effect on the noise voltages.
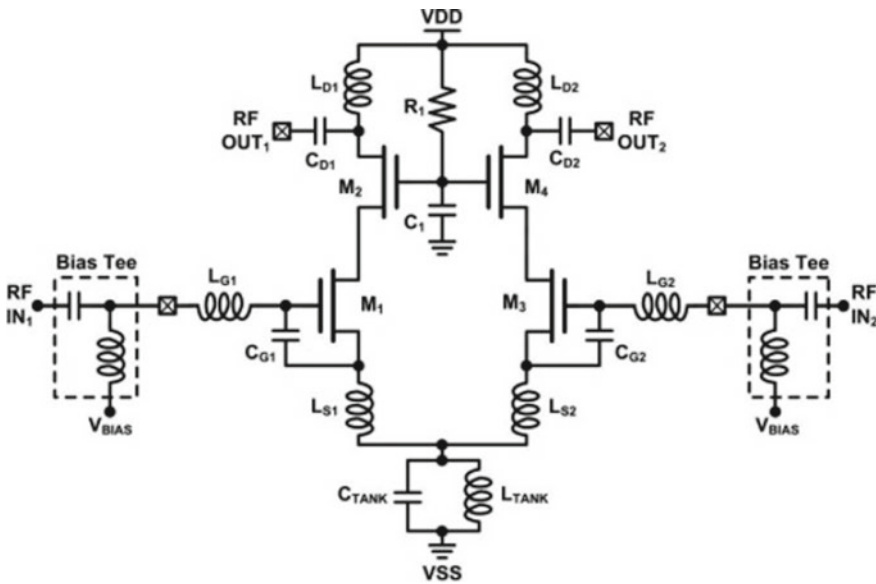
Fig. 2 Differentials LNA

In a CG configuration, the design proposed would achieve the lowest NF above the feedback amplifiers previously reported. The proposed design achieves simultaneous broadband impedance, low noise, high gain, improved linearity, and massive bandwidth using effective and stable dual negative feedback [22]. The M_1 matching impedance device improves the signal and provides the principal path of the front signal. The M_1 matching impedance device improves the signal and provides the principal path of the front signal. G_{m1} is increased by a typical source AFB amplifier (g_m of M_1). The M_3 source tracker affects the impedance of the LNA input with the g_{m2}/g_{m3} ratio, which controls gm and RL changes in the LNA input impedance [23]. The proposed LNA system can be divided into three parts: the cascade amplifier for shunting feedback, the interstage network, and the inductive high-speed amplifier cascade. A cascade amplifier with high reverse isolation and frequency response is used for the input stage [24]. The feedback resistance allows input feedback to be chosen to match the input, low NF, and even broadband gains simultaneously by choosing a suitable R_1. The first is made up of resonances of L_1 and C_1 and the second of resonances of L_2 and C_2. The third is made up of two LC circuits that match the input. To maintain a successful feedback balance, first and second resonance frequencies are located within the range. With an interstage matching inducer, a traditional cascade LNA configuration is used [25]. Two independent phases are considered to be the two transistors of the cascade structure. Two steps are used for the interstage inductor of the off-chip. This approach can improve overall gain and reduce the noise figure of the LNA as shown in Fig. 3 [26]. The nominal supply voltage is not ideal if two N_{MOS} transistors are stacked, however, to quickly scaling advanced C_{MOS} technology. The combination of a transistor P_{MOS} and N_{MOS}, the topology of current reuse, allows LC technology to be high-voltage stable between the two transmission lines. The cascade design has been commonly used for LNA designs because noise and power gain requirements are easily met [27].

In an analysis of cascade topology, though, the combination of the common source and the mechanism of the portal is often less stressed. The outcome of the common-source method should be carefully considered to achieve good isolation. Performance would be considerably improved if an interstage matching inductor was added [28, 29]. Also considered is the cascaded LNA Architecture (Ku and Huang 2012; Lin et al. 2004; Nguyen et al. 2004). This topology has a clear benefit, but multi-story topologies subject to the power budget (Fatin and Fatin 2014; Ho and Mirabbasi 2006). Certain literature uses a standard dual-band LNA, but this means that the consumption of power and energy is minimized [30]. In comparison to power gain, noise, and power consumption, a standard LNA (Hsu et al. 2013) source is better than the previous literature [31].

Figure 4a shows the schematic of Inductorless Active Load LNA. To minimize resistive loss, the lines and conductors of the fixing were placed on top of 2.34 mm thick metal. The LNA consisted of a cascaded, buffered CG stage. At the lower corner frequency (3 GHz) and the source terminal M_2, the peak induction LC and parasite power of the drain terminal M_1 were sequenced with the peak induction L_{D2} and C_{gs4}, resonant at the high frequency of the corner (10 GHz). The proposed T-Match input network will achieve broadband input impedance across the entire interest
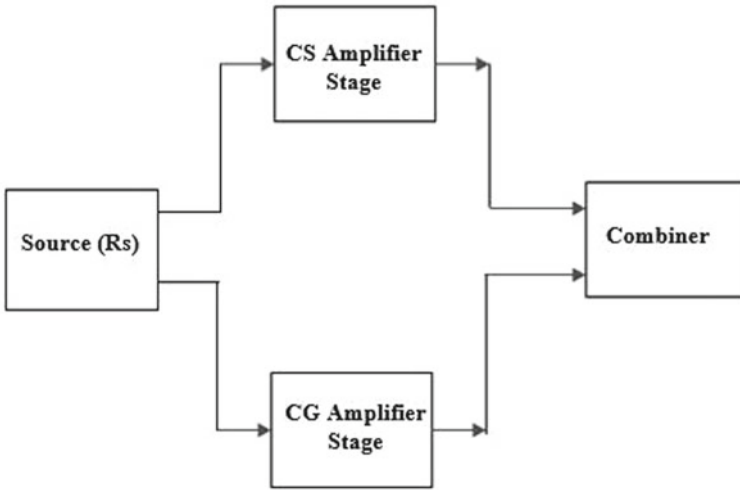
Fig. 3 Block diagram of noise cancellation technique

range; thanks to the two S_{11} dips [32]. For flat and high gain and enhanced reverse insulation in the proposed LNA, the CS M_1 and M_2 cascading transistors are used. Figure 4b shows the schematic of LNA with G_M Boosting Technique. The stabilized ports of the balun are directly connected to the CG transistor sources [33]. A DC-feed port for the balun is installed so that the headroom voltage can be conserved and the supply voltage reduced. The double g_m improvement decreases the voltage through the directly linked balun and ensures low power in this configuration. As the gm-boost CG amplifier is already amplified at the CG main amplifier door, the noise input can be removed from the major CG amplifier [34].

As the signal is connected to NM_{12}, however, when the gm value is NM_{12} at least, the gm-boost amplifier's contribution to noise is significant. Figure 5a shows the LC Reuse Configuration of LNA [35], the NM_{12} feed-in noise cancelation circuit is stacked with P_{MOS} amplifiers. The CG LNA usage-built and transformer feedback from two CMOS double feedback helped generate low NF and flat power over a wide variety of frequencies. CG LNA (CG LNA-1) uses a negative feedback topology and positive feedback in the shunt series to ease the balance between input and noise in the first shunt [36]. The combined influence of the transformer and the associated output component network of the secondary winding inductance from the peak-shunt series leads to resonance and an extension of the three-dB bandwidth gain. In comparison, the bandwidth of the input matched is somewhat improved [37, 38]. Figure 5b shows Small-Signal Model.

Figure 6 shows the schematic of Active Shunt Feedback LNA. Input impedance synchronization strategy of an LNA using mutually coupled inductors. This system not only provides for the cascade transistor, but also the transformation of the inter-stage impedance [39]. This system offers the necessary input impedance matching
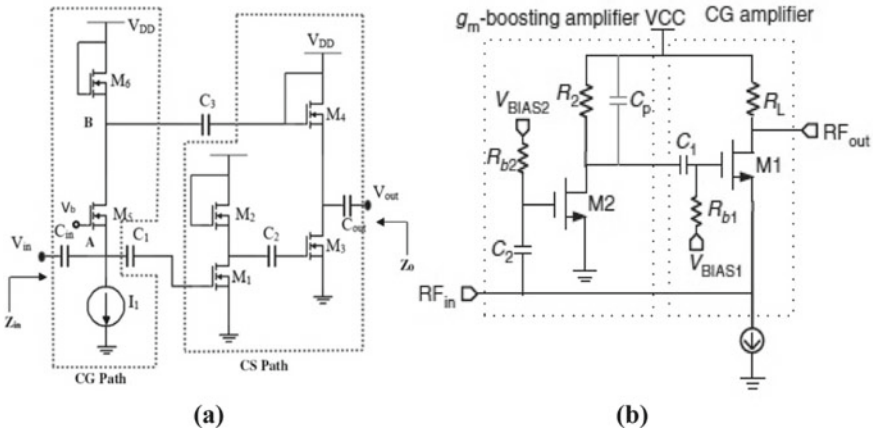
Fig. 4 a Inductorless active load LNA. b LNA with G_M boosting technique
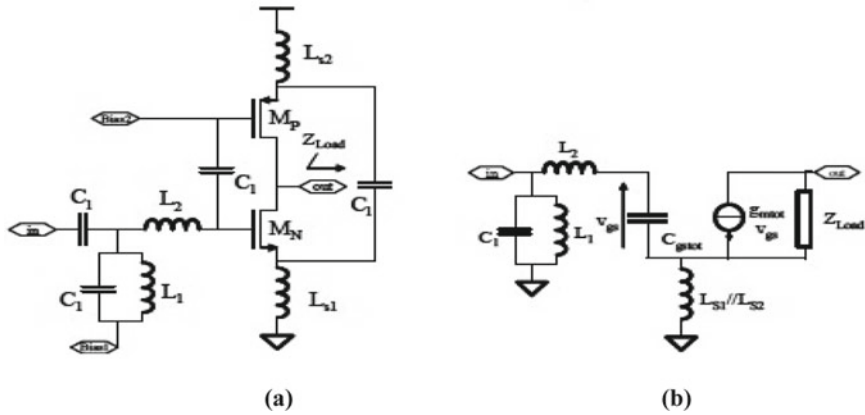
Fig. 5 a LC reuse configuration of LNA. b Small-signal model

not only for the cascaded transistor, but also for the transformation of interstage impedances. This approach uses 0.35 m normal complementary metal–oxide–semiconductor technology to design a mobile contact LNA device that is 900 MHz worldwide [40]. Typically, a cascaded configuration is used in the LNA to minimize the Miller effect and maximize reverse insulation of the input impedance. The interstage inducer is used for interstage matching. In coupled inductors (transformers) are used for feedback [41]. The reciprocal connection between the degeneration and inter-phase inducers is used to achieve another degree of freedom of design. As dc feed, transformers work to provide insulation between phases. If the transformer is lossless, the NF of the suggested CS feedback is similar to that of the CS, although the former has greater physical consistency in the input network architecture [42].
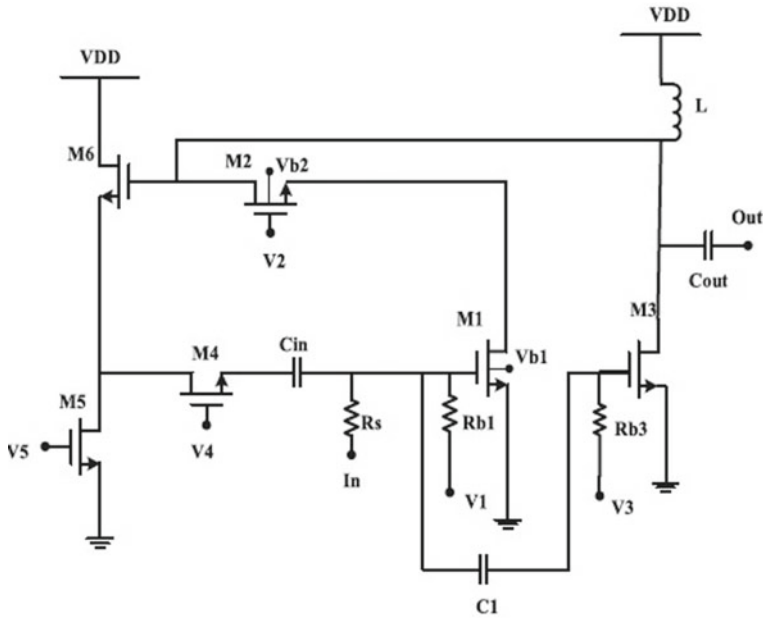
Fig. 6 Schematic of active shunt feedback LNA

The CCG stage helps form a frequency-dependent load from the source-degenerated CS stage. The input with a load reuse technique is convertible and enables simultaneous broadband gains, broadband matching, and NF flat across the target band to be achieved [43]. Cascaded complementary CG (CCG) and CS phases have a new broadband LNA topology, releasing the big chip area issue and dramatically improving LNA performance. It is also proposed and implemented on the first level a CCG Transformer pair, which greatly reduces the chip size by combining a transformer with two inducers and also saves dc power through the reuse of current [44]. Also, in LNA, the method for reuse of the load takes advantage of the CCG point, not only because the proposed LNA exceeds the size of a smaller chip and lower dc, but also because it provides greater bandwidth and enhanced linearity [45].

Four individual CS stages in the cascades are available for the LNA. The LNA contains four single CS stages in cascades [46]. This transformer saves the chip area and reduces losses in comparison with conventional broadband connection networks like a multi-line stub resonator. Figure 7 shows the schematic of Double G_M Enhancement LNA. The Particle Swarm Optimization (PSO) is a technique-driven, stochastic evolutionary calculation agent based on the movement and intelligence of swarms. Complex, multidimensional problems have been successfully simplified by the PSO methodology [47].

To optimize LNA linearity, a novel technique based on pre-distortion is proposed in the input matching circuit. The linearization technique uses a Capacitive Cross Common Coupled Gate (CCC-CG) configuration [48]. A weak inverse transistor is

Fig. 7 Schematic of double G_M enhancement LNA
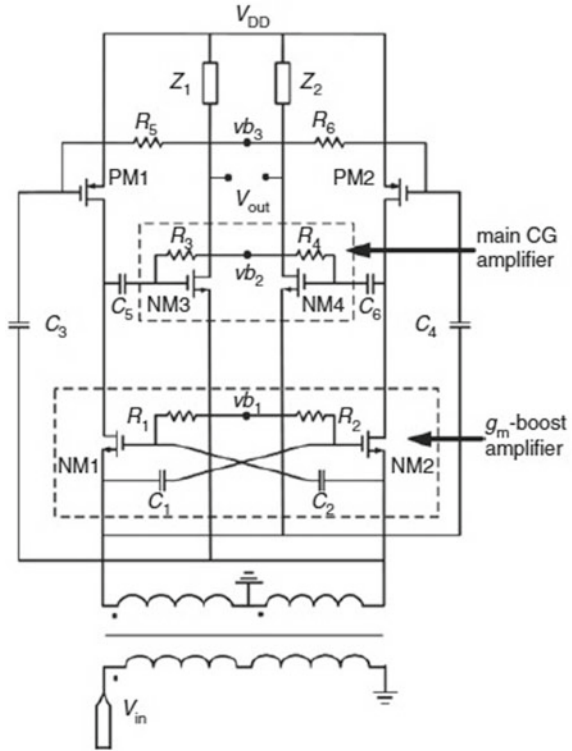
used to alter the nonlinearity of the input matching circuit. The nonlinearity of the input matching circuit has proved successful to offset the nonlinearity of transitivity (Gm) of the amplifier and increase the third input intercept point (IIP3). In addition, the additional transistor is used in an input direction giving a noise cancelation scheme. As a result, linearity is improved, in addition to the low-noise statistics [49]. Figure 8 shows the schematic of Complimentary Cascade Common Gate—Common Source LNA.

For the FET amplifier, linearization techniques based on optimum gate biasing have been suggested. Two parallel transistors, auxiliary and main transistor, which are biased, respectively, in extreme and mild inversion, are used in the derivative superposition technique [50]. Transistor bias and size are chosen if the negative peak of the main transistor nonlinear third-order coefficient (gm3) is linked to the positive peak of the auxiliary transistor nonlinear third-order co-factor. This approach does not reverse the second-order transistor nonlinearity and limits linearity [51]. Also, input matching is complicated by adding the auxiliary transistor to the LNA input. In comparison, a good candidate for improving IIP$_2$, IIP$_3$, and good feedback matching is the post-distortion (PD) technique. In this process, the transistors in the saturation region are biased; their stability is, therefore, high. In general, IIP$_2$ is important
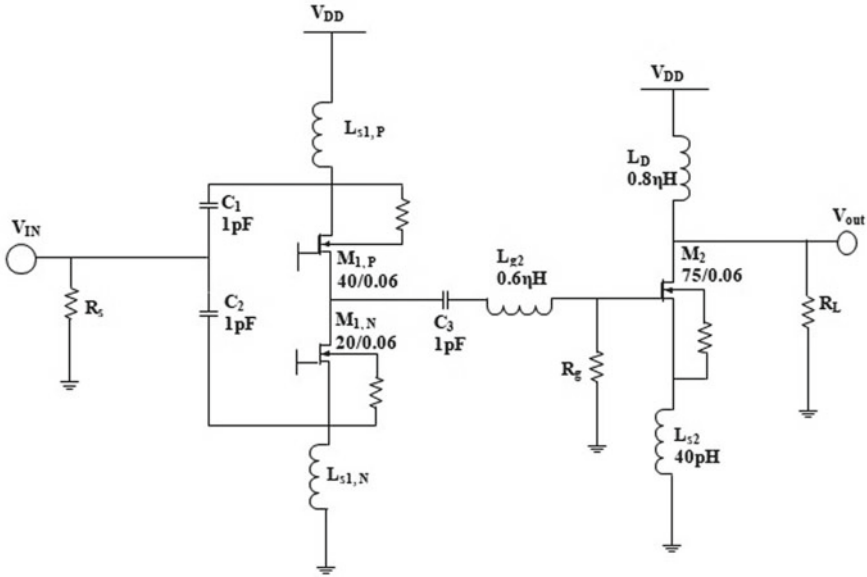
Fig. 8 Schematic of complimentary cascade common gate—common source LNA

for UWB receiving [52]. In low-noise amplifiers, CS and CG configurations are commonly used.

Although the CG configuration has lower input impedance, which makes it simpler for the LNA to balance the input impedance, due to its superior noise efficiency, the CS configuration is more widely used. Also, the input matching to 50 Ω can be facilitated by adding a degeneration inductor to the common-source amplifier. In the presence of such an inducer of degeneration, the LNA's input impedance is equal to

$$Zin(j\omega) = 1 j\omega Cgs + j\omega Ls + gmLs \ Cgs$$

In the above equation, the third term can be simplified to $Ls\omega T$ so for a MOS transistor, the transistor can be considered in $Ls\omega T$ or C_{gs}. Please note that the transit frequency of the transistor is $\omega T = 2\pi fT$ and f_T. F_T is a parameter that is dependent on technology and is a transistor channel length function. The rationale for using the inductive load is that it provides two cascade amplifier transistors with more voltage headroom than a resistive load. Also, the inductor supplies altering behavior along with the output node parasitic capacitance that can be used to change the LNA's bandwidth. The effect of the noise of the cascade transistor on the total noise figure is a problem with this design. It should be remembered that, at very high frequencies, the noise of the cascade system is only significant [53].

A powerful swarm optimizer with the Firefly Algorithm (FA) as an integrated setup of a low-noise amplifier (Several researchers used the firefly algorithm and released excellent results to solve various nonlinear engineering problems. For the

first time, FA is used to enhance LNA parameters, such as NF. By considering each parameter as a single target function, the optimization of these two parameters is achieved. To maintain the limits, the penalty factor strategy is considered. In contrast to FA's performance in reducing LNA parameters, modern algorithms such as PSO, HB-PSO, and tracking search algorithms are used to optimize particle swarm [54].

Xin-She Yang created the Firefly algorithm in 2007, which is based on the flickering action of fireflies during the night and the food search process. After extensive firefly experiments, Yang observed that a group of fireflies lead themselves to the brighter firefly during the food-seeking process. This technique tends to cut the gap between two fireflies, that is to say, the brighter and the firefly itself. This was the major observation of Xin-She Yang that helped him to develop the mathematical model for firefly upgrades. The way of contact between them is the flickering light produced by the firefly. There are around two thousand species of fireflies available, and for the numerous species, the pattern of flashes is different. Two forms of light are usually emitted, one is to indicate that food sources are present and another is to match [55].

Coupled inducers provide mutual inductance feedback so that high benefits and bandwidth in low-power consumption can be achieved simultaneously. The main benefits of topology are the strongly free gain, bandwidth, stability, and correspondence between the input impedances. Architectural guidelines have increased the LNA gain and bandwidth at low electricity consumption. The proposed LNA contains two parallel paths, one is the conventional CS path and the other the CG path. The CG path has the advantage of increasing the overall CS path, while the CS path is extremely effective if the broadband impedance at UWB matches. The CS path is used to minimize noise through the CG path by using a noise cancelation technique. Thermal noise cancelation and MOS distortion are the key advantages of this technique, with high linearity (IIP3 = + 14 dBm) and low NF but with a high tendency to biasing [56]. Figure 9 shows the schematic of Coupled Inductor LNA. The implementation of the standard for low noise and high linearity balun-low-noise amplifiers for large-band applications is a contemporary approach to noise cancelation, using the revised current-sanctioning method (CBLD) and a balanced load. The simple NF topology of CG-CS balun cannot be less than 3 dB. A practical topology is used to reduce NF with a CS transistor whose transitive value is N times the transistor of CG and often with a CS resistor with a resistor N times the CG resistor. Nevertheless, unchanged load resistors produce an increase in the differential output and a phase difference. The revised CBLD solution supported Balun-LNA to obtain differentially controlled output, low noise, and low-second distortion [57].

3 Comparative Study Table

Here, *G* denotes Gain, NF denotes Noise Figure, PC denotes Power Consumption, PS denotes Power Supply, IIP3 denotes the third input intercept point.

Fig. 9 Schematic of coupled inductor LNA
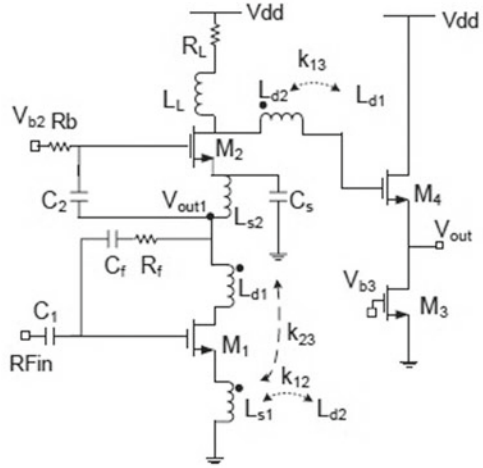
Publisher and year	Topology of LNA	G (dB)	NF (dB)	IIP3 (dBm)	PC (mW)	PS (V)	S11 (dB)
IEEE 1999	Inter-stage matching inductor	19	2.4	–	9	3	10
APMC 2004	Thermal noise	13.7	$<=2$	0	35	2.5	<-8
IEEE 2005	Distributed	8	2.9	-3.4	21.6	1.8	–
Electronics letter 2005	Mutually coupled	17	3.4	-5.1	13	2.3	-14
IEEE 2006	V-band 3-stage cascade	24.7	7.1	NA	72	1.8	–
IEEE journal 2008	Wideband balun	13–15.6	<3.5	>0	21	1.2	–
IEEE 2008	Current reuse CMOS	13.8	4.2	-5.8	8	1.4	<-10
EMC 2009	Forward body Bias	13	6.3	–	4.9	0.7	–
IEEE 2010	Shunt feedback	11	3.26 – 4.16	3.56	9.7	1.8	<-11.9
IEEE transaction 2010	Wideband inductorless	19	2.8 – 3.4	-4.2	5.7	1	<-9
IEEE transaction2010	Dual negative feedback	16.9	2.57	-0.7	12.6	1.8	-20
IEEE 2010	Resistive shunt feedback	15	4	2.5	21.5	1.8	<-7
ECCSC'10 2010	PSO optimized concurrent dual-band	8.8	2.2	-2.53	18	1.8	–

(continued)

Publisher and year	Topology of LNA	G (dB)	NF (dB)	IIP3 (dBm)	PC (mW)	PS (V)	S11 (dB)
IEEE 2011	Cascade cascode	14.47	5.5	–	6.66	1.8	− 32
Electronics letter 2011	T-match	7.9	6	–	0.99	1.1	< − 10.3
Electronics letter 2011	Self-body Bias	10.4	4.9	− 5.4	2.15	1.1	< − 10.1
IEEE journal 2012	Inductor less	20	4	−12	1.32	1.2	–
Electronics letter 2013	G_M boosting	18.3	2.5	− 7	14	1.5	− 10
IEEE 2013	Differential	18.56	1.85	− 7.75	7.59	1.2	−27.63
IEEE transaction 2013	Dual feedback	13.5–16.5	1.9 − 2.6	− 2 to 3	10.8	1.8	–
Electronics letter 2014	Double G_M enhancement	14	3.7 − 4.6	–	0.4	0.8	–
MC 2015	Common source	31.53	2.34	− 5.70	8.5	1.2	−9.14
IEEE 2015	Coupled inductor	13.8–14.2	3.22 − 4.1	− 14	4.8	1.5	< − 10
NC&A 2016	Fire flying algorithm	–	1.5	− 7	14	1.8	− 15
IJERT 2017	CS LNA with inductive degeneration	11	0.58	–	15.6	1.5	− 9.6
IEEE journal 2017	Noise canceling CMOS	17.5	2.9 − 3.5	10.6 − 14.3	21.3	2.2	–
IEEE transaction 2017	Cascade complimentary CG –CS	10.7	4.5 − 5.6	1.4	12.1	1	–
Microelectronics 2017	Pre-distortion	18.55	2.7	11	4.15	1.5	–
JLPEA 2018	Common gate	14.7	3.0 − 3.7	–	5.2	0.7	< −11.7
Electronics letter 2018	Transformer coupled	7.6	6.6	–	11.3	1.2	–
IEEE transaction 2018	Current bleeding technique and balance load	24–30	2.3 − 3.3	− 4.1	19.8	2.2	< − 10
ELSEVIER journal 2019	Active shunt feedback C_{MOS}	11	2.9 − 3.3	14	7	1.4	< − 10
ICEE 2019	Post-distortion	> 10	2 − 4.5	−5	10	1.8	< − 10
Frequenz 2020	Inductorless active load	13.87	1.15	–	0.92	1.1	< − 18.2

4 Conclusion

Different topologies of low-noise amplifiers have been done in this paper. Furthermore, each topology has been described with its diagram. Apart from it, all the topologies have been compared in the form of a table and the conclusion arises that a low-noise amplifier without an inductor is more suitable than others, and also in place of resistance a metal oxide semiconductor field-effect transistor can be used. Apart from it, a table has compared different parameters such as Gain, Noise Figure, Power Consumption, Power supply, S11, and IIP3. Apart from it, all the technologies have been compared.

References

1. Bijari A, Zandian S, Ebrahimipour M (2020) Optimum design of a new ultra-wideband LNA using heuristic multiobjective optimization. J Comput Electron 19:1295–1312
2. Yu X, Sun H, Xu Y, Hong W (2016) C-band 60 W GaN power amplifier MMIC designed with the harmonic tuned approach. Electron Lett 52(3):219–221
3. Limiti E, Ciccognani W, Cipriani E, Colangeli S, Colantonio P, Palomba M, Florian C, Pirola M, Ayllon N (2015) T/R modules front-end integration in GaN technology. In: 2015 IEEE 16th annual wireless and microwave technology conference (WAMICON), pp 1–6
4. Helali A, Gassoumi M, Gassoumi M et al (2020) Design and optimization of LNA amplifier based on HEMT GaN for X-band wireless-communication and iot applications. Silicon (2020)
5. Li N, Feng W, Li X (2017) A CMOS 3–12 GHz ultra-wideband low noise amplifier by a dual-resonance network. IEEE Microw Wirel Compon Lett 27(4):383–385
6. Arshad S, Ramzan R, Muhammad K et al (2015) A sub-10 mW, noise-canceling, wideband LNA for UWB applications. AEU Int J Electron Commun 69(1):109–118
7. Colangeli S, Bentini A, Ciccognani W, Limiti E, Nanni A (2013) GaN-based robust low-noise amplifiers. IEEE Trans Electron Devices 60(10):3238–3324
8. Colinge J-P, Colinge CA (2002) Physics of semiconductor devices. Kluwer Academic Publishers, Berlin. ISBN 0-306-47622-3
9. Metev SM, Veiko VP (1998) In: Osgood RM (edn) Laser-assisted microtechnology. Springer-Verlag, Berlin
10. Breckling J (ed) (1989) The analysis of directional time series: applications to wind speed and direction, ser. lecture notes in statistics, vol 61. Springer, Berlin
11. Ando Y, Okamoto Y, Miyamoto H, Hayama N, Nakayama T, Kasahara K, Kuzuhara M (2001) A110-W AlGaN/GaN heterojunction PET on a thinned sapphire substrate. IEDM Technical Digest, Washington, DC, pp 381–384
12. Campbell C, Lee C, Williams V, Kao MY, Tserng HQ, Saunier P, Balisteri T (2009) A wideband power amplifier MMIC utilizing GaN on SiC HEMT technology. IEEE J Solid-State Circ 44(10):2640–2647
13. Moujahed Gassoumi A, Helali M, Gassoumi C, Gaquière H, Maaref (2018) High frequency analysis and small-signal modeling of AlGaN/GaN HEMTs with Si02/SiN passivation. Silicon, pp 1–6
14. Papadimitriou A, Bucher M (2017) Multi-objective low-noise amplifier optimization using an analytical model and genetic computation. Circ Syst Sig Proc 36(12):4963–4993
15. Sahafi A, Sobhi J, Koozehkanani ZD (2016) Linearity improvement of gm-boosted common gate LNA: analysis to design. Microelectron J 56:156–162
16. Zhang Z, Dinh A, Chen L et al (2017) Wide range linearity improvement technique for linear wideband LNA. IEICE Electron Exp 14(4):1–10

17. Shin S-C, Lin C-S, Tsai M-D, et al (2006) A low-voltage and variable-gain distributed amplifier for 3.1–10.6 GHz UWB systems. IEEE Microw Wirel Compon Lett 16(4):179–181

18. Kolakaluri S, Nagura SS, Kar R, et al (2016) Optimization of low noise amplifier using particle swarm optimization. In: 2016 International conference on electrical, electronics, and optimization techniques (ICEEOT), Chennai, pp 2055–2058

19. Mallick S, Akhil JR, Dasgupta A, et al (2017) Optimal design of 5.5 GHz CMOS LNA using hybrid fitness-based adaptive De with PSO. In: International electrical engineering congress (IEECON), Pattaya, pp 1–4

20. Bhale V (2014) Design and optimization of CMOS 0.18 µm low noise amplifier for wireless applications. Int J Inf Electron Eng 4(2):92–97

21. Joshi D, Dash S, Malhotra A, et al (2017) Optimization of 2.4 GHz CMOS low noise amplifier using hybrid particle swarm optimization with Lévy flight. In: 2017 30th international conference on VLSI design and 2017 16th international conference on embedded systems (VLSID), Hyderabad, pp 181–186

22. Ghosh S, De BP, Kar R et al (2019) Optimal design of a 5.5-GHz low-power high-gain CMOS LNA using the flower pollination algorithm. J Comput Electron 18(2):737–747

23. Zandian S, Khosravi H, Bijari, A (2019) Design and heuristic optimization of a CMOS LNA for ultra-wideband receivers. In: 2019 27th Iranian conference on electrical engineering (ICEE). Yazd, Iran, pp 243–248

24. Mozaffari MH, Abdy H, Zahiri SH (2016) IPO: an inclined planes system optimization algorithm. Comput Inform 35(1):222–240

25. Karanicolas AN, A 2.7V 900 MHz CMOS LNA and mixer. In: IEEE ISSCC 96, Session 3, Paper TP 3. 2, pp 50–51

26. Lin Y-S, Chen C-Z, Yang H-Y, Chen C-C, Lee JH, Huang G-W, Shey Lu (2010) Analysis and design of a CMOS UWB LNA with dual-RLC-branch wideband input matching network microwave theory and techniques. IEEE Trans 58(2):287–296

27. Chen H-K, Lin Y-S, et Lu S-S (2010) Analysis and design of a 1.6–28-GHz compact wideband LNA in 90-nm CMOS using a pi-match input network. Microwave theory and techniques. IEEE Trans 58(8):2092–2104

28. Fukui H (1979) Optimal noise figure of microwave GaAs MESFET's. Electron Devices IEEE Trans 26(7):1032–1037

29. Jaemin S, Taejun Y, Jichai J (2013) Design of low power CMOS ultra-wideband low noise amplifier using the noise-canceling technique. Microelectron J 44(9):821–826

30. Meng-Ting H, Yi-Cheng C, Yu-Zhang H (2013) Design of low power UWB LNA based on common source topology with current-reused technique. Microelectron J 44(12):1223–1230

31. Chun- C, Yen-Chun W (2013) 3.1–10.6 GHz ultra-wideband LNA design using dual-resonant broadband matching technique AEU. Int J Electron Commun 67(6):500–503

32. Teyssandier C (2013) Cryogenic 8–18 GHz MMIC LNA using GaAs pHEMT. In: IEEE Asia-pacific microwave conference (APMC) proceedings, pp 261–263

33. Kim B, Gao W (2016) X-band robust current-shared GaN low noise amplifier for receiver applications. IEEE CSICS Digest, Austin Tx

34. Vittori M, Colangeli S, Ciccognani W, Salvucci A, Polli G, Limiti E (2017) High performance X-band LNAs using a 0.25 µm GaN technology. In: 13th conference on Ph.D. research in microelectronics and electronics (PRIME), pp 157–160

35. Sullivan PJ, Xavier BA, Ku WH (1997) An integrated CMOS distributed amplifier utilizing packaging inductance. IEEE Trans Microwve Theory Tech 45(10):1969–1976

36. Pipilos S, Tsividis Y, Fenk J, Papananos Y (1996) A Si 1.8 GHz RLC filter with tunable center frequency and quality factor. IEEE J Solid-State Circuits 31:1517–1525

37. Fong KL, Hull CD, Meyer RG (1997) A class AB monolithic mixer for 900 MHz applications. IEEE J Solid-State Circuits 32:1166–1172

38. Rudell JC, On J-J, Cho TB, Chien G, Brianti F, Weldon JA, Gray PR, A 1.9 GHz wide-band IF double conversion CMOS integrated receiver for cordless telephone applications. IEEE ISSCC 97, Session 18, Paper 18. 3, pp 304–305

39. Macedo J, Copeland M, Schvan P (1997) A 1.9 GHz silicon receiver with on-chip image filtering. In: IEEE 1997 CICC, pp 181–184
40. Wu C-Y, Hsiao S-Y (1997) The design of a 3-V 900 MHz CMOS bandpass amplifier. IEEE J Solid-State Circ 32(2):159–168
41. Meyer RG, Mack WD, A 2.5 GHz BiCMOS transceiver for wireless LAN. IEEE ISSCC97, Paper 18. 6, pp 310–311
42. Burghartz JN, Soyuer M, Jenkins KA, Kies M, Dolan M, Stein KJ, Malinowski J, Harame DL (1997) Integrated RF components in a SiGe bipolar technology. IEEE J Solid-State Circ 32(9):1440–1445
43. Schuppen A, Dietrich H, Gerlach S, Hohnemann H, Arndt J, Seiler U, Gotzfried R, Erben U, Schumacher H (1996) SiGe technology and components for mobile communication systems. In: Proceeding bipolar circuits and technology meeting, pp 130–133
44. Schuppen A, Gruhle A, Erben U, Kibbel H, Konig U (1994) Multi-emitter finger SiGe HBT's with Fmax up to 120 GHz. In: technology digital international electron devices meeting, pp 337–380
45. Ainspan H, Soyuer M, Plouchart JO, Burghartz J (1997) A 6.25 GHz low DC power low—noise amplifier in SiGe. In: IEEE CICC 1997, Paper 9.2. 1, pp 127–180
46. Van Der Ziel A (1976) Solid state physical electronics, Chapter 18, 3rd edn. Englewood Cliffs, Prince-Hall
47. Shaffer DK, Lee TH (1997) A 1.5 V 1.5 GHz CMOS low noise amplifier. IEEE J Solid-State Circ 32(5):745–759
48. Rhote H, Dahlk W (1956) Theory of noise four poles. Proc Instit Radio Eng 44(6):811–815
49. Goo JS, Ahn HT, Ladwig DJ, Yu Z, Lee T, Dutton RW (2002) A noise optimization technique for integrated low noise amplifiers. IEEE J Solid-State Circ 37(8)
50. Lee TH (1998) The design of CMOS radio-frequency integrated circuits. Cambridge University Press
51. Abidi AA (1986) High-frequency noise measurements of FETs with small dimensions. IEEE Trans Electron Devices 33(11):1801–1805
52. Van Der Ziel A (1986) Noise in solid-state devices and circuits. Wiley, New York
53. Scholten AJ, Timeijer LF, van Langeveld R, Havens RJ, Zegers ATA, Venezia VC (2003) Noise modeling for RF CMOS circuit simulation. IEEE Trans Electron Devices 50(3):618–632
54. Shaeffer DK (1998) The design and implementation of low-power CMOS radio receivers. Doctoral thesis, Stanford University
55. Karanicolas AN (1996) A 2.7 V 900 MHz CMOS LNA and mixer. IEEE J Solid-State Circ 31(12)
56. Youssef A, Sharaf K, Ragaie H, Marzouk M (2002) VLSI Design of CMOS image-reject LNA for 950 MHz wireless receivers. In IEEE international conference of circuits and systems for communications, ICCSC'02, Russia, pp 330–333
57. Guo W, Huang D (2002) The noise and linearity optimization for a 1.9-GHz CMOS low noise amplifier. In: IEEE international symposium on circuits and systems (ISCAS), pp 253–257

Wireless Implantable Medical Devices Security and Privacy: A Survey

Zankhana Patel, Yash Velankar, Chandan Trivedi, and Parita Oza

Abstract Wireless connectivity is now playing a critical role in healthcare systems for medical equipment. Numerous benefits are entitled to remote health control, care, and detection of critical cases. Even so, any downside to the protection of these devices against cyber-attacks could cause huge problems, such as exploitation of personal data, mistreatment, and even mortality. Medical devices save lives, but these devices also utilize these advancements to connect to the healthcare network as cellular technology continues its rapid growth. As a part of interconnectivity, due to security flaws with the hardware and applications used to manage patient information and run the system, networks face multiple security vulnerabilities. Security of medical equipment is a growing concern within the healthcare sector. An increasing number of medical instruments and services contain sensitive health-related information that needs to be protected in terms of accuracy, affordability, and secrecy. In the health care domain, managing protection, anonymity, welfare, and usefulness is a requirement in which body area networks (BANs) and IMDs have made it much easier to handle and treat a disease constantly and efficiently. This paper analyzes the limitations generated by technical and end-user demands and theoretical approaches to minimize wireless hazards. In terms of efficiency, mobility, and knowledge processing, the advantages of wireless medical services are incredible. By addressing vulnerabilities and reducing the expense of traumatic accidents, these advantages may be achieved. We also indicate some of the possible theoretical solutions as a countermeasure for security and privacy.

Z. Patel · Y. Velankar · C. Trivedi (✉) · P. Oza (✉)
Department of Computer Science and Engineering, Institute of Technology, Nirma University, Ahmedabad, Gujarat, India
e-mail: chandan.trivedi@nirmauni.ac.in

P. Oza
e-mail: parita.prajapati@nirmauni.ac.in

Z. Patel
e-mail: 19mcei05@nirmauni.ac.in

Y. Velankar
e-mail: 19mcei17@nirmauni.ac.in

69

1 Introduction

Security has become a hot-button topic concerning several socio-economic, safety,
and technical problems we face nowadays. It is an unusual newspaper or televi-
sion broadcast that does not address security problems linked to terrorism threats,
disruptive device attacks, or communications, electricity, and other utilities expo-
sure to any deficiencies in the infrastructure. The reality is that we add more possible
failure points as our culture evolves and continues to depend on more advanced
technology, each end of a string that could undo a vital component of the system
on which we have come to rely heavily if pulled. One such area where protection
is of growing importance is healthcare technology [1]. The causes for all of these
issues are primarily due to identifying current vulnerabilities and the inadequacy
and susceptibility to compromise healthcare technologies. For some time, the inad-
equacy of healthcare technologies has been recognized, and, subsequently, the U.S.
healthcare sector has been under tremendous efforts to increase the infrastructure for
information technology [1].

IMDs, like pacemakers, implantable cardiovascular defibrillators (ICDs), narcotic
conveyance strategies, and neuro-triggers, offer significant patient care advancements
by continuing to treat multiple conditions and saving millions of lives [2]. They
provide a tremendous benefit in realizing the promise of comprehensive wellbeing
that requires patients to be detected, tracked, and treated instantly, at any time. Such
instruments have now been installed in several people's bodies, and their use is
predicted to increase throughout the future [2]. Figure 1 illustrates various IMD.

To medical device firms, software that has earned previous clearance under regu-
latory requirements is essential as it helps to simplify the procedure by not adding
an unfamiliar device. Once these products hit the market, of course, the devices
have tremendous technical capacities and might operate on old-fashioned software
that has drawbacks to many new risks. Several flaws have been reported in testing,
primarily implantable devices such as insulin pumps, pacemakers, and implantable
cardiac defibrillators [2]. In a mass attack, the greatest danger is probably going to
be an attack on the usefulness or believability of clinical hardware inside a medical
services organization. Such an attack may prompt postponed treatment, ill-advised
determination, or the possible loss of Protected Health Details [3].

When labeled as a medical device, the FDA classifies such factors into different
types. Level 1 devices usually are less dangerous than Level 3 devices that have a
greater degree of risk. The level of oversight and scrutiny involving a Level 1 and
Level 3 product is also closely connected to the level of danger associated with
the device. In other terms, a lancing device would be a Level 1 device, as Table 1
indicates, while a Level 3 device will be an Artificial Pancreas [2].
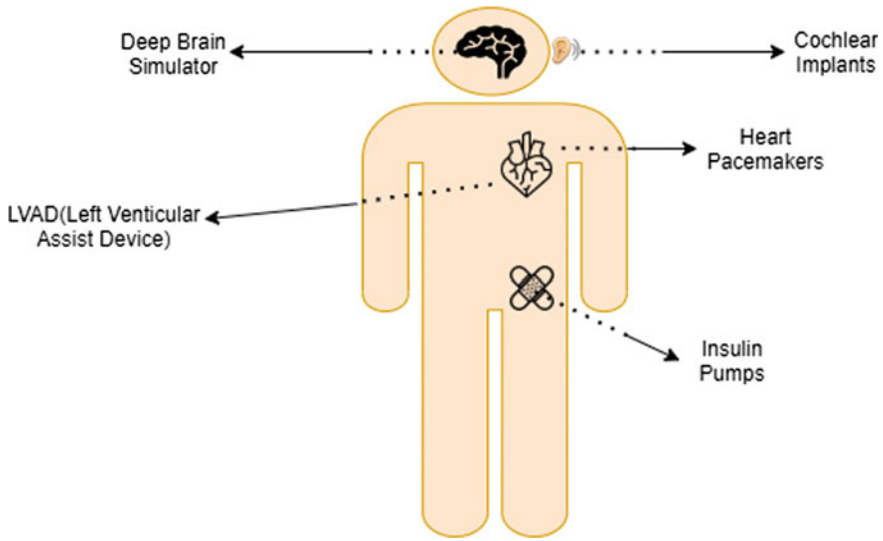
Fig. 1 Implantable medical devices [2]

Table 1 Various medical device class and attributes [2]

Medical device class	Attributes	Examples
Level 1	Ordinary, low complication, and low threat	Surgical knife and oral flaws
Level 2	More complication, relatively implanted, and more threat to patient	Endocrine pump, needle, and blood glucose monitoring
Level 3	Fully embedded, manage body functioning and higher threat	Continuous glucose monitoring, artificial pancreas and heart valves substitution

It is essential to explain that this has been such a concern in recent years once the classification methodology is known. The dilemma has arisen as the connectivity of medical equipment has been dramatically improved by technical gains. In comparison, medical devices use different software around the board, and manufacturers of medical devices are more concerned with the device's functionality and not with the software's stability [4]. Thus, the expanded use of IP-connected computers provides considerably more access points to a health organization network. The utilization of outdated programming with different potential flaws can put the organization in danger or result in an occasion because of the absence of ensured data amplifying this ascent to guide access toward the organization. A compromise in availability or honesty may lead to the loss of lives in the worst situation.

The possible dimensions of attack are various. As Mandeep Khera [5] writes, "in today's crop of medical devices, software vulnerabilities and misconfigurations are widely prevalent, as evidenced by an increasing body of research showing that a significant number of medical devices are imminently hackable." A portion of the primary weaknesses as for clinical devices, for the most part, fall into the accompanying classifications:

- Improper Software Architecture
- Glitch of Codes
- Lack of tamper-resistance
- Mediator Loopholes.

Above mentioned flaws lead to future accidents or contraventions. At that point, the inquiry becomes who ought to be considered responsible for the network protection issues with clinical devices? The Food and Drug Administration (FDA) directs clinical devices as requested by the president, yet the FDA's essential obligation lies in guaranteeing understanding government assistance. Although this is an exceptionally logical position, it doesn't fulfill the steadily changing insurance principles because of specialized improvements nearby wellbeing cares. The legislation focuses mainly on accepting life-saving technology. Still, there is a lack of laws on manufacturers of medical devices and such vendors' obligation when developing the system and the related applications to follow a security-oriented approach.

1.1   Motivation

With the emergence of the Internet of Things (IoT), computer automation, maintenance, and tracking have recently become pain-free and transparent. In recent years, intelligent health care has gained popularity as it provides for constant control of patients away from clinics and physicians. Nevertheless, through a surgical approach that entails embedded medical equipment, both patients and doctors increase their self-satisfaction every year. Today, these clinical instruments are an inescapable element of bleeding-edge clinical consideration. The major difference in the patient's quality of life is the clinical advancement to the degree that IMDs have brought. Nevertheless, the demand for modern drugs, devices, and long-term prescription usage has grown manifold with the extended life expectancy of the present life [1]. These technologies also increased physicians' abilities to analyze and treat illnesses apart from clinics, allowing outstanding dedication and supplying clinicians with self-gratification.

Alongside development, the healthcare system has evolved over time; currently, medical equipment range from basic wooden tongue retractors to dialysis machines that save lives. Although emerging technology is improving the healthcare sector, security issues around smart devices are also evolving. Medical equipment's industry value has hit 133 billion dollars in the United States alone, with over 6500 medical device firms [2]. The existing size of the market for medical devices, combined with

such a grab expense of about $34 million for medical devices, demonstrates that it is challenging to alter laws or switch suppliers of new medicines towards a more security-based approach during the design process [2].

The main motivation to write this survey is to embark the journey of wireless implantable medical devices and their security and privacy for the readers of the domain. We comprehensively reviewed various approaches that can help to achieve the security and privacy of implantable devices in the medical field.

1.2 Objective and Contribution

In comparison, the FDA is concerned only with digital issues that include the death toll. Subsequently, no obvious indicators about how accidents or violations can impact credibility or functionality directly affect patients, this is the core of the dilemma. Clinical devices are costly to produce and certify, and merchants are more cantered around selling devices than on-device protection. Although the systems are specifically intended to save lives and extend medical service alternatives, insurance is an untimely idea. The FDA regulations mandate that technological upgrades require further monitoring to ensure that such updates do not impede the medical devices' operation originally authorized. It will require as long as 180 days [3]. Those 180 days could feel like a long time in the virtual world, and these frameworks could keep on running on an organization with bugs that may harm the IT foundation, intrude on medical services, or bring about the insufficiency of Secure Health Data. The FBI issued a cyber threat alert that "Cyber actors are likely to increase cyber intrusions against health care systems." It is now more critical than ever for policymakers to collaborate with industry to create a sensible solution to ensure adequate cyber protection while ensuring patient safety. Patient assurance should start things out; however, controllers and providers should focus more on guaranteeing the security and accessibility of their frameworks from a digital perspective, not simply saving lives.

There are also several research on wireless body area network security that are compatible with IMDs [2, 5–7]. This paper, accommodates various solutions in terms of tackling wireless security challenges, in addition to the survey in order to comprehend existing concepts, their flaws, and advantages against various types of attackers. The focus of the paper is as follows:

- We recognize the security and privacy requirements of medical devices and their associated common security and privacy risks.
- We identified the impact of security risks in medical devices and possible attacks scenario.
- We recognize the existing aperture associated with data defense for medical devices.
- We discussed interim solutions to resolve existing compliance concerns.

2   Wireless IMD Security and Privacy Issues Overview

The arrangement of wireless advancements in the medical services setting cannot just offer advantages to the medical services experts yet in addition to patients. In contrast, the inescapability of wireless medical devices and applications may perhaps prompt potential abuse cases. For example, abuse can be when an adversary attacks a wireless medical system like an insulin pump to negotiate with patients by manipulating or stopping the drug dosages [3]. Adversaries that probably exist around an IMD client may danger the patient in various manners. An adversary may inactively stand by to get private wellbeing-related data communicated by IMD or effectively attempt to adjust the IMD parameter. It might be found close by the patient or extremely near the unit controlling the IMD from the emergency clinic.

Various malicious events that could occur by using IMD are described in the literature [3, 6, 8]. For instance, the usage of a pacemaker or an installed heart defibrillator or a ventricular assist device with inciting cardiovascular breakdown [9], bradycardia, tachycardia, and arrhythmia. Essentially, Radio Frequency Identification (RFID) empowered Wireless Medical Devices utilized for patients checking or continuing in the clinical focuses can be mishandled by a harmful software engineer utilizing a likely assault Implantable Identification Devices (lIDs, for example, the cloning assault) [3, 8]. The lIDs are, generally, implantable RFID marks with no force and powerless against risks. Henceforth the adversary can arrange the patients' security by getting the patients' interesting IDs through an outer RFID scanner [10].

Different classification of IMD security issues is given in the literature [2, 8, 11]. These issues are accumulated under three principles of malicious attack in wireless communication; eavesdropping, impersonation, and jamming attacks as shown in Fig. 2 [2].

Impersonation: Authentication can be considered the most fundamental issue in IMD security. If the entrance of a malicious hub to the IMD can't be prevented.
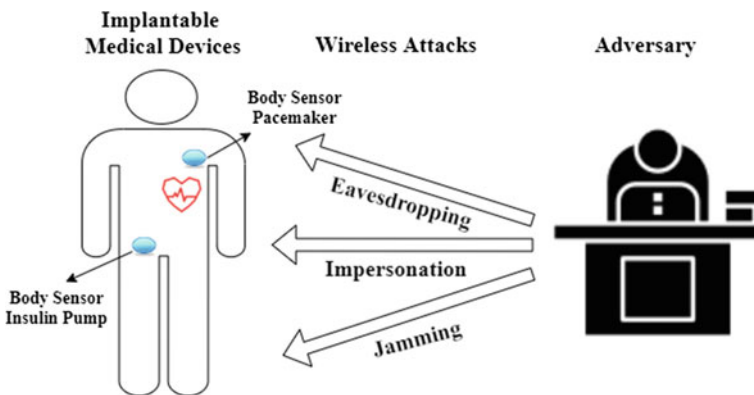
Fig. 2   Malicious attacks that compromise the safety of IMD

- Virus and malware sort of virtual products can be introduced in an IMD to make breakdowns, for example [2], keeping IMD continuously open to diminish battery life or disregarding a few orders from the actual developer.
- IMD can be hacked, and destructive exercises might be performed, for instance [2], mentioning an insulin siphon to apply an overabundance insulin imbuement or an implantable heart defibrillator to send a stun expected to impel a dangerous heartbeat.
- Information put away in IMD can be reached by unapproved hubs, which may prompt Identity thefts.

Instead of a malicious attack, an authentic hub may get to the wrong IMD incidentally, making an unacceptable IMD issue and the proposed one. Therefore, a strong mechanism controlling the access mechanisms to the IMD should be utilized to keep up their security and reliability.

Eavesdropping: Eavesdropping attacks negotiate the confidentiality of the transmitted private information, e.g., patient's data, clinical estimations, client location, and data that might be utilized to play out extra assaults, for example [2], cloning. While such an attack does not look as hazardous as an Impersonation attack, reaped data may empower unapproved clients to get to clinical devices or IMD regulator units. In this way, protecting the private patient's information is a fundamental issue for a safe framework plan.

Jamming Attacks: Besides all of the attacks mentioned above, medical devices may undergo jamming attacks that point to a Denial of Service (DOS) attack by flooding the working recurrence of clinical devices with an unessential signal. Keeping up the transmission of IMD under such assaults is very troublesome.

3 Security and Privacy Requirements for IMD

The objectives of security and privacy benefits in IMD are intended to guarantee the patient's information and the devices' resources. IMD should focus on the accompanying security and privacy properties while planning security as a board framework for clinical devices. Figure 3 represents various safety requirements in IMDs. Here we also discuss multiple security and privacy properties that IMD should target [6, 7].

Confidentiality: Information either put away in the devices or imparted through the remote connection must be perused by supported gatherings. Specifically, IMDs and the software engineer go on through the radio channel, and these trades are acquainted with an overhang dropper. In the event that interchanges are not encoded, the aggressor could uncover private information, for example, the IMD model or even clinical data of the patient. This could deal with the information assurance of the patient [5]. Regardless of whether correspondences are encoded, an assailant could recognize the embeds quality or, again, surprisingly more terrible, track its holder's developments. Consequently, confidentiality is one of the primary security
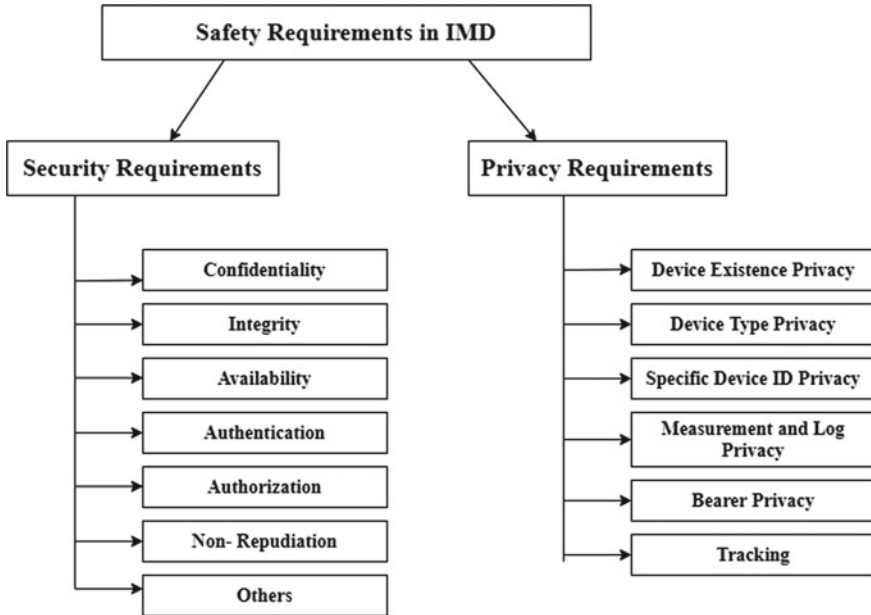
Fig. 3 Security and privacy requirements in IMD [6]

goals to guarantee that any unapproved individual won't approach sensitive data by sniffing the correspondence interface between remote devices.

Integrity: The inspiration driving the information integrity essential is to ensure that the information appearing at the arranged objective has not been subverted in any way during the far-off transmission. An adversary could alter patient information by exploiting the transmission normal for the remote organization, prompting profound implications under challenging cases [12]. To ensure that the information has not been subverted, the ability to recognize expected unapproved mutilations or controls is fundamental. Hence, the data prepared and dispatched off and from IMDs ought to be encoded or ought to have a more grounded validation framework that saves the data from being changed or defiled by illegitimate staff [6]

Availability: The essential objective of presenting IMD inside the patient's body is to have common and far away admittance to a specialist. Both patient and doctor have devices access available and perform certain operations as and when needed [6]. Therefore, administrations offered by the IMD ought to be available to the authentic gatherings reliably. An IMD could be passed on out of reach through the radio channel's blockage (dynamic staying). Obviously, the gadget may be over-inconvenience by flooding the IMD with network traffic over the radio channel. This could be utilized to thwart induction to the gadget or to exhaust its battery [5]. In the event that the battery runs out of power, the gadget will turn out to be everlastingly impossible, and the patient's success could be at risk.

Authentication: The identities of the communicating parties ought to be correctly verified before performing any other operations. Any devices in the framework (IMDs, External devices, or Programmers) can be impersonated inside the IMD domain. Henceforth, the gathered patient's physiological information ought to be confirmed not just during the correspondence through either wired or remote clinical organization, yet also while taking care of it in an electronic clinical record (EMR) or a patient wellbeing record (PHR) structure [3].

Authorization: An action should be executed just if the requester has adequate advantages to organize it. For instance, treatment boundaries (e.g., voltage, limits, current, activity mode, and so on) can't be refreshed by the patient. Just specialists should have the option to alter these. Then again [5], the IMD ought to be continued running on all occasions and be executed under remarkable conditions that may threaten the patient's life (e.g., heart operation with electro-burning gadgets). By ethicalness of pacemakers, an engaging field ought to be applied close to the contraption (over the patient's chest), and this method ought to be embraced by the cardiologist [5].

Non-repudiation: Tasks performed by/on the IMD are kept securely in an entrance log. The assailant could zero in on eradicating these commitments to demand to cover his/her path. Of course, not all IMDs are furnished with a logging system. In the event that this was the situation, the enemy could repeatability to get to the IMD without leaving in any case. Regardless of whether a logging framework is open, the limits would be logged notwithstanding no alert would be set out to caution the IMD holder if there should be an occasion of the harmful demonstration [5].

Others: Among all the above basic security principles, other security measures should also ensure secure IMD i.e.

- **Access Control**: IMDs ought to have the option to deny the permission of any unapproved clients.
- **Accountability**: IMDs should keep audit logs to follow for potential breakdowns on the devices.
- **Robustness**: The devices ought to be equipped for taking care of circumstances, for example, emergency conditions or some other anomalous circumstances.
- **Freshness**: Activities being performed should be new, additionally, non-repetitive. While keeping up trade logs further, in hostile DoS attack conditions, an intruder can positively endeavor to debilitate the device's memory by sending comparable tasks [6].

Apart from the above security goals, IMD should also satisfy the following privacy goals [7, 13].

Device Existence Privacy: An unapproved person could not have the option to verify that a patient has at least one IMDs remotely. An enemy may be a potential business ready to segregate against the evil or an individual from a sorted-out wrongdoing bunch looking to sell a significant device.

Device-type Privacy: If a device uncovers its reality, its sort ought to be discovered by approved entities. Patients most likely will not wish to impart that they have a particular device for reasons unknown.

Specific Device ID Privacy: Unapproved entities ought not to have the option to decide on the unique ID of an IMD. This is practically equivalent to worrying about using constant identifiers in RFIDs, 802.11 media access control (MAC), Bluetooth, and locations to bargain an individual's area protection.

Measurement and Log Privacy: Unapproved entities ought not to have the option to decide on distant telemetry or access put away data about the patient. The framework plan stage ought to incorporate a privacy assessment to determine fitting approaches concerning information access.

Bearer Privacy: An adversary ought not to have the choice to abuse an IMD's properties to see the transporter or concentrate private data about the patient. This data unites a patient's name, clinical history, or analysis subtleties.

Tracking: Unapproved entities do not have the option to influence the actual layer (e.g., by noticing basic sensors or organizing a radio unique finger impression) to follow or track down a patient.

4 Security Threats and Impacts in Wireless Medical Devices

The security dangers of remote clinical gadgets used in the clinical consideration region have been examined in this segment. Before getting into IMD attacks due to a lack of security and privacy, it is necessary to understand the adversary and its purposes. Table 2 describe various Security Threats and its Impacts in IMD [6, 14, 15].

4.1 Adversaries Model

Following the standard security approaches, an adversary can be classified based on their capabilities, goals, and relationship with the framework such as [5, 13].

Passive Adversary: A passive adversary can look at the channel and, in this way, get to the messages traded between the IMD and the developer. Enduring an unsure radio channel, a passive enemy is an impending risk to characterization and may bargain verification. By investigating messages, a passive enemy may pick if an individual passes on an embed or not; discover what kind of embed and other information, for example, its model and persistent number; get telemetry information and reveal private data about the patient, for instance, the ID of his success records, name, age, also, conditions. Taking everything together cases, the general outcome is a genuine trade off of the patient's security.

Active Adversary: An active adversary isn't just fit for getting messages traded over the radio channel, at any rate in like a way to send solicitations to the IMD, change messages on the way before they appear at the IMD or the developer, or

Table 2 Security threats, attack types and impact

Security threats	Attacks type	Impact
Communication attacks	Eavesdropping	An attacker can listen in on the communication between the gadgets and the gatekeeper
	Man-in-the-middle attack	The external gatecrasher undermines the communication between the two components to allow clinical data passed into it
	Denial of service	A device is incited to send repeated transmissions tenaciously
	Replay attack	An attacker can have unrestricted access to the patient's information and corrupt it
	Resource depletion attack	By crippling the battery, the attacker can deplete the assets of clinical devices
Internal attacks	Calibration attack	Changing the facts acquired in order to falsify a clinical patient's analytic cycle
	Battery failure attack	An attacker can make the gadget's memory deficient
	Malware software attack	An attacker can modify its software program to do harmful actions in order to infect devices with a virus
	Hardware/connection attack	An attacker can attack on hardware/connection failure point

simply square them with the target that they will not at any point show up. For example [5], he could recklessly demand data from the IMD to deplete its battery. He could similarly try to change the devices' plan, cripple medicines, or even impel a stunning state to the patient.

4.2 Attacks in IMDs

Cyber Attacks on IMDs are authentic and making danger. These attacks can debilitate the information's secret and endorsement by adjusting the association's reliability or changing and draining network availability. The attack's consequences can also be savage for patients as these unexpected changes can impact the patient's existence. The attacker arranges to fathom the patient's information to impact the patient's prosperity or stifle the device's idea with a negative arrangement from a genuine maker's site. The attack's weaknesses combine unsteady remote channels, lacking confirmation or then again check instruments, powerless audit frameworks, and insignificant memory limit. This part gives subtleties of such attacks found in IMD's [6, 14].

Communication Attack: The communication channel among IMD and guardian gives a route for unapproved individuals to get to the clinical devices. The affectability

of information being communicated and usage of decoded remote channels, insufficient validation, what's more, access control systems offer ascent to the communication attacks [16]. This assault can either allow the aggressors to get the clinical gadgets to trap and entry the data to some different gadgets or to deplete the gadgets' resources. The correspondence channel is decoded and can prompt explicit further assaults, for instance:

- **Eavesdropping**: An aggressor can sneak around on the correspondence occurring between the gadgets and the gatekeeper. This listening can permit an aggressor to get some answers concerning the gadgets related to the patient, the restrictions of the gadgets, or the headings and settings given to the gadgets and patient prosperity data. Through this data, an attacker can actuate point-by-point insights regarding the current status of the patient's challenges and track the patient.
- **Man-in-the-Middle Attack (MITM)**: It happens when the outer interloper inserts itself in-between the gadgets and gatekeeper, passing information among them and causing them to accept that they are communicating information to each other. The external gatecrasher weakens the communication between the two components by allowing the clinical gadgets' information to pass into it. This permits a gatecrasher to will calm information in an unapproved course by knowing the situation with the patient's prosperity.
- **Denial of Service (DoS) Attack**: In these, the IMD adversary and the guardian can dispose of the patient's data, inciting the device to send repeated transmissions tenaciously.
- **Replay Attack**: Replaying a past text exchanged in-between the gadgets and the watchman can trick the beneficiary into trusting in the assailant's realness. At the point when the association is set up, the assailant can have unapproved admittance to the patient information and degenerate it.
- **Resource Depletion Attack**: It attempts to drain clinical devices' assets by debilitating the battery by referencing power-devouring endeavors to them, for example, [6], DoS, or constrained validation assault.

Internal Attacks: Internal attacks are presented during clinical devices organization. Here, an attacker can hack pacemakers [16]. Furthermore, insulin siphons shut down specialist's office frameworks and take patients' information. The producer worker, patient, doctor, or clinic director can get hold of the internal system of IMD and present attacks, for example [6]:

- **Calibration Attack**: This attacker center around changing the gathered information to deceive the analytic cycle of a clinical patient.
- **Battery Failure Attack**: Battery Failure Attack happens when the processor and the radio used to handle devours an extraordinary energy arrangement while sending, taking care of, and tolerating data. A dangerous aggressor can make the gadget's memory deficient by introducing preparing assignments to make the gadgets counter profitable.

- **Malware Software**: An attacker can adjust its software program to do malicious activities to add a virus to the devices. For example [6], an assailant can intentionally ingest too much of the insulin entirely by either a solitary shot or persistent shot in the instance of a patient with diabetes.
- **Hardware/Connection Attacks**: There are hardware/connection failures that variables can bring about, for example [6], catastrophic events, malicious also, careless outsiders, or authentic activities of outsiders whose business interests' conflict.

5 Challenges in IMD Security and Privacy

In this segment, we discuss some common issues which are faced while inspecting the security and privacy of IMD. Securing IMD is a difficult task because of the limitations of restricting resources as far as energy flexibly, handling power, storage space, and so on [17]. Secure communication is considered one of the most fundamental issues for IMDs. In any case, a few problems clashing with essential IMD prerequisites rise in a secure framework plan. These challenges should be considered carefully to build up a sensible framework [2, 17]. IMD challenges are categorized into two categories as Power Challenges and Design Tension Challenges.

5.1 Power Challenges

Battery Life: An IMD is inserted in a patient's body and should work for some time or years. Normally, IMDs are energized by a non-battery-fueled battery, and replacement of the battery needs an operation, i.e. a medical procedure [6]. Recharging an IMD through an external RF electromagnetic source causes warm effects in body tissues and appropriately isn't proposed. May use AA-type or endless (e.g., sun-based) batteries, an IMD typically utilizes silver vanadium oxide batteries and in this manner is totally defenseless to the Resource Depletion (RD) assaults [6]. Thus, battery life should be long enough. Nonetheless, security algorithms corrupt battery life because of their operational complexity.

5.2 Design Tension Challenges

Emergency Access Control: During emergencies, a patient may be oblivious and can't give his accreditations (for instance, a key or a token) to the clinical staff, nor would he have the option to show his ID or advise the clinical work force about his clinical information. For the present circumstance, the security of patients surpasses the security and insurance stresses of IMDs. A respectable access control plot should

satisfy security, assurance, and wellbeing necessities so, IMD should be available to the medical personal for emergency treatment even if he/she is not authenticated previously.

Adaptability: To give security to any clinical devices, adaptable strategies that don't need any adjustment on IMDs are essential, particularly for the recently implantable devices.

Reliability: Security measurement present additional parts to the framework or run different algorithms which expands the weakness of IMDs against programming bugs what's more, hardware impairments, and lead to glitches. Accordingly, security components ought to be sufficiently robust to guarantee framework reliability.

6   Defense Mechanism

Security was not seen as a priority in older generation IMD's. However, with the rise in cyber threats, we agree that protecting IMD's from malware vulnerabilities is of the utmost importance as their communication grows [6]. IMD manufacturers must regard systems' protection as a focus from the preliminary design stage to prevent unintended errors. In this section, the security threats that we consider to be the most essential suggested strategies for protecting IMD's and possible proposed solutions are presented [6, 18].

6.1   Nearby Range Communication

Remote contact among IMDs and outside machines makes them entirely defenseless against attacks. Identification of the radio frequency with an RFID tag appended to the installed clinical gear and an RFID scanner is used to scrutinize the data in the tag [19]. A fluid seal protects the tag. It gives data about the patient and the unit, which the specialist must get. An outline of an injectable RFID medical care framework is VeriChip, which is a chip name inserted in a human body containing a special ID number associated with an information base containing patients' clinical history, manifestations, and contact numbers. The client can see subtleties on the names from 10 to 15 cm [10]. The contact between the database and implantable tag is found in Fig. 4.

Two dimensions should protect communication between the injectable hardware equipment and the repository: the correspondence between both the tag and the reader and the correspondence between both the reader and the data set over the network. [19]. Moosavi proposed a new protocol that enables the communication to be guarded between both the tag and the reader using elliptical hashing.

They also suggested a randomized hash lock calculation that tackles the issues of tracking and confidentiality. One encryption solution proposed is to add the hash function [20] any time a tag is read. This enhances anonymity but then, on the other
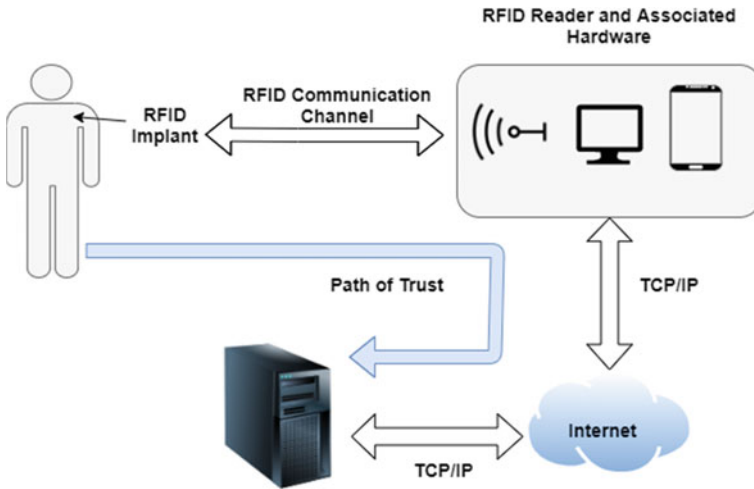
Fig. 4 Implantable tag and database communication [19]

side, raises the computing burden in the repository. This approach is unsuccessful since an intruder will always use a high transmitter to exploit the system at a distance of up to two meters from either of the victims. Near-Field Communication is also an advancement in RFID, where the operating gap is reduced to 20 cm. However, the intruder will also be able to decode the message with the appropriate equipment. Some other scientific avenue with the use of body-coupled contact, wherein the body is being used as a means of transport and connectivity, is only practicable in the vicinity of the patient. Rasmussen suggested a proximity-based intrusion detection system that uses infrared sensor boundary, which only provides attention to machines in the vicinity.

6.2 Cryptography

A cryptosystem approach for protecting IMDs has also been suggested. Various classes of cryptography may be used, symmetric key cryptography, in which contact bunches exchange a private key, and public-key cryptography, in which two keys are being utilized, one is public, and the other is a private [21–23]. For example, it offers an answer dependent on open key encryption, yet the principal drawback lies in utilizing this methodology's energy. Hosseini-Khayat has built up a vigorous symmetric key cryptography that can be reached out to insanely energy ASIC chips [6]. Zhend developed a one-time pad cryptography technique that takes an ECG signal to get a mutual authentication. Compression algorithms methods can be used to minimize energy consumption further.
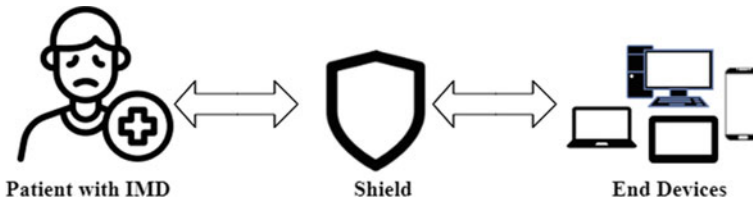
Fig. 5 Usage of external medical device [24]

6.3 External Devices

The utilization of convenient gadgets is one more technique initially supported by Denning. A generalized overview of the function of remote instruments is illustrated in Fig. 5. Requirements from terminal systems will be sent to remote devices rather than just being transmitted explicitly to the IMD [24]. The remote computer is accountable for verifying all user requests and defending the IMD against multiple threats. A portable unit is battery-powered and also has fewer size limitations than that of the IMD. Throughout the event of an emergency, the medical team may detach the external enclosure and share this information with either the IMD [24]. The downside to this approach would be that the person must still be near the outer unit. This approach is also sufficient if the IMD is still in the person's body and the protection applies equally subsequently.

6.4 Biometric Access

The use of biometric data to connect the IMD, including fingerprints, iris, and speech, could minimize the emergency access restriction [25]. Hei and Du suggested a two-venture access to the executive's framework, wherein the main level uses fingerprints, iris, shading, and tallness as biometric information for patients. In contrast, the second tier uses a robust iris authentication scheme. In an emergency, medical personnel may use biometric patients to access data that does not require any patient flexibility [25]. However, it does not help the user to recall any credentials or to carry any credential information.

6.5 Battery Constraint Mitigation

Battery drainage assaults pose a significant challenge to IMDs, as new batteries typically require surgical treatment [6]. Rather than reducing the battery usage while using streamlined cryptography and remote equipment, other methods can be used, such as easing the power limitation by making the implant remotely rechargeable or

using the human body's kinetic energy [18]. Not much research has been reported in this region. A bunch of studies need to be done both hypothetically, from a technical point of view, and medically to ensure this methodology's success [26].

7 Conclusion and Future Work

There seems to be a real challenge to the accessibility and safety of medical equipment, the threat to a pacemaker or insulin siphon may appear as though a circumstance expected by government specialists or related secret work. However, the risk is genuine. The possibility that we will see enhanced assassination attempts by such a unique pattern is small, but what's even more possible would be a significant collapse of the supply of much medical equipment in the hospital. This sort of event may lead to severe injury or death.

As this study has demonstrated, there have been realistic steps that healthcare providers should adopt with the place of legislation to protect the safety of patients. Although these improvements would be tedious, avoiding the threats raised by medical devices' flaws is reckless based on what is understood about the danger. In layman's terms, how could you defend the building when you don't know how many openings to the building there really are? A plain and inevitable reality is that you cannot protect your property unless you have the essential knowledge designed to eliminate the threat.

One single record structure must explain what the linked devices and company needs to become part of clinical care and analyze the devices' key access points. Security flaws can persist as companies gradually struggle with the complexity of the regulatory authorities. Development appears to be moving at increasing rates, so protection and defense are essential. Health technologies have provided numerous advantages to mankind by continuing to extend their lives. It'd be a total shame if, either at the end of the day, those equivalent life-saving contraptions, attributable to a security break, finished in what they were endeavoring to keep away from, calamity.

References

1. Martinez JB (2018)Medical device security in the IoT age. In: 2018 9th IEEE annual ubiquitous computing, electronics and mobile communication conference (UEMCON), pp 128–134.https://doi.org/10.1109/UEMCON.2018.8796531
2. Ankarali ZE, Abbasi QH, Demir AF, Serpedin E, Qaraqe K, Arslan H (2014) A comparative review on the wireless implantable medical devices privacy and security. In: 2014 4th international conference on wireless mobile communication and healthcare—transforming healthcare through innovations in mobile and wireless technologies (MOBIHEALTH), Athens, 2014, pp 246–249. https://doi.org/10.1109/MOBIHEALTH.2014.7015957

3. Kyaw AK, Cusack B (2014) Security challenges in pervasive wireless medical systems and devices. In: 2014 11th annual high capacity optical networks and emerging/enabling technologies (photonics for energy), Charlotte, NC, pp 178–185. https://doi.org/10.1109/HONET.2014.7029386

4. Kulaç S, Sazli MH, İlk HG (2018) External relaying based security solutions for wireless implantable medical devices: a review. In: 2018 11th IFIP wireless and mobile networking conference (WMNC), pp 1–4. https://doi.org/10.23919/WMNC.2018.8480911

5. Camara C, Peris-Lopez P, Tapiador JE (2015) Security and privacy issues in implantable medical devices: a comprehensive survey. J Biomed Inf 55:272–289. ISSN 1532-0464. https://doi.org/10.1016/j.jbi.2015.04.007

6. Rathore H, Mohamed A, Al-Ali A, Du X, Guizani M (2017) A review of security challenges, attacks and resolutions for wireless medical devices. In: 2017 13th international wireless communications and mobile computing conference (IWCMC), Valencia. pp 1495–1501.https://doi.org/10.1109/IWCMC.2017.7986505

7. Halperin D, Kohno T, Benjamin T, Fu K, Maisel W (2008) Security and privacy for implantable medical devices. Pervas Comput IEEE. 7:30–39. https://doi.org/10.1109/MPRV.2008.16

8. Malasri K, Wang L (2009) Securing wireless implantable devices for healthcare: ideas and challenges. IEEE Commun Mag 47(7):74–80. https://doi.org/10.1109/MCOM.2009.5183475

9. Trivedi C, Srivastava R (2018) Irregularity detection in clinical data of patients encountering heart surgery 7:331–339

10. Xinghua S, Cao J, Lu T, Chang V (2019) A survey on RFID security and privacy in smart medical: threats and protections, pp 278–285. https://doi.org/10.5220/0007713402780285

11. Ng HS, Sim ML, Tan CM (2006) Security issues of wireless sensor networks in healthcare applications. BT Technol J 24:138–144. https://doi.org/10.1007/s10550-006-0051-8

12. Sun Y, Lo FP, Lo B (2019) Security and privacy for the internet of medical things enabled healthcare systems: a survey. In: IEEE Access 7:183339–183355. https://doi.org/10.1109/ACCESS.2019.2960617

13. Rushanan M, Rubin AD, Kune DF, Swanson CM (2014) SoK: security and privacy in implantable medical devices and body area networks. In: 2014 IEEE symposium on security and privacy, San Jose, CA, 2014, pp 524–539. https://doi.org/10.1109/SP.2014.40

14. Yan R, Xu T, Potkonjak M (2014) Semantic attacks on wireless medical devices. SENSORS, 2014 IEEE, Valencia, Spain, pp 482–485. https://doi.org/10.1109/ICSENS.2014.6985040.

15. Hassija V, Chamola V, Bajpai BC, Naren SZ (2021) Security issues in implantable medical devices: fact or fiction? Sustain Cities Soc 66:102552. ISSN 2210-6707. https://doi.org/10.1016/j.scs.2020.102552

16. Rehman U, Rehman M, Khan H, Zeashan H (2020) Cyber-attacks on medical implants: a case study of Cardiac Pacemaker vulnerability. IJCDS J 9. https://doi.org/10.12785/ijcds/0906020.

17. Hei X, Du X (2013) Emerging security issues in wireless implantable medical devices. Springer

18. Newaz AI, Sikder AK, Rahman MA, Uluagac AS (2021) A survey on security and privacy issues in modern healthcare systems: attacks and defenses. ACM Trans Comput Healthcare 2(3), Article 27 (July 2021), 44p. https://doi.org/10.1145/3453176

19. Ren Y, Werner R, Pazzi N, Boukerche A (2010) Monitoring patients via a secure and mobile healthcare system. IEEE Wirel Commun 17(1):59–65. https://doi.org/10.1109/MWC.2010.5416351

20. Oza P, Kathrecha, Malvi P (2016) Encryption algorithm using Rubik's cube principle for secure transmission of multimedia files. In: Third international conference on multidisciplinary research and practice IJRSI 4:239–243

21. Patel N, Oza P, Agrawal S (2019) Homomorphic cryptography and its applications in various domains. In: Bhattacharyya S, Hassanien A, Gupta D, Khanna A, Pan I (eds) International conference on innovative computing and communications. Lecture notes in networks and systems, vol 55. Springer, Singapore. https://doi.org/10.1007/978-981-13-2324-9_27

22. Shah Y, Joshi S, Oza P, Agrawal S (2019) An insight of information security: a skeleton. Int J Recent Technol Eng 8(3):2600–2605

23. Yaqoob T, Abbas H, Atiquzzaman M (2019) Security vulnerabilities, attacks, countermeasures, and regulations of networked medical devices—a review. IEEE Commun Surv Tutor 21(4):3723–3768
24. Qiu H, Qiu M, Liu M, Memmi G (2020) Secure health data sharing for medical cyber-physical systems for the healthcare 4.0. IEEE J Biomed Health Inform 24(9):2499–2505. https://doi.org/10.1109/JBHI.2020.2973467
25. Pirbhulal S, Wu W, Li G (2018) A Biometric security model for wearable healthcare. In: 2018 IEEE international conference on data mining workshops (ICDMW), Singapore. pp 136–143. https://doi.org/10.1109/ICDMW.2018.00026
26. Liang Y, Zhou X, Yu Z et al (2014) Energy-efficient motion related activity recognition on mobile devices for pervasive healthcare. Mobile Netw Appl 19:303–317. https://doi.org/10.1007/s11036-013-0448-9

Trans-QZS Inverter for PV-Based Energy Conversion System

Arvind Yadav and Subhash Chandra

Abstract Traditional voltage source inverter (VSI) suffers from the voltage boost ability, thus are not appropriate for low-voltage producing sources. The magnetically coupled impedance source inverter (transformer based) is more appropriate for photovoltaic applications due to unconventional high boost ability. This paper presents the trans-qzs inverter for photovoltaic-based energy conversion systems; the performance of the inverter is compared with the transformer-based and non-transformer-based impedance source inverter. Various factors are considered for the comparison of different topology, and the effect of leakage inductance on converter is also visible. Results show the acclaimed performance of the trans-qzs inverter for PV applications.

Keywords Trans-qzs inverter · Photovoltaic · High boost · Voltage source inverter · Single-stage converter

1 Introduction

In the last decade, renewable energy generation has got world wide acclamation as it serves a solution to increasing energy demand; some of the promising renewable energy sources are photovoltaic (PV), wind, micro-hydro, geothermal, biomass, ocean waves and tides; output produced by some of the renewable sources is very low and thus required an intermediate converter for boosting and conditioning of input before feeding it to load. Single-stage topology is preferred over two-stage topology for an intermediate converter for various advantages [1, 2]. The drawbacks of two-stage topology were the decreased efficiency and increased cost; also, different controllers are to be employed for every stage. Many single-stage topologies

A. Yadav (✉) · S. Chandra
Department of Electrical Engineering, GLA University, Mathura, Uttar Pradesh 281004, India
e-mail: arvindyadavpec@gmail.com

S. Chandra
e-mail: subhash.chandra@gla.ac.in
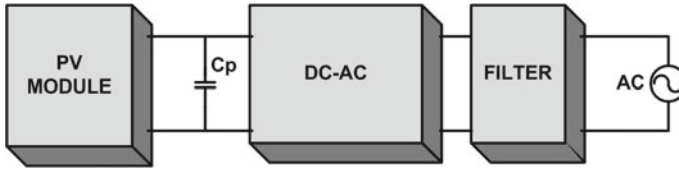
Fig. 1 Block diagram for a single-stage power converter

are derived; these proposed solutions have achieved reduced power stages, reduced components, high-power density with reduced cost [3–5]. Figure 1 shows the single-stage topology block diagram, where a PV module can be connected directly to a DC-AC converter avoiding a boost converter and transformer. The overall size and cost are reduced with increased power density. The Z-source inverter (ZSI) possesses the above characteristics and is suitable for low-power renewable energy sources; ZSI uses reduced number of components, can operate in buck boost mode, transfer energy via a single-stage power conversion [6, 7].

Magnetically coupled impedance source networks are different then conventional impedance source networks as they uses coupled winding or inductor; major topologies reported use either two or three coupled winding or inductors; they are different from each other in terms of the active and passive component used in that impedance network. MCIS network is capable of high boost at low shoot-through duty ratio (D_{ST}), uses lesser number of components for same features than non-transformer-based topologies, and has high-power density [8–10]. So far MCIS network is more versatile as they gives more design choices, more combination of control parameters are possible; high-power density will low core size thus improved efficiency.

2 T Source or Trans-Z Source Impedance Network

The network configuration of trans-qzs inverter impedance network is shown in Fig. 2; it consists of a coupled inductor, two capacitors (C_1, C_2), a diode (D), and an inductor (L_3). The impedance network has the unique ability of providing high boost as the inverter utilizes the shoot-through state. Theoretically, the gain can be infinite, however will pose high voltage stress and can lead to low modulation index; thus, a practical range is only considered for voltage boost.

2.1 Operating Principle

Trans-qzs inverter utilizes the additional shoot-through state other than the six active states and two zero states. The power is fed from source to load via a single-stage power conversion. The operating principle can be explained with help of two operat-
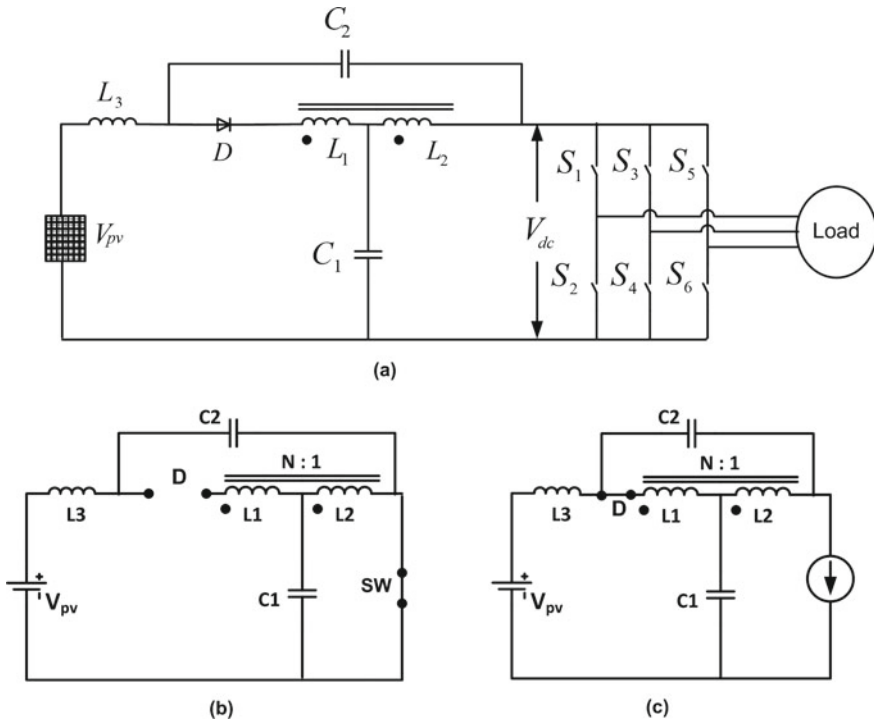
Fig. 2 Circuit configuration showing, **a** Trans-qzs inverter connected system, **b** operating mode I, **c** operating mode II

ing modes. Many modulation techniques are available for ZSI in literature [5, 11–13]; here, simple boost modulation technique is used here; three sinusoidal modulating signal, triangular carrier wave, and two shoot-through envelopes (V_p, V_n) are utilized in the simple boost technique as shown in Fig. 3.

Mode I: In this mode, the trans-qzs inverter utilizes the shoot-through state; the equivalent circuit configuration for the operating mode is shown in Fig. 2. Here, the upper and lower switches of inverter leg(s) are short-circuited; diode is open-circuited, and this state is represented by an equivalent switch (SW). The various switching states for the trans-qzs inverter are shown in Table 1. Energy transferred to the load is zero, where as it is stored in the passive elements, thus

$$V_{L2} = V_{C1} \tag{1}$$

$$V_{L1} = N V_{L2} = N V_{C1} \tag{2}$$

$$V_{L3} = V_{pv} + V_{C2} \tag{3}$$

Table 1 Shoot-through zero states for q-ZSI

Switching state	Conducting switches
S_{TH1}	S_1, S_2
S_{TH2}	S_3, S_4
S_{TH3}	S_5, S_6
S_{TH4}	S_1, S_2, S_3, S_4
S_{TH5}	S_1, S_2, S_5, S_6
S_{TH6}	S_3, S_4, S_5, S_6
S_{TH7}	S_1, S_2, S_3, S_4, S_5, S_6
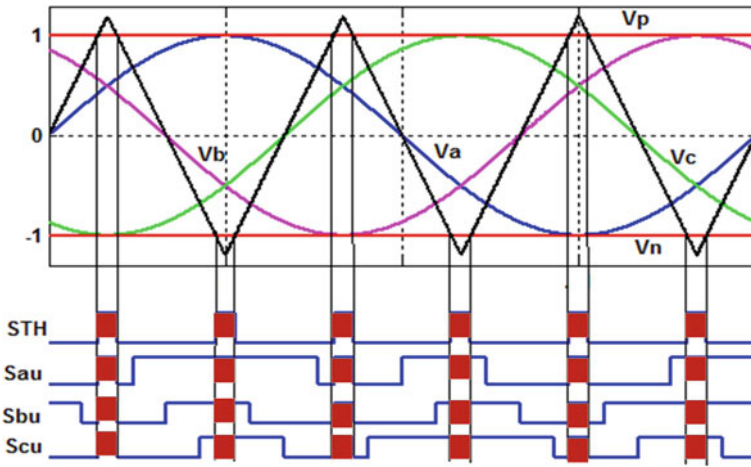
Fig. 3 Simple boost modulation scheme

Mode II: In this mode, the trans-qzs inverter utilizes the six active state and two zero state as that of conventional VSI; the circuit configuration for the same is shown in Fig. 2. Here, diode is active, and the power from the source along with the stored energy in passive components is delivered to the load, thus

$$V_{L1} + V_{L2} = -V_{C2} \tag{4}$$

$$V_{L3} = V_{pv} - V_{C1} - V_{L1} \tag{5}$$

$$V_{dc} = V_{C1} - V_{L2} \tag{6}$$

Voltages at the coupled inductor can be calculated by applying volt-second balance to L_1 and L_2, Eqs. (1) and (2) yield
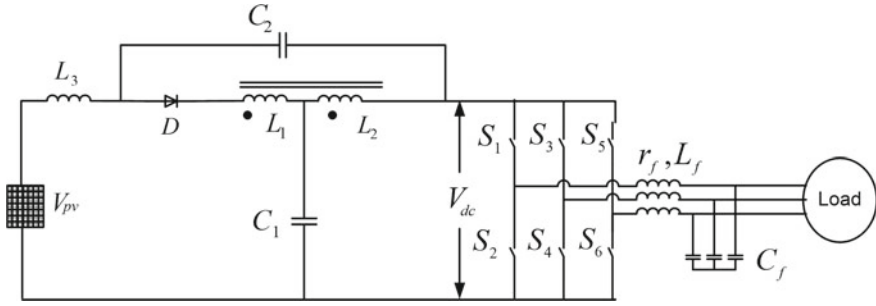
Fig. 4 System configuration of Trans-qzs inverter for PV-based energy conversion system

$$\begin{cases} V_{L1} = \dfrac{-ND_{ST}}{1 - D_{ST}}V_{C1} \\ V_{L2} = \dfrac{-D_{ST}}{1 - D_{ST}}V_{C1} \end{cases} \tag{7}$$

Substituting Eqs. (7) into (4), we have

$$\begin{cases} V_{C1} = \dfrac{1 - D_{ST}}{1 - (2 + N)D_{ST}}V_{pv} \\ V_{C2} = \dfrac{(1 + N)D_{ST}}{1 - (2 + N)D_{ST}}V_{PV} \end{cases} \tag{8}$$

Peak DC-link voltage at the trans-qzs inverter expressed in Eq. (6) can be rewritten as in Eq. (9), where D_{ST} is the shoot-through duty ratio and B is the boosting factor.

$$V_{dc} = \dfrac{1}{1 - (2 + N)D_{ST}}V_{pv} = BV_{pv} \tag{9}$$

3 Comparative Analysis for PV Applications

An intermediate power converter is essential when a PV module is used, as conditioning and boosting are required. The system layout of PV-assisted energy conversion system is shown in Fig. 4, where a suitable impedance network can be integrated between source and VSI; here, trans-qzs inverter is considered. Trans-qzs inverter is derived from the conventional qzs inverter topology, where an inductor is replaced by a magnetic core transformer with turn ratio $N : 1$. They have higher boost capabilities, draw continuous current from the source, suppress high starting inrush current, and provide resonant current suppression.
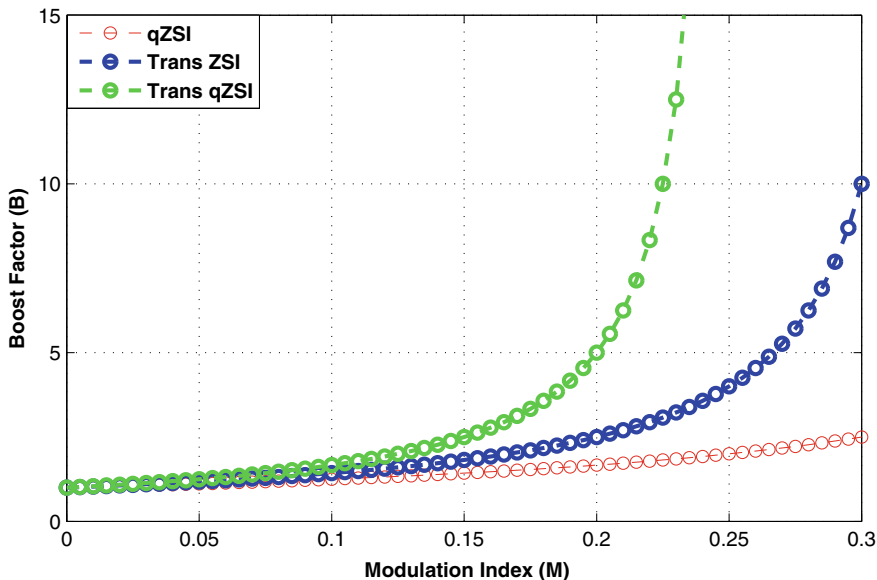
Fig. 5 Voltage boost ability of qZSI, Trans-ZSI, and Trans-qZSI

Peak DC-link voltage for qZS inverter is given in Eq. (10), where as for trans-z-source inverter is given in Eq. (12) where B_q and B_t are boosting factor for qZS and trans-z-source inverter as given in Eqs. (11) and (13), respectively. T_{ST} and T are shoot-through state time interval and switching time interval, respectively, and D_{ST} is shoot-through duty ratio.

$$V_{dc} = \frac{1}{1 - 2D_{ST}} V_{pv} = B_q V_{pv} \tag{10}$$

$$B_q = \frac{1}{1 - 2D_{ST}} = \frac{1}{1 - 2\left(\dfrac{T_{ST}}{T}\right)} \tag{11}$$

$$V_{dc} = \frac{1}{1 - (2 + N)D_{ST}} V_{pv} = B_t V_{pv} \tag{12}$$

$$B_t = \frac{1}{1 - (2 + N)D_{ST}} = \frac{1}{1 - (2 + N)(\dfrac{T_{ST}}{T})} \tag{13}$$

The voltage boost capability of trans-qzs inverter is superior compared to qzs inverter and trans-zsi; boosting factor for the different transformer-based and non-

Table 2 Comparison of qZSI, Trans-ZSI, and Trans-qZSI impedance network topology

	qZSI	Trans-ZSI	Trans-qZSI
Boost factor	$(1 - 2d_{st})^{-1}$	$(1 - (1 + N)d_{st})^{-1}$	$(1 - (2 + N)d_{st})^{-1}$
Component used			
capacitor	2	1	2
Inductor	2	–	1
Coupled inductor	–	2	2
Diode	1	1	1
Current drawn from source	Continuous, highly rippled	Discontinuous	Continuous
Draws inrush current	No	Yes	No
Comment	First modified ZSI, lower voltage stress for same voltage gain, reduced component rating	Higher gain, reduced component, LC i/p filter to suppress high inrush current	Highest gain, reduced component count (trans-zsi/qzsi with LC i/p filter)

transformer-based topology is plotted in Fig. 5. The voltage boost ability increases at a rapid pace compared to the counterparts can be inferred from the increased gap in the curves of Fig. 5 with increasing modulation index. Table 2 compares the different transformer-based and non-transformer-based topology's.

4 Results and Discussion

PV-assisted energy conversion system can be cost-effective with an appropriate intermediate power converter, which can reduce the number of PV modules for the same application by producing high boost output. In this study, a 96-cell PV module is used as an input source to the trans-qzs inverter system and the system configuration parameters are given in Table 3. The trans-qzs inverter has one additional control parameter (turn ratio) compared to qzs inverter; thus, high output voltage can be achieved with an appropriate combination of coupled inductor turn ratio (N), shoot-through duty ratio (D_{ST}), and modulation index (M).

As the inverter is considered as harmonic generator, therefore, a first-order filter is used between inverter and load. The output voltage of the PV module is 85 V under normal solar irradiance; the power is transferred to a 500 W inductive load using trans-qzs inverter. With turn ratio 1, trans-zsi will boost the voltage with same factor as that of qzs inverter, where as trans-qzsi boost factor will be highest among them. As the modulation index and shoot-through duty ratio are mutually restricted, then the turn ratio can be increased to get the desired DC-link voltage. With constant N, an increase in D_{ST} will increase the DC-link voltage, and with constant D_{ST}, an

Table 3 System configuration parameters

Elements	Parameter	Value
Trans-qZS inverter	Inductance (L_3)	390 µH
	Capacitance (C_1, C_2)	280 µF
	Transformer coil inductance	220 µH
	Switching frequency	20 kHz
LC filter	inverter side inductance (L_f, r_f)	1.3 mH, 0.1 Ω
	Filter capacitance (C_f)	7.5 µF
Load	Line frequency	50 Hz
	Nominal power	500 W
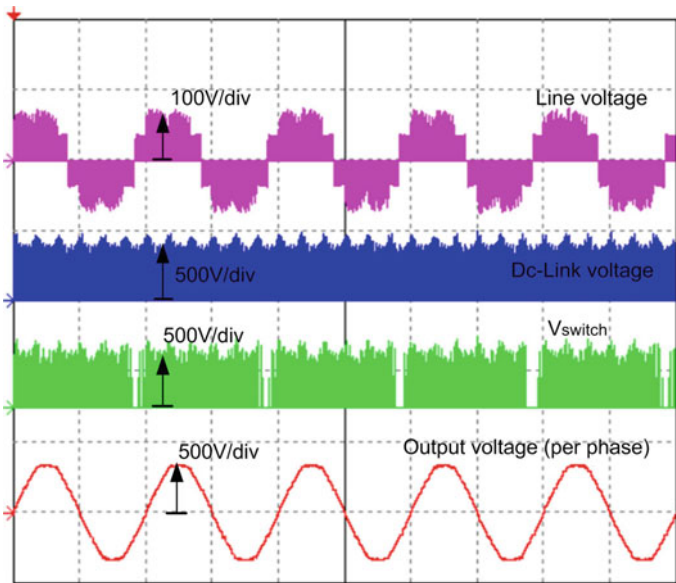
Fig. 6 Captured waveforms showing (top to bottom), V_{Line}, V_{dc}, V_{switch}, V_{o}

increase in N will also increase the DC-link voltage. Low modulation index range can be avoided be selecting low D_{ST} (Table 3).

For a 96-cell PV module, the output voltage obtained at the input of impedance network is 85 V, without utilizing the shoot-through state 34 V can be obtained with 0.8 modulation index. However, with $N = 2$, and $D_{\text{ST}} = 0.2$, the peak DC-link voltage obtained is 425 V. The output of inverter is full of harmonics, hence can not be used in the same form for an AC load; thus, a first-order filter is utilized to condition the output voltage. The peak DC-link voltage (V_{dc}) is 425 V; peak line voltage at inverter output (V_i) is 350 V; voltage across a switch is 425 V, and the output voltage at load side (V_{o}) is 170 V as shown in Fig. 6. The spikes in the peak DC-link voltage are due
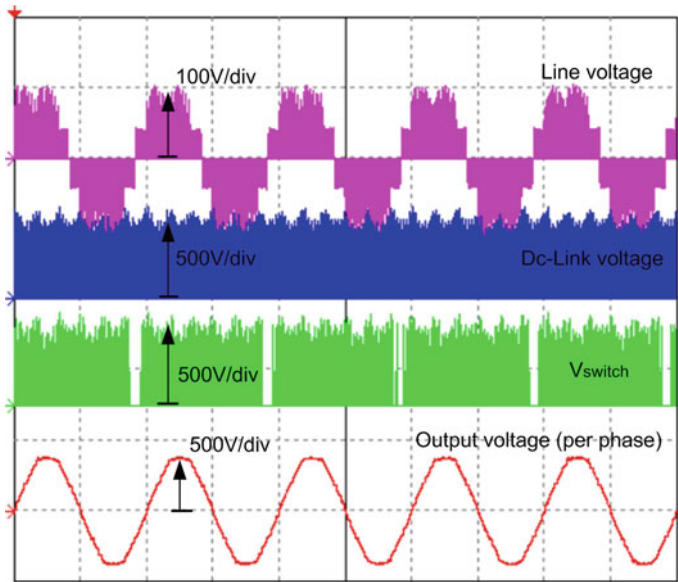
Fig. 7 Captured waveforms showing (top to bottom), V_{Line}, V_{dc}, V_{switch}, V_{o}

to the leakage inductance effect; thus, a tight coupling in coupled winding can ensure the acclaimed performance of the inverter; thus, a high value of leakage inductance can deteriorate the performance of trans-qzs inverter. Whereas, for $N = 2$, and D_{ST} = 0.22 the peak DC-link voltage (V_{dc}) is 705 V, peak line voltage at inverter output (V_i) is 535 V; voltage across a switch is 705 V, and the line voltage at load side (V_{o}) is 279 V as shown in Fig. 7. The THD level of output voltage and current is as per the IEEE std. 1547.

5 Conclusion

This paper presents the trans-qzs inverter for PV applications. The operating modes are described for the system configuration; a comparative assessment of the topology with transformer-based and non-transformer-based impedance source inverter is also presented. The voltage boost ability of the configuration is elaborated for a constant turn ratio, whereas the shoot-through duty ratio is kept variable. The results show the acclaimed performance of the trans-qzs inverter system for PV application; however, the spikes in the peak DC-link voltage depict the effect of leakage inductance on the output voltage; thus, a loose coupling in the coupled inductor can deteriorate the performance of the inverter.

References

1. Anand I, Senthilkumar S, Biswas D, Kaliamoorthy M (2018) Dynamic power management system employing a single-stage power converter for standalone solar PV applications. IEEE Trans Power Electron 33(12):10352–10362
2. Umaz R (2020) Design of a single-stage power converter operating in burst and continuous modes for low-power energy sources. IEEE Trans Circ Syst II: Express Briefs 68(1):421–425
3. Liu H, Ji Y, Wang L, Wheeler P (2017) A family of improved magnetically coupled impedance network boost DC-DC converters. IEEE Trans Power Electron 33(5):3697–3702
4. Loh PC, Blaabjerg F (2013) Magnetically coupled impedance-source inverters. IEEE Trans Ind Appl 49(5):2177–2187
5. Siwakoti YP, Peng FZ, Blaabjerg F, Loh PC, Town GE, Yang S (2014) Impedance-source networks for electric power conversion part II: review of control and modulation techniques. IEEE Trans Power Electron 30(4):1887–1906
6. Yadav A, Chandra S, Deolia V, Agrawal S (2017) Z source inverter application and control for decentralized photovoltaic system. In 2017 3rd international conference on condition assessment techniques in electrical systems (CATCON). IEEE, pp 52–57
7. Yadav A, Chandra S (2020) Single stage high boost Quasi-Z-Source inverter for off-grid photovoltaic application. In: 2020 International conference on power electronics and IoT applications in renewable energy and its control (PARC). IEEE, pp 257–262
8. Qian W, Peng FZ, Cha H (2011) Trans-Z-source inverters. IEEE Trans Power Electron 26(12):3453–3463
9. Nguyen MK, Lim YC, Park SJ (2013) Improved trans-Z-source inverter with continuous input current and boost inversion capability. IEEE Trans Power Electron 28(10):4500–4510
10. Fang X, Ma B, Gao G, Gao L (2018) Three phase trans-quasi-Z-source inverter. CPSS Tran Power Electron Appl 3(3):223–231
11. Diab MS, Elserougi AA, Massoud AM, Abdel-Khalik AS, Ahmed S (2015) A pulse width modulation technique for high-voltage gain operation of three-phase Z-source inverters. IEEE J Emerg Select Top Power Electron 4(2):521–533
12. Bradaschia F, Cavalcanti MC, Ferraz PE, Neves FA, dos Santos EC, da Silva JH (2011) Modulation for three-phase transformerless Z-source inverter to reduce leakage currents in photovoltaic systems. IEEE Trans Ind Electron 58(12):5385–5395
13. Erginer V, Sarul MH (2013) A novel reduced leakage current modulation technique for Z-source inverter used in photovoltaic systems. IET Power Electron 7(3):496–502

Diminish Shading Effect Through Altering PV Module Connections in an Array Using Game Puzzles

Rupendra Kumar Pachauri, Amarnath Bose, Shashikant, and Ahmad Faiz Minai

Abstract Partial shading conditions (PSCs) and their degrading effects on solar photovoltaic (PV) systems have inspired researchers to search for ways to diminish the shadowing effects. To decrease the impact of PSCs, an overall study is proposed in this paper about different PV array arrangements for Solar PV systems and various game puzzles for shade dispersion efficiently. The various PV array configuration models studied in this paper are Total Cross-Tied (TCT) PV array configuration, and Latin Square-Total Cross Tied (LS-TCT) PV array configuration. Apart from these configurations, various game puzzle configurations have also been presented i.e. Su-do-Ku (SDK) and Shape-do-Ku (SPDK) puzzles based on PV array configurations. The values of various performance indices, such as open-circuit voltage, short-circuit current, maximum voltage, maximum current, power at global maximum power point (GMPP) and local maximum power point (LMPP), power loss (PL), and fill factor (FF) are found out through MATLAB/Simulink and experimental study. As a whole, the study of this paper is useful for academicians and researchers working in the field of solar energy.

Keywords Solar energy · Partial shading · Power losses · Game puzzle · Shade dispersion

R. K. Pachauri (✉) · A. Bose
Electrical and Electronics Engineering Department, School of Engineering, University of Petroleum and Energy, Dehradun 248007, India
e-mail: rpachauri@ddn.upes.ac.in

A. Bose
e-mail: abose@ddn.upes.ac.in

Shashikant
Electrical Engineering Department, School of Engineering, Babu Banarasi Das University, Lucknow 226068, India

A. F. Minai
Electrical Engineering Department, Integral University, Lucknow 226026, India

1 Introduction

Renewable energy (RE) sources are clean, inexhaustible, and different from non-renewable sources of energy in the point of view of their diversity and plenty of availability on Earth [1]. The most important advantage of renewable energy (RE) sources is that they neither emit greenhouse gases (which have adverse effects on our environment and climate), nor they generate any other polluting emissions. The costs for using RE are decreasing at economic rates, while the costs for using non-renewable sources of energy, such as fossil fuels are rising despite their inconsistent nature [2, 3].

Solar energy (SE) is a fully clean source of energy as it neither pollutes the air, nor does it contaminate the water. It is the most important factor due to the scarcity of water on our planet. The other advantages of SE are that using it in our households reduces the electricity bills, low maintenance costs, etc. The major problem associated with SE is the partial shadowing conditions [4]. PSCs occur due to various factors, such as moving clouds, high rise buildings, telecom towers, advertisement holdings, trees standing aside, dry leaves, dust aerosol, etc. An evaluation of some recent literature is carried out to find the research gap in the present work.

The effect of PSCs on PV arrays lowers the power output and causes several P-V peaks responsible. The losses caused by PSCs are not proportional to the shaded area, but to the shading pattern, the exhibit, and the physical placement of the shaded PV modules in a column. In this paper, a new way of modifying the electrical connections of the PV modules is presented in order to improve the power output during PSCs [5, 6].

1.1 *Literature Review*

A substantial literature review on the present PV models is done to analyze them, depending upon the network, modeling, output, scale, connectivity with the grid, etc. These PV array arrangements are exclusively categorized depending upon traditional, hybrid, rearranged, and puzzle-based advanced arrangements. In the puzzle-based arrangement, various game puzzle methods are put forward, and productivity is assessed. The productivity of these puzzle-based arrangements is obtained more efficiently compared to traditional arrangements.

In [7], the authors have performed to observe the effect of shading on I-V and P-V performance characteristics nature. The PV array system is configured in series and series-parallel (SP) based electrical connections during MATLAB/Simulation and experimental validation. Critical observation is carried out in terms of performance indices e. g. PL and current decrement, FF increment, etc. [8]. Comprehensive observations are carried out to show the effect of PSCs on various conventional TCT, SP, BL and HC configurations. Also, the results were assessed with regard to the lowest possible PL and the improved FF values. In [9] the SP configured PV system is

tested during experimentation to analyze the effect of shadowing conditions during outdoor and laboratory scenarios. Under the observations, the level of obfuscated sun irradiance is taken into account, and it was discovered that PV modules connected in parallel methods have higher efficiency. To diminish the shadowing effect on PV modules, the authors of [10–12] developed a switch matrix array to reconfigure the PV module interconnections. The research being focused based hardware analysis on Series, SP, and TCT interconnections of PV array. Using the Latin square (LS) puzzle, conventional TCT connections are modified and titled as LS-TCT configuration [13]. Four numbers of shading conditions (progressive behavior) were carried out for investigation. In addition, LS-TCT has the highest GMPP location at 2279, 2139, 1806, and 1680 W and improved FF by 9.91, 9.26, 7.85, and 7.30%. At the part of losses in power re found worst as 330 W, 470 W, 803 W, 929 W respectively for all four shading scenarios.

1.2 Novelty of Work

The efficacy of the PV system is increased with respect to power output, FF, and minimum PL. Following points are addressed herewith to show the novelty of work as,

- The conventional TCT configuration is compared with game puzzle based LS-TCT, SDK and SPDK configurations to show shadow effects on PV performance.
- Higher shade dispersion capability is found for LS-TCT configuration compared to other configurations under experimental and MATLAB/Simulation studies.
- The performance evaluation is investigated with respect to GMPP location, enhanced FF and decreased PL etc.
- The MATLAB/Simulation results are validated using an experimental study, which shows the interest towards hardware study for new learners.

2 Solar PV Technology

2.1 Modeling of PV Cell

PV cell is envisioned as a variable current source and parallel to photodiode–current (I_{ph}). It can be formulated as,

$$I_{ph} = (I_{SC} + K_i \Delta T)\left(\frac{S_x}{S_{STC}}\right)\left(\frac{R_{sh} + R_{se}}{R_{sh}}\right) \qquad (1)$$

where, R_{se} and R_{sh} are stands for series and shunt resistance. In addition, I_{SC} is given to express short circuit current. Solar standard test conditions (STC) and actual

Fig. 1 Electrical equivalent
circuit of a PV cell [5]
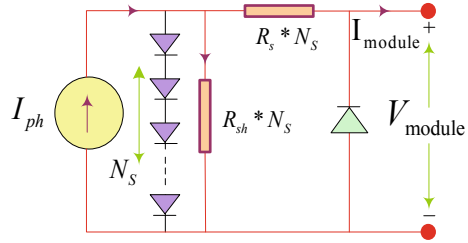
irradiances are presented as I_{SC} and S_x. K_i is represented to show cell temperature
coefficient [14, 15]. Actual temperature (T_x) and temperature at STC are used to
define the temperature difference as,

$$\Delta T = (T_x - T_{STC}) \tag{2}$$

PV module, equivalent PV cells and bypass diodes are interlinked to avoid any
damage due to hot-spot conditions under the shading effect. In Fig. 1, an equivalent
PV model is depicted [5]. The module current is evaluated and expressed in Eq. (3)
as,

$$
\begin{aligned}
I_{\text{mod}} = & \left\{ I_{\text{ph}} - I_o \left(e^{\frac{q(V_{\text{mod}} + R_s I_{pv})}{AKTN_s}} - 1 \right) - \frac{V_{\text{mod}} + R_s I_{pv}}{R_{sh} N_s} \right\} \\
& + \left\{ I_{\text{obypass}} \left(e^{\frac{-q(V_{\text{mod}})}{A_{\text{bypass}}}} - 1 \right) \right\}
\end{aligned}
\tag{3}
$$

where, A and I_o Ioare ideality factor and reverse saturation current. K: Stands for
Boltzmann constant (1.38×10^{-23} J/K) and T: temperature (K). Moreover, q: elec-
tron charge (1.6×10^{-19} °C) and output voltage of the module is represented as
V_{module}. To design a PV module, series connections of solar cells are represented as
N_s. $R_{S\text{-}mod}$ and $R_{sh\text{-}mod}$ are series and shunt module resistances respectively [18].

2.2 PV Array Configurations

(a) **Total cross-tied configuration**: The TCT model is achieved through the modi-
fication in the SP configured PV array system. The 4 × 4 size TCT array is
shown in Fig. 2.
(b) **LS-TCT configuration**: The LS game puzzle is utilized for altering the TCT
model and is entitled as LS-TCT configuration. In addition, the methodology is
given along with the LS-TCT configuration in Fig. 3a and b.
(c) **Su-do-Ku configuration**: The SDK based PV array model is made by taking
concepts of the famous SDK 'Number Place' puzzle which is done through
a 4 × 4 number matrix. Utilizing the rules on how to form a SDK puzzle, the

Fig. 2 TCT connection of modules in PV array
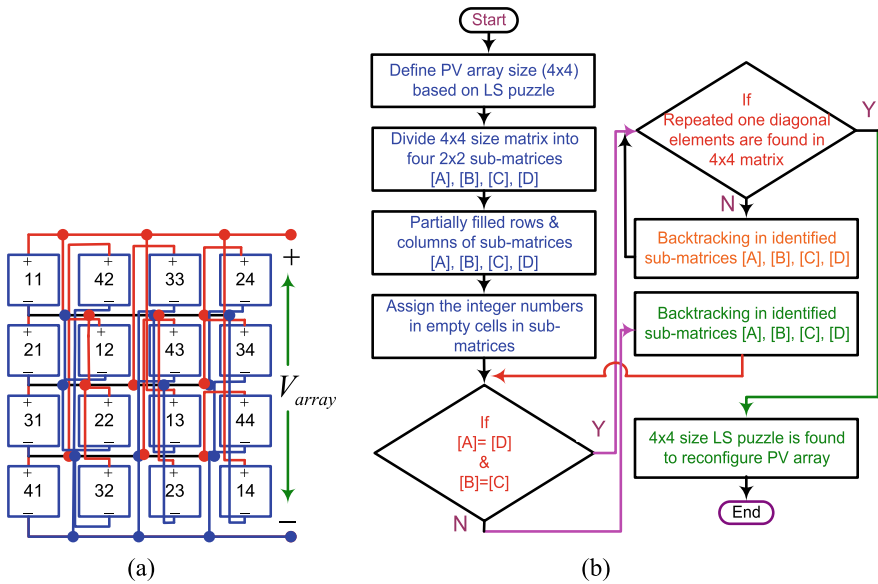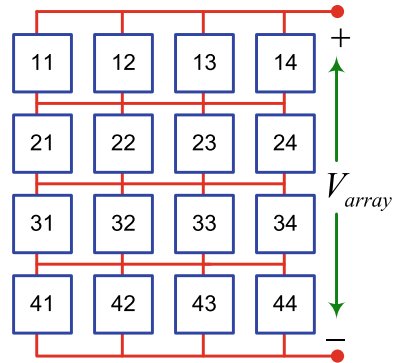
Fig. 3 **a** Module arrangement in LS-TCT configuration, **b** Methodology

values of every feasible grouping are noticed as uniformly dispersed throughout that matrix. The electrical connection of SDK configuration and methodology is given in Fig. 4a and b.

(d) **Shape-do-Ku configuration**: This SPDK configuration is an advance version of SDK configuration. The shading dispersion capability is higher than other game puzzle configurations. The PV module connections and methodology to achieve the SPDK based PV array configuration is shown in Fig. 5a and b as follows.
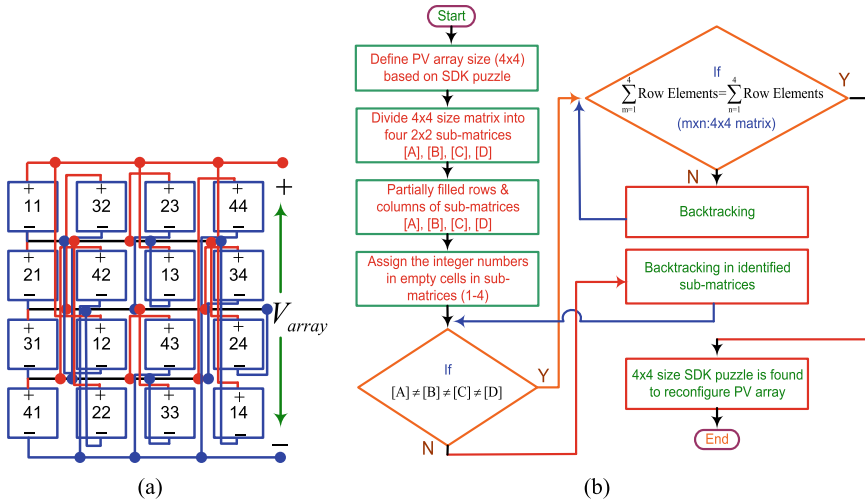
Fig. 4 **a** Module arrangement in SDK configuration, **b** Methodology
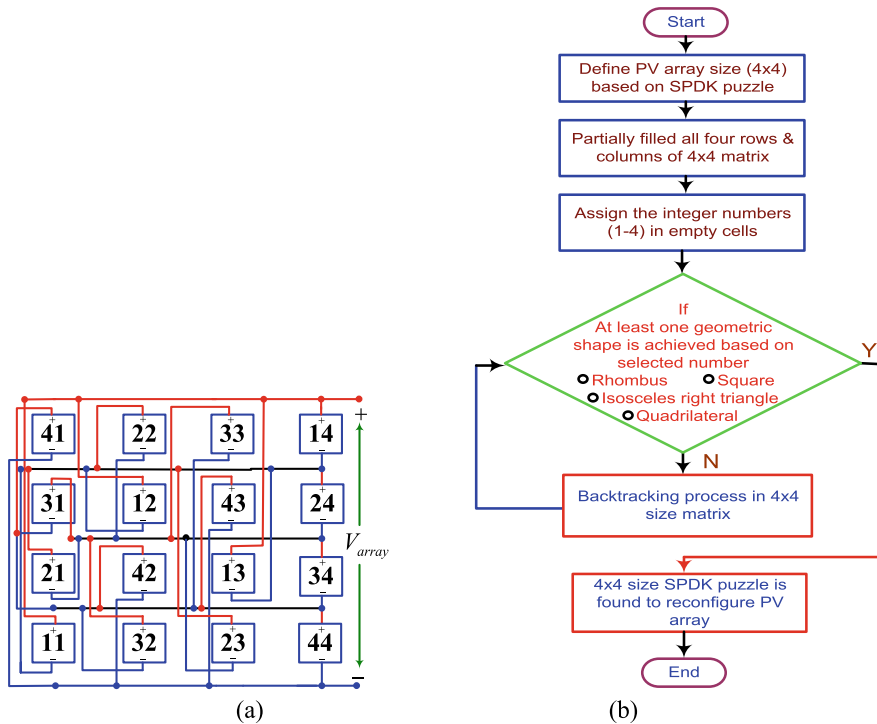
Fig. 5 **a** Module arrangement in SPDK configuration, **b** Methodology

3 Shading Scenarios and Performance Indices

For an extensive study of PSCs on considered PV array configurations such as TCT, LS-TCT, SDK and SPDK, the following two shading scenarios are considered and shown in Fig. 6a and b for performance analysis.

3.1 Global and Local MPP

It is observed that multiple power peaks are existed on P-V curves because of non-uniform shading conditions. Nearest/minimum power maxima and highest value of power maxim are called LMPP and GMPP respectively.

3.2 Misleading Power

Due to PSCs, the difference between power values at LMPP and GMPP are observed. The disadvantage condition of misleading power (ML) is observed during maximum power point tracking device.

$$ML \text{ power} = GMPP - LMPP \text{ under PSCs} \tag{4}$$

3.3 Power Loss and FF

Deviation between Maximum power at uniform irradiance and MPP at global point is responsive for power loss and expressed in Eq. (5). FF is the major performance index parameter to define the efficiency as well as easy to understand the PV performance in first perceptive and shown in Eq. (6) as,

Fig. 6 **a** and **b** PSCs for performance investigation of puzzle based PV array configurations
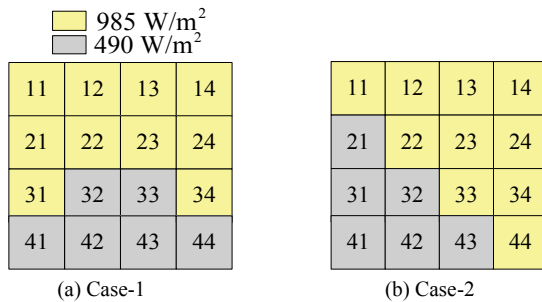
$$\text{PL} = \text{MPP at uniform} - \text{GMPP at PSCs} \tag{5}$$

$$\text{FF} = \frac{V_\text{m} \times I_\text{m}}{V_\text{OC} \times I_\text{SC}} \tag{6}$$

Theoretical analysis of the current calculation can be done with TCT, LS-TCT, SDK and SPDK configurations under shading cases 1–2. Current produced under shading cases 1–2 for TCT configuration in Eqs. (7-13) as follows,

Current produced for case-1

$$I_\text{r1} = I_\text{r2} = \left(\frac{985}{1000}\right)I_\text{m} + \left(\frac{985}{1000}\right)I_\text{m} + \left(\frac{985}{1000}\right)I_\text{m} + \left(\frac{985}{1000}\right)I_\text{m} \tag{7}$$

$$I_\text{r3} = \left(\frac{985}{1000}\right)I_\text{m} + \left(\frac{490}{1000}\right)I_\text{m} + \left(\frac{490}{1000}\right)I_\text{m} + \left(\frac{490}{1000}\right)I_\text{m} \tag{8}$$

$$I_\text{r4} = \left(\frac{490}{1000}\right)I_\text{m} + \left(\frac{490}{1000}\right)I_\text{m} + \left(\frac{490}{1000}\right)I_\text{m} + \left(\frac{490}{1000}\right)I_\text{m} \tag{9}$$

Current produced for case-2

$$I_\text{r1} = \left(\frac{985}{1000}\right)I_\text{m} + \left(\frac{985}{1000}\right)I_\text{m} + \left(\frac{985}{1000}\right)I_\text{m} + \left(\frac{985}{1000}\right)I_\text{m} \tag{10}$$

$$I_\text{r2} = \left(\frac{490}{1000}\right)I_\text{m} + \left(\frac{985}{1000}\right)I_\text{m} + \left(\frac{985}{1000}\right)I_\text{m} + \left(\frac{985}{1000}\right)I_\text{m} \tag{11}$$

$$I_\text{r3} = \left(\frac{490}{1000}\right)I_\text{m} + \left(\frac{490}{1000}\right)I_\text{m} + \left(\frac{985}{1000}\right)I_\text{m} + \left(\frac{985}{1000}\right)I_\text{m} \tag{12}$$

$$I_\text{r4} = \left(\frac{490}{1000}\right)I_\text{m} + \left(\frac{490}{1000}\right)I_\text{m} + \left(\frac{490}{1000}\right)I_\text{m} + \left(\frac{985}{1000}\right)I_m \tag{13}$$

4   Results and Discussion

4.1   *Analysis of P-V and I-V Curves Under Shading Case-1*

The performance evaluation is carried out to compare P-V and I-V curves under uniform and non-uniform conditions of sun irradiations such as 945 W/m^2 and 490 W/m^2 for shading cases 1–2 respectively. In uniform irradiance levels such as 945 W/m^2, , the maximum power point (MPP) is found as 80 W at a maximum
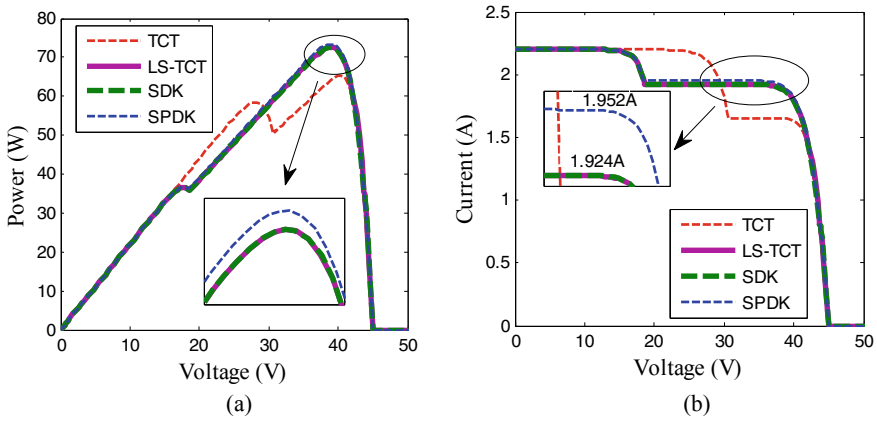
Fig. 7 **a** I-V, **b** P-V curves under shading case-1

voltage of 38.9 V. In shading cases 1–2, the observation on behavior of I-V and P-V curves is carried out to investigate the performance indices such as open circuit voltage (V_{OC}), short circuit current (I_{SC}), and GMPP locations.

During shading case-1, the values of I_{SC} for all the PV array configurations such as TCT, LS-TCT, SDK and SPDK are marked similar as 2.20 A. In addition, the values of V_{OC} are also found similar as 45.02 V. In addition, the values of V_{OC} are also obtained similar as 45.02 V for TCT, LS-TCT, SDK and SPDK configurations. It is observed that the GMPP location is found highest as 73.37 W for SPDK configuration under shading scenario-1 compared to TCT, SDK and SPDK configurations as similar value of 72.5 W. The effect of shading case-2 is shown on P-V and I-V curves, which are depicted in Fig. 7a and b as follows,

4.2 Analysis of P-V and I-V Curves Under Shading Case-2

Furthermore, the impact of shading case-2 is shown in highly non-linear conditions as observed in P-V curves behavior. In the aspect of performance parameters, the values of I_{SC} for all the PV array configurations such as TCT, LS-TCT, SDK and SPDK are marked similar as 1.92 A, 1.90 A, 1.92 A and 1.649 A respectively. In addition, the values of V_{OC} are also found similar as 45.03 V. The GMPP location is found highest as 55.59 W in the case of SPDK as compared to TCT (41.36 W), LS-TCT (47.95 W) and SDK (52.36 W) respectively. The impact of shading case-2 on P-V and I-V curves is shown in Fig. 8a and b as follows,
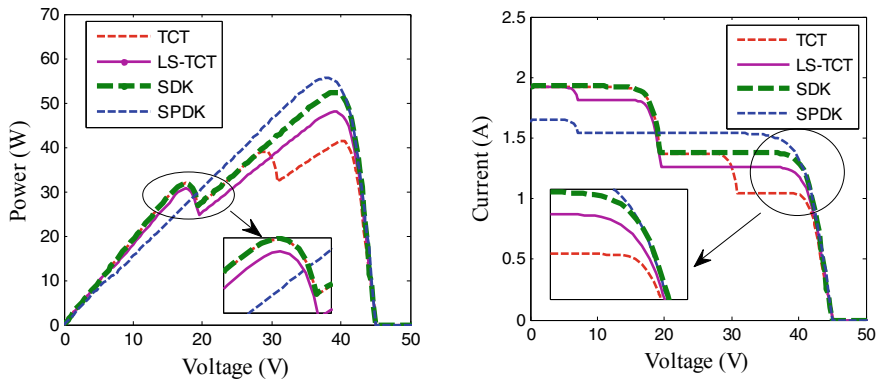
Fig. 8 **a** I-V, **b** P-V curves under shading case-2

Fig. 9 Power at GMPP
comparison
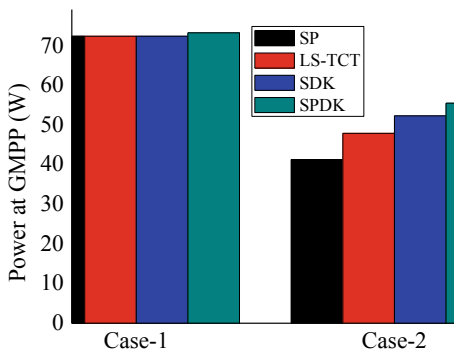
4.3 Power at GMPP

During the investigation of PV array systems under shading case 1, the highest GMPP
value is observed as 73.37 W, for SPDK configuration compared to other GMPP
locations as 72.5 W, 72.5 W and 72.5 W for TCT, LS-TCT and SDK configurations
respectively. Moreover, under shading case-2, the GMPP location for SPDK is found
highest as 55.59 W compared to TCT (41.36 W), LS-TCT (47.95 W) and SDK
(52.36 W) configurations. The power at GMPP is shown in Fig. 9.

4.4 Power Loss

PL calculation is performed to show statistical presentation using Fig. 10. In shading
case-1, power loss for SPDK configuration is found lowest (6.63 W) compared to
other PV array electrical arrangements i.e. LS-TCT, SDK and SPDK puzzle based.

Fig. 10 Power loss analysis
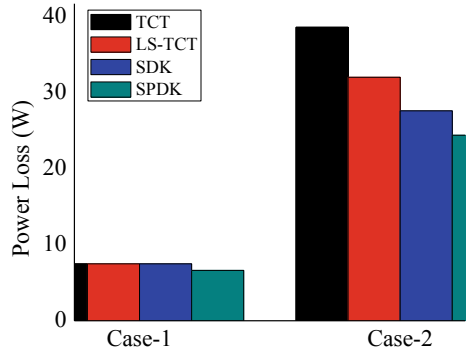
For further investigation during shading case-2, the power loss is found lowest as 24.41 W compared to LS-TCT (38.64 W), SDK (32.05 W) and SPDK (27.64 W) configurations respectively.

4.5 Fill Factor

The main performance parameters such as V_{OC}, I_{SC}, V_m, and I_m are responsible to calculate the FF under shading scenarios. The FF values are investigated highest as 0.740 and 0.748 for shading cases 1–2 respectively for SPDK configuration compared to other configurations. Quantitative observations of FF are depicted in Fig. 11 as follows,

The quantitative analysis of work was carried out to investigate the PV system performance with different PV module interconnections under shading scenarios. The performance indices are depicted in Table 1 as follows,

Fig. 11 Bar chart representation of FF
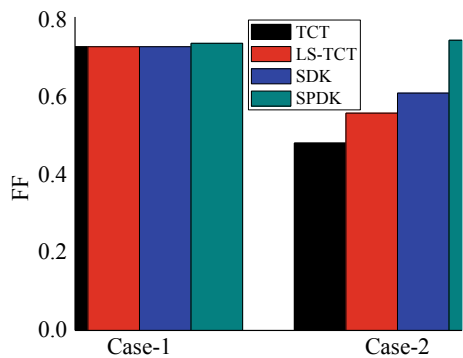
Table 1 Quantitative analysis of performance parameters under investigation

Performance parameters	Case-1				Case-2			
	TCT	LS-TCT	SDK	SPDK	TCT	LS-TCT	SDK	SPDK
$V_{OC}(V)$	45.02	45.02	45.02	45.02	45.03	45.03	45.03	45.03
$I_{SC}(A)$	2.20	2.20	2.20	2.20	1.92	1.90	1.92	1.649
$V_m(V)$	38.89	38.89	38.89	39.06	40.14	38.95	38.91	37.72
$I_m(A)$	1.864	1.864	1.864	1.878	1.030	1.231	1.345	1.473
$P_{GMPP}(V)$	72.5	72.5	72.5	73.37	41.36	47.95	52.36	55.59
PL(W)	7.5	7.5	7.5	6.63	38.64	32.05	27.64	24.41
FF	0.731	0.731	0.731	0.740	0.483	0.560	0.611	0.748

5 Conclusion

In this study, 4×4 size LS, SDK and SPDK puzzle based configurations have been investigated and compared under shading scenarios 1 and 2. During the investigation, the performance indices such as GMPP, PL and FF by using MATLAB/Simulink environment was done. Extensive observations have been carried out on SPDK puzzle based PV configuration arrangements, lowest PL and improved FF, to prove the superiority. Following salient points about the study are as follows,

- The higher GMPP locations under shading cases 1–2 are found 73.37 W and 55.59 W respectively compared to TCT, LS-TCT and SDK configurations.
- In SPDK configuration, the PL is quite less viz. 6.63 and 24.41 W compared to TCT (7.5 and 38.64 W), LS-TCT (7.5 and 32.05 W) and SDK (7.5 and 27.64 W) configurations under shading scenarios.
- In addition, the improved FF is also found as 0.740 and 0.748 for SPDK configuration compared to other PV array configurations under shading cases 1–2.
- Overall, SPDK puzzle based configuration improved the performance of the PV array system in terms of highest GMPP, minimized PL and raised FF compared to conventional TCT and most preferred SDK and LS-TCT configurations.

References

1. Pachauri RK, Mahela OP, Sharma A, Bai J, Chauhan YK, Khan B, Alhelou HH (2020) Impact of partial shading on various PV array configurations and different modeling approaches: a comprehensive review. IEEE Access 8:181375–181403
2. Pachauri RK, Chauhan YK (2014) Hybrid PV/FC stand-alone green power generation: a perspective for Indian rural telecommunication systems. In: Proceedings of IEEE international conference on issues and challenges in intelligent computing techniques, pp 802–810

3. Bhadoria VS, Pachauri RK, Tiwari S, Jaiswal SP, Alhelou HH (2020) Investigation of different BPD placement topologies for shaded modules in a series-parallel configured PV array. IEEE Access 8:216911–216921
4. Tao Y, Bai J, Pachauri RK, Sharma A (2020) Parameter extraction of photovoltaic modules using a heuristic iterative algorithm. Energ Convers Manage 224:1–18
5. Pachauri RK, Mahela OP, Khan B, Kumar A, Agarwal S, Alhelou HH, Bai J (2021) Development of arduino assisted data acquisition system for solar photovoltaic array characterization under partial shading conditions. Comput Electr Eng 92:1–12
6. Bai J, Sun L, Pachauri RK, Wang G (2021) Investigate on photovoltaic array modeling and the MPPT control method under partial shading conditions. Int J Photo Energ 2021:1–16
7. Patel H, Agarwal V (2008) MATLAB-based modelling to study the effects of partial shading on PV array characteristics. IEEE Trans Energ Convers 23(1):302–310
8. Karatepe E, Boztepe M, Çolak M (2007) Development of a suitable model for characterizing photovoltaic arrays with shaded solar cells. Sol Energ 81(8):977–992
9. Gao L, Dougal RA, Liu S, Iotova AP (2009) Parallel-connected Solar PV system to address partial and rapidly fluctuating shadow conditions. IEEE Trans Ind Electron 56(5):1548–1556
10. Nguyen D, Lehman B (2008) An adaptive solar photovoltaic array using model-based reconfiguration algorithm. IEEE Trans Ind Electron 55(7):2644–2654
11. Chaaban MA, Alahmad M, Neal J, Shi J, Berryman C, Cho, Y, Lau S, Schwer A, Shen Z, Stansbury J, Zhang T (2010) Adaptive photo-voltaic system. In: Proceedings of IEEE Conference Industrial Electronics Safety, pp 3192–3197
12. Quesada GV, Gispert FG, Lopez RP, Lumbreras MR, Roca AC (2009) Electrical PV array reconfiguration strategy for energy extraction improvement in grid connected PV systems. IEEE Trans Ind Electron 56(11):4319–4331
13. Pachauri R, Yadav AS, Chauhan YK, Sharma A, Kumar V (2018) Shade dispersion-based photovoltaic array configurations for performance enhancement under partial shading conditions. Int Trans Electr Energ Syst 28(7):1–32
14. Pachauri RK, Bai J, Kansal I, Mahela A, Khan B (2021) Shade dispersion methodologies for performance improvement of classical total-cross-tied photovoltaic array configuration under partial shading conditions. IET Renew Power Gener 10:1–16
15. Pachauri RK, Alhelou HH, Bai J, Golshan MEH (2021) Adaptive switch matrix for PV module connections to avoid permanent cross-tied link in PV array system under non-uniform irradiations. IEEE Access 9:45978–45992

A Fuzzy-Based Approach for Short Term Load Forecasting

Papia Ray and K. R. Satyajit

Abstract This paper proposes the development of a unique method of load forecasting. An essential factor in planning for developing counties in today's world is Load Forecasting (LF). In developing countries, a vast amount of power loss occurs in the generation, transmission and distribution, which is due to unpredictable load forecasting on a day-to-day basis. So, predicting accurate load forecasting has become a significant part of dropping the generation cost and optimizing the spinning reserve capability. The LF is done for managing power system energy. Earlier, many methods, Regression and Time Series, were used to forecast Load, but nowadays, intelligent methods like Fuzzy Logic (FL) are in practice, giving better forecasting accuracy. Here the presented technique for Load forecasting is FL using Mamdani Implication. From the simulation results, it has been noticed that the proposed FL-based load forecasting gives minor errors. Further, MATLAB and Simulink, Fuzzy Logic Toolbox and triangular membership function are used to obtain the forecasted load.

Keywords Load forecasting · Fuzzy logic · Actual percentage error (APE) · Mean absolute percentage error (MAPE) · Membership function

1 Introduction

Transmission of reliable power to customers is the prime duty of any utility. Consumer load demand in electric distribution systems varies because of person-to-person activities that follow daily cycles. During daylight, especially in the afternoon, the load demand is generally high due to industries and lighting. On the contrary, the demand is lesser in the evening and early morning. Load forecasting (LF) is like weather forecasting, as weather experts tell us about the weather conditions in the upcoming future [1]. Load forecasting allows the future estimation of load conditions, and power system planning can be done in the future. The energy requirement of the

P. Ray (✉) · K. R. Satyajit
Department of Electrical Engineering, Veer Surendra Sai University of Technology, Burla, Sambalpur, Odisha, India
e-mail: papiaray_ee@vssut.ac.in

clients varies each minute because of human activities that are not the same all day [2]. Thus, a significant priority for estimation of load demand is required in the future, and LF, therefore, plays a vital part in scheduling, operation and control of electrical power systems [3]. It approximates the variable(s) of the forecasted value at a future point in time. This paper mainly focuses on FL-based short term load forecasting (STLF) [4].

1.1 Literature Review

Balancing a power system is mostly done a day ahead of forecasted values given on the side of demand [5]. In nature, several types of loads make the performance highly nonlinear, which is quite dissimilar from the nonlinearity of the power system; then comes the fault due to which the system increases the price [6]. The methods used are based on regression analysis, time analysis, artificial neural network (ANN), similar day method, fuzzy logic, etc. [7]. Neutral Networks is a prolonged convergence period and a poor capability to process a large amount of variable quantity at a time; on the other side, Fuzzy logic provides a medium for representing and processing data in linguistic standings that makes the systems easily understandable [8–10]. The fuzzy forecasting method has widely been considered for forecasting dynamic and nonlinear type data in the last decade [11, 12]. In [13]. use Mamdani implication to attempt fuzzy logic for STLF. The basic rule of Fuzzy is prepared based on time, temperature and similar previous day load. Forecasts focus on minimization of the error among the actual and forecasted values [14]. A fuzzy-based STLF method that uses Gaussian membership function, If–Then rules and fuzzy logic process and further reduces the forecasted error and the processing time [15]. A methodology on STLF contains functioning mechanisms under the different regimes of power segment in India [16]. It also demonstrates the effects of load and temperature on generation, transmission and distribution. Here load forecasting is processed by using the function of triangular membership. Also, weather parameters such as temperature can be used to predict the consumption of energy based on week/special days with a support vector machine and generic neural regression network [17].

From the above literature survey, it is concluded that LF plays a significant role in the economic operation of a power system. The conventional methods used for STLF are Multiple Linear Regression (MLR) and Time Series (TS). The significant disadvantages of the MLR method are that this model is susceptible to temperature fluctuations. It needs a very accurate temperature forecast, as a minute variation in temperature leads to a significant change in load prediction and that of the TS method is it is difficult to use and is time-consuming. This encourages the author to implement an intelligent scheme like FL, which is more effective and faster than the abovementioned schemes.
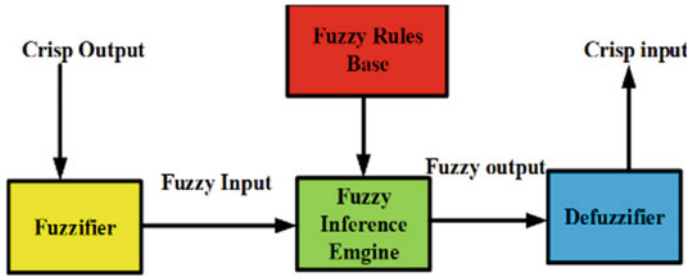
Fig. 1 Fuzzy logic configuration

2 Short-Term Load Forecasting (STLF)

The STLF is an integrated planning sector. Nowadays, demand-scheduling for several energy divisions like generation, transmission and distribution is required for designing a time-ahead power system, and STLF plays a significant role in that. It helps operators know about power systems with several decisions, including planning, generation reserve, system security, scheduling, demand side management, financial planning, and so forth. While it is essential for the time-ahead power system operation, inaccurate demand forecasting will cost the effectiveness of a spectacular financial loss.

2.1 Block Diagram and Flow Chart of the Proposed Scheme

For STLF, mathematical modelling is used for FL. The FL is multi-valued logic where the estimation of data is done according to Boolean logic (yes or no and true or false). The FL approach is one of the generalizations of Boolean logic. This logic is implemented for load forecasting weather data like temperature and humidity as the input and load as the output data. Figure 1 represents the configuration of the FL, which is implemented here. The block diagram in Fig. 2 presents an overview of FL methodology. Figure 3 presents the proposed intelligent scheme algorithm which depicts the stepwise implementation of the proposed work.

3 Model Description of Fuzzy Logic

3.1 Base Design

Make a note of the variable quantity of input and output by using arithmetical analysis with another user. This paper consists of 2 input and 1 output variable. Each variable
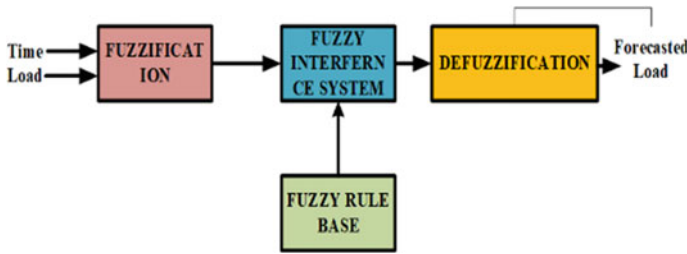
Fig. 2 Block diagram of fuzzy logic

is taken by resolving for membership value [0, 1]. After determining each variable, the input and output variable, the shape of fuzzy membership is selected and its shape can be triangular, trapezoidal, Gaussian or ballcapped. For all single variables, fuzzy membership functions are well-defined. The provided variables should not remain equal, but it is ensured that the variable must equal the number of functions. Next, the data needs to be trained in a fuzzy model. Couples of data is referred to as training sample and it is further said that if the time is midnight and the load is average, then the load is high.

3.2 Compute the Forecast Value

A nonlinear mapping is done by fuzzy if–Then rule implements a fuzzy inference system starting from input to output space. The centroid of the area of a numerical forecast is expressed as

$$\text{Centroid of area, } M_{coa} = \frac{\int z\mu_A(z)\,dz}{\int z\mu_A(z)z\,dz} \tag{1}$$

whereas membership function 'M' that defines the fuzzy set A is μ, on the universe Z.

3.3 Test Performance

For obtaining the accurateness of the STLF, it is verified by using old data. If it becomes improper, the shape of the membership function of fuzzy is changed, and a new rule base is formed. The testing system and membership function shapes are tested for several periods until the correct rule base system is developed. In the "train and set" method, the lowest error is measured for forecasting, which is very useful for large data sets.

Fig. 3 Flow chart of the proposed intelligent scheme
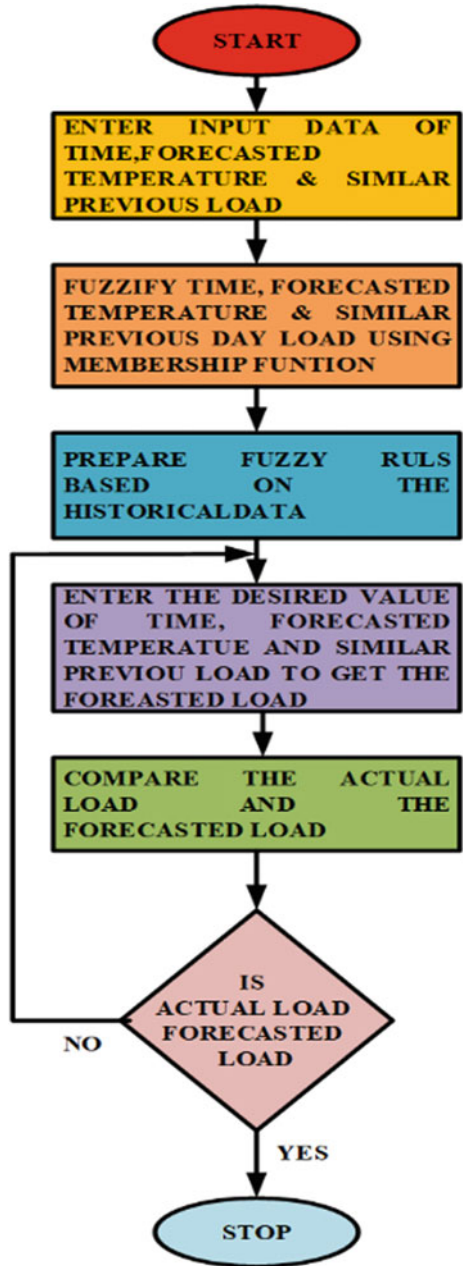
3.4 Error Analysis

To decrease the error in the system, STLF is done.

$$\text{APE} = \left(\frac{\text{actual load - forecasted load}}{\text{forecasted load}} \right) * 100 \tag{2}$$

$$\text{MAPE} = \frac{1}{n} \sum_{i=1}^{n} \left(\frac{\text{actual load}(i) \text{ - forecasted load}(i)}{\text{forecasted load}(i)} \right) \tag{3}$$

4 Modelling of FL for STLF

4.1 Fuzzification

Fuzzification can be defined as a procedure in which crisp values change the degree of membership related to the fuzzy set shown in Figs. 4, 5 and 6. The time which is divided into 6 sets of fuzzy are Midnight, Morning, Forenoon, Afternoon, Evening and Night.

4.2 Rule Base

The fuzzy rule base is considered an essential part of the fuzzy system. In this, If–then rule is used for getting the load forecasted output, some of which are mentioned below and shown in Figs. 7 and 8 as.

5 Results and Discussion

Fuzzy logic simulated for STLF is shown in Fig. 9. MATLAB software is used for simulation work. From the workshop file, actual load data and input data are taken and then simulated. The simulated diagram is shown in Fig. 9. The input data is given to the controller of fuzzy logic, block. "fis" of the fuzzy interference system is put in the fuzzy logic controller block. The controller block of fuzzy logic is prepared with the fuzzy rules, which gives the forecasted output as shown in Fig. 10.

It can be observed from Fig. 11 that the actual and forecasted load is almost identical, and significantly with less error.
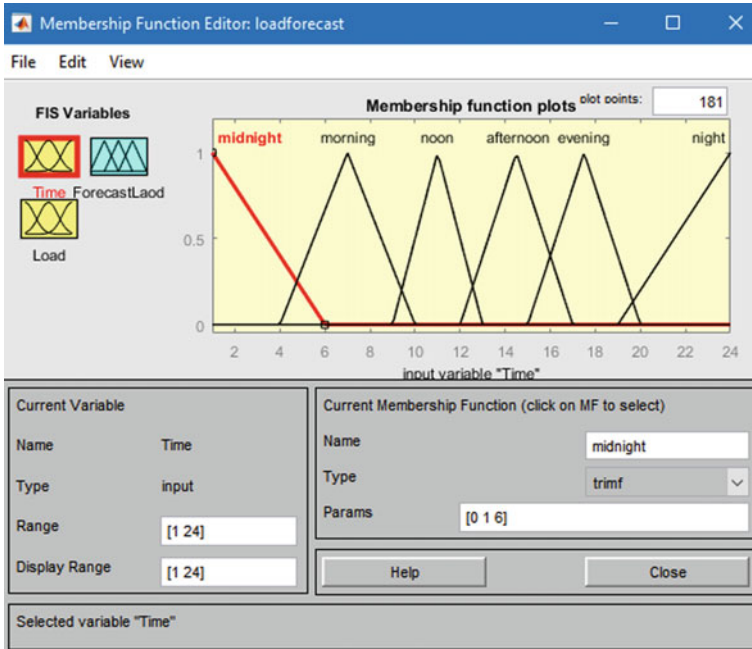
Fig. 4 Time membership function

From Table 1, it is concluded that the mean error found from the result obtained from the fuzzy logic is **1.60%** and the actual error range is between −2.63% to + 3.11%.

It is observed from Table 2 that the proposed method gives much less error as compared to other researchers' work. So, FL-based STLF is recommended.

6 Conclusion

In this report, the STLF methodology is discussed by using FL. For safety analysis of generation, STLF is a very useful tool. It has been observed that by using input data and by making a rule base, the load forecasting is predicted precisely and its margin error is between + 3.11% and −2.63%, and MAPE is 1.60%, which is relatively minor. Further, during simulation, it has been observed that the fuzzy logic toolbox is easy to understand because it works on the If–Then rule and the error can be reduced if the data is large and by using many memberships function.
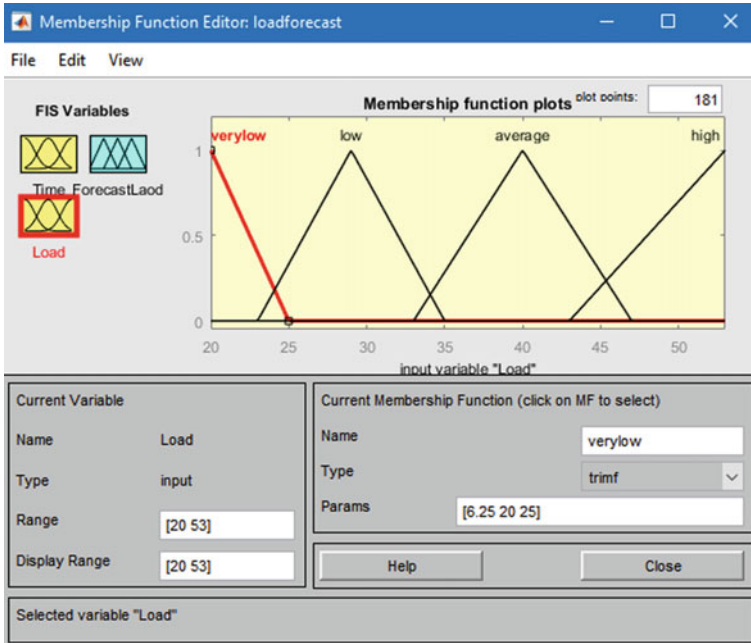
Fig. 5 Load membership functions
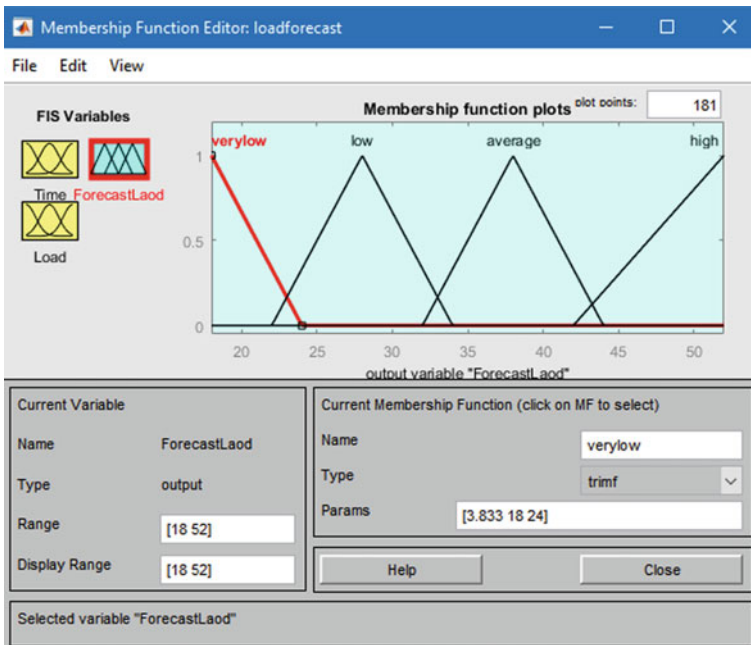
Fig. 6 Membership functions of forecasted load
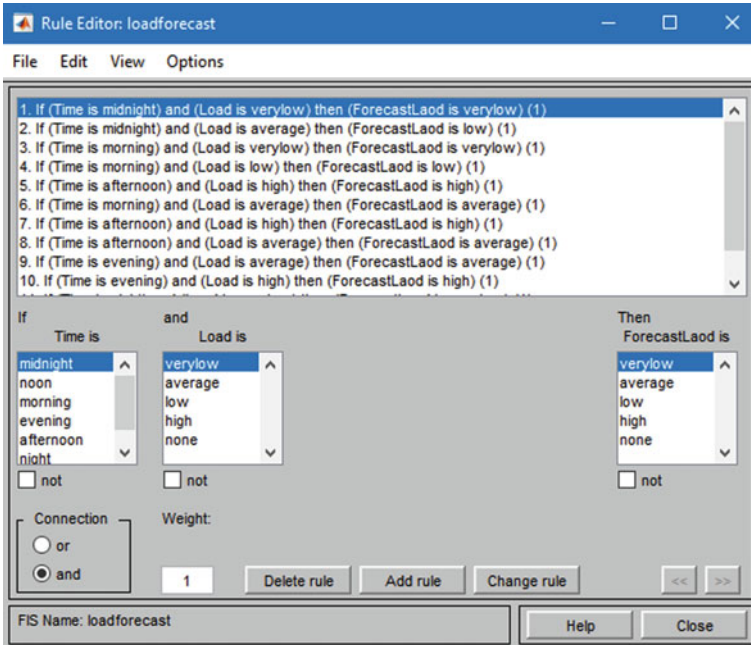
Fig. 7 Rule base of fuzzy
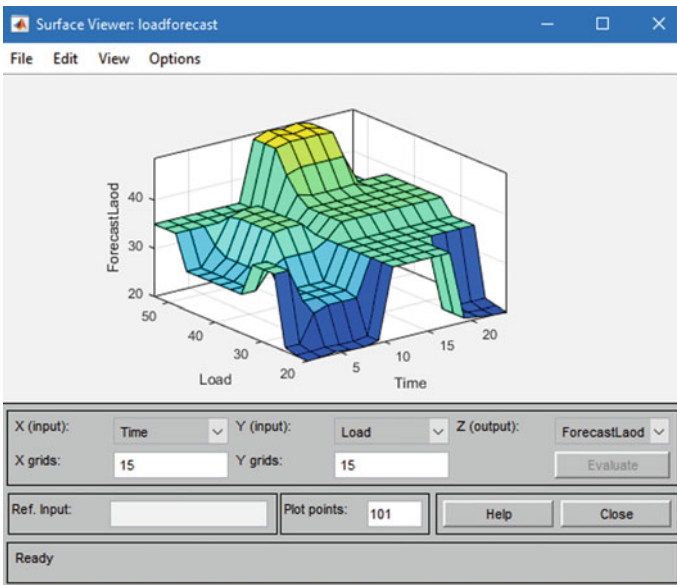
Fig. 8 Three-dimensional surface
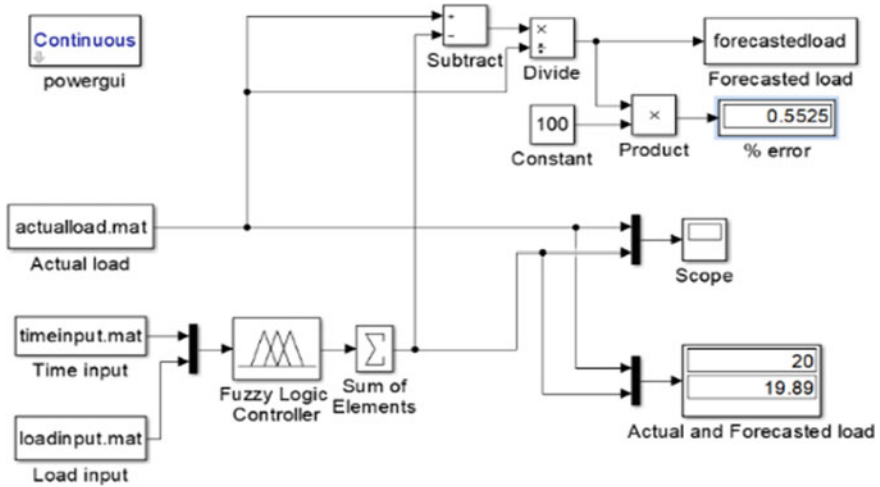
Fig. 9 Simulated FL-based STLF model
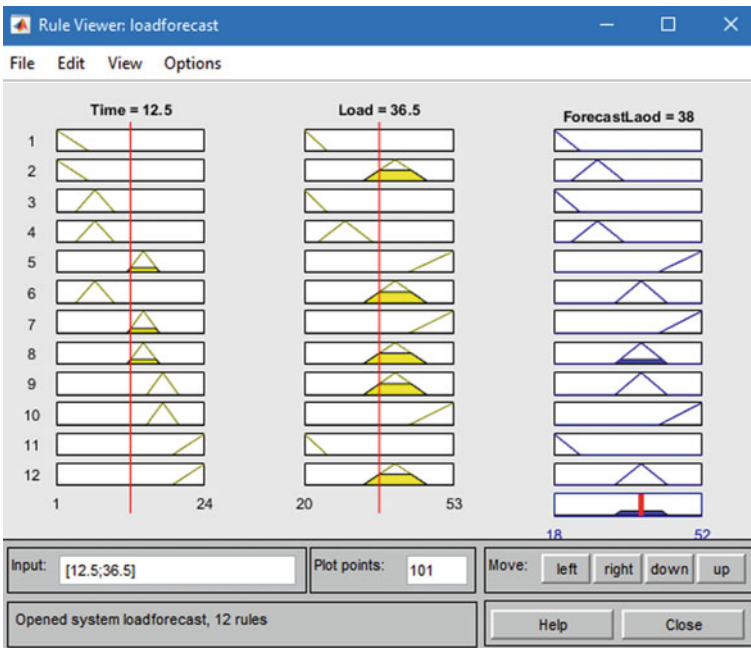
Fig. 10 Rule viewer of one sample data
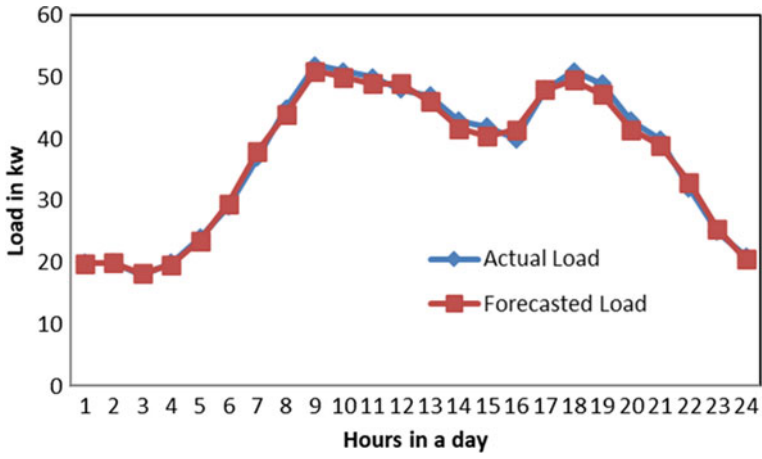
Fig. 11 Comparison of the actual and forecasted load of a day for FL

Table 1 Forecasted load and percentage error for 24 h

Time	Load	Actual load	Forecasted load	APE%
1	20	20	19.9	0.5
2	20	20	20	0
3	20	18	18.2	−1.09
4	26	20	19.7	1.5
5	31	24	23.5	2.12
6	34	29	29.5	−1.69
7	42	37	38	**−2.63**
8	53	45	44	2.27
9	49	52	51	1.96
10	48	51	50	2
11	46	50	49	2.04
12	46	48	49	−2.04
13	44	47	46.1	1.95
14	43	43	41.7	**3.11**
15	42	42	41.5	1.20
16	45	40	40.5	−1.23
17	47	48	48	0
18	53	51	49.5	3.03
19	46	49	47.8	2.51
20	39	43	42.5	1.17
21	37	40	39.7	0.75
22	32	32	32.5	−1.53
23	24	25	25.8	−0.77
24	22	21	20.7	1.44
			MAPE	1.60

Table 2 Comparison of different schemes

S No.	Scheme	MAPE (%)
1	[3]	3.75
2	[14]	2.69
3	**Proposed One**	**1.60**

References

1. Amirthavalli M (2015) Fuzzy logic and neural networks. SCITECH Publications
2. Hernandez L, Baladron C, Aguiar J, Carro B, Sanchez-Esguevillas A, Lloret J, Massana J, A survey on electric power demand forecasting: future trends in smart grids, microgrids and smart buildings. IEEE Commun Surv Tutorials 16(3):1460–1495
3. Singla MK, Hans S (2018) Load forecasting using fuzzy logic tool box. GRD J Eng 3(8):12–19

4. Ali D, Yohanna M, Puwu M, Garkida B (2016) Long-term load forecast modelling using a fuzzy logic approach. Pacific Sci Rev A: Nat Sci Engg 18(2):123–127
5. Yildiz B, Bilbao JI, Sproul AB (2017) A review and analysis of regression and machine learning models on commercial building electricity load forecasting. Renew Sustain Energy Rev 73:1104–1122
6. Clements AE, Hurn A, Li Z (2016) Forecasting day-ahead electricity load using a multiple equation time series approach. Eur J Oper Res 251(2):522–530
7. Khwaja A, Naeem M, Anpalagan A, Venetsanopoulos A, Venkatesh B (2015) Improved short-term load forecasting using bagged neural network. Electric Power Syst Res 125:109–115
8. Selakov A, Cvijetinovic D, Milovic L, Mellon S, Bekut D (2014) Hybrid PSO–SVM method for short-term load forecasting during periods with significant temperature variations in city of Burbank. Appl Soft Comput 16:80–88
9. Mamlook R, Badran O, Abdulhadi E (2009) A fuzzy inference model for short-term load forecasting. Energy Policy 37(4):1239–1248
10. Lee WJ, Hong J (2015) A hybrid dynamic and fuzzy time series model for mid-term power load forecasting. Int J Electr Power Energy Syst 64:1057–1062
11. Aggarwal S, Kumar M, Saini L, Kumar A et al (2011) Short-term load forecasting in deregulated electricity markets using fuzzy approach. J Engg Technol 1(1):21–27
12. Bart K(2006) Neural networks and fuzzy systems. Prentice Hall of India Private Limited, New Delhi
13. Driankov D, Hellendoorn H, Reinfrank M (2001) An introduction to fuzzy control. Narosa Publishing House
14. Manoj PP, Shah AP (2014) Fuzzy logic methodology for short-term load forecasting. Int J Res Eng Technol 3(4):2321–7308
15. Kaur J, Brar YS (2014) Short-term load forecasting using fuzzy logic of 220 kV transmission line. Int J Eng Res Technol 3(9):336–343
16. Alam SMM, Ali MH (2020) A new fuzzy logic based method for residential loads forecasting. In: 2020 IEEE/PES transmission and distribution conference and exposition (T&D), pp 1–5
17. Sharma S, Agrawal RK, Tripathi MM (2020) Synergism of recurrent neural network and fuzzy logic for short term energy load forecasting. In: 2020 fourth international conference on computing methodologies and communication (ICCMC), pp 165–216

A Microstrip Line Fed Hexagonal Square Shaped Fractal Monopole Antenna for Ultra-Wide Band Applications

Ranjeet Kumar, Rashmi Sinha, Arvind Choubey, Santosh Kumar Mahto, Pravesh Pal, and Praveen Kumar

Abstract A compact hexagonal-square shaped fractal monopole antenna is etched out from circular patch for ultra-wide band application. This proposed antenna has an overall physical dimension of 54×35 mm^2.The parameters of antenna such as Return loss, percentage Bandwidth, VSWR, E-plane and H-plane pattern, Gain, are analyzed. The partial ground plane and microstrip transmission line is employed to achieve ultra-wide band (UWB) operating bandwidth from 2.1 to 13.5 GHz (155%) with reflection coefficient close to -30 dB. This makes it suitable for the commercial, aerospace, and military telecommunication besides the traditional radar imaging application. The proposed antenna is fabricated. The simulated and measured outcomes are in very close agreement**.**

Keywords Antenna theory · Fractal · Ultrawideband (UWB)

1 Introduction

Nowadays, ultra-wideband antenna plays an essential role in transmit the information because of its desirable characteristics, such as light weight, very small electrical

R. Kumar (✉) · R. Sinha · P. Pal · P. Kumar
Department of Electronics and Communication Engineering, National Institute of Technology, Jamshedpur, India
e-mail: ranjeet77kumar@gmail.com

R. Sinha
e-mail: rsinha.ece@nitjsr.ac.in

A. Choubey
Department of Electronics and Communication Engineering, Indian Institute of Information Technology, Bhagalpur, India
e-mail: achoubey.ece@nitjsr.ac.in

S. K. Mahto
Department of Electronics and Communication Engineering, Indian Institute of Information Technology, Ranchi, India
e-mail: skumar@iiitranchi.ac.in

dimension and stable radiation patterns, immunity to multipath propagation [1–14]. However, the interference and radio-frequency wave congestion (RF) are major issues concerned with UWB antenna. The allocation of bandwidth is from 3.1 to 10.6 GHz for UWB system. Over the ultra-wide band spectrum several narrow band systems, such as, WiMAX, WLAN and X-band [11] exists. The ultra-wideband technique is more significant to several applications due to more bandwidth, higher data rate, and good time precision. In designing ultra-wideband antenna, a number of different technologies and methods have been proposed. Various conventional shape is used to design ultra-wideband monopole antennas [15–21]. For the ground penetrating radar (GPR) application, a hexagonal shape having a rectangular slot with resistive load is presented [22]. But these often have a limitation in bandwidth. In recently, fractal geometries are adopted to provides way to this limitation; It provides wide bandwidth and stable radiation patterns. Fractal is a set of similar structure, having two property, self-similarity or self-affinity and space-filling [23]. The space-filling technique ensures the compact and miniaturized antenna [24] and the self-similarity technique ensures increase the electrical dimension of antenna, which provide the good performances characteristics throughout the wide band. The researchers of the antenna community have designed fractal geometry-based antennas such as Von Koch, Minkowski, Sierpinski, Cantor, etc. In [25], the Sierpinski technique is presented to design a compact fractal antenna for multiband.

This paper presents an ultra-wideband antenna based on iterations of hexagonal-square geometries, fed by a microstrip transmission line, etched on a circular patch is proposed. The hexagonal-square geometry consists of square slots within the hexagonal patch. This antenna imparts stable radiation patterns and gain, which makes it useful for many applications.

2 Layout of Proposed Antenna

There is a number of fractal antennae designed so far, but the Sierpinski-based fractal Patch Antenna is frequently used. Inspired by these works, a fractal microstrip patch antenna has been designed. The proposed fractal geometry consists of quadrilateral and triangular arrow shaped on the circular patch, as is shown in Fig. 1. A hexagonal shape of radius R2 is etched out from a circle of radius R1, as depicted in Fig. 1a. A hexagonal and square shape is placed at about the same point as shown in Fig. 1b. A hexagonal shape is subtracted from the square, resulting in a quadrilateral and triangular arrow-like shape formed as shown in Fig. 1c. The same process is repeated to get a structure portrayed in Fig. 1d, e. The final fractal shape is achieved by filling Fig. 1e, in the void space formed in Fig. 1a. A maximum of three iterations are involved to achieve wide bandwidth. This radiating patch is fabricated on an FR4 epoxy substrate of dimension 54×35 mm^2 with material dielectric permittivity constant (ε) of 4.4, height 1.6 mm and partial ground plane (PGP). It is fed by a 50 Ω microstrip transmission line. The simulated fractal antenna is portrayed in Fig. 2a and the front and back view of the prototype is shown in Fig. 2b. Table 1 presents

the optimized dimension. The resonant frequency of the Hexagonal Square Shaped Fractal Monopole Antenna is given in Eq. (1) [10].

$$f_0 = \frac{T_{mn}C}{5.714 R_e \sqrt{\varepsilon_{\text{reff}}}} \tag{1}$$

where C = Electromagnetic wave speed of light in free space, $\varepsilon_{\text{reff}}$ = effective dielectric constant, the effective radius (R_e) of the circular patch antenna is given by Eq. (2) [10].

$$R_e = R_c \cdot \sqrt{\left(1 + \frac{2 \cdot h}{R_c \cdot \pi \cdot \varepsilon_r}\left[\ln\left(\frac{\pi \cdot R_c}{2 \cdot h}\right) + 1.7726)\right]\right)} \tag{2}$$

where $R_c = R_1$ is the radius of the circular patch antenna, h is the height of the substrate and ε_r is the dielectric constant.
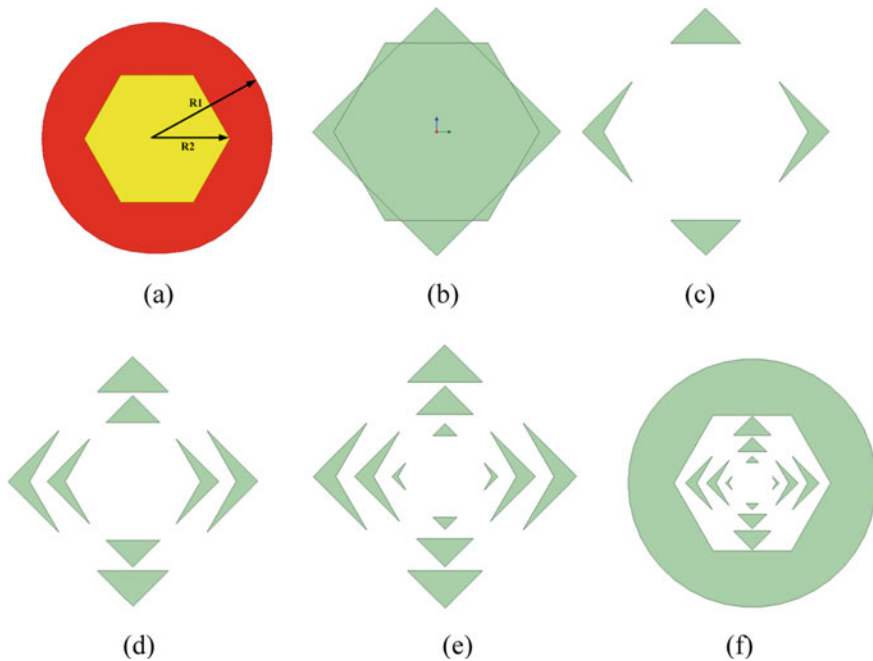
Fig. 1 A layout stage of proposed fractal antenna
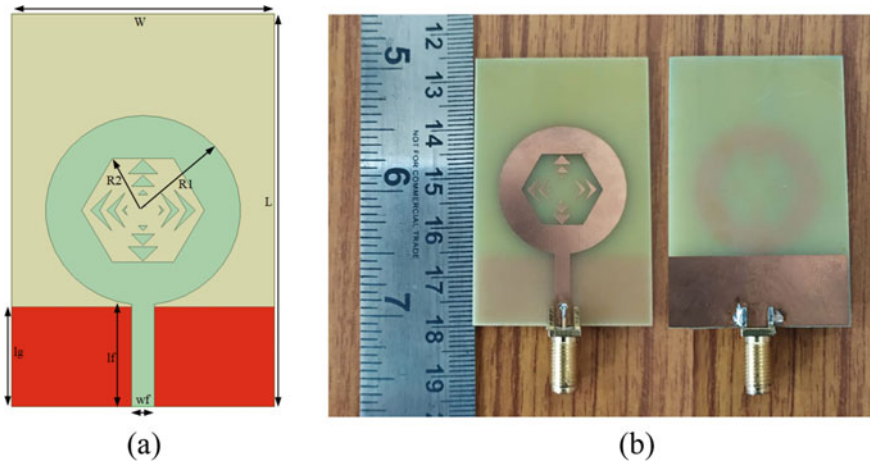
Fig. 2 **a** The small UWB fractal antenna, **b** prototype (front and rear view)

Table 1 Optimized designed parameters and the numerical value of fractal antenna

Abbreviation	Parameter	Dimension (mm)
L	Length of substrate	54
W	Width of substrate	35
lf	Length of feedline	14
Wf	Width of feedline	3
lg	Length of ground plane	13.68
R1	Radius of circular patch	13
R2	Hexagonal radius	8.2

3 Results and Discussion

The proposed fractal antenna is designed and simulated in HFSS and its results are verified in the antenna measurement laboratory. The measured and simulated reflection coefficient characteristics of the proposed antenna are depicted in Fig. 3. It can be seen that there are two resonance frequencies at 5.4 GHz and 10.4 GHz and have a return loss of around -35 dB, which works efficiently in the range of 2.1 to 13.5 GHz. It has a 146% of bandwidth frequency and the value of VSWR is less than 2, which indicates that the proposed antenna has perfect impedance matching.

The E-plane and H-plane of the fractal antenna at different frequencies, as indicated below, are depicted in Fig. 4. These radiation patterns are almost as same as dipole/monopole antenna. E-plane radiation patterns are nearly dumbbell shape and H-plane radiation patterns are omnidirectional, but as frequency increases, their patterns are directive in nature because of its diversified surface current and higher mode are activated.
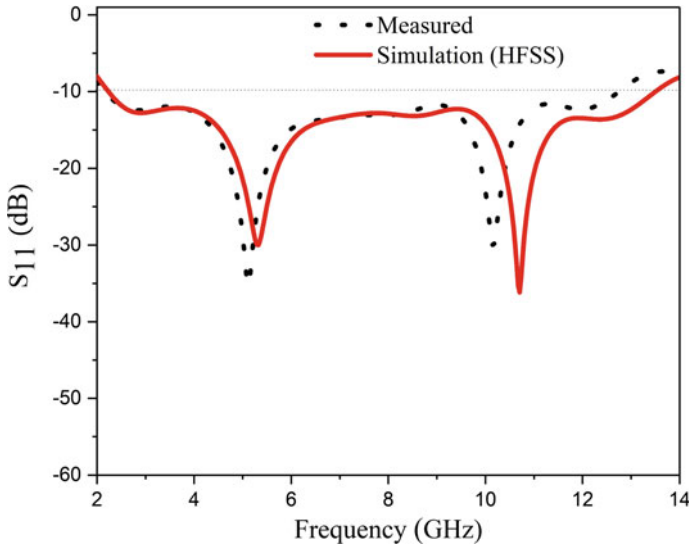
Fig. 3 Measured and simulated S_{11} parameter
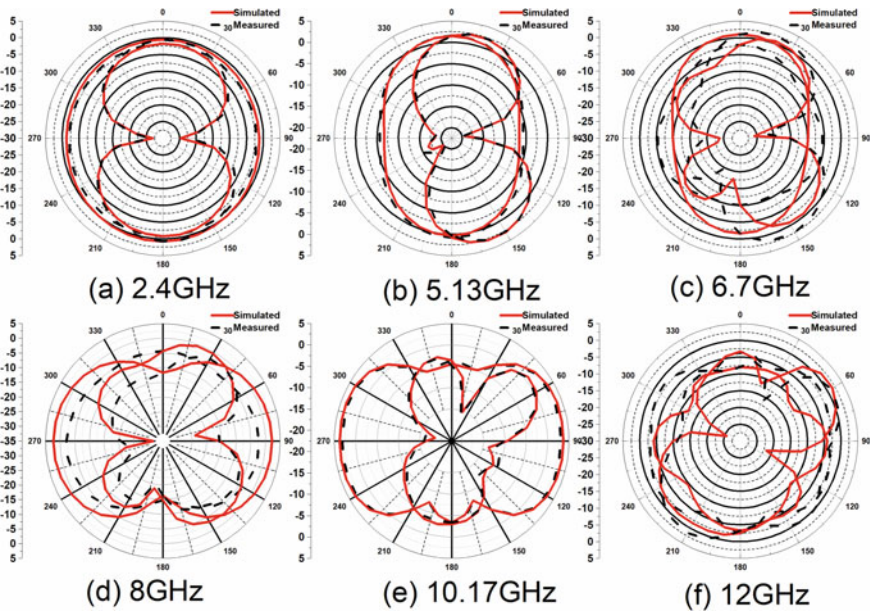
Fig. 4 E and H-plane of the fractal antenna at different frequencies
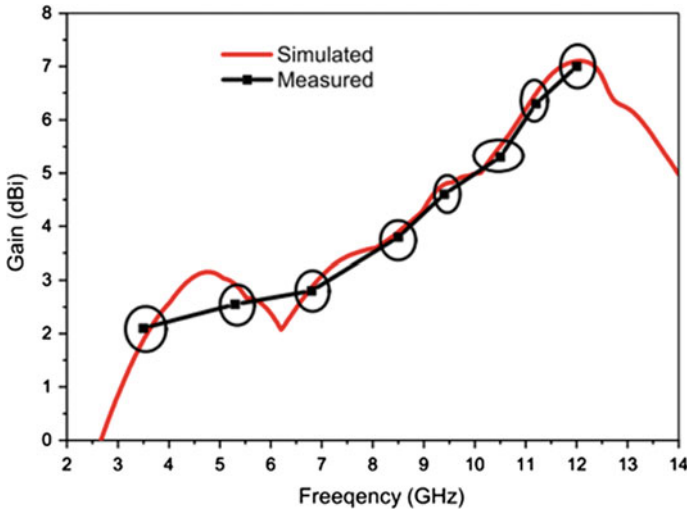
Fig. 5 Simulated and measured gain versus frequency

The gain plot is portrayed in Fig. 5. The simulated and measured gain are good and have positive values in the entire band. It can be seen from this gain plot is increasing as the operating frequency increases. The peak and average gain are 7.2 dB at 11.76 GHz and 3.9 dB in the entire bandwidth.

4 Conclusion

A fractal technique-based antenna is proposed by the combination of hexagonal-square shapes, etched out from a circular patch. The simulated results are compared with the measured one, which shows both outcomes are close in agreement. There is a little discrepancy, because of fabrication, and human-measured errors. This proposed antenna is suitable for Ultra-Wide Band (UWB) application.

References

1. Kang W, Ko KH, Kim K (2012) A compact beam reconfigurable antenna for symmetric beam switching. Progr Electromagnetics Res 129:1–16
2. Sze JY, Pan SP (2011) Design of broadband circularly polarized square slot antenna with a compact size. Progress In Electromagnetics Research 120:513–533
3. Peng H-L, Yin W-Y, Mao J-F, Huo D, Hang X, Zhou L (2011) A compact dual-polarized broadband antenna with hybrid beam-forming capabilities. Progr Electromagnetics Res 118:253–271

4. Weng W-C, Hung C-L (2012) Design and optimization ofa logotype antenna for multiband applications. Progr Electromagnetics Res 123:159–174
5. Ban YL, Chen JH, Sun SC, Li JL, Guo JH (2012) Printed wideband antenna with chip-capacitor-loaded inductive strip for LTE/GSM/UMTS WWAN wireless USB dongle applications. Progr Electromagnetics Res 128:313–329
6. Tiang J-J, Islam MT, Misran N, Mandeep JS (2011) Circular microstrip slot antenna for dual-frequency RFID application. Progr Electromagnetics Res 120:499–512
7. Xie J-J, Yin Y-Z, Ren J, Wang T (2012) A wideband dual polarized patch antenna with electric probe and magnetic loop feeds. Progr Electromagnetics Res 132:499–515
8. Azim R, Islam MT, Mandeep JS, Mobashsher AT (2012) A planar circular ring ultra-wideband antenna with dual band-notched characteristics. J Electromagnetic Waves Appl 26(14–15):2022–2032
9. Amin Y, Chen Q, Zheng LR, Tenhunen H (2012) Design and fabrication of wideband archimedean spiral antenna based ultra-low cost "green" modules for RFID sensing and wireless applications. Progr Electromagnetics Res 130:241–256
10. Chen A-X, Jiang T-H, Chen Z, Su D (2011) A novel low-profile wide band UHF antenna. Progr Electromagnetics Res 121:75–88
11. First Report and Order (2002) Revision of Part 15 of the commission's rule regarding ultra-wideband transmission system FCC 02 -48. Federal Communications Commission
12. Kumar G, Ray KP (2003) Broad band microstrip antennas. Norwood, MA, Artech House
13. Lin CC, Kan YC, Kuo LC, Chuang HR (2005) A planar triangular monopole antenna for UWB communication. IEEE Microwave Wireless Compon Lett 15:624–626
14. Yang HY (2005) Miniaturized printed wire antenna for wireless communication. IEEE Antenna Propag Lett 4:358–361
15. Huang CY, Hisa WC (2005) Planar elliptical antenna for ultra-wide band communication. Electron Lett 41:296–297
16. John M, Amman MJ (2005) Optimization of impedance bandwidth for the printed rectangular monopole antenna. Microwave Opt Technical Lett 47:153–154
17. Ammann MJ (2001) Control of the impedance bandwidth of wide band planar monopole antenna using a beveling technique. Microwave Opt Technical Lett 30:229–231
18. Zhang C, Fathy AE (2006) Development of an ultra-wide band elliptical disk planar monopole antennas with improved omni-directional performance using a modified ground. In: IEEE international antenna propagation symposium dig. Alburqueque, NM. pp 1689–1692
19. Chen ZN, See TSP, Qing XM (2007) Small printed ultra-wide band with reduced ground plane effect. IEEE Trans Antenna Propag 55(2):383–388
20. Roy KP, Tiwari S (2010) Ultra-wide band printed hexagonal monopoleantennas. IET Microwaves Antenna Propag 4(4):437–445
21. Shaalan AAM, Ramadan MI (2010) Design of a compact hexagonal monopole antenna for ultra-wideband applications. J Infrared Milli Terahz Waves 31:958–968
22. Pramudita AA, Kurniawan A, Bayu Suksmono A (2008) Hexagonal monopole strips with rectangular slot for 100 1000MHz SFCW GPR application. Int J Antenna Propag 1–6
23. Mandelbrot BB (1983) The fractal geometry of nature. W. H. Freeman and Company, New York
24. Gianvittorio JP, Rahmat-Samii Y (2002) Fractal antennas: a novel antenna miniaturization technique, and applications. IEEE Antennas Propag Mag 44(1):20–36
25. Nikolaou S, Kingsley ND, Ponchak GE et al (2009) UWB elliptical monopoles with a recon-figurable band notch using MEMS switches actuated without bias lines. IEEE Trans Antennas Propag 57(8):2242–2251

Fuzzy Logic Control-Based Maximum Power Point Tracking for a Three-Phase Grid Connected PV System

Anshuman Bhuyan, Basanta K. Panigrahi, Kumaresh Pal, and Subhendu Pati

Abstract This paper proposed a fuzzy logic control (FLC)-based maximum power point tracking (MPPT) for a three-phase grid integrated photovoltaic (PV) system. The suggested methodology for the present MPPT command employs fuzzy logic control to identify the size of the incremental current. A fuzzy logic controller has been designed for integrating a PV array to the utility grid via a three-phase line-commutated inverter. The controller monitors and supplies the electric system with the maximum amount of power possible. The linguistics variables have been chosen to modify the inverter's firing angle in order to track the maximum power. With the use of fuzzy logic, a PWM generator was employed to generate pulses for the thyristors in the inverter. The identical simulation setup was employed with the P&O methodology as well. Finally, a comparison between the two methodologies was conducted to demonstrate fuzzy logic's superiority.

Keywords Maximum power point tracking (MPPT) · Photovoltaic (PV) · Perturb and observe (P&O) method · Fuzzy logic control (FLC)

1 Introduction

With the advancement of the industry, the issue of energy scarcity is becoming increasingly acute. Renewable energy sources, particularly photovoltaic (PV) system technologies, are rapidly growing and playing an increasingly important role in electric power system, and are considered the new century's green energy [1]. Owing to the PV output power varies based on the load current, temperature, and irradiation, it can't be treated as continuous DC source. In most cases, MPPT is utilized to track the maximum power point of a PV system [2]. The MPPT control methodology, as

A. Bhuyan · B. K. Panigrahi · S. Pati
Department of EE, ITER, Siksha 'O' Anusandhan Deemed to Be University, Bhubaneswar, India

K. Pal (✉)
Department of EEE, ARKA JAIN University, Jamshedpur, India
e-mail: kumaresh.pal@rediffmail.com
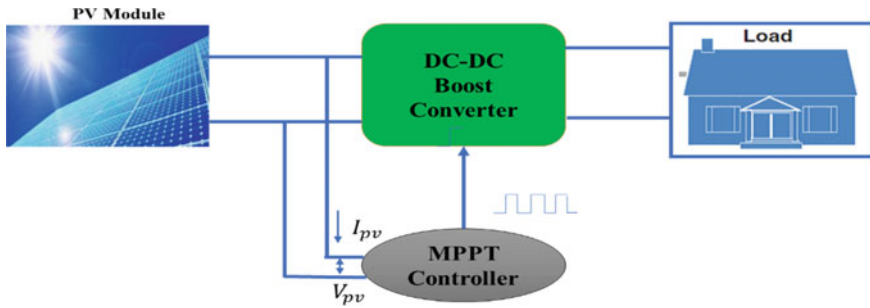
Fig. 1 A typical MPPT diagram in a PV system

well as the MPPT circuit, determine MPPT efficiency. In DC-DC converters, which are typically utilized as MPPT circuits, the MPPT control algorithm is widely used [3]. A sample diagram of MPPT connections in a photovoltaic system is illustrated in Fig. 1. MPPT has been implemented in a variety of ways, according to reports. To determine the maximum power point (MPP), the perturb and observe (P&O) approach requires calculating dP/dV. It is easy to establish, however, it would be unable to track the MPP whenever the irradiance varies quickly and instead oscillates across the MPP instead of directly monitoring it. MPP can be tracked quickly using the incremental conductance method, but it adds to the algorithm's complexity by requiring the calculation of dI/dV[4]. The constant voltage strategy, which utilizes the open circuit voltage of 76% as the MPP voltage, and the short-circuit current approach are both simple, however, they don't always monitor MPPs precisely [5]. When compared to traditional approaches, the fuzzy control technique can improve tracking performance for both linear and nonlinear loads.

The remaining of this paper is organized as follows. In Sect. 2, the Generalized Photovoltaic Circuit is thoroughly explained. MPPT technique is described in Sect. 3. Section 4 depicts the proposed system model, while Sect. 5 demonstrates the proposed work's result analysis, and finally, in Sect. 6, you will find the conclusions.

2 Generalized Photovoltaic Circuit

The photovoltaic (PV) cell converts solar heat into electric energy, which is then used to generate electricity. Whenever the sun's rays focus on the photovoltaic cell that generates current, the remaining holes and electrons are moved to some other Path of the cell due to the establishment of an electric field in the depletion region [6]. Figure 2 depicts a PV cell's single diode equivalent circuit, which includes a photocurrent, one resistor in parallel, one resistor in series, and a diode. The photo-generated current source is connected to a diode in this setup. The serial internal resistance of a PV cell is made up of carrier recombination in the PN junction's junction area, parallel internal resistance, and material resistance, whereas the contact resistance is made
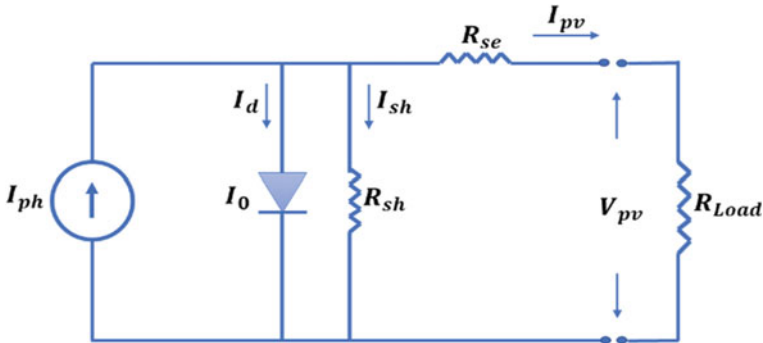
Fig. 2 PV cell equivalent circuit with a single diode

up of the leakage current at the edge, which takes into account the loss and resistance characteristics of PV cell materials [7].

The net PV current of a Photovoltaic module can be calculated using the following Eq. 1 [8]:

$$I_{pv} = I_{pv} - I_0 \left[\exp\left(\frac{(V_{pv} + I_{pv} R_{se})q}{a K T_c N_s} \right) - 1 \right] - \frac{(V_{pv} R_{se})}{R_{sh}} \tag{1}$$

where I_{pv} is the PV module's gross PV current in amps, I_{ph} is the photocurrent in amps, I_0 is the reverse saturation diode current in amps, V_{pv} is the PV array's output voltage in amps, R_{se} and R_{sh} are the series and shunt resistances, respectively, K denotes the Boltzmann constant ($K = 1.381\ 1023$ J/K), T_c is the temperature of Cell in K, q is electron charge ($q = 1.602\ 1019$C), and the PV cell numbers in series are denoted by N_s.

3 Maximum Power Point Tracking (MPPT) Techniques

A Photovoltaic cell's efficiency is extremely low. To improve efficiency, procedures must be implemented to correctly correlate the source and load. MPPT technology is employed to enhance the solar panel's efficiency [9]. The MPP is the bias potential where the solar cell generates the most net power [10]. The intensity of the irradiance, temperature of the device, and device deterioration are all factors that can cause the fluctuation of the MPP voltage [11].

3.1 Perturb and Observe (P&O) Technique

This approach is one of the most basic and extensively employed MPPT strategies. The fundamental idea behind this strategy is to force the system to run in a direction where the PV system's output power grows. Equation 2 describes the power change that determines the P&O technique's approach [12].

$$\Delta P = P_{\text{New}} - P_{\text{Old}} \tag{2}$$

If the change in power is positive, the incremental current command (increase or decrease PV current) will remain the same; whether the change is negative, the incremental current command will be changed to the other direction. In a steady state situation, this strategy works effectively (the radiation and temperature conditions change slowly). When the atmospheric conditions vary rapidly, however, the P&O technique fails to follow MPP [13].

3.2 Fuzzy Logic Control

MPPT with Fuzzy Logic Control has various advantages, including improved performance, robustness, and simplicity of design. Furthermore, this methodology does not necessitate a thorough understanding of the system's actual model [14]. Figure 3 depicts the essential components of Fuzzy Logic Control: fuzzification, rule-base, inference, and defuzzification. One of the most effective control systems is Fuzzy Logic Control which is described in two terms: multivariable considerations and multi-rules-based resolution. Over the last decade, fuzzy MPPT has been increasingly popular. FLC has the benefit of functioning with erroneous inputs, requiring no precise mathematical model, and handling nonlinearity [15]. Figure 3 depicts the proposed FLC with one output and two inputs.

Error (E) and the change of error (CE), both exhibit by Eq. 3 and 4, are the two fuzzy logic control input parameters [16].
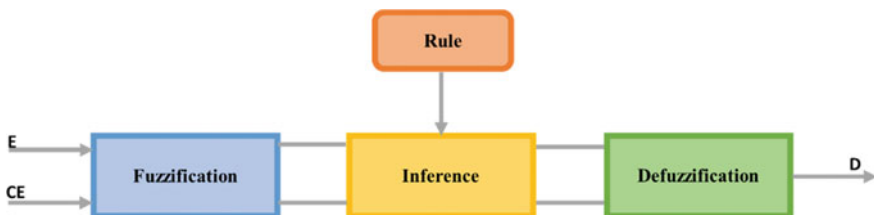
Fig. 3 The fuzzy logic Controller

$$E = \frac{\Delta P_{\text{pv}}}{\Delta V_{\text{pv}}} = \frac{P_{\text{pv}_{\text{New}}} - P_{\text{pv}_{\text{old}}}}{V_{\text{pv}_{\text{New}}} - V_{\text{pv}_{\text{Old}}}} \tag{3}$$

$$CE = E_{\text{New}} - E_{\text{Old}} \tag{4}$$

• Fuzzification

Fuzzification is the process of employing a fuzzy membership function to turn the system's real input values E and CE into linguistic fuzzy sets [17]. Basic fuzzy subsets are used to express these variables from the perspective of 5 linguistic variables like PB (positive big), PS (positive small), NB (negative big), NS (negative small), and ZE (zero) [18].

• Rule base and inference engine

A fuzzy rule base is a collection of if–then rules which include all of the data for the variables under consideration [19]. It is determined based on professional experience and system control operation. The fuzzy rule algorithm has 25 fuzzy control rules [20]. The fuzzy inference engine is a mechanism for making logical decisions based on fuzzy rule sets and converting fuzzy linguistic output from the fuzzy rule base.

• Defuzzification

Defuzzification of the inference engine, that employs a series of control actions to evaluate the rules for a particular set of fuzzy inputs. The inferred fuzzy control action is converted into a numeric value at the output by constructing the union of the outputs from each rule [21]. The output duty control parameter is being defuzzified using the center of area (COA) methodology. If E is NB, and CE is ZO, then increase the duty cycle if D is PB, If the operating point is far away on the right side of the MPP and the slope variability is almost negligible [22].

4 Proposed Model

In our proposed model, we have connected the designed PV panel with a 600/40MVA grid. For tracking maximum power and at the same time to match the generated voltage with the grid, we have used fuzzy logic. The same circuit has been tested when connected to the grid with the P&O MPPT technique. The PV array, a step-up transformer, a line commutated SCR inverter, and the MPPT are all part of this power generation scheme. The PV array converts solar energy into electricity and through dc link capacitance, sent to the six-pulse thyristor bridge, which works as a line-commutated inverter. The PV panel's stable direct current is obtained using this dc link capacitance. The line-commutated inverter transforms dc to ac and uses the step-up transformer to deliver power to the utility grid from the PV panels. The firing angle delay is provided by the PWM generator. To generate the pulse, a triangular
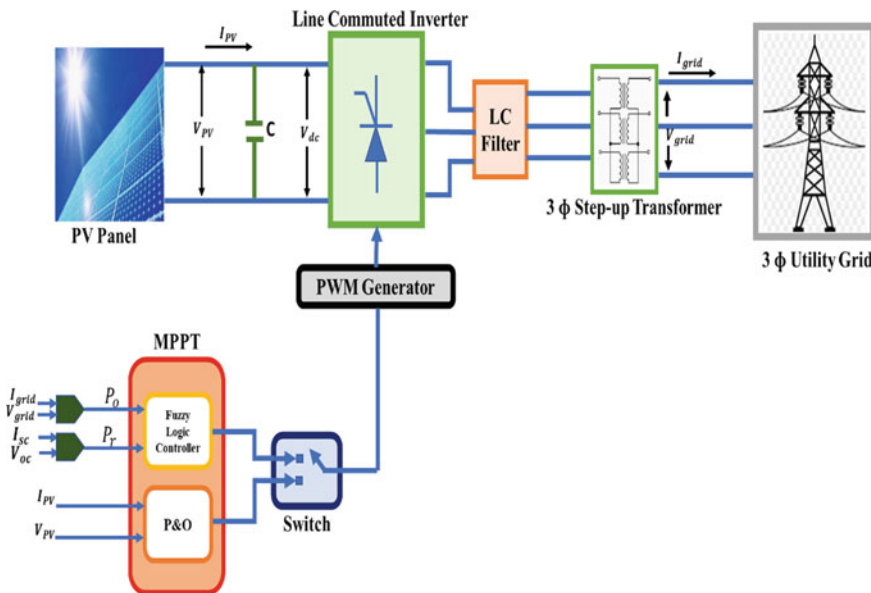
Fig. 4 Basic PV system integrated with 3 ϕ utility grid

carrier waveform is compared to a reference modulating signal. Figure 4 illustrates the proposed three-phase grid integrated photovoltaic system model.

The circuit has been tested when connected to grid with P&O MPPT technique. In this approach, the input current and voltage are used to calculate power and compared with its previous values by accessing previous values of voltage and current from the memory block. Depending on the difference in power, the predefined delta value is assigned to be multiplied by the D delta. Again, that delta value is compared with the previous one which will produce a pulse when combined with a reference repeating signal, which is then fed to an inverter which converts generated dc voltage to ac. When the circuit has been tested when connected to the grid with the Fuzzy logic MPPT technique. The FLC accepts two inputs: the real power output at the transformer's output and the maximal reference power, which is computed using the I_{sc} (short-circuit current) and V_{oc} (open-circuit voltage) of PV array. It should be noticed that the array's V_{oc} varies with temperature and I_{sc} varies with irradiation. The difference between the real and reference power is utilized to modulate the line-commutated inverter's firing angle delay, which transforms generated dc voltage to ac voltage. A LC filter is connected after the inverter to minimize the current harmonics created by the line-commutated inverter on the grid side. A two-winding transformer next to the LC filter steps up the PV 3 phased voltage to an approximate grid level and is supplied to the transmission line.

Fig. 5 I–V characteristic curves of the PV module
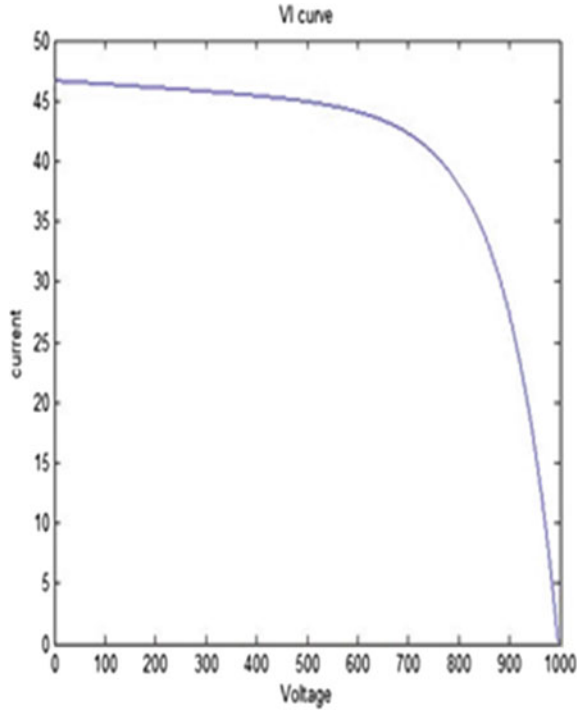
5 Result Analysis

Figures 5 and 6 illustrate the I–V characteristic curves and PV characteristic curves of the PV module, respectively.

In our proposed technique of fuzzy logic-based MPPT, we have compared the power of the grid side shown in Fig. 7 with the maximum possible power of PV panel to generate a pulse which is then fed to an inverter which converts generated dc voltage to ac. And then it is compared with the voltage levels of grid side and hence produces a three-phase signal shown in Fig. 8 with same frequency as of grid side and with no amplitude fluctuation. But when the same circuit has been tested when connected to grid with P&O MPPT technique & when compared with voltage levels of grid side with the PV three-phase voltage having same frequency as of grid side, there is some amplitude fluctuation shown in Fig. 9.

6 Conclusion

The designed PV panel has been simulated individually which provides a good PV response. It is then used with the grid with the generated three-phase voltage. At the

Fig. 6 PV characteristic
curves of the PV module
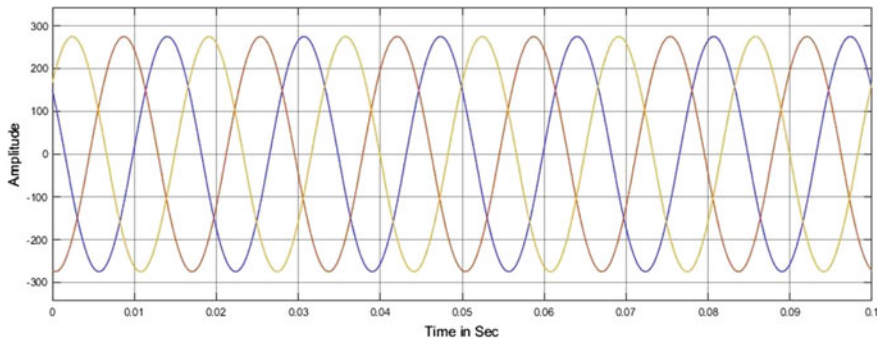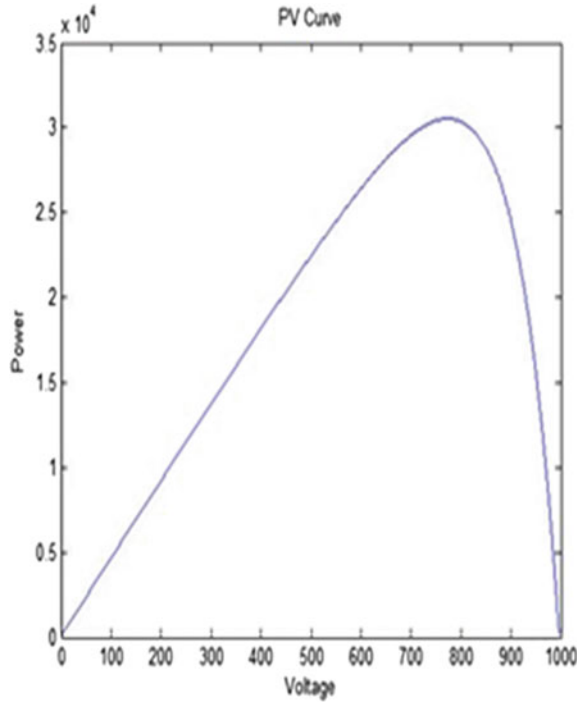
Fig. 7 Three-phase grid voltage

time of the P&O technique, it has been seen that it is able to track MPP but with a little fluctuation in amplitude level but with the use of FLC it is possible to track maximum power point with a steady output. So, our aim of synchronizing PV voltage with the grid has been achieved without any flicker in the output. So, in future, we will try to implement the same design with a multi-phase Boost converter to increase voltage level at the PV side, and at the same time generate an ac signal so that it can be applicable for on-grid connection without any transformer.
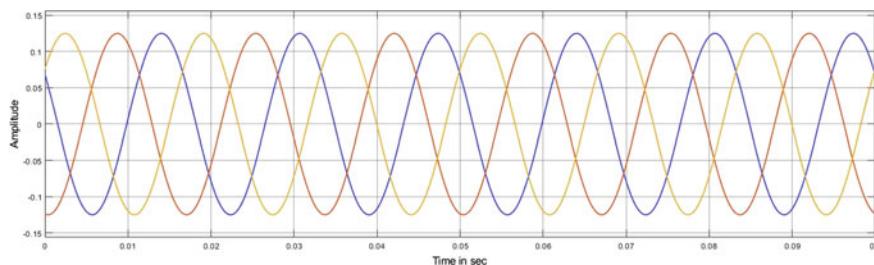
Fig. 8 Three-phase PV voltage with MPPT using fuzzy logic control method
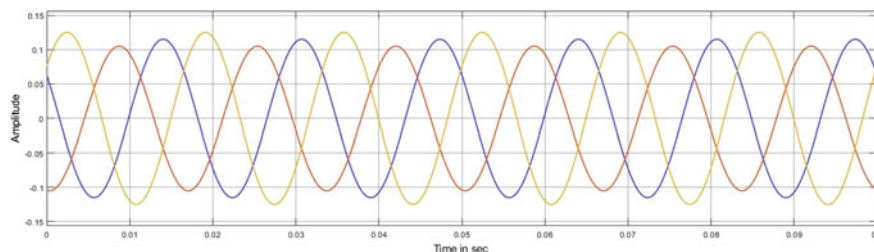
Fig. 9 Three-phase PV voltage with MPPT using P&O method

References

1. Jiandong D, Ma X, Tuo S (2018) A variable step size P&O MPPT algorithm for three-phase grid-connected PV systems. In: 2018 China international conference on electricity distribution (CICED). IEEE, pp 1997–2001
2. Abbadi A, Hamidia F, Morsli A (2018) New MPPT sliding mode approach for grid connected PV system. In: 2018 International conference on applied smart systems (ICASS). IEEE, pp 1–5
3. Keawthai S, Po-Ngam S (2015) Simplified active power and reactive power control with MPPT and islanding detection for three-phase grid-connected photovoltaic inverters. In: 2015 12th international conference on electrical engineering/electronics, computer, telecommunications and information technology (ECTI-CON). IEEE, pp 1–6
4. Suyata TI, Po-Ngam S (2014) Simplified active power and reactive power control with MPPT for three-phase grid-connected photovoltaic inverters. In: 2014 11th international conference on electrical engineering/electronics, computer, telecommunications and information technology (ECTI-CON). IEEE, pp 1–4
5. Hamadi A, Rahmani S, Al-Haddad K, Al-Turki YA (2011) A three-phase three wire grid-connect photovoltaic energy source with Sepic converter to track the maximum power point. In; IECON 2011–37th Annual Conference of the IEEE Industrial Electronics Society. IEEE, pp 3087–3092
6. Panigrahi BK, Bhuyan A, Satapathy AK, Pattanayak R, Parija B (2019) Fault analysis of grid connected wind/pv distributed generation system. In: International conference on intelligent computing and communication technologies. Springer, Singapore, pp 47–54
7. Pei T, Hao X (2019) A fault detection method for photovoltaic systems based on voltage and current observation and evaluation. Energies 12(9):1712
8. Bhuyan A, Panigrahi BK, Pati S (2021) Fault classification for DG integrated hybrid power system using wavelet neural network approach. In: 2021 1st Odisha international conference

on electrical power engineering, communication and computing technology (ODICON). IEEE, pp 1–5

9. Soufi Y, Bechouat M, Kahla S, Bouallegue K (2014) Maximum power point 5 1% 6 1% 7 1% 8 1% 9 1% 10 1% 11 1% tracking using fuzzy logic control for photovoltaic system. In: 2014 International conference on renewable energy research and application (ICRERA)

10. Modern maximum power point tracking techniques for photovoltaic energy systems. Springer Science and Business Media LLC (2020)

11. Kamarzaman NA, Tan CW (2014) A comprehensive review of maximum power point tracking algorithms for photovoltaic systems. Renew Sustain Energy Rev 37:585–598

12. Salman S, Xin AI, Zhouyang WU (2018) Design of a P-&-O algorithm based MPPT charge controller for a stand-alone 200W PV system. Protect Cont Mod Power Syst 3(1):1–8

13. Kamran M, Mudassar M, Fazal MR, Asghar MU, Bilal M, Asghar R (2020) Implementation of improved Perturb & Observe MPPT technique with confined search space for standalone photovoltaic system. J King Saud Univ-Eng Sci 32(7):432–441

14. Robles Algarín C, Taborda Giraldo J, Rodriguez Alvarez O (2017) Fuzzy logic based MPPT controller for a PV system. Energies 10(12):2036

15. Mahamudul H, Saad M, Ibrahim Henk M (2013) Photovoltaic system modeling with fuzzy logic based maximum power point tracking algorithm. Int J Photoenergy

16. Das SK, Panda PC, Samal S (2017) Grid connected PV system with fuzzy logic controller. In: 2017 International conference on communication and signal processing (ICCSP), pp 1177–1181. IEEE

17. Abraham Roy E, Beevi SS (2021) Control of BLDC motor driven standalone blower system using fuzzy logic controller. In: 2021 International conference on communication, control and information sciences (ICCISc)

18. Al-Majidi SD, Abbod MF, Al-Raweshidy HS (2018) A novel maximum power point tracking technique based on fuzzy logic for photovoltaic systems. Int J Hydrogen Energy 43(31):14158–14171

19. Ngan MS, Chee WT (2011) A study of maximum power point tracking algorithms for stand-alone photovoltaic systems. In: 2011 IEEE applied power electronics colloquium (IAPEC)

20. Mohamed A, Hannan MA (2009) Maximum power point tracking in grid connected PV system using a novel fuzzy logic controller. In: 2009 IEEE student conference on research and development (SCOReD). IEEE, pp 349–352

21. Sankar R, Velladurai S, Rajarajan R, Anitha Thulasi J (2017) II. PV system description: maximum power extraction in PV system using fuzzy logic and dual MPPT control. In: 2017 international conference on energy, communication, data analytics and soft computing (ICECDS)

22. Gounden NA, Peter SA, Nallandula H, Krithiga S (2009) Fuzzy logic controller with MPPT using line-commuted inverter for three-phase grid-connected photovoltaic systems. Renew Energy 34(3):909–915

An Assessment of Electricity Generation from Biogas Using Kitchen Waste with H$_2$S Removal by Pressure Swing Adsorption

Anup Kumar Rajak ⬤ **, Vaibhav Singh, Yash Verma, Kishan Kumar Mishra, Rajkumar Mishra, and Gaurav Kumar Pandey**

Abstract It is observed that a large amount of kitchen waste and other organic waste is obtained daily in our surroundings. It can be utilised for better purposes. Many places are still untouched with the supply of electricity due to graphical and economical reasons. If the places are in reach of power supply even after providing them a continuous power supply is also a big challenge due to low production of energy and high demand. So, keeping these problems in focus, the waste generated from kitchen and vegetable waste is given as feedstock to produce 0.4 m^3 of biogas per day with cow dung as a by-product. The Pressure Swing Adsorption technique purifies the CH4 gas generated from Biogas, and this is used for power generation. The biogas engine generator of 7 kVA is installed. This power is used for backup power for renewable energy lab lighting and fan load. Biogas can be used as an energy source and also for various purposes. The main objective of this study is the generation electricity by operating a generator with biogas.

Keywords Biogas electricity · Kitchen waste · PSA technique · Power generation

1 Introduction

Animals (cows, buffalo) dung square measure getting used from precedent days by farmers as associate energy supply to cook for. It's a way to use organic wastes; however, it is not economical and eco-friendly [1, 2]. Therefore, the government is promoting biogas, which can be useful in waste management and scale back dependency on renewable energy sources [3].

The correct definition of biogas may be a natural fuel obtained from "anaerobic digestion", i.e. the method of organic chemistry conversion that takes place in biological substances while not gas, at an acceptable temperature, and with the continual admixture of the substances used [4–6]. In observation, the assembly of

A. K. Rajak (✉) · V. Singh · Y. Verma · K. K. Mishra · R. Mishra · G. K. Pandey
Department of Mechanical Engineering, Rewa Engineering College, Rewa, Madhya Pradesh 486001, India
e-mail: anuprajak14@gmail.com

biogas consists of microorganisms breaking down complicated organic substances (lipids, protides, and glucides), contained in plants, sludge, and by-products of animal origin [7, 8].

Biogas is understood as an environmental-friendly energy supply as it alleviates 2 major environmental issues simultaneously:

- The reliance on conventional fossil fuel energy to satisfy world energy demand.
- The world waste pandemic releases hazardous levels of gas each day.

By changing domestic waste into energy, biogas utilizes nature's elegant tendency to recycle waste into productive resources [9–12]. Biogas generation recovers waste materials that will otherwise foul landfills, prevents the consumption of harmful chemicals in sewerage handling plants, and saves energy, material, and cash, by treating waste on the spot. Furthermore, biogas usage doesn't need fuel extraction to supply energy.

2 Material and Methodology

2.1 Digester

The Anaerobic digester is to undergo the formation of the kitchen waste, which is accessible in the hostel mess and within the college site. The anaerobic digester is premeditated to feed the daily kitchen waste of 250 kg max per day. The water added is 100 L max, and the retention time is 30 days. It has one inlet which is accompanied by the 2 hp crusher motor to crush the waste into 5–8 mm size. To carry the manure, the outlet is attached with a 4″ diameter pipe.

2.2 Floater

The generated biogas is collected in the floater or floating dome by the anaerobic digestion of the food inside the digester. The floating dome is lifted automatically, and as the gas is used, the dome comes to its original form (which means it touches the digester). The size of the floater is checked manually. It is attached to the outlet pipe to suck the biogas and transfer it to the filter at the pressure of 5 bar, with the help of a small booster pump. Floaters should be checked regularly for liquid level (oil/water can be used in the jacket) in the water jacket.

Fig. 1 Pressure swing adsorption-based filter unit

2.3 Filter Unit

To filter the CO_2, H_2O, and H_2S, this upgrading system uses the raw biogas and upgrades up to 90–94% methane, which is separate from other gases and retains the methane? The PSA (Pressure swing adsorption) technique is used for filtration. In this technique, three different cylindrical vessels are used to filter gases with adsorption material filled inside them by the surface adsorption and then release the gases from the surfaces after the mentioned period (Fig. 1).

2.4 Generator

The biogas is transformed into mechanical energy through an internal combustion engine. This mechanical energy rotates an iron core wrapped in copper wire inside a powerful magnet to create an electrical current. Further, it rotates the generator and generates electricity.

The biogas generator consists of a dual-fuel mode, diesel, and biogas, where a small amount of diesel is used to help the ignition of the biogas. The generator requires high-quality fuel. Harmful components such as Hydrogen sulphide (H_2S) in the biogas can drastically reduce a motor's lifecycle and cause severe damage.

This ought to be addressed in two ways:

Fig. 2 Biogas generator set (dual fuel-based- diesel and biogas)

- Use of suitable and strong motors and components; and
- Production of clean biogas.

For the use of biogas in diesel/gas/ petrol/gasoline engines, the biogas must carry out definite requirements:

- CH_4 should be as high as possible because it is the key combustible part of the biogas;
- CO_2 and water vapour content should be as low as possible, mainly because they lead to the low calorific value of the gas;
- Sulphur content in biogas, mainly in the form of H_2S, must be low because it produces corrosion—causing acids by condensation and combustion.

The standard calorific value of biogas is about 21–23.5 MJ/m^3. That means 1 m^3 of biogas corresponds to 0.5–0.6 L diesel fuel of about 6 kwh power. However, 1 m^3 of biogas can be converted only to around 1.7 kWh due to conversion losses [13, 14] (Fig. 2).

3 Result and Discussion

Retention time (r, measured in days) and Hydraulic loading (q, measured in m^3/day), are the two fundamental factors for digester volume. The feed rate (Q) is given by the mass of total solid (m kg) fed daily, divided by the proportion of total solid (T_s) in the mixed slurry (as summing the density of feed is 1000 kg/m^3) [15, 16].

$$Q = \frac{m}{T_s * 1000} \frac{m^3}{day} \tag{1}$$

The retention time (R_T) of any anaerobic digester is specified by the volume of the digester pit (V m^3) divided by the volume of the daily feed Q.

$$R_T = \frac{V}{Q} \tag{2}$$

The mass of volatile solids added each day per unit volume of the digester is defined as the loading rate [R (kg V_s/m^3/day)], and this is related to the mass feed rate.

$$R = \frac{m V_S}{Q} \tag{3}$$

The characteristic values for the loading rate are between 0.2 and 2.0 kg V_s/m^3/day.

3.1 Electricity Generation

Data obtained from this study revealed that biogas production is actually slow at the start and end of production. This is because of the slow activity level of the methanogenic bacteria, as the biogas production rate is directly equal to the specific growth of methanogenic bacteria. For this work, 40 kg of cow dung was used. From the biogas production and purification system, 1.565 m^3 of purified biogas is generated after a retention period of 30 days which is compressed into a 3 kg gas cylinder using a refrigerator compressor given a mass of 1.8 kg and a total mass of 4.8 kg. The produced biogas is used to run the power generating system.

3.2 Current and Voltage Reading

The engine's optimal performance at 100–800 W is partly due to the scrubbing efficiency of the scrubbing chamber which considerably reduced the carbon dioxide content of the raw biogas and improved the biogas thermal efficiency. Voltage and current readings were taken from the synchronous generator using a multi-meter at different load inputs ranging from 100 to 800 W (Table 1).

Table 1 Voltage output/load bearing capacity assessment

Load (W)	Power sources in renewable energy lab	Biogas	
		current reading	Voltage reading
80	2 tube light (40 W/tube light)	0.87	220
200	5 tube light (40 W/tube light)	1.36	220
300	5 tube light + 1 wall fan (100 W/fan)	1.82	219
400	5 tube light + 2 wall fan (100 W/fan)	2.31	218
800	5 tube light + 2 wall fan (100 W/fan) + Biogas Booster Pump (400 W)	2.72	210

3.3 Electricity Production from Biogas

From the biogas production and purification system, 1.565m^3 of purified biogas is generated. To determine the electricity production rate of the biogas generated, the volume of biogas is converted into megajoules, after which it is converted from megajoules to kilowatt-hour and multiplied by its helpful percentage energy [9, 17].

Biogas production rate $= 1.565 \text{m}^3$
Converting the volume of biogas produced to megajoules
1m^3 of biogas $= 19$ megajoules
1.565 m^3 of biogas $= 1.565 \text{ m}^3 \times 19$ megajoules$= 29.7$ megajoules
Converting to kilowatt-hour $= 29.7$ megajoules$/3.6 = 8.26$ kWh

When biogas is converted into electrical energy, 65% of the energy is lost as heat and other mechanical losses as the generator uses [12]. Hence, the electrical energy used for the generation of electricity becomes 35% of the kilowatt-hour.

35% of 8.26 kWh $= 0.35 \times 8.26$ kWh $= 2.88$ kWh. From the above result, 2.88 kwh is the electricity generated using 1.565 m^3 of biogas.

The biogas is scaled before and after it is run on the power generating system with a load input load of 800 W. Biogas is run on the power generating system. It is observed that 85% of biogas is consumed. Therefore, biogas will run for:

If biogas runs for 60 min, 1 kg will run for x minutes
0.85 kg $= 60$ min
1 kg $= X$ minutes
X minutes $= 60$ min$/0.85 = 71$ min

From the above result, biogas will run for 42 min with a load capacity of 800 W up to.

4 Conclusion

This study concluded the potential of biogas for power generation. A 250 kg kitchen waste-based biogas generation system is premeditated and implemented. We successfully modified the biogas generator, which is upgraded by the PSA technique. Comparatively, our result shows that biogas runs with a load capacity of 800 W for 42 min. Biogas is operated on the power generating system for 42 min, after which the system shut down due to complete consumption of the available fuel.

References

1. Voelklein MA, Rusmanis D, Murphy JD (2019) Biological methanation: strategies for in-situ and ex-situ upgrading in anaerobic digestion. Appl Energy 235:1061–1071. https://doi.org/10.1016/j.apenergy.2018.11.006
2. Amakom CN (2015) Comparative analysis on the biogas yield for chicken droppings and cow dung. In: 5th annual & international conference on renewable energy for sustainable environment, vol 5, 18th–21st June 2015, At Gregory University, Uturu, AbiaState, Nigeria
3. Sarker S, Lamb JJ, Hjelme DR, Lien KM (2019) A review of the role of critical parameters in the design and operation of biogas production plants. Appl Sci 9:1915. https://doi.org/10.3390/app9091915
4. Nsair A, Cinar SÖ, Abu-Qdais H, Kuchta K (2019) Optimizing the performance of a large-scale biogas plant by controlling stirring process: a case study. Energy Convers Manage 198:111931. https://doi.org/10.1016/j.enconman.2019.111931
5. Gebresemati M, Das G, JuPark B, Hee-Yoon H (2017) Electricity production from macroalgae by a microbial fuel cell using nickel nano particles as cathode catalysts. Int J Hydrogen Energy 42(50):29874–29880
6. Caposciutti G, Baccioli A, Ferrari L, Desideri U (2020) Biogas from anaerobic digestion: power generation or biomethane production. Energies 13(3):743. https://doi.org/10.3390/en13030743
7. Greenstone M (2014) Evidence paper: energy, growth and development. In: International Growth Centre (IGC), pp 2–42
8. Izhar TNT, Zakarya IA, Zaaba SK, Yusof AHM, Shahril NM (2021) A review of food waste characterization and treatment in anaerobic digestion. In: International conference on civil and environmental engineering, IOP Conference Series: Earth and Environmental Science, vol 646, p 012004. https://doi.org/10.1088/1755-1315/646/1/012004
9. Joshi A, Jose J, Bansiwal N, Soni N (2017) Study on electricity generation through biogas on small scale. Int J Innov Res Sci Eng Technol 6(4):6662–6669
10. Khan IU, Othman MHD, Hashim H, Matsuura T, Ismailb AF, Rezaei-DashtArzhandib MI, Azeleeb W (2017) Biogas as a renewable energy fuel—a review of biogas upgrading, utilization and storage. Energy Convers Manage 150:277–294
11. Müller FPC, Maack GC, Buescher W (2017) Effects of biogas substrate recirculation on methane yield and efficiency of a liquid manure-based biogas plant. Energies 10:325
12. Niemczewska J (2012) Characteristics of utilization of biogas technology. NAFTA-GAZ, ROK LXVIII, pp 293–297

13. Nkalo UK, Agwu EO (2019) Impactof electricity supply on economic growth: a Nigerian case study. J Elec Elect Eng 14(1):28–34
14. Octaviani NS, Semin S (2018) Technical overview of biogas utilization as fuel of boat engine. Int J Marine Eng Innov Res 2(2):171–175
15. Kumar D, Tewary T (2021) Techno-economic assessment and optimization of a standalone residential hybrid energy system for sustainable energy utilization. Int J Energy Res. https://doi.org/10.1002/er.6389
16. Ogwo JN, Dike OC, Mathew SO, Akabuogu EU (2012) Overview of biomass energy production in Nigeria: implications and challenges. Asian J Nat Appl Sci 1(4):46–51
17. Babaei A, Shayegan J (2020) Effects of temperature and mixing modes on the performance of municipal solid waste anaerobic slurry digester. J Environ Health Sci Eng 17:1077–1084. https://link.springer.com/article/10.1007%2Fs40201-019-00422-6

Biogas as an Alternate Vehicle Fuel

Anup Kumar Rajak [ORCID]**, Harsh Sharma, Abhinay Rangari, Aman Pandey, Rohit Sen, and Abhishek Mishra**

Abstract Anaerobic Digestion has been practiced for generations and ages. It has played a crucial role in generating renewable sources of energy to be used to make the environment clean and sustainable. One such example is the biogas generation plant which uses the daily waste, which helps in energy generation and fertiliser in agricultural practice. Biogas can be an efficient fuel that could give high calorific value. It could be helped in sustainable development of world by reducing environment hazards. An analysis through the engine rig rest will witness that biogas could be benefited to the environment as a fuel. It's performance could be as good as petrol and diesel. The need of the hour is to harness the potential of the renewable sources as the fossil fuels are fast depleting.

Keywords Anaerobic digestion · Anaerobic respiration process · Engine performance tests

1 Introduction

Biogas is a gaseous stream produced by the anaerobic digestion of organic matter. The key element of biogas is methane. It can be successful used as renewable source of energy [1, 2]. The maximum tremendous components of biogas depend on its decentralised global manufacturing and the environmental benefits of warding off methane emissions to the atmosphere simultaneously as using bio-methane to replace fossil fuels [3, 4]. With the purpose to use the power received in biogas, its production ought to be controlled. The biogas production from organic matter is a complex method concerning many distinctive bacterial groups.

A. K. Rajak (✉) · H. Sharma · A. Rangari · A. Pandey · R. Sen · A. Mishra
Department of Mechanical Engineering, Rewa Engineering College, Rewa, Madhya Pradesh 486001, India
e-mail: anuprajak14@gmail.com

153

Biomass

↓

Digester- Anaerobic Digestion
Hydrolysis → Acidogenesis → Acetogenesis → Methanogenesis

↓

Biogas

↓

Energy
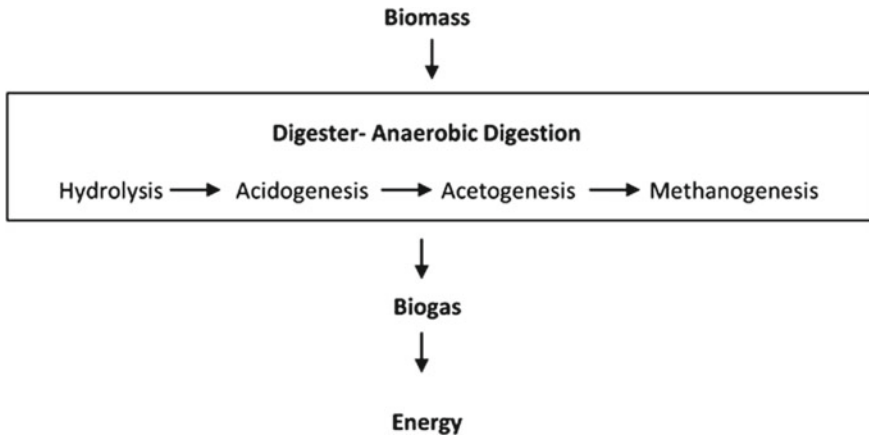
Fig. 1 Process involved in anaerobic respiration

2 Process

There are four main processes to convert organic matter to biogas which are as follows:

2.1 Hydrolysis

Biomass is initially served in the form of kitchen or animal waste which are generally complex organic matter which breaks off into simpler molecules with the help of microorganisms in this process [5, 6]. Hydrolysis is the process of breaking macromolecules into simpler molecules to initiate the process with the help of microorganisms. The outcome of this process is that it serves the purpose of rendering organic macromolecules that bacteria can utilise into their minor components. It could be seen that hydrolysis acts as the rate-determining step. Being the initial stage, it has its importance so that further stages could be performed unhindered [7–9] (Fig. 1).

2.2 Acidogenesis

With the absorption of the product of hydrolysis, acidogenic microorganisms can change them to intermediary volatile fatty acids and other products. It is believed that the acidogenesis stage generally occurs at a rapid rate than all different stages of anaerobic digestion. Acidogenic bacteria auxiliary break down the molecules into voletile fatty acids, H_2, H_2S and NH_3 [9, 10].

2.3 Acetogenesis

It is the process in which higher volatile fatty acids are converted into acetates with some amount of hydrogen produced. It converts the matter into H_2, CO_2 and acetic acid.

2.4 Methanogenesis

This is the final stage of anaerobic digestion, where the methanogenic microorganisms consume the matter to produce methane. These microorganisms are highly sensitive to oxygen and are confined to a small part of the matter. Acetoclasticmethanogenesis results in 2/3rd of the methane production, and hydrogenotrophic methanogenesis results in 1/3rd of the methane production [11].

3 Biogas Engine Testing Machine

Biogas engine testing machine is based on dual fuel, i.e. petrol and biogas fuel system. Both types of fuel can be utilised in this testing machine. Basically, it depends on a 4-stroke petrol engine which is upgraded for biogas fuel also. Block diagrams 1 and 2 of the engine testing machine are shown in Fig. 2.

4 Parameters

Brake power, specific fuel consumption, torque, brake thermal efficiency, mean effective pressure, indicated thermal efficiency, mechanical efficiency and exhaust temperature parameters at different speeds were compared with that run on petrol [12–14].

Some of these parameters are.

4.1 Brake Power

The brake power (BP) is defined as the power developed by an engine and measured at the output shaft.

Brake power

$$BP = \frac{2\pi NT}{60} \tag{1}$$

Fig. 2 Engine testing machine

where

N = Rotational speed of the engine, rpm
T = Torque, Nm

4.2 Indicated Power

Indicated Power is defined as the power developed in the cylinders, and thus forms the basis of an evaluation of combustion efficiency or the heat released in the cylinder.

$$IP = \frac{P_m LANK}{60} \tag{2}$$

where

P_m = Mean Effective Pressure, P_m
L = Length of the stroke, m
A = Area of the piston, m^2

$K = $ Number of cylinders

Mean Effective Pressure, P$_\mathbf{m}$, (N/m^2) is defined as a hypothetical/average pressure that is assumed to be acting on the piston throughout the power stroke. The difference between Indicated Power (IP) and Brake Power (BP) is called Friction Power (FP)

$$FP = IP - BP \tag{3}$$

4.3 Torque

$$\text{Torque}, T = (\text{BMEP} * A * L * k)/2\pi \tag{4}$$

4.4 Mechanical Efficiency

Mechanical efficiency is a measure of how much of the indicated power is converted into brake power. The difference between them is due to the frictional losses between the moving parts and the energy taken to run the auxiliary equipment such as the fuel pump, water pump, oil pump, etc.

$$\text{Mechanical Efficiency} = \frac{\text{BP}}{\text{IP}} \tag{5}$$

4.5 Indicated Thermal Efficiency

Indicated Thermal Efficiency is a measure of how much of the fuel power is converted into brake power

$$\text{Indicated Thermal Efficieny} = \text{Indicated power/Energy Supplied}$$
$$= ip/(mf \times Q_{\text{net},v}) \tag{6}$$

4.6 Brake Thermal Efficiency

Brake Thermal Efficiency is an indication of fuel power that is converted into brake power, i.e.

$$\text{Brake Thermal Effeciency} = \frac{BP}{\text{Energy Supply}} = \frac{BP}{m_f \times Q_{net,v}} \tag{7}$$

where

m_f = mass of fuel consumed per unit time
$Q_{net,v}$ = Lower calorific value of the fuel

4.7 Brake Specific Fuel Consumption

The amount of fuel consumed for each unit of brake power developed per hour is defined as brake specific fuel consumption. It is a clear sign of the efficiency with which the engine produces power from fuel

$$\text{BSFC} = \frac{(\text{Actual fuel} - \text{Air ratio})}{(\text{Stoichiometric fuel} - \text{Air ratio})}$$

5 Observation

Table 1 and Fig. 3 show the result of the calibration of the torque meter.

6 Result of Engine Performance Tests

Biogas engine testing machine is based on dual fuel, i.e. petrol and biogas fuel system. Both types of fuel can be utilised in this testing machine. Basically, it depends on a 4-stroke petrol engine which is upgraded for biogas fuel also. This study is based on running biogas on four-stroke internal combustion engine test machines.

7 Conclusion

Biogas is used as an internal combustion fuel which comes with difficulties. This study contains the modification in some parts of the engine and specifications. This

Table 1 Engine performance tests result using biogas as a fuel

S. No	Speed, RPM	Torque, Nm	Fuel Mass flow rate, kg/hr	Brake Power, kW	Specific Fuel Consumption, g/kWh	Brake Thermal Efficiency, %	Brake Mean Effective Pressure, N/m^2	Friction Power kW	Mechanical efficiency, %	Indicated Thermal Efficiency, %	Exhaust temperature, °C
1	1000	6.2	1.18	64.93	18.23	4.47	0.00017	27.44	0.70	3.37	350
2	1500	7.8	1.25	122.54	10.23	7.96	0.00021	16.02	0.88	8.65	410
3	2000	8	1.52	167.57	9.08	8.97	0.00022	17.18	0.91	10.76	440
4	2500	8.3	1.64	217.32	7.54	10.80	0.00023	13.62	0.94	16.96	460
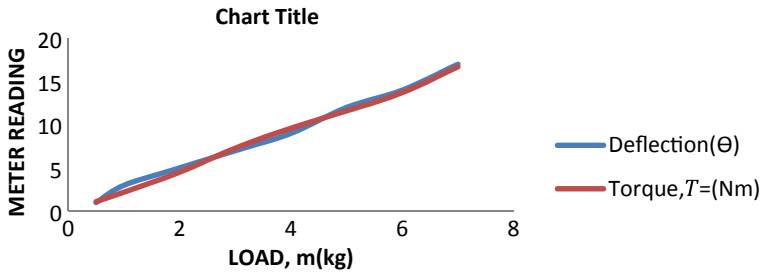
Fig. 3 The graph between Torque meter reading, T, (Nm) and a deflection against Applied load, m (kg)

research is based on a 250 kg domestic waste biogas digester system installed at Rewa Engineering College, Rewa. With this study, some salient features are immersed:

- This work is based on biogas production from kitchen waste. The waste contains all kitchen waste, vegetable waste and hotel waste. These wastes are mixed together, and a chemical reaction forms biogas which contains methane, carbon dioxide, water vapour and hydrogen sulphide from feeding solid waste.
- Engine testing rig machine is fuelled with biogas and generates more brake power, indicated power, torque, brake thermal efficiency and mean effective pressure but with less exhaust temperature and fuel consumption.

Consequently, it can be concluded that biogas is a genuine and feasible alternative for SI engine fuel. Biogas is more economical and environment friendly which also contribute as waste disposal and production of fertiliser.

References

1. Ali AM, Atefeh S, Akbari NK, Tala B, Antonio V (2019) Halophiles and their vast potential in biofuel production. Front Microbiol 10:1895. https://doi.org/10.3389/fmicb.2019.01895
2. Kasirajan L, Maupin-Furlow JA (2020) Halophilic archaea and their potential to generate renewable fuels and chemicals. Biotechnol Bioeng. https://doi.org/10.1002/bit.27639
3. Dar RA, Parmar M, Dar EA, Sani RK, Phutela UG (2021) Biomethanation of agricultural residues: potential, limitations and possible solutions. Renew Sustain Energy Rev 135:110217. ISSN 1364-0321. https://doi.org/10.1016/j.rser.2020.110217
4. Zhurka M, Spyridonidis A, Vasiliadou IA, Stamatelatou K (2020) Biogas production from sunflower head and stalk residues: effect of alkaline pretreatment. Molecules 25(1):164. https://doi.org/10.3390/molecules25010164

5. Piotrowska-Długosz A. Significance of the enzymes associated with Soil C and N transformation. In: Carbon and Nitrogen cycling in soil. Springer, Singapore. https://doi.org/10.1007/978-981-13-7264-3_12

6. Auma EO (2020) Anaerobic co-digestion of water hyacinth (Eichhornia crassipes) with ruminal slaughterhouse waste under mesophilic conditions. Thesis, University of Nairobi. http://erepository.uonbi.ac.ke/handle/11295/154487

7. Anthony A, Ali M, Muhammad N, Karin G (2019) A review of the chemistry of anaerobic digestion: methods of accelerating and optimizing process efficiency. Processes 7(8):2227–9717. https://doi.org/10.3390/pr7080504

8. Logroño W, Popp D, Kleinsteuber S, Sträuber H, Harms H, Nikolausz M (2020) Microbial resource management for ex situ biomethanation of hydrogen at alkaline pH. Microorganisms 8:4. https://doi.org/10.3390/microorganisms8040614

9. Voelklein MA, Rusmanis D, Murphy JD (2019) Biological methanation: strategies for in-situ and ex-situ upgrading in anaerobic digestion. Appl Energy 235:1061–1071. https://doi.org/10.1016/j.apenergy.2018.11.006

10. Bonk F, Popp D, Weinrich S, Sträuber H, Becker D, Kleinsteuber S, Harms H, Centler F (2019) Determination of microbial maintenance in acetogenesis and methanogenesis by experimental and modeling techniques. Front Microbiol 10:1–13. https://doi.org/10.3389/fmicb.2019.00166

11. Schulzke T (2019) Biomass gasification: conversion of forest residues into heat, electricity and base chemicals. Chem Pap 73:1833–1852. https://doi.org/10.1007/s11696-019-00801-1

12. Nsair A, Onen Cinar S, Alassali A, Abu Qdais H, Kuchta K (2020) Operational parameters of biogas plants: a review and evaluation study. Energies 13(15):3761. https://doi.org/10.3390/en13153761

13. Igoni H, Ayotamuno MJ, Eze CL, Ogaji SOT, Probert SD (2008) Designs of anaerobic digesters for producing biogas from municipal solid-waste. Appl Energy 85(6):430–438. https://doi.org/10.1016/j.apenergy.2007.07.013

14. Ashok Kumar S, Marimuthu C, Balaji EP, Shaker Riswan S (2014) Biogas production from kitchen waste water using USAB reactor. Int J ChemTech Res 06:4135–4142

Control and Operation of Microgrid Integrated with Solar PV and Wind Power (DFIG)

Paluru Venkatesh, Jai Prakash Sharma, Salauddin Ansari, and Om Hari Gupta

Abstract This paper presents modeling and simulation of a renewable energy-based microgrid in a MATLAB environment for a particular selected load in different operating conditions. The microgrid technologies, that merge distributed generations, energy storage sections, and loads, lead to an effective approach to solving the interconnection of large-scale distributed generations with the main power grid. Wind and solar can be compatible with each other in time, therefore wind and solar PV power systems could make great use of clean energy and have greater reliability. The proposed microgrid system consists of a doubly-fed induction generator (DFIG) dependent wind energy conversion system (WECS), solar PV array, and loads. The wind turbine system is interfaced to the main utility grid along with the solar PV array system while the PV array is linked via an inverter and a boost converter with a maximum power point tracking system. Finally, simulation and analysis of the microgrid are carried out for various operating conditions.

Keywords Distribution generation system · DFIG wind turbine · Solar photovoltaic · Microgrid · Maximum power point tracking

1 Introduction

Under this section Distributed generation system, wind generation system, DFIG system, and PV system will be introduced. With the centralized facilities, large-scale generation of electricity can be achieved, and is referred to "centralized generation" which is a conventional system. Nowadays, unlike centralized generation, with small-scale generating units, the generation of electricity will be achieved, and it is known as de-centralized generation also known as distribution generation (DGs). DG refers to a variety of technologies that produce electricity at or near where it will be needed. DG can carry by a single structure, like a home or business or it can be a portion of a microgrid (MG). Meanwhile, at the same time the worldwide energy disaster,

P. Venkatesh (✉) · J. P. Sharma · S. Ansari · O. H. Gupta
National Institute of Technology Jamshedpur, Jharkhand 831014, India
e-mail: 2019rsee006@nitjsr.ac.in

Electricity demand, and large-scale power interruptions are there so to mitigate this problem DG will play a vital role. Due to the various advantages of integrating DG, it is always a research topic. In modern years, DG has set off as a well-organized and a better substitute to the conventional energy resources and modern technologies are making DGs economically suitable [1]. DG minimizes the amount of energy loss in transmitting electricity, as the electricity is generated very near to the load where it is utilized. DG allows you to collect energy from many sources and may offer lower environmental impacts and greater reliability and stability [2, 3].

By using the power of wind, the wind turbines (WTs) will make mechanical energy and with that mechanical energy, it will drive an electric generator that generates electricity. Generally, across the blades, the wind passes over and creates lift, and produces a rotating force. The WT blades which are rotating will rotate a shaft inside the nacelle, i.e., from the blade's swept area the WT draws kinetic energy. The gearbox here is having an important role that will maximize the rotational speed of the WT to drive the shaft of the generator. Based on Faraday's law of magnetic induction, mechanical energy is converted to electrical energy. Generated electrical energy is then converted to desired voltage level with the help of a power transformer. The WECSs at present are the most inexpensive, available, and viable renewable energy systems which have accomplished rapid growth in modern years. Wind energy systems incorporated with DFIGs have been effectively utilized in high-power generation as they use power-electronic converters with ratings below the rating of the WT generators [4–7].

The frequently used machine nowadays is the DFIG. The induction machine can be operated either as a motor or generator. The DFIG and WTs have secured and prominence in the utilization of generators in water and wind power plants because of their efficient capability for maintaining and flexibility. In this paper, the DFIG system and its modeling have been described in brief.

A PV system utilizes solar panels to convert solar energy into usable electrical energy. It is having different segments that include the PV modules, mechanical and electrical links, mountings, and means of regulating and adapting the electrical output [8, 9]. The PV system, when hit by the sunlight, will generate DC electricity without any impact on the environment. The fundamental components of PV arrays are the solar cell and primarily it is a P–N junction that turns sunlight energy into electrical energy. The PV module's output characteristic depends upon the temperature of the module's cell, solar irradiation, and output voltage.

2 Microgrid (MG)

2.1 Introduction

An MG is a localized group, i.e., a small-scale power grid. It has a small-scale network of electricity consumers with a domestic origin of supply either by solar generation or by WT or by diesel generators, which is nominally coupled to a centralized national grid but it is also able to function independently i.e., islanded mode. Power systems nowadays turning into a noticeable change in the operational process mainly due to an increase in distributed energy resources (DER) and deregulation. Having microsources adjacent to the load has the benefit of mitigating transmission losses and resolving congestion in the network, nowadays it is called a microgrid [10].

From the end-user point of view, MG can give both thermal and electricity needs and with that, it improves local reliability, enhances power quality by encouraging voltage and mitigating voltage dip, and perhaps it supplies power at a lower cost. The use of distributed energy sources can bring down bids for distribution and transmission facilities from the utility point of view [11, 12].

2.2 Advantages of MG

i. A primary advantage of MG is its capability to seamlessly attached and detach itself from the utility grid and no disruption to the loads associated with the MG during a utility-grid disturbance.
ii. It reduces the utility grid burden in peak load periods by lowering the load on the grid.
iii. Usage of both electricity and heat allowed by the generator's close propinquity to the user, thereby increasing the overall energy efficiency.
iv. By generating numerous or whole of its electricity needs, MG can act to diminish the electricity costs to its users.

2.3 Disadvantages of MG

i. Voltage, frequency, and standard of power are the key points that must be contemplated and regulated according to appropriate standards while preserving the balance of power and energy.
ii. The storage of electrical energy in battery banks is required in an MG therefore there is a need for space as well as maintenance.
iii. It is difficult to resynchronize with the main grid.
iv. MG protection faces the most difficult challenge.
v. Issues related to stand-by charges and net metering may impede MG.
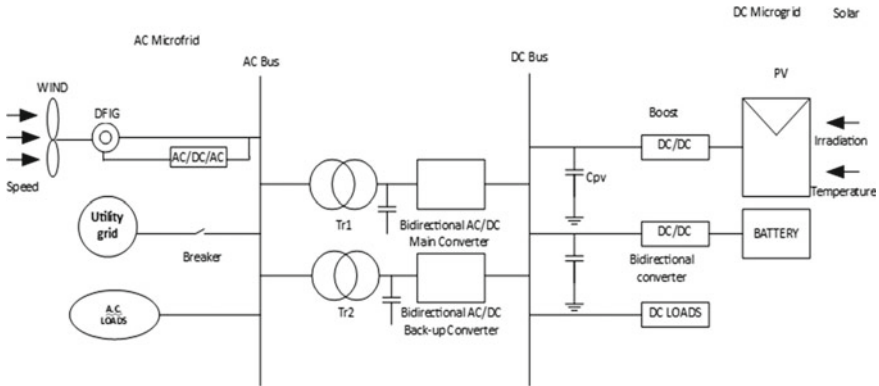
Fig. 1 A hybrid AC/DC MG system

2.4 Configuration of the Hybrid Microgrid (HMG)

Figure 1 deliberates the configuration of an HMG system that is consisting of AC and DC grids. These grids are having compatible sources, loads, power supplies, and a three-phase converter. The transformer and breaker are used to connect the AC bus to the main utility grid. In the proposed system, the PV array is linked to a DC bus to mimic DC sources with a boost converter. To mimic AC sources DFIG system is connected to an AC bus. To mimic the load which was connected in common to the grid and both the DFIG and solar PV system will deliver power to the load under different operating conditions.

3 Control and Modeling

3.1 DFIG

A comprehensive model of DFIG is described in Fig. 2. In the rotor circuit, two reverse transformers have been used. The main motivation of the machine side converter is that it can manage the real by handling the current units of the DC motor, while the grid-sided converter manages the DC-link voltage and make sure the operation of the unit's power factor supply and keeps reactive power "Q" of the power system at zero. The simulated DGID model is shown in Fig. 3. In this DFIG Model, the performance of the DFIG system is analyzed under different values of wind speed. A load of 2 MW was connected at the load end and results of different parameters under varying wind speed have been observed.
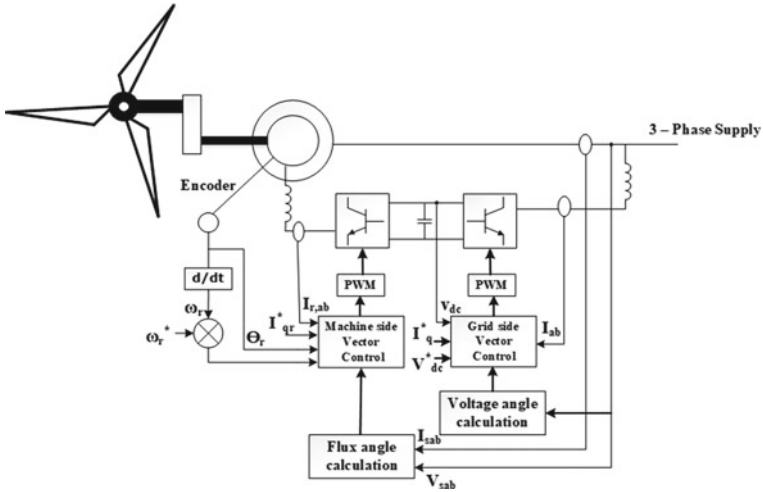
Fig. 2 Overall DFIG system
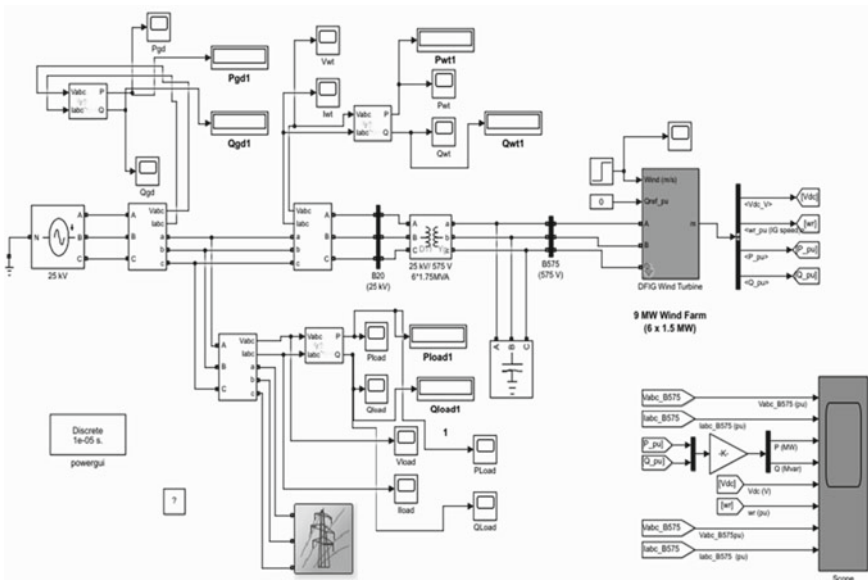
Fig. 3 DFIG model diagram

3.2 The Solar PV Array System

A comprehensive schematic diagram and model diagram of the solar PV array is represented in Figs. 4 and 5, respectively. The performance validation of the PV

array system had been carried out with variations in temperature and irradiance values. Here Max.PPT technique is used to track the maximum power peak point at which the panel has the peak energy. As from Fig. 4, the DC power obtained from the solar panel is converted into AC by using a 3-level bridge inverter after that the output level of the inverter will be converted to the desired level by using a transformer. The obtained AC supply is integrated into an already existed MG which is linked with DFIG to serve the resistive load of 2 MW which is connected at the end, and it can have been analyzed different parameters under variations in temperature and solar irradiance which is discussed in the result section.
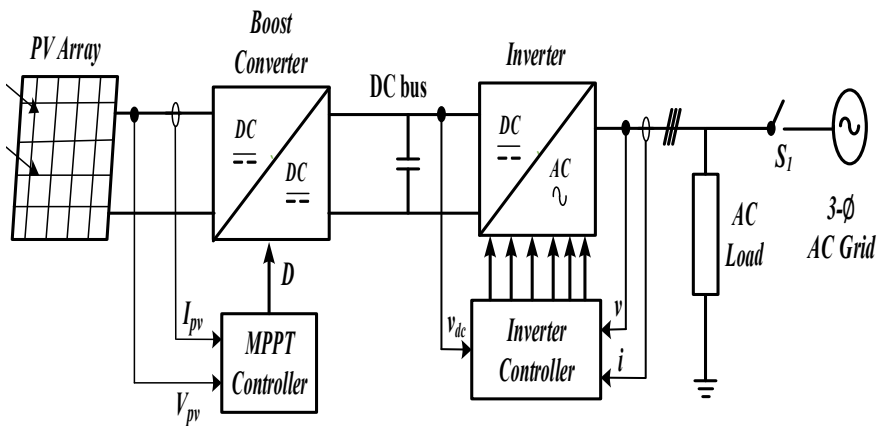
Fig. 4 Schematic diagram of Solar PV array system
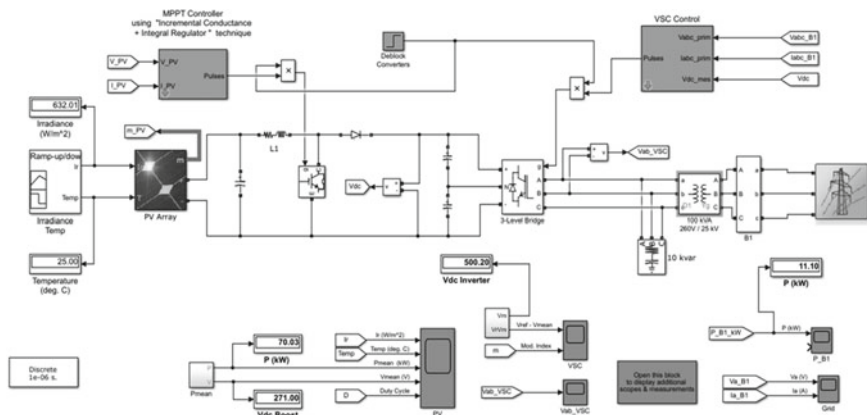
Fig. 5 Solar PV array model diagram

4 Results

An MG that is linked with a solar PV system and DFIG wind generation system is simulated using the MATLAB environment. The grid-connected mode has been considered for performance validation. The performance analysis is carried out with the HMG, DFIG, and PV Systems. With variation in the solar irradiation, the temperature of the cell, and the speed of the wind, a rigorous analysis of the MG has been done under MATLAB/Simulink environment.

4.1 PV Array Simulation

The only PV system is considered with the MG and corresponding simulated results are observed and discussed here. Figure 6 represents the output voltage (V_a) of the solar system, the output voltage taken at the secondary side of the boost transformer.

Figure 7 represents the output current (I_a) of the solar system, and it has been taken at the secondary side of the transformer.

Figure 8 depicts the output real power (P) which is produced by the solar PV system and here it produces slightly lesser than rated power of the PV system, i.e. 100 kW at steady state. The mean real power (P) produced by the solar system is 92.88 kW.

Figure 9 represents the output reactive power (Q)—as a purely resistive load has been taken, Q drawn by the load is 0 VAR. With a 2 MW load connected through a 5 km feeder, results of P and Q have been recorded. The temperature is kept at 50 °C
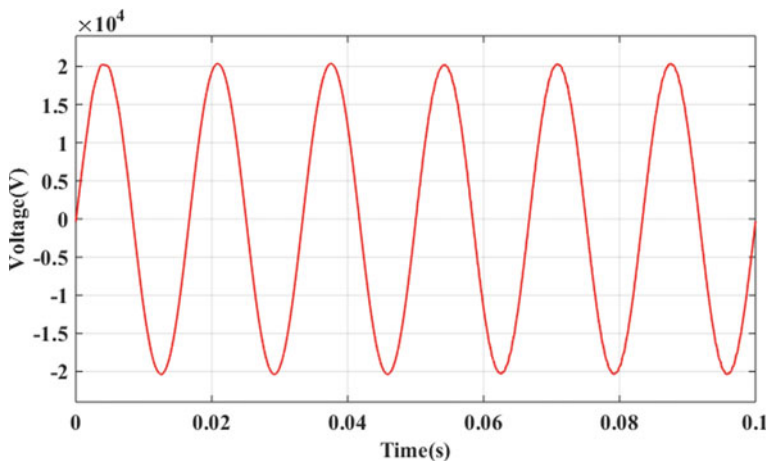
Fig. 6 PV array output voltage
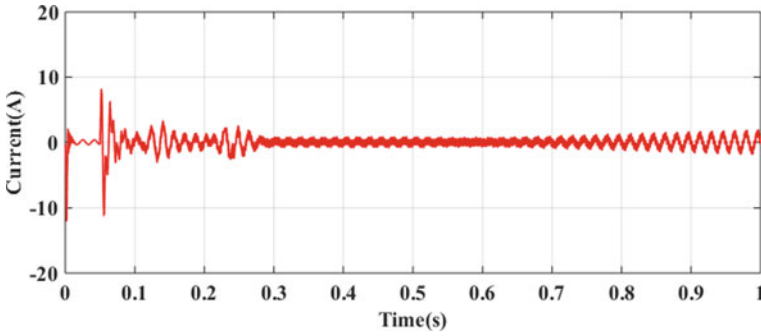
Fig. 7 PV array output current
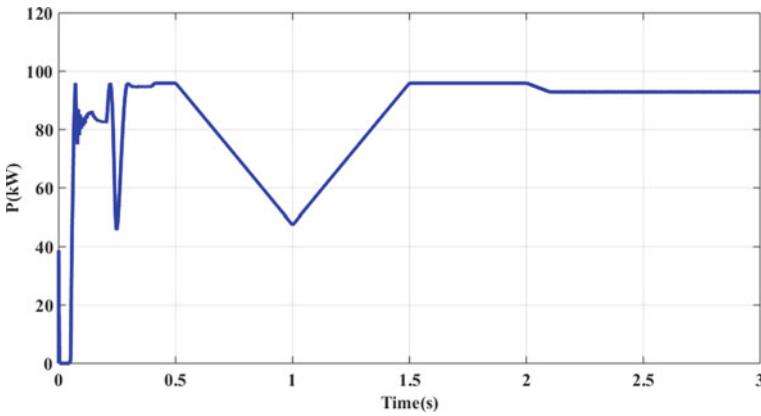
Fig. 8 Solar PV system output active power

and the solar irradiance at 1000 W/m^2 and P drawn by the load is 1.98 MW and the Q drawn by the load is 0 VAR—as the load is purely resistive.

In this simulation, Fig. 10 is showing the solar irradiance with variation in time. A signal builder has been taken such that the solar irradiance will vary from 0 s to 0.5 s it is 1000 W/m^2 and from 0.5 s it will bring down to 500 W/m^2 at 1 s and it raises from that point to 1000 W/m^2 and it continues to them till 3 s.

It can be seen from Fig. 11 that different values of the solar cell temperature have been considered. The temperature varies such that from 0 to 2 s it is at 40 °C and from that point, it increases to 50 °C and it continues to there till 3 s.
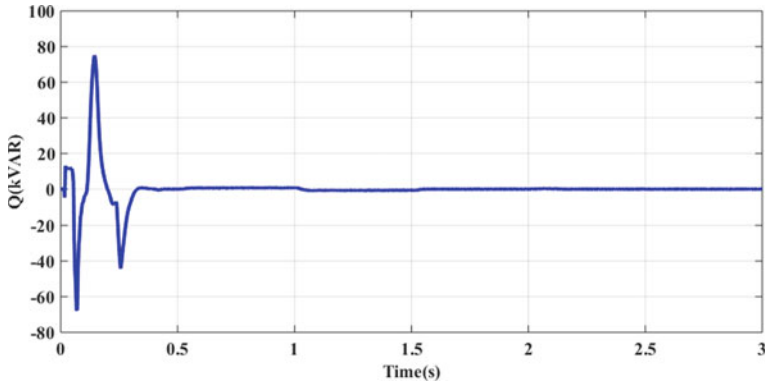
Fig. 9 Solar PV system output reactive power
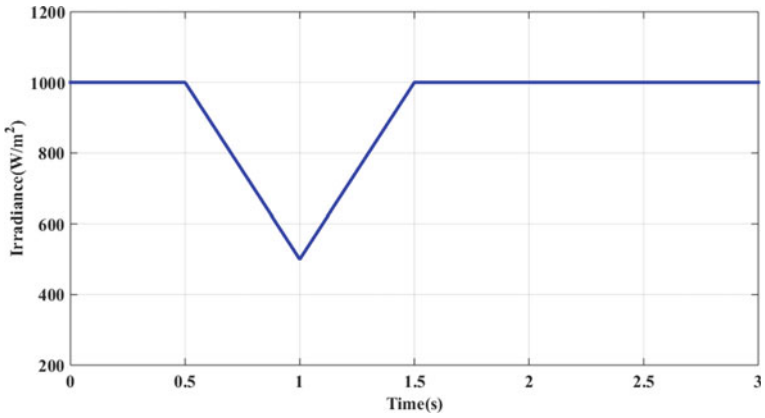
Fig. 10 Variation of irradiance considered
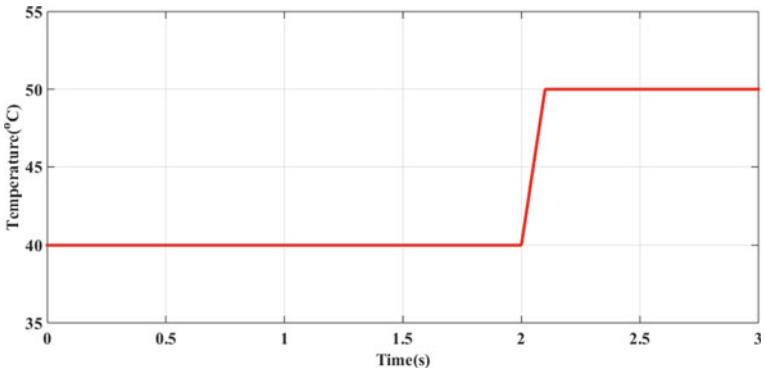
Fig. 11 Variation of solar cell temperature considered

4.2 DFIG Simulation

Here only the WGS with MG has been considered for performance evaluation. A DFIG WGS is connected to the main grid of 25 kV. In this model, the variation of wind speed considered is shown in Fig. 12. Initially, the wind speed is kept at 4 m/s after 2 s the wind speed increases to 40 m/s. The response of the wind speed is shown in Fig. 12.

In Fig. 13 the output voltage sampled at the output side of the WT was represented. Actually, in Fig. 13 the output voltage is represented per unit (P.U), the actual value of the output voltage which was generated by the DFIG WT is 575 V.

In Fig. 14 the output current sampled at the output side of the WT is represented. Actually, in Fig. 14 the output current is represented in the P.U system.

In Figs. 15 and 16, the output real power (P) and reactive power (Q) of the DFIG WGS are shown respectively. The P generated by the WGS at a steady state is nearly 8 MW and the Q is 0 VAR.
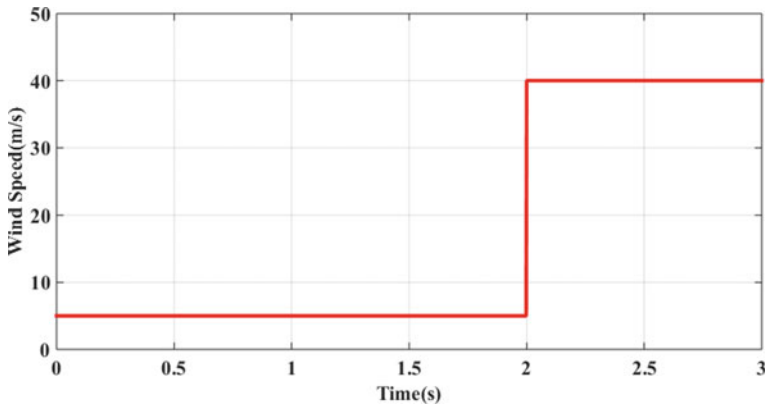
Fig. 12 Varying wind speed considered
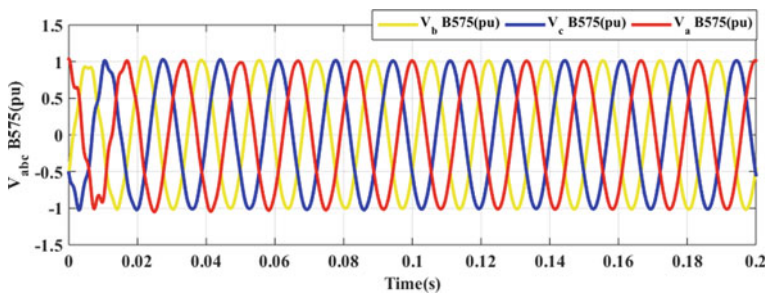
Fig. 13 DFIG 3-ϕ output voltage
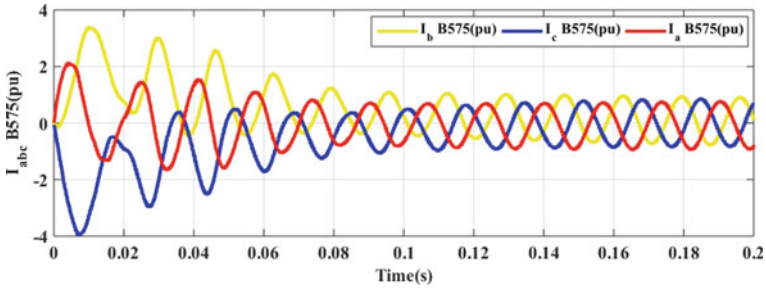
Fig. 14 DFIG 3- φ output current
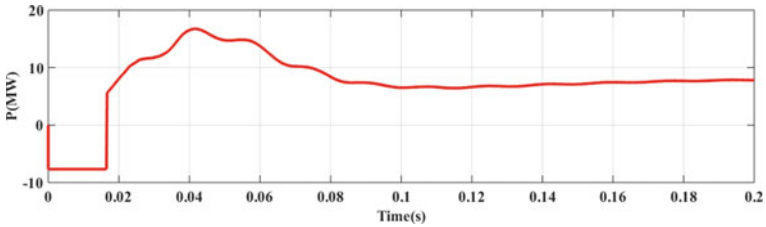
Fig. 15 DFIG output active power
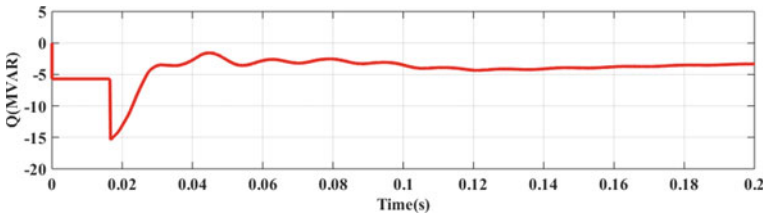
Fig. 16 DFIG output reactive power

In this model also a 2 MW load has been taken, which is connected at the end of a 5 km long feeder to the microgrid. The samples of P and Q have been used for analysis. The simulation runs for 3 s and at 3 s the P drawn by the load is 1.99 MW which is very much closer to the rated load and obviously, the reactive power drawn by the load is 0 VAR. The main utility grid taking 7.11 MW of P and 6.56 MVAR of Q and the load drawing P of 1.99 MW and the Q drawn is 0.7 kVAR which is the reactive VAR drawn by the feeder as the load is purely resistive. By observing these results, it is clear that the system is well balanced.

4.3 MG Simulation

In this Model, the PV array and the DFIG WT generation sources both are inter-connected to a common utility grid and it is finally coupled to the main power grid like Grid-tied mode and a load of 2 MW is connected at the end of a 5 km feeder as same as in the PV array model and DFIG WT model. In Fig. 17 Solar PV system generated real power (P_{pv}) sample which is taken at the output end side of the solar PV system is shown. Here the solar PV system generates 92.70 kW of P_{pv} which is shown in the figure. In Fig. 18 Solar PV system generated reactive power (Q_{pv}) sample which is taken at the output end side of the solar PV system is shown. Here the solar PV system generates 0.68 kVAR and which is giving to the main grid. In Fig. 19, the real power (P_{dfig}) generated by the DFIG WT is shown. Here at time 3 s the P_{dfig} generated is 9.66 MW.
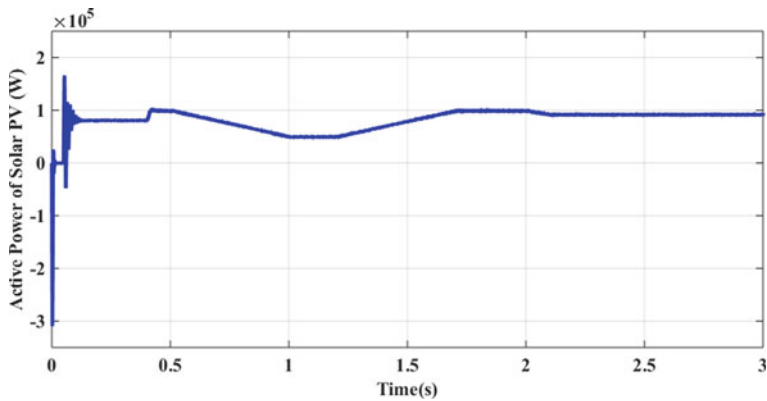
Fig. 17 Solar PV array real power
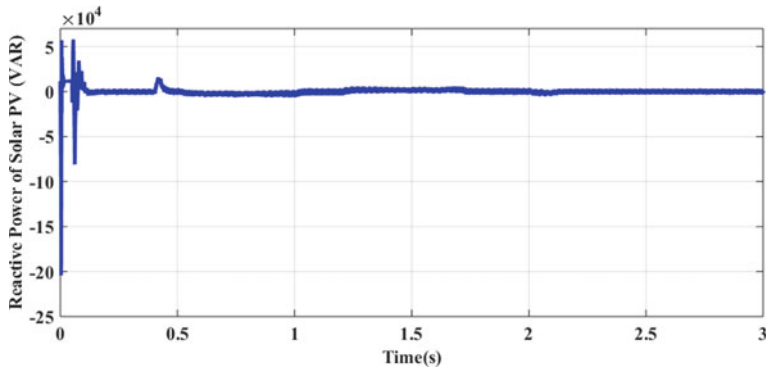
Fig. 18 Solar PV array's reactive power
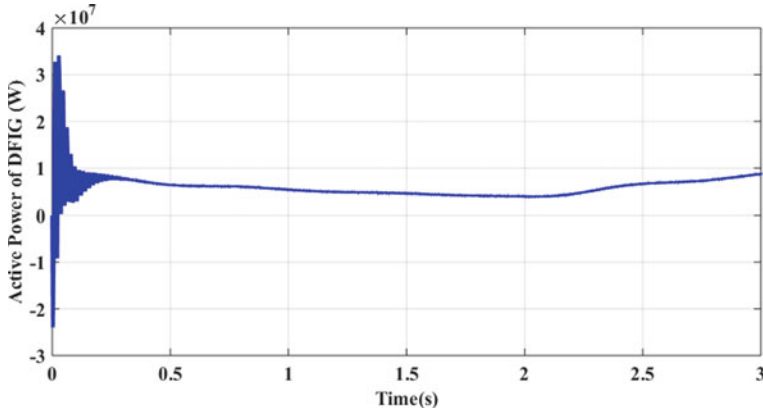
Fig. 19 DFIG real power

In Fig. 20, the Reactive power (Q_{dfig}) generated by the DFIG WT is shown. Here at time 3 s the Q_{dfig} generated is 8.26 MVAR. In Fig. 21 the real/active power (P_{load}) drawn by the load which is connected commonly to the MG is shown. Here the load drawing 1.99 MW of P_{load} from the grid at time 3 s.

In Fig. 22 the reactive power (Q_{load}) drawn by the load which is connected commonly to the MG is shown. Here the load drawing 0 VAR of Q_{load} from the grid at time 3 s but as we connected the load through a 5 km feeder so the feeder consuming some amount of reactive Vars which is 0.7 kVAR.

In this MG model, the P contributed by the DFIG WT generator is 9.66 MW, and the Q contributed by the DFIG WT generator is 8.26 MVAR, the P contributed by the PV array model is 92.7 kW and the Q contributed by the PV array is 676 VAR. Here it is observed that the power is received by the load at the starting of the feeder.
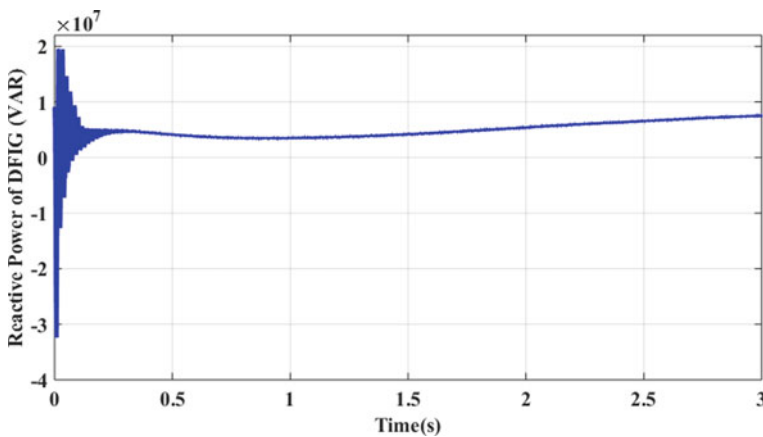
Fig. 20 DFIG reactive power
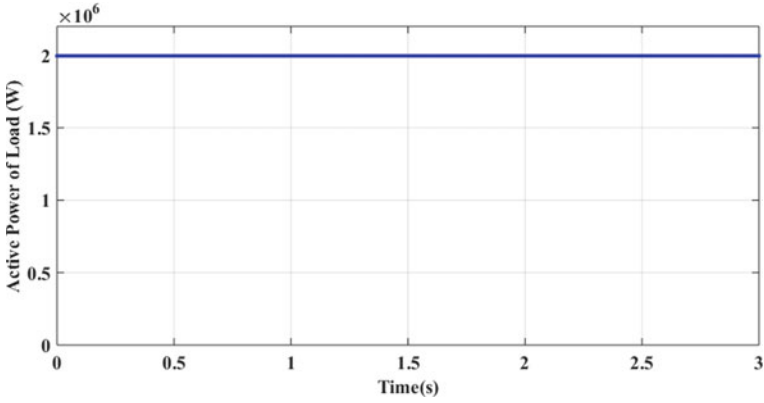
Fig. 21 Active power is drawn by the load
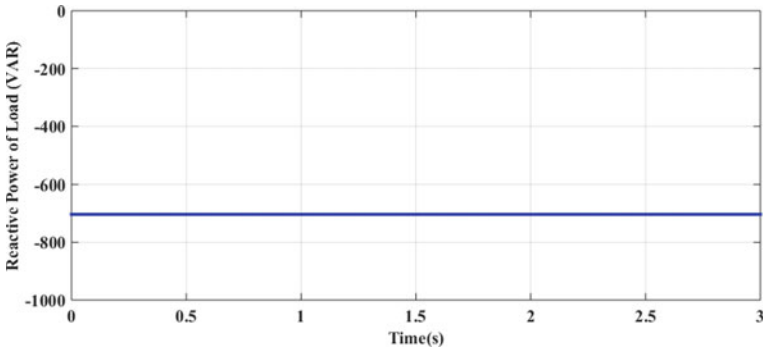
Fig. 22 Reactive power is drawn by the load

The samples of P and Q are taken, those values are 1.99 MW and -0.7 kVAR. Here the main power grid taking P of 3.54 MW and the Q taking by the main power grid is 3.83 MVAR. With a load of 2 MW and the load is drawing P of 1.99 MW, as it is a resistive load so the Q drawn by the load is 0 VAR.

5 Conclusion

A fully renewable-energy-dependent MG has been designed and the model was simulated for a particular chosen load and the simulation results are analyzed. From the simulation results, it was observed that the designed MG is successfully meeting the required load demand as a connected load of 2 MW, and the MG conveniently serving the load with 1.99 MW as the connected load is resistive so the reactive power

at the load end is zero. It is found that from this analysis, modeling of renewable energy-dependent MG was found to be feasible and functional for the desired load.

References

1. Guan FH, Zhao DM, Zhang X, Shan BT, Liu Z (2009) Research on distributed generation technologies and its impacts on power system. In: 1st international conference on Sustainable Power Generation and Supply, SUPERGEN '09
2. Kundu D (2008) An overview of the distributed generation (DG) connected to the GRID. In: 2008 joint international conference on Power System Technology POWERCON and IEEE Power India Conference, POWERCON 2008
3. Mozina CJ (2008) A tutorial on the impact of distributed generation (DG) on distribution systems. In: 2008 61st annual conference for protective relay engineers, pp 591–609
4. Chandrasekaran JS, Rossi C, Casadei D. Modeling and simulation of grid connected Doubly Fed Induction Generator (DFIG) based wind turbine with varying wind speed. IET Renew Power Generation J RPG-2012-0280 (Accepted)
5. Fan L, Yin H, Miao Z (2011) On active/reactive power modulation of DFIG-based wind generation for interarea oscillation damping. IEEE Trans Energy Convers 26(2):513–521
6. Muller S, Deicke M, De Doncker R (2002) Doubly fed induction generator systems for wind turbines. IEEE Ind Appl Mag 8(3):26–33
7. Tremblay E, Atayde S, Chandra A (2011) Comparative study of control strategies for the doubly-fed induction generator in wind energy conversion systems: ADSP-based implementation approach. IEEE Trans Sustain Energy 2(3):288–299
8. Qiao W (2009) Dynamic modeling and control of double fed induction generators driven by wind turbines. In: Power system conference and exposition, PSCE'09, IEEE/PES
9. Haque A, Zaheeruddin (2013) Research on solar photovoltaic (PV) energy conversion system: an overview. In: IET Conference Publications, vol 2013, no CP646, pp 605–611
10. Parida B, Iniyan S, Goic R (2011) A review of solar photovoltaic technologies. Renew Sustain Energy Rev 15:1625–1636
11. Modeling and simulation of a microgrid consisting solar PV & DFIG based wind energy conversion system for St.Martin's Island. Abir Muhtadi Department of Electrical & Electronic Engineering American International University-Bangladesh Dhaka, Bangladesh
12. Muhtadi A, Saleque AM (2018) Modeling and simulation of a microgrid consisting solar PV & DFIG based wind energy conversion system for St. Martin's Island. In: 2017 IEEE 3rd International Conference on Engineering Technologies and Social Sciences, ICETSS 2017, vol 2018-January, pp 1–6.

Parameterization of a Solar Cell Using Multivariable Newton Raphson and Particle Swarm Optimization Based on Single Diode Model

Divya Gupta, Kumari Namrata, and Akshit Samadhiya

Abstract The paper focuses on the parameterization of solar cells to study the electrical behavior based on a single diode model. The classical Newton–Raphson method and nature-inspired PSO algorithm technique are adopted to extract the unknown electrical parameters with a fair degree of accuracy. Parameter extraction becomes vital in designing and analyzing photovoltaic-based applications as these are not specified by the manufacturer. This paper discusses the methodologies for analyzing non-linear characteristics of the solar cell using the two techniques and provides specific remarks for each technique. The *N–R* method is an iterative approach which converges accurately provided a good initial guess of parameters while Particle Swarm Optimization (PSO) algorithm is a robust optimization tool which minimizes the objective function accurately and quickly to extract the given set of unknown parameters. Solarex MSX83 (36 cells) is considered as the test case for the validation of the two models. Electrical characteristics are plotted under varying irradiance which shows fair agreement with the actual curves present in the datasheet.

Keywords Jacobian matrix · Newton Raphson method (*N–R*) · Particle swarm optimization (PSO) · Photovoltaic (PV)

1   Introduction

With the gradual depletion of natural energy reserves and the degrading condition of the earth, researchers started to explore the inexhaustible energy sources, with the

D. Gupta (✉) · K. Namrata · A. Samadhiya
National Institute of Jamshedpur, Jamshedpur, Jharkhand, India
e-mail: divya.apt95@gmail.com

K. Namrata
e-mail: namrata.ee@nitjsr.ac.in

A. Samadhiya
e-mail: akspinnacle1@gmail.com

solar energy domain being explored widely. In the solar energy domain PV systems have gained huge popularity since the past few years because of their ability to convert sunlight energy directly into electrical energy. PV system's efficiency is determined by solar cell configuration, material used, and the technique with which maximum power point is traced [1]. Prior to working on the control algorithm we need to extract the parameters of the PV system. The solar cells have the ability to absorb 80–85% of the incoming solar radiation and are able to generate 15% of electricity. Accurate modeling of solar cells is required to control the quality of solar cells and to evaluate the performance of photovoltaic-based applications. The non-linearity in the electrical characteristics of solar cells makes the solar cell parameterization more complicated. Moreover the dependence of electrical parameters on varying atmospheric conditions leads to significant errors in the calculated parameters. Over the years various studies have been done by researchers on modeling PV cells and evaluating their parameters using varied simulation software. Different analytical, numerical, and meta-heuristic approaches have been adopted for the extraction of electrical parameters. Many research work related to parameter extraction were based on manufacturer datasheet, mathematical assumptions, and approximations in order to avoid solving non-linear current–voltage relationship [2, 3]. Various numerical methods and optimization techniques were implemented by the researchers which required the use of the manufacturer's datasheet to verify the accuracy of the models [1, 4]. Villalva and Rafael in [5] modeled the solar PV cell by formulating equations in Matlab/Simulink and compared results with datasheet but lacked a detailed stepwise approach to PV modeling. Vinod and Kumar in [6] framed commercial PV module (KC200GT) code in Matlab by using mathematical equations, computed maximum power obtainable from the PV module, and plotted characteristics for varied irradiance and temperature values. Pandirajan and Muthu in [7] proposed the MATLAB model of PV module and identified the characteristics curve by varying irradiation and temperature conditions. The author also described the effect of shading on PV module but the paper lacks step-wise modeling of PV module due to which difficulty is observed in simulating and understanding the model. From above review, there exists vast gap in the modeling and analysis of PV module. In [8, 9] reliable solar cell modeling techniques are discussed by considering the implicit single diode model. For evaluation of technique comparison factors like algorithm convergence time, mean absolute error and error at maximum power point are taken. Some methods like Newton Raphson proved to be best for the mono-crystalline sample and other methods like particle swarm optimization for polycrystalline and amorphous samples. The key factor for finding the optimal solution by Newton Raphson method is a good initial value and that for PSO is to properly limit boundary conditions. In [10] parameters are obtained using adaptive differential evolution algorithm using *I–V* data point and results obtained outperforms algorithms such as Genetic Algorithm (GA) and Artificial Bee Swarm Optimization (ABSO). Advanced Cuckoo Search algorithm known as Adaptive Cuckoo Search is proposed where in every iteration step size coefficient is modified.

Here unknown electrical parameters of the solar cell are found by the Multivariable Newton Raphson (*N–R*) method. For the *N–R* method to converge accurately

Fig. 1 Equivalent circuit of
a single diode PV model
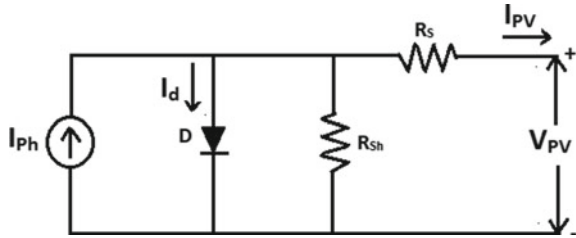
a good initial guess value is required [11]. The single diode output equation is non-linear in nature and has five unknown parameters namely I_{ph} (Photon current), I_O (Diode saturation current), n (ideality factor), R_S (Series Resistance), and R_{Sh} (Shunt resistance). Figure 1 shows the equivalent circuit diagram of a solar cell. To estimate the initial guess values for the parameters a simple to complex approach is followed. Initially, the ideal model (without considering the effect of resistances) is solved which consists of three unknowns only. Further R_s model (considering only series resistance), R_{Sh} model (consisting only shunt resistance) is solved to get a rough estimate of the two resistances. Finally, a single diode full model (considering both resistances) involving five unknowns is solved. A nature-inspired meta-heuristic algorithm namely PSO (particle swarm optimization) technique is also used to extract the parameters of a solar cell. PSO is a powerful technique inspired by the communication behavior of swarms and it achieves optimal solutions by iteratively improving the candidate solution [12]. Unlike *N–R*, PSO requires no initial assumption and can search a larger space for an optimal solution. The electrical characteristics, Voltage-current, and Power-Voltage curves are plotted for each computational technique and are compared with the curves provided in the datasheet. Here Root mean square error reflects the accuracy of the two techniques by calculating the difference between actual experimental data points and the calculated data points.

2 Single Diode Model-Based Photovoltaic Modeling

Data specified by the manufacturer in the solar cell datasheet is not sufficient to carry out the electrical analysis of a solar cell. Unknown data like photocurrent, diode reverse saturation current, ideality factor, series, and shunt resistances which affect the characteristics of the solar cell need to be evaluated. The output current of the solar cell is given by

$$I = I_{Ph} - I_O * \left(e^{\left(\frac{q(V+I \cdot R_s)}{A \cdot k \cdot T} \right)} - 1 \right) - \frac{V + I \cdot R_s}{R_{Sh}} \tag{1}$$

The accuracy of the converged solution given by Newton–Raphson Method depends upon the selected initial guess value. While a good initial value may help

in finding the result in less iteration, a bad guess value may lead to non-converging results. So here simple to complex approach is followed to find the unknown parameters of the solar cell. Four models i.e. an ideal model (without resistances), R_S model (considering the effect of series resistance), R_{Sh} model (considering the effect of shunt resistance), and final model (considering both series and shunt resistance) are discussed.

3 Model for Estimating Initial Value for Multivariable Newton–Raphson Method

3.1 Ideal Model

An ideal single diode model does not takes into account the practicalities associated with the solar cell i.e. neglects series and shunt resistances. Output current equation of an ideal cell is derived from Eq. (1) by neglecting resistances and is given by:

$$I = I_{Ph} - I_O * \left(e^{\left(\frac{q \cdot V}{A \cdot k \cdot T} \right)} - 1 \right) \tag{2}$$

The parameters unknown in the above equations are I_{Ph}, I_0, and A. To find these parameters we use three conditions of short circuit, open circuit, and maximum power point to formulate three equations:

$$I_{SC} = I_{Ph} \tag{3}$$

$$\text{Taking } V_{TC} = (kT/q), \ I_{SC} = I_0 * \left(e^{\frac{V_{OC}}{V_{TC} \cdot A}} - 1 \right) \tag{4}$$

$$I_{SC} - I_{MPP} = I_0 * \left(e^{\frac{V_{MP}}{V_{TC} \cdot A}} - 1 \right) \tag{5}$$

$$\text{Assuming } n = 1 \big/ A, \ a = 1 - \frac{I_{MPP}}{I_{SC}}, \ b = \frac{V_{OC}}{V_{TC}} \ and \ c = \frac{V_{MPP}}{V_{TC}} \tag{6}$$

Substituting Eq. (6) in Eqs. (1), (2), and (3) and rearranging gives

$$x = \frac{e^{zn} - 1}{e^{yn} - 1} \tag{7}$$

$$f(n) = e^{zn} - x \cdot e^{yn} - 1 + x \tag{8}$$

$$f(n) = z \cdot e^{zn} - x \cdot y \cdot e^{yn} \tag{9}$$

The classical Newton Raphson method is used to determine the optimal value of n. The value of n gets updated on each iteration using Eq. (10) until a tolerance in error reaches 10^{-6}.

$$x_{k+1} = x_k - \frac{f(n)}{f'(n)} \tag{10}$$

After finding the optimal value of n using Newton Raphson method the value of diode saturation current is calculated using the following equation:

$$I_0 = \frac{I_{SC}}{\left(e^{\frac{n \cdot V_{OC}}{V_{TC}}} - 1\right)} \tag{11}$$

3.2 R_{Sh} Model

R_{sh} model is formed by taking into account the effect of shunt resistance and neglecting series resistance. Thus using Eq. (1) we get,

$$I = I_{Ph} - I_0 * \left(e^{\frac{V}{A \cdot V_{TC}}} - 1\right) - \frac{V}{R_{Sh}} \tag{12}$$

where

$$V_{TC} = \frac{k \cdot T}{q}$$

Substituting $n = \frac{1}{A}$ and $b = \frac{1}{R_{Sh}}$ in Eq. (12) gives

$$I = I_{Ph} - I_0 * \left(e^{\frac{n \cdot V}{V_{TC}}} - 1\right) - b \cdot V \tag{13}$$

Applying general conditions to formulate equations to find four unknowns i.e. $I_{Ph}, I_0, n,$ and b.

As $I_{Ph} = I_{SC}$, three equations are considered as three independent functions to determine $I_0, n,$ and b iteratively through the Multivariable Newton–Raphson method.

$$f(I_0) = I_{SC} - I_0 * \left(e^{\frac{n \cdot V_{OC}}{V_{TC}}} - 1\right) - b \cdot V_{OC} \tag{14}$$

$$f(n) = I_{MPP} - I_{SC} + I_0 * \left(e^{\frac{n \cdot V_{MPP}}{V_{TC}}} - 1\right) - b \cdot V_{MPP} \tag{15}$$

$$f(n) = I_{MPP} - I_{SC} + I_0 * \left(e^{\frac{n \cdot V_{MPP}}{V_{TC}}} - 1\right) - b \cdot V_{MPP} \tag{16}$$

Defining unknown vector $X = [I_0 \; n \; b]$ and calculating partial derivatives of above mentioned three functions with respect to each unknown variable gives the Jacobian matrix as follows:

$$
\begin{bmatrix}
-(e^{\frac{n \cdot V_{OC}}{V_{TC}}} - 1) & -\frac{I_0 \cdot V_{OC}}{V_{TC}} e^{\frac{n \cdot V_{OC}}{V_{TC}}} & -V_{OC} \\[2ex]
(e^{\frac{n \cdot V_{MPP}}{V_{TC}}} - 1) & \frac{I_0 \cdot V_{MPP}}{V_{TC}} e^{\frac{n \cdot V_{MPP}}{V_{TC}}} & V_{MPP} \\[2ex]
\left(1 - e^{\frac{n \cdot V_{MPP}}{V_{TC}}} - \frac{n \cdot V_{MPP} \cdot e^{\frac{n \cdot V_{MPP}}{V_{TC}}}}{V_{TC}}\right) & \left[-\frac{I_0 \cdot V_{MPP}}{V_{TC}} e^{\frac{n \cdot V_{MPP}}{V_{TC}}} - \frac{I_0 \cdot V_{MPP}}{V_{TC}}\left(e^{\frac{n \cdot V_{MPP}}{V_{TC}}} + \frac{n \cdot V_{MPP} \cdot e^{\frac{n \cdot V_{MPP}}{V_{TC}}}}{V_{TC}}\right)\right] & -2V_{MPP}
\end{bmatrix}
\tag{17}
$$

Newton Raphson Method can be used to find the optimal value of unknown variables using the following equation:

$$
x_{k+1} = x_k - \text{inv}(J) * F \tag{18}
$$

3.3 R_S Model

Equations of the R_s model are derived from Eq. (1) by considering the effect of series resistance and neglecting shunt resistance which gives:

$$
I = I_{Ph} - I_0 * \left(e^{\frac{V + I \cdot R_S}{A \cdot V_{TC}}} - 1\right) \tag{19}
$$

In the above equation we have four unknowns i.e. I_{Ph}, I_0, A, and R_s. Four equations are required to find the unknowns. Three equations can be formed using three conditions of short circuit, open circuit, and maximum power point as follows:

$$
f(I_{Ph}) = I_{Ph} - I_0 * \left(e^{\frac{n \cdot I_{SC} \cdot R_S}{V_{TC}}} - 1\right) - I_{SC} \tag{20}
$$

$$
f(I_0) = I_{Ph} - I_0 * \left(e^{\frac{n \cdot V_{OC}}{V_{TC}}} - 1\right) \tag{21}
$$

$$
f(n) = I_{Ph} - I_0 * \left(e^{\frac{n \cdot (V_{MPP} + I_{MPP} \cdot R_S)}{V_{TC}}} - 1\right) - I_{MPP} \tag{22}
$$

To find the fourth unknown we need to formulate the fourth equation using condition $(dP/di)_{\text{at MPP}} = 0$ we get,

$$
f(R_S) = \frac{V_{TC}}{n} \ln\left(\frac{I_0 + I_{Ph} - I_{MPP}}{I_0}\right) - \frac{I_{MPP} \cdot V_{TC}}{n(I_0 + I_{Ph} - I_{MPP})} - 2I_{MPP} \cdot R_s = 0 \tag{23}
$$

Once equations are formulated we use Newton Raphson method to find the four unknowns

$$x_{k+1} = x_k - \text{inv}(J) * F \tag{24}$$

where x is the unknown variable vector $[I_{Ph}\ I_0\ n\ R_s]$, x_k is the initial vector, x_{k+1} is the updated vector, J is a 4×4 Jacobian matrix containing partial derivatives of functions with respect to the unknown values, and F is the function vector as given in Eq. (25)

$$J = \begin{bmatrix} \frac{\partial f(I_{Ph})}{\partial I_{Ph}} & \frac{\partial f(I_{Ph})}{\partial I_0} & \frac{\partial f(I_{Ph})}{\partial n} & \frac{\partial f(I_{Ph})}{\partial R_S} \\ \frac{\partial f(I_0)}{\partial I_{Ph}} & \frac{\partial f(I_0)}{\partial I_0} & \frac{\partial f(I_0)}{\partial n} & \frac{\partial f(I_0)}{\partial R_S} \\ \frac{\partial f(n)}{\partial I_{Ph}} & \frac{\partial f(n)}{\partial I_0} & \frac{\partial f(n)}{\partial n} & \frac{\partial f(n)}{\partial R_S} \\ \frac{\partial f(R_S)}{\partial I_{Ph}} & \frac{\partial f(R_S)}{\partial I_0} & \frac{\partial f(R_S)}{\partial n} & \frac{\partial f(R_S)}{\partial R_S} \end{bmatrix},\ F = \begin{bmatrix} f(I_{Ph}) \\ f(I_0) \\ f(n) \\ f(R_S) \end{bmatrix} \tag{25}$$

4 Parameter Extraction Using Multivariable Newton Raphson

The final model i.e. consisting of both series and shunt resistance involving five variables is solved by the Multivariable Newton–Raphson Method with the help of datasheet values and 2 experimental data points (V, I). To extract five variables, five equations are required which are given below:

$$f_i = I_{k_i} - I_{Ph} + I_0 * \left(e^{\frac{V_{k_i} + I_{k_i} \cdot R_S}{A \cdot V_{TC}}} - 1 \right) - \left(\frac{V_{k_i} + I_{k_i} \cdot R_S}{R_{Sh}} \right) = 0 \tag{26}$$

where f_i shows ith functions found by putting the 5 data points $\left(V_{k_i}, I_{k_i} \right)$ values. In the datasheet three points are easily available which are the Short circuit point $(0, I_{SC})$, Open circuit point $(V_{OC}, 0)$, and maximum power point (V_{MPP}, I_{MPP}). Rest two experimental data points are selected close to short-circuit and open-circuit points.

Unknown vector $X = [I_{ph}\ I_0\ n\ R_s\ b]$. The Jacobian matrix in Eq. (27) is found by computing partial derivatives of above-mentioned functions w.r.t. each unknown variable is to be found.

$$J = \begin{bmatrix} \frac{\partial f_1(I_{Ph})}{\partial I_{Ph}} & \frac{\partial f_1(I_{Ph})}{\partial I_0} & \frac{\partial f_1(I_{Ph})}{\partial A} & \frac{\partial f_1(I_{Ph})}{\partial R_S} & \frac{\partial f_1(I_{Ph})}{\partial R_{Sh}} \\ \frac{\partial f_2(I_0)}{\partial I_{Ph}} & \frac{\partial f_2(I_0)}{\partial I_0} & \frac{\partial f_2(I_0)}{\partial A} & \frac{\partial f_2(I_0)}{\partial R_S} & \frac{\partial f_2(I_0)}{\partial R_{Rs}} \\ \frac{\partial f_3(A)}{\partial I_{Ph}} & \frac{\partial f_3(A)}{\partial I_0} & \frac{\partial f_3(A)}{\partial A} & \frac{\partial f(A)}{\partial R_S} & \frac{\partial f(A)}{\partial R_{Sh}} \\ \frac{\partial f_4(R_S)}{\partial I_{Ph}} & \frac{\partial f_4(R_S)}{\partial I_0} & \frac{\partial f_4(R_S)}{\partial A} & \frac{\partial f_4(R_S)}{\partial R_S} & \frac{\partial f_4(R_S)}{\partial R_{Sh}} \\ \frac{\partial f_5(R_{sh})}{\partial I_{Ph}} & \frac{\partial f_5(R_{sh})}{\partial I_0} & \frac{\partial f_5(R_{sh})}{\partial A} & \frac{\partial f_5(R_{sh})}{\partial R_S} & \frac{\partial f_5(R_{sh})}{\partial R_{Sh}} \end{bmatrix},\ F = \begin{bmatrix} f_1(I_{Ph}) \\ f_2(I_0) \\ f_3(A) \\ f_4(R_S) \\ f_5(R_{Sh}) \end{bmatrix} \tag{27}$$

Below the Newton Raphson Method is used to find the unknowns

$$x_{k+1} = x_k - \mathrm{inv}(J) * F \tag{28}$$

The initial value for Newton Raphson is estimated using three models explained in Sect. 3.

5 Parameter Extraction Using Particle Swarm Optimization

James Kennedy and Eberhart developed particle swarm optimization. It is based on the social interaction among swarms to reach toward the optimal solution with the help of position gradients [13]. Complex problems can be easily solved by PSO as it improves the particle solution through the search space. In PSO N swarms are moved in search space in accordance with mathematical equations. These equations define the velocity and position of each swarm. The advantage of PSO is that candidate's movement is guided by both local and best-known solutions in the specified range. With each iteration, the candidate's position gets updated and therefore swarms move toward the optimum solution.

Consider N number of populations of particles having m dimensions. Each particle has a real fitness value. The fitness of the particles depends on the objective function of the problem. All the particles preserve their best-known position while a global best-known position is also maintained among the particles. Each particle moves toward a new position by adjusting its velocities considering its best solution and global best position. The velocity and position of each particle are updated by the following equations:

$$v_{k+1}^i = w_k \cdot v_k^i + C_1 \cdot \mathrm{rand}(P_k^i - x_k^i) + C_2 \cdot \mathrm{rand}(G_k^g - x_k^i) \tag{29}$$

$$x_{k+1}^i = x_k^i + v_{k+1}^i \tag{30}$$

C_1 and C_2 are the learning factor. The term multiplied by C_1 shows the local best position influence on the velocity while the term multiplied by C_2 shows the global best position influence on the velocity. The term w_i is the inertia weight to represent the particle's own inertial effect. The value of C_1 and C_2 ranges between 1 and 2 depending on the complexity of the objective function [14].

Here the best position of the swarm means the best solution to the unknown variable. To estimate unknown parameters, 62 experimental points (V_k, I_k) are used. The objective function given below which represents RMSE error is minimized.

$$\text{Obj.func(of)} = \sqrt[2]{\frac{1}{N} \sum_{k=1}^{k=N} g(V_k, I_k, x)^2} \tag{31}$$

$$g(V_k, I_k, x) = I_k - I_{Ph} + I_0 * \left(e^{\frac{(V_k + I_k \cdot R_S)}{A.V_{TC}}} - 1 \right) - \left(\frac{V_k + I_k \cdot R_S}{R_{Sh}} \right) \tag{32}$$

$$x = [I_{Ph}, I_0, A, R_S, R_{Sh}] \tag{33}$$

where N is the number of experimental points, x is the unknown parameters set, and V_k and I_k are voltage and current corresponding to kth iteration respectively.

The implementation of the particle swarm optimization algorithm is explained through a pseudo code given below:

1. *Initialize Particle population size (N) and set PSO parameters c_1, c_2, w_{max}, and w_{min}*
2. *Define the objective function using Eqs. (31), (32) and (33)*
3. *Randomly generate initial population of particles.*
4. *Evaluate the fitness of each particle and select initial position of all particles as P_{BEST}*
5. *while (iteration < Max iteration or stopping criteria is met)*
6. *Select G_{BEST} among all the particles having minimum fitness value $f(x_i)$*
7. *for i = 1:N*
8. *Evaluate the velocity of the particle xi using Eq. (29)*
9. *Update the position of each particle using Eq. (30)*
10. *End*
11. *for i = 1:N*
12. *Calculate the fitness of each update particle position x_i*
13. *if (fitness value of x_i < fitness value of P_{BESTi})*
14. *Update the particle best position, $P_{BESTi} = x_i$*
15. *end*
16. *if (fitness value of x_i < fitness value of G_{BEST})*
17. *Update the Global best position, $G_{BEST} = x_i$*
18. *end*
19. *end*
20. *end for while*

6   Results and Discussion

Solar cell's parameter estimation is done through two methods namely the multivariable Newton–Raphson method and particle swarm optimization. To validate the obtained results, a single cell of Solarex MSX83(81 W, 36 cells) datasheet at STC is considered. The values provided in the datasheet are mentioned in Table 1. The values

Table 1 Values of parameters provided in manufacturer's datasheet

Parameters in datasheet	Values
I_{SC} (A)	5.27
V_{OC} (V)	0.588
P_{Max} (W)	2.305
I_{MPP} (A)	4.85
V_{MPP} (V)	0.475

found out using multivariable Newton–Raphson and particle swarm optimization are listed in Tables 2 and 3 respectively.

For multivariable Newton Raphson method to converge a proper initial value is required. The initial guess value of five unknowns is calculated by three individual models as discussed above. By the ideal model value of the ideality factor is computed to be 1.7381. The ideal model estimates the value of power (2.305 W), which is close to the actual maximum, the value of voltage and current at MPP is 0.4780 V and 4.8208 A respectively. I_{Ph}, I_o, and A values computed from the ideal model are used as the initial guess for R_{Sh} model. However, R_{Sh} estimates the values of P_{max}, V_{MPP}, and I_{MPP} same as that of datasheet values still R_{Sh} model seems invalid in this case

Table 2 Electrical parameters estimated using Newton Raphson method

Parameters	Ideal model	R_{sh} model	R_s model	Final model
I_{Ph} (A)	5.27	5.27	5.27	5.27
I_0 (μA)	10.125	20.848	2.2922	0.387
A	1.7381	1.8366	1.5618	1.3934
R_S (Ω)	–	–	0.0024	0.00451
R_{Sh} (Ω)	–	6.9037	–	11,500
P_{Max} (W)	2.3044	2.3038	2.3008	2.306
I_{MPP} (A)	4.8208	4.85	4.854	4.88
V_{MPP} (V)	0.478	0.475	0.474	0.475

Table 3 Electrical parameters estimated using particle swarm optimization

Parameters	Boundary limits	Final model
I_{Ph} (A)	[5, 6]	5.2754
I_0 (μA)	[0, 1000]	0.3952
A	[1, 2]	1.396
R_S (Ω)	[0, 0.5]	0.0041
R_{Sh} (Ω)	[0, 10000]	980.927
P_{Max}	–	2.31
I_{MPP} (A)	–	4.885
V_{MPP} (V)	–	0.473

as $R_{Sh} = -6.9037$. The negative value of the resistance is not realizable. Hence, the initial value of R_{Sh} can be estimated as the negative slope of $V-I$ characteristics near the short circuit region. The initial value of R_{sh} lies in the range of (500–15,000) Ω. The R_S model computes the value of the series resistance to be 0.0024 Ω. The initial values of I_0 and A for the R_S model were taken from the result of the ideal diode model.

The comparison between the experimental $V-I$ curve and the curves estimated by Newton Raphson and particle swarm optimization is shown in Figs. 2 and 3. Figures 4 and 5 show Electrical characteristics of solar cell SOLAREX MSX83 at different irradiances estimated by Newton Raphson method and particle swarm optimization respectively.

The result obtained shows that the Newton Raphson estimated the maximum power point more precisely than the particle swarm optimization. However, the

Fig. 2 Comparison of $V-I$ characteristics estimated using $N-R$ Method and experimental $V-I$ curve
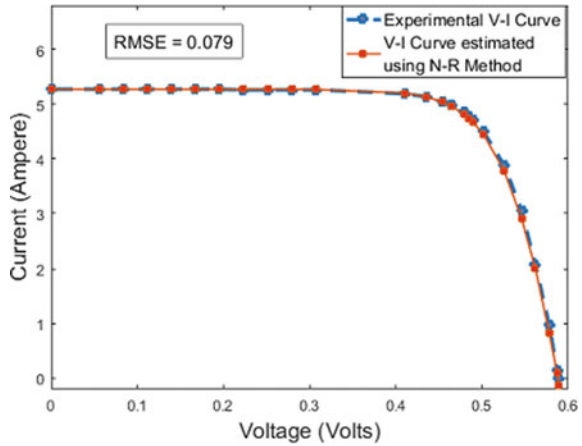
Fig. 3 Comparison between $V-I$ characteristics estimated using PSO and experimental $V-I$ curve
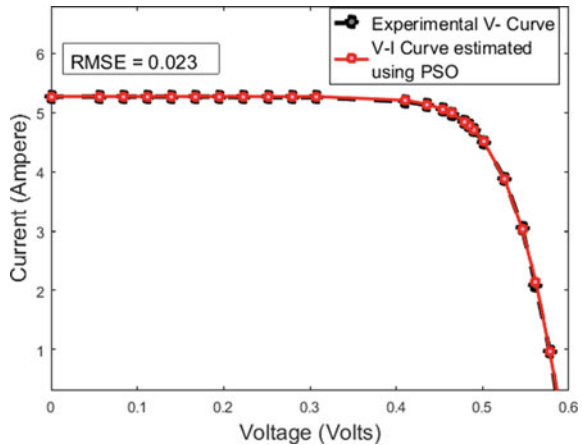
Fig. 4 *V–I* Characteristics estimated at different irradiance using *N–R* method
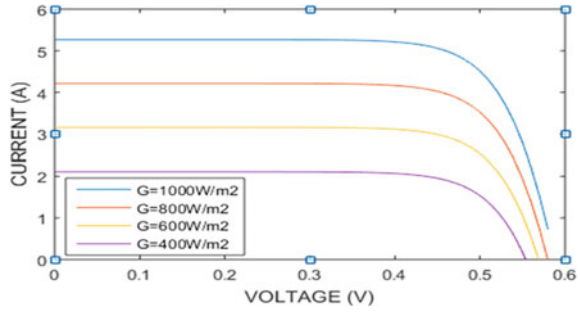
Fig. 5 *V–I* Characteristics estimated at different irradiance using PSO
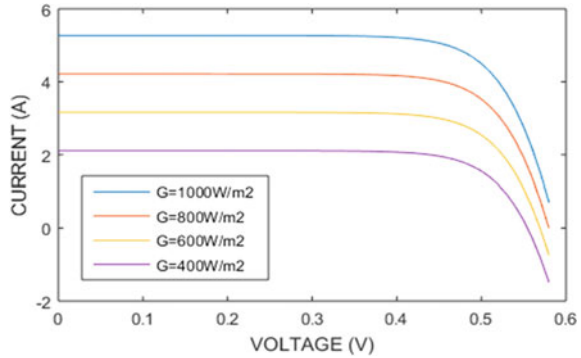
particle swarm optimization shows a better performance in terms of accuracy. PSO is more accurate in estimating electrical characteristics as it shows a lower root mean square error value.

The result obtained shows that the Newton Raphson estimated the maximum power point more precisely than the particle swarm optimization. However, the particle swarm optimization shows a better performance in terms of accuracy. PSO is more accurate in estimating electrical characteristics as it shows a lower root mean square error value.

7 Conclusions

To analyze, design, and accurately model photovoltaic systems, parameterization of PV cells is crucial. In this paper, two different kinds of techniques are discussed. For Newton Raphson method to converge, a proper initial guess value is required while particle swarm optimization requires boundary values of unknown variables and gives an accurate optimal solution. The convergence speed of the algorithm is comparable to the classical Newton Raphson but has the advantage of solving complex functions with ease.

References

1. Reis L, Camacho J, Novacki D (2017) The newton Raphson method in the extraction of parameters of PV modules. Renew Energy Power Qual J 1:634–639
2. Senturk A (2018) New method for computing single diode model parameters of photo-voltaic modules. Renew Energy 128(A):30–36
3. Vergura S (2016) A complete and simplified datasheet-based model of PV cells in variable environmental conditions for circuit simulation. Energies 9(5):326
4. Ayodele TR, Ogunjuyigbe ASO, Ekoh EE (2016) Evaluation of numerical algorithms used in extracting the parameters of a single diode photovoltaic model. Sustain Energy Technol Assess 13:51–59
5. Villalva M, Rafael J, Ruppet Filho E (2009) Comprehensive approach to modeling and simulation of photovoltaic arrays. IEEE Trans Power Electron 24
6. Vinod, Kumar R, Singh S (2018) Solar photovoltaic modeling and simulation: as a renewable energy solution. Energy Rep 4:701–712
7. Pandiarajan N, Muthu R (2011) Mathematical modeling of photovoltaic module with Simulink. In: Electrical Energy Systems, IEEE, pp 258–263
8. Kareem A, Bognar G, Plesz B (2020) Evaluation of different methods for solar cells/modules parameter extraction. Sol Energy 196:183–195
9. Chellaswamy C, Ramesh R (2016) Renew Energy 97:823. https://doi.org/10.1016/j.renene.2016.06.024
10. Farivar G, Asaei B (2010) Photovoltaic module single diode model parameters extraction based on manufacturer datasheet parameters. In: Proceedings 2010 IEEE international conference on power and energy, pp 929–934
11. Ghani F, Fernandez EF, Almonacid F, Donovan TSO, Miller EH (2017) The numerical computation of lumped parameter values using the multi-dimensional Newton-Raphson method for the characterisation of a multi-junction CPV module using the five-parameter approach. Sol Energy 149:302–313
12. Meiying Y, Xiaodong W, Yousheng X (2009) Parameter extraction of solar cells using particle swarm optimization. J Appl Phys 105:094502
13. Qin H, Kimball JW (2011) Parameter determination of photovoltaic cells from field testing data using particle swarm optimization. In: Proceedings 2011 IEEE power and energy conference, pp 1–4
14. Li Y, Shi J, Yu B, Duan B, Wu J, Li H, Li D, Luo Y, Wu H, Meng Q (2020) Joule 4(2):472. https://doi.org/10.1016/j.joule.2019.12.016

Symmetric Source Configuration of Nine Level Multi Level DC Link Inverter Topology Using Nearest Level Control and Unipolar Phase Disposition PWM Techniques

Kasoju Bharath Kumar, A. Bhanuchandar, Rajakumar Sakile, Bandela Supriya, Kowstubha Palle, and C. Mahesh

Abstract In this paper, a symmetric source configuration of 9-level Multilevel DC Link Inverter (MLDCL) topology using Nearest Level Control (NLC) and Unipolar Phase Disposition (UPD) Pulse Width Modulation (PWM) techniques have been reported clearly. This topology consists of 4 equal DC sources and 12 unidirectional switches for generating 9-level output. For generating this much output, 4 half-bridge cells are connected in a cascaded manner in the level generator side and a full bridge or backend H-bridge is connected in the polarity generator side. This topology provides an equal amount of voltage stress on each switch i.e., Vdc in the level generator side and similarly 4Vdc on each switch in the polarity generator side. With respect to PWM strategies, the fundamental switching frequency and high switching frequency methods have been applied to this topology. Then, a comparative assessment in terms of %THD in output voltage has been illustrated vividly with respect to both PWM strategies. Basically, the fundamental switching frequency method is a non-carrier method and it is possible to generate the nearest voltage level easily by taking the round function. Finally, the operation of 9L-MLDCL topology with respect to two PWM strategies has been validated clearly through the MATLAB/Simulink platform.

Keywords Multilevel DC link inverter · Pulse width modulation · Nearest level control · Unipolar phase disposition · Level generator · Polarity generator

K. B. Kumar (✉) · C. Mahesh
EEE Department, MGIT, Hyderabad, Telangana, India
e-mail: bharathchary15@gmail.com

A. Bhanuchandar
Electrical Engineering Department, NIT Warangal, Warangal, Telangana, India

R. Sakile
Electrical Engineering Department, NIT Jamshedpur, Jamshedpur, Jharkhand, India

B. Supriya · K. Palle
EEE Department, CBIT (A), Hyderabad, Telangana, India

193

1 Introduction

In the present research trend, in the area of power systems i.e. at generation, transmission, distribution, and utilization of that electrical energy DC-AC power conversion plays a crucial role which includes HVDC power transmission, Power Quality, Renewable Energy Applications (Wind, PV, DFIG, and Fuel cell), Flexible AC Transmission Systems (FACTS) and Electric Vehicles [1]. Generally, the modern inverters are divided as two-level inverters, quasi-square wave inverters, PWM inverters, and Multi-level Inverters (MLIs) [2]. Out of all these inverters, multi-level inverters have many advantages such as [3]

(i)   MLIs can guarantee equal voltage sharing among active switches.
(ii)   MLIs can considerably reduce the size.
(iii)   MLIs not only exhibit a better harmonic profile but also reduces dv/dt stresses on switches [4].
(iv)   MLIs produce small common mode voltage.
(v)   MLIs exhibits redundancy in switches.
(vi)   MLIs can draw input current with low distortion.
(vii)   MLIs can be easily interfaced with Renewable Energy Sources.

Hence, MLIs are presented to overcome certain disadvantages. Moreover, the replacement of IGBTs over GTOs can improve the performance of the system as IGBTs require less gate drivers [5, 6]. MLIs have a special and huge impact in several industries such as Electrical Vehicle Industry, Traction industry, marine industry including the power quality improvement industry such as FACTS and VAR compensation. The modern MLIs used in the industry are as follows: Diode clamped Multi-Level Inverter (DCMLI), Flying Capacitor Multi-Level Inverter (FCMLI), and Cascaded H-Bridge Multi Level Inverter (CHBMLI). The cascaded MLI is based on the cascade connection of single-phase full bridge inverters which give medium-level output voltage by using low-level voltage components [7]. The Cascaded H-Bridge Multi Level Inverter and Diode clamped Multi-Level Inverter can be operated with a single DC source but Flying Capacitor Multi-Level Inverter requires the number of DC sources [8, 9]. One of the most important properties in any Multi-Level Inverter is Modularity, which explains the extension of the number of levels. Generally, some practical results state that DCMLI and FCMLI are only used for low and medium power applications up to five levels. CHBMLI is used for high-power applications using a high level of operation [10]. Hence for high-level inverters, the control strategy is very difficult as it increases the number of switches. Therefore, it is very important to lessen the number of active switches in modular multi-level inverters. A new MLI is proposed to reduce the number of active semiconductor devices which is called a Reduced Device count Multilevel Inverter or Multi-Level DC link inverter (MLDCL). In the present classical topologies, the number of active switches required are $2*(s-1)$ for 's' level inverter whereas MLDCL inverter requires only $s + 3$ active switches [11]. Hence MLDCL is better when compared to other classical inverters as the number of switches is reduced, heat sinks will reduce, and gate driver circuits will reduce which is most economical [5] (Fig. 1).
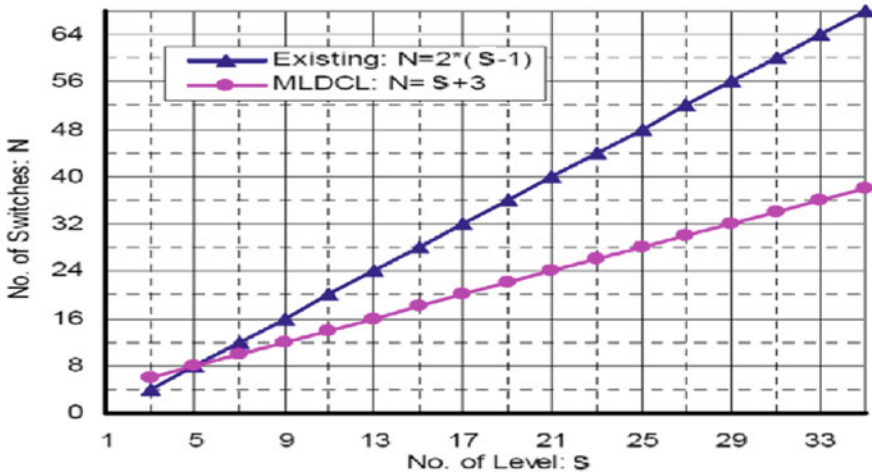
Fig. 1 Comparison with existing and MLDCL inverter

The rest of the paper is organized as follows. In this paper, in Sect. 2 operation of MLDCL topology is described. In Sect. 3 the UPD and NLC control schemes are described. In Sect. 4 the simulation results are discussed. Section 5 gives the conclusion.

2 MLDCL Topology

The traditional inverters require a large number of switches and clamping diodes, but an MLDCL inverter works with a reduced switch count which is highly economical as every switch require a gate driver circuit, control unit, and heat sink [3]. Generally, an MLDCL inverter consists of symmetrical DC sources and an H-bridge inverter [12]. The proposed MLDCL inverter has a separate level and polarity generator to generate multi levels with less ripples. The single-phase MLDCL inverter is shown in Fig. 2. From Fig. 2 it is clear that the MLDCL inverter consists of separate level and polarity generators. The level generator is used to decide the number of levels of the inverter and the polarity generator decides the polarity (sign) of the output. For a nine level inverter a level generator has four symmetrical DC sources connected in a cascade manner with four half-bridge converters (8 switches—S1, S2, S3, S4, S5, S6, S7, S8) where in the switches operate with low or fundamental switching frequency and the polarity generator has one single phase full bridge inverter (SPFB with 4 switches-H1, H2, H3, H4) where in the switches operate with high switching frequency [13]. To get the output as 4Vdc, the switches S1, S3, S5, S7 in the level generator side and H1, H4 from polarity generator side must be in conducting mode.

Fig. 2 Single phase 9-level
MLDCL inverter topology
with RL load
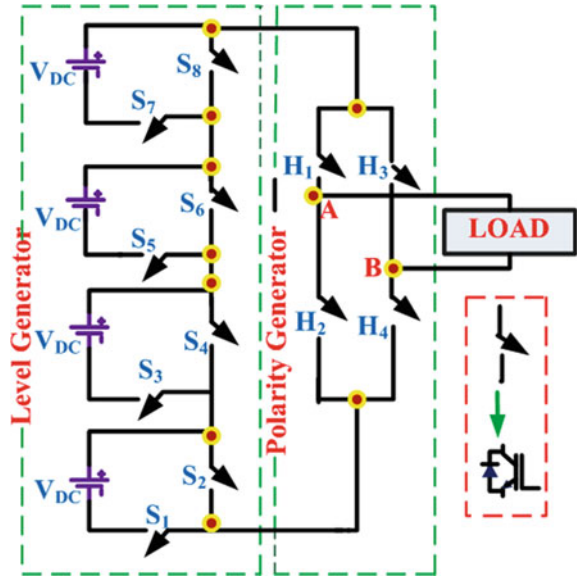
Table 1 Switching
configurations

Output voltage	ON state switches
$4V_{dc}$	S1-S3-S5-S7-H1-H4
$3V_{dc}$	S1-S3-S5-S8-H1-H4
$2V_{dc}$	S1-S3-S6-S8-H1-H4
$1V_{dc}$	S1-S4-S6-S8-H1-H4
0	S2-S4-S6-S8-H1-H4
$-1V_{dc}$	S1-S4-S6-S8-H2-H3
$-2V_{dc}$	S1-S3-S6-S8-H2-H3
$-3V_{dc}$	S1-S3-S5-S8-H2-H3
$-4V_{dc}$	S1-S3-S5-S7-H2-H3

All the other switching configurations are given in Table 1. The output generated by
the MLDCL inverter has very less switching and conduction losses [14].

3 Proposed Control Schemes

In this paper, two control schemes Uni Polar Phase disposition (UPD) and Nearest
level control (NLC) are to be presented and the performance of both the control
schemes is evaluated.
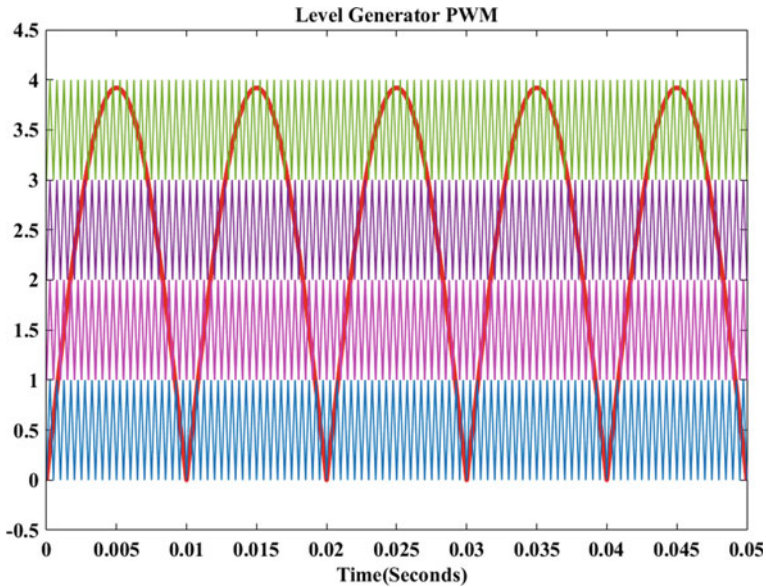
Fig. 3 UPD-PWM technique

3.1 Uni-Polar Phase Disposition (UPD) Technique

Generally, in any inverter the control scheme is very important. Based on the control logic, we can classify the inverters as PWM inverters and stepped low-frequency inverters. The most common and efficient control scheme is the phase disposition technique which uses (S-1) carriers to generate gate pulses for the 'S' level inverter. The advanced control scheme which is proposed in this paper is Uni Polar Phase Disposition (UPD) Technique which uses only (S-1)/2 carrier signals to generate gate pulses for 'S' level inverter. This operation is performed using absolute function, and the carrier count is reduced by half compared to Phase Disposition (PD) Technique. In this paper a nine-level inverter is presented, which takes four carrier signals and compares them with the absolute modulating signal to generate gate pulses. The proposed control scheme is shown in Fig. 3.

The single modulating signal is given to both the polarity and level generator. In case of level generator, the modulating signal is given to absolute function which reduces the carrier count by half.

3.2 Nearest Level Control Scheme

Another advanced control scheme presented in this scheme is the nearest level control (NLC) scheme which is highly recommended because the number of required voltage

Fig. 4 Nearest level control technique

(a) Waveform Synthesis

(b) Control Diagram
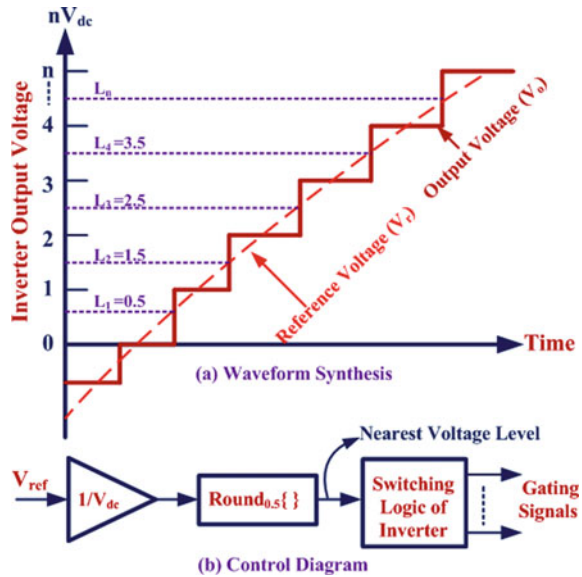
levels for an inverter topology is high. The NLC technique is used to efficiently synthesize the medium frequency voltages at the output. The working principle of the NLC scheme is to select the nearest voltage that can be generated by the inverter to the desired voltage reference [15]. The other PWM control schemes which use triangular carrier waves offer low Total Harmonic Distortion (THD) by they have a drawback of high switching losses. Hence NLC technique there is no need to use a triangular carrier wave and therefore it is easy to implement and switching frequency can be reduced [16]. The nearest voltage level (NVL) can be generated by using the formula.

$$\text{NVL} = (1/V_{\text{DC}}) * \text{round}\ (V_{\text{ref}}) \tag{1}$$

As discussed earlier, the NLC technique offers low THD but the drawback of this technique is it cannot be used for low-level inverters as it cannot eliminate specific harmonics. Therefore, NLC technique is highly recommended for inverters with an increased number of levels. The control technique is shown in Fig. 4.

4   Simulation Results and Discussion

In the UPD (Uni-Polar Phase Disposition) technique for nine-level inverter the required number of carrier waves is four. The reduced carrier strategy is shown in Fig. 3. The Nine level output voltage generated through this scheme and the switching states of all the switches is shown in Fig. 5.
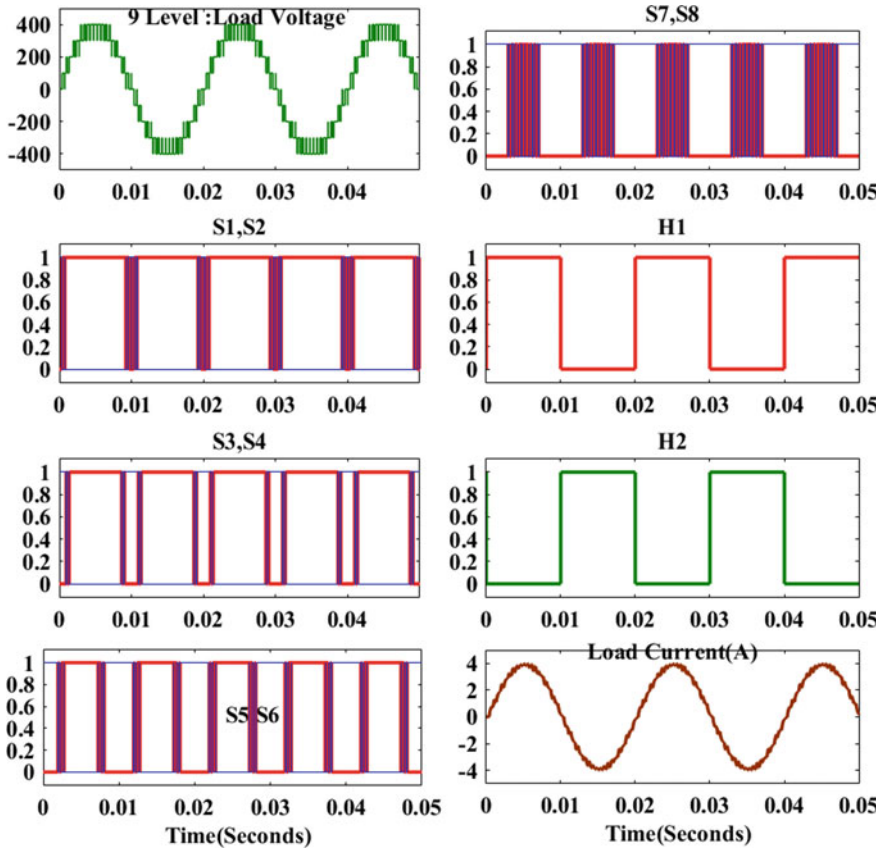
Fig. 5 Simulation results-UPD technique

At fundamental frequency, the line voltage is 393.2 V with 14.36% Total harmonic distortion with the use of the UPD technique. The FFT analysis through the UPD technique is shown in Fig. 6. Similarly, the simulation results of output voltage and switching states of the switches with the NLC (Nearest level Control) technique are shown in Fig. 7.

At fundamental frequency, the line voltage is 399.3 V with 9.76% Total harmonic distortion (THD) with the use of NLC technique. The FFT analysis through NLC technique is shown in Fig. 8 (Tables 2, 3 and 4).

Fig. 6 FFT analysis for nine level load voltage with UPD control technique
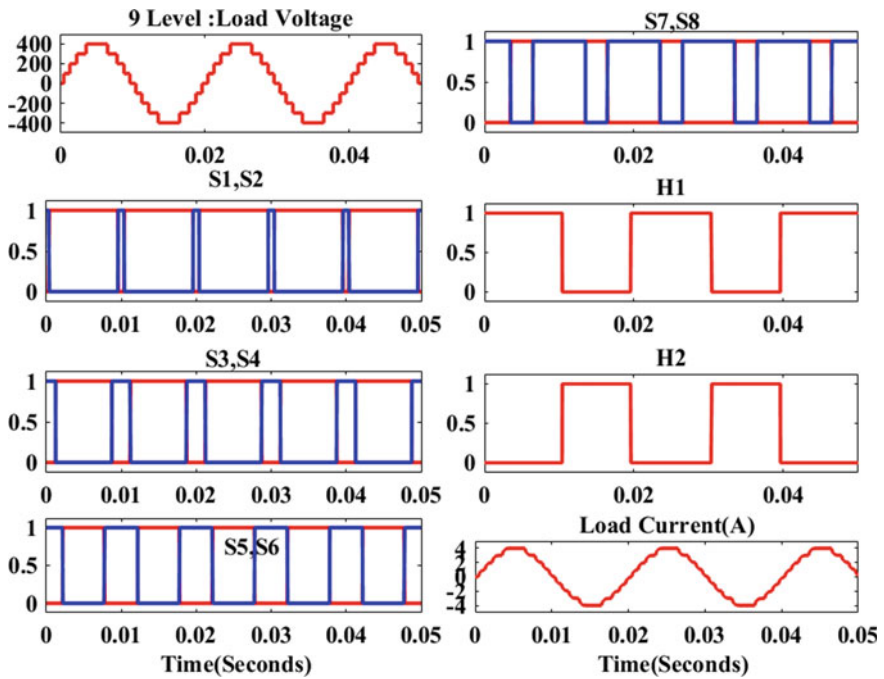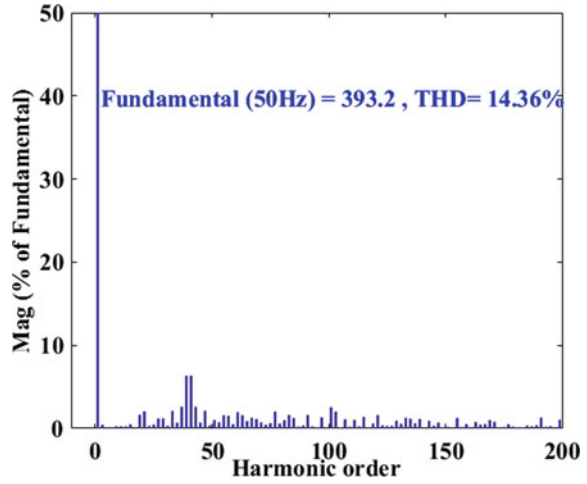
Fig. 7 Simulation results—NLC technique

Fig. 8 FFT analysis for nine level load voltage with NLC control technique
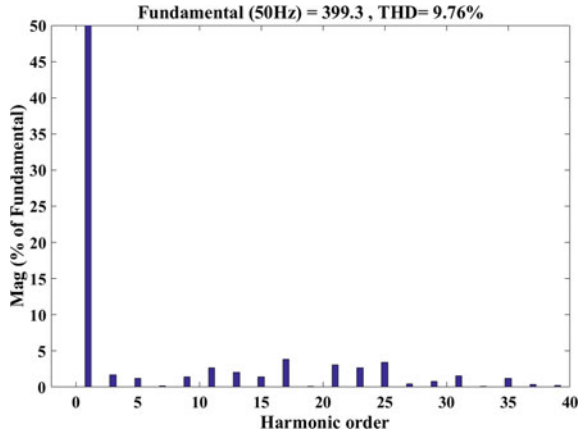
Table 2 Simulation parameters

Parameter	Parameter value
V_{DC}	100 V
Resistance (R)	100 ohms
Inductance (L)	22 mH
Switching frequency	2 kHz
Fundamental frequency	50 Hz
Modulation index (ma)	0.98
Total blocking voltage	6 p.u
Voltage gain	1

Table 3 Comparative assessment for %THD values

S No.	UPD		NLC	
	% THD	Peak value at 50 Hz	%THD	Peak value at 50 Hz
1	14.36%	393.2 V	9.76%	399.3 V

Table 4 Comparative study

S No.	Components	NPC	FC	CHB	9L-MLDCL
1	Main switches	16	16	16	12
2	Anti-parallel diodes	16	16	16	12
3	Clamping diodes	56	0	0	0
4	DC bus capacitors	8	8	4	4
5	Flying capacitors	0	28	0	0

5 Conclusion

In this paper a single phase MLDCL inverter is presented and compared the %THD values for two different control schemes. Generally, the UPD (Uni polar phase disposition) technique requires (s-1/2) carrier signals to generate the gate signals for switches in level and polarity generators but the % THD value for a nine-level inverter using UPD is presented as 14.36% and the line voltage at the fundamental frequency is 393.2 V. The new advanced technique called NLC (Nearest level Control) Technique is used for the same nine-level MLDCL inverter which uses a round function to select the nearest voltage. The % THD value for the line voltage output of the MLDCL inverter which uses NLC technique is presented as 9.76% and the line voltage at the fundamental frequency is 399.3 V.

References

1. Omer P, Kumar J, Surjan BS (2020) A review on reduced switch count multilevel inverter topologies. In: IEEE Access, vol 8, pp 22281–22302. https://doi.org/10.1109/Access.2020.2969551; Author F (2016) Article title. Journal 2(5):99–110
2. Kumawat RK, Palwalia DK, A comprehensive analysis of reduced switch count multilevel inverter. Australian J Electric Electron Eng. doi.org/https://doi.org/10.1080/1448837X.2019.1693884
3. Su GJ (2005) Multilevel DC-link inverter. IEEE Trans Ind Appl 41(3):848–854. https://doi.org/10.1109/TIA.2005.847306
4. Manjunatha YR, Anand BA (2014) Multilevel DC link inverter with reduced switches and batteries. Int J Power Electron Drive Syst 4(3):299–307; Author F, Author S (2016) Title of a proceedings paper. In: Editor F, Editor S (eds) Conference 2016, LNCS, vol 9999. Springer, Heidelberg, pp 1–13
5. Kumar KB, Bhanuchandar A, Mahesh C (2021)A novel control scheme for symmetric seven level reduced device count multi-level DC link (MLDCL) inverter. In: 2021 international conference on sustainable energy and future electric transportation (SEFET), pp 1–4. https://doi.org/10.1109/SeFet48154.2021.9375714
6. Bhanuchandar A, Murthy BK (2020) Single phase nine level switched capacitor based grid connected inverter with LCL filter. In: 2020 3rd international conference on energy, power and environment: towards clean energy technologies, pp 1–5. https://doi.org/10.1109/ICEPE50861.2021.9404491
7. Mariuz Malinowski J et al (2010) A survey on cascaded multilevel inverters. IEEE Trans on Ind Electr 57:2197–2206
8. Rodriguez J, Lai J-S, Peng FZ (2002) Multilevel inverters: a survey of topologies, controls, and applications. IEEE Trans Ind Electron 49(4):724–738. https://doi.org/10.1109/TIE.2002.801052
9. Sathisha D (2021) A simplified control approach of AC-DC-TLBC for bi-polar DC microgrid applications. Turkish J Comput Math Educ (TURCOMAT) 12(2):818–824. https://doi.org/10.17762/turcomat.v12i2.1090
10. Belekar RA, Nakade RP, et al. (2013) Single phase 9 level MLDCL inverter with half bridge cell topology: performance analysis. In: 2013 international conference on power, energy and control (ICPEC)
11. Rao SN, Kumar DVA, Babu CS (2013) New multilevel inverter topology with reduced number of switches using advanced modulation strategies. In: 2013 international conference on power, energy and control (ICPEC), pp 693–699. https://doi.org/10.1109/ICPEC.2013.6527745

12. Eguchi K, Shibata A, et al (2020) An inductor-less step-up/step-down multilevel inverter with a single input source. Energy Rep 6(2):146–152
13. Lai JS, Peng FZ (1995) Multilevel converters—a new breed of power converters. In: Conference record 1995 IEEE-IAS annual meeting, pp 2348–2356
14. Nabae A, Takahashi I, Akagi H (1981) A new neutral-point-clamped PWM inverter. IEEE Trans Ind Appl 17(5):518–523
15. Droguett G, Rojas F, Arancibia D, Díaz M, Mirzaeva G, Uriarte M (2018) Nearest level control for a three-phase to single-phase modular multilevel converter for solid state transformers. In: 2018 IEEE international conference on automation/XXIII congress of the chilean association of automatic control (ICA-ACCA), pp 1–6. https://doi.org/10.1109/ICA-ACCA.2018.8609787
16. Nguyen MH, Kwak S (2020) Nearest-level control method with improved output quality for modular multilevel converters. IEEE Access 8:110237–110250. https://doi.org/10.1109/ACCESS.2020.3001587

Voltage Multiplier Cell Based Five Level Asymmetrical Multilevel Inverter for Electrical Vehicle and Photo Voltaic Applications

Sumith Yellapu, J. Vijay Chandra, and K. Ravishankar

Abstract In the recent past, power generation using Photo Voltaic (PV) cells in the power sector and Battery Powered vehicles (BPV) in the automotive sector became popular. People are looking for DC-DC converters to conserve the energy of batteries to travel long distances with electric vehicles. This paper exhibits a configuration of Voltage Multiplier Cell-Based Boost Converter (VMCBC) with Dual-DC-Port Asymmetrical Multilevel Inverters (DPAMI). Voltage Multiplier Cell/Circuit (VMC) in VMCBC is efficient. It offers high DC voltage gain, i.e. improves boosting capabilities and reduces voltage stress on the switch. An enhancement in the voltage-boosting ratio makes the converter suitable for both BPV and PV applications. As fewer series-connected battery cells are required to get the desired voltage to drive an electric motor. DP-AMI is a five-level Multilevel inverter that reduces power conversion stages, voltage stress, current stress and improves the overall conversion efficiency DPAMI interfaces with low voltage, high voltage DC ports. These voltages are provided by VMCBC. The simulation model of the proposed configuration is tested through the MATLAB/SIMULINK simulation software environment. Simulink results of the simulation model configuration conform the accuracy and viability, and effectiveness is analysed through simulation.

Keywords Multi-level inverter (MLI) · Boost converter · Battery powered vehicle (BPV) · Voltage multiplier cell (VMC)

1 Introduction

By noticing, recent and past published literature surveys of multilevel inverters on Topologies, Control Strategies, Applications, and Reduced Device Count. DC to AC conversion using multilevel inverters offers some of the promising features as follows [1–5]:

S. Yellapu (✉) · J. Vijay Chandra · K. Ravishankar
Department of Electrical and Electronics Engineering, Lendi Institute of Engineering and Technology, Vizianzgaram, Andhrapradesh 535005, India
e-mail: sumithyellapu@gmail.com

- They can generate a high-quality waveform with low distortion on output voltages.
- They draw source current with low distortion.
- The voltage stresses on the power semiconductor devices (PSD) are a lot lesser when contrasted with the functional voltage. Subsequently, a high voltage (HV) waveform can be constructed with relatively switches with a low voltage rating, harvest a much smaller common-mode voltage and consequently, the pressure in the bearings of a motor can be diminished.
- They work with a lower switching frequency.
- The staircase waveform displays a superior consonant profile, which also decreases the dv/dt stresses. Consequently, filter requirements can be reduced (or even eliminated), and electromagnetic compatibility issues can be alleviated.
- The ability to obtain a specific voltage level using switching permutations. These redundant conditions can be employed to programme a fault-tolerant state.
- Non-conventional energy sources, such as photovoltaic, fuel cells, and Battery Powered vehicles (BPV), can be easily directly integrated into a multilevel converter system and organized for equal load allocation among input sources.

Comparison of three-phase and two-phase multilevel inverter depicts reduction of THD and switching losses with voltage balancing of two DC-links capacitors switching orders are selected conditional on the alteration in the capacitor voltages [6]. Five-level single-phase PWM and seven-level single-phase PWM inverters with deadbeat control schemes are proposed to maintain sinusoidal output voltage and current regardless of load variation and to reimburse for partial magnetization of filter inductor and high dynamic performances for grid incorporation with PV cells [7, 8].

In 2019, Naresh K. Pilli, M. Raghuram, Avneet Kumar, Santosh K. Singh, proposed a "Single DC-source-based seven-level boost inverter for electric vehicle application" [9] to produce two levels of different voltages without increased device count, the generation of unbalanced DC supplies from balanced DC supplies, which requires fewer battery cells due to the enhanced voltage generated by the low-input voltage of Battery, i.e. the demand for fewer DC supplies due to the multi-output facility and it transforms a single voltage level of DC power supply from BPV batteries to two distinct DC output voltages levels and offers asymmetrical DC source for seven-level operations [9].

Quasi-Z-source inverter (QZSI) offers for smoothening source current, reduced voltage stress on the capacitor for electric vehicles supplied with low voltage batteries. The inductor of Z-source in Quasi Switching Boost Inverter (QSBI) with conventional PWM inverter can be compact because of the escalation in ripple frequency for a particular inverter switching frequency [10–12]. However, the partial step-up voltage capability and modulation index, high current and voltage stresses and difficult to control make it complicated to achieve high efficiency with QZSI and QSBI inverters.

Solar panels and Boost converters are used to provide asymmetrical input voltages for the Dual-DC-Port T-type Asymmetrical multi-Level Inverter (DP-T-AMI), which helps to reduce switching losses and the size/volume of the passive filter on the output side. The stages of power conversion are shortened. The front-end DC-DC

converter's voltage and current stress may be minimized, resulting in a significant increase in conversion efficiency. To achieve maximum power from the renewable source, the high voltage port is regulated by DP-AMI, and the low voltage DC port is regulated by the boost/Step-up converter, but the Total Harmonic Distortion (THD) order of DP-T-AMI is above 37% with conventional Boost converter and complex control strategy (MPPT, SPWM, and PLL). Furthermore, the DP-low AMI's voltage is not a set value, which would be a disadvantage for the inverter in comparison to conventional multilevel inverters [13].

VMC's are efficient, minimal expense, and simple topologies. The VMC is widespread for high boost applications as they are simple to execute in any circuit to meet very extremely high voltage gain demand. They can usually achieve ultra-voltage gain with diminished stress on the components use multiple VMCs. However, these most researchers' capacitors arrangement with source in non-isolated DC-DC converter is not intuitive to achieve boosting in input voltage. Further in some arrangements, demands additional switches, components in VMC and condensers/capacitors require a current equivalent to either the source current or the load current [14–16].

Earlier some researcher studies carried on inverter with DC-DC converter for photo voltaic/Solar applications. However, past research on voltage boosting capabilities, stress on power semiconductor switching devices, and THD improvement with conventional and multilevel inverters have been inadequate. This paper proposes a configuration to modification of existing DP-T-AMI with a Conventional DC-DC converter. Cascade connecting between Voltage Multiplier Cell (VMC) and DP-T-AMI is dependent, without extending stages and with improving the boost factor, THDs and cascade linked battery cells with a suggested configuration.

2 Proposed System Configuration

The Proposed system configuration is presented in Fig. 1.It comprises of four stages. Stage-1: Single Boosting Stage, Stage-2: Double boosting stage (Capacitor-Diode Bridge configuration or Voltage multiplier cell), Stage-3: Filtering stage, and Stage-4: Multilevel Inverter (MLI) stage. This circuit configuration consists of one inductor, one switch S, two diodes (D_1, D_2), two capacitors (C_1, C_2), and one LC filter. Voltage Multiplier Cell (VMC) based Boost converter operates in two different modes as shown in Figs. 3 and 4. Stage1 and 2 operation purely depends on switch 'S' switching action. In the first mode, switch 'S' is turned on by a gate signal then the inductor is exciting. During the second mode, switch (S) is turned off by removing gate single then the inductor is discharged through the capacitors.

Charging states of capacitors C_1 and C_2 during two modes of operations are summarized in Table 1. The advantage of the converter is inductor and capacitors will charge in series and discharge in parallel.

Duty-ratio of switch 'S' governs the voltage offered across the capacitors $C1$ and $C2$.
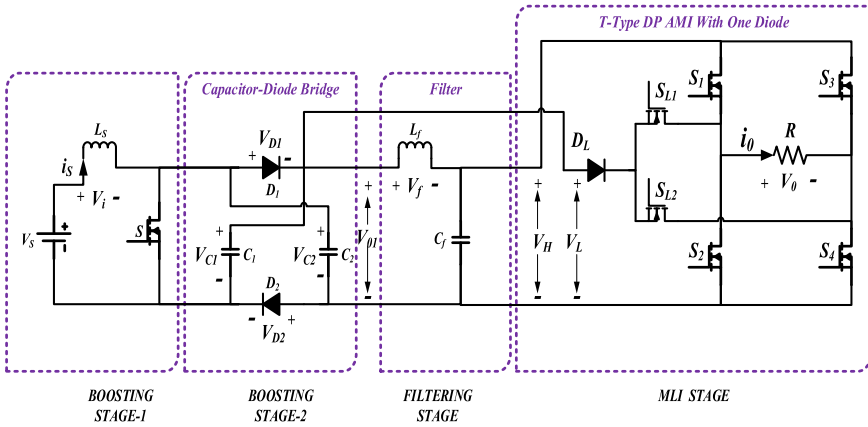
Fig. 1 Proposed system configuration—voltage multiplier cell (VMC) based 5-level asymmetrical multilevel inverter (VMC-5L-AMI)

Table 1 Charging and discharging states of capacitors according to modes of operation

MODE	S	C_1	C_2
1	On	Charging	Charging
2	Off	Discharging	Discharging

Table 2 Switching states of devices in DC-converter of the proposed configuration

S	Capacitances $(C1,C2)$	Output voltage (V_o)	Conducting devices
ON	Series	$V_o = V_{C1} + V_{C2}$	S
OFF	Parallel	$V_o = V_{C1} = V_{C2}$ $= V_S + V_i$	D_1, D_2

During two modes of operations, output voltage of the converter is summarized in Table 2.

2.1 Voltage Multiplier Circuits/Cells (VMC) Based Boost Converter and Its Operation

Average value of output voltage of Conventional Boost converter is (Fig. 2) [14]

$$V_0 = \frac{V_s}{1 - D}$$

Voltage Multiplier Circuits/Cells (VMC) based boost converter is derived from conventional boost converter by adding extra diode and capacitor.
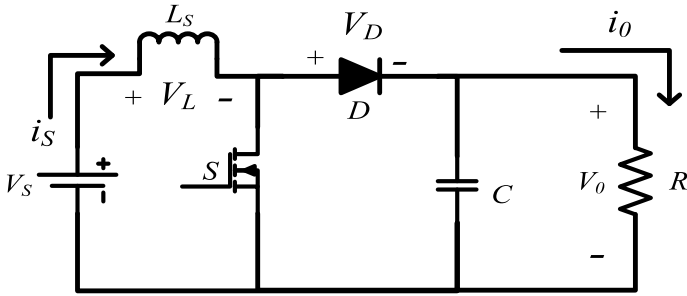
Fig. 2 Conventional boost converter
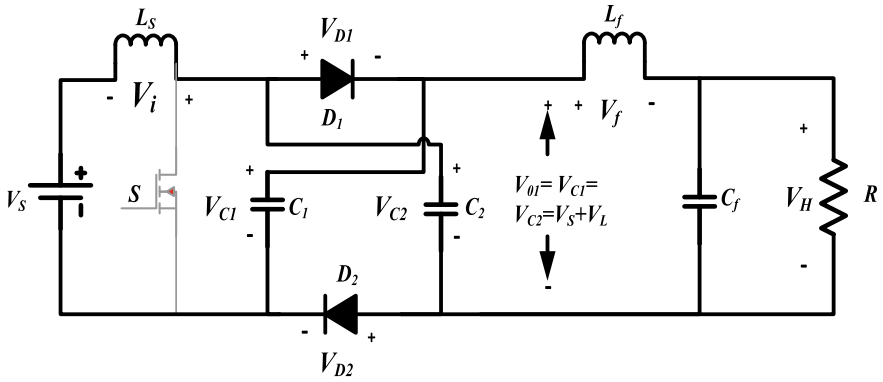
(a)
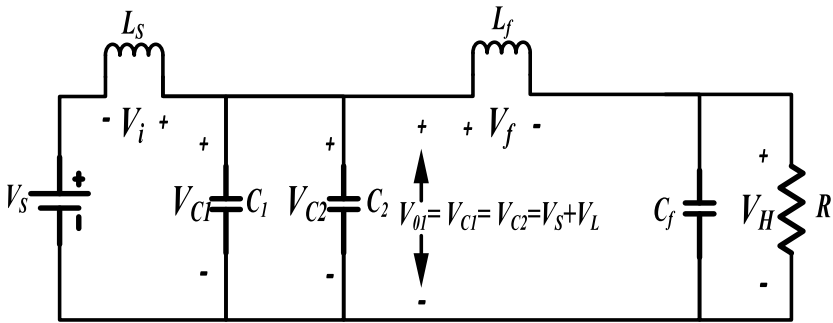
(b)

Fig. 3 Mode-1. **a** Operation of voltage multiplier cell (VMC) based Boost converter. **b** equivalent circuit of Fig. 3a is shown
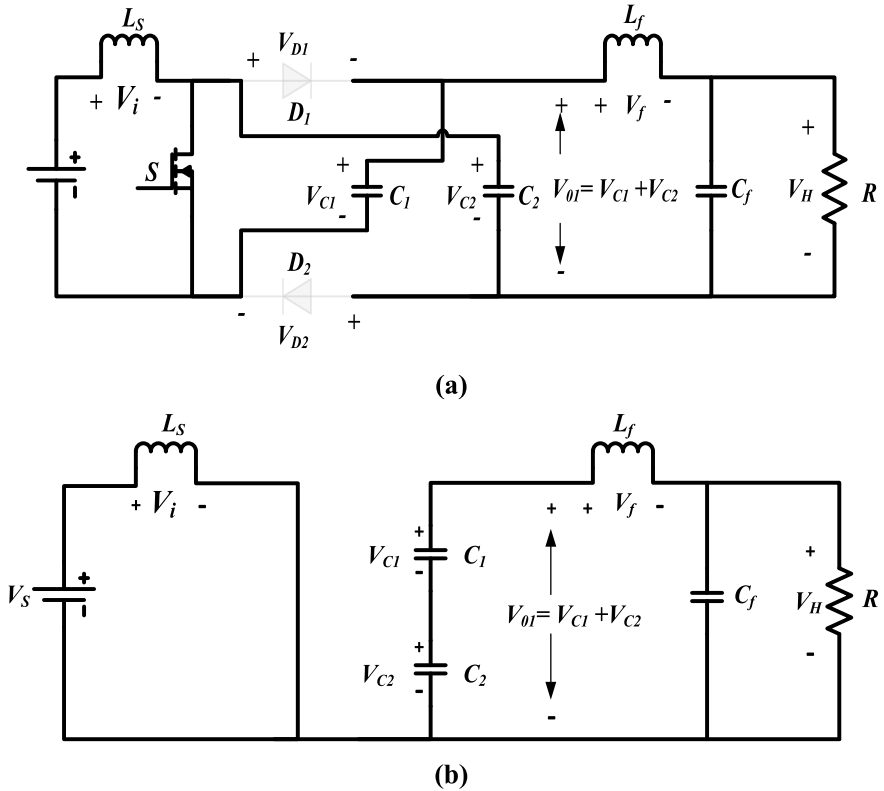
Fig. 4 **a**.Mode-2 operation of voltage multiplier circuits/cells (VMC) based boost converter. **b** Equivalent circuit of Fig. 4a is shown

Boosting factor or Voltage gain provided by Voltage Multiplier Circuits /Cells (VMC) is $\frac{(1+D)}{(1-D)}$.

Modes of VMC based Boost converter: VMC based boost converter operates in two modes:

Mode-1 (During 'S'-ON): 'S' is ON, inductor charges. Diode D_1, D_2 becomes reverse biased. Switch side terminals of capacitors are short circuited, and then capacitors comes to series. Capacitors discharges in series to load through filter. Output voltage is equal to sum of Capacitors C_1 and C_2 voltages (Fig. 3).

$$V_{01} = V_{C1} = V_{C2} = V_S + V_i \tag{1}$$

Mode-2 (During 'S'-OFF): 'S' is OFF both the Diodes become forward biased and capacitors become parallel to both input, output stage. In stage-2 (cross-coupled capacitor-diode or capacitor-diode bridge configuration), capacitors charges
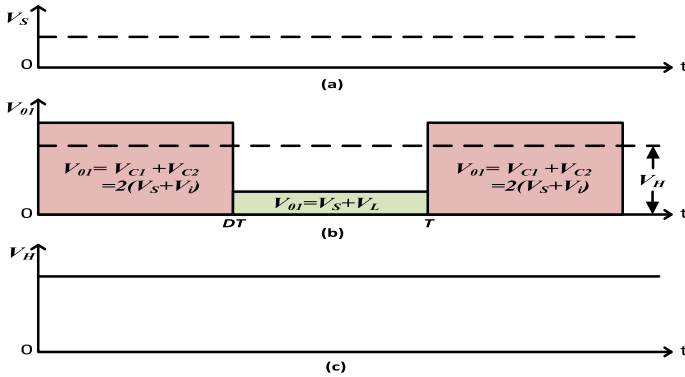
Fig. 5 **a** Input DC voltage. **b** Voltage multiplier circuits/cells (VMC) based boost converter output voltage without filter (V_{01}). **c** Voltage multiplier circuits/cells (VMC) based boost converter output voltage with filter (V_H)
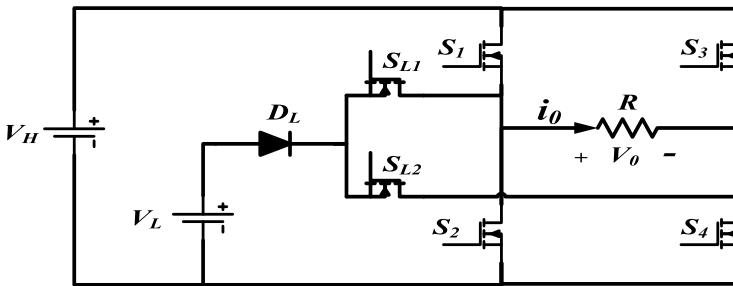
Fig. 6 Diagram of dual DC port five level asymmetrical multi level inverter (DP-5L-AMI)

in parallel to series connected source and inductor combination. The sum of the source and inductor voltages denotes the output voltage (Figs. 4, 5 and 6).

$$V_{01} = V_{C1} + V_{C2} = 2(V_S + V_i) \tag{2}$$

2.2 Dual DC Port Five Level Asymmetrical Multi Level Inverter (DP-5L-AMI) and Its Operation

Dual DC Port Five level Asymmetrical Multi Level Inverter (DP-5L-AMI) is derived from T-type inverter and Neutral Point Clamped (NPC) inverter. The DP-5L-AMI requires six switches and one clamping diode. In conventional inverter to produce three levels of voltages ($-V/2$, 0, $V/2$) uses capacitors as voltage dividers. The AMI

Table 3 Switching states of devices in AMI

Switching state	S_{L1}	S_{L2}	S_1	S_2	S_3	S_4	Output voltage
A	ON (1)	OFF (0)	OFF (0)	OFF (0)	OFF (0)	ON (1)	$+V_L$
B	OFF (0)	ON (1)	OFF (0)	ON (1)	OFF (0)	OFF (0)	$-V_L$
C	OFF (0)	OFF (0)	ON (1)	OFF (0)	OFF (0)	ON (1)	$+V_H$
D	OFF (0)	OFF (0)	OFF (0)	ON (1)	ON (1)	OFF (0)	$-V_H$
E	OFF (0)	OFF (0)	OFF (0)	OFF (0)	OFF (0)	OFF (0)	0

is supplied with two levels of voltages from a voltage multiplier cell-based boost converter (VMCBC) to operate the AMI as a five-level multilevel inverter [13]. Operation of Switches—S_{L1}, S_{L2}, S_2, and S_4 to create negative and positive levels of low voltages. Operation of Switches—S_1, S_2, $S_{3,}$ and S_4 to create negative and positive levels of high voltages. The switching states of devices in AMI are shown in Table 3. Operating modes and the output voltage of the AMI during a positive half cycle and a negative half cycle are shown in Fig. 7.

3   Matlab/Simulink-Simulation Results

See Figs. 8, 9 and 10.

Total Harmonic Distortion (THD) analysis of proposed configuration in MATLAB/SIMULINK:

See Figs. 11, 12 and 13.
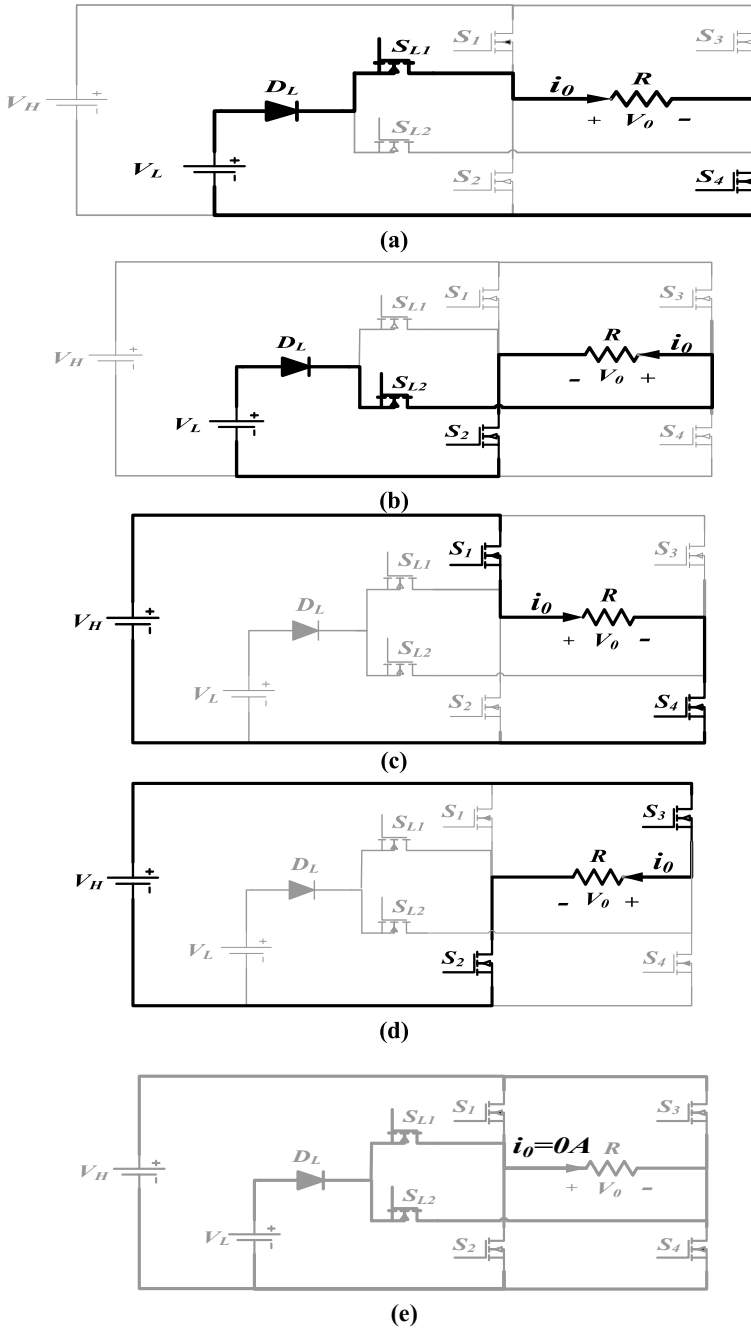
Fig. 7 Switching states of the AMI. **a** State—'A'. **b** State—'B'. **c** State—'C'. **d** State—'D'. **e** State—'E'
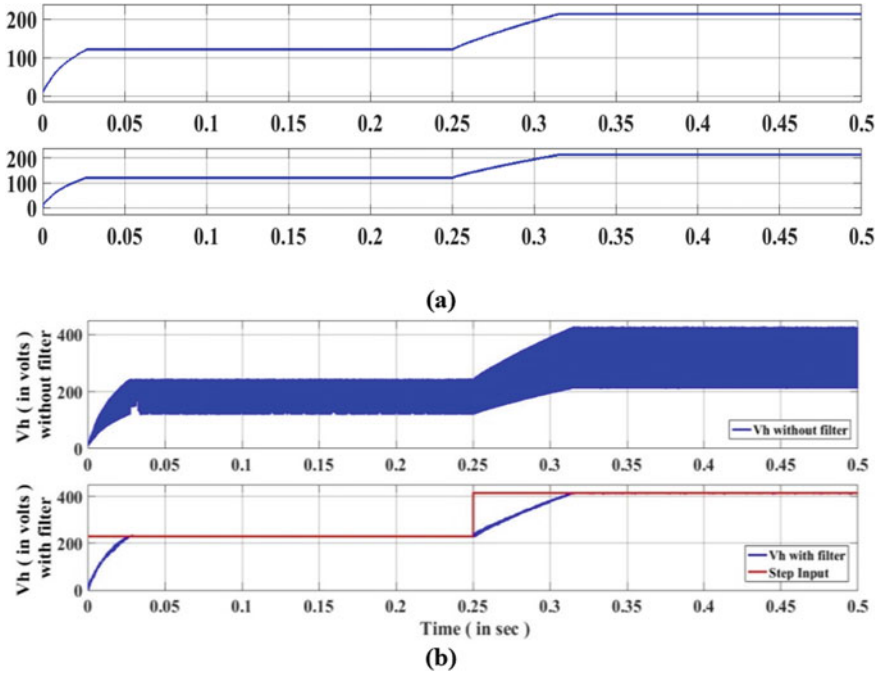
Fig. 8 Simulation results of the proposed configuration for Load of 250 W for a step-change in voltage reference signal from 230 to 415 V at $t = 0.25$ s for fixed 12 V, input DC supply. **a** Voltage across capacitors $C1$ and $C2$. **b** Voltage across VMC based boost converter output terminals-without and with filter

4   Circuit Parameters for Matlab/Simulink Simulation

Components	Value
Input source (in volts)	$V_S = 12$
Source inductance (in mH)	$L_S = 0.1$
Capacitors (in μF)	$C_1 = 560, C_2 = 560$
LC output filter (μH, μF)	$L_f = 560$
	$C_f = 10$
Switching frequency of proposed configuration (in kHz)	$f_C = 5$
Utility frequency (in Hz)	50
PI-controller gains	$K_P = 100, K_I = 0.1$
PLL controller gains	$K_P = 10, K_I = 0.1$
Load (in KW, VAR)	250,100
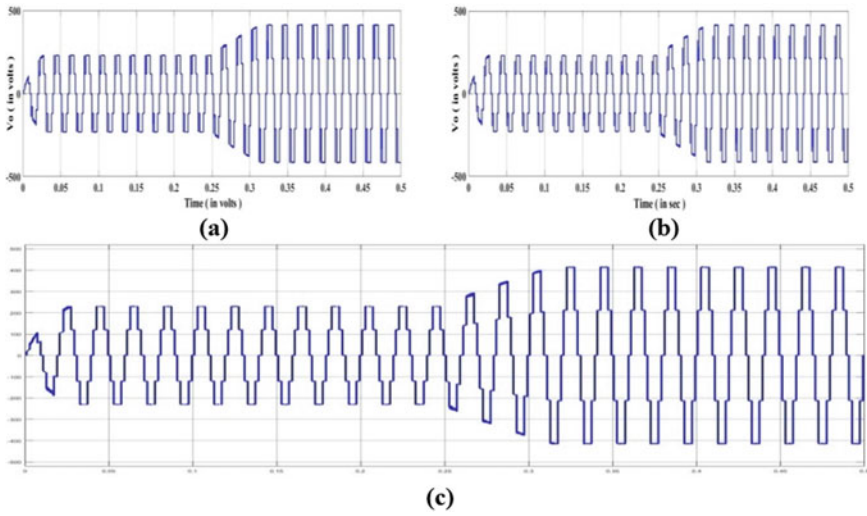
Fig. 9 Five level output voltages of the multi-level inverter (MLI) for 12 V input DC supply and a reference signal of 230 V. **a** Load at 250 W and 100VAR. **b** Load at 250 W and 500VAR. **c** Load at 250 W
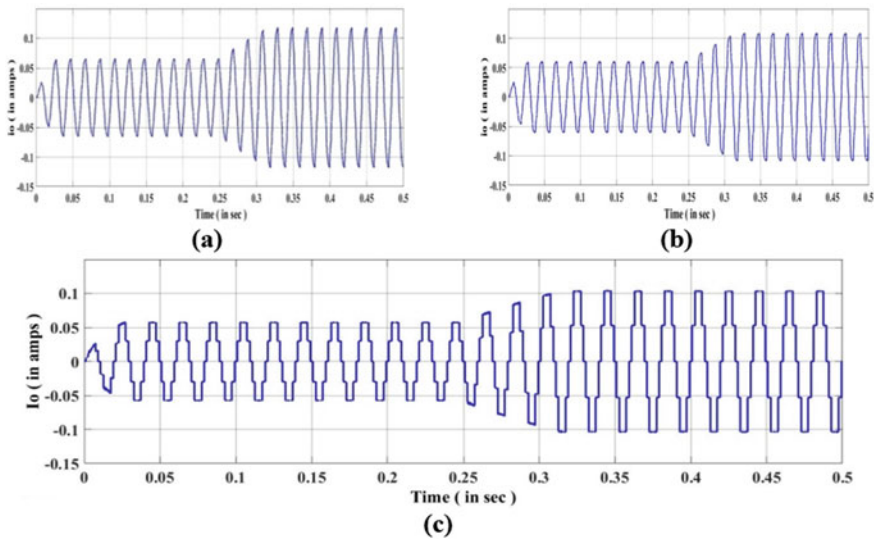
Fig. 10 Five level output currents of the multi-level inverter (MLI) for a step-change in voltage reference signal from 230 to 415 V at $t = 0.25$ s (12 V input DC supply). **a** Load at 250 W and 100VAR. **b** Load at 250 W and 500VAR. **c** Load at 250 W
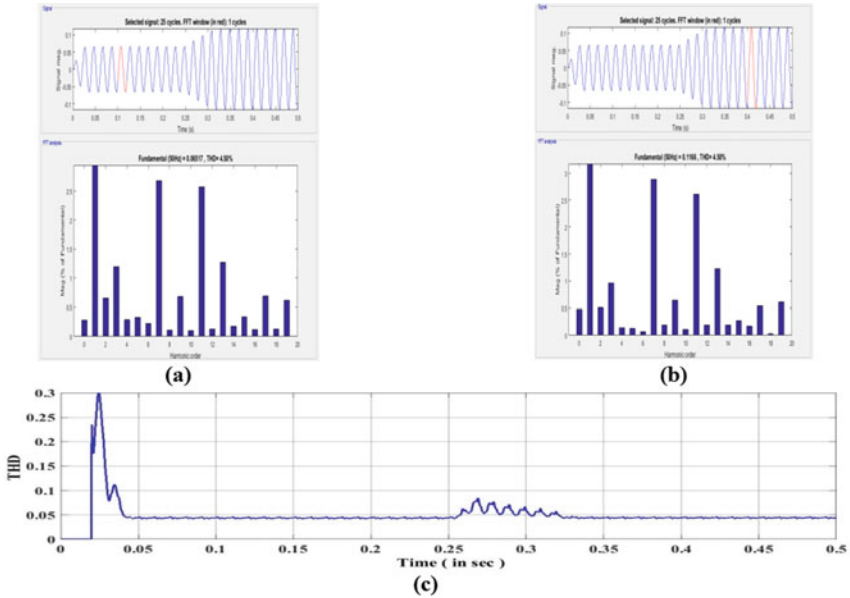
Fig. 11 THD analysis of 5 level inverters output current for load at 250 W and 100VAR. **a** THD analysis of proposed configuration at 230 V reference signal. **b** THD analysis of proposed configuration at 415 V reference signal. **c** THD graph of proposed configuration for a step-change in voltage reference signal from 230 to 415 V at 0.25 s

5 Conclusion

This paper proposes a voltage Multiplier Cell-based Asymmetrical Five level Multi-Level Inverter (VMC-DL-AMI). Closed-loop operation of VMC-5L-AMI with tracking of input command and simulation results is shown. VMC-5L-AMI produces five levels of AC output voltages with varying input voltage commands. Simulated results of the proposed configuration at different Load conditions reveal an improvement in the voltage-boosting ratio and also avoid a dependency of series-connected battery cells to produce a higher voltage. Comparison of simulation results of THD analysis clearly shows that suppression of even harmonics and reduction occurs for pure resistive load, reduction of THD at inductiveness of VMC-5L-MLI. As a result, the conversion efficiency is enhanced while conduction and switching losses are minimized.
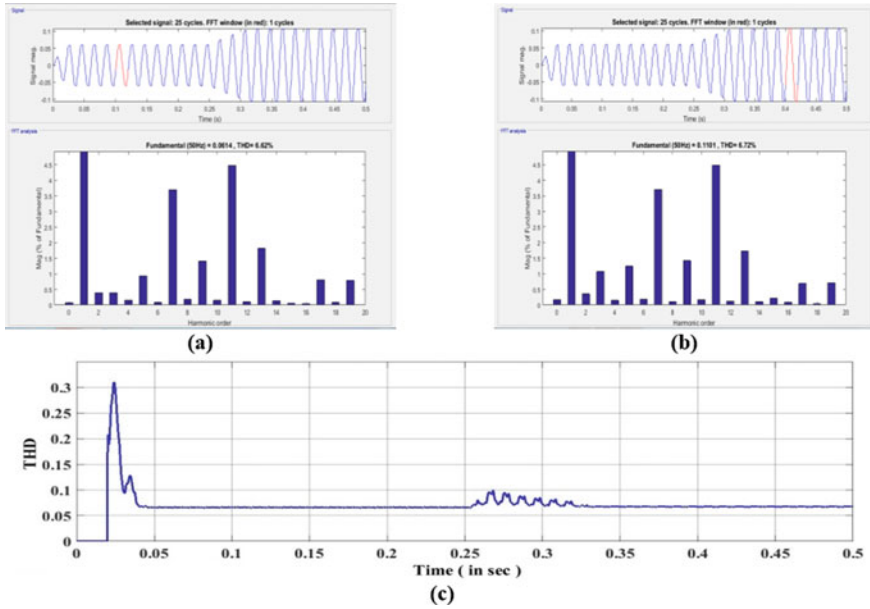
Fig. 12 THD analysis 5 level inverter output current for load at 250 W and 50VAR. **a** THD analysis of proposed configuration at 230 V reference signal. **b** THD analysis of proposed configuration at 415 V reference signal. **c** THD graph of proposed configuration for a step-change in voltage reference signal from 230 to 415 V at 0.25 s

Load	THD at 230 V (%)	THD at 415 V (%)
250 W and 100VAR	4.50	4.50
250 W and 50VAR	6.62	6.72
250 W and 0VAR	17.24	17.38
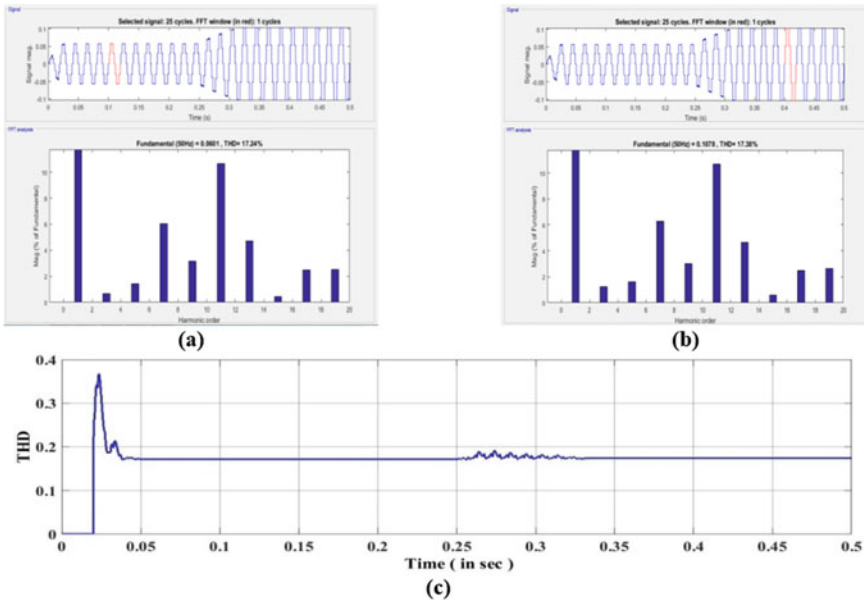
Fig. 13 THD analysis 5 level inverter output current for load at 250 W. **a** THD analysis of proposed configuration at 230 V reference signal. **b** THD analysis of proposed configuration at 415 V reference signal. **c** THD graph of proposed configuration for a step-change in voltage reference signal from 230 to 415 V at 0.25 s

References

1. Mittal N, Singh B, Singh SP, Dixit R, Kumar D (2012) Multilevel inverters: a literature survey on topologies and control strategies. In: ICPCES 2012–2012 2nd international conference on power, control and embedded systems, pp 1–11. https://doi.org/10.1109/ICPCES.2012.650 8041
2. Sandeep N, Yaragatti UR (2018) Design and implementation of active neutralpoint-clamped nine-level reduced device count inverter: an application to grid integrated renewable energy sources. IET Power Electron 11(1):82–91. https://doi.org/10.1049/iet-pel.2016.0951
3. Rodriguez J, Lai J-S, Peng FZ (2002) Multilevel inverters: a survey of topologies, controls, and applications. IEEE Trans Ind Electron 49(4):724–738. https://doi.org/10.1109/TIE.2002. 801052
4. Gupta KK, Ranjan A, Bhatnagar P, Sahu LK, Jain S (2016) Multilevel inverter topologies with reduced device count: a review. IEEE Trans Power Electron 31(1):135–151. https://doi.org/10. 1109/TPEL.2015.2405012
5. Salem A, Van Khang H, Robbersmyr KG, Norambuena M, Rodriguez J (2021) Voltage source multilevel inverters with reduced device count: topological review and novel comparative factors. IEEE Trans Power Electron 36(3):2720–2747. https://doi.org/10.1109/TPEL.2020.301 1908
6. Choudhury A, Pillay P, Williamson SS (2014) Comparative analysis between two-level and three-level DC/AC electric vehicle traction inverters using a novel DC-link voltage balancing algorithm. IEEE J Emerg Sel Top Power Electron 2(3):529–540. https://doi.org/10.1109/jes tpe.2014.2310140

7. Rahim NA, Chaniago K, Selvaraj J (2011) Single-phase seven-level grid-connected inverter for photovoltaic system. IEEE Trans Ind Electron 58(6):2435–2443. https://doi.org/10.1109/TIE.2010.2064278

8. Park SJ, Kang FS, Lee MH, Kim CU (2003) A new single-phase five-level PWM inverter employing a deadbeat control scheme. IEEE Trans Power Electron 18(3):831–843. https://doi.org/10.1109/TPEL.2003.810837

9. Pilli NK, Raghuram M, Kumar A, Singh SK (2019) Single dc-source-based seven-level boost inverter for electric vehicle application. IET Power Electron 12(13):3331–3339. https://doi.org/10.1049/iet-pel.2019.0255

10. Nguyen MK, Le TV, Park SJ, Lim YC (2015) A class of quasi-switched boost inverters. IEEE Trans Ind Electron 62(3):1526–1536. https://doi.org/10.1109/TIE.2014.2341564

11. Beer K, Piepenbreier B (2010) Properties and advantages of the quasi-Z-source inverter for DC-AC conversion for electric vehicle applications. In: 2010 emobility—electrical power train, EEPT 2010, pp 1–6. https://doi.org/10.1109/EMOBILITY.2010.5668100

12. Karthik VMV, Kottayil SK (2018) An improved PWM control of quasi-switched-boost inverter with reduced ripple magnitude and increased ripple frequency input current. In: Proceedings of 2017 IEEE international conference on technological advancements in power and energy: exploring energy solutions for an intelligent power grid, TAP energy 2017, 2018, pp 1–6. https://doi.org/10.1109/TAPENERGY.2017.8397255

13. Wu H, Zhu L, Yang F, Mu T, Ge H (2017) Dual-DC-Port asymmetrical multilevel inverters with reduced conversion stages and enhanced conversion efficiency. IEEE Trans Ind Electron 64(3):2081–2091. https://doi.org/10.1109/TIE.2016.2625772

14. Forouzesh M, Siwakoti YP, Gorji SA, Blaabjerg F, Lehman B (2017) Step-Up DC-DC converters: a comprehensive review of voltage-boosting techniques, topologies, and applications. IEEE Trans Power Electron 32(12):9143–9178. https://doi.org/10.1109/TPEL.2017.2652318

15. Schmitz L, Martins DC, Coelho RF (2020) Comprehensive conception of high step-Up DC-DC converters with coupled inductor and voltage multipliers techniques. C IEEE Trans Circuits Syst I Regul Pap 67(6):2140–2151. https://doi.org/10.1109/TCSI.2020.2973154

16. Prudente M, Pfitscher LL, Emmendoerfer G, Romaneli EF, Gules R (2008) Voltage multiplier cells applied to non-isolated DC-DC converters. IEEE Trans Power Electron 23(2):871–887. https://doi.org/10.1109/TPEL.2007.915762

Application of Renewable Energy in Charging Station for Electric Vehicles: A Comprehensive Review

Bugatha Ram Vara Prasad ⓘ **, Brundavanam Sesha Sai,**
Joddumahanthi Vijaychandra, and Rohit Babu

Abstract Nowadays with an increase in the demand for electric vehicles, we need to increase the charging stations to provide continuous power to the public for transportation. At the same time to decrease the pressure on the local grid we have to use alternative energy sources like solar and wind. Recently the entire world has seen the importance of renewable energy in charging stations which received great applause. In this paper, we review the different types of renewable energy-based charging stations. This paper covers research on critical aspects in this field, architecture, location, optimal designing and sizing. The research also incorporates studying power management and control of charging station and also investigates various challenges faced by charging stations and suggested proper solutions for those challenges. The main objective of the paper is to give an overview of charging stations with renewable energy for electric vehicles.

Keywords Electric vehicle · Charging station · Renewable energy · Solar · Wind · Vehicle to grid

1 Introduction

Worldwide there is an increase in the usage of electric vehicles (EVs) which resulted in the high demand for electrical energy all over the world. Worldwide the market for EVs has been increased exceptionally. In [1], according to the data the number of EVs on the road in the year 2010 was only in the hundreds but in the year 2017 around 3 million and in the year 2019 almost 6 million EVs are being used by the people across the globe. The best alternative to conventional vehicles (CVs) is EVs which have zero carbon emission and also the solution for decreasing the pollution which is caused by CVs. Using EVs the usage of biofuels would also be minimized which are in the stage of extinguish. The motors which are used in EVs have efficiency of

B. R. V. Prasad (✉) · B. S. Sai · J. Vijaychandra · R. Babu
Department of Electrical Engineering, Lendi Institute of Engineering and Technology, Jonnada, Vizianagaram 535005, India
e-mail: ramvaraprasad.bugatha@lendi.org

80–95% [2], where the CVs have an efficiency of below 20% [3], making EVs more choice than CVs. The disadvantages in EVs are pricing cost is more, charging time is more and speed is limited makes serious issues while promoting and due to above reasons, the usage of EVs are not up to mark [4].

Due to the fast increase in demand in EVs and EV charging most of researchers along with power generation companies are trying to reduce the pressure on local grid which is due to an increase in EV charging stations. The beneficial idea is to adopt the EV charging stations along with renewable energy sources like solar and wind [5].

As we know that there is high demand in EVs renewable energy-based charging stations (RCS) with the sources like solar and wind will be suited for charging of EVs [6]. Proper planning of RCS and direct current (DC) will satisfy the demand of charging the EV. Also, the conventional charging stations affect the stability of the grid with power quality issues like voltage fluctuations, harmonics, and power outages [7]. But RCS will have various advantages like simple planning, efficiency high [8], and low cost [9]. Compare to an alternating current (AC) -based charging station [10], DC-based system will have less power conversion levels more over RCS will reduce the carbon emission and also expands the involvement of renewable energy sources into energy domains.

The major problems seen while designing and implementing the RCS are the unpredictability of renewable energy sources (e.g., the wind speed is varied seasonally, variation in daily sun irradiance) and EVs load nature (e.g., initial charging state, charging start time, charging stop time, capacity of battery, types of EVs) [11].

Many research works are going on the above-mentioned topics and researchers are planning to design and implement the RCS considering various aspects like optimal placing, sizing and controlling, pricing, and load factors. Few reviewed the EVs but analysed technical points and not applied the concept of renewable energy sources [1]. Others reviewed the study of RCS which mainly concentrated on number of consumers and EVs interaction [12]. No one studied completely on RCS and talked over the recent advanced areas.

In EVs battery plays a vital role in today's transportation industry and there are various types of batteries incorporated to EVs. For proper selection of battery in EVs we have to consider the various characteristics like efficiency, price, capacity, energy storage, and safety. Most of the EVs utilize these four types of batteries 1. Lithium Ion (Li-Ion) 2. Molten salt (Na-NiCl$_2$) 3. Nickel Metal Hydride (Ni-MH) 4. Lithium Sulphur (Li–S). Among different types of batteries used in EVs Li-Ion is widely used due to its effective cost price, modern manufacturing technology, improved life cycles, lightweight and high storage of energy make an ideal solution to use in EVs [13].

This study investigates the latest advanced technologies in RCS and recent developments in this field. This paper talk about the advanced technology for designing RCS, sources of energy for RCS, sitting, optimal planning, optimal sizing, control and energy management, pricing, and difficulties faced by RCS.

2 Technical Architecture

Across the world in most of the countries the growth of EVs is increasing day by day due to a smaller number of charging stations restricting the usage of EVs across the globe [14]. Recently with an increase in EVs, the charging stations are also increased, installing a greater number of charging stations at public places [15] conventional type charging stations which use fossil fuels will affect the environment and grid. With renewable energy sources like solar photovoltaic (SPV) system and wind energy generates electricity to a greater potential will be an optimal solution to charge an EV and shows the advancement towards a clean green energy environment [16]. Due to variation in output power generated by the renewable energy sources (e.g., variation in solar radiation and variation in wind speed) most of studies show the hybrid installation of SPV systems and wind energy conversion system (WECS) along with grid is progressive and technically feasible [17].

Balancing of cells plays a vital role in improving the life of series-connected cells in batteries because without proper balancing system each cell voltage will vary over time and capacity of the battery pack will be discharged quickly. So, to improve the battery we need dynamic adjustment of equalization. In [18], the work shows the inductor-based bidirectional losses equalization circuit for series-connected cells and the experimental results show that the equalization circuit helps to decrease the charging current of high voltage battery and also decrease the discharging current of low voltage battery during the discharge process.

The battery will be unbalanced due to variation in cells which makes the degradation process and also effect the state of health of battery. The researcher in [19], has explained the balancing of modular battery with different degradation levels and researcher has proposed the new model called linear regression which is used to analyse the degradation of battery and to find the difference in degradation level between each cell.

2.1 Storage of Energy and Quick Charging Systems

Uncontrolled charging in EV stations will lead to overloading of feeders and transformers and affect the power supply also [20]. Therefore, after many papers investigation the optimal solution is to storage the energy and quick charging stations will reduce the difficulties faced by the system. Storage of energy will enhance the stability of the charging station and provide enough energy during emergency conditions [21]. Many literature suggested the benefits of using storage energy along with fast charging stations [22]. Anyhow, to acquire such benefits, we have to plan for optimum sizing of the storage energy system along with load nature of EVs [23].

There are some problems during quick charging of battery that are to be identified and proper modelling has to be done to improve the charging process and state of

health of the battery. Many researchers have done modelling and simplified the partial differential equations to predict the battery dynamics [24].

2.2 Controller and Battery Storage

To store the excess energy produced by the solar photovoltaic (SPV) systems there is necessity of controller in the system which is connected to the battery. Figure 1. Shows the schematic diagram of EVs charging station with SPV system. Many literature have done an investigation on a controller which is used in SPV systems. In this process they mentioned there is improvement in SPV systems generation while using maximum power point tracker (MPPT) and pulse width modulated (PWM) techniques [25].

Using solar-powered battery storage in charging stations will reduce the stress on the grid. There are different types and ranges of batteries that are used in solar charging stations. Mostly used batteries for SPV systems are lithium-ion, lead-acid battery, and flow battery [26].
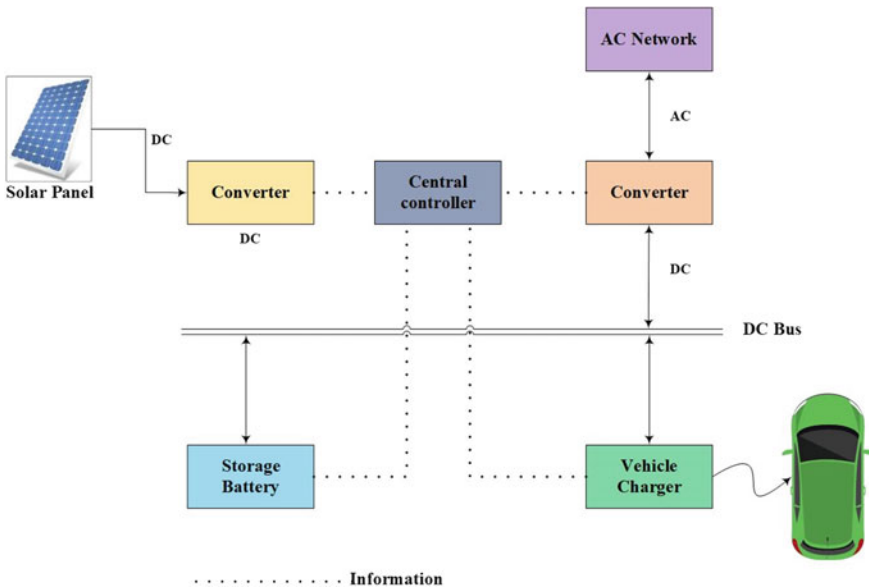
Fig. 1 EV charging station with a solar PV system

2.3 Converters

They are different types of converters used in RCS for charging of EVs, the different converters are DC/DC converters, and AC/DC converters used in charging stations. Mostly in SPV systems DC/DC converters are used to extract the maximum power from the PV arrays using the MPPT or PWM technique. The power coming from the grid is mostly AC but to charge the electric vehicles we need DC so we use AC/DC converter. Therefore, converters play an important role in SPV-based charging stations for energy conversion [27]. These converters improve the overall efficiency of SPV arrays and make the system to operate in maximum conditions.

3 Significance of Renewable Energy Sources

Solar and wind power are treated as the best alternative sources to conventional sources because of environmental advantages and economic considerations [28]. Anyhow, there is one major disadvantage in renewable energy sources that is unstable energy and we will not get continuous power all the time and they may vary. However, a few researchers suggested the solar-based charging stations of low and medium range for charging the EVs [22]. In [29], the work shows the EVs charging using solar power and DC link because to decrease the burden on the distribution network.

Many research works have been done on the control and optimization of wind turbine and show that wind energy is also suitable option for the EV charging station. In [30], the research work shows the various advantages of applying wide-range wind turbines in EV charging stations. The researcher in [31], investigated the chances of utilizing wind power as a direct source of power for charging of EVs. The researcher implemented the EV charging station with WECS considering various factors like average wind speed data, various turbine constructions, high resolution wind speed. Therefore, the investigation shows that wind energy with constant power will be sufficient for wide range EV charging stations.

In [32], the researcher developed favourable charging station based on wind energy with various charging modes. The wind energy–based charging station is connected to the grid and also having storage of energy. The optimized power was 52, 84 and 116 kW for charging EV with slow, medium, and fast charging modes. In this paper the study also shows the energy storage system to improve the wind energy system.

However, from the above data we can say that both solar and wind energy are suitable sources for EV charging stations. With the help of storage system, we can provide hybrid (solar and wind) or nonhybrid-based charging stations for charging of EVs with different types of charging modes like fast, medium, slow charging.

4 Location

4.1 Residential Charging

In [33], most of researcher's studies have observed that home charging is considered as reason for purchasing of EVs as it is simple to access. constructing a greater number of residential charging (RC) stations will also increase the buying of EVs, mainly in metro-cities [34]. According to the USA, report by energy efficient and renewable energy shows that nearly 80% of the installed charging stations is for RC, EVs charging areas are mostly in residential areas [35]. Using on-grid the EVs charging takes place and most of the EV charging takes place in home or residential areas. Utilizing renewable energy (e.g., solar, wind energy) based charging station in residential areas will decrease the stress on the grid and increases the demand for EVs also it is better use of clean energy resources which results the decrease in greenhouse gases release in the environment and pollution free.

4.2 Workstation Charging

Most of the companies has started to implement charging stations at workplaces for their staff and companies showing their commitment towards development of green energy environment. Considering the workstation charging (WC) as the second-best location after RC stations for employees to charge their EVs because they spend more time at work places and having extended parking in companies to charge EVs. In [12], the survey shows that 15–25% of charging takes place at the workstations and it is best opportunity to charge the EVs at parking areas in companies. Some companies like Google, DirecTV are offering free charging to employees, also adopting the renewable energy-based charging stations which will reduce the stress on grid. WC will lead to increase in utilizing of EVs and parking vehicles can be treated as distributed source of electricity provide to grid also known as vehicle to grid (V2G) integration of EVs and grid will utilize the renewable energy sources effectively and V2G concept will solve the fluctuations in renewable energy sources.

4.3 Public Charging

The public charging (PC) stations are the places where the EVs can be charge easily and best suited for executing the renewable energy sources than home areas. Residential areas or home areas having few disadvantages like availability of parking area, large buildings like gated communities where there is less space for installing SPV panels, installing problems in wind farms can be overcome by utilizing the PC stations [36].

The various public charging stations are:

4.3.1 Common Charging Stations

Common charging stations (CCSs) are the place where the EVs can be charge at public areas. Mostly CCSs are installed at shopping malls, hotels, airports, railway stations, parks where the EVs are parked for more than hour [37]. There will be an agreement between CCSs and drivers of EVs. The EVs operators have to pay amount as monthly subscription package, pay-as-you-go plans, in some cases for free also.

4.3.2 Fast Charging Stations

Fast charging stations (FCSs) or quick time charging stations are developed to solve the problem of charging time which plays a crucial role in purchasing of EVs. The purpose of fast charging is to charge the charge the vehicle quickly which is not possible in conventional charging stations. The role of fast charging in EVs are crucial in increasing the demand of EVs which reduce the time to charge the vehicle. Most of the EVs will have off-board fast charging module and the ratings of those stations will be usually 35 kW and above and the current range is 20–200 Amperes and the voltage profile will be 45–450 V [32]. These ranges are so high we need to install the monitoring system to control the station.

4.3.3 Swapping Stations

A swapping station is place where the EV drivers can easily replace their discharged battery with complete charged battery at swapping stations. Swapping stations will provide benefits like quick time to exchange the battery. Most popular company Tesla helps the drivers of EV to swap the batteries in less than 90 s. The advantages of using battery swapping at stations are drivers of EV can quickly exchange the batteries which reduce the charging of EVs during peak demand [38], low maintenance, long life for battery, low power consumption [39]. The disadvantages of swapping stations are high investment cost, battery management system (BMS) cannot give assurance to battery safety [32].

5 Optimal Designing

Table 1 shows the charging station designing and various parameters related to station type, sources, design methodology while designing charging station. Few researchers suggested the integration of renewable energy sources with V2G while designing the

Table 1 Charging station planning

Study	Modelling technique	Source	Station type
[41]	Stochastic programming	Grid, solar	Charging station
[42]	Mixed-integer linear programming (MILP)	Grid, wind, vehicle to grid (V2G)	Charging station
[40]	Two-stage stochastic MILP	Grid, solar	Battery exchange station and charging station
[43]	Two-stage stochastic MILP	Grid, wind, V2G	Charging station
[44]	Stochastic optimization	Grid, wind	Charging station
[45]	Probabilistic model	Grid, wind, solar	Charging station
[46]	Two-stage stochastic MILP	Grid, solar	Battery exchange station
[47]	MILP	Grid, wind	Charging station

infrastructure of charging stations. In [40], the researchers concentrated on battery swapping stations (BSS).

Designing the charging stations is a difficult task. However, while designing the charging station we have to consider the various factors like accessibility of renewable energy, nature of location, unpredictable demand, peak time of grid, V2G technology. While designing we have to consider the location, size, operation time in hours, usage of grid power, number of charged/discharged batteries, storage capacity, V2G, apart from the above considerations we have to include the fast charging technology also. In design process of RCS, the other factors are the cost, reliability, environment and social factors. Hence, while designing the charging stations optimal designing is suggested.

6 Optimal Sizing

In the past few years, vehicle industries noticed that there is rapid increase in EVs and the aim to ensure sustainability of the network. The latest advanced technologies in batteries made people to choose the EVs. Thus, the demand for EVs is increased which adds extra load to the distribution system. With increase in load we need to enhance and increase the load capacity in the distribution system to avoid overloading problems. Integration of renewable energy sources with power systems will solve the overloading problems. The most challenging task is to meet the demand of EVs using optimal sizing and operating the charging stations.

In [48], the researcher has designed the software for sizing the renewable energy and load sharing. Hybrid optimization model for electric renewables (HOMER) is designed in software for EV charging station with hybrid power sources like solar, wind. The total installed capacity of wind turbine (WT) and PV panels is 200 kW

and total power is 250 kW, total annual generation of 843,150 kWh was obtained. This designed charging station has the capacity of charging 5 EVs at a time in one hour. In [49], the mathematical modelling was developed in MATLAB environment for optimal sizing, allocating the load using differential evolution (DE) algorithm for integrating wind energy with EV charging station [49].

Wind generator with 200 kW has installed and used at charging station to charge the EVs and the demand of EVs can be achieved by the hybrid system. In [49], the researcher has designed multi objective optimization problem based on DE algorithm for optimal sizing of EV charging stations and implementation of the proposed technique is estimated in MATLAB for various grids. After simulation results, we get the data of optimal sizing of charging stations for EVs depends on various factors like load factor, loss of power, voltages losses. In [50], the researcher used the hybrid improved optimization technique based on Genetic Algorithm-Particle Swarm Optimization (GA-PSO) for optimal sizing of renewable energy sources (RES) and EVs.

In [51], the researcher presented the comparative analysis of optimal sizing for an isolated EV charging station and also grid connected charging stations. In this study the researcher explained utilizing of various sources like diesel-based, SPV with battery swapping system, integration of diesel-SPV-BSS system. The studies also show the simulation is done using HOMER software with minimum cost for charging stations.

With increase in demand for EVs which results increase in charging stations for EV drivers so there is necessity to provide fast charging to EVs. In [52], considering the quick charging time concept the researcher analysed the technical and economic factors designed an off grid SPV -based storage system with batteries for quick-time charging of EVs. In this paper the optimal sizing was done using HOMER software to improve the results of load scheduling. Using 50 kW DC fast charging station with 281.52 kW power generated from PV modules and the total no EVs which are recharged are 12 EVs each of 35 kWh are charged for the period of 13.5 h per day.

In [53], the researcher implemented a new approach of sizing of battery energy storage system within a fast charging station. The results of mathematical model show the demand of quick charging stations depends on various factors like charging level, number of EVs connected in station, size of batteries in EVs. In [54], the researcher proposed a new technique for optimal sizing and allocation of EVs called probabilistic planning model. Also, queuing theory (QT) was designed for EVs charging demand and using poisoning process the demand for EVs charging is estimated and also by applying the exponential distribution we can get the service time of charging devices.

7 Power Management and Control

While integrating the charging stations to grid especially renewable energy-based charging stations will leads to various problems. While integrating with grid voltage fluctuations, induced harmonics, power quality issues will rise especially when we connect with quick time charging stations [55]. Therefore, it is necessary to control

the charging stations while integrating with grid to decrease the effects. In [56], the study shows the necessity of control and energy management of charging station which will reduce the voltage fluctuations, controlling grid peak demand, effective utilization of load characteristics of the grid. In [57], the researcher explained the effect of EVs on the distribution system, [58] investigated the impact of charging stations on the system complete losses. In [59], proposed a new model called probabilistic method to study the effects of EV charging on distribution system.

By governing the charging process in a controlled mode will increase the charging capacity of EVs and also increasing number of EVs. By utilizing the maximum energy generated by the renewable sources and integrated with grid will reduce the load stress on the grid and secure clean energy. By controlling the renewable sources, we can reduce the voltage fluctuations and enhance the system reliability and integrating the energy storage will reduce the load from the grid [55].

In [60], the study shows that parking time for EVs is around 95% per day in parking area only which make use of V2G technology. In this paper the investigation concludes that EV can be charge at low cost value and discharge at high cost value during peak hours which makes EV to act as a distributed source. This procedure makes the operators of EVs to decrease the charging cost which make a huge difference. The advanced technologies integrating with the grid and EV stations will execute the smart charging and discharging programme [61].

Many papers after investigation the studies shows that there is a problem in energy management for EVs connected with renewable energy sources. In [62], the studies show a new algorithm was implemented to control the EV charging connected with PV in smart design. This method is based on PV energy and demand power and this methodology does not considered about the uncertainties in EV charging. Another researcher in [63], proposed a new methodology for implementing smart buildings with reduced greenhouse gasses emission and thus study not focused on resilience of EV charging demand.

Many researchers' studies showed the different control strategies for EV charging and in [64] the researcher proposed the algorithm for controlling the EV charging Based on storage system and renewable energy. In [65], he implemented the optimal scheduling method for charging stations connected with grid. In [66], the study shows the various methodologies and various pricing plans on EVs charging price. Table 2 Shows the various advanced studies on power management of renewable energy-based charging stations. It is observed that main study is concentrated on PV network with energy management which is integrated to the grid. Moreover, there is less focused on wind turbines (WT) with energy storage systems.

8   Charging Plans

In worldwide they are minimal charging programs that are offered to EVs and few existing charging plans are at Austin (USA) and Saint Paul (France). Only few charging plans or programs are being used by the EVs to charge their vehicles. These

charging plans helps the customers to charge at promising rate which is an advantage to the consumers. Many companies are offering solutions to charge the EVs for employees, retailers and commercial consumers. Best charging plans comes with

Table 2 Energy management studies related to renewable energy-based charging stations

Study	Configuration	Aim	Method	Remarks
[67]	Standalone hybrid renewable systems	Minimizing the use of battery storage and maximizing the use of renewable sources with zero charging rejection	The simulation was developed to find the minimum of a constrained non-linear multi-variable function	Different scenarios are introduced and analyzed
[68]	Standalone hybrid renewable systems	Optimal scheduling for power supply	The energy resources and realistic EV charging data were simulated	The power scheduling was optimized
[69]	PV–WT-Grid	Maximizing use of renewable sources	Experimenting with the maximum power point tracking technique	The infrastructure is capable of providing sufficient energy in response to the load demand
[70]	PV–BESS–Grid	Support of high charging rates and penetration of the energy system into the grid	Simulation and prototype experimental	They demonstrated the effectiveness and benefits of a hybrid grid-connected energy system
[71]	PV–Grid	Discussing critical aspects of renewable resources-based fast charging	Review	Recommendations and useful information related to renewable energy-based DC fast charging
[72]	WT–Diesel Generator–BESS	Minimizing use of the dump load normally associated with diesel operation	Simulation	Optimizes charging/discharging cycles of the storage system and system operation cost
[73]	PV–Grid	Improving self-consumption of PV energy and lower its impacts on the grid	Simulation-based on real-time data acquisition of the demand and generation without forecasting	Proves the proposed strategy's efficiency that can be used in embedded systems for real-time allocation of the EV charging rate

Table 2 (continued)

Study	Configuration	Aim	Method	Remarks
[74]	PV–Grid	Comparing an optimal charge-scheduling strategy with an uncontrolled charging case	An hourly simulation was used by considering statistical data for driving distances, different types of vehicles, parking time, installation cost, tax rebates and incentives	Confirms feasibility of PV-based infrastructure, benefits to EV's drivers and the garage owner and the need for an optimal charging controller
[62]	PV–Grid	Determining optimal schedules of EV according to the predicted PV power and demand	Simulation and prototype	Demonstrates the effectiveness of the proposed smart EV charging method
[75]	PV–Grid	Minimizing operation costs	Simulation and economic analysis	Confirms applicability of the strategy to DC distribution buildings, for energy cost reduction
[76]	PV–Grid	Providing a day-ahead upper limit profile of the charging infrastructure's power consumption	Simulations and sensitivity analysis	Demonstrates feasibility and relevance of the proposed strategy
[77]	PV–WT–Fuel Cells–Grid	Minimizing the total cost	Simulations based on the genetic algorithm method	Presents the optimal number of parking lots under optimal scheduling of PHEVs
[78]	PV–WT– Thermal Storage –BESS–Grid	Minimizing operating costs and CO_2 emissions	Case study	Demonstrates reduction in costs and CO_2 emissions
[79]	PV–WT– Fuel Cells –Grid	Integrating scheduling and management of intermittent renewable generation and EVs in a microgrid	Case study	Satisfies technical and financial objectives of infrastructure and economic and security issues of the microgrid
[80]	PV–BESS–Grid	Reducing operation cost	Simulation based on two algorithms and a case study	The case study confirms effectiveness of the proposed algorithms in reducing the cost

renewable energy sources which encourages the drivers of EV to charge their vehicles. RCS with effective pricing plans, time of charge are the key factors which influence the consumers to charge the vehicles. Many other plans have been introduced among them time of use (TOU) rates can be useful and attracted by the commercial and residential consumers to charge the EVs with renewable energy sources which leads to effective cost savings during off-peak time. Table 3 Shows the Comparison of different existing charging plans.

Table 3 Renewable's charging programs

Approach	Advantages	Programs/plans	Example of costing	Utility
Renewables' network charging	– Enables customers to charge with renewable sources – Encourages drivers to charge at beneficial times	– Pay per use – Monthly flat fee	2 USD per h 4.17 USD per month	Austin energy
Offers for time-shifting and renewables' access	– Encourages charging at more suitable times for the grid by considering the availability of renewables and avoiding peak hours	– Charging with renewable energy – Merge TOU rates with renewable's pricing program	No extra cost for wind energy or 0.02 USD per kWh	Great river energy and potomac electric power Co
Pair on-site renewables' charging with EV charging	– Free management and control charging	– Beneficial charging rate – Free employee charging	Cost varied	San Diego's solar and Google LLC
Smart charging	– Allows utilities to control charging remotely to meet grid needs	– Managed charging program	Cost varied	Pacific gas and electric/BMW
Matching rate with surplus renewable energy	– Shifts charging loads to times when there is excess renewable energy generation on the grid	– Time of use (TOU) rates	Varies from 0.9 to 1.5 USD per kWh	Xcel energy

9 Challenges of Renewable Energy-Based Charging Station

There are many challenging issues while implementing the charging stations using renewable energy's and many problems while installing issues like selection of land, pricing plans, stability and power quality issues. Few research papers studies explain major issues while designing and implementing the RCSs.

9.1 Power Quality Issues

Power quality problem looks like one of the serious issues which influence the reliability of RCS. It is observed that generation of renewable energy is the main reason for creating the power quality problems. In [81], the study shows the change in wind nature, variation of solar power generates discontinuous power which is cannot controlled by the operator. Therefore, while developing the RCS the major challenging issues is power quality problem.

9.2 Stability

It is necessary to recover the power system network after blackouts which can be done by controlling the voltage and frequency. However, the stability issues occurred mainly because of extra power from renewable energy and storage of battery can also affect the RCS [82]. By proper controlling of system stability, we can enhance the performance of the power system.

9.3 Charging Plans

As number of EVs are increasing rapidly the renewable charging stations also increases. Thus, the initial cost will be high and structural pricing will me more. To achieve profits in charging stations we should run the stations long life. Mostly, beneficial programs offered by the charging stations are very limited because of availability of residential charging stations [83]. There is necessary to increase the charging stations at workplaces, public areas like shopping malls, theatres, parks so that it can be profitable.

9.4 Locality

For installation of moderate and wide-range wind farms in urban areas is practically not possible at everywhere. However, for installation of WECS need large area which is difficult in many areas and especially in cities the tall buildings are primary drawback for wind speed. Although, we can install at rural areas but EVs are majorly in cities so installing of charging stations should be in urban areas only. Therefore, optimal planning and scheduling of charging stations are the main factors that are considered while designing RCSs [36].

10 Conclusions

In future EVs will be the mode of transportation with integrated renewable energy sources. The EVs charging with RCSs will reduce the fossil fuels and have zero emission of carbon into the environment. Still, there are some drawbacks while installing charging stations integrated with renewable sources. The challenging problems while installing the wind farms are location and environmental aspects and WT are not suitable at urban areas due to the requirement of huge land and noise. Similarly, the issues while implementing the solar systems are discontinuous power because they produce power in day time only.

Solar and wind power are treated as the best sources for EV charging stations. Integration of EVs, V2G technology, and energy storage can build efficient RCS with the grid. The several challenging issues while implementing the RCS are variation in renewable power output, unpredictable demands, difficulty in selection of location, grid peak time, and V2G concept. The major concern in RCS is not considering real-time data for enhancing the control approach and sizing. In energy management and control, by bridging the gap between RCS and long-range EVs tends to the concept of smart charging and discharging approach. The way the charging plans are utilized shows that very few numbers of consumers are preferring renewable sources and adopting residential charging only. Effective price plans have to be introduced for large-capacity vehicles at public charging stations.

References

1. Das HS, Rahman MM, Li S, Tan CW (2020) Electric vehicles standards, charging infrastructure, and impact on grid integration: a technological review. Renew Sustain Energy Rev 120. https://doi.org/10.1016/j.rser.2019.109618
2. Canals Casals L, Martinez-Laserna E, Amante García B, Nieto N (2016) Sustainability analysis of the electric vehicle use in Europe for CO_2 emissions reduction. J Clean Prod 127:425–437. https://doi.org/10.1016/j.jclepro.2016.03.120
3. Åhman M (2001) Primary energy efficiency of alternative powertrains in vehicles. Energy 26(11):973–989. https://doi.org/10.1016/S0360-5442(01)00049-4

4. Kempton W (2016) Electric vehicles: driving range. Nat Energy 1(9). https://doi.org/10.1038/nenergy.2016.131

5. Von Jouanne A, Husain I, Wallace A, Yokochi A (2003) Innovative hydrogen/fuel cell electric vehicle infrastructure based on renewable energy sources. In: Conference record—IAS annual meeting (IEEE Industrial Applications Society, Naias 2000 vol 2. pp 716–722 . https://doi.org/10.1109/ias.2003.1257598

6. Harakawa T, Tujimoto T (2001) Efficient solar power equipment for electric vehicles: Improvement of energy conversion efficiency for charging electric vehicles. In: Proceedings IEEE international vehicle electronics conference 2001, IVEC 2001, pp 11–16. https://doi.org/10.1109/IVEC.2001.961718

7. Pieltain Fernández L, Gómez San Román T, Cossent R, Mateo Domingo C, Frías P (2011) Assessment of the impact of plug-in electric vehicles on distribution networks. IEEE Trans Power Syst 26(1):206–213. https://doi.org/10.1109/TPWRS.2010.2049133

8. Huang Y, Ye JJ, Du X, Niu LY (2014) Simulation study of system operating efficiency of EV charging stations with different power supply topologies. Appl Mech Mater 494–495:1500–1508. https://doi.org/10.4028/www.scientific.net/AMM.494-495.1500

9. Hammerstrom DJ (2007) AC versus DC distribution systems-did we get it right?. In: 2007 IEEE power engineering society generation meeting PES, pp 1–5. https://doi.org/10.1109/PES.2007.386130

10. Xu L, Chen D (2011) Control and operation of a DC microgrid with variable generation and energy storage. IEEE Trans Power Deliv 26(4):2513–2522. https://doi.org/10.1109/TPWRD.2011.2158456

11. Shukla A, Verma K, Kumar R (2019) Impact of EV fast charging station on distribution system embedded with wind generation. J Eng 2019(18):4692–4697. https://doi.org/10.1049/joe.2018.9322

12. Hardman S et al (2018) A review of consumer preferences of and interactions with electric vehicle charging infrastructure. Transp Res Part D Transp Environ 62:508–523. https://doi.org/10.1016/j.trd.2018.04.002

13. Delvasto P (2017) Comparison of different battery types for electric vehicles comparison of different battery types for electric vehicles. https://doi.org/10.1088/1757-899X/252/1/012058

14. Prasad BRV, Deepthi T, Satyavathi N, Satish Varma V, Hema Kumar R (2021) Solar charging station for electric vehicles. Int J Adv Res Sci Commun Technol 7(2):316–325. https://doi.org/10.48175/IJARSCT-1752

15. Mohammad A, Zamora R, Lie TT (2020) Integration of electric vehicles in the distribution network: a review of PV based electric vehicle modelling. Energies 13(17). https://doi.org/10.3390/en13174541

16. Khan S, Ahmad A, Ahmad F, Shafaati Shemami M, Saad Alam M, Khateeb S (2018) A comprehensive review on solar powered electric vehicle charging system. Smart Sci 6(1):54–79. https://doi.org/10.1080/23080477.2017.1419054

17. Dallinger D, Gerda S, Wietschel M (2013) Integration of intermittent renewable power supply using grid-connected vehicles—a 2030 case study for California and Germany. Appl Energy 104:666–682. https://doi.org/10.1016/j.apenergy.2012.10.065

18. Guo X, Kang L, Huang Z, Yao Y, Yang H (2015) Research on a novel power inductor-based bidirectional lossless equalization circuit for series-connected battery packs. Energies 8(6):5555–5576. https://doi.org/10.3390/en8065555

19. Wang X, Li S, Wang L, Sun Y, Wang Z (2020) Degradation and dependence analysis of a lithium-ion battery pack in the unbalanced State

20. Alkawsi G, Ali N, Baashar Y (2021) The moderating role of personal innovativeness and users experience in accepting the smart meter technology. Appl Sci 11(8). https://doi.org/10.3390/app11083297

21. Ehsan A, Yang Q (2020) Active distribution system reinforcement planning with EV charging stations-part II: Numerical results. IEEE Trans Sustain Energy 11(2):979–987. https://doi.org/10.1109/TSTE.2019.2915383

22. Bao Y, Luo Y, Zhang W, Huang M, Wang LY, Jiang J (2018) A bi-level optimization approach to charging load regulation of electric vehicle fast charging stations based on a battery energy storage system. Energies 11(1). https://doi.org/10.3390/en11010229

23. Prasad BRV, Prasanthi C, Jyothika Santhoshini G, Kranti Kumar KJSV, Yernaidu K (2020) Smart electrical vehicle. i-Manager's J Digit Signal Process 8(1):7. https://doi.org/10.26634/jdp.8.1.17347

24. Zou C, Manzie C, Anwar S (2014) Control-oriented modeling of a lithium-ion battery for fast charging, 19(3), IFAC

25. Ingole JN (2012) Pic based solar charging. 4(02):384–390

26. Ibrahim H, Dimitrova M, Dutil Y, Rousse D, Ilinca A (2012) Wind-diesel hybrid system : energy storage system selection method. In: 12th international conference energy storage, pp 1–10

27. Loxbo E, Johansson S (2016) Charging electric cars from solar energy

28. Overview A (2010) A state of the art of DC microgrids for electric vehicle charging electrical department, vol 3. no. Dc

29. Goli P, Shireen W (2014) PV integrated smart charging of PHEVs based on DC Link voltage sensing. IEEE Trans Smart Grid 5(3):1421–1428. https://doi.org/10.1109/TSG.2013.2286745

30. Short W, Denholm P (2006) A preliminary assessment of plug-in hybrid electric vehicles on wind energy markets a preliminary assessment of plug-in hybrid electric vehicles on wind energy markets. Contract, April

31. Noman F, Alkahtani AA, Agelidis V, Tiong KS, Alkawsi G, Ekanayake J (2020) Wind-energy-powered electric vehicle charging stations: resource availability data analysis. Appl Sci 10(16). https://doi.org/10.3390/app10165654

32. Alkawsi G, Baashar Y, Dallatu Abbas Y, Alkahtani AA, Tiong SK (2021) Review of renewable energy-based charging infrastructure for electric vehicles. Appl Sci 11(9). https://doi.org/10.3390/app11093847

33. Nicholas M, Tal G, Ji W (2021) Lessons from in-use fast charging data: why are drivers staying close to home?. Inst Transp Stud, January 2017

34. Peterson SB, Michalek JJ (2013) Cost-effectiveness of plug-in hybrid electric vehicle battery capacity and charging infrastructure investment for reducing US gasoline consumption. Energy Policy 52:429–438. https://doi.org/10.1016/j.enpol.2012.09.059

35. Franke T, Krems JF (2013) Understanding charging behaviour of electric vehicle users. Transp Res Part F Traffic Psychol Behav 21:75–89. https://doi.org/10.1016/j.trf.2013.09.002

36. Lopez-Behar D, Tran M, Froese T, Mayaud JR, Herrera OE, Merida W (2019) Charging infrastructure for electric vehicles in multi-unit residential buildings: mapping feedbacks and policy recommendations. Energy Policy 126:444–451. https://doi.org/10.1016/j.enpol.2018.10.030

37. Lunz B, Sauer DU (2015) In: Electric road vehicle battery charging systems and infrastructure. Elsevier Ltd.

38. Zheng Y, Dong ZY, Xu Y, Meng K, Zhao JH, Qiu J (2014) Electric vehicle battery charging/swap stations in distribution systems: comparison study and optimal planning. IEEE Trans Power Syst 29(1):221–229. https://doi.org/10.1109/TPWRS.2013.2278852

39. Shareef H, Islam MM, Mohamed A (2016) A review of the stage-of-the-art charging technologies, placement methodologies, and impacts of electric vehicles. Renew Sustain Energy Rev 64:403–420. https://doi.org/10.1016/j.rser.2016.06.033

40. Quddus MA, Kabli M, Marufuzzaman M (2019) Modeling electric vehicle charging station expansion with an integration of renewable energy and Vehicle-to-Grid sources. Transp Res Part E Logist Transp Rev 128:251–279. https://doi.org/10.1016/j.tre.2019.06.006

41. Zhang H, Moura SJ, Hu Z, Qi W, Song Y (2018) Joint PEV charging network and distributed PV generation planning based on accelerated generalized benders decomposition. IEEE Trans Transp Electrif 4(3):789–803. https://doi.org/10.1109/TTE.2018.2847244

42. Haddadian G, Khalili N, Khodayar M, Shahidehpour M (2016) Optimal coordination of variable renewable resources and electric vehicles as distributed storage for energy sustainability. Sustain Energy Grids Netw 6:14–24. https://doi.org/10.1016/j.segan.2015.12.001

43. Liu C, Wang J, Botterud A, Zhou Y, Vyas A (2012) Assessment of impacts of PHEV charging patterns on wind-thermal scheduling by stochastic unit commitment. IEEE Trans Smart Grid 3(2):675–683. https://doi.org/10.1109/TSG.2012.2187687

44. Jin C, Sheng X, Ghosh P (2014) Optimized electric vehicle charging with intermittent renewable energy sources. IEEE J Sel Top Signal Process 8(6):1063–1072. https://doi.org/10.1109/JSTSP.2014.2336624

45. Liu H, Zeng P, Guo J, Wu H, Ge S (2015) An optimization strategy of controlled electric vehicle charging considering demand side response and regional wind and photovoltaic. J Mod Power Syst Clean Energy 3(2):232–239. https://doi.org/10.1007/s40565-015-0117-z

46. Pan F, Bent R, Berscheid A, Izraelevitz D (2010) Locating PHEV exchange stations in V2G. pp 173–178. https://doi.org/10.1109/smartgrid.2010.5622037

47. Ortega-Vazquez MA, Bouffard F, Silva V (2013) Electric vehicle aggregator/system operator coordination for charging scheduling and services procurement. IEEE Trans Power Syst 28(2):1806–1815. https://doi.org/10.1109/TPWRS.2012.2221750

48. Ekren O, Hakan Canbaz C, Güvel ÇB (2021) Sizing of a solar-wind hybrid electric vehicle charging station by using HOMER software. J Clean Prod 279:123615. https://doi.org/10.1016/j.jclepro.2020.123615

49. Moradi MH, Abedini M, Tousi SMR, Hosseinian SM (2015) Optimal siting and sizing of renewable energy sources and charging stations simultaneously based on differential evolution algorithm. Int J Electr Power Energy Syst 73:1015–1024. https://doi.org/10.1016/j.ijepes.2015.06.029

50. Mozafar MR, Moradi MH, Amini MH (2017) A simultaneous approach for optimal allocation of renewable energy sources and electric vehicle charging stations in smart grids based on improved GA-PSO algorithm. Sustain. Cities Soc 32:627–637. https://doi.org/10.1016/j.scs.2017.05.007

51. Hafez O, Bhattacharya K (2017) Optimal design of electric vehicle charging stations considering various energy resources. Renew Energy 107:576–589. https://doi.org/10.1016/j.renene.2017.01.066

52. Grande LSA, Yahyaoui I, Gómez SA (2018) Energetic, economic and environmental viability of off-grid PV-BESS for charging electric vehicles: case study of Spain. Sustain Cities Soc 37:519–529. https://doi.org/10.1016/j.scs.2017.12.009

53. Hussain A, Bui VH, Kim HM (2020) Optimal sizing of battery energy storage system in a fast EV charging station considering power outages. IEEE Trans Transp Electrif 6(2):453–463. https://doi.org/10.1109/TTE.2020.2980744

54. Aghapour R, Sepasian MS, Arasteh H, Vahidinasab V, Catalão JPS (2020) Probabilistic planning of electric vehicles charging stations in an integrated electricity-transport system. Electr Power Syst Res 189:106698. https://doi.org/10.1016/j.epsr.2020.106698

55. Bai S, Du Y, Lukic S (2010) Optimum design of an EV/PHEV charging station with DC bus and storage system. In: 2010 IEEE energy conversation congress exposition. ECCE 2010−proceedings, pp 1178–1184. https://doi.org/10.1109/ECCE.2010.5617834

56. Abronzini U et al (2016) Optimal energy control for smart charging infrastructures with ESS and REG. In: 2016 international conference electrical systems aircraft, railway ship propulsion and road vehicles and international transportation electrification conference ESARS-ITEC 2016, pp 1–6. https://doi.org/10.1109/ESARS-ITEC.2016.7841427

57. Green RC, Wang L, Alam M (2011) The impact of plug-in hybrid electric vehicles on distribution networks: a review and outlook. Renew Sustain Energy Rev 15(1):544–553. https://doi.org/10.1016/j.rser.2010.08.015

58. Amini MH, Kargarian A, Karabasoglu O (2016) ARIMA-based decoupled time series forecasting of electric vehicle charging demand for stochastic power system operation. Electr Power Syst Res 140:378–390. https://doi.org/10.1016/j.epsr.2016.06.003

59. Bai C, Gao W, Li J, Liao H (2012) Analyzing the impact of electric vehicles on distribution networks. In: 2012 IEEE PES innovation smart grid technology ISGT 2012. https://doi.org/10.1109/ISGT.2012.6175645

60. Song J, Suo L, Han M, Wang Y (2019) A coordinated charging/discharging strategy for electric vehicles based on price guidance mechanism. In: IOP conference series material science engineering, vol 677(5). https://doi.org/10.1088/1757-899X/677/5/052103

61. Xu Z, Su W, Hu Z, Song Y, Zhang H (2016) A hierarchical framework for coordinated charging of plug-in electric vehicles in China. IEEE Trans Smart Grid 7(1):428–438. https://doi.org/10.1109/TSG.2014.2387436

62. Wi YM, Lee JU, Joo SK (2013) Electric vehicle charging method for smart homes/buildings with a photovoltaic system. IEEE Trans Consum Electron 59(2):323–328. https://doi.org/10.1109/TCE.2013.6531113

63. Shimomachi K, Noritake M, Hara R, Hoshi H, Kita H, Hirose K (2014) Development of energy management system for DC microgrid for office building. In: Power systems computing conference

64. Liao YT, Lu CN (2015) Dispatch of EV charging station energy resources for sustainable mobility. IEEE Trans Transp Electrif 1(1):86–93. https://doi.org/10.1109/TTE.2015.2430287

65. Carpinelli G, Mottola F, Proto D (2014) Optimal scheduling of a microgrid with demand response resources. IET Gener Transm Distrib 8(12):1891–1899. https://doi.org/10.1049/iet-gtd.2013.0758

66. Kumar KN, Sivaneasan B, So PL (2015) Impact of priority criteria on electric vehicle charge scheduling. IEEE Trans Transp Electrif 1(3):200–210. https://doi.org/10.1109/TTE.2015.2465293

67. Bokopane L, Kusakana K, Vermaak HJ (2015) Optimal energy management of an isolated electric Tuk-Tuk charging station powered by hybrid renewable systems. In: Proceedings 23rd conference domestics use energy, DUE 2015, May, pp 193–201. https://doi.org/10.1109/DUE.2015.7102981

68. Wang H, Balasubramani A, Ye Z (2018) Optimal planning of renewable generations for electric vehicle charging station. In: 2018 International conference computing network communications ICNC 2018, pp 63–67. https://doi.org/10.1109/ICCNC.2018.8390352

69. Fathabadi H (2017) Novel wind powered electric vehicle charging station with vehicle-to-grid (V2G) connection capability. Energy Convers Manag 136:229–239. https://doi.org/10.1016/j.enconman.2016.12.045

70. Badawy MO, Sozer Y (2015) Power flow management of a grid tied PV-battery powered fast electric vehicle charging station. In: 2015 IEEE energy conversation congress exposition, ECCE 2015, March, pp 4959–4966. https://doi.org/10.1109/ECCE.2015.7310359

71. Ashique RH, Salam Z, Bin Abdul Aziz MJ, Bhatti AR (2017) Integrated photovoltaic-grid dc fast charging system for electric vehicle: a review of the architecture and control. Renew Sustain Energy Rev 69:1243–1257. https://doi.org/10.1016/j.rser.2016.11.245

72. Ross M, Hidalgo R, Abbey C, Joós G (2011) Energy storage system scheduling for an isolated microgrid. IET Renew Power Gener 5(2):117–123. https://doi.org/10.1049/iet-rpg.2009.0204

73. Liu N et al (2015) A heuristic operation strategy for commercial building microgrids containing EVs and PV system. IEEE Trans Ind Electron 62(4):2560–2570. https://doi.org/10.1109/TIE.2014.2364553

74. Tulpule PJ, Marano V, Yurkovich S, Rizzoni G (2013) Economic and environmental impacts of a PV powered workplace parking garage charging station. Appl Energy 108:323–332. https://doi.org/10.1016/j.apenergy.2013.02.068

75. Byeon G, Yoon T, Oh S, Jang G (2013) Energy management strategy of the DC distribution system in buildings using the EV service model. IEEE Trans Power Electron 28(4):1544–1554. https://doi.org/10.1109/TPEL.2012.2210911

76. Pflaum P, Alamir M, Lamoudi MY (2018) Probabilistic energy management strategy for EV charging stations using randomized algorithms. IEEE Trans Control Syst Technol 26(3):1099–1106. https://doi.org/10.1109/TCST.2017.2695160

77. Chen C, Duan S (2014) Optimal integration of plug-in hybrid electric vehicles in microgrids. IEEE Trans Ind Inform 10(3):1917–1926. https://doi.org/10.1109/TII.2014.2322822

78. Bracco S, Delfino F, Pampararo F, Robba M, Rossi M (2015) A dynamic optimization-based architecture for polygeneration microgrids with tri-generation, renewables, storage systems and electrical vehicles. Energy Convers Manag 96:511–520. https://doi.org/10.1016/j.enconman.2015.03.013

79. Honarmand M, Zakariazadeh A, Jadid S (2014) Integrated scheduling of renewable generation and electric vehicles parking lot in a smart microgrid. Energy Convers Manag 86:745–755. https://doi.org/10.1016/j.enconman.2014.06.044

80. Wu D, Zeng H, Lu C, Boulet B (2017) Two-stage energy management for office buildings with workplace EV charging and renewable energy. IEEE Trans Transp Electrif 3(1):225–237. https://doi.org/10.1109/TTE.2017.2659626

81. Liang X (2017) Emerging power quality challenges due to integration of renewable energy sources. IEEE Trans Ind Appl 53(2):855–866. https://doi.org/10.1109/TIA.2016.2626253

82. Nijhuis M, Gibescu M, Cobben JFG (2016) Application of resilience enhancing smart grid technologies to obtain differentiated reliability. In: EEEIC 2016—international conference environmental electrical engineering. https://doi.org/10.1109/EEEIC.2016.7555598

83. Otsuki T (2017) Costs and benefits of large-scale deployment of wind turbines and solar PV in Mongolia for international power exports. Renew Energy 108:321–335. https://doi.org/10.1016/j.renene.2017.02.018

Energy Efficiency in Charging Stations for Electric Vehicles with Minimum Affection to the Electrical Distribution Network Through Resource Allocation

Maria Carolina Ramos Chávez, Javier Martínez-Gómez, Jhonatan Meza, Deepa Jose, and S. Anthoniraj

Abstract The primary objective of the Response to Demand (DR) is to manage the required demand, by allocating existing resources in a way in which to allow it to be used without the need to increase new generation capacity. The DR focused on the grid load due to the insertion of Electric Vehicles (EVs), and it promotes a great emphasis on the impact they cause on the electrical systems. Therefore, this work develops an optimal response to demand with respect to the impact generated by EVs, in addition to the different types of loads toward the electrical network with various scenarios. A heuristic model is presented that is based on the Hungarian algorithm in MatLab, that is, in this specific work it was intended to achieve the adequate allocation of energy resources for the charging of EVs. Posing several load scenarios that focus on DR among which the types of loads that will be used have been modeled and determined: (a) slow, (b) fast, and (c) ultra-fast that allowed us to evaluate the different behaviors. It also describes the different types of batteries and which EVs are using them, as well as having a response demand taking advantage of the penetration of conventional and unconventional energies and in turn also with the influence of solar radiation in winter and summer cases to the EV load will be those coming from renewable energies.

Keywords Resource allocation · Hungarian algorithm · Demand response · Electric vehicles · Matching · First section

M. C. R. Chávez · J. Martínez-Gómez
Universidad Internacional SEK, Quito 170134, Ecuador
e-mail: mcramos.mee@uisek.edu.ec

J. Meza
Instituto Superior 17 de Julio, Ibarra, Ecuador

D. Jose (✉)
KCG College of Technology, Karapakkam, Chennai 600097, India
e-mail: deepajose11@gmail.com

S. Anthoniraj
Department of CSE, MVJ College of Engineering, Whitefield, Bangalore 560067, India

1 Introduction

Renewable energy as an alternative appears in recent decades instead of conventional power generation plants. Its greatest benefit is supported by the easy installation in places close to the load and also by not having too many losses or voltage variations and investment costs.

In many countries of the continent and the world, like Ecuador some years ago, the main sources of electricity generation were through the use of fossil fuels. Currently and with an electrification plan that aims to increase the production of electrical energy by using renewable energy to 80% by 2025. Currently, April 2020, 60.75% of the nominal power in generation in the country were from renewable sources, on the other hand, 39.25% were through fossil fuel generation plants (Diesel, bunker, Fuel oil, etc.).

Adding to this, the transmission and distribution losses in the country that are around 12.20%, however with a demand for electricity that increases exponentially and in turn the availability of fossil fuel is decreasing, the gap between the generation resource and demand is growing at an alarming rate.

The model to solve the energy efficiency problem for EVs is a NPL optimization problem (non-linear programming), due to the number of variables involved and it is also due to the proposed restrictions. Therefore, the proposed techniques have been evaluated in scenarios that address different types of electrical devices with different energy requirements, on different scales the performance of the technique has been compared with different baselines [1–4]. On the other hand, inserting EVs electric vehicles provides us with a more feasible option for reducing fossil fuels and also reducing the high impact they produce on the environment. In such a way that car dealers and producers have inserted proposals and technological innovations focused on electric vehicles that have been increasing in a very short time, these innovations have resulted in the mitigation of CO_2 emissions into the environment. However, by inserting electricity generation from renewable energies and that vary according to time in the distribution systems, they cause a greater need for reliability and stability in the network and generate a balance by optimizing for electric vehicles included in the network [4, 5] so much so that it is possible to reduce air pollution.

For charging EVs, their charging stations will be those that contain the stored energy in this case from renewable energies, as a clear example one of them is the energy that comes from the sun or also called Photovoltaic, this energy is injected the distribution system just at the moment it is generated, which provides us with clean, optimal energy and without so many losses, which avoids affecting the grid. The immense amount of solar energy is highly effective and helps because it reaches the earth is approximately 101 PWh per hour, which in approximate figures is the same amount as the world demand for energy, that is, the Photovoltaic (PV) renewable energy is gradually improving as part of the solution.

Different technological innovations among which we have battery electric vehicles, hybrid electric vehicles, and hydrogen fuel cell vehicles [6–8], the high possibility and risk of battery degradation, that is, the useful life of the battery is shortens more and more depending on the load and discharge ratio that is carried out.

Energy efficiency applied to optimal resource consumption in charging stations denotes the way in which the change in electricity supply is carried out and at the same time how the consumption of electricity varies by consumers before the respective distribution companies and with the expected price patterns established for a time in which incentives are given, in order to reduce consumption and minimize peaks in times of high demand for electricity consumption and avoid inconveniences or danger of system failures [9]. The primary objective of energy efficiency is to manage the required demand, by allocating existing resources in a way that allows it to be used without the need to increase new generation capacity. The issue of energy efficiency offers us a very positive commercial interest, but it does not yet have a concrete maturity in other areas, as is the case of residential [10].

In this document, the energy resource allocation problem is considered based on a concept of energy efficiency in the optimization processes using Matlab's Munkres algorithm that solves allocation problems within a period of time that in this case has been analyzed hourly. One time for a day. In accordance with the aforementioned, the proposed heuristic model will allow modeling an optimal system of response to demand that minimizes the impact of charging electric vehicles in a distribution system, in this way a strategy is proposed that manages to adequately achieve the allocation of resources energy referred to the literature on electric vehicles. Some indices are introduced that will allow us to estimate the effectiveness of the proposed model.

The model to solve the DR problem for EVs is a NPL (nonlinear programming) optimization problem, due to the number of variables involved and it is also due to the proposed restrictions. Therefore, the proposed techniques have been evaluated in scenarios that address different types of electrical devices with different energy requirements, on different scales the performance of the technique has been compared with different baselines [11]. On the other hand, inserting EVs electric vehicles provides us with a more feasible option for reducing fossil fuels and also reducing the high impact they produce on the environment. In such a way that car dealers and producers have inserted proposals and technological innovations focused on electric vehicles that have been increasing in a very short time, these innovations have resulted in the mitigation of CO2 emissions into the environment [12]. However, by inserting electricity generation from renewable energies and that vary according to time in the distribution systems, they cause a greater need for reliability and stability in the network and generate a balance through optimization for electric vehicles included in the network [4], so much so that it is possible to reduce pollution to the atmosphere. Different technological innovations among which we have: battery electric vehicles, hybrid electric vehicles and hydrogen fuel cell vehicles [13], the high possibility and risk of battery degradation, that is, the battery life becomes shorter and shorter depending on the charge and discharge ratio that is performed.

Renewable energy as an alternative appears in recent decades instead of conventional power generation plants. Its greatest benefit is supported by the easy installation in places close to the load and also by not having too many losses or voltage variations and investment costs. Being inserted into the electrical distribution network leads to too many challenges since it has a randomness of generation. With which storage systems such as batteries with high capacity arise, which will help to contain the network?

The immense amount of solar energy is highly effective and helps because it reaches the earth is approximately 101 PWh per hour [10], which in approximate figure is the same amount as the world demand for energy, that is, that the Photovoltaic (PV) renewable energy is gradually improving as part of the solution [11]. To charge EVs, their charging stations will be those that contain the stored energy in this case from renewable energies [9]. As a clear example, one of them is the energy that comes from the sun or also called Photovoltaic, this energy is injected into the distribution system just at the moment it is generated, which provides us with clean, optimal energy, and without so many losses, which avoids impact on the network. The present work shows the study of the impact of the load assumed by the network when inserting EVs, the Hungarian Algorithm was used for the allocation of energy resources by having a charging station, in which 4 vehicles enter randomly during 24 h, for which will be taken into account that the charge will be different, so it has been presented that there are 4 types of charges: slow charge, fast charge, and two ultra-fast charges (Fig. 1).
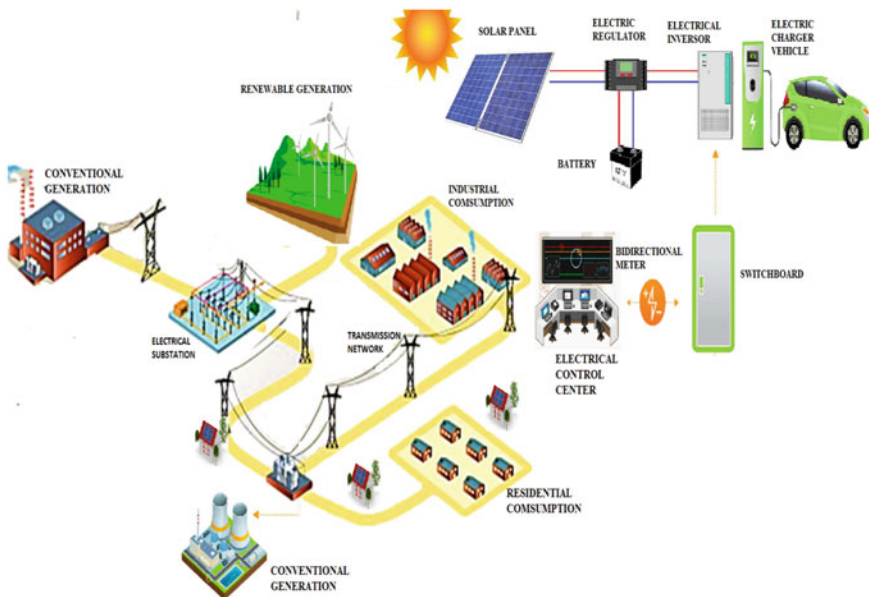
Fig. 1 Resource allocation

2 Theoretical Framework

2.1 Electric Vehicles EVs

Given that concerns about oil depletion and security of supply remain as serious as ever and faced with the consequences of climate change due to greenhouse gas emissions, it is increasingly being considered that alternatives to traditional technologies are being sought road transport. Electric vehicles EVs are considered a promising technology, which could lead to the decarbonisation of the light vehicle fleet and independence from oil. Battery electric vehicles, also called EVs, and more frequently called EVs, are fully electric vehicles with rechargeable batteries and no gasoline engine. Battery electric vehicles store electricity on board with high-capacity battery packs. Battery power is used to power the electric motor and all electronic components on board. BEVs do not emit harmful emissions or hazards caused by traditional gasoline-powered vehicles. EVs are charged with electricity from an external source. Electric vehicle (EV) chargers are classified according to the speed with which they recharge an electric vehicle battery.

Among the components that make up an electric vehicle, we can observe:

- **Battery**

Drives the electric motor. Its capacity is defined in Ah. The battery design includes complex calculations that determine various parameters of the battery.

- **Power convertor**

The electrical energy stored in the battery is fixed DC which must be converted to variable DC or variable AC, which depends on the type of electric motor used to drive the wheels.

- **Electric Motor**

In the previous stage, induction motors of the DC series were used. Now the scope has shifted to special electrical machines (Fig. 2).
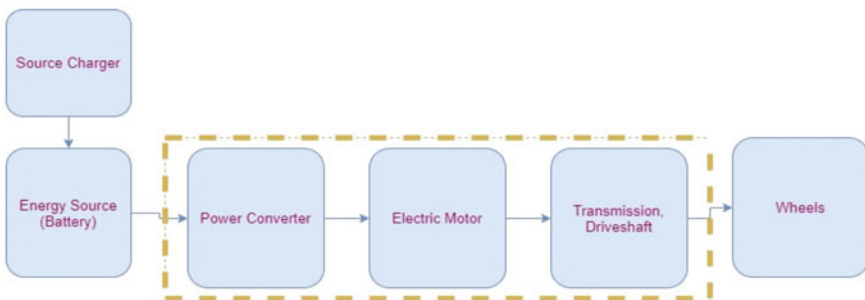
Fig. 2 Block Diagram with the structure of EVs

The use of electric vehicles is one of the most plausible solutions since they are very friendly to the environment, they do not emit harmful gases, and it is a means to protect the environment, as well as a way of using electrical energy that comes from clean sources and naturally [eleven]. It can be said that EVs have up to 80% greater efficiency compared to traditional vehicles and, being more ergonomic, they are less complex due to their electric motor and rechargeable battery (Table 1).

The benefits that EVs transmit to us have increased their production markets such as: Renault, Kia, Nissan, and General Motors which have gained popularity among consumers who are mostly industrialized countries that have proposed as a method of reducing pollution in their countries (Fig. 3).

Table 1 Electric energy consumption in EVs according to the brand of manufacture [15]

Brand	kWh
Audi E-tron	95
BMW i3	22
BYD E6	54
Chevrolet volt	16
Citroen C-Zero	14,5
Ford focus	23
Hyundai Ioniq	28
KIA soul	27
Mercedes ED	36
Mercedes SLS AMG	60
Mitsubishi i-MiEV	16
Nissan leaf	24
Opel Ampera	16
Opel Ampera-e	60
Peugeot iOn	14,5
Peugeot partner electric	22,5
Renault fluence ZE	22
Renault Kangoo ZE	24
Renault Twizy	6,1
Renault Zoe	22
VW e-Golf	26,5
VW e-UP	18,7
Tesla model III	90
Tesla model S	85
Tesla model X	75
Tesla roadster	53
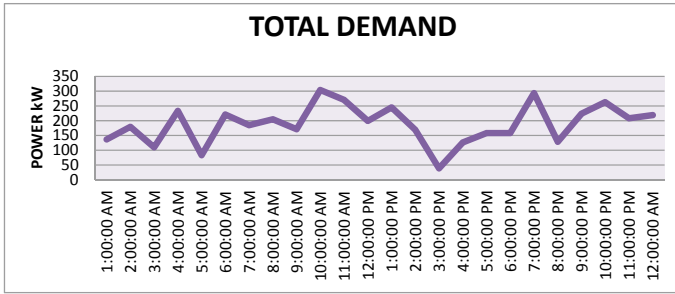
Fig. 3 Total demand versus power KW

2.2 Electric Vehicle Batteries

The use of energy storage becomes mandatory when such microgrids are used to supply quality power to the loads. Microgrids have two modes of operation, namely grid-connected and island modes. During island mode, the primary responsibility for storage is energy balancing. During grid-connected mode, the objective is to avoid the propagation of intermittency from the renewable source and load fluctuations to the grid [11]. These equipments or rather devices that are used for the storage of energy produced in a chemical way to later be converted into electrical energy at the time of use [14]. There are different and diverse types of materials from which batteries are built, but the most widely used are lithium-ion batteries. In the materials that make up the battery we have a small electric cell which is made up of an electrochemical element made up of an electrolyte and two electrodes inside [14]. This electrolyte is loaded with an immense amount of ions and substances that the electrodes contain, these are semiconductors and allow the battery to store energy [15].

Type of load

We have three categories for the types of charge, which are divided according to their characteristics (type of power, time and there are several other electrical parameters) which determine the speed of (100%) battery charge. Table 2 shows the charging of a 24kWh capacity battery.

Table 2 Characteristics of EV battery charging types [15]

Type of load	Type of feeding	# phases	V	I	t_load (24 kWh)
Slow	C. Alternate	One	127 V	16–30 A	6-8 h
		Two	230 V	16–30 A	6-8 h
Fast		3	400 V	64 A	3–4 h
Ultra fast	C. Continuous	1 + , 1−	400 V	400 A	15–30 min

We have very important characteristics for lithium ion batteries which are positioned as the main ones in the market, among the best known are their weight and voltage level. The condition of the reduced weight is due to having Lithium and Carbon electrodes. Since Lithium, being a very reactive metal, has an immense potential energy that is stored in its atoms, which are contained in extremely small spaces, which leads to a battery with a smaller volume and a greater amount of charge. How much with a very high voltage level 4 V per cell (4 V/cell) and also has a number of charge/discharge cycles which does not affect its performance [14, 15].

2.3 Photovoltaic Energy

Solar energy is one of the fastest developing renewable energies in the world. The global photovoltaic solar power market has been outpacing future market projections and the giant untapped markets are just now waking up [16], the great inclusion of solar power has been in great magnitude due to the clean way and its constant source of production of Energy. This type of electrical energy production fully depends on the hours of sunshine that the solar panels capture, radiation is another very important factor, which is why different radiation values are obtained that for our study we have considered for winter and summer as shown in Fig. 4.
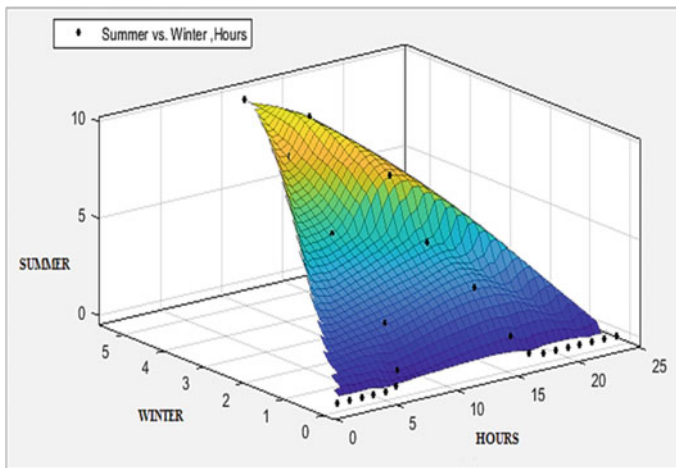
Fig. 4 Solar panel radiation curves

3 Methodology and Problem Formulation

A heuristic model is proposed that is based on the Hungarian algorithm, that is, an efficient use of energy resources was achieved for charging EVs. It also explains the different batteries and what types of EVs will use them, at the same time achieving optimal use of energy resources with the use of conventional and non-conventional energies, by taking advantage of solar radiation, two study scenarios are proposed: winter and summer. Therefore, the present work implements an energy efficiency system in the charging stations, which develops an optimal response to the demand regarding the impact generated by EVs, in addition to the different types of charge towards the electricity grid with various scenarios. A heuristic model is proposed that is based on the Hungarian algorithm, that is, an efficient use of energy resources was achieved for charging EVs. At the same time achieving optimal use of energy resources with the use of conventional and non-conventional energies, by taking advantage of solar radiation, two study scenarios are proposed: winter and summer. Therefore, the present work implements an energy efficiency system in the charging stations, which develops an optimal response to the demand regarding the impact generated by EVs, in addition to the different types of charge towards the electricity grid with various scenarios. A heuristic model is proposed that is based on the Hungarian algorithm, that is, an efficient use of energy resources was achieved for charging EVs. At the same time achieving optimal use of energy resources with the use of conventional and non-conventional energies, by taking advantage of solar radiation, two study scenarios are proposed: winter and summer. Therefore, the present work implements an energy efficiency system in the charging stations, which develops an optimal response to the demand regarding the impact generated by EVs, in addition to the different types of charge towards the electricity grid with various scenarios. A heuristic model is proposed that is based on the Hungarian algorithm, that is, an efficient use of energy resources was achieved for charging EVs. The present work implements an energy efficiency system in the charging stations, which develops an optimal response to the demand regarding the impact generated by EVs, in addition to the different types of charge towards the electricity grid with various scenarios. A heuristic model is proposed that is based on the Hungarian algorithm, that is, an efficient use of energy resources was achieved for charging EVs. The present work implements an energy efficiency system in the charging stations, which develops an optimal response to the demand regarding the impact generated by EVs, in addition to the different types of charge towards the electricity grid with various scenarios. A heuristic model is proposed that is based on the Hungarian algorithm, that is, an efficient use of energy resources was achieved for charging EVs.

The problem statement is given as the optimal allocation of energy resources for a response to demand based on the Hungarian algorithm, through which it will be possible to reduce the load impact that EVs produce on the electrical distribution network, in its different types charging and at different time periods.

3.1 Randomness of EVs

For the study, an analysis was carried out hour after hour during a day, for which our EV charging station has four islands through which the energy will be randomly dispatched, in other words the EVs will have a different type of charge each hour and they will be able to enter any of the four islands available in the station, this means that no type of load is the same and the four islands can be occupied just as none can be used.

3.2 Resource Allocation Using Hungarian Algorithm

The Hungarian algorithm has been created as a solution for the optimal allocation of resources and solving allocation problems, through the theorem about zero elements of a matrix, it uses as an optimal allocation plan, which refers to assigning a single task from a set of tasks to a single person within a group of people, all this seen from the efficiency of each person to solve each task. The model to be proposed is idealized in the theory of an optimal allocation plan that does not change more than a constant number of rows or columns of the matrix that shows the efficiency.

Resource allocation
Data entry: Potmax, Potmin   **Initialize** Islands $= 4$ **Step 1:** Expand the sum
$Dem_{TOTAL} = Islas + Dem_{base}$

Step 2: Make the decisions
 If $8 > = hours > = 16$ If PotSis <PotPanel
 Assign the PotPanel resource
 Else
 Assign the PotSolar $+$ Red resources
 End If
 Else
 If $8 > = hours > = 16$
 If PotSis <PotBattery
 Assign the Battery resource
 Else
 Assign the Battery $+$ Network resources
 End If
 Else
 Assign the Red resource
 End If
 End If

Step 3: Optimal allocation of resources
Step 4: Optimal resource allocation   Case1 $=$ Summer Assignment   Case2 $=$ Winter Assignment

(continued)

Step 5: Graph
Plot (hours, case1)
Plot (hours, case2)

4 Analysis of Results

The objective of the work presented was to obtain energy efficiency by assigning energy resources to obtain an optimal load in electric vehicles using the Munkres algorithm of Matlab, it should be taken into account that by managing to distribute the available energy resources, we managed to reduce the demand peaks of electricity to the grid required to recharge the EVs, which is beneficial to both the electric distribution companies and the owners of the EVs, the results obtained in the case studies are detailed below.

4.1 Study Cases

The objective of the work to obtain energy efficiency by introducing electric vehicles to the network and was achieved by optimizing energy resources, in our case two case studies were taken into account in which the allocation of energy resources was analyzed for the optimal response to the demand both in winter and summer.

4.1.1 Summer

In this case, it is taken into account that the solar radiation index is at its maximum point as indicated in Fig. 4 in such a way that the energy production generated by the solar panels will be greater than the case study in winter, however the battery bank will have the same capacity both in this case and in the winter one.

Figure 5 shows the base demand in blue and the effect on the base demand in red when electric vehicles enter the grid, having the maximum peak at night. It can be analyzed how the insertion of EV affects the base demand by increasing the demand of the network for this case in 505.17 kWh [15], in the same way the figure indicates an energy efficiency through the optimal allocation of energy resources such as is shown in the green curve, which allows us to reduce the power required for this case, it is 308.24 kWh but there are still significant peaks, but a significant flattening of the peak curve is evidenced, which shows that it was possible to apply energy efficiency in the time of completion of electric vehicle charging for optimal allocation of energy resources [15].
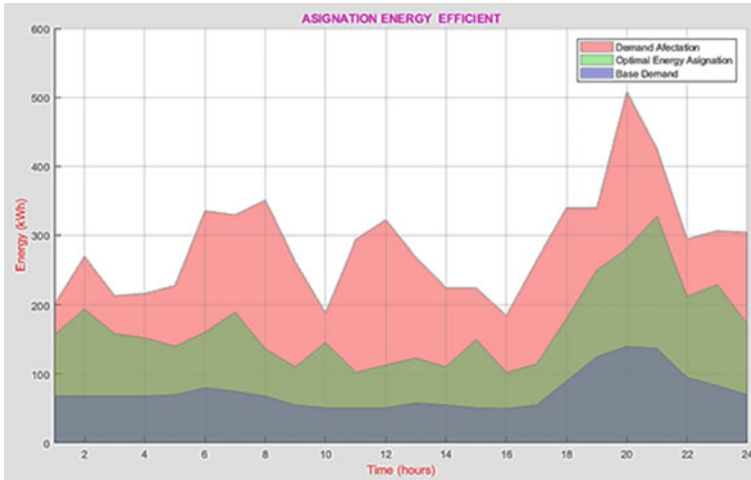
Fig. 5 Impact of summer demand

In Fig. 6 we can clearly see how the energy resources are assigned in the charging station for the summer case, being here that the greatest resource to use is the battery bank and the solar panels achieving a significant decrease in energy from the network [15]. The allocation of energy resources in summer can be seen that the photovoltaic panels work from the morning until a few hours in the afternoon, having a production that has its maximum in the noon hours, this is due to the high solar radiation rates that exist in this case study.

There are hours of greater radiation that is where solar panels are used to generate electricity in this way to meet the highest demand.

Battery banks are dispatched from 5 a.m. to 9 p.m., they deliver all the capacity they have to meet the demand for power on the grid by entering electric vehicles, unlike photovoltaic energy. Unconventional energy type is not influenced by winter and summer seasons.

In addition, the hours in which the batteries are recharged is at night, consuming energy from the electricity grid, having a lesser impact since the battery bank recharges slowly.

In the case of summer, unconventional energy sources such as battery banks and solar panels contribute 33% to the grid through the allocation of resources, while with the help of the Hungarian algorithm they contribute 53% of electrical energy, in this way they alleviate the supply that the network has to deliver by half.
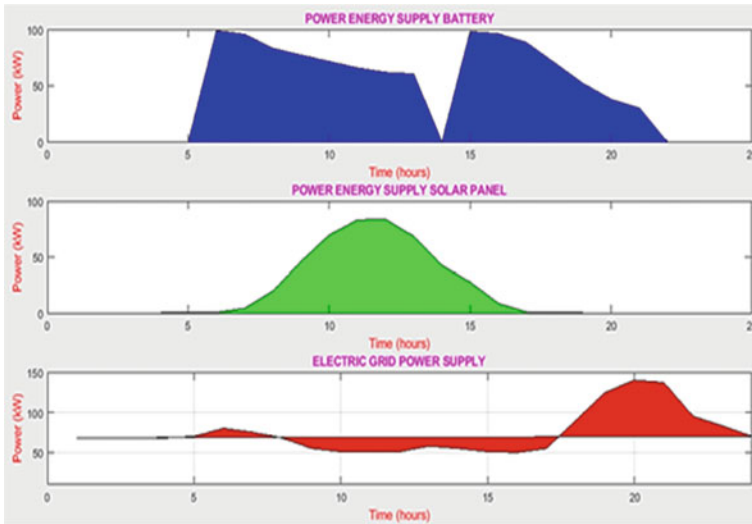
Fig. 6 Energy efficiency through optimal allocation of energy resources in summer

4.1.2 Winter

In this case, as in the summer, we apply the same study, but in the case of winter, radiation decreases notably compared to summer, so the generation of solar panels will be much lower in the same way.

When assigning energy resources using the Hungarian algorithm, we can see in Fig. 7 that the curve of the affectation reduces the excessive peaks that were had, thus optimizing the response to the demand for the entry of electric vehicles to the network, in turn, it decreases the energy that must be delivered to the grid is 243.7960 kWh, that is, 53% less, achieving the objective by reducing the impact of electric vehicles when entering the grid. In the case of winter, we can say that the highest or peak demand occurs at night, having to supply 398.67 kWh through the network. It is also observed how when allocating resources the increase produced by the insertion of EVs is considerably reduced, the green curve shows how energy resources are allocated optimizing the demand curve that produced significant peaks due to the insertion of load of EV, using the Munkres algorithm, was able to considerably reduce the impact of the network through energy efficiency, optimizing the allocation of energy resources.

With the help of the Hungarian algorithm, unconventional energy sources contribute 52% to the system, leaving the network to supply half of the demand that exists.

In Fig. 8 the way in which energy resources are dispatched can be analyzed, in such a way that for the winter case the production of solar panels decreases due to the low radiation that exists in this case, at the end of the dispatch of these banks of batteries are recharged by surplus energy from the grid or by solar panels that will
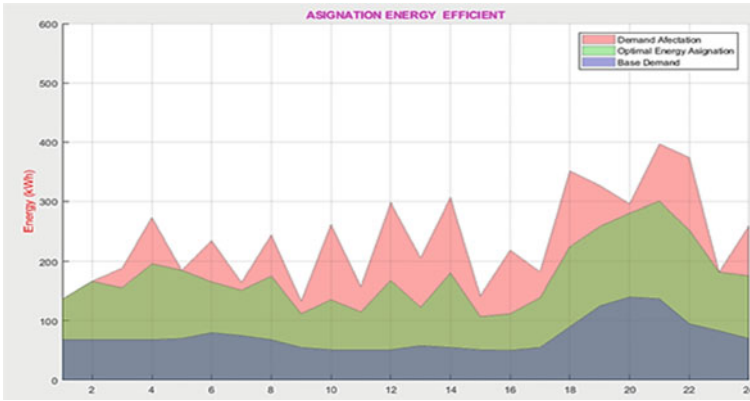
Fig. 7 Impact on winter demand

then be used to charge electric vehicles. With the help of the Hungarian algorithm, unconventional energy sources contribute 52% to the system, leaving the grid to supply the electricity, half of the demand you have.

The allocation of energy resources in the case of winter varies compared to the case of summer since solar radiation influences the generation of energy from solar panels, reducing the power generated, however the optimal response to demand by allocating resources for Electric vehicles can cover all the energy required without having to use the network, the battery banks work normally and at their full capacity in the same way in summer and winter, dispatching energy from morning to night [16].

At the end of dispatching the battery banks, they will be recharged using the energy supplied by the network, taking into account that the demand for energy at night decreases and the load of the battery banks does not influence so much on the electrical network as they are charging slow.
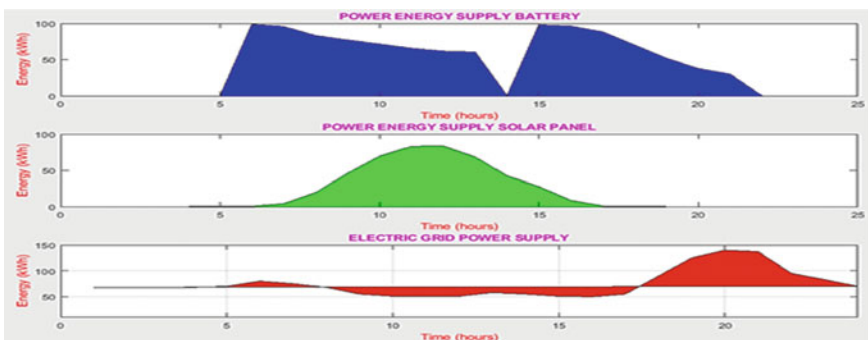
Fig. 8 Energy resource allocation winter

5 Conclusions

The use of energy from renewable sources such as solar panels, gives us a great help to reduce pollution when using fossil fuels, as well as represents an alternative to use energy in places that do not have conventional electricity generation. By dispatching energy resources in an optimal way and achieving a response to the demand for EVs through the Hungarian algorithm, it is of great help to greatly reduce the peaks in the demand curve in hours of high load, which generally is at night and in this way to achieve that the EVs are charged in hours that there is no significant load and thus reduce the increase in load to the network to avoid failures.

By allocating energy resources using the Hungarian algorithm, it helps the network because it provides in an efficient way the resources that will be used to later recharge the EVs, thus balancing the load through the use of available resources and not directly from the electricity network distribution.

References

1. Selvam R, Velavan R, Soundarrajan A (2019) A sustainable energy management soft computing system for photovoltaic/wind hybrid power generation system. Int J Environm Sustain Developm 18(3):238–258. https://doi.org/10.1504/IJESD.2019.100997
2. Ramya LN (2015) A case study on effective consumption of energy using sensor based switching system. In: ICIIECS 2015 IEEE international conference on innovations in information, embedded and communication systems. https://doi.org/10.1109/ICIIECS.2015.7192908
3. Muratori M, Schuelke-Leech BA, Rizzoni G (2014) Role of residential demand response in modern electricity markets. Renew Sustain Energy Rev 33:546–553. https://doi.org/10.1016/j.rser.2014.02.027
4. Nan S, Zhou M, Li G (2018) Optimal residential community demand response scheduling in smart grid. Appl Energy 210:1280–1289. https://doi.org/10.1016/j.apenergy.2017.06.066
5. Wang J, Zhong H, Ma Z, Xia Q, Kang C (2017) Review and prospect of integrated demand response in the multi-energy system. Appl Energy 202:772–782. https://doi.org/10.1016/j.apenergy.2017.05.150
6. Dusparic I, Taylor A, Marinescu A, Golpayegani F, Clarke S (2017) Residential demand response: Experimental evaluation and comparison of self-organizing techniques. Renew Sustain Energy Rev 80:1528–1536. https://doi.org/10.1016/j.rser.2017.07.033
7. Ruelens F, Claessens BJ, Vandael S, De Schutter B, Babuska R, Belmans R (2016) Residential demand response of thermostatically controlled loads using batch reinforcement learning. IEEE Trans Smart Grid 1–11. https://doi.org/10.1109/TSG.2016.2517211
8. Martínez-Lao J, Montoya FG, Montoya MG, Manzano-Agugliaro F (2017) Electric vehicles in Spain: an overview of charging systems. Renew Sustain Energy Rev 77:970–983. https://doi.org/10.1016/j.rser.2016.11.239
9. Nunes P, Brito MC (2017) Displacing natural gas with electric vehicles for grid stabilization. Energy 141:87–96. https://doi.org/10.1016/j.energy.2017.09.064
10. Figueiredo R, Nunes P, Brito MC (2017) The feasibility of solar parking lots for electric vehicles. Energy 140:1182–1197. https://doi.org/10.1016/j.energy.2017.09.024
11. Meza-Cartagena JF et al (2020) Analysis and study of energy efficiency in the electric system of the millennium education schools . SUMAK YACHANA WASI of Imbabura Province in Ecuador 29(7):14040–14050

12. Garcia Torres EM, Benalcazar Lopez BD, Idi Amin IM (2017) Analysis of the voltage profile by the insertion of electric vehicles in the distribution network considering response to demand. In: 2017 international conference information system computing science, pp 7–13. https://doi.org/10.1109/INCISCOS.2017.26

13. García Torres EM, Isaac I (2016) Demand response systems for integrating energy storage batteries for residential users

14. Moreno P, Garcia Torres EM (2016) Respuesta a la Demanda para smart home Utilizando Procesos Estocásticos. I+D Tecnológico 12

15. García Torres EM, Isaac Ì (2017) Multi-objective optimization for the management of the response to the electrical demand in commercial users. In: INCISCOS 2017—international conference information system computing science, pp 14–20. https://doi.org/10.1109/INCISCOS.2017.25

16. Meza Cartagena JF, García Torres EM (2018) Asignación de recursos para la recarga de vehículos eléctricos en estaciones de servicios basado en la respuesta a la demanda. I+D Tecnológico 14(2):66–73. https://doi.org/10.33412/idt.v14.2.2075

A Current Control Scheme of Three Phase Three-Level Neutral Point Clamped Grid Connected Inverter Using Min–Max Algorithm Approach

Bandela Supriya, Kowstubha Palle, A. Bhanuchandar, Rajakumar Sakile, Dongari Vamshy, and Kasoju Bharath Kumar

Abstract In this paper, a Current Control Scheme (CCS) for three phase 3-level Neutral Point Clamped (NPC) Inverter using Min–Max (MM) algorithm approach has been presented. The inverter topology basically consists of four unidirectional switches, two clamping diodes per phase and common split dc link capacitors have been provided for all phases at input side. At the input side of an inverter, balanced dc link capacitors are considered through the application of either dc link chopper or Three Level Boost Converter (TLBC) circuits. An LCL filter is connected to the output of inverter circuit and is integrated with the grid to achieve higher ripple attenuation capability. Here, the MM algorithm is nothing but an offset addition to the respective modulating signals then it follows like Space Vector Pulse Width Modulation (SVPWM) technique without the need of any dwell time calculations and finally control complexity can be reduces. Here, a Synchronous Reference Frame (SRF) Phase Locked Loop (PLL) has been utilized to generate reference grid variable for grid synchronization. In the grid connected closed loop operation, an inverter current feedback system is used. The d-axis and q-axis current reference values were utilized to inject active and reactive powers into the grid respectively. Usually, the d-axis current reference is taken from the dc link voltage controller and for Unity Power Factor Operation (UPF) of the grid, the q-axis current reference is taken as zero. Finally, the operation and control approach of grid connected inverter with LCL filter has been validated through MATLAB/Simulink environment.

B. Supriya (✉) · K. Palle
EEE Department, CBIT (A), Gandipet, Hyderabad, Telangana, India
e-mail: supriyasarada17@gmail.com

A. Bhanuchandar
Electrical Engineering Department, NIT Warangal, Warangal, Telangana, India

R. Sakile
Electrical Engineering Department, NIT Jamshedpur, Jamshedpur, Jharkhand, India

D. Vamshy · K. B. Kumar
EEE Department, MGIT, Hyderabad, Telangana, India

1 Introduction

The demand for power is continuously increasing, causing a major resource constraint challenge. Thus, there is a need to improve the generation of electricity with good efficient system. Energy conversion is a constant requirement in today's environment. The main application of the modern power conversions is at Grid Connected systems (GC). This process of conversion accomplished through two methods: rectifying and inverting [1]. Solar energy, wind turbines, and hydropower plants are all being used to generate electricity at an increasing rate, and research is ongoing in this area [2–4]. Because power conversion is so important in renewable resources, converters are required.

Converters are available in a wide range of shapes and sizes, and they can be utilized in both low and high-power applications [5]. The two types of high-power drives are direct and indirect DC link drives. Voltage Source Inverters (VSI) are used in indirect DC link drives. The Neutral Point Clamped, Flying Capacitor, and Cascaded H Bridge (CHB) inverter topologies are the three major multilevel inverter topologies used in VSI inverters. An asymmetric seven level CHB has been developed using various modulation techniques such as multi carrier in-phase dis-position [6]. Low harmonic distortion and medium voltage operation are realized by cascading two H-bridge cells with 1:2 stiff dc source configurations [7]. A reduced device count for symmetric seven level [8] and a Capacitor Based with LCL filter for nine level[9], Bi-Polar DC Micro grid control approach [10] have been presented for Grid connected applications.

The most important research area in the realm of Power Electronics is the development of control schemes for various power converters. Modulation techniques are employed to ensure proper switching timing, i.e. when the devices turn on and off. Fundamental and high switching frequency modulation approaches are classified based on the type of switching frequency. A high switching frequency has been proposed for high-power drives. The most commonly implemented approach in high switching frequency is Space Vector Pulse Width Modulation. The three-level technique appears to be the most promising option in terms of harmonic reduction and high dc link voltage level. At an analogous switching frequency, the harmonic content of a three-level inverter is better than a two-level inverter, so the switching device's blocking voltage is half that of the dc link voltage. As a result, the three-level inverter design is commonly used in high-performance, high-voltage drive systems.

The rest of the paper is organized as follows. Section 2 describes the operation of 3 phase grid connected 3-level NPC inverter with LCL filter. Section 3 describes the Proposed Control algorithm. Section 4 gives Simulation Studies. Section 5 gives Conclusion.

2 Description and Operation of 3 Phase Grid Connected 3-Level NPC Inverter with LCL Filter

In high-power applications (several megawatts), neutral-point-clamped (NPC) inverters are the most extensively used topology of multilevel inverters [11]. NPC inverter with three level topology was first proposed by Nabae et al. [12]. Figure 1 represents a 3 phase grid connected 3-level NPC inverter with LCL filter. Each leg of a 3 phase 3-level inverter is made up of switching devices coupled by anti-parallel diodes, and also with other devices called as clamping diodes, to improve the inverter's performance. To reduce the harmonic distortion or to get a smooth sinusoidal wave at the output of Inverter, usually a low pass filter is connected. In this paper, inverter with higher order LCL filter is considered for the following reasons [13–17]. The reasons are, (i) they provide regulatory requirements at compact size and weight as per of standards such as IEEE 519–1992 and IEEE P1547.2- 2003. (iii) Compact size for the filter elements 3. Higher ripple attenuation capability.

In order to avoid stability problems, LCL filter values were designed carefully. One of the major problems with higher order filters is the occurrence of resonance. The problem of resonance can be reduced with active damping method. Designing of filter elements is done as per the procedures given in reference [15]

Table 1 gives the Switching pattern for three-level NPC inverter circuit. Table 2 demonstrates that when switch ga_1 is switched on, switch ga_3 is turned off, suggesting that the two switches are complimentary, just as switch ga_2 and switch ga_4 are. For the same operational requirements, a three-level three-phase NPC inverter has lower THD and dv/dt than a two-level inverter. The static voltage equalization is obtained

Fig. 1 Three phase grid connected 3-level NPC inverter with LCL filter

Table 1 Switching pattern for three-level NPC inverter circuit

Switching state	ON state devices of phase A	Pole voltage, V_{AZ}
1	$ga_1 - ga_2$	E
0	$ga_2 - ga_3$	0
−1	$ga_3 - ga_4$	−E

Table 2 Simulation parameters for NPC GCI with LCL filter

Grid specifications	100kVA, Grid Voltage (L-L) = 415 V, f = 50 Hz
DC bus voltage in volts	$V_{dc1} = V_{dc2} = 400$ V
Switching frequency	$f_{sw} = 10$ kHz
Filter inductor values (L1 & L2)	490μH
Filter capacitor values C	95μF

in NPC, only when the leakage current flow of switches ga_1 and ga_4 in a leg is lower than that of switches ga_2 and ga_3.

Space Vector Pulse Width Modulation Techniques (SVPWM) is most popularly used in multilevel inverters [18–20]. Space Vector is a mathematical concept used for visualizing the effect of MMF. The switching states of the space vector are determined by the level and phase of the inverters. For three phase and three level NPC, the space vectors will have 27 switching states. Based upon the magnitude the switching states are classified into four sectors i.e.; zero vector, small vector, medium vector and large vector, as depicted in Fig. 2.

Fig. 2 Representation of vectors in SVPWM

3 Proposed Control Algorithm

The proposed Min–Max (MM) algorithm approach becomes a simplified version of space vector modulation Technique implemented on NPC grid connected Inverter in the aspects reduction of dwell time calculation and complexity of the circuit. Figure 3 gives the block diagram of proposed control scheme of Three Phase Three Level NPC –GCI Inverter as given in Fig. 1 (Min–Max algorithm) which can overcome the drawbacks incurred with SVM approach.

The explanation of the proposed control scheme is given as under on the grid side, three-phase abc voltages are initially converted into αβ frames by using Clark's transformation. The generated V_{α} and V_{β} are given to PLL for grid synchronization purpose to produce desired phase angle (wt). The α-β frame voltages are converted in d-q frame to produce V_d and V_q components. Now, on the Inverter side, three-phase load currents are initially converted into αβ frames by using Clark's transformation. These α-β frame currents are converted in d-q frame currents. The obtained I_d and I_q values are compared with I_{dref} and I_{qref} respectively and the obtained output signals are given to PI controller. The components E_d and E_q are obtained as per the procedure reflecting in Fig. 3. Then E_d and E_q are converted in to 3 phase abc signals and they act as modulating signals.

In order to get the desired Modified Modulating (M2) Signal to be fed to the PWM block as shown in Fig. 3, the following approach is adopted. In order to get these signals for three phases, an offset value is added to each phase as indicated below.

$$V_{AM} = V_m \sin(\theta) + x$$
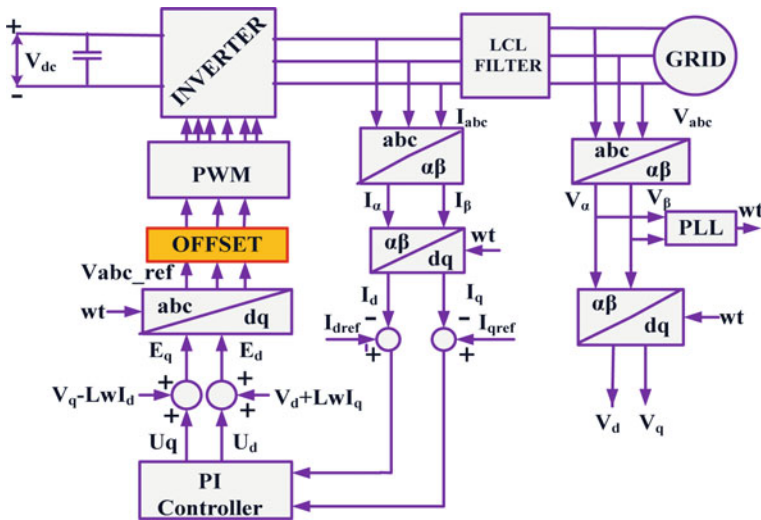
Fig. 3 Block diagram of proposed control scheme for NPC –GCI (Min –Max algorithm)

$$V_{BM} = V_m \sin\left(\theta - \frac{2\pi}{3}\right) + x$$

$$V_{CM} = V_m \sin\left(\theta + \frac{2\pi}{3}\right) + x$$

where $x =$ offset. The offset value is taken as

$$\text{Offset} = -\frac{V_{\max} + V_{\min}}{2}; \ \ V_{\max} = \max\{V_{AM}, V_{BM}, V_{CM}\}$$
$$\text{and} \ \ \ V_{\min} = \min\{V_{AM}, V_{BM}, V_{CM}\}$$

This offset addition approach is called as MM algorithm. Adding first offset /common mode injection to the modulating signals then it produces camel hump waveform as like 3rd harmonic injection PWM technique. Because of this, the DC bus utilization can become increases. However, the duration of starting and ending vectors not be equal means that it does not follows the actual SVM Technique. To make equal time durations, one more offset should be added to the camel hump waveform then it produces Modified Modulating (M2) signal as given in Fig. 4, which represents the generation of M2 signals with the addition of first and second offset. This M2 signal is finally compared with single high frequency carrier signal, then the required gate pulses has been generated to the inverter.
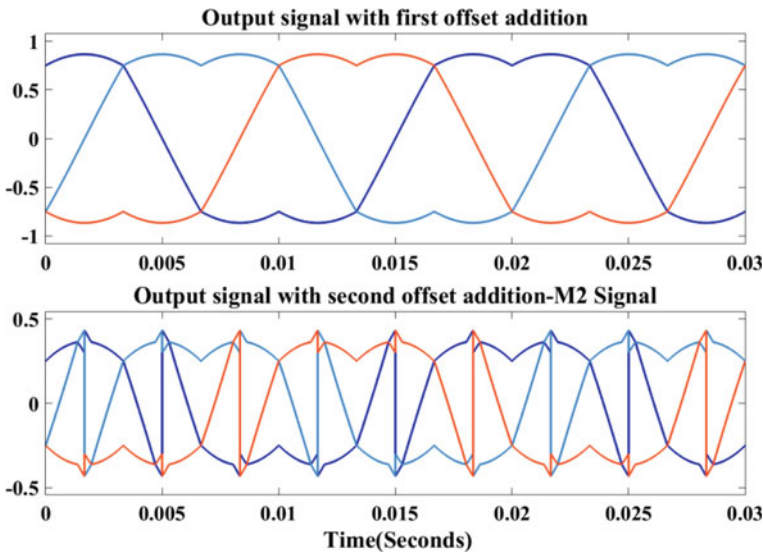
Fig. 4 Generation of M2 signals with the addition of first and second offset

4 Simulation Studies

The Simulation parameters for this NPC Grid Connected Inverter (NPC-GCI) are represented in Table 2. On implementing the proposed control scheme on NPC-GCI, the following obtained outputs were discussed below.

4.1 Case I: I_{dref} is Taken as 150A and $I_{qref} = 0$

For this case of taken reference currents, it is required to inject grid current as I_{dref} and with $I_{qref} = 0$ gives unity power factor operation at the grid side. This is visualized through the simulation results obtained for NPC-GCI with the specifications given in the Table 2 with the proposed MM control algorithm from Fig. 3. Figure 5 gives the simulation results for this case of $I_{dref} = 100A$, Fig. 5 is further divided as (a), (b), (c), (d), (e). The proposed control scheme with the mentioned simulation parameters gives a 3 level and 5 pole and line voltages with a peak value of 400 and 800 V respectively as depicted in Fig. 5a and b.

Figure 5c and d give the grid voltage and grid currents. It is clear from the figure that grid voltage is 586.81 V with a pure sinusoidal waveform after getting smoothened with LCL filter on inverter side. From the applied control scheme, the injected grid current exactly tracks according to I_{dref} value. Figure 5e represents Grid Voltage and Current waveforms for One Phase: UPF operation mode. From this figure it is clear that grid voltage and grid current are in phase indicating the unity power
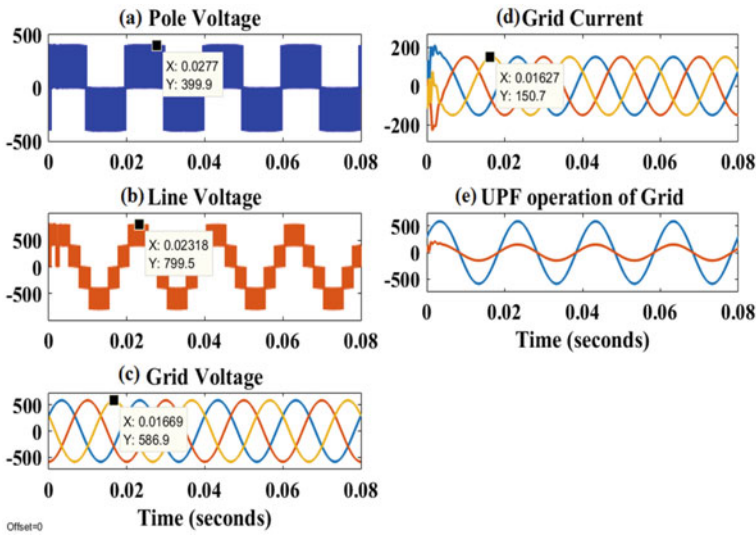
Fig. 5 Simulation results with $I_{dref} = 150A$
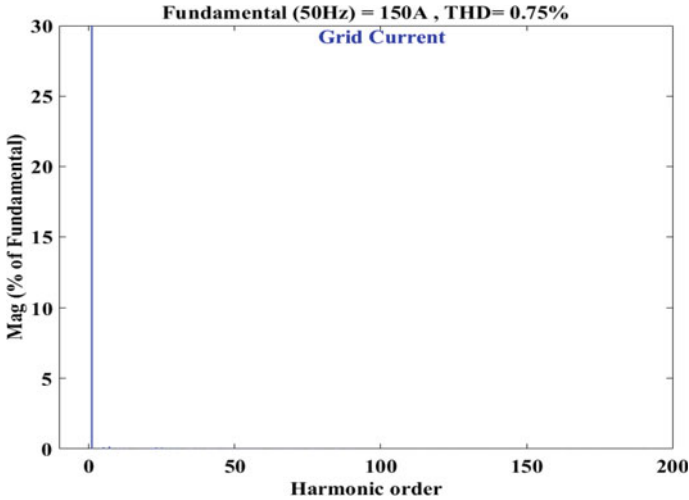
Fig. 6 FFT analysis-grid current

factor operation. Figure 6 shows the FFT analysis for Grid Current in which it is observed that THD is obtained as 0.75%. The meaning of I_{dref} indicates the active power transferring to the grid.

4.2 Case II: I_{dref} is Taken as 100A and $I_{qref} = 0$

For this case of taken reference currents, it is required to inject grid current as I_{dref} and with $I_{\text{qref}} = 0$ gives unity power factor operation at the grid side. This is visualized through the simulation results obtained for NPC-GCI with the specifications given in the Table 2 with the proposed MM control algorithm from Fig. 3. Figure 7 gives the simulation results for this case of $I_{\text{dref}} = 100A$, Fig. 7 is further divided as (a), (b), (c), (d), (e). The proposed control scheme with the mentioned simulation parameters gives a 3 level and 5 pole and line voltages with a peak value of 400 and 800 V respectively as depicted in Fig. 7a and b.

Figure 7c and d gives the grid voltage and grid currents. It is clear from the figure that grid voltage is 586.81 V with a pure sinusoidal waveform after getting smoothened with LCL filter on inverter side. From the applied control scheme, the injected grid current exactly tracks according to I_{dref} value. Figure 7e represents Grid Voltage and Current waveforms for One Phase: UPF operation mode. From this figure it is clear that grid voltage and grid currents are in phase indicating the unity power factor operation.
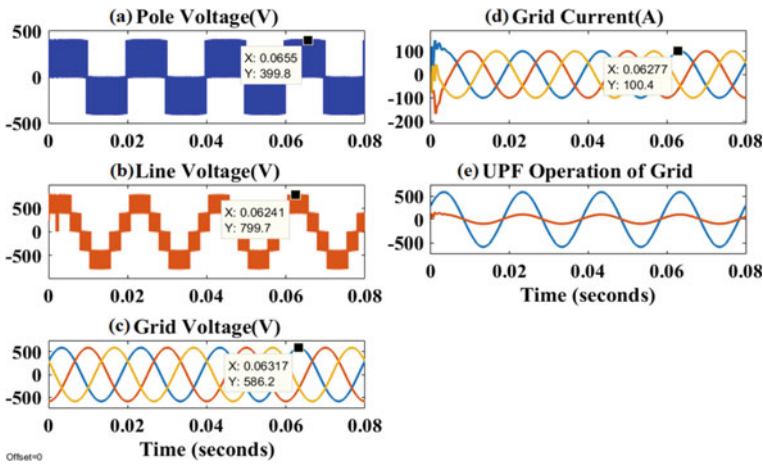
Fig. 7 Simulation results with $I_{\text{dref}} = 100A$

5 Conclusions

A CCS for 3- φ, 3- level NPC Inverter with LCL filter using Min–Max (MM) algorithm approach has been presented in this paper. The proposed MM algorithm produces the M2 signal that follows like Space Vector Pulse Width Modulation technique without the need of any dwell time calculations and finally control complexity can be reduces. The proposed control algorithm provides good tracking capability of grid current with respect to I_{dref} and finally the UPF operation of Grid has been achieved with less harmonic distortion and also the grid current follows IEEE-519 standards according to grid code requirement. Finally, the operation and control approach of grid connected inverter with LCL filter is explained clearly.

References

1. Erickson RW, Maksimovic D (2007) Fundamentals of power electronics. Springer, Berlin, Germany
2. Gee AM, Robinson FVP, Dunn RW (2013) Analysis of battery lifetime extension in a small-scale wind-energy system using super capacitors. IEEE Trans Energy Convers 28(1):24–33
3. Gee AM, Dunn RW (2010) Novel battery/super capacitor hybrid energy storage control strategy for battery life extension in isolated wind energy conversion systems. In: Proceedings 45th international university power engineering conference (UPEC), pp 1–6
4. Karki R, Billinton (2001) Reliability/cost implications of PV and wind energy utilization in small isolated power systems. IEEE Trans Energy Convers 16(4):368–373
5. Palle K, Bhanuchandar A (2020) A novel modified voltage oriented control of an active front-end rectifier used for PMSG based wind turbine systems. Int J Innov Technol Exploring Eng (IJITEE) 9(8)

6. Palle K, Supriya B, Mahesh C, Vamshy D (2021) Multi carrier IPD-PWM technique for three phase diode clamped and cascaded H-bridge multilevel inverters. AEGAEUM J 9(5). ISSN: 0776–3808

7. Kowstubha P, Krishnaveni K, Supriya B, Mahesh C (1945) A new hybrid control scheme for seven level asymmetric cascaded H-bridge multilevel inverter, April/2021 13(4). ISSN:0022–1945

8. Kumar KB, Bhanuchandar A, Mahesh C (2021) A novel control scheme for symmetric seven level reduced device count multi-level DC Link (MLDCL) inverter. In: 2021 international conference on sustainable energy and future electric transportation (SEFET), pp 1-4.https://doi.org/10.1109/SeFet48154.2021.9375714

9. Bhanuchandar A, Murthy BK (2020) Single phase nine level switched capacitor based grid connected inverter with LCL filter. In: 2020 3rd international conference on energy, power and environment: towards clean energy technologies, pp 1–5. https://doi.org/10.1109/ICEPE50861.2021.9404491

10. Sathisha D (2021) A simplified control approach of AC-DC-TLBC for Bi-polar DC micro grid applications. Turkish J Comput Mathem Educ (TURCOMAT) 12(2):818–824. https://doi.org/10.17762/turcomat.v12i2.1090

11. Seo JH, Choi CH et al (2001) A new simplified space vector PWM method for three-level inverters. IEEE Trans Power Electron 16(4):545–555

12. Nabae A, Takahashi I, Akagi H (1981) A new neutral-point-clamped PWM inverter. In: IEEE transactions on industry applications, September, vol IA-17(5), pp 518–523. https://doi.org/10.1109/TIA.1981.4503992

13. Wang T, Ye Z et al (2003) Output filter design for a grid-interconnected three phase inverter. In: Power electronics specialist conference, 2003. PESC '03. 2003 IEEE 34th annual

14. Parikshith BC, John V (2008) Higher order output filter design for grid connected power converters. In: 5th national power systems conference (NPSC), pp 614–619

15. Jiao Y, Lee FC (2015) LCL filter design and inductor current ripple analysis for a three-level NPC grid interface converter. IEEE Trans Power Electron 30(9):4659–4668

16. Lindgren M (1995) Feed forward-time efficient control of a voltage source converter connected to the grid by low pass filters. In: Proceedings IEEE PESC '1995, pp 1028−1032

17. Lindgren M (1998) Control of a voltage-source converter connected to the grid through an LCL filter—application to active filtering. In: Proceedings IEEE-PESC'1998, pp 229−235

18. Ratnayake KRMN et al (1999) Novel PWM scheme to control neutral point voltage variation in three-level voltage source inverter. In: IEEE industry application society conference (IAS), pp 1950–1955

19. Abu-Sharkh S, Sykuski J etc. (2000) Current control of three-phase PWM inverters for embedded generators. In: Proceedings international conference: on power electronics and variable speed drives, pp 524–529

20. Rodriguez J, Bernet S, Steimer PK, Lizama IE (2010) A Survey on neutral-point-clamped inverters. IEEE Trans Industr Electron 57(7):2219–2230

Computational Study of CH$_3$NH$_3$PbI$_{3-x}$Cl$_X$ Perovskite Solar Cell with Record Efficiency of 33.19%

Ayush Tara , **Vishal Bharti** , **Susheel Sharma** , **and Rockey Gupta**

Abstract Mixed halide perovskites are found to be more stable and bandgap tunable along with enhanced carrier transportation. Here we present a CH$_3$NH$_3$PbI$_{3-x}$Cl$_x$ perovskite solar cell (PSC) having Spiro-oMeTAD as HTL and Zn(O$_{0.3}$,S$_{0.7}$) as ETL which is simulated in SCAPS-1D software with initial output parameters as: V_{OC} = 1.2632 V, J_{SC} = 23.53 mA/cm^2, FF = 76.35% and PCE = 22.71%. In order to optimize the device performance, an exhaustive study has been performed for obtaining the critical specifications of device, in terms of the thickness, defect density and bandgap of the active layer. The optimized thickness, defect density and bandgap of active layer is found to be 1000 nm, 2.5 × 10^{11} cm^{-3} and 1.50 eV respectively. It has been found that optimized value of ETL thickness for better efficiency of device is 20 nm and HTL thickness has no impact on output device parameters. Moreover, the influence of back metal contact work function has also been investigated with its optimized value as 5.4 eV. Finally, when simulation is done with all the optimized values, the device performance has been found to be greatly enhanced with V_{OC} = 1.4215 V, J_{SC} = 27.62 mA/cm^2, FF = 84.51%, and PCE = 33.19%.

Keywords Mixed halide perovskite · Zn(O0.3,S0.7) · SCAPS

1 Introduction

With the increasing population, the consumption of energy is increasing exponentially by time [1]. The non-renewable energy sources like fossil fuels will be depleted from the earth if their effective replacements are not found [2]. Also, the usage of

A. Tara (✉) · S. Sharma · R. Gupta (✉)
Department of Electronics, University of Jammu, Jammu 180006, India
e-mail: ayushtara512@gmail.com

R. Gupta
e-mail: rockeygupta@gmail.com

V. Bharti
Department of Physics, School of Sciences, Cluster University of Jammu, Jammu, India

fossil fuels as the primary source of energy cause major environmental concern, which lead to the progress toward renewable energy. Solar energy is considered to be the most effective replacement of fossil fuels as it is the cleanest form of energy with no hostile impact on the environment [3]. The photovoltaic market has been dominated by silicon based solar cells for decades until researchers found perovskites as an excellent candidate for developing efficient photovoltaic solar cells [4, 5].

Due to wide spectral absorption, high charge carrier mobilities, long charge diffusion lengths, small exciton binding energy, and solution-processing abilities, the perovskite solar cells (PSC) have made tremendous progression with power conversion efficiency (*PCE*) increasing from 3.8% in 2009 to a certified *PCE* of 25.5% in 2021 [6–10].

Organo-metal lead iodide based perovskites ($CH_3NH_3PbI_3$) are being extensibly employed as active layers in perovskite solar cells because of their capability to absorb photons at a better rate, having great charge transport properties, convenient band gap (approximately $= 1.55$ eV) and longer carrier diffusion length [11, 12]. Snaith et al. [13, 14] in 2012, demonstrated that the mixed halide $CH_3NH_3PbI_{3-x}Cl_x$ shows better stability and charge carrier mobility when compared to $CH_3NH_3PbI_3$. Mixed halides exhibit enhancement in carrier diffusion length when compared to its pure organo-metal lead iodide equivalent ($\sim$100 nm) which results in better carrier accumulation with a power conversion efficiency (*PCE*) of 10.9%. Further, Snaith and group [15] in late 2013, reported an efficiency of 15.4% by proposing a two source thermal evaporation method for the deposition of $CH_3NH_3PbI_{3-x}Cl_x$ uniform films with improved morphology. Fan and co-workers [16] demonstrated the improvement in the performance of $CH_3NH_3PbI_{3-x}Cl_X$ based perovskite solar cells by forming good morphology active films having nominal photocurrent hysteresis.

Besides all these experimental reports, a lot of computational studies have also been carried out in the recent past for better performance of mixed halides based perovskite solar cells. In 2018, Zhao et al. [17] reported a maximum *PCE* of 22% in mixed halide based perovskite solar cells having architecture: ITO/NiO/$CH_3NH_3PbI_{3-x}Cl_x$/PCBM/Ag using SCAPS-1D software. Further, they also studied the influence of doping concentration and thickness of NiO along with thickness of active layer and found the optimized doping concentration of NiO $= 1 \times 10^{17}$ cm^{-3}, the optimized thickness of NiO $= 30$ nm, along with optimized thickness of active layer as 450 nm.

Gupta et al. [18] have proposed an interface layer free solar cell structure with $CH_3NH_3PbI_{3-x}Cl_x$ as absorber layer, FTO as the front electrode and Au as back contact. They have concluded that perovskite layer thickness and back electrode metal greatly influence the output parameters of the device. The best device performance has been found to be at absorber thickness of 2.3 μm with FTO as the front electrode and Au as the back electrode giving a maximum *PCE* of 22.7%. Another mixed halide based perovskite solar cell structure having inverted planar architecture: glass/FTO/TiO_2/$CH_3NH_3PbI_{3-x}Cl_X$ /Spiro-OMeTAD/Ag has been simulated by Iseo and group [19] in 2020. The thickness of FTO, TiO_2, and $CH_3NH_3PbI_{3-x}Cl_X$ has been varied to ascertain their impact on the output parameters of the device and found that the ETL thickness has no substantial impact on the performance of solar

cells while the 300−400 nm is the best range for absorber layer thickness to achieve higher efficiency of 29.56%.

In this paper, we have proposed a CH$_3$NH$_3$PbI$_{3-x}$Cl$_X$ based solar cell structure having an inverted planar configuration and investigated the dependence of the performance of the device upon variation of defect density, band gap and thickness of absorber layer.

2 Computational Details and Device Structure

The proposed solar cell structure in inverted planar configuration consists of CH$_3$NH$_3$PbI$_{3-X}$Cl$_X$ absorber layer which is interjected between zinc oxysulphide (Zn(O$_{0.3}$,S$_{0.7}$)) and 2,2′,7,7′-Tetrakis[N,N-di(4-methoxyphenyl)amino]-9,9′-spirobifluorene(Spiro-oMeTAD) as electron transport layer (ETL) and hole transport layer (HTL) respectively, as illustrated in Fig. 1. The presented solar cell device employs fluorine doped SnO$_2$ (FTO) and Gold (Au) as cathode and anode respectively. The proposed solar cell device has the architecture of: FTO/Zn(O$_{0.3}$,S$_{0.7}$)/CH$_3$NH$_3$PbI$_{3-}$materials employed in device structure is displayed in Fig. 2.

Fig. 1 Device architecture of proposed solar cell
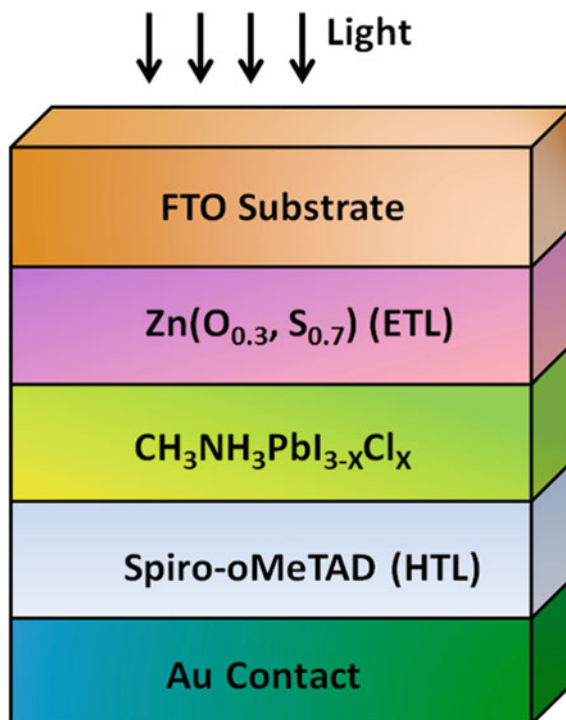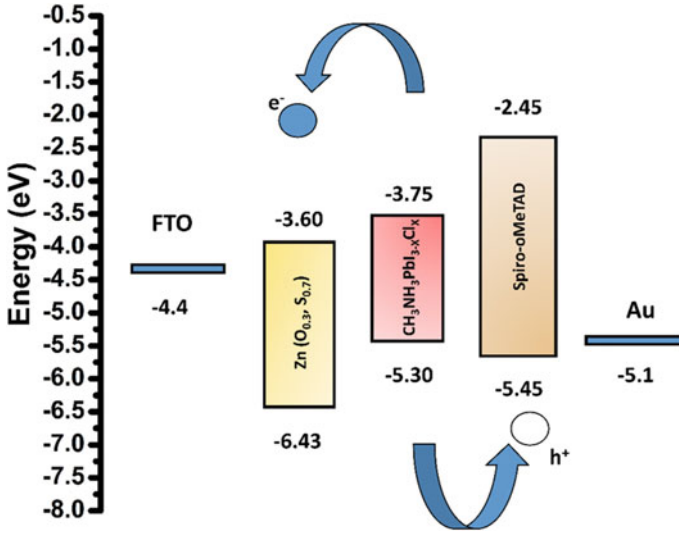
Fig. 2 Energy band alignment for proposed structure

The computational study of the proposed solar cell structure is executed using solar cell capacitance simulator (SCAPS) software (version 3.3.09). The SCAPS software is primarily based on the Poisson's Eq. (1), and the Continuity equations for electrons (2) and holes (3) respectively [20, 21];

$$\nabla^2 \psi = \frac{q}{\in}(n - p + N_A - N_D) \tag{1}$$

$$\nabla \cdot J_n + q\frac{dn}{dt} = +qR \tag{2}$$

$$\nabla \cdot J_p + q\frac{dp}{dt} = -qR \tag{3}$$

where symbols have the following meaning:

$\in$ = permittivity,

q = elementary charge,

ψ = electrostatic potential,

n = concentration of free electrons,

p = concentration of free holes,

N_D = donor concentration.

N_A = acceptor concentration.

and J_n and J_p are, current densities for electrons and holes respectively.

Drift–Diffusion current equations are:

$$J_n = qn\mu_n E + qD_n\nabla_n \tag{4}$$

$$J_p = qp\mu_p E + q D_p \nabla_p \tag{5}$$

where D_p and D_n are diffusion coefficients for holes and electrons respectively.

Basic parameters used to perform simulation have been collected from various published reports summarized in Table 1 [18, 19, 22]. Parameters including energy bandgap (E_g), relative permittivity (ϵ_r), electron affinity (χ), electron mobility (μ_n), hole mobility(μ_p), defect density (N_t), N_c and N_v are the efficient density of states for conduction band and valence band respectively. The bulk type in each layer is considered to achieve reasonable results, as displayed in Table 2. The electron and hole thermal velocity have been set as 10^7 cm/s. Gold with work function = 5.1 eV and FTO with a work function of 4.4 eV are used as the back contact and front contact respectively [23].

Table 1 Basic parameters utilized for simulation

Parameters	FTO	Zn(O$_{0.3}$, S$_{0.7}$)	CH$_3$NH$_3$PbI$_{3-x}$Cl$_X$	Spiro-oMeTAD
Thickness (nm)	500	10	500	50
Eg (eV)	3.5	2.83 [22]	1.55 [18]	3.0 [19]
χ (eV)	4	3.6 [22]	3.90 [18]	2.45 [19]
ϵ_r	9	9 [22]	6.50 [18]	3.0 [19]
'Nc' (cm^{-3})	2.2×10^{18}	2.2×10^{18}	2.2×10^{18}	2.2×10^{18}
'Nv' (cm^{-3})	1.8×10^{19}	1.8×10^{19}	1.8×10^{19}	1.8×10^{19}
μ_n(cm^2/vs)	20	100 [22]	2 [18]	2×10^{-4} [19]
μ_p(cm^2/vs)	10	25 [22]	2 [18]	2×10^{-4} [19]
N_D (cm^{-3})	2.0×10^{19}	1.0×10^{18} [22]	1.0×10^{18}	0
N_A(cm^{-3})	0	0	—	2.0×10^{18} [19]
N_t (cm^{-3})	1.0×10^{15}	1.0×10^{15}[22]	2.5×10^{13} [18]	1.0×10^{15} [19]

Table 2 Defect types of various layer used in simulation

	FTO	Zn(O$_{0.3}$, S$_{0.7}$)	CH$_3$NH$_3$PbI$_{3-x}$Cl$_X$	Spiro-oMeTAD
Type	Neutral	Neutral	Neutral	Neutral
Capture cross section of electrons (σ_n)	1×10^{-15}	1×10^{-15}	1×10^{-15}	1×10^{-15}
Capture cross section for holes (σ_p)	1×10^{-15}	1×10^{-15}	1×10^{-15}	1×10^{-15}
Energy(eV)	$> E_V$	$> E_V$	$> E_V$	$> E_V$

3 Results and Discussions

3.1 *Variation of Thickness of Absorber Layer*

The perovskite absorber layer plays a crucial role in designing efficient perovskite solar cells and its thickness highly influences the efficiency of PSC [24, 25]. The effect of variation of thickness of absorber layer on the output performance of the presented solar cell structure is studied by changing its value from 500 to 1500 nm and the corresponding change in the device output parameters are displayed in Fig. 3. As evident from Fig. 3a, c, the open circuit voltage (V_{OC}) and fill factor (FF) start decreasing monotonically with an increase in the thickness. PCE firstly increases with the increasing thickness of absorber layer until the thickness of 1000 nm is reached, as more photons are absorbed by perovskite absorber layer at a larger thickness as shown in Fig. 3d. The increase in the number of photo-generated charge carriers results in enhanced short circuit current density (J_{SC}) as depicted in Fig. 3b. Further, when we increase the absorber layer thickness beyond 1000 nm, PCE falls. This is due to the fact that at a larger thickness more photons are absorbed which results in a higher recombination rate as carrier diffusion length becomes smaller than absorber layer thickness. Thus, the absorber layer thickness of 1000 nm has been chosen as the optimized value for an efficient solar cell device.
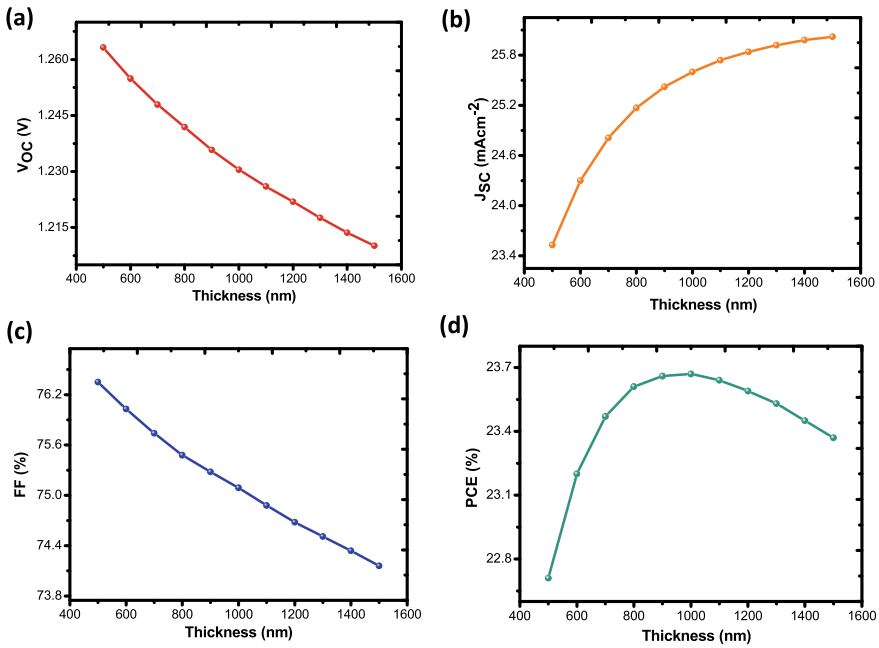
Fig. 3 Effect of thickness of absorber layer on output parameters
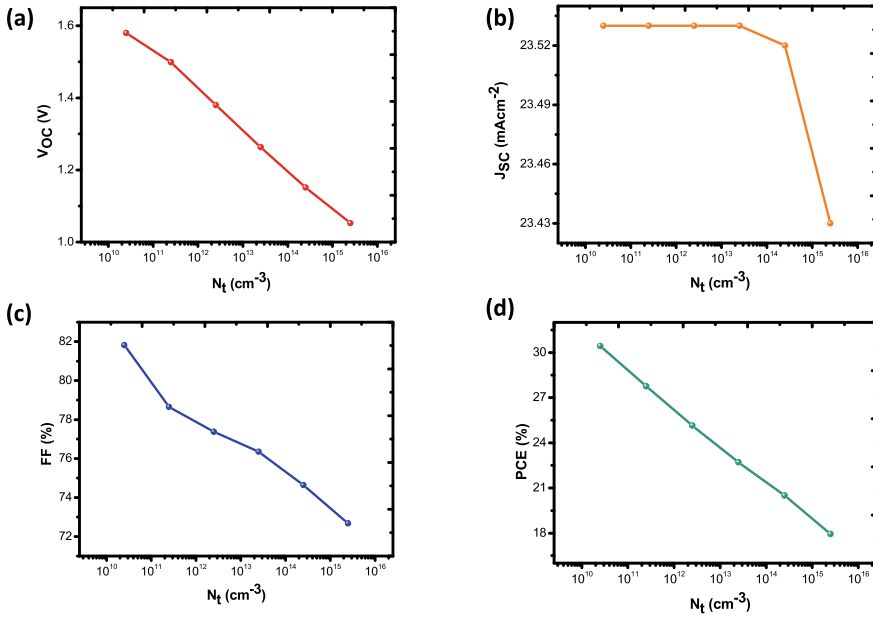
Fig. 4 Effect of N_t in absorber layer on output parameters

3.2 Variation of Density of Trap States in Absorber Layer

Perovskite films contain a number of trap states that have a significant influence on its physical and electrical properties, and thereby on the performance of solar cell [26, 27]. An inferior quality active perovskite film has a greater number of trap states which results in non-radiative recombination that leads to *deterioration* of V_{OC}. Therefore, the impact of the density of trap states (N_t) in the perovskite layer on device output parameters needs to be explored. The value of N_t in the absorber layer is altered from 2.5×10^{10} cm^{-3} -2.5×10^{15} cm^{-3} and the corresponding variation in output parameters is displayed in Fig. 4. PCE increases with decreasing N_t, however, degradation of N_t below 2×10^{11} cm^{-3} demands a high cost of fabrication [28]. Thus, the improved value of N_t is selected as 2.5×10^{11} cm^{-3} resulting in the enhanced output parameters as: $V_{OC} = 1.4990$ V, $J_{SC} = 23.53$ mA/cm^2, $FF = 78.65\%$ and $PCE = 27.76\%$.

3.3 Variation of Bandgap of Absorber Layer

Since perovskite materials are highly band gap tunable [29], the variation of energy band gap (Eg) from 1.50 to 1.60 eV of the absorber layer is done to investigate its impact on the performance of the proposed structure. As depicted in Fig. 5b, J_{SC}

(a)

(b)

(c)

(d)
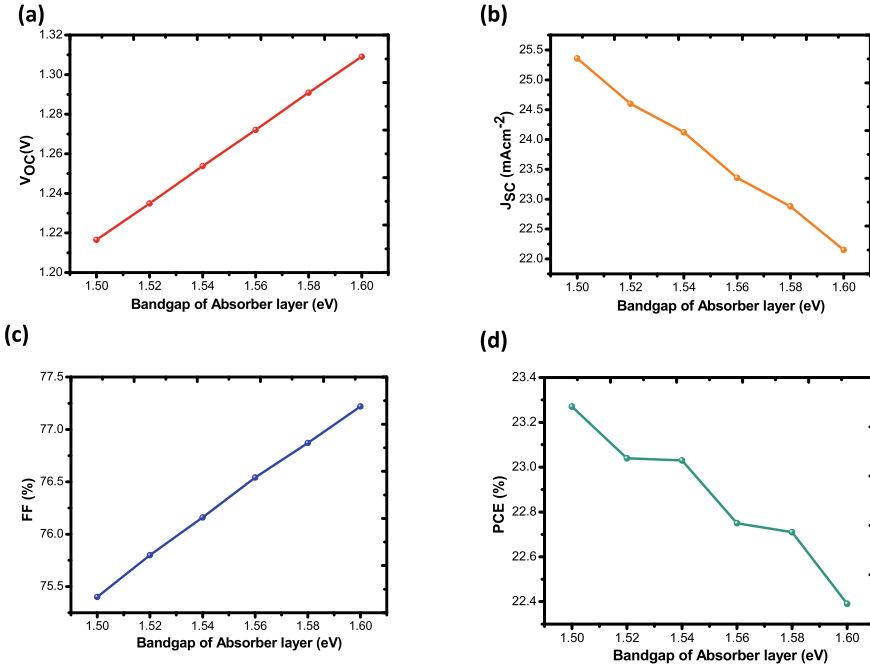
Fig. 5 Effect of Eg in absorber layer on output parameters

decreases with increasing energy band gap because of depletion in photon absorption having energy lower than Eg of the perovskite absorber layer. V_{OC} and FF increase with an increase in Eg as depicted in Fig. 5a, c. PCE decreases continuously with an increase in Eg of the absorber layer as shown in Fig. 5d. When Eg is optimized at 1.50 eV, it results in PCE of 23.27%, FF of 75.40%, J_{SC} of 25.36 mA/cm^2 and V_{OC} of 1.2166 V.

3.4 Variation of ETL Thickness

Further, the variation in output parameters of the proposed device as a function of ETL thickness is depicted in Fig. 6. V_{OC} remains constant throughout the variation and J_{SC} starts decreasing after 30 nm of ETL thickness as depicted in Fig. 6a, b. PCE of the proposed device increases with an increase in ETL thickness reaching a value of 22.71% at an ETL thickness of 20 nm and thereafter it saturates as shown in Fig. 6d. FF also shows a similar variation as that of PCE (Fig. 6c). Since the PCE saturates at 20 nm thickness, so, ETL thickness is optimized at 20 nm resulting in output performance parameters of the presented PSC as: $PCE = 22.71\%$, $FF = 76.35\%$, $J_{SC} = 23.54$ mA/cm^2 and $V_{OC} = 1.2632$ V. The dependence of device
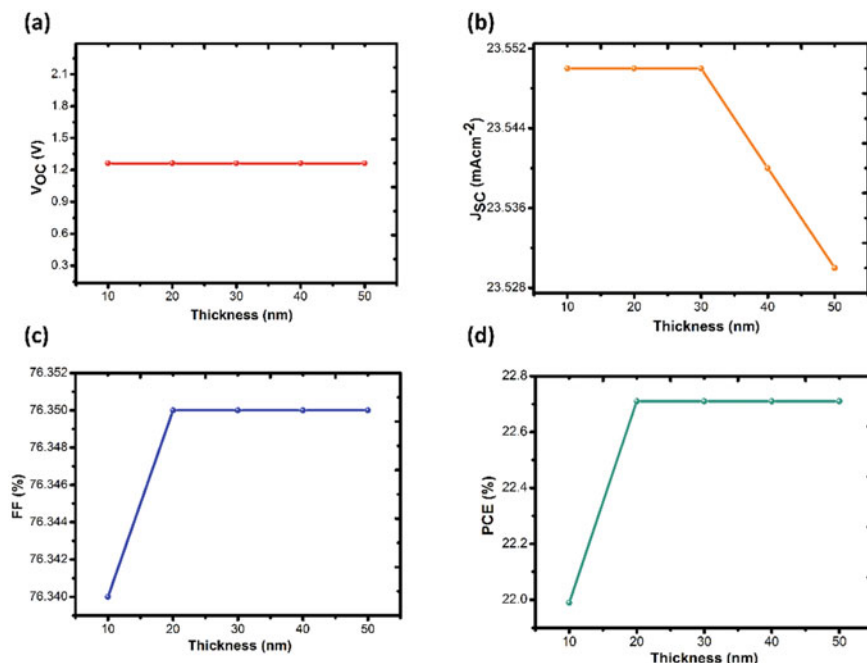
Fig. 6 Effect of ETL thickness on output parameters

performance parameters on HTL thickness has also been investigated and it has been found that there is no effect of HTL thickness on the device performance.

3.5 Dependence of PCE of Device on Back Metal Contact Work Function

Selection of suitable back metal contact is also crucial for crafting efficient perovskite solar cells [30, 31]. Figure 7 shows the dependence of *PCE* of the proposed device on the back metal contact work function. The work function of back metal contact is varied from 4.7 to 5.5 eV and as examined from Fig. 7, *PCE* increases with an increase in work function and attains a value of 25.01% at 5.4 eV work function and thereafter it saturates. So, the improved value of back metal contact work function is chosen as 5.4 eV.

Finally, when the proposed structure is simulated by using the optimized parameters, the solar cell performance is found to be improved with enhanced output parameters as: $V_{OC} = 1.4215$ V, $J_{SC} = 27.62$ mA/cm^2, $FF = 84.51\%$ and $PCE = 33.19\%$. Figure 8 compares the J-V characteristics and QE curves of the proposed solar cell structure, before and after the optimization of the device.
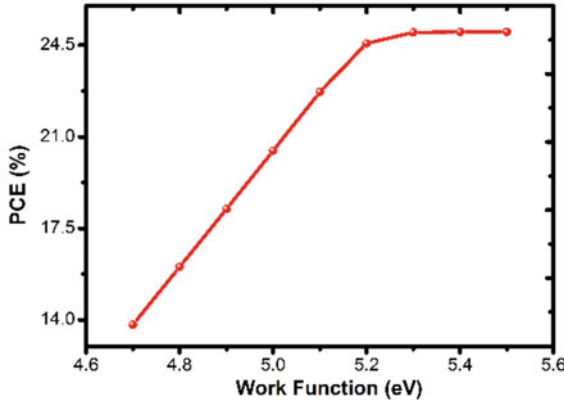
Fig. 7 PCE dependence on back metal contact work function
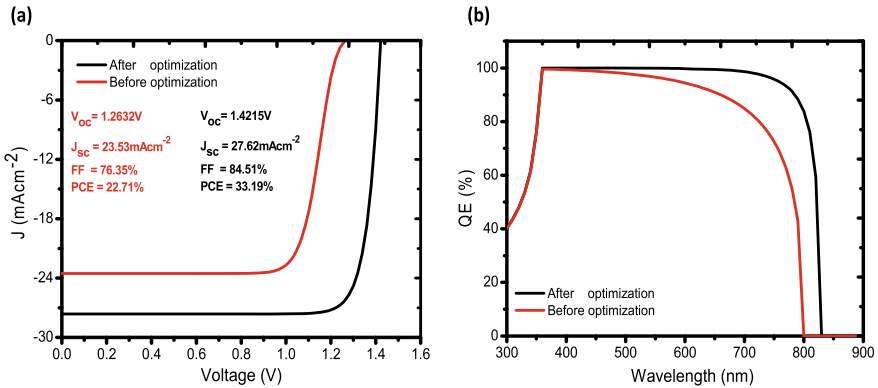
Fig. 8 a J-V characteristics and **b** QE curve; before and after optimization

4 Conclusion

A novel solar cell structure based on mixed halide perovskite $CH_3NH_3PbI_{3-x}Cl_X$ with Spiro-oMeTAD as HTL and $Zn(O_{0.3},S_{0.7})$ as ETL has been proposed. The simulation of the proposed solar cell structure has been carried out using SCAPS-1D software with initial parameters as: $V_{OC} = 1.2632$ V, $J_{SC} = 23.53$ mA/cm^2, $FF = 76.35\%$ and $PCE = 22.71\%$. The crucial parameters of the device have been thoroughly investigated and the optimized thickness, defect density and bandgap of the absorber layer were obtained as 1000 nm, 2.5×10^{11} cm^{-3} and 1.50 eV respectively. Impact of ETL and HTL thickness have also been studied and found that there is no effect of HTL thickness on output device parameters. The optimized value of ETL thickness has been obtained as 20 nm for better efficiency of the device. Moreover, the influence of the back metal contact work function has also been investigated with its optimized

value as 5.4 eV. Finally, when simulated with all the optimized values, the device performance has been found to be greatly enhanced with *PCE* of 33.19%, *FF* of 84.51%, J_{SC} of 27.62 mA/cm^2 and V_{OC} of 1.4215 V.

References

1. Höök M, Tang X (2013) Depletion of fossil fuels and anthropogenic climate change—a review. Energy Policy 52:797–809
2. Scheffran J, Felkers M, Froese R (2020) Economic growth and the global energy demand. Green Energy to Sustainability: Strategies for Global Industries 1–44
3. Kannan N, Vakeesan D (2016) Solar energy for future world:-a review. Renew Sustain Energy Rev 62:1092–1105
4. Park NG (2015) Perovskite solar cells: an emerging photovoltaic technology. Mater Today 18(2):65–72
5. Ansari MIH, Qurashi A, Nazeeruddin MK (2018) Frontiers, opportunities, and challenges in perovskite solar cells: a critical review. J Photochem Photobiol, C 35:1–24
6. Kojima A, Teshima K, Shirai Y, Miyasaka T (2009) Organometal halide perovskites as visible-light sensitizers for photovoltaic cells. J Am Chem Soc 131(17):6050–6051
7. Leijtens T, Eperon GE, Pathak S, Abate A, Lee MM, Snaith HJ (2013) Overcoming ultraviolet light instability of sensitized TiO_2 with meso-superstructured organometal tri-halide perovskite solar cells. Nat Commun 4(1):1–8
8. Zhou H, Chen Q, Li G, Luo S, Song TB, Duan HS, Hong Z, You J, Liu Y, Yang Y (2014) Interface engineering of highly efficient perovskite solar cells. Science 345(6196):542–546
9. Wu Y, Yang X, Chen W, Yue Y, Cai M, Xie F, Bi E, Islam A, Han L (2016) Perovskite solar cells with 18.21% efficiency and area over 1 cm 2 fabricated by heterojunction engineering. Nature Energy 1(11):1–7
10. National Renewable Energy Laboratory (2021) Best research-cell efficiency. https://www.nrel.gov/pv/cell-efficiency.html
11. Noh JH, Im SH, Heo JH, Mandal TN, Seok SI (2013) Chemical management for colorful, efficient, and stable inorganic–organic hybrid nanostructured solar cells. Nano Lett 13(4):1764–1769
12. Dong Q, Fang Y, Shao Y, Mulligan P, Qiu J, Cao L, Huang J (2015) Electron-hole diffusion lengths>175 μm in solution-grown $CH_3NH_3PbI_3$ single crystals. Science 347(6225):967–970
13. Lee MM, Teuscher J, Miyasaka T, Murakami TN, Snaith HJ (2012) Efficient hybrid solar cells based on meso-superstructured organometal halide perovskites. Science 338(6107):643–647
14. Stranks SD, Eperon GE, Grancini G, Menelaou C, Alcocer MJ, Leijtens T, Herz LM, Petrozza A, Snaith HJ (2013) Electron-hole diffusion lengths exceeding 1 micrometer in an organometaltrihalide perovskite absorber. Science 342(6156):341–344
15. Liu M, Johnston MB, Snaith HJ (2013) Efficient planar heterojunction perovskite solar cells by vapour deposition. Nature 501(7467):395–398
16. Fan B, Peng D, Lin S, Wang N, Zhao Y, Sun Y (2015) Enhanced efficiency of planar-heterojunction perovskite solar cells through a thermal gradient annealing process. RSC Adv 5(71):58041–58045

17. Zhao P, Liu Z, Lin Z, Chen D, Su J, Zhang C, Zhang J, Chang J, Hao Y (2018) Device simulation of inverted $CH_3NH_3PbI_{3-X}Cl_X$ perovskite solar cells based on PCBM electron transport layer and NiO hole transport layer. Sol Energy 169:11–18

18. Kaifi M, Gupta SK (2019) Simulation of Perovskite based solar cell and photodetector using SCAPS software. Int J Eng Res Technol 12(10):1778–1786

19. Isoe W, Mageto M, Maghanga C, Mwamburi M, Odari V, Awino C (2020) Thickness dependence of window layer on $CH_3NH_3PbI_{3-X}Cl_X$ Perovskite solar cell. Int J Photoenergy

20. Rakocevic L, Gehlhaar R, Merckx T, Qiu W, Paetzold UW, Fledderus H, Poortmans J (2016) Interconnection optimization for highly efficient perovskite modules. IEEE J Photovoltaics 7(1):404–408

21. Stuckelberger M, Nietzold T, Hall GN, West B, Werner J, Niesen B, Ballif C, Rose V, Fenning DP, Bertoni MI (2016) Charge collection in hybrid perovskite solar cells: relation to the nanoscale elemental distribution. IEEE J Photovoltaics 7(2):590–597

22. Bansal S, Aryal P (2016) Evaluation of new materials for electron and hole transport layers in perovskite-based solar cells through SCAPS-1D simulations. In: 2016 IEEE 43rd photovoltaic specialists conference (PVSC), pp 0747–0750

23. Patel PK (2021) Device simulation of highly efficient eco-friendly $CH_3NH_3SnI_3$ perovskite solar cell. Sci Rep 11(1):1–11

24. Zhang B, Zhang MJ, Pang SP, Huang CS, Zhou ZM, Wang D, Wang N, Cui GL (2016) Carrier transport in $CH_3NH_3PbI_3$ films with different thickness for perovskite solar cells. Adv Mater Interfaces 3(17):1600327

25. Roy P, Sinha NK, Tiwari S, Khare A (2020) Influence of defect density and layer thickness of absorption layer on the performance of tin based perovskite solar cell. In: IOP conference series: materials science and engineering, vol 798(1), pp 012020, IOP Publishing

26. Kim H, Lim KG, Lee TW (2016) Planar heterojunction organometal halide perovskite solar cells: roles of interfacial layers. Energy Environ Sci 9(1):12–30

27. Ahmadian-Yazdi MR, Zabihi F, Habibi M, Eslamian M (2016) Effects of process parameters on the characteristics of mixed-halide perovskite solar cells fabricated by one-step and two-step sequential coating. Nanoscale Res Lett 11(1):1–11

28. Shi D, Adinolfi V, Comin R, Yuan M, Alarousu E, Buin A, Chen Y, Hoogland S, Rothenberger A, Katsiev K, Losovyj Y (2015) Low trap-state density and long carrier diffusion in organoleadtrihalide perovskite single crystals. Science 347(6221):519–522

29. Chae J, Dong Q, Huang J, Centrone A (2015) Chloride incorporation process in $CH_3NH_3PbI_{3-x}Cl_X$ perovskites via nanoscale bandgap maps. Nano Lett 15(12):8114–8121

30. Sultana NA, Islam MO, Mahmood ZH (2017) Utilization of low cost metals as back contact with Perovskite solar cell. Dhaka University J Appl Sci Eng 4(1):35–38

31. Behrouznejad F, Shahbazi S, Taghavinia N, Wu HP, Diau EWG (2016) A study on utilizing different metals as the back contact of $CH_3NH_3PbI_3$ perovskite solar cells. J Mater Chem A 4(35):13488–13498

Multi-input Single-Output Superboost DC-DC Converter for Solar-Powered Electric Vehicle

Divya Chandran, A. Haseena, and K. Biju

Abstract As the pollution is increasing due to fossil fuel usage, electric automobile is gaining popularity. Among electric vehicles, solar-powered electric vehicle is getting more focus. In this paper; a multi-input single-output superboost DC-DC converter for solar-powered electric vehicle is proposed. Here, solar, battery, and the supercapacitor are the three inputs. The energy developed due to regenerative breaking is stored in supercapacitor and later used for high-speed operation along with photovoltaics (PV) and battery. The presence of supercapacitor increases the system reliability and efficiency. The operation principle, analysis, and detailed waveform of different modes are presented in this study. The performance of the MISB converter is verified through simulations.

Keywords Multi-input converter · Solar photovoltaic · DC-DC converter · State of charge (SOC) · Supercapacitor

1 Introduction

As the consumption of fossil fuel is increasing, the pollution increases as well as the fossil fuel depletion occurs. In order to reduce the use of fossil fuel, an alternative solution is sustainable energy sources. Nowadays, solar-powered electric vehicles (SPEVs) become popular and leading. In [1], a dual-input superboost converter has been discussed. The energy from regenerative breaking is fed back to a breaking

D. Chandran (✉) · A. Haseena
Department of Electrical Engineering, Rajiv Gandhi Institute of Technology, Kottayam, Kerala, India
e-mail: divyachandrandivya@gmail.com

A. Haseena
e-mail: haseenaa@rit.ac.in

K. Biju
Department of Electrical Engineering, College of Engineering, Munnar, Kerala, India
e-mail: bijuk@ieee.org
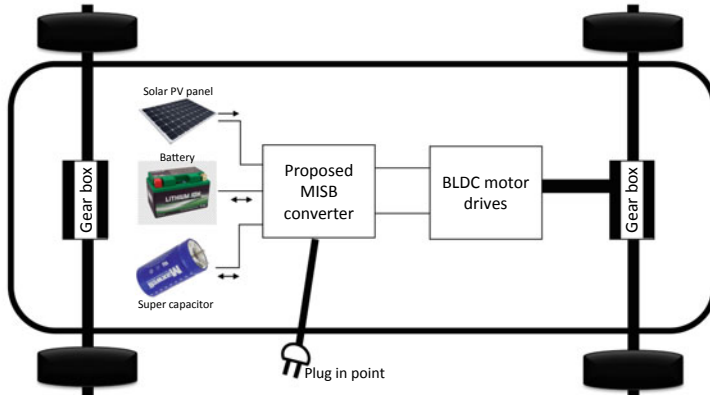
Fig. 1 PV-operated vehicle with MISB converter

resistance, and the energy is dissipated as heat. In order to extract this energy, a multi-input single-output superboost DC-DC converter (MISB) for solar-powered electric vehicle is proposed. Non-isolated topology is used for the converter to obtain high voltage; it needs only less number of turns. The output voltage is controlled by voltage regulator [2]. In [3], a three-port series resonant DC-DC converter is discussed. It uses three ports, first and second port for the input sources and third for the load. In [4], an interleaved three-port converter is discussed for hybrid energy systems where diode is coupled to full bridge rectifier through a high-frequency transformer. The three-port converter configuration is realized using boost converter topology and the voltage equalizer circuit used for balancing the voltage levels of the connected batteries [5]. The three-port rectifier for AC input and two DC output was designed [6]. In [7], a power management scheme for a modular three-port converter used in satellite application is discussed. Battery state of charge control is done based on the modes of operation. In [8], advantages of non-isolated three-port converter have been discussed which include reduced number of components, cost-effectiveness, and compact in size. In [9], a voltage multiplier-based DC-DC converter has been discussed. The system can act as a multiport converter when two sources are available and operate in the interleaved mode when connected to a single source. In [10], different types of multiport converter systems and control methods used have been discussed. In [11, 12] discusses isolated three-port DC-DC converter that operates in both boost and buck modes of operation and incorporates flyback topology. In [13], the system consists of magnetic switch used for maintaining continues input current of solar PV, and a control strategy is proposed for the generation of battery management command and satisfying load power demand. In [14] designed a single inductor-based non-isolated three-port converter for interfacing both photovoltaic and battery energy management systems. Implementation of application of isolated full bridge three-port converter for interfacing renewable energy sources is discussed in [15].

In commercial electric vehicles (EVs), during braking, regenerative energy is generated due to rotational inertia. The energy developed due to regenerative braking

is expended as heat through a dynamic brake resistor. To overcome this drawback, a novel multi-input single-output superboost DC-DC converter for solar-powered electric vehicle is proposed in this paper. The proposed MISB converter enables to integrate multiple inputs. The three inputs are PV, battery, and supercapacitor. The power generated due to braking is fed back to the supercapacitor and used for high-speed operation along with PV and battery. Figure 1 shows the configuration of PV-operated electric vehicle with the proposed converter configuration. It allows the EV to integrate multiple inputs and does not require a separate charge controller and DC-DC converter to charge the battery. There is a plug in point which helps to charge through an external source. Moreover, it can also provide power to the utility grid thereby reduce the peak demand, and in addition, it maintains the frequency and voltage of the utility grid.

By using conventional configuration in commercial electric automobile, for operating in six modes, three separate converters are required. Proposed converter reduces the cost and complexity from conventional configuration as it requires less number of devices in each mode to perform same operations. It is more reliable and has extensive range of speed control with less ripple and finer dynamic characteristics. The operating waveform, equations, and simulation results under six different modes are explained comprehensively in the succeeding sections.

2 Operation Principle

There are six modes of operation for the proposed MISB converter,

1. PV-operated mode
2. Cell-operated mode
3. Stationing at daytime
4. Stationing at nighttime
5. Supercapacitor-operated mode
6. Superboost mode.

The circuit diagram for the proposed MISB converter is shown in Fig. 2. It allows to restore the battery from multiple inputs like grid and supercapacitor. This will give smooth and clean operation of battery and increases the life of batteries. The presence of supercapacitor enables to store the energy from breaking, and also, this enables fast braking and increases system reliability and efficiency.

The proposed converter operates under six modes. In mode 1 that is battery state of charge (SOC) >80%, the motor is run by the power from solar radiation; therefore, it is called PV-operated mode, and switch S_2 is ON. With no solar irradiation, the motor is run by the power from battery. This is called cell-operated mode. It is similar to mode 1. Here, S_2 is continuously ON. In mode 3, vehicle is in parking lot at day time, the PV either charges battery or to the external source depends on the SOC. The energy developed from PV is given to the external source V_{ext} if SOC>80% otherwise used to recharge the battery or cell. In mode 4, the EV is in parking lot at nighttime;
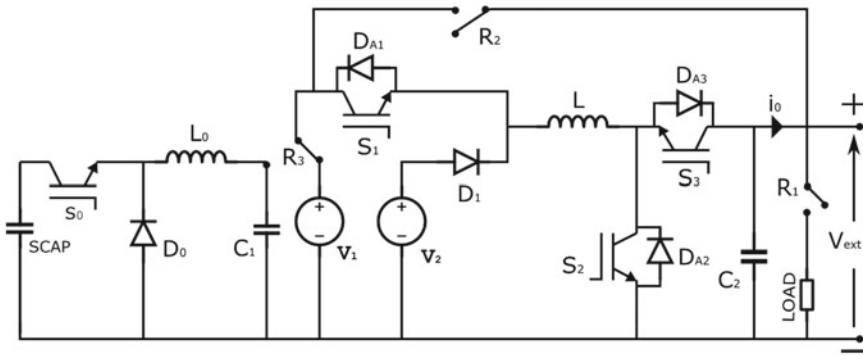
Fig. 2 Circuit diagram of proposed MISB converter

an external source is used to charge the battery. This operational mode is called stationing at nighttime. Here, the converter operates in buck mode. During braking, the regenerative braking power is extracted and given to the supercapacitor till null speed achieves. This mode is called supercapacitor-operated mode. In superboost mode, the energy supplied from PV, battery, and supercapacitor is used for high-speed operation or superboost operation. This mode is called superboost mode.

As mentioned above, except on high-speed operation, the converter either operates on boost or buck operation. In high-speed operation, the power supplied to the motor by PV, cell, and supercapacitor. The combined energy is released to the motor. This is a distinctive feature of the proposed converter. Initially, the energy stored in the supercapacitor is fed to the battery, and the voltage across the battery becomes v_1'.

The operating waveform for high-speed operation is illustrated in Fig. 3. It shows the gate pulse for switch S_1 and S_2, v_L and i_L, respectively. From 0 to t_1, S_1 is turned ON, the current i_L increases from i_{L0} to i_{L1} due to v_1'. At instant t_1, S_1 is turned off, and from t_1 to t_2, current rises from i_{L1} to peak i_{Lp} due to source V_2. At t_2, S_2 is switched off, and inductor current starts discharging up to T_s. The voltage across the inductor is $v_2 - v_0$.

The average value of inductor voltage is null as per voltage time balance principle. Therefore, the equation becomes

$$v_1'd_1 + v_2(d_2 - d_1) + (v_2 - v_0)(1 - d_2) = 0 \tag{1}$$

where d_1 and d_2 be the duty ratio of switch S_1 and S_2. After simplifying (1), the voltage output of the proposed MISB converter is

$$V_0 = \frac{v_1'd_1 + v_2(1 - d_2)}{1 - d_2} \tag{2}$$

At $d_1 = 0.6$ and $d_2 = 0.8$ during high-speed operation, the maximum output voltage is obtained as
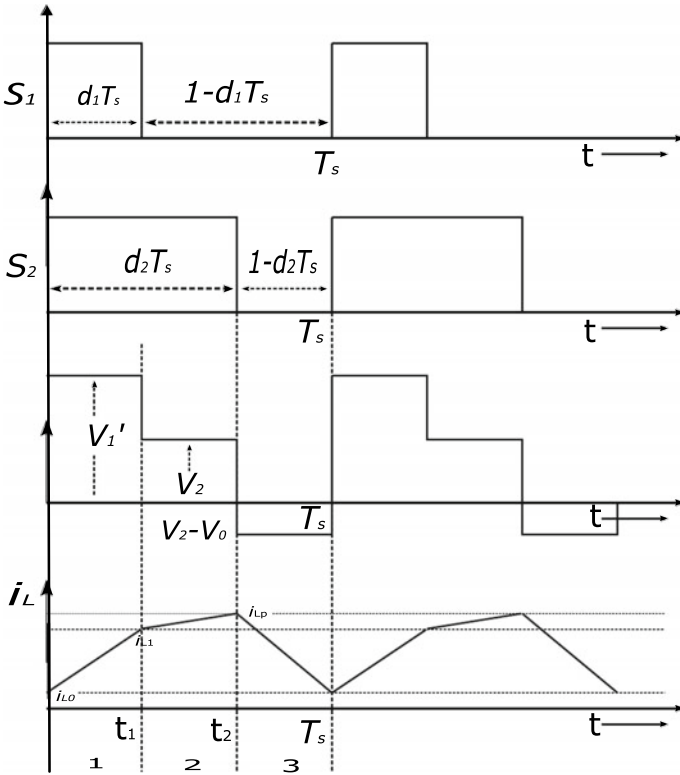
Fig. 3 High-speed operating waveform

Table 1 Active devices in each mode

Operating modes	Switches	Active devices diodes	Relays
Solar mode	S_2	D_1, D_{A3}	R_1
Battery mode	S_1, S_2	D_{A3}	R_1, R_3
Parking in daytime mode SOC<80%	S_2	D_1, D_{A3}	R_2, R_3
Parking in daytime mode SOC>80%	S_2	D_1, D_{A3}	None
Parking in nighttime mode	S_3	D_{A1}, D_{A2}	R_3
Regenerative mode	S_0	None	R_1, R_2, R_3
High-speed mode	S_1, S_2, S_0	D_1, D_{A3}	R_1, R_3

$$V_{\max} = 3V_1 + 2V_2 \tag{3}$$

The output voltage increases as d_1 and d_2 increases. By this, it is understandable that a broad range of speed control can be obtained. The equivalent circuit of proposed
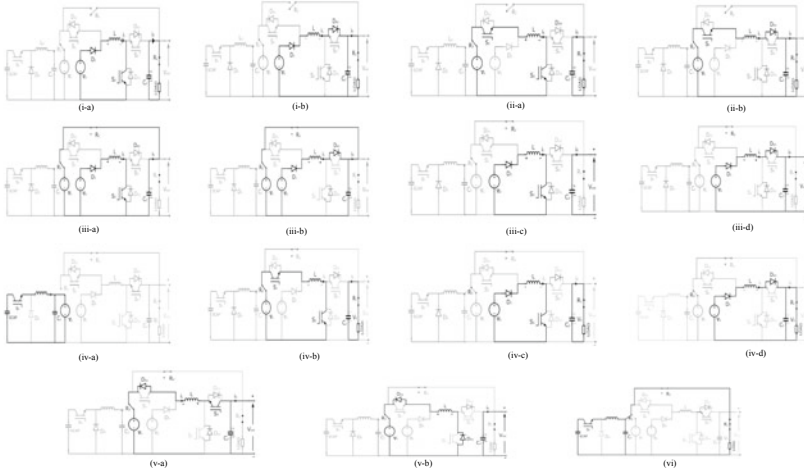
Fig. 4 Equivalent circuit of MISB converter

MISB converter is depicted in Fig. 4. Inductor L stores energy from V_2 when S_2 is turned ON as seen in Fig. 4i(a). Inductor L releases its power to the motor through D_{A3} as shown. This mode is PV-operated mode. The equivalent diagram for cell-operated mode is depicted in Fig. 4ii. The mode 2 is similar to mode 1. Here, S_2 is continuously ON. Inductor stores energy from V_1, when S_1 is ON, and it discharges to load through D_{A3}. While the automobile is in parking lot at daylight, the inductor stores energy from V_2. The equivalent circuit is depicted in Fig. 4iii. If the battery SOC < 80%, the inductor delivers its energy to the cell battery as in Fig. 4iii(b), else inductor L delivers its energy to external source V_{ext}.

The unique feature of the converter is superboost mode, the equivalent circuit of superboost operation as depicted in Fig. 4iv. In this superboost mode, the energy stored in supercapacitor from regeneration is discharged to the cell V_1 and the inductor L initially stores energy from V_1 and then by V_2 is clearly seen in Fig. 4iv(b) and Fig. 4iv(c). This combined power is finally delivered to the motor depicted in Fig. 4iv(d). The power is controlled by S_1 and S_2. The equivalent circuit of stationing at nighttime mode is depicted in Fig. 4v. In this, the inductor L stores energy from $_{Vext}$, and it is discharged to the battery V_2. Here, S_3 controls the power. In this mode, the converter is in buck operation. The equivalent circuit of supercapacitor-operated mode is seen in Fig. 4vi. In supercapacitor-operated mode, the energy developed due to rotational inertia during braking is given back to a supercapacitor. Supercapacitor stores this energy and used for high-speed operation. This mode is similar to parking in nighttime mode. The active devices in each mode are shown in Table 1.

3 System Design

The various working stages linked with the topology are depicted in Fig. 1. Solar array, proposed MISB converter, and brushless DC motor are chosen suitably to get better performance with their ideal design. The design strategies of these system parts are explained in this section.

3.1 Design of Solar Array

A photovolatic cell is an electrical device that converts solar or light energy to electrical energy by the photovoltaic effect. When exposed to light, electrical characteristics such as current, voltage, and resistance vary [13]. Equation (1) describes the current drawn from the solar cell.

$$I = I_{\text{sh}} - I_{\text{d}} = I_{\text{sh}} - I_0 \frac{e^{(V+IR_{\text{s}})}}{aKT_{\text{c}}} \tag{4}$$

where a is the idealizing aspect, k be the Boltzmann's constant and V is the voltage imposed across the cell. The essential parameters of a solar cell are following: The maximum developed electrical current under short-circuit instants is called short-circuit current (Isc) in which voltage across a cell is null. The voltage of cell during absence of solar radiation is called open-circuit voltage in which generated current is null and is given by the equation

$$V_{\text{opencircuit}} = V_{\text{t}} \ln \frac{I_{\text{sh}}}{I_0} \tag{5}$$

3.2 Design of Proposed Converter

The voltage available at the converter input is the solar PV array voltage Vpv and the battery voltage. The output voltage is kept as 240 V which is given to the BLDC motor.

The relation between V_{in}, V_{o} and duty ratio, D is given by,

$$V_0 = \frac{v_1 d_1 + v_2(1 - d_2)}{(1 - d_2)} \tag{6}$$

$$L = \frac{V_{\text{in}} D}{\Delta I_L f_{\text{s}}} \tag{7}$$

Table 2 Simulation parameters

Parameters	Specification
Source V_1	36 V
Source V_2	38 V
Supercapacitor	40 V
Capacitor C	470 μF
Capacitor C_0	470 μF
Inductor L	3 mH
Inductor L_0	1 mH
Switching frequency	20 kHZ

$$C = \frac{I_o D}{f_s v_o} \qquad (8)$$

$$L_0 = \frac{D V_{\text{in}}}{f_s \Delta I_{L0}} \qquad (9)$$

where f_s is the switching frequency and ΔI_L is ripple in the current through L (Table 2).

3.3 Battery

A battery is a 36 V, 80 Ah lithium-ion (Li-ion) cell. This is the most prominent electrochemical energy storage device which uses lithium ions as the major component of its electrochemistry. Lithium atoms in the anode are ionised and separated from their electrons during discharge cycle. These Li-ions move from the negative electrode anode to positive electrode cathode through the electrolyte. In positive electrode, lithium ions recombine with their electrons and electrically neutralize. Between the positive and negative electrodes, there is a micro-permeable separator through which these ions move as these ions are small. Moderately, due to the small size of lithium (third only to hydrogen and helium), lithium-ion cells have high charge storage per unit mass and high cell voltage.

3.4 BLDC Motor

1000 W BLDC motor is used for electric automobile. Brushless DC motor produces both rotor and stator magnetic fields. The BLDC motor has high speed, high power-to-weight ratio, extensive life, lower losses, high starting torque has a higher efficiency without brushes and mechanical commutator. There are many configu-

rations of BLDC motor. Out of many, in electric automobiles, three-phase motors are broadly used and most accepted in electric cars. A hub motor is selected for the vehicle is as the motor replaces the hub of the wheel. Without using belts or chains, mounting would be easier that minimizes weight and size of the automobile. Coupling loss is reduced.

3.5 *Comparison with Existing Topology*

In [1], a dual-input superboost DC-DC converter has been discussed where PV and battery are the two inputs, three switches, three diodes, one inductor, and one capacitor. PV can provide power to the motor moreover can charge and discharge the battery, but the source voltage of the one input source should be always larger than the other. The efficiency of the dual-input converter is 87–93%. During regenerative breaking, the power generated is given to breaking resistor, and the energy is dissipated as heat. To overcome this drawback, the proposed MISB converter is introduced with four switches, four diodes, two inductor, and two capacitor. Here, the regenerative energy is given back to the supercapacitor, and this stored energy is later used for superboost operation.

4 Simulation Results

The algorithm was built using MATLAB simulink. The motor speed in rpm is depicted in Fig. 5. Figures 6 and 7 show the simulation result of each mode. It shows the inductor current, output current, inductor voltage, and output voltage, respectively. The simulation result of PV-operated mode and stationing at daytime mode is depicted in Fig. 6. In mode 1 and mode 2, the results are almost similar. The inductor current rises due to V_2 and decays when S_2 is OFF in mode 1 as shown in Fig. 6a.

Fig. 5 Motor speed
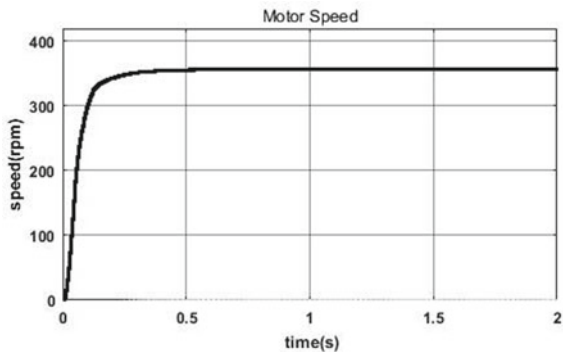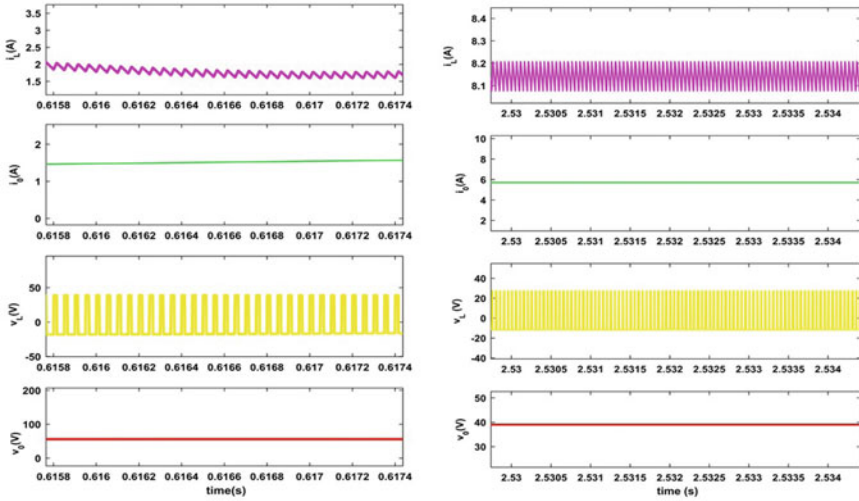
Fig. 6 Simulation result of PV-operated mode and stationing at daytime
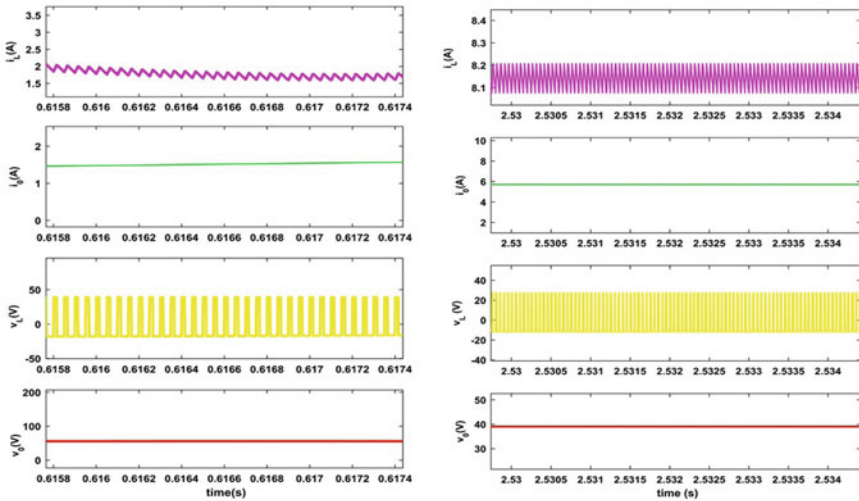
Fig. 7 Simulation result of supercapacitor mode and superboost mode

While in mode 2, i_L increases by V_1 and decays during off state of S_1. The simulation result of stationing at daytime mode is depicted in Fig. 6b. The simulation result of supercapacitor mode is shown in Fig. 7a, From the result, the inductor current obtained has a negative value due to regeneration. In supercapacitor mode, an external voltage is supplied at the load side and made to operate the MISB converter in buck mode. In superboost mode as shown in Fig. 7b, inductor get charged in two stages. The inductor current rises because of V_1 and again increases because of V_2 and

finally decays when S_1 and S_2 are turned OFF. The output is ripple free. As the output voltage is ripple free, battery has a better life cycle. When compared to conventional converter, we can summarize that MISB converter has greater efficiency.

5   Conclusion

A multi-input single-output superboost DC-DC converter for solar-powered electric automobile is modeled, simulated, and examined using MATLAB/SIMULINK tool. The proposed MISB converter efficiently uses the PV energy by working in six different modes. Also, it has the advantages of extracting regenerative energy and broad range of speed control thereby increasing the efficiency. The detailed analysis of the proposed system is presented with necessary waveforms. The performance of the proposed system is validated through simulations. Results confirm that the MISB converter is more suitable for electric automobile applications.

References

1. Guru Kumar G, Sundaramoorthy K, Athikkal S, Karthikeyan V (2019) Dual input super boost DC-DC converter for solar powered electric vehicle. IET Power Electron 12:2276–2284. https://doi.org/10.1049/iet-pel.2018.5255
2. Chien L, Chen C, Chen J, Hsieh Y (2014) Novel three-port converter with high-voltage gain. IEEE Trans Power Electron 29:4693–4703. https://doi.org/10.1109/tpel.2013.2285477
3. Krishnaswami H, Mohan N (2009) Three-port series-resonant DC-DC converter to interface renewable energy sources with bidirectional load and energy storage ports. IEEE Trans Power Electron 24:2289–2297. https://doi.org/10.1109/tpel.2009.2022756
4. Mira M, Zhang Z, Knott A, Andersen M (2017) Analysis, design, modeling, and control of an interleaved-boost full-bridge three-port converter for hybrid renewable energy systems. IEEE Trans Power Electron 32:1138–1155. https://doi.org/10.1109/tpel.2016.2549015
5. Wu J, Jou H, Hung C (2016) Three-port power converter for a solar charger. Int J Electron 104:355–368. https://doi.org/10.1080/00207217.2016.1216180
6. Wu H, Han M, Zhang Y (2017) Three-port rectifier-based AC-DC power converters with sigma architecture and reduced conversion stages. IEEE J Emerg Selected Top Power Electron 5:1091–1101. https://doi.org/10.1109/jestpe.2017.2648859
7. Zhang J, Wu H, Xing Y et al (2016) Power management of a modular three-port converter-based spacecraft power system. IEEE Trans Aerospace Electron Syst 52:486–492. https://doi.org/10.1109/taes.2015.140808
8. Zhang N, Sutanto D, Muttaqi K (2016) A review of topologies of three-port DC-DC converters for the integration of renewable energy and energy storage system. Renew Sustain Energy Rev 56:388–401. https://doi.org/10.1016/j.rser.2015.11.079
9. Prabhala V, Fajri P, Gouribhatla V et al (2016) A DC-DC converter with high voltage gain and two input boost stages. IEEE Trans Power Electron 31:4206–4215. https://doi.org/10.1109/tpel.2015.2476377
10. Mihai M (2015) Multiport converters—a brief review. In: 2015 7th international conference on electronics, computers and artificial intelligence (ECAI). https://doi.org/10.1109/ecai.2015.7301246

11. Sun X, Shen Y, Li W, Wu H (2015) A PWM and PFM hybrid modulated three-port converter for a standalone PV/Battery power system. IEEE J Emerg Select Top Power Electron 3:984–1000. https://doi.org/10.1109/jestpe.2015.2424718

12. Hu Y, Xiao W, Cao W et al (2015) Three-Port DC-DC converter for stand-alone photovoltaic systems. IEEE Trans Power Electron 30:3068–3076. https://doi.org/10.1109/tpel.2014.2331343

13. Zhu H, Zhang D, Liu Q, Zhou Z (2016) Three-port DC/DC converter with all ports current ripple cancellation using integrated magnetic technique. IEEE Trans Power Electron 31:2174–2186. https://doi.org/10.1109/tpel.2015.2433675

14. Chen Y, Zhang P, Zou X, Kang Y (2014) Dynamical modeling of the non-isolated single-inductor three-port converter. In: 2014 IEEE applied power electronics conference and exposition—APEC 2014. https://doi.org/10.1109/apec.2014.6803591

15. Hu W, Wu H, Xing Y, Sun K (2014) A full-bridge three-port converter for renewable energy application. In: 2014 IEEE applied power electronics conference and exposition—APEC 2014. https://doi.org/10.1109/apec.2014.6803289

Solar Photovoltaic (SPV) Fed Water Pumping—A Review

Raj Kumar and K. B. Yadav

Abstract Amongst all of the renewable energy sources available, solar energy is known as the more significant. In the agricultural and industrial sectors, solar water pumping systems are attracting comprehensive publicity as they are environmentally sustainable and free from the cost of fuel. Conventional electricity-driven water pumps appear to be inefficient and the fuel cost of diesel pumps has risen. The key purpose of this report is to provide a detailed survey and analysis of solar PV powered water pumping systems that uses AC IM (Induction Motor), Permanent Magnet Brushless DC (PMBLDC) motors and DC brushed motors. Due to its high performance, high consistency and low maintenance requirements, the PMBLDC motor is a better alternative for AC IM and DC brushed motors in the application of water pumping. The study emphases on the study results of solar PV liquid pumping arrangements with dc-dc converters and without dc-dc converters using different motor drives.

Keywords Solar PV (Photovoltaic) · Water pump · DC-DC converter · Permanent magnet brushless DC (PMBLDC) motor · AC IM (induction motor)

1 Introduction

Due to population growth, industrialization and transportation, energy demand is growing considerably nowadays. That fossil with this rise in energy demand, fuel depletion is high. Sincere attempts are being made around the world to exploit green energies. Sources and the adoption of those energy sources for their financial and community growth. Solar energy is considered amongst all existing renewable energy sources to be the most viable source of energy, and successful production can easily

R. Kumar (✉) · K. B. Yadav
Department of EE, NIT Jamshedpur, Jharkhand 831014, India
e-mail: rajk7250@gmail.com

K. B. Yadav
e-mail: kbyadav.ee@nitjsr.ac.in

satisfy the world's current demand for energy. Solar photovoltaic arrangements have developed today as an auspicious solution for industrial usage, space jet, domestic applications, and irrigation in a nation like India with ample sunbeams but minimal fossil-fuel asset [1]. As an agriculture sector-dominated country employing approximately half of the community, solar driven water pumping arrangements are rapidly becoming an efficient, nature friendly and inexpensive solution for farmers' irrigation needs, minimizing the use of traditional diesel and electric pumps. By eliminating CO_2 emissions, the addition of fossil-fuel water pumping with solar driven water pumping pays to nature protection. Due to the constraints of grid-based electricity supply in rural and isolated zones, separate PV powered water pumping arrangements are evolving as an interesting resolution to encounter power needs.

2   Solar Photovoltaic (SPV) Water Pump Arrangement

Since there are no moving parts in solar PV structures, they are flexible and operation cost is low. Solar photovoltaics have a relatively longer span of life, and it requires less maintenance. PV systems, on the other hand, it has a high starting setup cost, conversion of solar-to-electricity yield is poor, and nonlinear voltage-current (I-V) characteristics. PV systems have been introduced as one of the most powerful renewable energy sources for feeding stand-alone applications when compared to grid electricity. The main focus of research is on shortening the payback time in terms of increased productivity and output, and also trying to decrease the amount of components to reduce the overall costs. As a result, researchers have concentrated their efforts on three key areas.

- Method of construction of solar PV arrays: Several scientific attempts have been made to develop the material and PV cell production process [2].
- Controlling the amount of sunlight that reaches the solar PV: solar collectors for the tracking of sun or reconfiguration of solar module in the solar PV arrangement leads to improvements in several factors to increase the amount of insolation striking on the array's surface [3, 4].
- Consumption of solar arrays' output electric power [5]: In off-grid [6–10] or on-grid solar photovoltaic systems [11–15], attempts are being made to increase the efficient use of solar energy [16, 17].

Solar photovoltaic water pumping arrangement is generally classified as AC and DC motor pumping structures shown in Figs. 1, 2 and 3 [18–21]. In industrial development and growth in the human community, electric drives show a vital role. About 40 percent of energy disbursement arises in motors in drive systems. Therefore, in applications involving electric drives, such as PV powered liquid pumping, engines play a significant role [22]. Conventional brushed DC motors were initially used for water pumping applications. Owing to the presence of brushes and commutators, drawbacks such as low performance and constant maintenance for DC motors contribute to the operation of the AC IM for liquid pumping utilization.
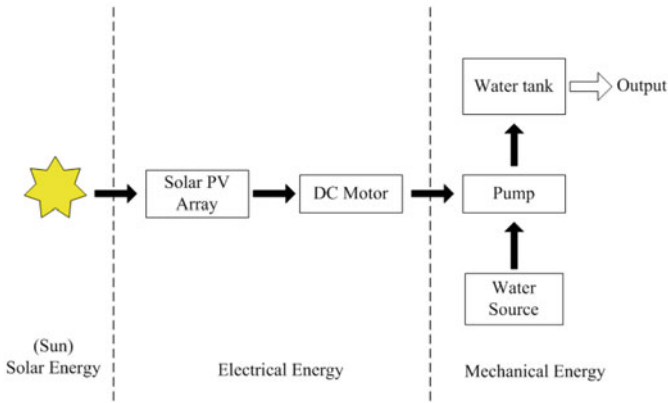
Fig. 1 Solar PV fed water pump with DC motor
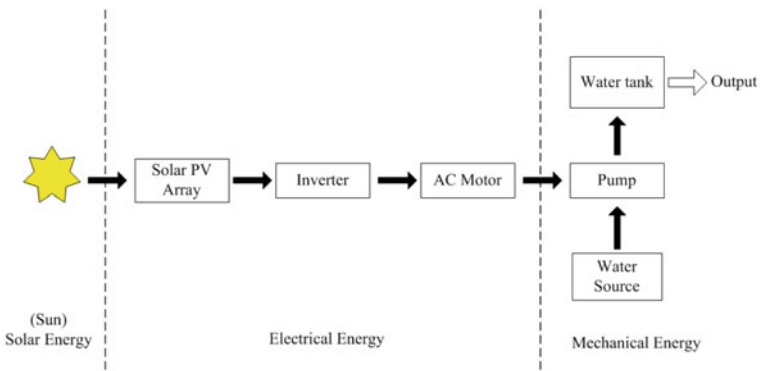
Fig. 2 Solar PV fed water pump with AC motor
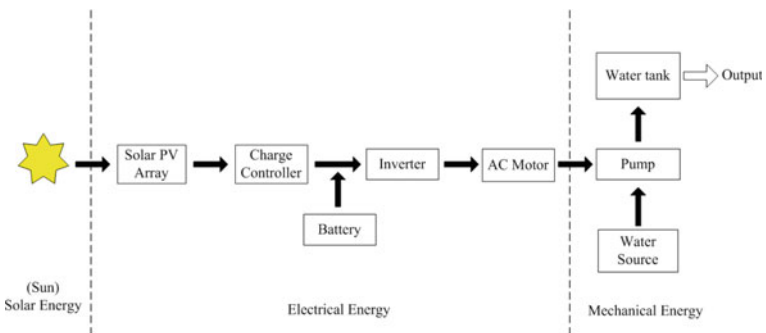
Fig. 3 Solar PV fed water pump with AC motor and battery backup
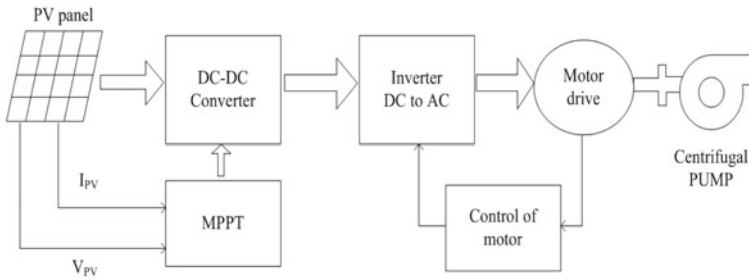
Fig. 4 Pumping of water with a motor drive powered by solar PV

For photovoltaic applications without transitional converters [23], the transient outputs [24], steady state, and the starting of solar power fed brushed DC motors for constant load torques and water pump load torques were studied in the early 1980s [25–27]. These motors were large and needed to be serviced often. Solar-powered PMBLDC motors with and without intermediate converters are being used for water pumping applications [28–31] (Fig. 4).

A power electronic converter is used in conjunction with one of the maximum power monitoring algorithms to map a maximum power point. The maximum power point tracking controller's goal is to determine the maximum voltage V_m and maximum current I_m at which the photovoltaic device has to be run in order to maximize photovoltaic power P_m at several changing atmospheric conditions. In a DC-DC converter type maximum power point tracking controller [32], the reference current and voltage are perturbed either with a negative step if the power slope is negative [33] or with a positive step if the power slope is positive to approach the maximum power point using either voltage mode control or current mode control to approach the maximum power point [34].

PMBLDC motors have been increasingly common in recent years [35]. Since it does not have brushes, the PMBLDC motor is electronically commutated. PMBLDC motors have a number of benefits, including heavy-duty operation, a higher speed-to-torque ratio, lower noise, better dynamic response, a wider speed range, and a more durable design. Due to these benefits PMBLDC motors are used in water pumps instead of other DC and AC motors.

3 Literature Survey

In 1996, a low-cost and extremely efficient PV driven PMBLDC motor drive arrangement for the application of pumping of liquid was suggested by Singh et al. [36]. Without any external DC-DC converters, the structure used a sensor-less control process. The system's conceptual model was created, and the dynamic characteristics of the PMBLDC motor drive arrangement were tested using a simple low-cost

microcontroller. With experimental values and the simulated results obtained were tested and at multiple power levels, the planned model was found to work well.

In 2010, the performance of PV fed water pump using a permanent magnet brushless DC (PMBLDC) motor was described by Hosseini et al. In this MPPT (maximum power point tracking) technique Zero-source inverter (ZSI) was used to feed the PMBLDC motor [37]. For the abolition of swing at the point of operating, developed a fuzzy-logic based INC-MPPT. For the control of PMBLDC, motor speed PSO (particle swarm optimisation) algorithm was used so that its dynamic response is better. In this paper, using PSCAD/EMTDC and MATLAB tools, the implementation of the developed arrangement was computed for various working situations of the PV array. Small torque ripples were accomplished by the inverter voltage regulation control, according to the simulation performance.

In 2012, For PV powered water pumping arrangements, the author Terki et al. examined the output of a PMBLDC motor operated by a hysteresis current loop. In this paper two types of controllers were used, fuzzy-logic and classical PI controller [38]. The system's control by these kinds of controllers was analyzed at load and no load, as well as the overall system output. For both controllers, the results demonstrate that the speed meets the reference speed very easily with zero steady state error and without overshoot, but the Fuzzy-Logic (FL) controller confirms much improved dynamical possessions for nonlinear and complex control systems.

In 2013, To search for a result that better fits the MPPT, the author Taghvaee et al. identified related studies on nonisolated DC-DC CUK, boost, buck, buck-boost, and single-ended primary-inductor (SEPIC) converters [39]. The analysis was divided into four categories: converter topology, operating area, implementation, and topologies' merits and demerits. An analysis of converters was also performed. The buck-boost converter had the highest efficiency rating of 96.2%, according to the report, as opposed to other converters that had lower efficiencies. The buck-boost DC-DC converter was found to be the finest kind of converter for Photo Voltaic systems, as it had the capability to guarantee maximum MPPT output for each load condition, cell temperature, and solar irradiation while correspondingly improving the system's performance.

In 2014, The author Kumar and Singh created a solar PV powered LUO converter-based PMBLDC motor-operated liquid pumping arrangement [40]. A negative output basic LUO converter was chosen because it provided advantages such as an infinite MPPT operating area, a continuous process mode, and decreased output current ripple. According to simulation results, the PMBLDC motor driven pump directories achieved their rated values under steady state, and under less solar irradiation, the motor also sustained a speed larger than 1100 rpm.

In 2014, The author Kumar and Singh discusses and designs a CSC (canonical switching cell) converter for use as an alternative DC-DC converter in a PV-fed PMBLDC motor drive for a liquid pumping arrangement [41]. Unlike buck and boost converters, the canonical switching cell converter doesn't have a limited MPPT operating range. The maximum power was tracked using the Incremental Conductance MPPT algorithm. The proposed water pumping system's comprehensive output for different modes of operation was obtained by simulation, and the outcomes indicated

that the system achieved steady state values for the provided irradiance levels, as well as gentle starts of the PMBLDC motor.

In 2016, Kumar and Singh proposes a PMBLDC motor drive for a solar PV array-powered water pumping arrangement that is quick, cost-effective, and reliable. The full capacity available from the SPV array is obtained using a zeta converter [42]. The suggested method removes phase current sensors and adapts the voltage source inverter (VSI) to a fundamental frequency switching mode, eliminating power losses due to excess frequency switching. The BLDC motor's speed is adjusted with no supplementary controls or circuitry. Soft starting of the BLDC motor is possible with proper zeta converter regulation through the incremental conductance (INC) based maximum power point tracking (MPPT) algorithm. The machine under investigation has demonstrated a number of desirable features, including optimal power extraction from the solar PV array, lenient starting of the PMBLDC motor drive, fundamental frequency switching of the VSI with decreased switching errors, speed modulation of the PMBLDC motor drive with absence supplementary control, and removal of phase current and dc line voltage detecting, all of which result in lower cost and complexity.

In 2017, Quéval et al. suggest the use of photovoltaic transistors (PVTs) in a solar-fed SRM drive is demonstrated. A traditional photovoltaic (PV) cell used as a light-controlled power transistor is referred to as a "PVT" [43]. The control is accomplished by using a motor rotor-driven shutter to modulate the amount of sunlight entering the PVTs. The operation of photovoltaic transistors is first discussed in this paper by the suggestion and justification of a model. The working theory of a PVT inverter is then explained. Lastly, the first photovoltaic transistors inverter-fed SRM experimental and numerical findings are discussed.

In 2017, The author Kumar and Singh demonstrated a single-stage energy conversion system for the applications of water pumping using a PV-fed PMBLDC motor drive. The PMBLDC motor pump was fed directly from the solar PV array via a VSI [44]. In contrast to an AC IM based system, the proposed arrangement had a high efficiency power conversion due to the removal of phase current sensors and DC-DC converters. Control of the solar photovoltaic array working point via INC-MPPT methodology, PMBLDC motor drive are electronically commutation, voltage source inverter's switching pulse generation, and regulating the speed of the PMBLDC by the optimal power of the solar photovoltaic array were the four main components of the single-stage system's control. Even under dynamic conditions, the motor retained its smooth performance.

In 2018, The author Shukla and Singh discusses a solar feeded single-stage speed sensor-less vector driven AC IM drive for water pumping systems that outperforms traditional motor drives [45]. The calculated stator flux is used to calculate the speed. To get the most power out of a PV panel, an INC based MPPT algorithm is used. When the irradiance changes, the PV array's power is retained at its highest level and this is maintained by the INC based MPPT algorithm. The vector control of an AC IM allows for a smooth motor start.

In 2019, a solar photovoltaic array driven IM control powered water pumping arrangement with an adaptive speed finder is proposed by Shukla and Singh [46]. It

focuses on the implementation of a VSI with no current sensors using space vector modulation (SVM). The dc line current is used to approximate the motor phase currents. To boost drive efficiency, a global integrator-based flux variation technique is used. Furthermore, an updated model reference adaptive device based on stationary frame currents and rotor fluxes increases its reliability across the working spectrum. In the MATLAB/Simulink environment, the overall system, which includes a single-stage PV operated SVM based VSI fed IM controlled liquid pump, is demonstrated and its output is simulated. The suggested solar PV driven induction motor drive has a less sensor driven, cost-effective system that consists of one current sensor and a robust speed variation technique.

In 2020, Murshid and Singh suggest an autonomous Solar Water Pumping System with Reduced Sensor-Based PMSM [47]. In order to get the most power out of a solar photovoltaic (PV) array, the nonlinear I-V characteristic of PV cells necessitates the use of the MPPT technique. One voltage and one current sensor are required by conventional MPPT methods. This paper suggests an innovative maximum power point tracking technique which is based on single sensor-based for solar photovoltaic array-powered water pumping arrangement using a PMSM (permanent magnet synchronous motor) drive. The solar water pumping system can be made cheaper and more reliable by using a sensor-less speed monitor. The PV array's energy is used to fuel the permanent magnet synchronous motor, which rotates the pump that is attached to it.

In Table 1 the environmental and economic viability of solar photovoltaic fed water pumping has been determined. The main conclusions of the environmental and economic study of solar photovoltaic fed water pumping are summarized (Table 2).

Table 1 Solar PV fed water pump uses a variety of motors and its advantages and limitation

Motor types	Pump types	Advantages	Limitations
BLDC	Centrifugal Pump, Helical rotor pump	BLDCMs have highly efficient (80–90%), a higher speed-to-torque ratio, lower noise, better dynamic response, a wider speed range and require little maintenance. PSI/e was used to analyze the entire system and disregarding the array system, the system's efficiency was between 30 and 50% [48]	BLDC motors are more expensive than other types of motors. Operation of BLDC motors are not easy as that of brushed motors
IM	Centrifugal Pump	In an Induction motor, greater the frequency, the better the system efficiency, however it is recommended to run at a nominal frequency. The simulated obtained results were compared to experimental data from a system placed in Jordan's desert area, and the outputs were quite similar [49]	The control of speed of the Induction motor is very difficult and Induction motor has poor starting torque

(continued)

Table 1 (continued)

Motor types	Pump types	Advantages	Limitations
SRM	Centrifugal Pump	In comparison to DC or induction motors, SRM has a better efficiency and cheaper cost. The motor efficiency may reach up to 85%, while the system efficiency can reach up to 95%. The pump and pipe system suffered the most losses, accounting for 1/3 of the total energy available [50]	SRM motors are very noisy. In SRM for the finding rotor position, external sensors are required
DC Shunt Motor	Centrifugal Pump	A mathematical model is created, and it is then applied to a steady state dynamic analysis. The motor runs at a steady speed for almost the whole day, with an efficiency of above 75%. Current and voltage overshoots are only present for a brief time [51]	DC shunt motor runs at a steady speed. Size of the DC shunt motor is larger compared to other motors

Table 2 PV water pumping systems with motor drive control and maximum power point techniques used by authors

Converter	Control strategy of MPPT	Control of motor drive
Cuk, Zeta, Buck-Boost,	Incremental Conductance (IMC) Method	Control of Commutation of PMBLDC Motor
Boost	F-Logic (Fuzzy) Controlled Algorithms	Control of Hysteresis Current
LUO	Hybrid ANFIS-Flower Pollination Optimization	Control of Commutation of PMBLDC Motor
Z-Source Inverter	F-Logic (Fuzzy) Controlled Incremental Conductance (IMC) Method	Sensor-less control
Landsman	Incremental Conductance (IMC) Method	F-Logic (Fuzzy) Controlled Algorithms
No intermediate converter	Single sensor MPPT algorithm	Sensor-less control of PMSM

4 Conclusion

This survey paper examines the results of solar photovoltaic powered water pumping arrangement using different motor drives in single and multi-stage setups. The water pumping arrangement and its constituents such as the photovoltaic array, the MPPT control system, the motor drive and the pumping system are explained in the first section. The next step is to conduct a literature review that focuses on study results from both the multi-stage and single-stage pumping arrangements. For the feeding of water pump nowadays PMBLDC motor is used because this motor is better than all other motors (IM, DC shunt motor, SRM). Due to its high cost of installation, PV water pumping is still not commonly used, particularly for the irrigation of large

areas and water supplies. More encouragement would be given by governments to make this system more appealing in comparison to conventional fuel-based pumps and electricity-based water pumping.

References

1. Chandel SS, Nagaraju Naik MN, Chandel R (2015) Review of solar photovoltaic water pumping system technology for irrigation and community drinking water supplies. Renew Sustain Energ Rev 49:1084–1099
2. Salameh ZM, Borowy BS, Amin ARA (1995) Photovoltaic module-site matching based on the capacity factors. IEEE Trans Energ Convers 10(2):326–332. https://doi.org/10.1109/60.391899
3. Yeager KE (1992) Electric vehicles and solar power: enhancing the advantages. IEEE Power Eng Rev 12(10):13. https://doi.org/10.1109/MPER.1992.159923
4. Saied MM, Jaboori MG (1989) Optimal solar array configuration and DC motor field parameters for maximum annual output mechanical energy. IEEE Trans Energ Convers 4:459–465
5. Alghuwainem SM (1996) Speed control of a PV powered DC motor driving a self-excited 3-phase induction generator for maximum utilization efficiency. IEEE Trans Energ Convers 11(4):768–773. https://doi.org/10.1109/60.556377
6. Daud A-K, Mahmoud MM (2005) Solar powered induction motor-driven water pump operating on a desert well, simulation and field tests. Renew Energ 30:701–714
7. Kaldellis JK, Spyropoulos GC, Kavadias KA, Koronaki IP (2009) Experimental validation of autonomous PV-based water pumping system optimum sizing. Renew Energ 34:1106–1113
8. Mokeddem A, Midoun A, Kadri D, Hiadsi S, Raja IA (2011) Performance of a directly coupled PV water pumping system. Energ Convers Manage 52:3089–3095
9. Ghoneim AA (2006) Design optimization of photovoltaic powered water pumping systems. Energ Convers Manage 47(11–12):1449–1463 ISSN 0196-8904
10. Firatoglu ZA, Yesilata B (2004) New approaches on the optimization of directly coupled PV pumping systems. Solar Energ 77:81–93
11. Hiyama T, Kouzuma S, Imakubo T, Ortmeyer TH (1995) Evaluation of neural network based real time maximum power tracking controller for PV system. IEEE Trans Energ Convers 10:543–548
12. Hiyama T, Kouzuma S, Imakubo T (1995) Identification of optimal operating point of PV modules using neural network for real time maximum power tracking control. IEEE Trans Energ Convers 10:360–367
13. Hiyama T, Kitabayashi K (1997) Neural network based estimation of maximum power generation from PV module using environmental information. IEEE Trans Energ Convers 12:241–247
14. Enslin JHR, Wolf MS, Snyman DB, Swiegers W (1997) Integrated photovoltaic maximum power point tracking converter. IEEE Trans Ind Electron 44:769–773
15. Enslin JHR, Snyman DB (1991) Combined low-cost, high-efficient inverter, peak power tracker and regulator for PV applications. IEEE Trans Power Electron 6(1):73–82. https://doi.org/10.1109/63.65005
16. Altas IH, Sharaf AM (1996) A novel on-line MPP search algorithm for PV arrays. IEEE Trans Energ Convers 11(4):748–754. https://doi.org/10.1109/60.556374
17. Alghuwainem SM (1994) Matching of a DC motor to a photovoltaic generator using a step-up converter with a current-locked loop. IEEE Trans Energ Convers 9(1):192–198. https://doi.org/10.1109/60.282492
18. Campana PE, Li H, Yan J (2013) Dynamic modelling of a PV pumping system with special consideration on water demand. Appl Energ 112:635–645

19. Badoud AE, Khemliche M, Bouamama BO, Bacha S, Villa LFL (2013) Bond graph modeling and optimization of photovoltaic pumping system: simulation and experimental results. Simul Model Pract Theory 36:84–103
20. Benghanem M, Daffallah KO, Joraid AA, Alamri SN, Jaber A (2013) Performances of solar water pumping system using helical pump for a deep well: a case study for Madinah, Saudi Arabia. Energ Convers Manage 65:50–56
21. Moechtar M, Juwono M, Kantosa E (1991) Performance evaluation of a.c. and d.c. direct coupled photovoltaic water pumping systems. Energ Convers Manage 31:521–527
22. Singh B, Swamy CLP, Singh BP (1998) Analysis and development of a low-cost permanent magnet brushless DC motor drive for PV-array fed water pumping system. Sol Energ Mater Sol Cells 51:55–67
23. Akbaba M, Qamber I, Kamal A (1998) Matching of separately excited DC motors to photovoltaic generators for maximum power output. Sol Energ 63:375–385
24. Senjyu T, Veerachary M, Uezato K (2002) Steady-state analysis of PV supplied separately excited DC motor fed from IDB converter. Sol Energ Mater Sol Cell 71:493–510
25. Singer S, Appelbaum J (1993) Starting characteristics of direct current motors powered by solar cells. IEEE Trans Energ Convers 8:47–53
26. Fam WZ, Balachander MK (1988) Dynamic performance of a DC shunt motor connected to a photovoltaic array. IEEE Trans Energ Convers 3:613–617
27. Appelbaum J (1986) Starting and steady-state characteristics of DC motors powered by solar cell generators. IEEE Trans Energ Convers EC 1:17–25
28. Swamy CLP, Singh B, Singh BP (2000) Experimental investigations on a permanent magnet brushless DC motor fed by a PV array for a water pumping system. J Sol Energ 122:129–132
29. Mummadi VC (2000) Steady-state and dynamic performance analysis of PV supplied DC motors fed from intermediate power converter. Sol Energ Mater Sol C 61:365–381
30. Appelbaum J, Sarma MS (1989) The operation of permanent magnet DC motors powered by a common source of solar cells. IEEE Trans Energ Convers 4:635–642
31. Appelbaum J (1986) Performance characteristics of a permanent magnet DC motor powered by solar cells. Sol Cells 17:343–362
32. Chee Wei T, Green TC, Hernandez-Aramburo CA (2005) An improved maximum power point tracking algorithm with current-mode control for photovoltaic applications. In: Proceedings of the power electronics and drives systems, pp 489–494
33. Salameh ZM, Dagher F, Lynch WA (1991) Step-down maximum power point tracker for photovoltaic systems. Sol Energ 46:279–282
34. Salameh Z, Taylor D (1990) Step-up maximum power point tracker for photovoltaic arrays. Sol Energ 44:57–61
35. Kumar R, Anwar MN (2021) Optimal design of permanent magnet brushless DC (PMBLDC) motor using PSO algorithm. In: Malik H, Fatema N, Alzubi JA (eds) AI and machine learning paradigms for health monitoring system. Studies in big data, vol 86. Springer, Singapore. https://doi.org/10.1007/978-981-33-4412-9_33
36. Swamy CLP, Singh B, Singh BP, Murthy SS (1996) Experimental investigations on a permanent magnet brushless DC motor fed by PV array for water pumping system. In: Proceedings of the 31st Intersociety Energy Conversion Engineering, IECEC. IEEE, vol 3. pp 1663–1668
37. Hosseini SH, Nejabatkhah F, MozafariNiapoor SAKH, Danyali S (2010) Supplying a brushless dc motor by z-source PV power inverter with FL-IC MPPT. In: International conference on green circuits and systems. IEEE, pp 485–490
38. Terki A, Moussi A, Betka A, Terki N (2012) An improved efficiency of fuzzy logic control of PMBLDC for PV pumping system. Appl Math Model 36:934–944
39. Taghvaee MH, Radzi MA, Moosavain SM, Hizam H, Marhaban MH (2013) A current and future study on non-isolated DC–DC converters for photovoltaic applications. Renew Sustain Energ Rev 17:216–227
40. Kumar R, Singh B (2014) Solar photovoltaic array fed Luo converter based BLDC motor driven water pumping system. In: 9th international conference on industrial and information systems (ICIIS). IEEE, pp 1–5

41. Kumar R, Singh B (2014) Solar photovoltaic array fed canonical switching cell converter based BLDC motor drive for water pumping system. In: Annual IEEE India conference (INDICON). IEEE, pp 1–6
42. Kumar R, Singh B (2016) BLDC motor-driven solar PV array fed water pumping system employing zeta converter. IEEE Trans Ind Appl 52:2315–2322
43. Quéval L, Coty A, Vido L, Gottkehaskamp R, Multon B (2017) A switched reluctance motor drive using photovoltaic transistors: principle, prototype, experimental, and numerical results. IEEE Trans Ind Appl 53(5):4886–4893. https://doi.org/10.1109/TIA.2017.2718493
44. Kumar R, Singh B (2017) Single stage solar PV fed brushless DC motor driven water pump. IEEE J Emerg Sel Top Power Electron 5(3):1377–1385. https://doi.org/10.1109/JESTPE.2017.2699918
45. Shukla S, Singh B (2018) Single-stage PV array fed speed sensorless vector control of induction motor drive for water pumping. IEEE Trans Ind Appl 54(4):3575–3585. https://doi.org/10.1109/TIA.2018.2810263
46. Shukla S, Singh B (2019) Reduced-sensor-based PV array-fed direct torque control induction motor drive for water pumping. IEEE Trans Power Electron 34(6):5400–5415. https://doi.org/10.1109/TPEL.2018.2868509
47. Murshid S, Singh B (2020) Reduced sensor-based PMSM driven autonomous solar water pumping system. IEEE Trans Sustain Energ 11(3):1323–1331. https://doi.org/10.1109/TSTE.2019.2924012
48. Langridge D, Lawrance W, Wichert B (1996) Development of a photo-voltaic pumping system using a brushless d.c. motor and helical rotor pump. Sol Energ 56(2):151–160. https://doi.org/10.1016/0038092X(95)00077-5
49. Daud A-K, Mahmoud MM (2005) Solar powered induction motor-driven water pump operating on a desert well, simulation and field tests. Renew Energ 30(5):701–714. https://doi.org/10.1016/j.renene.2004.02.016
50. Metwally HMB, Anis WR (1994) Performance analysis of photovoltaic-powered water-pumping systems using switched reluctance motor drives. J Power Sources 52(1):141–147. https://doi.org/10.1016/0378-7753(94)01946-0
51. Metwally HMB, Anis WR (1996) Dynamic performance of directly coupled photovoltaic water pumping system using D.C. shunt motor. Energy Convers Manage 37(9):1407–1416. https://doi.org/10.1016/0196-8904(95)00226-X

Artificial Neural Network Based Power Control of DC Microgrid

Rahul Sharma, Akanksha Kashyap, and Vijay Kumar Singh

Abstract This paper proposed the data driven artificial neural network (ANN) learning based control scheme for the DC microgrid. In the proposed control scheme, ANN is used to regulate DC link voltage and achieve proper power sharing control between parallel sources in the DC microgrid. Both the transient and dynamic behavior of the system is improved by using the proposed ANN control. The Ripple content of dc link voltage is also reduced significantly and improved the power sharing between the two sources through the Levenberg-Marquardt algorithm based neural network in spite of using the traditional PI controller technique. Along with it, the effect of cable impedance is also found to be negligible in the proposed control. DC microgrid voltage control is conventionally controlled by dual loop control which is used to take more time to provide desired results. The proposed system is based on optimal data set which is independent of system complexity. Hence, the overall time is also reduced using the proposed method.

1 Introduction

The continuous increasing demand of electricity, scantiness of fossil fuels and environmental concerns are the driving forces to introduce microgrids as the future of the electricity market. Currently, the majority of power is produced and delivered based on conventional sources (e.g., thermal power generation) which are harmful

R. Sharma · A. Kashyap · V. K. Singh (✉)
NIT, Kurukshetra, India
e-mail: vsc9717@gmail.com

R. Sharma
e-mail: rahulsharma.knit2006@gmail.com

A. Kashyap
e-mail: manu051196@gmail.com

303

to the environment and its scope to expand with the increasing demand of power is also low due to the depletion of fossil fuels. Therefore, researchers are considering microgrids as the future and replacement of traditional power systems. Microgrid has achieved tremendous popularity in the last few years because of its benefit to use non-conventional sources like Solar PV, Wind turbine systems etc., to expand the generating system as per the requirement. İt also reduces significant transmission losses comparatively with conventional one. Microgrid is emerged as one of the best option to supply electricity in rural/remote areas where electrification is still pending.

Microgrids are of two types: AC and DC. DC microgrid has a more easy structure than AC and also it has higher efficiency because there is no reactance losses, no skin effect and no need of frequency regulation and reactive power compensation. Despite the complexity of AC microgrid, it is popular till now due to the existing AC power system. That's why AC microgrid has been studied thoroughly. Most of the renewable energy generation system has dc output (e.g., solar PV, fuel cell) and especially nowadays solar PV system is used extensively at the level of commercial and domestic both for which DC microgrid is more compatible [1].

Microgrids are used in both ways i.e. grid connected and islanded (isolated) mode. The control of grid connected microgrid is easy because it has an infinite source (AC main grid) to balance itself. But the main problem with islanded grid is voltage stability and load sharing between distributed generators. Constant power load shows the characteristics of non-linearity and negative impedance [2]. Due to which marge of voltage stability decreases and it can make the system unstable.

There are many strategies for controlling the dc microgrid. In centralized control (master slave control), a large size control unit (e.g., inverter or battery) which work as a master unit, is used which sends reference signal to the other slave units. Here communication channel is required which makes the system more susceptible to fault, and costlier and also it can only be used for short distance networks [3–5]. Droop control is very popular for DC microgrid to implement decentralized control. In this controller, a virtual resistance is connected to the output of the source which increases the overall resistance and provides a better interconnection between source and load [6–8]. Due to increment in resistance, droop gain also increases which ensures the load sharing accuracy but shrinks the stability margin [9]. Most of the stability analysis are used with some specific values of CPL and studies on an equilibrium condition [10]. In practical cases, equilibrium changes with the change in load and source. So, there is a requirement of a novel control technique to make the system work even under variable equilibrium conditions.

For the past few years, artificial neural networks is gaining popularity in the power system protection. ANN is basically influenced by biological neural networks. This paper has proposed a control technique based on data driven ANN learning to control the DC microgrid [11]. The proposed scheme is able to settle the dc bus voltage on its desired value by achieving very less settling time, smoothening out the voltage and increasing the power/current sharing accuracy.

The rest of the paper is arranged as follows:

Section 2 gives a brief introduction. The rest of the paper is arranged as follows.
Section 3 Introduces the ANN based proposed control strategy of DC microgrid.

Section 4 Results are discussed and compared with the conventional one.

Section 5 Concludes the findings of the study and the outcome of the paper.

2 Tradıtıonal Control of DC Mıcrogrıd

The Droop control technique is the most commonly used control scheme for DC link voltage control and proper load sharing in DC microgrid environment as shown in Fig. 1 where multiple energy sources are connected in parallel to the loads. In this scheme, communication link is not used for maintaining the system voltage unlike centralized master salve control. The Droop control schemes generally used a virtual impedance strategy to compensate for the effect of line impedances and provide proper voltage control and current/power sharing. But, the difference between currents shared by multiple sources starts decreasing due to an increase in resistance. Also, DC link voltage regulation becomes worse. So, it is clear that the voltage regulation is bartered for load sharing even if it costs the stability of the system under variable line impedance conditions [12].

To control dc bus voltage, two droop control units are used which consists of a DC voltage source and a DC-DC boost converter.

The state equations are given below:
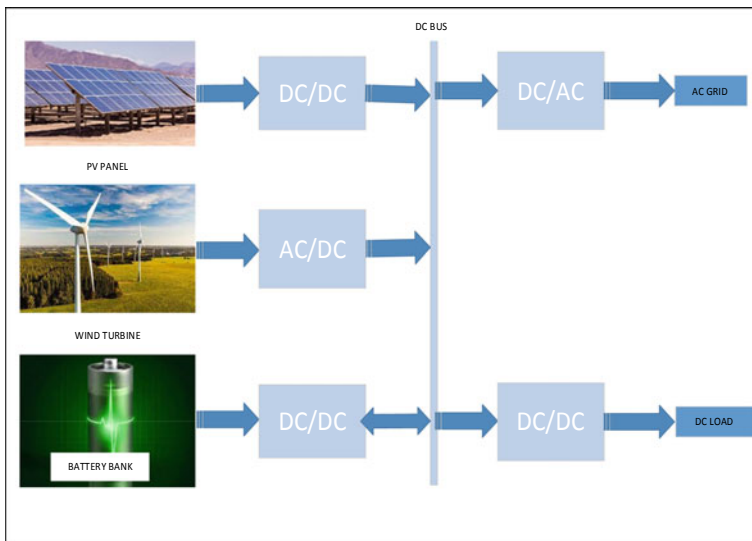
Fig. 1 Basic block diagram of DC microgrid
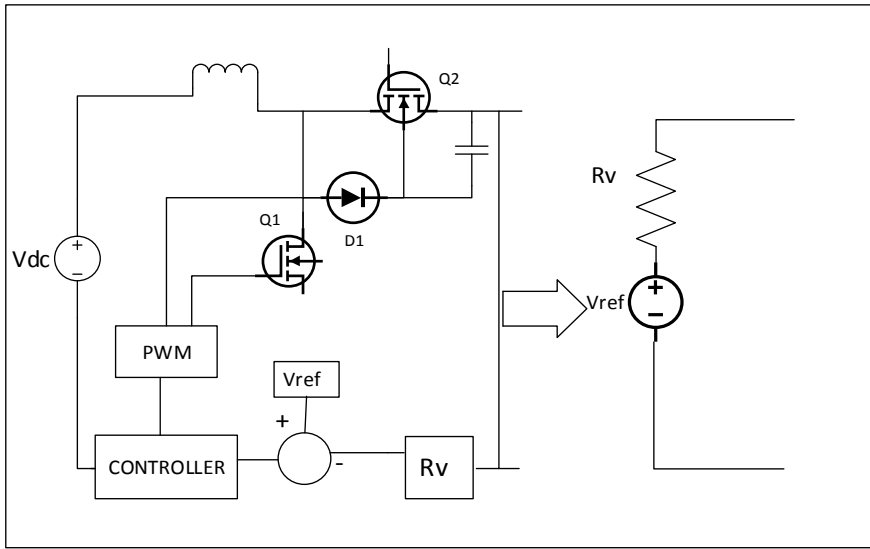
Fig. 2 Circuit diagram of droop control unit

$$C_i \frac{\mathrm{d}u_{oi}}{\mathrm{d}t} = (1 - d_i)i_{Li} - i_{oi}$$

$$V_{si} = R_i i_{Li} + L_i \frac{\mathrm{d}i_{Li}}{\mathrm{d}t} + (1 - d_i)u_{oi} \qquad (1)$$

$$u_{oi} = \mathrm{Re}_i i_{oi} + \mathrm{Le}_i \frac{\mathrm{d}i_{oi}}{\mathrm{d}t} + u_{dc}$$

In Eq. (1), C, R, L, u, d represent capacitor, resistance, inductor, output voltage of converter, and duty cycle respectively and i is used for the number of units ($i = 1$, 2,..). Re and Le are representing the line impedance (Fig. 2).

Droop control system contains two loops: one is the voltage control loop and other is the current control loop. Voltage loop gives the reference current and current loop adjust the value of the output current. Both the voltage and current loops use PI controllers.

In voltage loop, output voltage is compared with a reference voltage in a comparator and then the obtained signal is divided by droop resistance which gives the reference current. Here, the proportional gain works the same as a resistance connected in series with the source.

$$I_{\mathrm{ref}} = \frac{U_{\mathrm{set}\,i} - U_i}{R_{\mathrm{droop}}}$$

$$k_{\mathrm{p}} = \frac{1}{R_{\mathrm{droop}}} \qquad (2)$$

Reference current can be calculated from the above Eq. (2). In current loop, current coming from the source is compared with reference current and the obtained signal is given to PI based current controller. The output from here is applied to the PWM generator from where a pulse is generated. This pulse works as a triggering pulse for the respective switch.

The value of k_p and k_i can be found by the Ziegler Nichols Tuning method but the value of load affects the performance of the system [13]. That's why PI gain has to be tuned according to the fluctuated load.

3 ANN Based Proposed Control of DC Microgrid

The droop control scheme is discussed where the stability of the system is compromised for the accuracy of load sharing and also there is a need of PI controller tuning. Therefore, this paper proposed data based ANN controller to regulate DC bus voltage and proper power sharing. ANN is basically designed with the idea of biological neural networks like neurons are connected with each other and transmit data. Similarly, ANN has different layers and it is trained with the set of operating data to get the targeted output for different input conditions [14].

3.1 Function Fitting Neural Network

There are different types of wizards in neural networks. The fitting app is used in the proposed work. In fitting app, neural network is trained with a set of numeric inputs and respective numeric outputs to form a generalized relation between input and output. In a fitting network, there are hidden layers in which neurons perform all the computational work. In the proposed work, the Levenberg-Marquardt algorithm is used for training. Along with it, source current, output current, converter voltage of respective droop control units and load current are used as input. In the hidden layer, 10 neurons are used as shown in Fig. 3.
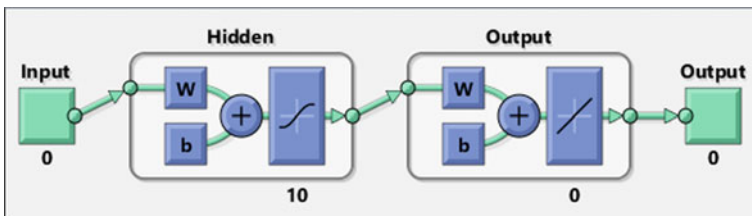
Fig. 3 Layout used in neural network
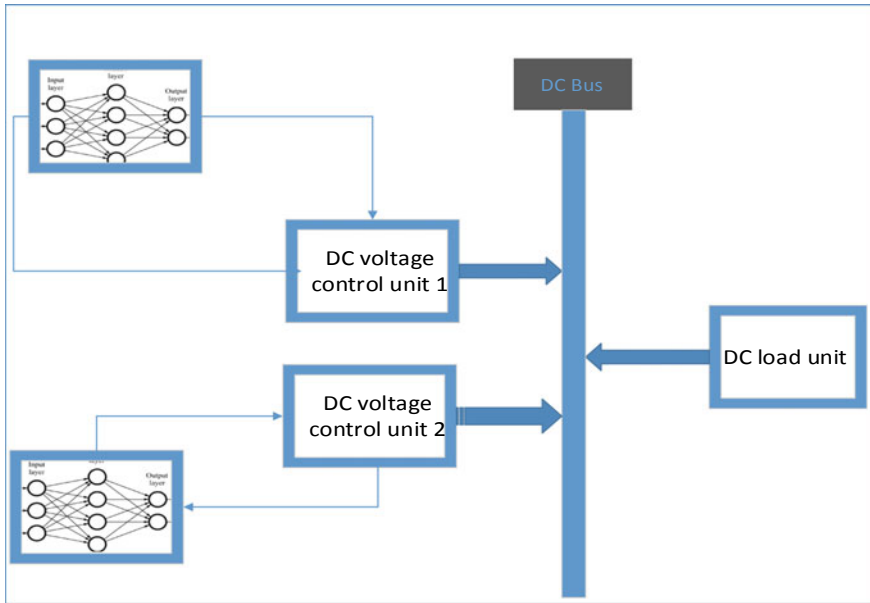
Fig. 4 Block diagram of proposed scheme

In the proposed work, two function fitting neural networks are used for the two droop control units. The output of the fitting network is applied to generate a reference voltage signal to modulate the gating pulses of the converter. The ANN controlled gating pulses actually regulate the DC link voltage and power injection into the common DC bus (Fig. 4).

3.2 Data Set

The network is trained from the data procured from the optimization method using mathematical equations which are stated in the traditional control section. The set contains 80 samples for different values of load resistance. Most of the samples are used for training around 75%. In the remaining, some are used for validation and some are used for testing.

4   Results and Discussions

4.1   *Effect on DC Link Voltage by Variation in Load Resistance*

Results are observed by comparison of traditional scheme output and proposed scheme output. First of all, in Figs. 5 and 6 comparison of DC link voltages has been done. On the observation, it can be seen clearly that the settling time of the proposed scheme gives a satisfactory result. In proposed scheme, DC link voltage is settled at around 0.7 s whereas in traditional approach it settled down at 0.97 s. In proposed scheme, steady state value of DC link voltage is 199.8 V whereas; the steady state value of DC link voltage is 199.3 V in traditional scheme. Desired value of DC link voltage was 200 V hence proposed scheme increased DC link voltage by 0.25%. With the help of proposed scheme, the output of DC link voltage accuracy goes from 99.65 to 99.9%.

Variation in load resistance is done at 1 s. The effects of variation can be observed easily in Fig. 6. When a disturbance in load resistance is introduced at 1 s, it's found that in traditional approach significant drop of 27.1 V is observed at DC link voltage and it is sustained for a longer period of time and takes around 1.2 s to maintain steady state value. After settling down at a steady state, its value is also reduced by 2.3 V from 199.3 to 197 V. On the other hand, observing the behavior of the proposed system variation in load resistance does not have much effect on its DC link voltage. At the time of switching load resistance, the value of DC link voltage oscillates for 0.3 s and achieved its steady state value but, it settled at 198.2 by reduction of 1.6 V from 199.8 V.
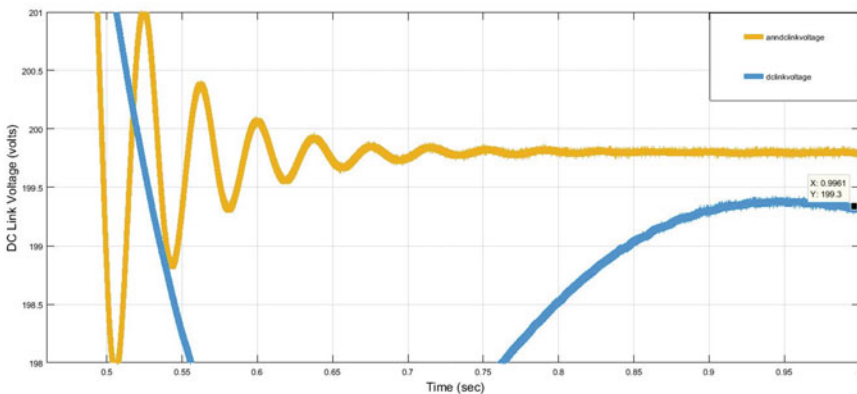
Fig. 5   DC Link voltages of proposed scheme and traditional scheme
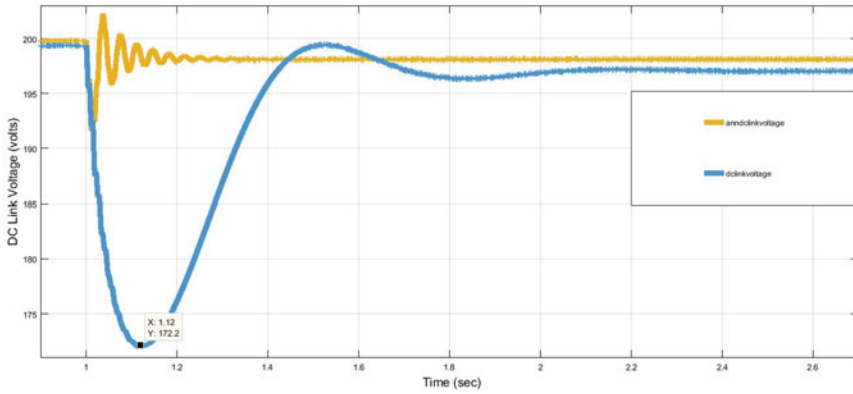
Fig. 6 Effects of variation in load resistance on DC link voltages

4.2 Effect on DC Link Voltage on the Variation at Line Impedance

On the variation of line impedance, at the time of switching load at t = 1 s, it's clearly observed that the waveform is taking a lot of time to gain steady state value in the traditional droop control scheme. It takes around 1.2 s, whereas proposed ANN scheme takes around 0.07 s to regain its steady state value. Also, traditional droop control scheme is regulating DC link voltage at 197 V in steady state, whereas proposed scheme regulates the DC link voltage at 199.9 V. The waveform behavior shows that the proposed scheme yields better results than the traditional one (Fig. 7).
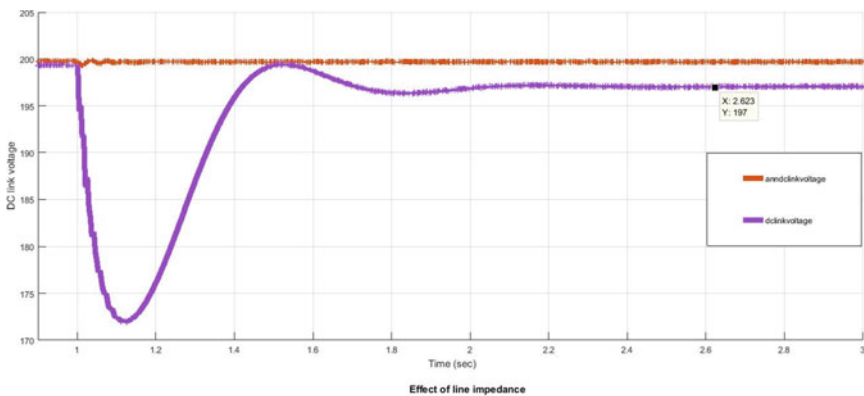
Fig. 7 Effect of variation in line impedance on DC link voltage

5   Concusion

The results reflected clearly that the proposed ANN based control scheme is able to manage DC link voltage stability and load sharing both at the same time in the DC microgrid. The proposed scheme is able to maintain the DC bus voltage constant at the desired value even under the variation in load as well as line impedances. The settling time is also improved which reflects the better transient and dynamic behavior of the system under the proposed scheme. It smoothens out the ripple content of the output voltage. Also, the ANN relates with optimal data is better targeted output with variable input which is more effective to regulate the system parameters. It concludes that the uncertain environment of the microgrid can be better handled with ANN which introduces more reliable operation with improved performance.

References

1. Adhikari S, Xu Q, Tang Y, Wang P (2017) Decentralized control of DC microgrid clusters. In: 2017 IEEE 3rd international future energy electronics conference and ECCE Asia (IFEEC 2017—ECCE Asia), pp 567–572. https://doi.org/10.1109/IFEEC.2017.7992101
2. Belk JA et al (2016) Stability and control of ad hoc dc microgrids. In: Proceedings of IEEE 55th annual conference on decision and control CDC, Dec 2016, pp 3271–3278
3. Kumar M, Srivastava SC, Singh SN (2015) Control strategies of a DC microgrid for grid connected and islanded operations. IEEE Trans Smart Grid 6(4):1588–1601
4. Chen D, Xu L (2012) Autonomous DC voltage control of a DC microgrid with multiple slack terminals. IEEE Trans Power Syst 27(4):1897–1904
5. Vivek K (2019) Design and analysis of voltage droop control technique for DC microgrids. In: 2019 3rd international conference on electronics, communication and aerospace technology (ICECA), pp 795-799. https://doi.org/10.1109/ICECA.2019.8822144
6. Tahim PN, Pagano DJ, Lenz E, Stramosk V (2015) Modeling and stability analysis of islanded DC microgrids under droop control. IEEE Trans Power Electron 30(8):4597–4607. https://doi.org/10.1109/TPEL.2014.2360171
7. Lu X, Sun K, Guerrero JM, Vasquez JC, Huang L, Wang J (2015) Stability enhancement based on virtual impedance for DC microgrids with constant power loads. IEEE Trans Smart Grid 6(6):2770–2783. https://doi.org/10.1109/TSG.2015.2455017
8. Hamzeh M, Ghafouri M, Karimi H, Sheshyekani K, Guerrero JM (2016) Power oscillations damping in DC microgrids. IEEE Trans Energ Convers 31(3):970–980. https://doi.org/10.1109/TEC.2016.2542266
9. Li X et al (2018) Observer-based DC voltage droop and current feed-forward control of a DC microgrid. IEEE Trans Smart Grid 9(5):5207–5216. https://doi.org/10.1109/TSG.2017.2684178
10. Zonetti D, Ortega R, Schiffer J (2016) A tool for stability and power sharing analysis of a generalized class of droop controllers for high-voltage direct-current transmission systems. arXiv:1609.03149
11. Chawla G, Sachdev MS, Ramakrishna G (2005) Artificial neural network applications for power system protection. In: Canadian conference on electrical and computer engineering, 2005, pp 1954–1957. https://doi.org/10.1109/CCECE.2005.1557365
12. Gao F, Kang R, Cao J, Yang T (2019) Primary and secondary control in DC microgrids: a review. J Mod Power Syst Clean Energ 7(2):227–242. https://doi.org/10.1007/s40565-018-0466-5

13. Bharath KR, Dayal A, Kanakasabapathy P (2017) A simulation study on modified droop control for improved voltage regulation in DC microgrid. In: 2017 International conference on ıntelligent computing, ınstrumentation and control technologies (ICICICT), pp 314–319. https://doi.org/10.1109/ICICICT1.2017.8342581
14. Dong W, Li S, Fu X (2018) Artificial neural network control of a standalone DC microgrid. In: 2018 Clemson university power systems conference (PSC), pp 1–5. https://doi.org/10.1109/PSC.2018.8664030

Experimental Validation of the Effects of Non-uniform Light Irradiance and Series Resistance on Solar Photovoltaic System Performance Using an Emulator

Chandrakant D. Bhos , **Javed Sayyad** , **and Paresh Nasikkar**

Abstract Solar Photovoltaic (SPV) innovation ends up being gradually helpful, starting late with the advance of material science among the key wellsprings of a sustainable power source. The SPV system's output performance is determined by environmental parameters like solar light irradiation and operational temperature. In this article, MATLAB Simulink simulates an SPV array with 4 series-connected SPV panels to examine the effect of 4 different levels of Partial Shading (PS) on the performance of the SPV system. A test set-up with an SPV emulator was developed for experimental validation. Sequential examinations were carried out to observe the effect of PS and series resistance on the performance parameters such as maximum power, fill factor, and efficiency of the SPV system. 25–63% reduction in the maximum power due to partial shading was reported after examining the simulated and experimental results. Also, it is noted that 2.5 times increase in the series resistance results in a 52% reduction in the maximum power, 66% reduction in fill factor, and 67% reduction in the efficiency of the system.

Keywords Solar photovoltaic · Partial shading · Series resistance · Maximum power · Renewable energy

Nomenclature

I	Total current (Amps)
I_{pv}	PV current (Amps)
I_s	Saturation current (Amps)
I_d	Diode current (Amps)
q	Charge on an electron ($1.60217662 \times 10^{-19}$ C)

C. D. Bhos · J. Sayyad · P. Nasikkar (✉)
Department of Electronics and Telecommunication Engineering, Symbiosis Institute of Technology (SIT), Symbiosis International (Deemed University) (SIU), Lavale, Pune, Maharashtra 412115, India
e-mail: paresh.nasikkar@sitpune.edu.in

k	Boltzmann constant (1.380649×10^{-23} J/K)
V	PV cell voltage (Volts)
T	Temperature (K)
N_s	Number of cells connected in series
a	Constant of diode ideality factor
R_s	Series resistance (Ω)
R_p	Parallel resistance (Ω)
V_{oc}	Open-circuit Voltage (Volts)
I_{sc}	Short-circuit current (Amps)
V_{MPP}	Voltage at maximum power point (Volts)
I_{MPP}	Current at maximum power point (Amps)
P_{MPP}	Power at maximum power point (Watts)
FF	Fill factor
η	Efficiency

1 Introduction

Energy resources impose a vitally important influence on economic growth, urbanization level, and environmental issues [1]. The need for electricity has risen significantly in the past two decades. The energy consumption for the residential sector is increased by 30% in the COVID-19 pandemic situation in 2020 [2]. The link between gross domestic product (GDP) and the energy consumption is well discussed in the literature. Improvements in energy efficiency have expected a 40% reduction in greenhouse gas emissions over the next two decades [3]. As per the estimation by International Energy Agency, an increase of about 1500 Mtoe (Mega Tonnes of Oil Equivalent) in energy demand is expected by 2030 in India. About 30–40% of the production cost lies in energy costs in small and medium-sized enterprises [4]. Mainly the energy is produced using petroleum resources. However, because of the release of ozone-depleting compounds in the air, these non-renewable energy sources are restricted and quickly exhausting, and their continuous usage has adverse effects on the planet. Therefore, it wants a renewable, environmentally sustainable energy supply. One of the primary solutions to the aforementioned issues is the use of Solar Energy (SE). It is a key source of renewable energy all around the world. A total of 4.2 million tonnes of solar mass are converted into various types of energy. Because the sun weighs about 333 times the weight of the Earth, Sun can provide the energy needs for the next 5 billion years [2].

Around 60% of energy generation from the total European energy generation is targeted from the solar photovoltaic system [5]. SPV development is one means of generating light-emitting energy. As SPV panel-based power plants contrast with other renewable power sources, they have multiple points of concern, such as low emissions, lower operating costs, and abundant availability. The most recent information shows that excellent outcomes are acquired in SPV-based systems. As indicated

by information from the National Renewable Energy Laboratory (NREL), the efficiency of SPV cells has surpassed 45%. This circumstance shows that the eventual fate of SPV technology is very brilliant, and it will continue to increase in the distant future.

There are significant impacts on SPV efficiency due to the parameters such as solar irradiance, temperature, series resistance, and shunt resistance. All SPV modules in a system are ensured to be indistinguishable as far as the electrical properties are concerned. These modules are adversely affected by variable irradiance, however. To judge the system's effectiveness, an investigation of the system's performance under Partial Shading (PS) is necessary. Numerous literature analyses are related to the influence of shading and other parameters on the SPV system, such as series resistance, shunt resistance, cell temperature, and light irradiance [6–13]. Significant shading on SPV panels degrades the system's performance and never achieves its specified yield level [14]. The electrical characteristics deviate from the expected one due to PS, and reduced power output is observed [15]. PS caused by nearby buildings, trees, and birds is an important consideration related to photovoltaic performance. A method for accurate modelling of SPV systems under the influence of PS and mismatch conditions is implemented using a five-parameter equivalent circuit to study the multi-peak characteristics of SPV systems [16]. The shadow by obstacles with an irregular shape close to the photovoltaic arrays exhibits imprecise simulation results. However, good simulation results are obtained for obstacles far away from the SPV array [17]. A comprehensive review of the energy models with different complexity, accuracy, and applicability is discussed by Batzelis et al. [18]. The impact of three different patterns of PS on Series-parallel and total-cross tied configurations of SPV array is reported by Kumar and Vadhera [19]. The researchers have discussed parallel-connected solar SPV systems to overcome the shading losses and achieved promising results [20]. The model for characterizing the SPV array under the influence of PS achieves promising results, as discussed by Karatepe et al. [21]. The higher deformations in I-V characteristics and a significant reduction in VMPP due to an increased level of shading are observed by Alonso-Garcia et al. [22]. The effect of shading on the performance of the SPV system is experimentally validated by researchers and noted the significant losses in the output power [23]. SPV panel electrical characteristics concerning multiple maximum power points are also affected by PS [24]. Researchers have experimentally investigated the power output under uniform and non-uniform irradiance by analyzing different module configurations under PS [25]. Yadav et al. have investigated the output performance of different configurations of SPV modules under non-uniform shading patterns and found that proposed configurations with puzzle shade dispersion as an efficient one [26]. Yin and Babu proposed the mathematical analysis process with one-diode and two-diode models for finding the performance of SPV systems under normal and partially shaded conditions [27]. The performance of various SPV array topologies was analyzed under PS by Pendem and Mikkili for different shading patterns [28]. Hariharan et al. presented a technique for identifying the defect and PS in an SPV array by monitoring light irradiance, array voltage, and array current [29]. The effect of three different PS patterns on the shape of the output I-V curve of the SPV system

was experimentally analyzed by Sebbagh et al. [30]. Pannebakker et al. discussed the performance of the SPV system under PS with one bypass diode per cell and achieved promising results [31]. Experimental work about finding several MPP for SPV systems under PS and the performance of different configurations of SPV array was carried out by Lappalainen and Valkealahti [32]. Kunz et al., in their work, found that the losses in the maximum power for shingled SPV modules are larger than that for conventional ones [33]. The Odd–even configuration of the SPV array was proposed by Yadav et al. to overcome the power losses due to PS [34]. The main purpose of the proposed work in this paper is to analyze the effect of PS and series resistance on the performance of SPV systems. Section 2 describes the mathematical model used for SPV cells. MATLAB Simulink work and experimental validation using SPV emulator are presented in Sects. 3 and 4, respectively.

2 Mathematical Modelling of SPV Cell

The SPV panel configuration with one diode is a parallel connection between a current source and a diode, as shown in Fig. 1. Parallel and series resistance implies obstruction to the flow of electrons from the negative charge region (n region) to the positive charge region (p region) and the flow of current, respectively.

An equation for total current (I) is as follows:

$$I = I_{pv} - I_s \left[\exp \frac{q(V + IR_s)}{N_s kTa} - 1 \right] - \frac{V + IR_s}{R_p} \tag{1}$$

The SPV current is influenced by many factors such as solar irradiance, ambient temperature, diode ideality factor, and the number of series-connected cells. A
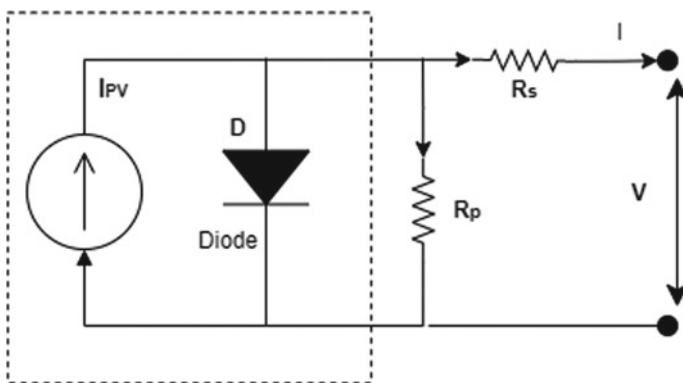
Fig. 1 SPV cell modelling with a single diode
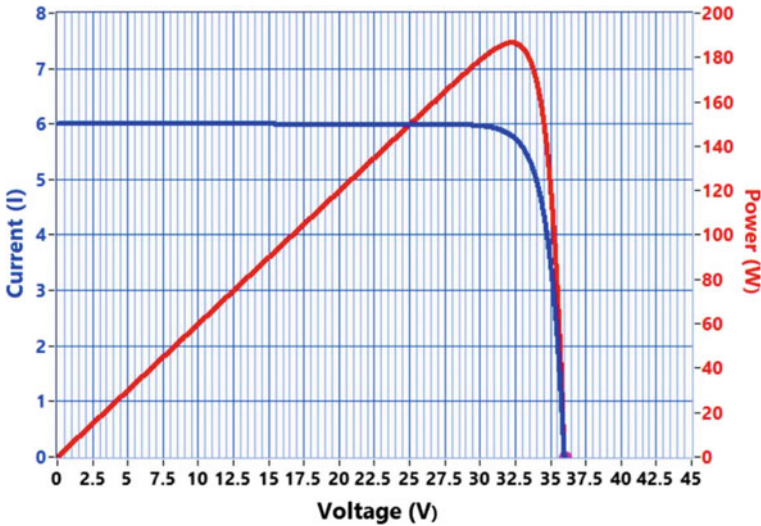
Fig. 2 Typical current-voltage (I-V) and power–voltage (P-V) curves of SPV system

photovoltaic module has non-linear Current-Voltage (I-V) and Power-Voltage (P-V) curves, as shown in Fig. 2.

3 Modelling of SPV Array Under *PS* in MATLAB/SIMULINK

Figure 3 depicts a MATLAB Simulink model of an SPV array consisting of 4 series-connected '1Soltech 1STH-215-P' SPV panels, each with a maximum power of 213.15 W. Each module internally contains 60 cells in series. It is used to investigate the effect of PS on SPV panel performance. Table 1 lists the dimensions of the aforementioned SPV panel.

Figures 4, 5, 6, 7, 8, 9, 10 and 11 depict the simulated output I-V and P-V curves with four different levels of light irradiance, and Table 2 summarizes the corresponding data.

The system can generate a maximum power of 851 W_p with uniform irradiance levels on all panels, as in case 1. However, in the following situations, PS drastically decreases the system's maximum power harnessed. The decreased solar irradiance causes a reduction in the total photo-current and the amount of maximum power. It also results in an increase in the number of local maxima points. This effect creates hurdles to the conventional maximum power point tracking algorithms in tracking the true maxima.
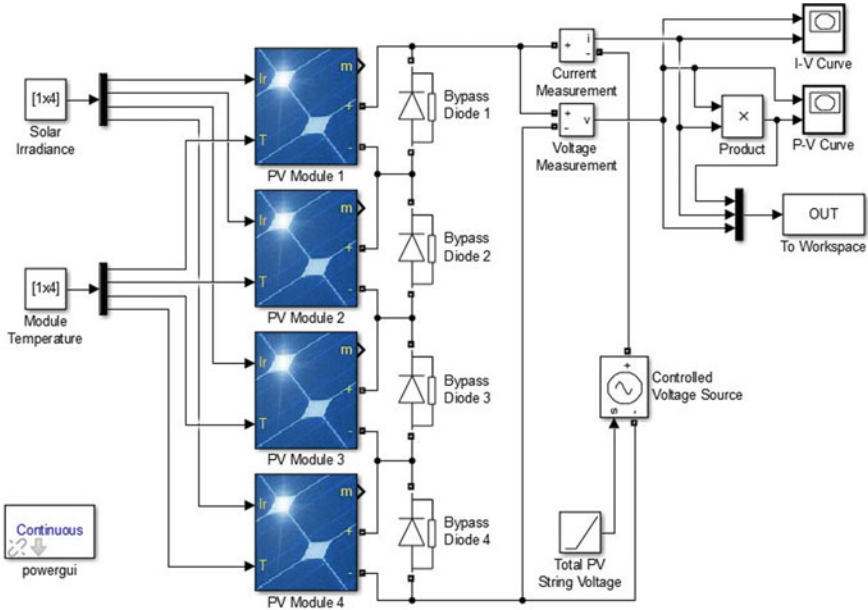
Fig. 3 MATLAB simulink model of SPV array

Table 1 Specifications 1Soltech 1STH-215-P SPV module

SPV module electrical parameter	Specifications/value
N_s	60 numbers
V_{oc}	36.3 V
I_{sc}	7.84 Amps
V_{MPP}	29 V
I_{MPP}	7.35 Amps
P_{MPP}	213.15 Watts
R_s	0.39383 Ω
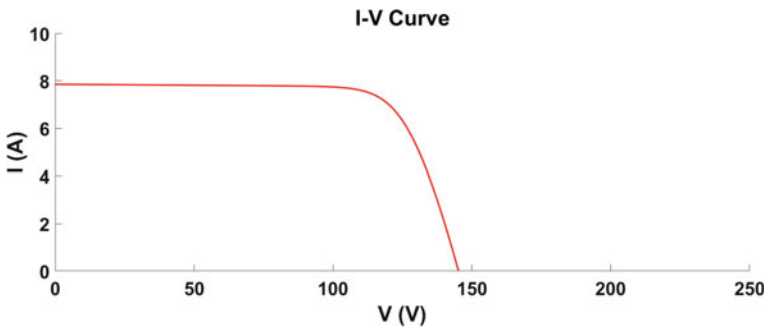
Fig. 4 Output I-V curve at four different irradiance levels for case 1 [1000, 1000, 1000, 1000]
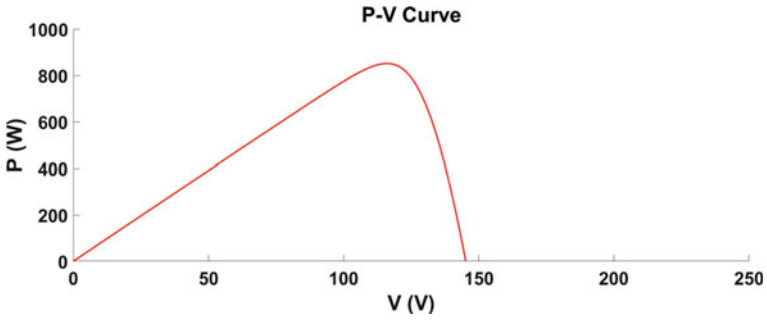
Fig. 5 Output P-V curve at four different irradiance levels for case 1 [1000, 1000, 1000, 1000]
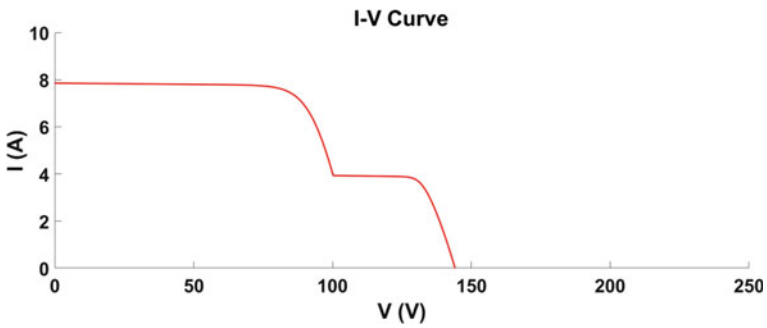
Fig. 6 Output I-V curve at four different irradiance levels for case 2 [1000, 1000, 1000, 500]
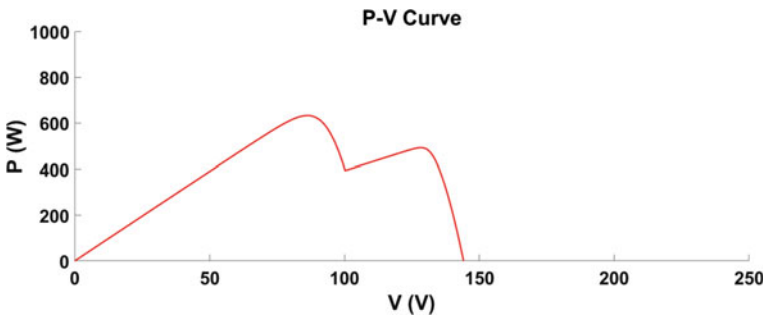
Fig. 7 Output P-V curve at four different irradiance levels for case 2 [1000, 1000, 1000, 500]
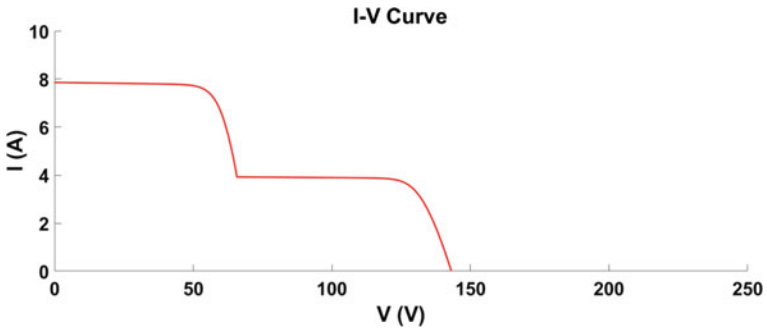
Fig. 8 Output I-V curve at four different irradiance levels for case 3 [1000, 1000, 500, 500]
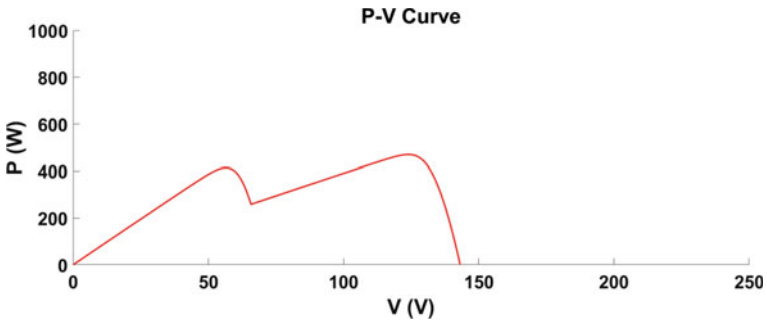
Fig. 9 Output P-V curve at four different irradiance levels for case 3 [1000, 1000, 500, 500]
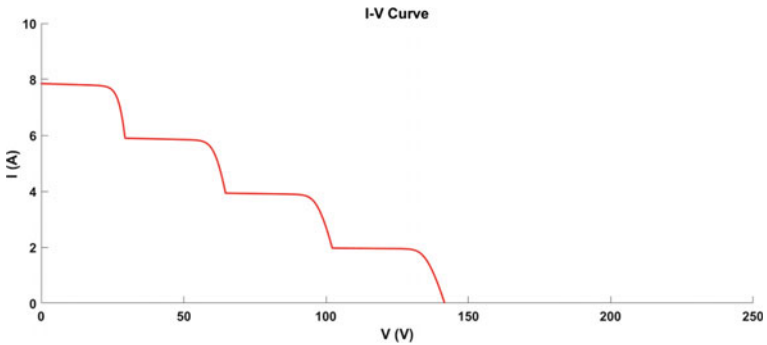
Fig. 10 Output I-V curve at four different irradiance levels for case 4 [1000, 750, 500, 250]
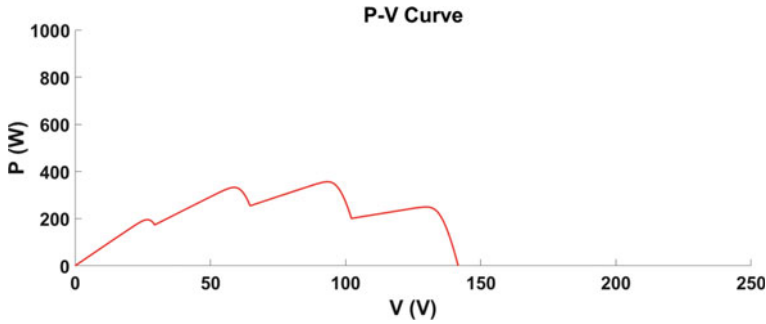
Fig. 11 Output P-V curve at four different irradiance levels for case 4 [1000, 750, 500, 250]

Table 2 Outcome performance of an SPV array at four different irradiance levels

Case	Light irradiance on module 1 (W/m^2)	Light irradiance on module 2 (W/m^2)	Light irradiance on module 3 (W/m^2)	Light irradiance on module 4 (W/m^2)	Maximum power (Watts)	Number of local maxima
1	1000	1000	1000	1000	851	1
2	1000	1000	1000	500	643	2
3	1000	1000	500	500	462	2
4	1000	750	500	250	376	4

4 Experimental Validation Using SPV Emulator

4.1 *Effect of PS*

This experiment employs Ecosense Sustainable Solutions Pvt. Ltd.'s SPV Emulator Model SPVE001, which validates the influence of PS on the performance of an SPV array. The actual set-up used for the experiment is shown in Fig. 12. A series of experiments were conducted using 4 different shading patterns. Parameters for the SPV Emulator were set as described in Table 3, and the values of MPP, VMPP, IMPP, FF, and η were noted. Figures 13 and 14 illustrate the output I-V and P-V curves in 4 different levels of light irradiance using the SPV emulator and Table 4 summarizes their findings.

The system generates a maximum power of 251.5 W with uniform solar irradiance on all SPV panels, as shown in case 1. In the subsequent cases, the maximum power decreases as non-uniformity in solar irradiance increases. Also, the number of local maxima increases. The experimental results validate the correctness of simulated results.
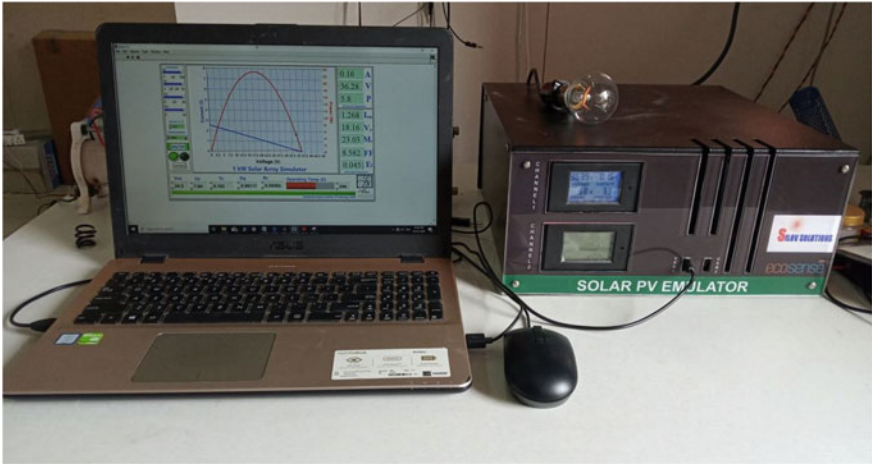
Fig. 12 Actual experimental set-up using SPV emulator model SPVE001

Table 3 SPV emulator parameters during the experiment

Electrical parameter	Specifications/value
V_{oc}	36.3 V
I_{sc}	7.84 Amps
T_c	0.102
A	0.98117
R_s	0 Ω
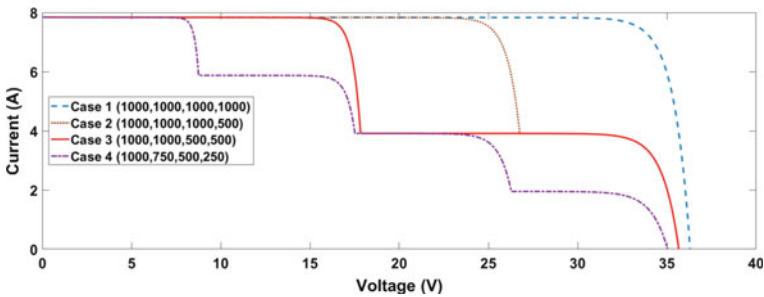
Fig. 13 Output I-V curves of SPV emulator for four different light irradiance levels

4.2 Effect of Series Resistance (R_s)

To validate the effect of change in the value of R_s on the performance curve of the SPV at different settings of irradiance are experimented using an emulator, and observations are noted down for further analysis.
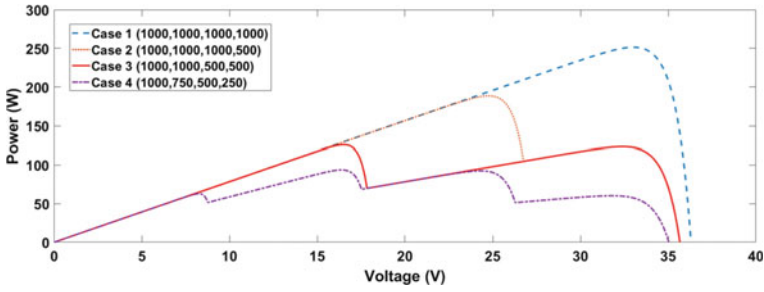
Fig. 14 Output P-V curves of SPV emulator for four different light irradiance levels

Table 4 Outcome performance parameters of the SPV array under four different light irradiance levels using SPV emulator

Case	Irradiance levels (W/m^2)	I_{MPP} (Amps)	V_{MPP} (Volts)	P_{MPP} (Watts)	Fill factor	Efficiency
1	1000, 1000, 1000, 1000	7.619	33.01	251.5	88.38	0.4005
2	1000, 1000, 1000, 500	7.619	24.76	188.6	67.45	0.3433
3	1000, 1000, 500, 500	7.619	16.51	125.8	44.97	0.2670
4	1000, 750, 500, 250	5.711	16.38	93.53	34.04	0.2383

With R$_s$ = 0.039383 Ω

The output I-V and P-V curves derived for Rs = 0.039383 Ω are shown in Figs. 15 and 16, respectively, and noted performance parameters for different cases are tabulated in Table 5.
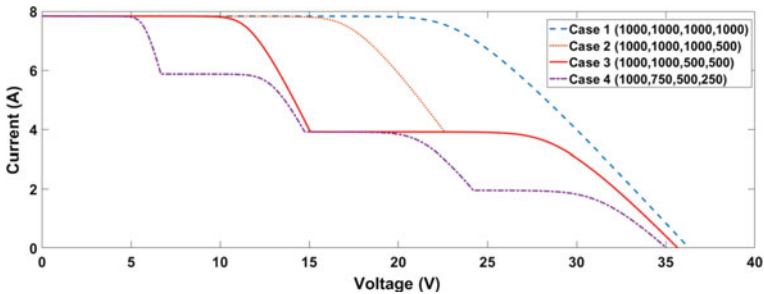
Fig. 15 Output I-V curves for 4 different cases having different light irradiance levels using SPV emulator with R$_s$ = 0.039383 Ω
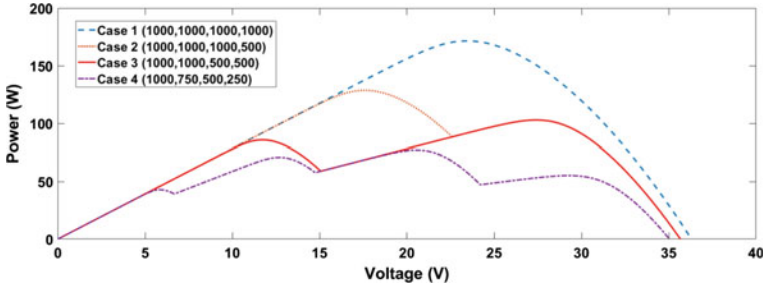
Fig. 16 Output P-V curves for 4 different cases having different light irradiance levels using SPV emulator with $R_s = 0.039383\ \Omega$

Table 5 Output performance parameter of SPV array under 4 different light irradiance levels using SPV emulator with $R_s = 0.039383\ \Omega$

Case	Irradiance levels (W/m²)	I_{MPP} (Amps)	V_{MPP} (Volts)	P_{MPP} (Watts)	Fill factor	Efficiency
1	1000, 1000, 1000, 1000	7.32	23.44	171.6	60.32	0.2732
2	1000, 1000, 1000, 500	7.32	17.58	128.7	46.03	0.2342
3	1000, 1000, 500, 500	3.755	27.41	102.9	36.82	0.2185
4	1000, 750, 500, 250	3.755	20.56	77.18	28.11	0.1966

With $R_s = 0.1\ \Omega$

The I-V and P-V curves derived for Rs = 0.1 Ω are shown in Figs. 17 and 18, respectively, and noted performance parameters are tabulated in Table 6.
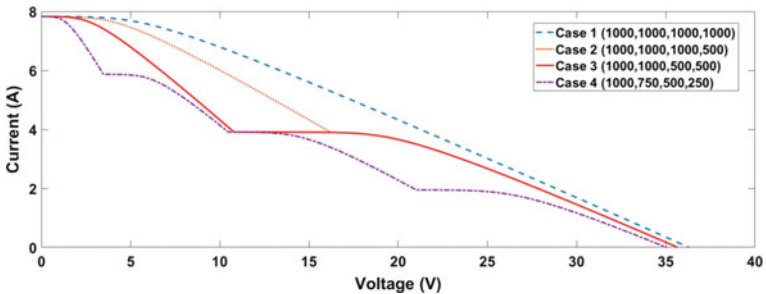
Fig. 17 Output I-V curves for 4 different cases having different light irradiance levels using SPV emulator with $R_s = 0.1\ \Omega$
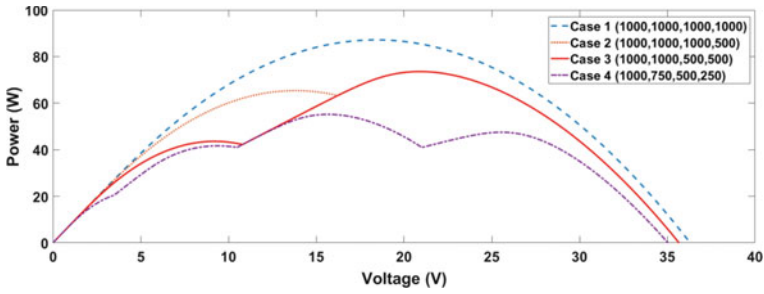
Fig. 18 Output P-V curves for 4 different cases having different light irradiance levels using SPV emulator with $R_s = 0.1\ \Omega$

Table 6 Output performance parameters of SPV array under 4 different light irradiance levels using SPV emulator with $R_s = 0.1\ \Omega$

Case	Irradiance levels (W/m^2)	I_{MPP} (Amps)	V_{MPP} (Volts)	P_{MPP} (Watts)	Fill factor	Efficiency
1	1000, 1000, 1000, 1000	4.732	18.42	82.17	30.67	0.1388
2	1000, 1000, 1000, 500	3.52	20.9	73.57	26.34	0.1339
3	1000, 1000, 500, 500	3.52	20.9	73.57	26.34	0.1562
4	1000, 750, 500, 250	3.52	15.67	55.18	20.11	0.1406

5 Discussion

After analyzing the results in MATLAB Simulink and SPV Emulator, it is clear that the maximum power harnessed from the system is significantly reduced due to PS on SPV panels. The considerable effect of PS on MPP is experimented with using an SPV emulator shown in Fig. 19. Increasing the value of series resistance up to 0.1 Ω has a considerable influence on the system's overall performance. It reduces the value of maximum power by 52%, which is represented in Fig. 20. As seen in Figs. 21 and 22 shows that a modest increase in the value of the series resistance reduces the FF by 66% and the efficiency by 67%.

6 Conclusion

An accurate guess of power production performance from the SPV system can achieve better operational efficiency. In the presented work, an equivalent circuit of the SPV array is modeled in MATLAB Simulink to symbolize the effect of PS
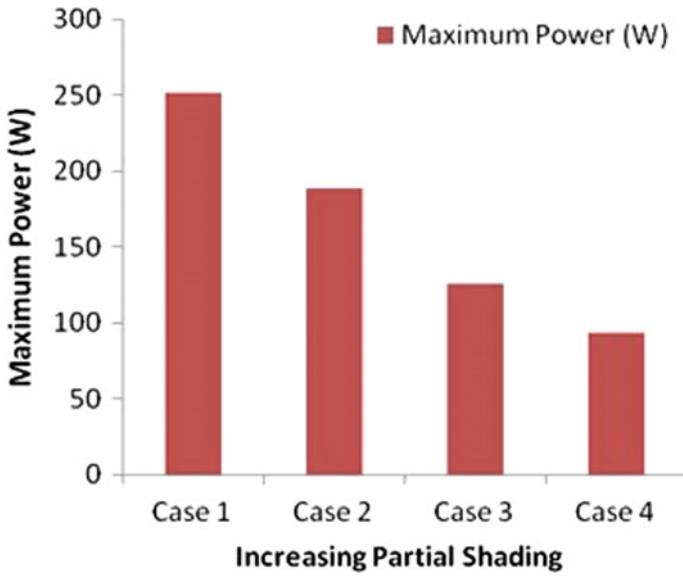
Fig. 19 Comparative study of effect due to partial shading on MPP
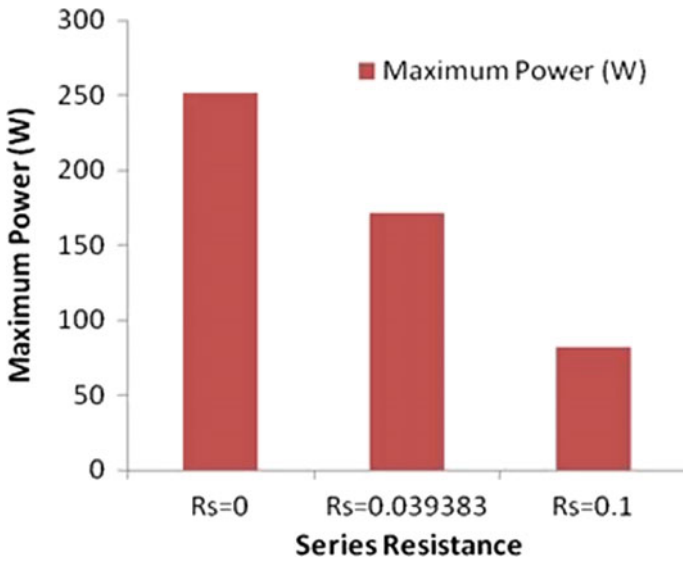
Fig. 20 Comparative study of effect due to change in series resistance on MPP
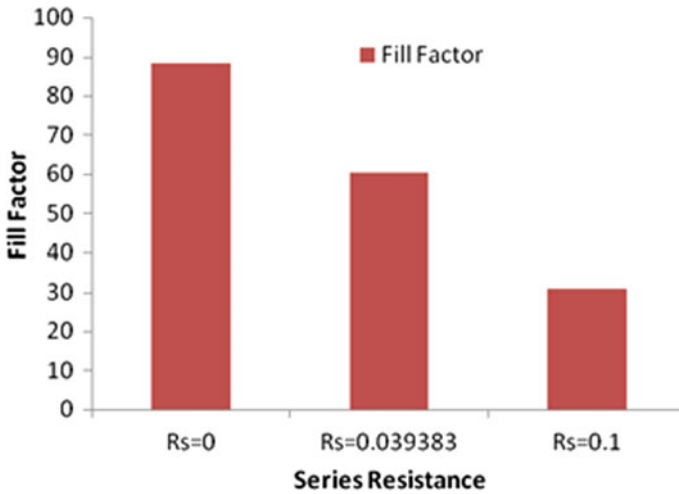
Fig. 21 Comparative study of effect due to change in series resistance on FF (fill factor)
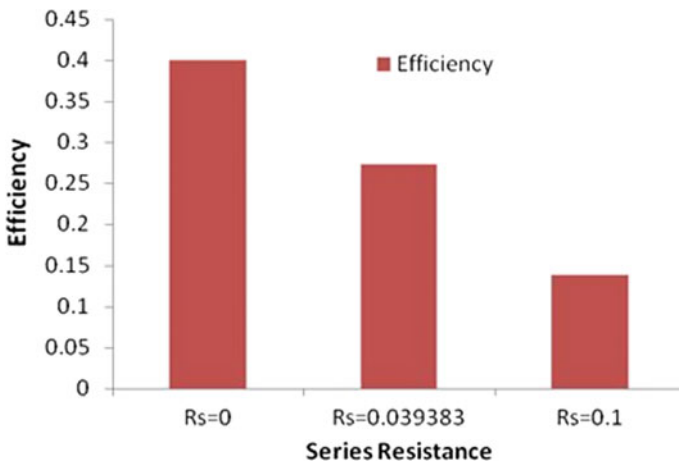
Fig. 22 Comparative study of effect due to change in series resistance on η (efficiency)

on the SPV system. Besides, an experimental investigation with SPV Emulator to validate the simulation results was done. The results clearly show that PS diminishes the power generation efficiency of an SPV system and forms the basis of a hot spot problem. Further work in the paper also puts insight into the effect of the series resistance of the SPV panel on the performance of the SPV system. The investigations show that the series resistance has a severe adverse effect on the maximum power generated from the system, FF, and the efficiency of the SPV system. The work carried out in the paper forms a foundation for the judgment about SPV system

performance under shading and change in the series resistance. It focuses significantly on the need for an efficient way to address these destructive factors to increase the overall performance of the SPV system.

References

1. Armeanu DS, Joldes CC, Gherghina SC, Andrei JV (2021) Understanding the multidimensional linkages among renewable energy, pollution, economic growth and urbanization in contemporary economies: quantitative assessments across different income countries' groups. Renew Sustain Energ Rev 110818. https://doi.org/10.1016/j.rser.2021.110818
2. Nahidan MH, Niroomand M, Dehkordi BM (2021) Power enhancement under partial shading condition using a two-step optimal PV array reconfiguration. Int J Photoenergy. https://doi.org/10.1155/2021/8811149
3. Brockway PE, Sorrell S, Semieniuk G, Heun MK, Court V (2021) Energy efficiency and economy-wide rebound effects: a review of the evidence and its implications. Renew Sustain Energ Rev 110781. https://doi.org/10.1016/j.rser.2021.110781
4. Lalith Pankaj Raj GN, Kirubakaran V (2021) Energy efficiency enhancement and climate change mitigations of SMEs through grid-interactive solar photovoltaic system. Int J Photoenergy 1–19. https://doi.org/10.1155/2021/6651717
5. Cotfas DT, Sera D, Kaplani E, Cotfas PA, Rezaniakolaei A (2019) Advancements in photovoltaic cell and system technologies. Int J Photoenergy. https://doi.org/10.1155/2019/8129137
6. Nasikkar PS, Sayyad JK (2020) Internet of Things (IoT) based outdoor performance characterisation of solar photovoltaic module. In: E3S web of conferences. EDP Sciences
7. Sayyad J et al (2021) Capacitive load-based smart OTF for high power rated SPV module. Energies 14(3):788
8. Sayyad J, Nasikkar P (2021) Design and development of low cost, portable, on-field IV curve tracer based on capacitor loading for high power rated solar photovoltaic modules. IEEE Access 9:70715–70731
9. Nasikkar PS, Bhos CD, Sayyad JK (2021) Two-step experimental validation of impact of irregular irradiance on solar photovoltaic system's performance. Innovations in electrical and electronic engineering. Springer, Berlin, pp 203–215
10. Sayyad JK, Nasikkar PS (2020) Capacitor load based I-V curve tracer for performance characterisation of the solar photovoltaic system. Appl Sol Energ 56(3):168–177
11. Sayyad JK, Nasikkar PS (2020) Solar photovoltaic module performance characterisation using single diode modeling. In: E3S web of conferences. EDP Sciences
12. Sayyad J, Nasikkar P (2020) Solar photovoltaic performance monitoring: a bibliometric review, research gaps and opportunities
13. Sayyad JK, Nasikkar PS (2019) An overview of methods used for outdoor performance characterisation of photovoltaic module string up to 10 kWp. Int J Instrum Technol 2(2):114–134
14. Boukenoui, R., Salhi, H., Bradai, R., Mellit, A.: A new intelligent MPPT method for stand-alone photovoltaic systems operating under fast transient variations of shading patterns. In: Solar Energy (2016)
15. Jazayeri, M., Uysal, S., Jazayeri, K.: A comparative study on different photovoltaic array topologies under partial shading conditions. In: Proceedings of the IEEE Power Engineering Society Transmission and Distribution Conference (2014)
16. Bai J, Cao Y, Hao Y, Zhang Z, Liu S, Cao F (2015) Characteristic output of PV systems under partial shading or mismatch conditions. Sol Energ 112. https://doi.org/10.1016/j.solener.2014.09.048

17. Woyte A, Nijs J, Belmans R (2003) Partial shadowing of photovoltaic arrays with different system configurations: literature review and field test results. Sol Energ. https://doi.org/10.1016/S0038-092X(03)00155-5
18. Batzelis EI, Georgilakis PS, Papathanassiou SA (2015) Energy models for photovoltaic systems under partial shading conditions: a comprehensive review. IET Renew Power Gener. https://doi.org/10.1049/iet-rpg.2014.0207
19. Kumar J, Vadhera S (2015) Maximum power of PV plant for SP and TCT topologies under different shading conditions. In: India international conference on power electronics, IICPE
20. Gao L, Dougal RA, Liu S, Iotova AP (2009) Parallel-connected solar PV system to address partial and rapidly fluctuating shadow conditions. IEEE Trans Ind Electron. https://doi.org/10.1109/TIE.2008.2011296
21. Karatepe E, Boztepe M, Çolak M (2007) Development of a suitable model for characterizing photovoltaic arrays with shaded solar cells. Sol Energ. https://doi.org/10.1016/j.solener.2006.12.001
22. Alonso-García MC, Ruiz JM, Herrmann W (2006) Computer simulation of shading effects in photovoltaic arrays. Renew Energ. https://doi.org/10.1016/j.renene.2005.09.030
23. Alonso-García MC, Ruiz JM, Chenlo F (2006) Experimental study of mismatch and shading effects in the I-V characteristic of a photovoltaic module. Sol Energ Mater Sol Cells. https://doi.org/10.1016/j.solmat.2005.04.022
24. Manjunath, Suresh HN, Rajanna S (2019) Performance enhancement of hybrid interconnected solar photovoltaic array using shade dispersion magic square puzzle pattern technique under partial shading conditions. Sol Energ. https://doi.org/10.1016/j.solener.2019.10.068
25. Bana S, Saini RP (2017) Experimental investigation on power output of different photovoltaic array configurations under uniform and partial shading scenarios. Energy. https://doi.org/10.1016/j.energy.2017.03.139
26. Yadav AS, Pachauri RK, Chauhan YK (2016) Comprehensive investigation of PV arrays with puzzle shade dispersion for improved performance. Sol Energ. https://doi.org/10.1016/j.solener.2016.01.056
27. Yin OW, Babu BC (2018) Simple and easy approach for mathematical analysis of photovoltaic (PV) module under normal and partial shading conditions. Optik (Stuttg). https://doi.org/10.1016/j.ijleo.2018.05.037
28. Pendem SR, Mikkili S (2018) Modelling and performance assessment of PV array topologies under partial shading conditions to mitigate the mismatching power losses. Sol Energ. https://doi.org/10.1016/j.solener.2017.12.010
29. Hariharan R, Chakkarapani M, Saravana Ilango G, Nagamani C (2016) A method to detect photovoltaic array faults and partial shading in PV systems. IEEE J Photovoltaics. https://doi.org/10.1109/JPHOTOV.2016.2581478
30. Sebbagh T, Kelaiaia R, Zaatri A (2018) An experimental validation of the effect of partial shade on the I-V characteristic of PV panel. Int J Adv Manuf Technol. https://doi.org/10.1007/s00170-018-1858-4
31. Pannebakker BB, de Waal AC, van Sark WGJHM (2017) Photovoltaics in the shade: one bypass diode per solar cell revisited. Prog Photovoltaics Res Appl. https://doi.org/10.1002/pip.2898
32. Lappalainen K, Valkealahti S (2020) Number of maximum power points in photovoltaic arrays during partial shading events by clouds. Renew Energ. https://doi.org/10.1016/j.renene.2020.01.119
33. Kunz O, Evans RJ, Juhl MK, Trupke T (2020) Understanding partial shading effects in shingled PV modules. Sol Energ. https://doi.org/10.1016/j.solener.2020.03.032
34. Yadav K, Kumar B, Swaroop D (2020) Mitigation of mismatch power losses of PV array under partial shading condition using novel odd even configuration. Energ Rep. https://doi.org/10.1016/j.egyr.2020.01.012

Identification and Validation of Prominent Features for Predicting Mortality in Heart Patients with Left Ventricular Dysfunction Using Machine Learning

R. Subha, Rekha Radhakrishnan, P. Sumalatha, and B. R. Nayana

Abstract Machine Learning (ML) is a strong tool for medical prognosis, and it has the potential to give this branch of medicine a huge boost by allowing doctors to make accurate predictions about a patient's future health using various forms of medical data. ML algorithms have proven to be reliable and effective in decision making with good classification accuracy. They can model nonlinear relationships, which are frequent in medical data, and apply them to predictive tasks such as forecasting a future event. In this paper, an attempt has been made to predict the mortality of heart patients with left ventricular dysfunction. Feature selection methods have been used to rank the input features in the dataset and identify four prominent features. Different combinations of these prominent features have been applied to five ML algorithms namely, Decision Tree, Gradient Boost, Random Forest, Support Vector Machine and k Nearest Neighbors to find the best performing combinations using F1-Score and AUC ROC. Considering additional performance parameters, further analysis is carried out to identify the best feature combination and the most effective ML algorithm for predicting mortality and the results are provided for the same.

Keywords Cardiovascular disorder · Classification · Decision trees · Machine learning · Medical prognosis

1 Introduction

Machine Learning (ML) is a dominant strategy aimed at medical prognosis since it is capable of bringing out hidden patterns in clinical data to make accurate predictions about a patient's future health. There are many applications of ML algorithms

R. Subha (✉)
Department of Electrical and Electronics Engineering, M S Ramaiah Institute of Technology, Bangalore, India
e-mail: subha.mvit@gmail.com

R. Radhakrishnan · P. Sumalatha · B. R. Nayana
Department of Electrical and Electronics Engineering, Sir M Visvesvaraya Institute of Technology, Bangalore, Karnataka, India

in the medical field. Logistic regression based classifier has been used to detect ovarian tumors using obstetric ultrasound imaging in [1]. Based on microarray data with average shrinkage, a Nave Bayes based model for biomarker identification and cancer classification has been built [2]. A k–Nearest Neighbor (KNN) classifier has been used for epilepsy diagnosis in [3]. For the prediction of diabetes, Random Forest (RF) algorithm has been used in [4]. Patients' heart failure has been detected using the Support Vector Machine (SVM) [5]. Decision Tree (DT) has been used to classify premature brain injury using MRI data in [6]. Early detection of Cardiovascular disorder plays a vital role in medical prognosis as it is a major cause of death worldwide annually [7]. Heart failure happens when the heart cannot pump enough blood to the body, commonly caused by diabetes, excessive blood pressure, or other heart problems [8]. Early diagnosis and prognosis can bring down the mortality rate in patients with cardiovascular disorders. Various ML algorithms applied to heart ailments are reported in the literature [9–16].

This paper attempts to predict the event of death in heart patients with left ventricular dysfunction using five different ML algorithms namely Gradient Boost (GB), KNN, SVM, DT, and RF. The dataset in use is obtained from UCI Machine Learning Repository. All patients of age 40 years and above with left ventricular systolic dysfunction and falling in classes III and IV as per the New York Heart Association (NYHA) have been included in the dataset. Left ventricular dysfunction occurs when the left ventricle is either defective or damaged. The data set consist of 13 features and are described in detail in the next section. However, it is perceived that the authors in [17] have attempted to predict mortality in patients for the same dataset with various ML algorithms using two features [17]. The results, however, reveal a low true positive rate, which is unacceptably high for medical applications. In [18] the authors have employed biostatistical techniques to the same dataset to analyze the survival rate of heart patients.

This paper presents a detailed description of the dataset and feature selection techniques used to identify prominent features. The effectiveness of the feature combinations has been evaluated using various ML algorithms and the best performing feature combinations for the prediction of mortality have been identified. The paper further analyzes the result using more elaborate performance parameters to identify and validate the most effective ML model for predicting mortality in heart patients with left ventricular dysfunction.

2   Dataset Description

The dataset used for the study in this paper contains the data of 299 heart patients with left ventricular dysfunction collected during the period April to December of 2015. NYHA classifies patients on the basis of the stages of heart failure. Patients with no symptoms during ordinary activity are categorized as class I and those with discomfort during physical activity and symptoms during rest period as class IV. All patients under study belonged to classes III or IV as per NYHA classification. The data set

consists of 13 features which include clinical parameters like age, gender, high blood pressure, anaemia, creatinine phosphokinase (CPK), Diabetic_condition, Ejection-Fraction (EF), Platelet_count, Serum Creatinine and Serum Sodium, patient habits like smoking, time duration of the follow-up and death event (whether the subject died or survived during the follow-up period). The subjects under study belonged to the age group of 40–95 years. Clinical parameters like anaemic_condition, high blood pressure, diabetic_condition, gender, and Smoking_habit are presented as binary values. The dataset reflects a value of '1' to indicate an anaemic patient if the patient's hematocrit level is less than 36%. Patients with high blood pressure were marked as '1' and those with normal blood pressure were marked as '0'. Diabetic patients were marked as '1' and non diabetic patients were marked as '0'. The study group consisted of 105 women (shown as '0') and 194 men (shown as '1'). The mortality rate in women was found to be 35.42% which was significantly lower than that of men which were found to be 64.58%. Another parameter provided in the dataset is the smoking habit of patients. Among the 203 non-smokers, 66 of them died during the study period with a mortality rate of 68.75%. Creatinine Phosphokinase (CPK) indicates the levels of CPK enzyme in the bloodstream. CPK enzyme is produced by a damaged heart muscle and hence high levels of CPK are considered a marker for heart failure or injury. Ejection fraction is the percentage of blood that is pumped out of the left ventricle during each contraction. Serum creatinine is a waste product generated during the break down of muscle cells. The level of serum creatinine indicates the condition of the kidney. High levels of serum creatinine are indicative of kidney dysfunction. Sodium is necessary to ensure the proper functioning of muscles and nerves. Significantly lower levels of serum sodium may be caused by heart failure and is considered an important parameter in the diagnosis and treatment of heart patients. The death event used in the dataset states if the patient died ('1') or was alive ('0') at the end of the follow-up period. The parameters of the dataset and its description are summarized in Table 1.

3 Feature Selection and Classification

Feature Selection is the procedure of recognizing the features which contribute extremely to the output variable. Accuracy of the model can decrease if data contains features which are not relevant. Feature selection minimizes the problem of overfitting, enhances accuracy and decreases training computation time. In this paper three feature selection methods—correlation matrix, chi-square test and feature importance map have been considered. Correlation matrix gives the correlation between the input features and prediction variables. Correlation value can be positive or negative depending on the relationship between the two variables. A chi-square test is a statistical test to determine the independence of two events. Chi-Square measures the deviation between expected count and observed count. For independent features, the observed count and expected count are close to each other, thus resulting in a lower chi-square value. Feature importance, a built-in class which comes along with

Table 1 Dataset parameters and their description

Sl. No.	Parameter name	Description	Data type	Range [min, max]
1	Age	Patient's age in years	Int	[40, 95]
2	Anaemic_condition	Low count of red blood cells	Binary	[0, 1]
3	Creatinine_phosphokinase	Creatinine phosphokinase enzyme level in blood	Int	[23, 7861]
4	Diabetic_condition	Whether patient is diabetic	Binary	[0, 1]
5	Ejection_fraction	Blood leaving the heart during each contraction in percentage	Int	[14, 80]
6	High_blood_pressure	Whether patient has hypertension	Binary	[0, 1]
7	Platelet_count	Platelet count/ml of blood	Float	[25000, 850000]
8	Serum_creatinine	Creatinine level in blood	Float	[0.5, 9.4]
9	Serum_sodium	Sodium level in blood	Integer	[114, 148]
10	Gender	Patients gender	Binary	[0, 1]
11	Smoking_habit	Whether the patient smokes	Binary	[0, 1]
12	Time	Follow-up period in days	Int	[4, 285]
13	Death_Event	Death of the patient during the follow-up period	Binary	[0, 1]

tree related classifiers, provides a score for every feature in the data with a greater score for features that are more relevant. These methods have been used to rank the features and to identify prominent features. ML based classifiers have been used to predict mortality using combinations of the prominent features as input to identify the most effective combination.

ML algorithms use classification as a predictive tool to predict an outcome for a given input dataset. The performance of the classifier is based on the kind of the dataset. The classifiers widely used in medical prognosis include Decision Tree, Random Forest, Gradient Boost, K Nearest Neighbors, and Support Vector Machines (SVM) [3–6]. Decision Tree is one of the most preferred ML algorithms in medical applications due to its capability to deal with continuous and categorical data, its interpretability and the speed at which we can train them. It is also good at modeling

the nonlinear relationships that exist in medical data. Random Forest is a group of several decision trees that works as an ensemble. The results of many uncorrelated decision trees when combined together will produce a result better than the isolated trees. Gradient boosting algorithm is another robust technique to build predictive models in view of weak prediction models and ensembles. KNN algorithm is one among the easiest ML algorithms that compute the correspondence between available and the new data and put the new data into the class if it is almost identical. SVM is an ML algorithm that finds the most optimal hyperplane in an N-dimensional space which classifies the data points distinctly.

The performance of a classifier can be evaluated using a set of performance parameters. The performance parameters used in this paper are Accuracy, True Positive Rate (TP Rate), True Negative Rate (TN Rate), Precision, F1-Score, and AUC—ROC. Accuracy measures the percentage of observations classified correctly. Accuracy is not an accurate metric in the case of the imbalanced dataset. Hence other performance parameters also need to be considered. TP Rate, also familiar as Sensitivity or Recall, refers to the percentage of positive data points that are classified by the algorithm exactly. TN Rate, also called as Specificity, refers to the percentage of negative data points which are grouped by the algorithm correctly. Precision refers to the positive percentage rate. Harmonic mean of precision and TP Rate gives F1-Score. Area under the ROC curve refers as AUC ROC. The AUC ROC score gives us the likelihood of a randomly selected positive specimen being graded higher than a randomly selected negative specimen. The higher the area under the ROC curve is, the better will be the classification algorithm. Precision and TP Rate are two important metrics for evaluating the performance of a model. However, both these parameters cannot be maximized at the same time. As F1-Score considers both false positives (FP) and false negatives (FN), it is a more useful performance parameter than accuracy in the case of the imbalanced data set. For medical applications, TP Rate is a very crucial performance metric as False Negative results are to be kept as low as possible in medical applications.

4 Results and Discussion

4.1 Identification of Prominent Feature Combination

To identify the prominent features, the scores for each of the input features and its rank have been evaluated using the three feature selection methods namely correlation matrix, chi-square test and feature importance, and the results are tabulated in Table 2.

All three feature selection methods, as seen in the table, rank serum_creatinine, ejection-fraction and age as the top three features. The feature serum_sodium is ranked as fourth by the correlation method and feature importance method, whereas chi-square test method ranks it as the sixth feature. Based on the ranking obtained

Table 2 Feature scores and their rank

Input features	Correlation		Chi-squared test		Feature importance	
	Score	Rank	Score	Rank	Score	Rank
Age	**0.2537**	**3**	**2.3688**	**2**	**0.1380**	**3**
Anaemic_condition	0.0663	6	0.7466	5	0.0292	10
Creatinine_phosphokinase	0.0627	7	0.2520	7	0.1099	5
Diabetic_condition	−0.0019	11	0.0007	11	0.0403	7
Ejection_fraction	**−0.2686**	**2**	**1.8945**	**3**	**0.1753**	**1**
High_blood_pressure	0.0794	5	1.2215	4	0.0311	10
Platelet_count	−0.0491	8	0.0350	8	0.1069	6
Serum_creatinine	**0.2943**	**1**	**3.4716**	**1**	**0.1745**	**2**
Serum_sodium	**−0.1952**	**4**	**0.2674**	**6**	**0.1186**	**4**
Gender	−0.0043	10	0.0020	10	0.0372	9
Smoking_habit	−0.0126	9	0.0323	9	0.0391	8

using the three methods, the prominent features for the prediction of mortality are identified as serum_creatinine, ejection-fraction, age, and serum_sodium. Different combinations of these features have been used to predict mortality using different ML algorithms to identify the best combination.

In this paper, five ML algorithms have been used for prediction. A Decision Tree algorithm with maximum depth restricted to 3 (DT-3), Random Forest algorithm with maximum depth restricted to 3 (RF-3), Gradient boosting algorithm, kNN algorithm with the number of neighbors as 3 (KNN-3) and SVM algorithm with radial basis function (SVM RBF) have been implemented. To evaluate the five ML algorithms with different feature combinations as inputs, the performance metrics F1-Score and AUC ROC are considered as these two metrics give us a fair idea about the overall performance of the model. The nomenclature used in this paper for ML models developed using different feature combinations is shown in Table 3. Figure 1a and b show a plot of the performance metric F1-Score and AUC ROC respectively for the five ML algorithms developed using different feature combinations along with the maximum value for each algorithm. From Fig. 1, the three feature combinations that give the highest F1-Score and AUC ROC values for the five algorithms are tabulated in Table 4. Based on Table 4, the best performing feature combinations are identified as SC_EF and SC_EF_age. In the next section, further analysis of the results is carried out for the feature combinations SC_EF and SC_EF_age, to identify the best ML algorithm and feature combination.

4.2 Comparison of ML Algorithms

Based on the results from the previous section, the best performing feature combinations have been identified as SC_EF and SC_EF_age. In this section, additional

Table 3 Nomenclature for models developed for different feature combinations

Sl. No.	Nomenclature	Feature's used for prediction
1	SC_EF	serum_creatinine and ejection-fraction
2	SC_age	serum_creatinine and age
3	SC_SS	serum_creatinine and serum_sodium
4	EF_age	ejection-fraction and age
5	EF_SS	ejection-fraction and serum_sodium
6	age_SS	age and serum_sodium
7	SC_EF_age	serum_creatinine, ejection-fraction and age
8	SC_EF_SS	serum_creatinine, ejection-fraction and serum_sodium
9	SC_age_SS	serum_creatinine, age and serum_sodium
10	EF_age_SS	ejection-fraction, age and serum_sodium
11	SC_EF_age_SS	serum_creatinine, ejection-fraction, age and serum_sodium
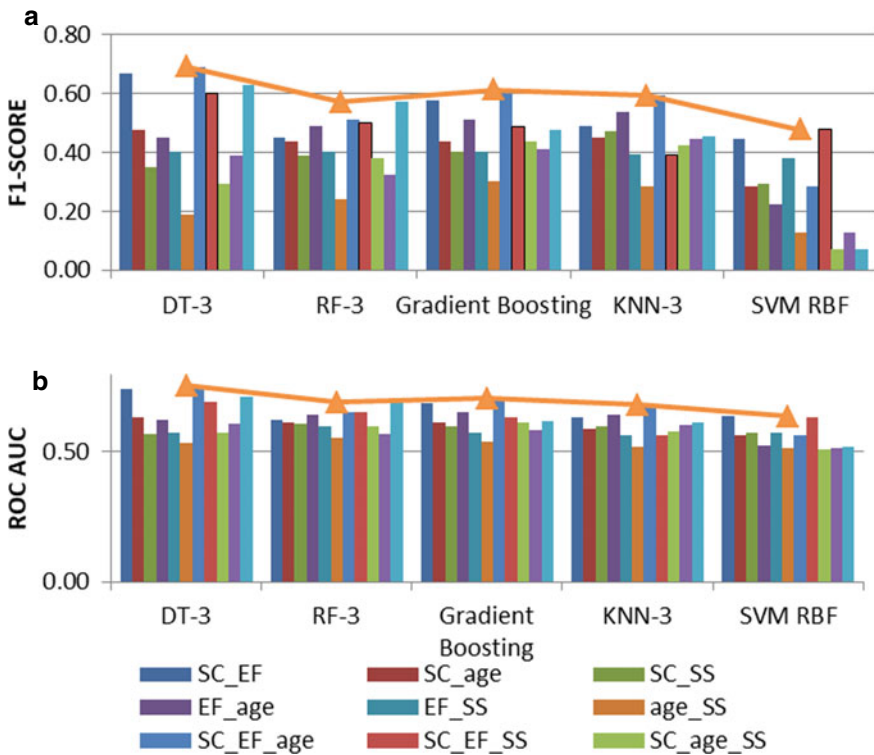
Fig. 1 **a** F1-SCORE **b** ROC AUC for different ML algorithms for each feature combination

Table 4 Top three feature combinations

Sl. No.	Parameter	Performance metric	1	2	3
1	DT-3	F1-Score	**SC_EF_age**	**SC_EF**	SC_EF_age_SS
		ROC AUC	**SC_EF_age**	**SC_EF**	SC_EF_age_SS
2	RF-3	F1-Score	SC_EF_age_SS	**SC_EF_age**	SC_EF_SS
		ROC AUC	SC_EF_age_SS	**SC_EF_age**	SC_EF_SS
3	GB	F1-Score	**SC_EF_age**	**SC_EF**	EF_age
		ROC AUC	**SC_EF_age**	**SC_EF**	EF_age
4	KNN-3	F1-Score	**SC_EF_age**	EF_age	**SC_EF**
		ROC AUC	**SC_EF_age**	EF_age	**SC_EF**
5	SVM RBF	F1-Score	SC_EF_SS	**SC_EF**	EF_SS
		ROC AUC	SC_EF_SS	**SC_EF**	EF_SS
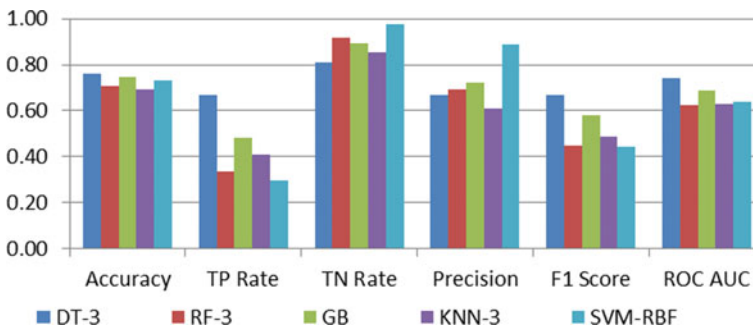
Fig. 2 Performance of SC_EF feature combination for different ML algorithms

performance parameters have been included to further analyze the results to identify the best feature combination and the classification algorithm suitable for predicting mortality for this application. Figures 2 and 3 shows a plot of the performance parameters for the five ML algorithms with the feature combination SC_EF and SC_EF_age respectively. As seen from the two graphs, the TP rate is relatively lower than the TN rate for all algorithms. This is due to the fact that the dataset used here is not a balanced dataset. It has more negative cases than positive ones. Due to the imbalanced nature of the dataset, accuracy is not a very good performance metric to evaluate the algorithms. All algorithms except the Decision Tree algorithm, give a higher precision value and TN Rate but a very low TP Rate, resulting in lower F1-Score and AUC ROC. As Decision Tree algorithm gives a higher TP Rate, F1-Score and AUC ROC, it would be the most suitable algorithm for predicting the mortality in this application. The Performance parameters for SC_EF and SC_EF_age with Decision Tree algorithm is shown in Table 5. Comparing values in Table 5, as the feature combination SC_EF_age gives a significantly higher TP Rate with better F1-Score and ROC AUC, it can be concluded that, the feature combination SC_EF_age performs
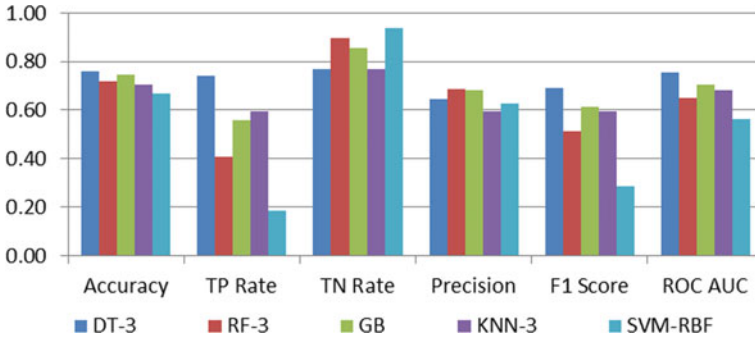
Fig. 3 Performance of SC_EF_age feature combination for different ML algorithm

Table 5 Performance parameters for SC_EF and SC_EF_age with decision tree algorithm

Sl. No.	Parameter	SC_EF	SC_EF_age
1	Accuracy	0.76	0.76
2	TP rate	0.67	**0.74**
3	TN rate	0.81	0.77
4	PPV	0.67	0.65
5	F1-score	0.67	**0.69**
6	ROC AUC	0.74	**0.76**

better than the feature combination SC_EF with Decision Tree algorithm. Hence it is concluded that, Decision Tree classifier with the features serum_creatinine, ejection_fraction and age as inputs is the most suitable model for this application. A visual representation of the Decision Tree classifier is shown in Fig. 4.
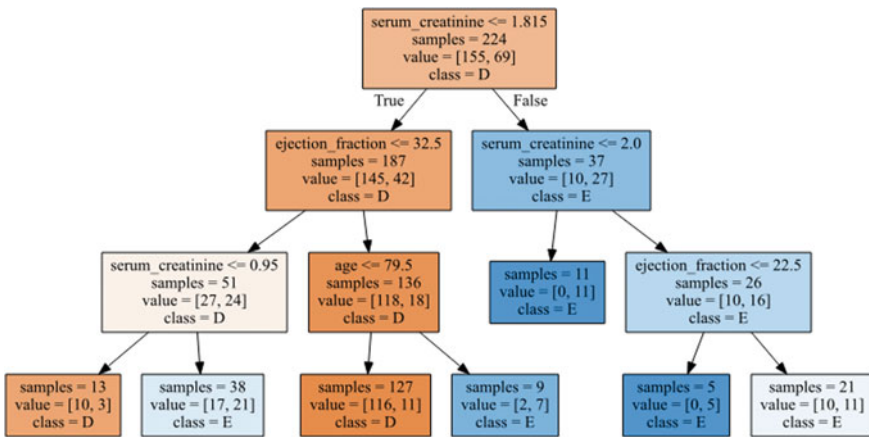
Fig. 4 Visual representation of decision tree classifier

5 Conclusions

This paper presents the identification and validation of prominent features for predicting mortality in patients with left ventricular dysfunction. Three different feature selection algorithms were used to rank the features and based on the ranking, four prominent features were identified as serum_creatinine, ejection_fraction, age, and serum_sodium. Five ML algorithms namely Decision Tree, Random Forest, Gradient Boosting, kNN, and SVM algorithms were implemented and their performance was evaluated for different combinations of the prominent features using F1-Score and ROC AUC. Based on the results it was concluded that the feature combinations SC_EF andSC_EF_age were the best performing feature combinations. Further analysis of the results for more performance parameters showed that Decision Tree algorithm is a good choice of classifier for this application as it gives the highest TP rate, F1-Score and AUC ROC. Comparing the results of feature combinations SC_EF_age and SC_EF with Decision Tree classifier, it was further concluded that the feature combination SC_EF_age gives better results with Higher TP Rate and good F1-Score and AUC ROC. Hence it is concluded that Decision Tree based classifier with the features serum_creatinine, ejection_fraction and age as input features would be the best model for predicting mortality in patients with left ventricular dysfunction.

References

1. Zhang Z, Han Y (2020) Detection of ovarian tumors in obstetric ultrasound imaging using logistic regression classifier with an advanced machine learning approach. IEEE Access 8:44999–45008
2. Wu M, Dai D, Shi Y, Yan H, Zhang X (2012) Biomarker identification and cancer classification based on microarray data using laplace naive bayes model with mean shrinkage. IEEE/ACM Trans Comput Biol Bioinf 9:1649–1662
3. Wang Z, Na J, Zheng B (2020) An improved kNN classifier for epilepsy diagnosis. IEEE Access. 8:100022–100030
4. VijiyaKumar K, Lavanya B, Nirmala I, Caroline SS (2019) Random forest algorithm for the prediction of diabetes. In: 2019 IEEE international conference on system, computation, automation and networking (ICSCAN), pp 1–5
5. Geweid GGN, Abdallah MA (2019) A New Automatic identification method of heart failure using improved support vector machine based on duality optimization technique. IEEE Access 7:149595–149611
6. Yu W, Xiaowei Y (2016) Application of decision tree for MRI images of premature brain injury classification. In: 2016 11th International conference on computer science & education (ICCSE). IEEE, Nagoya, Japan, pp 792–795
7. UK heart disease fatalities on the rise for first time in 50 years, the Guardian. http://www.theguardian.com/society/2019/may/13/heart-circulatory-disease-fatalities-on-rise-in-uk. Last accessed 25 Oct 2019
8. Heart Failure, NHLBI, NIH. https://www.nhlbi.nih.gov/health-topics/heart-failure. Last accessed 12 Sept 2020
9. Al'Aref SJ, Anchouche K, Singh G, Slomka PJ, Kolli KK, Kumar A, Pandey M, Maliakal G, Van Rosendael AR, Beecy AN, Berman DS, Leipsic J, Nieman K, Andreini D, Pontone G,

Schoepf UJ, Shaw LJ, Chang H-J, Narula J, Bax JJ, Guan Y, Min JK (2019) Clinical applications of machine learning in cardiovascular disease and its relevance to cardiac imaging. Eur Heart J 40:1975–1986

10. Al'Aref SJ, Singh G, van Rosendael AR, Kolli KK, Ma X, Maliakal G, Pandey M, Lee BC, Wang J, Xu Z, Zhang Y, Min JK, Wong SC, Minutello RM (2019) Determinants of in-hospital mortality after percutaneous coronary intervention: a machine learning approach. J Am Heart Assoc 8:e011160

11. Dunn WB, Broadhurst DI, Deepak SM, Buch MH, McDowell G, Spasic I, Ellis DI, Brooks N, Kell DB, Neyses L (2007) Serum metabolomics reveals many novel metabolic markers of heart failure, including pseudouridine and 2-oxoglutarate. Metabolomics 3:413–426

12. Gallagher J, McCormack D, Zhou S, Ryan F, Watson C, McDonald K, Ledwidge MT (2019) A systematic review of clinical prediction rules for the diagnosis of chronic heart failure. ESC Heart Fail 6:499–508

13. Ambale-Venkatesh B, Yang X, Wu CO, Liu K, Hundley WG, McClelland R, Gomes AS, Folsom AR, Shea S, Guallar E, Bluemke DA, Lima João AC (2017) Cardiovascular event prediction by machine learning. Circ Res 121:1092–1101

14. Can machine-learning improve cardiovascular risk prediction using routine clinical data? (n.d.). Available at: https://journals.plos.org/plosone/article?id=https://doi.org/10.1371/journal.pone.0174944. Accessed 12 Nov 2020

15. Panahiazar M, Taslimitehrani V, Pereira N, Pathak J (2015) Using EHRs and machine learning for heart failure survival analysis. Stud Health Technol Inform 216:40–44

16. Tripoliti EE, Papadopoulos TG, Karanasiou GS, Naka KK, Fotiadis DI (2017) Heart failure: diagnosis, severity estimation and prediction of adverse events through machine learning techniques. Comput Struct Biotechnol J 15:26–47

17. Chicco D, Jurman G (2020) Machine learning can predict survival of patients with heart failure from serum creatinine and ejection fraction alone. BMC Med Inform Decis Mak 20:16

18. Ahmad T, Munir A, Bhatti SH, Aftab M, Raza MA (2017) Survival analysis of heart failure patients: a case study. Plos One 12:e0181001

Design of Wideband Metamaterial Absorber for X-Band Application

Praveen Kumar, Rashmi Sinha, Arvind Choubey, Santosh Kumar Mahto, Pravesh Pal, and Ranjeet Kumar

Abstract In this paper, an ultrathin Swastik shape unit cell structure of a metamaterial absorber (MA) is capable of increasing absorption in the X-band spectrum for a variety of applications. The structure of the MA is arranged periodically and has a swastika shape with lumped resistor resonator. In addition to having an intuitive design, the unit cell structure is able to absorb more than 80% of the desired band. The simulated result shows two absorption peaks at 5.05 and 12.60 GHz with more than 95% absorptivity. A proposed absorber provides absorption bandwidths between 4.19 and 13.33 GHz (9.14 GHz) in Full-Width Half Maxima (FWHM). An ultrathin absorber has a thickness of 0.035 mm, which is nearly $\lambda/10$ corresponding to the absorption central frequency of 8.67 GHz. The unit cell's size of MA is 9×9 mm^2, with a thickness of 3.2 mm (0.0346 λ).

Keywords Lumped resistor · Metamaterial · Ultrathin · Wideband absorber

P. Kumar (✉) · R. Sinha · P. Pal · R. Kumar
Department of Electronics and Communication Engineering, National Institute of Technology, Jamshedpur, Jharkhand, India
e-mail: 2018rsec005@nitjsr.ac.in

R. Sinha
e-mail: rsinha.ece@nitjsr.ac.in

A. Choubey
Department of Electronics and Communication Engineering, Indian Institute of Information Technology, Bhagalpur, Bihar, India
e-mail: achoubey.ece@nitjsr.ac.in

S. K. Mahto
Department of Electronics and Communication Engineering, Indian Institute of Information Technology, Ranchi, Jharkhand, India
e-mail: skumar@iiitranchi.ac.in

343

1 Introduction

In the last few years, there has been increasing curiosity about metamaterials due to their unusual electromagnetic properties. Based on the properties of metamaterial, it finds application in filters [1], cloaking [2], antennas [3], resonators [4], sensors [5], and MA. The MA has many superior qualities, including lightweight, ultra-thinness, near-unity absorption, etc. Conventional absorbers such as multilayers [6] are large, fragile, and have fabrication complexity with respect to the proposed metamaterial absorbers. In 2008, Landy proposed the first single-band MA [7]. After this, many MAs have been reported for multiband, wideband, and single-band absorption [8, 9]. Several of the earlier proposed MAs have limited with less bandwidth and their practical applications [10–15].

Various MAs have been proclaimed for a wide span of applications but it suffers from the limitation that it has an absorption phenomenon at a particular frequency. To obtain wideband resonance phenomena, various configurations like multi-resonant [17], multilayer [16], and single layer [7] have been reported. Multilayer and multi-resonant absorbers find limitations in creating thin absorbers. A variety of applications have been reported for single-layer MA that overcomes the above limitations [18].

The simulated result shows absorption peaks with more than 95% absorptivity at 5.05 and 12.60 GHz. The proposed MA provides an FWHM bandwidth of 9.14 GHz from 4.19 to 13.33 GHz. The MA is of an ultrathin thickness of 0.035 mm that is nearly $\lambda/10$ corresponding to the absorption center frequency of 8.67 GHz. The proposed design was optimized parametrically to match its impedance with the free space at the desired frequency.

2 Proposed Unit Cell Structure

Figure 1 shows three layers design of MA, which consists of two copper layers, and the dielectric substrate is sandwiched between the copper layers. A frequency selective surface (FSS) is an upper layer made up of a periodic metallic unit cell geometry, and a copper ground is beneath it. The dimensions of MA are optimized to maximize the absorption magnitude due to a field coupling among the loops. Equation (1) can be used for determining the absorptivity of the MA.

$$A(W) = 1 - |S_{11}|^2 - |S_{21}|^2 \tag{1}$$

Where reflection and transmission coefficient are represented by S_{11} and S_{21}, respectively. The bottom layer of copper completely blocks out the incident wave because it is completely covered with copper. Thus, there is no power transmitted ($S_{21} = 0$), parameter S_{11} represents the quantity of energy absorbed by MA. A higher S_{11} value indicates more MA absorption.

Fig. 1 Three-layer design of MA
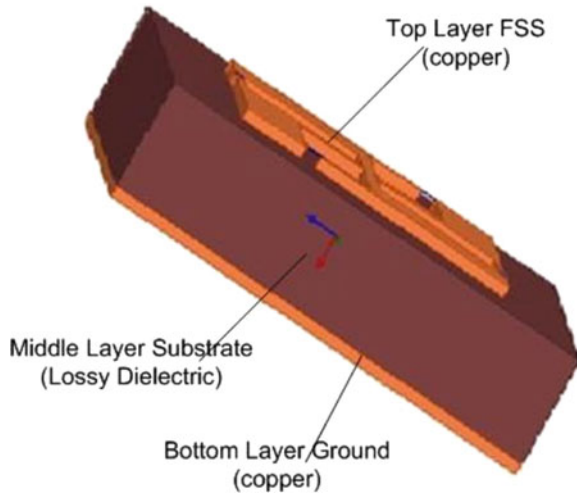
The primary and secondary boundary conditions are applied to the sidewalls of a unit cell to simulate a metamaterial periodic structure. Using these boundary conditions, the electric fields on one surface correspond to the electric fields on the other. With the application of these boundary conditions, the electric field at each point on the slave boundary is forced to match the electric potential within a phase difference corresponding to the master boundary. These boundary conditions help simulate the structures such as infinite arrays.

A unit cell structure of the proposed MA is illustrated in Fig. 1. The structure is composed of two panels of metal (top and ground layer), each fabricated from copper, separated by FR-4 dielectric substrate, and thickness of 3.2 mm, top layer is a Swastik shape structure as shown in Fig. 2a. The peak absorption frequencies are 4.2 and 13 GHz. Its absorptivity is very less at peak 50% and 75%, respectively. So, this structure cannot produce the desired response. We desire to produce a wideband with more than 80% absorptivity. Due to narrow bandwidth and less absorptivity percentage of basic structure, we introduce four Lumped Resistors in the proposed structure. According to the proposed structure, the Swastik shapes are interconnected by resistors and arranged in a periodic array as shown in Fig. 2b. The bottom surface is entirely capped with copper to stop incidents wave pass through MA. The optimized dimensions of the proposed MA are given in Table 1.

3   Result and Discussion

The simulated result appears a wideband of absorption, and it shows two absorption peaks at 5.05 and 12.60 GHz with more than 95% absorptivity is shown in Fig. 3a. The simulated reflection coefficient of the metamaterial absorber is shown in Fig. 3b.

(a) Without resistor   (b) With resistor
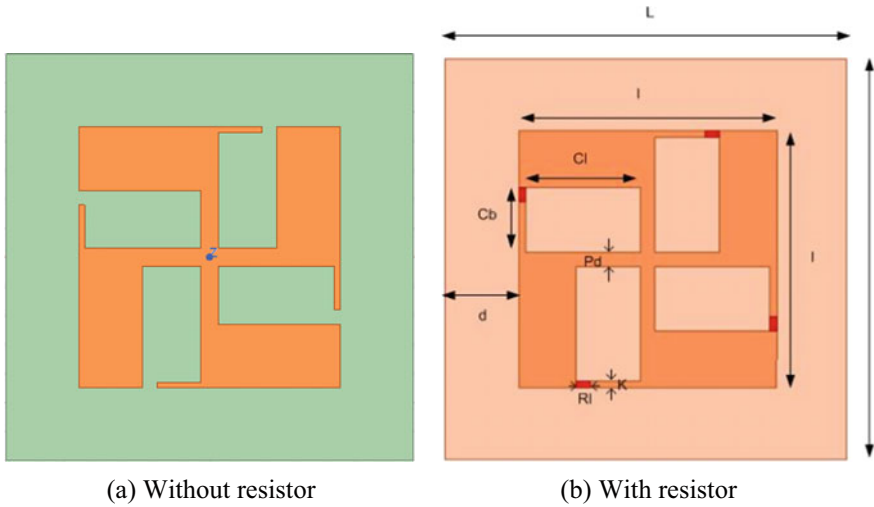
Fig. 2 Top-view of the proposed MA

S. No	Parameters	Dimension (mm)
1	L	14
2	I	9
3	Cl	4
4	d	2.5
5	K	0.25
6	Pd	0.5
7	Cb	2.25
8	Rl	0.5

Table 1 Optimized dimensions of the proposed wideband ultrathin MA

The proposed absorber provides a full-width half maxima bandwidth from 4.19 to 13.33 GHz. It consists of an ultrathin sheet with 0.035 mm thick, which is nearly $\lambda/10$, and its center frequency is 8.67 GHz.

The real and imaginary part of the input impedance is shown in Fig. 4. At desired frequency bands, the real part of input impedance is stable whereas the imaginary part is nearly zero. This means that the input impedance of the proposed MA is almost equal to the impedance of free space for incident waves. Thus, the maximum power of the incident wave propagates into the MA and is trapped.

The representation of surface current distributions is shown in Figs. 5 and 6 at 5.02 and 12.60 GHz. According to the observations, the lumped resistor of the structure is responsible for the high current. Additionally, the unit cell's inner corner also exhibits a high surface current. The unit cell and ground plane surfaces of the proposed MA show antiparallel surface current distribution at the peak absorption
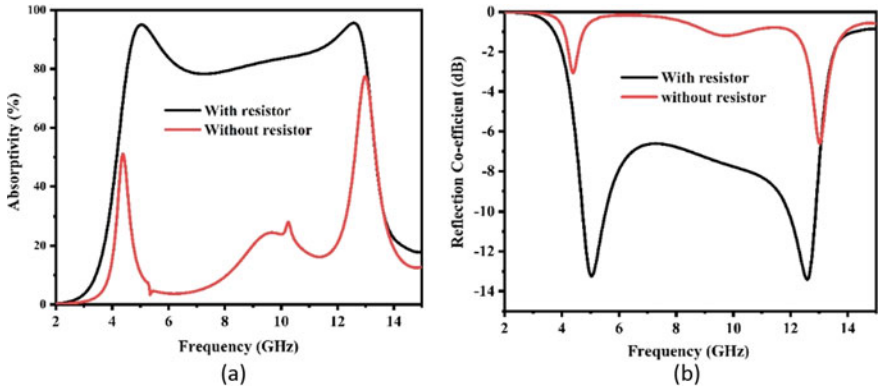
Fig. 3 **a** Absorptivity and **b** reflection coefficient of the proposed MA
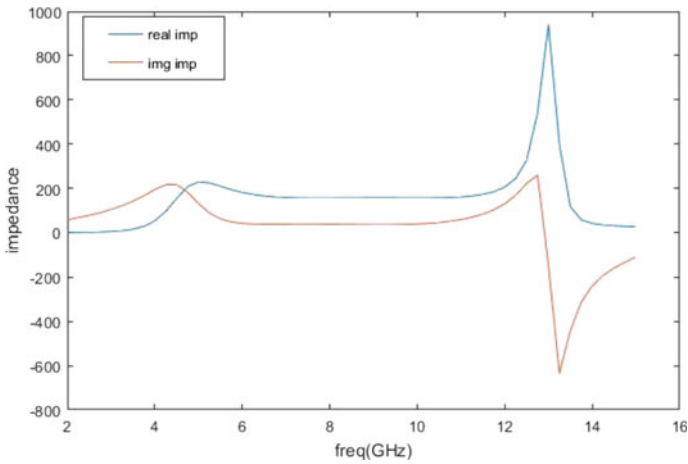
Fig. 4 Input impedance of the proposed MA

frequencies (5.05 and 12.60 GHz). The current at these frequencies increases the strength of the magnetic resonance frequencies.

Comparison between the proposed work and recently reported work is depicted in Table 2. FWHM of the proposed structure is more than all previous work. In [17, 22] has less unit cell size but these structures are polarization sensitive.

4 Conclusion

A novel design of ultrathin ($\lambda/10$) broadband MA has been presented. Simulated results indicate that the proposed MA provides an FWHM bandwidth of 9.14 GHz.

(a) 5.05 GHz   (b) 12.56 GHz
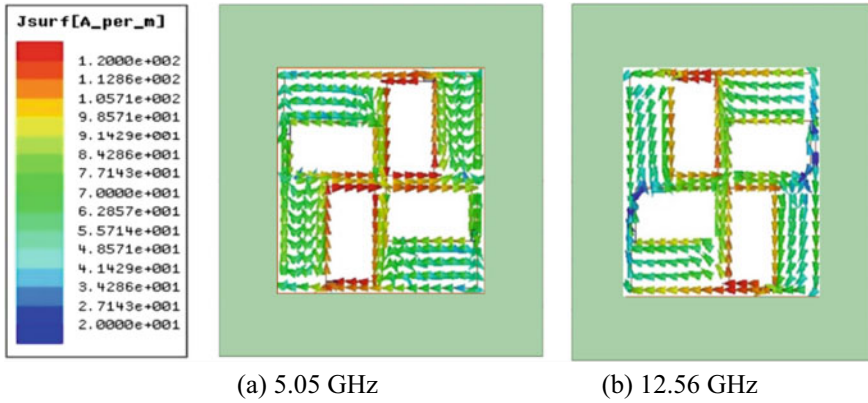
Fig. 5 Surface current distribution at the top

(a) 5.12 GHz   (b) 12.55 GHz
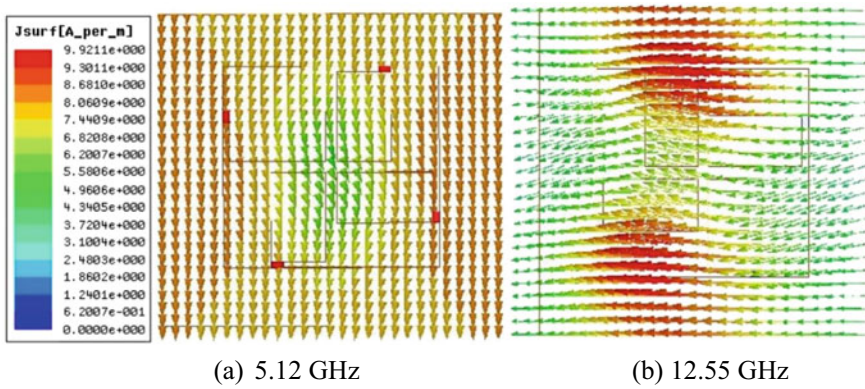
Fig. 6 Surface current distribution at the bottom

Table 2 Comparison between the proposed MA with the previous reported absorbers

References	Center frequency (GHz)	Unit cell size (mm)	Thickness	FWHM (%)	Polarization insensitivity
[19]	10	14.2	0.6 (0.02λ)	11	Yes
[20]	9.98	7.2	1 (0.033λ)	11.52	Yes
[17]	15.13	6.4	3.65 (0.18λ)	95	No
[21]	10.15	13.8	5.6 (0.19λ)	45	Yes
[22]	10.05	7.1	2 (0.067λ)	72.64	No
This work	**8.86**	**14**	**3.2 (0.1λ)**	**104**	**Yes**

The incidence angle for TM and TE polarizations is up to 45 degrees. Moreover, the proposed MA shows higher than 80% absorption from 4.5 to 13 GHz. The simulation indicates two distinct maximum absorption frequencies at 5.05 GHz and 12.60 GHz, corresponding to absorption values of 95% and 95.6%, respectively. The distributions of surface currents and electromagnetic fields are illustrated at the absorption frequencies to better understand absorption mechanisms. A performance analysis is also conducted on the MA under normal incidence for a variety of incident angles and polarization angles.

References

1. Li C, Xiao Z, Li W, Zou H (2018) Tunable multiband band-stop filter based on graphene metamaterial in the frequency. J Electromagn Waves Appl 32(18):2481–2489
2. Bae KU, Kim H, Kim Y, Yang W-Y, Myung N-H (2016) Improvement of FDTD method regarding cloaking metamaterials by interpolation. J Electromagn Waves Appl 30(10):1366–1379
3. Majid HA, Abd Rahim MK, Masri T (2009) Microstrip antenna's gain enhancement using left-handed metamaterial structure. Prog Electromagn Res 8:235–247
4. Si L-M, Lv X (2008) CPW-fed multi-band omni-directional planar microstrip antenna using composite metamaterial resonators for wireless communications. Prog Electromagn Res 83:133–146
5. Wang W, Yan F, Tan S, Zhou H, Hou Y (2017) Ultrasensitive terahertz metamaterial sensor based on vertical split ring resonators. Photonics Res 5(6):571–577
6. Ranjan P, Choubey A, Mahto SK (2018) A novel approach for optimal design of multilayer wideband microwave absorber using wind driven optimization technique. AEU-Int J Electron Commun 83:81–87
7. Landy NI, Sajuyigbe S, Mock JJ, Smith DR, Padilla WJ (2008) Perfect metamaterial absorber. Phys Rev Lett 100(20):207402
8. Ranjan P, Choubey A, Mahto SK, Sinha R (2018) An ultrathin five band polarization insensitive metamaterial absorber having hexagonal array of 2d-bravais-lattice. Prog Electromagn Res 87:13–23
9. Ranjan P, Choubey A, Mahto SK, Sinha R (2018) A six-band ultra-thin polarization-insensitive pixelated metamaterial absorber using a novel binary wind driven optimization algorithm. J Electromagn Waves Appl 32(18):2367–2385
10. Ma B, Liu S, Bian B, Kong X, Zhang H, Mao Z, Wang B (2014) Novel three-band microwave metamaterial absorber. J Electromagn Waves Appl 28(12):1478–1486
11. Qiu K, Feng S (2016) A novel metamaterial absorber with perfect wave absorption obtained by layout design. J Electromagn Waves Appl 30(4):523–535
12. Tak J, Jeong E, Choi J (2017) Metamaterial absorbers for 24-GHz automotive radar applications. J Electromagn Waves Appl 31(6):577–593
13. Ranjan P, Mahto SK, Choubey A (2019) BWDO algorithm and its application in antenna array and pixelated metasurface synthesis. IET Microw Antennas Propag 13(9):1263–1270
14. Chaurasiya D, Ghosh S, Bhattacharyya S, Srivastava KV (2015) An ultrathin quad-band polarization-insensitive wide-angle metamaterial absorber. Microw Opt Technol Lett 57(3):697–702
15. Zheng D, Cheng Y, Cheng D, Nie Y, Gong RZ (2013) Four-band polarization-insensitive metamaterial absorber based on flower-shaped structures. Prog In Electromagn Res 142:221–229

16. Chen Z, Han N, Pan Z, Gong Y, Chong T, Hong M (2011) Tunable resonance enhancement of multi-layer terahertz metamaterials fabricated by parallel laser micro-lens array lithography on flexible substrates. Opt Mater Express 1(2):151–157
17. Costa F, Genovesi S, Monorchio A (2012) A chipless RFID based on multiresonant high-impedance surfaces. IEEE Trans Microw Theory Tech 61(1):146–153
18. Watts CM, Liu X, Padilla WJ (2012) Metamaterial electromagnetic wave absorbers. Advanced Materials 24(23):OP98–OP120
19. Smith DR, Padilla WJ, Vier D, Nemat-Nasser SC, Schultz S (2000) Composite medium with simultaneously negative permeability and permittivity. Phys Rev Lett 84(18):4184
20. Skolnik MI (2008) Radar handbook. McGraw-Hill Education
21. Rufangura P (2015) Wide-band perfect metamaterial absorber for solar cells applications. Master's thesis, Middle East Technical University
22. Wang C-M, Chang Y-C, Abbas MN, Shih M-H, Tsai DP (2009) T-shaped plasmonic array as a narrow-band thermal emitter or biosensor. Opt Express 17(16):13526–13531

Experimental Investigation of PV Microinverter Technology for Low-Power Applications

Ruchira, R. N. Patel, and Sanjay Kumar Sinha

Abstract In this paper, an experimental investigation of PV microinverter technology for low-power application was done. The experiment was conducted on a 1 kW rooftop solar system installed in a residential complex and connected to the household load. The system is connected through DPST switch to two separate converter setups. Physical circumstances have an effect on the performance of photovoltaic systems. As a result, the performance of both PV inverter designs was monitored for a period of 10 days. In MATLAB, a graphical user interface was created to compare the central inverter and microinverter. The comparison is based on experimental findings achieved for a 1 kW system comprised of four 250 W panels, four microinverters, and one central inverter. Apart from the system's equipment, a lux meter, a digital voltmeter, laser temperature sensor and an ammeter were used to conduct the investigation. The designed GUI will show how temperature and solar irradiation change over time, as well as the effect on power output whether connected to a central inverter or a microinverter under normal, shading, and dusty situations.

Keywords Photovoltaic · Microinverter · Central inverter

1 Introduction

Renewable energy sources include sunlight, wind, rain, tides, and geothermal heat. These resources are renewable and can be replenished naturally. Thus, unlike depleting traditional fossil fuels, these resources can be deemed inexhaustible. The

Ruchira (✉) · S. K. Sinha
Amity University Uttar Pradesh, Noida, Uttar Pradesh, India
e-mail: er.ruchiragarg@gmail.com

S. K. Sinha
e-mail: sksinha6@amity.edu

R. N. Patel
National Institute of Technology, Raipur, India
e-mail: rnpatel.ee@nitrr.ac.in

global energy crisis has re-energised efforts to expand and develop Clean and Renewable Energy Sources Organizations from all over the world are adopting Clean Development Mechanisms (CDMs). Apart from the world's increasingly diminishing fossil fuel supplies, another significant element pushing against fossil fuels is the pollution produced by their combustion. In comparison to conventional energy sources, renewable energy sources are believed to be cleaner and produce energy without the adverse consequences of pollution.

Among all of these renewable energy sources, the most abundant and sustainable is the sun, which provides the Earth with around 150,000 TW of energy. Even though half of this energy is lost before it reaches the earth's surface and only a small fraction is practically usable for electricity generation, the total amount of energy is more than sufficient to meet world energy needs. One of the most significant technological and scientific issues we face today is developing cost-effective methods for collecting, converting, storing, and utilising solar energy [3]. Solar energy can be used in three ways: to provide energy for biomass growth, to gather heat from the sun in solar thermal systems, or to convert solar irradiation into electricity in photovoltaic systems. A photovoltaic (PV) system utilises solar panels to generate usable electricity, and these solar panels are typically equipped with an inverter that converts their output DC power to AC power for distribution to users via an electric power grid. PV technology is a relatively new development in comparison to other renewable energy sources. PV systems have been employed in specific applications for 50 years but have been used as grid-connected systems for only 20 years [8]. The relatively high cost of PV systems and the inconvenience of being without power at night are the primary impediments to wider adoption in the industry. However, the cost of photovoltaic cells has continuously reduced from US $20 per watt in 1990 to less than US $0.7 per watt in 2014. Along with the remarkable advancements in the semiconductor sector, we are confident that the photovoltaic industry has a bright future and will play a larger part in electricity generation as a dependable and inexpensive green energy supply in the near future [1–3].

In addition to the system's equipment, numerous measurement devices were used for the investigation, such as the lux meter, the digital voltmeter and the clamp meter. Three different circumstances were investigated, namely, normal, shading, and dusting. The graphs given depict data collected every half hour of the day at specified intervals. In normal circumstances, observations on both MI and CI were made under the same conditions. In typical conditions, no continuous shading has been presumed due to any tree or other obstruction. However, cloud darkening is conceivable that is not within our control. The second condition is the shade condition, where partial shade conditions were manually developed to take into account the effect of shade, commonly through trees and surrounding walls etc. The effects of shade have been studied in different places and times [4]. The third condition is that of dusting, in which the effect of dust collection on solar panels was taken into account [5].

2 PV Inverter Technology

Inverters are critical components of every photovoltaic system's equipment. Inverters are used to convert the energy generated by solar panels into alternating current (AC) electricity that can be consumed immediately or connected to the grid via household devices. Over the last few decades, inverter technology has advanced gradually to enable homeowners to get the maximum amount of energy possible from their photovoltaic systems. Additionally, it monitors and regulates the PV system's operation. Central inverters, string inverters, and microinverters are the three types of photovoltaic inverters. We are comparing central inverters and microinverters in this paper. Both central inverters and microinverters accomplish this task differently and have their own set of advantages and disadvantages, which are explained below. Solar panels are connected in series with central inverters, and the DC electricity generated by these panels is converted to AC power, as illustrated in Fig. 1.

A typical central inverter is located in a sheltered area away from extreme weather and is typically located near the main power panel. This architecture collects DC energy from all solar panels in a single combiner and transfers it to a central inverter
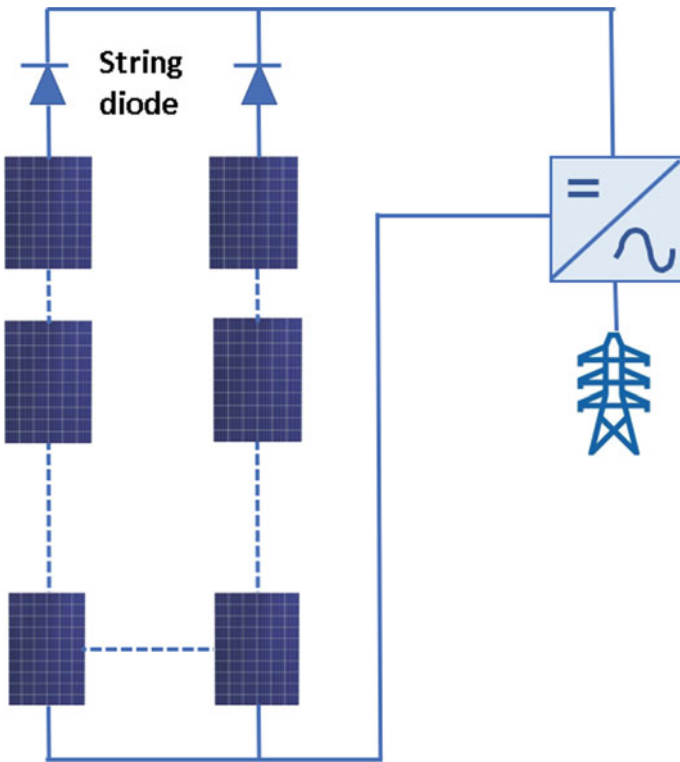
Fig. 1 PV with central inverter
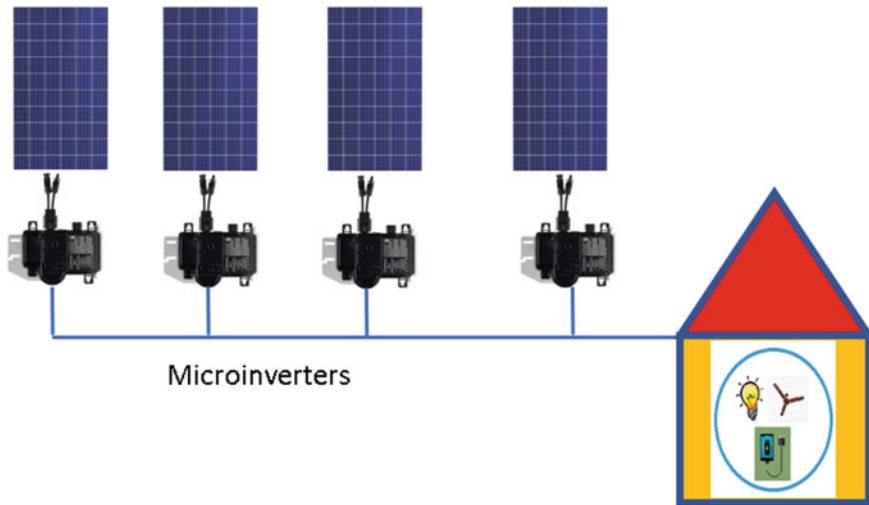
Fig. 2 PV with microinverter supplying domestic load

for conversion to alternating current electricity. As a result, the central inverter's voltages can reach quite high levels, occasionally exceeding 600 V DC [3].

A solar microinverter is a plug-and-play photovoltaic device that converts direct current to alternating current, as seen in Fig. 2. In comparison to microinverters, typical central inverters are made up of a single inverter coupled to a number of solar panels. However, the output of microinverters can be aggregated and frequently supplied to the electric grid.

Microinverters for solar energy have a variety of advantages over conventional inverters. The key benefit is that they electrically separate the panels, ensuring that small shading, debris, or snow lines on any one solar module, or even a complete module failure, do not greatly reduce the array's output. Each microinverter maximises energy harvesting by performing maximum power point tracking (MPPT) on the modules it is connected to. Additionally, microinverter technology benefits include simplified system design, reduced amperage cables, improved inventory management, and increased safety [6–14].

3   Experimental Setup

An experimental comparison was made between a central inverter and a microinverter coupled to a 1 kW roof photovoltaic system, as illustrated in Fig. 3. The study collected data from a 1 kW grid panel solar installation in Bhilai, Chhattisgarh, India on the top of a building. The test system consists of a 1 kW system with four 250 W panels, four microinverters and a central inverter. The PV system has been connected

to either the central inverter or the microinverter by means of DPST switches. Since the panel location and the conditions of input remain constant, the use of a DPST switch results in a more productive way. The Hoymiles MI-250 microinverter was used in this study. Tables 1, 2, and 3 tabulates the specifications of microinverter, photovoltaic panel, and central inverter respectively used in this investigation [15].

Fig. 3 Experimental setup for CI and MI performance analysis

Table 1 Specifications of solar microinverter

Input ratings	Output ratings
Maximum input voltage = 60 V	Nominal output voltage = 230 V A.C
Maximum input current = 10A dc	Nominal output frequency = 50 Hz
Maximum input short circuit current = 15 A	Output power factor = 0.99
	Maximum output current = 1.08 A A.C
	Maximum continuous output power = 250 W
	Maximum output overcurrent protection = 20 A

Table 2 Specifications of photovoltaic panel

Parameter	Value
Maximum power (PMP)	250Wp
Open circuit voltage	44 V
Short circuit current	7.6 A
Voltage at maximum power	36 V
Current at maximum power	6.95 A
Maximum system voltage	DC 1000 V
Normal operating cell temperature	44.6 °C
Temperature coefficient	-1.036 W/°C

Table 3 Specifications of central inverter

Parameter	Value
Output power	1 kW
Output frequency	230 V
Input voltage	250 V
Efficiency	97.4%
Output current	11.5 A
MPP tracker	Single
MPPT efficiency	99.5%
Output voltage	230 V

In addition to the system's equipment, numerous measurement devices were used for the investigation, such as the lux meter, the digital voltmeter and the clamp meter. Three different circumstances were investigated, namely, normal, shading, and dusting. The graphs given depict data collected every half hour of the day at specified intervals. In normal circumstances, observations on both MI and CI were made under the same conditions. In typical conditions, no continuous shading has been presumed due to any tree or other obstruction. However, cloud darkening is conceivable that is not within our control. The second condition is the shade condition, where partial shade conditions were manually developed to take into account the effect of shade, commonly through trees and surrounding walls etc. The effects of shade have been studied in different places and times. The third condition is that of dusting, in which the effect of dust collection on solar panels was taken into account [12].

4   Ohmic Loss Calculations

As we know, every material has its own internal resistance and the value of that internal resistance is different for every material. Cable size is one of the most important factors affecting the power output of the PV system. Cable size means

the wires connected from PV system to the various load and measuring instruments. Variation in cable size and cable length creates resistive losses. If the PV system is not designed with proper cable size and thickness, the output of the system decreases due to extra unwanted voltage drop.

$$\therefore \quad \Rightarrow \text{Resistance} = \rho \times \frac{l}{a}$$

where,

ρ resistivity of material.
l length of material.
a cross-sectional area.

Resistance of material depends on temperature, directly proportional to length of conductor and inversely proportional to area of conductor.

Ohmic losses, when current flows through any conductor, due to its internal resistance unwanted $i^2 R$ Losses take place. As the unit of resistance is Ohm. That's why this loss is called as Ohmic losses.

$$\Rightarrow \text{Ohmic loss}_{\text{microNC}} = \sum_{0}^{i} (I_{\text{micro}})^2 \times k \tag{1}$$

where,

i sequence number of set of data to be
k Ohmic loss calculation factor, i.e. resistance per m for 4 sqmm wire.

(Source—Havells PVC Insulated Industrial Grade Flexible Cable Catalogue 2017–18)
Standard value for k is 4.95 Ω/Km.
So, calculating Ohmic loss factor per meter for 4 sqmm conductor used.
$\Rightarrow k = 4.95/1000$ ($\therefore$ 1 km $= 1000$ m)
$\Rightarrow k = 0.00495 \, \Omega/\text{m}$
The calculations of Ohmic losses under normal condition are as follows
Putting value of k in Eq. (1).

$$\Rightarrow \text{Ohmic loss}_{\text{microNC}} = \sum_{0}^{i} (I_{\text{microNC}})^2 \times 0.00495 \, \text{Watt}$$

$$\Rightarrow \text{AvgOhmic loss}_{\text{microNC}} \text{perm} = (\text{Avg} I_{\text{microNC}})^2 \times 0.00495 \, \text{Watt} \tag{2}$$

$$\Rightarrow \text{Avg} I_{\text{microNC}} = \frac{\sum_{0}^{i} I_{\text{microNC}}}{n} = 1.1933 A \, (\text{from readings}) \tag{3}$$

Putting value of $\mathrm{Avg}I_{\mathrm{microDC}}$ from (3) into Eq. (2)

$$\Rightarrow \mathrm{AvgOhmic\,loss}_{\mathrm{microNC}}\mathrm{per\,m} = (1.1933)^2 \times 0.00495 = 0.0070490\,\mathrm{Watt}$$

$$\Rightarrow \mathrm{Total\,Ohmic\,loss}_{\mathrm{microNC}} = 0.70490 \times 2 = 0.014098\,\mathrm{Watt} \qquad (4)$$

$\therefore$ In our experimental setup, 2 m connecting wire of 4mm^2 is used for interconnection in case of PV system with microinverter.

As microinverter is installed just on the back side of each PV module so, direct conversion of DC power into AC takes place at panel only unlike Central inverter in which DC power of all PV modules is added then it is fed to the central inverter connected far away. Large length of wires is required in case of central inverter whereas microinverter requires only few m lengths of wire, which is very less. Now, calculating Ohmic losses in case of PV system installed with central inverter.

$$\Rightarrow \mathrm{Ohmic\,loss}_{\mathrm{centralNC}} = \sum_{0}^{i} (I_{\mathrm{centralNC}})^2 \times 0.00495\,\mathrm{Watt}$$

$$\Rightarrow \mathrm{AvgOhmic\,loss}_{\mathrm{centralNC}}\mathrm{per\,m} = (\mathrm{Avg}I_{\mathrm{centralNC}})^2 \times 0.00495\,\mathrm{Watt} \qquad (5)$$

$$\Rightarrow \mathrm{Avg}I_{\mathrm{centralDC}} = \frac{\sum_{0}^{i} I_{\mathrm{centralNC}}}{n} = 1.3422\,A\,(\mathrm{from\,experimental\,readings}) \qquad (6)$$

Putting value of $Avg I_{\mathrm{microNC}}$ from Eq. (6) into Eq. (5)

$$\Rightarrow \mathrm{AvgOhmic\,loss}_{\mathrm{centralNC}}\mathrm{per\,m} = (1.3422)^2 \times 0.00495 = 0.00891\,\mathrm{Watt}$$

$$\Rightarrow \mathrm{Total\,Ohmic\,loss}_{\mathrm{centralNC}} = 0.008917 \times 15 = 0.13376\,\mathrm{Watt}$$

$\therefore$ In our experimental setup, 15 m interconnecting wire of 4 mm^2 is used for connection in case of PV system installed with central inverter.

% Ohmic loss saving in microinverter case under normal condition is given by

$$\Rightarrow \mathrm{\%ohmic\,loss\,saving}$$
$$= \left(\frac{\mathrm{Total\,Ohmic\,loss}_{\mathrm{centralNC}} - \mathrm{Total\,Ohmic\,loss}_{\mathrm{microNC}}}{\mathrm{Total\,Ohmic\,loss}_{\mathrm{microNC}}} \right) \times 100$$

Or simply Ohmic loss saving in case of microinverter is

$$\Rightarrow \mathrm{\%ohmic\,loss\,saving\,microinverterNC} = \frac{0.014098}{0.133765} \times 100 = 10.539\%$$

Table 4 Comparison of parameters under normal, shading, and dusting conditions

Parameter	Normal condition (%)	Shading condition (%)	Dusting condition (%)
How much per cent more output is given by the PV system installed with microinverter than that given by PV system installed with central inverter	9.694	15.756	10.645
How much per cent of Ohmic losses takes place in PV system installed with microinverter than that takes place in PV system installed with central inverter	10.539	17.589	13.408

Above calculation concludes that Ohmic losses in PV system installed with microinverter are only 10.539% of the losses incorporated by the PV system installed with central inverter. Similarly, the losses are calculated for shading and dusting conditions and also the results are compiled in Table 4.

5 Results and Discussion

The experimental investigation of central inverter and microinverter technology connected to 1 kW photovoltaic system has been done, and the different parameters have been recorded at discrete intervals. Figures 4, 5 and 6 show the comparison curves of microinverter (MI) and central inverter (CI) technology under three different conditions—normal, shading and dusting. From Figs. 4, 5, and 6, it can be inferred that MI technology performs significantly better than CI technology. Table 4 mentions the percentage difference in output power and Ohmic losses obtained with microinverter and central inverter technology under normal, shading, and dusting conditions.

6 Conclusion

Experimental 1 kW PV system installed with microinverter and the same system with central inverter is completely analysed based on the parameters recorded during performing experiment. MATLAB GUI is used for plotting graphs; mathematical calculations were made, which gives the following conclusion:
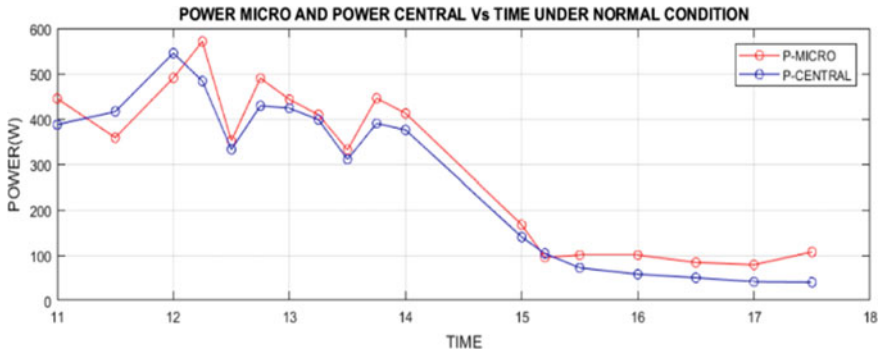
Fig. 4 Comparison of output power obtained with CI and MI under normal condition
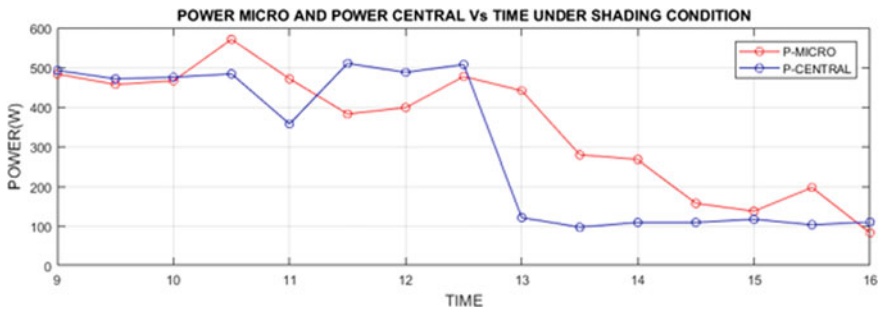
Fig. 5 Comparison of output power obtained with CI and MI under shading condition
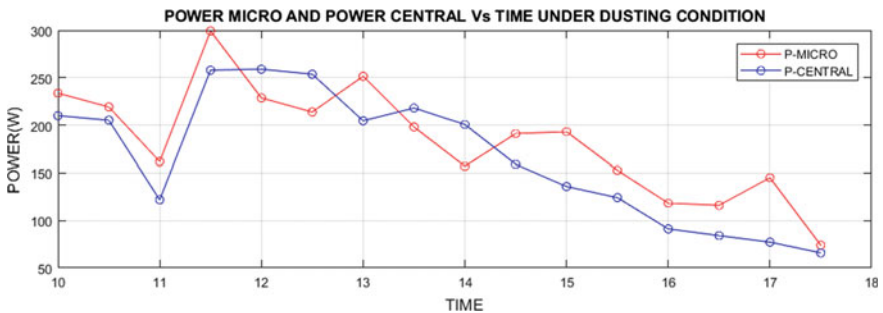
Fig. 6 Comparison of output power obtained with CI and MI under dusting condition

1. Under normal condition
   Research work concludes that Ohmic loss in PV system installed with microinverter is only 10.539% of the losses incorporated by the PV system installed with central inverter.

     Under normal condition, power output of system with microinverter is 9.694% more than that of power output of system with central inverter of our installed 1 kW experimental setup.

2. Under partial shade condition

     Above calculation concludes that Ohmic loss in PV system installed with microinverter is only 17.589% of the losses incorporated by the PV system installed with central inverter.

     Under partial shading condition, power output of system with microinverter is 15.756% more than that of power output of system with central inverter of our installed 1 kW experimental setup.

3. Under dust condition

     Above calculation concludes that Ohmic loss in PV system installed with microinverter is only 13.408% of the losses incorporated by the PV system installed with central inverter.

     Under dusting condition, power output of system with microinverter is 15.756% more than that of power output of system with central inverter of our installed 1 kW experimental setup.

References

1. Zhou X, Liu M, Ma Y, Gao Z (2018) An overview of photovoltaic system. In: 2018 Chinese control and decision conference (CCDC), pp 4949–4954. https://doi.org/10.1109/CCDC.2018.8407988
2. Pali BS, Vadhera S (2016) Renewable energy systems for generating electric power: a review. In: 2016 IEEE 1st international conference on power electronics, intelligent control and energy systems (ICPEICES), pp 1–6. https://doi.org/10.1109/ICPEICES.2016.7853703
3. Karabanov S, Kukhmistrov Y, Miedzinski B, Okraszewski Z (2010) Photovoltaic systems. Mod Electric Power Syst 2010:1–5
4. Ramabadran R (2009) Effect of shading on series and parallel connected solar PV modules. Mod Appl Sci 3(10):32–41
5. Appels R, Muthirayan B, Beerten A, Paesen R, Driesen J, Poortmans J (2012) The effect of dust deposition on photovoltaic modules. In: 2012 38th IEEE photovoltaic specialists conference, pp 001886–001889. https://doi.org/10.1109/PVSC.2012.6317961
6. Kjaer SB, Pedersen JK, Blaabjerg F (2005) A review of single-phase grid-connected inverters for photovoltaic modules. IEEE Trans Ind Appl 41:1292–1306
7. Bzura JJ (2010) The AC module: an overview and update on self-contained modular PV systems. In: 2010 IEEE Power and Energy Society General Meeting, pp 1–3
8. Janardhan K, Mittal A, Ojha A (2020) Performance investigation of stand-alone solar photovoltaic system with single phase micro multilevel inverter. In: Energy Reports, vol 6. pp 2044–2055, ISSN 2352-4847
9. Alluhaybi K, Batarseh I, Hu H (2019) Comprehensive review and comparison of single-phase grid-tied photovoltaic microinverters. IEEE J Emerg Sel Top Power Electron 8(2):1310–1329. https://doi.org/10.1109/JESTPE.2019.2900413
10. Mundada AS, Nilsiam Y, Pearce JM (2016) A review of technical requirements for plug-and-play solar photovoltaic microinverter systems in the United States. Sol Energ 135:455–470 ISSN 0038-092X

11. Pal D, Koniki H, Bajpai P (2016) Central and micro inverters for solar photovoltaic integration in AC grid. In: National power systems conference (NPSC)
12. Lee DM, Raichle BW (2012) A side by side comparison of micro and central inverters in shaded and unshaded conditions. In: World Renewable Energy Forum, Denver, USA
13. Scholten DM, Ertugrul N, Soong WL (2013) Micro-inverters in small scale PV systems: a review and future directions. In: 2013 Australasian universities power engineering conference (AUPEC), pp 1–6. https://doi.org/10.1109/AUPEC.2013.6725465
14. Mallwitz R (2016) Photovoltaic Inverters in Micro-scale. In: CIPS 9th international conference on integrated power electronics systems, ISBN 978-3-8007-4171-7
15. Ruchira, Sao A, Patel RN, Sinha SK (2018) GUI supported experimental investigation of central inverter and microinverter integrated with 1kW system. In: ICRAIE international conference on recent advances and innovations in engineering, Nov 2018, pp 23–25

Design and Simulation of Wireless Power Transfer System for Electric Vehicle Application

R. Aiswarya, Elby Barnabas, R. S. Hari Shankar, S. Nandagopal, and A. N. Archana

Abstract The exceedingly developed automotive industry and increasing use of automobiles around the world are causing serious environmental problems, so further efficient, cleaner and safer vehicles are needed. The development of electric drive train technologies is the most auspicious vehicle solution for the future. As an effort to overcome this downside as well as to reduce the transmission and distribution losses of the existing charging systems, highly efficient wireless power transmission is initiated. A wireless power transfer system using resonant magnetic coupling, intended to charge a battery is designed. Primary and secondary coils resonate at same frequency. Resonant compensation is done so that the complication due to intrinsic low coupling and large leakage inductance can be overcome. Series-series resonant topology with feedback design has the advantages of circuit clarity, easy analysis and control. The coils are designed on ANSYS Maxwell 3D software. It is exported to ANSYS Twin Builder/Simplorer where the high-efficiency wireless power transfer circuit is simulated to determine the power transfer efficiency.

Keywords Power transfer efficiency · Resonant frequency · Wireless power transfer

1 Introduction

According to Maxwell's electromagnetic theory [1], electromagnetic waves move at the speed of light, hence it was determined that light itself was an electromagnetic wave. Hertz later conducted an experiment [2] by using pulsed wireless energy transfer that was able to produce and detect microwaves in the ultra-high frequency region. Nikola Tesla in 1890 conducted an experiment [3] by transmitting power by capacitive as well as inductive coupling, using radio frequency resonant transformers known as Tesla coils that can generate high AC voltages. In order to develop wireless

R. Aiswarya (✉) · E. Barnabas · R. S. Hari Shankar · S. Nandagopal · A. N. Archana
Department of Electrical and Electronics Engineering, Mar Baselios College of Engineering and Technology, Trivandrum, Kerala 695015, India
e-mail: aiswaryakulathinkara@gmail.com

lighting [4] system based on capacitive as well as near-field inductive coupling, Geissler tubes and incandescent light bulbs were illuminated in several public events conducted. Tesla also found that it is possible to increase the distance at which the lamp could be lit by using resonant inductive coupling [5].

Wireless power transfer (WPT) system [6] also called electromagnetic power transfer system is the type of transmission of electricity without physical wires. In WPT [7], a time-varying electromagnetic field generated by a transmitter device is transmitted to receiver device and supplied to an electrical load. The electric power can be transfigured across the air gap [8] with a variety of techniques such as radio frequency waves, optical links, capacitive power transfer etc. Radio frequency (RF) waves can be used to transmit power as waves that can travel through vacuum [9]. In optical links, the light in the ultraviolet, visible or infrared spectrums are used for transmitting power in the high-frequency range [10]. Ultrasonic waves, mainly used for low-power data transmission, propagate with an interchange of kinetic and potential energy in the medium of transmission. Piezoelectric crystals are the key to convert the ultrasound wave to electricity [11] and vice versa. Inductive power transfer uses the principle of time-varying magnetic [12] field between mutually coupled coils for power transfer. In resonant magnetic coupling [13] a compensating network is added to the coil so as to produce resonance, thereby increasing the coefficient of coupling and WPT efficiency.

The WPT system technology [14] can eliminate the usage of wires, hence helping to increase the mobility, convenience and safety of all users. Wireless charging has the advantage of reducing the battery size [15] and weight since it decreases the charging intervals. Currently, laptops, mobile phones, tablets, televisions, etc., have already started imbibing this technology. Other promising applications that are widely researched include electric vehicle (EV) charging, wireless railway charging and some special biomedical implant devices.

2 Literature Survey

A highly efficient WPT system using series-series resonant topology with resonant frequency feedback design is considered for electric vehicle applications [16]. A 500 W test site prototype is erected, and the demonstration is carried out in 15 cm air gap. Two DSP processors control the primary and secondary sides. Wireless feedback communication is taken via resonant frequency modules. The resonating frequency is 182 kHz. When resonance takes place, the power transfer is done efficiently.

EV batteries are advantageously charged using wireless power transfer system with inductive coupling [17]. Transmitting sector is connected to power supply circuitry and receiving sector is connected to power conditioning circuitry. The paper denotes the design and implementation of WPT battery charger. Primary segment consists of AC-DC converter cascaded with high-frequency inverter. Secondary segment comprises of diode rectifier cascaded with chopper. The coupling coefficient of spiral coils is designed with the help of Finite Element Method (FEM). The

prototype is tested to authenticate the design procedure. Controller used in primary side needs to be taken care to avoid losses so that the overall efficiency of the system is not affected.

Electric, hybrid electric and fuel cell fired drive train technologies are the most hopeful vehicle blends for the foreseeable future and [18] put forward the casting of an electric bicycle by considering the forces acting on it. The different types of batteries used for EVs and their properties are also mentioned. The collation allying the different kinds of motors like Induction Motor (IM) etc. used for EV is also outlined.

3   Methodology

As shown in Fig. 1, the WPT circuit is mainly divided into two sections; the primary side and the secondary side, separated by an air gap. On the primary side, a 230–240 V AC input is provided. This is given as the input of the full bridge rectifier. The rectifier has an output of 24 V and 10A, thus giving a total output power of 240 W. As the rectifier has an efficiency of 87%, an output power of around 210 W is expected. This is passed onto an inverter. A 250 W rated inverter circuit is used, and it has a switching frequency of 125 kHz. An inverter circuit is used to provide a high switching frequency as well as to convert the current to ac.

The output ends of the inverter circuit are connected to the two ends of the transmitter coil that has a black ferrite sheet attached to it. The ferrite sheet helps to increase the magnetic flux density, which in turn helps in increasing the overall power transfer efficiency of the circuit. Similar to the transmitter coil, the receiver coil also has a ferrite sheet. From the receiver coil, the transferred power is passed onto the buck-boost converter where the power is adjusted to obtain the required current rating and voltage rating. After obtaining the required current rating and voltage rating by adjusting the buck-boost converter, the output is connected to two 12 V, 7.5Ah lead acid batteries that are connected in parallel configuration for the charging phase.

The wireless power transfer coils discerned over a distance are simulated in industry standard ANSYS Maxwell 3D tool. Dynamic calculation of self and mutual

Fig. 1   Block diagram of WPT circuit

inductance is also computed. It can be seen that by using ANSYS simulation, when air gap distance is varied, there are changes in mutual coupling of coils that has a great role in power transmission. Copper coils with rectangular cross-section are used for simulation. This software helps to resolve complex electromagnetic systems before physical implementation that guides to choose efficient coil for power transfer.

4 Coil Design

Designing of coils applies the same analogy for both transmitter and receiver coils except for the reduction in their dimensions. The moulding of coils is carried out in ANSYS Maxwell electromagnetic suite with transient analysis. The mutual inductance, M (in henry), for power transfer capabilities is given by

$$M = k\sqrt{L_1 L_2}$$

Here, k is the coefficient of coupling; L_1 and L_2 are the inductance of coils in henry.

4.1 Design Parameters (Selected Values)

- Polygon segment is the number of cross-section polygon segments (4).
- Polygon radius is the outer radius of cross-Section (1 mm).
- Start helix radius is the radius from polygon centre to helix centre of coil (10 mm).
- Radius change is the distance difference between two consecutive turns (2.05 mm).
- Segment per turn is the total number of segments per turn (36).
- Turns is the number coil turns (10).
- Pitch is the height in z-direction (helix) with coil in x–y direction (0 mm).

4.2 Design of Transmitter Coil (Tx)

Open a new project in ANSYS electronic desktop and then go to project. On project magnetostatic tab appears. To create transmitter coil, enter the required design parameters as mentioned above in user-defined primitive operations table as shown in Table 1 that appears in polygon helix tab. After entering the required details, the transmitter coil is obtained as shown in Fig. 2 of the desired value. Material assigned for the transmitter coil is copper for better conduction.

To attach terminals for transmitting coil, create two boxes box1 and box2 at either end of coil and then from either of these two boxes extend another two boxes box3
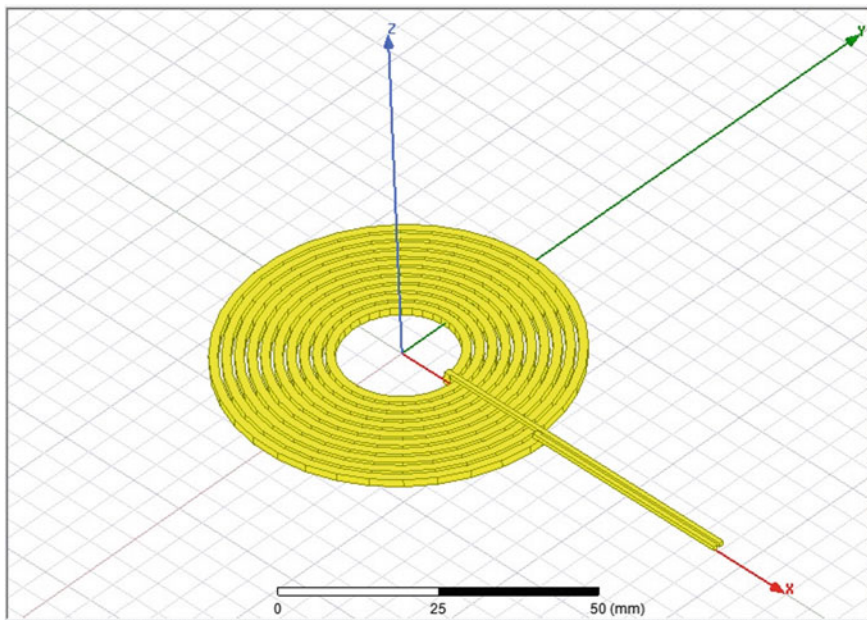
Fig. 2 Transmitter coil
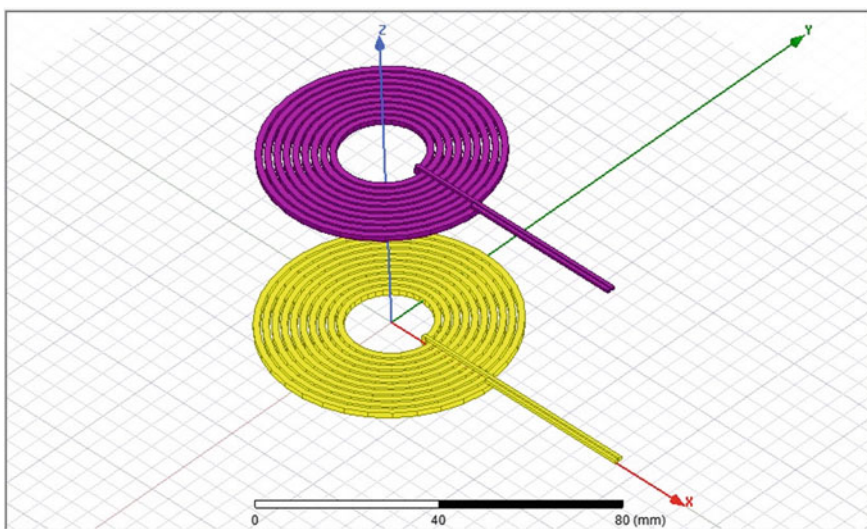
Fig. 3 Transmitter coil (yellow) and receiver coil (purple)

and box4 along the x-axis up to a sufficient length as required. Then unite the Tx coil and terminals by clicking on it.

4.3   Design of Receiver Coil (Rx)

The design procedure for receiver coil is same as that of the transmitter coil. As transmitter coil receives more power, it is usually designed for larger dimension with respect to receiver coil as shown in Fig. 3. To create air gap between the coils, select the Rx coil and assign x, y, z coordinate values depending on the axis along which the Rx coil is shifted (here z-direction). For validation purpose, the air gap is varied from 20 to 100 mm.

After creating the transmitter and receiver coils with terminals, whole design is enclosed in a box assigned with vacuum. Create another region outside the vacuum box that is required for simulation to run. An excitation current of 6A is given as input to both Tx and Rx coils. Apply mesh operation on the coils by selecting a suitable air gap distance between them. Before simulation of coils, the limit has to be set. In setup, dialog box gives maximum number of cycle passes, percentage error range and minimum number of cycles as input. Then apply iteration to the coil structure to obtain the final geometric design.
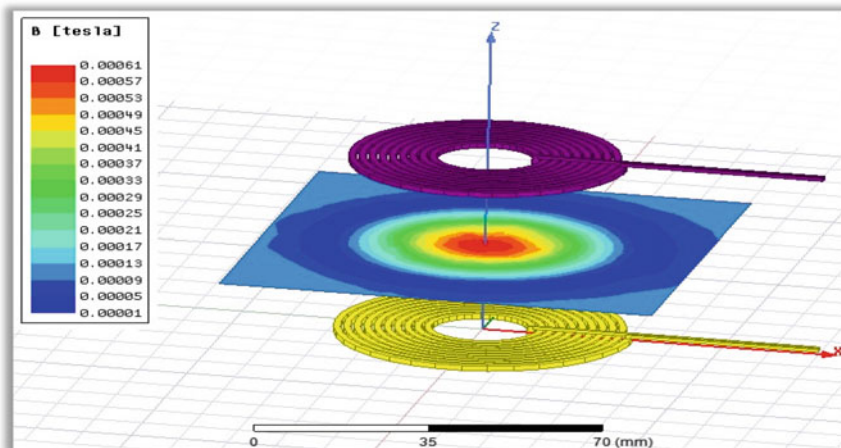
Fig. 4   ANSYS simulated wireless power transfer coil
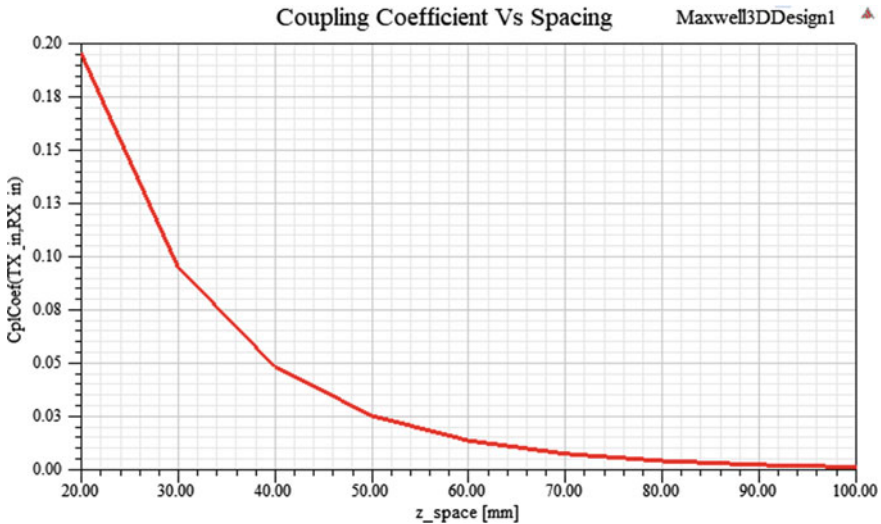
Fig. 5 Graph showing variation of coupling coefficient with air gap distance

4.4 Coil Analysis

The coil analysis is done to find out coupling coefficients, self-inductance and mutual inductance between coils. These parameters can be automatically calculated for variable distances by using a pre-defined parameter for sweep analysis. The magnetic field strength between the transmitter and receiver coils is shown in Fig. 4. in the form of a heat map.

For analysis results, right click on to generate magnetostatic report and enter the parameters for the generation of required waveforms. In first matrix category, enter coupling coefficient and spacing parameters and click OK to give rise to coupling coefficient vs spacing graph as shown in Fig. 5. Follow the similar procedure for creating the rectangular plot that shows the variation of mutual inductance with spacing as shown in Fig. 6.

The results so obtained are tabulated as shown in Table 2. From the table, it's clear that the coupling coefficient and mutual inductance vary considerably with air gap.

5 Experiment and Result

After the design of coil in Maxwell software, it is exported to Twin Builder as shown in Fig. 7 for simulation purpose. From the vast library of Twin Builder software, the components that give the desired result across each selected node of circuit are selected. The circuit is modelled with step-by-step verification of output at each stage to ensure its proper functioning.
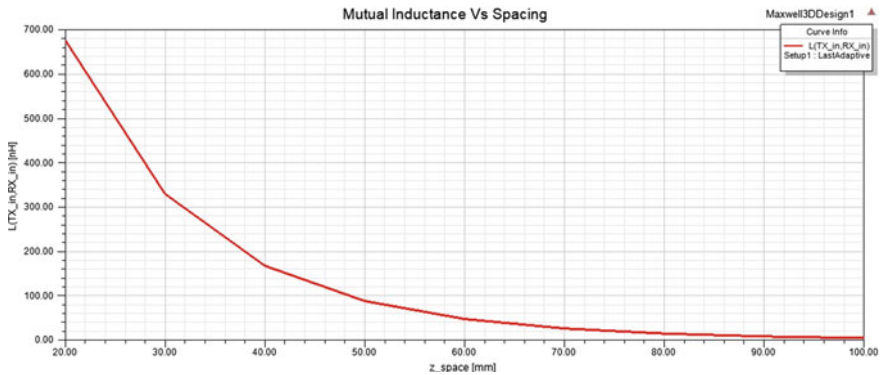
Fig. 6 Graph showing variation of mutual inductance with air gap distance
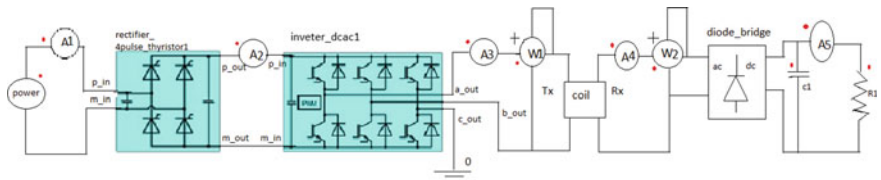
Fig. 7 Wireless power transfer circuit in ANSYS twin builder

The WPT system is modelled with a power source of 240 W, 50 Hz as input followed by an ammeter to record the values of current and to ensure the flow of current in the circuit. The input then enters the full bridge SCR rectifier circuit after little losses. The use of SCR helps in better control of AC power from the beginning itself. The AC power input is rectified into DC power with ripples less than 20% by the effective filter capacitor of 176nF in rectifier. Now the rectified output is verified by the ammeter connected. The output of rectifier is given as the input of inverter circuit.

From the library of ANSYS Twin Builder, three-phase PWM inverter using SCR is chosen, and the thyristors are triggered by the internal PWM circuit to which frequency of 125 kHz is given. This triggers the SCR and makes the inverter work as a high-frequency inverter, which in turn converts DC power into high frequency AC power, suitable for power transmission. The three-phase inverter is transformed as 1 phase inverter by grounding the third phase. The output from inverter is validated by the ammeter and wattmeter that succeeds it. It measures about 210 W after considerable amount of loss in halfway path before power transfer. The high frequency AC power is transfigured to the secondary side of the coil when both the coils resonant at radio frequency of 125 kHz, and this phenomenon is defined as resonant magnetic coupling. The received power is substantiated by the wattmeter in the receiver section. High-power frequency AC used for power transfer is to overcome the losses in air gap, so desired power can be given for the load in need. The output of secondary coil

Table 1 User-defined primitive operation tab

Name	Value	Unit	Evaluated value	Description
Command	CreateUserDefinedPart			
Coordinate System	Global			
Name	SegmentedHelix/PolygonHelix.dll			
Location	syslib			
Version	1.0			
PolygonSegments	4		4	Number of cross-section polygon segments, 0 for circle
PolygonRadius	1	mm	1 mm	Outer radius of cross-section polygon
StartHelixRadius	10	mm	10 mm	Start radius from polygon centre to helix centre
RadiusChange	2.05	mm	2.05 mm	Radius change per turn
Pitch	0	mm	0 mm	Helix pitch
Turns	10		10	Number of turns
SegmentsPerTurn	36		36	Number of segments per turn, 0 for true surface
RightHanded	1		1	Helix direction, non-zero for right-handed

is put in as input to diode rectifier to get rectified DC power output. Diode rectifier is used because of the moderate power in the secondary side. The rectified out is filtered by a standard capacitor of 470nF. Finally, DC power is fed into the load for charging purposes.

Result of ANSYS Twin Builder analysis is obtained in graphical form as shown in Fig. 8. The coils designed for wireless power transmission resonate at 125 kHz switching frequency. From the graph, it can be understood that at an air gap of 50 mm between the coils the total efficiency is 44% with losses. Therefore, when 210 W is transferred from primary side to secondary side, around 93 W is obtained. In physical system due to the accompanying rectifier circuit followed by a converter, nearly 86 W power is obtained across the load after losses. So, an output current of around 7A and 12 V output voltage are generated.

Table 2 Data table representing the variation of coupling coefficient, self-inductance, mutual inductance with air gap

	Air gap	Coupling coefficient		Self-inductance (μH)		Mutual inductance (Nh)
	z-space (mm)	Self-coupling	Mutual coupling	Transmitter coil	Receiver coil	
1	20	1	0.195529	3.867031	3.089374	675.826057
2	30	1	0.095430	3.867265	3.087005	329.727036
3	40	1	0.048602	3.867416	3.087875	167.956202
4	50	1	0.025630	3.868271	3.094372	88.675090
5	60	1	0.013949	3.867674	3.090127	48.221753
6	70	1	0.007800	3.867983	3.090590	26.967576
7	80	1	0.004475	3.868848	3.091637	15.477007
8	90	1	0.002627	3.868184	3.088738	9.081597
9	100	1	0.001575	3.867807	3.085377	5.440975
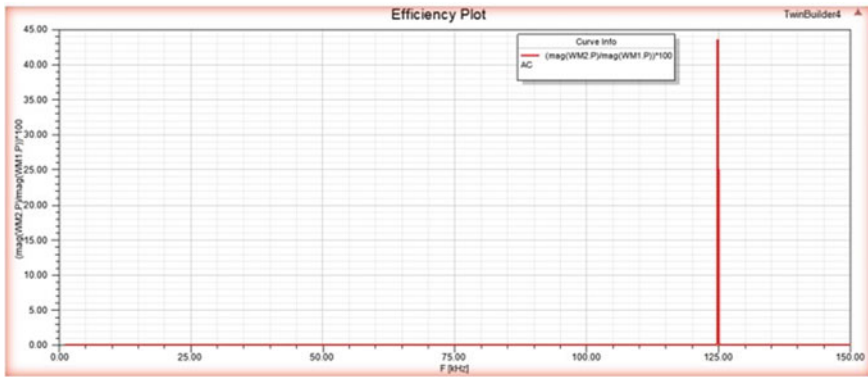
Fig. 8 Efficiency verses resonant frequency

6 Conclusion

For operating high-energy efficient power mechanisms in high-frequency environments, wireless power transmission is introduced. The study and simulation of a high-efficiency wireless power transfer can be used for electric vehicle charging applications. From the literature survey conducted, the design of wireless charging system is obtained. The perfect charging system is designed to balance the power transfer and losses. The designed circuit for wireless power transfer is simulated and verified in ANSYS software tool. The coil is designed in ANSYS Maxwell 3D software, and it is imported to ANSYS Twin Builder to test the efficiency of the coil. The results show that the efficiency of the system and power transfer distance can be improved by changing the geometric design and turns of the coil. The simulation

result shows that 44% power transfer efficiency was possible and nearly 86 W power will reach the load. With the necessary research and development in this field, the power transfer efficiency can be improved even further and in the near future, there is every possibility that electric vehicles and its charging methods will be embraced over conventional vehicles.

References

1. Tran DH, Choi W (2017) Design of a high-efficiency wireless power transfer system with intermediate coils for the on-board chargers of electric vehicles. IEEE Trans Power Electron 33(1):175–187
2. Liou CY, Kuo CJ, Mao SG (2016) Wireless-power-transfer system using nearfield capacitively coupled resonators. IEEE Trans Circuits Syst II Express Briefs 63(9):898–902
3. Mi CC, Buja G, Choi SY, Rim CT (2016) Modern advances in wireless power transfer systems for roadway powered electric vehicles. IEEE Trans Industr Electron 63(10):6533–6545
4. Lu F, Zhang H, Hofmann H, Mi CC (2016) A dynamic charging system with reduced output power pulsation for electric vehicles. IEEE Trans Industr Electron 63(10):6580–6590
5. Lu F, Zhang H, Hofmann H, Mi C (2017) A dual-coupled LCC-compensated IPT system to improve misalignment performance. In: 2017 IEEE PELS workshop on emerging technologies: wireless power transfer (WoW), pp 1–8
6. Ramezani A, Narimani M (2018) A wireless power transfer system with reduced output voltage sensitivity for EV applications. In: 2018 IEEE PELS workshop on emerging technologies: wireless power transfer (Wow), pp 1–5
7. Zhao X, Li R, Li X (2019) Review and research status of dynamic bidirectional-energy-interaction-based wireless power transfer technology. In: 2019 22nd international conference on electrical machines and systems (ICEMS), pp 1–6
8. Vienglek P, Nutwong S, Sangswang A, Naetiladdanon S, Mujjalinvimut E (2020) Comparative study of magnetically coupled coil used in dynamic wireless battery charger for electric vehicles. In: 2020 23rd international conference on electrical machines and systems (ICEMS), pp 1775–1778
9. Ramezani A, Narimani M (2019) High misalignment tolerant wireless charger designs for EV applications. In: 2019 IEEE transportation electrification conference and expo (ITEC), pp 1–5
10. Chowdary KV, Kumar K, Behera RK, Banerjee S (2020) Overview and analysis of various coil structures for dynamic wireless charging of electric vehicles. In: 2020 IEEE international conference on power electronics, smart grid and renewable energy (PESGRE2020), pp 1–6
11. Tang C, Long H, Shi K, Xu B, Wang Z, Su Y (2020) Study of integrated pickup compensation inductance for EV wireless charging system with doublesided LCC topology. In: 2020 IEEE PELS workshop on emerging technologies: wireless power transfer (WoW), pp 326–329
12. Jo H, Kim J, Seo S, Bien F (2020) A wireless power transfer system with uniformly high transfer efficiency for free arrangement of the receiver in a wide area. In: 2020 IEEE PELS workshop on emerging technologies: wireless power transfer (WoW), pp 312–315
13. Diep NT, Nguyen KT, Tran TM (2020) Wireless power transfer system design for electric vehicle dynamic charging application. Int J Power Electron Drive Syst 11(3):1468
14. Zhang Q, Song S, Dong S, Zhu C (2021) A receiver-side-oriented simulator for dynamic wireless charging system with I-type transmitter and multi-phase-receiver. IEEE Trans Ind Electron 68(5):3906–3916
15. Ramezani A, Narimani M (2019) A dynamic wireless charging system with a robust output voltage respect to misalignment. In: 2019 IEEE PELS workshop on emerging technologies: wireless power transfer (Wow), pp 292–296

16. Hsieh YC, Lin ZR, Chen MC, Hsieh HC, Liu YC, Chiu HJ (2016) High efficiency wireless power transfer system for electric vehicle applications. IEEE Trans Circuits Syst II Express Briefs 64(8):942–946
17. Jiang Y, Wang L, Wang Y, Liu J, Wu M, Ning G (2018) Analysis, design, and implementation of WPT system for EV's battery charging based on optimal operation frequency range. IEEE Trans Power Electron 34(7):6890–6905
18. Du G, Cao W, Hu S, Lin Z, Yuan T (2018) Design and assessment of an electric vehicle power train model based on real-world driving and charging cycles. IEEE Trans Veh Technol 68(2):1178–1187

On-Board EV Charging with Switched Mode Rectifier-Based Bidirectional Converter in CC-CV Mode

Pramit Parichha, Jajati Keshari Parida, Medha Chaudhary, and Kumari Namrata

Abstract In this paper, the efficient way of charging and discharging of electric vehicle has been implemented with the aim of correcting the power factor in the input side. In the initial stage, switched mode rectifier (SMR) along with boost converter with sinusoidal pulse width modulation control has been implemented with power factor correction (PFC) approach. In the next state, the non-isolated DC-DC bidirectional converter is being implemented to charge the battery in one mode and to use the battery as source for load supply using the same bidirectional converter in another mode. In the later stage, constant current and constant voltage (CC-CV) has been discussed, and it has been implemented for an efficient way of charging the battery. For various load applications, required constant output voltage is being properly maintained. All the works have been successfully simulated in MATLAB-SIMULINK, and it can be considered for future work as a reference for multiple load applications and economic way of using it for long-term application.

Keywords Switched mode rectifier · Non-isolated DC-DC bidirectional converter · Constant current–constant voltage algorithm

1 Introduction

The world is now concerned with the depletion of conventional energy sources and rising pollution and hazardous effect caused by the vigorous use of this conventional energy. In the recent time, we use our conventional grid power for charging purpose. We not only focus on various modes of charging but also we need an efficient one with proper algorithm to implement. The limitation of charging a battery in constant current (CC) or constant voltage (CV) is overcome by the method of charging it in constant current along with constant voltage (CCCV) mode of operation [1]. The conventional power we use varies a lot based on location and time. So, there is a need for proper input to our charging system to maximize the efficiency. The unidirectional

P. Parichha (✉) · J. K. Parida · M. Chaudhary · K. Namrata
Department Electrical Engineering, NIT Jamshedpur, Jamshedpur, India
e-mail: pramitparichha1998@gmail.com

way of charging is commonly used due to its simple operating mode and control. But in the future run, there is a need to use battery as source to supply outer loads, which is possible by using bidirectional mode of operation. Battery can not only be used for vehicle application as backup resource, but it can also be used for supplying constant uninterrupted supply to outer load. The provision for power output panel in an EV can serve as emergency source, as a household load by supplying power as an auxiliary source along with inverter. In the larger context, it can be used to improve power quality, as a part of community microgrid to control the voltage profile [2–6]. With advancement of technology, the need for AC to DC converters is increasing rapidly. As the requirement of DC power supply is increasing at the same time regulatory agencies are enforcing Harmonics to the system, which causes degradation in power quality. So high-frequency converters like SMR that has high-speed switches are used. SMR, also called as power factor corrector Rectifier be formed by inserting a suitable DC-DC converter cell between diode rectifier and output capacitor filter [7–10].

The objective of this paper is to create an onboard electric vehicle charger, which has high efficiency and injects fewer harmonics to the system. Thus, less loss with improved power factor can be achieved.

2 Proposed Charger for Electric Vehicle

In this paper, an onboard charger is proposed that has two stages as shown in Fig. 1. In the first stage, AC to DC conversion operation is done by SMR, and in the second stage, DC to DC conversion is done by DC-DC bidirectional converter. A LI-ion battery is connected at the end of the BDC converter, which is charged with CC-CV charging technique.

2.1 Switched Mode Rectifier

SMR is used to convert an AC power to DC power with a high-power factor, i.e., near to unity and low line current harmonic distortion. It consists of a diode rectifier and a DC-DC converter. A suitable DC-DC converter is placed between diode rectifier and an output capacitive filter. The SMR circuit is shown in Fig. 2. In this paper, boost converter is used as a DC-DC converter. This combination of diode rectifier and a boost converter gives us a better power factor. For getting desired output, switching speed is increased. High-frequency converter needs smaller reactive components, which lead to reduced volume and compactness of the device [7]. There are several benefits of using SMR and one of those is that there is a very small input current harmonic. The input line current that is drawn by the SMR will have better power quality, and it will provide adjustable and controlled DC output voltage by proper control and operation. Here, we have used sinusoidal PWM technique to reduce
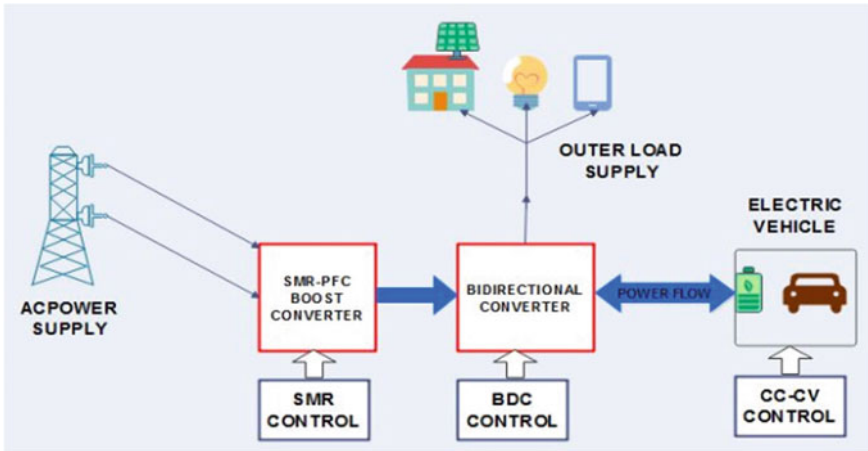
Fig. 1 Block diagram charging technique of EV
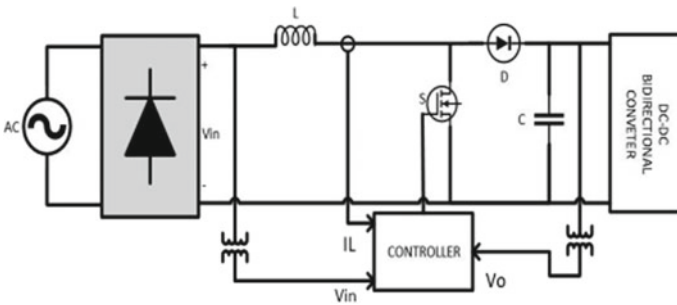
Fig. 2 SMR circuit

harmonics. The input filter and output filter have been calculated according to the SPWM technique [8]. It is highly reliable, efficient and enhances the performance of the equipment.

2.2 Bidirectional Converters

Bidirectional converter is the modified version of conventional DC-DC converter with anti-parallel diode connected with MOSFET/IGBT. The mode of operation is adjusted with the proper control of switches. The bidirectional converter on the basis of protection and power requirement is basically of two types, i.e. non-isolated and isolated. Non-isolated being the easier to control and compact design are mostly used for various purposes like in PV hybrid system, continuous power supply in the

Fig. 3 DC-DC bidirectional
converter
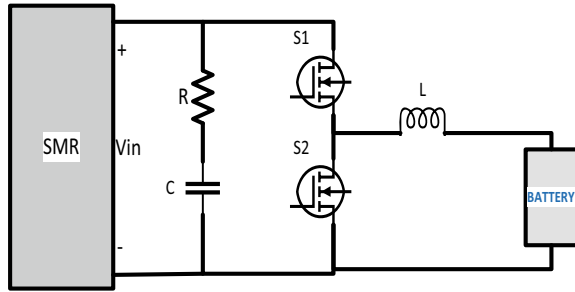
absence of conventional or renewable primary source from storage device, battery
charging. The bidirectional converter as shown in Fig. 3 has the following mode of
operation.

Buck Mode of Operation

For charging a battery with reduced controlled voltage and current, the controlled
switch is so operated that it acts as a buck converter. The operation in buck mode of
charging the EV can be explained as shown in Fig. 4. In Mode 1, when S-1 is ON, the
power from the rectifier starts charging the battery through the L and R. The inductor
and output capacitor are chosen as described below. Mode 2 starts when S-1 is OFF
and the inductor discharges through battery and the anti-parallel diode D-2 [6].

Boost Mode of Operation

In general, we use a separate circuit for discharging a battery for various purposes like
car lighting system, household application, inverter application, hybrid PV system,
etc. As the EV batteries have enough ability to provide power for its locomotion as
well for outer power requirement. There is always a requirement of controlled output
with higher voltage for practical applications. So, we require a Boost converter to
meet the requirement. The bidirectional converter acts as Boost converter as shown
in Fig. 5, when the S-2 is ON, and the inductor gets charged in Mode 1 of operation
in boost mode. The Mode 2 of boost mode starts with S-2 being OFF. The battery
discharged along with stored energy of inductor through D-1. The capacitor in the
load end is chosen as described below.

Fig. 4 Buck mode of BDC
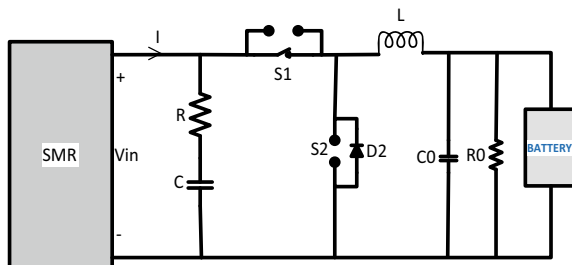
Fig. 5 Boost mode of BDC
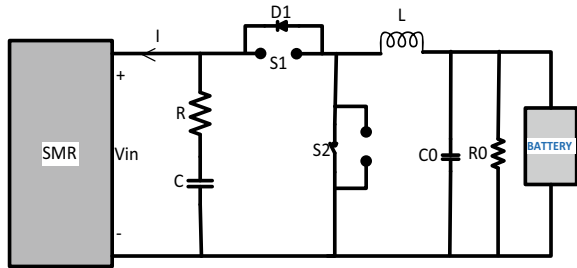
2.3 Battery Charging Technique

In this paper, Li-ion battery is used to charge the EV. There are various methods of charging the battery. Here, we have used CC-CV (Fig. 6) charging method because of its high efficiency with lesser complexity and lower cost. In this method, at first the battery is charged up to a pre-specified voltage value while keeping the current constant. This pre-specified voltage value is known as preset value or, cut-off value. When the voltage reaches the pre-set value, constant voltage mode of charging is started. In this mode, the voltage is kept constant at the cut-off value while the current reduces simultaneously. The charging of the battery stops when the current value decreases to 1% of the total current capacity of the battery [11–18].

Fig. 6 CC-CV mode of charging
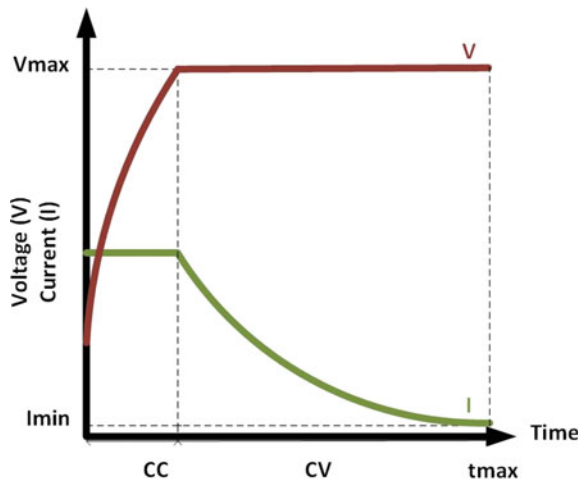
3 Simulation Results

The simulation of the above-proposed charger has been done as shown in Fig. 7. An AC voltage source having 230 V RMS value has been connected to the SMR. The waveform of input voltage and current is shown in Fig. 8. The parameters of the SMR are given in Table 1. The input voltage is rectified and boosted to 530 V DC having a ripple of $\pm 2\%$ as shown in Fig. 10. The input RMS voltage and the inductor current of SMR have been compared, and we have found that they were in the same phase. This shows that the input source side power factor of the proposed system was close to unity. The power factor has been calculated in MATLAB simulation and its value was 1. Hence, the objective of this paper was fulfilled.
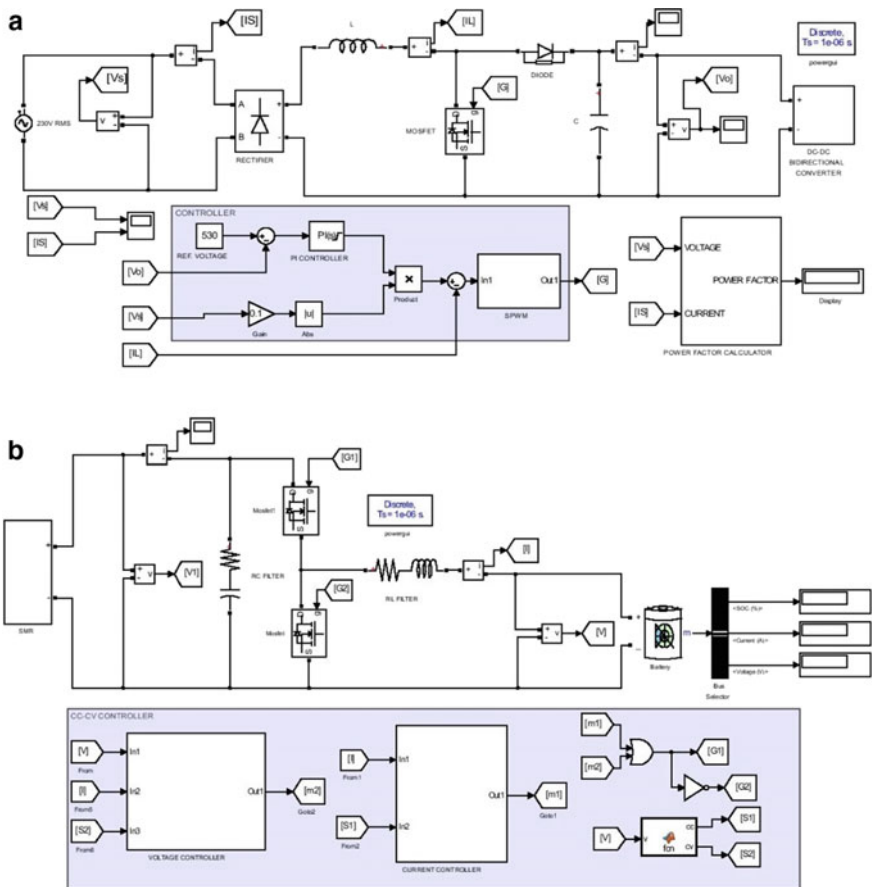
Fig. 7 a Simulation circuit of SMR. **b** Simulation circuit of DC-DC BDC with CC-CV controller
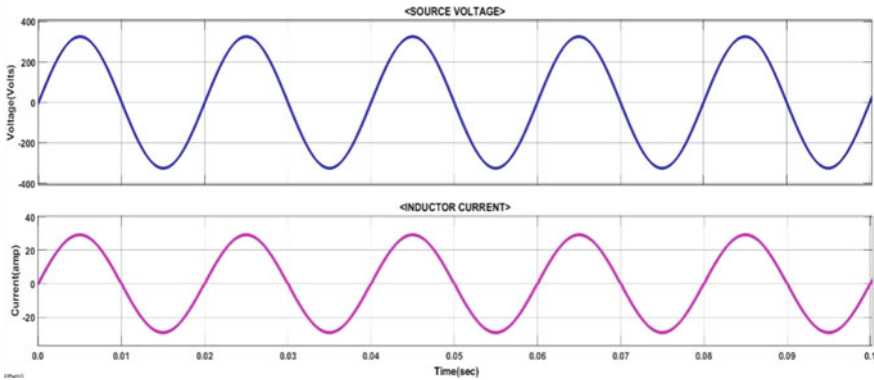
Fig. 8 Input AC source voltage and input source current

Table 1 Parameters of SMR

Symbol	Device	Parameter
V_s	Input ac source voltage	230 V RMS, 50 Hz
L	Inductor in SMR	1.528 mH
C	Capacitor in SMR	4527 μF
V_0	Output voltage of SMR	530 V DC
R-L filter	R-L Filter of DC-DC BDC Converter	0.001 Ω, 5.76 mH
R-C filter	R-C Filter of BDC Converter	0.001 Ω, 1000 μF
SOC	State of charge of battery	0–100%
V_b	Battery terminal voltage	–
I_b	Battery terminal current	–

The harmonics of the input inductor current has been calculated through FFT analysis as shown in Fig. 9. The THD value was less than 3%, which is desirable (Fig. 10).

A DC-DC bidirectional converter has been connected to the SMR. The output voltage of the SMR has been given as the input DC voltage to the BDC. It was operated in buck mode for charging of the battery.

A battery was connected to the BDC having initial SOC of 20%. It has nominal voltage of 100 V, rated capacity of 100Ah, fully charged voltage is 109 V, nominal discharge current of 43.473 A and internal resistance of 0.01 Ω. When the battery started charging, the SOC started to rise from 20%. The voltage at 20% SOC was less than the maximum voltage. It was charged in CC-mode until the battery voltage reached the maximum voltage, i.e. 109 V. After reaching 109 V, it started charging in CV-mode at constant 109 V. During this time, current started decreasing. This change in mode occurred at 50% SOC. The CC-CV graph is shown in Fig. 11.
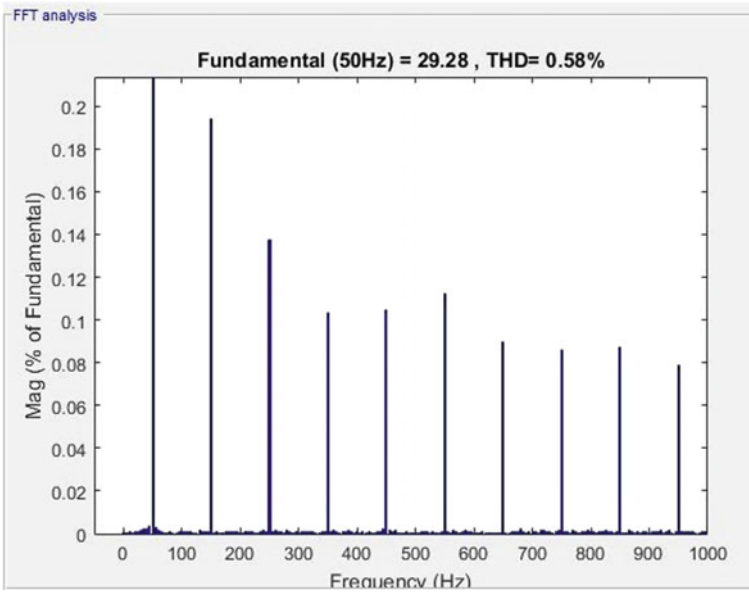
Fig. 9 FFT analysis
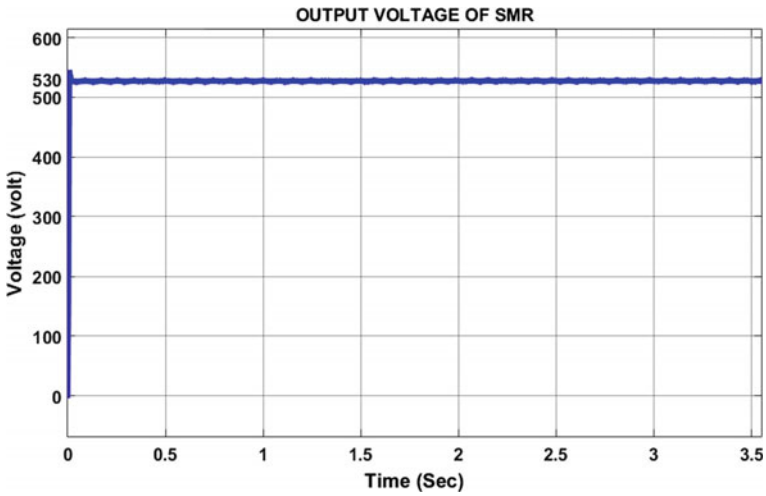
Fig. 10 SMR output voltage

The efficiency of the proposed EV charger at different SOC is shown in Table 2.
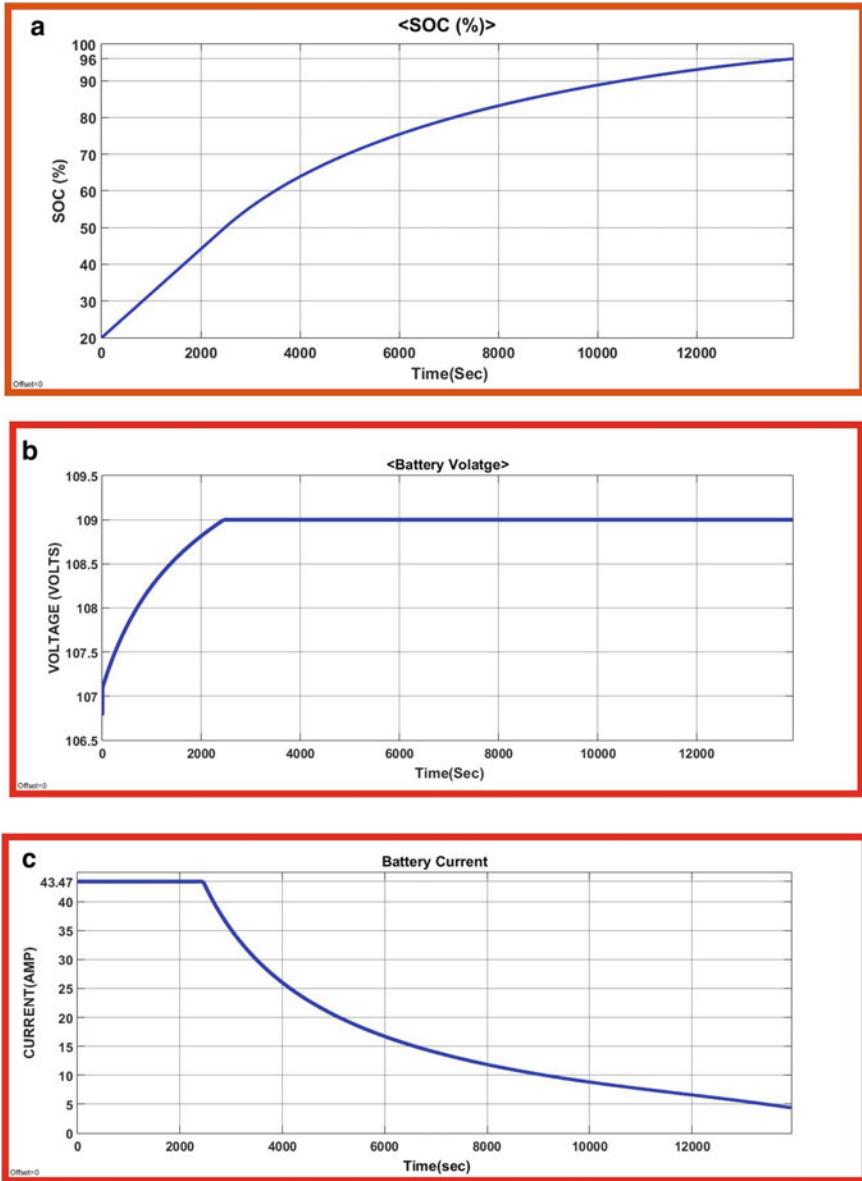
Fig. 11 **a** SOC%. **b** Battery voltage. **c** Battery current

Table 2 Efficiency of proposed EV charger

SOC%	Input power	Output power	Efficiency
20	4591	4460	97.15
30	4823	4700	97.45
40	4833	4725	97.76
50	4831	4740	98.12
60	3556	3489	98.11
70	2759	2697	97.75
80	1539	1495	97.14
90	992	963.4	97.12

4   Conclusion

The proposed model of charger is efficient along with a wide range of applications. The SMR PFC-Boost converter having a unity power factor has been simulated, and this gives the finest approach towards the control of power flow. Bidirectional converter proposed here having the most effective control gives us the reliability of controlling the flow of power of charging and discharging for efficient use for outer load application. The FFT shows the lesser harmonic content. The CC-CV charging algorithm proves to be an efficient method of charging along with other proposed parameters. This module gives a realistic approach for the multifunction ability of EV with onboard charging system. This gives a great initiative and further use in future for an efficient and compact way of EV battery charging and load application.

References

1. Hussein AA, Batarseh I (2011) A review of charging algorithms for nickel and lithium battery chargers. IEEE Trans Veh Tech 60(3):830–838
2. Garcia O, Zumel P, de Castro A, Cobos A (2006) Automotive DC-DC bidirectional converter made with many interleaved buck stages. IEEE Trans Power Electron 21(3):578–586
3. Inoue S, Akagi H (2007) A Bidirectional DC–DC converter for an energy storage system with galvanic isolation. IEEE Trans Power Electron 22(6):2299–2306
4. Yilmaz M, Krein PT (2013) Review of battery charger topologies, charging power levels, and infrastructure for plug-in electric and hybrid vehicles. IEEE Trans Power Electron 28(5):2151–2169
5. Liaw C, Hu K (2013) On a bidirectional adapter with G2B charging and B2X emergency discharging functions. IEEE Trans Ind Electro
6. Zahid ZU, Dalala ZM, Chen R, Chen B, Lai J (2015) Design of bidirectional DC–DC resonant converter for vehicle-to-grid (V2G) applications. IEEE Trans Transp Electrific 1(3):232–244
7. Naraharisetti K, Channegowda J, Green PB (2021) Design and modeling of CCM average current control PFC AC-DC Boost converter. In: 2021 IEEE green technologies conference (IEEE-Green)
8. Pandey R, Singh B (2018) A power factor corrected electric vehicle battery charger using boost converter. In: India international conference on power electronics, IICPE, vol 2018

9. CM, YC (2011) Chapter 11 some basic issues and applications of switch-mode rectifiers on motor drives and electric vehicle chargers. IntechOpen

10. Singh B, Singh BN, Chandra A, Al-Haddad K, Pandey A, Kothari DP (2003) A review of single-phase improved power quality AC-DC converters. IEEE Trans Ind Electron 50(5):962–981

11. Ayoub E, Karami N (2015) Review on the charging techniques of a Li-Ion battery. In: Third international conference on technological advances in electrical, electronics and computer engineering (TAEECE). Beirut, pp 50–55

12. Liu L, Kong F, Liu X, Peng Y, Wang Q (2015) A review on electric vehicles interacting with renewable energy in smart grid. Renew Sustain Energy Rev 51:648–661

13. Wang S, Liu Y, Wang X (2020) Resonant converter for battery charging applications with CC/CV output profiles. IEEE Access 8:54879–54886

14. Thomson SJ, Thomas PAR, Rajan E (2018) Design and prototype modelling of a CC/CV electric vehicle battery charging circuit. In: 2018 international conference on circuits and systems in digital enterprise technology (ICCSDET)

15. Shen W, Vo TT, Kapoor A (2012) Charging algorithms of lithium-ion batteries: an overview. In: 2012 7th IEEE conference on industrial electronics and applications (ICIEA)

16. Jadhav S, Devdas N, Nisar S, Bajpai V (2018) Bidirectional DC-DC converter in solar PV system for battery charging application. In: 2018 international conference on smart city and emerging technology (ICSCET), pp 1–4

17. Jang Y, Jovanovic MM (2009) A bridgeless PFC boost rectifier with optimized magnetic utilization. IEEE Trans Power Electron 24(1):85–93

18. Awwad R, Das R, Arabi T, Hajj H (2012) A fast charging Multi-C technique for mobile devices. In: 2012 international conference on energy aware computing

Single-Step Ahead Solar Irradiance Forecasting Using Hybrid WT-PSO-Based Neural Network

Anuj Gupta, Kapil Gupta, and Sumit Saroha

Abstract Solar irradiance forecasting accuracy is a major concern for grid stability, and it has been studied from various angles including precision and complexity. So, in order to enhance the forecasting accuracy, this paper proposed a hybrid solar irradiation forecasting machine in which wavelet transform is used to deconstruct the original data into a set of understandable series, and particle swarm optimization is utilized to solve the correlation problem by selecting the input parameters (weight and biases) properly whereas feed forward neural network is trained by meaningful series. For the proposed work, 3-year data from 2012 to 2014 have been collected from National Solar Radiation Database for a Delhi location. The proposed model is trained using 2-year data and tested for 1 year on different seasons by following the single-step ahead. The proposed model performance is determined in terms of Mean Absolute Percentage Error (MAPE) and Mean Absolute Error (MAE). The developed model performance indicates that it outperforms the Naïve Predictor, standalone neural network model and particle swarm optimization-based neural network model in terms of precision and complexity.

Keywords Neural network · Wavelet transform · Particle swarm optimization · Time series data

1 Introduction

Renewable energy resources are becoming more popular in today scenario to fulfill electricity demand of a reconfigured electricity market. Among all renewable energy resources, solar energy has rapid growth and emerged as an alternative option of fossil fuel. Now a day's energy from solar is highly popular resource of energy

A. Gupta (✉) · K. Gupta
Maharishi Markandeshwar (Deemed to be University), Mullana-Ambala, India
e-mail: annu11gupta@gmail.com

S. Saroha
Guru Jambheshwar University of Science and Technology, Hisar, India

that is naturally available on earth surface but forecasting of solar energy is necessary because it is variable in nature, and solar forecasting provides grid operators with means to forecast and align electricity production and consumption [1]. Many academicians, scientist and power system engineers around the world have been working to improve the accuracy of solar irradiance forecasting by considering all the uncertainties and complexity associated with solar. The accurate forecasting of solar irradiation is very useful for planning, state assessment, maintenance scheduling and estimation of cost for production. The solar irradiation is estimated using two methods: statistical and physical methods [2]. The statistical approach depends on the previous time series data of solar irradiation as input and does not depend on the internal phase of the model. Persistence model, neural network, auto regressive integrated moving average, fuzzy logic include in the statistical method whereas physical methods depend on the total sky imagers, numerical weather prediction and physical parameters include temperature, cloud cover, humidity etc. The forecasting is divided into single-step and multistep ahead prediction. Multistep ahead prediction is more complex as comparison to single-step ahead forecasting because it involves some additional difficulties like as compounding of error at each stage and more ambiguities [3]. In the literature various models have been developed to forecast solar irradiation at various origins along with different-2 preprocessing techniques to improve the forecasting accuracy. Mohammadi et al. used a wavelet transform-based support vector machine model for predicting solar irradiation in which wavelet transform decomposed the original raw data. The performance of developed model outperforms the performance of traditional model in terms of Mean Absolute Percentage Error, Root Mean Square Error (RMSE) and correlation coefficient [4]. Yiting Wang et al. introduced modified empirical mode decomposition with back propagation neural network model to predict solar irradiation. Ensemble EMD is used to extract the original data into IMF's and a residue. The proposed model shows better performance as comparison to standalone BPNN in terms of MAPE, MBE and R^2 [5]. Hussain et al. introduced a Bayesian E-Kalman filter to adjust the weight of multilayer perceptron model. The proposed models outperform the benchmark model performance in terms of R^2 and modeling [6]. However, Kalman filter also used by the Che et al. to improve the forecast accuracy in terms of RMSE and mean bias error (MBE) [7]. Dong et al. present a hybrid model using SOM-SVR-PSO. SOM has a strong capability of dividing the time series data into uniform characteristics [8]. The proposed hybrid model outperforms the traditional forecasting model in terms of normalized root mean square error and normalized mean bias error. As per above-given literature, researchers used optimization algorithm with preprocessing technique to increase the forecasting accuracy. In the proposed work, wavelet transform is used as a preprocessor in which divides the original solar irradiation data into approximations and detailed subseries whereas particle swarm optimization is used to select the input parameters (weight and biases) of the neural network and feed forward neural network is used as a learning model.

2 Proposed Architecture for WT-PSO-FFNN

Wavelet transform is used to manage non-linear historical solar irradiation time series data. Wavelet is able to generate a suitable local representation of the signal in both temporal and in frequency domain. The original signal is split into low frequency (approximations) and high frequency (detailed component) subseries using WT-based multi-scale analysis and decomposition [9]. These constitutive series outperform the forecasting performance of original solar irradiation data. The data subseries were applied to FFNN together with a time lag solar irradiation series based on the Auto Correlation Function (ACF). A PSO-based learning algorithm is used to optimize the weight and biases parameter of learning model [10]

2.1 Wavelet Transform

The accuracy of the prediction model is highly dependent on the quality of input variables. The data gathered from multiple sites are usually in raw format and lack the necessary qualities to give adequate accuracy. As a result, the data need to be analyzed before it can process with the model [11]. In this paper, WT is used as a preprocessor in which divide the original time series data into low- and high-frequency subseries. The consecutive subseries performance is better than the raw solar irradiation input data and hence good forecasting accuracy is achieved. WT is a Fourier transform-based signal processing technique but it is having an advantage over Fourier transform that it analyzes decomposed subseries with higher resolution [12]. It is classified into two types, depends on the type of signal: Discrete wavelet transform and continuous wavelet transform. The continuous wavelet transform for a solar irradiation input signal $f(t)$ is defined from –infinity to infinity, and it is shown by below equation

$$w(x, y) = x^{\frac{1}{2}} \int_{-\infty}^{\infty} f(t)\psi * \left(\frac{t - y}{x}\right) dt \tag{1}$$

In Eq. (1), mother wavelet $w(x, y)$ is resized by x, translation is done by y and * indicates complex conjugate. The scaling and translation of mother wavelet is corresponding to either low pass filter gives approximate information or high pass filter gives the detailed component of solar irradiation whereas in discrete wavelet transform scale index parameter (x) and time shifting parameter (y) are represented in discrete form with $x = 2^i$, $y = k2^i$. The discrete wavelet transform decomposition of solar irradiation signal is given by [4]

$$w(x, y) = \frac{1}{\sqrt{2}} \sum_{-\infty}^{\infty} f(t)\psi * \left(\frac{t - 2^i k}{2^i}\right) dt \tag{2}$$
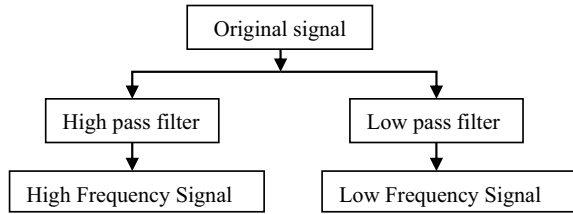
Both high-pass and low-pass filters are used in DWT to decompose and recreate the original solar irradiation input data pattern as shown in Fig. 1.

The wavelet transform performs suitable signal smoothness with respect to wavelength resulting in optimal behavior of input data pattern for a solar irradiation forecast tool. The solar irradiation input series decomposed into approximated and detailed component by Daubechies wavelet as shown in Fig. 2. The approximation signal depicts the frequency curve of solar irradiation signal, whereas detailed component represents the high-frequency curve.

2.2 Feed Forward Neural Network

Feed forward means it transfers the value in a forward direction only. It means the input value move from input layer to hidden layer and hidden layer output transferred to the output layer. The non-linear structure of feed forward neural networks is inspired by the human brain. The supply terminals in the input layer transfer the input signal to the hidden layer neurons. The hidden layer outputs act as an input of output layer. The output signals of the output layer make up the network total response [13].

2.3 Particle Swarm Optimization

Particle swarm optimization is based on how diverse animals use social and cooperative behavior to fulfill their demands in the search space. This method uses personal experience (Pbest), global experience (Gbest) and presents the movements of the particles to estimate the particles' next location in the search space. Furthermore, two factors, g_1, g_2, as well as two random values created between [0 1] accelerate the experiences, and current movement is amplified by an inertia factor Y fluctuating between $[Y_{min} \ Y_{max}]$.

Suppose the initial size of the population is X and dimension H is indicated as $Z = [Z_1, Z_{2....}Z_x]^T$ where T represents the transpose operator. Every individual particle Z_i ($i = 1, 2, 3...X$) is denoted by Z_i $[Z_{i,1}, Z_{i,2}...Z_{i,H}]$. The initial velocity of the population is indicated by $U = [U_1, U_2...U_N]^T$ and the velocity of the individual
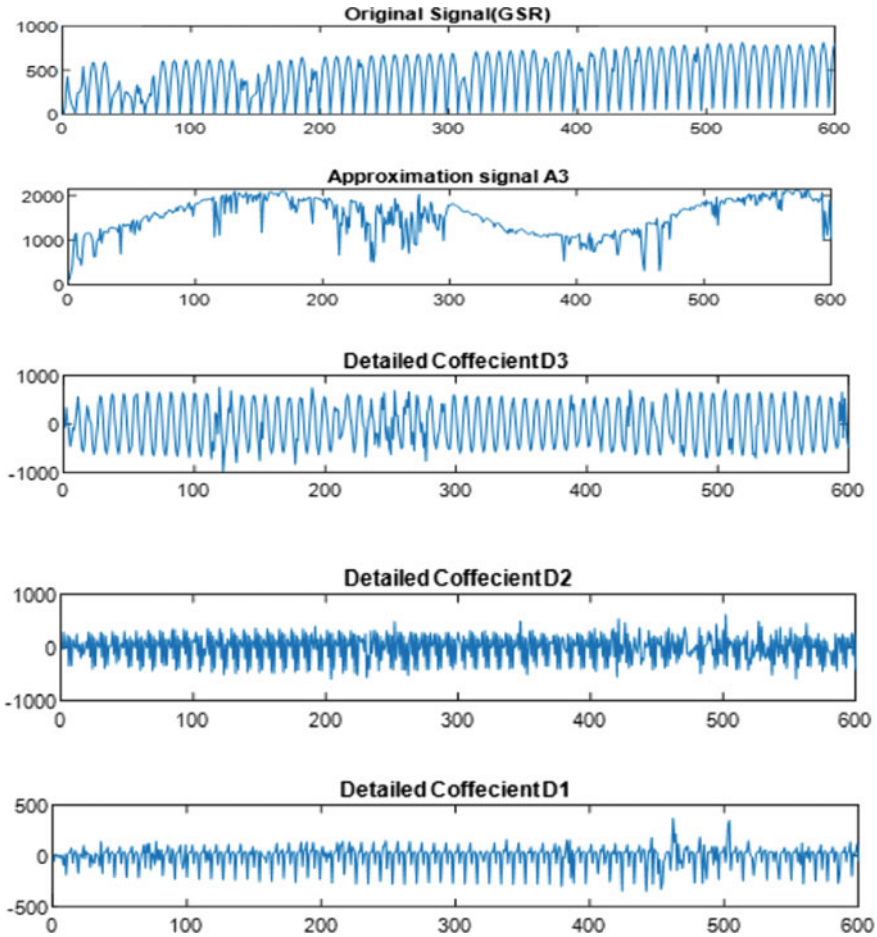
Fig. 2 Solar irradiation, detailed and approximated signal by wavelet decomposition

particle is U_i ($i = 1, 2, 3…X$) is denoted by $U_i[U_{i,1}, U_{i,2},…U_{i,H}]$. The value of i ranges from 1 to X and J value ranges from 1 to H. For completeness, the detailed algorithm of multiple approaches is presented here

$$U_{i,j}^{k+1} = Y \times U_{i,j}^k + g_1 \times r_1 \times \left(\text{Pbest}_{i,j}^k - Z_{i,j}^k\right) + g_2 \times r_2 \times \left(\text{Gbest}_j^k - Z_{i,j}^k\right) \quad (3)$$

$$Z_{i,j}^{k+1} = Z_{i,j}^k + U_{i,j}^{k+1} \quad (4)$$

In Eq. (3), $\text{Pbest}_{i,j}^k$ indicates personal best value where Gbest_j^k denotes the global best value.

The steps of PSO are as follows:

i. Select parameter C_1, C_2 and w_{min}, w_{max} of PSO
ii. Particles population initialization having position Z and velocity U
iii. Set $k = 1$ as the number of iterations
iv. Determine particle fitness $F_i^k = f(Z_i^k)$ and calculate the index of the best particle b
v. Select Pbest and Gbest value
vi. $Y = Y_{max} - k \times \frac{Y_{max} - Y_{min}}{maxite}$
vii. Update position and velocity of the particle
viii. Evaluate Fitness $F_i^{k+1} = f(Z_i^{k=1})$ and calculate the index of the best particle b1
ix. Reboot personal best value of population
x. Reboot Global best of population
xi. If the value of $k <$ Maxite then $k = k + 1$, if it is satisfied move to next step otherwise move to step 6
xii. Display Gbest optimum value

The detailed flowchart of PSO considering above steps is given as (Fig. 3).
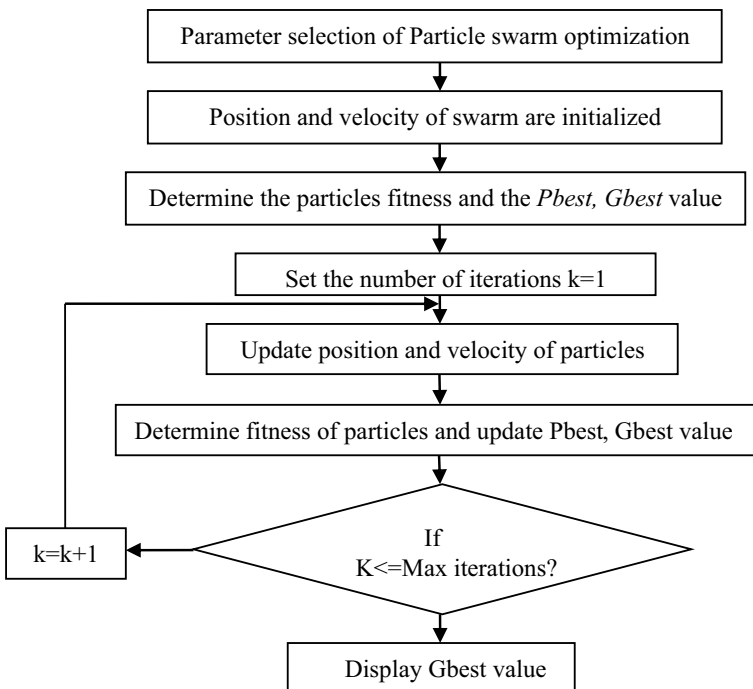
Fig. 3 PSO flowchart

2.4 Proposed Hybrid Forecasting Model

Various researchers used a preprocessing technique to enhance the forecasting accuracy of machine learning models while some of them used an optimization algorithm to select the optimum value of forecasted model. In this paper, the proposed model is implemented by combination of three strategies: firstly, the original global horizontal irradiation data are dividing into detailed (D1, D2, D3) and approximated (A3) solar irradiation signal by three wavelet decomposition using Daubechies (Db) wavelet. The input to the three-layer neural network structure for the proposed model is seven (Three solar irradiation time lags by autocorrelation function and four wavelet transform decomposed solar irradiation signal). Secondly, the optimization technique PSO is used to optimally select the parameters related to neural network, and finally, feed forward neural network is used to train the three time-series lags along with low-level signal (approximated) and high-level signal (detailed) [14]. The steps used for developing the proposed model are given as (Fig. 4):

Step 1: The original solar irradiation time-series data used as an input for the proposed model.

Step 2: WT is used to decompose the input time-series data into a detailed (D_1, D_2, D_3) and approximated signal (A_3).

Step 3: Rebuild the signal using approximated and detailed signal.

Step 4: Autocorrelation function is used to find the time lags l from the input signal.

Step 5: The detailed and approximate signal of 2-year data set along with three time-lag series created using autocorrelation function used as training data for neural network.
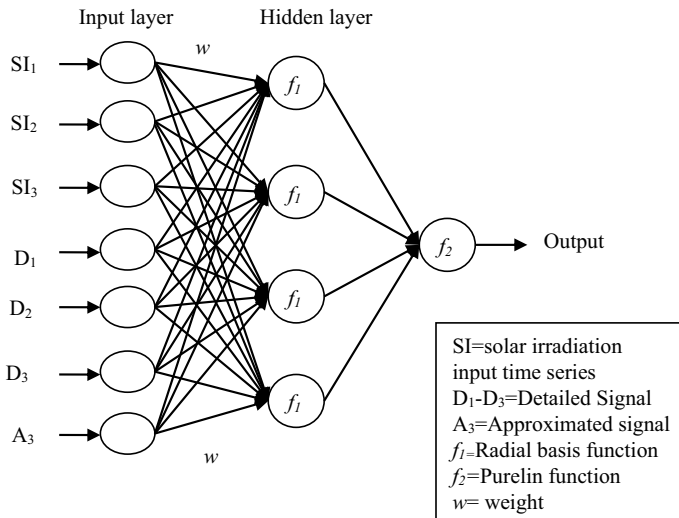
Fig. 4 Proposed model structure

Step 6:   Evolutionary technique PSO used to optimize the parameters related to
          neural network.
Step 7:   In the last step, the forecasted global horizontal irradiation value is compared
          with the actual solar irradiation.

3   Evaluation Metrics

The aim of the evaluation metrics is to compare the actual observed value with the
forecasted value. In this paper, mean absolute percentage error and mean absolute
error are used to judge the performance of proposed model [11, 15]

$$\text{MAPE} = \left(\frac{1}{n} \sum_{i=1}^{n} \frac{\left| \text{GSR}_{i(\text{prediction})} - \text{GSR}_{i(\text{actual})} \right|}{\text{GSR}_{i(\text{actual})}} \right) \times 100 \tag{5}$$

$$\text{MAE} = \frac{1}{n} \sum_{i=1}^{n} \left| R_{\text{prediction},i} - R_{\text{actual},i} \right| \tag{6}$$

4   Result and Analysis

The data set of the prime location of India is considered to evaluate the performance
of developed model. The paper collected the data set of 'Delhi' location, capital of
India and its geographical value is shown in Table 1. The data set was gathered from
National Solar Radiation Database for the year of 2000–2014. However, the model
used 2-year data, i.e. 2012–13 for training and 1 year data, i.e. 2014 for testing.
The testing of model is performed on seasonal basis. The training data were used for
model creation, whereas testing data were utilized to assess the model's performance
on untrained data. Geographical location of Delhi station is shown in Table 1.

MATPAB 2019a was employed for neural network training and testing. Table
2 displays the results of all constructed models in terms of MAPE and MAE. The
proposed model is compared with three existing models on single-step ahead basis
up to 1 year by using 2-year training data set. FFNN and PSONN both use three input
neuron, number of hidden neuron is 25, learning rate is 0.001, 2-year training data and
1-year testing data (divided into different seasons), Levenberg Marqaurdt algorithm is
used for training the neural network with tangential sigmoid and pure linear activation

	Serial number	Place	Latitude/Longitude	Altitude
Table 1 Geographical location of Delhi [16]	1	Delhi	28°38′/77°13′	216

Table 2 Comparative analysis of forecasted models

| | 1-h ahead | | | | | | | |
| | Model 1 | | Model 2 | | Model 3 | | Model 4 | |
Seasons	MAPE	MAE	MAPE	MAE	MAPE	MAE	MAPE	MAE
Winter	22.1	51.3	18.1	49.1	17.6	47.2	7.2	24.9
Spring	19.7	48.5	16.8	45.2	15.7	44.1	6.4	22.4
Summer	10.2	44.7	9.6	40.2	9.1	39.8	4.6	20.1
Monsoon	26.6	63.4	20.8	57.1	18.2	55.7	9.3	28.5
Autumn	12.4	46.9	7.1	39.2	6.4	38.6	4.1	19.2
Average	18.2	50.9	14.4	46.1	13.4	45.0	6.3	23.0

Model 1—Naïve Predictor, Model 2—FFNN, Model 3—PSOFFNN, Model 4—WTPSOFFNN

Fig. 5 Histogram of all models showing their MAPE (%) and MAE (w/m^2)
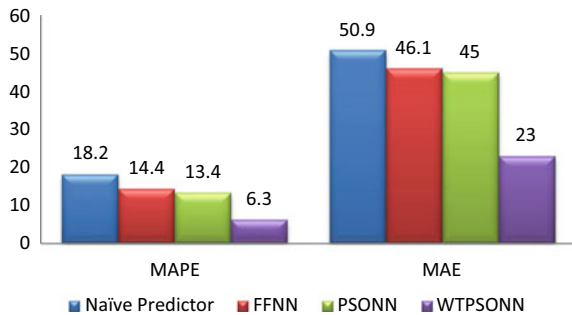
function. Naïve Predictor forecasts the future value based on previous value. It is also known as persistence model

The proposed model is already discussed in the above section. The MAPE value obtained by proposed model is 6.3%, which is far better than other two models tested for a duration of 1 year on seasonal basis (January 2014 to December 2014). The accuracy of proposed model is also judged by using MAE, which describes uniform forecasting error. The MAE value obtained by proposed model is 23w/m^2, which is much better than FFNN and PSONN (Fig. 5).

5 Conclusion

This research developed a hybrid model (WTPSOFFNN) for forecasting the solar irradiation. Three-year data (2012–14) collected from NSRDB for a Delhi location. Two-year data are used for training, and 1-year data are used for testing of model on seasonal basis. The proposed model forecasts solar irradiation for a single-step ahead basis in time-series framework. An efficient forecasting of solar irradiation was made by proper selection of input neuron, learning algorithm, time legs, learning rate,

training data to achieve better accuracy. The performances of all developed models are judged on the basis of MAPE and MAE evaluation metrics. The forecasting accuracy of the proposed model (MAPE = 6.3%) and (MAE = 23 w/m^2) is far better than FFNN and PSONN and persistence model. So, this model is very much useful for predicting solar irradiation in renewable energy system.

References

1. Gupta A, Gupta K, Saroha S. A review and evaluation of solar forecasting technologies. Mater Today Proc. https://doi.org/10.1016/j.matpr.2021.04.491
2. Yang D, Wu E, Kleissl J (2019) Operational solar forecasting for the realtime market. Int J Forecasting 35(4):1499–1519
3. Prasad R, Ali M, Kwan P, Khan H (2018) Designing a multistage multivariate empirical mode decomposition coupled with ant colony optimization and random forecast model to forecast monthly solar radiation. Appl Energy 236:778–792
4. Mohammadi K, Shamshirband S, Tong C, Arif W, Petkovic M, DCh S (2014) A new hybrid support vector machine-wavelet transforms approach for estimation of horizontal global solar radiation. Energy Convers Manage 92:162–171
5. Tan WY, Yide WG, Kai G, Shan T (2020) Adoption of ensemble empirical mode decomposition algorithm and back propagation neural network in net surface solar radiation prediction. J Phys 16519
6. Hussain S, AlAlili A (2016) Online sequential learning of neural network in solar radiation modeling using hybrid Bayesain hierarchical approach. J Solar Energy Eng 138(6)
7. Che Y, Chen L, Zheng J, Yuan L, Xiao F (2019) A novel hybrid model of WRF and clearness index based kalman filter for day ahead solar radiation forecasting. Appl Sci 9
8. Dong Z, Yang D, Reindl T, Walsh WM (2015) A novel hybrid approach based on self organizing maps, support vector regression and particle swarm optimization to forecast solar irradiance. Energy 82:570–577
9. Li F-F, Wang S-Y, Wei J-H (2018) Long term rolling prediction model for solar radiation combining empirical mode decomposition and artificial neural network techniques. J Renew Sustain Energy 10:013704
10. Harender YK, Yash P, Madan TM (2020) Short term PV power forecasting using empirical mode decomposition in integration with back propagation neural network. J Inf Optimization Sci 41(1):25–37
11. Anuj G, Kapil G, Sumit S (2021) Solar irradiation forecasting technologies: a review, strategic planning for energy and environment, vol 39, issue 1–4, pp 319–354. https://doi.org/10.13052/spee1048-4236.391413
12. Huang D, Wu Z (2017) Forecasting outpatient visits using empirical mode decomposition coupled with back propagation artificial neural networks optimized by particle swarm optimization. Plos One 12
13. Awajan Ahmad M, Tahir IM, Al Wadi S (2019) A review on empirical mode decomposition in forecasting time series. Italian J Pure Appl Math 42:301–323
14. Monjoly M, Andre R, Calif Soubdhan T (2017) Hourly forecasting of global solar radiation based on multistage decomposition methods: a hybrid approach. Energy 119:228–298
15. Shamshirband S, Mohammadi K, Khorasanizadeh H (2016) Estimating the diffuse solar radiation using a coupled support vector machine-wavelet transform model. Renew Sustain Energy Rev 56:428–435
16. https://delhitourism.gov.in/delhitourism/aboutus/seasons_of_delhi.jsp

Real-Time Power Quality Monitoring System in LabVIEW Using Wavelet Transform and Stockwell Transform

Papia Ray, Surender Reddy Salkuti, and K. R. Satyajit

Abstract Power quality (PQ) standards have become a concern, which in turn becomes intensified due to day-to-day increase usage of power electronic and electricity demand devices. Now, it has become a challenge for engineers to identify and analyze qualitatively and quantitatively these issues. Hence, it has become a significant concern for developing hardware, PQ monitoring systems for real time. Some of these problems have been cited in this paper. Continuous use of wavelet and Stockwell transforms and monitoring PQ are solutions to some of the main issues. Using LabVIEW, we can compare both the advantages and disadvantages of the above-said schemes. In LabVIEW, PQ monitoring is designed and implemented, which help to display result like harmonic components, values of root mean square (RMS), power quality factor (PQF), values of total harmonic distortion (THD), and 3D S-transform plots and plots of wavelet transform (WT) in the proposed real-time system.

Keywords Power quality · Power quality factor · Wavelet transform · S-transform · Total harmonic distortion

1 Introduction

All the commercial and industrial electricity users have a significant concern about the power quality (PQ), with all its negative impact being posed in the system as the problem. By acquiring all the knowledge of the PQ thoroughly, voltage, harmonics, frequency, and other indicators of steady-state are not the only thing to be focused on, but the values of voltage swells, transient overvoltage, voltage sags, and transient oscillation need to be focused to get more perfect PQ information in real time [1].

P. Ray · K. R. Satyajit
Department of Electrical Engineering, Veer Surendra Sai University of Technology, Burla, India
e-mail: papiaray_ee@vssut.ac.in

S. R. Salkuti (✉)
Department of Railroad and Electrical Engineering, Woosong University, Daejeon, Republic of Korea
e-mail: surender@wsu.ac.kr

Therefore, the critical precondition of dynamic compensation of PQ is realizing the real time and effectively detecting these disturbance signals.

According to IEEE standards, a utility defines PQ as reliable and shows statistics that demonstrate a 99.98% reliable system. PQ is featured as power supply characteristics, which is also an indicator that the manufacturer is working appropriately or not. It depends upon these characteristic types of equipment, and they can be voltage, current, or frequency [2]. The currents that specific loads may draw cannot be controlled by the power supply system, thus controlling the quality of the voltage. However, impedances incur various disturbances that may affect the voltage while the current passes through [3, 4].

1.1 Literature Review

Different monitoring methods have been proposed related to PQ and a firm monitoring system using LABVIEW. Some of the ways are discussed below.

To monitor by using a real-time PQ system using S transform is proposed in [5], which sites a bright idea about using S transform to watch the power quality issue, thus real-time calculation and detection of PQ problems by LabVIEW. By using LabVIEW, the modeling and analysis of a virtual tool for the online real-time monitoring of PQ are proposed in [6]. PQ monitoring by distributing wavelet energy of a signal, mapped in time and frequency domain using discrete wavelet transform is proposed in [7]. Techniques to digitally filter with the use of WT are viewed in reference [8] to display various disturbances in PQ.

Power disturbances monitoring using Lab VIEW is used in [9] to accommodate both hardware and software to enhance the PQ. In reference [10], the data for PQ disturbances events are gathered experimentally and synthetically. PQ classification proposed in [10] has comparatively high performance than other approaches presented in the literature for both the actual data and simulations. Reference [11] suggests a multifunctional real-time and hardware implementation of PQ monitoring system with the use of Stockwell transform (*S*-transform) in a LabVIEW environment that can depict real-time harmonic components, root mean square values, fast Fourier transform (FFT) plots, 3D plots of *S*-transform, and importance of total harmonic distortion (THD) of three-phase voltages. A comprehensive overview of PQ for real-time applications has been presented in reference [12].

A comprehensive review of PQ monitoring that is large and long-running involving most distribution network service providers (DNSPs) of Australia is proposed in [13]. An oscillography system is applied remotely for the PQ monitoring; allowing the users to control a terminal using Ethernet networks, analyzing data, and capturing waveforms from modules remotely in real-time and is proposed in [14]. To find PQ monitors, a new technique is accrued to optimize the prize of the distributed monitoring system that takes into the data redundancy and is proposed in [15]. Reference [16] proposes a power monitoring system that is real-time based on a field-programmable gate array platform. Reference [17] considers the potential

harmonic resonance conditions and suggests an enhanced procedure of PQ meters in a medium voltage distribution system. Various power quality parameters such as RMS values, values of harmonic components, values of THD, PQF, and 3D plots of wavelet transform (WT) and S-transform can be calculated and compared by using the LabVIEW.

1.2 Objective

The main aim of this work is to monitor PQ events precisely. To fulfill it, analysis of harmonics, calculation of THD of a distorted wave, application of filters and analysis of filtered voltage, calculation of PQF, implementation of wavelet and Stockwell transform, comparison between Stockwell and wavelet transform are executed in this paper.

The organization of the rest of the contents is in the following manner: Sect. 2 presents the PQ, PQ concern, and various distortions like voltage sag, swell, interruption, waveform distortion, and harmonics. Section 3 describes the calculation of PQF and THD of a system-generated PQ profile and application of filters to condition the distorted voltage waveform and comparison of THD of both the distorted signal and filtered signal. The description of Stockwell transforms and wavelet transform has been shown in Sect. 4. Finally, Sect. 5 concludes the manuscript, and the results obtained are discussed.

2 Power Quality Concepts

Electric power system devices are now dramatically changed from linear to highly non-linear due to the intervention of solid-state devices like converter inverters, variable speed regulators, FACTS devices. These devices are highly non-linear because of high switching operation and incorporation of the diode, diac, transistors, thyristor, triac, and GTO, etc. These non-linear elements considerably affect the PQ of the electric power supply by introducing the harmonics [18]. Therefore, monitoring the supply network to detect harmonics has become a significant issue in the power quality research area.

Maintaining a smooth PQ profile has become a challenge for utilities and supply systems due to power quality issues. Voltage sag is defined as reducing RMS voltage for a short duration due to overload, short circuit, or starting of electric motors [19]. It occurs when 10 and 90% of the RMS voltage decrease from nominal voltage for half cycle to 1 min.
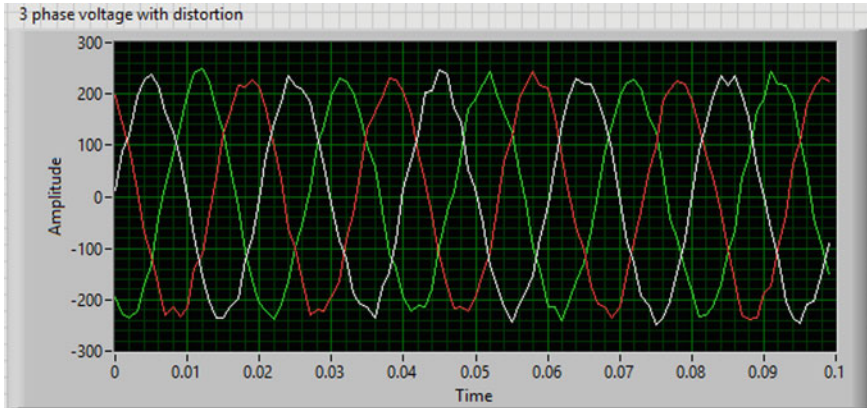
Fig. 1 LabVIEW model of a three-phase voltage

2.1 Waveform Distortion

A sine wave of ideal characteristics with a power frequency that is mainly characterized by deviation's spectral content is known as steady-state deviation. Harmonics, notching, inter harmonics, DC offset, and noise are types of waveform distortion [20]. Figure 1 depicts the model of a $3-\Phi$ system having waveform distortion in LabVIEW.

Electronic equipment with an internal switch-mode power supply (SMPS) to draw a non-linear current waveform is called voltage waveform distortion. In contrast, a sine wave current is produced by a linear load. The pulses in current by applied voltage waveform are drawn by SMPS [21]. There is an increase in nonlinear current with the addition of every device. The voltage drop is seen at the peak portions created by a combination of nonlinear current and the circuit conductor impedance and the power source. The root mean square (RMS) voltage drop increases with the heaviness of loading [22]. The amplitude of the current is decreased by the recent changes in the design and efficiency of SMPS.

2.2 Harmonics

These are the sinusoidal waveforms of voltage or current that are integral multiple of frequencies at which the design is done for its operation (fundamental frequency). Waveforms that are distorted periodically can be used for a sum of fundamental frequency and the harmonics [23]. Figure 2 depicts the waveform showing the noise and harmonic.
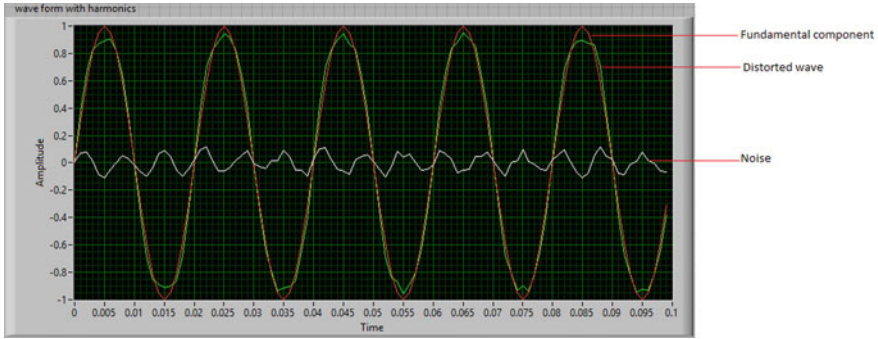
Fig. 2 Waveform showing noise and harmonic

2.3 Total Harmonic Distortion (THD)

In most cases, the transmission voltage system has less than 1% of distortion. But there is a growth in distortion when moved closer to the load. Harmonics cause this distortion. The Fourier series concept is used universally to study harmonics [24]. For $1-\Phi$, total current harmonics distortion THD$_I$ and THD$_V$ are defined as,

$$\text{THD}_I = \frac{\sqrt{\sum_{h \neq 1} I_h^2}}{I_1} \tag{1}$$

$$\text{THD}_V = \frac{\sqrt{\sum_{h \neq 1} V_h^2}}{V_1} \tag{2}$$

where h is the order of harmonics, the fundamental component is represented by 1 [25]. The fundamental RMS voltage and current are represented by V1 and I1.

THD of a signal measures the distortion. THD characterizes linearity in audio systems of PQ of electric power systems. Distortion factor is generally used as a synonym. The distortion of a waveform for pure sinewave can be measured by using LABVIEW and it is shown in Fig. 3.

3 Stockwell (S) and Wavelet Transform

The two intelligent methods used to analyze PQ events in this paper are S and Wavelet transforms. Details of the methods are given below.
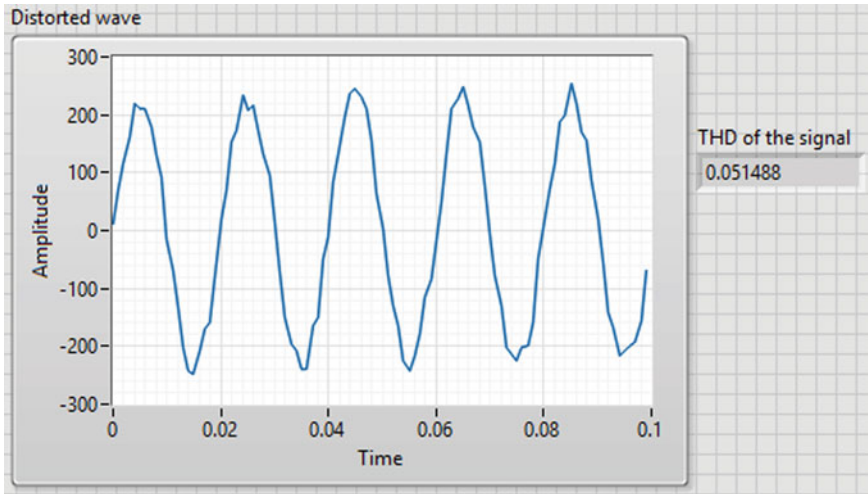
Fig. 3 THD of a signal using LABVIEW

3.1 Stockwell (S) Transform

Stockwell transform or S transform was developed in 1994 as a time–frequency distribution to analyze geophysics data. The STFT [26] is an extension of continuous WT and overcomes some of its disadvantages and is generalized by S-Transform. Sinusoids are fixed with respect to the time axis for one modulation, which limits the dilations in scalable Gaussian window and translations in S transform [27]. The cross-term problem cannot be seen in the S transform, but the clarity of the signal is better than the Gabor transform. S transforms have many disadvantages that include the requirement of higher complexity computation (because of inability in using FFT).

3.1.1 Mathematical Formulation

If $f(t)$ is input signal, WT and $W(t, d)$ are a continuous function of $f(t)$ and is defined as,

$$W(\tau d) = \int_{-\infty}^{\infty} f(t)w(w(t - \tau, d)\mathrm{d}t) \tag{3}$$

where $W(\tau, d)$ is the fundamental wavelet for scaled reproduction. A phase factor of S-transform is defined as,

$$S(\tau, f) = e^{i2\pi f \tau} W(\tau, d) \tag{4}$$

where wavelet is defined for this case as,

$$W(t, f) = \frac{|f|}{\sqrt{2\pi}} e^{-\left(\frac{t^2 f^2}{2}\right)} e^{-i2\pi f \tau} \tag{5}$$

d is the dilation factor of inverse frequency f and S-transform is expressed as,

$$S(\tau, f) = \frac{|f|}{\sqrt{2\pi}} \int_{-\infty}^{\infty} f(t) e^{-\left(\frac{t^2 f^2}{2}\right)} e^{-i2\pi f \tau} \, \mathrm{d}t \tag{6}$$

Gaussian window is given by,

$$\sigma(f) = T = \frac{1}{|f|} \tag{7}$$

As local spectra are a representation of S-transform, Fourier or by averaging it through inverse ST can be obtained directly by time average spectrum and is given by [28],

$$f(t) = \int_{-\infty}^{\infty} \left\{ \int_{-\infty}^{\infty} S(\tau, f) \mathrm{d}t \right\} e^{-i2\pi f \tau} \, \mathrm{d}f \tag{8}$$

The discrete s-transform can be represented as follow,

$$S\left(jT, \frac{n}{NT}\right) = \sum_{m=0}^{N-1} F\left(\frac{m+n}{NT}\right) G(m, n) e^{\left(\frac{i2\pi m j}{N}\right)} \tag{9}$$

where

$$G(m, n) = e^{-\left(\frac{2\pi^2 m^2 \alpha^2}{n^2}\right)} \tag{10}$$

3.2   Wavelet Transform (WT)

In mathematics, square integral is represented as wavelet series function (complex or real valued) by some orthonormal series generated by it [29], and it is defined as [10],

$$[W_\Psi f](a, b) = \frac{1}{\sqrt{|a|}} \int_{-\infty}^{\infty} \Psi\left(\frac{x - b}{a}\right) f(x)\mathrm{d}x \tag{11}$$

The wavelet coefficients are then given by,

$$c_{ik} = [W_\Psi f]\left(2^{-j}, k2^{-j}\right) \tag{12}$$

4 Results and Discussion

PQF is termed as the Fourier technique that expresses power transfer quality in three-phase system power. The fundamental frequency is accepted by harmonics of current and voltage when phase voltages are not balanced. The standard parameters to measure are voltage, current, and frequency. The waveform of harmonics in voltages or currents is fundamental to integral multiple [30]. As power electronic and nonlinear equipment are present, so there are harmonics in the power system. When this standard does not meet electric power, then a reduction in PQ occurs. The PQF indicates PQ supply. All PQ is represented in one indicator which are,

$$POF = \sum_i x_i (1 - PQ_i) \tag{13}$$

where x_i is maximum value is up to one. In previous sections, dissimilar PQ_i is expressed. The PQF is unity for pure sinusoidal current and voltage, and is in phase for a balanced system. A low value in an unbalanced system is caused due to higher-order harmonics in PQF. Figure 4 depicts PQF of a three-phase system. After comparing different, it shows a significant reduction.

In the front panel of total voltage harmonics distortion (THD$_V$), which shows total voltage harmonic distortion and frequency of $3-\Phi$ system, PQ1 = 17.6926%, which is shown in Fig. 5. $Z_{an} = Z_{bn} = Z_{cn} = 100\ \Omega$ and 0.2 A of third harmonic is added in the current signal load and is taken to balance. In Fig. 6 $3-\Phi$ current signal is shown. Similarly, in Fig. 6, detected fundamental as shown in the front panel of total current harmonics distortion (THD$_I$), a current signal of third harmonic frequency and total THD$_I$, PQ2 = 23.6386% is shown.

Similarly, PQ3, PQ4, and PQ5 are simulated, and PQ3 = 0.707109%, PQ4 = 0.707223%, and PQ5 = 0.61458, respectively as in Fig. 6. Various approaches have been implemented in recent years to progress the power quality system. Some of them are series-connected filters, shunt-connected filters, passive filters, active filters, isolation transformers, and FACTS devices.

Using internal LabVIEW programs, unlike noise or turbulences, were produced for sighting different simulated signals of PQ and three staged Butterworth filters to condition the system. The detailed simulation and front panel of LabVIEW are
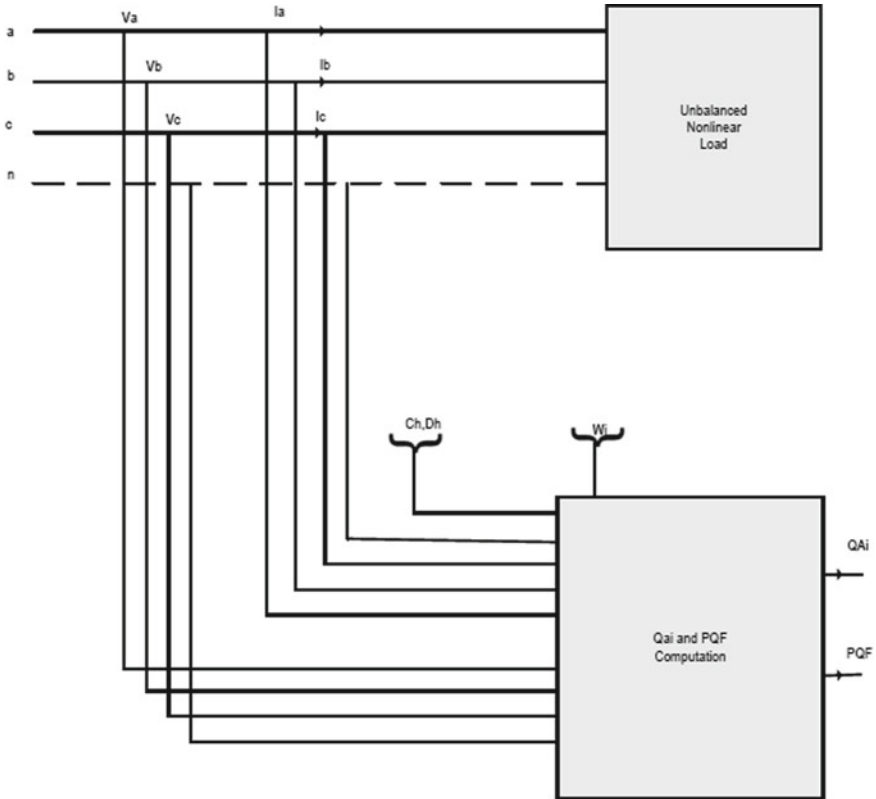
Fig. 4 PQF of three-phase system
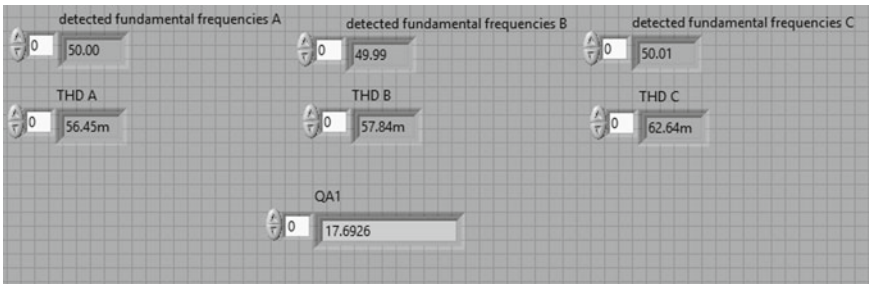
Fig. 5 Simulated PQ1 aspect for VTHD shown in LabVIEW

shown in Figs. 7 and 8, which may provide some view regarding power quality conditioning.
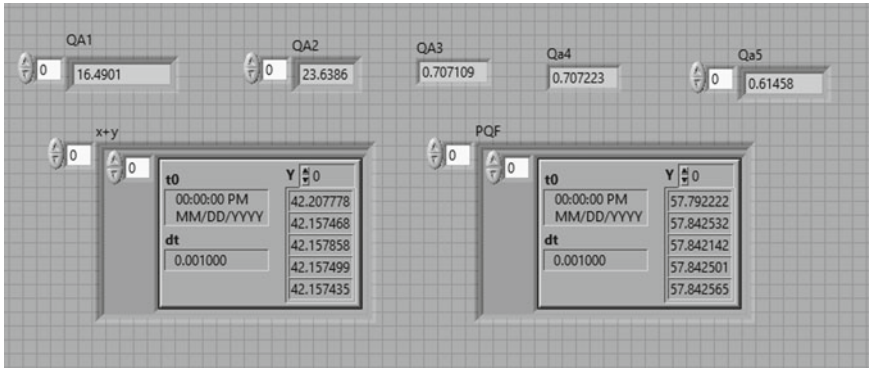
Fig. 6 Simulated all quality aspect harmonics contain signal and unbalanced PQF
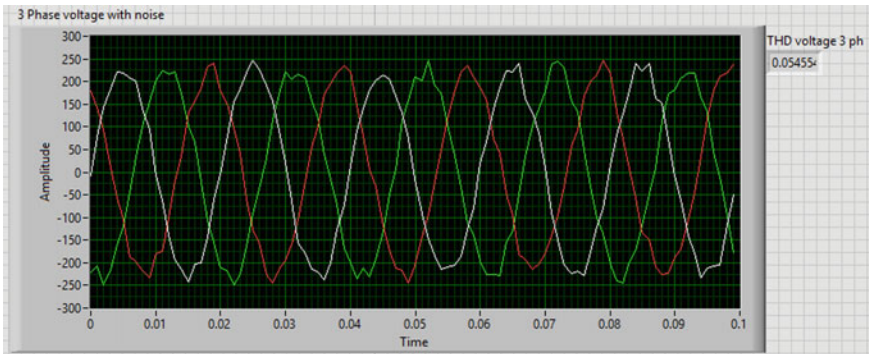
Fig. 7 Three-phase voltages with harmonics and THD of the system
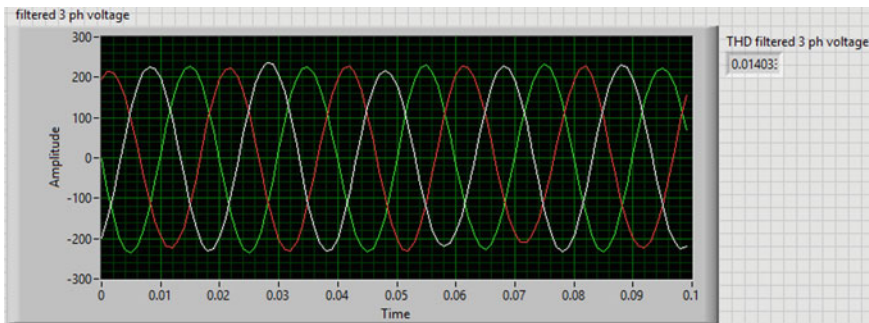
Fig. 8 Filtered three-phase voltage with less THD

5 Conclusions

This paper presented various factors that include total harmonic distortion (THD) of signals that contain harmonics and the said filtered signal calculated and compared, and PQF of the designed system has been estimated to monitor the PQ system. It is depicted from the simulation results that it improves the performance of reliability of the system by using such measurement and monitoring scheme. S-Transform and Wavelet Transform are implemented here for the proposed schemes. Thus, comparing above said transform techniques it is concluded that the proposed scheme provides advantages over each other, resulting in a better power quality monitor system.

References

1. Mishra DP, Ray P (2015) Calculation of power quality factor of supply system using LabVIEW. In: Michael Faraday IET international summit 2015, pp 150–155
2. Malik H, Iqbal A, Joshi P, Agrawal S, Bakhsh FI (2021) Metaheuristic and evolutionary computation: algorithms and applications. In: Studies in computational intelligence, vol 916. Springer, Singapore
3. Reddy MJB, Sagar K, Mohanta DK (2014)A multifunctional real-time power quality monitoring system using Stockwell transform. IET Sci Meas Technol 8(4):155–169
4. Barros J, de Apraiz M, Diego RI (2009) A virtual measurement instrument for electrical power quality analysis using wavelets. Measurement 42(2):298–307
5. Xu RL, Liu Y, Xu X, He JJ (2013) Power quality monitoring system based on LabVIEW. Adv Mater Res 711:358–362
6. Isdawimah N, Nadhiroh A, Aji D, Ismujianto (2019) Real-time monitoring of power quality for web based electrical power panel using LabVIEW. In: International Conference on Electrical Engineering and Computer Science (ICECOS), pp 217–221
7. Singh S, Jain B, Jain S (2016) Wavelet based real-time power quality monitoring. IEEE Canadian Conference on Electrical and Computer Engineering (CCECE), pp 1–6
8. Lee KS, Lee YJ, Kim DH, Kim YM (2003) A real time monitoring system of power quality disturbances using digital filtering techniques. In: IFAC proceedings volumes, vol 36, issue 20, pp 845–850
9. Abidin AF, Yusoh MATM (2021) LabVIEW as power disturbances classification tools (Online First), IntechOpen. https://doi.org/10.5772/intechopen.96079. Available from: https://www.intechopen.com/online-first/labview-as-power-disturbances-classification-tools
10. Karasu S, Saraç Z (2020) Classification of power quality disturbances by 2D-Riesz Transform, multi-objective grey wolf optimizer and machine learning methods. In: Digital signal processing, vol 101
11. Reddy MJB, Sagar K, Mohanta DK (2014) A multifunctional real-time power quality monitoring system using Stockwell transform. IET Sci Meas Technol 8(4):155–169
12. Igual R, Medrano C (2020) Research challenges in real-time classification of power quality disturbances applicable to microgrids: a systematic review. Renew Sustain Energy Rev 132
13. Elphick S, Ciufo P, Drury G, Smith V, Perera S, Gosbell V (2017) Large scale proactive power-quality monitoring: an example from Australia. IEEE Trans Power Deliv 32(2):881–889

14. Auler LF, d'Amore R (2009) Power quality monitoring controlled through low-cost modules. IEEE Trans Instrum Meas 58(3):557–562
15. Eldery MA, El-Saadany EF, Salama MMA, Vannelli A (2006) A novel power quality monitoring allocation algorithm. IEEE Trans Power Deliv 21(2):768–777
16. Zhao L, Matsuo IBM, Salehi F, Zhou Y, Lee W (2019) Development of a real-time web-based power monitoring system for the substation of petrochemical facilities. IEEE Trans Ind Appl 55(1):43–50
17. Bottura FB, Oleskovicz M, Le TD, Petit M (2019) Optimal positioning of power quality meters for monitoring potential conditions of harmonic resonances in a MV distribution system. IEEE Trans Power Deliv 34(5):1885–1897
18. Chen, Yang Y, Xu T, Cao Y, Wang X (2009) Power quality disturbances detection based on hilbert phase-shifting. In: Asia-Pacific power and energy engineering conference, 1–4
19. P. Li, L. Zhao, H. Bai, Y. Zhang.: Power Quality Monitoring of Power System Based on Spectrum Analysis. International Conference on E-Product E-Service and E-Entertainment, pp 1–4
20. Keerthana SV, Madhuridevi L, Sindhuja K (2014) Development of software tool for class-room teaching of power quality using LabVIEW. In: International Conference on Advances in Electrical Engineering (ICAEE), pp 1–6
21. Talavera MDB, Bravo JC, Arroyo CÁ (2021) Instantaneous disturbance index for power distribution networks. Sensors 21:1–17
22. Ray P, Salkuti SR (2020) Smart branch and droop controller based power quality improvement in microgrids. Int J Emerging Electric Power Syst 21(6)
23. Enshaee P (2018) A new S-transform based method for identification of power quality disturbance. Arab J Sci Eng 43:2817–2832
24. Akorede MF, Hizam H (2009) Wavelet transforms: practical applications in power systems. J Electrical Eng Technol 4(2):168–174
25. Das SR, Mishra DP, Ray PK, Salkuti SR, Sahoo AK (2021) Power quality improvement using fuzzy logic-based compensation in a hybrid power system. Int J Power Electronics Drive Syst (IJPEDS) 12(1):576–584
26. Gupta N, Seethalekshmi K, Datta SS (2021) Wavelet based real-time monitoring of electrical signals in Distributed Generation (DG) integrated system. Eng Sci Technol Int J 24(1):218–228
27. Abidullah NA, Abdullah AR, Shamsudin NH, Ahmad NHTH, Jopri MH (2013) Real-time power quality signals monitoring system. In: IEEE student conference on research and developement, pp 433–438
28. Das B, Panigrahi PK, Das SR, Mishra DP, Salkuti SR (2021) Power quality improvement in a photovoltaic based microgrid integrated network using multilevel inverter. Int J Emerging Electric Power Syst. https://doi.org/10.1515/ijeeps-2021-0040
29. Talavera MDB, Bravo JC, Arroyo CA (2021) Instantaneous disturbance index for power distribution networks. Sensors 21(4)
30. Jung WK, Park YC, Lee JW, Suh ES (2020) Remote sensing of sewing work levels using a power monitoring system. Appl Sci 10(9)

An IOT-Based Cost-Effective Home Automation System for Energy Saving

Arjun Baliyan, Majid Jamil, and M. Rizwan

Abstract In this era of digitalization, automation has been the most vital revolution. Nowadays, internet is an integral part of human life. Internet of things (IOT) provides a platform that allows devices to connect, sense and control remotely across a network infrastructure. In this paper, the focus is made on home automation through IOT over app-based switching operation with ESP32 as the central processor. The IOT devices control and monitor the electronic and electrical appliances in a typical household load. IOT enables us to control the appliances over internet from any part of the world. The proposed ESP32 microcontroller-based home automation is achieved with the help of Virtual Sphere app that allows smooth controlling of lighting and air-conditioning loads, and the complete setup is very economical and easy to implement. It gives the brief insight of the use of controllers and sensors that can help the researchers to design and deploy them in real-time industrial applications.

Keywords Internet of things (IOT) · Relay · ESP32 microcontroller · IR sensor · DHT 11 sensor

1 Introduction

Energy that is a part of everyone's life is directly proportional to the cost endorsed by the supplier on the consumer. Hence, it must be used efficiently so as to minimize the cost of consumption. Therefore, in order to do so we can monitor the different devices through mobile phones and tablets and can control their functioning with the help of microcontrollers. Also, with the rapid increase in a number of companies manufacturing microcontrollers, their cost is becoming reasonable day by day.

A. Baliyan (✉) · M. Jamil
Department of Electrical Engineering, Jamia Millia Islamia, New Delhi 110025, India
e-mail: arjunbaliyaneee@gmail.com

M. Rizwan
Department of Electrical Engineering, Delhi Technological University, Delhi 110042, India

Apart from this due to user-friendly mobile development programs, the IOT-based home/building automation is becoming popular among the users.

Initially, the devices used to communicate with each other using the RFID tags but now it has gained a much wider scope due to the evolving technology [1]. The IOT is not limited to the home/building automation only but it can be used for traffic lights controlling as well as for the different manufacturing machines in the industries. The concept behind all this is that it gathers information from different devices and further converts them into the viable information. According to the data available, there were around 500 million devices that interact among themselves in 2003, and the number is expected to increase up to 50 billion till the end of 2021 [2]. At present time, there is a complete transformation in our workplaces, homes and the surroundings nearby and the whole credit goes to the IOT. For example, be it a lighting and controlling of electrical appliances [3], monitoring the energy consumption of different heating and air conditioning devices such as refrigerators and air conditioners [4, 5], getting the information about the weather conditions [6], smart classrooms [7], smart farming that not only enables the soul nourishment but also help in the increase of farm production [8] are important parts of our lives. Smart home is nothing but the combination of different controlling and monitoring devices that interacts with each other. These devices communicate with the help of gateways that is basically a control system with user interface, which interact with the mobile phones and laptops and the whole network connectivity is managed by the IOT [9]. Smart Home eases the human efforts by centrally controlling all the electrical appliances via IOT irrespective of the time and the location it is installed [10]. It not only provides comfort to the users but also ensures safety and device operability at all the times [11]. Mobile devices are comfortable for the residents of smart homes since they can use them anytime and from anywhere instead of physically operating the devices [12]. In this article, an IOT-based system is implemented for the lighting and air conditioning control of a smart home/building.

The developed system has the following characteristics:

- User can operate and control the electrical appliances via Android-based mobile application.
- Include the facility to set the time for the particular switches to ON/OFF for a certain interval of time as per requirement

The proposed system provides the facility to monitor and control the electrical appliances with the android-based Graphic user interface (GUI). Hence, the system not only provides the comfort to the individual but also plays an important role in the energy savings to the industries as well as to the households.

The paper is structured as follows: Home automation is briefed in Sect. 2. Section 3 gives the hardware requirement, Sect. 4 includes the graphic user interface (GUI) system, Sect. 5 shows the analysis of energy consumption, and finally Sect. 6 concludes the paper.

Fig. 1 Layout of home automation system

2 Home Automation

It is basically a system that allows the consumer to not only control the different appliances in a very easy manner but it also serves the purpose of energy saving. It is easily implementable and therefore very common in industries and offices [13]. Apart from the energy saving, it also adds comfort to the consumer since it allows centralized controlling of all heating, lighting and the air conditioning loads from a central point [14]. Therefore, it leads to the overall reduction in electricity consumption which is a main concern today for different categories of consumer. Wired communication played an important role in the home automation in the past but it has the drawback of higher cost. Therefore, home automation with Wi-Fi is becoming very popular nowadays [15]. In [16], a node microcontroller unit has been used as a Wi-Fi gateway to connect to the different sensors. It also stores the information on the server along with Google Assistant to control the different appliances for the comfortability of the consumer. There are various benefits of home automation system, out of which some are energy saving, user comfortability, peace of mind to the individual and better control with home safety [17]. In [18–20], a recent study about the ongoing work and the development in the field of home automation is explained in detail. A basic structure of the above system is shown in Fig. 1.

3 Hardware Required

The hardware part basically consists of two sections: First is the master node with ESP32 microcontroller, SD card reader, and the real-time clock (RTC) that is used to keep the accurate time for proper operation of the various devices connected to it. The second one consists of a slave node that basically comprises of relay/switch along with the ESP32 microcontroller, DHT 11 sensor, card reader, memory card, IR sensor and IR receiver. The block diagram of the proposed system is shown in Fig. 2.

Fig. 2 Block diagram of the proposed architecture
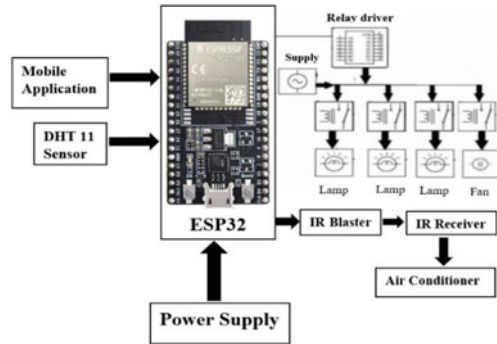
4   Graphic User Interface (GUI)

In order to control and monitor the various devices, a graphic user interface (GUI) system has been implemented in the Smart Home. Virtual sphere app has been used to track the real-time performance and the devices are adjusted to run according to the preset time. The app requires a Wi-Fi connection to add the lighting and air-conditioning devices. Figure 3 shows the home page of the proposed application. The flowchart of the proposed system is given in the Appendix.

Fig. 3 Virtual sphere mobile app
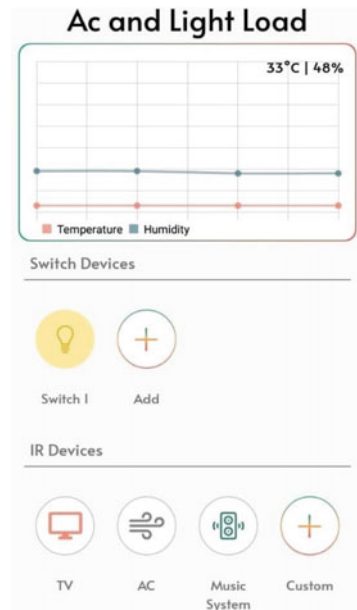
Fig. 4 DTH 11 sensor
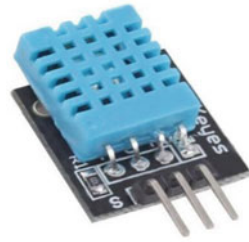
4.1 Air Conditioning and Lighting Unit

To control the air conditioning and the lighting unit, it consists of DHT11 sensor, IR sensor, IR receiver, Opto-coupler Relay and the ESP32 microcontroller.

DTH 11 sensor. DTH 11 sensor (shown in Fig. 4) is a digital humidity and temperature sensor used to control the appliances, here air conditioner.

The specifications are as follows:

(a) *Operating Voltage*: 3.5 V to 5.5 V
(b) *Operating Current*: 0.3 mA (measuring) 60uA (standby).
(c) *Output*: Serial data.
(d) *Temperature range*: 0–50 °C
(e) *Humidity range*: 20–90%
(f) *Resolution*: Temperature and humidity are 16-bit
(g) *Accuracy*: ±1 °C and ±1%

Opto-coupler Relay. A four-channel optocoupler relay has been used with one normally closed contact and one normally open contact. The operating voltage of the relay ranges between 3.3 and 5 V.

Real-Time Clock (RTC). Real-time clock has been used to automate the operation of appliances at a preset time. It switches the appliance on and off at a preset time. It is inbuilt in the ESP32.

RSP32 Microcontroller. The ESP32 has been used as the CPU. The specifications of the CPU used are as follows: two levels of headings should be numbered. Lower-level headings remain unnumbered; they are formatted as run-in headings. The specifications of the CPU used are as follows.

(a) *Processors:*

- CPU: Xtensa dual-core (or single-core) 32-bit LX6 microprocessor, operating at 160 or 240 MHz and performing at up to 600 DMIPS.
- ULP: Ultra-low power co-processor

(b) *Memory:* 520 KiB SRAM, 448 KiB ROM
(c) *Wireless connectivity:*

- Wi-Fi: 802.11 b/g/n
- Bluetooth: v4.2 BR/EDR and BLE (shares the radio with Wi-Fi)

5   Experimental Setup

Once the hardware is tested for proper controlling the devices, it is then implemented to control two led bulbs of 9 * 2 Watts and one air conditioning unit of 7.17 horse-power. The master node and the slave node are depicted in Fig. 5, which includes all the components required for the setup.

Apart from the above setup, one single phase submeter was also installed to capture the number of units consumed in a day normally during the working hours from 9 am to 5 pm. Figure 6 shows that the single-phase meter has rating 240 V, 10–40 amp, 50 Hz frequency.

In order to show the efficacy of the proposed system over the existing one, the energy saving and simple payback period of the device used are calculated according to the Uttar Pradesh, India household traffic and is shown below:

Cost of Controller: 1080 Rs.

- ESP 32 microcontroller: 490 Rs
- Relay/Switch: 60 Rs
- Single Phase Meter: 250 Rs
- Micro SD Card: 220 Rs
- IR sensor: 30 Rs

Fig. 5 Experimental setup
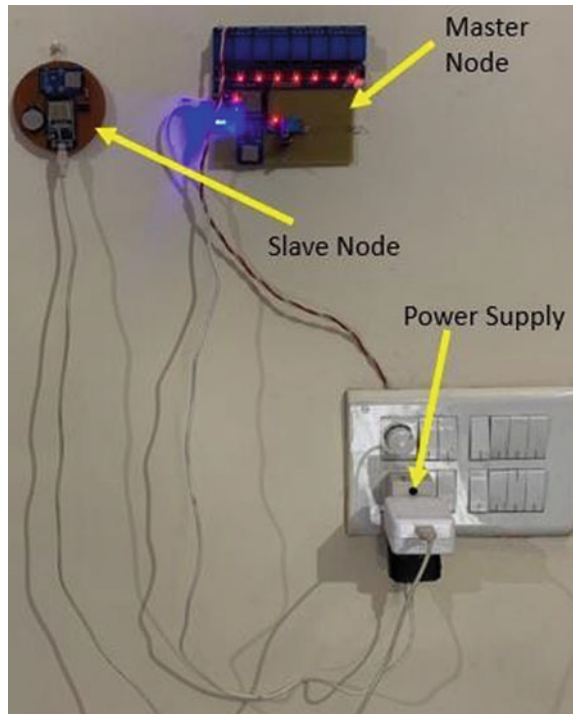
Fig. 6 Single phase meter
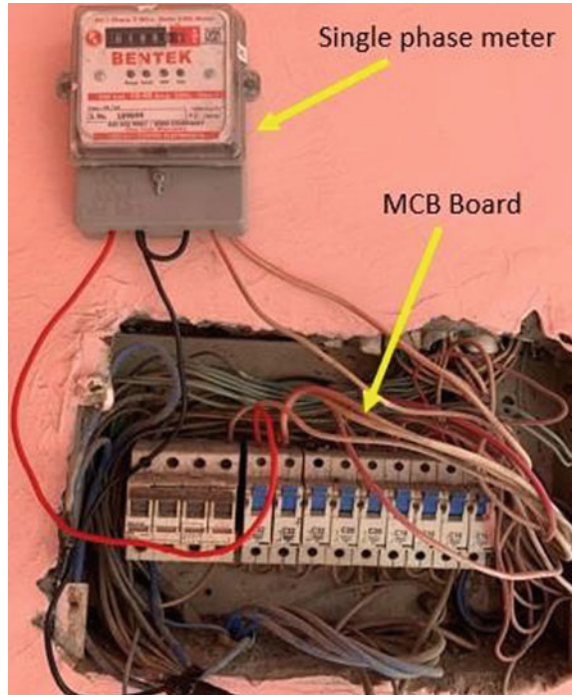
- IR Receiver: 10 Rs
- Real Time Clock: 20 Rs

The analysis was done for a day say for 8 h from 9 am to 5 pm, and it was observed that unit consumption was around 38 units without installing the proposed system but then on the next day when the analysis was done with the IOT-based system then consumption was reduced by 4 units by proper controlling and monitoring the devices with the GUI-based mobile app.

Figures 7 and 8 represent the reading of the meter for the whole day with the above setup installed in the home. At 9 am, the meter reading was noted down, and it was around 18801units, which is shown in Fig. 7. Again, the meter reading was noted down at 5 pm, and it was 18,835 units, which can be seen in Fig. 8. So, it was clear that the above proposed system helps in the energy saving of around 12% for a single day.

Saving in a day (**Rs**):
$$= (\text{KWh (not install)} - \text{KWh (Install)}) * 7$$
$$= (38 - 34) * 7$$
$$= 28 \, \text{Rs}$$

Fig. 7 Initial meter reading

Fig. 8 Final meter reading

Saving per month approximately:
$$= 28 * 30$$
$$= 840 \, \text{Rs}$$

Saving per year (**Rs**):
$$= (\text{KWh (not install)} - \text{KWh (Install)}) * 7$$
$$= 28 * 30 * 12$$
$$= 10{,}800 \, \text{Rs}$$

So, it is clear from the above calculation that the payback period of the above controller is around one and half months. It must be also noted down that the saving will increase for the large buildings because the energy consumption will be more in that case as compared to the smaller area.

6 Conclusion

A prototype for controlling the lighting and the air conditioning loads has been designed and implemented in the room. The achievement of the proposed system is that it provides 12% saving even for a single-day implementation. The payback period of the controller is very less, and the energy saving can be increased further if the system is implemented for a large scale. The above system can be implemented in industries and office applications.

Appendix

Flowchart of the proposed system
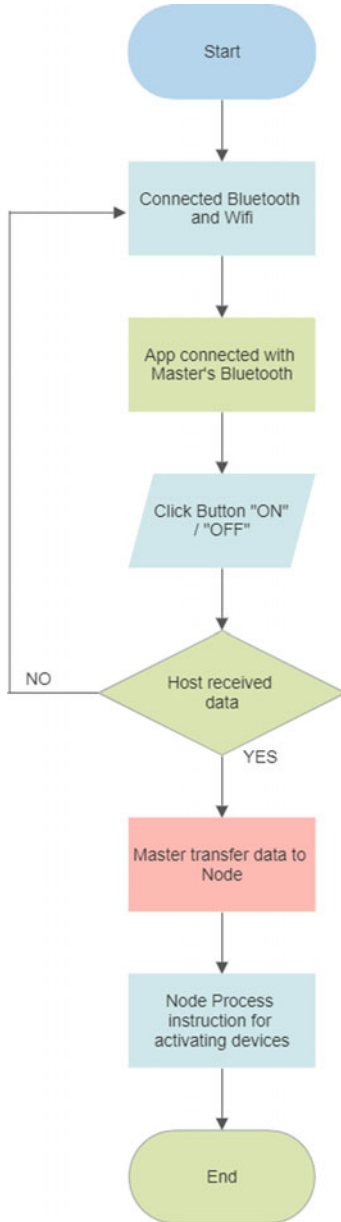
References

1. Misra S, Muthucumaru M, Salman H (2017) System model for the internet of things. In: Security challenges and approaches in internet of things. Springer, Cham, pp 5–17
2. Gubbi J, Buyya R, Marusic S, Palaniswami M (2013) Internet of Things (IoT): a vision, architectural elements, and future directions. Futur Gener Comput Syst 29(7):1645–1660
3. Pirbhulal S, Zhang HE, Alahi M, Ghayvat H, Mukhopadhyay S, Zhang YT, Wu W (2017) A novel secure IoT-based smart home automation system using a wireless sensor network. Sensors 17(1):69
4. Pocero L, Amaxilatis D, Mylonas G, Chatzigiannakis I (2017) Open source IoT meter devices for smart and energy-efficient school buildings. HardwareX 1:54–67
5. Morello R, De Capua C, Fulco G, Mukhopadhyay SC (2017) A smart power meter to monitor energy flow in smart grids: the role of advanced sensing and IoT in the electric grid of the future. IEEE Sens J 17(23):7828–7837
6. Chapman L, Simon JB (2018) High-resolution monitoring of weather impacts on infrastructure networks using the Internet of Things. Bull Am Meteorol Soc
7. Gökozan H, Taştan M, Sarı A (2017) Smart cities and management strategies, II. International Strategic Research Congress, Antalya, Turkey, pp 327–331
8. Debauche O et al (2021) Data management and internet of things: a methodological review in smart farming. Internet Things 14:100378. ISSN 2542-6605
9. Galinina O, Mikhaylov K, Andreev S, Turlikov A, Koucheryavy Y (2015) Smart home gateway system over bluetooth low energy with wireless energy transfer capability. EURASIP J Wirel Commun Netw 1:178
10. Samuel S, Sujin I (2016) A review of connectivity challenges in IoT-smart home. In: 2016 3rd MEC International Conference on Big Data and Smart City (ICBDSC), IEEE
11. Alohali B, Merabti M, Kifayat K (2014) A secure scheme for a smart house based on Cloud of Things (CoT). In: Computer Science and Electronic Engineering Conference (CEEC), 2014 6th, pp 115–120
12. Ye X, Huang J(2011) A framework for cloud-based smart home. In: 2011 International Conference on Computer Science and Network Technology (ICCSNT), vol 2. IEEE, pp 894–897
13. Guth J et al (2018) A detailed analysis of IOT platform architectures: concepts, similarities, and differences. Springer, Heidelberg
14. Al Kuwari M, Ramadan A et al (2018) Smart-home automation using IOT-based sensing and monitoring platform. In: IEEE 12th international conference on compatibility, power electronics and power engineering
15. Smart Security System. Int J Adv Res Comput Commun Eng 6(4), April 2017
16. Jabbar WA et al (2019) Design and fabrication of smart home with Internet of Things enabled automation system. IEEE Access 7:144059–144074
17. Kunal D, Tushar D, Pooja U, Vaibhav Z, Lodha V (2016) Smart home automation using IoT. Int J Adv Res Comput Commun Eng 5(2)
18. Zielonka A, Woźniak M, Garg S, Kaddoum G, Piran MJ, Muhammad G (2021) Smart homes: how much will they support us? A research on recent trends and advances. IEEE Access 9:26388–26419
19. Singh U, Ansari MA (2019) Smart home automation system using Internet of Things. In: Proceedings of the 2019 2nd international conference on Power Energy, Environment and Intelligent Control (PEEIC), Noida, India, 18–19 Oct 2019, pp 144–149
20. Ozeer U, Letondeur L, Ottogalli F-G, Salaun G, Vincent J-M (2019) Designing and implementing resilient IoT applications in the fog: a smart home use case. In: Proceedings of the 2019 22nd Conference on Innovation in Clouds, Internet and Networks and Workshops (ICIN), Paris, France, 19–21 Feb 2019, pp 230–232

Simulation of Modular Fly-Back Current-Fed Push–Pull DC-DC Converter for High Voltage Low Current Applications

D. Beula, M. S. Indira, and N. Balaji

Abstract A DC-DC converter has been proposed using Fly-back Current-fed Push–Pull topology with multiple secondary windings for high voltage low current applications. The converter is modular at the output which gives the flexibility to cater to specific output voltage levels. The High Voltage Transformer (HVT) with multiple secondary windings and rectifier with voltage doublers result in a smaller turns ratio for higher voltage conversion. The rectifier components on the high voltage side are subjected to lower voltages that reduce the voltage stress on the rectifier component, compared to HVT with the single secondary winding. The converter is operated in complete energy transfer mode (Discontinuous conduction mode) for effective utilization of stored energy in the fly-back inductor as it is fed-back to the source. The discontinuous current-fed scheme provides an instantaneous current limiting facility for short circuits at the load side. Zero current turn-on of switches due to the discontinuous mode of operation reduces switching losses and the non-overlapping mode of power switches minimizes conduction loss. The operation of the converter is analyzed under steady-state conditions. A design procedure is established and the converter is designed for a typical load of 5 kV, 500 W at a switching frequency of 20 kHz. The performance of the converter is verified by simulation.

Keywords Current-fed · DC-DC converter · Modular · Energy feedback · High voltage application

---

D. Beula (✉)
Department of Electrical and Electronics Engineering, Sir M Visvesvaraya Institute of Technology, Bangalore, Karnataka, India
e-mail: beula_eee@sirmvit.edu

M. S. Indira
M.S. Ramaiah University of Applied Sciences, Bangalore, Karnataka, India

N. Balaji
Department of Electrical and Electronics Engineering, Dayananda Sagar College of Engineering, Bangalore, Karnataka, India

1 Introduction

High voltage converters find applications in medical X-ray units, Electrostatic Precip-
itator (ESP), traveling wave tubes, and many other areas [1–4]. Conventionally, these
systems convert low voltage from a single/three phase source to high voltage DC typi-
cally of several kilovolts. In most of these applications, isolated DC-DC converters are
used. For high voltage applications, voltage-fed isolated converters are not preferred
due to the presence of an output filter inductor that experiences large voltage stress
making them bulky and expensive [5–7]. In the case of multi-output applications
inductor is necessary at each output circuit. Compared to voltage-fed converters,
current-fed DC-DC converters are used in high voltage applications as the output
inductor can be transferred to the primary side [8]. It has one single inductor on the
input side that makes a good choice for multiple output power supplies. In case of flux
imbalance, the inductor controls the peak current and protects against transformer
saturation. In current-fed push–pull converters, the switches need to be operated in an
overlapping mode to avoid sudden interruption of current when the switch is opened.
The converter used in high voltage applications requires HVT of high voltage trans-
formation ratio resulting in large parasitic capacitance and leakage inductance. Such
converters use these stray components of HVT to achieve Zero Current Switching
(ZCS) operation [9, 10]. Another current-fed topology is the fly-back current-fed
push–pull DC-DC converter [11–13]. In this, the series inductor can be used as a
fly-back transformer by providing a secondary winding to feed the energy to either
input or output. In all these topologies, the rectifier used in the high voltage side of
HVT with a single secondary winding has series-connected low voltage diodes in
each rectifier branch, to achieve a high voltage output. This result in voltage imbal-
ance among the diodes and compensation techniques are required to mitigate voltage
imbalance [14].

   In this paper, a high voltage power supply based on fly-back current-fed push–pull
topology with multiple secondary winding and voltage doublers rectifier is proposed.
It has a fly-back transformer at the input side in series with a push–pull primary and
the fly-back secondary is connected back to the input. The fly-back inductance can be
designed to limit the short circuit current. Operating the converter in discontinuous
conduction mode makes effective utilization of the energy stored, by returning to the
source. The power supply circuit is modular in nature, easy to realize required high
voltage levels by connecting multiple secondary circuits in series. In this scheme,
the rectifier components experience less voltage stress because each rectifier diode
is directly supplied from the secondary of the transformer and it eliminates a series
of connected diodes also the associated voltage mis-sharing. Zero current turn-on
of power switches due to the discontinuous mode of operation reduces switching
losses. Non-overlapping of power switches owing to buck mode of operation reduces
conduction losses of switches. Operation of the converter at high-frequency results
in reduced size of magnetic and filter components.

2 Operation of DC-DC Converter

The DC-DC converter circuit is shown in Fig. 1. Push–pull transformer (HVT) has a center tapped primary (L_{1p}) with multiple secondary windings (L_{s1}-L_{sn}). The series inductor L_{2p} is brought in the form of a fly-back transformer with its secondary winding (L_{2s}) returned to the input. The turns ratio of push–pull and fly-back are n_1 and n_2 respectively. The push–pull center tap voltage is denoted as V_{ct}. Each secondary of the push–pull transformer is connected to a rectifier and voltage doubler circuit. D1 and D2 are the rectifier diodes in the first secondary winding of a push–pull transformer. The total output voltage, V_o is obtained across load resistance R_L, by connecting secondary circuits in series. The fly-back transformer secondary winding, diode D3, capacitor C and D4 form an energy feedback circuit. This configuration can operate by overlapping "ON" times of switches S1 and S2 with a duty cycle greater than 0.5 and non-overlapping of these switches with a duty cycle less than 0.5. Analysis of the circuit is done in the non-overlapping mode of ON times of power switches. There are four operating modes in one switching cycle. The transformer is assumed to be ideal in this analysis.
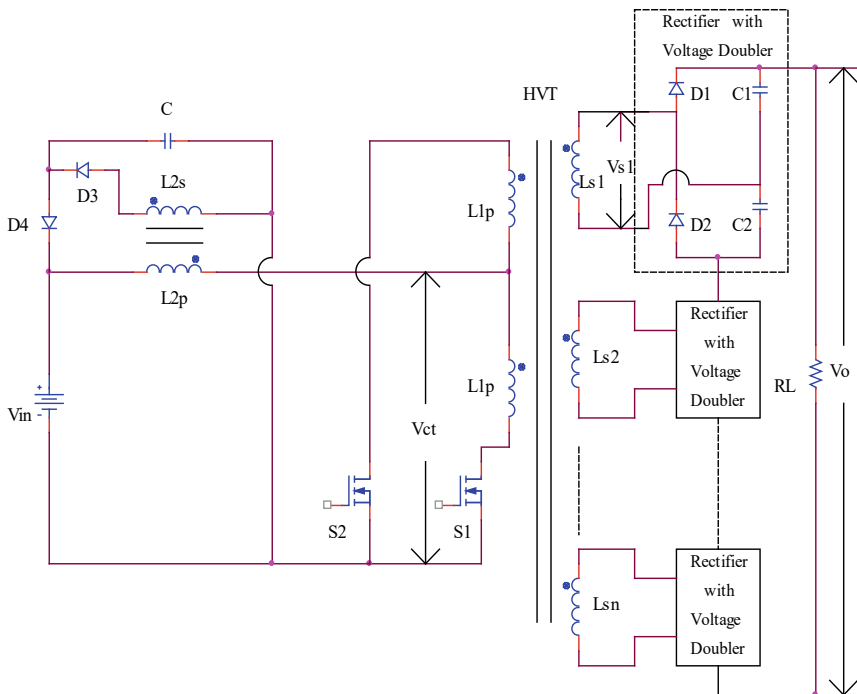
Fig. 1 Schematic of DC-DC converter

2.1 Mode 1: Switch S1 Closed and S2 Open

During the interval when S1 is "ON" current flows through L_{2p}, L_{1p}, and switch S1. This operation establishes the voltage across fly-back primary (L_{2p}) and push–pull primary winding (L_{1p}). The voltage across L_{1p} reflected on to the push–pull secondary windings (L_{s1} to L_{sn}) is $n_1 \times V_{ct}$, that forward biases rectifier diode D1 due to selected dot polarity and charges capacitor C1, to a voltage equal to V_{s1}. When the switch S1 is ON, energy is transferred from the source to the load. The diode D2 is reverse biased and the reverse voltage is equal to two times secondary induced voltage. During the same time, the dot end of fly-back secondary (L_{2p}) is negative with respect to non-dot end that reverses biases diode D3. Therefore no current flows through the secondary of the fly-back transformer.

2.2 Mode 2: Switch S1 Open and S2 Still Open

When the ON switch S1 turns OFF, the current forces a reversal of polarities in the winding, and dot end of L_{2p} goes positive. The dot end of L_{2s} also goes positive which makes diode D3 forward biased enabling the primary current transfer to the secondary fly-back transformer and also charges capacitor C in the feedback circuit. The circuit is designed to operate in discontinuous current mode. The energy stored in the fly-back inductance during the period when switch S1is ON, is transferred completely to the fly-back secondary and back to the source. The current in the secondary of fly-back decreases to zero before the next switch S2 goes ON. When both switches are OFF the polarity of push–pull secondary winding makes the diode D2 forward biased and makes a path through the capacitor C2. In this mode, no energy transfers from source to load.

2.3 Mode 3: Switch S2 Closed and S1 Open

During the interval when S2 is "ON" current flows through L_{2p}, L_{1p}, and switches S2. This operation is similar to the mode 1 operation. The voltage across L_{1p} is reflected across the push–pull secondary winding L_{s1}, which makes the diode D2 forward biased and charges capacitor C2 to a voltage equal to V_{s1}. The diode D3 in the feedback circuit is reverse biased and no current flows through the secondary of the fly-back transformer.

2.4 Mode 4: Switch S2 Open and S1 Still Open

When the ON switch S2 turns OFF, the dot end of L_{2s} goes positive and diode D3 gets forward biased. This operation is similar to mode 2. When both switches S1 and S2 are OFF the polarity of the push–pull secondary winding makes D1 forward biased and makes a path through C1. Energy stored in the fly-back inductor gets transferred to the source and there is no energy transfer from source to load.

3 Design Considerations

In developing a high voltage power supply system it is customary to make a preliminary design and verify through established simulation techniques. The design considerations are converter to be modular at the output end, short circuit limit capability, and energy feedback operation.

The first objective is to obtain high voltage by connecting multiple secondary circuits in series. This helps in achieving high voltages at the output making the unit modular with the reduction in the voltage stress across rectifier diodes.

The second objective is to limit the short circuit current at the load side. The drop across the primary of fly-back is assumed to be 25% of input DC voltage at rated load. When there is a short circuit at the load, the voltage across the primary fly-back increases and the short circuit current gets limited to four times the rated current.

The third objective is to make the system energy efficient. When power switches are conducting, energy is stored in the fly-back inductor. By operating it in discontinuous conduction mode, the stored energy is completely fed-back to the source when the switches are not conducting. Therefore the switches S1 and S2 are to be operated in non-overlapping mode with a duty cycle less than 0.5.

3.1 Design Specifications

To simulate the converter following design parameters are considered and the details are given in Table 1.

3.2 Design Steps

Determination of duty ratio: Maximum duty cycle occurs at a minimum value of input DC voltage (V_{in}) and minimum load resistance.

The relation between the output voltage at one of the secondary circuits and ON time for the non-overlapping mode of operation [15] is given by

Table 1 Design specifications

Output Power (P_o)	500 W
Output voltage (V_o)	5 kV
Output ripple	1% of V_o
Switching frequency	20 kHz, $T = 50\,\mu s$
DC input voltage	24 V nominal, $\pm15\%$
Discontinuous current mode and non-overlapping of power switches	

$$V_{o1} = \left[\frac{2V_{in}N_s}{N_P} \frac{T_{on}}{T} \right] \tag{1}$$

where V_{o1} is the voltage across one secondary circuit, V_{in} is the input voltage, N_P and N_S denote the number of turns in primary and secondary push–pull transformer, T_{on} is the on-time of the power switch, T is the switching period and D is the duty cycle. Let the turns ratio $N_S/N_P = n_1$ and duty ratio $T_{on}/T = D$. From Eq. (1)

$$D = \frac{V_{o1}}{2 \times n_1 V_{in}} \tag{2}$$

To calculate the maximum duty ratio, the minimum input voltage is taken as 15% less than the nominal voltage. The high voltage transformer has multiple secondary winding and each secondary winding has a rectifier with a voltage doubler circuit. In the present design, the number of secondary windings is assumed as four. Using Eq. (2) the maximum duty ratio obtained is 0.375 which is less than 0.5 indicating non-overlapping switches.

Calculation of primary and secondary inductance of push–pull transformer: The size of a transformer is designated by a parameter known as area product [15, 16]. Let A_p area product, P_o output Power in Watts, η transformer efficiency, B_m maximum flux density in Gauss, f_s switching frequency in Hz, J current density in A/cm^2, and k window utilization factor.

$$A_p = \frac{P_o\left(\sqrt{2} + \sqrt{2}/\eta\right) \times 10^8}{4B_m f_s k J} \; \text{cm}^4 \tag{3}$$

Using the value of output power and assumed value of η (0.9), B_m (2000), k (0.15), and J (200), the area product is calculated. Suitable core is selected from the core data book [17], which satisfies the area product requirement is E70/33/32. Let the primary number of turns required is N_p [17] and calculated using Eq. (4).

$$N_p = \frac{V_{ct}T_{on} \times 10^8}{A_c \times \Delta_B} \; \text{Turns} \tag{4}$$

Secondary number of turns N_s is obtained from the turns ratio n_1. The calculated value of turns ratio is 41, considering four secondary windings. This can be reduced by selecting more number of windings. Knowing the reluctance of core, values of primary and secondary inductance can be calculated and the corresponding values 35 µH and 64.7 mH, respectively.

Calculation of fly-back inductance: The fly-back inductance is designed, such that the drop across it is 25% of source voltage at rated current. The peak value of input current I_{pk} is calculated from the average input current at rated load. For discontinuous current mode of operation, peak-peak ramp amplitude ΔI is I_{pk}. When the switch is ON, the current starts from zero and ramps up linearly to a peak value I_{pk} in *2DT/2* interval. The frequency of the input current is twice that of the switching frequency. The average current is given as

$$i_{ave} = \frac{\frac{1}{2}2D\frac{T}{2}I_{pk}}{\frac{T}{2}} = DI_{pk} \tag{5}$$

Equation (5), gives the peak input current $I_{pk} = i_{ave}/D$.

Current through the secondary rectifying diodes is proportional to the input current and the load current is the average value of the rectifier current. The primary load current is the addition of all secondary windings currents reflected onto the primary side with their respective turns ratio. The peak input current,

$$I_{pk} = \frac{i_{ave}}{D}n_1 \times n \times 2 \tag{6}$$

Peak value of input current [15] at the end of ON time is

$$I_{pk} = \frac{(V_{in} - V_{ct})T_{on}}{L_{2p}} \tag{7}$$

L_{2p} is the fly-back inductance, n is the number of the secondary winding. The voltage drop across the inductance is assumed as 25% of the V_{in}. Fly-back inductance is calculated by using Eq. (7). The turns ratio n_2 of the fly-back transformer is selected such that the secondary current reduces to zero before the start of the next switch turn-on, for discontinuous mode. If the current ramp-down time is taken as t_f, then t_f is less than $(1 - 2D)T/2$. The secondary inductance (L_{2s}) is determined from the turns ratio (n_2) using, $\sqrt{L_{2s}/L_{2p}} = n_2$.

Calculation of output capacitance: The peak-peak voltage ripple is usually given as a percentage of the output voltage. The filter capacitor (C) is designed for an output ripple of 1% of V_o. The output ripple [18] is given by

$$\frac{\Delta V_0}{V_0} = \frac{1 - 2D}{32 \times L_{2p}' \times C \times f_s^2} \tag{8}$$

The value of the capacitor obtained from Eq. (8) is 1.09 μF.

4   Simulation Results and Discussion

The converter is simulated using Orcad PSPICE to validate the performance. The designed values of circuit parameters are $D = 0.375$, Turns ratio of high voltage transformer (Push–pull) $= 41$, Primary inductance and secondary inductance are $L_{1p} = 35$ μH, $L_{s1} = 64.7$ mH, Fly-back inductance $L_{2p} = 1.12$ μH, and filter capacitance $C = 1.09$ μF. Ideal switches and diodes are used therefore ON-state voltage drops are neglected. Simulation of DC-DC converter is carried out with designed values of circuit parameters. The schematic diagram of the simulation used to perform the time domain analysis is given in Fig. 2.
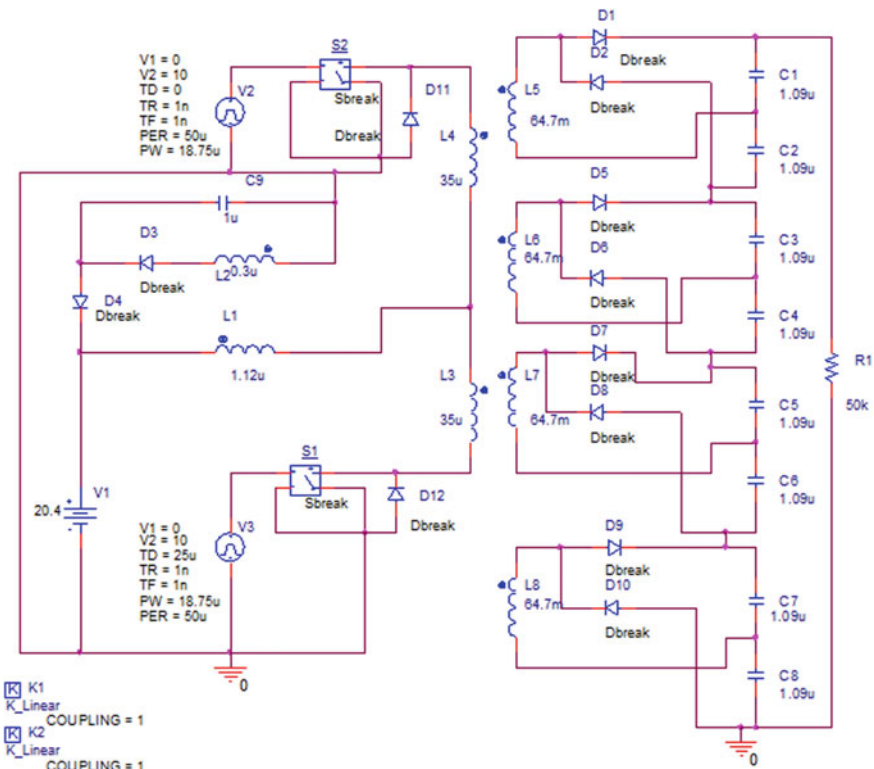
Fig. 2   Schematic diagram of the simulation

4.1 Modularity

High voltage transformer is designed to have a modular design in order to use it for different voltage levels. Being modular, failure of any one secondary circuit does not interrupt the output of the system, but can operate at reduced voltage making it a more reliable operation. As the high voltage transformer is designed to have four secondary windings each secondary circuit gives an output of 1.25 kV. The total output voltage obtained by connecting four secondary circuits in series is 5 kV. The simulated results of the output voltage of each secondary winding (V_{o1}-V_{o4}) and the total output (V_o) are shown in Fig. 3a.

The converter is more reliable compared single secondary circuit. In case of any one secondary circuit being open, output is available with the remaining secondary circuits, but at reduced voltage. Due to the reduction of one winding, the load current gets reduced and the reflected input current also reduces. This decreases the drop across the fly-back primary and higher voltage across push–pull primary winding. Figure 3b. shows the total output voltage (V_o) at maximum duty ratio with secondary circuit three being open is 4.239 kV. The voltage at the secondary circuit three (V_{o3}) is 770.756 mV.

Figure 4a shows the simulation results of the voltage, current, and power for 5 kV at 500 W output. Further the circuit is also designed and simulated for 50 kV at 1 kW from a 48 V input and the simulation results are shown in Fig. 4b. This ensures the design is robust and the converter is suitable for the generation of appropriate output voltage and power levels based on the application.
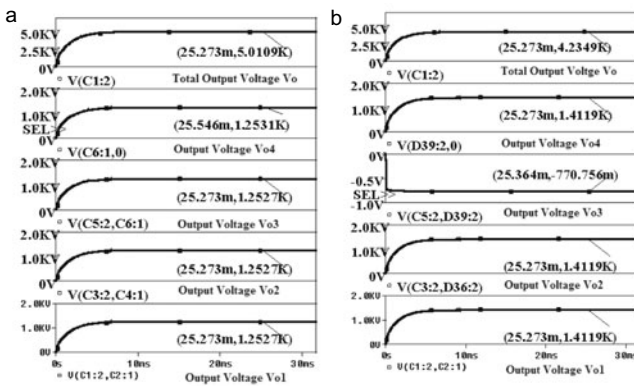
Fig. 3 **a** Output voltage of each secondary circuit and total output voltage, **b** output voltage of each secondary circuit when winding three is opened
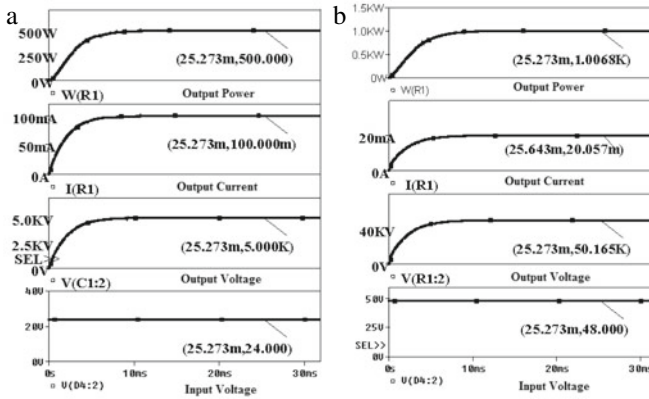
Fig. 4 **a** Simulation results for 5 kV, 500 W, **b** simulation results for 50 kV,1 kW

4.2 Voltage Stress on Rectifier Diodes

In the conventional high voltage power a supply, the transformer consists of a single secondary winding with high turns ratio to obtain high output voltages. In such conditions, a single commercially available diode cannot meet the required voltage rating and they need to be connected in series. Under such circumstances the series-connected diodes do not share reverse voltage equally though they are from a single manufacturer. To overcome this problem balancing resistors and capacitors are connected across each diode to take care of static and dynamic voltage mis-sharing.

The proposed converter use series-connected multiple secondary winding circuits to obtain the required high voltage. If there are "*n*" secondary winding with voltage doublers, then the turns ratio of each secondary winding gets reduced by a factor $1/2n$ as compared to the HVT with a single secondary winding. Each rectifier diode is directly supplied from a secondary high voltage transformer, therefore the rectifier devices have better reverse voltage sharing and reduction in voltage stress. Therefore commercially available diodes can be used, which reduces the overall cost of the circuit.

To verify this operation, the converter circuit with four secondary windings is simulated. Hence the voltage across anyone of the secondary winding is 625 V. When the rectifier diode is OFF, the maximum reverse voltage and hence the voltage stress across it is two times the voltage across the secondary winding. The maximum voltage stress on diode is 1.25 kV. Since each rectifier diode is directly supplied from the secondary of the transformer, string of series-connected diodes get eliminated, and the associated voltage mis-sharing. The voltage across the diode is 1.25 kV when it is OFF as shown in Fig. 5.
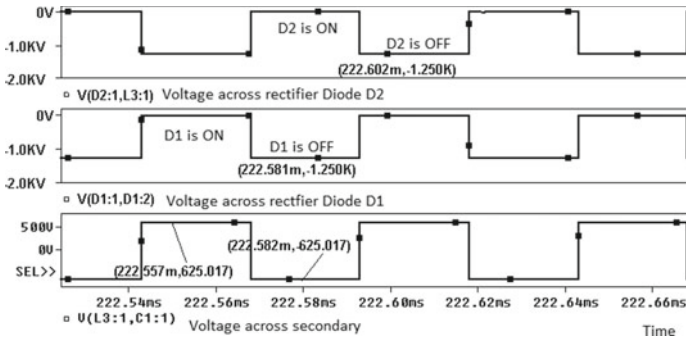
Fig. 5 From bottom to top: Trace 1. Voltage across one secondary of HVT, Trace 2 and 3. Voltage across rectifier diodes D1 and D2

4.3 Zero-Current Turn-On Operation and Short Circuit Limit

Zero-Current Turn-on Operation: When the converter is operating at higher switching frequencies switching losses and higher. Zero-voltage or zero-current switching reduces switching losses. As the converter is designed to operate in discontinuous conduction mode, the current starts building up linearly from zero. This ensures zero-current turn-on operation and minimizes the switching losses. This is achieved without any additional components. Zero current switch-off condition is not maintained in the circuit.

Zero current turn-on operation is verified through simulation and the results (waveforms) for rated load current of 100 mA are shown in Fig. 6a. At the instant when switch S1 is ON, the current through the switch starts increasing from zero linearly and reaches the peak value. There is a dead time where the current remains zero. Similar operation occurs with switch S2 also. Discontinuous operation is maintained in other load conditions also.

Short Circuit Limit: The fly-back transformer in the input side is an advantage in limiting the short circuit current at the load side. If there is a short circuit at load side, drop across the fly-back primary is increased. The drop across the fly-back primary is increased to 18.2 V, when the load current is 350 mA (3.5 times of rated current) as shown in Fig. 6b. This indicates the instantaneous current limiting capability under short circuit.

4.4 Recovery of Stored Energy by Feedback Operation

When the power switch is ON, considerable amount of energy is stored in the magnetic field of fly-back transformer. If the stored energy available is not properly handled, it gets lost and the efficiency of the converter also decreases. Therefore to recover the stored energy, it is transferred to the secondary side when switches
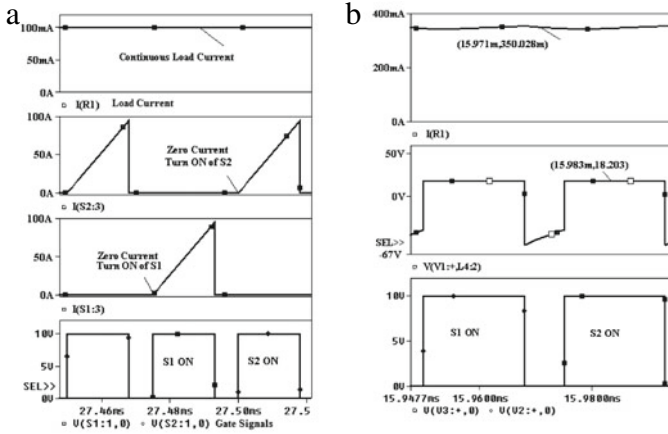
Fig. 6 **a** From bottom to top: Trace 1: gate signals S1 and S2, Trace 2: switch current S1, Trace 3: switch current S1, Trace 4: load current, **b** From bottom to top: Trace 1: gate signals S1 and S2, Trace 2: drop across fly-back inductance Trace 3: load current

are OFF. For the effective transfer of stored energy, the secondary inductance is designed such that discontinuous conduction mode (DCM) is ensured. This makes the effective transfer of stored energy and also resetting of flux in the magnetic core. When the switch S1 is closed, the fly-back primary winding current starts building up linearly from zero and the energy gets stored in the fly-back inductor. During the same time diode D3 is reverse biased due to the polarity of induced emf on the secondary winding of fly-back, and no current flows in the secondary winding L_{2s} of fly-back transformer. When switches S1 and S2 are OFF, reversal of polarity on the fly-back secondary winding makes the diode D3 forward biased. The fly-back secondary current decays to zero before next power switch S2 is ON, resulting in complete transfer of energy to the fly-back secondary and then back to the source.

The energy stored during ON time of switch is

$$E_{\text{Stored}} = \frac{L_{2P} \, I_{\text{pk}}^2}{2} \tag{9}$$

I_{pk} denotes the magnitude of fly-back primary peak current at the end of conduction period. By knowing the values of L_{2p} and I_{pk} from Eqs. (6) and (7), theoretical value of energy stored calculated at rated load condition using Eq. (9) is 4250 μJ. The value of energy stored obtained from the simulated waveform shown in the Trace 2 and 4 of Fig. 7.

$$E_{\text{Stored}} = 1.12 \, \mu\text{H} \times 87.73^2/2 = 4257 \, \mu\text{J}$$

Figure 7 Trace 3 shows that the secondary current reduces to zero before switch S2 is ON. This shows the circuit is operating in the discontinuous conduction mode and
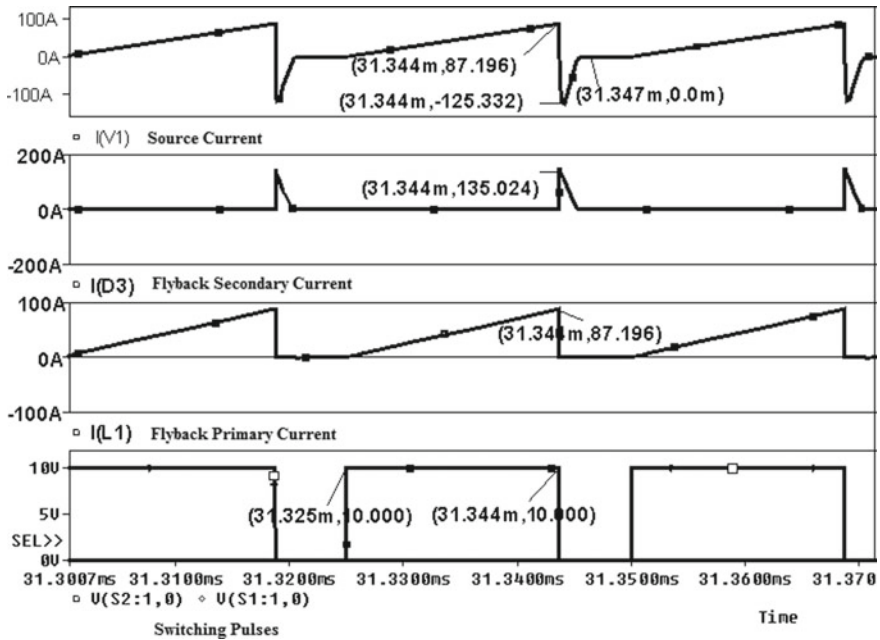
Fig. 7 From bottom to top: Trace 1: gate signals S1 and S2, Trace 2: fly-back primary current, Trace 3: fly-back secondary current, Trace 4: source current

energy is completely transferred to the source via fly-back secondary. The negative polarity on source current is shown in Trace 4, of Fig. 7 indicates current being fed-back to the source. Thus the energy fed-back to the source can be calculated as follows

$$
\begin{aligned}
E_{\text{Fed-back}} &= V_{\text{in}} \times \left(I_{\text{pk}}/2\right) \times t_f \\
&= 20.4 \times (125.33/2) \times 3\mu = 3835\,\mu\text{J}
\end{aligned}
\tag{10}
$$

Hence 90.09% of the total stored energy is fed-back to source while the remaining energy is stored in capacitor C of the feedback circuit. From the simulated waveforms and energy calculations, it is clear that the energy stored in the magnetic core of fly-back transformer during ON time of the switch is effectively transferred to the source during OFF time of the switch. The average current drawn from the source obtained using simulation is 31A. If the input source is the battery, then the energy feedback aids in charging the battery during OFF time of switches.

5   Conclusion

This paper presents a fly-back current-fed push–pull DC-DC converter suitable for high voltage low current applications. The four modes of operations of the converter over one switching cycle are analyzed. With an established design procedure the converter is designed for an output of 5 kV, 500 W from a 24 V source, operating at non-overlapping mode with four secondary windings simulated. The results obtained show that the converter with series-connected multiple secondary windings along with voltage doublers gives the flexibility in high voltage levels obtained at the output. Rectifier diodes are subjected to less voltage stress therefore commercially available diodes can be used which results in reduced cost. Zero current turn-on of switches ensures zero turn-on switching losses. Short circuit current at load side gets limited by dropping the voltage across the fly-back inductance. Energy feedback is effective due to Fly-back secondary connected back to the source. Simulation results show that at rated current, 90.09% of stored energy is fed-back to the source during OFF time, making the system energy efficient. The output of the converter for a voltage of 50 kV at 1 kW power level is also presented to validate the design procedure. The proposed converter is more suitable for small-scale ESP power supply applications.

References

1. Babri I, Gules R (2003) Isolated DC-DC converters with high-output voltage for TWTA telecommunication satellite applications. IEEE Trans Power Electronics 18(4):975–984
2. Martin-Ramos JA, Prenia AM, Diaz J et al (2008) Power supply for high-voltage application. IEEE Trans Power Electronics 23(4):1608–1619
3. Verma R, Mishra E, Shukla R, Banerjee P et al (2014) Design and development of a portable flash X-ray source driven by battery powered compact Marx generator. In: XXVI international symposium on discharges and electrical insulation in vacuum. IEEE, Mumbai, India, pp 605–607
4. Lin B-R, Lin G-H, Jian A (2019) Resonant converter with voltage-doubler rectifier or full bridge rectifier for wide-output voltage and high power applications. J Electronics 8(3):1–16
5. Iannello C, Luo S, Batarseh I (2002) Full bridge ZCS PWM converter for high-voltage high-power applications. IEEE Trans Aerosp Electronic Syst 38(2):515–524
6. Maiti D, Mondal N, Biswas SK (2010) Design procedure of a push-pull current fed DC-DC converter. In: Conference proceedings of national power electronics conference, Roorkee, India, pp 1–7
7. Anand V, Kaushik Basu G, Ranganathan G (2018) Resonance based current-fed isolated DC/DC converter for high voltage applications. In: International conference on power electronics, drives and energy systems. IEEE, Chennai, India, pp 1–6
8. Chan W-C, Liang T-J, Yang L-S et al (2010) Current-fed DC-DC converter with current ZCS for high voltage application. In: International power electronics conference. IEEE, Sapporo, Japan, pp 56–62
9. Chen R-Y, Liang T-J, Chen J-F et al (2008) Study and implementation of a current-fed full-bridge boost DC-DC converter with zero-current switching for high voltage applications. IEEE Trans Ind Appl 44(4):1218–1226
10. Liang T-J, Chen R-Y, Chen J-F et al (2007) Buck-type current-fed push-pull converter with ZCS for high voltage applications. In: Region 10 conference. IEEE Taipei, Taiwan, pp 1–4

11. Mazumder SK, Acharya K, Tan CM (2008) Design of an All-SiC parallel DC/DC Weinberg converter unit using RF control. IEEE Trans Power Electronics 23(6):2893–2904
12. Tong Q, Zhang H, Zhang D (2018) A ZVS and ZCS DC-DC converter based on Weinberg topology for high voltage application. In: IEEE conference on industrial electronics and applications, Wuhan, China, pp 177–180
13. Tong Q, Zhang H, Zhang D (2018) Research on a high power density DC/DC converter based on Weinberg topology. In: 2nd advanced information management, communicates, electronic and automation control conference. IEEE, Xi'an, China, pp 2346–2350
14. He Y, Perreault DJ (2020) Diode evaluation and series diode balancing for high-voltage high-frequency power converters. IEEE Trans Power Electronics 35(6):1–13
15. Pressman AI, Billings K, Morey T (2009) Switching power supply design, 3rd edn. McGraw Hill Publisher, New Delhi
16. Umanand L, Bhat SR (2017) Design of magnetic components for switched mode power converters. New Age International Publishers, New Delhi, Reprint
17. EPCOS data Book Ferrites and Accessories (2012) Corporate communication, Munich, Germany
18. Hart DW (2011) Power electronics. McGraw Hill Publisher, New York, US

Convolutional Neural Network-Based Lung Cancer Detection

K. R. Satyajit, Sai Samarpita, and Papia Ray

Abstract Medical image analysis involves solving medical problems using different techniques to analyze images for efficient extraction of information. There has been the use of algorithms of machine learning to study the medical image in recent years for the better extraction of compact information to make medical image analysis systems better in comparison to the methods used earlier. Deep learning provides state-of-the-art results and thus acts as a breakthrough in machine learning techniques. Recently, deep learning in utilizing deep convolutional neural networks has been applied to medical image analysis that provides superior results. Because of this reason, this paper proposes research on the application of the Convolutional Neural Network (CNN)-based algorithm on magnetic resonance imaging (MRI). Here the architecture of CNN VGG-16 and ResNet-50 have been used for predicting lung diseases. From simulation results, it has been observed that the proposed scheme (CNN technique) has better accuracy than earlier researchers' work.

Keywords Convolution Neural Network · Deep learning · Lung diseases · Layers · Architecture

1 Introduction

Nowadays diseases are increasing day by day and medical science is growing. A lot of methods have been found to predict which type of disease a person is going through. We can dictate diseases through CNN or artificial neural network (ANN), or image processing method. CNN is a method by which we can predict if we know its architecture. This paper proposes the identification of lung diseases.

K. R. Satyajit · S. Samarpita · P. Ray (✉)
Department of Electrical Engineering, Veer Surendra Sai University of Technology, Burla, Sambalpur, Odisha, India
e-mail: papiaray_ee@vssut.ac.in

Lung diseases are increasing. For its identification, many methods and architectures are used. Some of the architectures are LeNet-5, Alex-Net, VGG-16, Inception-V1, Inception-V3, ResNet-50, etc. Here we have compared accuracies for VGG-16 and ResNet-50.

1.1 Literature Review

Deep learning (DL) is used widely in research involving computer vision and analysis of natural language speech. This method is suited mainly for analyzing a large amount of data and to suffice the requirement of human-like intelligence. Simple convolutional neural network on image classification, and further also analyzed different methods of learning rate set and different optimization algorithm of solving the optimal parameters of the influence on image classification [1–3]. The deep neural networks (DNN), especially the CNNs are significant in their performance since 2012 in changing the tasks for classifying images through strategies that make classifying images on small datasets better. Here, the case of primary lung cancer is considered, where optimal thresholding and gray level characteristics are used for segmentation of lung nodules from the lung volume area. Image denoising is a critical pre-processing task preceding further preparation of the image like feature extraction, segmentation, surface examination, etc. This paper deals with the improvement of the quality of lung image and diagnosis of lung cancer by reducing misclassification [4–6]. Advancements have greatly benefited medical imaging in designing hardware, and procedures to ensure safety and capability to store data by segmenting, classifying, and detecting abnormalities in clinical imaging modalities generated images. Deep feature extraction using pre-trained convolutional neural networks (CNNs) has recently been successfully applied in some image domains, including the detection of lung cancer [7–9]. Medical images that are highly accurate, precise, sensitive, and specific directly affect clinical diagnosis. Deep learning methods are best suited for purposes like computer-aided vision. Influenced by the success of deep learning in natural and medical image classification tasks, the proposed idea is about exploring the performance of deep transfer learning for lung nodules malignancy classification [10–15].

1.2 Contributions

- A survey with various architectures of CNN has been carried out to detect lung disease.
- After a thorough investigation, it was found that CNN provides better detection accuracy as compared to other techniques mentioned in the literature.

The organization of the paper follows the concept of CNN in Sect. 2. This section consists of the description of CNN layers and their advantages of CNN. The following Sect. 3 talks about the detection of diseases with its methodology and process. Section 4 describes the detailed methods with various CNN architecture used here. Section 5 evaluates the performance of the reported method. The sixth section discusses the results.

2   Concept of CNN

In a neural network, the messages are exchanged between systems of interconnected artificial neurons having tuned numeric weights during the training process to make them respond to images or patterns to recognize. The network has multiple layers of feature-detecting "neurons", with each layer responding to combinations of inputs from the previous layers. In Fig. 1, the first layer detects primitive patterns in the input. The second layer detects different ways of patterns.

Training is performed using a "labeled" dataset of inputs in which representative input patterns are assorted. They are tagged with output response intended by determining the weights for intermediate and final feature neurons. Figure 2 shows the block-level diagram for the same.

Input layer   **Hiddebn layer**   **Output layer**
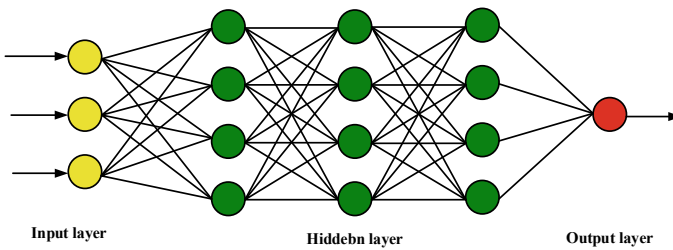
Fig. 1 Layers of CNN

Fig. 2 The training process at a block-level
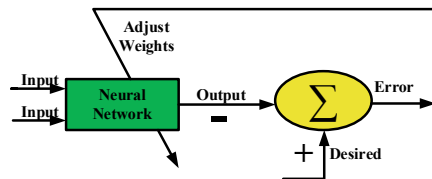
2.1 Layers of CNN

A. **Convolution layer**

The convolution layer is the primary building block of a CNN. We get scalar results by taking the filter's dot product and chunks of the input image by sliding them over the complete picture to generate a new image. The convolution layer consists of independent filters convolved with the image.

B. **Pooling Layer**

The reduction of the spatial size of the representation occurs by being progressively inserted in between successive convolution layers and decreasing the number of factors and computation in the network, thereby helping to control overfitting.

C. **Fully Connected Layer**

A CNN also consists of layers of the neuron at the end that is also fully connected to all activations in the previous layer, and they look and work just like the regular neural networks.

3 Diseases Detection

Lung diseases lack easiness in airways and other structural parts of the lung; for example—pneumonia and tuberculosis (TB). As per International Respiratory Societies, 334 million peoples are asthmatic, 1.4 million people are killed by TB every year, and 1.6 million people lose their life because of cancer in the lungs. Deep learning works excellent for detecting lung disease, unlike the traditional method, which is done through a sputum test. Deep learning relates to algorithms. Recent advancements focus on supporting the quantification and classification of patterns in medical images through learning features from data by deep learning.

3.1 Methodology

A. **Process**

The application of deep learning through three significant steps, namely, image pre-processing, training, and classification for the detection of lungs disease, is described in this section. The detection deals with the classification of an image into lungs that are healthy or infected. The model is obtained through training a neural network to detect a similar set of images. Therefore, to apply deep learning for detecting disease of lungs, gathering images of infected lungs with the disease to be classified is done at the beginning. In the second step, the

class of images not seen by the model before is predicted. The last step is the classification of new images.

B. **Image Acquisition Phase**

The initial step is acquiring images. For this, the computer must learn as many images and their recognition. In the surveyed work, images are accurate data required for the detection of lung disease. The result of this step is the image that will be used for model training.

C. **Processing Phase**

In this step, the quality of the image is improved. Performing Contrast Limited Adaptive Histogram Equalization (CLAHE) can increase image contrast. Modification of images such as segmentation of lung and bone elimination could be done to identify the Region of Interest (ROI). The detection is done in ROI. Edge detection can represent related data. Application of Data augmentation will result in an increment of available data associated with the image.

D. **Training Phase**

This phase involves selecting the deep learning algorithm, usage of transfer learning and use of an ensemble. Many deep learning algorithms have various learning styles, and multiple data work better with respective algorithms. The nature of the data should decide the choice of the deep learning algorithm. CNN works better with images. Transfer learning is the transfer of knowledge among different models. This generates models from the data learned as its output.

E. **Classification Phase**

In the last step, the model is trained to predict the category an image fits into. For example, suppose the model's training was done to distinguish between healthy lungs and lungs that TB infects through their respective X-Ray images. In that case, it should classify new images into healthy lungs or infected lungs through a score representing how probable an image belongs to a particular category as depicted in Fig. 3.

4 Different Architecture of CNN

A. **VGG-16**

Visual Geometry Group (VGG) invented the VGG-16 having 13 convolution and three fully connected layers, stacks a greater number of layers onto Alex-Net, by using smaller filters (2×2 and 3×3). Table 1 gives the performance parameter of the architecture VGG-16.

From Table 1, it can be noticed that the accuracy is relatively high (99.7%), and the error rate is low (0.5%).

B. **ResNet-50:**

Fig. 3 Overview of using deep learning for lung disease detection
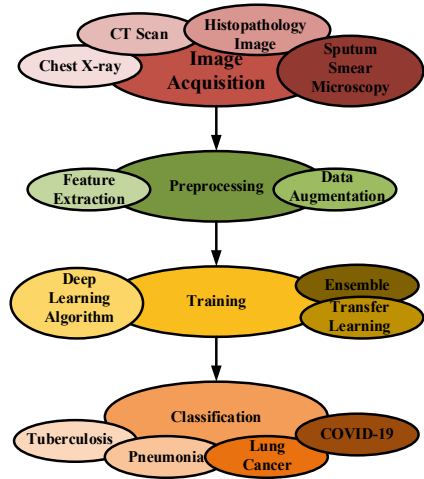
Table 1 Performance measure parameter of improved VGG-16

Train accuracy	100%
Test accuracy	99.59%
Precision	100%
Overall accuracy	*99.7%*
Recall	99.3%
Confusion matrix	
Total testing images	600
True Negative	300
True Positive	298
False Negative	0
False Positive	2
Error rate	*0.5%*

With the increase in depth of the network, a saturation of the accuracy occurs, followed by its rapid degradation. Table 2 cites the performance measure of ResNet-50 architecture of CNN.

From Table 2, it can be seen that the overall accuracy (98.5%) of ResNet-50 architecture of CNN is a bit less than VGG-16 architecture. Also, the error is high (0.8%) using ResNet-50 architecture of CNN than VGG-16. So, it can be said that the VGG-16 architecture of CNN is preferable for detecting lung disease and recommended.

Table 2 Performance measure parameter of improved ResNet-50

Train accuracy	100%
Test accuracy	98%
Precision	99%
Overall accuracy	*98.5%*
Recall	98.3%
Confusion matrix	
Total testing images	600
True Negative	300
True Positive	298
False Negative	0
False Positive	2
Error rate	*0.8%*

5 Evaluation Method and Criteria

$$\text{Precision} = \frac{\text{True Positive}}{\text{True Positive} + \text{False Positive}} \qquad (1)$$

$$\text{Recall} = \frac{\text{True Positive}}{\text{True Positive} + \text{False Positive}} \qquad (2)$$

$$F1 = 2 \times \frac{\text{Prescision} \times \text{Recall}}{\text{Prescision} + \text{Recall}} \qquad (3)$$

$$\text{Accuracy} = \frac{\text{TN} + \text{TP}}{\text{TN} + \text{FP} + \text{TP} + \text{FN}} \qquad (4)$$

where 'TN' is a true negative, 'TP' is true positive, 'FP' false positive, and 'FN' false negative.

6 Result Analysis

We have examined 3600 samples of lung cancer histopathological images using architecture VGG-16; We got 100% training accuracy and 99.7% testing accuracy with CNN. In this process, we have used two architectures of CNN, i.e., VGG-16 and ResNet-50. From ResNet-50, we got a testing accuracy of 98.5% and from VGG-16, the testing accuracy is 99.7%. After comparison, we concluded that VGG-16 is the best model for CNN. Table 3 and Fig. 5 show the comparison of different schemes by other researchers with the proposed method.

Table 3 Performance measure parameter of improved

Scheme	Methodology used	Testing accuracy (%)
[7]	ANN	92.7
[11]	ANFIS	88.4
[12]	Fuzzy	83
Proposed one	*CNN*	*99.7*

Fig. 5 Performance measure parameter comparison
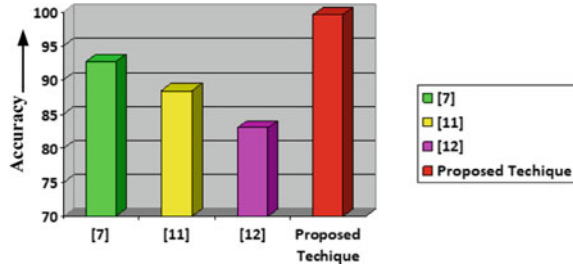
7 Conclusion

Through this paper, the review of the applications of various deep learning techniques in medical image analysis is done in a detailed manner. It is inferred that CNN-based methods of deep learning are highly acceptable in all related fields of medical image analysis. CNN-based methods can learn and select features automatically and more precisely than traditional ones. The addition of visualization for improving the understanding and explanation of the results of the system based on CNN would translate into systems with improvised computer-aided detection. A comparison with two architectures, i.e., VGG-16 and ResNet-50, is also carried out and it is found from the simulation results that VGG-16 is a better choice. The success shows that these techniques of deep learning would help in advancing medical image analysis.

References

1. Guo T, Dong J, Li H, Gao Y (2017) Simple convolutional neural network on image classification. In: Proceedings of 2017 IEEE 2nd international conference on big data analysis (ICBDA), pp 721–724
2. Krizhevsky IS, Hinton GE (2017) ImageNet classification with deep convolutional neural networks. Commun ACM 60(6):84–90
3. Rao P, Pereira NA, Srinivasan R (2016) Convolutional neural networks for lung cancer screening in computed tomography (CT) scans. In: Proceedings 2016 2nd international conference on contemporary computing and informatics (IC3I), pp 489–493
4. Aggarwal T, Furqan A, Kalra K (2015) Feature extraction and LDA based classification of lung nodules in chest CT scan images. In: Proceedings 2015 international conference on advances in computing, communications and informatics ICACCI 2015, pp 1189–1193

5. Khumancha MB, Barai A, Rao CBR (2019) Lung cancer detection from computed tomography (CT) scans using convolutional neural network. In: Proceedings 2019 10th international conference on computing communication and networking technologies (ICCCNT), pp 1–7
6. Shakeel P, Burhanuddin MA, Desa M (2019) Lung cancer detection from CT image using improved profuse clustering and deep learning instantaneously trained neural networks. Measurement 145:702–712
7. Song Q, Zhao L, Luo X, Dou X (2017) Using deep learning for classification of lung nodules on computed tomography images. J Healthcare Eng 1–8
8. Paul R, Hawkins SH, Hall LO, Goldgof DB, Gillies RJ (2016) Combining deep neural network and traditional image features to improve survival prediction accuracy for lung cancer patients from diagnostic CT. In: Proceedings of 2016 IEEE international conference on systems man and cybernetics (SMC), pp 2570–2575
9. Jakimovski G, Davcev D (2019) Using double convolution neural network for lung cancer stage detection. Appl Sci 9(3):1–12
10. Kuruvilla J, Gunavathi K (2013) Lung cancer classification using neural networks for CT images. Comput Methods Programs Biomed 113(1):202–209
11. Da Nóbrega RV, Peixoto SA, da Silva SP, Rebouças Filho PP (2018) Lung nodule classification via deep transfer learning in CT lung images. In: 2018 IEEE 31st international Symposium on computer-based medical systems, pp 244–249
12. Tariq Z, Shah SK, Lee Y (2019) Lung disease classification using deep convolutional neural network. In: Proceedings of 2019 IEEE international conference on bioinformatics and biomedicine (BIBM), pp 732–735
13. Armato SG et al (2015) Lung challenge for computerized lung nodule classification: reflections and lessons learned. J Med Imaging Bellingham Wash 2(2):1–6
14. Patil S, Kuchanur M (2012) Lung cancer classification using image processing. Int J Eng Innov Technol 2(3):37–42
15. Al-Tarawneh MS (2012) Lung cancer detection using image processing techniques. Leonardo Electron J Practices Technol 11(21):147–158

Closed-Loop Analysis of Multi-input KY Boost Converter Applying Fuzzy Logic Controller

M. Pushpavalli, N. M. Jothi Swaroopan, R. Harikrishnan, P. Abirami, P. Sivagami, V. Geetha, and M. Kavitha

Abstract The hybrid system always focuses on individual converters for renewable sources. It leads to inflation in the volume and expenditure of the system. This researcher mainly focuses on multi-input converter system. This multi-input contains two sources where wind and solar energy can connect to the system. These hybrid systems choose the DC-coupled system. The performance of multi-input converters designed through the boost nature with converter configurations is Multi-Input KY Boost converter. Dynamic behavior is tested and checked with the help of MATLAB simulation. The researcher designed a new novel multi-input KY boost converter for RE with a very high-power factor and less THD. This converter is connected to FLC. The Fuzzy logic controller is identified as a better controller for attaining fast-tracking and less Total Harmonic Distortion. Hardware results evaluated for open-loop of Multi-Input KY boost converter. The Hybrid RES, PV, and wind system are performed including the energy storage arrangement. This configuration is mainly used to give AC loads.

Keywords Multi-input · KY boost converter · Fuzzy Logic Controllers (FLC)

M. Pushpavalli (✉) · P. Abirami · P. Sivagami · V. Geetha · M. Kavitha
Sathyabama Institute of Science and Technology, Chennai, India
e-mail: pushpavalli.eee@sathyabama.ac.in

N. M. Jothi Swaroopan
R.M.K Engineering College, Chennai, India

R. Harikrishnan
Symbiosis International Deemed University, Pune, India

P. Abirami
Assistant Professor, B. S. Abdur Rahman Crescent Institute of Science and Technology, Chennai, India

1 Inception

These movements merge the power generation of Renewable Energy (RE) Resources and the measure of fewer carbon outflows. A worldwide temperature alteration is a tremendous risk that is being achieved by expending the coal, oil, and vaporous petroleum. It is dangerous for the planet and living animals. Renewable Energy (RE) Resources can replace these fossil fuels [17, 18].

2 Analysis on KY Converters

The analysis of KY converter is taken from various papers and tabulated in Table 1. From that single stage, KY boost converter is identified for high-power applications. Hwu et al. [8] developed KY boost converter combined with the boost converter. This converter is suitable to connect PV and wind [19].

3 Multi-input KY Boost Converter

Hwu et al. [8] developed KY boost converter combined with the boost converter. One more stage was added and developed the multi-input KY boost converter given in Fig. 1.

3.1 Multi-input KY Boost Converter Using FLC

Figure 2 gives the circuit layout of KY boost converter with closed-loop FLC controller. The circuit diagram 2 denotes multi-input KY boost converter. It contains two energy sources, and one input is joined to solar energy, and another input is joined to wind energy. The PV and wind energy specifications are given in Table 2. The solar cell assumed uniform irradiance and temperature. This PV cell maintains a constant voltage and current of 48 V and 7.95 amperes, respectively. The other input source is fed from wind energy. The wind energy is maintained with constant wind speed and constant pitch control. The 50 V AC voltage is generated from the windmill, and it is rectified using a rectifier circuit and converted into 48 V DC voltage. The output voltage across the capacitance maintains the constant DC voltage. This fixed DC voltage is applied to three-phase inverter circuits which generate the three-phase AC voltage waveform for resistive load. The constant DC bus voltage parallelly charges the battery. Figure 3 shows the voltage across the converter.

Table 1 Analysis of KY converter

Converter stage	Methodology	Supplementary components	Accomplished objectives
Boost converter [1]	Novel boosting KY converter	One energy transferring capacitor and one switch	Fast transient response, low output voltage ripple, and continuous current
KY converter [2]	KY converter combined with 1 + D converter	Derivative converter	The continuous change starting with one structure and then onto the next structure
KY converter [3]	KY converter combined with soft switching	Single resonant capacitor and inductor	current spike reduced and used in Industrial applications
Buck boost converter [4]	Two types of KY boost converters	Energy transferring capacitor	Fast transient response, suitable for low power applications
KY converter [5]	Bidirectional converter works in buck and boost mode	Using three switches only	Battery charging and discharging
KY buck boost converter [6]	Negative output KY buck boost converter	–	No bilinear characteristics
KY converter[7]	Combining the KY converter with its derivatives	Second order KY converter analyzed	To increase the output voltage
Boost converter [8]	KY converter and boost converter	–	Suitable for low ripple applications and continuous current
KY converter [9]	KY converter with ZVS	One switching capacitor	ZVS improved efficiency and used in industrial load
Buck boost converter [10]	KY and SR buck converter	No additional components	Positive voltage and no right-hand plane zeros
Step Up converter [11]	KY converter and buck boost converter	–	Reduce the current stress and voltage ripple
Cuk converter [12]	Innovated buck boost converter combining the feature of Cuk converter	One power switch	Low output voltage ripple
KY converter [13]	Improved KY converter	Charge pump capacitor and tapped coupled inductor	Improving voltage conversion ratio and increasing the efficiency
Boost converter [14]	KY combined with a SR Boost topology	Coupled inductor	Voltage gain improved and ZVS turn ON

(continued)

Table 1 (continued)

Converter stage	Methodology	Supplementary components	Accomplished objectives
KY converter [15]x	Integrated KY converter with buck and boost characteristics	Parasitic resistance	Fast transient response, reduced voltage ripple, and high efficiency
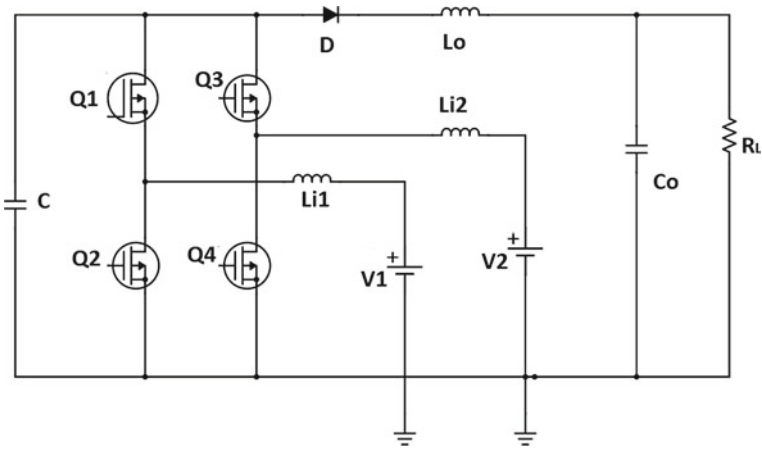
Fig. 1 Multi-input KY boost converter
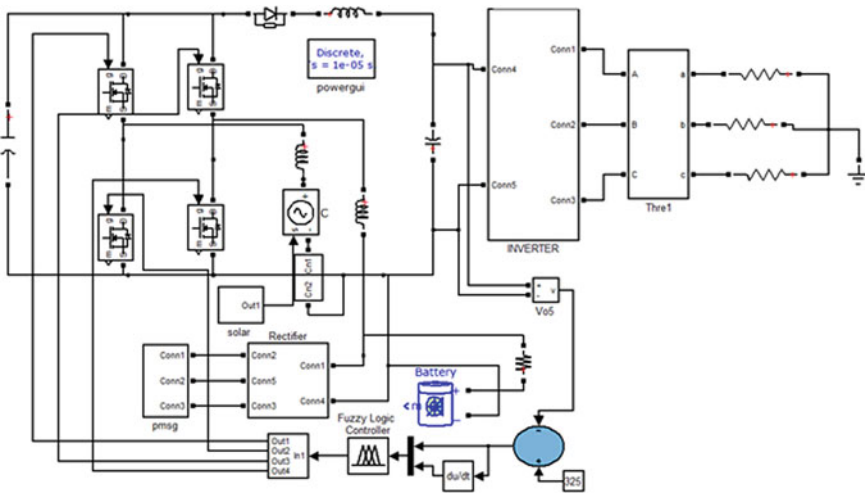
Fig. 2 Circuit layout of KY boost converter with FLC

Table 2 Renewable energy variable

Design	Values
Panel voltage (Vpv)	48 V
Panel current (Ipv)	7.95 Amps
Rectified DC wind voltage	50 V
Rectified DC current	5 A

Fig. 3 Voltage across KY boost converter

4 Simulation Analysis of Multi-input KY Boost Converter Using FLC

Figure 4 shows the FLC to realize the firing angle tracking of multi-input KY converter. The information to the FLC is the error signal and the derivative (du/dt) of this error signal. The command signal of the FLC is indicating the change of the duty cycle of the multi-input KY converter.

Error signal (e) indicating the distinction between the Vref and Vout.

$$e(k) = \text{Vref} - \text{Vout}(k) \tag{1}$$

Change in error,

$$ce(t) = e(k) - e(k-1) \tag{2}$$
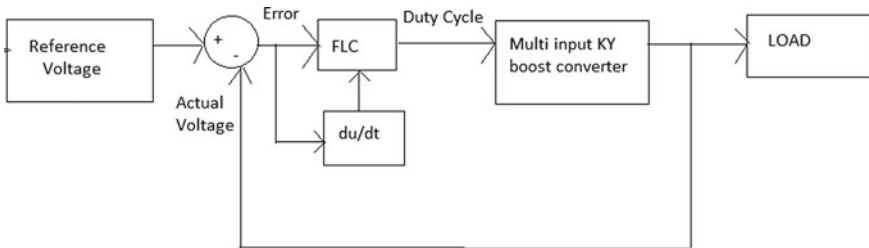
Fig. 4 Block diagram of closed-loop FLC controller

Table 3 Rule base of FLC-triangular member function

Error (e)	Change in error ($ce(t)$)				
	NB	NS	Z	PS	PB
NB	PB	PB	PS	PS	Z
NS	PB	PS	PS	Z	NS
Z	PS	PS	Z	NS	NS
PS	PS	Z	NS	NS	NB
PB	Z	NS	NS	NB	NB

The FLC, which consists of three foremost members, is fuzzification, inference engine, and defuzzification. Five fuzzy subsets represent fuzzification. The inference method uses the max–min operator for this work. Table 3 explains the rule of FLC. Defuzzification applies the centroid technique to determine the duty ratio for the converter. Table 3 explains the rule table of FLC. Error and change in error are the two information linguistic variables. Duty cycle is the yield linguistic variable. Negative Big-NB, Negative Small-NS, Positive Big-PB, Zero-Z, and Positive Small-PS.

Figures 5, 6, and 7 give the output voltage, current, real, and reactive power obtained using FLC.

$$3\oslash\text{Phase voltage Vph} = \frac{\text{Vdc}}{\pi} * 1.742 = 180 \text{ V}$$

$$3\oslash \text{ Line voltage VL} = \text{Vph} * 1.742 = 310 \text{ V}$$

$$\text{RMS value of Current Irms} = \sqrt{\frac{2}{3} * \left(\frac{\text{Vdc}}{2\text{R}}\right)^2} = 2.61 \text{ Amps}$$
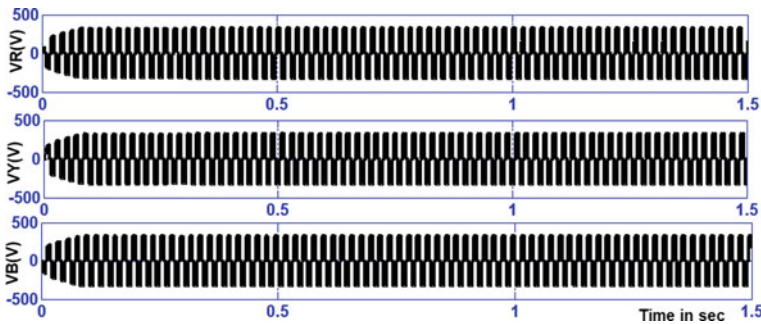
Fig. 5 Three-phase inverter voltage (simulation outputs in the closed loop conditions)
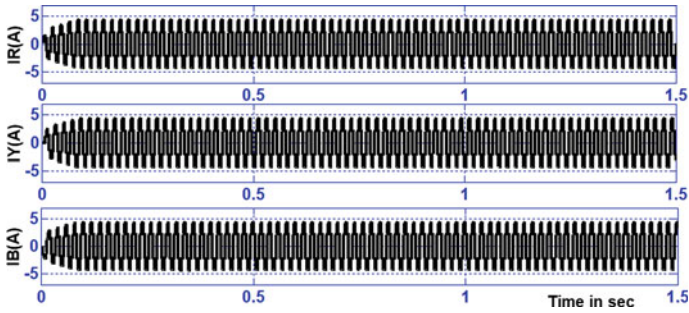
Fig. 6 Three-phase inverter current (simulation outputs in the closed loop conditions)
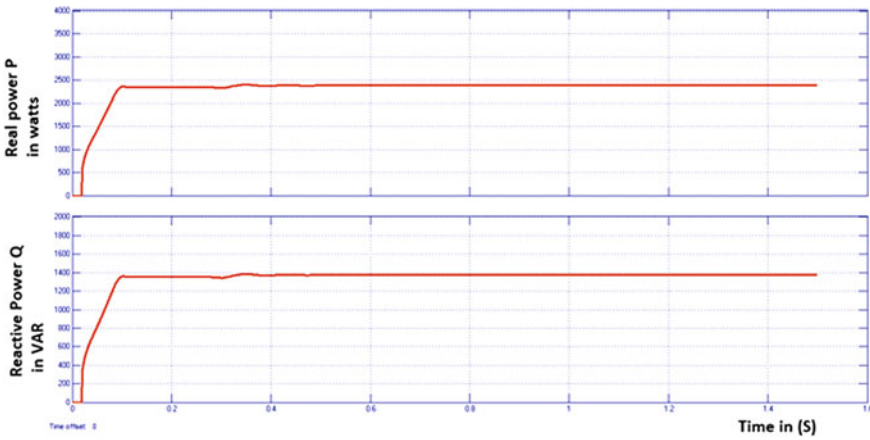
Fig. 7 Active and wattless power

Active Power $P = \sqrt{3}$VL ILCos$\oslash$ = 2400 Watts.
Reactive Power $Q = \sqrt{3}$VL IL sin $\oslash$ = 1400 VAR.
Figure 8 shows the THD value of 4.95% (Table 4).

5 Compare PI and FLC

Closed-loop system of multi-input KY boost converter hybrid system already discusses PI controller by this author [16]. Comparisons of the time domain parameter of PI and FLC are shown in Figs. 9 and 10. From the analysis it can be concluded that the Rise period (Tr), Settling period (Ts), Peak period (Tp), and Steady State Error (ESS) get reduced by using FLC than using PI. It is compared by taking two reference voltage Vref = 325 V and 400 V, and it is tabulated in Tables 5 and 6. Dynamic behavior is tested and checked with the help of MATLAB simulation, and
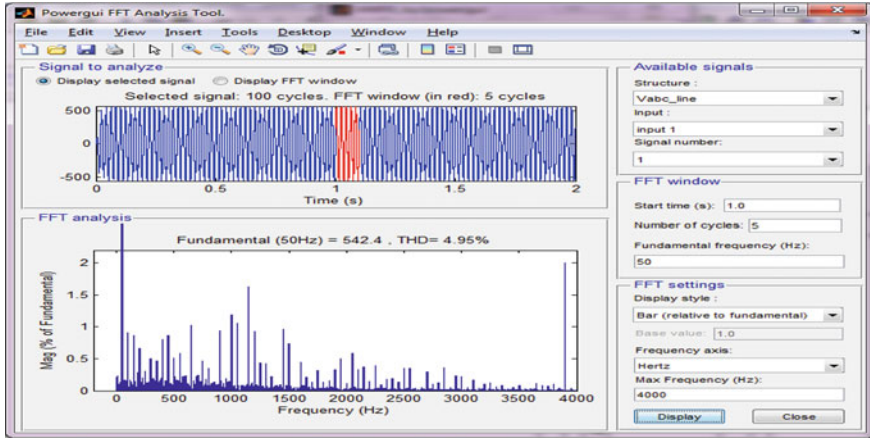
Fig. 8 THD

Table 4 Output values of closed-loop summary of multi-input KY boost converter using FLC

Parameter	Formula	Values
Vin	Vpv + Vwind	98 V
Vo	$\frac{2-D}{1-D}*Vi$	325 V
Vph	Vph = $\frac{\text{Vdc}}{\pi}*1.742$	180 V
VL	Vph*1.742	310 V
Irms	Irms = $\sqrt{\frac{2}{3}*\left(\frac{\text{Vdc}}{2R}\right)^2}$	2.61 A
P	$P = \sqrt{3}$VL ILCos$\oslash$	2400 watts
Cos$\oslash$	Cos$\oslash = \frac{P}{\sqrt{3}\text{VLIL}}$	0.988
Q	$\sqrt{3}VLIL\sin\oslash$	1400 VAR

a suitable controller is identified. PI and FLC controller performances are investigated under closed-loop conditions (Table 7).

All the review results state that the fuzzy model always gives better results for renewable systems. Results show that FLC gives better performance than the PI controller. In this, FLC has less THD nearly 4.96%, Power factor 0.988, Settling time 0.47 s, and good transient response than PI controllers.

6 Hardware Results

The hardware results shown in this section have been observed during the measurement stage of the open-loop system of multi-input KY boost converter hybrid network. The whole hybrid experimental arrangement is mentioned in Fig. 11. The

Fig. 9 Evaluation of time-domain parameters keeping reference voltage 325 V
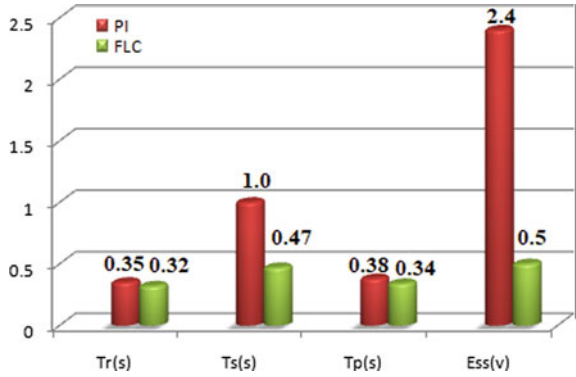
Fig. 10 Evaluation of time-domain parameters keeping reference voltage 400 V

Table 5 Evaluation of time-domain parameters keeping reference voltage 325 V

Controlling systems	Tr-Rise Time (s)	Ts-Settling Time (s)	Tp-Peak Time (s)	Ess-Steady State Error (V)
PI-Proportional Integral [16]	0.35	1.00	0.38	2.4
FLC-Fuzzy Logic Controller	0.32	0.47	0.34	0.5

Table 6 Evaluation of time-domain parameters keeping reference voltage 400 V

Controlling techniques	Tr-Rise Time (s)	Ts-Settling Time (s)	Tp-Peak Time (s)	Ess-Steady State Error (V)
Proportional Integral [16]	0.38	1.32	0.43	2.9
Fuzzy Logic Controller	0.34	0.51	0.38	0.8

Table 7 Parameters comparison of PI and FLC

Parameters	PI [16]	FLC
THD	7.08%	4.96%
Power factor	0.8844	0.988
Power P in Watts	2100 W	2400 W
Steady-state error	2.9 V	0.8 V
Settling time	1.00 S	0.44 S

hardware model consists of two input sources of the PV panel (V1) and AC voltage source (V2), which acts as a wind source [20]. Multi-input KY boost converter which switches and receives the pulse from the control circuit board. The corresponding waveforms are given in Figs. 12, 13, 14, and 15 (Table 8).

The desired PWM pulses were applied to switch Q1, Q2, Q3, and Q4. The duty ratio applied to Q1 and Q4 is D. The duty ratio applied to Q2 and Q3 is $1-D$.

The output voltage across multi-input KY boost converter 82 V.

$Vo = \frac{2-D}{1-D} * Vi$ where $D = 0.5$ and Vi = 24 V.

Three Phase Line voltage $Vph = \frac{Vdc}{\pi} * 1.742$.

Three Phase Line voltage $VL = Vph * 1.742 = 80$ V.

RMS value of Current $Irms = \sqrt{\frac{2}{3} * \left(\frac{Vdc}{2R}\right)^2} = 1.1$ Amps.
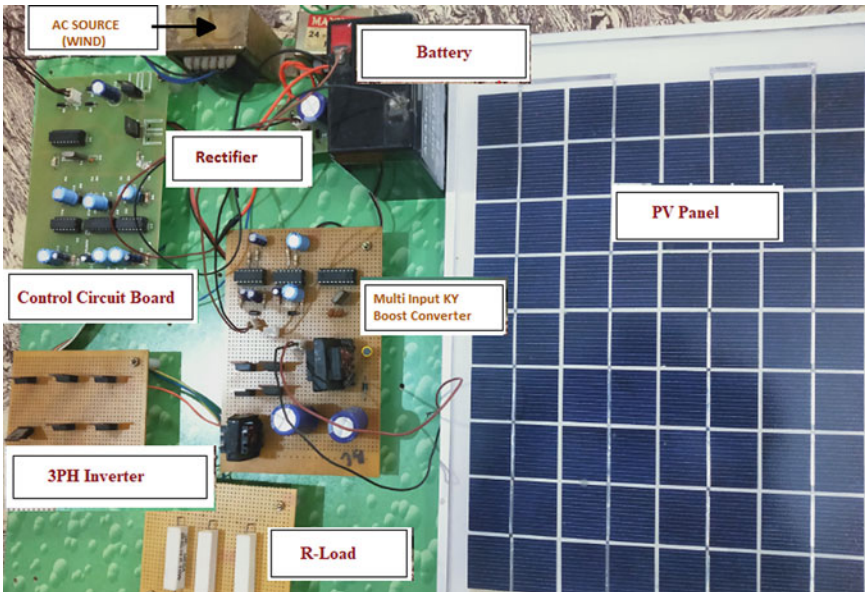
Fig. 11 Hardware snapshot of open-loop system of multi-input KY converter hybrid system

Fig. 12 Switching pulse of multi-input KY boost converter
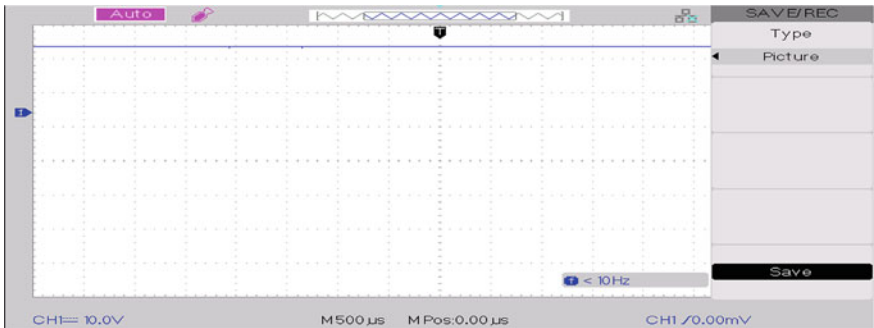
Fig. 13 Voltage across multi-input KY boost converter
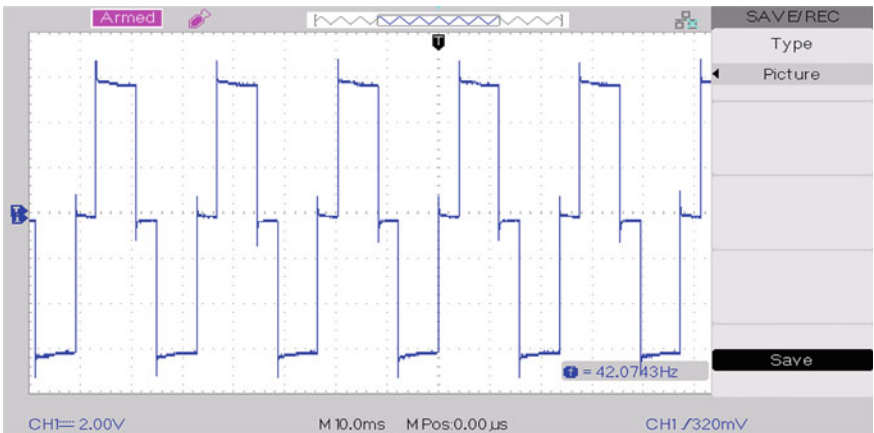
Fig. 14 Three-phase inverter voltage (hardware outputs in the open loop condition)
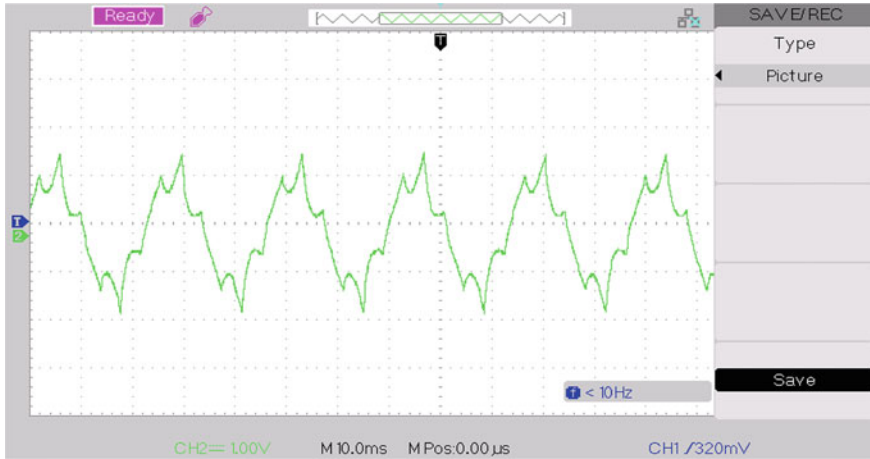
Fig. 15 Three-phase inverter current (hardware outputs in the open loop condition)

Table 8 Hardware results

Results	AC source voltage (Wind)	Rectified DC voltage V2	PV panel voltage V1	KY boost converter voltage	Three-Phase voltage	Three-phase current
Simulation	24 V	12 V	15 V	80 V	70 V	1.1 Amps
Hardware	24 V	12 V	12 V	82 V	80 V	1.0 Amps

7 Conclusion

Solar and wind are nonlinear sources because of its climatic conditions. This integrated system is intelligently controlled under the supervision of FLC. The PWM of multi-input KY converter switches is adjusted using FLC. The intelligent controller using fuzzy to increase the efficiency, convergence speed, fast response, and supply the uninterrupted power provided to the load. The DC bus maintains constant DC bus Voltage, and the storage device manages the power when there is no supply from the input side. The whole arrangement is simulated using MATLAB. This novel multi-input KY boost converters connected to the hybrid renewable energy system under the open-loop and closed-loop conditions. PI and FLC controller performances are investigated under closed-loop conditions. In this, FLC has less THD nearly 4.96%, Power factor 0.988, Settling time 0.47 s, and good transient response than PI controllers.
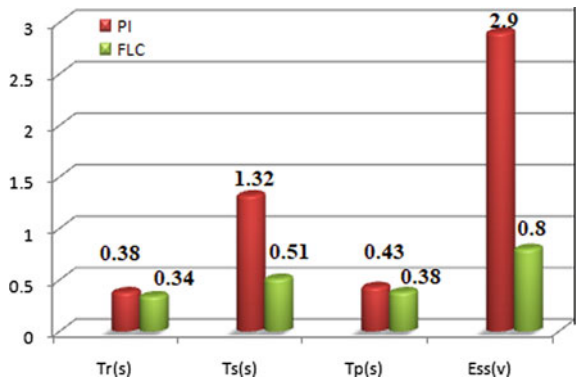
References

1. Hwu KI, Yau YT (2007) A novel voltage-boosting converter: KY converter. In: IEEE applied power electronics conference and exposition, pp 368–372
2. Hwu KI, Yau YT (2008) Soft switching of KY converter. In: IEEE applied power electronics conference and exposition, pp 1477–1482
3. Hwu KI, Yau YT (2008) Topology exchange between KY converter and its derivative. In: IEEE applied power electronics conference and exposition, pp 1675–1678
4. Hwu KI, Yau YT (2009) KY converter and its derivatives. IEEE Trans Power Electron 24:128–137
5. Hwu KI, Yau YT (2009) Two types of KY buck–boost converters. IEEE Trans Industr Electron 56:2970–2980
6. Hwu KI, Yau YT (2009) Voltage-boosting converter based on charge pump and coupling inductor with passive voltage clamping. IEEE Trans Industr Electron 57:1719–1727
7. Hwu KI, Chen YH, Lin ZF (2009) Negative-output KY buck-boost converter. In: IEEE conference on industrial electronics and applications pp 3347–3350
8. Hwu KI, Yau YT (2010) Inductor-coupled KY boost converter. Electron Lett 46:1624–1626
9. Hwu KI, Yau YT (2010) KY converter with zero voltage switching. In: IEEE conference on industrial electronics and applications, pp 1103–1106
10. Hwu KI, Peng TJ (2011) A novel buck–boost converter combining KY and buck converters. IEEE Trans Power Electron 27:2236–2241
11. Hwu KI, Huang KW, Tu WC (2011) Step-up converter combining KY and buck-boost converters. Electron Lett 47:722–724
12. Ajami A, Ardi H, Farakhor A (2014) Design, analysis and implementation of a buck–boost DC/DC converter. IET Power Electron 7:2902–2913
13. Hwu KI, Jiang WZ, Chen HM (2015) Improved KY converter. J Electr Eng Technol 10:1578–1588
14. Hwu KI, Jiang WZ (2017) A KY converter integrated with a SR boost converter and a coupled inductor. J Power Electron 17:621–631
15. Zhang Y, Li D, Lu H, Fan S, Chen Z, Wang Y, Geng L (2017) Analysis and implementation of a high-performance-integrated KY converter. IEEE Trans Power Electron 32:9051–9064
16. Pushpavalli M, JothiSwaroopan N (2020) Development of wind-solar hybrid system using multi input KY boost converter results from the simulation model. J Green Eng 10(1):238–254
17. Pushpavalli M, Jothi Swaroopan NM (2020) KY converter with fuzzy logic controller for hybrid renewable photovoltaic/wind power system. Tran Emerg Telecommun Technol 31(12):e3989
18. Mehrjerdi H (2020) Modeling, integration, and optimal selection of the turbine technology in the hybrid wind-photovoltaic renewable energy system design. Energy Convers Manage 205:112350
19. Murugan P, Mony JS (2020) Implement using KY converter for hybrid renewable energy applications: design, analysis, and implementation. In: Advanced statistical modeling, forecasting, and fault detection in renewable energy systems. Intech Open
20. Alajmi BN, Ahmed KH, Finney SJ, Williams BW (2011) Fuzzy-logic-control approach of a modified hill-climbing method for maximum power point in microgrid standalone photovoltaic system. IEEE Trans Power Electron 26:1022–1030

A Particle Swarm Optimization-Based Maximum Power Point Tracking Scheme Employing Dynamic Inertia Weight Strategies

Suraj Joshi and R. Subha

Abstract Photovoltaic (PV) systems are one of the most popular forms of Renewable Energy Sources. It is extremely important that these systems be operated at the Maximum Power Point (MPP). Under uniform insolation conditions, we observe a single peak in the *P–V* characteristics of a PV array. In contrast, under Partial Shading Condition (PSC) the *P–V* curve is highly non-linear and has multiple peaks that can be classified as Local and Global Peaks. Conventional MPPT Algorithms have failed to deliver satisfactory results under PSC. Hence, nature inspired optimization techniques such as the Particle Swarm Optimization (PSO) algorithm have been applied to MPPT under PSC and have proven to be an effective solution to the problem. In this paper, we employ a set of simple and dynamic Inertia weight strategies which are independent of factors such as maximum number of iterations and can be exploited to increase the speed of tracking of the PSO-based MPPT approach. An inertia weight that is dynamic, simple, and intuitive has also been proposed. The proposed Inertia Weight (IW) is independent of the current iteration number as well as a predetermined value for the maximum number of iterations necessary to converge to the MPP. A significantly lower convergence time and lesser tracking losses are obtained using the proposed IW. The performance of all these techniques has been evaluated using simulations under different shading conditions and validated with hardware implementation.

Keywords MPPT · PSC · PSO · Inertia weight · PV systems · Dynamic · Simulated annealing inertia weight · Global–local best inertia weight

S. Joshi
Department of Electrical and Electronics Engineering, Sir M. Visvesvaraya Institute of Technology, Bengaluru, India

R. Subha (✉)
Department of Electrical and Electronics Engineering, M S Ramaiah Institute of Technology, Bangalore, India
e-mail: subha.mvit@gmail.com

461

1   Introduction

Solar photovoltaic systems are of great importance in the field of renewable power generation due to the abundance of sunshine available during the day which can be converted into electrical energy. In addition, they can be incorporated into any location with minimum amount of difficulty and have a wide number of applications in which they can be utilized. The power output of a PV cell is a function of its temperature and the magnitude of irradiance. When uniformly irradiated, there exists only one peak in the P-V Characteristics of the array. The function of an MPPT Controller is to continuously track this unique point under any given condition.

In a PV array, there is often the possibility that one or more group of cells or a module gets shaded. Under such conditions, the P-V characteristics no longer has a single peak but is multimodal in nature and the peaks obtained can be classified as Local Peaks and Global Peaks. An MPPT algorithm under PSC must be able to track this global peak for any shading pattern. Conventional MPPT algorithms like the Hill Climb and Incremental Conductance as well as other MPPT algorithms have been analyzed in [1, 2]. These algorithms fail miserably to track the global peak under PSC (when the global peak is not the first peak).

Several attempts have been made to modify these algorithms to incorporate Global tracking capability under PSC [3–8] but these only make the tracking process longer and more complicated. Thus, there exists a need to use an approach that is both simple and effective. In [9] a PSO-based MPPT scheme has been described. PSO-based MPPT proves to be a simple and effective solution to the problem. In [10–12], various modifications to the PSO algorithm have been proposed. Inertia weight plays a key role in exploiting the global search ability of the PSO algorithm [13, 14]. Various Inertia Weights are summarized in [13]. In this paper, a modified inertia weights variation strategy is proposed and evaluated.

2   Partial Shading Conditions

MATLAB R2016b has been used for our simulations. This version of MATLAB is fully equipped with its own PV Array block which allows us to directly view the P-V and I-V Characteristics of the array under uniform insolation conditions. Under PSC, the P-V and I-V curves can then be plotted for the gradual variation in voltage. An example of these curves is shown in Fig. 1a, b.

3   PSO-Based MPPT Scheme

The PSO algorithm was inspired by the flocking nature of birds and the schooling nature of fishes and is hence an example of an algorithm that employs swarm intelligence for optimization. It performs a global search process by employing global
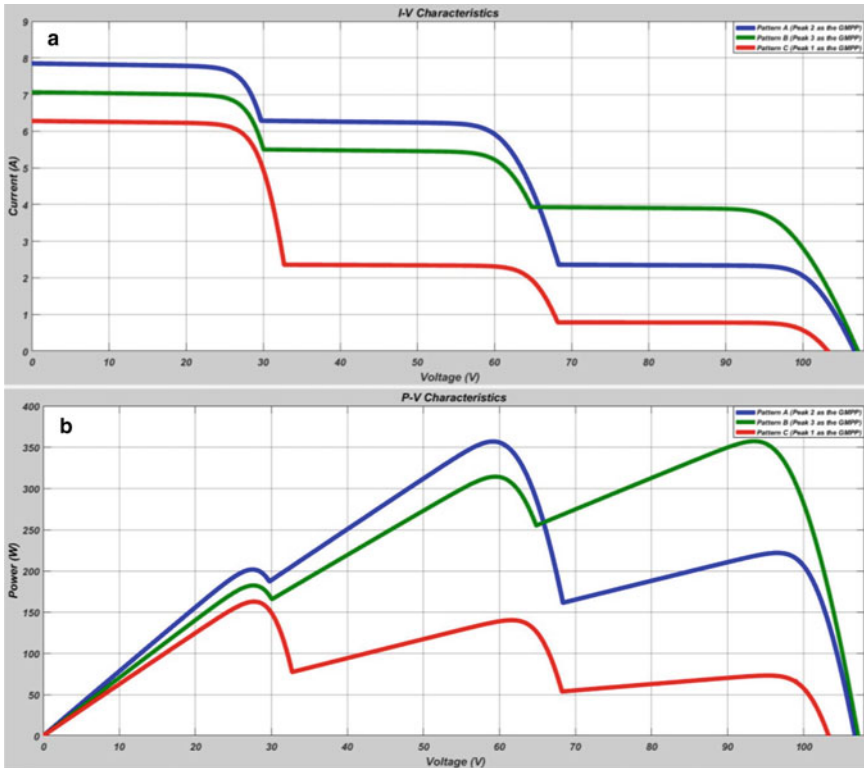
Fig. 1 **a** I-V Characteristics, **b** P-V Characteristics of a 3×1 PV Array under PSC

communication among individual units of the swarm (called particles) [15]. The positions of each particle are updated to search the entire search space for an optimum solution. The algorithm has a deterministic as well as a stochastic component. Within the stochastic component, there exists both a cognitive behavior-based component (Pbest) and a social behavior-based component (Gbest). Two main parameters are used in the PSO algorithm which are called the position (x) and the velocity (v) of a particle. These parameters are varied every iteration until convergence to the optimum solution occurs.

3.1 Particle Velocity and Position Update

The PSO velocity and position update for each particle i at an iteration t (for the next iteration $t + 1$) are

$$v_i^{t+1} = \omega^t v_i^t + c_1 r_1 \left(P_{\text{best}_i}^t - x_i^t \right) + c_2 r_2 \left(G_{\text{best}}^t - x_i^t \right) \tag{1}$$

$$x_i^{t+1} = x_i^t + v_i^{t+1} \tag{2}$$

where $c1$ and $c2$ are acceleration constants or learning parameters and $r1$ and $r2$ are random numbers between 0 and 1. ω is the inertia weight which can be time varying or constant. The position xi corresponds to the reference voltage V_{ref} which is generated by the MPPT controller to vary the duty cycle of the converter. Thus, for n particles we have

$$x_i^t = \left[V_{ref_1}^t, V_{ref_2}^t, V_{ref_3}^t \ldots \ldots \ldots V_{ref_n}^t \right] \tag{3}$$

3.2 Inertia Weight Strategies

Inertia weight plays a key role in exploiting the global search ability of the PSO algorithm. This component is desired to have a high value in the initial stage and its value should slowly decrease as the particles approach the MPP. The Inertia Weights (IW) considered in this study are.

Constant Inertial Weight (CIW):

$$\omega = k \tag{4}$$

where k is a constant

Simulated Annealing Inertia Weight (SAIW):

$$\omega^t = \omega_{min} + (\omega_{max} - \omega_{min})\lambda^{t-1} \tag{5}$$

where $\lambda = 0.95$

Global–Local Best Inertia Weight (GLbestIW)

$$\omega^t = 1.1 - \frac{G_{best}^t}{P_{best_i}^t} \tag{6}$$

Modified GLbestIW (M GLbestIW)

$$\omega^t = 1.1 - \frac{P_{best_i}^t}{G_{best}^t} \tag{7}$$
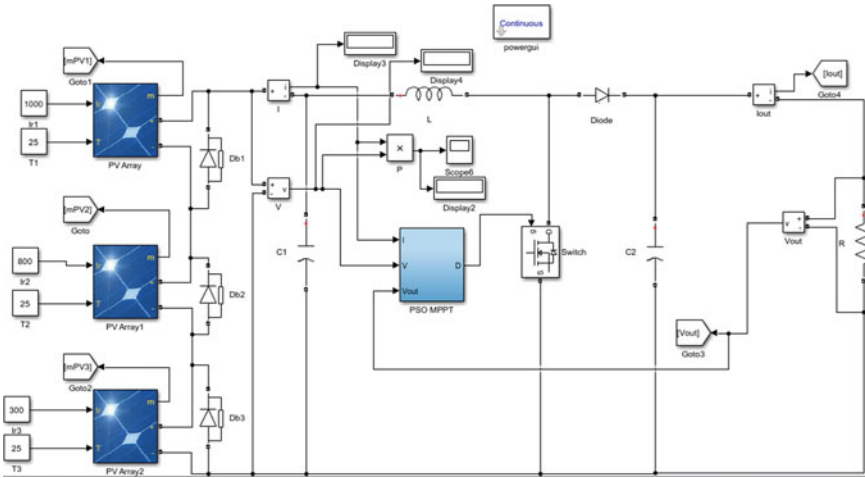
Fig. 2 Simulink Implementation of PSO-Based MPPT

3.3 MATLAB Simulink Implementation

The simulation for the proposed PSO-based MPPT is carried out using MATLAB Simulink. A 3 × 1 PV array has been considered to study the process of MPPT under PSC. The PSO Algorithm is implemented using a MATLAB function block. The inputs to the block are the PV array voltage and current. In addition, for computing the duty cycle we utilize the output voltage across a load resistor as an input to the system. A boost converter acts as the intermediate stage between the PV array and the load. The input capacitor is selected using [16]. The converter is employed to vary the operating voltage of the PV array and hence arrive at the voltage at which maximum power can be harnessed from the array, i.e., VMPP. The Simulink implementation is shown in Fig. 2.

3.4 Steps in Implementing PSO-Based MPPT

The steps involved in implementing the PSO-based MPPT are similar to those described in [17, 18] with the necessary modifications. The steps are as follows:

1. The particle positions are initialized. We have selected four particles at [0.8 0.6 0.4 0.2]*V_{OC}. The values of c1 and c2 are fixed as constants.
2. The inertia weight for each iteration and particle is computed for the corresponding method using equations (4), (5), (6), or (7).
3. For each particle "", the corresponding duty cycle (D) at an iteration "t" is computed using (8) and a pulse is generated. The generated pulse is fed to the DC-DC boost converter.

$$D(i) = 1 - \frac{V_{\text{ref}_i}^t}{V_0} \qquad (8)$$

4. A small delay is provided and the power derived from the PV array is computed as the product of the input voltage and current for each particle position.
5. For a given particle, its position at which maximum power was obtained is stored as its Personal Best.
6. Among all the best positions, one particular position stands out as the absolute best position at which the input power is maximum. This position is stored as the Global Best position.
7. The velocity vector and corresponding particle position are updated using equations (1) and (2), respectively.
8. The convergence criterion is evaluated. If it is not satisfied, the algorithm continues from the second step. Otherwise, the positions of all the particles are fixed at the last computed Global Best position.

The convergence criterion is satisfied when all the components of the velocity vector become less than a given tolerance limit. It must be noted that V_{ref} has been kept between the threshold values of 0.1*Voc and 0.9*Voc as the MPP for any array configuration and shading pattern lies between 10 and 90% of Voc. Also, the values of c1 and c2 are fixed so as to view the effects of the inertia weight alone on the tracking speed. When these factors are also tuned to be time varying, the convergence time will reduce even further and the system will reach the MPP much faster. This is of utmost importance as reduced convergence times lead to lesser energy loss during the process of tracking (resulting in higher energy efficiency).

3.5 Hardware Implementation

For the hardware implementation, a 100 kHz Boost Converter is implemented. An Arduino UNO board is utilized as the MPPT Controller. The steps described in the previous section apply to the hardware implementation as well. The inputs to the controller are the input voltage, input current, and output voltage. The pulse generated by the microcontroller is fed to the MOSFET via a driver circuit.

4 Results and Discussion

Figures 3, 4, 5 and 6 are the simulation results for CIW, SAIW, GLbestIW, and MGLbestIW PSO approaches, respectively, corresponding to the characteristics of pattern A shown in Fig. 1a, b. Figures 7, 8, 9 and 10 are the hardware results for the CIW, SAIW, GLbestIW, and MGLbestIW PSO approaches, respectively. The following can be observed:
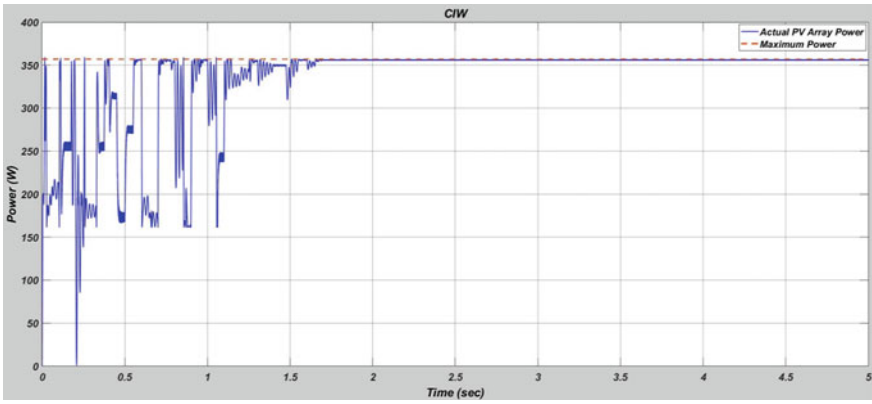
Fig. 3 Power output for CIW-PSO
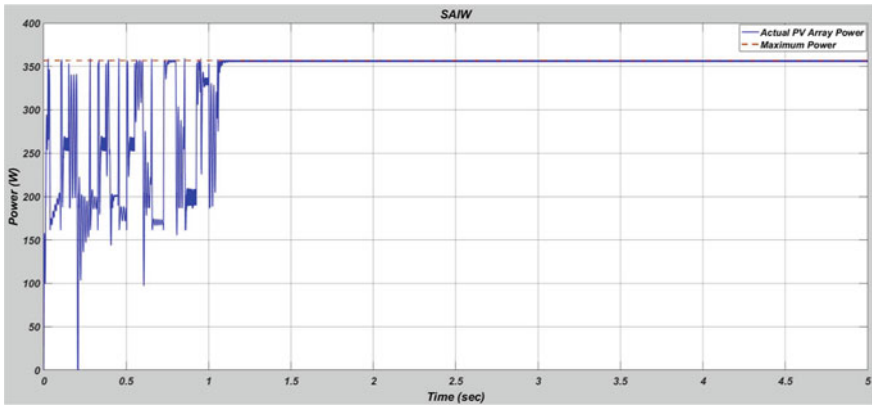
Fig. 4 Power output for SAIW-PSO
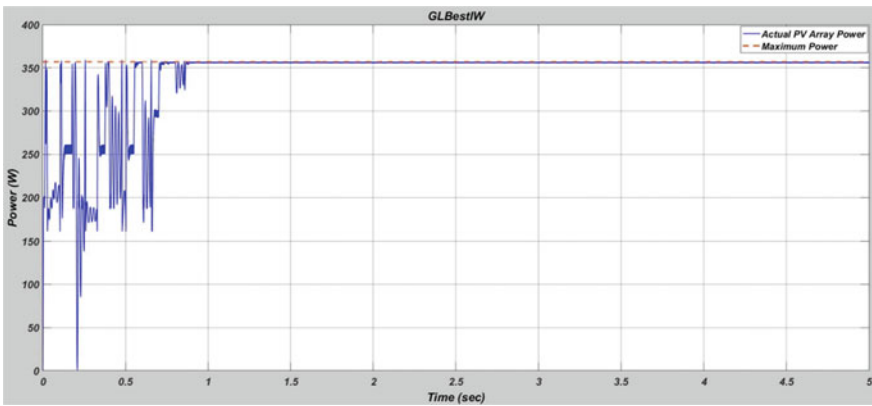
Fig. 5 Power output for GLbestIW-PSO
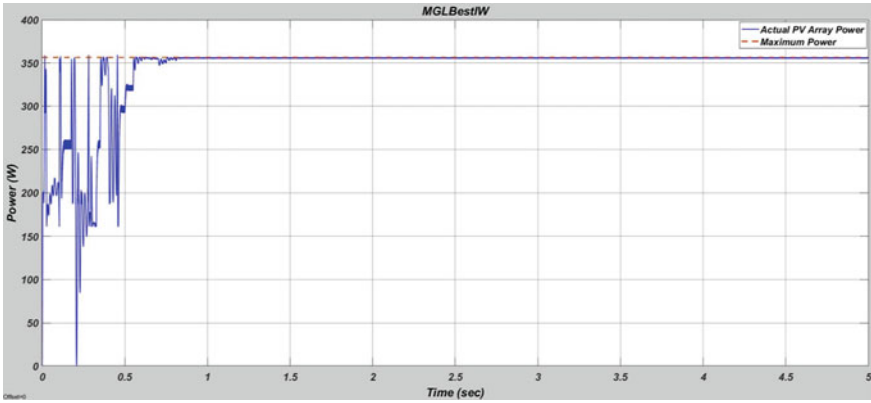
Fig. 6 Power output for MGLbestIW-PSO

Fig. 7 V_{PV}, I_{PV}, and P_{PV} for CIW-PSO
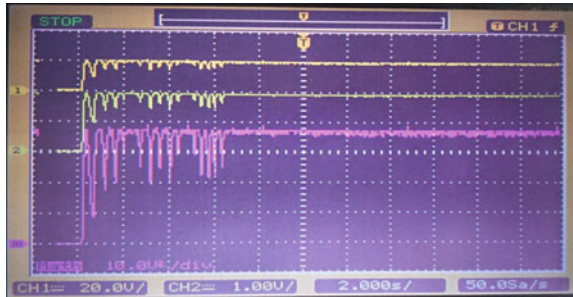
Fig. 8 V_{PV}, I_{PV}, and P_{PV} for SAIW-PSO
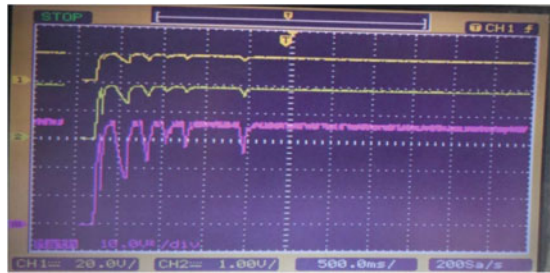
- The CIW-PSO takes the largest amount of time to converge to the MPP.
- The SAIW-PSO takes comparatively lesser time to converge to the MPP. It depends on the current iteration number and must be utilized with a suitable velocity clamping. Hence, it requires some tuning.

Fig. 9 V_{PV}, I_{PV}, and P_{PV} for GLbestIW-PSO
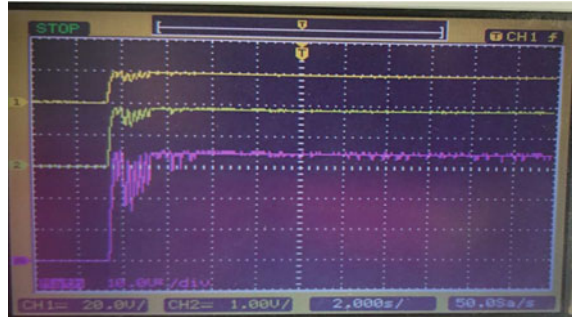
Fig. 10 V_{PV}, I_{PV}, and P_{PV} for MGLbestIW-PSO
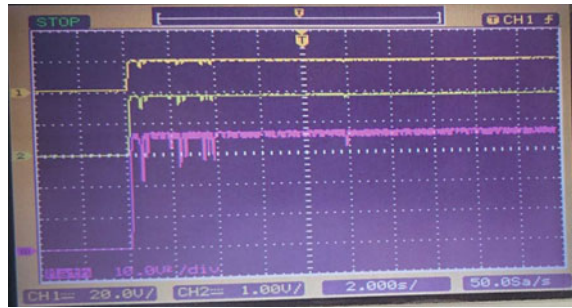
- The GLbestIW-PSO has a comparatively better performance and seems to converge to the MPP faster than the above approaches. This is because the positions of the particles near the Global Peak are perturbed to a lesser extent than other particles. (When Gbest = Pbest, $\omega = 0.1$)
- The proposed MGLbestIW-PSO has the most preferable convergence speed among all the four approaches. This is because the positions of the particles near the Global Peak are perturbed to a lesser extent as mentioned above. In addition, particles away from the Global Peak are perturbed to a greater extent when compared to the same particles in the GLbestIW-PSO approach (as Pbest is always less than or equal to Gbest).

Thus, it can be inferred that the inertia weight plays a key role in the tracking speed of the PSO algorithm. Additionally, compared to all the available IW strategies the MGLbestIW has many advantages. The fact that it does not depend on the iteration number and the maximum number of iterations along with easy hardware implementation is what makes it more preferable. Also, it is directly related to the ratio of the position best and global best variables. Table 1 highlights the time required to converge to the MPP and the Energy Lost while tracking when each IW strategy is utilized for 15 different shading patterns. When c1 and c2 are also tuned to be time varying, these values will further decrease and faster tracking will be achieved. The system successfully tracks the MPP for multiple shading patterns in the hardware implementation as well.

Table 1 Comparison of inertia weight strategies for PSO-Based MPPT

Pattern number	Global peak	VMPP (V)	PMPP (W)	CIW		SAIW		GLbestIW		MGLbestIW	
				Conv Time (sec)	Energy Loss (J)	Conv Time (sec)	Energy Loss (J)	Conv Time (sec)	Energy Loss (J)	Conv Time (sec)	Energy Loss (J)
1	1st	27.59	181.9	1.51	61.5	1.06	56.7	0.91	49.7	0.80	38.1
2		27.70	162.3	1.46	46.2	1.05	44.3	0.96	41.0	0.82	30.2
3		27.48	201.1	1.47	77.0	1.01	74.5	0.98	67.2	0.70	48.6
4		27.77	137.5	1.38	50.0	1.10	45.4	0.90	43.0	0.81	39.4
5		27.66	71.20	1.40	38.5	1.12	30.3	0.88	27.4	0.79	23.2
6	2nd	57.50	357.3	1.67	81.3	1.13	76.2	0.89	66.0	0.74	51.4
7		59.10	311.8	1.41	72.3	1.15	70.4	0.80	59.2	0.66	54.6
8		60.22	273.2	1.43	58.6	1.11	57.4	0.87	49.6	0.61	42.0
9		60.62	206.5	1.35	60.9	1.09	58.7	0.92	50.2	0.65	42.4
10		58.59	154.6	1.48	46.2	1.14	45.1	0.97	41.7	0.70	35.0
11	3rd	93.47	356.9	1.42	61.4	1.16	59.5	0.86	54.1	0.75	47.2
12		92.71	460.0	1.47	81.5	1.12	75.6	0.82	63.2	0.72	53.6
13		94.27	216.3	1.43	51.0	1.09	46.3	0.90	34.5	0.69	25.6
14		93.62	143.2	1.39	38.6	1.16	35.9	0.84	29.3	0.73	24.5
15		90.82	82.10	1.44	29.7	1.02	26.3	0.93	24.3	0.77	16.4

5   Conclusion

The study reveals the effect of the inertia weight of the PSO algorithm on the convergence time of the system for a Partially Shaded PV Array. When the inertia weight has a high value in the initial set of iterations and it decreases gradually to a low value in the final few iterations (when the particles have nearly reached VMPP), there exists a good tracking response. A dynamic inertia weight independent of the iteration number and directly dependent on the Pbest and Gbest variables is observed to give the most satisfactory results. The MGLbestIW effectively exploits the global search capability of a standard dynamic inertia weight. Hence, this IW strategy is preferable when compared to the existing strategies utilized in PSO-based MPPT for Partially Shaded PV Arrays.

References

1. Hohm DP, Ropp ME (2000) Comparative study of maximum power point tracking algorithms using an experimental, programmable, maximum power point tracking test bed. In: Conference record of the twenty-eighth IEEE photovoltaic specialists conference—2000 (Cat. No.00CH37036), pp 1699–1702
2. Esram T, Chapman PL (2007) Comparison of photovoltaic array maximum power point tracking techniques. IEEE Trans Energy Convers 22:439–449
3. Ahmad J, Spertino F, Di Leo P, Ciocia A (2016) A variable step size perturb and observe method based MPPT for partially shaded photovoltaic arrays. In: PCIM Europe 2016; international exhibition and conference for power electronics, intelligent motion, renewable energy and energy management pp 1–8
4. Spertino F, Ahmad J, Ciocia A, Di Leo P (2015) A technique for tracking the global maximum power point of photovoltaic arrays under partial shading conditions. In: 2015 IEEE 6th International Symposium on power electronics for distributed generation systems (PEDG), pp 1–5
5. Koutroulis E, Blaabjerg F (2012) A new technique for tracking the global maximum power point of PV arrays operating under partial-shading conditions. IEEE J Photovoltaics 2:184–190
6. Chen K, Tian S, Cheng Y, Bai L (2014) An improved MPPT controller for photovoltaic system under partial shading condition. IEEE Trans Sustain Energy 5:978–985
7. Kobayashi K, Takano I, Sawada Y (2003) A study on a two stage maximum power point tracking control of a photovoltaic system under partially shaded insolation conditions. In: 2003 IEEE power engineering Society General Meeting (IEEE Cat. No.03CH37491), vol 4, pp 2612–2617
8. Carannante G, Fraddanno C, Pagano M, Piegari L (2009) Experimental performance of MPPT algorithm for photovoltaic sources subject to inhomogeneous insolation. IEEE Trans Industr Electron 56:4374–4380
9. Miyatake M, Toriumi F, Endo T, Fujii N (2007) A Novel maximum power point tracker controlling several converters connected to photovoltaic arrays with particle swarm optimization technique. In: 2007 European conference on power electronics and applications, pp 1–10
10. Ishaque K, Salam Z, Amjad M, Mekhilef S (2012) An improved particle swarm optimization (PSO)–based MPPT for PV with reduced steady-state oscillation. IEEE Trans Power Electron 27:3627–3638
11. Ishaque K, Salam Z (2013) A deterministic particle swarm optimization maximum power point tracker for photovoltaic system under partial shading condition. IEEE Trans Industr Electron 60:3195–3206

12. Phimmasone V, Endo T, Kondo Y, Miyatake M (2009) Improvement of the maximum power point tracker for photovoltaic generators with particle swarm optimization technique by adding repulsive force among agents. In: 2009 International conference on electrical machines and systems, pp 1–6
13. Bansal JC et al (2011) Inertia weight strategies in particle swarm optimization. In: 2011 Third World Congress on nature and biologically inspired computing. IEEE, pp 633–640
14. Shi Y, Eberhart R (1998) A modified particle swarm optimizer. In: 1998 IEEE international conference on evolutionary computation proceedings. IEEE World Congress on Computational Intelligence (Cat. No.98TH8360), pp 69–73
15. Yang XS (2014) Nature-inspired optimization algorithms. Elsevier Insights
16. Hayat A, Faisal A, Javed MY, Hasseb M, Rana RA (2016) Effects of input capacitor (cin) of boost converter for photovoltaic system. In: 2016 International conference on computing, electronic and electrical engineering (ICE Cube), pp 68–73
17. Subha R, Himavathi S (2016) Accelerated particle swarm optimization algorithm for maximum power point tracking in partially shaded PV systems. In: 2016 3rd International conference on electrical energy systems (ICEES), pp 232–236
18. Rajendran S, Srinivasan H (2016) Simplified accelerated particle swarm optimisation algorithm for efficient maximum power point tracking in partially shaded photovoltaic systems. IET Renew Power Gener 10:1340–1347

Improved Fractional Filter IMC Controller Design for Fractional Order System

R. Ranganayakulu [ID]**, T. Kiranmayi, Ch.V. L. Aditya, I. Tanoj Kumar, and G. Uday Bhaskar Babu** [ID]

Abstract Most of the real-time applications are being dealt with fractional order controllers. Choosing a non-integer order controller has made the design worthful for many systems, especially for processes modeled as fractional order systems. A yielding method for designing a non-integer order controller is represented here for a non-integer order system using internal model control (IMC). IMC technique is picked up to implement the controller design by considering filter of fractional order due to its flexibility and robust nature. The system performance with the proposed controller is estimated for nominal model and for variations in the model. Performance is boosted with the proposed method, especially in reduced controller effort by studying system and parameter variations. Further, the controller fragility is estimated for perturbations in the controller parameters. The proposed method is extended for the delayed fractional model and its fragility is investigated.

Keywords Fractional filter controller · Internal model control · Fragility

1 Introduction

A proportional integral derivative (PID) controller is largely used in industries and a variety of other applications due to its simple design and robust to tuning the mismatches of models [1–3]. However, it is not suitable for processes with nonlinearities and quickly changing set points. An alternative for this comes in the form of fractional controller developed with the help of fractional calculus [4].

Fractional-order control is a special branch of control that uses the fractional calculus for designing the control system. The use of fractional calculus (FC)

R. Ranganayakulu · T. Kiranmayi · Ch.V. L. Aditya · I. Tanoj Kumar
Department of ECE, Vignan's Foundation for Science, Technology & Research, Vadlamudi, Andhra Pradesh 522213, India

G. Uday Bhaskar Babu (✉)
Department of Chemical Engineering, National Institute of Technology, Warangal, Telangana 506004, India
e-mail: udaybhaskar@nitw.ac.in

enhances the scope of existing and widely accepted control strategies [5]. The fractional order (FO) PID controller consists of gains along with fractional powers of integrator and differentiator. These fractional powers in FOPID controller make it flexible and offer robustness for uncertainties than PID controller. Due to this unique feature, it gained much attention in the control domain [6–9]. Several tuning rules are available for FOPID controller for the IO process [10]. There are various techniques to determine the settings of PID controller. In the direct synthesis (DS) method, controller is designed after assuming the desired closed-loop transfer function [11].

IMC is a proved controller design scheme and IMC-based controller tuning rules yield a robust performance when used with a wide variety of processes. There are several analytical tuning rules for IMC-PID controllers developed for different types of stable time delay systems [12–15]. A single and two-degree of freedom FOPID controller was developed for a fractional order system based on predefined bandwidth [16]. The performance of any IMC controller depends on the model which is used for design and the requirements related to the performance given by the designer. Perfect control is possible if the model used for IMC controller design is an exact representation of the process [17]. The IMC control predicts output change for change in set point using open loop step response transfer functions with the time constant and gain [18]. This is the major advantage of IMC controller structure over others. A fractional IMC (FIMC) controller is developed for gas turbine system by considering fractional order model [19]. In [20], a fractional filter PID (FFPID) controller is proposed for first-order models based on IMC scheme.

In the present work, a fractional controller is proposed for a fractional order system using IMC method. The design uses a fractional IMC filter and is hence named as fractional filter IMC (FFIMC) controller. The main motive for designing the fractional controller is that it can reject the disturbance in a better way than PID controller. The proposed controller performance is compared with FIMC controller [19] and FOIMC-PID controller [16]. The performance is analyzed for variations in the model and controller parameters.

The paper is structured as follows. Section 2 discusses the preliminaries of the proposed controller and performance measures required during analysis. Proposed controller design is explained in Sect. 3. Discussion about the results and analysis is mentioned in Sect. 4 and the conclusion is given in Sect. 5.

2 Preliminaries

A clear picture of the IMC and feedback loop is provided in Fig. 1. Implementation of controller using IMC method involves the following steps.

1. Identify the stable and unstable parts from the process model

$$G_m(s) = G_m^+(S)G_m^-(S) \tag{1}$$
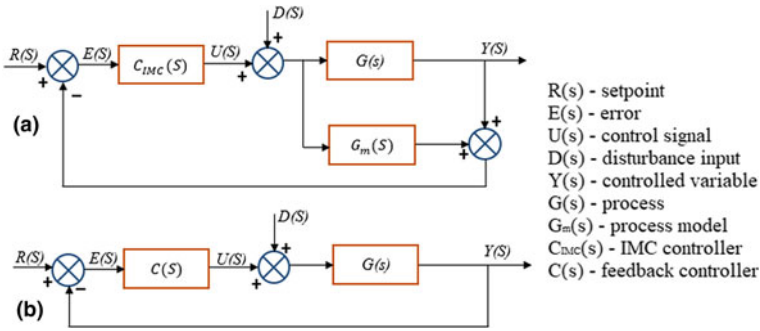
Fig. 1 **a** IMC scheme. **b** Feedback loop

Table 1 Metrics used for performance assessment

ISE	IAE	ITAE		ISI	TV
$\int_0^T e^2(t)dt$	$\int_0^T |e(t)|dt$	$\int_0^T t(e)dt$		$\int_0^T u^2(t)dt$	$\sum_{i=0}^{\infty} |u_{i+1} - u_i|$

$G_m^+(S)$ is noninvertible and contains unstable zeros and time delays. $G_m^-(S)$ is invertible and contains stable portions like poles and system gain.

2. Generate the IMC controller using Eq. (2)

$$C_{\text{IMC}}(s) = \frac{1}{G_m^-(s)} F(s); \; F(s) - \text{IMC filter} \qquad (2)$$

3. Obtain feedback controller $C(s)$ using Eq. (2) and process model

$$C_{\text{FFIMC}}(s) = \frac{C_{\text{IMC}}(s)}{1 - C_{\text{IMC}}(s)G_m(s)} \qquad (3)$$

In the current work, the closed-loop performance is determined through error functions ISE (integral square error), IAE (integral absolute error), and ITAE (integral time absolute error) (Table 1). The controller performance is assessed through Total Variation (TV) and Integral of the squared input (ISI) (Table 1).

2.1 Fragility Analysis of Proposed Controller

The controller fragility [21] is investigated in terms of loss of performance for variation in tuning parameters using the performance fragility index (PFI) (Eq. 4).

$$PFI_{\Delta\varepsilon} = \frac{IAE_{\delta\varepsilon}}{IAE_{actual}} - 1 \tag{4}$$

where $\Delta\varepsilon$ is the variation in the controller parameter; $IAE_{\delta\varepsilon}$ is the absolute error for variation in the controller parameter and IAE_{actual} is the nominal value of error.

The fragility of any controller for performance is decided using $PFI_{\Delta20}$. The controller is said to be resilient, non-fragile, and fragile if $0 < PFI_{\Delta20} < 0.1$, $0.1 < PFI_{\Delta20} < 0.5$ and $PFI_{\Delta20} > 0.5$, respectively.

3 Proposed Controller Design

3.1 Controller Design for Model Without Delay

The process model used here is a representation of the complex gas turbine system. Despite the different mathematical models [22, 23] available, the following fractional model is considered which is derived through system identification [24].

$$G_m(s) = \frac{K}{as^\alpha + bs^\beta + c} \tag{5}$$

The IMC Controller

$$C_{IMC}(s) = \frac{1}{G_m^-(s)} F(s) \tag{6}$$

The fractional IMC filter, $F(s) = \frac{1}{\gamma s^P + 1}$ (γ-filter time constant; p-fractional order) is used for realizing the controller. Then, the IMC controller becomes

$$C_{IMC}(s) = \frac{as^\alpha + bs^\beta + 1}{K} \frac{1}{\gamma s^P + 1} \tag{7}$$

The feedback controller $C_{FFIMC}(s)$ using (5) and (7) is given by Eq. (8)

$$C_{FFIMC}(s) = \frac{as^\alpha + bs^\beta + 1}{K\gamma s^P} \tag{8}$$

where γ and p are the tuning parameters

Table 2 Approximation of the term e^{-Ls}

1st order approximation	2nd order approximation
$\frac{1-0.5LS}{1+0.5LS}$	$\frac{1-0.5Ls+0.0833L^2s^2}{1+0.5Ls+0.0833L^2s^2}$

3.2 Controller Design for Model with Delay

A small delay has been introduced in Eq. (5). The modified model (Eq. 9) with delay is

$$G_m(s) = \frac{K}{as^\alpha + bs^\beta + c} e^{-Ls} \tag{9}$$

where L is time delay.

The FFIMC controller for Eq. (9) using Eqs. (2), (3), and $F(s) = \frac{1}{\gamma s^p + 1}$ is given in Eq. (10)

$$C_{\text{FFIMC}}(s) = \frac{\left[as^\alpha + bs^\beta + c\right]}{K\left[(\gamma s^p + 1) - e^{-Ls}\right]} \tag{10}$$

The two proposed controllers after approximating the time delay term (Table 2) in Eq. (10) are given by (11) and (12). Proposed 1 and 2 represents the FFIMC controller equations obtained after rationalizing the FFIMC controller equation for model with delay using pade's 1st and 2nd order of approximation, respectively.

$$C_{\text{Proposed 1}}(s) = \frac{0.5aLS^{\alpha+1} + 0.5bS^{\beta+1} + aS^\alpha + bS^\beta + 0.5LS + c}{0.5K\gamma LS^{p+1} + K\gamma s^p + KLS} \tag{11}$$

$$C_{\text{proposed 2}}(s) = \frac{\begin{array}{c}0.0833aL^2s^{\alpha+2} + 0.0833L^2bs^{\beta+2} + 0.5aLs^{\alpha+1}\\ +0.5bs^{\beta+1} + 0.0833L^2s^2 + 0.5Ls + as^\alpha + bs^\beta + c\end{array}}{0.833K\gamma L^2s^{p+2} + 0.5K\gamma Ls^{p+1} + K\gamma s^p + KLs} \tag{12}$$

4 Results and Discussion

4.1 Example 1

The model (Eq. 13) used for simulation [25] is

$$G_m(s) = \frac{103.9705}{0.0073s^{1.6807} + 0.1356s^{0.8421} + 1} \tag{13}$$

The proposed FFIMC controller with γ and p chosen as 0.007 and 1.01 is in Eq. (14)

$$C_{\text{FFIMC}}(s) = \frac{0.0073s^{1.6807} + 0.1356s^{0.8421} + 1}{0.7277\ s^{1.01}} \tag{14}$$

The other controllers [16, 19] used for comparison are given in Eq. (15) and Eq. (16)

$$C_{\text{FIMC}}(s) = \frac{0.0073s^{1.6807} + 0.1356s^{0.8421} + 1}{0.7277\ s} \tag{15}$$

$$C_{\text{FOIMC-PID}}(s) = 0.06205 + \frac{0.4582}{s^{0.8421}} + 0.0033s^{0.8386} \tag{16}$$

The closed-loop performance of this example is verified for the nominal model and for parametric variations of the model. The response for unit step excitation plus a disturbance of amplitude -0.2 given at $t = 0.15$ s is presented in Fig. 2. It is clear from Fig. 2 that the set point has been reached quickly by both proposed FFIMC and FIMC, Whereas FOIMC-PID takes longer to reach the set point than the others. The control signal corresponding to the three methods is illustrated in Fig. 3 and the control effort of the FFIMC is low compared to FIMC followed by FOIMC-PID. The proposed method is preferable with the low value of TV followed by FIMC and FOIMC-PID (Table 3).

The ISI value listed in Table 3 signifies the amount of energy required by the control system. Though, the ISI value of the FOIMC-PID is low compared to FFIMC followed by FIMC in Fig. 4, the overall performance of the FOIMC-PID is not up to the mark in terms of performance measures: errors and TV. It is proved based upon the
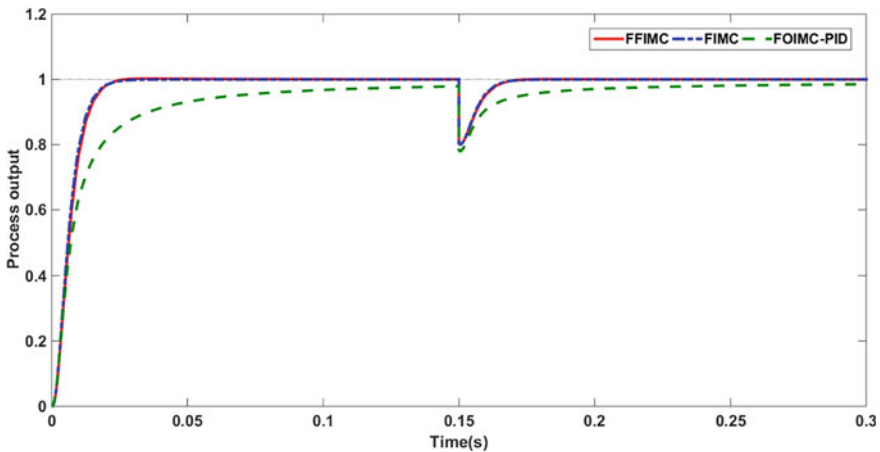
Fig. 2 Response for the nominal model in Eq. (13)
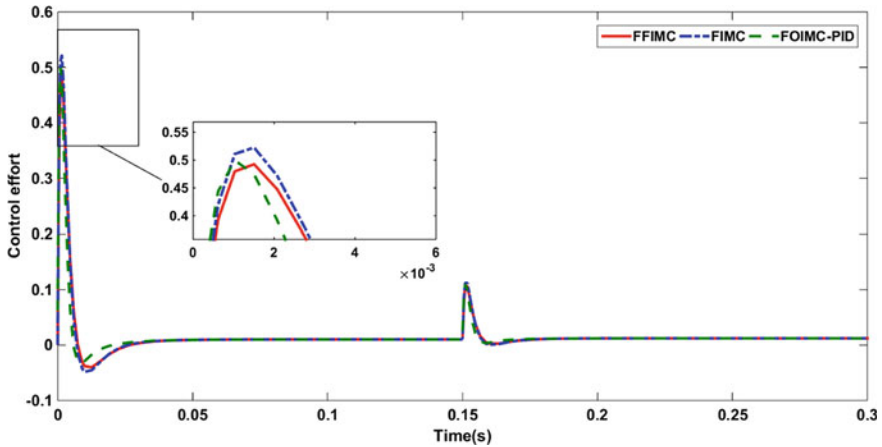
Fig. 3 Controller output for the model in Eq. (13)

results that the FFIMC controller is secured with low TV and IAE followed by FIMC and FOIMC-PID. The proposed method is preferable with respect to performance measures even at perturbations of +5% in model parameters followed by FIMC and FOIMC-PID. This is evident from the measures presented in Table 4.

Fragility analysis based on the performance of the controller was analyzed and the results were shown in Fig. 5. It is observed that all the three controllers FFIMC, FIMC, FOIMC-PID are non-fragile in nature for +20% shift in the tuning parameter of the respective controller as the PFI value exists between 0.1 and 0.5 (Table 5). Due to the non-fragile nature, these controllers can be returned based on our requirements.
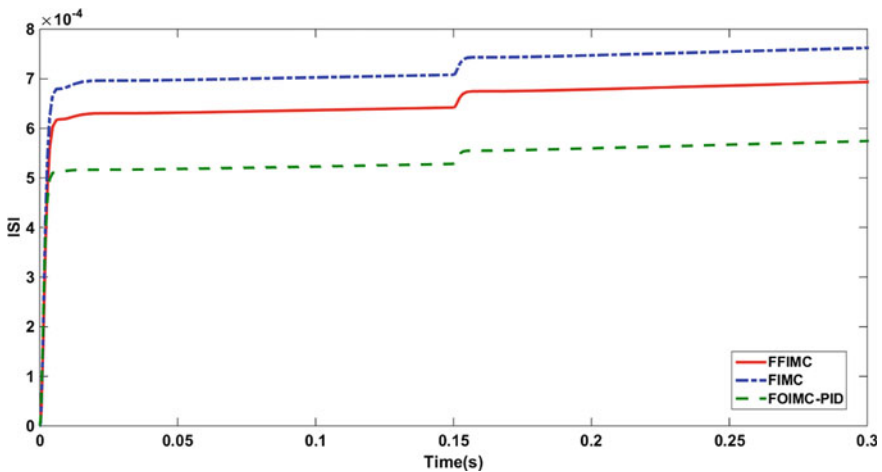
Fig. 4 Trends of ISI for step response of the model in Eq. (13)

Table 3 Performance measures for nominal process model

Method	ISE	IAE	ITAE	ISI	TV
FFIMC	0.004946	0.008399	0.0002333	0.0006935	0.1041
FIMC [19]	0.004759	0.008899	0.000252	0.0007621	0.1284
FOIMC-PID [16]	0.006561	0.02154	0.001549	0.0005743	0.1679
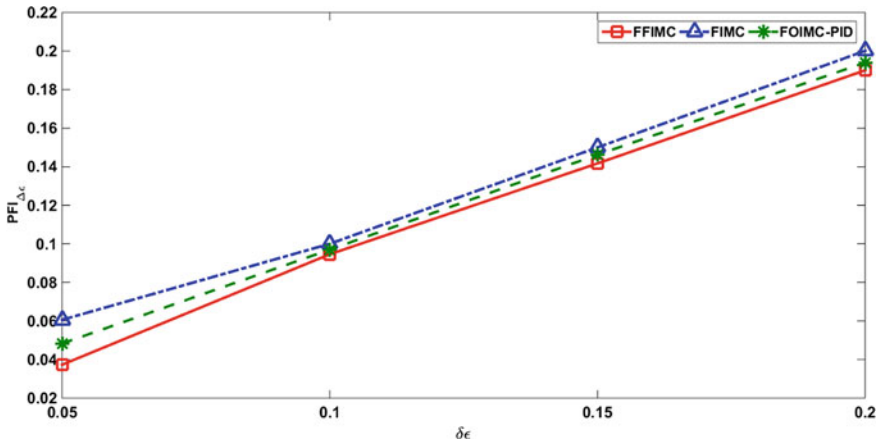
Fig. 5 Fragility plot for the model in Eq. (13)

Table 4 Measures for perturbed model

Method	ISE	IAE	ITAE	ISI	TV
FFIMC	0.006704	0.01434	9.429×10^{-5}	0.0007723	0.0987
FIMC [19]	0.006452	0.01362	0.0001149	0.0008471	0.0913
FOIMC-PID [16]	0.00827	0.02052	0.001228	0.0006105	0.1239

Table 5 PFI values for the three methods

Method	$\Delta\varepsilon$				
	5%	10%	15%	20%	25%
FFIMC	0.03730	0.0946	0.1417	0.1900	0.2799
FIMC [19]	0.06060	0.10001	0.15001	0.2001	0.25014
FOIMC-PID [16]	0.04828	0.0970	0.1462	0.1940	1.2743

4.2 Example 2

The fractional order model with a delay of 0.005 s in Eq. (13) is given by Eq. (17)

$$G_m(s) = \frac{103.9705}{0.0073s^{1.6807} + 0.1356s^{0.8421} + 1}e^{-0.005s} \tag{17}$$

The two proposed controllers for the model in (17) are given in Eqs. (18) and (19) with $\gamma = 0.007$ and $p = 1.01$.

$$C_{\text{proposed 1}}(s) = \frac{\begin{array}{c}0.00001825s^{2.6807} + 0.000339s^{1.8421} + 0.0073s^{1.6807} \\ +0.0025\ s + 0.1356\ s^{0.8421} + 1\end{array}}{0.2599s^{2.01} + 103.9705s^{1.01} + 0.519s} \tag{18}$$

$$C_{\text{proposed 2}}(s) = \frac{\begin{array}{c}\left(1.52 * 10^{-8}\right)s^{3.6807} + \left(2.825 * 10^{-7}\right)s^{2.8421} + \left(1.825 * 10^{-5}\right)s^{2.6807} \\ +\left(2.08 * 10^{-6}\right)s^2 + 0.000339s^{1.8421} + 0.0073\ s^{1.6807} \\ +0.1356s^{0.8421} + 0.0025\ s + 1\end{array}}{2.166\ s^{3.01} + 0.2599\ s^{2.01} + 103.9705\ s^{1.01} + 0.5198\ s} \tag{19}$$

The closed-loop response for unit step excitation plus a disturbance of amplitude -0.2 given at $t = 0.15$ s is depicted in Fig. 6. The associated measures are listed in Table 6. Both the proposed controllers reached the set point at the same time, whereas control effort is more with proposed 2 compared to proposed 1. The rate of error and TV is falling with rise in the approximation order of e^{-Ls} while the amount of energy consumed by the controller is increasing (ISI trends in Fig. 7). The response provided in Fig. 7 is justified through the ISI values in Table 6.

The fragility analysis carried out with Proposed 1 and Proposed 2 controllers proves that the controllers are non-fragile up to $+20\%$ variation in controller settings (Fig. 8 and Table 7).
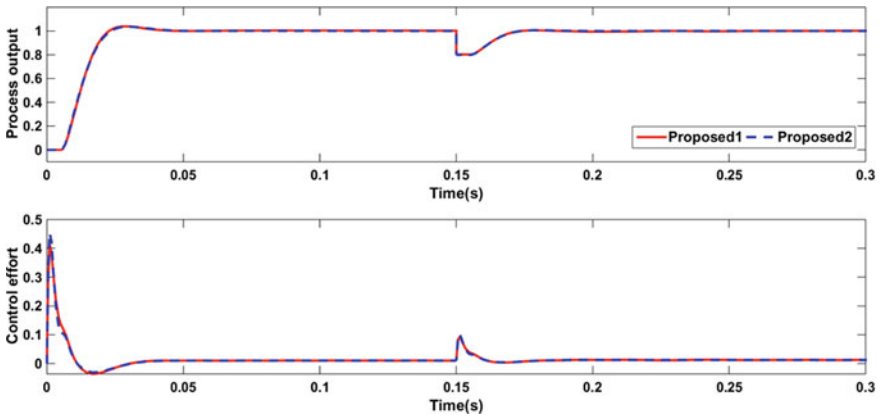
Fig. 6 Response for the model in Eq. (17)
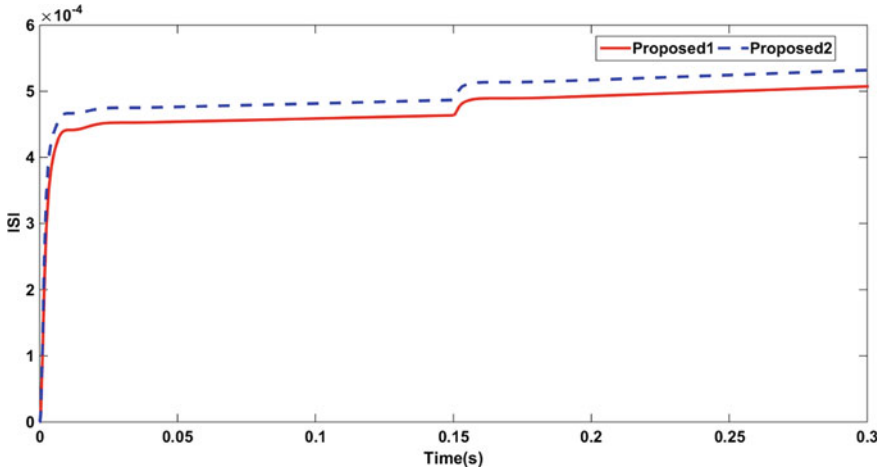
Fig. 7 Trends of ISI for step response of Example 2
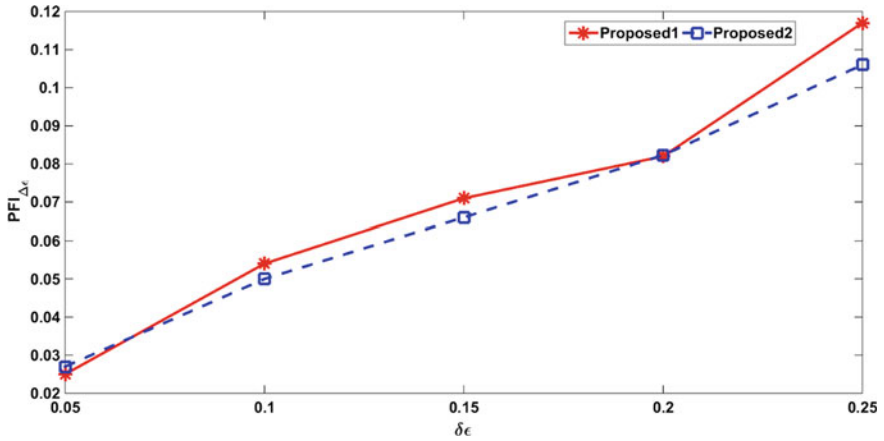
Fig. 8 Fragility plot of Example 2

Table 6 Performance measures for the model in Eq. (17)

Method	ISE	IAE	ITAE	ISI	TV
Proposed 1	0.0108	0.01629	0.0002333	0.0005074	0.1342
Proposed 2	0.01073	0.01615	0.001549	0.000532	0.1126

Table 7 PFI values for Example 2

Method	$\Delta\varepsilon$				
	5%	10%	15%	20%	25%
Proposed1	0.025	0.054	0.071	0.082	0.117
Proposed2	0.027	0.05	0.066	0.0823	0.106

5   Conclusion

A non-integer order controller is accomplished using a fractional IMC filter for a complex gas turbine system represented as a fractional order model. Performance measures of the proposed controller for nominal process model and perturbations have been compared with previous methods and found that it has better performance in various terms like error, reaching set point quickly, disturbance rejection, and control effort indicated by TV. Fragility analysis based on performance has been analyzed and discovered that it is non-fragile in nature. The controller designed for the fractional model with delay resulted in an improved performance with low errors and the two proposed controllers were found non-fragile for tuning parameter variation. The design of the FFIMC controller based on maximum sensitivity can be the future work ensuring robust performance.

References

1. Vilanova R, Visioli A (2012) PID control in the third millennium. Springer, London
2. Seborg DE, Edgar TF, Mellichamp DA (2004) Process dynamics and control, 2nd edn. John Wiley and Sons, New York
3. Yee SK, Milanovic JV, Hughes FM (2008) Overview and comparative analysis of gas turbine models for system stability studies. IEEE Trans Power Syst 23(1):108–118
4. Miller KS, Ross B (1993) An introduction to the fractional calculus and fractional differential equations. A Wiley-Inderscience Publication
5. Ruszewski A, Sobolewski A (2012) Comparative studies of control systems with fractional controllers. Electr Rev 88:204–208
6. Das S (2011) Functional fractional calculus. Springer Science & Business Media
7. Padula F, Visioli A (2011) Tuning rules for optimal PID and fractional-order PID controllers. J Process Control 21(1):69–81
8. Aguila-Camacho N, Ponce C (2018) Improving the control energy use for first order plus time delay plants with fractional proportional integral controllers: a preliminary analysis. In: 2018 IEEE international conference on automation/XXIII Congress of the Chilean Association of Automatic Control (ICA-ACCA). IEEE, Oct 2018, pp 1–6
9. Li X, Gao L (2021) Robust fractional-order PID tuning method for a plant with an uncertain parameter. Int J Control Autom Syst 19(3):1302–1310
10. Tepljakov A, Petlenkov E, Belikov J, Finajev J (2013) Fractional-order controller design and digital implementation using FOMCON toolbox for MATLAB. In: 2013 IEEE conference on computer aided control system design (CACSD). IEEE, Aug 2013, pp 340–345
11. Chen D, Seborg DE (2002) PI/PID controller design based on direct synthesis and disturbance rejection. Ind Eng Chem Res 41(19):4807–4822
12. Vanavil B, Anusha AVNL, Perumalsamy M, Rao AS (2014) Enhanced IMC-PID controller design with lead-lag filter for unstable and integrating processes with time delay. Chem Eng Commun 201(11):1468–1496
13. Gül O, Tan N (2019) Application of fractional-order voltage controller in building-integrated photovoltaic and wind turbine system. Meas Control 52(7–8):1145–1158
14. Aleksei T, Eduard P, Juri B (2012) A flexible MATLAB tool for optimal fractional-order PID controller design subject to specifications. In: Proceedings of the 31st Chinese control conference. IEEE, July 2012, pp 4698–4703

15. Chiluka SK, Ambati SR, Seepana M, Gara UBB (2020) A new VRFT approach for IMC-PID feedback-feedforward controller design based on robustness. IFAC-PapersOnLine 53(1):147–152
16. Vinopraba T, Sivakumaran N, Narayanan S, Radhakrishnan TK (2012) Design of internal model control based fractional order PID controller. J Control Theory Appl 10(3):297–302
17. Rivera DE, Morari M, Skogestad S (1986) Internal model control: PID controller design. Ind Eng Chem Process Des Dev 25(1):252–265
18. Padula F, Visioli A (2014) Advances in robust fractional control. Springer, London, UK
19. Sondhi S, Hote YV (2014) Fractional IMC design for fractional order gas turbine model. In: 2014 9th International conference on industrial and information systems (ICIIS). IEEE, Dec 2014, pp 1–5
20. Ranganayakulu R, Babu GUB (2021) Analytical design of fractional filter PID controller for improved performance of first order plus time delay plants. ICIC Express Letters 15(2):135–142
21. Alfaro VM, Vilanova R (2012) Fragility evaluation of PI and PID controllers tuning rules. In: PID control in the third millennium. Springer, London, pp 349–380
22. Rowen WI (1983) Simplified mathematical representations of heavy-duty gas turbines. J Eng Gas Turbines Power 105:865–869
23. Al-Hamdan QZ, Ebaid MS (2006) Modeling and simulation of a gas turbine engine for power generation. J Eng Gas Turbines Power 128:302–311
24. Lennart L (1999) System identification: theory for the user. PTR Prentice Hall, Upper Saddle River, NJ, 28
25. Nataraj PSV, Kalla R (2010) Computation of spectral sets for uncertain linear fractional-order systems. Commun Nonlinear Sci Numer Simul 15(4):946–955

Simulation and Design of 3 × 3 Rectenna for Wireless Power Transfer Using Microwave Frequency at 2.45 GHz

Ankit Singh, Nafees Ahamad, Abhay Chhetri, Abhay Mishra, and Neha Mishra

Abstract In this paper, we have presented a physical model of wireless power transfer (WPT) which is used to transmit electrical power without wires by using microwave energy. In this model, WPT is done by using a magnetron which transmits the microwaves at 2.45Ghz. Whereas, at the receiving end, we have simulated and designed a 3 × 3 rectenna which is used to convert the electromagnetic waves into DC electricity. This model significantly reduces the amount of power dissipation during transmission and can transmit up to 700 watts of electricity to a 90 cm distance. Also, the simulation results confirm the efficacy of the designed system. And in the future, this method would be one of the most cost-saving and reliable methods for transmitting power.

Keywords Wireless power transfer · Microwave energy · Magnetron · Rectenna

1 Introduction

The word wireless power transmission was introduced by Nikola Tesla in 1891. He showed us that the electrical power which is to be transmitted wirelessly is dependent upon the electrical conductivity of the material. In this era, power transmission is using distribution wires. However, as the power demand is increasing, the power generation is also and so the losses are increasing which occur generally during the generation and transmission of electrical power. If we can reduce the power dissipation during transmission and distribution, the overall efficiency of the system

A. Singh (✉) · N. Ahamad · A. Chhetri
Department of Electrical and Electronics and Communication Engineering, DIT University, Dehradun, India
e-mail: ankitsingh23jan@gmail.com

A. Mishra
Department of Mechanical Engineering, DIT University, Dehradun, India

N. Mishra
Depatment of Energy Science and Technology, Dr. A.P. J. Abdul Kalam Technical University, Lucknow, India

will increase which results in cost reduction. To reduce these losses, various scientists have developed unique techniques to transmit power wirelessly which means that there is no physical connection between the input and output mechanisms. There are three categories of WPT namely inductive coupling, EM waves, and magnetic resonant coupling [1]. Wireless power transfer of all kinds has its own set of properties and applications [2]. A transmitting antenna and an RF-DC conversion circuit are housed in the rectenna (Rectifying Antenna) [3]. One or two Schottky diodes and a DC output filter are often used in RF-DC conversion circuits. A resistive factor that reflects the input impedance of the system to be operated is usually used to load a rectenna. To consider this theory familiar to the new investigator's history, innovations and emerging technologies were examined for future advancement [4]. Microwave power transmission must transmit electromagnetic (EM) waves or radio frequency (RF) power over long distances before converting the RF power to direct current (dc) power via the rectenna. Microwave transmission RF needs to be received on separate MPT networks [5].

In this article, a physical model for wireless power transfer using microwave energy is designed. A magnetron that transmits microwave energy at 2.45 GHz is used along with a 3×3 rectenna to receive the electricity from this microwave. Simulated results, using MATLAB©, are compared with the practical data to show the effectiveness of the designed system. The organization of the paper is as follows: Sect. 2 discusses the basics of wireless power transfer; Sect. 3 covers the rectenna simulation and design for WPT; Sect. 4 illustrates the Microwave Transmitter; and experimental setup, result, and discussion are done in Sect. 5 followed by a conclusion.

2   Microwave Power Transmission

Microwaves, like radio waves, ultraviolet, X rays, and gamma rays, are electric sources of radiation [6]. There are various uses of microwaves, including networking and radar. This technology uses geosynchronous receiving and transmitting satellites to transfer high power from one emitter to a receiver in a direct line of sight. This technology makes for objects to acquire magnetron control from the base station. Microwave power gives energy transfer efficiency, but it is easily hard to concentrate the beam in a small area [5]. A typical diagram of energy transmission using the microwave is shown in Fig. 1. Energy is transferred in the form of microwaves and is received by the rectennas.

3   Rectenna Simulation and Design

The rectifying antenna (Rectenna) is one of the main components of the microwave transmission system. If such systems are inexpensive on land or at scattered sites, the converting efficiency between the microwave and the dc of the rectenna must be

Fig. 1 Microwave power transmission
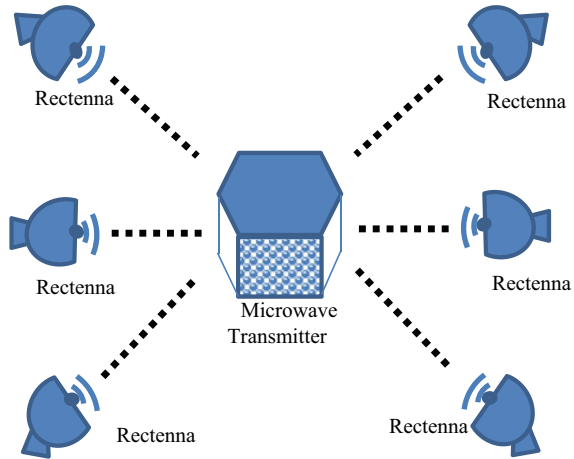
high. The Rectenna was originally designed in the sixties for 2.45 GHz [7]. Since then, conversion performance has grown from 38 to over 85% [8]. The major element behind improving diode and circuit construction efficiency is high-power input [9]. Efficiency in diode conversion is a key element of successful microwave transmission systems [10]. The rectenna has a type of GaAs Schottky barrier diode which transforms the incoming beam into usable dc. Computer methods may be used to adjust rectenna performance diode settings. The capacity to experimentally characterize the diode in high-power circumstances permits efficiency in the construction of the rectenna circuit. The diode may be examined using the microstrip test mount both in small and large signal conditions. Various operating frequencies of rectenna have been researched and investigated. The transmission components of the microwave power were generally 2.45 GHz and were updated to 5.8 GHz lately [11]. It has a modest aperture of 2.45 GHz. Both frequencies have relatively small air loss, low component availability, and excellent conversion efficiency. This study proposes a new rectenna of duality at 2.45 and 5.8 GHz simultaneously (ISM bands) [12].

3.1 Rectenna Simulation

Firstly, a rectenna is designed in MATLAB© by the Array Antenna designer toolbox which is shown in Fig. 2. This antenna patch has a dimension of 60mmx10mm and a gap of 10 mm. The center-to-center distance is chosen as 30 mm.

A dual-band configuration with a different polarization (orthogonal) for each band is considered here. The base squared patch is used to connect the side patches to operate (2.45 GHz ISM) in parallel with the Schottky diode.

Gain Pattern. The radiation field pattern of the above antenna at 2.45 GHz is drawn in Fig. 3. The amplitude of the gain is the function of angular direction.
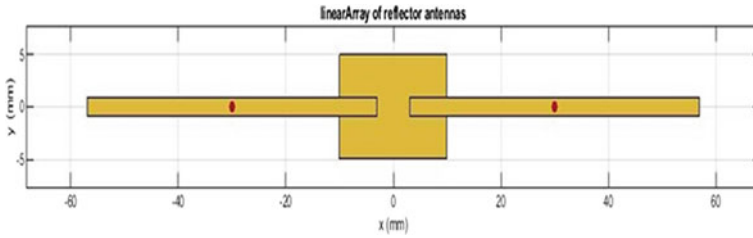
Fig. 2 Antenna patch design
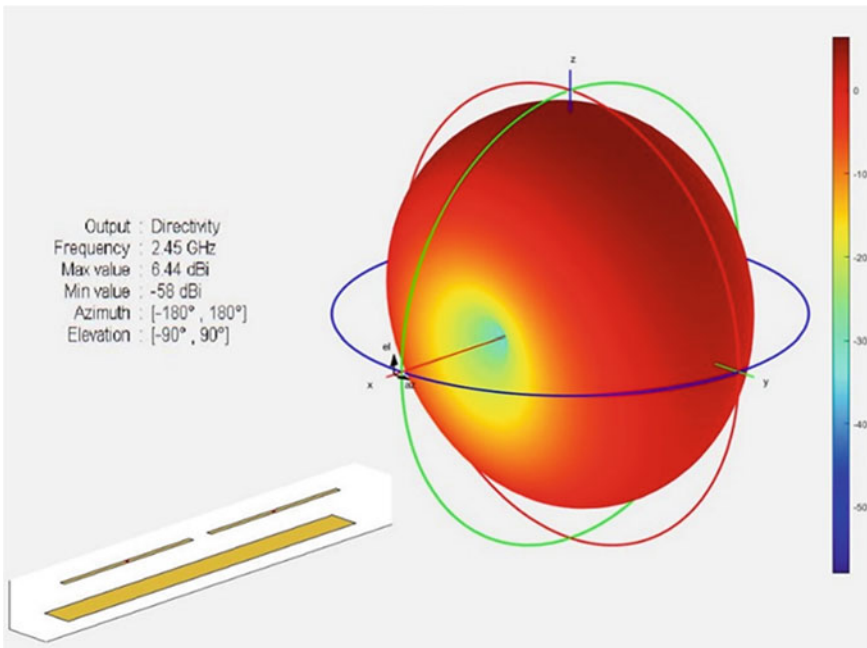
Fig. 3 Gain pattern of designed antenna at 2.45 GHz

In this figure, the minimum value of side lobe value is -58 dBi and its maximum value is 6.44dBi. In general, it is very challenging to achieve a maximum side lobe gain higher than 6 dB in antenna design.

Rectenna Impedance. The impedance of the rectenna indicates the power that is either excised or absorbed within the rectenna. The imaginary portion of the impedance shows power stored in the rectenna. The simulated resistance and reactance of the rectenna are found in Fig. 4 and their values are 25 and -18 ohms, respectively.

Total impedance is calculated as
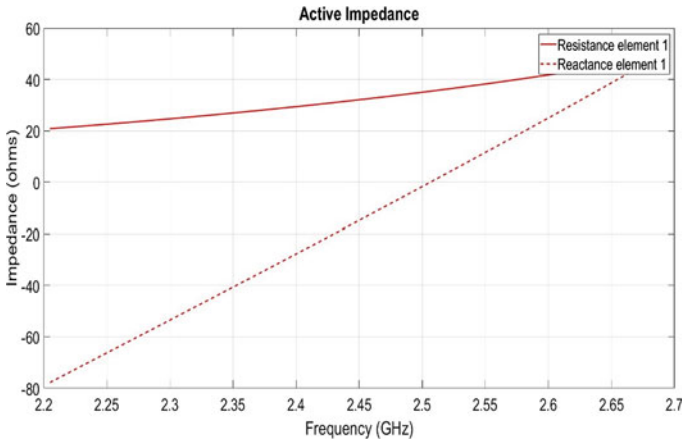
Fig. 4 Rectenna impedance

$$|z| = \sqrt{R^2 + X^2}\,\text{Ohm}$$

where

R Resistance of Rectenna = 25 Ω
X Reactance of Rectenna = −18 Ω

$$|z| = \sqrt{625 + 324}\,\text{Ohm}$$

$$|z| = 30.805\,\text{Ohm}$$

Azimuth and Elevation of Rectenna. The rotation of the entire antenna around a vertical axis refers to azimuth. It is the lateral angle you typically loosen the main mounting bracket and swing the entire dish around in a circle of 360°. The North is described as 0°, the East as 90°, the South as 180°, and the West as 270. The simulated radiation patterns in azimuth and elevation are shown in Figs. 5 and 6, respectively. Antenna Alignment Tool (AAT) is used for the Azimuth and Elevation setup of rectenna alignment.

S-parameters of Rectenna. The input and output connection ports (or terminals) in the power system are defined by S-parameters. In the case of two ports, for example, Port 1 and Port 2, S12 is the power transferred from Port 2 to Port 1. The power transferred from Port 1 to Port 2 is represented by S21. S11 represents that the reflected power Port 1 is trying to deliver to Port 2. The parameters S11 and S12 are simulated and shown in Fig. 7. These S-parameters of the simulated rectenna are as per the desired values (<0).

Fig. 5 Radiation pattern in
Azimuth of designed
rectenna
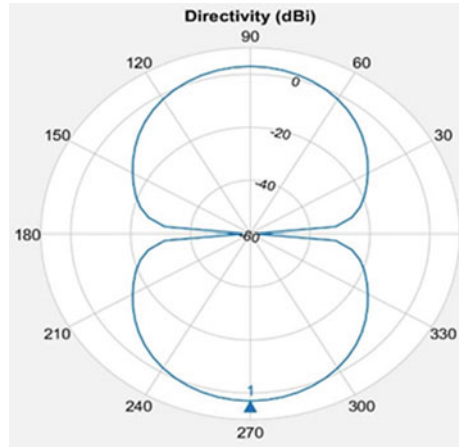
Fig. 6 Radiation pattern in
Elevation of designed
rectenna
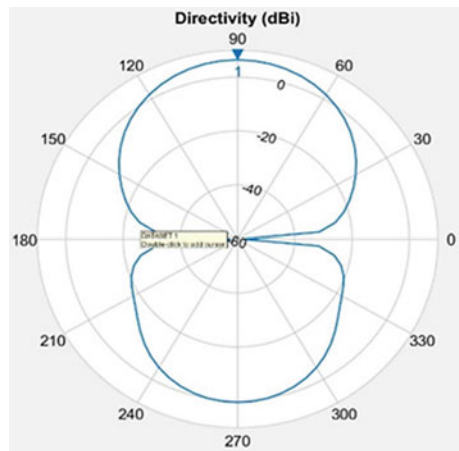
3.2   Rectenna Design

As the rectifier's aim is to directly convert RF energy from the microwave to DC
electricity, so, in designing the patches, Schottky diodes (1 N 5819 40V1A0041) are
used between the two side patches. Because Schottky diode has low voltage drop and
greater switching speed with less power consumption [11], the conversion efficiency
and voltage rise, which is extremely successful for low-power transformation, when
the input power goes from -20 to 0 dBm [7]. Now, using nine antenna patches,
a rectenna is designed which is shown in Fig. 8. In this rectenna, there are three
columns that are connected in parallel, and in each column, patches are connected
in series. The rectenna is shown in Fig. 8 and is printed on a copper plate using
ferric-chloride. The one-side patch is having 30 mm length and 10 mm width.
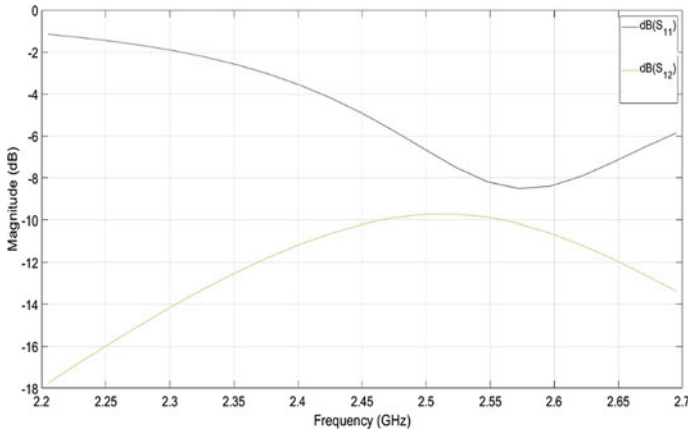
Fig. 7 S11 and S12 parameters of designed rectenna

Fig. 8 A 3 × 3 designed rectenna

4 Microwave Transmitter

A Galanz Magnetron, M24FA-210A, with a power input of 1100 W and output of about 700 W operating at 2.45 GHz frequency is used in the experimental setup. In the magnetron filament, the beginning temperature is 40 °C, the highest is 260 °C, and it is made of 42% of thallic bromide and 58% of thallium iodides. Magnetron contains a transformer along with an LC oscillation circuit and it provides an electromagnetic field to another coil (Figs. 9 and 10).

The electromagnetic waves go as radiation in cavity magnetron. In thermionic emission, there is one cathode and one filament, and the current flows from the

Fig. 9 Galanz Magnetron
M24FA-210A
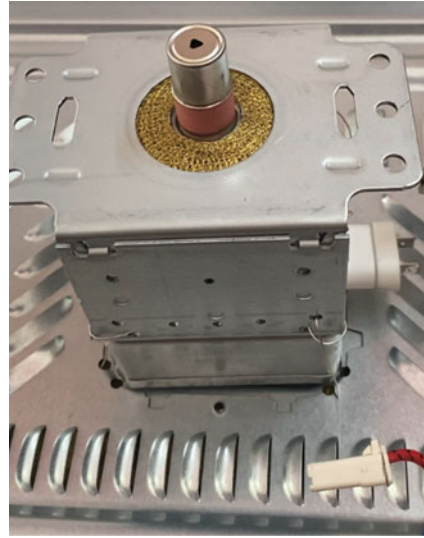
Fig. 10 Cover of
Magnetron's antenna

filament, producing heat and electrons, which return to the cathode, and there is an anode form coil in the magnetron cavity, so the electron flows to the anode [3]. The permanent magnet is then connected to the anode, and the magnetic field forces the electron to take a curved path, and the timing of the spending electron in the structure is known as hull magnetron [6]. The hull magnetic efficiency increases when we are using LC oscillators to create an oscillation anode in the cavity design [8]. The metal belt is meant to provide an anode and a second cathode for oscillation. The result is the radiation and the antenna, and the radiation is transmitted as a microwave [3].

Using the Planck-Einstein relation, the electric field generated by the magnetron is given as

$$E = h * f$$

where

h Planck's constant = 6.6260693*10^{-34}
f Operating frequency = 2.45 GHz

So, $E = 6.6260693*10^{-34} * 2.45 * 10^9$ eV

$$E = 1.62338679 * 10^{-24} \text{ eV}$$

Wavelength is calculated as

$$\lambda = \frac{C}{f}$$

where

C Velocity of light = 3 * 10^8 m/s

$$\lambda = \frac{3*10^8}{2.54 \times 10^9}$$

$$\lambda = 0.1224 \mu m$$

5   Experimental Setup, Result, and Discussion

The complete setup for microwave power transmission is shown in Fig. 11. It consists of a Galanz Magnetron (M24FA-210A) along with a 3 × 3 rectenna. It operates at a frequency of 2.45 GHz and an input of 700 watts, and the distance between magnetron and rectenna is about 120 cm.

At this distance, the voltage varies from 120 to 190 V, with an average voltage of about 176.25 V and a current of about 3.1 amperes, resulting in an output of about 546.3 W. The distance between the magnetron and rectenna is varied and different parameters are recorded which are shown in Table 1.

In this table, the distance between source and magnetron is mentioned along with generated voltage, current, and efficiency for the designed wireless power transmission. At the distance of 160 cm, the voltage and current are 50 V and 0.15 amps, respectively, resulting in the lowest efficiency of about 1.07% because most of the

Fig.11 The designed complete setup for microwave power transmission

Table 1 WPT parameters at different distances

S. No.	Distance (cm)	Voltage	Current	Power (W)	Efficiency (%)
1	60	190	3	570	81.42
2	90	188	2.98	560.24	80.03
3	100	174	2.86	497.64	71.09
4	110	182	2.7	507.6	72.51
5	120	185	2.45	453.25	64.75
6	130	175	1	175	25
7	140	150	0.5	75	10.714
8	150	100	0.25	25	3.57

radiation does not integrate into the rectenna. Now, when the distance is decreased to 60 cm, the obtained values of voltage, current, and efficiency are 190 V, 3 amps, and 81.42%. We obtain reasonable efficiency (80.03%) at a distance of around 90 cm. The graphical representation of WPT data is shown in Fig. 12. It can be concluded that between 60 and 90 cm distance, reasonable values of voltage, current, and efficiency are obtained.

6 Conclusion

In this paper, we have simulated and designed a 3×3 rectenna using Schottky diodes (1 N 5819 40V1A0041) for wireless power transfer (WPT) at a 2.45 GHz frequency. Rectenna gain pattern, S11, and S12 parameters are also simulated. A Galanz Magnetron, M24FA-210 of 700 watts output, is used with the designed

DISTANCE VS POWER-VOLTAGE-EFFICIENCY

Orange(Power), Blue (Voltage), Green (Efficiency)
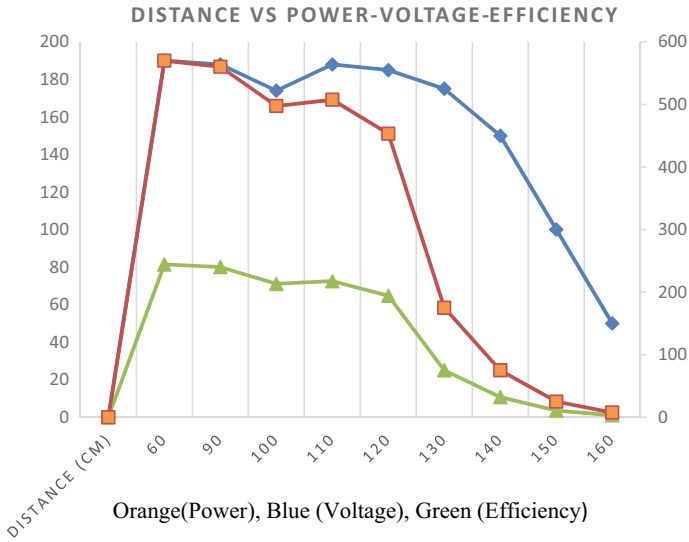
Fig. 12 Graphical representation of WPT parameters at different distances

rectenna for WPT. Here, in the experiment, the distance between Megatron and rectenna is varied from 60 to 160 cm and various parameters of WPT are recorded. The obtained voltage, current, and efficiency at a distance of 90 cm are reasonably good. Further, looking into the successful implementation of WTP using the 3 × 3 rectenna with around 80% efficiency, the rectenna may be modified to get higher efficiency at a larger distance.

References

1. Xie L, Shi Y, Hou YT, Lou A (2013) Wireless power transfer and applications to sensor networks. Wireless Commun IEEE 20(4):140,145
2. Pawade S, Nimje T, Diwase D (2012) Goodbye wires: approach to wireless power transmission. Int J Emerg Technol Adv Eng ISSN: 2250-2459
3. Collins GB (Ed) (1948) Microwave magnetrons. Collins GB [under the Supervision of the] office of scientific research and development, National Defense Research Committee. McGraw-hill Book Company
4. Brown WC (1984) The history of power transmission by radio waves. IEEE Trans. Microwave Theory Tech., vol MTT-32, pp 1230–1242
5. Brown WC, Triner JF (1982) Experimental thin-film, etched-circuit rectenna. In: IEEE MTT-S international microwave symposium digest, pp 185–187
6. Zhang H-L, Tang M-X, Song S-X (2005) Study on dual-frequency planarmonopole antennas. In: IEEE 2005 international symposium on microwave, antenna, propagation and EMC technologies for wireless communications, Beijing, China, pp 399–402
7. Kumar D, Chaudhary K (2018) High efficiency harmonic harvester rectenna for energy storage application. Int J Power Electron Dri Syst (IJPEDS) 9(1):252–259

8. Yang JW, Tsai TY, Chan CC, Sim CYD (2016) Small size circularly polarized patch antenna for 2.4 GHz WLAN applications. In: 2016 IEEE 5th Asia-Pacific conference on antennas and propagation (APCAP), pp 153–154

9. Dickinson RM (1980) Beamed microwave power transmitting and receiving subsystems radiation characteristics. Jet Propulsion Laboratory, California Institute of Technology, Pasadena, Publication pp 80–11

10. McSpadden JO, Chang K (1992) Suppression of rectenna harmonic radiation by a frequency selective surface. Presented at 1992 IEEEAPS/ URSI/NEM joint symposia, Chicago

11. Chuc DH, Duong BG (2015) Investigation of rectifier circuit configurations for microwave power transmission system operating at S Band. Int J Electr Comput Eng (IJECE) 5(5):967–974

12. Uysal S, Ng JWP (1999) A compact coplanar stripline lowpass filter. In: Asia–pacific microwave conference, vol 2, pp 307–310

The Correntropy Kalman Filter: A Robust Estimator for GPS Applications

P. Sirish Kumar and V. B. S. Srilatha Indira Dutt

Abstract India suffers from low satellite visibility. If any GPS receiver is operated in urban canyons, the visibility further reduces. These system constraints lead to many challenges in providing precise GPS position accuracy over the Indian subcontinent. Among all these factors, the predominant factors that significantly influence the receiver position accuracy are selecting a user/receiver position estimation algorithm. In this article, a novel kinematic positioning algorithm is proposed designated as the Correntropy Kalman Filter (CKF) that adopts the robust correntropy criterion as the optimality criterion instead of using the well-known minimum mean square error (MMSE). A novel fixed-point algorithm is then used to update the posterior estimates. A sufficient condition that guarantees the convergence of the fixed-point algorithm is also given. The proposed algorithm results are then compared with the Least Square Estimator (LSE), traditional Kalman Filter (KF), and Extended Kalman Filter (EKF) algorithms. Results prove that the proposed CKF algorithm exhibits significant improvement in position estimation compared to the other three recursive algorithms (i.e., LSE, KF, and EKF). And Statistical position Accuracy Measures (SAM) like DRMS, CEP, SEP, etc. are additionally used for performance evaluation of the proposed algorithm.

Keywords Correntropy kalman filter · Fixed-point algorithm · Minimum mean square error · SAM · DRMS · CEP · SEP

1 Introduction

Precise positioning and robust surveillance systems are essential to safeguard countries like India with a long geographic border and an extensive coastline. This has led

P. Sirish Kumar (✉)
Department of ECE, Aditya Institute of Technology and Management, Tekkali 532201, India
e-mail: sirishdg@gmail.com

V. B. S. Srilatha Indira Dutt
Department of ECE, GITAM (Deemed to be University), Visakhapatnam 530048, India

to the development and evolution of numerous such systems. Some of these systems' real-world applications include aviation, marine, mining, military, medicine, and agriculture. These systems can be segregated into two categories depending on the nature of operation and system coordinate origin. They are (i) Source Localization System and (ii) Global Positioning System. Source localization system is a relative positioning system used to find an unknown radiating source (like radar) close to a fixed point. Some examples of source localization systems are radar tracking, mobile unit tracking, and Unmanned Ariel Vehicle (UAV) tracking system [1].

On the other hand, the Global Positioning System (GPS) allows each receiving unit/object (like ship, aircraft, and handheld navigator) to find its position anywhere globally. Contrary to the source localization system, this system considers the earth's center as the positioning system coordinate origin. It uses the range of information obtained from the known location of the radiating sources or spacecraft to find the user/object position. The accuracy of source localization and Global Positioning System is affected by several factors such as measurement technique, environmental effects on the measurements, and positioning solution. Among these factors, identifying an optimal measurement technique is considered significant because an improper measurement technique provides a diverging solution [2]. For instance, a measurement technique that provides good results for a positioning application with air as a medium may not show the same performance in the underwater environment.

Nevertheless, the predominant factor in the usage of an appropriate ionospheric model and satellite configuration is the receiver position estimation algorithm, which is not accessible in the public domain because of trade-related and secrecy-oriented justification. Moreover, these may show optimal performance in mid-latitude (35°N-75°N) regions where the ionospheric effects are minimum coupled with improved satellite receiver geometry [3]. Hence, it is expedient to construct a proper navigational framework for precise positioning and a different GPS application that suits the Indian subcontinent (6 °N–36 °N latitude).

1.1 Motivating Applications

1. The investigations carried out on finding the optimal measurement technique for source localization systems are useful for precise position estimation of an unknown radiating source, mobile phone localization using base station signals, indoor positioning in mines, buildings, etc.
2. As per the ICAO, the currently used primary navigation systems for air traffic control will be replaced by GNSS/GPS-based navigation systems by the year 2017. The work presented in this article is aimed at strengthening the proposed GNSS/GPS-based navigation system.
3. The proposed CKF algorithm used in this article is useful for navigation and surveying in urban canyons and dense forest areas where the satellite visibility is low.

4. In this article, the proposed correntropy-based Kalman Filter (CKF) performance is evaluated with real-time pseudo-range GPS data and can be implemented straight away to carrier phase measurement-based critical GPS applications like surveying and farming.
5. The iterative algorithms presented in this article are used for receiver position estimation and can also solve various other optimization problems encountered in the control and automation industry. They are also useful for Geographic Information System (GIS) and accurate aerial mapping applications.

2 Related Work

The basic premises and system details of positioning systems (i.e., source localization and global positioning system), measurement techniques, GPS signal structure, GPS observables, and iterative and recursive navigational techniques covering linear algebra are essential. In [4], the authors have proposed a useful positioning method with two GNSS satellites in urban areas such that estimates of their position can be obtained with the least number of satellites. This method eliminates the problem by causing multi-path or non-line-of-sight (NLOS). In [5], the authors have discussed KF and EKF thoroughly. In general filtering, it is observed that in linear and Gaussian scenarios, the standard filter matches with KF, which is suitable for estimating state to minimize the error. KF is evaluated by comparing the raw data and a simple moving average filter. According to the results, the Kalman Filter reduces the variance in comparison with raw data [6]. In [7], the authors have proposed a method based on EKF for UAV position estimation and collision avoidance in outdoor search scenarios by utilizing received signal strength from an onboard module of communication. In [8], the authors have proposed a unique, fast, and accurate GPS positioning technique employing a Weighted Kalman Filter (WKF) that supported the variance estimation approach. In [9], the authors have proposed a modified EKF algorithm with delayed update (DU-EKF) for speeding up the convergence rate without the receiver's approximate initial position as required on normal EKF. This method, additionally, improves the accuracy of positioning and velocity measurement. In [10], the authors have analyzed linearised and extended Kalman filter and given critical remarks with geodetic navigation examples. In [11], the authors have analyzed the difference between the Extended Strong Tracking Filter (ESTF) and Extended Kalman Filter (EKF) in the content of carrier tracking estimation. In [12], the authors have proposed a hybrid algorithm based on multiple-decrease factor cubature Kalman filter (MDF-CKF) and random forest (RF) for GPS/INS systems during GPS outages. The MDF-CKF guarantees restricted filter divergence and increases robustness. In [13], the authors proposed a novel adaptive filter based on a nonlinear Cubature Kalman filter (CKF) and an estimate of variance–covariance components (VCE). CKF is used to solve nonlinearity, but VCE was used for the nonlinear system's real-time estimation noise correlation matrix. In [14–16], the authors have

proposed a novel Kalman filter based on MCC called MCKF. The optimality condition is decided by MCC instead of the traditional MMSE used in the regular Kalman filter suitable for Gaussian assumptions.

Literature survey unveils that to increase demand for an accurate positioning system, optimal measurement strategies and precise navigation solutions are necessary. For critical GPS applications like CAT-I aircraft landings, low variance in estimation is crucial besides the estimated position accuracy. Moreover, the number of onboard system parameters and dynamics needs to be analyzed while estimating the position.

3   Correntropy Kalman Filter (CKF)

3.1   Comparison Between Minimum Mean Square Error and Correntropy

If 'A' and 'B' are two random variables and $E = B - A$, MSE(A, B) is defined as $a = b$

$$\text{MSE}(A, B) = E\big[(A - B)^2\big] = \iint\limits_{a,b} (a - b)^2 = \int\limits_{e} e^2 J_{f_E}(e)\mathrm{d}e \qquad (1)$$

whereas, correntropy [17] is defined as

$$V(A, B) = E[k(A - B)] = \iint\limits_{a,b} k(a - b) f_{AB}(a, b)\mathrm{d}a\mathrm{d}b = \int\limits_{e} k(e) J_{f_E}(e)\mathrm{d}e \quad (2)$$

It may be noted that Minimum Mean Square Error (MMSE) is quadratic for the joint space having a valley accompanying the line $a = b$. Similarity measures how distinctive 'A' is from 'B' in terms of possibility; the intuitive explanation is that MMSE is also a similarity measure on the joint space. The improvement in values on the $a = b$ line corresponds to an improved contribution of samples well removed from the typical error distribution. However, this is also why other data patterns can make MMSE non-optimal, especially when the error dispersion owns outliers and is non-symmetric or has a non-zero value of the mean. It can be inferred that two similarity metrics assess similarity in different ways when comparing MMSE with correntropy: first, correntropy is local while MMSE is global. The global term implies that whole samples will consider the quantity of the similarity measure. The local name suggests the kernel function's value and quality along the ling $a = b$. Hence, correntropy of error may be utilized as a cost function for adaptive training of the system [18]. This is termed as Correntropy Criterion (CC). It perceives that

CC, having the advantage of being local, can be useful for situations in which the measurement noise has a non-zero mean, non-Gaussian pattern with large outliers.

3.2 Derivation of the Algorithm

Contemplate a linear system having the following state and measurement equations:

$$\vec{\mathbf{U}}_k = \boldsymbol{\Phi}_{k-1}\vec{\mathbf{U}}_{k-1} + \mathbf{q}_{k-1} \tag{3}$$

$$\vec{\mathbf{z}}_k = \mathbf{H}_k\vec{\mathbf{U}}_{\mathbf{k}} + \mathbf{r}_k \tag{4}$$

where $\vec{\mathbf{U}}_{\mathbf{k}}$ is the n-dimensional state vector, $\vec{\mathbf{z}}_{\mathbf{k}}$ is the m-dimensional measurement vector for instant 'k,' Φ is the system matrix, and $\mathbf{H}$ is the observation matrix; the mutually uncorrelated process noise is $\mathbf{q}_{\mathbf{k}-1}$ and measurement noise is $\mathbf{r}_{\mathbf{k}}$.

$$E\left[\mathbf{q}_{k-1}\mathbf{q}_{k-1}^T\right] = \mathbf{Q}_{k-1}, E\left[\mathbf{r}_k\mathbf{r}_k^T\right] = \mathbf{R}_k \tag{5}$$

Kalman filter has, in general, two steps: Predict and Update.

Predict: The prior mean and covariance matrices are given by

$$\vec{\mathbf{U}}_{k|k-1} = \boldsymbol{\Phi}_{k-1}\vec{\mathbf{U}}_{k-1|k-1} \tag{6}$$

$$\mathbf{P}_{k|k-1} = \boldsymbol{\Phi}_{k-1}\mathbf{P}_{k-1|k-1}\boldsymbol{\Phi}_{k-1}^T + \mathbf{Q}_{k-1} \tag{7}$$

Update: The gain of KF is computed as

$$\mathbf{K}_k = \mathbf{P}_{k|k-1}\mathbf{H}_k^T\left(\mathbf{H}_k\mathbf{P}_{k|k-1}\mathbf{H}_k^T + \mathbf{R}_k\right)^{-1} \tag{8}$$

It is observed that the posterior state is the prior state coupled with innovation weighted by the KF gain

$$\vec{\mathbf{U}}_{k|k} = \vec{\mathbf{U}}_{k|k-1} + \mathbf{K}_k\left(\vec{\mathbf{z}}_k - \mathbf{H}_k\vec{\mathbf{U}}_{k|k-1}\right) \tag{9}$$

Further, the posterior covariance is updated recursively

$$\mathbf{P}_{k|k} = (\mathbf{I} - \mathbf{K}_k\mathbf{H}_k)\mathbf{P}_{k|k-1}(\mathbf{I} - \mathbf{K}_k\mathbf{H}_k)^T + \mathbf{K}_k\mathbf{R}_k\mathbf{K}_k^T \tag{10}$$

For the linear model depicted in the above equations, we have

$$\begin{bmatrix} \widehat{\vec{U}}_{k|k-1} \\ \vec{z}_k \end{bmatrix} = \begin{bmatrix} \mathbf{I} \\ \mathbf{H}_k \end{bmatrix} \vec{U}_k + c_k \tag{11}$$

where I is $n \times n$ identity matrix, and c_k is $c_k = \begin{bmatrix} -\left(\vec{U}_k - \vec{U}_{k|k-1}\right) \\ \mathbf{r}_k \end{bmatrix}$,

with $E\left[c_k c_k^T\right] = \begin{bmatrix} \mathbf{P}_{k|k-1} & 0 \\ 0 & \mathbf{R}_k \end{bmatrix} = \begin{bmatrix} \mathbf{D}_{p_{k|k-1}} \mathbf{D}_{p_{k|k-1}}^T & 0 \\ 0 & \mathbf{D}_{r_k} \mathbf{D}_{r_k}^T \end{bmatrix} = \mathbf{D_k D}_k^T \tag{12}$

Here $\mathbf{D_k}$ may be available through Cholesky decomposition of $E\left[c_k c_k^T\right]$. Multiplication of both sides of Eq. (11) by $\mathbf{D}_k^{-1}$

$$\mathbf{Y}_k = \mathbf{W}_k \vec{U}_k + \mathbf{e}_k \tag{13}$$

Here $\mathbf{Y}_k = \mathbf{D}_k^{-1} \begin{bmatrix} \widehat{\vec{U}}_{k|k-1} \\ \vec{z}_k \end{bmatrix}$, $\mathbf{W}_k = \mathbf{D}_k^{-1} \begin{bmatrix} \mathbf{I} \\ \mathbf{H}_k \end{bmatrix}$, $\mathbf{e}_k = \mathbf{D}_k^{-1} c_k$, since $E\left[\mathbf{e}_k \mathbf{e}_k^T\right] = \mathbf{I}$.

where $\mathbf{e}_k$ is a white residual error. Here, the following CC-based cost function is proposed:

$$M_N\left(\vec{U}_k\right) = \frac{1}{N} \sum_{i=1}^{N} G_\Omega\left(y_{i_k} - \mathbf{w}_{i_k} \vec{U}_k\right) \tag{14}$$

where y_{i_k} is the ith element of $\mathbf{Y_k}$, w_{i_k} is the ith row of $\mathbf{W}_k$ & $N = n + m$ is the dimension of $\mathbf{Y_k}$.

For *CC*, the optimal estimation of $\vec{U}_k$ is

$$\widehat{\vec{U}}_k = \arg\max_{\vec{U}_k} M_N\left(\vec{U}_k\right) = \arg\max_{\vec{U}_k} \sum_{i=1}^{N} G_\Omega\left(e_{i_k}\right) \tag{15}$$

where e_{i_k} is the ith element of $\mathbf{e}_k$:

$$e_{i_k} = y_{i_k} - \mathbf{w}_{i_k} \vec{U}_k \tag{16}$$

Thus, the optimal solution can be made available by solving

$$\frac{\partial M_N\left(\vec{U}_k\right)}{\partial \vec{U}_k} = \sum_{i=1}^{N} \left[G_\Omega\left(e_{i_k} w_{i_k}^T\right)\left(y_{i_k} - \mathbf{w}_{i_k} \vec{U}_k\right)\right] = 0 \tag{17}$$

It follows easily that

$$\vec{\mathbf{U}}_k = \left(\sum_{i=1}^{N} \left[G_\Omega(e_{i_k} \mathbf{w}_{i_k}^T \mathbf{w}_{i_k}) \right] \right)^{-1} \times \left(\sum_{i=1}^{N} \left[G_\Omega(e_{i_k} \mathbf{w}_{i_k}^T y_{i_k}) \right] \right) \tag{18}$$

As $e_i = y_{i_k} - \mathbf{w}_{\mathbf{i}_k} \vec{\mathbf{U}}_k$, Eq. (18)'s optimum solution is a fixed-point equation of $\vec{\mathbf{U}}_k$. It can be restated as

$$\vec{\mathbf{U}}_k = \mathbf{f_a}\left(\vec{\mathbf{U}}_k\right) \tag{19}$$

with

$$\mathbf{f_a}\left(\vec{\mathbf{U}}_k\right) = \left(\sum_{i=1}^{N} \left[G_\Omega\left(y_{i_k} - \mathbf{w}_{i_k} \vec{\mathbf{U}}_k\right) \mathbf{w}_{i_k}^T \mathbf{w}_{i_k} \right] \right)^{-1} \times \left(\sum_{i=1}^{N} \left[G_\Omega\left(y_{i_k} - \mathbf{w}_{i_k} \vec{\mathbf{U}}_k\right) \mathbf{w}_{i_k}^T y_{i_k} \right] \right)$$

At this stage, a fixed-point iterative technique can be quickly made available as

$$\vec{\mathbf{U}}_{k_{n+1}} = \mathbf{f_a}\left(\vec{\mathbf{U}}_{k_n}\right) \tag{20}$$

where $\vec{\mathbf{U}}_{k_n}$ gives the solution against fixed iteration 'n'. The fixed-point Eq. (18) can be rewritten as

$$\vec{\mathbf{U}}_k = \left(\mathbf{W_k^T X_k W_k} \right)^{-1} \mathbf{W_k^T X_k Y_k} \tag{21}$$

where $\mathbf{X}_k = \begin{bmatrix} \mathbf{X}_k^a & 0 \\ 0 & \mathbf{X}_k^b \end{bmatrix}$, with

$$\mathbf{X}_k^a = \mathrm{diag}\big(G_\Omega\big((e_{r_{1_k}}), \cdots G_\Omega(e_{r_{n_k}})\big)\big),$$
$$\mathbf{X}_k^b = \mathrm{diag}\big(G_\Omega\big((e_{r_{n+1_k}}), \cdots G_\Omega(e_{r_{n+m_k}})\big)\big)$$

Equation (21) can be further rewritten as per the following:

$$\vec{\mathbf{U}}_k = \widehat{\vec{\mathbf{U}}}_{k|k-1} + \mathbf{K}_k\left(\vec{z}_k - \mathbf{H}_k \widehat{\vec{\mathbf{U}}}_{k|k-1}\right) \tag{22}$$

Here

$$\begin{cases} \bar{\mathbf{K}}_k = \bar{\mathbf{P}}_{k|k-1} \mathbf{H}_k^T \left(\mathbf{H}_k \bar{\mathbf{P}}_{k|k-1} \mathbf{H}_k^T \bar{\mathbf{R}}_k \right)^{-1} \\ \bar{\mathbf{P}}_{k|k-1} = \mathbf{D}_{p^{k|k-1}} \mathbf{X}_k^{a^{-1}} \mathbf{D}_{p^{k|k-1}}^T \\ \bar{\mathbf{R}}_k = \mathbf{D}_{r_k} \mathbf{X}_k^{b^{-1}} \mathbf{D}_{r_k}^T \end{cases} \tag{23}$$

3.3   Steps in Computing Correntropy Kalman Filter

Equation (22) is a fixed-point type for $\vec{\mathbf{U}}_k$ as $\overline{\mathbf{K}}_k$ is dependent on $\overline{\mathbf{P}}_{k|k-1}$ and $\overline{\mathbf{R}}_k$, which are related to $\vec{\mathbf{U}}_k$ via $\mathbf{X}_k^a$ and $\mathbf{X}_k^b$. Hence further, the optimal solution of Eq. (22) also depends on the prior estimate $\vec{\mathbf{U}}_{k|k-1}$, which can be computed by Eq. (6) utilizing the latest estimate $\vec{\mathbf{U}}_{k-1|k-1}$. From the above assumptions, the proposed CKF algorithm can be summed up as follows:

Step 1. A proper kernel bandwidth $\boldsymbol{\Omega}$ is selected along with a positive number $\boldsymbol{\xi}$. An initial estimate $\widehat{\vec{\mathbf{U}}}_{0|0}$ and an initial covariance matrix $\mathbf{P}_{0|0}$ are assumed with $k = 1$.

Step 2. Equations (6) and (7) are used to obtain $\widehat{\vec{\mathbf{U}}}_{k|k-1}$ and $\mathbf{P}_{k|k-1}$, and the Cholesky decomposition is used to obtain $\mathbf{D}_{p_{k|k-1}}$.

Step 3. It is assumed that $n = 1$ and $\widehat{\vec{\mathbf{U}}}_{k|k_n} = \widehat{\vec{\mathbf{U}}}_{k|k-1}$, where $\widehat{\vec{\mathbf{U}}}_{k|k_n}$ represents the estimated state at iteration 'n' of the fixed-point type.

Step 4. Equations (24)–(30) are used to compute $\widehat{\vec{\mathbf{U}}}_{k|k_n}$

$$\widehat{\vec{\mathbf{U}}}_{k|k_n} = \widehat{\vec{\mathbf{U}}}_{k|k-1} + \overline{\mathbf{K}}_k\left(\vec{\mathbf{z}}_k - \mathbf{H}_k\widehat{\vec{\mathbf{U}}}_{k|k-1}\right) \tag{24}$$

with

$$\overline{\mathbf{K}}_k = \tilde{\mathbf{P}}_{k|k-1}\mathbf{H}_k^T\left(\mathbf{H}_k\tilde{\mathbf{P}}_{k|k-1}\mathbf{H}_k^T + \tilde{\mathbf{R}}_k\right)^{-1} \tag{25}$$

$$\tilde{\mathbf{P}}_{k|k-1} = \mathbf{D}_{p^{k|k-1}}\tilde{\mathbf{X}}_k^{a^{-1}}\mathbf{D}_{p^{k|k-1}}^T \tag{26}$$

$$\tilde{\mathbf{R}}_k = D_{r_k}\tilde{\mathbf{X}}_k^{b^{-1}}\mathbf{D}_{r_k}^T \tag{27}$$

$$\tilde{\mathbf{X}}_k^a = \text{diag}\big(G_\Omega\big((\tilde{e}_{1_k}), \cdots\cdots\cdots G_\Omega\big(\tilde{e}_{n_k}\big)\big)\big) \tag{28}$$

$$\tilde{\mathbf{X}}_k^b = \text{diag}\big(G_\Omega\big((\tilde{e}_{n+1_k}), \cdots\cdots\cdots G_\Omega\big(\tilde{e}_{n+m_k}\big)\big)\big) \tag{29}$$

$$\tilde{e}_{i_k} = y_{i_k} - \mathbf{w}_{i_k}\widehat{\vec{\mathbf{U}}}_{k|k_{n-1}} \tag{30}$$

Step 5. The estimation of the current step and the last step is compared. For Eq. (31) to be valid, set $\widehat{\vec{\mathbf{U}}}_{k|k} = \widehat{\vec{\mathbf{U}}}_{k|k_n}$ and proceed to step 6. Otherwise, $n + 1 \rightarrow n$, and go back to step 4.

$$\frac{\widehat{\mathbf{U}}_{k|k_n} - \widehat{\mathbf{U}}_{k|k_{n-1}}}{\widehat{\mathbf{U}}_{k|k_{n-1}}} \leq \xi \tag{31}$$

Step 6. The posterior covariance matrix is updated by Eq. (32), $k + 1 \rightarrow k$, and the return is made to step 2.

$$\mathbf{P}_{k|k} = \left(I - \tilde{\mathbf{K}}_k \mathbf{H}_k\right) \mathbf{P}_{k|k-1} \left(I - \tilde{\mathbf{K}}_k \mathbf{H}_k\right)^T + \tilde{\mathbf{K}}_k \mathbf{R}_k \tilde{\mathbf{K}}_k^T \tag{32}$$

The CKF algorithm reacts to Eqs. (6), (7), (24)–(30), and (32).

4 Results and Discussion

In this article, four algorithms (LSE, KF, EKF, and CKF) are examined, and the obtained results are analyzed. The data used to evaluate the navigation algorithms' performance concerning the IISc, Bangalore, GPS receiver is collected from the Scripps Orbit and Permanent Array Centre (SOPAC) database. The collected data is processed and used in receiver position estimation. The true receiver position coordinates are $X = 1,337,936.309$ m, $Y = 6,070,317.116$ m, and $Z = 1,427,876.908$ m. These values conform to the GPS receiver position surveyed at IISc, Bangalore, India. The GPS receiver position is estimated using the proposed Correntropy Kalman Filter (CKF), and error analysis is carried out.

Table 1 compares the error in estimated mean position over an hour due to the LSE, KF, EKF, and CKF algorithms (in X, Y, and Z-directions). The observed minimum and maximum error in position estimate corresponding to the four algorithms are shown in the following table with bold numbers along with its mean.

Figure 1a represents the mean position error over an hour compared in receiver X, Y, and Z-directions reported with the four algorithms (LSE, KF, EKF, and CKF) in a two-dimensional surface. Similarly, Fig. 1b represents the mean position error comparison over an hour among the four algorithms in a three-dimensional surface which are tabulated in Table 1.

From the above figures, it is observed that the receiver's estimated mean positions over an hour due to the CKF algorithm seem close to the true receiver position (surveyed position) with less variance in contrast to the other three algorithms (i.e., LSE, KF, and EKF).

4.1 Statistical Error Characterization in the One-Dimensional Surface

A normal or Gaussian curve of a probability distribution is produced by computing the 22-h data statistics overlaid in Fig. 2a–l. These curves simultaneously exhibit
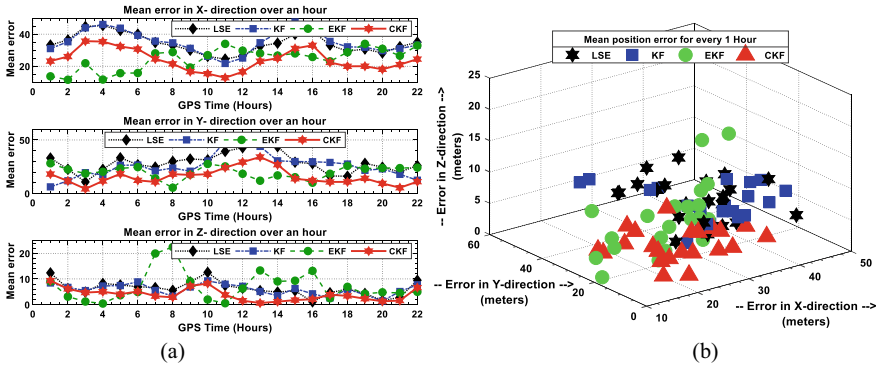
Table 1 Mean position error comparison among four algorithms

GPS time (h)	Mean position error (in meters)											
	X-direction				Y-direction				Z-direction			
	LSE	KF	EKF	CKF	LSE	KF	EKF	CKF	LSE	KF	EKF	CKF
00–01	33.2	31.0	13.7	23.2	33.1	**6.1**	**28.2**	18.1	12.4	8.4	9.0	**9.4**
01–02	36.4	35.3	**11.6**	26.0	22.6	11.8	22.4	11.6	6.2	6.7	3.1	6.1
02–03	44.8	43.9	21.8	**35.6**	**10.7**	19.4	18.6	**4.2**	4.9	5.5	1.2	4.7
03–04	**45.4**	46.0	11.7	35.4	22.6	17.3	20.3	11.7	8.2	7.3	**0.4**	5.0
04–05	42.3	43.7	15.7	32.3	33.3	26.3	23.4	18.3	7.6	7.4	3.6	4.1
05–06	40.0	39.2	15.8	30.7	26.8	26.6	24.6	12.2	7.0	8.9	4.9	5.1
06–07	34.7	35.6	28.0	24.5	24.7	21.1	14.1	10.7	6.6	5.5	19.9	3.3
07–08	33.0	34.6	28.8	21.5	30.0	23.7	**5.4**	18.0	5.6	3.3	**22.4**	2.8
08–09	30.0	31.1	19.2	16.6	32.1	20.8	17.7	17.3	8.8	6.9	9.0	7.2
09–10	26.1	26.2	26.9	15.4	31.5	30.4	27.6	18.0	**12.6**	**9.3**	2.0	8.2
10–11	**24.5**	**21.7**	33.9	**12.8**	39.3	48.5	25.3	24.1	7.4	8.0	0.5	3.8
11–12	26.5	25.1	29.7	16.5	42.8	**51.4**	18.4	29.3	6.4	7.2	6.3	1.5
12–13	32.6	34.7	28.0	23.1	**47.6**	44.0	11.9	**34.1**	5.5	5.1	13.3	**0.6**
13–14	34.4	40.9	26.6	25.0	43.7	30.5	16.8	26.9	4.9	3.5	9.0	1.1
14–15	39.9	**47.6**	28.0	31.1	29.2	29.8	15.2	13.7	5.4	6.3	9.3	1.8
15–16	41.8	45.0	25.7	33.0	27.9	29.6	10.0	12.1	**1.1**	4.2	13.1	2.1
16–17	33.2	35.5	23.0	22.3	16.3	29.0	18.4	10.7	4.6	2.6	2.5	3.9
17–18	29.4	32.1	28.7	19.9	16.1	27.5	25.8	10.8	6.1	6.0	6.9	3.4
18–19	30.7	31.8	**34.0**	20.0	28.1	21.6	23.2	14.1	4.3	3.9	4.2	2.3
19–20	28.3	29.7	30.9	18.1	24.6	23.0	23.8	9.4	1.6	**1.4**	4.8	1.3
20–21	32.2	31.0	26.5	21.0	20.0	17.9	23.7	5.3	2.8	5.1	4.5	1.6
21–22	35.0	33.2	32.9	24.4	26.0	12.4	24.2	11.0	9.5	7.7	5.0	6.6
Mean	**34.3**	**35.2**	**24.6**	**24.0**	**28.6**	**25.9**	**20.0**	**15.5**	**6.3**	**5.9**	**7.0**	**3.9**

what a normal distribution seems and ease graphically representing the underlying truth. It is seen that there is a valid bell-shaped curve (Red, Blue, and Black color bell-shaped curves) on the figures (Fig. 2a–l). It is also evident whether GPS errors obey the normal distribution or the Gaussian one.

Tables 2, 3 and 4 exhibit the histogram's statistical error distribution that is plotted in Fig. 2a–d in X-direction, Fig. 2e–h in Y-direction, Fig. 2i–l in Z-direction using four algorithms (LSE, KF, EKF, and CKF), respectively, along with the obtained minimum and maximum error. The estimated position error for 22 h of data (in X, Y, and Z-directions) is partitioned into the number of bins, and these bins accommodate a specified range (based on the minimum and maximum error). The total estimated position error points are lying in those bins according to their error value.

Fig. 1 Mean position error comparison in **a**. Two-dimensional surface and **b**. Three-dimensional surface
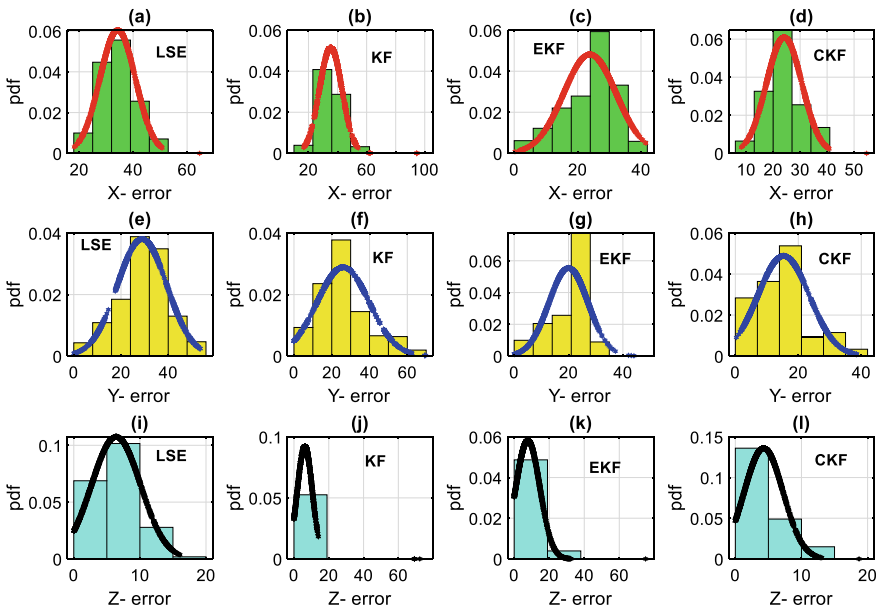
Fig. 2 Gaussian distribution of position error in the one-dimensional surface using four algorithms in *X, Y, Z*-directions

It is noted from Table 2 concerning *X*-direction that mostly 88.1% of the position errors lie within 25–46 m due to LSE, 90.4% of the errors are within 23–49 m due to KF, 72.3% of the errors are within 18–36 m due to EKF, and 86% of the errors are within 13–34 m due to CKF, respectively.

It is noted from Table 3 concerning *Y*-direction that mostly 73.7% of the errors lie within 16–40 m due to LSE, 75.8% of the errors are within 10–40 m due to KF,

Table 2 Statistical distribution of position error in *X*-direction

X-direction

LSE		KF		EKF		CKF	
Bin limits: [18 67]		Bin limits: [9 97]		Bin limits: [0 42]		Bin limits: [6 55]	
No. of bins: 7		No. of bins: 7		No. of bins: 7		No. of bins: 7	
Bin width: 7 m		Bin width: 13 m		Bin width: 6 m		Bin width: 7 m	
Bin edge (m)	No. of error points	Bin edge (m)	No. of error points	Bin edge (m)	No. of error points	Bin edge (m)	No. of error points
[18 25]	181	[10 23]	132	[0 6]	96	[6 13]	117
[25 32]	813	[23 36]	1379	[6 12]	190	[13 20]	593
[32 39]	1011	[36 49]	971	[12 18]	344	[20 27]	1177
[39 46]	465	[49 62]	109	[18 24]	435	[27 34]	464
[46 53]	128	[62 75]	4	[24 30]	925	[34 41]	247
[53 60]	0	[75 88]	0	[30 36]	518	[41 48]	0
[60 67]	1	[88 101]	7	[36 42]	91	[48 55]	1
[25 46] → 88.1%		[23 49] → 90.4%		[18 36] → 72.3%		[13 34] → 86%	
X_{err_min}: 18.19 m		X_{err_min}: 16.66 m		X_{err_min}: 0.24 m		X_{err_min}: 8.19 m	
X_{err_max}: 64.64 m		X_{err_max}: 94.51 m		X_{err_max}: 41.49 m		X_{err_max}: 54.64 m	

Table 3 Statistical distribution of position error in *Y*-direction

Y-direction

LSE		KF		EKF		CKF	
Bin limits: [0 56]		Bin limits: [0 70]		Bin limits: [0 49]		Bin limits: [0 42]	
No. of bins: 7		No. of bins: 7		No. of bins: 7		No. of bins: 6	
Bin width: 8 m		Bin width: 10 m		Bin width: 7 m		Bin width: 7 m	
Bin edge (m)	No. of error points	Bin edge (m)	No. of error points	Bin edge (m)	No. of error points	Bin edge (m)	No. of error points
[0 8]	90	[0 10]	242	[0 7]	181	[0 7]	516
[8 16]	226	[10 20]	612	[7 14]	373	[7 14]	662
[16 24]	384	[20 30]	981	[14 21]	467	[14 21]	978
[24 32]	807	[30 40]	376	[21 28]	1409	[21 28]	173
[32 40]	725	[40 50]	172	[28 35]	162	[28 35]	209
[40 48]	270	[50 60]	165	[35 42]	4	[35 42]	61
[48 56]	97	[60 70]	51	[42 49]	3	–	–
[16 40] → 73.7%		[10 40] → 75.8%		[7 28] → 86.5%		[0 21] → 83%	
Y_{err_min}: 0.04 m		Y_{err_min}: 0.05 m		Y_{err_min}: 0.03 m		Y_{err_min}: 0.34 m	
Y_{err_max}: 53.51 m		Y_{err_max}: 69.75 m		Y_{err_max}: 44.06 m		Y_{err_max}: 38.51 m	

Table 4 Statistical distribution of position error in Z-direction

Z-direction							
LSE		KF		EKF		CKF	
Bin limits: [0 20]		Bin limits: [0 76]		Bin limits: [0 76]		Bin limits: [0 20]	
No. of bins: 4		No. of bins: 4		No. of bins: 4		No. of bins: 4	
Bin width: 5 m		Bin width: 19 m		Bin width: 19 m		Bin width: 5 m	
Bin edge (m)	No. of error points	Bin edge (m)	No. of error points	Bin edge (m)	No. of error points	Bin edge (m)	No. of error points
[0 5]	894	[0 19]	2594	[0 19]	2404	[0 5]	1768
[5 10]	1320	[19 38]	0	[19 38]	194	[5 10]	636
[10 15]	361	[38 57]	0	[38 57]	0	[10 15]	194
[15 20]	24	[57 76]	5	[57 76]	1	[15 20]	1
[0 15] → 99.1%		[0 19] → 99.8%		[0 19] → 92.5%		[0 10] → 92.5%	
Z_{err_min}: 0.02 m		Z_{err_min}: 0.01 m		Z_{err_min}: 0.0 m		Z_{err_min}: 0.0 m	
Z_{err_max}: 16.08 m		Z_{err_max}: 72.33 m		Z_{err_max}: 75.0 m		Z_{err_max}: 18.71 m	

86.5% of the errors are within 7–28 m due to EKF, and 83% of the errors are within 0–21 m due to CKF, respectively.

It is noted from Table 4 concerning Z-direction that mostly 99.1% of the errors lie within 0–15 m due to LSE, 99.8% of the errors are within 0–19 m due to KF, 92.5% of the errors are within 0–19 m due to EKF, and 92.5% of the errors are within 0–10 m due to CKF, respectively.

4.2 Statistical Position Accuracy Measures (SAM)

Whenever you notice the position of a GPS receiver over time, it will be identified. Should these moving positions be put on a graph, it gives a distribution map. The investigation of this specific distribution depends on the characteristics you want to obtain. The position is typically three-dimensional, but not everyone considers three-dimensional accuracy. Somebody would require horizontal accuracy; another would need vertical accuracy. The obtained statistical position accuracy metrics[a] in the 2-D and 3-D surface due to the four algorithms are provided in Table 5 and graphically described in Figs. 3 and 4, respectively.

Figure 3 compares the horizontal position error (X and Y) scatter plot with CEP among the four algorithms. Further, Fig. 4 compares the horizontal and vertical position error (X, Y, and Z) scatter plot in a three-dimensional surface with SEP among the four algorithms.
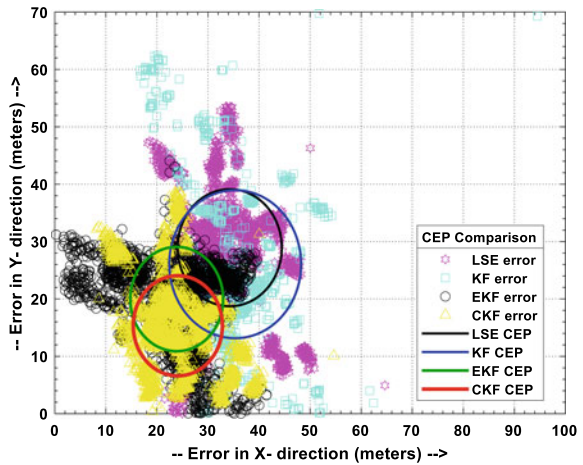
It is evident that from Fig. 3 the CEP circle (Red color solid line circle) due to the CKF algorithm is miniature and seems closer to the origin than the other three

Table 5 Statistical position accuracy measures[a] (SAM) comparison in a 2-D and 3-D surface

Statistical position accuracy measure (SAM)		Probability (%)	(In meters)			
			LSE	KF	EKF	CKF
2-D	DRMS	65	12.39	15.83	10.97	10.46
	2DRMS	95–98	24.78	31.66	21.93	20.93
	CEP	50	10.20	12.90	9.09	8.73
	R95	95	21.21	26.82	18.92	18.15
3-D	SEP	50	10.61	13.20	11.38	9.00
	MRSE	61	12.94	16.41	12.93	10.87
	SAS	90	17.33	21.56	18.59	14.69
	SAS	99	23.34	29.04	25.04	19.79

[a]The statistical position accuracy measures mentioned in the above table are calculated for the entire data range after neglecting other correctable error sources

Fig. 3 Horizontal position error scatter plot with CEP among four algorithms

Fig. 4 3-D position error scatter plot with SEP among four algorithms
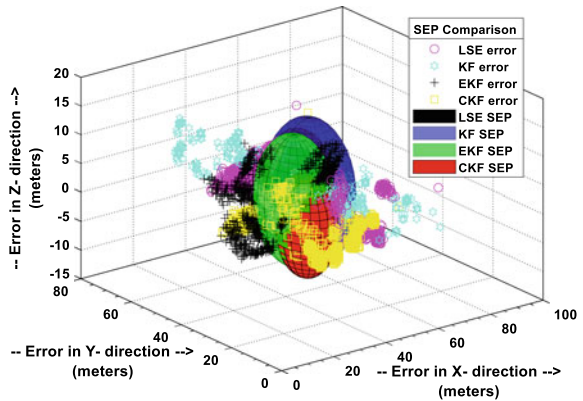
algorithms (LSE, KF, and EKF). Similarly, it is evident that from Fig. 4 the SEP sphere (Red color sphere) due to the CKF algorithm is miniature and seems closer to the origin than the other three algorithms (LSE, KF, and EKF).

5 Conclusion

A precise navigation algorithm is always essential under low satellite visibility conditions to provide the user with an accurate position on or above the earth's surface. Therefore, the Correntropy Kalman Filter (CKF) algorithm is developed, and the performance is compared with the LSE, KF, and EKF algorithms. The four algorithms' overall performance, i.e., LSE, KF, EKF, and CKF, is validated with real-time data collected from a dual-frequency GPS receiver located in India's southern region. For performance evaluation, Statistical position Accuracy Measures (SAM) such as DRMS, CEP, MRSE, and SEP are used. The results show that the position estimated with CKF is more accurate and precise among these four algorithms. For instance, the difference in CEP and SEP values between CKF and KF is 4.17 m and 4.2 m, respectively. Hence, with due consideration of all correctable errors, it is concluded that the proposed CKF algorithm provides a significant improvement in position accuracy. The proposed algorithm is only tested for the Space-Based Augmentation System (SBAS). It can also be tested for Ground-Based Augmentation System (GBAS) and Local Area Augmentation System (LAAS) that provide the CAT-II and III aircraft landing requirements.

References

1. Oxely A (2017) Uncertainties in GPS positioning-a mathematical discourse. Academic Press, Elsevier. ISBN: 978-0-12-809594-2
2. Anjasmara IM, Pratomo DG, Wahyu Ristanto K (2019) Accuracy analysis of GNSS (GPS, GLONASS and BEIDOU) Obsevation for positioning. E3S web of conferences, vol 94 EDP Sciences
3. Santra A et al (2019) Precision of satellite based navigation position solution: a review using NavIC data. J Inf Optim Sci 40(8):1683–1691
4. Hatano H, Kitani T, Fujii M, Watanabe Y, Onishi H (2013) A helpful positioning method with two GNSS satellites in Urban area. MOBILITY 2013: The third international conference on mobile services, resources, and Users, pp 41–46. ISBN: 978-1-61208-313-1
5. Ribeiro MI (2004) Kalman and extended kalman filters: concept, derivation and properties. Inst Syst Rob 43:46
6. Eliasson M (2014) Kalman filter approach to reduce position error for pedestrian applications in areas of bad GPS reception. Bachelor's Programme in computing science, UMEA University
7. Luo C, McClean SI, Parr G, Teacy L, De Nardi R (2013) UAV position estimation and collision avoidance using the extended kalman filter. IEEE Trans Veh Technol 62(6):2749–2762. https://doi.org/10.1109/TVT.2013.2243480,July
8. Shokri S, Rahemi N, Mosavi MR (2020) Improving GPS positioning accuracy using weighted kalman filter and variance estimation methods. CEAS Aeronaut J 11(2):515–527

9. Hao Y, Xu A, Sui X, Wang Y (2018) A modified extended kalman filter for a two-antenna GPS/INS vehicular navigation system. Sensors 18:3809. https://doi.org/10.3390/s18113809
10. Jwo D-J, Cho T-S (2010) Critical remarks on the linearised and extended Kalman filters with geodetic navigation examples. Measurement 43(9):1077–1089
11. Ge Q, Shao T, Chen S, Wen C (2017) Carrier tracking estimation analysis by using the extended strong tracking filtering. In: IEEE transactions on industrial electronics, 64(2):1415–1424. https://doi.org/10.1109/TIE.2016.2610403
12. Zhang Y, Shen C, Tang J, Liu J (2018) Hybrid algorithm based on MDF-CKF and RF for GPS/INS system during GPS outages. In IEEE Access 6:35343–35354. https://doi.org/10.1109/ACCESS.2018.2849217
13. Zhang Y et al (2017) Adaptive cubature Kalman filter based on the variance-covariance components estimation. J Glob Positioning Syst 15(1):1–9
14. Liu X, Chen B, Zhao H, Qin J, Cao J (2017) Maximum correntropy kalman filter with state constraints. IEEE Access 5:25846–25853. https://doi.org/10.1109/ACCESS.2017.2769965
15. Wang H, Li H, Zhang W, Zuo J, Wang H (2018) Maximum correntropy derivative-free robust kalman filter and smoother. IEEE Access 6:70794–70807. https://doi.org/10.1109/ACCESS.2018.2880618
16. Kumar PS, Srilatha Indira Dutt VBS, Ganesh L (2020) Implementation of new navigation algorithm based on cross-correntropy for precise positioning in low latitude regions of South India. Int J Speech Technol 23(4):747–756
17. Fan X, Wang G, Han J, Wang Y (2021) Interacting multiple model based on maximum correntropy kalman filter. In: IEEE transactions on circuits and systems II: express briefs. https://doi.org/10.1109/TCSII.2021.3068221
18. Zhang Z, Qiu J, Ma W (2019) Adaptive extended kalman filter with correntropy loss for robust power system state estimation. Entropy 21(3):293

A Novel Arithmetic Optimization Algorithm-Based 2DOF Tilted-Integral-Derivative Controller for Restructured LFC

Mrinal Ranjan and **Ravi Shankar**

Abstract During the last decade, the electrical power system has experienced several changes raised by increasing privatization and the newly deregulation policy. Further, the load–frequency control (LFC) job becomes more challenging due to the integration of non-conventional energy resources such as nuclear, wind, solar, and fuel into the power system. If the demand of consumers varies, then the voltage along with the frequency of the multiple area interconnected power system also changes. Therefore, these changes must be kept within a certain range to supply better quality of electricity to the consumers. The study in this article is focused upon the Load–Frequency Control (LFC) of a double area deregulated power system along with multiple generation sources using Tilted-Integral-Derivative Controller (TIDC) with 2DOF. LFC is the mechanism by which the power system tries to restore its nominal frequency after it has been subjected to load fluctuations. The control areas considered for this paper comprise a reheat turbine and gas unit in addition to the thermal generating unit. Considering the practical scenario of operation, an appropriate generation rate constraint (GRC) has been included for each unit. The gain parameters of the 2DOF Tilted-Integral-Derivative Controller have been optimized by Arithmetic Optimization Algorithm (AOA). Later, the supremacy of the suggested algorithm is verified among the other well-known meta-heuristic approaches such as particle swarm optimization (PSO), Teaching learning-based optimization (TLBO), and Artificial bee colony (ABC) by evaluating under the same test conditions. The dynamic response of the proposed controller to load disturbances has been compared with prevalent controller schemes to bring about the efficacy of the prospective work.

Keywords Load–frequency control · Arithmetic optimization algorithm · Deregulated power system · 2DOF-TIDN controller

M. Ranjan (✉) · R. Shankar
National Institute of Technology, Patna, India
e-mail: mrinalr.phd19.ee@nitp.ac.in

R. Shankar
e-mail: ravi@nitp.ac.in

1 Introduction

The effective operation of multi-area power systems requires the total generation must be equal to total power demand by load plus transmission losses. Day by day technology is going to be advanced and the power system gets more complex and interrelated for any interest. As time passes, the operation of the multiple area interconnected power, system shifts, and hence the power system may experience variation from a rated frequency of the system and tie-line for power exchanging of the double areas interrelated power system [1]. The load–frequency regulation in a multiple area renewable-based system is one of the effective control problems in a power system [2, 3]. A very large variation in the system frequency, as well as tie-line for power exchange in a multiple area power system, can harm appliances, account for the instability of the appliances, possess the life of the equipment, and finally direct to power system instability [4]. To eliminate this problem, the LFC approach [5–7] is proposed for two areas to restructure power systems. LFC is important to create a superior control to get less deviation on change in frequency of the power system and tie-line for power exchange of the distinct control areas [8].

Due to the presence of vertically integrated units (VIUs) in interconnected power systems, it handles all three phases of power transfer, i.e. generation, transmission, and distribution [9, 10]. Because there is no competition in the efficiency of power, the system also decreases. Hence, the Restricting of the power system is introduced to enhance the power system efficiency [11, 12]. Due to the independence of each company, it is free to contact each other. The working of deregulated power system is performed in various forms such as unilateral and bilateral transactions and contract violations. A pool-based transaction is known as a unilateral transaction in which the GENCOs supply power in their area only. GENCOs of any area of an interconnected power system are free to participate in supplying power to DISCOs of their own area as well as to the DISCOs of other areas in a bilateral transaction. In case of contract violation, the uncontracted power dispatch by generation company (GENCOs) is supplied to the distribution company of the same area [13].

Different soft computing approaches are used for tuning intelligent controllers in modern power systems [14, 15]. Hence for tuning different controllers, modern progressive soft computing algorithms are developed. Formally, many authors have concentrated on traditional controllers such as I, PI, PD, and PID in the secondary control of the LFC of the system [16, 17]. To remove the drawback of secondary conventional controllers such as slow response speed, more liable to disturbance, and adverse convergence in a complex system, the author proposed different methods [18, 19]. Various of them are (1) Utilization of modern intelligent controllers such as sliding mode controller, linear matrix inequality controller, fuzzy proportional-integral (FPI) controller, and Predictive and adaptive controller; (2) Application of fractional-order controllers; (3) To increase the DOF of the secondary controller; and (4) Use of cascade controllers. Modern optimization techniques are used by many researchers for optimizing the gain parameter of secondary controllers [20, 21]. These include Particle Swarm Optimization, Whale Optimization, Gray Wolf Optimization,

Fruit Fly Algorithm, Sine–cosine algorithm, symbiotic organisms search algorithm, differential search algorithm (DSO), backtracking search algorithm (BSA), Artificial Bee Colony (ABC), Ant colony, and teaching learning-based optimization (TLBO).

In the paper, a recent meta-heuristic approach that is called as Arithmetic optimization Algorithm (AOA) is proposed by the author, which is based on the distribution nature of the arithmetic operator. Due to the presence of gradient-free approach and high local optimal prevention capability approach of the proposed algorithm, it overrules conventional optimization algorithms. To show the dominancy, the proposed algorithm is compared with the traditional meta-heuristic approach. From the literature, the survey author concluded that most of the meta-heuristic techniques deteriorate their performance by certain deficiencies. The main cause of lower speed of operation per iteration in a Genetic-algorithm (GA) is the involvement of crossover and mutation. There is the possibility of particles diverging in the case of particle swarm optimization for a complex problem. In comparison to other meta-heuristic approaches, the Arithmetic Optimization algorithm is free from any derivative term and does not settle in local minima. Hence, it can perform superior to the other well-known optimization algorithms. Thus, in the paper, a new experiment has been done to design a 2DOF-Tilted-Integral-Derivative Controller and optimize its parameters using the Arithmetic Optimization Algorithm (AOA) approach. In a deregulated environment of a double area power system, the proposed controller performance is verified by comparing its performance with various meta-heuristic techniques such as teaching learning-based optimization, particle swarm optimization (PSO), and Artificial bee colony. The detailed descriptions of the research works are as follows:

(1) A double area deregulated power system considering the thermal constraints such as generation rate constraint (GRC) and governor dead band (GDB) having multiple generations is proposed.
(2) For the secondary LFC system, a TIDC with 2DOF is proposed.
(3) Arithmetic Optimization Algorithm (AOA) is proposed to get optimal gain parameters of the Secondary controller.
(4) The System dynamic performance characteristic of the 2DOF-TIDC approach is correlated with PID and PD(1 + PI) controller.
(5) Robustness of the suggested controller scheme is investigated by performing the sensitivity analysis.
(6) The dominancy of the suggested algorithm is presented by correlating with other meta-heuristic algorithms.

2 Proposed System

The linearized block diagram of investigated power under deregulation has been proposed in Fig. 1. The study of a double area multi-source interconnected power system is carried out under deregulated conditions. The generating units considered in both areas are a thermal reheating turbine unit and a gas unit. Taking into account practical operating scenarios and thermodynamic considerations, thermal units of

both control areas are provided with an open-loop GRC non-linearity of value 3% per minute. The objective function considered is the Integral-time-square-error (ITSE) which is given as

$$F_{\text{ITSE}} = \int_0^{T_{\text{sim}}} \left\{ |\Delta f_1|^2 + |\Delta f_2|^2 + |\Delta P_{\text{tie}}|^2 \right\} \cdot \text{tdt} \tag{1}$$

Deregulation refers to the rules governing economic commitment between electric power companies to ensure healthy open market competition. The deregulation of the power system model is realized by the introduction of the DISCO Participation Matrix (DPM). This conveys the correlation of load distribution between generating and distributing companies. The transmission companies are generally included with the distribution of two generating and distributing companies in each area and the DPM for this scenario can be given by
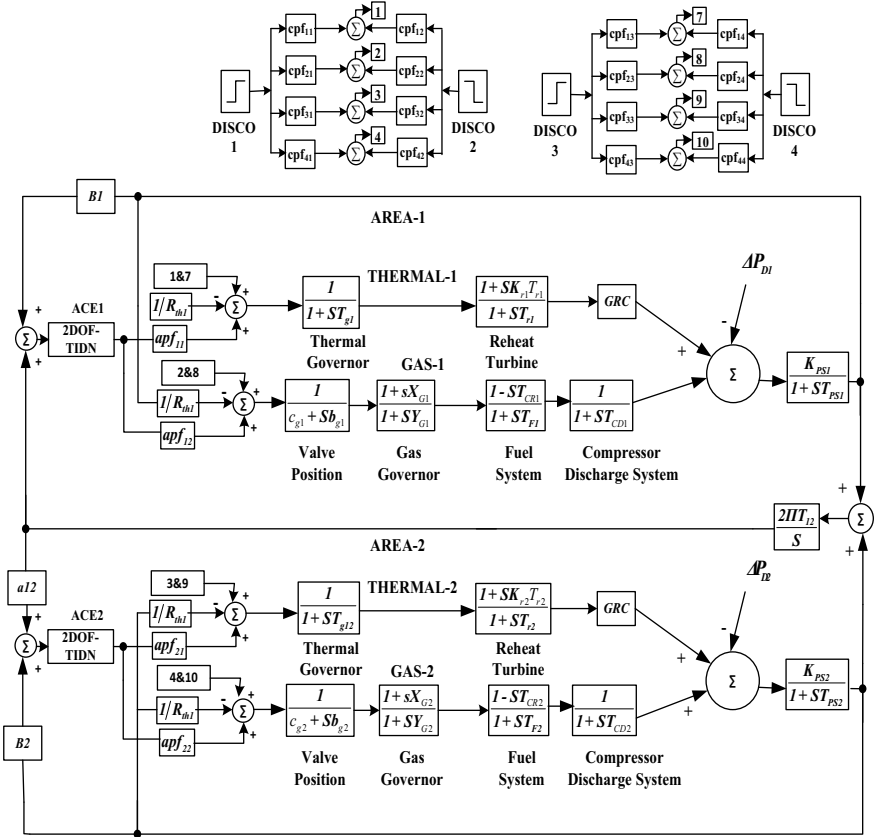

Fig. 1 Transfer function model of a twin-area scheduled system in restructured environment

$$DPM = \begin{bmatrix} \mathrm{cif}_{11} & \cdots & \mathrm{cif}_{14} \\ \vdots & \ddots & \vdots \\ \mathrm{cif}_{41} & \cdots & \mathrm{cif}_{44} \end{bmatrix} \tag{2}$$

where cif is the contract involvement factor. It gives the value of a power-sharing agreement between the two electrical utilities associated in that area.

3 The Proposed Controller

The main function of a proportional controller as a conventional controller in a two-area system is to decrease the rise time of the time domain response of the system but it declines to remove the error in a steady state. The Integral controller removes the error of the steady state but it increases the order of the system, although the purpose of the derivative controller is to enhance the transitory response of the system by decreasing maximum overshoot and enhancing the stability of the system. Filter coefficient (N) combined with a derivative controller is used for mitigating the noise in the system. This paper is discussed with the 2DOF-TIDN controller to improve overall time domain specification [22].

The suggested intelligent controller mixes the properties of the 2DOF structure and TIDF controller in the treated LFC Scenario. The no. of closed-loop transfer in the proposed system is decided by the degree of freedom of the controller. The suggested controller receives two inputs. $R(s)$ is the first reference input signal in the proposed controller, which contains Area Control Error (ACE), and $Y(s)$ is the second input signal, which measures the output signal indicated by area frequency deviation in the two-area system. Figure 2 Shows the simple structure of a 2DOF-TIDN controller. TIDF controller is a simple form of fractional-order controller. The TIDN system dynamics are analogous to a proportional-integral-derivative filter controller. The only discrepancy between the two controllers is that Proportional is changed by a tilted controller. Equation (3) shows the transfer function of the TIDN controller.

$$G_{\mathrm{TIDN}} = K_p \left(\frac{1}{s^{\frac{1}{n}}} \right) + K_i \left(\frac{1}{s} \right) + K_d \left(\frac{sN}{s+N} \right) \tag{3}$$

The proposed 2DOF-tilted-integral-derivative filter controller contains seven tuning parameters in two areas of the investigated system. All the seven parameters are optimized by Arithmetic Optimization Algorithm subjected to.

$K_{p\ \min} < K_p < K_{p\ \max}$, $K_{i\ \min} < K_i < K_{i\ \max}$, $K_{d\ \min} < K_d < K_{d\ \max}$, $b_{\min} < b < b_{\max}$, $c_{\min} < c < c_{\max}$, $(1/n)_{\min} < 1/n < (1/n)_{\max}$, $N_{\min} < N < N_{\max}$.

Where K_p, K_i, K_d, c, b, $\frac{1}{n}$, and N represent the tuning parameters of the proposed controller.
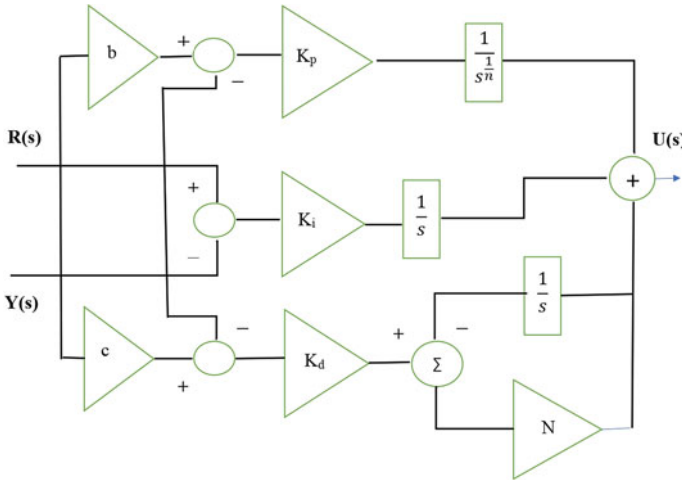
**Fig. 2** Modeling of proposed 2DOF-TIDN controller

4 Optimization

Seyedali Mirjalili [23] has presented an Arithmetic Optimization Algorithm (AOA). The dispersion properties of the main arithmetic operations such as (Addition(A), subtraction(S), Division (D), and Multiplication(M)) are used by the proposed Algorithm (AOA). To execute the optimization procedure in an extensive range of search space, a mathematical model of the proposed algorithm is used. Involved steps in the proposed algorithm are as follows.

4.1 Initialization Phase

The proposed optimization procedure starts with randomly generated candidate solutions(x) as shown in Eq. (4). To get the best-obtained solution, an optimal value in every iteration of the candidate solution is calculated. It uses the two-phase search, i.e. exploration and exploitation before going to start the proposed algorithm (AOA).In Algorithm A function coefficient called Math-optimizer-accelerated (MOA) evaluated in Eq. (5) is used during the exploration and exploitation search phases. Figure 3 shows the general ranking of four Arithmetic operators and their influence from the outer side to the inner side.

Fig. 3 Ranking of various arithmetic operators (influence decreases from top to down)
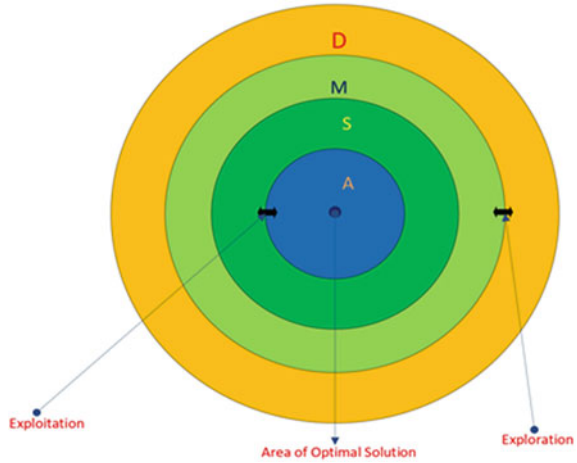
$$x = \begin{bmatrix} x_{1,1} & \cdots \cdots & x_{1,j} & x_{1,n-1} & x_{1,n} \\ x_{2,1} & \cdots \cdots & x_{2,j} & x_{2,n-1} & x_{2,n} \\ \cdots & \cdots \cdots & \cdots & \cdots & \cdots \\ \vdots & \vdots \ \vdots & \vdots & \vdots & \vdots \\ x_{N-1,1} & \cdots \cdots & x_{N-1,j} & x_{N-1,j} & x_{N-1,n} \\ x_{N,1} & \cdots \cdots & x_{N,j} & x_{N,n-1} & x_{N,n} \end{bmatrix} \tag{4}$$

$$\text{MOA}(C\_\text{Iter}) = \text{Min} + C\_\text{Iter} \times ((\text{Max} - \text{Min})/(M\_\text{Iter})) \tag{5}$$

4.2 Exploration Phase

The arithmetic optimization Algorithm (AOA) uses the exploration operator which is modeled in Eq. (6) to get the optimal solution depending on two main search approaches (such as Division (*D*) approach and the Multiplication (*M*) search approach) by exploring the search space randomly on various regions.

$$x_{i,j}(C_{\text{Iter}} + 1) = \begin{cases} \text{best}(x_j) \div (\text{MOP} + \in) \times ((\text{UB}_j - \text{LB}_j) \times \mu + \text{LB}_j), & r2 < 0.5 \\ \text{best}(x_j) \times \text{MOP} \times ((\text{UB}_j - \text{LB}_j) \times \mu + \text{LB}_j), & \text{otherwise} \end{cases} \tag{6}$$

$$\text{MOP}(C\_\text{Iter}) = 1 - \frac{C\_\text{Iter}^{1/\infty}}{M\_\text{Iter}^{1/\infty}} \tag{7}$$
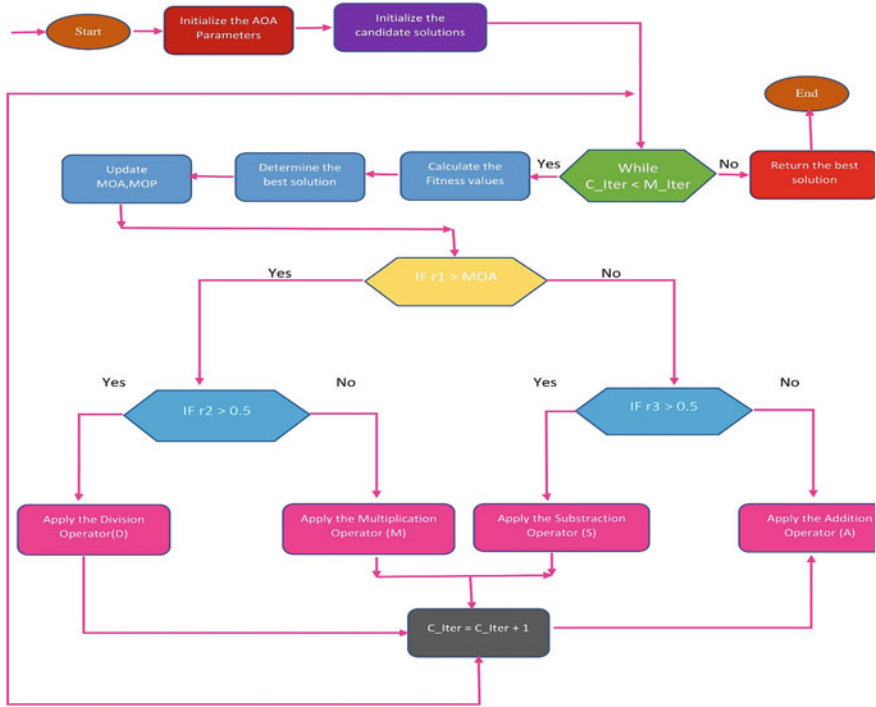
Fig. 4 Flowchart of the proposed AOA

4.3 Exploitation Phase

Arithmetic Optimization Algorithm (AOA) uses the exploitation operator which is modeled in Eq. (8) to get the optimal solution depending on two main search approaches (such as Addition (*A*) approach and Subtraction (*S*) search approach) by exploring the search space intensely on various dense regions. The perceptive and extensive procedure of AOA is shown in Fig. 4.

$$
x_{i,j}(C_{\text{Iter}} + 1) = \begin{cases} \text{best}(x_j) - (\text{MOP} + \epsilon) \times \left((\text{UB}_j - \text{LB}_j) \times \mu + \text{LB}_j\right), & r3 < 0.5 \\ \text{best}(x_j) + \text{MOP} \times \left((\text{UB}_j - \text{LB}_j) \times \mu + \text{LB}_j\right), & \text{otherwise} \end{cases}
$$

$$(8)$$

5 Results and Discussion

To examine the system dynamic response, i.e. frequency deviation in two areas dereg-ulated system, a step-load disturbance (SLD) of 0.1 per unit in area-1 is considered

by keeping area-2 undisturbed. The DPM for deregulation is considered as a pool-based transaction (PBT) in which the DISCO of an area is restricted to purchase power from the GENCO associated with the same area. In pool-based transaction (PBT), let us consider load demand is uniformly distributed by GENCOs locally in every area and load variation appears only in area-1. In two areas restructure power system area-participation factor(apf) for every GENCO is considered as 0.5. The change in total demand in area-2 is zero due to the presence of load disturbance in area-1. The DISCO participation matrix is given as

$$\text{DPM}_P = \begin{bmatrix} 0.5 & 0.5 & 0 & 0 \\ 0.5 & 0.5 & 0 & 0 \\ 0 & 0 & 0 & 0 \\ 0 & 0 & 0 & 0 \end{bmatrix} \tag{9}$$

The simulation was carried out using MATLAB and SIMULINK R2020a Toolbox. The 2DOF-TIDN controller gains were tuned for the optimal control setting using Arithmetic Optimization Algorithm (AOA) considering ITSE as the cost function. The no. of initial search agents and maximum iterations considered were 10 and 10, respectively. The obtained response was compared in two different ways as follows.

Case 1: Comparison of the dynamic response of proposed controllers with different Optimization Algorithms.

The dynamic response and convergence curve using Arithmetic Optimization Algorithm (AOA) are compared with other well-known evolutionary techniques like particle swarm optimization (PSO), Teaching–learning-based optimization (TLBO), and Artificial bee colony (ABC) with the same condition on the investigated system. The proposed Arithmetic Optimization Algorithm (AOA)-optimized 2DOF-TIDN controller showed enhanced transient and steady-state response with reduced settling time, undershoot, and overshoot in obtaining frequency regulation in addition to controlling power transfer in the tie-line connection. From the convergence curve, it can also be predicted that the proposed optimization algorithm converges very fast in comparison to other Evolutionary techniques. The dynamic response and convergence curve for proposed algorithm schemes along with the other evolutionary techniques is depicted in Figs. 5 and 6. Comparison of the dynamic response of the proposed controller with different Algorithms is shown in Table 1.

Case 2: Comparison of the dynamic response of different controllers.

The 2DOF-TIDN controller gains were tuned for the optimal control setting using Arithmetic Optimization Algorithm (AOA) considering ITSE as the cost function. The no. of initial search agents and maximum iterations considered were 10 and 10, respectively. The obtained response was compared with PSO-optimized PID and PD(1 + PI) controllers. The proposed AOA-optimized 2DOF-TIDN controller showed enhanced transient and steady-state response with reduced settling time, undershoot, and overshoot in obtaining frequency regulation in addition to controlling
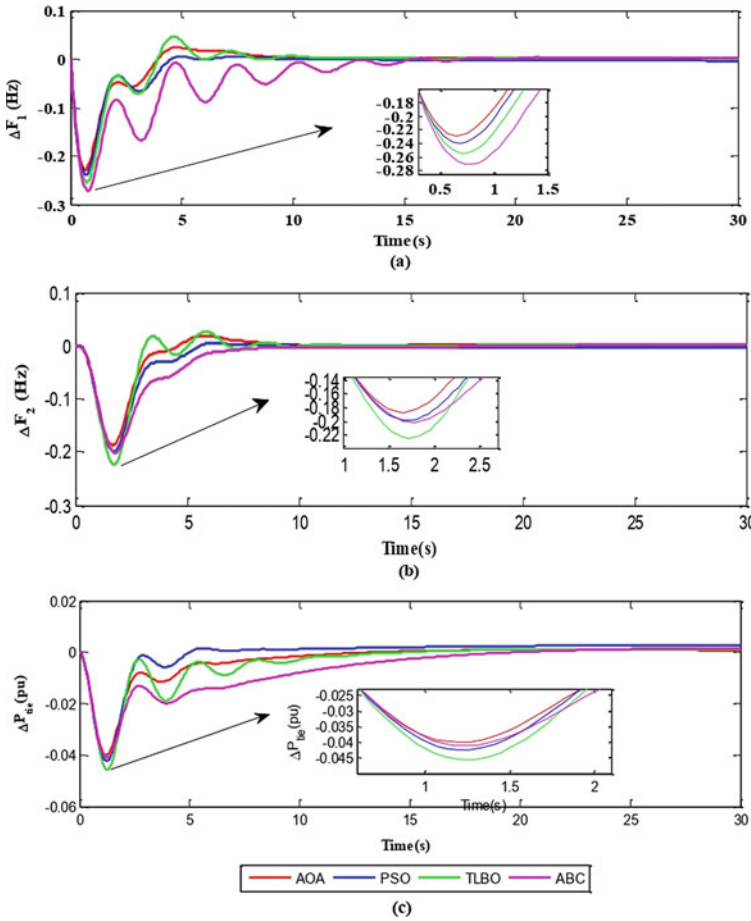
Fig. 5 **a** Frequency fluctuation vs time in area-1. **b** Frequency fluctuation vs time in area-2. **c** Power flow fluctuation in Tie-line verse time
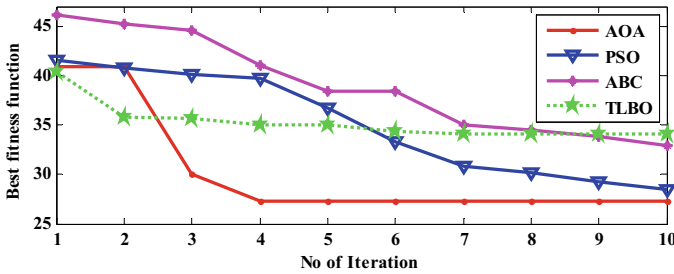

Fig. 6 Best fitness verses number of iterations

Table 1 Comparison of dynamic response of proposed controller with different Algorithms

Maximum deviation	ΔF_1	ΔF_2	ΔP_{tie}
AOA optimization	− 0.221	− 0.181	− 0.0389
PSO optimization	− 0.242	− 0.198	−0.041
TLBO optimization	− 0.249	−0.22	−0.045
ABC optimization	− 0.269	− 0.199	−0.041
% improvement of proposed Algorithm w.r.t ABC algorithm	17.84	9.00	5.12

the power transfer in the tie-line connection. The dynamic response for prevalent controller schemes along with the proposed 2DOF-TIDN is depicted in Fig. 7.
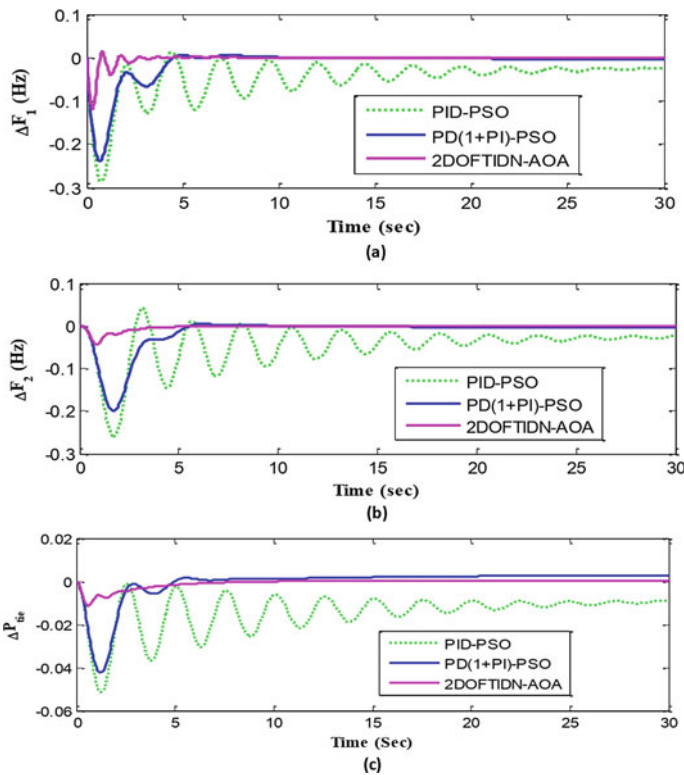
Fig. 7 **a** Frequency fluctuation verses time in area-1. **b** Frequency fluctuation verses time in area-2. **c** Power flow fluctuation in tie-line verses time

6 Conclusion

A new concept has been made to introduce the dynamic response of diverse deregulated power systems using an Arithmetic Optimization Algorithm based on 2DOF-TIDC. The effect of GDB and GRC is also considered in dynamic response. The gain parameter of the proposed controller is optimized by using an Arithmetic Optimization Algorithm optimizer. The recommended optimization algorithm is compared with other algorithms for 1% SLP in area-1 to show its superiority. It is stated from the system dynamic response curve that in area-1 frequency change is improved by 17.84 and 9% in area-2 while tie-line power is improved by 5.12%. From the convergence curve, it can also be predicted that the proposed optimization algorithm converges very fast in comparison to other Evolutionary techniques. A step ahead the proposed control scheme is compared with other popular classical controllers like PID and PD(1 + PI) to show its dominancy. The proposed research work could be further continued to a triple-area power system integrated with non-conventional energy resources such as biomass energy, wind energy, solar energy, etc.

References

1. Shankar R, Pradhan SR, Chatterjee K, Mandal R (2017) A comprehensive state of the art literature survey on LFC mechanism for a power system. Renew Sustain Energy Rev 76:1185–1207. https://doi.org/10.1016/j.rser.2017.02.064
2. Aryan P, Shankar R, Ranjan M (2020) Equilibrium optimized AGC of multi-area restructured power system using cascaded fractional fuzzy controller. In: International conference on emerging frontiers in electrical and electronic technologies (ICEFEET), NIT Patna, pp 1–6. https://doi.org/10.1109/icefeet49149.2020.9187014
3. Aryan P, Shankar R, Ranjan M (2021) Deregulated LFC scheme using equilibrium optimized type-2 fuzzy controller. In: Proceeding of international conference on innovative development in engineering application (IDEA). WEENTECH, Bodhgaya, pp 495–501. https://doi.org/10.32438/WPE.442021
4. Barik AK, Das DC (2018) Expeditious frequency control of solar photovoltaic/biogas/biodiesel generator based isolated renewable microgrid using a grasshopper optimization algorithm. Instit Eng Technol 12(14):1659–1667. https://doi.org/10.1049/iet-rpg.2018.5196
5. Kumar D, Mathur HD, Bhanot S, Bansal RC (2019) Frequency regulation in islanded microgrid considering a stochastic model of wind and PV. Int Trans Electric Energy Syst 29:1–17. https://doi.org/10.1002/2050-7038.12049
6. Latif A, Hussain SMS, Das DC, Ustun TS (2021) Double-stage controller optimization for load frequency stabilization in hybrid wind-ocean wave energy based maritime microgrid system. Appl Energy 282(Part A):0306–2619. https://doi.org/10.1016/j.apenergy.2020.116171
7. Shankar R, Kumar A, Raj U, Chatterjee K (2021) Fruit fly algorithm-based automatic generation control of multi-area interconnected power system with FACTS and AC/DC links in deregulated power environment. Int Trans Electr Energy Syst 29(1):1–25. https://doi.org/10.1002/etep.2690
8. Pathak N, Bhatti TS, Verma A, Nasiruddin I (2018) AGC of two area power system based on different power output control strategies of thermal power generation. IEEE Trans Power Syst 33:2040–2052
9. Aryan P, Shankar R, Ranjan M (2020) Equilibrium optimized AGC of multi-area restructured power system using cascaded fractional fuzzy controller. Int Conf Emerg Front Electr Electron Technol ICEFEET. https://doi.org/10.1109/ICEFEET49149.2020.9187014

10. Morsali J, Zare K, Hagh MT (2018) A novel dynamic model and control approach for SSSC to contribute effectively in AGC of a deregulated power system. Electr Power Energy Syst 95:239–253. https://doi.org/10.1016/j.ijepes.2017.08.033
11. Prakash A, Kumar K, Parida SK (2020) PIDF(1+FOD) controller for load frequency control with SSSC and AC–DC tie-line in a deregulated environment. IET: Instit Eng Technol 14(14):2751–2762. https://doi.org/10.1049/iet-gtd.2019.1418
12. Nayak N, Mishra S, Sharma D, Sahu BK (2019) Application of modified sine cosine algorithm to optimally design PID/fuzzy-PID controllers to deal with AGC issues in deregulated power system IET Gener. Transm Distrib 13(12):2474–2487. https://doi.org/10.1049/iet-gtd.2018.6489
13. Raj U, Shankar R (2020) Deregulated automatic generation control using novel opposition-based interactive search algorithm cascade controller including distributed generation and electric vehicle. Iran J Sci Technol—Trans Electr Eng. https://doi.org/10.1007/s40998-019-00306-3.
14. Prakash A, Murali S, Shankar R (2019) Bhushan R (2019) HVDC tie-link modeling for restructured AGC using a novel fractional order cascade controller. Electric Power Syst Res 170:244–258. https://doi.org/10.1016/j.epsr.2019.01.021
15. Mohanty B, Panda S, Hota PK (2014) Controller parameters tuning of differential evolution algorithm and its application to load frequency control of multi-source pwer system. Electr Power Energy Syst 54:0142–0615. https://doi.org/10.1016/j.ijepes.2013.06.029o
16. Khokhar B, Dahiya S, Parmar PKS (2020) A novel fractional order proportional integral derivative plus second-order derivative controller for load frequency control. Int J Sustain Energ 40:235–252. https://doi.org/10.1080/14786451.2020.1803861
17. Safari A, Babaei F, Farrokhifar M (2018) A load frequency control using a PSO-based ANN for micro-grids in the presence of electric vehicles. Int J Ambient Energy 42(6):688–700. https://doi.org/10.1080/01430750.2018.1563811
18. Mohanty D, Panda S (2021) A modified moth flame optimisation technique tuned adaptive fuzzy logic PID controller for frequency regulation of an autonomous power system. Int J Sustain Energ 40(1):41–68. https://doi.org/10.1080/14786451.2020.1787412
19. Sahu PC, Prusty RC, Panda S (2020) Frequency regulation of an electric vehicle operated micro grid under WOA tuned fuzzy cascade controller. Int J Ambient Energy. https://doi.org/10.1080/01430750.2020.1783358
20. Guha D, Roy PK, Banerjee S (2020) Grasshopper optimization algorithm-scaled fractional-order PI-D controller applied to reducedorder model of load frequency control system. Int J Model Simul 40(3): 217–242. https://doi.org/10.1080/02286203.2019.1596727
21. Bhuyan M, Barik AK, Das DC (2020) GOA optimised frequency control of solarthermal/seawave/biodiesel generator based interconnected hybrid microgrids with DC link. Int J Sustain Energ 39(7):615–633. https://doi.org/10.1080/14786451.2020.1741589
22. Sharma P, Prakash A, Shankar R, Parida SK (2019) A Novel hybrid salp swarm differential evolution algorithm based 2DOF tilted-integral-derivative controller for restructured AGC. Electric Power Comp Syst 47(19–20):1775–1790. https://doi.org/10.1080/15325008.2020.1731870
23. Abualigah A, Diabat A, Mirjalili S, Elaziz MA, Gandomi AH (2021) The Arithmetic optimization algorithm. Comput meth Appl Mech Eng 376(113609). https://doi.org/10.1016/j.cma.2020.113609

Zeta Converter Interfacing in a Single-Stage Boosting Inverter for Solar Photovoltaic Array

S. Narasimha and Surender Reddy Salkuti

Abstract With the drastic increase in power demand in the future, the dependability on renewable energy sources (RESs) is increasing leading to research on power electronic devices for high-efficiency operation. In this paper, the Zeta converter is interfaced with a high gain booster single-stage inverter. The RESs like solar photovoltaic array (PVA), wind generator, fuel cell, and battery generate a voltage at a very low amplitude which is boosted using this converter. The proposed single-stage boosting inverter (SSBI) has several advantages when compared to the conventional two-stage one in terms of the requirement of fewer components and simple topology. Single-cycle control with a non-linear controller is employed with the high gain SSBI to provide the controlled pulses to the switches to produce an ac output voltage. The Zeta converter is a typical DC-DC converter and generates boosted DC voltage with a normal gain value. The DC output of the Zeta converter is further fed to SSBI for high gain boost inverting operation. The modeling of the converter is carried out in MATLAB with all results represented with dynamic voltage changes.

Keywords DC-DC converter · Solar PV array · Zeta converter · Renewable sources · Simulink

1   Introduction

The micro-inverters that are designed for the solar photovoltaic (PV) are single-stage, two-stage, and multi-stage. The multi-stage small-scale inverters are typically including a step-up DC-DC converter with an optimal power point tracking (OPPT)

S. Narasimha
Department of Electrical and Electronics Engineering, TKR College of Engineering and Technology, Hyderabad, Telangana, India

S. R. Salkuti (✉)
Department of Railroad and Electrical Engineering, Woosong University, Daejeon, Republic of Korea
e-mail: surender@wsu.ac.kr

control [1]. The two-stage smaller scale inverter can be outlined falling an OPPT-controlled stride with a network-tied high-frequency inverter and a DC-DC converter, while the single-stage needs to play out voltage step-up, OPPT, and DC-AC reversal works across the board stage. To change over and to connect the solar power to the utility grid, the low voltage of the solar PV board must be stepped up to coordinate the utility level. It represents a test to the architect of solar PV inverters as a customary lift converter cannot give the required pick up at high efficiency [2, 3]. The common problem of the single-stage DC-AC power framework is the AC-DC power decoupling issue [4].

Correct and suitable types of power converters are required for solar PV systems to meet various needs, and applications have a significant influence to obtain the optimum performance [5] as they act as an interface between the utility/main grids and/or residential loads and solar PV systems. Various modeling methods for grid-connected step-up PV systems intended to include different tools for the control design are presented in reference [6]. A detailed review of the various single-stage inverter (SSI) approaches in solar PV systems is presented in [7]. In reference [8], a Zeta converter with a coupled inductor is utilized for efficient recycling of leakage inductor energy. As the PV array (PVA) depicts as the floating source, there is an enhancement in the overall safety of the system. It also discusses operating principles, steady-state analysis, and stress on active components of the converter are also presented. The important characteristics of DC/DC converters as well as various MPPT approaches are analyzed and reviewed in [9].

Reference [10] describes the design and detailed operation of a Cuk-derived, common-ground PV micro-inverter. The present state-of-the-art approaches available for micro-inverters with a comprehensive overview of various technical characteristics such as grid compatibility abilities, control structures, power circuit configuration, energy harvesting capabilities, decoupling capacitor placement, and various mechanisms required for safety are presented in [11]. The classification of the PV system, various inverter types, the global status of the PV market, configurations of grid-connected PV inverters, and topologies are reviewed in [12].

The decoupling of AC–DC power is accomplished on a high-voltage dc link and hence it needs generally low capacitance esteem. The one-cycle control (OCC) has a quick reaction and low affectability to dc-transport voltage swell permitted applying yet littler decoupling capacitor esteem, what's more, has shown low THD output for various sorts of profoundly nonlinear burdens.

2   Proposed Modules and Functionalities

Several single-stage topologies which can understand voltage step-up and reversal in a single-stage are presented in the literature. In a double lift inverter load is associated with yields of two bidirectional lift converters. Figure 1 depicts the DC-AC boost converter. Subsequently, this topology takes a typical H-bridge with boosting inductors associated with the midpoints of legs [13, 14]. The negative marks of this

Fig. 1 Boost DC-AC converter
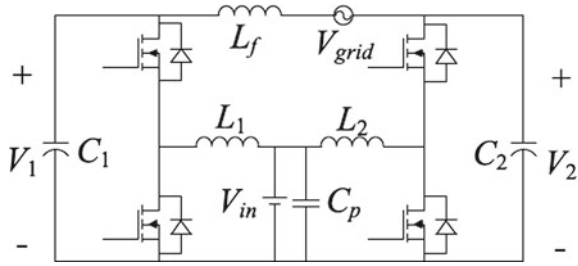
Fig. 2 Single-stage DC-AC converter
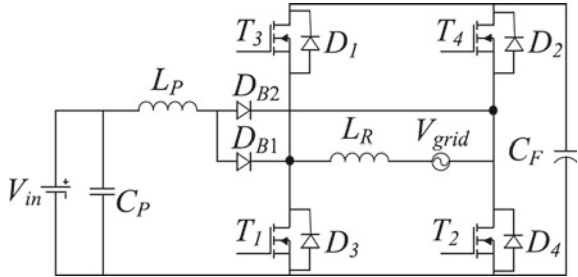
topology are the constrained DC step-up increase, flowing currents, which disable the efficiency; and to some degree entangled control.

Figure 2 depicts another single-stage arrangement of the DC-AC converter. Contrasted with the topologies utilization of single lift inductor, no coursing currents and have a high voltage DC-link [15]. Likewise, customary control strategies can be connected. Also, the proposed topologies may give different decisions to single-stage arrangements.

In any case, the restricted dc step-up requires utilizing more costly high-voltage PV boards with 70–100 V_{dc} yield keeping in mind the end goal to get coveted DC-transport voltage good to network-associated inverters [16, 17]. On the other hand, utilizing the famous crystalline silicon modules with the 25–50 V_{dc} maximum power point (MPP) extend. In the field operating conditions, substantial electrolytic capacitors have a short life and impede the framework's unwavering quality. Hence, the decoupling issue ends up one of the significant worries in the miniaturized scale inverter outline. An enhanced topology using the spillage vitality reusing showed 86% pinnacle efficiency [18, 19]. Some other fly back-based topology likewise makes utilization of an extra power decoupling circuit.

Another nonlinear control system, one-cycle control is presented for steady-state frequency operation. However, the SSBI can be able to control by any existing control techniques. Figure 3 depicts the high-gain SSBI. Contrasted with the topologies utilization of a single lift inductor, have a high voltage DC-link [20], no coursing currents, and a small decoupling capacitor. Likewise, customary control strategies
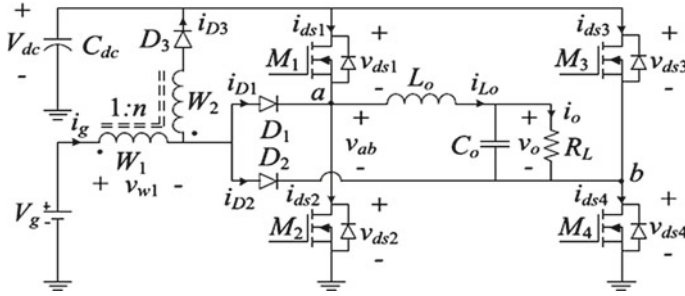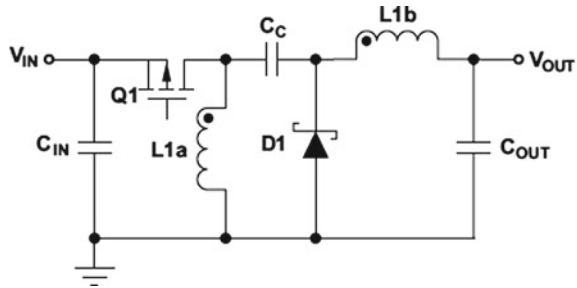
Fig. 3 High-gain SSBI

Fig. 4 Zeta converter

can be connected. Also, the proposed topologies give different decisions in single-stage arrangements [21, 22]. The schematic view of the Zeta converter is depicted in Fig. 4.

To achieve a higher conversion ratio of voltage, with higher efficiency, higher gain enhancement techniques were implemented previously [23]. A boost converter is a power converter. Here in this converter, its DC voltage at the output is more prominent than its DC voltage at its input. The SSBI topology works in discontinuous conduction mode (DCM) all through the lattice cycle if it supports the operation of DCM through peak interim [24]. By applying the condition for the DCM or critical conduction mode (CCM) through peak interim yields the critical estimation of the adjustment file as beneath

$$M = \frac{1}{\left(1 + \frac{V_{\text{in}}}{V_{\text{p}}}\right)} \tag{1}$$

where M is the modulation index, V_{in} is the input voltage, and V_{p} is the peak value of output voltage.

3 Implementation of High Gain SSBI for PV Array in Simulink

As mentioned earlier, the Zeta converter interfacing in an SSBI for PVA has been implemented in MATLAB Simulink software. MATLAB gives one of the successful modeling instruments and reenactment apparatus called Simulink. In engineering, it needs to represent the information graphically. MATLAB Simulink can be used for several applications such as image processing, signal processing, power electronics, basic electrical and electronics measurements, and instrumentation. Simulink is a piece graph condition for multi-space amusement and model-based outline. It underpins the recreation customized code age and steady tests and checks [25, 26]. Here viably gives a graphical depiction, can changes square libraries, and can agree to demonstrating and recreating dynamic structures. Along these lines, it is joined with MATLAB figuring into models and sends reenactment results to MATLAB for assist investigation.

This section presents the software design of the proposed models. Figure 5 depicts a simulation model of a high gain single-stage boosting inverter (implemented in Simulink model of MATLAB software) which is controlled by one cycle controller. It operates at an input voltage of 48 V, switching at 50 kHz frequency, and the output voltage at 436 V.

The PV array (PVA) comprises 8 PV cells, and all of them are associated in series to get a coveted voltage yield. Contingent upon required load control, the total number of parallel branches is expanded to at least 2. The impacts of solar irradiation and temperature levels are spoken to by two variables picked up. These
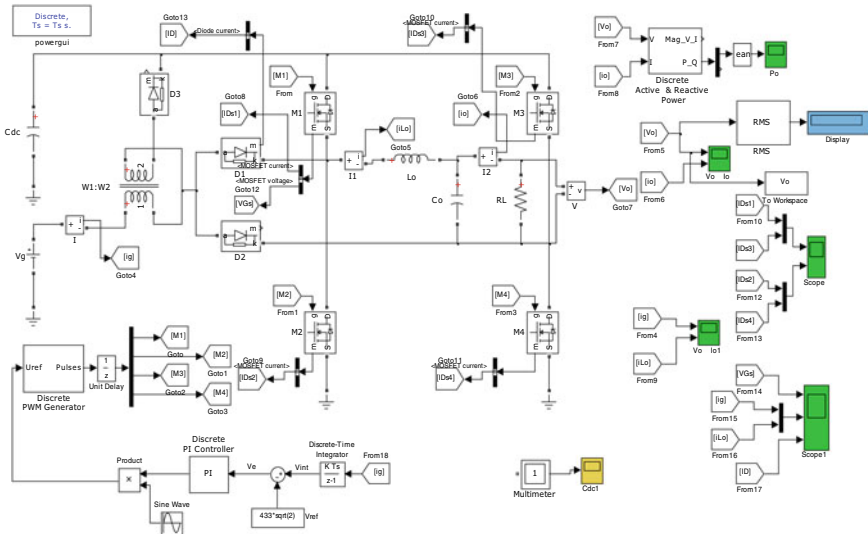

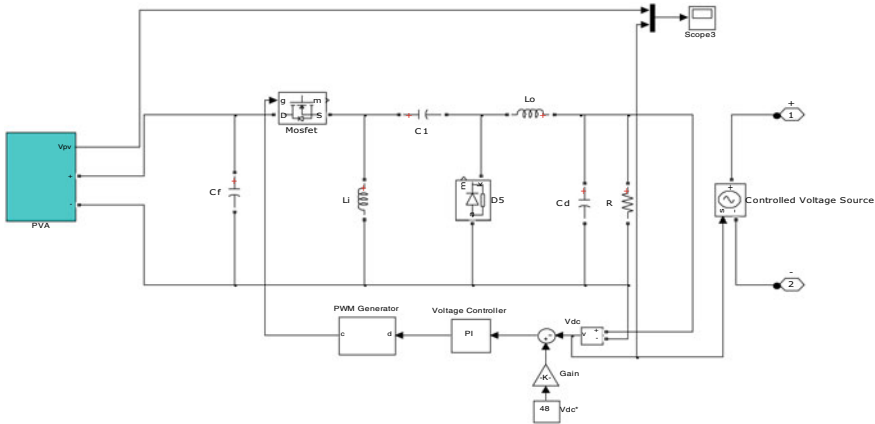**Fig. 5** Implementation of high gain SSBI in Simulink

Fig. 6 Design of Zeta converter simulation model for PV Array

are changed by dragging the slider pick-up modifications of these blocks named variable solar insolation and temperature. The design of the Zeta converter in the simulation approach and which is implemented in MATLAB is depicted in Fig. 6.

Figure 7 depicts the simulation model of the design and integration of Zeta converter in high gain SSBI. Here, the PVA, ZETA converter, and high gain SSBI are cascaded respectively. The output of the PVA is given as input to the Zeta converter and in the same way, the output of a Zeta converter is given as an input to the high gain SSBI, and the output is fed to the load. The Simulink model of PVA is connected to a Zeta converter. The Simulink model of PVA fed Zeta converter is integrated into high gain SSBI in the Simulink model. This Simulink model is a discrete-time system, and simulation is switched at a frequency of 50 kHz.

4   Results and Discussion

This section presents the output results of the proposed models. In this work, PSIM simulation is utilized to confirm the DCM voltage conversion proportion. Simulation parameters are as per the following: input voltage (V_g) = 48 V, $L_m = 150\mu H$, $T_s = 20\,\mu s$, boost duty cycle ($Đ_{bst}$) = 0.64, $n = 3$, and $R_{eq} = 4000\,\Omega$. Connecting these variables leads to $M_{cal} = 10.96$, though mimicked result $M_{sim} = 10.58$ emphatically supporting the hypothetical desire. CCM–DCM boundary condition is checked by simulation utilizing the accompanying parameters: $V_g = 48$ V, $L_m = 150\,\mu H$, $T_s = 20\,\mu s$, $Đ_{bst} = 0.64$, and n is 3. The detonated perspective of input current I_g shows that SSBI is in reality at CCM–DCM boundary. The reproduced power output obtained as $P_{ob} = 68$ W and coordinated the hypothetically expected estimation of $P_{ob} = 68.36$ W. Figure 8 presents the output waveforms of the input current (i_g)
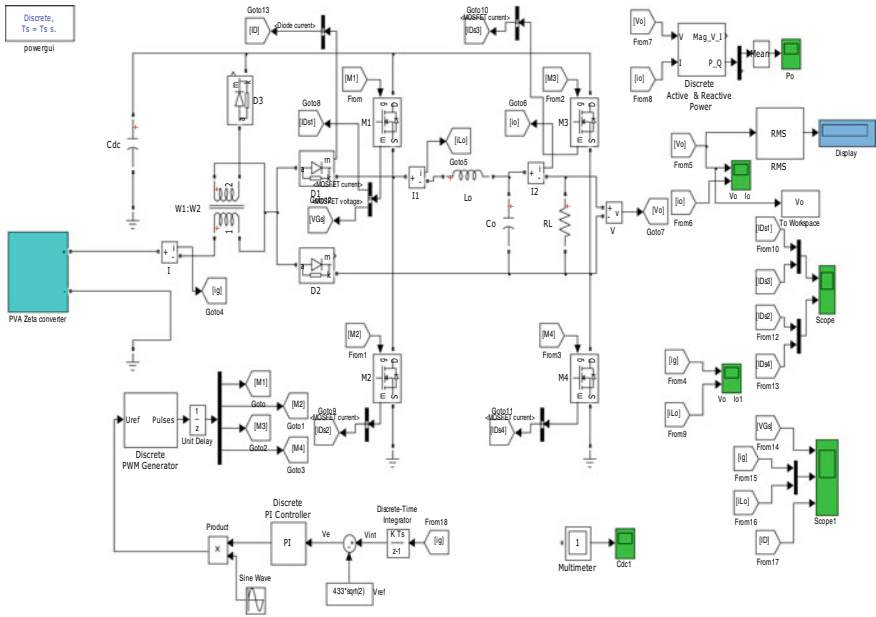
Fig. 7 Simulation model of Zeta converter interference in high gain SSBI for PV Array

and inductor current (i_{LO}) of SSBI. The decoupling capacitance (C_{dc}) of DC-link capacitor between the inputs and output has been depicted in Fig. 9.
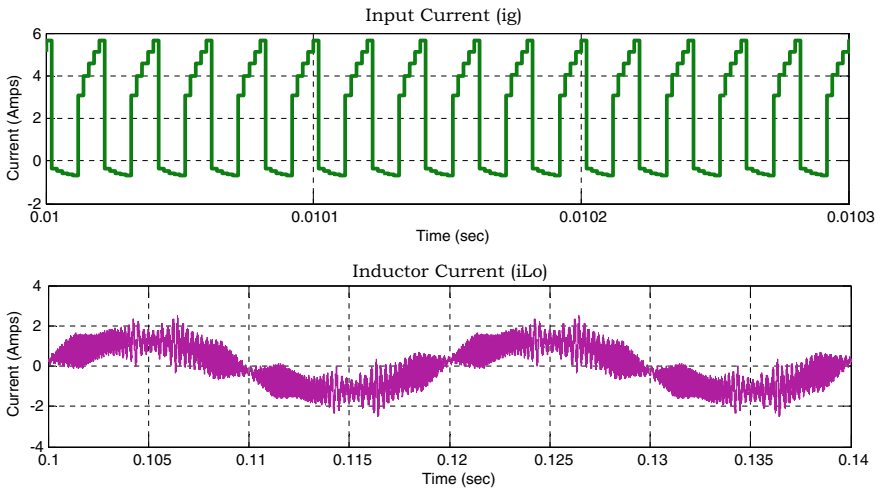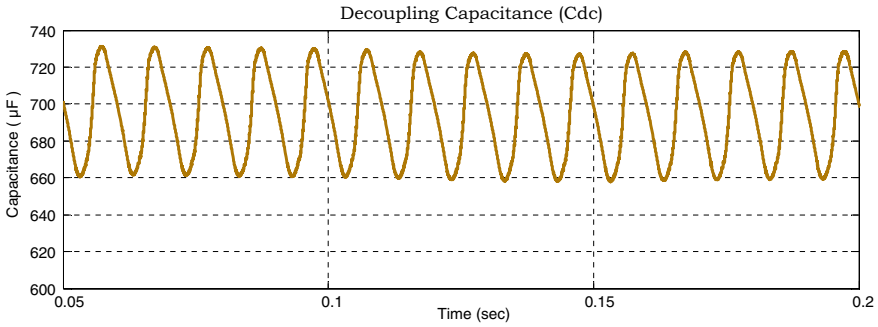

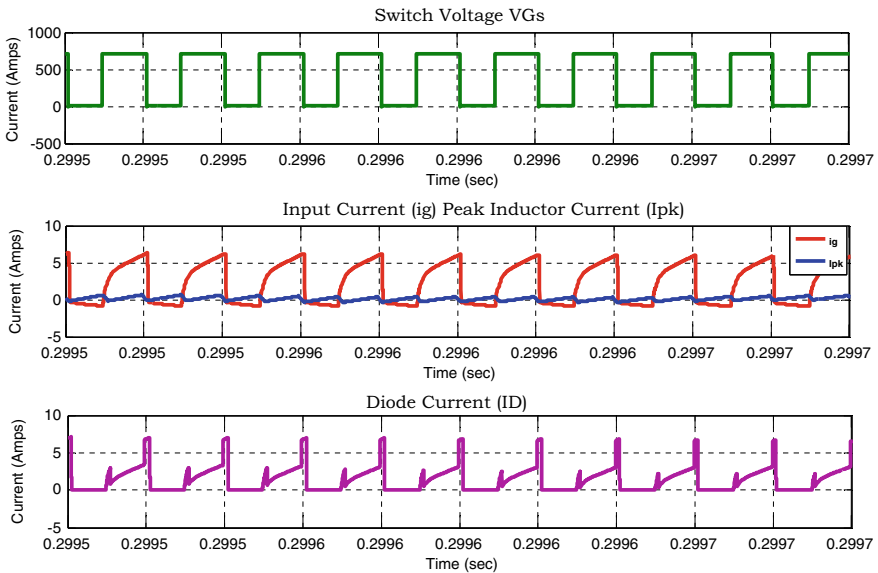**Fig. 8** Simulation waveforms of input current (i_g) and inductor current (i_{LO})

Fig. 9 Simulation waveform of decoupling capacitance ($\mathbf{C}_{dc}$)

The value of C_{dc} depends on P_{dc} and f at line conditions, V_{dc} and allowed peak-to-peak swell (ΔV). The C_{dc} value can be calculated by

$$C_{dc} = \frac{P_{dc}}{2\pi \int V_{dc} \Delta V} = \frac{160}{2\pi \times 35 \times 6} = 2.4\,\mu\mathrm{F} \tag{2}$$

Figure 10 depicts the waveforms of the diode current (I_D), input current (i_g), , inductor peak current (I_{pk}), and input voltage (V_g). Figure 11 presents the current waveforms through each switch in SSBI.

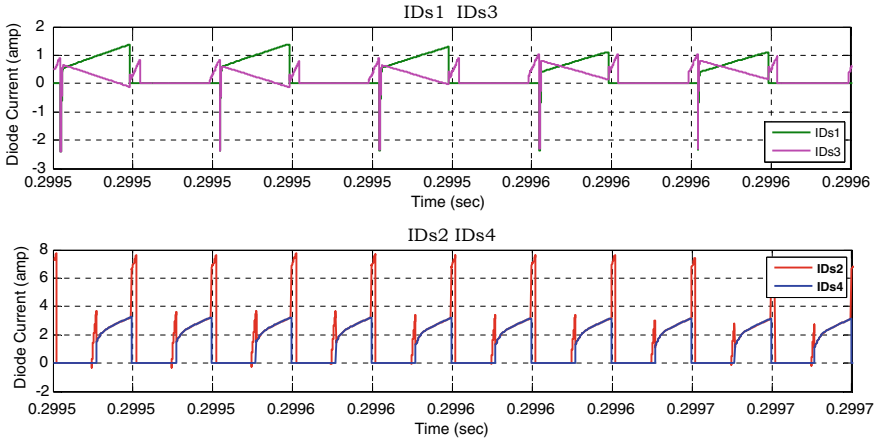**Fig. 10** Simulation waveforms of i_g, I_D, V_g, and I_{pk}

Fig. 11 Current waveforms through each switch in SSBI

The output current (I_o) and output voltage (V_o) waveforms define the differences between input and output waveforms, and they are depicted in Fig. 12. Figure 13 depicts the output power of high gain SSBI.

The waveforms in Fig. 12 represent the nature of output voltage below and above the P_{omin} In Fig. 13, P_o is simply above P_{omin} and it does not cause any distortion in the waveform. In Fig. 13, Po is just underneath the beginning of peak-shaving distortion. Parameters utilized as a part of the simulation are $V_g = 48$ V, $V_{dc} = 380$ V, and Output current $I_o = 0.8981$A. Figure 14 depicts the operation of Zeta converter when it is integrated with a high gain SSBI.
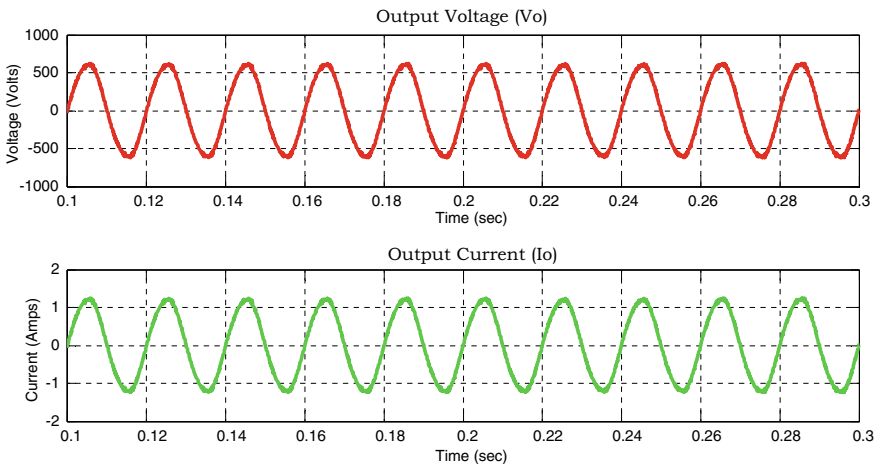

Fig. 12 Output voltage ($\mathbf{V_o}$) and output current ($\mathbf{I_o}$) waveforms of SSBI
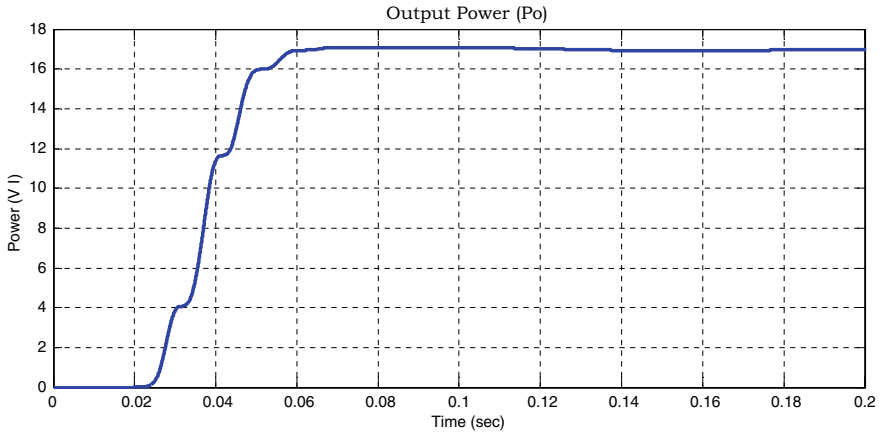
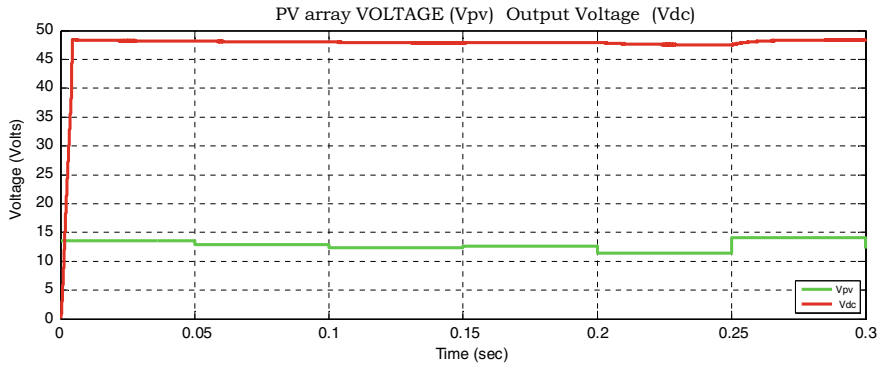**Fig. 13** Waveform depicting the output power of high gain SSBI

Fig. 14 Output voltage (V_{dc}) and PV array voltage (V_{PV}) of Zeta converter

The variable voltage from the PV array is given to a high-gain SSBI. Then SSBI produces the variable output voltage for each particular level of input voltage from the PV array as the output of the PV array is variable from time to time so to stabilize the output of SSBI, and the Zeta converter is integrated with between PV array and single-stage boosting inverter. When the V_{pv} 38 V of PV array is applied to the Zeta converter then it produces 48 V DC voltage and is applied to the high-gain SSBI as V_g then output voltage V_o is 435 V. In another case, V_{pv} 58 V of PV array is applied to the Zeta converter then it produces 48 V DC voltage and is applied to the high-gain SSBI as V_g then output voltage V_o is 435 V. The output of the Zeta converter is always constant even if the input is above or below the level of output voltage. By this, the variable renewable source output is maintained stable and the converter achieves the high voltage conversion.

5   Conclusions

The integration of Zeta converter in high-gain SSBI for elective vitality age applications has been described in this paper. Here high gain SSBI utilizes a TI to accomplish a high-input voltage step-up and, therefore, permits operation from the low dc input voltage. This paper determines the standards of operation, hypothetical investigation of nonstop, and irregular modes of operation by considering the increase in voltage and current stresses. Here, two remaining solitary models with 48 and 35 V inputs are studied and simulated. Hypothetical discoveries remain in great assertion with simulation and trial comes about. Satisfactory efficiency was accomplished with a low dc input voltage source. The Zeta converter provides positive output power from variable solar irradiance to the SSBI topology. The high gain SSBI provides the upside of high voltage step-up, and it can be additionally expanded by modifying the TI turns proportion.

References

1. Mthew D, Naidu RC (2020) Investigation of single-stage transformerless buck-boost microinverters. IET Power Electron 13(8):1487–1499
2. Mumtaz F, Yahaya NZ, Meraj ST, Singh B, Kannan R, Ibrahim O (2021) Review on non-isolated DC-DC converters and their control techniques for renewable energy applications. Ain Shams Eng J
3. Raj TAB, Ramesh R, Maglin JR, Vaigundamoorthi M, Christopher IW, Gopinath C, Yaashuwanth C (2014) Grid connected solar PV system with SEPIC converter compared with parallel boost converter based MPPT. Int J Photoenergy 2014:1–12
4. Mohammad N, Quamruzzaman M, Hossain MRT, Alam MR (2013) Parasitic effects on the performance of DC-DC SEPIC in photovoltaic maximum power point tracking applications. Smart Grid Renewable Energy 4(1)
5. Dogga R, Pathak MK (2019) Recent trends in solar PV inverter topologies. Sol Energy 183:57–73
6. Trejos A, Gonzalez D, Paja CAR (2012) Modeling of step-up grid-connected photovoltaic systems for control purposes. Energies 5(6):1900–1926
7. Ankita, Sahooa SK, Sukchaib S, Yaninec FF (2018) Review and comparative study of single-stage inverters for a PV system. Renew Sustainable Energy Rev 91:962–986
8. Dheesha J, Murthy B (2014) Simulation of micro inverter with high efficiency high step up Dc-Dc converter. Int J Innovat Res Electr Electron Inst Contr Eng 2(2):974–984
9. Raghavendra KVG, Zeb K, Muthusamy A, Krishna TNV, Kumar SVSVP, Kim DH, Kim MS, Cho HG, Kim HJ (2020) A comprehensive review of DC–DC converter topologies and modulation strategies with recent advances in solar photovoltaic systems. Electronics 9(1)
10. Ajith A, Thiyagarajan R, Nagalingam A, Ilango R, Purushothaman G (2018) A novel topology using cuk converter in PV microconverter with transformerless injection. Int J Eng Res Technol (IJERT) 6(7):1–7
11. Çelik Ö, Tan ATA (2018) Overview of micro-inverters as a challenging technology in photovoltaic applications. Renew Sustain Energy Rev 82(3):3191–3206

12. Zeb K, Uddin W, Khan MA, Ali Z, Ali MU, Christofides N, Kim HJ (2018) A comprehensive review on inverter topologies and control strategies for grid connected photovoltaic system. Renew Sustain Energy Rev 94:1120–1141
13. Dileep G, Singh SN (2017) Selection of non-isolated DC-DC converters for solar photovoltaic system. Renew Sustain Energy Rev 76:1230–1247
14. Jana J, Saha H, Bhattacharya KD (2017) A review of inverter topologies for single-phase grid-connected photovoltaic systems. Renew Sustain Energy Rev 72:1256–1270
15. Abramovitz A, Zhao B, Smedley K (2016) High-gain single-stage boosting inverter for photovoltaic applications. IEEE Trans Power Electron 31(5):3550–3558
16. Hu H, Harb S, Kutkut NH, Shen ZJ, Batarseh I (2013) A single-stage microinverter without using electrolytic capacitors. IEEE Trans Power Electron 28(6):2677–2687
17. Narasimha S, Salkuti SR (2018) Design and implementation of smart uninterruptable power supply using battery storage and photovoltaic arrays. Int J Eng Technol 7(3):960–965
18. Narasimha S, Salkuti SR (2018) Dynamic and hybrid phase shift controller for dual active bridge converter. Int J Eng Technol 7(4):4795–4800
19. Hu H, Harb S, Fang X, Zhang D, Zhang Q, Shen ZJ, Batarseh I (2012) A three-port flyback for PV microinverter applications with power pulsation decoupling capability. IEEE Trans Power Electron 27(9):3953–3964
20. Narasimha S, Salkuti SR (2020) An improved closed loop hybrid phase shift controller for dual active bridge converter. Int J Electr Comput Eng 10(2):1169–1178
21. Chien-Ming W (2004) A novel single-stage full-bridge buck-boost inverter. IEEE Trans Power Electron 19(1):150–159
22. Abramovitz A, Zhao B, Heydari M, Smedley K (2014) Isolated flyback half-bridge OCC micro-inverter. Proc IEEE energy convers. Congr Expo 2967–2971
23. Narasimha S, Salkuti SR (2020) Design and operation of closed-loop triple-deck buck-boost converter with high gain soft switching. Int J Power Electron Drive Syst 11(1):523–529
24. Hu H, Kutkut N, Batarseh I, Harb S, Shen ZJ (2013) A review of power decoupling techniques for microinverters with three different decoupling capacitor locations in PV systems. IEEE Trans Power Electron 28(6):2711–2726
25. Kim SC, Narasimha S, Salkuti SR (2020) A new multilevel inverter with reduced switch count for renewable power applications. Int J Power Electron Drive Syst 11(4):2145–2153
26. Zhao B, Abramovitz A, Smedley K (2014) High gain single-stage boosting inverter. IEEE Energy Convers Congress Expos (ECCE) 4257–4261

Investigation of Performance of BLDC-Driven Dumbwaiter Elevator System Fed from SPV Array and Diesel Generator

Manju Panickar and V. Sreelekha

Abstract This paper presents a dumbwaiter elevator driven by a brushless direct current (BLDC) motor and fed from a standalone photovoltaic system. Dumbwaiter elevators are freight elevators used to carry food, clothes, etc. in hotels and shopping malls. Its capacity ranges from 40 to 400 kg. Elevators operate in motoring and braking modes. The braking power is regenerated by using the BLDC drive and is utilised for the charging of battery in the standalone photovoltaic system. The elevators consume a considerable part of electrical energy in high-raised buildings which is reduced by utilising the regeneration capability of BLDC motors. The other advantages of BLDC drive for elevator applications are smooth speed control, high power density and less complexities in power converter and controller when worked with dc supply. The proposed system drives the dumbwaiter elevator using the BLDC motor fed from a standalone photovoltaic source. A diesel generator is added as a back-up source to ensure more reliability for the system. The entire system is designed and simulated in MATLAB Simulink model.

Keywords Brushless direct current (BLDC) motor · Solar photovoltaic array · Dumbwaiter elevator · Regeneration · Diesel generator

1 Introduction

The technological advancements made life more comfortable in this hectic world. Nowadays, hotels, shopping malls and multi-storied buildings are very common. The transportation of goods within the high-raised buildings is made more convenient by the dumbwaiter elevators. BLDC motors are popular in industrial applications like conveyers and elevators because of the recent advancements in power electronics help the BLDC motors to overcome its drawbacks. Standalone photovoltaic systems with MPPT are a best option to be used ac supply source for the elevators in multi-

M. Panickar (✉) · V. Sreelekha
Department of Electrical Engineering, Rajiv Gandhi Institute of Technology,
Kottayam, Kerala, India
e-mail: manjupanickar1998@gmail.com

storied buildings. The maximum power from the solar modules under all conditions can be extracted by using the maximum power point tracking (MPPT) circuit thereby ensuring the best utilisation of solar PV modules. There is a possibility for the set-up of a dc microgrid in the top of high-raised buildings. DC microgrid with renewable energy sources have the advantages of less stages of power conversion, easy control, absence of harmonics and reactive power, ease of connecting storage devices, etc. A 400 V ac supply and V/f control is required for a three-phase induction motor which demands a dc source of more than 500 V. It will lead to an additional power conversion stage, thereby adding more complexity when used with dc microgrid. The most suitable motor for the elevator application is BLDC motor, when operated with a standalone PV source. In the case of elevators, which operates in both motoring and braking modes, the power loss occurs most at the time of braking and it can be recovered by regeneration of power during braking and it is possible by the four quadrant operation of the BLDC drive.

The initial motors used in elevator applications were dc motors. The dc motors persisted in this application because its speed control can be done by changing the magnitude of voltage and changing the polarity of the supply will help to reverse the direction of rotation of motor. Three-phase induction motors are generally used in elevator applications. Less maintenance due to absence of the parts like brushes, commutators, etc. is the main advantage of induction motors compared to dc motors. The speed control of induction motor was difficult before the arrival of variable speed drive. Therefore, smooth running dc motors were used as elevator drives for many years. There was a vast advancement and growth in the power electronics field in the second half of 20th century. The elevator motor technology was abruptly changed after the development of variable frequency drive. The VFD made possible the precise speed control of ac motor by changing the supply frequency since both synchronous and asynchronous motors' speeds depend on the supply frequency. To find out the most suitable motors to be used in elevator applications is an active research area. The number of elevators in the world increases day by day. Clean and efficient motors are needed in the elevator market as well. Induction motors with the mechanical gearbox are used in the conventional systems. These systems are neither clean nor efficient. PMSM would be a better alternative to solve some certain problems [1]. The windings of the PMSM should be properly designed to reduce harmonic components in the induced back EMF and to reduce torque ripple. In the former systems with induction motors, a mechanical gearbox is used to reduce motor's angular speed to the desirable speed. For the smooth operation, it must be lubricated frequently. This lubrication is very dirty work and is an environment threat. The floor absorbs the oil in long time operation and it will cause unpleasant smell. Gearboxes are not efficient. The speed can be changed to any value with the use of PMSM and inverter, as a result, the gearboxes can be eliminated. Use of permanent magnets in rotor or stator will end up reducing the electrical energy consumption and will give high efficiency. Permanent magnet synchronous motors have recently come into the market because of their high efficiency, large power density and control simplicity. Therefore, PMSMs are preferred by companies for elevator applications. Electrical energy consumption of elevator drives with permanent magnet machines are studied

[2, 3]. The research was returned to BLDC motors because of the less availability and complex maintenance of PMSMs. The development of a nine-phase permanent magnet motor which is suitable for an ultra-high speed elevator and its testing in the world's highest elevator test tower is done [4]. Linear switched reluctance motors were studied to be implemented as elevator motor drive [5, 6].

The proposed system consists of a dumbwaiter elevator driven by a BLDC motor. A standalone PV system is used to harvest the available solar energy in the top of high-raised buildings. A Cuk converter is used to boost the output of the PV system. Section 2 consists of the description of the block diagram, BLDC motor control, four quadrant operation of BLDC motor, control of PFC Cuk converter and the design. The simulation studies are presented in Sect. 3 followed by conclusion in Sect. 4.

2 Description of Proposed System

2.1 Block Diagram Explanation

The block diagram of the complete system is shown in the Fig. 1. In the source side, there is a standalone PV system and a diesel generator connected to the common dc bus. The output from the PV array is boosted by using a Cuk converter. To operate the PV array always at its maximum power point, perturb and observe maximum power point technique is used to generate the gate pulses for the Cuk converter. Since it is a standalone PV system, a battery back-up is necessary. The battery is connected to the common dc bus via a synchronous boost converter. The diode in the boost converter is replaced by a MOSFET to enable bidirectional power flow. It performs the function of a bidirectional buck-boost converter. The regenerated voltage from the BLDC motor and the excess voltage from the PV array will charge the battery by buck operation and the battery will discharge through boost operation of the converter whenever it is necessary, i.e. when the power supply from the PV array is not sufficient to meet the load demand. The control loop of this converter is formed so as to maintain the dc bus voltage constant.

A diesel generator is also added to the source side to ensure more reliability for the system. The output of the diesel generator is rectified and is fed to the power factor corrected Cuk converter. Power factor correction is necessary to meet the power quality standards. The diesel generators role is to intermittently intercept and to act as a back-up source only when two conditions are satisfied, i.e. when the standalone PV system is not sufficient to meet the load demand and when the battery is at its maximum admissible discharge limit. The diesel generator will get disconnected when the standalone PV system is able to meet the load demand.

After necessary controls in the source side, it is connected to the BLDC motor via an inverter. The BLDC motor is coupled to the elevator. The upward and downward motion of the elevator corresponds to forward and reverse rotation of the motor. The BLDC motor is operated in four quadrants to drive the dumbwaiter elevator. It is done
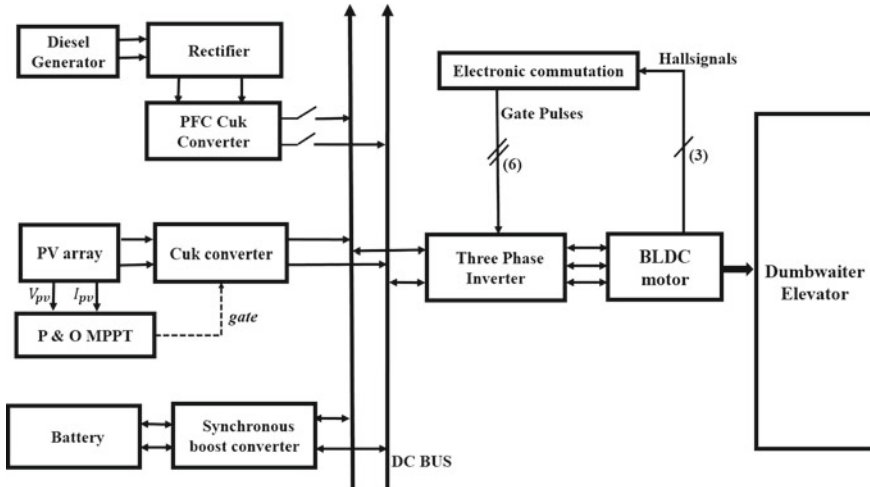
**Fig. 1** Block diagram of the proposed system

by the switching of MOSFETs in the inverter in the required pattern. For this, hall sensor signals from the motor are used. The elevator consists of an elevator cabin and a counterweight. Both are connected via suspension cables and are guided through a mechanical pulley. The mechanical pulley is coupled with the BLDC motor-gear system. The circuit diagram of the proposed system is shown in the Fig. 2. The explanation of the circuit diagram is same as that of the block diagram.

2.2 Control of BLDC Motor

The BLDC motor control has to be done in such a way to operate the dumbwaiter elevator in four quadrants. The MOSFETs in the three-phase inverter are switched according to the specific pattern for the forward and reverse rotation of BLDC motor. The actual rotor position is identified by the three hall sensors in the BLDC motor. It is able to generate a switching table to operate the motor in required pattern by utilising the information provided by the hall sensors.

The motor is operated in both forward and reverse directions with constant speed for this application. At a time two switches, one from the top and other from the bottom will conduct. As the quadrant changes, the torque will also change. As the torque varies, the speed shows a slight variation from its constant value and then returns to the previous value. The change in speed may generate a positive or negative speed error, and this sign change is used to create a direction input. If it is zero, the motor will rotate in forward direction, otherwise the rotation will be in reverse direction. This is by the simultaneous conduction of top and bottom switches of the same leg. The logic is used the simulation to obtain the required results is as mentioned above.

Fig. 2 Four quadrant operation [7]
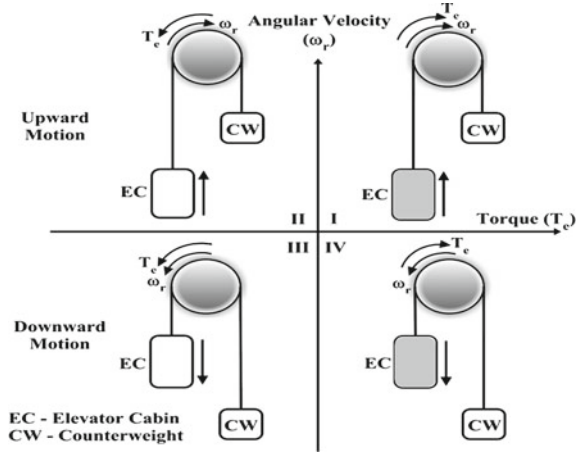
2.3 Four Quadrant Operation

The elevator consists of the elevator cabin and counter weight. The half of the weight of fully loaded elevator is assigned for the counter weight. To drive the dumbwaiter elevator, the BLDC motor is operated in four quadrants. In Fig. 2, torque is represented by x-axis and and speed is represented by the y-axis. Both speed and torque are positive in the first quadrant. The drive is in forward motoring mode in first quadrant. The loaded cabin moves upwards, therefore, applied torque and load torque are in same direction. In second quadrant, the speed remains positive, but the torque is negative. The empty cabin moves upwards. The weight of empty cabin is much lesser than the counter weight, so there is chance of sudden lifting. Therefore, applied torque and load torque are in opposite direction, i.e. braking. The second quadrant indicates the forward braking mode.

Both the speed and torque are negative in the third quadrant. This quadrant refers to the case of empty cabin moving downwards. Torque must be applied as the same direction of load torque, so it is reverse motoring mode. In the fourth quadrant loaded cabin moves downwards. Here, the applied torque is opposite to that of load torque. So, this mode is reverse braking. In both the braking modes, there is a power loss. The conventional drives waste this braking power in external resistors. By utilising the regeneration capability of BLDC motor and with a suitable gear system, this power can be recovered and can be used for other applications.

2.4 Control of Power Factor Corrected (PFC) Cuk Converter Used for the Incorporation of Diesel Generator

The required dc bus voltage is combined with the actual dc bus voltage. The error is fed to a PI controller. The PI controller output is multiplied with the absolute voltage
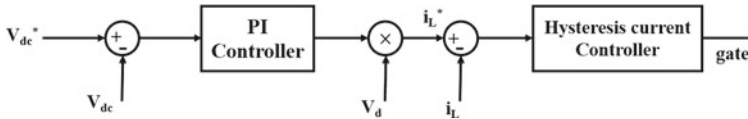
Fig. 3 Block diagram of PFC Cuk converter control

output of diode rectifier. Thus, the reference current is generated. This reference current is compared with the actual current and the error is fed to a hysteresis current controller. It compares the load current and band limit given to it. When it crosses the upper band limit, the switches turns off, when current crosses the lower band limit, switches turns on (Fig. 3).

2.5 Design of Proposed System

The weight of fully loaded elevator cabin, diameter of pulley, rated top speed, counter weight ratio and shaft and gear box efficiency is assumed, and the BLDC motor to operate the elevator in the simulation is chosen. The motor used is 48 V, 750 W BLDC motor. The battery design which is used as a back-up source is done as per the following steps. The assumption considered is the battery must operate the dumbwaiter elevator for three hours. The energy required by lift from the battery at the motor output side is 2250 Wh. It is then divided by the efficiencies of motor, inverter and synchronous boost converter, so the exact energy required as the battery output energy is 3096 Wh. A 24 V lithium ion battery with 80% Depth of Discharge (DoD) is selected. Dividing the energy by system voltage and then by DoD gives the required ampere hour value of the battery. A 24 V/200 Ah lithium ion battery is chosen as per the energy requirements of the load.

PV array is sized as per the following steps. The output power rating of the motor is 750 W. The energy required to drive the elevator from PV array is calculated by multiplying the motor output power rating with the hours to be operated output. Thus, obtained energy output is divided by the efficiencies of motor, inverter, Cuk converter and cable to find the required output energy at the PV side. Multiplying the energy then by 1.25 will compensate the additional system losses. The panel capacity required for the load is then calculated by considering the insolation at the place. Additional panel capacity required to charge the battery is calculated, and both these values are summed to obtain the total panel capacity. A 225 Wp panel is selected. The total panel capacity is divided by 225 W to obtain the number of panels. A 1 kVA three-phase voltage source inverter is used for the safe and reliable operation.

CUK Converter design

The Cuk converter is used to boost the output voltage of the PV array instead of a boost converter. Cuk converters are a type of buck-boost converter with same voltage gain and inverted output. The configuration of the converter is like a boost converter

followed by a buck converter. Certain components are eliminated and some are added to form the configuration of the Cuk converter. A capacitor is used as the main energy storage element. This mutual capacitor couples the input side with the output side. Cuk converters offer smooth current at both input and output sides. A buck converter has pulsating input current due to the absence of the inductor at the input side, and the boost converter has pulsating output current due to the absence of inductor at the output side. But Cuk converter has inductors on both input and output sides which will ensure smooth input and output currents. These converters are one of the most suggested converters to be used with renewable energy sources like wind and solar energy, where power production depends on varying atmospheric conditions. It offers stable and fast response when operated with PV array and Perturb and observe MPPT algorithm. The switching frequency is 25 kHz. The components are designed as per the following equations.

The duty cycle is obtained from Eq. 1

$$V_o = \frac{-V_{in}D}{(1-D)}, D = 0.62 \tag{1}$$

$$L_1 = \frac{V_s D}{\Delta I_{L1} f} \tag{2}$$

$$L_2 = \frac{V_s D}{\Delta I_{L2} f} \tag{3}$$

$$C_1 = \frac{V_s D}{Rf \Delta V_{c1}} \tag{4}$$

$$C_2 = \frac{(1-D)}{8L_2 \frac{\Delta V_o}{V_o} f^2} \tag{5}$$

Synchronous boost converter

Synchronous boost converter (Fig. 4) is not very different from a boost converter. The diode in the boost converter is replaced with a switch to obtain the configuration of a synchronous boost converter. It is to enable bidirectional power flow. It performs the function of a bidirectional buck-boost converter. Bidirectional dc–dc converter is an important device to interface storage devices between source and load in renewable energy system. It is to ensure continuous flow of power, because the output of the renewable energy system varies according to the changes in weather conditions. A 24 V battery is used and the dc bus voltage is 48 V. So, the components are designed as per the input and output voltage values. The duty cycle is calculated using the same equation of the boost converter.
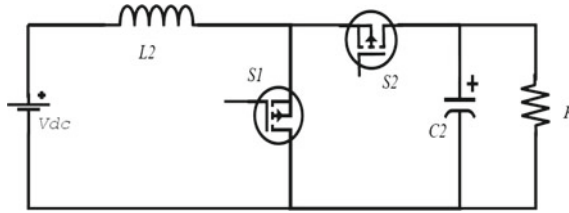
$$L = \frac{V_o D(1-D)}{2I_s f} \tag{6}$$
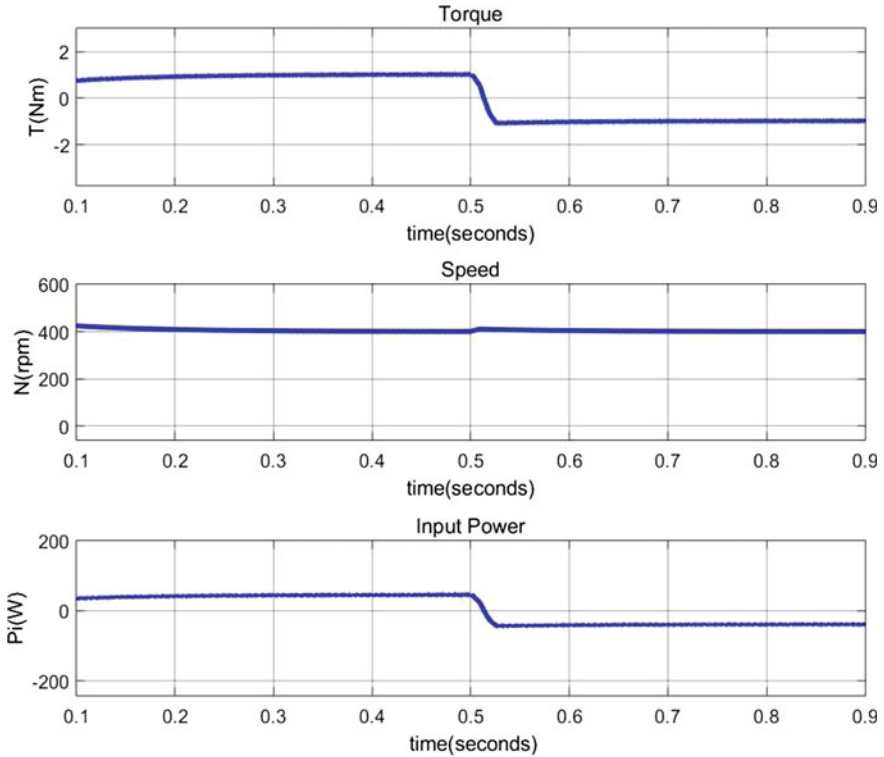
Fig. 4 Synchronous boost converter

Fig. 5 Motor parameters during first and second quadrant operation

$$C = \frac{V_o D}{R f \Delta V_c} \tag{7}$$

PFC Cuk converter design

   The PFC Cuk converter is designed as per the following equations. $V_d = \sqrt{2}V_s = \sqrt{2} \times 220 = 312V$, $V_{dco} = 48V$ $V_{smin} = 85V$, $V_{dcomax} = 48V$, $P_{max} = 982W$, $f_s = 25000\,Hz$ $\eta = 0.25$, $\lambda = 0.25$, k= 0.1, $\omega = 314$, $\delta = 0.4$
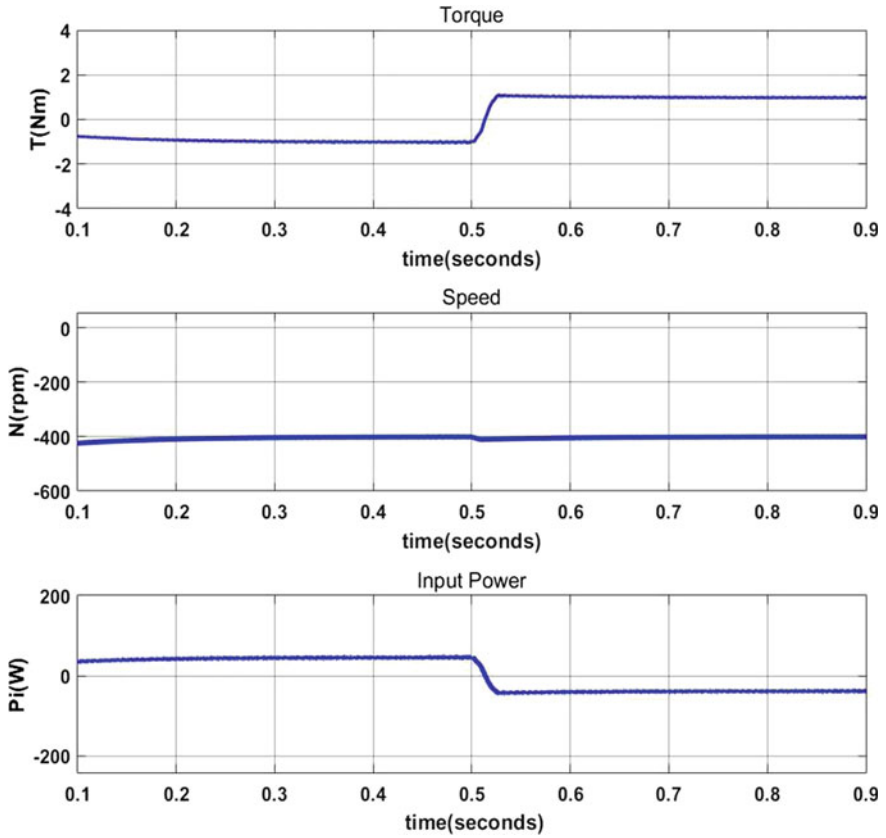
Fig. 6 Motor parameters during third and fourth quadrant operation

$$L_1 = \frac{1}{\eta f_s} \left(\frac{V_{smin}^2}{P_{max}} \right) \left(\frac{V_{dcomax}}{\sqrt{2}V_{smin} + V_{dco}} \right) \tag{8}$$

$$L_2 = \frac{V_{dcmax}}{\lambda \sqrt{2}V_{smin} f_s} \left(\frac{V_{smin}^2}{P_{max}} \right) \left(\frac{V_{dcomax}}{\sqrt{2}V_{smin} + V_{dcomax}} \right) \tag{9}$$

$$C_1 = \frac{P_{max}}{k f_s (\sqrt{2}V_{smin} + V_{dcomax})^2} \tag{10}$$

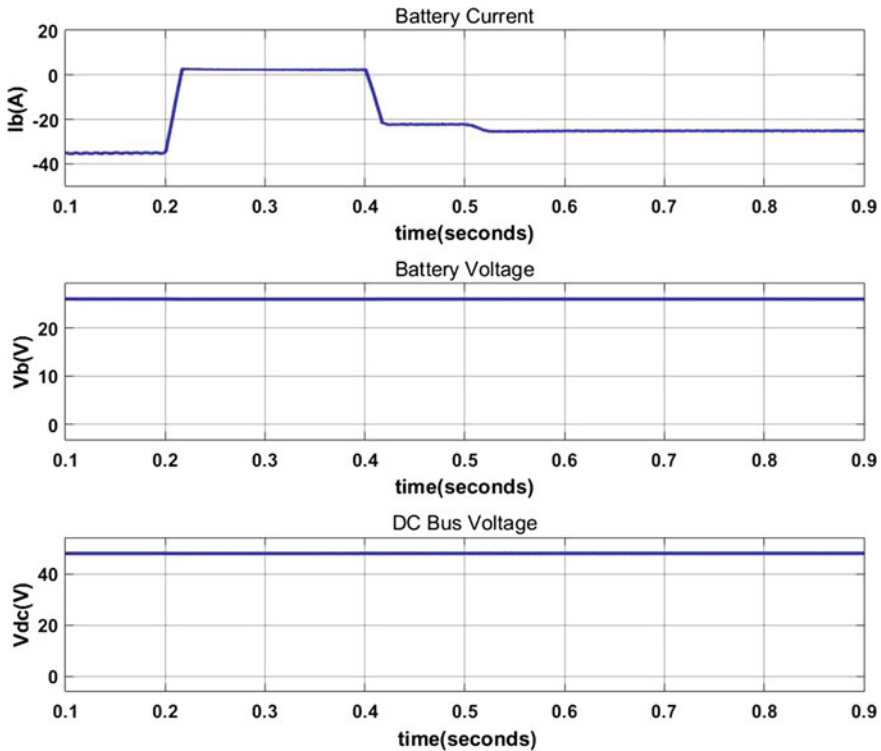$$C_2 = \frac{P_{max}}{2\omega\delta V_{dcmin}^2} \tag{11}$$

Fig. 7 Battery parameters

2.6 Diesel Generator

Diesel generator can be used as a back-up source to ensure the reliability of a stan-dalone system. It consists of an electrical generator and a diesel engine to generate electrical energy. The primary fuel used in the diesel generators is liquid fuels or natural gas. It works based on the air compression and fuel. Air is blown into the generator till it is that compressed, so that the injection of fuel will generate heat thereby leads to the inflammation of fuel. The generator will then starts to produce energy. Here, it is connected to dc bus only if the load demand is more than the power supplied from the PV array and when the battery is at its maximum discharge limit. Considering the power requirement at the source side, a 2 kVA, 220 V, 50 Hz single-phase diesel generator is selected.

3 Simulation and Results

The complete simulation was done in MATLAB Simulink using the components taken from Simulink library. The main sections in the simulation are PV section,
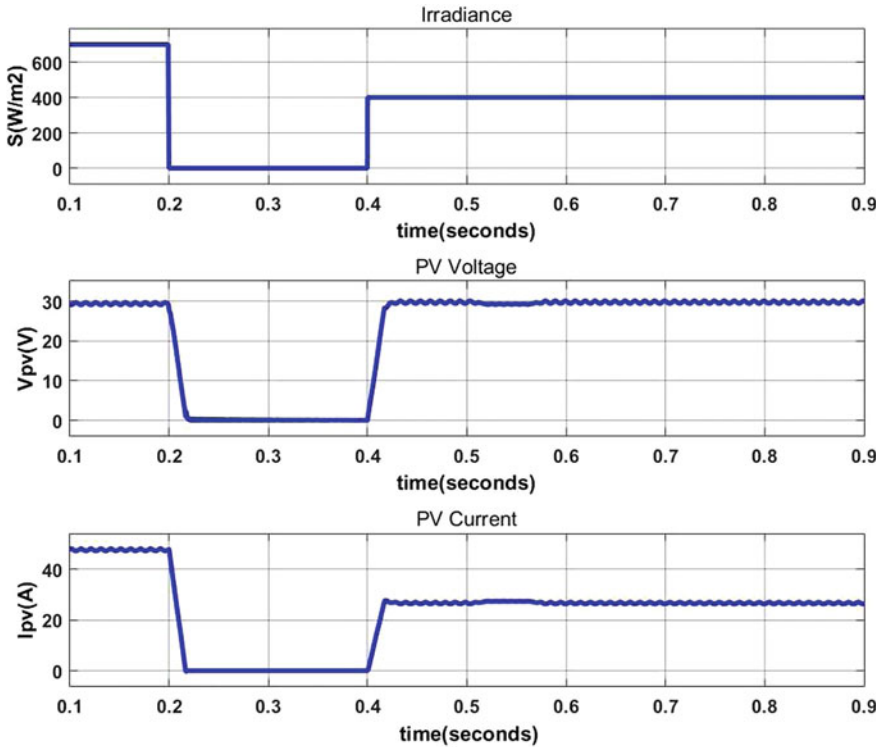
Fig. 8 PV parameters

battery section, motor section and diesel generator section. The quadrant is changed at 0.5 s and the irradiance is reduced to 0 from 0.2 to 0.4 s. It is to show the discharge of battery. The battery discharges and supply the load during this time interval. At 0.4, the irradiance is increased, thereby charging the battery. At 0.5 s, there is a further dip in the battery power curve which shows that during second quadrant, the regenerated power from the BLDC motor is charging the battery. The speed is maintained at 400rpm. In first and second quadrants, speed is positive, while in the second quadrant, the torque is negative. The input power waveform in Fig. 6 is negative at second quadrant. The power is regenerated at second quadrant (Fig. 5).

The battery current is negative, while the battery is charging and it is positive from 0.2 to 0.4, while the battery is discharging. Figures 7, 8 and 9 show the mentioned parameters for first and second quadrant operation for 1Nm load torque. It is same for third and fourth quadrant operation for the same load torque. The dc bus voltage is maintained at 48V which is the input voltage of the BLDC motor. The PV voltage is constant when there is irradiance rather than the increase or decrease of the irradiance value. It is because of the use of perturb and observe MPPT technique. The PV current is varied according to the variation of irradiance.
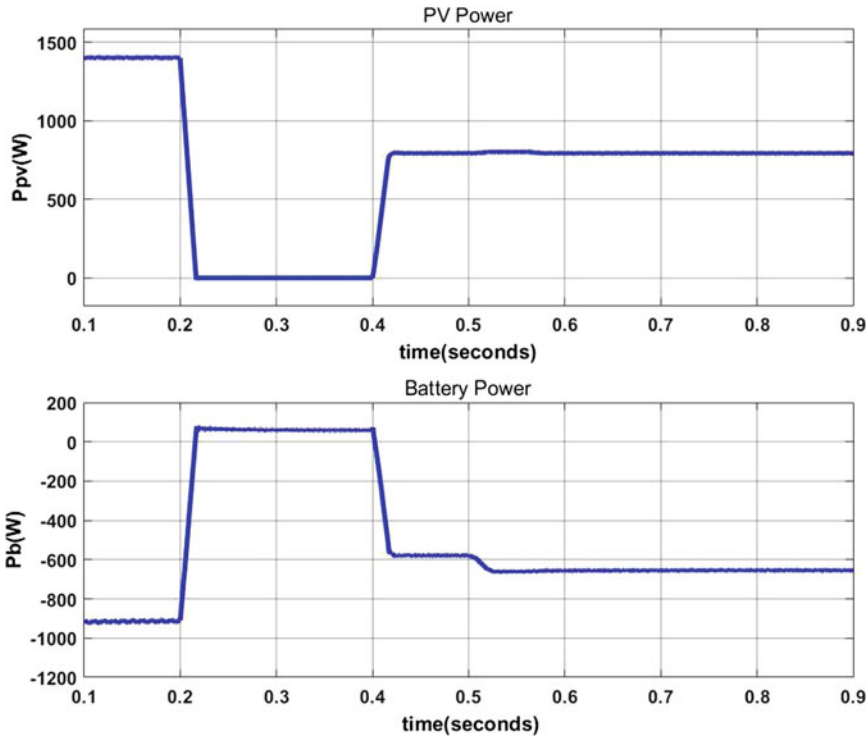
Fig. 9 PV and battery power

Third and fourth quadrant refers to the reverse rotation of the motor. The speed is at $-400\,$rpm which indicates the reverse rotation of motor. The torque is $-1\,$Nm in third quadrant and it changes to 1Nm in fourth quadrant. The quadrants are changed at 0.5 s. In third quadrant, both torque and speed are negative, the mode is motoring. The positive input power during this interval indicates the motoring operation. In fourth quadrant, the input power is negative, which refers to the reverse braking mode and battery is charged by the regenerated power from the motor during this mode.

An AC source is added to the source as a representation of diesel generator output. Prior to the connection of this ac source to the dc bus, rectification and power factor correction is to be done. Former sections detail the design and control methods used in this section. The power factor of the system must be as close as possible to unity. The supply voltage and current must be in phase to realise this condition and the total harmonic distortion (THD) of the supply current must be below five percentage. The dc bus voltage is controlled to be 48 V, since the BLDC motor voltage input is 48 V (Fig. 10).
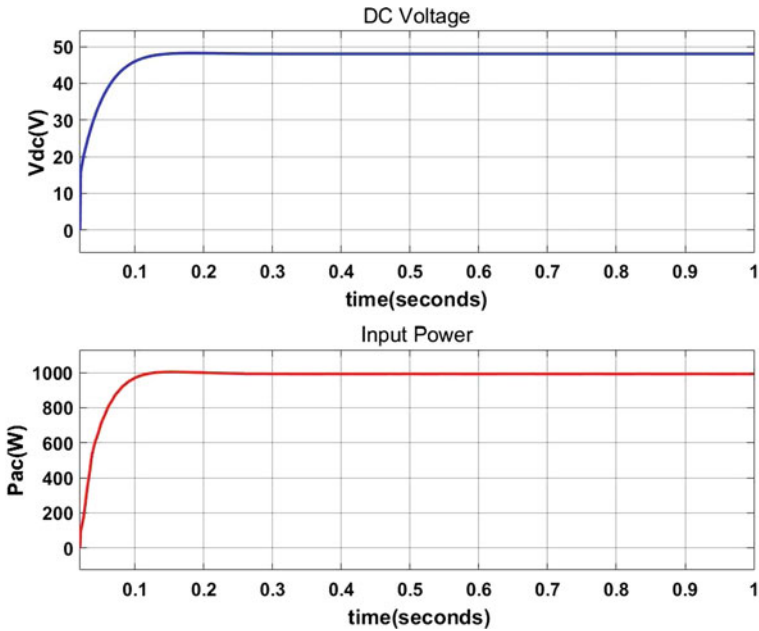
Fig. 10 Output dc voltage and input power

4 Conclusion

Investigation of performance of BLDC-driven dumbwaiter elevator fed from a SPV array and diesel generator is done through MATLAB simulations and verified the results. The regeneration mode of BLDC motor is utilised for charging the battery and is investigated using simulation studies. The renewable energy source makes the proposed system cost effective and efficient. It is found that BLDC motor is suitable for standalone PV array fed dumbwaiter elevator, and diesel generator adds more reliability to the system.

References

1. Bakhtiarzadeh H, Polat A, Ergene LT (2017) Design and analysis of permanent magnet synchronous motor for elevator applications. 978-1-5090-4489-4
2. Georgiev I, Mirchevski S (2012) Analysis of electrical energy consumption in elevator drives. In: 15th international power electronics conference
3. Anand R, Mahesh M (2016) Analysis of elevator drive energy consumption with permanent magnet machines. In: 4th international smart energy grid engineering conference
4. Jung E, Yoo H, Sul S-K, Choi H-S, Choi Y-Y (2012) A nine-phase permanent-magnet motor drive system for an ultra high-speed elevator. IEEE Trans Ind Appl 48(3):987–995

5. Onat A, Kazan E, Takahashi N, Miyagi D, Komatsu Y, Markon S (2010) Design and implementation of a linear motor for multicar elevators. IEEE/ASME Trans Mechatron 15(5):685–693

6. Lim HS, Krishnan R, Lobo NS (2008) Design and control of a linear propulsion system for an elevator using linear switched reluctance motor drives. IEEE Trans Ind Electron 55(2):534–542

7. Das D, Kumaresan N, Nayanar V, Navin Sam K, Ammasi Gounden N (2016) Development of BLDC motor based elevator system suitable for DC microgrid. IEEE Trans/ASME Mechatronics 21

8. Strunz K, Abbasi E, Huu DN (2013) DC microgrid for wind and solar power integration. IEEE J Emerg Sel Topics Power Electron 2(1):115–126

9. Anand S, Fernandes BG (2010) Optimal voltage level for DC microgrids. In: Proceedings of 36th annual conference IEEE industry electronics society, Glendale, AZ, pp 3034–3039

10. Yuhang Z, Muyan MA (2010) Implementation of six-layer automatic elevator controller based on FPGA. In: Proceedings 6th international conference wireless communication network mobile computing, Chengdu, pp 1–4

Pixelated Wideband Metamaterial Absorber for X-band Applications

Prakash Ranjan, Chetan Barde, Komal Roy, Rashmi Sinha, Sanjay Kumar, and Debolina Das

Abstract This report presents a pixelated wideband Metamaterial Absorber (MA) that operates in a microwave region. The proposed metamaterial absorber contains two same-shape resonators made-up of splitted squares in the form of pixels that have been obliquely placed opposite to each other. Wideband absorption of 5.67 GHz (52.88%) that ranges from 6.40 to 12.07 GHz with absorptivity above 90% has been achieved, which covers the X (8 to 12 GHz) band. The Full Width Half Maxima (FWHM) of the structure is 6.84 GHz (58.82%) which ranges from 5.96 to 12.80 GHz. The presence of metamaterial properties in the region of interest has been explained by plotting an Electromagnetic (EM) parameter, real and imaginary curves. The high absorption phenomenon is explained using surface current and electric field distribution at three absorption peaks (6.8, 8.5 and 11.9 GHz). The sensitivity of the polarization for the structure has been examined under normal and oblique incident of the wave. The proposed structure has been designed using ANSYS HFSS 19.1. The advantage of the proposed MA is the wideband absorption with an overall dimension of $16.5 \times 16.5 \times 3.2$ mm in contrast to that of the other reported microwave MAs.

1 Introduction

EM waves have played a key role in our everyday life and have found applications in the various field of sensing, imaging, communications, optical fibers, light sources,

P. Ranjan · C. Barde (✉)
Department of Electronics and Communication Engineering, Indian Institute of Information Technology Bhagalpur, Bihar, India
e-mail: 2017rsec004@nitjsr.ac.in

K. Roy · R. Sinha · D. Das
Department of Electronics and Communication Engineering, National Institute of Technology Jamshedpur, Jharkhand, India

S. Kumar
Department of Computer Science Engineering, National Institute of Technology Jamshedpur, Jharkhand, India

filters, antennas, absorbers etc. [1–4]. These waves have received huge interest from the researchers and scientists all over the world ranging from low frequencies to Gamma rays [5, 6]. The interconnection between materials and waves has led to numerous applications and devices such as reflection, transmission, diffraction and refraction [7–9]. Materials' response to EM waves is determined by their macroscopic EM parameters, namely the dielectric permittivity (ε) and the magnetic permeability (μ). Natural occurring materials generally have positive ε and μ. The response from the naturally occurring materials has only been a small fraction that one can access theoretically. The material response can be expanded by designing artificial structures, the so-called metamaterials [10, 11].

Metamaterials are artificially engineered structures with properties commonly not similar to the naturally occurring materials; therefore, these materials are artificially made in nature and are called as manmade materials. The properties possessed by metamaterials are used for various applications such as clocking [12], super lens [13], nonlinear metamaterial [14], sub-wavelength waveguides [15], antennas [16], filters [17] and metamaterial absorbers (MAs) [18].

In recent years, MAs conquers conventional absorbers due to their perfect EM absorption, compactness, fine width, and low profile. These advantages lead to different MAs in single-band [19], dual-band [20], multi-band [21, 22] and wideband [23] applications in all frequency regions. Despite of various applications MAs suffer from narrow bandwidth. To enhance the bandwidth different techniques are implemented such as multilayers [23] and multiresonant structures [24]. The first one suffers from thickness constraint and the latter one suffers from the larger size. To overcome the above problems single layer MAs are proposed, which have moderate thickness and enhanced bandwidth [25].

This article presents two same-shape resonators made-up of splitted squares in the form of pixels with that have been obliquely placed opposite to each other. Wideband absorption of 5.67 GHz (52.88%) that ranges from 6.40 to 12.07 GHz with absorptivity above 90% has been achieved, which covers the X (8 to 12 GHz) band. The Full Width Half Maxima (FWHM) of the structure is 6.84 GHz (58.82%) that ranges from 5.96 to 12.80 GHz. The high absorption phenomenon is explained using surface current and electric field distribution at three absorption peaks (6.8, 8.5 and 11.9 GHz). The sensitivity of the polarization for the structure has been examined under normal and oblique incidents of the wave. The proposed structure has been designed using ANSYS HFSS 19.1.

2   Structure Synthesis

The synthesis of structure is done using WDO (Wind Driven Optimization technique) in pixelated form as described in [22]. Synthesis of wideband MCP is done by using interface techniques. This technique involves interfacing of MATLAB with commercially available ANYSS-HFSS. BWDO algorithm runs in MATLAB, and pixelated unit cell structure develops in FEM solver (ANYSS-HFSS). Figure 1 shows

the flowchart for the synthesis process of pixelated unit cell structure which is used for wideband MCP.

The proposed unit cell structure consists of two same-shape resonators made up of splitted squares in the form of pixels that have been obliquely placed opposite to each other as shown in Fig. 2 with EM field directions. The overall dimension of the structure is 16.5 × 16.5 mm. The unit cell structure is comprised of three layers as shown in Fig. 3. The top and bottom layers are made up of copper with a thickness of 0.035 mm, and the middle layer is made up of lossy dielectric FR-4 substrate with a thickness of 3.2 mm. The structure has been designed using ANSYS HFSS 19.1, with periodic master and slave boundary condition and floquet port excitation.
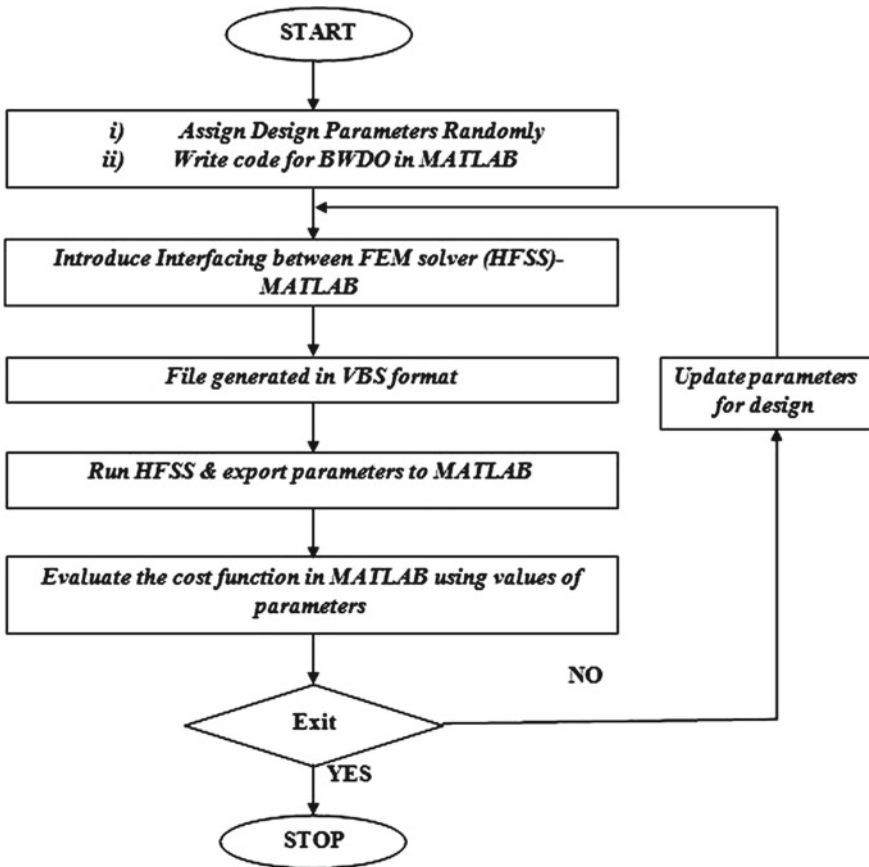
Fig. 1 A typical scheme for synthesis of unit cell of metamaterial
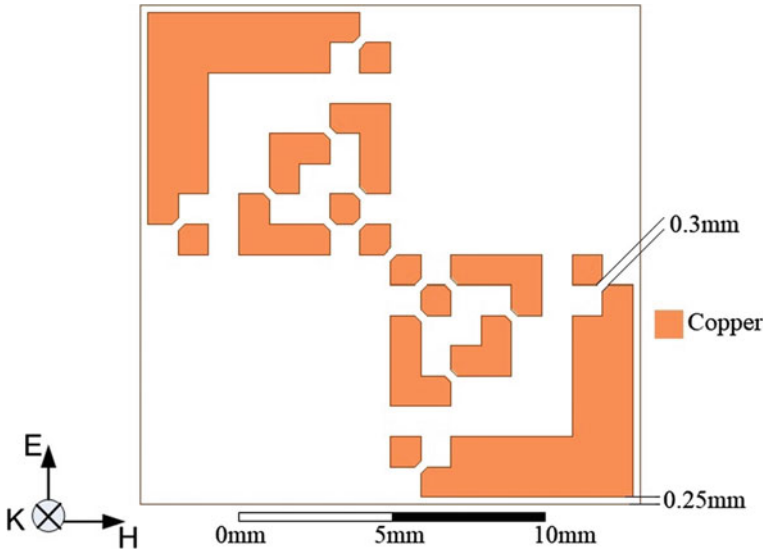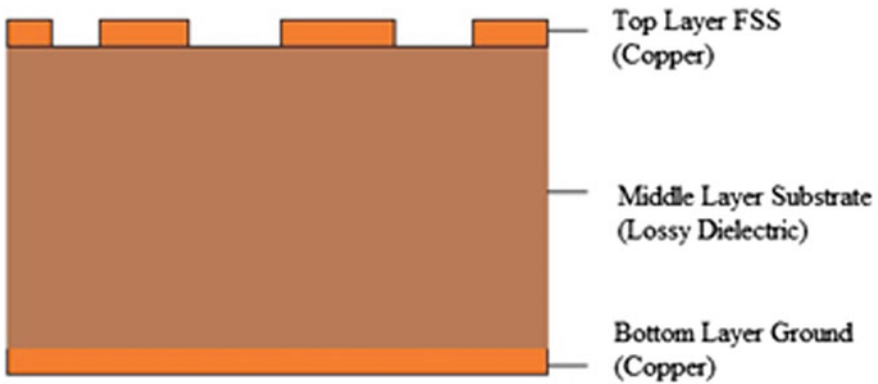
Fig. 2 Front view of proposed MA

Fig. 3 Unit cell structure of the proposed MA

3 Simulation Analysis

From Eq. 1, absorptivity $A(\omega)$ has been calculated that depends on the reflected (S_{11}) and transmitted (S_{21}) power, but as the lower layer is completely covered with copper, the transmitted power in Eq. 1 becomes zero and absorptivity completely depends on reflected power as specified in Eq. 2. The absorptivity of the structure can be increased by minimizing the reflected power from the surface.

$$A(\omega) = 1 - |S_{11}(\omega)|^2 - |S_{21}(\omega)|^2 \tag{1}$$
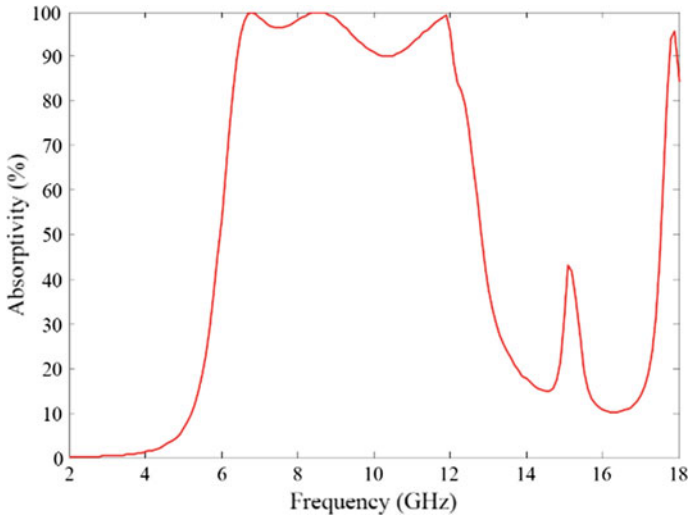
Fig. 4 Absorptivity curve of proposed MA

$$A(\omega) = 1 - |S_{11}(\omega)|^2 \tag{2}$$

The proposed structure has obtained a wideband absorption of 5.67 GHz (6.40 to 12.07 GHz) at 90% absorptivity with three absorption peaks (6.8, 8.5 and 11.9 GHz) and FWHM of 6.84 GHz (5.96 to 12.80 GHz) as shown in Fig. 4.

3.1 Absorption Mechanism

The absorption mechanism can be explained by considering MA as a homogeneous medium. The normalized impedance can be evaluated by Eq. 3.

$$Z = \sqrt{\frac{(1 + S_{11})^2 - S_{21}^2}{(1 - S_{11})^2 - S_{21}^2}} \tag{3}$$

As the bottom layer is completely covered with copper, therefore transmitted power (S_{21}) is zero.

$$Z = \frac{(1 + S_{11})^2}{(1 - S_{11})^2} \tag{4}$$

But to evaluate the normalized impedance transmitted power (S_{21}) play an important role. In order to calculate S_{21} the bottom layer is cut from all four corners
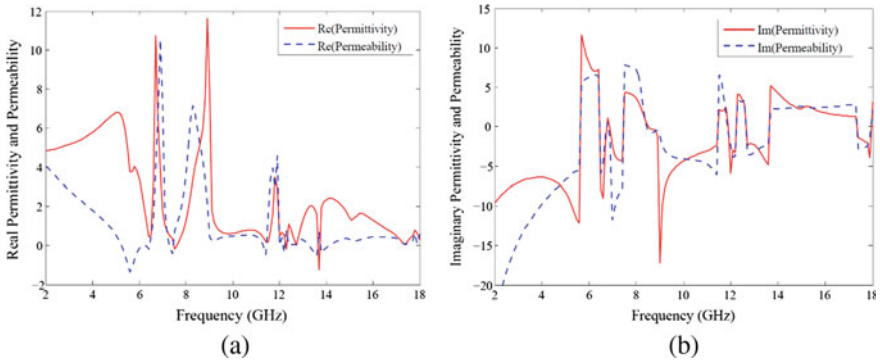
Fig. 5 EM parameter curve for **a** Real part, **b** Imaginary part

such that absorption frequency does not swerve. The normalized impedance at three absorption peaks (6.8, 8.5 and 11.9 GHz), the real and imaginary parts approaching towards unity and zero respectively indicates that a perfect impedance has been achieved which eventually leads to the maximum absorption.

The real part approaching towards unity in Fig. 5 occurs due to a speedy change in values of ε_{eff} and μ_{eff} at absorption frequency, satisfying the electric and magnetic resonance condition.

The effective ε_{eff} and μ_{eff} has been calculated using Electric susceptibility (Es) and Magnetic susceptibility (Ms), mentioned in Eqs. 5–8.

$$E_s = \frac{2jS_{11} - 1}{kS_{11} + 1} \tag{5}$$

$$E_s = \frac{2jS_{11} + 1}{kS_{11} - 1} \tag{6}$$

$$\varepsilon_{\text{eff}} = 1 + \frac{E_s}{d} \tag{7}$$

$$\mu_{\text{eff}} = 1 + \frac{M_s}{d} \tag{8}$$

where K is a wave number and d is the distance travelled by the incident EM wave. The real and imaginary part of EM parameters are shown in Fig. 5a and b respectively.

3.2 Absorption Phenomena

The phenomenon of absorption can be described by surface current distribution at two absorption peaks (9.44 and 11.47 GHz). The surface current distribution at the top
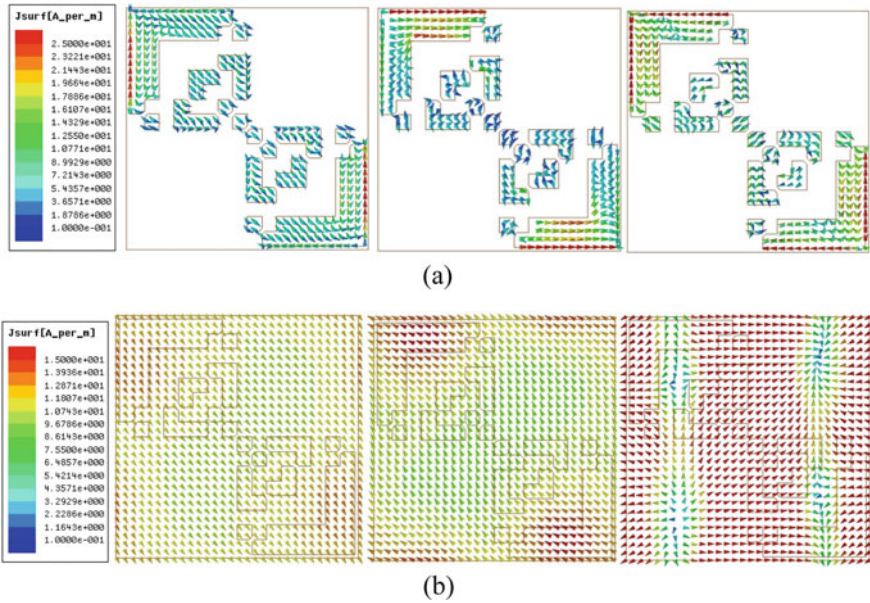
Fig. 6 Surface current distribution. **a** Top surface. **b** Bottom surface

and bottom layers of the proposed structure is shown in Fig. 6a and b. It is observed that the current is anti-parallel at top and bottom layer, resulting in a circulating current that is in a perpendicular direction to the magnetic field, creating magnetic excitations.

3.3 Analysis of MA Under Normal and Oblique Incident

The polarization sensitivity of MA has been studied under normal and oblique incidents for TE and TM mode. The electric field direction has been fixed, and the wave vector and magnetic field direction have been changed so as to analyze the absorption. Under normal incidents the structure is rotated from horizontal polarization ($\phi = 0^0$) to a vertical polarization ($\phi = 90^0$), and the reflection coefficient is measured at every 15^0 increments. When the polarization angle changes the absorptivity decreases up to 45^0 and then again increase after that up to 90^0 which confirms that the proposed MA is polarization sensitive as shown in Fig. 7.

Under oblique incident for TE and TM polarization, wide absorption is achieved up to 45^0 but absorptivity response decreases gradually as the angle is increased further as shown in Fig. 8a and b respectively.
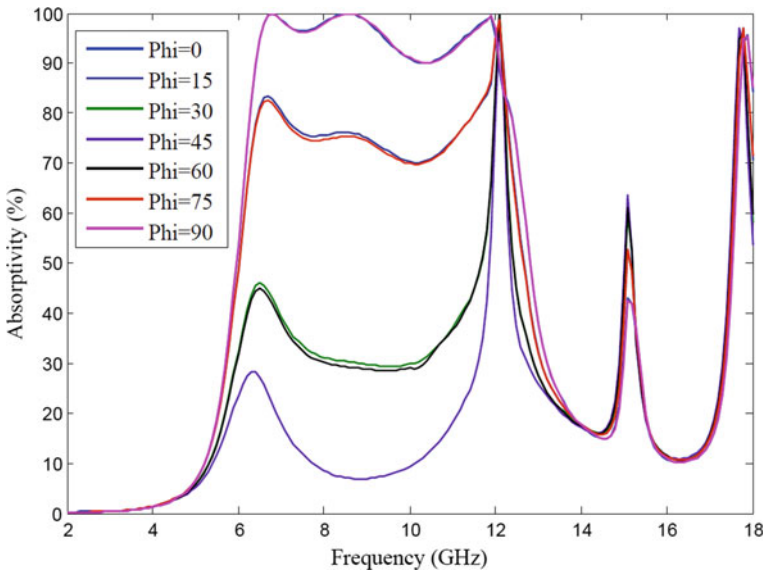
Fig. 7 Oblique incident curve
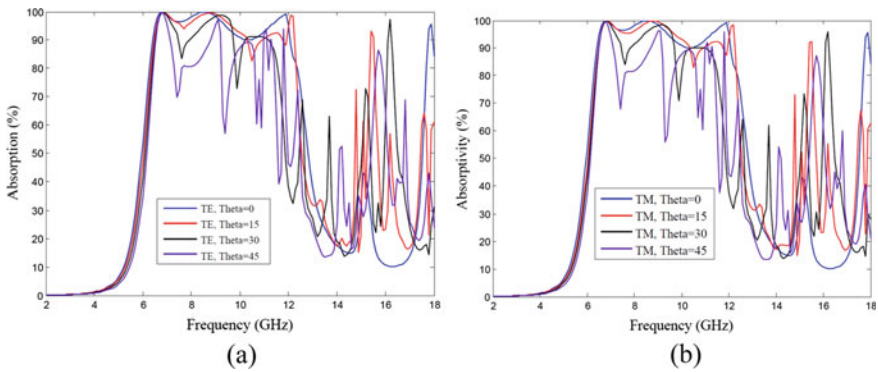

Fig. 8 Normal incident curve. **a** TE. **b** TM

3.4 Comparison with Reported Literature

The proposed work is compared with already reported literature in Table 1, in terms of −10 dB bandwidth, thickness, design configuration and design methodology.

Table 1 Comparison between proposed and reported MA

Ref	Central frequency (GHz)	Unit cell size (mm)	Thickness (mm)	−10 dB bandwidth (%)	Design configuration	Design methology
Tao et al. [20]	14.69	6.4	3.65	85.9	Multilayer	Hit and trial
Barde et al. [21]	8.78	12.0	4.0	86.6	Multilayer	Hit and trial
Ranjan et al. [22]	11.51	9	1.6	46.2	Dual layer	Hit and trial
Barde et al. [23]	10.15	13.8	5.6	45.0	Dual layer	Hit and trial
Ranjan et al. [24]	5.9	10.0	3.2	44.0	Single layer	Hit and trial
Guo-Dong et al. [25]	14.05	5.5	1.6	51.2	Single layer	Hit and trial
Proposed work	9.62	16.5	3.2	52.8	Single layer	Pixelated using WDO

4   Conclusion

A wideband MA has been proposed for X band applications. The bandwidth of 5.67 GHz (52.88%) ranging from 6.40 to 12.07 GHz which almost covers the X band has been achieved. The proposed absorber has three absorption peaks (6.8, 8.5 and 11.9 GHz) with FWHM bandwidth of 6.84 GHz (58.2%) ranging from 5.96 to 12.80 GHz that operates at a central frequency of 10.58 GHz. The overall dimension of the structure is $16.5 \times 16.5 \times 3.2$ mm. The presence of metamaterial properties in the region of interest has been explained by plotting EM parameters (real and imaginary) curves. The high absorption phenomenon is explained by surface current distribution. The unit cell structure is further examined under normal and oblique incidents of the wave. The proposed structure is simulated using ANSYS HFSS 19.1. The proposed MA has larger wideband absorption bandwidth, percentage bandwidth, FWHM and percentage FWHM bandwidth compared to that of other reported microwave MAs, hence finds application in satellite, stealth and radar.

References

1. Kong LB et al (2013) Recent progress in some composite materials and structures for specific electromagnetic applications. Int Mater Rev 58(4):203–259
2. Lian Y, et al (2020) Solvent-free synthesis of ultrafine tungsten carbide nanoparticles-decorated carbon nanosheets for microwave absorption. Nano-Micro Lett 12(1):1–13

3. Pelluri R, Appasani B (2017) Genetic algorithm optimized X-band absorber using metamaterials. Progress Electromag Res Lett 69:59–64
4. Cheng Y, et al (2020) A flexible and lightweight biomass-reinforced microwave absorber. Nano-Micro Lett 12(1):1–15
5. Sarkar D, Khan T, Talukdar FA (2020) Analysis of electromagnetic band gap structure using artificial neural network for UWB applications. In: 2020 Advanced communication technologies and signal processing (ACTS). IEEE
6. Lo W, et al (1997) Controlled processing and properties of large Pt-doped YBaCuO pseudo-crystals for electromagnetic applications. J Mater Res 12(11):2889–2900
7. Fiedziuszko S, Electromagnetic transmission line elements having a boundary between materials of high and low dielectric constants. U.S. Patent Application No. 09/749, 153
8. Liang X, et al (2020) Environment-stable Co x Ni y encapsulation in stacked porouscarbon nanosheets for enhanced microwave absorption. Nano-Micro Lett 12:1–12
9. Zhao H, et al (2019) Biomass-derived porous carbon-based nanostructures for microwaveabsorption. Nano-Micro Lett 11(1):24
10. Landy NI et al (2008) Perfect metamaterial absorber. Phys Rev Lett 100(20):207402
11. Watts CM, Liu X, Padilla WJ (2012) Metamaterial electromagneticwave absorbers. Adv Mater 24(23):OP98-OP120
12. Chen H, Chan CT (2007) Acoustic cloaking in three dimensions using acousticmetamaterials. Appl Phys Lett 91(18):183518
13. Zhang X, Liu Z (2008) Superlenses to overcome the diraction limit. Nat Mater 7(6):435–441
14. Wurtz GA, et al (2011) Designed ultrafast optical nonlinearity in a plasmonic nanorodmeta-material enhanced by nonlocality. Nature nanotechnology 6(2):107–111
15. Halir R, et al (2018) Subwavelength-grating metamaterial structures for silicon photonicdevices. Proc IEEE 106(12):2144–2157
16. Caloz C, Rennings A (2009) Overview of resonant metamaterial antennas. In: 2009 3rd European conference on antennas and propagation. IEEE
17. Gil M, et al (2007) Composite right/left-handed metamaterial transmission lines basedon complementary split-rings resonators and their applications to very wideband and compact filter design. IEEE Trans Microw Theor Tech 55(6):1296–1304
18. Barde C, Choubey A, Sinha R (2019) Wide band metamaterial absorberfor Ku and K band applications. J Appl Phys 126(17):175104
19. Zhong J, et al. (2012) Single-/dual-band metamaterial absorber based on crosscircular-loop resonator with shorted stubs. Appl Phys A 108(2):329–335
20. Tao H, et al (2010) A dual band terahertz metamaterial absorber. J Phys D: Appl Phys 43(22):225102
21. Barde C, et al (2020) A compact wideband metamaterial absorber for Ku band applications. J Mater Sci: Mater Electron 31(19):16898–16906
22. Ranjan P, et al (2018) A six-band ultra-thin polarization-insensitive pixelated metamaterial absorber using a novel binary wind driven optimization algorithm. J Electromag Waves Appl 32(18):2367–2385
23. Barde C, et al (2020) A compact wideband metamaterial absorber for Ku band applications. J Mater Sci: Mater Electron 1–9
24. Ranjan P, et al (2018) An ultrathin -ve-band polarization insensitive metamaterialabsorber having hexagonal array of 2D-bravais-lattice. Prog Electromag Res 87:13–23
25. Guo-Dong W, et al (2013) Multi-band microwave metamaterial absorber based on co-planar Jerusalem crosses. Chinese Phys B 23(1):017802

An Improved Regenerative Braking and Drive Cycle Analysis of BLDC Motor for Electric Vehicles Using Fuzzy Logic

Arya Sreekumar, A. Prince, and Ginu Ann George

Abstract Regenerative braking method can extend the driving range and can improve energy usage efficiency of an electric vehicle. Regenerative braking system of EV driven by BLDC motor is recommended because of its rugged construction, efficiency, reliability and life span. It can be done efficiently by making use of hybrid energy storage system (HESS) comprising both battery and supercapacitor. During regenerative braking, the voltage across the dc link is boosted by controlling the switching of lower switches of the inverter. So in this method, an inverter is used alone to drive the motor. This regenerated energy can be stored into battery–supercapacitor system. The simulation is done by using MATLAB Simulink. Drive cycle analysis of electric vehicle system also done through this work. Drive cycle analysis helps to determine the optimum parameters of the electric vehicle.

Keywords Brushless dc motor · Regenerative braking · Battery · Supercapacitor · Fuzzy logic · Drive cycle

1 Introduction

As the atmospheric pollution and economic concerns caused by the internal combustion engine vehicles are very high, the need of electric vehicles become more needy. Most EV's utilise the energy stored in battery. One of the major challenge in EV's is to effectively utilise battery's energy. The major problem associated with the battery includes its limited life cycle, limited power density, and also high cost. Supercapac-

A. Sreekumar (✉) · A. Prince · G. A. George
Department of Electrical Engineering, Rajiv Gandhi Institute of Technology, Kottayam, Kerala, India
e-mail: aryasreekumar1996@gmail.com

A. Prince
e-mail: prince@rit.ac.in

G. A. George
e-mail: ginuanngeorge@rit.ac.in

563

itors also known as electric double layer capacitors are high capacitance capacitors with high power density, wide operating temperature range, and also long life cycle [1]. The energy density of supercapacitor is relatively very small so it cannot be used as main energy source [2].

When compared to brushed dc motor and induction motors, brushless dc motor have many advantages. Brushless dc (BLDC) motors are ideally suitable for EVs because of their high power densities, good speed-torque characteristics, high efficiency, wide speed ranges, and low maintenance [3]. With the help of regenerative braking in EV's the energy wasted during braking can be effectively utilised.

Regenerative braking is the process of supplying the energy back to the battery from the motor drive. In conventional IC engine vehicles, the kinetic energy of the vehicle wasted as heat. But in electric vehicles, this energy is converted into electrical energy and is stored back to battery. But the electrical energy that is generated will be insufficient to charge the battery directly. So inorder to boost this regenerated energy, either we can use an additional boost converter or use the motor's own winding inductance. The first method causes an increase in cost as well as size of the system [4]. While making a comparison study conducted the driving range of EV's using regenerative braking is 15% more than EV's not using regenerative braking method [5]. The current control of BLDC motor is done by using PI controller, and fuzzy logic is used for braking force distribution [6].

The organisation of the paper is as follows: Sect. 1 is introduction. Section 2 presents the structure of hybrid energy storage system. Section 3 deals with BLDC motor and its modes of operation.Fuzzy logic controller is explained in Sect. 4. Section 5 presents drive cycle analysis, and Sect. 6 presents Results and Conclusion.

2   Hybrid Energy Storage System

Figure 1 demonstrates the basic block diagram of regenerative braking employing battery–supercapacitor hybrid energy system.

The battery pack and the supercapacitor are connected parallel through diode D1. This diode remains reverse biased until the battery pack voltage is less than the supercapacitor voltage.

Fig. 1 Block diagram of hybrid energy storage system
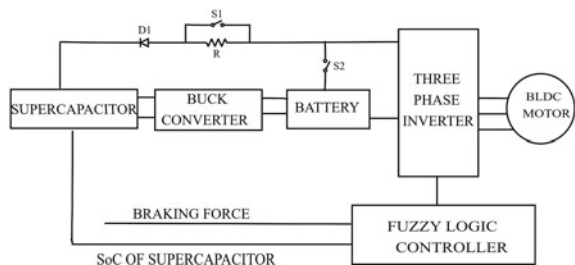
For the protection of battery, a limiting resistance is added in series with the diode D1. There are two modes of operation, normal mode with battery alone and regenerative braking with both battery and supercapacitor. In normal mode, current flows from battery to the motor. During braking, the motor acts as generator which causes the reversal of power flow. The regenerated energy is boosted by controlling the switching pattern of inverter. Now the diode D1 gets forward biased because boosted voltage becomes greater than supercapacitor voltage, and energy gets stored in the supercapacitor module. The supercapacitor used is of high voltage compared to battery, so energy stored is step down using the buck converter, and then battery is charged simultaneously.

3   BLDC Motor and Modes of Operation

Brushless dc motor has higher power density, better speed-torque characteristics, and they possess high speed range. All these characterstics make it suitable for EV application. BLDC motor comes under the family of synchronous motor because the stator and rotor magnetic field rotates at same frequency. The main controlling part used in BLDC control is the inverter also known as commutator. The commutation is achieved by sensing the rotor position. Hall effect sensors are used for the purpose. A multilevel H-bridge inverter is shown in the Fig. 2
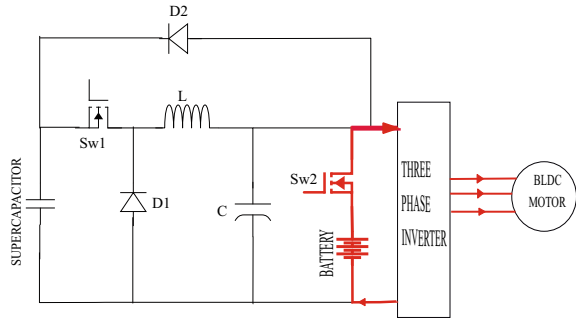
3.1   *Normal Mode Of Operation*

During the motoring mode of operation, the power flows from battery to motor [7].The supercapacitor taken is of high voltage when compared to battery voltage so diode D1 will be reverse biased. So the supercapacitor has no role in motoring operation. Hence, the buck converter is in OFF state. The power flow during normal mode of operation is shown in Fig. 3.
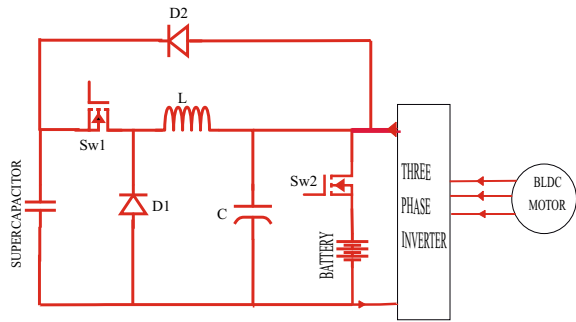

Fig. 2 H-bridge inverter
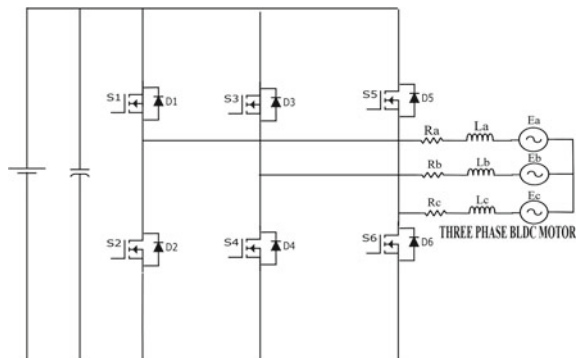
Fig. 3 Vehicle in normal mode of operation

Fig. 4 Vehicle in regenerative braking mode of operation
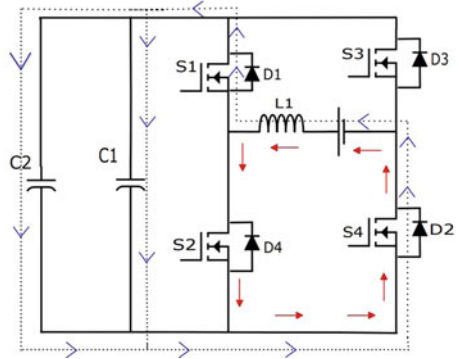

3.2 Regenerative Braking Mode of Operation

In regenerative braking mode of operation, the regenerated energy is not sufficient to store in the battery. So this energy has to be boosted. This is achieved by controlling the switching pattern of inverter. During motoring mode, both upper and lower switches are controlled while during regenerative braking mode to ensure boosting operation upper switches are turned OFF and lower switches are controlled in PWM technique.

Here the diode D2 gets forward biased, and energy gets stored into the supercapacitor module. The working of this equivalent boost converter is explained in Sect. 5. So the need of an extra dc-dc converter can be eliminated thus reducing the components used and also the overall cost [8].

Fig. 4 shows energy flow during regenerative braking mode.

When a brake signal is applied, the dc link voltage gets boosted and the regenerated energy gets stored into supercapacitor. The supercapacitor used is of high voltage when compared to battery voltage. Therefore, a buck converter is used to step down the supercapacitor voltage to the battery voltage and the battery can be charged.

Fig. 5 Equivalent boost converter

Fig. 6 Switching pulses given to inverter during motoring and braking mode of operation
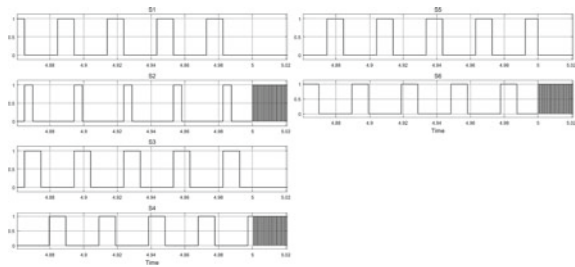
### 3.2.1 Equivalent Boost Circuit

During the normal mode of operation, both upper and lower switches are turned ON and OFF periodically. But during regenerative braking mode, the upper switches are turned OFF and pwm is applied to the lower switches S2, S4, and S6 of the inverter. Figure 5 demonstrates the operation of equivalent boost circuit [9].

The inverter switches are controlled via a high-frequency PWM signal. When the upper switches are turned OFF, the diodes conduct current to the battery side [10]. During the motoring mode, both upper and lower switches are operated while during regenerative braking mode, upper switches are turned OFF, and PWM switching is given to lower switches alone. This is evident from the waveforms demonstrated in Fig. 6.
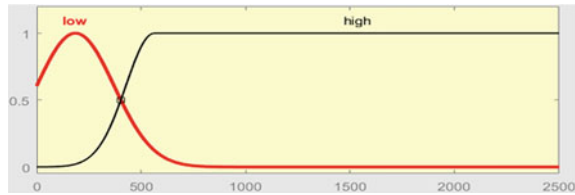
4 Fuzzy Logic Controller

In 1965 L.L.A. Zadeh was introduced fuzzy theory for the first time. Conventional classical theory concentrates much on precision rather than simple and efficient controlling mechanism. The fuzzy sets have a certain degree of membership for each element which was not there in classical set [11].

Fig. 7 Fuzzy logic controller (Mamdani)
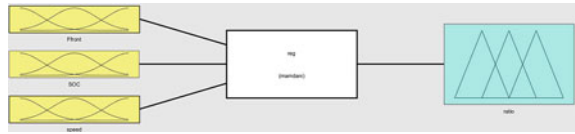
Fig. 8 Membership function for speed

Fuzzification, fuzzy rule-based inference system, and defuzzification are the main components/process of fuzzy logic controller. Fuzzy sets works on certain rules, and these rules are the most important requirement for the fuzzy logic system [12]. The rule has a general form of If-Then which consist of two parts: Antecedent and Consequence. The 'If' statement is the Antecedent and the Then statement is the Consequence. The output is controlled by these rules on input.

Fuzzy logic controller has certain advantages which make it preferable to the other controllers. They are: i. Very easy to comprehend because the concept behind the control is very simple. ii. It can work well even with noisy inputs. iii. It can be worked with multiple inputs and can provide multiple outputs as it solely works on rule basis. iv. Creating the rule base for fuzzy control is easier than optimising the parameters for PID control. v. It operates very well even in highly nonlinear systems adapting to the situation. But designing other conventional controllers to adjust in case of nonlinearity in characteristics is very difficult.

In fuzzy logic controller, the inputs and outputs are defined with ceratin membership functions. Mamdani-type fuzzy logic controller is used here, and the model is demonstrated in Fig. 7.

Fuzzy logic control is used for distribution of braking force between front and rear wheels. The factors affecting distribution of braking force are SoC of supercapacitor, speed of the motor and braking force, etc. [13]. The inputs for the fuzzy logic controller include driver's required braking force, vehicle speed, SoC of supercapacitor, and output is ratio between regenerative braking force to the total braking force.

When SoC is less than 10%, battery is unsuitable for charging so the proportion of required braking force should be low. When SoC lies between 10% and 90%, the proportion of regenerative braking force can be increased as batteries which can be charged with full current. For SoC greater than 90%, it is better to keep the value of regenerative braking force as low else the battery gets damaged due to Li ion deposits (Fig. 8).

When vehicle is running at low speed, the amount of regenerative braking force also should be low and for medium speed, it can be increased to a proper value. For

Fig. 9 Membership function for braking force
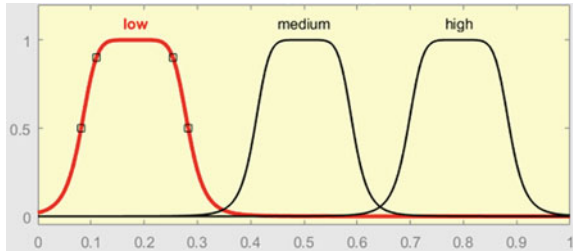
Fig. 10 Membership function for SoC
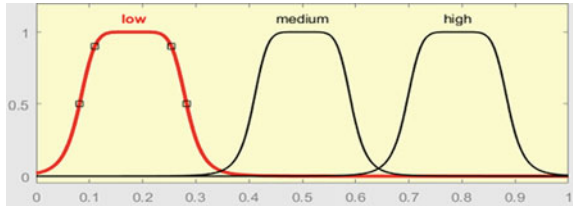
Fig. 11 Membership function for fuzzy logic output ratio

high speed, the regenerative braking force is set at the highest, so that maximum energy can be harvested [10].

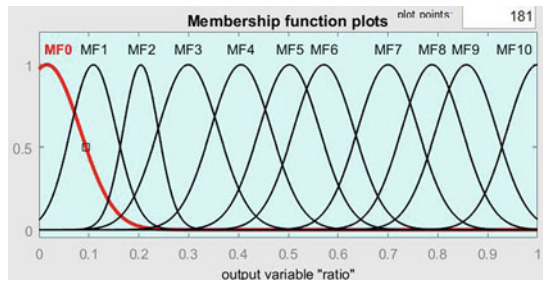If braking force is large, vehicle should be stopped in short distance and in little time so the required braking force should be reduced. For a medium braking force, the ratio of regenerative braking force should be increased, and for small braking force, the regenerative braking force should be very large.

Figure 9 shows the membership function for braking force where the concourse selected is low, medium, high

The membership function for SoC is demonstrated in Fig. 10, the concourse is chosen as low, medium, and high. The membership function for speed is chosen as low and high also the universe of discourse selected is [0, 2500]. The membership function for speed is demonstrated in Fig. 8. The membership function for output variable is demonstrated in Fig. 10. The rule is of the form IF premise1, premise2, and premise3 THEN conclusions [3] (Fig. 11).

Fig. 12 Motor speed
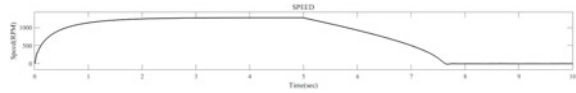
Fig. 13 Electromagnetic torque
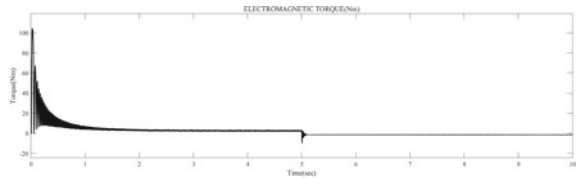
5 Drive Cycle Analysis

A driving cycle is a set of data points that show the speed of a vehicle as a function of time. A standard or user-specified longitudinal drive cycle is generated as a result of this. The longitudinal speed of the vehicle is the block output. A signal builder or slider gain can be used to create a user-defined drive cycle. Different countries and organisations establish standard and customised driving cycles to assess the performance of vehicles in various ways, such as fuel economy, electric vehicle autonomy, polluting emissions, etc.

Battery state and energy consumption in electric vehicles are analysed with the help of drive cycle and to simulate vehicle model prior to the actual development. Initial acceleration, cruising at rated vehicle speed, cruising at maximum vehicle speed and retardation are the main informations obtained from the driving cycle.

6 Results and Conclusion

Here the simulation of the system was done in MATLAB Simulink. After the brake signal is applied, the upper leg switches are turned OFF, and PWM switching is given to lower switches alone. With the help of PI controller, the battery current is controlled. The reference to the PI controller is given as the output of FLC.

After the brake signal is applied, the regenerated energy is boosted, and it gets stored in the supercapacitor and simultaneously the battery is charged with the help of buck converter. A total simulation time of 10 s is applied. The first 5 s is dedicated for motoring operation and after that, brake signal is applied as step input.

The speed of motor increases and reaches the reference speed during motoring period and speed decreases, reaches zero during braking mode. The waveform of speed is shown in Fig. 12. The electromagnetic torque produced by motor is positive during motoring and becomes negative during regeneration. The waveform of electromagnetic torque is shown in Fig. 13.
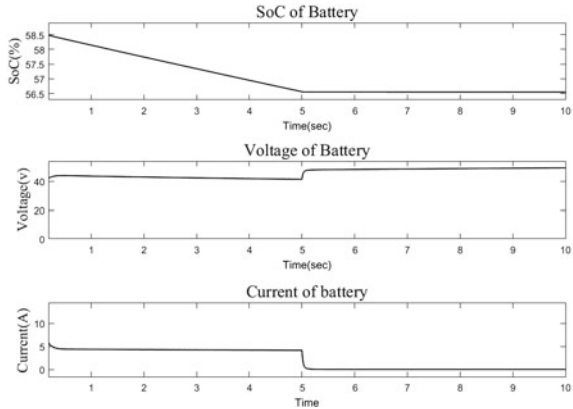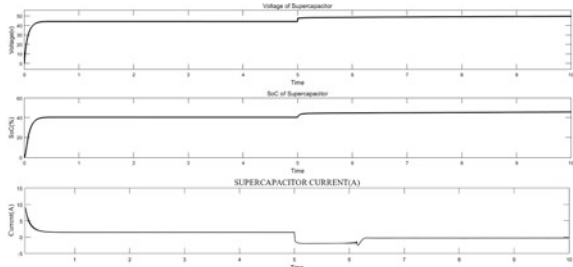
Fig. 14 Battery parameters

Fig. 15 Supercapacitor parameters

The voltage and SoC of battery are shown in Fig. 14, respectively. From the waveform of battery parameters, it can be inferred that during motoring mode of operation, both the SoC and voltage of battery reduces showing battery is supplying power to motor and during regenerative braking mode, the battery voltage increases along with a slight increase in SoC. The battery current becomes negative during regeneration.

The supercapacitor parameters are shown in Fig. 15. During normal mode, i.e., up to 5s simulation time, the supercapacitor voltage and SoC remains constant. During regenerative braking mode, the voltage and SoC increases and current becomes negative which indicates the charging of supercapacitor.

The power rating of the motor used here is 800 W and from the Fig. 16, it is inferred that almost 33% of power is regenerated back.

A drive cycle is a set of values generally velocity vs time graph which represents how a vehicle travels through a path. A drive cycle with acceleration, deceleration, and constant speed is developed. From the Figs. 17 and 18, it can be inferred that actual vehicle speed follows the reference speed and Fig. 17 shows a standard drive cycle of FTP75. Figure 18 shows a customised drive cycle generated with the help of a signal builder, which is also follows the commands. SoC also varies with the speed of the vehicle.

Fig. 16 Motor power
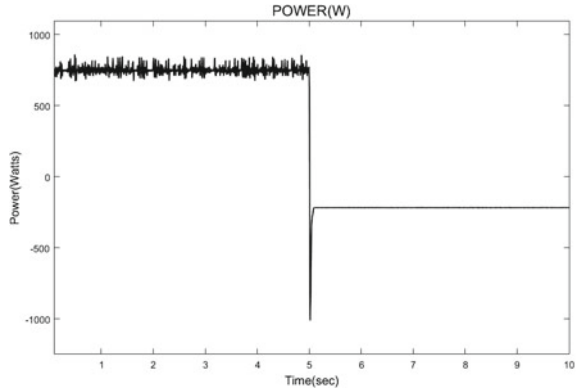
Fig. 17 Drive cycle (FTP 75)
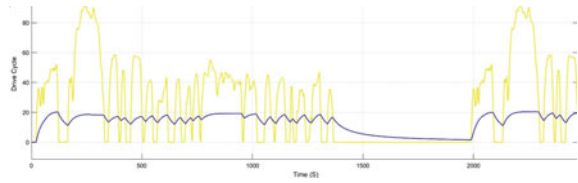
Fig. 18 Drive cycle (signal builder)
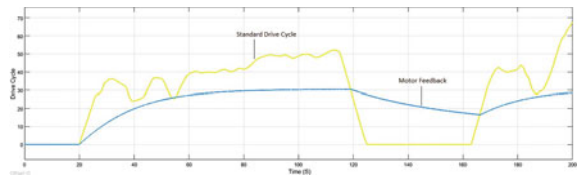
Fig. 19 Throttle and brake commands
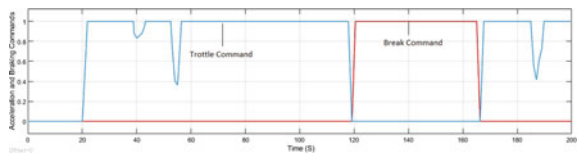
The vehicle input signals are acceleration and brake. The input commands act according to the drive cycle. Trottle and brake commands corresponding to the drive cycle FTP 75 are shown in Fig. 19 and the Soc variations in Fig. 20.

A simulation of regenerative braking of BLDC motor for electric vehicles with battery supercapacitor hybrid energy storage has been done in MATLAB Simulink. Regenerative braking helps to improve the driving range of vehicles. By using combination of both Fuzzy logic and PI controller, constant brake torque can be obtained and thereby smooth transitions and vehicle safety can be ensured. And also by this technique, more energy can be regenerated.

Drive cycle analysis of electric vehicle system also done. From the drive cycle, informations such as initial acceleration, cruising at rated vehicle speed, cruising at

Fig. 20 SoC variations with drive cycle
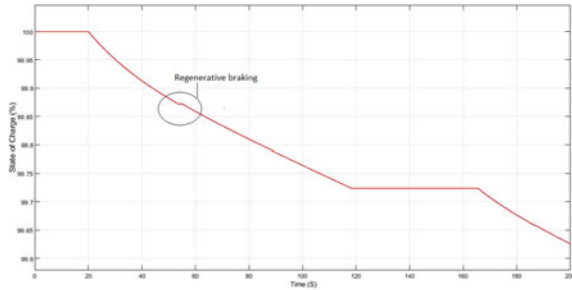
maximum vehicle speed and retardation, etc., are analysed. Drive cycle also helped to analyse battery state and energy consumption in electric vehicles and to simulate vehicle model prior to the actual development.

References

1. Khaligh A, Li Z (2010) Battery, ultracapacitor, fuel cell, and hybrid energy storage systems for electric, hybrid electric, fuel cell, and plug-in hybrid electric vehicles: state of the art. IEEE Trans Veh Technol 59(6):2806–2814
2. Farshid N, Ebrahim F, Teymoor G (2017) An efficient regenerative braking system based on battery/supercapacitor for electric, hybrid, and plug-in hybrid electric vehicles with BLDC motor. IEEE Trans Veh Technol 66(5):3724–3738
3. Nian X, Peng F, Zhang H (2014) Regenerative braking system of electric vehicle driven by brushless DC motor. IEEE Trans Ind Electronics 61(10):5798–5807
4. Kivanc OC, Ustun O, Tosun G, Tuncay RN (2016) On regenerative braking capability of BLDC motor. Industrial Electronics Society, IECON 2016—42nd annual conference of the IEEE, pp 1710–1715
5. Zhang X, Wang Y, Liu G, Yuan X (2016) Robust regenerative charging control base on T-S fuzzy sliding mode approach for advanced electric vehicle. IEEE Trans Transp Electrification 2(1):52–65
6. Yang M-J, Jhou H-L, Ma B-Y, Shyu K-K (2009) A cost-effective method of electric brake with energy regeneration for electric vehicles. IEEE Trans Ind Electronics 56(6):2203–2212
7. Shi Q, Zhang C, Cui N (2012) An improved electric vehicle regenerative braking strategy research. In: Jin D, Lin S (eds) Advances in computer science and information engineering. Advances in intelligent and soft computing, vol 169. Springer, Heidelberg. https://doi.org/10.1007/978-3-642-30223-7101
8. Liu W, Qi H, Liu X et al (2020) Evaluation of regenerative braking based on single-pedal control for electric vehicles. Front Mech Eng 15:166–179 (2020). https://doi.org/10.1007/s11465-019-0546-x
9. Biao J, Xiangwen Z, Yangxiong W et al (2021) Regenerative braking control strategy of electric vehicles based on braking stability requirements. Int J Automot Technol 22:465–473 (2021). https://doi.org/10.1007/s12239-021-0043-1
10. Aswathi ER, Prathibha PK, Nair JR (2018) Regenerative braking of BLDC motor using fuzzy control for electric vehicles. In: Second International Conference on Inventive Communication and Computational Technologies (ICICCT), pp 1661–1665. https://doi.org/10.1109/ICICCT.2018.8473242

11. Dang PS, Haran RR (2020) Fuzzy regenerative braking strategy. In: Reddy A, Marla D, Simic M, Favorskaya M, Satapathy S (eds) Intelligent manufacturing and energy sustainability. Smart innovation, systems and technologies, vol 169. Springer, Singapore. https://doi.org/10.1007/978-981-15-1616-073

12. Zhang H, Xu G, Li W, Zhou M (2012) Fuzzy logic control in regenerative braking system for electric vehicle. IEEE Int Conf Inf Autom 2012:588–591. https://doi.org/10.1109/ICInfA.2012.6246881

13. Akhila M, Ratnan P (2016) Brushless DC motor drive with regenerative braking using adaptive neuro based fuzzy inference system. In: International conference on electrical, electronics, and optimization techniques, pp 748–751

Short-Term Energy Yield Prediction of Dust Accumulated Standard, Half-Cut and Quarter-Cut PV Modules Using Multi-layer Neural Network Algorithm

Faisal Saeed, Muhammad Hassan Yousuf, Asad Idrees, Haider Ali Tauqeer, Mujahid Farooq, Waqar Aslam, and Haroon Ahmad

Abstract In this paper, the implementation of a multi-layer artificial neural network (ANN) algorithm is discussed to predict short-term photo-generated power of dust accumulated mono-crystalline PV modules variants; PV modules with full, half-cut, and quarter-cut solar cells. The datum to train neural networks was obtained from real-time results. Experimental observations were performed under standard irradiance conditions, i.e., 1000 W/m^2 over consecutive three months. To have targeted output, 70% of the data set is utilized in the training of neural networks. Comparison of neural network predicted results and experimental outcomes is discussed based on calculations of root mean square error (RMSE) as well as coefficient of determination R^2. The performance indices account RMSE = 0.17631 and R^2 = 0.99923 for standard cell PV modules, RMSE = 0.83192 and R^2 = 0.99969 for half-cut technology and RMSE = 0.90929 and R^2 = 0.99971 for the quarter-cut solar cell-based PV module which dictates the efficacy of the ANN algorithm in the power estimation of PV modules.

Keywords Standard solar cell PV module · Half-cut PV module · Quarter-cut PV module · ANN · Energy prediction

F. Saeed (✉) · A. Idrees · H. A. Tauqeer
SBA School of Science and Engineering, Lahore University of Management Sciences (LUMS), Lahore 54792, Punjab, Pakistan
e-mail: 19060005@lums.edu.pk

M. H. Yousuf
Department of Electrical Engineering, University of Engineering and Technology Lahore, Lahore 44000, Punjab, Pakistan

M. Farooq · W. Aslam
Department of Electrical Engineering, University of Engineering and Technology Lahore, Faisalabad Campus, Faisalabad 38000, Punjab, Pakistan

H. Ahmad
Department of Electrical Engineering, Technische Universität (TU) Dortmund, North Rhine-Westphalia, 44227 Dortmund, Germany

1 Introduction

Photovoltaic technology experienced expeditious deployment over last few years [1–3]. Since the development of the first solar cell, researches have been in progress to enhance the efficiency of the solar cells [4–9]. A way to enhance the efficiency as well as the performance of PV modules is to cut the PV cells in half [10–12]. Figure 1 depicts an electroluminescence image of a PV module with full-size, half-cut, and quarter-cut solar cells and demonstrates the difference of cell divisions in the above-mentioned PV technologies [13]. Note that number of cells is double in half-cut solar cells compared to the full-size solar cell wafer of the same size and is four times of full-size PV wafer in quarter-cut and double to half-cut solar cells. Half-size and quarter-size silicon wafer solar cells have been accounted to exhibit better output performance as compared to standard silicon wafers [10–13]. PV modules with half-cut and quarter-cut solar cells started seeking attention on a commercial scale in more or less equal proportionality as that of PV modules with full-size solar cells in developed countries in the last few yet this technology need years to be as common as standard PV modules with full-size solar cells globally [12].

The efficiency of PV modules gradually degrades with time due to environmental constraints, i.e., dust deposition over the surface of PV modules, soiling losses, partial shading, hot spot issues, climatic conditions, etc. apart from care of scheduled cleaning and maintenance [14–18]. Therefore, for large-scale and seamless penetration of PV systems to meet global energy demand, estimation of the future energy yield of the PV systems over a certain time is also an important concern. Adoption of artificial neural networks for these concerns can aid in optimal forecasting of energy yield [19].

The literature lacks a discussion on the combine performance analysis of three PV module cell variant systems; PV modules with full-size solar cells, half-cut solar
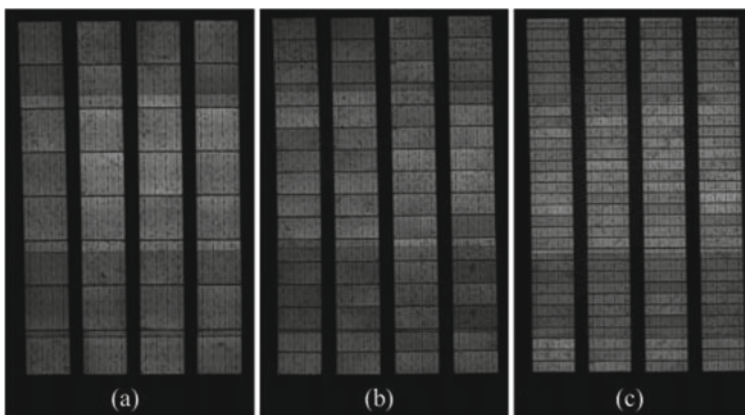
Fig. 1 Electroluminescence image of photovoltaic modules with **a** full size solar cells **b** half-size solar cells **c** quarter size solar cells [13]

Fig. 2 Experimental setup (left) photovoltaic modules with (1) full-size (2) half-cut and (3) quarter-cut solar cells (right) Indoor experimental setup

cells, and quarter-cut solar cells using any of the conventional or neural network algorithms [19–26]. This case study is particularly focused on studying the impact of dust accumulation on the performance of three earlier mentioned PV module cell variant systems using a multi-layer neural network approach. Further aspects are discussed in later sections.

2 Material and Methods

2.1 Experimental Setup

To train the neural network, data set is acquired from the experimental setup. Monocrystalline PV modules with full-size silicon wafers, half-cut, and quarter-cut employed for this case study are depicted in Fig. 2. (i.e., left setup). The output characteristics such as maximum power point (P_{mp}), voltage at P_{mp} (V_{mp}), current at P_{mp} (I_{mp}), short-circuit current (I_{sc}), and open-circuit voltage (V_{oc}) were extracted by using current–voltage measurement electronic device JETSPIN BAV2 as shown in Fig. 2 (i.e., right setup). Irradiance data is extracted using irradiance sensor SOZ-3 and a Type-T thermocouple was used to note temperature readings.

2.2 Adoption of Multi-layer Neural Network Algorithm

An artificial neural network (ANN) is a computational model with a functioning principle like the biological network. In such a network neuron is a processing unit that foremost linearly contemplates the input and subsequently concludes the sum by an activation function and then finally directs the results to the following neurons. In this study multi-layer neural network is used with sigmoid as an activation function. Irradiance (I_r), temperature (T), V_{mp} and I_{mp} data set recorded for 3 months is utilized

as an input for a neural network and the target is the P_{mp} of the PV modules. A pictorial illustration of the employed approach is shown in Fig. 3. The mathematical relation of such a neural network with $x_1, x_2 \ldots x_n$ as the input signals and $w_1, w_2 \ldots w_n$ as the weight of input is given as by (1) [26].

$$Z = \sum_{n=1}^{N} w_n x_n + \alpha \tag{1}$$

where Z is the argument of the activation function. A part of the implementation of the multi-layer feed-forward approach is depicted in Fig. 4. Comparison of the neural network generated results and experimental figures is discussed based on root mean square error (RMSE), and coefficient of determination R^2, evaluated using the expressions (2) and (3), respectively, wherein P_{Ex} is the experimentally obtained power, P_{ES} is the estimated power value, P_A is the average power value and n is the number of days [26].

Fig. 3 Algorithm for short-term power forecast of photovoltaic system

```
net = feedforwardnet([10 10]);  % implementation of multi-layer Neural ANN
net = train(net,input',output');
view(net)
y = net(input);
```

Part of MATLAB ANN Alogrithm to
Generate Multi-layer Neural Network
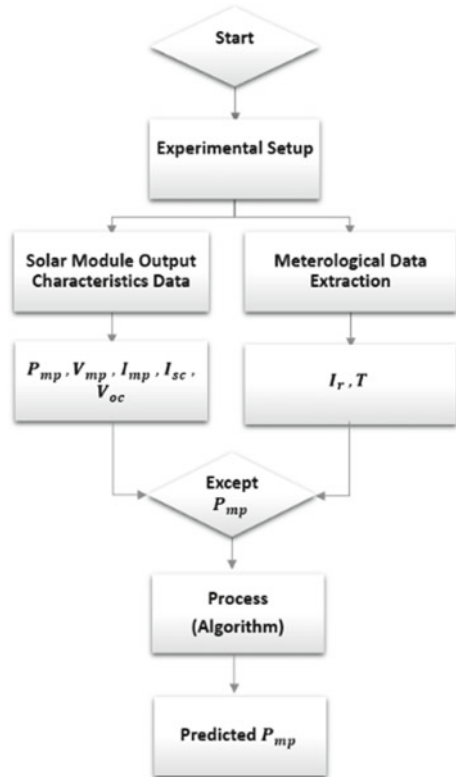
Fig. 4 Part of MATLAB code of implementation of multi-layer neural network
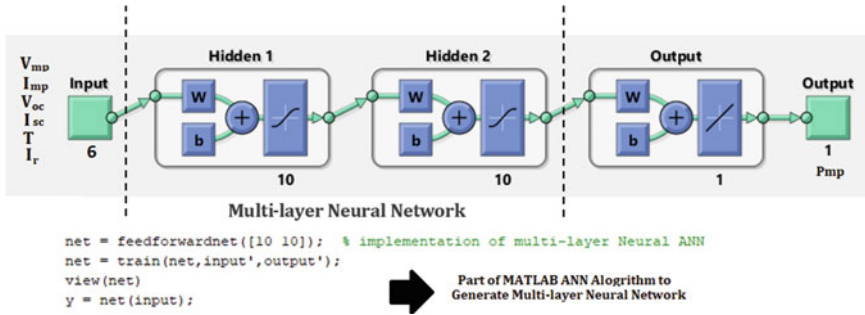
$$\text{RMSE} = \sqrt{\frac{1}{n}\sum_{1}^{n}(P_{\text{Ex}} - P_{\text{Es}})^2} \tag{2}$$

$$R^2 = 1 - \frac{\sum_{k=\pm1}^{n}(P_{\text{Ex}} - P_{\text{Es}})}{\sum_{k=\pm1}^{n}(P_{\text{Ex}} - P_A)} \tag{3}$$

The closer the RMSE to 0, the lesser the error and the closer the R^2 to 1 better the results.

3 Results and Discussions

An effort is made to obtain PV module characteristics under standard irradiance conditions yet experimental values deviated only 1% from the standard, i.e., irradiance lies in the range of 999–1000 W/m². However, Fig. 5 depicts the PV modules power characteristics on day1 (D1), after the first month (M1), second month (M2), and third month (M3). It can be observed that the power of the PV modules gradually decreased over time. Also the decline in open-circuit voltage and short-circuit current can be observed. It is to be noted that during the experimental duration no cleaning of PV modules was performed. The experimentally obtained output power values for the PV module with a full-size solar cell on D1 is 170 W_p, after M1, M2, and M3 is 153.3 W_p, 146 W_p, and 139 W_p, respectively. For PV module with a half-size solar cell, site recorder values for D1 is 330 W_p, after M1, M2, and M3 is 313 W_p, 290 W_p, and 265 W_p, respectively. for the PV module with quarter-cut- solar cell on D1 is 30 W_p, after M1, M2, and M3 is 26 W_p, 24.3 W_p, and 18 W_p, respectively. However, Fig. 5 clearly illustrates the impact of dust accumulation on the output characteristics of the PV modules. The summarized impact of the output power of the PV module technologies from D1 to M3 is enlisted in Table 1.

The training datum is based on 370 different values. Out of this, 70% of the information is utilized for training of the neural networks. This method was followed

Fig. 5 Each day power datum of PV modules with full-size, half-cutand quarter-cut solar cells over a specific duration
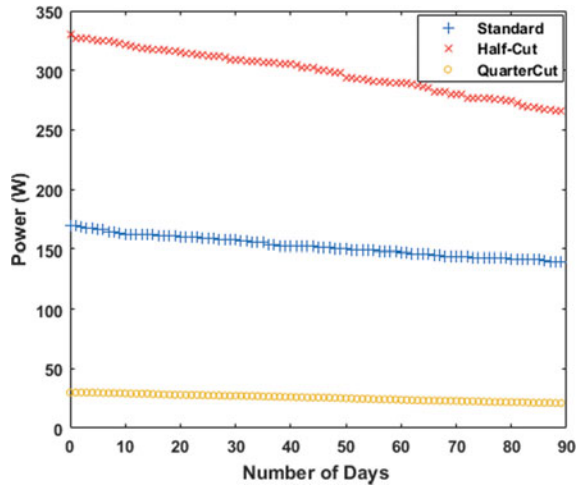
Table 1 Photovoltaic modules output characteristics extracted form experimental results

	$P_{mp}(W)$	$V_{oc}(V)$	$I_{sc}(A)$	$V_{mp}(V)$	$I_{mp}(A)$
a. Standard					
After M1	153.3	44.1	4.9	33.8	4.7
After M2	146	43.6	4.7	33.1	4.4
After M3	139	42.5	4.2	32.3	4.2
b. Half-cut					
After M1	313	43.0	8.9	37.3	8.3
After M2	290	42.6	8.1	36.9	7.8
After M3	265	41.8	7.9	36.2	7.3
c. Quarter-cut					
After M1	26	19.2	1.7	14.8	1.7
After M2	24.3	18.9	1.6	14.5	1.6
After M3	18	18.6	1.4	14.1	1.2

equally for the PV modules with full-size solar cells, half-cut as well as quarter-cut solar cells. Figures 6 and 7 illustrate the R^2 relation between experimental and predicted power values for the PV modules with full-size, half-cut, and quarter-cut solar, respectively. The figures depict the overall coefficient of determination, obtained after validation and testing of the data. The results demonstrate the efficient training of the neural networks R^2, a co-relation of the efficacy of the experimental and ANN predicted results. The R^2 for PV modules with full-size solar cells is 0.99923, for PV modules with half-size solar cells, is 0.99969 and for PV modules with quarter-cut solar cells is 0.99971.

Fig. 6 Coefficient of determination relation for experimental and predicted power values of photovoltaic modules with (upper) full size solar cells (bottom) half-size solar cells
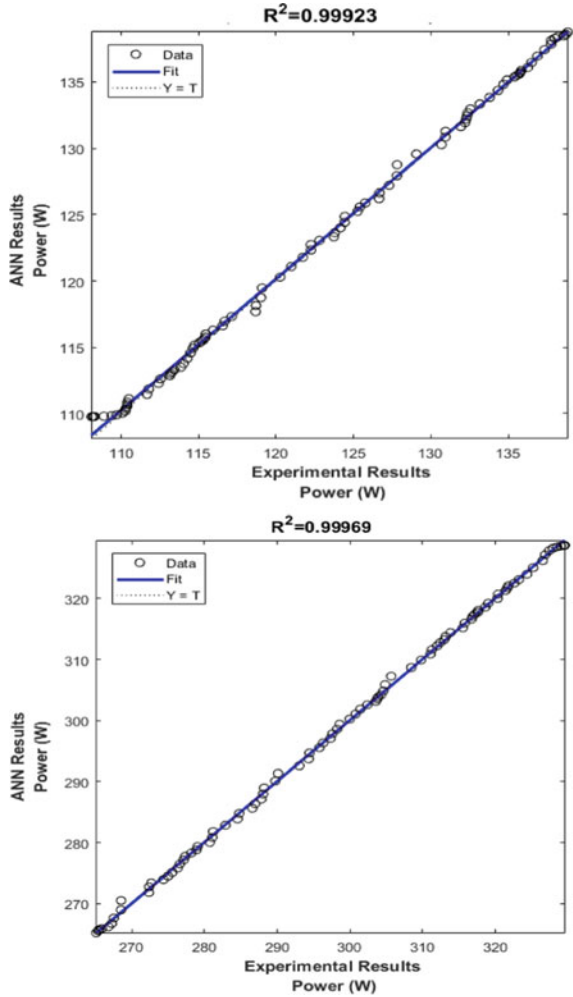
The 15 days ahead energy yield forecast of ANN results is closely related to the experimentally evaluated values as illustrated in Fig. 8. The experimentally obtained output power value for the PV modules with full-size solar cells is 139 W_p and ANN-based results are 136.2 W_p. Similarly, for PV modules with half-cut, the experimental recorded output power is 265 W_p and ANN-based results are 264.42 W_p and for PV module with quarter-cut solar cells, the experimental output power is 18.01 W_p. and ANN-based results are 18.02 W_p. The RMSE of PV modules with full-size solar cells, half-cut, and quarter-cut solar cells is 0.17631, 0.83192, and 0.90929, respectively.

Fig. 7 Coefficient of determination relation for experimental and predicted power values of photovoltaic modules with quarter-size solar cells
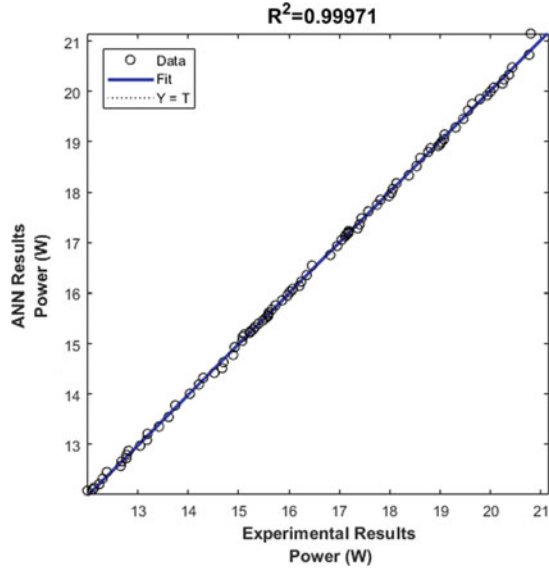
Fig. 8 Comparative representation of experimental and 15-days ahead energy yield predicted results using ANN
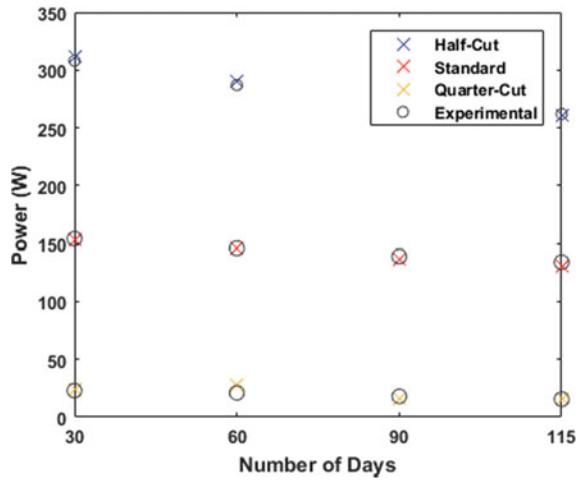
4 Conclusion

A real-time short term, i.e., 15 days ahead, energy yield prediction of three PV module systems; PV module with full-size, half-cut, and quarter-cut solar cells is comprehensively elaborated using a multi-layer neural network algorithm. The efficacy of the case study is evaluated with the aid of performance indices, RMSE and R^2 that map the efficiency relationship between the experimental and neural network algorithm evaluated results. It has been found that RMSE $= 0.17631$ and $R^2 = 0.99923$ for

standard cell PV modules, RMSE $= 0.83192$ and $R^2 = 0.99969$ for half-cut technology and RMSE $= 0.90929$ and $R^2 = 0.99971$ for the quarter-cut solar cell-based PV module system. The percentage error between ANN predicted output power and experimental results for M3 $+ 15$ days for PV module with full-size silicon wafer is 2.01%, for PV module with half-cut silicon cell is 0.2% and for the quarter-cut is 0.05% which dictates the efficiency of the proposed research effort.

References

1. Nayak PK, Mahesh S, Snaith HJ, Cahen D (2019) Photovoltaic solar cell technologies: analysing the state of the art. Nat Rev Mater 4
2. Dixit S (2020) Solar technologies and their implementations: a review. Mater Today: Proc
3. Tauqeer HA, Saeed F, Yousuf MH, Ahmed H, Idrees A, Khan MH, Gelani HE (2021) Proposed model of sustainable resource management for smart grid utilization. World Electr Veh J 12
4. Bhattacharya S, John S (2019) Beyond 30% conversion efficiency in silicon solar cells: a numerical demonstration. Sci Rep 9
5. Sheoran M, Sharma S, Kumar P (2021) Life cycle reassessment strategy for existing bulk and thin-film photovoltaic materials in indian context. Lecture Notes Electric Eng
6. Ghosh S, Yadav R (2021) Future of photovoltaic technologies: a comprehensive review. Sustain Energy Technol Assess 47
7. Saeed F, Tauqeer HA, Idrees A, Ali MZ, Raza A, Khan MA (2021) Buffer layered PbS colloidal quantum dot solar cell with enhanced efficiency. In: 2021 4th international conference on energy conservation and efficiency, ICECE 2021—proceedings
8. Garcia-Gutierrez L, Bressan M, Sferlazza A, Jimenez F, De-Las-Heras S, Alonso C (2020) Development of a high granularity photovoltaic model that considers complex nonuniform shadow conditions and different cell temperatures. Lecture Notes Electric Eng
9. Heath GA, Silverman TJ, Kempe M, Deceglie M, Ravikumar D, Remo T, Cui H, Sinha P, Libby C, Shaw S, Komoto K, Wambach K, Butler E, Barnes T, Wade (2020) A research and development priorities for silicon photovoltaic module recycling to support a circular economy. Nat Energy 5
10. Akram MW, Li G, Jin Y, Zhu C, Javaid A, Akram MZ, Khan MU (2020) Study of manufacturing and hotspot formation in cut cell and full cell PV modules. Sol Energy 203
11. Xia L, Chen J, Liao K, Huang L, Li Q, Luo X (2020) Influence of laser cutting conditions on electrical characteristics of half-size bifacial silicon solar cells. Mater Sci Semicond Process 105
12. Buratti Y, Sowmya A, Evans R, Trupke T, Hameiri Z (2020) End-of-line binning of full and half-cut cells using deep learning on electroluminescence images. In: Conference record of the IEEE photovoltaic specialists conference
13. Tang T, Gan C, Hu Z, Niu H, Si J, Luo X (2017) A quantitative comparison between double glass photovoltaic modules using half-size cells and quarter-size cells. IEEE J Photovoltaics 7
14. Brecl K, Bokalič M, Topič M (2021) Annual energy losses due to partial shading in PV modules with cut wafer-based Si solar cells. Renew Energy 168
15. Liang K, Ai D, Zhang H, Zhao Y, Zhang Y, Chen H (2021) Experimental performance analysis of the concentrated crystalline silicon solar cell—slicing cell. Sol Energy 224
16. Aïssa B, Isaifan RJ, Madhavan VE, Abdallah AA (2016) Structural and physical properties of the dust particles in Qatar and their influence on the PV panel performance. Sci Rep 6
17. Liu X, Yue S, Lu L, Li J (2021) Investigation of the dust scaling behaviour on solar photovoltaic panels. J Clean Prod 295
18. Xiao K, Wu X, Song X, Yuan J, Bai W, Wu C, Huang C (2021) Study on performance degradation and damage modes of thin-film photovoltaic cell subjected to particle impact. Sci Rep 11

19. Deo RC, Şahin M (2017) Forecasting long-term global solar radiation with an ANN algorithm coupled with satellite-derived (MODIS) land surface temperature (LST) for regional locations in Queensland
20. Saeed F, Yousuf MH, Tauqeer HA, Akhtar MR, Abbas ZA, Khan MH (2021) Performance benchmark of multi-layer neural network based solar MPPT for PV applications. In: 2021 international conference on emerging power technologies, ICEPT 2021
21. Abdel-Basset M, Hawash H, Chakrabortty R.K, Ryan M (2021) PV-Net: an innovative deep learning approach for efficient forecasting of short-term photovoltaic energy production. J Clean Prod 303
22. Chang R, Bai L, Hsu CH (2021) Solar power generation prediction based on deep learning. Sustain Energy Technol Assess 47
23. Pérez-Romero Á, Mateo-Romero HF, Gallardo-Saavedra S, Alonso-Gómez V, Alonso-García MDC, Hernández-Callejo L (2021) Evaluation of artificial intelligence-based models for classifying defective photovoltaic cells. Appl Sci 11
24. Moreira MO, Balestrassi PP, Paiva AP, Ribeiro PF, Bonatto BD (2021) Design of experiments using artificial neural network ensemble for photovoltaic generation forecasting. Renew Sustain Energy Rev 135
25. Rizzo SA, Scelba G (2015) ANN based MPPT method for rapidly variable shading conditions. Appl Energy 145
26. Adıgüzel E, Özer E, Akgündoğdu A, Yılmaz E (2019) A prediction of dust particle size effect on efficiency of photovoltaic modules with ANFIS: an experimental study in Aegean region, Turkey. Sol Energy 177

BLDC Motor-Based Electric Three-Wheeler with Regenerative Braking for Increased Driving Range

Sohail Mohammed Abdul Latheef, M. Muhammed Munavir, M. P. Arif, Shehzad, Sooraj Suresh Kumar, and P. Jayaprakash

Abstract This paper analyses energy conversion in BLDC motors during regenerative braking for an electric three-wheeler. For a BLDC motor to act in braking mode the back emf generated should be greater than the terminal voltage. So, the back emf is boosted to a high voltage so that braking can be applied to lower speeds. The step-up of the back emf is accomplished by modifying the switching scheme to the inverter, utilizing the winding inductance. This ultimately acts as a boost converter which eliminates the use of an extra inductor and converter. MATLAB Simulink model is developed for BLDC motor in drive mode and regenerative braking mode. A driving scenario that incorporated both running and braking modes is considered. The simulation results verify the regenerative braking operation of the proposed system. Energy recovery calculations showing how much this strategy is useful are depicted. Moreover, a hardware prototype is developed and tested in the laboratory.

Keywords BLDC motor · Electric vehicle · Regenerative braking

1 Introduction

An electric vehicle uses one or more electric motors for propulsion. The environmental impact of petroleum transportation alone with the hike in oil price will increase the interest in electric vehicles. The market demand is very less for electric vehicles especially three-wheelers due to less driving range. So, increasing driving range is a much-needed solution that will help to build the demand for EVs in the market [1].

Brushless DC motors (BLDC) motors are leading in the automotive industry, and due to their simple operation, permanent magnet excitation, and their high regenerative capability it has an upper hand over other motors for use in light electric vehicles. BLDC motors can also provide high torque which is useful during uphill driving.

S. M. Abdul Latheef · M. Muhammed Munavir · M. P. Arif · Shehzad · S. Suresh Kumar (✉) ·
P. Jayaprakash
Electrical and Electronics Engineering Department, Government College of Engineering, Kannur, India
e-mail: sooraj1173@gmail.com

Regenerative braking is possible if there is an efficient conversion of the kinetic energy into electricity which can be dumped into the battery [2]. Due to limited battery capacity, regenerative braking is essential for all types of electric vehicles [3]. Speed limitation is needed mostly during downhill driving and that is when regenerative braking can be made useful [4, 5]. Although numerous methods and approaches are presented in recent literature, most of them accommodate complex mathematical modeling or additional circuits and those extra features diminish the possibilities of the practical application of regenerative braking. Without compromising the regenerative braking performance, strategies can be implemented by not using any auxiliary circuits [6, 7]. The fundamental principle of regeneration is implemented by using the inverter as a boost converter and machine stator windings as the boosting inductors. However, this method has some limitations in using the inverter as a boost converter and utilizing them due to the nonlinear effects of the drive circuit. The limitations in voltage boosting are mainly caused by SoC and the thermal structure of a battery pack, winding resistance, non-ideal effects, and voltage drops of semiconductors [8]. Simple hardware in the control circuit has been developed to operate the motor in four quadrants [9]. In this work, the energy regeneration is performed by an appropriate switching pattern of VSI by controlling the switches in PWM mode [10]. In [11], the sensorless operation is performed using the back-emf of the motor. A detailed literature review on sensorless control has been done by Acarney and Watson in [12].

The rest of the paper is organized as follows: In Sect. 2, the principle of the BLDC motor is presented. The proposed BLDC drive with various modes, the braking strategy, and circuit analysis are presented. Further in Sect. 3, the simulation results of the two modes and the combined mode of operation are discussed and proposed. The power calculation is also discussed. Hardware results are discussed in Sect. 4 along with the energy recovery calculation by using a solar panel. Finally, the conclusion is presented in Sect. 5. The results of the study on the proposed method provide some important clues for the highly efficient regenerative braking performance on BLDC motors.

2 Proposed BLDC Motor-Based EV

BLDC motor works similarly to a conventional DC motor, except for the fact that in DC motors the conductors are placed on the rotor, and the rotor starts rotating. However, in a BLDC motor, the current-carrying conductor is the stator coils and the rotor is made of permanent magnets.

The stator of a BLDC motor is energized based on different switching states. A combined magnetic field is produced when two phases of the stator are energized. In order to align itself with the stator magnetic field the rotor rotates. Excitation of coil pairs can be done in 6 possible ways. By switching two phases at a time we get a rotating magnetic field at the stator. The rotor follows this field causing it to rotate

continuously. The controller should know the exact position of the rotor to properly switch the phases at the right time. This is done with the help of hall effect sensors.

2.1   EV in Motoring Mode

The electronic control circuit makes the necessary switching actions to operate the motor. **BLDC motor drive circuit** which consists of a MOSFET bridge, BLDC motor, hall effect sensor, and an electronic controller is shown in Fig. 1. Hall-effect sensors help in identifying the rotor position and the speed. Since the MOSFETs need a gate voltage greater than its threshold voltage it needs a driver circuit to turn on. Logic-level MOSFETs generally do not need a driver as they can turn on from the power of a microcontroller.

During motoring mode, two switches of two different phases are operated. For example, when phase A and phase B are to be energized then S1 and S6 are to be operated. In addition to the switching, the speed control is mainly implemented using PID controllers.

The 120-degree switching logic is one of the most common strategies to control the six-step VSI. In this method, each phase will be conducted two times in one full cycle with a span of 120 electrical degrees each time. Therefore, to have a balanced operation of the BLDC, the hall sensors are spatially placed at 120 degrees apart. Based on the Hall sensor signals, 6 switching pulses are generated as shown in Table 1 [13].
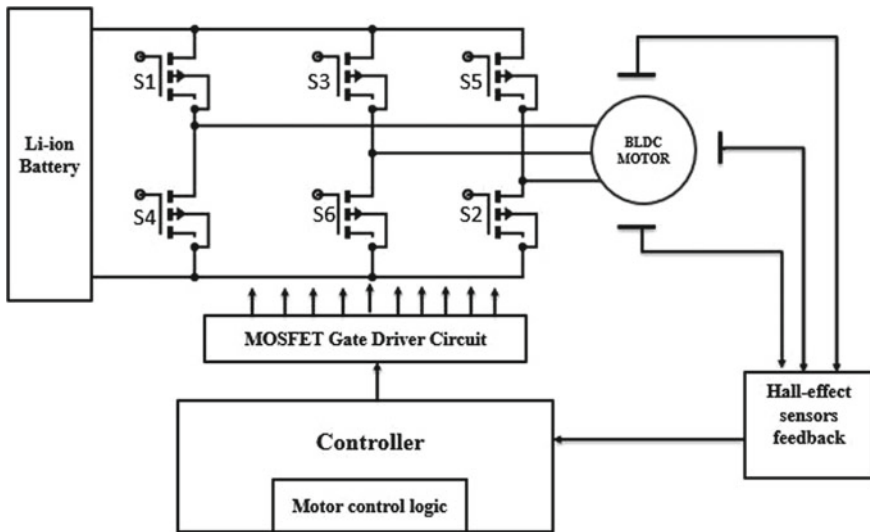

Fig. 1   BLDC motor drive circuit

Table 1 Switching state for electronic commutation for BLDC motor

Hall signal state			EMF of phase			Switching state					
Ha	Hb	Hc	e_a	e_b	e_c	Q1	Q2	Q3	Q4	Q5	Q6
0	0	0	0	0	0	0	0	0	0	0	0
0	0	1	0	−1	+1	0	0	0	1	1	0
0	1	0	−1	+1	0	0	1	1	0	0	0
0	1	1	−1	0	+1	0	1	0	0	1	0
1	0	0	+1	0	−1	1	0	0	0	0	1
1	0	1	+1	−1	0	1	0	0	1	0	0
1	1	0	0	+1	-1	0	0	1	0	0	1
1	1	1	0	0	0	0	0	0	0	0	0

The VSIs are switched at the fundamental frequency which is obtained by the electronic commutation controller. From the above table, the system equations can be derived as:

$$Q1 = HaH^-bH^-c + HaH^-bHc = HaH^-b(H^-c + Hc) = HaH^-b$$
$$Q2 = H^-aHbH^-c + H^-aHbHc = H^-aHb(H^-c + Hc) = H^-aHb$$
$$Q3 = H^-aHbH^-c + HaHbH^-c = HbH^-c(H^-a + H^-a) = HbH^-c$$
$$Q4 = H^-aH^-bHc + HaH^-bHc = H^-bHc(H^-a + Ha) = H^-bHc$$
$$Q5 = H^-aH^-bHc + H^-aHbHc = H^-aHc(H^-b + Hb) = HcH^-a$$
$$Q6 = HaH^-bH^-c + HaHbH^-c = HaH^-c(H^-b + Hb) = H^-cHa$$

The Pulse Width Modulated (PWM) technique is used to turn ON or OFF the switches. By changing the duty cycle of the PWM pulse we can vary the DC link voltage and hence the speed of the motor. For proper variation, the PWM pulse should have a very high frequency than the BLDC motor frequency. The Simulink model of BLDC drive in motoring mode has been shown in Fig. 2. There are two control loops used to drive the motor. The inner loop helps with the switching pulses for the inverter, and the outer loop controls the speed of the motor by changing the dc-link voltage. The load torque applied to the motor shaft is 2.3 Nm. The parameter of the motor used for modelling has been given in Table 2.

2.2 Regenerative Braking

A BLDC motor has windings on its stator and is made of a permanent magnet rotor. The magnetic field of varying magnitude will be induced in the stator if the rotor is rotated. In Fig. 3 the equivalent circuit of the BLDC machine is shown. At lower speeds, the back emf induced on the stator winding is much lower compared to the
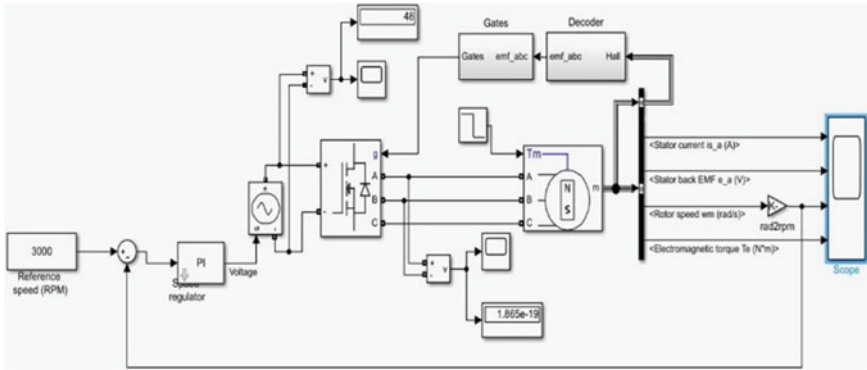
Fig. 2 BLDC drive in motoring mode

Table 2 Motor parameters

Parameters	Value
Stator phase resistance	2.875 Ω
Stator phase inductance	8.5 mH
Flux linkage	0.35 wb
Viscous damping	0.001 Nm−s
Inertia	0.008 kg m^2
Pole pairs	4

dc-link voltage of the converter. Hence, there will be no current flow to the battery and hence regenerative action is not possible. Hence this issue has to be eliminated.

The converter operates as a rectifier when the power flows from the BLDC machine to the dc-link. If no switches are turned on the MOSFETs act as a diode, thus the output voltage is the same as that from a 3-phase diode rectifier.

To enable the power to flow into the battery, the output voltage of the rectifier must be higher than the battery voltage which is at the input side. An idea based
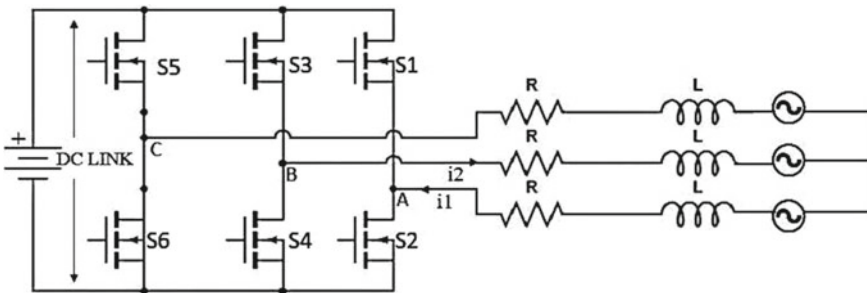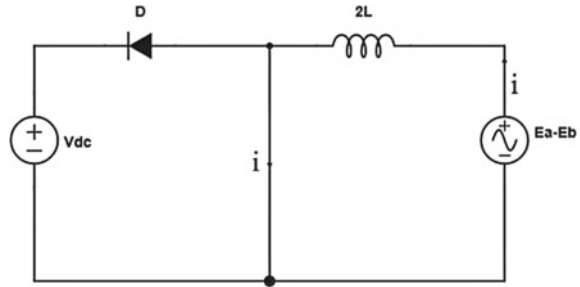

Fig. 3 Equivalent circuit of BLDC machine

Fig. 4 BLDC machine in generating mode

on the operation of a DC-DC boost converter can be derived to reach the desired condition. Turning off all the upper switches S1, S3, and S5, and operating the lower switches S6, S4, and S2 make us reach our desired condition. The equivalent circuit formed using this methodology is shown in Fig. 4. There are 2 modes of operation to be formed for the boost converter: the first is the energy-storing mode for the inductor (phase winding), and the second is the energy transfer mode to the load side (dc-link).

For the source of boost converter, phase windings that have maximum and minimum back emf must be used. In the equivalent circuit which is shown in Fig. 4. the phase inductances of both the phases add up to 2L and when phase-b and phase-a windings have the lowest and highest back emf, the resultant emf is $E_a - E_b$.

2.3 Combined Drive

A driving scenario where the motor is first running at 3000 rpm for five seconds and after a brake signal is applied forcing the motor to stop in two seconds is considered. The Simulink model of BLDC drive with both modes of operation is shown in Fig. 5. The simulation was run for ten seconds in the Simulink. For the realization of regenerative braking, the signal sent to the MOSFETs was changed after the fifth second after that the motor could be stopped by its inertia.

Run and brake blocks are used to provide necessary switching pulses to the respective elements. Run block is derived from a unit step signal up to five seconds. On the other hand, the brake block is derived from inverting the run signal. Control logic is developed from battery current so that the brake signal is active only when the current is negative. A logic is also included to limit the battery current within the safe limits.
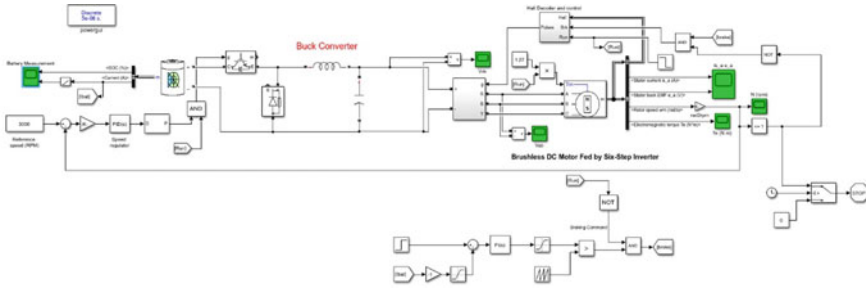
Fig. 5 Simulink model of BLDC drive with both modes

3 Results and Discussion

3.1 Motoring Mode

Figure 6 shows the simulation results of the BLDC machine in the motoring mode of operation. The back emf, stator current, speed, and torque are shown in the results.

3.2 Regenerative Braking

For a reverse current to flow which is into the battery, the motor back emf should be greater than the battery terminal voltage. Hence, we have to boost the voltage developed from the motor higher than the battery. Since this motor is rated for 48-V, the battery terminal voltage would be 48-V. To generate 48-V from the motor (or higher voltage), the motor should run at a speed of 3000 rpm or higher. So practically we have to run our motor at higher speeds to achieve regenerative braking. To eliminate this problem we have to boost the back EMF generated by the motor so that even at lower speeds, we can achieve regenerative braking. By developing a necessary switching action which is discussed in Sect. 2.2, a Simulink model was developed to see how the boost operation is being carried out.

In Fig. 7 there is an increase in SOC which shows that the power is being generated. The dc voltage was boosted up to 50 V which is more than the terminal voltage of the battery which is 48 V. This result proves that boost operation can be easily carried out using the proposed switching action.

3.3 Combined Motoring and Regenerative Action

In Fig. 8, there is a steep decrease in SOC during running. But after that, there is a slow increase in SOC. The battery current also got negative after braking which
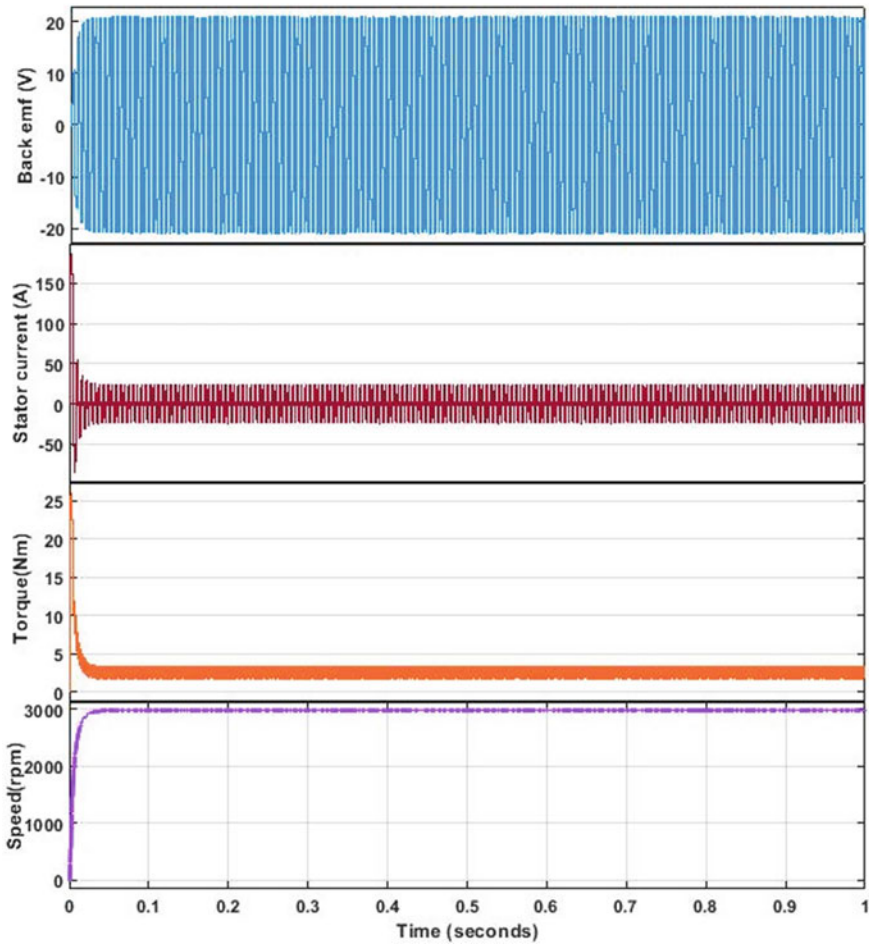
Fig. 6 Simulation results of Back emf, Stator current, Torque and Speed

shows that the power flow is reversed. The back emf is decreased as the motor brakes, and the torque jumps to negative at the braking period as shown in Fig. 9. The speed plot shows that the motor reaches a halt after 7 s.

From Fig. 10 the power was generated for almost 2.6 s which is a considerable amount of time. And also Fig. 11 shows that the power maxed out to −363 W. An average value of −125 W of power was generated during braking. By calculating the area under the power-time graph energy around 0.0902 Wh was obtained under a single braking instant.

Considering semi-urban traffic from "Thana" to "Caltex" which is 1.9 km long as shown in Fig. 12. Assuming 12 braking instants,

Energy required to travel 1mile i.e., 1.6 km is 20 Wh [14]

Energy required to travel 1.9 km = 23.75 Wh.
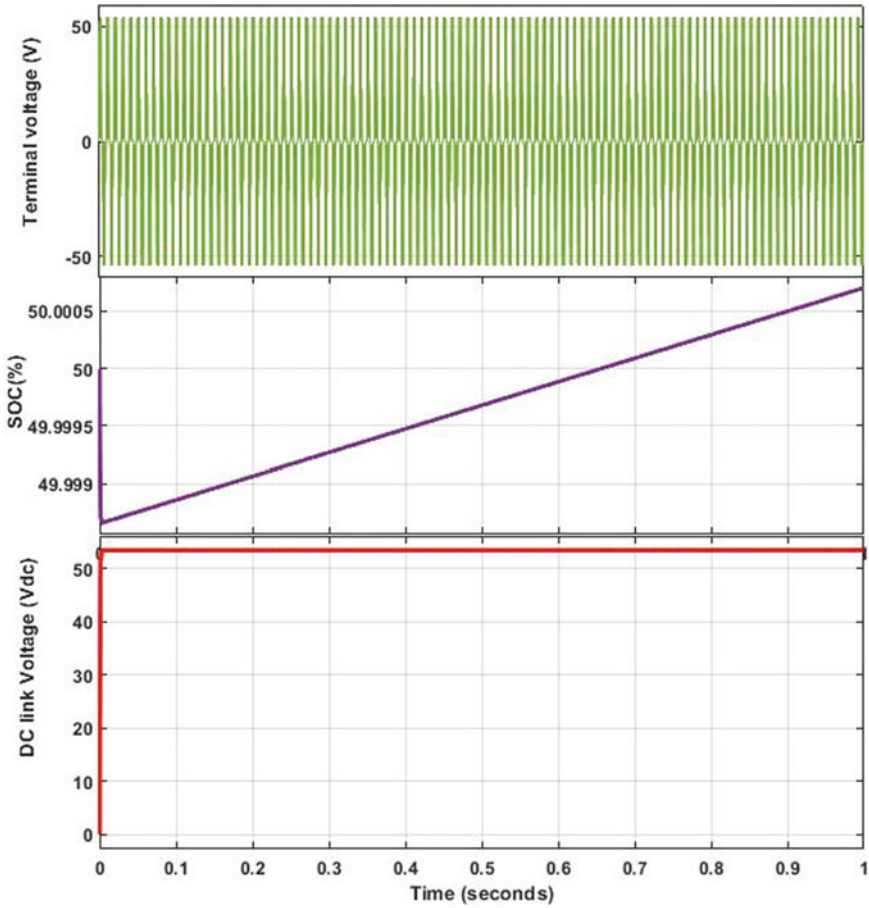
Fig. 7 Simulation result of terminal voltage, DC voltage, and SOC

Energy due to regenerative braking at an instant $= 0.0902$ Wh.
Total energy generated $= 1.0824$ Wh.
Percentage of energy recovery $= (1.0824/23.75) * 1\,00 = \mathbf{4.55\%}$

4 Hardware Results

4.1 BLDC Motor Parameter Calculation

$F_{\mathrm{rr}} =$ Force due to tire rolling resistance.
$F_{\mathrm{AD}} =$ Force due to aerodynamic drag.
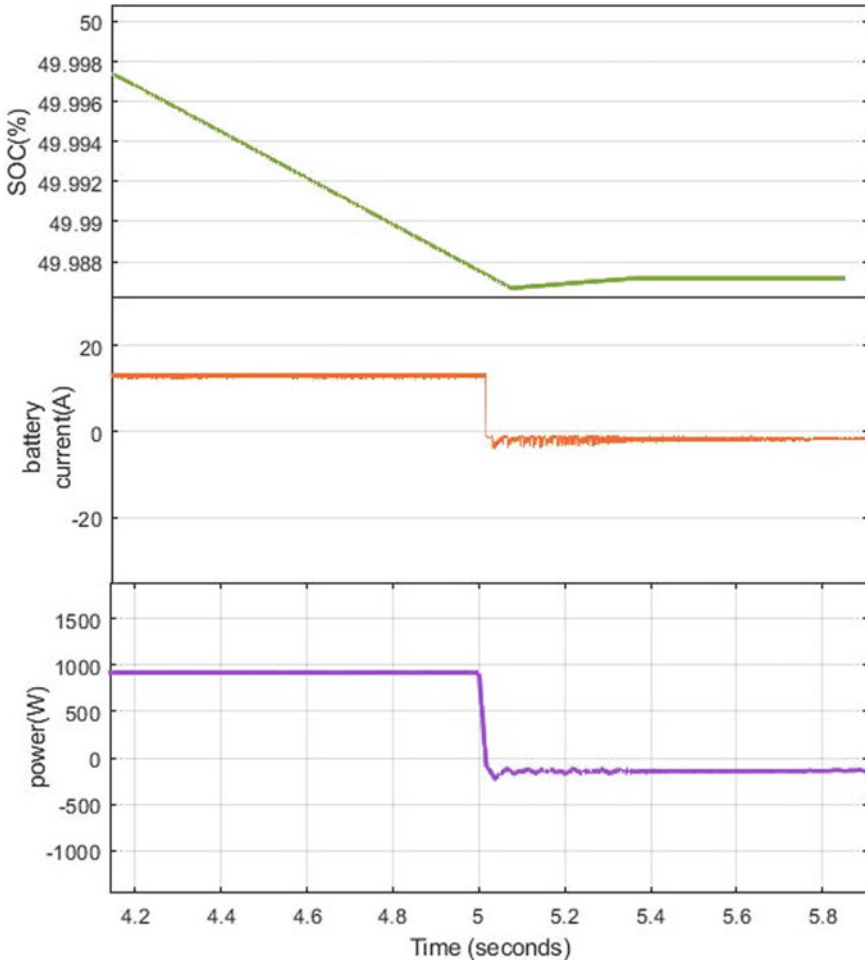
Fig. 8 Simulation result of SOC, battery current, and battery power

F_{AD} = Force due to aerodynamic drag.
F_G = Force to overcome inertia while negotiating slope.
F_I = Inertial forces (acceleration, deceleration).

The main forces opposing the vehicle which are considered for vehicle dynamics are shown in Table 3.

Total road load, $F = F_g + F_r + F_a$.

The torque required at wheel, $T = F * r$.

Power required $= T * w$.

The vehicle is considered with a maximum velocity of 60 km/h. The vahicle parameters considered for the calculation has been given in Table 4.

Rolling Resistance $= 34.3$ N.
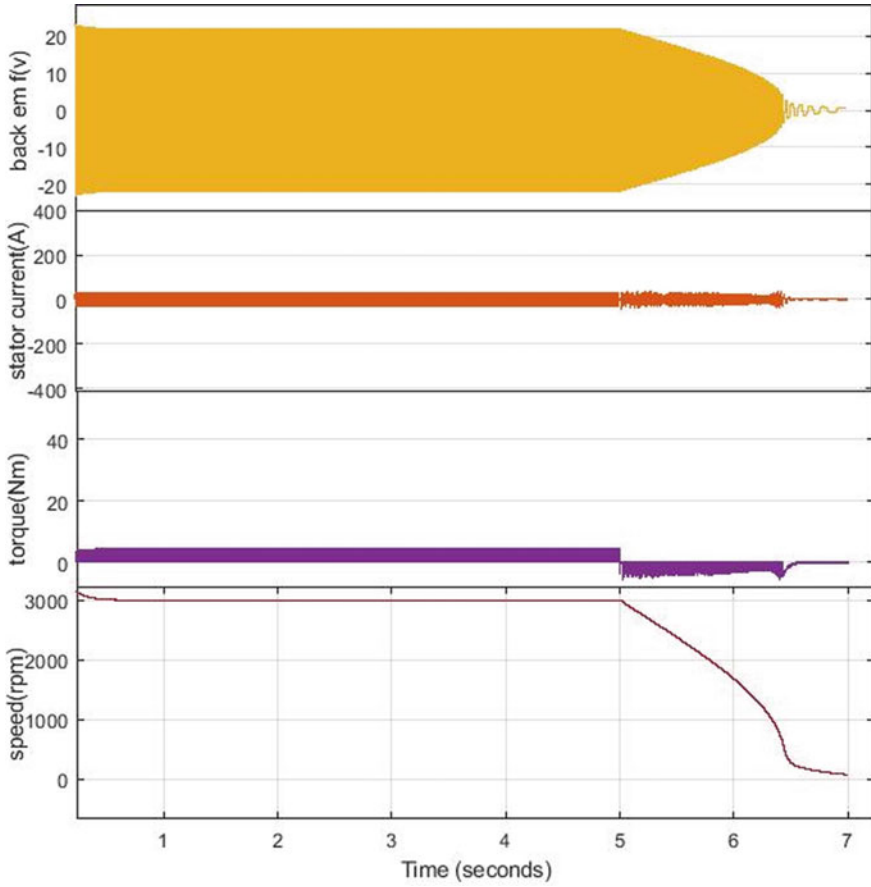
Fig. 9 Simulation result of back emf, stator current, torque and speed during first 5 s running and the next two seconds braking
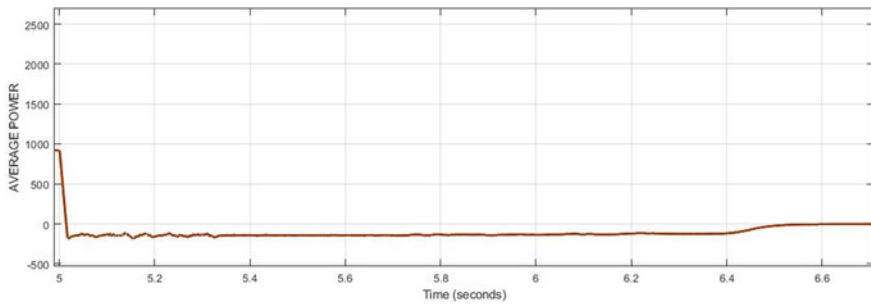
Fig. 10 Simulation result of average power

Fig. 11 Signal statistics

⫶ ▼ Signal Statistics		⬏ ✕
	Value	Time
Max	-3.636e+00	6.593
Min	-2.221e+02	5.038
Peak to Peak	2.185e+02	
Mean	-1.252e+02	
Median	-1.356e+02	
RMS	1.303e+02	
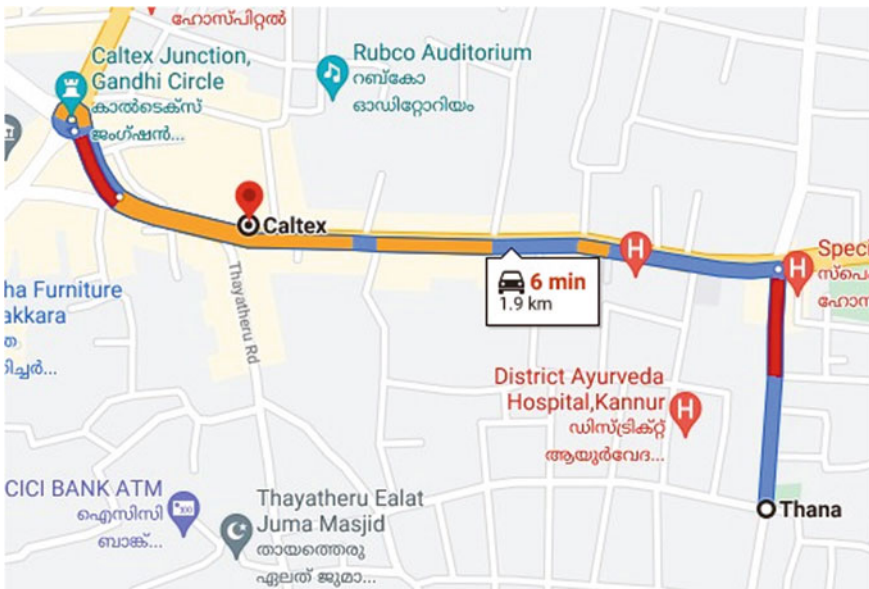
Fig. 12 Distance traveled from thana to Caltex

Table 3 Main opposing forces

Grade tresistance F_g	$m_g \sin\alpha$
Rolling resistance, F_r	$m_g C_r$
Air drag, F_a	$0.5 \, \rho C d A f V^2$

Table 4 Vehicle parameters

Kerb mass of the vehicle	350 kg
Radius of the tyre	0.21 m
Length	2.178 m
Width	0.995 m
Height	1.799 m
Frontal area	1.79 m^2

Power required to overcome rolling resistance = 571 W.
Air Drag = 0.85 N.
Power required against air drag = 247 W.
Total Power required = 571 + 247 = 818 W.

Considering the transmission losses such as losses during battery charging and electric drive system losses [15], we choose 1 Kw motor.

4.2 Experimental Study

To assess the motor performance load test was done. Figure 13 shows the experimental setup. The motor was attached to a brake drum. At first, the motor was made to run in no-load condition and then the load was increased step by step by increasing the weight on the motor until the rated current of the motor is reached. By adjusting the tension of the belt the load on the motor can be adjusted. Four 12 V Lead Acid Batteries were connected in series. Current vs Torque and Speed vs Torque characteristics were plotted in Figs. 14 and 15 respectively.

Fig. 13 Load test setup

Fig. 14 Current versus
torque characteristics
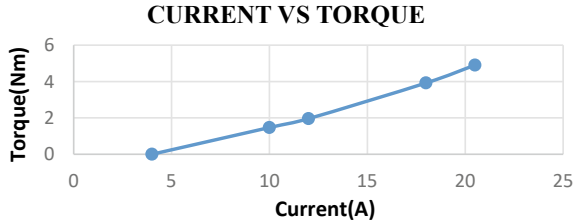
CURRENT VS TORQUE

Fig. 15 Speed versus torque
characteristics

SPEED VS TORQUE
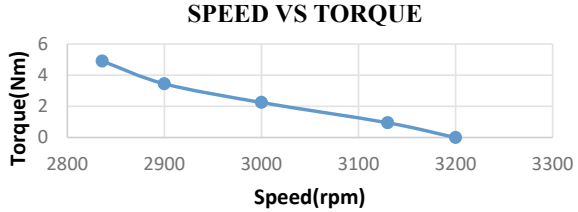
The maximum torque of 4.9 Nm was obtained at the rated current of 20.8 A as shown in Fig. 14.

At no load the speed was noted to be 3200 rpm and as the load is increased the speed reduced to around 2820 rpm. The result is plotted in Fig. 15.

4.3 Range Extension Using Solar Panel

To increase the driving range of the three-wheeler solar was chosen as an added feature. The roof of the vehicle was replaced with a 200 W solar panel as shown in Fig. 16.

By using a 200 W solar panel, it gives 200 Wh energy in 1 h.

Fig. 16 Installed 200 W
solar panel on EV

Therefore, Considering the six-minute duration from thana to Caltex 200 * 0.1 = 20 Wh.

So % of energy recovery due to solar panel = (20/23.75) * 100 = **84.21%**

5 Conclusion

Regenerative braking is one of the most considerable solutions to the reduced range issue associated with electric vehicles. In this paper, a model was developed to calculate how much power was generated at the braking instant. This power generated can determine how much extra range can be produced in an electric vehicle. From the results, we could see a small increase in SoC after braking. A lead-acid battery bank is used due to its robustness and safer behavior. The regenerative performance can be changed according to battery type, state, and condition. From the results, 4.55% of energy recovery was found due to regenerative braking. Adding solar panels gave around 84.21% energy recovery. The efficiency of regeneration with a controlled braking action is entirely dependent on the operation points of the electrical machine, the converter, and the battery pack. The non-ideal effects of motor and motor converters must be considered to reflect more realistic regeneration performance.

References

1. Bhurse SS, Bhole AA (2018) A review of regenerative braking in electric vehicles. In: 2018 international conference on computation of power, energy, information and communication (ICCPEIC), pp 363–367
2. Kivanc OC, Ustun O, Tosun G, Tuncay RN (2016) On regenerative braking capability of BLDC motor. In: 42nd annual conference of the IEEE industrial electronics society (IECON), pp 1710–1715
3. Xu W, Chen H, Wang J, Zhao H (2019) Velocity optimization for braking energy management of in-wheel motor electric vehicles. IEEE Access 7:66410–66422
4. Liu H, Lei Y, Fu Y, Li X (2020) An optimal slip ratio-based revised regenerative braking control strategy of range-extended electric vehicle. Energies 13:1526
5. Xiao B, Lu H, Wang H, Ruan J, Zhang N (1875) Enhanced regenerative braking strategies for electric vehicles: dynamic performance and potential analysis. Energies 2017:10
6. Chen YC, Tu CH, Lin CL (2019) Integrated electromagnetic braking/driving control of electric vehicles using fuzzy inference. IET Electr Power Appl 13:1014–1021
7. Xiao B; Lu H, Wang H, Ruan J, Zhang N (2017) Enhanced regenerative braking strategies for electric vehicles: dynamic performance and potential analysis. Energies 10:1875
8. Marcetic DP, Matic PR (2020) Non-regenerative braking of permanent magnet synchronous motor. IEEE Trans Ind Electron 67:8186–8196
9. Joice CS, Paranjothi SR, Kumar VJS (2013) Digital control strategy for four quadrant operation of three phase BLDC motor with load variations. IEEE Trans Ind Inf 9(2):974–982
10. Riyadi S, Dwi Setianto YB (2019) Analysis and design of BLDC motor control in regenerative braking. 2019 international symposium on electrical and electronics engineering (ISEE), Ho Chi Minh, Vietnam. pp 211–215

11. Sundeep S, Singh B (2018) Robust position sensorless technique for a PMBLDC motor. IEEE Trans Power Electron 33(8):6936–6945
12. Sameeullah M, Chandel S (2016) Design and analysis of solar electric rickshaw: a green transport model. In: 2016 international conference on energy efficient technologies for sustainability (ICEETS), Nagercoil, pp 206–211
13. Kukde H, Lilhare AS (2017) Solar powered brushless DC motor drive for water pumping system. In: 2017 International conference on power and embedded drive control (ICPEDC)
14. https://www.industrialbicycles.com/blog/How-to-calculate-your-ebike-range.
15. Young-kyoun Kim S-HR, Jung I-S (2010) Parameter determination of the BLDC motor considering the dynamic equation of vehicle. In: The XIX international conference on electrical machines ICEM

Grid-Connected DFIG-Based Wind Energy Conversion System with ANFIS Neuro-Fuzzy Controller

Megha Vyas, Vinod Kumar, Shripati Vyas, and Raju Kumar Swami

Abstract An adaptive neuro-fuzzy controller (ANFC) for grid-connected doubly fed induction generator (DFIG)-based wind energy conversion system (WECS) is presented in this paper. The ANFC architecture based on the adaptive network-based fuzzy inference system (ANFIS) has the exceptional feature of quick convergence while combining the flexibility of fuzzy logic with the suppleness of neural networks. For the proper functioning of isolated DFIG-based WEC system, the grid side converter (GSC) control is developed using the ANFIS. The proposed system reveals better dynamic performance during the fluctuating load conditions and wind speed by keeping the output voltage stable. The turbine rotation varies with varying wind speed while the supply frequency to the load stays consistent with the precise management of GSCs. The simulation results reveal the exceptional performance of controller in terms of limiting the supply frequency and load-voltage regulation during varying load demand and wind speed.

Keywords DFIG · ANFIS · WECS · RSC · GSC

1 Introduction

The DFIGs are most popular currently, due to their capacity to operate over a larger speed range than their rivals [1]. High magnetizing currents are drawn from the power grid by traditional squirrel cage asynchronous generators while the DFIGs allow for the employment of low-power converters in rotor side and grid side converters functioning in super-synchronous and sub-synchronous modes, further for decoupled real and reactive power control. Power electronics interfaces are built into the machine to manage frequency and voltage in order to maintain power variations from source

M. Vyas (✉) · V. Kumar · S. Vyas
Department of Electrical Engineering, College of Technology and Engineering, Udaipur, India
e-mail: megha.vyas14@gmail.com

R. K. Swami
Department of Electrical Engineering, Pacific University, Udaipur, India

side. Different control techniques for controlled functioning of DFIG also supplying the grid side control have been proposed so far [2–4].

Some of the researchers proposed direct power control and vector control to adjust the power output of DFIG in both balanced and unbalanced modes. To support asymmetric loads, authors developed direct voltage control technique using negative-sequence technique in another study [5]. However, the reliability of the wind power management under applied torque and fluctuating wind speed has not been demonstrated in the proposed technique.

Novel control methods like neural networks (NN), neuro-fuzzy control (NFC) and adaptive network-based fuzzy inference system (ANFIS) are yet to be substantially researched for standalone DFIG operation. Because of its hybrid learning, ANFIS is one of the most adaptable NFC systems when it comes to selecting membership functions. Furthermore, the ANFIS structure has the unique ability to represent a highly nonlinear system because it blends fuzzy reasoning's ability to handle uncertainty with the learning ability of a neural network from a complicated system [6].

To the author's best knowledge, very few studies are available which discussed the novel technique dealing to handle the nonlinearities and uncertainties in induction machines, considering the case of variable wind speed. In this paper, the ANFIS-based NFC approach for converter control has been proposed. The recommended controller is designed to keep the terminal voltage and frequency at a predetermined level. The responses of the DFIG-WECS under transient conditions with the PI controller was created to supply the sample data (input/output) to train the ANFIS structure. The overall configuration of the DFIG-WECS based on ANFIS is shown in Fig. 1.
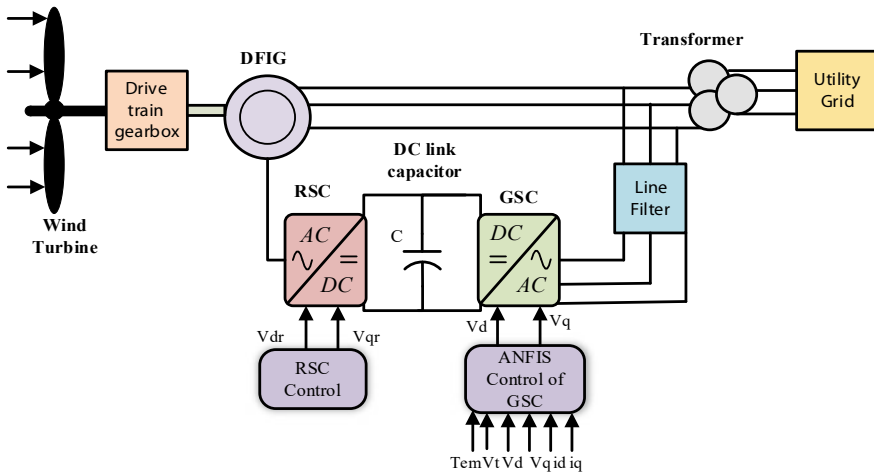
Fig. 1 Overall configuration of the DFIG-WECS based on ANFIS

2 DFIG Modelling

As illustrated in (1)–(8), the mathematical modelling of DFIG may be derived with the flux equations and d-q axis voltage. The d-q transformation model is achieved by substituting the arbitrary speed with the synchronous speed in the arbitrary reference frame model of the DFIG.

$$v_{ds} = R_s i_{ds} + p\Psi_{ds} - \omega_s \Psi_{qs} \tag{1}$$

$$v_{qs} = R_r i_{dr} + p\Psi_{qs} + \omega_s \Psi_{ds} \tag{2}$$

$$v_{dr} = R_r i_{dr} + p\Psi_{dr} - (\omega_s - \omega_r)\Psi_{qr} \tag{3}$$

$$v_{qr} = R_r i_{qr} + p\Psi_{qr} + (\omega_s - \omega_r)\Psi_{dr} \tag{4}$$

The d-q axis flux connections may be connected to the relevant currents using the equations described in (5)–(8)

$$\Psi_{ds} = (L_{ls} + L_m)i_{ds} + L_m i_{dr} = L_s i_{ds} + L_m i_{dr} \tag{5}$$

$$\Psi_{qs} = (L_{ls} + L_m)i_{qs} + L_m i_{qr} = L_s i_{qs} + L_m i_{qr} \tag{6}$$

$$\Psi_{dr} = (L_{lr} + L_m)i_{dr} + L_m i_{ds} = L_r i_{dr} + L_m i_{ds} \tag{7}$$

$$\Psi_{qr} = (L_{lr} + L_m)i_{qr} + L_m i_{qs} = L_r i_{qr} + L_m i_{qs} \tag{8}$$

Here,

$v_{dr}, v_{qr}, v_{ds}, v_{qs}$	Voltages of d-q axis rotor and stator in Volt
$i_{dr}, i_{qr}, i_{ds}, i_{qs}$	Currents of d-q axis rotor and stator in Ampere
$\Psi_{dr}, \Psi_{qr}, \Psi_{ds}, \Psi_{qs}$	Flux-linkages of d-q axis rotor and stator in Weber
ω_s, ω_r	Angular speed in Radian/Sec.
p	derivative operator ($p = \mathrm{d}/\mathrm{d}t$).
R_r, R_s	Rotor and stator winding resistances (Ω)
L_{lr}, L_{ls}	Leakage inductances Rotor and stator in Hennery
L_m	Magnetizing inductance (H)
$L_s = L_{ls} + L_m$	Stator self-inductance in Hennery
$L_r = L_{lr} + L_m$	Rotor self-inductance in Hennery

3 Converter Control Operation

The different conditions like irregular wind speed, fluctuating power demand of load make the functioning of wind energy systems difficult. During these conditions, it is difficult to maintain frequency and voltage output of DFIG constant. To satisfy demand in the event of an energy deficit and to store energy during surplus production of wind power, a battery storage system is designed analogous to the dc link side. In order to keep balance between the load demand and supply for the isolated system, a power management algorithm is necessary. When the storage unit becomes over-supplied, the extra energy is dispersed through dumping load. For the isolated mode of operation of DFIG [11, 12], the GSC and RSC control techniques are described in the subsections below.

(a) **Grid side converter control**

In spite of the course of power flow, the grid side converter (GSC) adjusts the current dc-link voltage in order to match the reference value [13]. To eliminate the influence of voltage dips across the GSC, the negative sequence current component of reference iqg* and idg* are set to zero. As shown in Fig. 2, the hysteresis current controller evaluates the reference and real current components as of the grid via the GSC and sends pulses to the converter for managing the dc-link voltage.

(b) **Rotor Side Converter Control**

When there is no negative or natural flux, the rotor side converter regulates actual and reactive power flow of DFIG by adaptive neuro-fuzzy control during normal
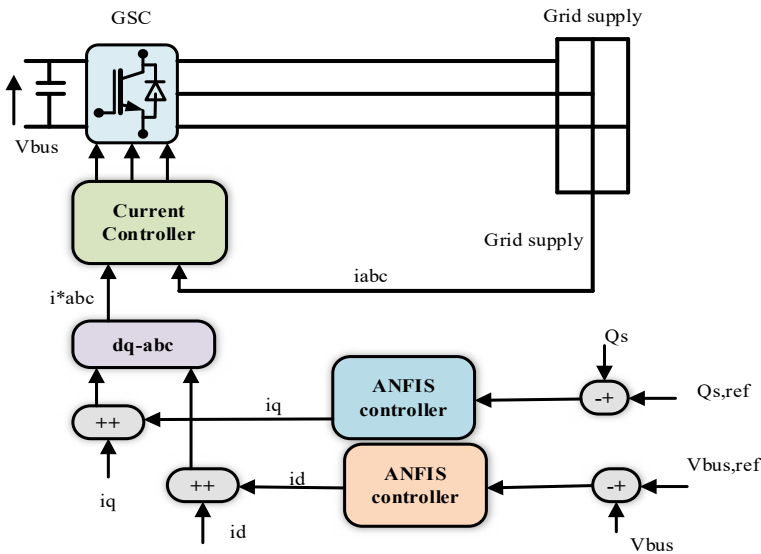

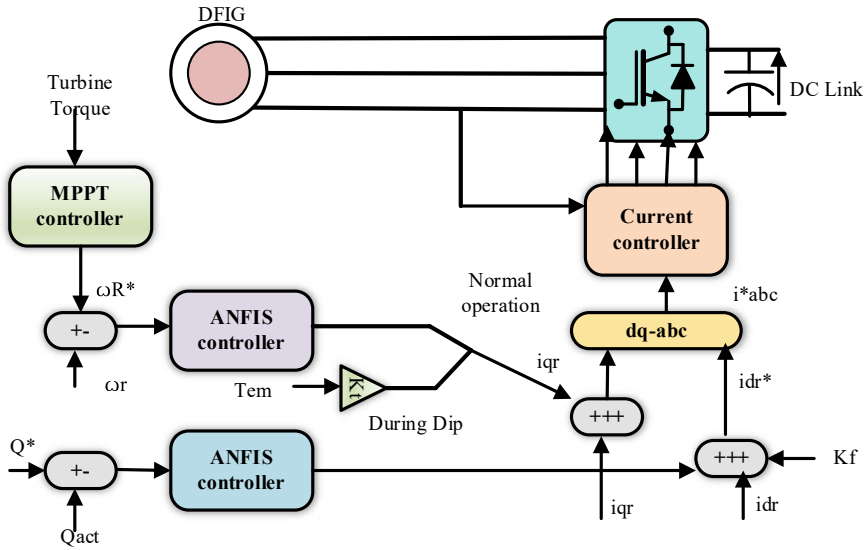**Fig. 2** Schematic diagram of the GSC control

Fig. 3 Schematic diagram of the rotor side converter control

operating conditions. An indirect MPPT control approach is used to obtain the reference rotor speed through control with no voltage dip. For mitigating the voltage sag effect, a demagnetizing current is provided into the control system during voltage dips [14]. Figure 3 shows a block schematic of the rotor side converter control.

(c) **ANFIS controller**

During the designing of a linear controller for DFIG-WECS, the controller needs some modifications for functioning in an actual wind turbine system. But it has some difficulties in making an ideal simulation model of actual DFIG-WECS since it comprises multiple unknown dynamics [15–17]. In adaptive neuro-fuzzy inference system, the membership functions may be recreated with the assistance of a genuine input–output data set. The gradient descent technique [18–20] is used to determine the parameter connected through the membership functions. For membership function parameter estimation, ANFIS use a mixture of backpropagation and least squares estimation. The basic structure of the suggested ANFIS is depicted in Fig. 4.

The ANFIS structure is described in depth in [21–27]. To reduce the load voltage error function, the method creates the appropriate voltage references to impel the rotor side converter using the numerical data set. The method uses a neuro-fuzzy model to change membership function parameters. After determining the gradient vector, it adjusts the parameters using one of its optimization strategies to lower the error function described as

$$V_{\text{err}} = V_x^{\text{ref}} - V_x^{\text{mes}} \tag{9}$$
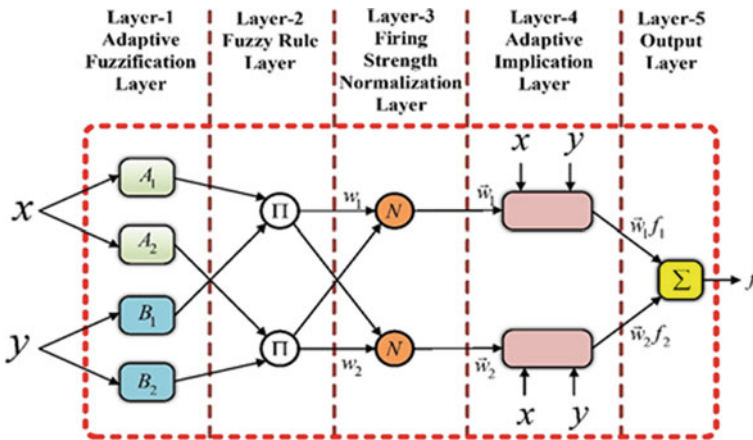
Fig. 4 ANFIS structure

Here, V_x^{ref} = grid side voltage of reference d, q axis taken for training

V_x^{mes} = reference voltage as measured for iteration process

The following are the node functions of each layer:

Layer 1: This layer assigns some membership functions to every input, called fuzzification layer. The Gaussian membership functions are used in the proposed method, as shown in Fig. 5

The Gaussian membership function has the following equations:

$$f(x) = e^{-\frac{(x-m_i)}{2\delta_i}} \tag{10}$$

where x = input for the layer

δ_i and m_i = standard deviation and mean value of data, respectively, for the corresponding membership function.

Fig. 5 Membership function for input data x

Layer 2: The output is to be sent to the succeeding level, indicating the rule's separate firing capacity μ_i.

$$\mu_i = \mu_{a_1}^i(x_1)\mu_{b_1}^i(x_2) \tag{11}$$

Layer 3: Every block estimates the proportion of the ith rule's firing μ_i capacity to the addition of all rules' firing capacity, called the normalization step.

$$\mu_1 = \frac{\mu_1}{\mu_1 + \mu_2 + \mu_3} \tag{12}$$

Layer 4: The liner activation function is used to calculate the functional output (f_i) in this layer.

$$f_i = a_0^i + a_1^i x_j, \quad i, \; j = 1, 2, 3 \tag{13}$$

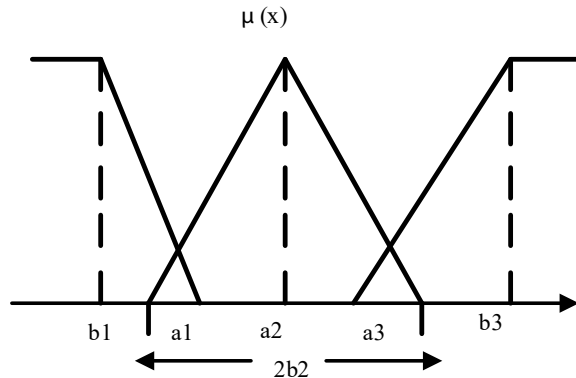Parameters a_0 and a_1 are designed as a function of input at this stage (x). The term "consequent parameters" refers to these parameters.

Layer 5: Output layer is the final layer that combines the input data to generate the overall result.

$$V^* = \mu_1 f_1 + \mu_2 f_2 + \mu_3 f_3 \tag{14}$$

4 Results and Discussion

The performance of the suggested ANFIS controller-based DFIG-WECS is evaluated for standalone mode during various operating conditions like fluctuating load and wind speed using MATLAB Simulink. The GSC control's goal is to maintain the DFIG's output voltage and frequency at a constant level. Filter capacitors are also necessary to eliminate the rotor side and grid side converters' switching frequency harmonics. The capacitors also offer some of the magnetization's reactive power. To keep the suggested system simple, the filtering circuit is not shown in the control structure. This section describes the transient condition generated due to change of rotor speed and variations in power demanded by load during the provision of nonlinear and linear loads. Figure 6a shows the variation in wind speed; a sudden change from 8 to 12 m/s in wind speed is applied at time $t = 7$ s and again decrease the wind speed from 12 to 8 m/s in order to analyse the system response in an abrupt change in wind speed.

Figure 6b shows the wind turbine generated power; it can be seen from the waveform that power output of the wind energy system increases as the speed of wind

(a)

(b)
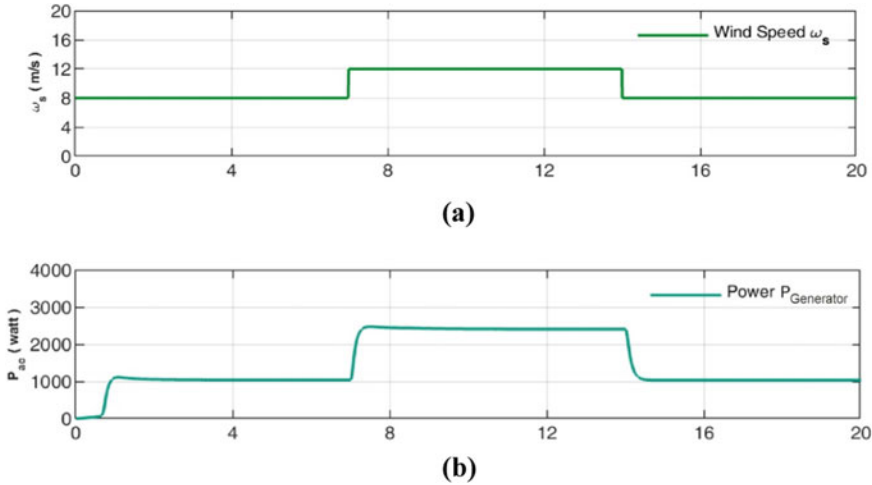
Fig. 6 Performance of the developed ANFIS controller for **a** step change in wind speed **b** variation in generator power

increases and vice versa. The response of the grid voltage and current in steady state condition are shown in Figs. 7 and 8, respectively.

Figure 9 depicts electromagnetic torque and mechanical torque, whereas Fig. 10 shows the direct axis and quadrature axis current of the generator, indicating projected controller performance. Figure 11 shows the generator output voltage, indicating that the control approach is performing well.
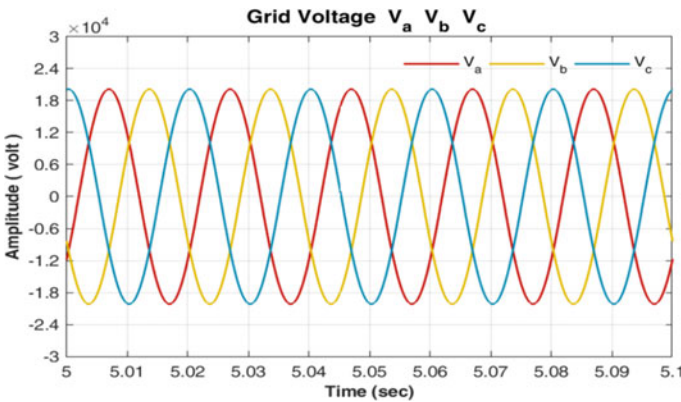
Fig. 7 Grid voltage
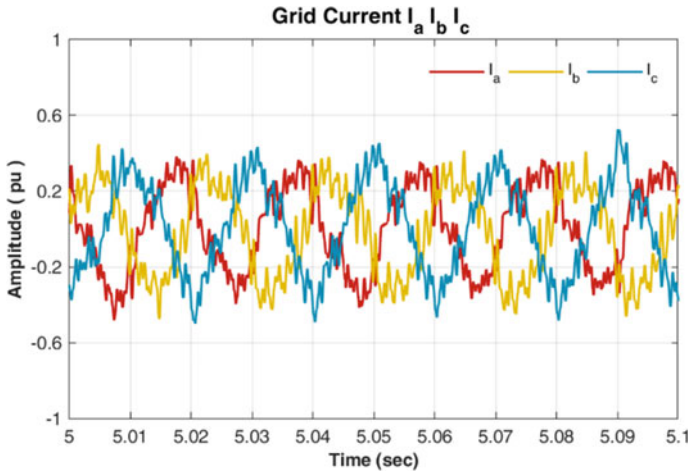
Fig. 8 Grid current
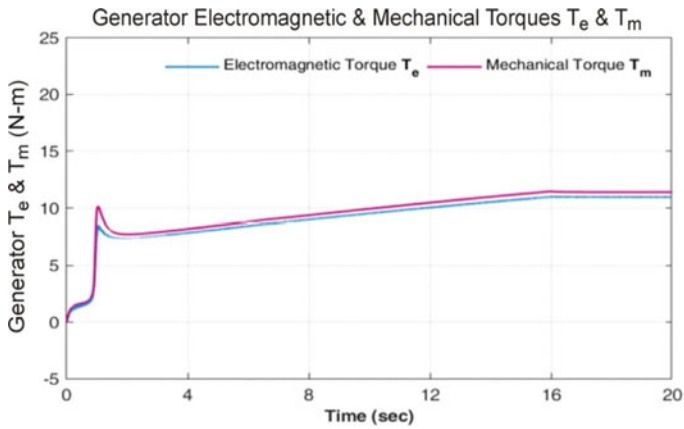
Fig. 9 Electromagnetic and mechanical torque at various wind speed conditions

5 Conclusion

ANFIS-based NFC is presented as a unique solution for DFIG-operated WECS. The suggested controller's performance is studied for isolated loads during various operating situations. The results show that RSC and GSC controllers work together to regulate reactive and real power by modifying machine torque and rotor speed when wind speed changes. Furthermore, even when the wind speed abruptly changes, the controller at the load end maintains a constant voltage and frequency. The suggested controller's inherent learning capability provides adaptive compensation for the uncertainty of the entire system and the nonlinearity of DFIG-WECS. In the
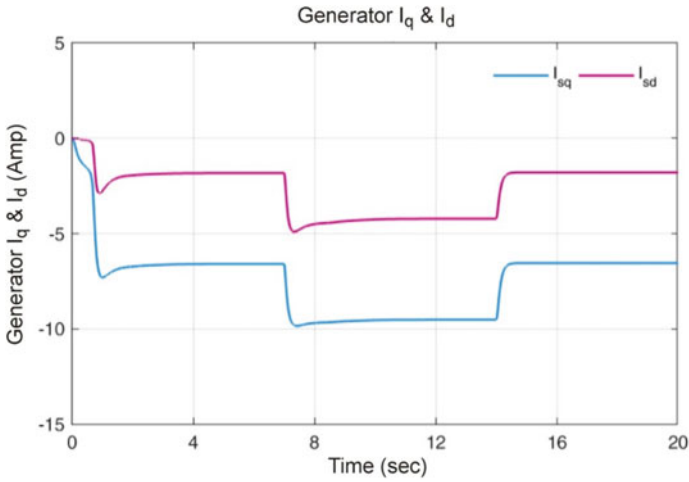
Fig. 10 Direct and quadrature current of generator
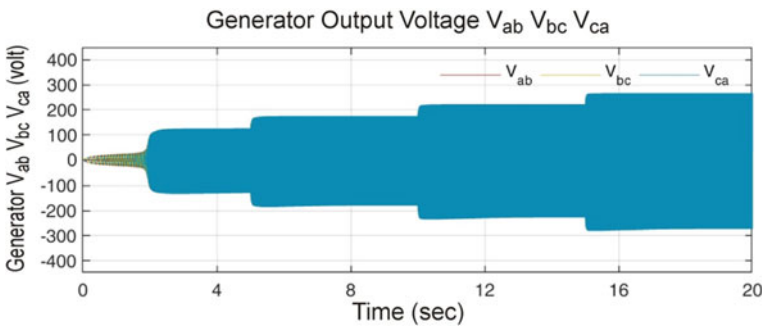
Fig. 11 Output voltage of wind generator

standalone working mode of DFIG-WECS, the study of the proposed method reveals that the provided ANFIS architecture-based controller is superior and resilient.

References

1. Dali M, Belhadj J, Roboam X (2010) Hybrid solar–wind system with battery storage operating in grid-connected and standalone mode: control and energy management-experimental investigation. Energ J 35(6):2587–2595
2. Peña R, Cardenas R, Escobar E, Clare J, Wheeler P (2009) Control strategy for a doubly-fed induction generator feeding an unbalanced grid or stand-alone load. Electric Power Syst Res 79(2):355–364
3. Kumar CES, Jasper J, Pregitha RE (2018) Soft computing techniques used power quality enhancement of doubly fed induction generator based wind energy conversion system. Taga J

Swansea Printing Technol Ltd 14:2785–2798

4. Bharti OP (2017) Controller design of DFIG based wind turbine by using evolutionary soft computational techniques. Eng Technol Appl Sci Res 7(3):1732–1736

5. Ataji AB, Miura Y, Ise T, Tanaka H (2015) Direct voltage control with slip angle estimation to extend the range of supported asymmetric loads for stand-alone DFIG. IEEE Trans Power Electron 31(2):1015–1025

6. Chy MI, Uddin MN (2009) Development and Implementation of a new adaptive intelligent speed controller for IPMSM drive. IEEE Trans Ind Appl 43(3):1106–1115

7. Wu B, Lang Y, Zargari N, Kouro S (2011) Power conversion and control of wind energy systems. Wiley, IEEE Press, pp 27–29

8. Abad G, López J, Rodríguez M, Marroyo L, Iwanski G (2011) Doubly fed induction machine, modelling and control for wind energy generation. Wiley Publications, IEEE Press Series on Power Engineering, p 538

9. Liu M, Member S, Pan W, Zhang Y (2019) A dynamic equivalent model for DFIG-based wind farms. IEEE Access 7:74931–74940

10. Eltamaly ALIM (2020) Dynamic control of a DFIG wind power generation system to mitigate unbalanced grid voltage. IEEE Access 8:39091–39103

11. Zhou Y, Member S, Bauer P, Member S, Ferreira JA, Pierik J (2009) Operation of grid-connected DFIG under unbalanced grid voltage condition 24(1):240–246

12. Xiong L, Wang J, Mi X, Khan MW (2017) Power control of grid-connected DFIG. IEEE Trans Power Syst Fractional 8950:0885–8950

13. Buddha S (2019) Rotor side and grid side converters fault in DFIG based WECS. Indian J Appl Res 9(7):7–9

14. Galdi V, Piccolo A, Siano P (2008) Designing an adaptive fuzzy controller for maximum wind energy extraction. IEEE Trans Energy Convers 23(2):559–569

15. Amin IK, Uddin MN, Marsadek M (2019) ANFIS based neuro-fuzzy control of DFIG for Wind Power Generation in Standalone Mode. In: IEEE international electric machines & drives conference (IEMDC), pp 2077–2082

16. Dhal PK (2018) Dynamic performance analysis of double fed induction generator using adaptive neuro-fuzzy interference system in microgrid. In: 2018 International conference on recent innovations in electrical, electronics & communication engineering (ICRIEECE), pp 1933–1938

17. Jang JSR (2020) ANFIS: adaptive-network-based fuzzy inference system. IEEE Trans Syst Man Cybern 23(3):665–685

18. Dzung PQ, Bao AN, Lee HH (2011) New artificial neural network based direct virtual torque control and direct power control for DFIG in wind energy systems. In: IEEE PEDS 2011, Singapore, 5–8 Dec

19. Diab AAZ, Maksoud SAA, Kotin DA (2016) Performance of doubly-fed induction generator based wind turbine using adaptive neuro-fuzzy inference system. In: IFOST-2016: mechatronics, electrical engineering and power electronics, pp 145–149

20. Kumar A, Giribabu D (2016) Performance improvement of DFIG fed wind energy conversion system using ANFIS controller. In: International conference on advances in electrical, electronics, information, communication and bio-informatics (AEEICB16) performance, vol 978, no 10

21. Elsisi M, Lehtonen M, Darwish MMF (2021) Robust design of ANFIS-based blade pitch controller for wind energy conversion systems against wind speed fluctuations. IEEE Access 9:37894–37904

22. Hussain J, Mishra MK (2020) An efficient wind speed computation method using sliding mode observers in wind energy conversion system control applications. IEEE Trans Ind Appl 56(1):730–739

23. Ali MN, Mahmoud K, Lehtonen M, Darwish MMF (2021) An efficient fuzzy-logic based variable-step incremental conductance MPPT method for grid-connected PV systems. IEEE Access 9:26420–26430

24. Liang H, Liu G, Zhang H, Huang T (2020) Neural-network-based event triggered adaptive control of nonaffine nonlinear multiagent systems with dynamic uncertainties. IEEE Trans Neural Netw Learn Syst
25. Li H, Wu Y, Chen M (2021) Adaptive fault-tolerant tracking control for discrete-time multiagent systems via reinforcement learning algorithm. IEEE Trans Cybern 51(3):1163–1174
26. Elsisi M, Mahmoud K, Lehtonen M, Darwish MMF (2021) An improved neural network algorithm to efficiently track various trajectories of robot manipulator arms. IEEE Access 9:11911–11920
27. Elsisi M (2020) New design of robust PID controller based on meta-heuristic algorithms for wind energy conversion system. Wind Energ 23(2):391–403

A Taxonomical Review of MOS Power Transistor for Electronic Circuits and Devices

Malti Bansal and Raaghav Raj Maiya

Abstract This literature survey dives deep in the theory of power MOSFET discussing every aspect of its development starting from the very beginning of its invention, covering the advancements in the device structure to its applications. The research paper also includes the study of various structures of the power MOSFET while comparing their features at the same time. The study of various power MOSFET structures based on the parameters like device structure, thermal stability, conductivity, breakdown voltage, and the on-state resistance has been included in the paper. The paper also researches and concludes the best device structure for use in the present world.

Keywords MOSFET · Vertical · On-state · Resistance · Gate · Trench · Silicon · Breakdown voltage

1 Introduction

The power MOSFET is a modified version of the conventional MOSFET, developed for the power applications. The device boasts the higher switching speed and requires less current as compared to the conventional MOS. The device has three terminals. These terminals have a different naming than BJT, the terminals of the device are the source terminal, the gate terminal, and the drain terminal. The device possesses junction with depletion layer at different depths. The device finds a lot of advantage over the other devices, like positive temperature coefficient, operating frequency over 100 kHz and the various device structures possible, which allows us to get the desired properties.

M. Bansal (✉) · R. R. Maiya

Department of Electronics and Communication Engineering, Delhi Technological University (DTU), Delhi 110042, India

e-mail: maltibansal@gmail.com

2 History

The MOSFET was a huge stepping stone in the history of modern electronics, just like the BJT proved to be a revolutionary invention, power MOSFET impacted the electronics world on the same scale. This breakthrough idea was developed in the bell laboratories. It was invented by Mohamed Atalla and Dawon Kahng in the year 1959. After this invention, a MOSFET solved a lot of problem at the places where BJT was not a suitable device to use. The conventional MOSFET still faced some challenges in working effectively in the place where high power is required or where high switching speed is required. This reason became one of the guiding reasons for development of Power MOSFET. The first power MOSFET was introduced by Hitachi in 1969, ten years after the invention of conventional MOSFET. The MOSFET developed had a vertical configuration and hence was known as VMOS or Vertical groove MOSFET. In the same year, Tarui, Toshihiro Sekigawa, and Y. Hayashi of the Electrochemical Laboratory (ETL) developed the doubly diffused MOSFET abbreviated as DMOS. The structure of DMOS possessed self-Aligned Gates. In the coming year of 1977, the research team of John Moll at HP labs designed VDMOS which was essentially a mix or combined form of VMOS and DMOS. This research was carried out at the HP laboratories. They also demonstrated the advantage which the DMOS possess over the VMOS. DMOS have a higher breakdown voltage and lower on-resistance as compared to VMOS. In the same year, the Hitachi technologies developed the lateral DMOS, another form of DMOS abbreviated as LDMOS. In the year of 1977 itself, we witnessed the development of yet another type of power MOS, known as HEXFET, which was developed by Alex Lidow at Stanford University. In the next year of 1978, Shozo Shirota and Shigeo Kaneda developed a super-junction MOSFET at Osaka University. The idea behind this development was using P+ columns, these columns were penetrated in the oppositely charge epitaxial layer, the N-epitaxial layer. So we can deduce that after the development of MOSFET in the year 1959 which paved a way for power MOSFET invention, maximum developments took place between the year 1969 and 1989 in the field of power MOSFET [1–8].

3 Power MOSFET and Its Fabrication

A power MOSFET is simply a modified type of field effect transistor. The power MOSFETs are specially designed to work under high power condition. Depending on the requirements of the circuit, different structures of the power MOSFET have been developed which lead to different breakdown voltage, on-state resistance, and other parameters (Fig. 1).

Fig. 1 Power MOSFET
equivalent circuit
(Reproduced from [4])
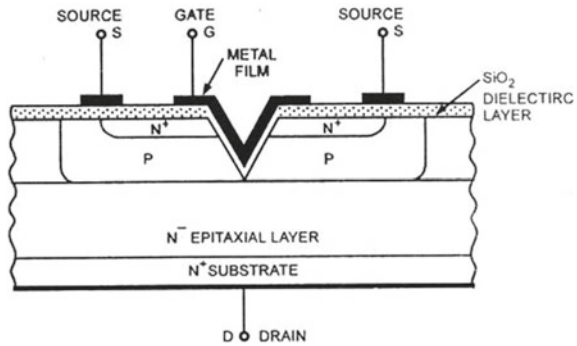
3.1 Fabrication

Over the years there have been several configurations of the MOSFET devices with
each having some structural change and some properties advantage over the other.
So, in this paper, the V-configuration or the vertical configuration has been explained.
Starting from the top, the MOSFET features four terminals, two are source metal
electrodes. The gate electrode is in between the source electrodes. The drain electrode
is connected to N+ substrate layer in the bottom of the MOSFET. Special care needs
to be taken that we do not connect the source and the drain electrode physically
otherwise it will disrupt the biasing of the MOSFET device. The electrode is not
connected to the n-type and p-type material directly, and there is a dielectric S02
layer between the two. This dielectric layer acts as an insulator between the two and
prevents any kind of charge flow between the electrodes and the substrate. The motion
of electrode is only within the substrate which happens when a potential difference
is applied to the electrode of the MOSFET. For use in high power conditions, the
drain region of the MOSFET needs to have a low doping concentration and a short
channel length. The drain contact in the case of VMOS which is the first developed
power MOSFET is formed on the substrate. Due to the V shape structure present
in the device, the flow of current is in the vertical direction which is basically from
drain to source. If we want to achieve a high current rating, this can be achieved using
the metallization process. In this process, we basically cascade or join several MOS
together one after another. The depth of diffusion controls the length of the channel
through which the current flows [9–15]. Due to the higher resistance present in the
epitaxial layer as compared to the p-channel region, there is higher power dissipation
in this region. The reason for higher power loss is because of the lower doping in
this region which leads to higher resistance. The current crowding leads to caging
of the current and voltage rating at the tip region. The problem mentioned can be
easily solved by truncated MOSFET. The MOSFET have two successive diffusion
steps, and these basically represent the two p-n junctions which the MOSFET device
possess. These junctions are essentially present at different depths in the MOSFET
structure, both the structure having their own biasing. If these dual diffusion layers
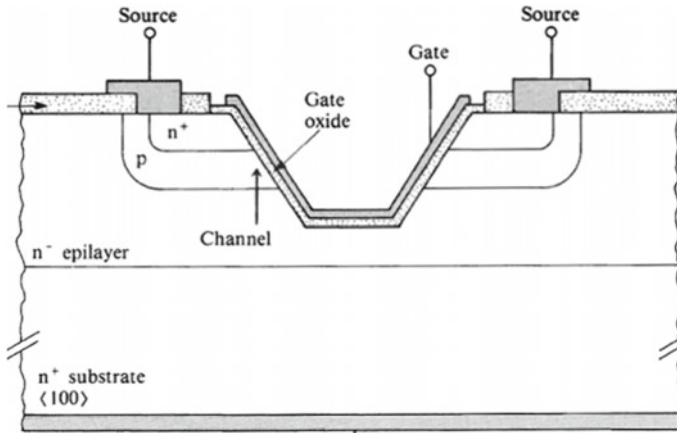
Fig. 2 Front view of VMOSFET (Reproduced from [7])

are present laterally then the MOSFET structure is termed as LDMOS, otherwise it is a VMOSFET (Fig. 2).

4 Working of Power MOSFET

The power MOSFET has a similar working as that of the conventional MOSFET. Talking about the structure, the power MOSFET has a gate electrode in between the source electrodes. The drain electrode is connected to N+ substrate layer in the bottom of the MOSFET. Special care needs to be taken that we do not connect the source and the drain electrode physically otherwise it will disrupt the biasing of the MOSFET device. The electrode is not connected to the n-type and p-type material directly, and there is a dielectric S02 layer between the two. This dielectric layer acts as an insulator between the two and prevents any kind of charge flow between the electrodes and the substrate. The motion of electrode is only within the substrate which happens when a potential difference is applied to the electrode of the MOSFET. The power MOSFET works on the enhancement mode principle where there is no channel formation on the structure in the initial stage or basically when there is no voltage applied to the electrodes of the device. The power MOSFET possesses several junctions at different depths of its structure. These junctions have a depletion layer when the electrodes are not connected to any electrode. The biasing to these junctions is provided by the voltages applied on the gate. The power MOFET has three working stages just like a conventional MOSFET. The three regions are the cutoff region, the active region, and the saturation region. Talking about the three regions of working, the MOSFET is in the first working state when no applied voltage is present on the terminal (Fig. 3).

Fig. 3 Drain characteristics of the power MOSFET (Reproduced from [4])
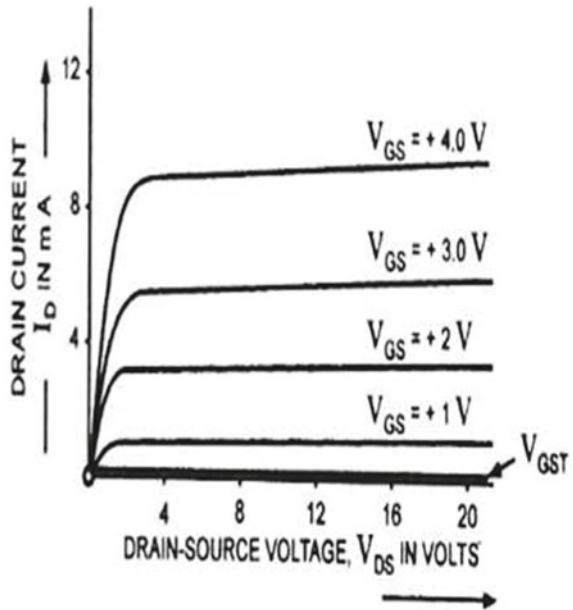
During this region the current through the drain is zero, the device acts as a closed switch and no current is allowed to flow from the device. Talking about the active region of the device, as the name suggests, the MOSFET device is active in this region or basically the MOSFET acts as a closed switch and the channel has been formed between the source electrode, by the potential difference which is applied to the source and the gate electrode. The third stage is the saturation stage, in this region of working the current flowing through the channel has been saturated or in simple terms the current flowing through the channel has reached its maximum value and cannot increase any further. The three stages have been represented in the graph below. The power MOSFET has two graphs, the transfer characteristics and the output characteristics (Fig. 4).

5 Characteristics of Power MOSFET

5.1 Resistance

The power MOSFET is known to have a lot of parameters out of which one is resistance. Talking about the resistance, the power MOSFET dc circuit has a use of lot of resistance. Each of the resistance is named either based on the function it does or based on its properties, like high resistance or the resistors are either named on the basis of the point in the circuit they are connected to like suppose id the resistance is
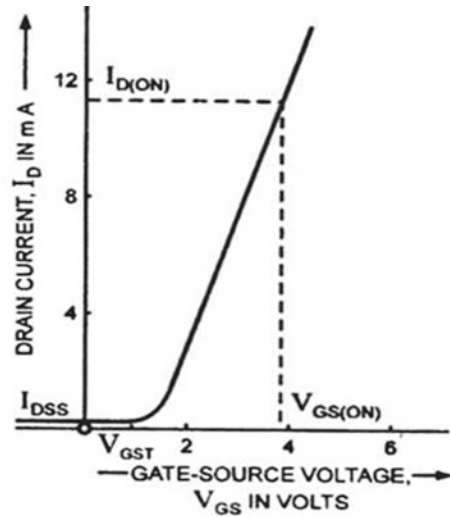
connected to the substrate so the abbreviation for the resistor is R_{sub}. The resistance of the inverted channel of the MOSFET is abbreviated as R_{ch}. The inverted channel resistance is related to the width of the channel inversely [16–22]. The resistance or to be more specific the spreading resistance of the accumulation region formed in the epitaxial layer. The resistance of the drain region and bulk semiconductor is abbreviated as R_{do}. This resistance can be further divided into two types, one is R_{jfet} and the other is Rd. Talking about R_{jfet}, as can be guessed from the abbreviation it is also known as JFET region resistance. The other type is the Rd which is basically the resistance between the region occurring under the p-body and highest most part or the topmost part of our substrate of the device. The on-resistance of the device or basically the type of MOSFET we are dealing with out of all MOSFET devices should be set to a low value. If the value of on-resistance is high this will lead to huge power loose.

5.2 Breakdown Voltage

In the voltage of the MOSFET, we are concerned about the breakdown voltage of the MOSFET which is abbreviated as V_b and depends on several factors. The factors on which the breakdown voltage of the MOSFET depends are (1) Avalanche, (2) Punch Through, (3) Zener Breakdown, and (4) Di-electric Breakdown. The breakdown voltage of the MOSFET is basically the maximum potential difference existing between the drain and the source of the MOS, which it can handle without experiencing a avalanche breakdown. The problem in the case of Ron and breakdown voltage is that as the Ron increases, the breakdown voltage also goes on increasing.

But for a MOSFET it is what we can say very desirable to have a very high value of the resistance to be specific, and high breakdown together which is not possible as both are directly proportional. The above-defined problem of basically doping is related to the layer of the device which we are talking about, these two actors control basically the value of breakdown voltage. V_b also depends on the semiconductor material, and V_b increases if the material changes from Si to SiC.

5.3 Threshold Voltage

The threshold voltage of the MOSFET transistor is basically defined as voltage applied to the gate when an interface is formed in the structure of the device. The threshold voltage is a very important parameter as we can clearly see in the working or the formulas of the device where it is having its presence in almost all the formulas. Not only the threshold voltage is present in almost all the formulas, but various parameters are dependent on the threshold voltage of the device. The threshold voltage and value above of the mentioned voltage are where basically transistor will work in the on state, but for the values below, the transistor goes in the off state.

6 Types of Power MOSFET

6.1 LDMOS

In the laterally diffused metal oxide semiconductor, it is the MOSFET structure which was made at the initial stage of the MOSFET development. The structure is not widely used these days due to the high resistance it offers to current flow. This all leads to what we can say as the high loss which our through various reasons in the concerned device. Now talking about the breakdown voltage range, the MOSFET breakdown voltage range lies between 20 and 80 V. The current in the MOS is a polynomial function of the width of the channel through which the current flows. The breakdown voltage of the LDMOS is also a function of the length of the channel. The LDMOS decreases the value of its on-resistance by doping the JFET region and also by changing the material of the plates (using SiC instead of Si) (Fig. 5).

6.2 VDMOS

In the vertical doubly diffused MOSFET, this power MOSFET is named so because of its current flow direction. If we look closely at the circuit diagram below, we can clearly see that the source is over the drain which results in a vertical flow of current.
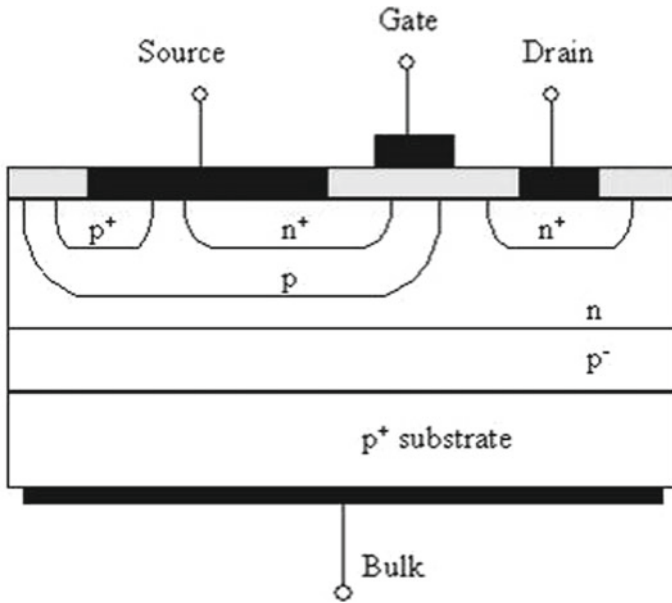
Fig. 5 Cross section LMOS view (Reproduced from [1])

Mostly the devices are structured in this fashion. In this fabrication, the current carrying terminals are placed opposite to each other because of which a uniform rate of flow of charges is maintained. In the VDMOS, the voltage ratings generally are dependent on the thickness of the epitaxial layer and also the doping of substrate. The current rating of the VDMOS depends upon the width of the channel through which current flows. In the structure mentioned below the MOS has JFET resistance which affects the total on-resistance value of device (Fig. 6).

Fig. 6 Cross section view of VDMOS (Reproduced from [2])
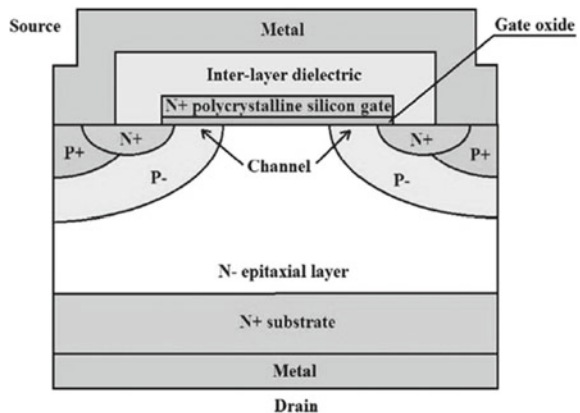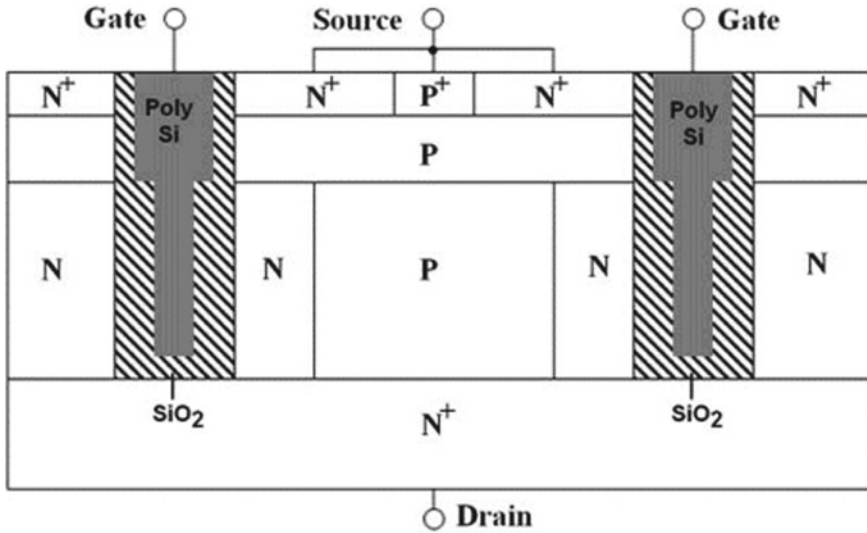
Fig. 7 Cross section view of trench MOSFET (Reproduced from [4])

6.3 Trench MOSFET

Nowadays, the major power MOSFET which is used in the electronics industry is the trench MOSFET, it is because of the various reasons which contribute to its lower on-resistance and less power dissipation. The Trench MOSFETs are also known as the UMOSFET. The reason for the decrease in the on-resistance is the removal of JFET region, one more reason which contributes to the decrease is the small cell pitch. The reason for the decrease in the JFET resistance is because of the channel through which the current flows is formed on the vertical sidewalls. The value of on-resistance can be said to be cut by 60% of that of the resistance value of the planar MOS or simple one, for the value of same doping concentration. The Trench MOSFET possesses gate charges which lead to the switching delays. So our target is to reduce the gate charge without affecting the on-resistance. One of the possible solutions for the problem is to introduce the n+ and -p junction, and this will reduce the gate charge by half of original value. The other type of trench MOSFET reduces the value of Rb as well as affect the value of breakdown voltage. The lateral power MOSFET introduces the concept of double extended trench gates (Fig. 7).

6.4 Super Junction MOSFET

Super Junction MOSFETs generally have a large breakdown voltage due to the structure they possess. The drift layer which was present in the device structure
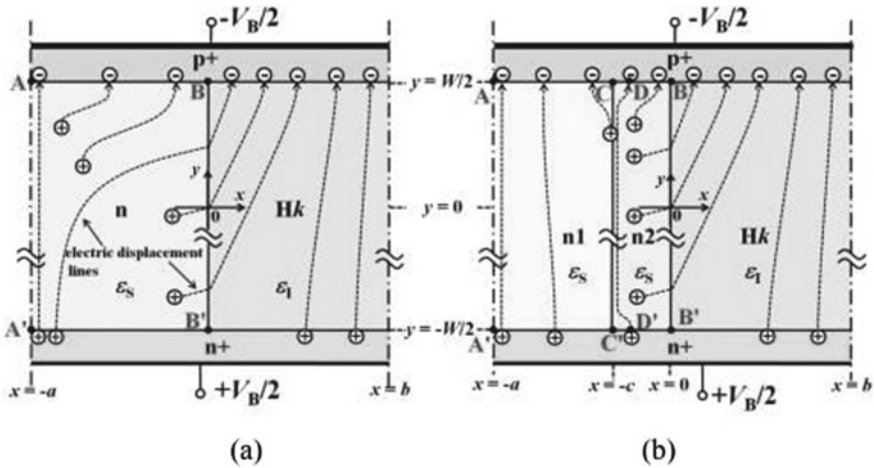
Fig. 8 Cross section view of super junction MOS (Reproduced from [12])

termed as the planar power MOS field effective transistor which is basically replaced by the pillars which are charged as same as the layer they are replacing. The pillars used in the super junction MOSFET share the vertical boundary. This structure used by the super junction results in a higher speed and an increase in the breakdown voltage. Not only this we can also increase the aspect ratio of the pillars in the SJMOS, which will result in a decrease in on-resistance of device. The super-junction MOSFET still experience some challenges because of the charge imbalance it faces due to the negative charges. The above charge imbalance also results in impact ionization. To solve this problem we need to achieve low on-resistance with high breakdown voltage. This drawback has been solved in another configuration of the MOSFET which was developed at a later stage. The MOSFET which overcome this issue is the multi-gate MOSFET abbreviated as MG MOSFET (Fig. 8).

6.5 FLI—MOSFET

This MOSFET structure uses P+ layer which is buried in the N drift region. The buried P+ layer can be seen in figure below in which the layer is surrounded by negatively charged drift region. So to basically decrease the magnitude of the highest value of the electric field or the electric field with value of highest order in the device structure we are talking about, the electric field and to be more precise the triangular electric field is separated into compartment which ultimately helps in achieving a lower electric field in the device. With this structure, we are able to achieve an lower access resistance and a lower drift resistance which leads to a smaller value of resistance of the device. And we can easily guess that the current value increases due to the above, as well as the depletion region increase due to the P+ floating
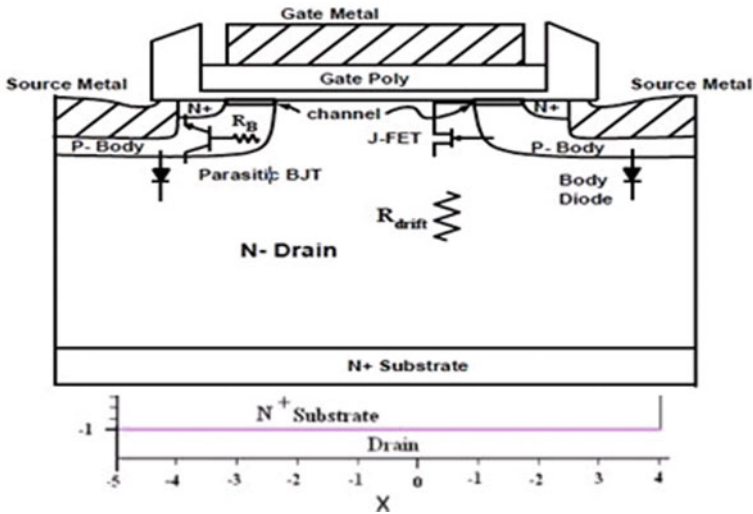
Fig. 9 Cross section view of FLI MOSFET (Reproduced from [13])

rings in the structure of the device. To overcome the limitation of the FLI MOSFET, a new MOSFET structure in which a combination of two pre-existing MOSFET structured was proposed. The new structure basically uses the quasi-saturation effect of the FLIMOS and basic design or the structure of the used device. The structure in the below picture reduces the peak electric current by 30% which improves the on-resistance and the breakdown voltage (Fig. 9).

7 Types Based on Semiconductor Material

Due to the change in the material of which the semiconductor device is made a lot of parameters like the saturation voltage, breakdown field strength, and the thermal conductivity is affected.

(a) Silicon Carbide
(b) Strained Silicon
(c) Gallium Nitride

All the three semiconductor devices based on the use of different material have been discussed in detail while studying the effect on the property of device due to change in material.
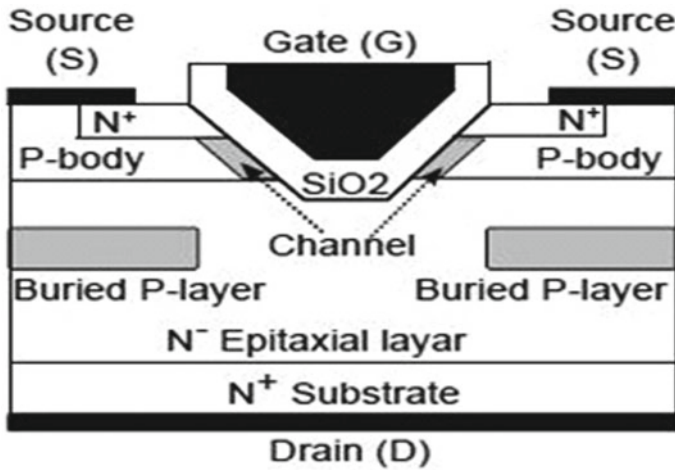
Fig. 10 Structured V-groove MOS (Reproduced from [8])

7.1 Silicon Carbide Semiconductor (SiC-MOS)

Due to the change in material of which the semiconductor device is made a lot of parameters like the saturation voltage, breakdown field strength, and the thermal conductivity is affected. The wide band gap materials were used in the initial stage but after the use of SiC, the scientist saw an improvement in lot the desired properties of the MOSFET. Like there was an increase in the breakdown field strength also in the saturation velocity and in the thermal conductivity. The V MOSFET with the grove has the p-layers buried in the n-layers. This structure leads to further advantage. Like the electron mobility is increased and the breakdown voltage is increased. The above parameters have been defined in comparison to the MOSFET which uses the Si material. There are also some limitations of using this material. We have to face the problem of the interface traps in the device. The MOSFET also suffers from tunneling effect (Fig. 10).

7.2 Strained Silicon Semiconductor (SS-MOS)

To develop this type of MOSFET, the scientist took the help of the strain engineering. The major problem which the MOSFET device structure provides is the problem of inverse proportionality of the two very frequently mentioned quantities of this device but a very opposite or what you can say a contrasting behavior is desired as the ideal condition for the working of the power MOSFET (Fig. 11).

This problem was solved by making the MOSFET channel through which the current flow for the strained-Si. The silicon is not used alone to produce the strain
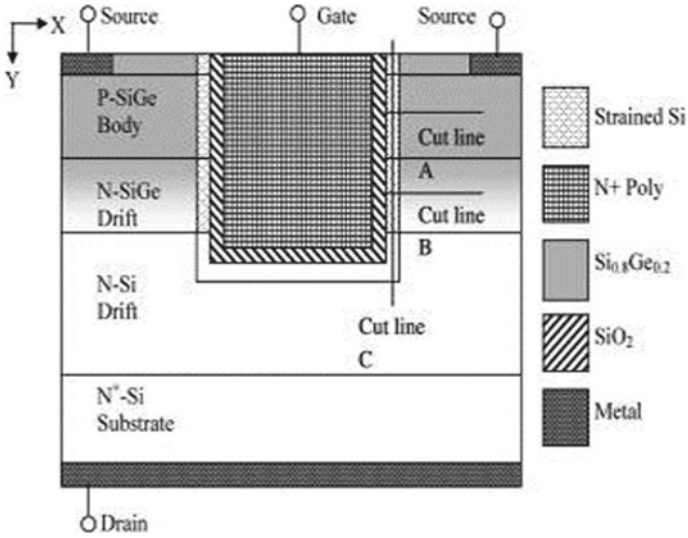
Fig. 11 Trench gate MOSFET strained-Si (Reproduced from [6])

in the channel, a mixture of silicon and germanium is used. The better tradeoff also leads to other benefits. The MOSFET also gets the advantage of the improvement in the drive current and trans-conductance (Fig. 12).
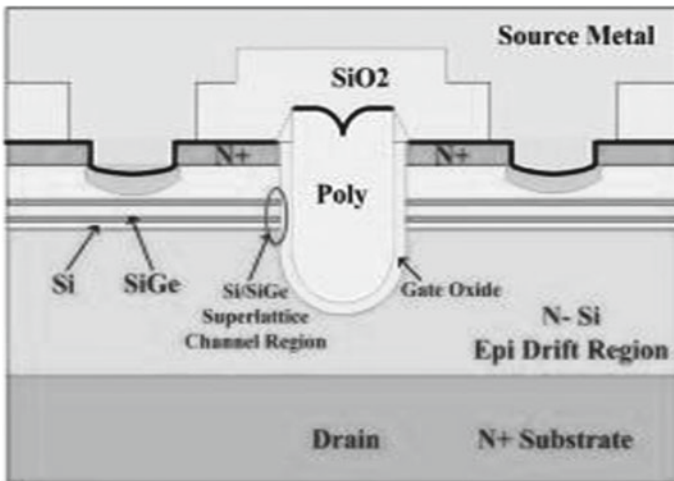
Fig. 12 Strained silicon MOSFET (Reproduced from [5])
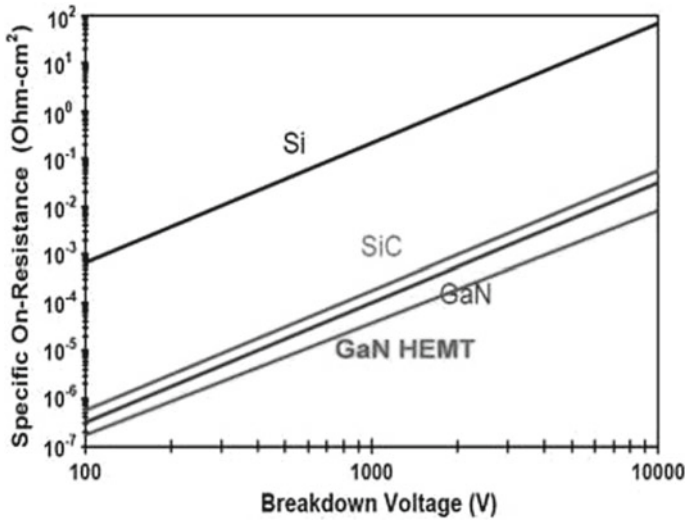
Fig. 13 Breakdown voltage vs on-state resistance [7]

7.3 Semiconductor Gallium Nitride (GaN)

Yet another type of MOSFET is based on the semiconductor material used in the making of the device. The MOSFET has been possible due to the advancement in the material science. Due to this, the limitations of the wideband material as discussed above in the material have been minimized. The use of gallium nitride for making the power MOSFET devices has resulted in a higher breakdown field. The use of gallium nitride has also led to increase in the electron saturation velocity. The on-state resistance of the MOSFET made with gallium nitride is lesser than that of one made from silicon carbide. As it is less than that of the silicon carbide, so it has a huge difference from the MOSFET devices which are made from the Silicon. Due to the better on-state resistance of the device, its effect is visible on the other properties as well like the chip size and cost which reduces significantly [13–17]. Also talking about the switching speed, it has also improved a lot as compared to other devices (Fig. 13).

8 Applications

The power MOSFET is the highest or the most used device in the amplifier market. It has the highest market capture even more than the RF power amplifier and the insulated-gate bipolar transistor. In the year 2018, more than 50 billion power MOSFETs we shipped and the number has been doubled since then. The power MOSFET has a strong use in the communication channels which communicate using

the radio frequency. They are used in the radios and to amplify the radio signals. The power MOSFET are also used in the communication channel to amplify the attenuated signal so that they can travel a longer distance. The power MOSFET is used in the electronic circuitry of the computer mother motherboard as a switch, the MOSFET allows the current from the source to pass when there is a gate current, and acts as an off switch if the gate current is zero. It is used in the heavy machinery in industries where we need to switch heavy currents. They are used extensively in the DC-DC converter, DC relay, and brushless DC motor.

9 Conclusion

The power MOSFET is a landmark in the history of electronics industry. Ever since its invention, its market share has been growing at an exponential rate due to the wide variation possible in its structure. Every structure is built according to different requirements of different circuits and hence finding its application at numerous places. This paper provides a concise and an effective and a concise study on the different structures of the power MOSFET discussing their properties and their relation in great detail. The paper also discusses the history of development in the power MOSFET and how modifications were made to main a balance in on-state resistance and breakdown voltage. The paper also discusses the different types of MOSFET available on the basis of semiconductor material used for their construction. In the nutshell, even after finding several applications in the present world, power MOSFET performance still provides an opportunity for several modifications by using hybrid structure and different semiconductor materials [23–28].

References

1. Sharma S, Gupta V, Saxena S (2016) A Review on VDMOS as a Power MOSFET. IOSR J Electro Commun Eng (IOSR-JECE). e-ISSN: 2278–2834, p- ISSN: 2278–8735
2. Saxena G, Saxena S, Jharia S (2017) Process Simulation of Super Junction Power MOSFET. Int J Innovative Res Sci Eng Technol 6(4):2347–6710
3. Fayyaz A, Romano G, Castellazzi A (2016) Body diode reliability investigation of SiC power MOSFETs. Microelectron Reliab 64:530–534
4. Jonathan Dodge PE (2006) Power MOSFET tutorial. Adv Power Technol Application Note APT-0403 Rev B
5. WadeElectrical.com Power MOSFET Applications
6. Baliga BJ (2013) Gallium nitride devices for power electronic applications. Semicond Sci Technol 28(7):074011
7. Sun S, Yuan JS, Shen ZJ (2011) Performance of trench power MOSFET with strained Si/SiGe multilayer channel. IEEE Trans Electron Devices 58(5):1517–1522
8. Galle J (2016) Suppression of dislocation-induced drain leakage current in power VD MOSFET structures. IEEE Trans Device Mater Reliab 16(4):556–560
9. Lyu X, Chen X (2013) Vertical Power $\mathrm{H}\,k$-MOSFET of Hexagonal Layout. IEEE Trans Electron Devices 60(5):1709–1715

10. Shintani M, Oishi K, Zhou R, Hiromoto M, Sato T (2016) A circuit simulation model for V-groove SiC power MOSFET. In 2016 IEEE 4th workshop on wide bandgap power devices and applications (WiPDA)
11. Lyu X, Chen X (2013) Vertical power MOSFET of hexagonal layout. IEEE Electron Devices 60
12. Vaid R, Padha N (2011) A novel trench gate power MOSFET (TG-FLIMOSFET). Microelectron Eng 88
13. Bansal M, Ranjan R (2017) CMOS instrumentation amplifier design. Int J Electron Electr Comput Syst (IJEECS) 6(11):86–91
14. Bansal M (2021) Machine learning perspective in VLSI computer aided design at different abstraction levels. Shakya S et al (eds) Mobile Computing and sustainable informatics, Lecture notes on data engineering and communications technologies, vol 68. Springer, Singapore. https://doi.org/10.1007/978-981-16-1866-6_6
15. Raghav N, Bansal M (2017) Analysis of power efficient 6-T SRAM cell with performance measurements. In: 2017 International conference on innovations in control, communication and information systems (ICICCI), Greater Noida, India, pp 1–4. https://doi.org/10.1109/ICICCIS.2017.8660819
16. Bansal M, Singh J (2020) Comparative analysis of 4-bit CMOS vedic multiplier and GDI vedic multiplier using 18nm FinFET technology. In: 2020 International conference on smart electronics and communication (ICOSEC), Trichy, India, pp 1328–1332. https://doi.org/10.1109/ICOSEC49089.2020.9215317
17. Bansal M, Singh J (2020) Qualitative analysis of 2-bit CMOS magnitude comparator and GDI magnitude comparator using FinFET technology (18nm). In: 2020 International conference on smart electronics and communication (ICOSEC), Trichy, India, pp 1323–1327. https://doi.org/10.1109/ICOSEC49089.2020.9215251
18. Bansal M, Priya (2020) Application layer protocols for internet of healthcare things (IoHT). In: 2020 Fourth international conference on inventive systems and control (ICISC), pp 369–376. https://doi.org/10.1109/ICISC47916.2020.9171092
19. Bansal M, Priya (2021) Performance comparison of MQTT and CoAP Protocols in different simulation environments. In: Ranganathan G, Chen J, Rocha Á (eds) Inventive communication and computational technologies, Lecture Notes in Networks and Systems, vol 145. Springer, Singapore. https://doi.org/10.1007/978-981-15-7345-3_47
20. Bansal M, Nanda M, Husain MN (2021) Security and privacy aspects for internet of things (IoT). In: 2021 6th international conference on inventive computation technologies (ICICT), pp 199–204 https://doi.org/10.1109/ICICT50816.2021.9358665
21. Bansal M, Gupta S, Mathur S (2021) Comparison of ECC and RSA algorithm with DNA encoding for IoT security. In: 2021 6th international conference on inventive computation technologies (ICICT), pp 1340–1343. https://doi.org/10.1109/ICICT50816.2021.9358591
22. Bansal M, Chopra T, Biswas S (2021) Organ simulation and healthcare services: an application of IoT. In: 2021 6th international conference on inventive computation technologies (ICICT), pp 205–208. https://doi.org/10.1109/ICICT50816.2021.9358677
23. Bansal M, Garg S (2021) Internet of things (IoT) based assistive devices. In: 2021 6th international conference on inventive computation technologies (ICICT), pp 1006–1009. https://doi.org/10.1109/ICICT50816.2021.9358662
24. Bansal M, Adarsh N, Kumar N, Meena M (2020) 24×7 Smart IoT based integrated home security system. In: 2020 Fourth international conference on inventive systems and control (ICISC), pp 477–481. https://doi.org/10.1109/ICISC47916.2020.9171051
25. Bansal M, Srivastava R, Lal C, Kamalasanan MN, Tanwar LS (2009) Carbon Nanotube based organic light emitting diodes. Nanoscale 1(317–330)
26. Bansal M, Srivastava G (2020) Design and implementation of LNA for biomedical applications. In: Pandian A, Ntalianis K, Palanisamy R (eds) Intelligent computing, information and control systems. ICICCS 2019. Advances in Intelligent Systems and Computing, vol 1039. Springer, Cham. https://doi.org/10.1007/978-3-030-30465-2_18

27. Bansal M, Sirpal V, Choudhary MK (2021) Advancing e-Government using internet of things. Shakya S et al (eds) Mobile computing and sustainable informatics, Lecture Notes on Data Engineering and Communications Technologies, vol 68. Springer, Singapore. https://doi.org/10.1007/978-981-16-1866-6_8

28. Bansal M, Bharti V, Chander V (2021) Comparison between conventional fast multipliers and improved fast multipliers using PTL logic. IOP Conf Ser Mater Sci Eng 1126(012041):1–12. https://doi.org/10.1088/1757-899X/1126/1/012041

Lncosh-Based Adaptive Control Algorithm for Single-Stage SPV Grid-Interfaced System

Mohammad Nair Aalam, Majid Jamil, and Ikhlaq Hussain

Abstract This work proposes the use of a logarithmic hyperbolic cosine (Lncosh)-based adaptive algorithm for a single-stage solar photovoltaic (SPV) grid-interfaced system. The design incorporates a VSC coupled SPV array to provide active power along with reactive power compensation. It also serves to offer load balancing, reduction of harmonics, and power factor correction. A maximum power point (MPP) extraction method based on the incremental conductance (InC) technique, integrated with the VSC control algorithm, is employed to ensure that the SPV array operates at the MPP under varying levels of irradiation. The Lncosh-based algorithm simultaneously offers benefits of both the least mean squares (LMS) and sign-error LMS algorithms, providing faster convergence without sacrificing the mean-square-error (MSE) performance. The proposed configuration is implemented for simulation in MATLAB with the Simulink environment; the steady-state and the dynamic behavior is observed and verified to be well within recommended limits.

Keywords SPV · Lncosh · LMS · Power quality · Power electronics · MPPT

1 Introduction

The last few decades have seen the decay of fossil-fuel-based energy sources as the demand for energy consumption continued to grow. Along with an increasing concern for the global environment, this has motivated the search and development of renewable alternatives. Among these alternatives, there has been widescale adoption of technologies such as SPV systems in the form of distributed energy resources (DERs) [1].

M. N. Aalam (✉) · M. Jamil
Department of Electrical Engineering, Jamia Millia Islamia, New Delhi 110025, India
e-mail: nairaalam22@gmail.com

I. Hussain
Department of Electrical Engineering, University of Kashmir, Srinagar 190006, India

There is a host of difficulties to be tackled when interfacing SPV systems with the utility grid. The majority of these include poor reliability, voltage instability, and degraded power quality [2]. SPV systems may be integrated with the utility grid in either single-stage or double-stage topologies. The double-stage topology performs MPP extraction in the first stage and output power control in the second stage, while the single-stage topology achieves both functions in one stage. Several MPPT techniques have been discussed in [3].

The integration of SPV arrays with the utility grid is done with the help of power electronic converters, mainly VSCs [4]. The converter can be controlled to offer load balancing, reduction of harmonics, power factor correction, and/or zero voltage regulation (ZVR). Numerous algorithms have been reported for the control of VSC coupled SPV systems [5–8].

The use of algorithms based on adaptive filtering theory, for unfamiliar systems, has confirmed the capability of the theory to track variations in the properties of such systems [2]. The algorithm parameters are self-adjusted in response to changes in the surrounding environment, ensuring that the behavior of the system remains appropriately in order. The least mean squares (LMS) algorithm [9] and sign-error LMS (SELMS) algorithm are two such algorithms that have been used for the control of VSC coupled SPV [10]. The LMS algorithm offers faster convergence compared to the SELMS algorithm [11]; however, the SELMS algorithm offers better mean-square-error (MSE) performance.

Recently a Lncosh-based algorithm, consisting of a cost function employing the natural logarithm of the hyperbolic cosine function, has been proposed in [12]. The Lncosh-based algorithm provides convergence characteristics akin to the LMS algorithm and robustness analogous to the SELMS algorithm [13]. It offers advantages of both the algorithms, performing similar to the LMS algorithm for errors of small magnitude and like the SELMS algorithm for errors of large magnitude [14].

In this work, the proposed Lncosh-based algorithm is implemented for the grid integration of a VSC coupled SPV array. The proposed configuration is implemented for simulation in MATLAB with the Simulink environment for Unity Power Factor (UPF) correction mode of operation as well as load balancing and reduction of harmonics.

1.1 Configuration of Proposed System

A composite circuit/block diagram representing the proposed configuration is shown in Fig. 1. The procedure for the calculation of the system parameters is given in [15]. The parameters for the proposed configuration are given in the Appendix.
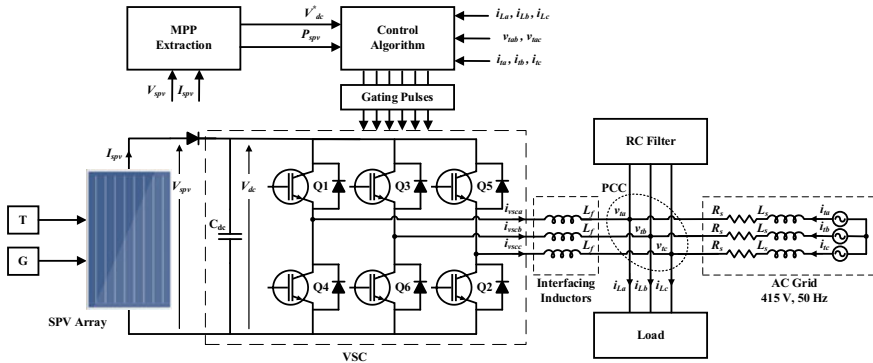
Fig. 1 Configuration of proposed system

2 Control Algorithm

The proposed control algorithm is developed for a single-stage three-phase configuration and consists of two parts: MPP Extraction Control and VSC Control.

The following signals are sensed: SPV array current and voltage (I_{spv}, V_{spv}), grid line-voltages at the PCC (v_{tab}, v_{tbc}), VSC DC-link voltage (V_{dc}), three-phase load currents (i_{La}, i_{Lb}, i_{Lc}), and three-phase grid currents (i_{ta}, i_{tb}, i_{tc}).

2.1 MPP Extraction Control

The goal of the MPP Extraction control is to ensure that the SPV array operates at the MPP under varying levels of irradiation, and provide a VSC DC-link reference-voltage (V_{dc}^r) for the sensed VSC DC-link voltage (V_{dc}) to track.

The output power of the SPV array is proportional to the amount of incident radiation. As a result, peak power extraction is needed to increase performance. An InC-based MPP extraction method is used to acquire the desired power maxima. The method uses incremental changes in V_{spv} and I_{spv} to estimate the result of a voltage shift.

In case of the proposed SPV system, the V_{dc} equals the V_{spv}. At steady-state, the V_{dc} equals the SPV array voltage at maximum power (V_{MPP}). The InC-based MPP extraction method, besides being high-speed and accurate under a variety of environmental conditions, is easy to implement.

2.2 VSC Control

The VSC control algorithm focuses on the generation of a series of trigger signals for the appropriate switching of the converter switches. The algorithm may also offer ancillary services such as load balancing, reduction of harmonics, improved PCC voltage regulation, and power factor correction.

A Lncosh-based converter control algorithm, shown in Fig. 2, is proposed [12].

The PCC phase voltages (v_{ta}, v_{tb}, v_{tc}) are evaluated from the grid line-voltages (v_{tab}, v_{tbc}) sensed at the PCC, using (1).

$$v_{ta} = \frac{2v_{tab} + v_{tbc}}{3}, \; v_{tb} = \frac{-v_{tab} + v_{tbc}}{3}, \; v_{tc} = \frac{-v_{tab} - 2v_{tbc}}{3} \tag{1}$$

From the phase voltage measurements, the unit templates in-phase (x_{pa}, x_{pb}, x_{pc}) with the grid voltage are estimated using (2)

$$x_{pa} = \frac{v_{ta}}{V_{PCC}}, \; x_{pb} = \frac{v_{tb}}{V_{PCC}}, \; x_{pc} = \frac{v_{tc}}{V_{PCC}} \tag{2}$$

where V_{PCC} is the magnitude of the PCC terminal voltage, given using (3).

$$V_{PCC} = 0.816\sqrt{(v_{ta}^2 + v_{tb}^2 + v_{tc}^2)} \tag{3}$$

The unit templates in-quadrature (x_{qa}, x_{qb}, x_{qc}) with the grid voltage are derived from x_{pa}, x_{pb}, x_{pc} using (4).

$$x_{qa} = \frac{-x_{pb} + x_{pc}}{\sqrt{3}}, \; x_{qb} = \frac{3x_{pa} + x_{pb} - x_{pc}}{2\sqrt{3}}, \; x_{qc} = \frac{-3x_{pa} + x_{pb} - x_{pc}}{2\sqrt{3}} \tag{4}$$
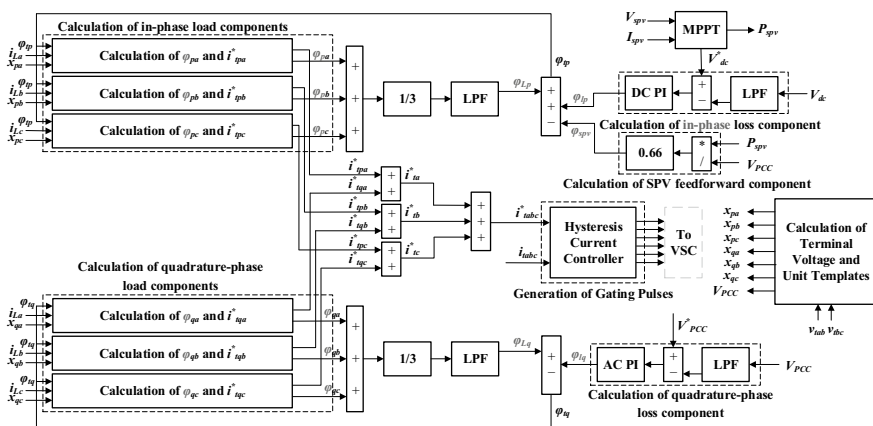

Fig. 2 Lncosh-based control algorithm for voltage source converter control

The VSC DC-link voltage (V_{dc}) is controlled by a P.I. controller in such a way that it tracks the VSC DC-link reference-voltage (V^r_{dc}). The VSC DC-link voltage error (V_{dce}) is determined for the ith sampling instant using (5)

$$V_{dce}(i) = V^r_{dc}(i) - V_{dc}(i) \tag{5}$$

and supplied to the DC-P.I. controller. The DC-P.I. controller provides the in-phase loss component (φ_{lp}) required to maintain V_{dc} at V^r_{dc}. φ_{lp} is estimated for the ith sampling instant using (6).

$$\varphi_{lp}(i+1) = \varphi_{lp}(i) + \lambda_{DCp}(V_{dce}(i+1) - V_{dce}(i)) + \lambda_{DCi}(i+1)V_{dce}(i+1) \tag{6}$$

where λ_{DCp} and λ_{DCi} are respectively the values of proportional gain constant and integral gain constant for the DC-P.I. controller.

Similarly, another P.I. controller, termed the AC-P.I. controller, regulates the terminal voltage (V_{PCC}) so that it tracks the reference terminal voltage (V^r_{PCC}) (set to 0.816 * 415 = 340 V). The terminal voltage error (V_{PCCe}) is given using (7)

$$V_{PCCe}(i) = V^r_{PCC}(i) - V_{PCC}(i) \tag{7}$$

and acts as input to the AC-P.I. controller. The AC-P.I. controller outputs the quadrature-phase loss component (φ_{lq}) which is used to regulate V_{PCC} at V^r_{PCC}. φ_{lq} is estimated for the ith sampling instant using (8).

$$\varphi_{lq}(i+1) = \varphi_{lq}(i) + \lambda_{ACp}(V_{PCCe}(i+1) - V_{PCCe}(i)) + \lambda_{ACi}(i+1)V_{PCCe}(i+1) \tag{8}$$

where λ_{ACp} and λ_{ACi} are respectively the values of proportional gain constant and integral gain constant for the AC-P.I. controller.

To improve the performance of the SPV system under dynamic conditions, the control algorithm includes an SPV feed-forward component. The SPV feed-forward component (φ_{spv}) for the ith sampling instant is given using (9)

$$\varphi_{spv}(i) = 0.66 * \frac{P_{spv}(i)}{V_{PCC}} \tag{9}$$

where $P_{spv}(i)$ is the SPV array power output for the ith sampling instant.

The in-phase load component of phase-a (φ_{pa}), for the ith sampling instant, is evaluated from the proposed Lncosh-based algorithm using (10)

$$\varphi_{pa}(i+1) = \varphi_{pa}(i) + \tau_s \tanh[\eta_{pa}(i)]x_{pa}(i) - \rho\frac{\text{sgn}[\varphi_{pa}(i)]}{1 + \varepsilon|\varphi_{pa}(i)|} \tag{10}$$

where τ_{s} is the step-size, ρ is the zero-attractor coefficient, and ε^{-1} is the shrinkage coefficient [10, 12]. $\eta_{\mathrm{pa}}(i)$ is the error of the in-phase current component of phase-*a*, given for the *i*th sampling instant using (11)

$$\eta_{\mathrm{pa}}(i) = i_{\mathrm{La}}(i) - x_{\mathrm{pa}}(i)\varphi_{\mathrm{pa}}(i) \tag{11}$$

where $i_{\mathrm{La}}(i)$ is the sensed load current in phase-*a* for the *i*th sampling instant.

Correspondingly, the in-phase load components of phase-*b* (φ_{pb}) and phase-*c* (φ_{pc}), for the *i*th sampling instant, are estimated using (10) for the phases *b* and *c*.

The quadrature-phase load component of phase-*a* (φ_{qa}), for the *i*th sampling instant, is evaluated using (12)

$$\varphi_{\mathrm{qa}}(i + 1) = \varphi_{\mathrm{qa}}(i) + \tau_{\mathrm{s}} \tanh\left[\eta_{\mathrm{qa}}(i)\right]x_{\mathrm{qa}}(i) - \rho\frac{\mathrm{sgn}\left[\varphi_{\mathrm{qa}}(i)\right]}{1 + \varepsilon\left|\varphi_{\mathrm{qa}}(i)\right|} \tag{12}$$

where τ_{s} is the step-size, ρ is the zero-attractor coefficient, and ε^{-1} is the shrinkage coefficient [10, 12]. $\eta_{\mathrm{qa}}(i)$ is the error of the quadrature-phase current component of phase-*a*, given for the *i*th sampling instant using (13).

$$\eta_{\mathrm{qa}}(i) = i_{\mathrm{La}}(i) - x_{\mathrm{qa}}(i)\varphi_{\mathrm{qa}}(i) \tag{13}$$

Correspondingly, the quadrature-phase load components of phase-*b* (φ_{qb}) and phase-*c* (φ_{qc}), for the *i*th sampling instant, are estimated using (12) for the phases *b* and *c*.

The total in-phase grid reference-current component (φ_{tp}) is given using (14)

$$\varphi_{\mathrm{tp}} = \varphi_{\mathrm{Lp}} + \varphi_{\mathrm{lp}} - \varphi_{\mathrm{spv}} \tag{14}$$

where the average in-phase load component ($\varphi_{L\mathrm{p}}$) is given using (15).

$$\varphi_{\mathrm{Lp}} = \frac{\left(\varphi_{\mathrm{pa}} + \varphi_{\mathrm{pb}} + \varphi_{\mathrm{pc}}\right)}{3} \tag{15}$$

Similarly, the total quadrature-phase grid reference-current component ($\varphi_{t\mathrm{q}}$) is given using (16)

$$\varphi_{\mathrm{tq}} = \varphi_{\mathrm{lq}} - \varphi_{\mathrm{Lq}} \tag{16}$$

where the average quadrature-phase load component ($\varphi_{L\mathrm{q}}$) is given using (17).

$$\varphi_{\mathrm{Lq}} = \frac{\left(\varphi_{\mathrm{qa}} + \varphi_{\mathrm{qb}} + \varphi_{\mathrm{qc}}\right)}{3} \tag{17}$$

The in-phase reference-currents $(i_{tpa}^*, i_{tpb}^*, i_{tpc}^*)$ and the quadrature-phase reference-currents $(i_{tqa}^*, i_{tqb}^*, i_{tqc}^*)$ are estimated using (18) and (19), respectively.

$$i_{tpa}^* = \varphi_{tp}x_{pa}, \, i_{tpb}^* = \varphi_{tp}x_{pb}, \, i_{tpc}^* = \varphi_{tp}x_{pc} \qquad (18)$$

$$i_{tqa}^* = \varphi_{sq}x_{qa}, \, i_{tqb}^* = \varphi_{sq}x_{qb}, \, i_{tqc}^* = \varphi_{sq}x_{qc} \qquad (19)$$

The summation of $i_{tpa}^*, i_{tpb}^*, i_{tpc}^*$ and $i_{tqa}^*, i_{tqb}^*, i_{tqc}^*$ for each phase respectively gives the three-phase total reference-currents $(i_{ta}^*, i_{tb}^*, i_{tc}^*)$.

$$i_{ta}^* = i_{tpa}^* + i_{tqa}^*, \, i_{tb}^* = i_{tpb}^* + i_{tqb}^*, \, i_{tc}^* = i_{tpc}^* + i_{tqc}^* \qquad (20)$$

For the generation of VSC trigger signals, a hysteresis current controller (HCC) is brought into use. The HCC takes as input a 3×1 vector of error signals generated from calculating the difference between $i_{ta}^*, i_{tb}^*, i_{tc}^*$ and i_{ta}, i_{tb}, i_{tc} for each individual phase, respectively and generates the appropriate trigger signals.

3 Simulation Results and Discussion

The proposed configuration is implemented for simulation in MATLAB with the Simulink environment for UPF correction mode of operation, and its steady-state and dynamic behavior is verified under various conditions.

3.1 Steady-State Behavior Under Non-linear Load

The behavior of the proposed configuration, under steady-state, with a non-linear load connected at the PCC is simulated, and the results are shown in Fig. 3. V_{dc} is sustained at the V_{MPP} of the SPV array. The active power output (P_t) of the grid is negative as the VSC is supplying some of the active power generated by the SPV array (P_{spv}) back to the grid. Since the VSC meets the load's reactive power requirements, the grid's reactive power output (Q_t) is zero. The power factor at the grid side is corrected to unity and the grid side total harmonic distortion (THD) values are in agreement with the IEEE-519 standard [16].

3.2 Dynamic Behavior Under Variable Irradiance

Figure 4 Illustrates the dynamic behavior of the configuration for a simulated change in irradiance G from 1000–600 W/m^2 at 0.6 s. As G is reduced, the power output
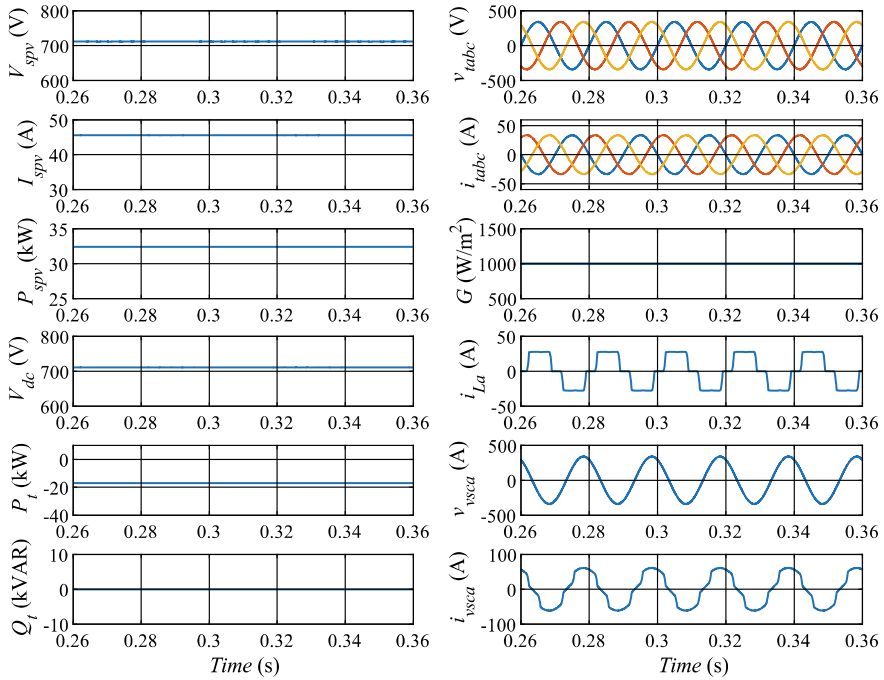
Fig. 3 Steady-state behavior under non-linear load

P_{spv} of the SPV array drops; as such P_t rises to a value, less negative than earlier. The output current I_{spv} of the SPV array and the grid currents i_{tabc} also decrease. The power factor at the grid side is maintained at unity and the grid side THD values comply with [16].

3.3 Dynamic Behavior Under Imbalanced Load

At 0.35 s, the load connected at phase a is disconnected to simulate an imbalance in load, and the behavior of the configuration is observed. The findings are depicted in Fig. 5. V_{dc} is maintained as per the MPP extraction control. The further decrease in the value of P_t can be accounted for by the fact that more of the SPV array power P_{spv} is available to be transferred to the grid side after the loss of load. The voltage and the current waveforms on the grid side are sinusoidal with unity power factor, showing the proper operation of the control algorithm for load balancing. The THD values on the grid side are again observed to be in compliance with the IEEE-519 standard.
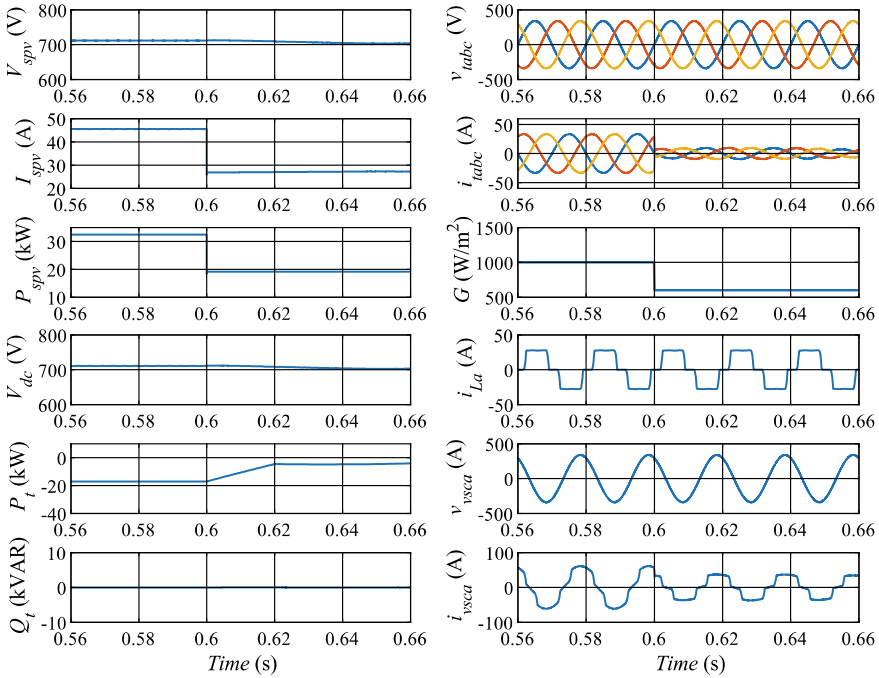
Fig. 4 Dynamic behavior of the configuration for change in solar irradiance

3.4 Comparison with LMS and SELMS Algorithm

In Fig. 6, a comparison of the average in-phase load component (φ_{Lp}) under a simulated imbalance in load, from 0.25–0.45 s, is shown for the proposed Lncosh-based algorithm, the LMS algorithm, and the SELMS algorithm. The convergence characteristics of the Lncosh-based algorithm are similar to the LMS algorithm and much faster than the SELMS algorithm. The oscillations in φ_{Lp} for the proposed algorithm are observed to be less than that in the case of LMS and comparable to that for the SELMS algorithms. The THD values for the grid current are 1.60%, 2.87% and 1.53%, respectively, for the proposed Lncosh-based algorithm, the LMS algorithm, and the SELMS algorithm.

4 Conclusion

The Lncosh-based adaptive algorithm has been described for the grid interfacing of a single-stage three-phase SPV system. The proposed configuration is implemented for simulation in MATLAB with the Simulink environment. The steady-state behavior and the dynamic behavior of the configuration under conditions of variable irradiance

Fig. 5 Dynamic behavior of the configuration for imbalance in load

Fig. 6 Comparison of the Lncosh-based algorithm against LMS and SELMS algorithms

and load imbalance are shown to be reliable. The tracking of the MPP is proper under varying levels of irradiance. Moreover, the response of the proposed control algorithm for a simulated imbalance in load is observed to be better than conventional LMS and SELMS algorithms. The results show correspondence with IEEE-519 standards.

Appendix: System Parameters

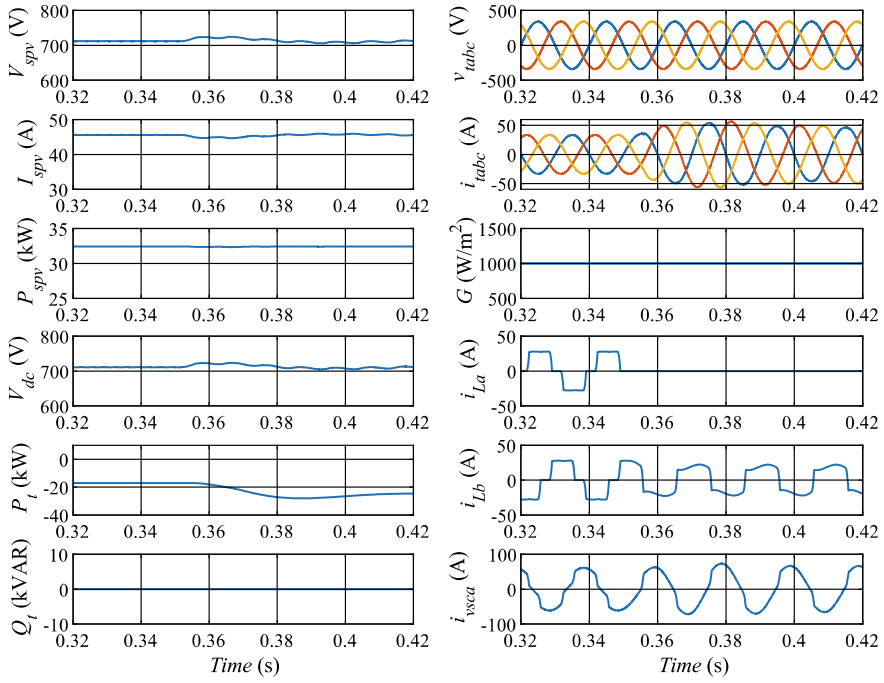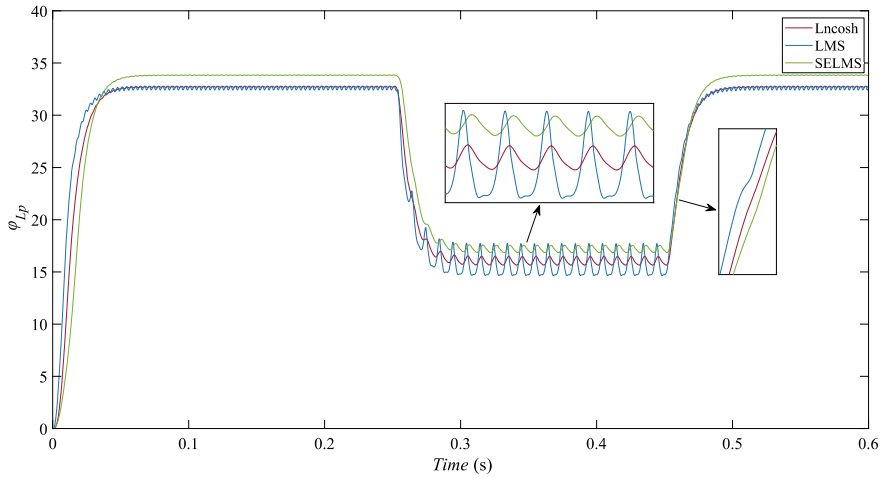Grid voltage, V_{LL} = 415 V (rms); SPV array parameters: V_{MPP} = 710 V, I_{MPP} = 46 A, P_{MPP} = 32 kW (all parameters at G = 1000 W/m^2); VSC DC-link voltage, V_{dc} = 700 V; interfacing inductance, L_f = 2 * 10^{-3} H; DC-link capacitance, C_{dc} = 8 * 10^{-3} F; sampling time, T_s = 1 * 10^{-6} s; ripple filter parameters, R_{rf} = 5Ω, C_{rf} = 1 * 10^{-5} F; AC-P.I. controller parameters, λ_{ACp} = 0.7 and λ_{ACi} = 0.5; DC-P.I. controller parameters, λ_{DCp} = 0.7 and λ_{Dci} = 0.5; load parameters, 3-phase diode-bridge rectifier feeding a series RL load of 20 Ω and 1 * 10^{-1} H; Hysteresis bandwidth = 0.01.

References

1. Sangwongwanich A, Blaabjerg F, Kim KA, Yang Y (2018) In: Advances in grid-connected photovoltaic power conversion systems, 1st edn. Woodhead Publishing
2. RK Agarwal 2016 LMF-based control algorithm for single stage three-phase grid integrated solar PV system IEEE Trans Sustain Energy 7 4 1379 1387
3. B Subudhi R Pradhan 2013 A comparative study on maximum power point tracking techniques for photovoltaic power systems IEEE Trans Sustain Energy 4 1 89 98
4. LBG Campanhol 2017 Single-stage three-phase grid-tied pv system with universal filtering capability applied to DG systems and AC microgrids IEEE Trans Power Electron 32 12 9131 9142
5. Chacko FM, George SA (2014) Comparison of different control methods for integrated system of MPPT powered PV module and STATCOM. In: Proceedings—2013 international conference on renewable energy and sustainable energy, ICRESE 2013. IEEE, Coimbatore, India, pp 207–212
6. Singh B et al (2013) IRPT based control of a 50 kw grid interfaced solar photovoltaic power generating system with power quality improvement. In: 2013 4th IEEE international symposium on power electronics for distributed generation systems, PEDG 2013. IEEE, Rogers, AR, USA
7. B Singh 2014 ILST control algorithm of single-stage dual purpose grid connected solar PV system IEEE Trans Power Electron 29 10 5347 5357
8. Kumar S et al (2015) Performance of grid interfaced solar PV system under variable solar intensity. In: India international conference on power electronics, IICPE. IEEE, Kurukshetra, India
9. E Walach B Widrow 1984 The least mean fourth (LMF) adaptive algorithm and its family IEEE Trans Inf Theor 30 2 275 283
10. S Choudhury 2020 Comparative analysis of LMS-based control algorithms for grid integrated PV system R Sharma Eds IEPCCT 2019, LNEE 630 Springer Singapore 571 581
11. V Mathews S Cho 1987 Improved convergence analysis of stochastic gradient adaptive filters using the sign algorithm IEEE Trans Acoustics, Speech, Sig Proc 35 4 450 454

12. C Liu M Jiang 2020 Robust adaptive filter with Lncosh cost Sig Proc 168 107348
13. Salman MS, et al (2020) A zero-attracting sparse lncosh adaptive algorithm. In: 2020 IEEE 40th international conference on electronics and nanotechnology, ELNANO 2020. IEEE, Kyiv, Ukraine, pp 565–568
14. K Kumar 2021 Joint logarithmic hyperbolic cosine robust sparse adaptive algorithms IEEE Trans Circuits Syst II Express Briefs 68 1 526 530
15. Singh B, Ambrish C, Al-Haddad K (2014) Power quality: problems and mitigation techniques, 1st edn. John Wiley & Sons
16. IEEE recommended practice and requirements for harmonic control in electric power systems, IEEE Std. 519, 1992. https://ieeexplore.ieee.org/document/6826459. Last accessed 21 Jun 2021

Modelling of Electric Vehicle Using Modified SEPIC Converter Configuration to Enhance DC–DC Converter Performance Using MATLAB

Lone Faisal, V. Siva Brahmaiah Rama, Subhajit Roy, and Sudeshna Nath

Abstract The paper presents a systematic model for an electric vehicle. To check the flexibility and predications of the system, the model has been verified on controlling and triggering parameter simulations in MATLAB. Simulations verify that the model can be effective in improving DC–DC converter performance. Moreover, the paper focuses on the integration and synchronization of the CC-CV method of charging with a SEPIC converter and the economic and environmental advantages of electric vehicles. Secondly, the research proposes novel methods by which the efficiency of the electric vehicle can be enhanced and focuses on the use of supercapacitors for providing the required continuous output voltage, thus increasing the durability of the electric vehicle to a larger extent.

1 Introduction

The inception of electric vehicles goes to the era when Nikola Tesla invented alternating current in 1887. It was a major milestone in the field of science that paved the way for the invention of the electric vehicle, which became a reality after a century.

The craze for electric vehicles has increased manifold in the last few decades. The Tesla model is the perfect example of the emergence of electric vehicles as it won the motor trend car of the year in 2013 [1]. Researchers show that electric vehicle car sales have increased by 91.6% and thus in the near future, we might not get surprised while seeing electric vehicles hitting the roads everywhere due to the reduction in fossil fuel reservoirs and hike in the price of petrol and diesel. The beauty of electric

L. Faisal (✉)
Department of Electrical Engineering, Mewar University, Chittorgarh, Rajasthan, India
e-mail: lonefaisal@mewaruniversity.co.in

V. S. B. Rama · S. Roy · S. Nath
Department of Electrical Engineering, BBIT, Kolkata, West Bengal, India

vehicles is that there rely on the cleanest form of technology with almost no emission of carbon to the environment [2]. Thus, electric vehicles could be handy in tackling the ongoing environmental degradation. We live in the era of energy crisis, thus the growth of electric vehicles is the need of the hour to meet the energy needs of current and future generations. Environmental degradation has become a global issue, thus it is the responsibility of every nation to follow the protocols of environmental regulation and use environmentally friendly technology like electric vehicles [3]. The electric vehicle does not contain any fuel tank thus there is no emission of greenhouse gases. Electric vehicles are quieter than gas- and diesel-based vehicles and are instrumental in reducing noise pollution. Electric vehicles are employed with lithium-ion batteries which are homologous to electric motors. A battery is to an electric vehicle what a motor is to a normal vehicle running on fuel [4]. Thus, the selection of a battery for an electric vehicle plays a crucial role in the durability of the electric vehicle. Lithium batteries are the best choice for electric vehicles as their life cycle is about 12–14 years. Moreover, the charging methods of batteries also have a handful of impacts on the batteries. The unavoidable advantage of electric vehicles is regenerative braking. With the application of regenerative braking, the electric vehicle can convert the kinetic energy of wheels into chemical energy. The same chemical energy gets stored in the battery and is later used to run the vehicle. Power conversion is the most important phenomenon in the case of electric vehicles as they contain an electric motor instead of an IC engine. The supply of continuous constant voltage is mandatory for the smooth running of electric vehicles [5]. DC–DC converters are mainly used in the power conversion of electric vehicles and are treated as the most important equipment of the power electronic circuit of electric vehicles. The paper describes the proposed design of SEPIC converters suitable for the performance of electric vehicles. SEPIC converters are the solution to many of the problems observed in convectional DC–DC converters as they are efficient, economical and better in performance. Moreover, DC converters are compatible with the judicious charging of Li-ion batteries and regenerative braking. Secondly, the paper discusses the constant current and constant voltage method of charging for Li-ion batteries. The research also explains the novel methods by which we can enhance the performance of electric vehicles and the economic and environmental impact of electric vehicles.

2 Modelling of Electric Vehicle Embedded with Modified SEPIC Converter and Lithium-Ion Batteries

Figure 1 shows the configuration of electricity embedded with a modified SEPIC converter. The SEPIC converter is a DC–DC converter; its operation mimics the buck–boost converter though there are various advantages of the SEPIC converter over convectional DC–DC converters [6]. The SEPIC converters can be controlled by duty ratio and provide increased or decreased voltage ratios accordingly [7]. Figure 1

below shows a rechargeable lithium-ion battery that powers the electric vehicle and provides the required traction [8]. The DC–DC converter supplies a low-voltage DC to the lithium-ion battery while recharging it. The DC motor powers the wheels. There is an onboard charger that continuously monitors lithium-ion battery characteristics such as voltage, current, temperature and state of charge while charging it to ensure peak performance [9]. The transmission system transfers mechanical power from the motor to the wheels. The lithium-ion battery receives power during charging via a bidirectional SEPIC converter through a high-voltage bus; the voltage is stepped down before transferring to the lithium-ion battery. The SEPIC converters have a low ripple factor [10]. Approximately 49% of commercially sold batteries are lithium-ion batteries.

They were first introduced by Sony and Asahi Kasei in the year 1991. The best part of lithium-ion batteries is the huge energy density ratio, thus they can store a huge amount of energy with low maintenance. The lithium-ion batteries have better durability and a life cycle of about 500 charge cycles. The unique feature of lithium-ion batteries is their secondary life that means after using lithium-ion batteries for a longer period for electric vehicles, they can be then used for inverters also. The increasing trend of lithium-ion batteries in the share market can turn out to be a big win for India. India is the second-largest producer of graphite that is used as anode in lithium-ion batteries [11]. Lithium-ion batteries are considered one of the best inventions in the last few decades. Stanley Whittingham, John Goodenough and Akira Yoshino were jointly awarded the prestigious Noble Prize in 2019 for the development of lithium-ion batteries [12]. The major limitation of a lithium-ion battery is the range of power. The state of charge can help optimize it. State of charge prevents overcharging and undercharging of battery due to which the life cycles of
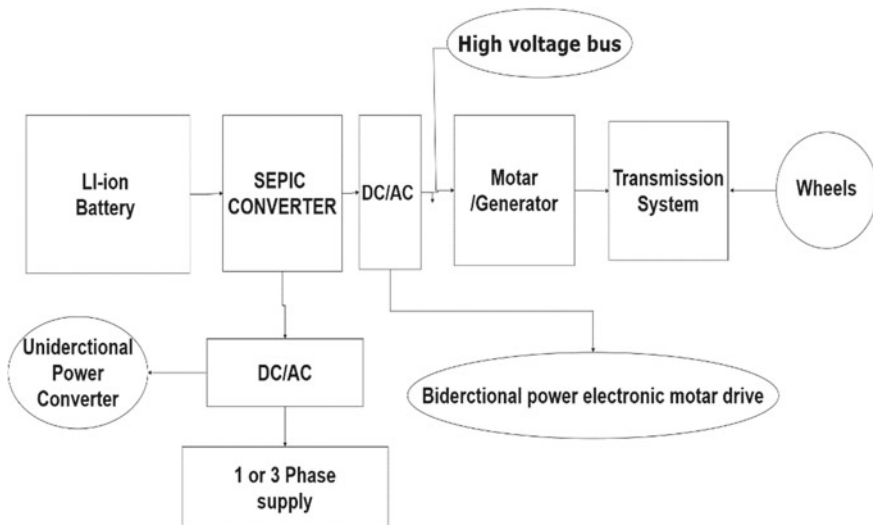

Fig. 1 Scheme of power converter in electric vehicle

the battery can be increased. Moreover, shortly, we can charge batteries with solar or wind energy that might lead to a fuel-free society and the earth can be a better place to live in. Lithium sulphur batteries can be more efficient batteries. The cost of production of lithium sulphur is comparatively low. They are safer and sulphur is abundantly available in the earth's crust. Lithium sulphur batteries have high power density and more critical density. The nations that develop more efficient batteries and advance in the field of electric vehicle technology might be considered as the next technology superpower of the world.

3   Charging Methods for Lithium-Ion Batteries

An electric vehicle needs a power electronic system between a power grid and a Li-ion battery fitted inside the vehicle that can be charged at regular intervals. The electronic system is divided into two halves, a charging station that also acts as electric vehicle service equipment and off-board charger or onboard charger fitted inside the electric vehicle. The charging station is the special part of the grid installed at a particular accessible location with the primary role of charging the battery of the electric vehicle. However, the onboard charger helps in the final stage charging of the battery pack.

There are three levels of charging lithium-ion batteries. Level I requires a 120-V plug and outlet. It can be easily carried out at home though it takes the longest time. Level II requires a 240-V plug, usually installed by a trained professional. It can either be carried out at home or at a commercial charging outlet. It is faster than the level I charging. The electric vehicle usually takes about 2 h for full charging. Level III charging requires electric vehicle supply equipment chargers. It is the fastest mode of charging and can charge the electric vehicle in just 20 min. This service can be accessed by payment mode only at a commercial point.

The two modes of charging, i.e. constant current (CC) and constant voltage (CV), are best suited for lithium batteries. While charging the lithium-ion battery, up to 80% constant current (CC) is supplied and after that the current gradually reduces at the near end of full charging. The constant current and constant voltage method of charging help in high-voltage protection and also maintain the battery life cycle. The constant current and constant voltage method with a modified SEPIC converter are best suited for the correction of the power factor. It is also beneficial in reducing power loss and also improves power quality [13].

4   Proposed Design of SEPIC Converters for Electric Vehicles with Optimization and Control Techniques

The SEPIC converters have been derived from boost converters. Figure 1 shows that the SEPIC converters are embedded with two capacitors, one on the input side and the other on the output side. The capacitor connected on the input side acts as a filter. Furthermore, a diode, inductor and MOSFET have been added to the circuit. The MOSFET acts as a power switch in the circuit.

The SEPIC converters produce the same output voltage at a lower duty cycle. Therefore, the proposed design of SEPIC converters is best suited for high power rating electric chargers. The average output voltage is given by

$$V_O = d/1 - d \cdot V_s \tag{1}$$

In Eq. 1, V_o and V_s are the output voltage and input supply, respectively.

The polarity inversion of the output voltage is not observed leading to the simplicity of the circuit [. The input inductor in the SEPIC reduces the current ripple. The proposed SEPIC converter has various advantages over conventional converters, the major advantage being that they show peak performance during steady-state operation. The main focus is to achieve a unity power factor as per IEC61000-3–2 guidelines and that can be achieved by SEPIC converters. The sustainable architecture of electric vehicles must contain a SEPIC converter that boosts its performance to the next level [14]. The charging and battery cycle typically depend on the performance of a SEPIC converter [15]. The conventional buck–boost converter provides a discrete current that halts the performance of an electric vehicle. To obtain the gain in the output voltage, we can add a transformer to the input side of an electric vehicle. SEPIC converters provide a proper constant and continuous output voltage. The proposed SEPIC converter produces increased voltage gain that is far better than conventional converters. The converter efficiency is also improved by the simulation tested in MATLAB.

AC conversion techniques are easy due to the employment of transformers, however, the DC–DC conversion techniques have always been a tough job. As shown in Fig. 2 when a SEPIC converter is in on condition, inductor 1 is charged by the input voltage and inductor 2 is charged by the capacitor. The diode remains in off condition and the required output voltage is maintained by the capacitor.
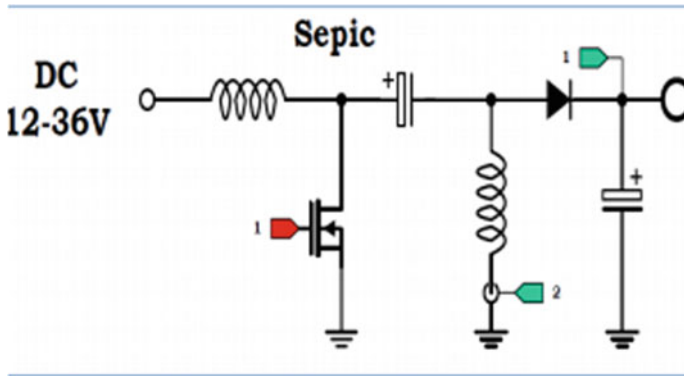
Fig. 2 Simscape model of DC–DC SEPIC Converter

Figure 3 below depicts that the SEPIC converter is triggered by a high-voltage frequency pulse. Consequently, when the SEPIC converter gets a low pulse, it takes the SEPIC converter in an off condition. The output voltage is achieved through a diode.

The controlling of a pulse is very important as if the pulse lasts for too long then the capacitor would not be able to charge the circuit, and it can be solved by using a supercapacitor which can store a tremendous amount of energy and thus can be highly impactful here.

Figure 4 shows the DC–DC SEPIC converter open-loop duty. The duty cycle decides the step up and step down voltage levels of the SEPIC converter.

Choosing inductance for the SEPIC converter is a pivotal job. The higher value of inductance leads to the peak performance of the circuit as shown in Fig. 4. However,

Fig. 3 SEPIC converter configuration
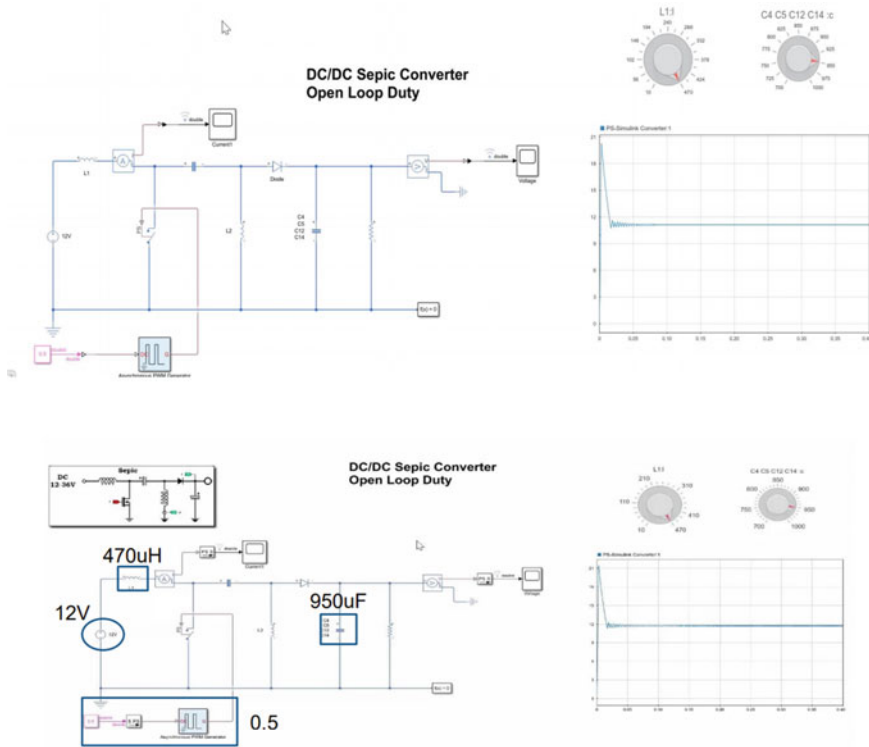
Fig. 4 DC–DC SEPIC Converter open-loop duty

larger inductance value means high internal resistance that decreases the efficiency of the SEPIC converter. So the best option is to choose the value of inductance that is just good enough to maintain the voltage and current ratio. The capacitance helps in the reduction of ripple and also helps in the change of reflected voltage. The beauty of SEPIC co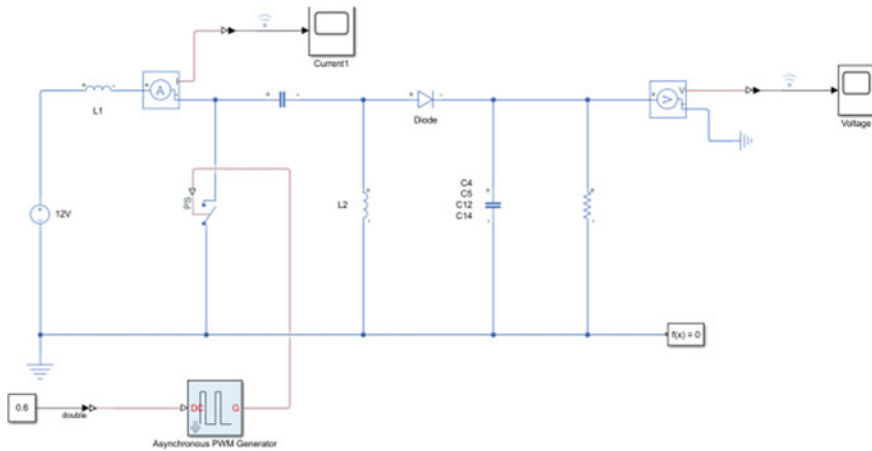nverters lies in the fact that by varying duty cycles, we can increase or decrease the voltage level more efficiently and easily as compared to conventional converters which proves that SEPIC converters are more reliable and flexible in performance.

The convectional power factor correction circuits have many limitations with efficiency and performance, so SEPIC converters come to a rescue here. The best thing about SEPIC converters is that they always operate with a power factor of 1 and the conduction losses are comparatively low.

The conventional energy system is used to balance fluctuations of the power between the source side and load side. It is the beauty of the DC–DC converter that interconnects the energy system with the DC bus. In the current scenario, we have three different topologies available that are generally classified as a buck converter, boost converter and buck–boost converter. The major findings of this research are the SEPIC converter that has unique non-inverter output best suited for the energy
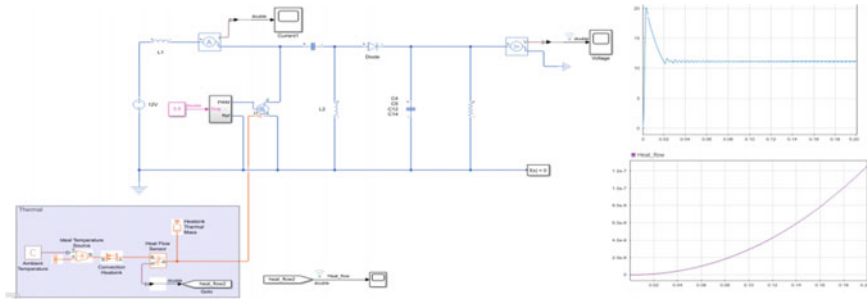
Fig. 5 DC–DC converter with nonlinear switching dynamics

conversion of electric vehicles. Moreover, the results show that it reduces the current–voltage ripple on the output/input side. The SEPIC converters have comparatively better performance than buck converters and boost converters, so they are best suited for electric vehicles. Moreover, as compared to other DC–DC converters, the SEPIC converters are best suited for charging and longer life cycle of Li-ion batteries due to their ability to convert direct current from one voltage level to another voltage level by the directly varying duty cycle. Figure 4 depicts that a pulse with just 0.5 width is able to trigger the converter smoothly that is the least value as compared to all the conventional converters. Figure 4 shows that an input voltage of 12 V has been supplied to the SEPIC converter and consequently the output voltage is maintained in the respective waveform as compared to the results of Niranjana et al. [16]. Furthermore, research depict that SEPIC converters have better efficiency as compared to other converters.

5 Result

The overall performance of the system is tested and verified in MATLAB. The results are analysed for the improvement of the entire system behaviour. The proposed design strategy proves a handful of improving power factors. Figures 5 and 6 show the results of a SEPIC converter with nonlinear switching dynamics and voltage mode control of SEPIC converters simulated in MATLAB. The results in Fig. 7 prove that by controlling PID parameters, we can control the on and off conditions of SEPIC converters.

6 Conclusion and Future Scope

In summary, the proposed design of a SEPIC converter is very feasible for the performance of an electric vehicle, and the switching dynamics and voltage mode control of
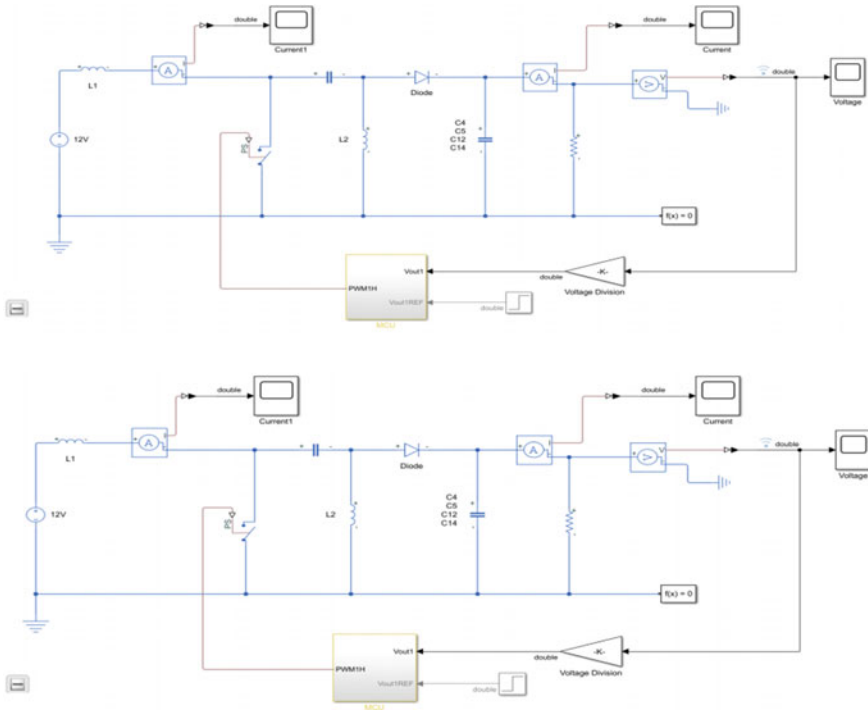
Fig. 6 DC/DC SEPIC converter voltage mode control (VMC)

SEPIC converters are faster. The SEPIC converters produce the same output voltage at a comparatively lower duty cycle. The two-way method of charging lithium-ion batteries is very beneficial to improving the durability and life cycle of lithium-ion batteries. Soon with the implementation of lithium sulphur batteries, electric vehicle range would be increased to the next level. Supercapacitor technology can be used to improve the power density of electric vehicles leading to an ecofriendly society.
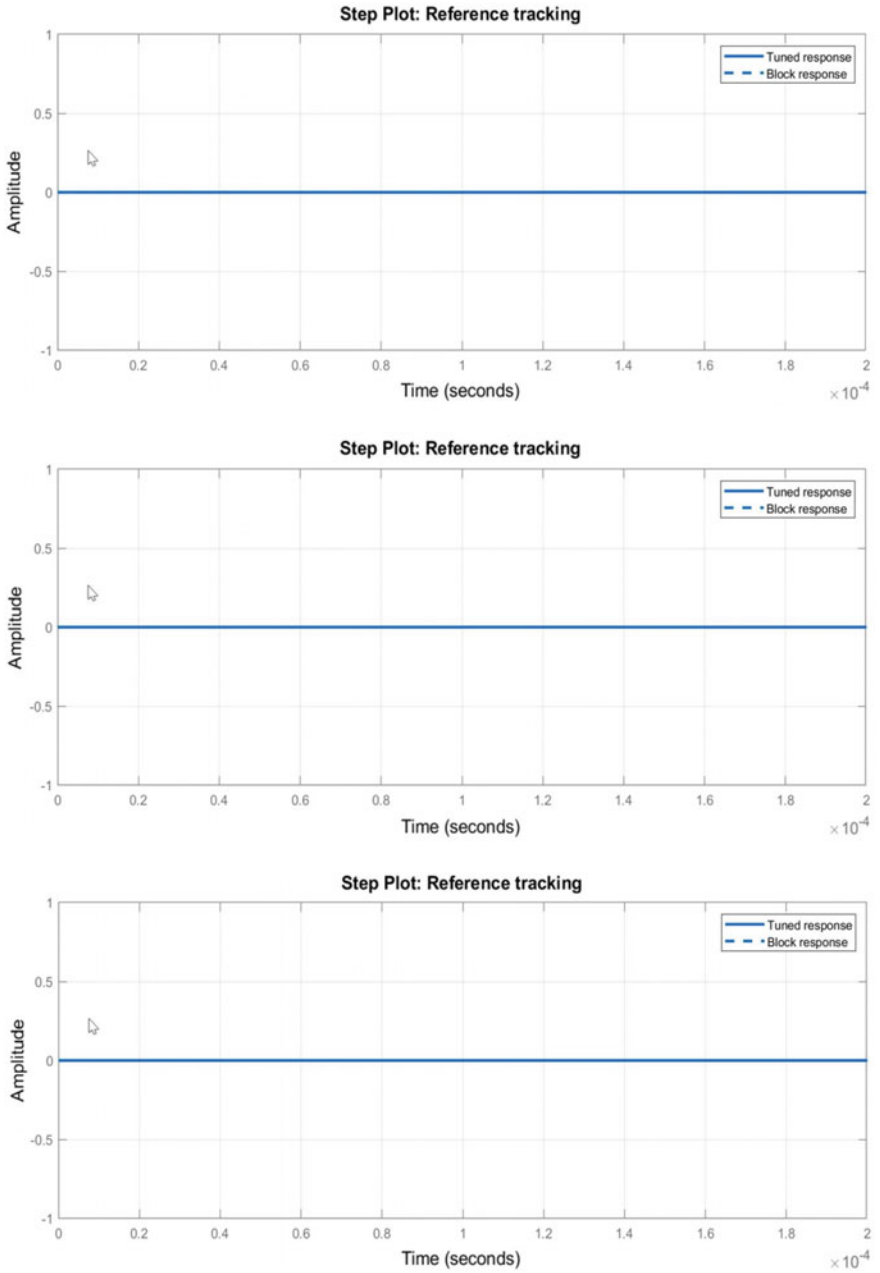
Fig. 7 Controlling PID parameters

References

1. Khaligh A, D'Antonio M (2022) Global trends in high-power onboard chargers for electric vehicles. Early Access IEEE Trans Vehicul Technol
2. Williamson SS, Rathore AK, Musavi F (2015) Industrial electronics for electric transportation: current state-of-the-art and future challenges. IEEE Trans Indus Electron 62(5):3021–3032
3. Gomez JC, Morcos MM (2003) Impact of EV battery chargers on the power quality of distribution systems. IEEETransactions Power Del 18(3):975–981
4. Kazimierczuk MK (2008) Pulse-width modulated DC-DC power converter. Willey, USA
5. Shahir FM, Babaei E, Farsadi M (2017) Analysis and design of voltage-lift technique-based non-isolated boost DC–DC converter. IET Power Electron. 11(6):1083–1091. https://doi.org/10.1049/iet-pel.2017.0259
6. Liu H, Ji Y, Wang L, Wheeler P (2018) A family of improved magnetically coupled impedance network boost DC–DC converters. IEEE Trans Power Electron 33(5):3697–3702
7. Hannan MA, Lipu MSH, Hussain A, Mohamed A (2017) A review of lithium-ion battery state of charge estimation and management system in electric vehicle applications: challenges and recommendations. Renew Sustain Energy Rev 78(May):834–854
8. Zhang C, Wang LY, Li X, Chen W, Yin GG, Jiang J (2015) Robust and adaptive estimation of state of charge for lithium-ion batteries. IEEE Trans Ind Electron 62(8):4948–4957
9. Jo C, Lee S, Song H, Cho Y, Kim I, Hyun D, Kim H (2010) Design and control of an upper-wedge-type electronic brake. J Automobile Eng 224(11):1393–1405
10. Singh B, Kushwaha R (2016) A PFC based EV battery charger using a bridgeless SEPIC converter. IEEE PIICON'16
11. Lan Z, Li Y, Gao F, Qiao F (2020) Research and implementation of step high voltage constant current closed-loop pre-charging technology. In: 2020 3rd international conference on advanced electronic materials, computers and software engineering (AEMCSE), pp 810–815
12. Maroti PK, Padmanaban S, Blaabjerg F, Wheeler P, Martirano L (2018) A novel high gain non-inverting, single switch configurations of modified SEPIC DC-DC converter for high-voltage/low-current renewable energy applications. In: 2018 20th European conference on power electronics and applications (EPE'18 ECCE Europe), pp P.1−P.9
13. Mohan N, Undeland TM, Robbins WP (2009) Power electronics: converters, applications and design. Wiley, Hoboken, USA
14. "Lithium-Ion Batteries" (2018) Polymer-based nanocomposites for energy and environmental applications
15. Khalid M, Sheikh SS, Janjua AK, Khalid HA (2018) Performance validation of electric vehicle's battery management system under state of charge estimation for lithium-ion battery. In: 2018 International conference on computing, electronic and electrical engineering (ICE Cube), pp 1–5
16. Siddharthan N, Balasubramanian B (2019) Performance evaluation of SEPIC, Luo and ZETA converter. Int J Power Electron Drive Syst 374–380

Automatic Generation Control of De-centralized Power System with V2G-Enabled HEV Fleets for Distributed Generation Management

K. Mohammed Roshan and C. Ismayil

Abstract Ancillary service provision by Hybrid Electric Vehicle (HEV) fleets to the Automatic Generation Control (AGC) of an interconnected deregulated power system is discussed in this paper. EVs can take part in the AGC through Vehicle to Grid (V2G) technology along with conventional thermal generators. To keep up with the exponential growth of energy demand, there is a gradual increase in the installation of Distributed Generators (DG), especially in isolated grids. The intermittent nature of such renewable sources combined with load deviations often imparts frequency deviations and stability issues in the power system. The embedded batteries of EV fleets are used to provide the inertia required for grid-related frequency regulation services. Their fast-acting batteries can supply quick impulsive power as required for frequency regulation. The AGC task becomes much more tedious as the power system is deregulated where various key players emerge in the market for generation, transmission and distribution of electrical energy. The efficiency of the system is validated for different power contracts that exist in the energy sector.

Keywords Deregulated power market · Hybrid electric vehicle (HEV) · Independent system operators · Renewable energy sources (RES)

1 Introduction

The introduction of smart grids enables the common customer to be an active part of the power market and earn profit. To combat the rise in fossil fuel prices and carbon emission, the emergence of electric vehicles on the market is on the rise. Since the electric vehicles have embedded batteries within them, a fleet of electric vehicles can be deemed as a mobile reserve power that can be used at any part of the grid when required [1]. Such an ancillary service provision from electric vehicles to the power system by aiding the Load Frequency Control (LFC) [2, 3]. This can ensure

K. Mohammed Roshan (✉) · C. Ismayil
Department of Electrical and Electronics, Government College of Engineering, Kannur, Kerala, India
e-mail: roshan.karikuzhi@gmail.com

655

reliable power flow even in remote islanded microgrids. Since the demand for energy is only growing, various means are being used in order to ensure a reliable power grid like the installation of distributed generators [4]. Hybrid power systems incorporate thermal plants, solar farms, diesel, etc. Coordination controls to maintain such a hybrid power system are also suggested [5, 6]. De-centralization or deregulation of the conventional electricity market leads to the surfacing of private key players in functions like energy generation, transmission and distribution [7]. In a deregulated power system, power generation is managed by generating companies termed as GENCOs. Various such GENCOs will be present in an interlinked power system. Likewise, transmission and distribution are privatized as TRANSCOs and DISCOs, and an Independent System Operator (ISO) coordinates all three with the customer [8, 9]. There are various forms of renewable energy sources used as DG like solar and wind farm. As such sources are very volatile and intermittent, they often impart stability issues and disturbances in the grid due to their low inertia [6, 10–12]. This is proved in the case of a deregulated system where ultracapacitors were connected to the grid to provide the additional inertia required to balance the power deviation [13]. Similarly in the proposed project, the electric vehicles are put to use to manage the distributed generation. After deregulation, every consumer will have different choices to choose from to get the power they need in an affordable tariff [14, 15]. By the incorporation of sophisticated charging control, hybrid electric vehicles can be used as a secondary reserve to be used for grid-related ancillary services.

The structure of the paper is as follows: Chap. 2 deals with the description of automatic generation control of a liberalized two-area power system. It also provides the modeling of the RES and the electric vehicle fleet. Chapter 3 provides the simulation results of the two-area system with renewable source and electric vehicles. Finally, conclusions drawn are mentioned in the last and final Chap. 4.

2 AGC of Power Considered System Under Deregulation

After the deregulation of electric power, the single entity generation, transmission and distribution do not exist. Rather, companies like GENCOs, TRANSCOs and DISCOs emerge to facilitate power flow. In the considered deregulated scenario for automatic generation control, two areas with each area having two DISCOs and two GENCOs are considered. The GENCOs considered are reheat thermal plants to ensure high thermal efficiency. Both power system control areas are interconnected via a tie line. The aggregate model of the entire power system is depicted in Fig. 1.

The various power contracts that may exist in the deregulated power system can be visualized in the form of a matrix known as the DISCO Participation Matrix (DPM). The conceptualization is used as described in the generalized model of deregulated power system [9]. Such a DPM is provided in Eq. (1).
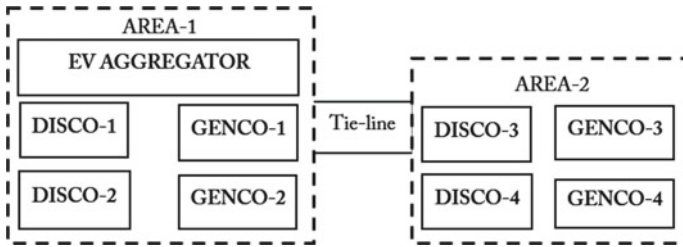
Fig. 1 Schematic diagram of power system control areas

$$\text{DPM} = \begin{bmatrix} \text{Cpf11} & \text{Cpf12} & \text{Cpf13} & \text{Cpf14} \\ \text{Cpf21} & \text{Cpf22} & \text{Cpf23} & \text{Cpf24} \\ \text{Cpf31} & \text{Cpf32} & \text{Cpf33} & \text{Cpf34} \\ \text{Cpf41} & \text{Cpf42} & \text{Cpf43} & \text{Cpf44} \end{bmatrix} \qquad (1)$$

The entries of this matrix are termed as the contract participation factors (CPF), and they are defined as per Eq. (2):

$$\text{cpf}_{ij} = \frac{j\text{th DISCO power demanded out of } i\text{th GENCO in p.u MW}}{j\text{th DISCO total power demand in p.u MW}} \qquad (2)$$

2.1 Modeling of Electric Vehicle and Solar Farm

In the mentioned two-area system, the EV fleets are provided in the first area and their combined power output is used to manage the instantaneous energy mismatch between generated and consumed power. Figure 2 represents a lumped model of an EV aggregator. The aggregators communicate with the EVs and provide the EVs for the AGC task according to their SoC and availability. The lumped model of the electric vehicle has the primary frequency control ability via V2G power transfer.

Fig. 2 EV lumped model

The dead band addresses a nonlinear case where a chance can occur that all the EVs are abruptly disconnected from the grid. This will result in an und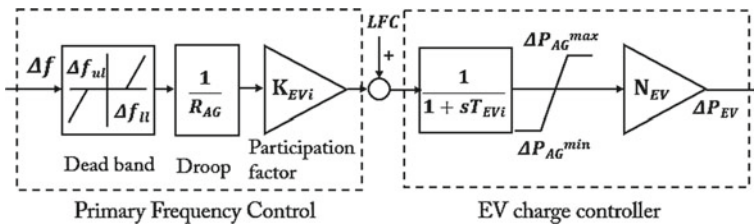esired frequency imbalance. As a preventive measure, dead band functions are provided with droop characteristics. A value of 10 mHz is chosen for the upper limit (Δf_{UL}) and for the lower limit (Δf_{LL}), it is taken as -10 mHz. The EV aggregators droop coefficient (R_{AG}) is considered 2.4 Hz/p.u. MW which is the same as the thermal units. For the embedded lithium-ion battery of the vehicles, the K_{EV} value differs according to the SOC [2]. The EVs will only power the grid when they have enough battery potential within 50 and 90% SoC.

The renewable source considered in the deregulated power system is a 300 MW solar PV farm. It constitutes of series and parallel arrangement of photovoltaic panels to generate the required power. Input to the PV array is Φ (solar insolation) from the sun. Power output from the PV array is represented by Eq. (3).

$$P_{PV} = \eta S\phi[1 - 0.005(T_a + 25)] \tag{3}$$

Here, the conversion efficiency of the cells is denoted as η and has a varied range from 7 to 12%. The area of the PV array is depicted as S in (m^2). The insolation from the sun is represented as Φ (kW/m^2). T_a corresponds to ambient temperature in (°C). S and η are taken uniform for the PV farm.

$$G_{PV} = \frac{K_{PV}}{1 + sT_{PV}} \tag{4}$$

The power delivered by the PV array depends on T_{PV} and Φ. A much plainer transfer function is deducted as per Eq. (4).

3 Simulation Results of Two-Area Deregulated Power System with EV and RES

The combined block diagram representation of the overall system is provided in Fig. 3. Along with the conventional reheat thermal plant in the first area, solar power as the intermittent renewable energy source is also integrated. Two GENCOs and two DISCOs are present in both areas. The output of a solar farm is around 200 MW. The entity that manages the scheduling of the EVs based on their availability and state of charge is the Independent System Operators (ISO). The efficiency of the HEV fleets in managing the intermittency of solar power is analyzed for various power contracts that exist in the energy market. Power system parameters are provided in Table 1.
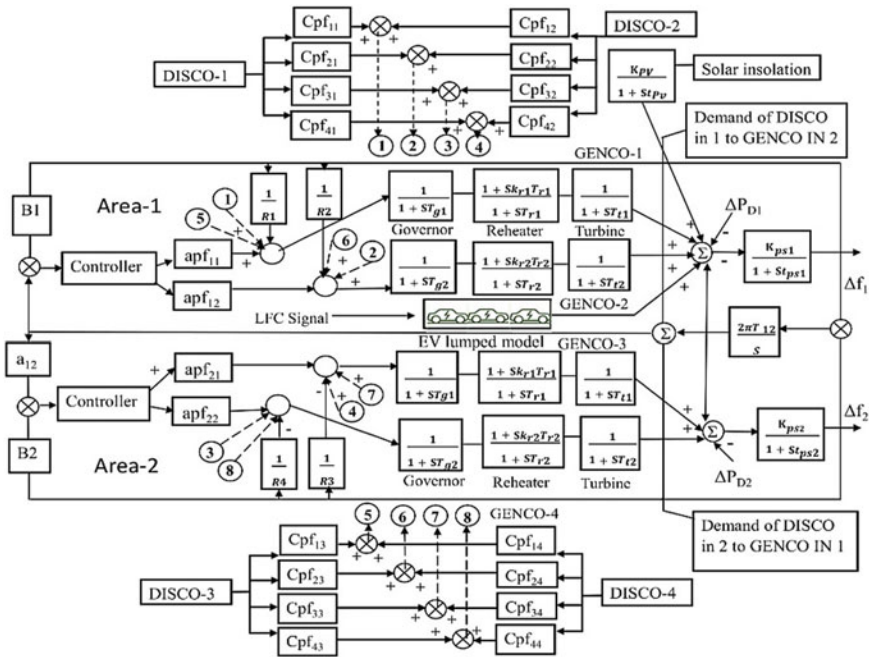
Fig. 3 LFC of a two-area deregulated power system with EV

Table 1 Power system parameters

Parameter	Value
Rated power, P_{R1}, P_{R2}	1000 MW
Rated frequency, f	50 Hz
Frequency bias factor, β_1	0.425 p.u MW/Hz
Frequency bias factor, β_2	0.416 p.u MW/Hz
Reheater gain constant, K_e	3
Time constant of governor, T_g	0.08s
Time constant of turbine, T_t	0.4s
Droop regulation constant, R	2.4 Hz/p.u MW
Power system damping coefficient	0.08 pu.MW.sec
Power system inertia, H	5s
Power system gain constant, K_{PS}	120 Hz/p.u MW
Power system time constant, T_{PS}	20s
Gain constant of solar PV, K_{pv}	1
Time constant of solar PV, T_{pv}	1.8s

3.1 Unilateral Contract

In the unilateral power contract, only one party or GENCO is involved in the contract. The power delivery by GENCO is solely based on the need in the specified area. Here, the time duration of the contract is determined by the operating GENCO only. The

$$
DPM = \begin{bmatrix} 0.5 & 0.5 & 0 & 0 \\ 0.5 & 0.5 & 0 & 0 \\ 0 & 0 & 0 & 0 \\ 0 & 0 & 0 & 0 \end{bmatrix}, \text{Disco Matrix} = \begin{bmatrix} 0.1 \\ 0.1 \\ 0 \\ 0 \end{bmatrix}, \text{Apf} = \begin{bmatrix} 0.5 \\ 0.5 \\ 0.5 \\ 0.5 \end{bmatrix} \tag{5}
$$

DPM and APF matrix is demonstrated in Eq. (5). Since it is a unilateral contract, DISCO loads for the second area are zero. The DISCO loads are taken as 100 MW each for DISCO1 and DISCO2, respectively. So the total DISCO load is 200 MW. The local load is 200 MW. As a result, the area 1 total load becomes 400 MW. Here, the (APF) is taken as 0.5 for each generator.

The 200 MW DISCO loads are met by the GENCOs 1 and 2 as they produce 100 MW. Their outputs are represented in Fig. 4. Since there are no DISCO loads in area 2, the output of GENCOs 3 and 4 are zero as they are not supplying any power. The improvement in the frequency profile is clearly portrayed in Fig. 5. After the EV fleets were incorporated into the AGC. The Power delivered from the EV fleet is 10–15 MW during normal operation, and it is portrayed in Fig. 6. This Power is used to compensate for the energy mismatch from the RES and improve overall system performance.

Since power does not flow from one area to the other area in a unilateral contract, tie-line deviations are not present here.

3.2 Bilateral Contract

For a bilateral contract, unlike the unilateral contract which has only one party, here two or more parties are involved in the transaction. The Power sharing through tie line should be based on strict mutual terms. The DPM is portrayed in Eq. (6). Here, the total DISCO load sums up to 400 MW. The local load of the first area is taken as 100 MW and for the second area, the load is taken as 400 MW.

$$
DPM = \begin{bmatrix} 0.2 & 0.1 & 0.2 & 0 \\ 0.3 & 0.4 & 0.2 & 0 \\ 0.5 & 0 & 0.4 & 0.5 \\ 0 & 0.5 & 0.2 & 0.5 \end{bmatrix}, \text{Disco Matrix} = \begin{bmatrix} 0.1 \\ 0.1 \\ 0.1 \\ 0.1 \end{bmatrix}, \text{Apf} = \begin{bmatrix} 0.5 \\ 0.5 \\ 0.5 \\ 0.5 \end{bmatrix} \tag{6}
$$

Hence, the total power system load is 900 MW. Area Participation Factor (APF) is taken as 0.5 for each generator hence all GENCOs have equal participation.
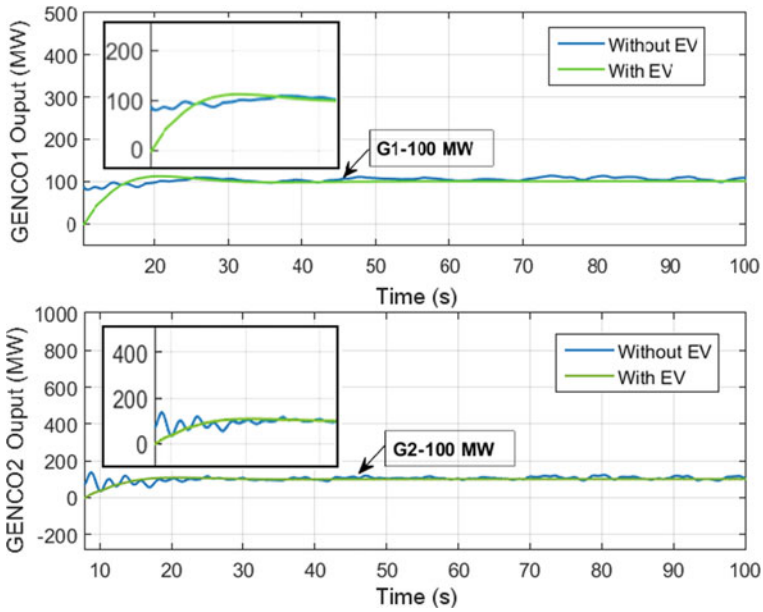
Fig. 4 Area-1 GENCO output power
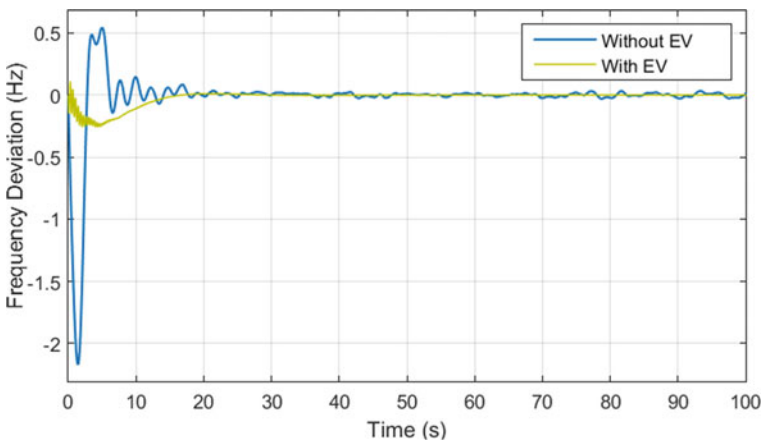
Fig. 5 Frequency deviation of area-1

The enhancement in the frequency profile is clearly portrayed in Fig. 8. The tie-line power deviations provided in Fig. 9 demonstrate the effect of EVs on the deregulated generation. The GENCOs G2 and G2 deliver an output power of 51MW and 92 MW respectively as per Fig. 7. For the GENCOs G3 and G4, the output power is 280 MW and 260 MW, respectively. This power along with the volatile 200 MW solar RES
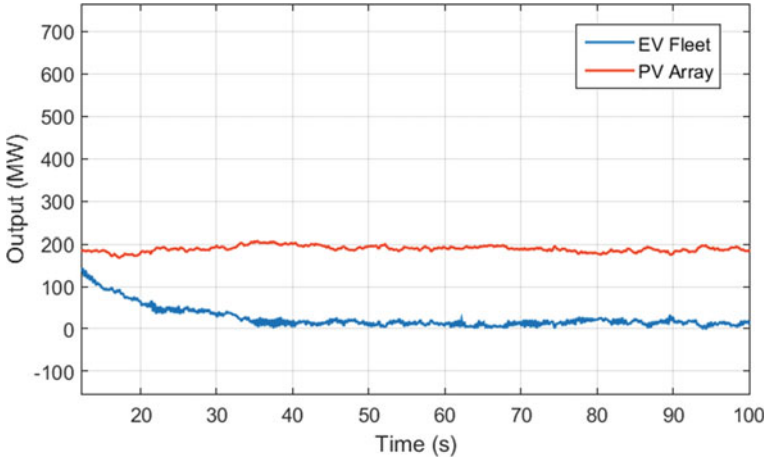
Fig. 6 Power output of EV and PV array

power sums up to 883 MW. Since this power is varying in nature due to the presence of PV arrays, here when the electric vehicles are integrated the power the rest power required within range of 10–15 MW is constantly supplied by EV fleets with their embedded lithium-ion batteries.

3.3 Contract Violation

There exists a condition in which the companies breach the mutual agreements when DISCOs demand more power than on the agreed terms. Such contracts are termed as contract violations.

Consider a bilateral case but here the DISCO load at DISCO1 of the first area is increased from 100–200 MW. So an unprecedented load of 100 MW is considered as the uncontracted load. This sudden load from the DISCO1 is projected as a contract violation. Even in contract violation condition, the deregulated power system has managed to maintain the frequency profile in its nominal values with EV fleet. This is demonstrated in Fig. 10 which represents the frequency deviations.

The contribution of the EV fleets to the automatic generation control of the power system varies according to the SoC levels of the combined batteries. Normally, the EVs get connected to the grid only when they are trying to recharge. So connecting a 30% SoC is not favorable for the grid. Similarly after 90% SoC, the EVs may get disconnected from the charging station as the battery is close to full.

The best battery state to participate in the AGC is with a SoC of 60% as per Fig. 11 and Table 2. The hybrid electric vehicle also has an internal combustion engine to run the vehicle and auxiliary power generating techniques like regenerative braking.
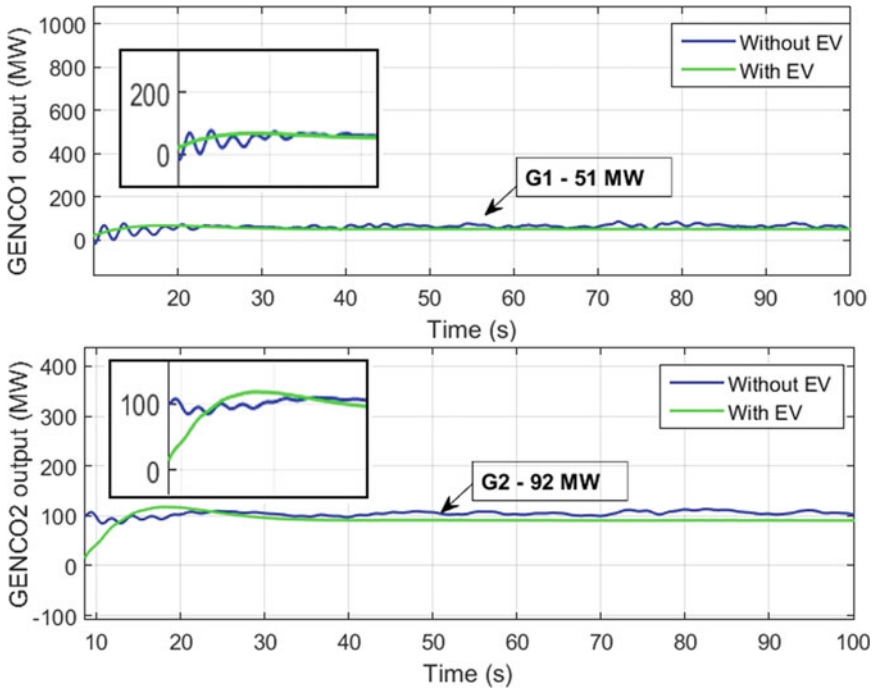
Fig. 7 Area-1 GENCO output power
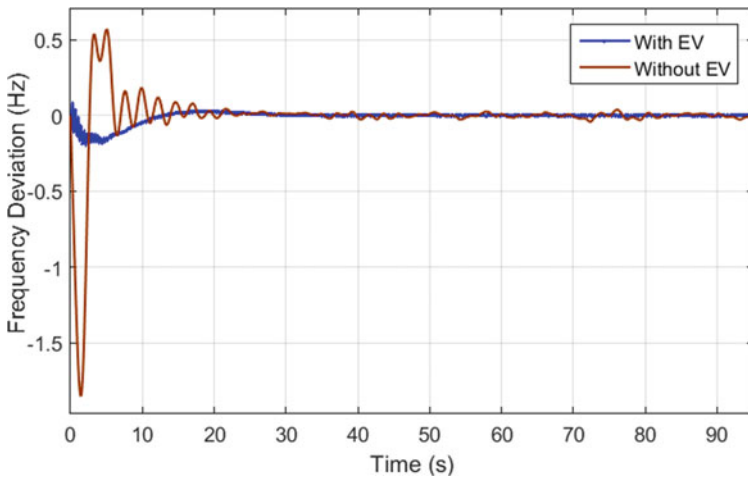
Fig. 8 Frequency deviation of area-1
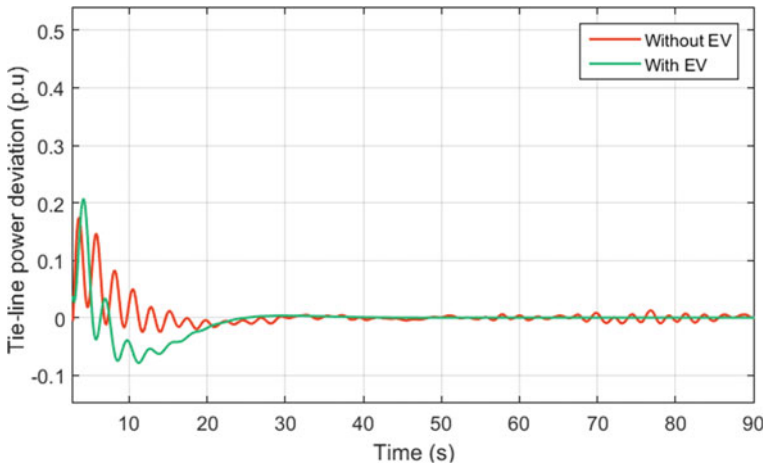
Fig. 9 Tie-line power deviations
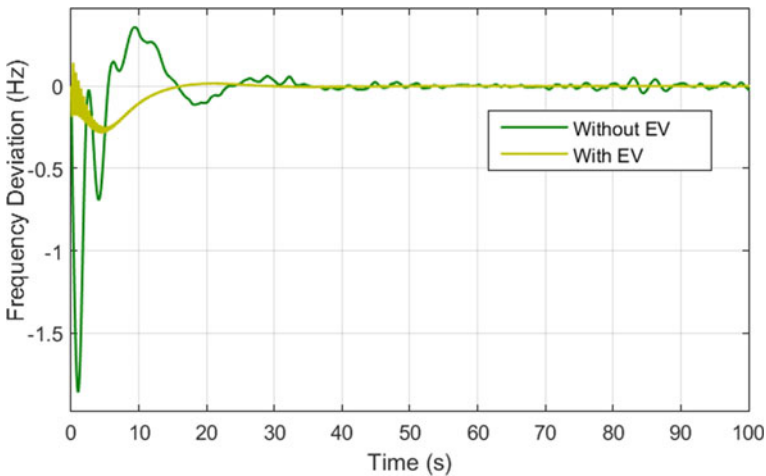
Fig. 10 Frequency deviation of area-1

4　Conclusion

The effect of the intermittent power from a 200 MW PV farm on the power system is seen to be detrimental as sustained oscillations are present in the frequency profile. This reduced inertia of the power system when RES is increased is managed with a fleet of 500 Hybrid Electric Vehicles (HEV). The ability of the EV to participate in grid-related ancillary services like frequency regulation through active energy measurement is measured. The lithium-ion batteries of the EV with a 60% SoC showed improved participation to provide impulsive power to the grid via V2G
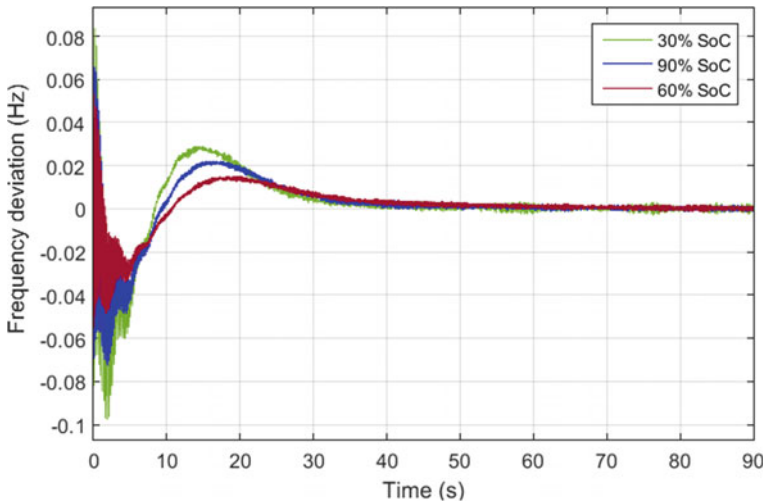
Fig. 11 Frequency deviation of area-1 under 30, 60 and 90% SoC

Table 2 Frequency deviations verses SoC

Cases	Peak overshoot (ΔHz)	Peak undershoot (ΔHz)
30% SoC	0.6316	−0.08816
60% SoC	0.01636	−0.04314
90% SoC	0.02706	−0.06414

aiding by primary frequency control. The experimental setup is simulated in a Matlab/Simulink environment under different power contract cases like a unilateral contract, bilateral and contract violation. The results obtained are promising as the fleet of EVs are able to supply power varying from 10 to 15 MW via the V2G technique. This smart grid maintains a constant generation load balance at all instants keeping the frequency and tie-line deviations to zero at all power contracts.

References

1. Dutta A, Debbarma S (2018) Frequency regulation in deregulated market using vehicle to grid services in residential distribution network. IEEE Syst J 12(3):2812–2820
2. Izadkhast S, Garcia-Gonzalez P, Fras P (2014) An Aggregate model of plug-in electric vehicles for primary frequency control. IEEE Trans Power Syst 10(11):885–895
3. Liu H, Hu Z, Song Y, Wang J, Xie X (2015) Vehicle-to-grid control for supplementary frequency regulation considering charging demands. IEEE Trans Power Syst 30(6):3110–3119
4. Raju PS, Farook S (2011) AGC controllers to optimize LFC regulation in deregulated power system. Int J Adv Eng Technol 1(5):278–289
5. Das DC, Roy AK, Sinha N (2012) GA based frequency controller for solar-thermal-diesel-wind

hybrid energy generation/energy storage system. Int J Electric Power Energy Syst 43(1):262–279

6. Datta A, Bhattacharjee K, Debbarma (2015) Load frequency control of a renewable energy sources based hybrid system. In: IEEE international conference on systems, process and control (ICSPC). Sunway, Malaysia, pp 34–38

7. Elgerd OI, Fosha CE (1970) Optimum megawatt-frequency control of multi area electric energy systems after deregulation. IEEE Trans Power Apparatus Syst 89(4):556–566

8. Chathoth I, Ramdas SK, Krishnan ST (2015) Fractional order Proportional-integral-derivative based automatic generation control in deregulated power systems. Electric Power Comp Syst 43(17):1931–1945

9. Donde V, Pai MA, Hiskens IA (2001) Simulation and optimization in an AGC after deregulation. IEEE Trans Power Syst 16(3):481–489

10. Bhongade S, Tyagi B (2012) AGC Scheme including photo-voltaic generating system for interconnected power system. In: National power systems conference, Paper id-12057, Indian Institute of Technology, Kanpur, India, pp 1–6

11. Annamraju, Nandiraju (2019) Robust frequency control in a renewable penetrated power system: an adaptive fractional order-fuzzy approach environments. Protection Control Mod Power Syst 4(16):130–138

12. Tungadio DH, Sun Y (2019) LFC considering renewable energy integration in power system. Energy Rep 5(1):436–453

13. Peddakapu K et al (2020) Performance analysis of distributed power flow controller with ultracapacitor for regulating the frequency deviations in restructured power system. J Energy Storage 31(6):20–31

14. Christie RD, Bose R (1996) LFC issues in power system operations after deregulation. IEEE Trans Power Syst 11(3):1191–1200

15. Tan W, Zhang H (2012) Decentralized load frequency control in deregulated environments. Electric Power Energy Syst 41(1):16–26

Retinal Image Enhancement for Detection of Medical Complications—A Summary

Ashanand and Manpreet Kaur

Abstract Retinal Image is an image obtained from a Fundus camera which is used for the detection of abnormalities and unwanted growth of cells. For proper identification of abnormalities (Retinal Diseases) present in an image, an adequate amount of image enhancement is required. The presence of any medical complications may lead to loss of eye vision, thus a diagnostic system is extremely required. Diabetic retinopathy is one of the majorly present medical complications that affect human vision. In this paper, the retinal image enhancement techniques using histogram equalization, adaptive histogram equalization, brightness preserving bi-histogram equalization, dual-tree complex wavelet transform, and contrast limited adaptive histogram equalization techniques are discussed. For comparison of these techniques, parameters like mean square error, peak signal-to-noise ratio, structural similarity index metrics, absolute mean brightness error, and root mean square error are available. These parameters can help in an early-stage diagnosis of retinal complications.

Keywords Image enhancement · Peak signal-to-noise ratio · Structural similarity index · Absolute mean brightness error · Root mean square error

1 Introduction

The eye is one of the sensitive organs of vision. The vision is directly related to the proper functioning of the human body. Retinal images not only provide information about the visual system but also signify a general state of health of the entire body. Production of retinal images requires a fundus camera normally which is capable of obtaining high-resolution images of the inner surfaces of the eye. The presence of any abnormality causes adverse effects on sensation parts also [1]. Due to the recent way of lifestyle, the retina of the human eye got easily affected by various infections that result in visual impairments. This leads to different abnormalities occurring in

Ashanand · M. Kaur (✉)
Sant Longowal Institute of Engineering and Technology, Sangrur, Punjab, India
e-mail: aneja_mpk@yahoo.com

Table 1 Diabetic retinopathy levels and corresponding features [6, 7]

Diabetic retinopathy level	Specific feature(s)
No retinopathy (No DR)	No abnormality
Mild non-proliferative diabetic retinopathy (Mild NPDR)	Microaneurysms only
Moderate non-proliferative diabetic retinopathy (Moderate NPDR)	Numerous microaneurysms and retinal hemorrhages
Severe non-proliferative diabetic retinopathy (Severe NPDR)	Numerous microaneurysms and retinal hemorrhages in 4 quadrants of the retina
Proliferative diabetic retinopathy (PDR)	Neovascularization and maybe vision loss

the retina. Diabetic retinopathy is one of the most serious abnormalities of diabetic Mellitus resulting in blindness for the age group 30–69 years [2–4].

In this disease, the retinal blood vessels get damaged with leakage of fats and proteins. These particles are known as exudates. Sometimes, it leads to hemorrhages and microaneurysms [2]. Microaneurysms usually have a diameter smaller than 125 µm which makes their detection a more complicated task. According to the latest report of the World Health Organization, 422 million people have diabetes, majorly in low- and middle-income countries [5].

Depending upon the presence of these abnormalities, Diabetic Retinopathy (DR) can be categorized into two classes: Non-proliferative diabetic retinopathy (NPDR) and proliferative diabetic retinopathy (PDR). Diabetic retinopathy abnormality is classified into five levels based on its severity as per Table 1: No DR, Mild NPDR, Moderate NPDR, Severe NPDR, and PDR [6, 7].

Another retinal complication is age-related macular degeneration which occurs in the retinal site of old age people. It mostly happens when Bruch's membrane doesn't work properly. It performs the function of passing waste products and nutrients through it. The improper functioning of this membrane leads to its leakage. The leaked waste products and nutrients are known as exudates [8]. Glaucoma is also an abnormality that occurs due to the breakdown of nerve fiber which puts pressure on the Optic Nerve Head (ONH). The ONH carries image vision information signals to the brain. When a significant number of ONH nerves are damaged, it may lead to permanent image loss too [9, 10]. For timely detection of these abnormalities, a proper enhancement is required. These abnormalities are not properly visible through clinical investigations; proper methodology should be there for early-stage diagnosis of these exudates.

In this paper, available enhancement techniques are discussed based on the parameters: Peak Signal-to-Noise Ratio (PSNR), Mean Square Error (MSE), Entropy, Mean Absolute Error (MAE), Structural Similarity Index Metrics (SSIM), Normalized Cross-Correlation (NCC), Absolute Mean Brightness Error (AMBE), and Root Mean Square Error (RMSE) [11, 12]. The evaluation of these enhancement parameters seems to be sufficient for retinal disease diagnosis. Parametric calculations can identify the presence of abnormality. There are many methods proposed by

researchers, and all methods require a preprocessed image for its operation and the preprocessed image needs proper enhancement.

The need for enhancement is extremely crucial as acquiring fundus images through a high-resolution camera undergo from non-uniform illumination, noise, and poor contrast. Various enhancement techniques like Contrast Stretching (CS), Log Transformations, Power-Law Transformations, Histogram Equalization (HE), Bi-histogram Equalization with Adaptive Sigmoid Function (BEASF), and Contrast Limited Adaptive Histogram Equalization (CLAHE) are available for enhancement.

2 Database Available

Dataset is the collection of records and useful information applied by some set of instructions. Table 2 describes the universally available datasets for retinal images. Images are taken with high-resolution fundus cameras for each dataset with their Field of View (FOV) angle.

2.1 DIARETDB0

DIARETDB0 is a publicly available database for diabetic retinopathy detection from digital retinal images in which the calibration level is 0. It contains 130 fundus images of the retina of which 20 are normal images and 110 images are prone to diabetic retinopathy (hard exudates, soft exudates, microaneurysms, hemorrhages, and neovascularization). Images were taken here with a digital fundus camera at an angle of 50°. This database can be used for evaluating the performance of the diagnosis method used for diabetic retinopathy detection [13, 14].

2.2 DIARETDB1

DIARETDB1 is a publicly available database used for the detection of diabetic retinopathy from digital fundus images in which the calibration level is 1. It contains 89 color fundus images of resolution 1500 × 1152 pixels out of which 84 images contain the sign of MNPDR (microaneurysms) and 5 images are normal. Images were taken here with a digital fundus camera at an angle of 50°. Markings of four independent experts were collected for annotation purposes. These annotations can be used for evaluating the certainty of getting accurate results [15, 16].

Table 2 Diabetic retinopathy database

Dataset name	Number of images	Resolution	Camera	Availability
DIARETDB0	130 (110 DR, 20 Normal)	–	Digital fundus camera with FVO 50°	Available online
DIARETDB1	89 (84 DR, 5 Normal)	1500 × 1152	ZEISS FF 450plus fundus camera with Nikon F5 digital camera, FOV 50°	Available online
Retinopathy online challenge	100	–	Topcon NW 100, a Topcon NW 200, Canon CR5-45NM, 2 differently shaped FOVs	Available on registration
RCB-RGB-MA	250	2595 × 1944	DRS non-mydriatic fundus camera, FOV45°	Available online
RC-SLO-MA	58	1024 × 1024	An EasyScan camera (i-Optics Inc., the Netherlands), FOV45°	Available online
IDRiD	516	4288 × 2848	A Kowa VX-10 alpha digital fundus camera, FOV 50°	Available online
MESSIDOR	1200	1440 × 960 2240 × 1488 2304 × 1536	A color video 3CCD camera on a Top-con TRC NW6 non-mydriatic retino-graph with FOV 45°	Available on registration
MESSIDOR-2	1748	1440 × 960 2240 × 1488 2304 × 1536	A Topcon TRC NW6 non-mydriatic fundus camera with FOV45°	Available on registration
e-Optha EX	47 exudates and 35 healthy	Ranging from 1440 × 960 to 2544 × 1696	–	Available on registration
e-Optha MA	148 with MA 233 healthy	Ranging from 1440 × 960 to 2544 × 1696	–	Available on registration

Table 2 (continued)

Dataset name	Number of images	Resolution	Camera	Availability
DDR	13,673	Mixed	42 types of fundus cameras with a 45° FOV	Available online
Kaggle/EyePACS	35,126 train, 53,576 test	–	Multiple fundus cameras and different fields of views	Available on registration
DRIVE	40	768 × 584	Canon CR5 camera with a 45° FOV	Available online
HRF	45	–	Canon CR1 fundus camera with a 45° FOV	Available online

2.3　Retinopathy Online Challenge (ROC)

The retinopathy online challenge is a dataset for diabetic retinopathy detection. It is available only after having online registration. The purpose of this database is to provide a computer-aided detection system for diabetic retinopathy detection. It contains 100 retinal images obtained from Topcon NW100, Topcon NW200, and Canon CR5-45NM fundus cameras at different FOVs [17, 18].

2.4　Microaneurysms Detection: RC-RGB-MA Dataset

The RC-RGB-MA is a universally available database for the detection of diabetic retinopathy. The images were collected in the framework of the Retina Check project managed by the Eindhoven University of Technology, the Netherlands. It contains 250 RGB images obtained from a DRS non-mydriatic fundus camera with a resolution of 2595 × 1944 pixels and a FOV of 45°. This dataset was specially designed for Mild NPDR detection. The annotations were provided by two medical experts using Microaneurysms Annotation Tool (RC-MAT) [19].

2.5　Microaneurysms Detection: RC-SLO-MA Dataset

The RC-SLO-MA is a universally available dataset available for the detection of microaneurysms which is MNPDR. The images were taken from an Easy Scan camera (i-Optics Inc., the Netherlands) with a resolution of 1024 × 1024 pixels and

FOV45°. The green and infrared lasers were used for image acquisition. The annotations of microaneurysms are provided by 2 medical experts. One expert annotated using green images and the second expert manually labeled microaneurysms with the help of infrared images [19].

2.6 IDRiD—Indian Diabetic Retinopathy Image Dataset

The IDRiD retinal image dataset is based on diabetic retinopathy segmentation and grading challenge. It contains 516 retinal images captured by a retinal specialist using Kowa VX-10 alpha digital fundus camera, at FOV 50° at an eye clinic situated in Nanded in Maharashtra, India. This database provides precise pixel-level annotations of abnormalities with the help of binary masks. It contains 81 images associated with microaneurysms, 81 with hard exudates, 80 with hemorrhages, and 40 with soft exudates. A binary mask is also here for optic disk regions for all images [20, 21].

2.7 MESSIDOR

It is a public dataset for the detection of diabetic retinopathy that is available online. It compares and evaluates segmentation methodologies for detecting lesions. The French Ministry of Research and Defense supported MESSIDOR through the TECHNO-VISION initiative. Total 1200 images of the human retina were captured using a non-mydriatic radiograph with a 45° field of view. Generally, the Topcon TRC NW6 radiograph is used. The images are having a resolution of 2240×1488 pixels in TIFF format and are divided into 3 sets each having four zipped folders containing 100 images each. Medical experts provided annotations about the risk of macular edema and type of retinopathy grade. Depending upon the presence of these abnormalities, the grading of diabetic retinopathy is categorized. Type 0 (no abnormality), Type 1 (microaneurysms ≤ 5), Type 2 ($5 <$ micro aneurysms < 15 or hemorrhages < 5), and Type 3 (microaneurysms ≥ 15 or hemorrhages < 5 or neovascularization $= 1$) are its four types [22, 23].

2.8 MESSIDOR-2

The availability of the MESSIDOR-2 database is online for DR detection. It is different from other databases of MESSIDOR as it contains a collection of evaluations consisting of two macula-centered eye fundus images. Total 1748 images are captured with resolution 2240×1488 pixels using Topcon NW6 non-mydriatic fundus camera at a 45° field of view. The only drawback here is no availability of any ground truth or annotations. Medical experts from outside of the MESSIDOR 2

team have provided these annotations but were not included in the original database [24, 25].

2.9　e-Optha EX

e-Optha EX is a diabetic retinopathy detection database available universally. As the name indicate EX, indicates the detection of Exudates only. It contains 82 colored retinal images in total, 47 images are available with exudates and 35 images are healthy with a resolution ranging from 1440 × 960 pixels to 2544 × 1696 pixels [26, 27].

2.10　e-Optha MA

e-Optha MA is a diabetic retinopathy detection database available universally. MA here denotes microaneurysms. It deals with the detection of microaneurysms only. It contains 381 colored retinal images in total, 148 images are available with microaneurysms or small lesions, and 233 images have no sign of lesions. The resolution of these images ranges from 1440 × 960 pixels to 2544 × 1696 pixels [28, 29].

2.11　DDR

DDR is a dataset for the detection of diabetic retinopathy available online for screening of DR. It is a general-purpose dataset containing a total of 13,673 High-quality colored digital retinal images with mixed resolution are available here for research work. 12 different digital fundus cameras are used for image acquisition at a 45° FOV [30].

2.12　Kaggle/EyePACS

Kaggle/EyePACS is a database for diabetic retinopathy detection available on registration. Medical experts rated the presence of diabetic retinopathy on a scale of 0–4. Here, 0 denotes no sign of diabetic retinopathy, 1 signifies mild, 2 signifies moderate, 3 signifies severe, and 4 signifies proliferative diabetic retinopathy. It contains 35,126 train images and 53,576 test-colored retinal images. These images are captured with the help of multiple digital fundus cameras at a different FOV [31, 32].

2.13   Digital Retinal Images for Vessel Extraction (DRIVE)

DRIVE is an online available database used for the evaluation of results obtained from the segmentation of blood vessels for colored retinal images. The images with the 768 × 584-pixel resolution were taken using a Canon CR5 camera at a 45° FOV from the screening population consisting of 400 diabetic patients in 25–90 years of age group. A total of 40 images are divided into training and test categories [33–35].

2.14   High-Resolution Fundus (HRF) Image Database

HRF is also an online available color retinal image database used for the detection of retinal complications. It contains 15 images with no sign of any abnormality, 15 images with diabetic retinopathy, and 15 images with glaucoma captured by a high-resolution Canon CR1 fundus camera. A group of medical experts has provided binary gold standard vessel segmentation as a benchmark [34, 36, 37].

3   Literature Review of Enhancement Techniques

Previously performed works under retinal image enhancement are reviewed in this section. Enhancement is extremely required as medical images are extremely prone to noise and bad contrast. The related works are discussed:

Zimmerman et al. [38] proposed a methodology in which the effectiveness of Adaptive Histogram Equalization (AHE) and intensity windowing was used for contrast enhancement. As per the results obtained, there was a less significant difference between AHE and intensity windowing methods for depicting luminance contrast [38].

Polesel et al. [39] provided an adaptive algorithm for contrast enhancement in which sharpening action was performed only where significant dynamics were present. This led to reduced amplification of noise for better contrast enhancement. It was capable of handling overshoot artifacts [39].

Qureshi and Shaheed [35] suggested a real-time mechanism of fundus image enhancement for early grading of abnormalities. International Commission on Illumination Color appearance model was used for enhancement. Further texture and color features were calculated. For evaluation of results, PSNR, a contrast to noise ratio, and SSIM were calculated. Enhancement through the technique outperformed the HE technique [35].

Duan and Qiu [40] provided a histogram processing algorithm for color image enhancement using original image pixel distribution. A single parameter was used here to control the degree of contrast enhancement that provided better results.

Initially, an algorithm for the luminance channel was developed, and then it was used for color components [40].

Foracchia et al. [41] suggested a methodology for luminosity and contrast normalization for retinal images. It was based on the estimation of luminosity and contrast variability in the background part of an image. It was provided with better normalization. They reduced luminance variability and increased image contrast of retinal images [41].

Feng et al. [42] provided a contrast enhancement technique using contour transform. It provided better enhancement than wavelets. The method was compared with wavelet transform HE, local normalization, and linear unsharp masking. It was found more satisfactory for low contrast and dynamic range images for vessel segmentation [42].

Ibrahim and Kong [43] suggested a method for brightness preserving dynamic histogram equalization that provided an output image with a mean intensity equal to the mean intensity of input. This method was found to be better than HE methods [43].

Nirmala et al. [44] provided a simple method to assess the quality of compressed retinal images. The overall quality of the image were given by Laplacian MSE. For evaluating the performance, MSE, PSNR, and SSIM were calculated [44].

Liao et al. [45] suggested a methodology for enhancement of retinal vessels based on multiscale top-hat transformation along with histogram stretching. The characteristics of enhanced retinal images were then analyzed using measurement of contrast and Contrast Improvement Index (CII) [45].

Khan et al. [46] explained retinal image enhancement using Laplacian pyramidal multi-scaling. Images were converted into scales using gray conversion, texture analysis, and desired frequencies were extracted. Reconstruction of the image was performed by adding extracted frequencies with the original image. Enhanced images appeared as a better source for edge detection and vessel extraction based on object background contrast ratio, contrast noise ratio, and 2D contour plot [46].

Jintasuttisak and Intajag [47] suggested a methodology for color retinal image enhancement using Rayleigh CLAHE. They utilized an improved nonlinear hue-saturation-intensity color model for preserving color information of original retinal images [47].

Rani and Kumar [48] acquired a technique for image contrast enhancement with a weighting distribution approach and better adaptive gamma correction. The contrast and brightness of the original image were enhanced by preserving its features for image analysis purposes [48].

Soomro and Gao [49] suggested a non-invasive contrast normalization and denoising technique for retinal images. It was based on the Retinex algorithm and stationary wavelet transform for noise removal. The performance was measured using peak signal-to-noise ratio and contrast improvement factor [49].

Shamsudeen and Raju [50] described enhancement of fundus images using a color model adequate channel to be equalized and histogram specification provided with maximum gray level contrast. It was observed that the RGB model outperformed the HSV model in all aspects [50].

Bandara and Giragama [51] devised a system for blood vessel segmentation using retinal image enhancement. They presented an assessment of the adaptive contrast enhancement technique for retinal images for segmentation. The technique was integrated with the Tyler Coye algorithm. A comparison was performed based on the techniques using wavelet transform, CLAHE, local normalization, linear un-sharp masking, and contourlet transform [51].

Kumar et al. [52] presented a technique for iris contrast enhancement using histogram equalization and CLAHE using a high-resolution fundus iris database. The performance was measured in terms of PSNR and MSE [52].

Sahu et al. [12] described a technique for denoising and enhancement of retinal images using CLAHE. Integration of filters was used for denoising. The performance of the method was evaluated by PSNR, SSIM, correlation coefficient, and edge preservation index with maximum improvements over the other methods [12].

Das et al. [53] suggested a scheme for region selective information augmentation for retinal images. It utilized a patch-based region selective approach in which enhancement was performed by contrast stretching. The performance was evaluated using PSNR and SSIM [53].

Sabri and Yazid [54] provided data about image enhancement methods for fundus retina images. Seven preprocessing steps were combined and presented. The images obtained from these datasets were categorized into dark and light images. Based on the results obtained, the best value of log transformation was applied after the power-law function was set to 0.7 for the dark image and 0.9 for the brighter image [54].

Kumar et al. [55] suggested equalization techniques for the enhancement of retinal fundus image quality using noise filtering and contrast enhancement techniques. Noise adaptive fuzzy switching median filter and block-matching 3D filtering techniques were implemented for denoising. HE, AHE, CLAHE, and Exposure-based Sub-Image Histogram Equalization (ESIHE) techniques were investigated one by one. ESIHE was found to be optimal. Performance evaluation of these techniques was carried out by determining the performance parameters such as histogram, SNR, entropy, AMBE, and PSNR of processed retinal fundus images [55].

Bannigidad and Deshpande [56] provided a hybrid approach for fundus images using enhancement techniques. It utilized CLAHE, mean filtering, Gaussian filtering, and morphological operations. Performance evaluation was performed by the measurement of PSNR, MSE, precision, and F measure [56].

Zulfahmi et al. [57] proposed an improved quality of image with CLAHE and filter variation. CLAHE was combined with filter order statistics, median filters, Gaussian filters, and Wiener filters for improving the quality of retinal images. The measurements of MSE and PSNR as parameters were performed for comparison between methods [57].

Arjuna et al. [58] described the performance analysis of various contrast enhancement techniques with illumination equalization. The quality of images was improved using contrast enhancement and illumination equalization techniques. Performance

of different contrast enhancement techniques with and without illumination equalization was analyzed for retinal fundus images. MSE and PSNR were the two performance metrics evaluated [58].

Jadhav and Shaikh [14] proposed a method to improve the quality of retinal images using optimization techniques. Median filter, average filter Weiner filter, and FFT were applied for noise removal. The performance of the method was evaluated using PSNR, RMSE, and correlation coefficient [14].

You et al. [59] proposed the Cycle Convolutional Block Attention Module (Cycle CBAM) method to realize the relocation from poor-quality fundus images to good-quality fundus images. They used Cycle CBAM to alleviate the texture and detail degeneration induced by training unpaired images. The improved fundus image was quantitatively and qualitatively examined. In addition, a Diabetic Retinopathy (DR) classification module was introduced to evaluate the DR level of the fundus images before and after enhancement. The Cycle CBAM was observed to have superior outcomes [59].

Gupta and Tiwari [60] suggested a method for overall contrast enhancement for retinal images. The Quantile-based histogram equalization method was used for increasing overall visibility. For evaluation purposes, PSNR and SSIM features were measured [60].

Palanisamy et al. [61] provided an improved technique for luminosity and contrast enhancement for feature preservation in color fundus images. The singular value equalization technique was applied for luminosity enhancement. $L * a * b$ color space model and CLAHE were used for contrast enhancement. The performance was analyzed using PSNR, AMBE, entropy, and measure of enhancement [61].

Bhardwaj et al. [62] proposed a technique for automatic blood vessel extraction of retinal images using a fuzzy approach. For enhancement of CLAHE was used. The performance parameters PSNR, SSIM, and RMSE value assured that the method was better as compared to the Kirsch algorithm [62].

Singh et al. [63] suggested a histogram equalization technique for enhancement of low-radiance retinal images for detection of diabetic retinopathy. To solve the problem of low light radiance, the technique focused on Radiance indicator-based histogram equalization for retinal vessel enhancement and Radiance indicator-based histogram equalization for recursive retinal vessel enhancement. Performance evaluation of these techniques was done by entropy, PSNR, SSIM, and Euclidian distance [63].

Listyalina et al. [64] described a method for retinal image quality improvement for diabetic retinopathy. The global and adaptive histogram equalization were used to enhance the images. Performance was evaluated by measuring MSE, PSNR, and SNR [64].

Setiawan et al. [65] provided a methodology in which the quality of fundus images improved by denoising the Convolutional Neural Network. The performance was evaluated using parameters like PSNR, MSE, and SSIM [65].

Jeyalaksshmi et al. [66] suggested a methodology for hard exudates detection from diabetic retinopathy using fuzzy logic. The HSV color model was used here

for the work. Hard exudates were separated using an adaptive fuzzy logic algorithm. MSE and PSNR were used as performance metrics [66].

Indumathi and Mangai [16] developed a technique in which an analysis was performed for fundus images using a convolutional neural network, hybrid neural network, and recurrent neural network along with the top-hat filter. As per the measurements of performance metrics like PSNR, MSE, and SSIM, hybrid neural network classifiers were found to be better [16].

Pal et al. [67] introduced an evaluation of the effectiveness of image enhancement techniques with application to retinal images. These enhancement techniques were CLAHE, Adaptive Gamma Correction (AGC), morphological enhancement operation, and Hessian matrix-based ridge enhancement. Visual information-based and statistical error-based performance metrics were used as Image Quality Assessment (IQA) indexes. These metrics were PSNR, AMBE, SSIM, correlation coefficient, and entropy [67].

Kandpal et al. [68] suggested a method of retinal image enhancement using Edge-based Texture Histogram Equalization (ETHE). They demonstrated that edge-based texture histogram equalization can correct contrast and illumination complications. ETHE was applied to retinal images in order to improve their quality that was detected using Blind Reference less Image Spatial Quality Evaluator. The image quality was improved by ETHE and was comparable in performance with Dominant Orientation-based Histogram Equalization (DOTHE), providing similar image quality improvement [68].

Bashir et al. [23] provided a contrast enhancement technique for fundus images. Enhancement was performed using B-Spline interpolation by passing through every point of the curve. The intensity transformation curve was computed based on control points of the curve [23].

Shen et al. [69] suggested a technique of modeling and enhancing low-quality images. As the low-quality fundus images may lead to misdiagnosis, they proposed a methodology in which initially the ophthalmoscope imaging system was analyzed and simulated a reliable degradation of major inferior-quality factors. Then based on the degradation model, a fundus enhancement network (cofe-Net) was proposed to suppress global degradation factors. Here the anatomical structures and pathological characteristics were preserved [69].

Wang et al. [70] proposed a methodology for retinal fundus image enhancement with image decomposition and visual adaption. They conducted image decomposition to divide the input image into three layers: base, detail, and noise layer. Illumination correction, detail enhancement, and denoising were conducted on these three layers. The datasets used were DIARETDB0 and DIARETDB1. Results obtained revealed that the method was much better as compared to other methods [70].

Alwazzan et al. [71] suggested a hybrid algorithm for the enhancement of color retinal fundus images using the Wiener filter and CLAHE. Out of three channels, the green channel of the colored image was passed through the Wiener filter followed by CLAHE. The performance of the method was measured using a contrast improvement index and linear index of fuzziness [71].

Bataineh and Almotairi [72] provided an enhancement algorithm for color retinal images based on structural details and illumination improvements for the HSV color model. Bilateral filters were used for enhancement and compared with histogram equalization, contrast stretching, and adaptive histogram equalization. For performance measurement, PSNR, entropy, and SSIM were evaluated [72].

4 Enhancement Techniques

Medical image enhancement is always a vital area of interest for researchers. These enhancement methods can be categorized into two parts, i.e. spatial domain and transform domain [73].

4.1 Spatial Domain Techniques

In the spatial domain, the enhancement is performed directly on the image pixels, whereas the transform domain involves frequency transformations. These digital techniques are observed to be more satisfactory as compared to photographic techniques. In spatial domain enhancement techniques, the pixel values are manipulated in the enhanced image.

4.2 Log Transformation Technique

The log transformation is one of the basic image enhancement techniques of the spatial domain. It can be used for contrast enhancement of dark images. In this technique, the gray levels of image pixels are varied. It maps a small range of gray values of input into wide range gray levels [74]. The general equation for log transformation can be written as given in Eq. 1.

$$S = c \log(1 + r) \tag{1}$$

S is gray output, c is constant, and r is gray level input (assumed that $r \geq 0$).

4.3 Power-Law Transformation Technique

Power-law transformation is another spatial domain for the gray level. It is performed by raising the input gray level using power. It is the same as log transformation but the difference is here the fractional value of power law maps a wide range of dark input

values into a large range of output by increasing contrast [54]. The basic equation for power-law transformation is as given in Eq. 2:

$$S = br^{\gamma} \tag{2}$$

Here, S is gray output, b is constant, and γ is power for which level of input is raised, and r is input gray level.

4.4 Frequency Domain Transformations

In frequency domain transformations, input image is converted into frequency domain first. Fourier transform of images is performed first; after processing in frequency form again it is converted back to resultant image using an inverse Fourier transform. Image brightness, contrast, and gray level distribution are increased in this technique [74, 75].

4.5 Contrast Stretching

The contrast stretching technique is one of the frequency domain techniques used to stretch the dynamic range of an image. Dynamic range can be defined as the range between minimum intensity and maximum intensity of an image. Mathematically, it can be expressed as per Eq. 3.

$$A'(i.j) = \frac{d}{(A_{\max} - A_{\min})}(I(i, j) - A_{\min}) + A_o \tag{3}$$

Here, d is the new dynamic range value, $A'(i, j)$ is the new dynamic range image, $A_{\min}$ is the minimum intensity of input image, $A_{\max}$ is the maximum intensity of input image, and A_o is the offset point. This transformation provides satisfactory visual representation [76].

4.6 Histogram Equalization (HE)

Histogram equalization is a technique used for enhancement in which an image histogram is used for contrast adjustment and helps in redistributing intensity distribution. A uniform histogram is obtained with this method which improves contrast values. It is further of three types, global histogram equalization, adaptive histogram equalization, and block-based histogram equalization [76–78].

Global histogram equalization (GHE): In GHE, each pixel is assigned a new pixel value. The cumulative histogram needs to be equalized by 255 for an enhanced image. Mathematically, it can be written as per Eq. 4:

$$A'(i.j) = \frac{d}{(C_{\max} - C_{\min})}(C(i) - \mathrm{I}_{\min}) + A_o \tag{4}$$

Here, d is the dynamic range value, $A'(i, j)$ is the new dynamic range image, $C(i)$ is the normalized cumulative value, and $C_{\min}$ is the minimum value of normalized cumulative value. A_o is the offset point [76, 79, 80].

Adaptive Histogram equalization (AHE): AHE is a type of histogram technique used to enhance the contrast of dull images. AHE focuses on overall contrast whereas histogram equalization focuses on local contrast values. With the help of AHE, images having dull contrast, lighter or darker can be easily enhanced [79, 81].

Block-based histogram equalization (BHE): BHE is an advanced version of GHE and AHE. Here, overlapped blocks are used for enhancement. The input image is divided into small blocks, and HE is applied to each block. Blocks are overlapped half by each other to overcome the problem of block discontinuity [82].

$$A(i, j) = \sum_{b=1}^{N} g_b(i, j) \times A_b(i, j) \tag{5}$$

Here, b is the block of input image, $A_b(i, j)$ is intensity value of block b, and $A(i, j)$ is smoothed image. The value of the N block will depend upon the position of the image block. $g_b(i, j)$ is weighting function which is equal to the product of individual weighting function in i and j directions.

4.7　Brightness Preserving Bi-Histogram Equalization

Brightness preserving bi-histogram equalization (BBHE) is a form of histogram equalization whose main objective is to preserve the mean brightness of an image [83, 84]. The image under consideration is divided into two parts by BBHE. The intensity of each partition is expressed in the average intensity of each pixel of the image [52, 78, 85, 86].

4.8 *Contrast Limited Adaptive Histogram Equalization (CLAHE)*

CLAHE is a variant of histogram equalization in which the input image is divided into non-overlapping parts of equal size. Here, pixels of an image are mapped using a linear combination of nearest regions [87–89]. CLAHE has two key parameters, block size (BS) and clip limit (CL). These two parameters control the quality of an enhanced image. With an increase in the CL value, brightness of the low-intensity input image increased. The histogram also gets flattened with increased CL value. Because the size of BS is large, the dynamic range becomes large with an increase in contrast [90].

4.9 *Dual-Tree Complex Wavelet Transform (DTWCT)*

Dual-tree complex wavelets method is an advanced form of wavelet transform which solves the problem of shift variance as well as low directional selectivity in two or higher dimensions. The main purpose of DTWCT is texture classification and recovery of images based on content. The noise removal capability of DTWCT is quite high [91–94].

Table 3 shows different enhancement techniques used by various researchers for the enhancement of retinal images.

5 Performance Parameters

5.1 *Peak Signal-To-Noise Ratio*

Peak signal-to-noise ratio (PSNR) is the ratio of an image's maximum possible power value to the power of noise produced, which impacts image quality. It is a metric for describing the quality of an image after any enhancement approach has been applied. If the value of PSNR is high, the quality of the reconstructed image is said to be better [52, 84].

Mathematically, the expression for PSNR can be written as given in Eq. 6:

$$PSNR = 10 \, Log_{10} \frac{(Peak \ Value)^2}{MSE} \tag{6}$$

where the Peak value is the maximum difference in input image value and MSE is the mean square error.

Table 3 Enhancement techniques

Enhancement technique	Name of author(s)
Histogram equalization	Chen and Ramli [78]
	Abdullah-Al-Wadud et al. [79]
	Wang and Ward [92]
	Ibrahim and Kong [43]
	Zakaria et al. [76]
	Dehghani et al. [95]
	Fazli et al. [79]
	Zuo and Sui [80]
	Yang et al. [77]
	Kumar [52]
	Kumar et al. [55]
	Singh et al. [63]
	Karthi and Subhashini [74]
	Indumathi [16]
	Kandpal and Jain [68]
Adaptive histogram equalization	Zimmerman et al. [38]
	Wu et al. [96]
	Saleh et al. [89]
	Raja et al. [97]
	Fazli et al. [81]
	Vaidya and Doiphode [98]
	Priyadharshini and Anitha [99]
	Listyalina et al. [64]
Contrast limited adaptive histogram equalization	Reza [87]
	Saleh et al. [89]
	Jintasuttisak and Intajag [47]
	Setiawan et al. [100]
	Dai et al. [101]
	Ma et al. [90]
	Bannigdad and Deshpande [56]
	Maheshan et al. [102]
	Mazlan et al. [88]
	Erwin et al. [57]
	Sonali et al. [12]
	Patil and Patil [103]
	Santos et al. [104]
	Tian et al. [105]

(continued)

Table 3 (continued)

Enhancement technique	Name of author(s)
	Yadav et al. [106]
	Alwazzan et al. [71]
Brightness preserving bi-histogram equalization	Chen and Ramli [86]
	Chen and Ramli [78]
	Wang and Ye [83]
	Abdullah-Al-Wadud et al. [79]
	Moniruzzaman et al. [85]
	Tang and Isa [84]
	Kumar [52]
	Singh et al. [63]
	Wang et al. [75]
Dual-tree complex wavelet transform	Selesnick et al. [91]
	Priya and Rajesh [93]
	Chitchian et al. [107]
	Baby et al. [108]
	Galshetwar et al. [109]
	Li et al. [110]
	Goyal and Meenpal [94]
	Liu et al. [111]

5.2 Mean Square Error

Mean square error (MSE) can be defined as the mean of squared error between an enhanced image and an original image. MSE can be used to quantify the difference between values implied by an estimator. It denotes a risk function corresponding to the expected value of squared error. The mean square error can be computed as per Eq. 7:

$$\text{MSE} = \frac{1}{M \times N} \sum_{i=0,\, j=0}^{M-1, N-1} (A(i, j) - B(i, j))^2 \qquad (7)$$

Here, $M \times N$ describes the size of an image and $A(i, j)$ is the enhanced image, and $B(i, j)$ is the original image [11].

5.3 Structural Similarity Index

The structural similarity index metric is a performance metric used to examine image quality. It is the evaluation of the amount of similarity between enhanced and original images. If the value of SSIM is high, the images are said to be structurally identical and better enhanced [63].

Mathematically, it can be written as per Eq. 8:

$$SSIM(i, j) = \left[lu(i, j)^p . Cs(i, j)^q . St(i, j)^r \right] \tag{8}$$

Here, i, j are windows of the same dimension. Luminance, structure, and contrast are lu, Cs, and St. The p, q, and r are the weights of these parameters. Equations 9, 10, and 11 denote the calculation of lu, Cs, and St.

Luminance

$$lu(i, j) = \frac{2u_i u_j + c_1}{u_i^2 + u_j^2 + c_1} \tag{9}$$

Contrast

$$Cs(i, j) = \frac{2v_i v_j + c_2}{v_i^2 + v_j^2 + c_2} \tag{10}$$

Structure

$$St(i, j) = \frac{v_{ij} + c_3}{v_i v_j + c_3} \tag{11}$$

Here, u_j = average of the reconstructed image, u_i = average of the original image, u^2 is the variance of i, v_j^2 = variance of j, and $v_i v_j$ = covariance of i and j. c_1 and c_2 parameters are used for denominator stabling and $c_3 = c_2/2$. If the value of SSIM is 1, it signifies perfect similarity between enhanced and original images [112].

5.4 Absolute Mean Brightness Error (AMBE)

Absolute mean brightness error is a performance metric used for the measurement of mean brightness error between enhanced and original images. If the value of AMBE is found low, the enhancement is said to be better. The purpose of AMBE is to check how much glitter is safeguarded in the enhanced image. It is also known as an intemperate brightness change in images. Mathematically, it can be given as per Eq. 12 [48, 86]:

$$\text{AMBE} = [E(o) - E(e)] \tag{12}$$

Here, '*o*' is the original image, and '*e*' is the enhanced image, E denotes the mean of an image, $E(o)$ is the mean of the original image, and $E(e)$ is the mean of the enhanced image.

5.5 Root Mean Square Error (RMSE)

Root mean square error is a performance metric that denotes an average of squared intensities of original and enhanced image. It normally denotes the root of a mean square error value. A higher value of mean square error and root mean square error denotes the best enhancement with less distortion [11].

Mathematically, it can be given as per Eq. 13:

$$\text{RMSE} = \sqrt{\frac{1}{M \times N} \sum_{i=0, j=0}^{M-1, N-1} [A(i, j) - B(i, j)]^2} \tag{13}$$

Here, $M \times N$ describes the size of the image and $A(i, j)$ is the enhanced image, and $B(i, j)$ is the original image.

5.6 Entropy

Entropy is a performance feature that represents the average information content of an enhanced image. It is used to characterize the texture of an image. Mathematically, entropy can be written as

$$\text{Entropy} = - \sum_{i=1}^{n} p(i) \log_2 p(i) \tag{14}$$

Here, i denotes the intensity level of an image, $p(i)$ denotes the probability density function, and n denotes the number of gray levels [35, 78, 113–115].

5.7 *Feature Similarity Index Metrics (FSIM)*

A feature similarity index metric is a performance metric that signifies the quality of an enhanced image. It uses phase congruency and gradient magnitude as a feature of the image. If the value of FSIM is nearby unity, the enhanced image is said to have all the features of the original image. Mathematically, FSIM can be written as

$$\text{FSIM} = \frac{\sum_{i \in \Omega} S_L(i) \text{PC}_m(i)}{\sum_{i \in \Omega} \text{PC}_m(i)} \tag{15}$$

Here, S_L denotes overall similarity of enhanced, Ω denotes spatial domain of whole image and original image, and PC_m denotes overall congruency between original and enhanced image [116–118]. Table 4 shows the performance metrics comparison of various features of a retinal image with their mathematical equation and corresponding authors.

6 Conclusions

Enhancement plays an important role in the identification of an abnormality in any medical image. We have studied the various enhancement techniques that were used by researchers to enhance the quality of retinal images in terms of various image quality assessment metrics. As per the above study, researchers are using various histogram equalization and wavelet transformation techniques for retinal image enhancement. In some methods, the combinations of various filters and histogram equalization techniques are used. These methods and techniques can give a solid base for further research work in the field of retinal image analysis.

Table 4 Performance
metrics used in literature

Feature metrics	Authors
Peak signal-to-noise ratio (PSNR)	Bhardwaj et al. [62] Bannigidad and Deshpande [56] Das et al. [53] Gupta and Tiwari [60] Jadhav and Shaikh [14] Kumar et al. [52] Nirmala et al. [44] Tang and Isa [84] Palanisamy et al. [61] Singh et al. [63] Sonali et al. [12] Soomro and Gao [49]
Structural similarity index metrics (SSIM)	Bhardwaj et al. [62] Das et al. [53] Gupta and Tiwari [60] Indumathi [16] Setiawan [65] Sonali et al. [12] Singh et al. [63]
Mean square error (MSE)	Asamoah et al. [11] Bannigidad and Deshpande [56] Bashir et al. [23] Jadhav and Shaikh [14] Karthi and Subhashini [74] Kothandaraman et al. [119] Kumar et al. [52] Listyalina et al. [64] Ma et al. [90] Nirmala et al. [44] Ramasubramanian and Selvaperumal [120] Rani and Kumar [48] Triwijoyo and Adil [121]
Root mean square error (RMSE)	Asamoah et al. [11] Jadhav and Shaikh [14] Nirmala et al. [44] Patton et al. [122] Triwijoyo and Adil [121]
Absolute mean brightness error (AMBE)	Chen and Ramli [86] Tang and Isa [84] Asamoah et al. [11] Indumathi [16] Karthi and Subhashini [74] Nirmala et al. [44] Rani and Kumar [48]
Entropy	Chen and Ramli [78] Mendonca et al. [113] Qureshi et al. [35] Yu et al. [114] Subramani and Veluchamy [115]

Table 4 (continued)

Feature metrics	Authors
Feature similarity index metrics (FSIM)	Patil et al. [123] Zhang et al. [116] Gandhamal et al. [118]

References

1. Klein R, Klein BE, Moss SE, Davis MD, DeMets DL (1984) The Wisconsin epidemiologic study of diabetic retinopathy. III. Prevalence and risk of diabetic retinopathy when age at diagnosis is 30 or more years. Arch Ophthalmol (Chicago, Ill. 1960) 102:527–32
2. Gargeya R, Leng T (2017) Automated identification of diabetic retinopathy using deep learning. Ophthalmology 124:962–969
3. Abràmoff MD, Reinhardt JM, Russell SR, Folk JC, Mahajan VB, Niemeijer M, Quellec G (2010) Automated early detection of diabetic retinopathy. Ophthalmology 117:1147–1154
4. Datta NS, Saha P, Dutta HS, Sarkar D, Biswas S, Sarkar P (2015) A new contrast enhancement method of retinal images in Diabetic Screening System. In: 2015 IEEE 2nd international conference on recent trends in information systems (ReTIS), pp 255–260
5. Atlas IDFD (1955) International diabetes federation. Lancet 266:134–137
6. Fadzil MHA, Nugroho HA, Nugroho H, Iznita IL (2009) Contrast enhancement of retinal vasculature in digital fundus image. In: International conference on digital image processing, pp 137–141
7. Nugroho HA, Dharmawan DA, Hidayah I, Listyalina L (2015) Automated microaneurysms (MAs) detection in digital colour fundus images using matched filter. In: 2015 international conference on computer, control, informatics and its applications (IC3INA), pp 104–108
8. Seoud L, Chelbi J, Cheriet F (2015) Automatic grading of diabetic retinopathy on a public database. In: Proceedings of the ophthalmic medical image analysis second international workshop, pp 97–104
9. Ricard P (2009) Vision loss and visual hallucinations: the Charles Bonnet syndrome. Community Eye Heal 22:14
10. Bock R, Meier J, Nyúl LG, Hornegger J, Michelson G (2010) Glaucoma risk index: automated glaucoma detection from color fundus images. Med Image Anal 14:471–481
11. Asamoah D, Ofori E, Opoku S, Danso J (2018) Measuring the performance of image contrast enhancement technique. Int J Comput Appl 181:6–13
12. Sonali, Sahu S, Singh AK, Ghrera SP, Elhoseny M (2019) An approach for de-noising and contrast enhancement of retinal fundus image using CLAHE. Opt Laser Technol 110:87–98
13. Kauppi T, Kalesnykiene V, Kamaranen J, Lensu L, Sorri I (2006) DIARETDB0: evaluation database and methodology for diabetic retinopathy algorithms. In: Machine vision and pattern recognition research group, Lappeenranta University of Technology, Finland, pp 1–17
14. Jadhav ML, Shaikh MZ (2019) Optimization of noise removal techniques for diabetic retinopathy. 9:66–72
15. Kauppi T, Kalesnykiene V, Kamarainen JK, Lensu L, Sorri I, Raninen A, Voutilainen R, Uusitalo H, Kälviäinen H, Pietilä J (2007) The DIARETDB1 diabetic retinopathy database and evaluation protocol. In: Proceedings of the British machine vision conference 2007, pp 15.1–15.10
16. Indumathi P (2020) Performance analysis of diabetic fundus images using CNN, RNN, HNN algorithms. 9:7822–7830
17. Niemeijer M, Van Ginneken B, Cree MJ, Mizutani A, Quellec G, Sánchez CI, Zhang B, Hornero R, Lamard M, Muramatsu C, Wu X (2010) Retinopathy online challenge: automatic detection of microaneurysms in digital color fundus photographs. IEEE Trans Med Imaging 29:185–195

18. Ali Shah SA, Laude A, Faye I, Tang TB (2016) Automated microaneurysm detection in diabetic retinopathy using curvelet transform. J Biomed Opt 21:101404

19. Dashtbozorg B, Zhang J, Huang F, ter Haar Romeny BM (2018) Retinal microaneurysms detection using local convergence index features. IEEE Trans Image Process 27:3300–3315

20. IDRiD—Indian-diabetic-retinopathy-image-dataset. https://ieee-dataport.org/open-access/indian-diabetic-retinopathy-image-dataset-idrid

21. Momeni Pour A, Seyedarabi H, Abbasi Jahromi SH, Javadzadeh A (2020) Automatic detection and monitoring of diabetic retinopathy using efficient convolutional neural networks and contrast limited adaptive histogram equalization. IEEE Access 8:136668–136673

22. Messidor Database. http://www.adcis.net/en/third-party/messidor, http://www.adcis.net/en/third-party/messidor/

23. Bashir T, Asghar K, Saddique M, Hussain S, Ul I (2020) Enhancement of fundus images for diagnosing diabetic retinopathy using B-spline. Int J Adv Comput Sci Appl 11:233–239

24. Messidor 2 Database. http://www.adcis.net/en/third-party/messidor2/

25. Saxena G, Verma DK, Paraye A, Rajan A, Rawat A (2020) Improved and robust deep learning agent for preliminary detection of diabetic retinopathy using public datasets. Intell Med 3–4:100022

26. E-Optha EX. http://www.adcis.net/en/third-party/e-ophtha/

27. Reshma Chand CP, Dheeba J (2015) Automatic detection of exudates in color fundus retinopathy images. Indian J Sci Technol 8:1–8

28. E-Optha MA. http://www.adcis.net/en/third-party/e-ophtha/

29. Wu B, Zhu W, Shi F, Zhu S, Chen X (2017) Automatic detection of microaneurysms in retinal fundus images. Comput Med Imaging Graph 55:106–112

30. Li T, Gao Y, Wang K, Guo S, Liu H, Kang H (2019) Diagnostic assessment of deep learning algorithms for diabetic retinopathy screening. Inf Sci (Ny) 501:511–522

31. Kaggle/EyePACS. https://www.kaggle.com/c/diabetic-retinopathy-detection/data

32. Kaplan S, Lensu L, Laaksonen L, Uusitalo H (2020) Evaluation of unconditioned deep generative synthesis of retinal images, pp 262–273

33. DRIVE. https://drive.grand-challenge.org/

34. Budai A, Bock R, Maier A, Hornegger J, Michelson G (2013) Robust vessel segmentation in fundus images. Int J Biomed Imaging 2013:1–11

35. Qureshi I, Ma J, Shaheed K (2019) A hybrid proposed fundus image enhancement framework for diabetic retinopathy. Algorithms 12:14

36. Annunziata R, Garzelli A, Ballerini L, Mecocci A, Trucco E (2016) Leveraging multiscale hessian-based enhancement with a novel exudate inpainting technique for retinal vessel segmentation. IEEE J Biomed Heal Inform 20:1129–1138

37. Amin J, Sharif M, Yasmin M, Ali H, Fernandes SL (2017) A method for the detection and classification of diabetic retinopathy using structural predictors of bright lesions. J Comput Sci 19:153–164

38. Zimmerman JB, Pizer SM, Staab EV, Perry JR, McCartney W, Brenton BC (1988) An evaluation of the effectiveness of adaptive histogram equalization for contrast enhancement. IEEE Trans Med Imaging 7:304–312

39. Polesel A, Ramponi G, Mathews VJ (1997) Adaptive unsharp masking for contrast enhancement. In: Proceedings of international conference on image processing, vol 1, pp 267–270

40. Duan J, Qiu G (2004) Novel histogram processing for colour image enhancement. In: Third international conference on image and graphics (ICIG'04), pp 55–58

41. Foracchia M, Grisan E, Ruggeri A (2005) Luminosity and contrast normalization in retinal images. Med Image Anal 9:179–190

42. Feng P, Pan Y, Wei B, Jin W, Mi D (2007) Enhancing retinal image by the Contourlet transform. Pattern Recognit Lett 28:516–522

43. Ibrahim H, Pik Kong N (2007) Brightness preserving dynamic histogram equalization for image contrast enhancement. IEEE Trans Consum Electron 53:1752–1758

44. Nirmala SR, Dandapat S, Bora PK (2007) Image quality assessment in retinal image compression systems. IET Semin Dig 737–742

45. Liao M, Zhao Y, Wang X, Dai P (2014) Retinal vessel enhancement based on multi-scale top-hat transformation and histogram fitting stretching. Opt Laser Technol 58:56–62

46. Khan S, Qidwai U, Muhammad H, Qidwai U (2014) Retinal image enhancement using Laplacian pyramidal multi-scaling. In: IEEE region 10 symposium, pp 141–146

47. Jintasuttisak T, Intajag S (2014) Color retinal image enhancement by Rayleigh contrast-limited adaptive histogram equalization. In: 2014 14th international conference on control, automation and systems (ICCAS 2014), pp 692–697

48. Rani S, Kumar M (2014) Contrast enhancement using improved adaptive gamma correction with weighting distribution technique. Int J Comput Appl 101:47–53

49. Soomro TA, Gao J (2016) Non-invasive contrast normalisation and denosing technique for the retinal fundus image. Ann Data Sci 3:265–279

50. Shamsudeen FM, Raju G (2016) Enhancement of fundus imagery. In: 2016 international conference on next generation intelligent systems (ICNGIS), pp 1–5

51. Bandara AMRR, Giragama PWGRMPB (2017) A retinal image enhancement technique for blood vessel segmentation algorithm. In: International conference on industrial and information systems (ICIIS), pp 1–5

52. Kumar M (2017) A performance analysis on iris image enhancement using histogram techniques. 8:28–32

53. Das V, Dandapat S, Bora PK (2018) Region selective information augmentation for retinal images. In: 2018 twenty fourth national conference on communications (NCC), pp 1–5

54. Binti Sabri NR, Yazid HB (2018) Image enhancement methods for fundus retina images. In: 2018 IEEE student conference on research and development (SCOReD), pp 1–6

55. Kumar S, Choudhary S, Gupta R, Kumar B (2018) Performance evaluation of joint filtering and histogram equalization techniques for retinal fundus image enhancement. In: 2018 5th IEEE Uttar Pradesh section international conference on electrical, electronics and computer engineering (UPCON), pp 1–5

56. Bannigidad P, Deshpande A (2017) A hybrid approach for digital fundus images using image enhancement techniques. Int J Comput Eng Appl 12:122–131

57. Zulfahmi R, Noviyanti DS, Utami GR, Harison AN, Agung PS (2019) Improved image quality retinal fundus with contrast limited adaptive histogram equalization and filter variation. In: International conference on informatics, multimedia, cyber and information system (ICIMCIS), pp 49–54

58. Arjuna A, Rose RR (2019) Performance analysis of various contrast enhancement techniques with illumination equalization on retinal fundus images. In: 2019 international conference on smart systems and inventive technology (ICSSIT), pp 406–411

59. You Q, Wan C, Sun J, Shen J, Ye H, Yu Q (2019) Fundus image enhancement method based on CycleGAN. In: 41st annual international conference of the IEEE engineering in medicine and biology society (EMBC), pp 4500–4503

60. Gupta B, Tiwari M (2019) Color retinal image enhancement using luminosity and quantile based contrast enhancement. Multidimens Syst Sig Process 30:1829–1837

61. Palanisamy G, Ponnusamy P, Gopi VP (2019) An improved luminosity and contrast enhancement framework for feature preservation in color fundus images. Sig Image Video Process 13:719–726

62. Bhardwaj C, Jain S, Sood M (2019) Automatic blood vessel extraction of fundus images employing fuzzy approach. Indones J Electr Eng Inform 7

63. Singh N, Kaur L, Singh K (2019) Histogram equalization techniques for enhancement of low radiance retinal images for early detection of diabetic retinopathy. Eng Sci Technol Int J 22:736–745

64. Listyalina L, Yudianingsih Y, Dharmawan DA (2020) Retinal digital image quality improvement as A diabetes retinopatic disease detection effort. J. Electr Technol UMY 4:53–60

65. Setiawan W, Utoyo MI, Rulaningtyas R (2020) Denoising convolutional neural network for fundus patches quality. J Phys Conf Ser 1569:022061

66. Jeyalaksshmi S, Padmapriya D, Midhunchakkravarthy D, Ameen A (2020) Detection of hard exudate from diabetic retinopathy image using fuzzy logic, pp 543–550

67. Pal MN, Banerjee M (2020) Evaluation of effectiveness of image enhancement techniques with application to retinal fundus images. In: 2020 4th international conference on computational intelligence and networks (CINE), pp 1–6

68. Kandpal A, Jain N (2020) Retinal image enhancement using edge-based texture histogram equalization. In: 2020 7th international conference on signal processing and integrated networks (SPIN), pp 477–482

69. Shen Z, Fu H, Shen J, Shao L (2021) Modeling and enhancing low-quality retinal fundus images. IEEE Trans Med Imaging 40:996–1006

70. Wang J, Li Y-J, Yang K-F (2021) Retinal fundus image enhancement with image decomposition and visual adaptation. Comput Biol Med 128:104116

71. Alwazzan MJ, Ismael MA, Ahmed AN (2021) A hybrid algorithm to enhance colour retinal fundus images using a wiener filter and CLAHE. J Digit Imaging

72. Bataineh B, Almotairi KH (2021) Enhancement method for color retinal fundus images based on structural details and illumination improvements. Arab J Sci Eng

73. Victoria LB (2015) A study on spatial domain and transform domain steganography techniques used in image hiding. Int J Innov Technol Creat Eng 5:273–276

74. Karthi M, Subhashini K (2020) An comprehensive analysis and implementation of different image enhancement techniques. Psychol Educ 57:2049–2058

75. Wang W, Wu X, Yuan X, Gao Z (2020) An experiment-based review of low-light image enhancement methods. IEEE Access 8:87884–87917

76. Firdaus Zakaria M, Ibrahim H, Azmin Suandi S (2010) A review: image compensation techniques. In: 2010 2nd international conference on computer engineering and technology, vol. 7, pp V7-404–V7-408

77. Yang J, Zhong W, Miao Z (2016) On the image enhancement histogram processing. In: 2016 3rd international conference on informative and cybernetics for computational social systems (ICCSS), pp 252–255

78. Chen S-D, Rahman Ramli A (2004) Preserving brightness in histogram equalization based contrast enhancement techniques. Digit Sig Process 14:413–428

79. Abdullah-Al-Wadud M, Kabir M, Akber Dewan M, Chae O (2007) A dynamic histogram equalization for image contrast enhancement. IEEE Trans Consum Electron 53:593–600

80. Zuo C, Chen Q, Sui X (2013) Range limited bi-histogram equalization for image contrast enhancement. Optik (Stuttg) 124:425–431

81. Fazli S, Samadi S, Nadirkhanlou P (2013) A novel retinal vessel segmentation based on local adaptive histogram equalization. In: 8th Iranian conference on machine vision and image processing (MVIP), pp 131–135

82. Xie X, Lam K-M (2005) Face recognition under varying illumination based on a 2D face shape model. Pattern Recogn 38:221–230

83. Wang C, Ye Z (2005) Brightness preserving histogram equalization with maximum entropy: a variational perspective. IEEE Trans Consum Electron 51:1326–1334

84. Tang JR, Mat Isa NA (2014) Adaptive image enhancement based on bi-histogram equalization with a clipping limit. Comput Electr Eng 40:86–103

85. Moniruzzaman M, Shafuzzaman M, Hossain MF (2014) Brightness preserving Bi-histogram equalization using edge pixels information. In: 2013 international conference on electrical information and communication technology (EICT), pp 1–5

86. Chen S-D, Ramli AR (2003) Minimum mean brightness error bi-histogram equalization in contrast enhancement. IEEE Trans Consum Electron 49:1310–1319

87. Reza AM (2004) Realization of the contrast limited adaptive histogram equalization (CLAHE) for real-time image enhancement. J VLSI Sig Process Syst Sig Image Video Technol 38:35–44

88. Mazlan N, Yazid H, Sabri NR (2018) Enhancement of retinal images for microaneurysms detection in diabetic retinopathy. In: 2018 IEEE student conference on research and development (SCOReD), pp 1–5

89. Saleh MD, Eswaran C, Mueen A (2011) An automated blood vessel segmentation algorithm using histogram equalization and automatic threshold selection. J Digit Imaging 24:564–572

90. Ma J, Fan X, Yang SX, Zhang X, Zhu X (2018) Contrast limited adaptive histogram equalization-based fusion in YIQ and HSI color spaces for underwater image enhancement. Int J Pattern Recogn Artif Intell 32:1854018

91. Selesnick IW, Baraniuk RG, Kingsbury NC (2005) The dual-tree complex wavelet transform. IEEE Sig Process Mag 22:123–151

92. Wang Q, Ward R (2007) Fast image/video contrast enhancement based on weighted thresholded histogram equalization. IEEE Trans Consum Electron 53:757–764

93. Priya KJ, Rajesh RS (2010) Local statistical features of dual tree complex wavelet transform on parallelogram image structure for face recognition with single sample. In: 2010 international conference on recent trends in information, telecommunication and computing, pp 50–54

94. Goyal A, Meenpal T (2021) Patch-based dual-tree complex wavelet transform for kinship recognition. IEEE Trans Image Process 30:191–206

95. Dehghani A, Moghaddam HA, Moin M-S (2012) Optic disc localization in retinal images using histogram matching. EURASIP J Image Video Process 2012:19

96. Wu D, Zhang M, Liu J-C, Bauman W (2006) On the adaptive detection of blood vessels in retinal images. IEEE Trans Biomed Eng 53:341–343

97. Raja NSM, Kavitha G, Ramakrishnan S (2012) Analysis of vasculature in human retinal images using particle swarm optimization based Tsallis multi-level thresholding and similarity measures, pp 380–387

98. Vaidya YM, Doiphode SE (2014) Comparison of pre-processing methods for segmentation and approximation of optic disc boundary from processed digital retinal images. In: International conference on devices, circuits and communications (ICDCCom), pp 1–6

99. Priyadharshini MLG, Anitha JA (2014) Region growing method of optic disc segmentation in retinal images. In: 2014 international conference on electronics and communication systems (ICECS), pp 1–5

100. Setiawan AW, Mengko TR, Santoso OS, Suksmono AB (2013) Color retinal image enhancement using CLAHE. In: International conference on ICT for smart society, pp 1–3

101. Dai P, Sheng H, Zhang J, Li L, Wu J, Fan M (2016) Retinal fundus image enhancement using the normalized convolution and noise removing. Int J Biomed Imaging 2016:1–12

102. Maheshan MS, Harish BS, Nagadarshan N (2018) On the use of image enhancement technique towards robust sclera segmentation. Procedia Comput Sci 143:466–473

103. Patil BP (2020) Retinal fundus image enhancement using adaptive CLAHE methods. J Seybold Rep 15:3476–3484

104. dos Santos JCM, Carrijo GA, dos Santos Cardoso CDF, Ferreira JC, Sousa PM, Patrocínio AC (2020) Fundus image quality enhancement for blood vessel detection via a neural network using CLAHE and Wiener filter. Res Biomed Eng 36:107–119

105. Tian F, Li Y, Wang J, Chen W (2021) Blood vessel segmentation of fundus retinal images based on improved Frangi and mathematical morphology. Comput Math Methods Med 2021:1–11

106. Yadav D, Karn AK, Giddalur A, Dhiman A, Sharma S, Yadav AK (2021) Microaneurysm detection using color locus detection method. Measurement 176:109084

107. Chitchian S, Mayer MA, Boretsky AR, van Kuijk FJ, Motamedi M (2012) Retinal optical coherence tomography image enhancement via shrinkage denoising using double-density dual-tree complex wavelet transform. J Biomed Opt 17:116009

108. Baby CG, Chandy DA (2013) Content-based retinal image retrieval using dual-tree complex wavelet transform. In: International conference on signal processing, image processing an pattern recognition, pp 195–199

109. Galshetwar GM, Waghmare LM, Gonde AB, Murala S (2017) Edgy salient local binary patterns in inter-plane relationship for image retrieval in Diabetic Retinopathy. Procedia Comput Sci 115:440–447

110. Li D, Zhang L, Sun C, Yin T, Liu C, Yang J (2019) Robust retinal image enhancement via dual-tree complex wavelet transform and morphology-based method. IEEE Access 7:47303–47316

111. Liu H, Lin S, Ye C, Yu D, Qin J, An L (2020) Using a dual-tree complex wavelet transform for denoising an optical coherence tomography angiography blood vessel image. OSA Contin 3:2630

112. Rohani M, Avanaki AN (2009) A watermarking method based on optimizing SSIM index by using PSO in DCT domain. In: 14th international CSI computer conference (CSICC 2009), pp 418–422

113. Mendonça AM, Cardoso F, Sousa AV, Campilho A (2012) Automatic localization of the optic disc in retinal images based on the entropy of vascular directions, pp 424–431

114. Yu H, Barriga S, Agurto C, Zamora G, Bauman W, Soliz P (2012) Fast vessel segmentation in retinal images using multiscale enhancement and second-order local entropy. In: van Ginneken B, Novak CL (eds), p 83151B

115. Subramani B, Veluchamy M (2019) Fuzzy contextual inference system for medical image enhancement. Measurement 148:106967

116. Zhang L, Zhang L, Mou X, Zhang D (2011) FSIM: a feature similarity index for image quality assessment. IEEE Trans Image Process 20:2378–2386

117. Kulkarni S, Kamble R, Kokare M (2017) Automatic field of view extraction with variable enhancement of color fundus images. In: 14th IEEE India council international conference (INDICON), pp 1–5

118. Gandhamal A, Talbar S, Gajre S, Hani AFM, Kumar D (2017) Local gray level S-curve transformation—a generalized contrast enhancement technique for medical images. Comput Biol Med 83:120–133

119. Kothandaraman D, Balasundaram A, Korra S, Sudarshan E, Vijaykumar B (2020) Enhancing dull images using discrete wavelet families and fuzzy. IOP Conf Ser Mater Sci Eng 981

120. Ramasubramanian B, Selvaperumal S (2016) A comprehensive review on various preprocessing methods in detecting diabetic retinopathy. In: International conference on communication and signal processing (ICCSP), pp 642–646

121. Triwijoyo BK, Adil A (1979) Analysis of medical image resizing using Bicubic interpolation algorithm. J Ilmu Komput 14:20–29

122. Patton N, Aslam TM, MacGillivray T, Deary IJ, Dhillon B, Eikelboom RH, Yogesan K, Constable IJ (2006) Retinal image analysis: concepts, applications and potential. Prog Retin Eye Res 25:99–127

123. Patil S, Kulkarni V, Bhise A (2018) BEASF-based image enhancement for caries detection using multidimensional projection and neural network. Int J Artif Life Res 8:47–66

Electric Vehicle Charging Using Solar Energy

Rahul Kumar, Vinay Dhar Dwivedi, and Ananyo Bhattacharya

Abstract The concept of electric vehicle is mainly proposed for its less or no carbon emission qualities. With an increase in the number of electric vehicles on the road, charging the electric vehicle with a fossil fuel-based grid is not efficient and degrades the quality of less emission of EV. Thus, a renewable energy-based charging station finds immense potential and control for electric vehicle charging. This paper proposes a charging technique based on PV cells, i.e., use of PV cells for charging the batteries of electric vehicles. This method can be applied in remote areas where electricity is not available easily or at home also. The simulation of the above-proposed method is done on MATLAB.

1 Introduction

Electricity has been the greatest invention that not only morphed the lifestyle, but has been a pioneer for various other inventions, one such inventions is an electric vehicle. Electric vehicles are nowadays encouraged by many agencies in different countries of the world. As it is nature-friendly, i.e., it does not emit carbon. The use of an electric vehicle is increasing day by day, and the demand for energy to charge the vehicles is rising. As fossil fuels are limited, so as an alternative, we came up with renewable energy resources that are non-exhaustible and abundant in nature.

R. Kumar (✉) · V. D. Dwivedi · A. Bhattacharya
Electrical Engineering Department, National Institute of Technology (NIT), Jamshedpur, Jharkhand, India
e-mail: 2020pgeepe04@nitjsr.ac.in

V. D. Dwivedi
e-mail: 2020pgeepe09@nitjsr.ac.in

A. Bhattacharya
e-mail: ananyo.ee@nitjsr.ac.in

Among several renewable resources, solar energy is one of the most abundant and easily available. Solar radiance reaching the exosphere has the power of 1366 W per square meter (W/m^2) in which the atmosphere and ground absorb 70% of them and reflects back around 30% [1, 2]. Solar Irradiance at the earth surface is 1000 W/m^2.

Charging stations in India are limited to almost around 950 in total [3]. India is planning to have charging stations in around 3000 m radius in cities and at every 25 km on highways. Also, there should be at least one charging point at every refueling center. Implementation of such a huge plan on the grid will exert a lot of pressure on the grid. This pressure can be reduced by implementing solar cells for charging the batteries of the vehicles. Here, in this paper, an EV charging station based on solar energy is explained with a battery bank that supports the charging station at night when there is no solar irradiance [4]. This method can be installed at home also, where it can support the household electricity demand. The proposed method will be in an isolated condition, i.e., it is not connected to the power grid [5].

2 Charging Methodology

Figure 1 shows the block diagram of the process of charging of vehicle using a PV panel and battery bank. DC-DC converter provides the requirement of DC power to the bus by PV panel at sufficient solar irradiance. This DC-DC converter after solar cell in Fig. 1 provides the impedance matching and implements the MPPT technique [6]. Here P&O is used due to simplicity [7]. MPPT technique is used to obtain the maximum power from the PV system. The output of this converter is fed to the DC bus where Buck–Boost converter (charger) and Bidirectional converter are connected parallelly.
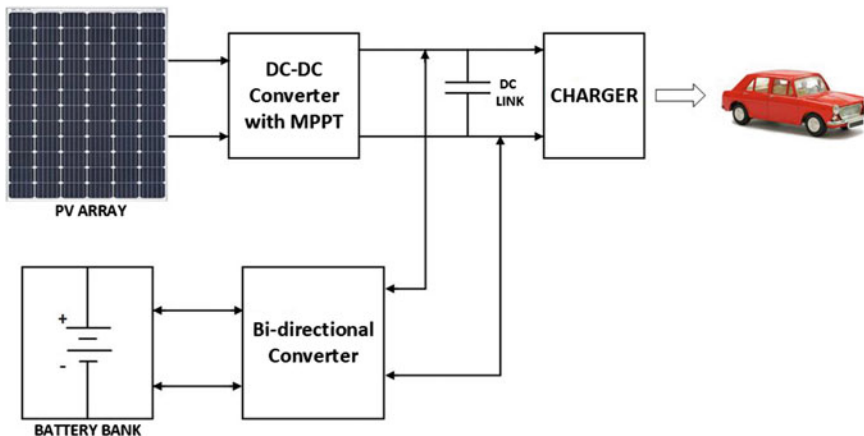
Fig. 1 Representation of EV charging station with solar cell

Here charger is Buck–Boost converter which is maintaining the terminal voltage at the charging point [8]. It is capable of working in both modes (i.e., buck and boost). If the bus voltage is greater than the nominal voltage of the battery, the converter works in buck mode and if the bus voltage is less than the nominal battery voltage, the converter works in boost mode [9, 10].

Closed loop control of the converter is implemented here to provide duty cycle w.r.t the reference voltage. The error between the output voltage and reference voltage is fed to the integral controller using suitable gain. The output of the controller is passed to the relay block as shown which provides the required duty cycle to the switch. This duty cycle will decide the output voltage [11, 12]. The simulation of the closed loop buck–boost converter is shown in Fig. 2. Average output voltage and current of the converter is given by

$$V_o = -\frac{d}{1-d} * V_{in}$$

$$I_o = \left(\frac{1-d}{d} * I_{in}\right)$$

where

V_o = Output voltage
V_{in} = Input voltage
I_o = Output current
I_{in} = Input current
d = Duty cycle
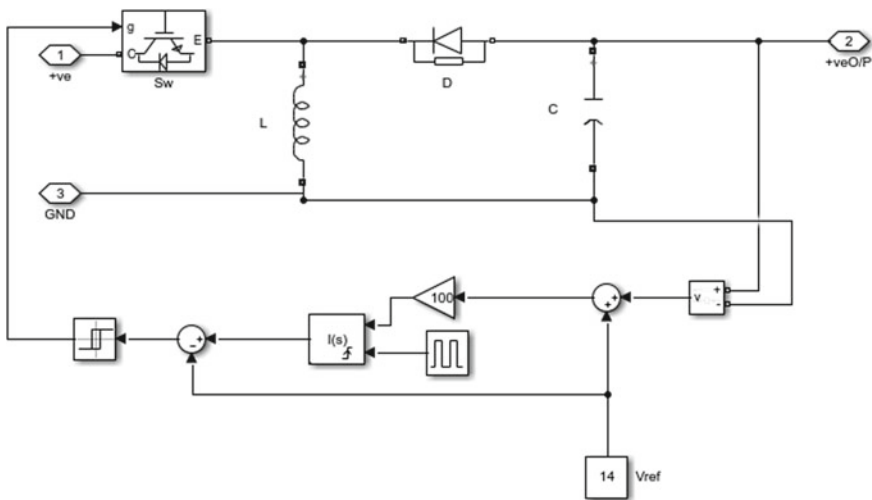
Fig. 2 Simulation of closed loop buck–boost converter
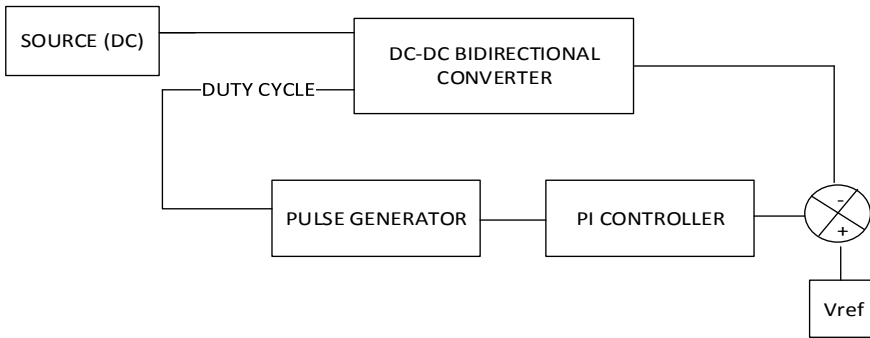
Fig. 3 Closed loop bidirectional converter

A bidirectional converter provides power flow in both directions. Here it is connected between the DC bus and battery bank to provide bidirectional power flow [13]. Both the switches can't be on at the same time. In its two modes of operations, when switch m_1 is on and m_2 is off in mode 1, it is operating in buck mode and the power is flowing from source to load (i.e., from Bus to Battery bank).

When switch m_2 is on and m_1 is off, it is operating in boost mode and the power is flowing from load to source (i.e., from Battery bank to DC Bus). When switches (m_1 or m_2) are off, they act as a diode in opposite direction [14, 15].

Figure 3 and 4 shows the block diagram and simulation of closed-loop controlled bidirectional converter respectively. The difference (error) between the reference voltage and the bus voltage is provided to the PI controller. The output is differentiated with the charging current of the battery and the difference is fed to another PI controller which produces the signal for the DC pulse generator block which further produces the triggering signal for the switches m_1 and m_2 [16] (for m_2 the signal is provided after passing through not gate) (Fig. 3).

3 Result and Discussion

Table 1 shows the values of the parameters that are selected in this paper.

Figures 5, 6, 7, and 8 show the curve of the vehicle battery and the battery bank during daytime. The curves are appearing with a positive slope which means the batteries are charging.

The battery bank voltage in Fig. 5 was initially at 53 V (approx.) and is reaching 54 V (approx.). Similarly, the SOC (State of Charge) of the bank in Fig. 6 is also increasing from 25 to 25.01.

For EV battery also, the battery voltage and SOC are increasing from 12.1 to 12.4 V nearly and from 12.50% to 12.54%, respectively. During the daytime with sufficient irradiance, the PV panel is able to charge both the batteries simultaneously.
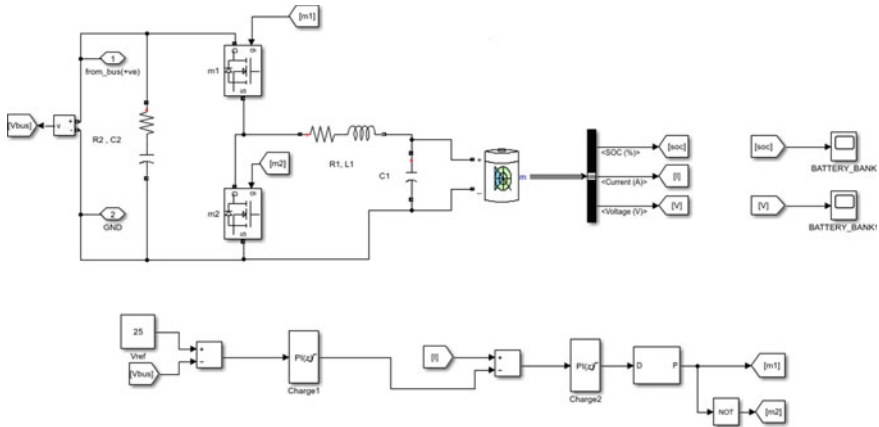
Fig. 4 Simulation of bidirectional converter in closed loop

Table 1 Selected values of different parameters

Irradiance (for day time)	1000 w/m^2
Irradiance (for night)	0 w/m^2
Battery rating (Battery bank)	50 (nominal) volts, 50 AH
Initial %SOC (Battery bank)	25%
Battery rating (EV)	12 (nominal) volts, 25 AH
Initial %SOC (EV)	12.5%
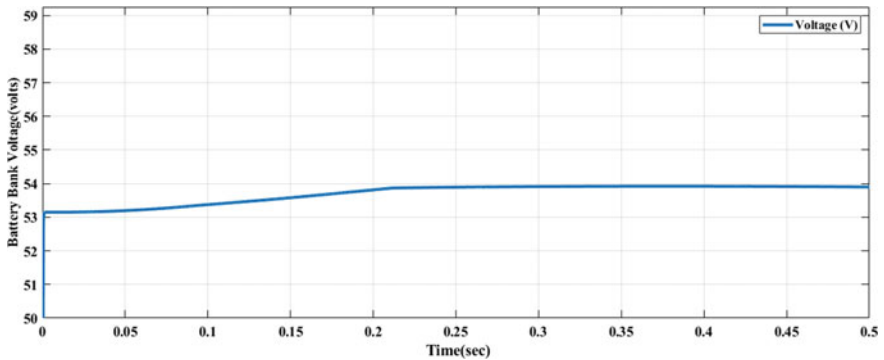
Fig. 5 Battery bank voltage curve

During the nighttime, with an irradiance of 0 w/m^2, the vehicle battery is getting charged. Figure 9 shows the curve of battery voltage and %soc with a positive slope represents the charging of the vehicle.

Now in Fig. 10, it can be seen that the voltage of the battery bank and %soc have with negative slope. This means the battery bank is providing voltage to the bus
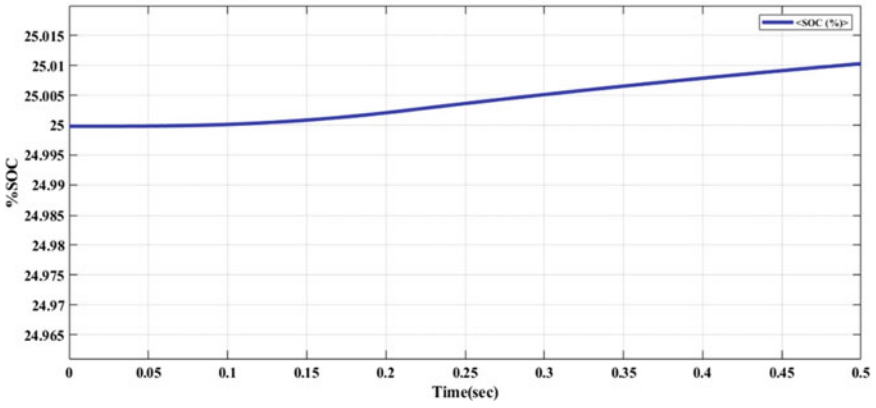
Fig. 6 Battery bank %SOC
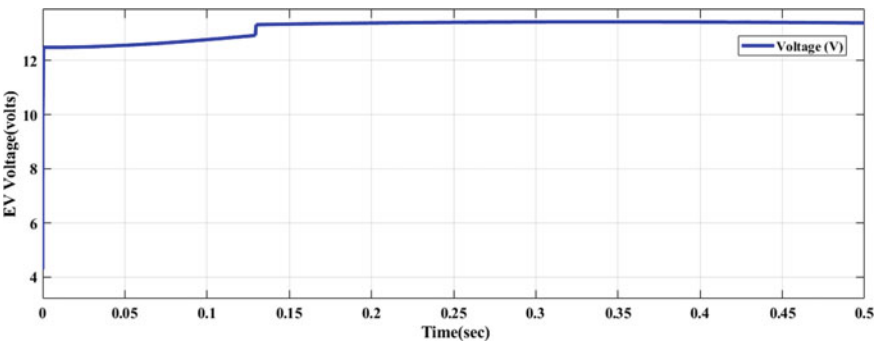
Fig. 7 EV battery voltage curve
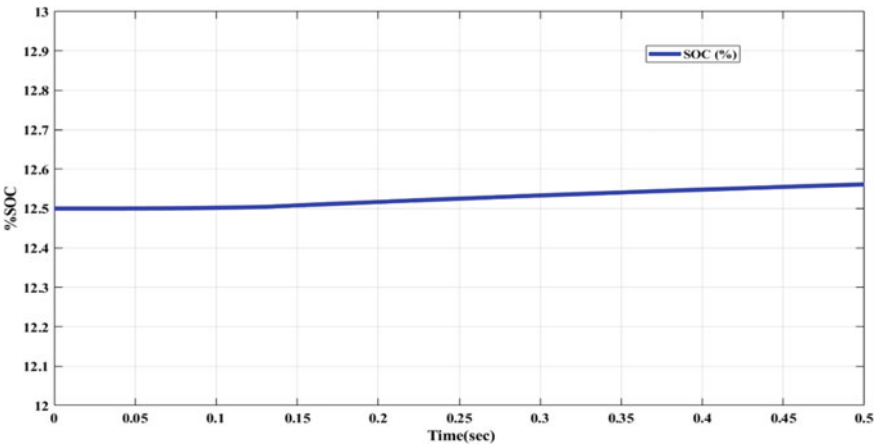
Fig. 8 EV battery %SOC curve (during night)
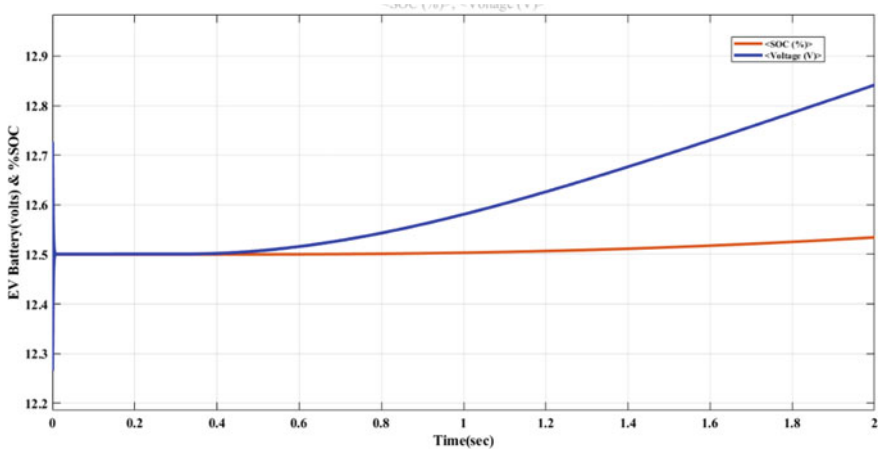
Fig. 9 EV battery voltage and %SOC curve (during night)

during the night as the PV panel is not able to charge the battery due to insufficient irradiance.
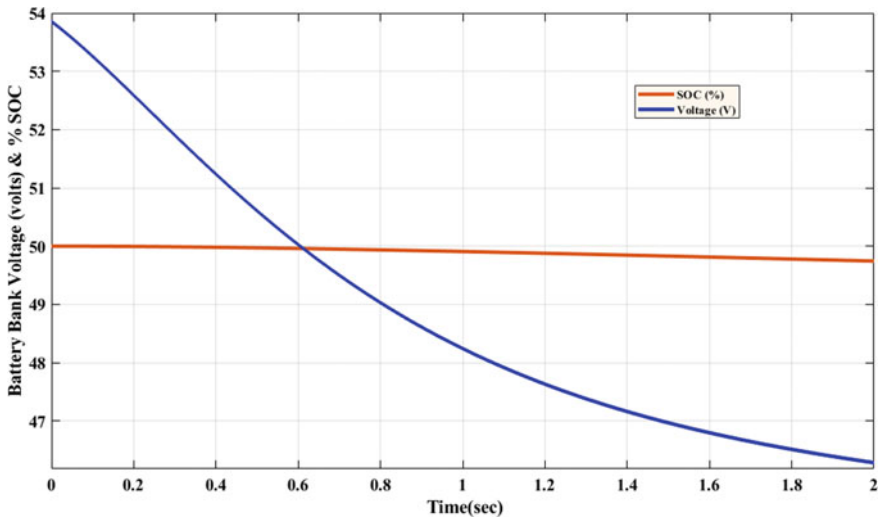
Fig. 10 Battery bank voltage and %SOC curve (during night)

4 Conclusion

In this paper, electric vehicle charging with the help of solar cells is shown. The electric vehicle and the battery bank are charged using a solar cell. When there is insufficient irradiance, the battery bank provides the required charging voltage. The method is designed using MATLAB. Implementation of this technique can be done in the remote area where electricity is not easily available. It can be used at home as a small-scale microgrid which will provide power to relevant loads when idle and will charge the vehicle when necessary. The process is eco-friendly. Since it is used in an isolated mode (i.e., not grid connected), it will not pollute the AC grid with harmonics which degrades the power quality of the grid.

References

1. (2016) Earth's heat budget, oceans and climate. In: Webb P (ed) Introduction to oceanography
2. Willson RC, Gulkis S, Jamssen M, Hudson HS, Chapman GA (1981) Observation of solar irradiance variability. Science 211:700
3. Amendments in EV charging guidelines by ministry of power EVreporter. EVreporter, 7 October 2019. Retrieved 26 May 2020
4. Zhao H, Burke A (2015) An intelligent solar powered battery buffered EV charging station with solar electricity forecasting and EV charging load projection functions. In: 2014 IEEE international electric vehicle conference (IEVC), December 2015
5. Akshya S, Ravindran A, Srinidhi AS, Panda S, Kumar AG (2017) Grid integration for electric vehicle and photovoltaic panel for a smart home. In: 2017 international conference on circuit, power and computing technologies (ICCPCT), April 2017
6. Gergaud O, Multon B, Ben Ahmed H (2002) Analysis and experimental validation of various photovoltaic system models. In: 7th international ELECTRIMACS congress, Montréal, Canada, pp 1–6
7. Femia N, Petrone G, Spagnolo G, Vitelli M (2005) Optimization of perturb and observe maximum power point tracking method. IEEE Trans Power Electron 20:963–973
8. Coates E (2017) Boost converters
9. Choudhary V, Hegarty T, Pace D (2016) Under the hood of a noninverting buck-boost converter. In: TI power supply design seminar
10. Poole I Buck-boost converter or DC-DC regulator
11. Poole I Step down buck regulator/converter
12. Tusahar M Comparative study on DC-DC converters. Brac University
13. Li X, Zhang W, Li H, Xie R, Xu D (2011) Design and control of bidirectional DC/DC converter for 30 kW fuel cell power system. IEEE
14. Karshenas HR, Daneshpajooh H, Safaee A, Jain P, Bakhshai A Bidirectional DC-DC converters for energy storage systems. In: Carbone R (ed) Energy storage in the emerging era of smart grids. ISBN 978-953
15. Zhang J (2008) Bidirectional DC-DC power converter design optimization, modeling and control. Diss. Virginia Polytechnic Institute and State University
16. Mousavi A, Moschopoulos G (2009) Analysis and design of a non isolated bidirectional ZVS-PWM DC-DC converter with coupled inductors. In: IEEE TPEL 2009

Modeling of a Grid-Connected Sustainable Energy Source Based Hybrid System for Pollution-Free Future

Uttara Das, Somudeep Bhattacharjee, Sarbani Mandal, and Champa Nandi

Abstract The sustainability of the earth for a sustainable developed future is the most important factor for today's world. Because of modernization, people are focusing on advance to advance technologies, industrialization, etc. which is directly and indirectly hampering our future generation through climate change. Electricity production sectors are playing such a big role in climate change as they are heavily dependent on conventional energy sources. So, this paper aims to model and optimize a grid-connected sustainable energy sources based hybrid system for Er Roseires town, Sudan. The purpose of this simulation model is not only to investigate the relation of greenhouse gas emissions, energy consumption from the grid and its sale-back, and economic growth but also to propose a new hybrid energy approach that will be reliable for the coming future. The modeling and optimization of the system are done by using HOMER Pro® software. The optimization result shows that the hybrid model can satisfy the total load demand of the particular location taking no power from the grid.

Keywords Climate change · Sustainable source · Hybrid system · Pumped hydro storage · Wind

1   Introduction

To attain a sustainable future for the earth, many countries started following towards sustainable development framework. "Agenda 2030", a most focused sustainable development pathway set by the United Nations General Assembly in 2015, shows 17 sustainable development goals and their 169 targets to save the earth from various inequality, injustice, etc. In this agenda, sustainable development goal 7 proclaims to ensure access to affordability, reliability, and sustainable and modern energy for all [1]. The idea of living and meeting own demands by the human without hampering the future generation is known as sustainable development [2]. Sustainable development

U. Das · S. Bhattacharjee · S. Mandal · C. Nandi (✉)
Tripura University, Agartala, Tripura 799022, India
e-mail: chmpnandi@gmail.com

is not possible without sustainable energies. The energy which comes from sources that don't require to be replenished is called sustainable energy. But the energy that comes from the sources which can be exhausted due to over consumption is called conventional energy. Almost 60% of global greenhouse gases are emitted from the burning of conventional energy sources [3]. Most of the countries of the world including North African countries depend on conventional sources of energy for their demand. The emission of greenhouse gases in these countries is going high to high due to severe population growth and their attention on modernization. Around 50% of carbon dioxide (CO_2) is emitted from the electricity and heat production sectors in the MENA (Middle East and North Africa) countries [4, 17].

These greenhouse gases are rapidly increasing due to human activities which have driven the Earth towards climate change. It is seen that sea-level rise, droughts, floods, and freshwater scarcities are the most common problem in every country under North Africa due to climate change. The countries like Algeria, Morocco, Libya, Egypt, Tunisia, Sudan, and Western Sahara have come under the North African empire. These countries are the battlefront fighter in the climate change war [5]. If we look at the environmental pollution scenario, these countries remain the most affected countries in the world. The study says the population within 100 km of the coast is highest in these countries. So, more population movement in coastal areas results in sea-level rise. Thus, coastal areas of these countries are facing extreme floods and the inland areas are facing severe drought [6]. Now, if we look at energy or electricity background, 99% of North African people have the access to electricity. Most of the energy sectors, mainly the electricity sectors of this region are primarily dependent on conventional energy sources. Here, almost 97% of the electricity comes from fossil fuel-based energy sources [7, 15]. This rapid increase of fossil fuel combustion across the North African countries is likely to increase the stress of pollution. Overall, conventional energy sources are not a proper option in the case of electricity generation.

To get redeemed from the use of conventional energy sources in the field of electricity generation, sustainable energy sources are a significant solution [18, 19]. Sustainable energy sources are abundantly available in nature and they are freely available. But the use of a single source of sustainable energy has different difficulties. The most common difficulty is they are not available all the time. Sustainable energy sources are heavily dependent on natural effects. So, to get a probable solution from this type of uncertainty, a hybrid system has been proposed earlier [8, 20]. In this paper, we proposed a hybrid system to analyze the performance of the location concerning load. This hybrid system is structured focusing on the wind-based pumped hydro storage concept. The aim of this paper is not only to investigate the relation of CO_2 emissions, energy consumption, and economic growth but also to propose a new hybrid energy approach that will be reliable for the coming future.

2   Materials and Method

2.1   The Study Area

The Blue Nile is one of the regional states of the Republic of Sudan. This state lies between the longitude of 34° 4′ East to latitude of 11° 16′ North. The name of this state comes from the Blue Nile River. Blue Nile River is one of the tributaries of the Nile River. The Nile is the major north-flowing river of North Africa and it is the primary source of water in Sudan. The Blue Nile River is the home of hydroelectric power in Sudan. Ad-Damazin is the state capital of Blue Nile. Ad-Damazin falls under a hot semi-arid climate. In Ad-Damazin, a dam was constructed on the river Blue Nile in 1966, upstream of Er Roseires. This Er Roseires is a town in Sudan, which is located 60 km away from the Ethiopian border. The name of the dam located in the Blue Nile River comes from the location where it has constructed. This dam has various units to continue the service to generate electricity. Here, we consider only one unit of the Roseires hydroelectric plant to get a more efficient outage for continuous services [9, 10]. Some information about the Roseires dam is given in Table 1.

Table 1 Some information about the Dam [9]

Particular	Information
Name of the Dam	Roseires Dam hydroelectric Power Plant
Type of the Dam	Dam on river with reservoir
State	Blue Nile
Town	Er Roseires
Latitude	11° 79′ North
Longitude	34° 37′ East
River	Blue Nile River
Project owner and Operating agency	National Electricity Corporation of Sudan (NEC)
Construction began	1961
Opening of dam	1966
Surface area	290 km^2
Height of dam	68 m
Length of dam	24,410 m
Capacity of main reservoir	7.4 km^3
Design capacity of Dam	280 MW
No. Of units	7
Capacity of Each unit	40 MW
Water Allocation	Hydroelectric, irrigation, drinking, industry

Fig. 1 Roseires hydroelectric Dam view [12]

This Roseires dam project was executed in two different stages. The first one was done by attaching a hydroelectric plant in 1966 and the second one was completed in 2013 [11]. The Arial view of the Roseires dam is given in Fig. 1 [12].

2.2   Data Collection

The case study data include average annual hydro availability in a particular reservoir with hydro flow rate and wind speed along electric load. Here, our system is proposed based on Hydro and wind, as they are considered sustainable energy sources. All this data used in this paper are taken from the database of the NASA Power website [9, 12, 13].

Wind Speed. Due to the temperate variation, the pressure of any area also varies.

The wind speed of any particular area directly depends on the pressure of that area. Wind always blows in the horizontal position from a low-pressure area to a high-pressure area. In Ad-Damazin, the average yearly wind speed is 3.8 m/s. This wind speed data are collected from the hub which is located 50 m high up from the plane of the earth floor.

The average maximum speed of wind in this area is found in June which is 4.9 m/s and the average minimum speed of wind in this area is found in October which is 2.4 m/s [12, 13]. Figure 2 shows monthly average information about wind speed.

Water Availability. Power generation of any hydroelectric plant relies on the flow rate of water and the water head. When the water flows from the upper reservoir to the lower reservoir, the water head and the flow rates are taken into account [16]. Water head means the height of the flowing water. Flow rate defines as the rate of water flow in liters for one second. When the maximum head is found, it is counted as the maximum flow rate. The maximum average water flow rate of this area is found in June and the minimum average water flow rate of this area is found in August [9]. Figure 3 shows monthly average information of water head and water flow rate.
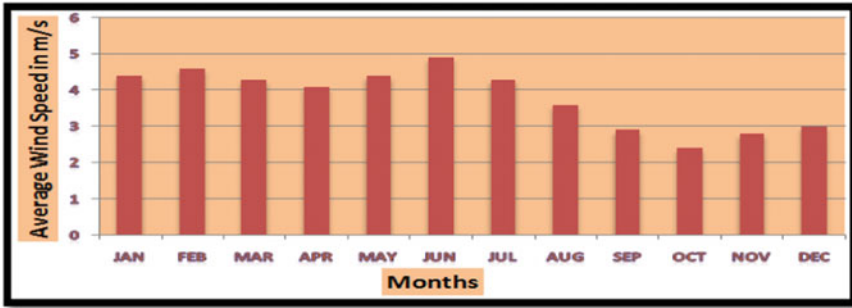
Fig. 2 Monthly average information of wind speed [12, 13]

Fig. 3 Monthly average information of head in (m) and water flow rate in (m/s) [9]

Electric Load. We have considered one single unit of Roseires Dam Hydroelectric Power Plant for our proposed system. This grid-connected proposed system will serve for fulfilling load demand in Er Roseires town. A constant load is taken in every month of a year for this proposed system. The load is considered as domestic load, small-scale industries, community load, etc. To establish an adjustable load profile, we considered a day-to-day variation of 15% and a time-step variation of 20% [14].

2.3 Simulation Model

A grid-connected sustainable energy sources based hybrid system is formulated in the HOMER Pro® software. This integrated system is analyzed in one unit of Roseires Dam Hydroelectric Power Plant. This simulation model consists of an existing hydroelectric project, a newly proposed pumped hydro system, windmill, power converter, electric load, and a grid connection. Figure 4 shows the simulation model of the sustainable energy source based hybrid system.
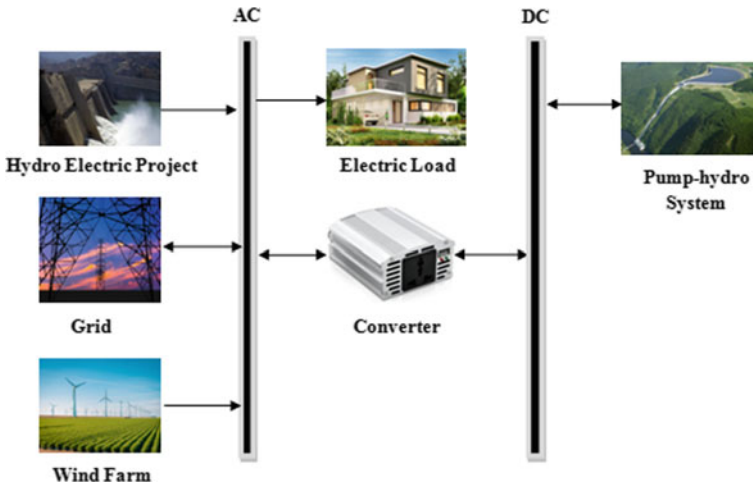
Fig. 4 Proposed simulink model of sustainable energy sources based integrated framework

Hydro Project. The hydroelectric project used in the model is manufactured by Generic. It has a capacity of 40 MW with an efficiency of 90%. The lifetime of this hydroelectric project is 25 years. The capital cost of the hydroelectric project is 98,807 US$, and its operation and maintenance (O&M) cost is 450,000 US$/year. The system considers the real-time temperature effect also.

Pumped Hydro System. The Generic pumped hydro has a reservoir that can store water. It can discharge water for 12 h period. A total of 12,250 MW pumped storage system is used in this proposed system. 50 units of pump hydro storage are used where each unit has 245 kWh capacity. The lifetime of this pumped hydro system is 7 years. The capital cost of the hydroelectric project is 22,000 US$ per pump, and its O&M cost is 2000 US$/year/pump.

Wind Mill. The wind turbine used in the windmill is manufactured by the company of Generic. 15 numbers of 1.5 MW wind turbines were used in this proposed windmill. The lifetime of this windmill is 20 years. The total capacity of the wind farm is 22.5 MW for 15 numbers of wind turbines. The capital cost of the wind turbine is 3,000,000 US$ per wind turbine, and its O&M cost is 3000 US$/year/wind turbine. The hub height of the turbine is 80 m.

Power Converter. This power converter has 95% efficiency. This converter is manufactured by the Generic Company. The power converter has a total capacity of 12,300 kW. It has 15 years lifetime. The capital cost of the power converter is only 300 US$ and its O&M cost is practically zero. The replacing cost of this converter is 300 US$.

Electric Grid. In this simulation model, the main purpose of the grid is to give power when required and to consume when excess power is generated. Overall, after

fulfilling the load demand of the particular area, if surplus energy produces, in that time, this surplus energy can be exchanged with the grid. Elseways, during the energy crisis, we can choose grid-energy-purchase option. Here, the energy buying from the grid price is 0.21 US$/kWh, and the grid net-excess price is 0.163 US$/kWh.

3 Result and Discussion

All the input data for the simulation of the proposed hybrid system is given in Sect. 2.2. This study consists of an existing hydroelectric project, a newly proposed pumped hydro system, windmill, power converter, electric load, and a grid connection. The net present cost of the whole proposed system is shown in Table 2.

The overall net present cost of the hybrid system is (188,511,000)$. The Levelized cost of the system is 0.04405$. Table 3 shows the annualized cost of the whole proposed system. Here, O&M represents operational and maintenance costs.

The total annualized operating cost of the system is (26,660,417)$. The total power production of the system is 332,559,596 kWh/yr. The total production, consumption, and greenhouse gas emission summary of the proposed system is shown in Table 4.

It is clear from Table 4 that, our proposed system is environmentally friendly and doesn't emit any greenhouse gases. Now, Table 5 shows the total energy purchased from the grid and total energy sales to the grid scenario of the hybrid system.

In Table 5, we can see that the energy purchase from the grid is zero for all the year. Moreover, we can sell the produced energy from our proposed system to the grid. Now, Fig. 5 indicates the total energy production from the windmill over the year. Here, we can see that our windmill is giving sufficient energy in all the years except October and November. In those months, the windmill is supplying comparatively low energy.

Figure 6 shows the total electricity produced from the Pumped Hydro Unit. Here we can see that the pumped hydro unit gives comparatively low energy in the month of August because of the low water flow rate and water head. Now, Fig. 5 shows the total electricity production from the windmill and pumped hydro unit of the proposed system. This figure also indicates that grid-purchased energy is not required fulfilling the load demand. So, all load demand of the particular area is fulfilled by our proposed system (Fig. 7).

4 Conclusion

It can be concluded from the case study work that the sustainable energy sources based hybrid proposed system is much more profitable as per economic and climatic aspects. This proposed hybrid system used 100% sustainable energy sources for fulfilling the load demand. In the case of satisfying load demand, we can see that the proposed system is neither taking any energy from the grid, nor it is using any

Table 2 Net present cost of the integrated framework

Name	Capital ($)	O&M ($)	Replacement ($)	Salvage ($)	Resource ($)	Total ($)
Hydroelectric	98,807,040	5,817,382	0.00	0.00	0.00	104,624,422
Wind mill	45,000,000	5,817,382	14,346,330	(8,085,077)	0.00	57,078,635
Pumped Hydro	1,100,000	1,292,751	35,514	(2566)	0.00	2,425,699
Grid	0.00	(357,580,503)	0.00	0.00	0.00	(357,580,503)
Converter	3,675,000	0.00	1,559,206	(293,458)	0.00	4,940,747
System	148,582,040	(344,652,986)	15,941,051	(8,381,102)	0.00	(188,510,997)

Table 3 Annualized cost of the integrated framework

Name	Capital ($)	O&M ($)	Replacement ($)	Salvage ($)	Resource ($)	Total ($)
Hydroelectric	7,643,157	450,000	0.00	0.00	0.00	8,093,157
Wind Mill	3,480,947	450,000	1,109,751	(625,416)	0.00	4,415,282
Pumped Hydro	85,089	100,000	2747	(198)	0.00	187,638
Grid	0.00	(27,660,417)	0.00	0.00	0.00	(27,660,417)
Converter	284,277	0.00	120,611	(22,700)	0.00	382,188
System	11,493,471	(26,660,417)	1,233,110	(648,314)	0.00	(14,582,150)

Table 4 Production, consumption and emissions scenario of the integrated framework

Production summary		
Component	Production (kWh/yr)	Percent (%)
Wind mill	17,667,738	5.31
Hydro	314,891,858	94.7
Grid purchases	0	0
Total	332,559,596	100
Consumption summary		
Component	Production (kWh/yr)	Percent (%)
AC primary load	161,622,000	48.8
DC Primary load	0	0
Deferrable load	0	0
Grid sales	169,435,941	51.2
Total	331,057,941	100
Emissions summary		
Pollutant	Emission quantity	Unit
Carbon dioxide	0	g/KWh
Carbon monoxide	0	g/KWh
Unburned hydrocarbons	0	g/KWh
Particular matter	0	g/KWh
Sulfur dioxide	0	g/KWh
Nitrogen oxide	0	g/KWh

conventional energy. Moreover, grid sale is possible as the proposed system can satisfy all the load demand. So, it is important to say that, if the grid fails to work, in that time also our proposed system can work alone and it can fulfill the load demand. So, this proposed system would not hamper the environment anyway and it will produce clean energy for the upcoming future. The low net present cost of the proposed system defines that this framework is economically preferable. At last, this

Table 5 Monthly energy purchases and monthly energy sales of the integrated framework

Month	Energy purchased (kWh)	Energy sold (kWh)	Net energy purchased (kWh)	Peak load (kW)	Energy charge	Demand charge	Total
January	0	15,135,242	−15,135,242	0	−$2.47 M	$0.00	−$2.47 M
February	0	14,284,656	−14,284,656	0	−$2.33 M	$0.00	−$2.33 M
March	0	14,376,283	−14,376,283	0	−$2.35 M	$0.00	−$2.35 M
April	0	13,973,882	−13,973,882	0	−$2.28 M	$0.00	−$2.28 M
May	0	15,378,872	−15,378,872	0	−$2.51 M	$0.00	−$2.51 M
June	0	14,967,881	−14,967,881	0	−$2.44 M	$0.00	−$2.44 M
July	0	14,985,383	−14,985,383	0	−$2.45 M	$0.00	−$2.45 M
August	0	12,849,403	−12,849,403	0	−$2.10 M	$0.00	−$2.10 M
September	0	12,765,449	−12,765,449	0	−$2.08 M	$0.00	−$2.08 M
October	0	13,150,172	−13,150,172	0	−$2.15 M	$0.00	−$2.15 M
November	0	13,247,923	−13,247,923	0	−$2.16 M	$0.00	−$2.16 M
December	0	14,320,796	−14,320,796	0	−$2.34 M	$0.00	−$2.34 M
Annual	0	169,435,936	−169,435,936	0	−$27.7 M	$0.00	−$27.7 M
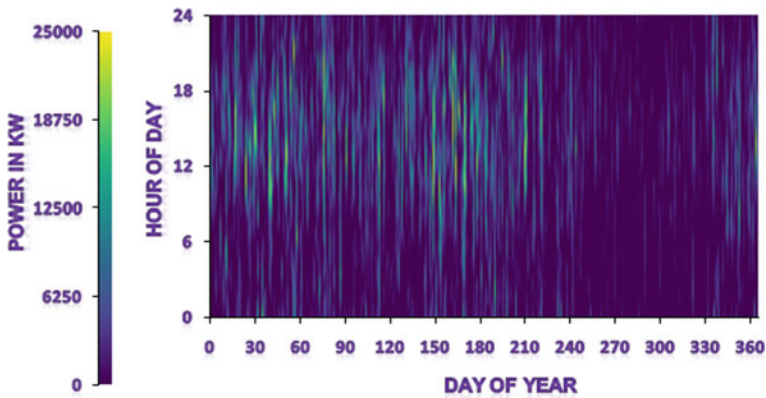
Fig. 5 The total electricity production from the Wind Mill

research work can be further extended by integrating other sustainable sources like solar, biomass, etc.
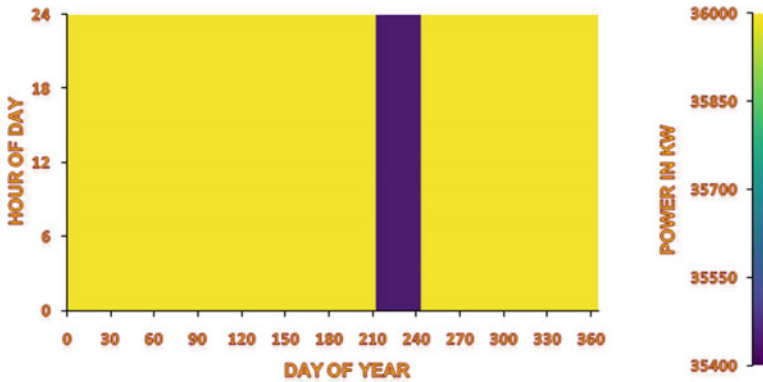
Fig. 6 The total electricity production from the pumped hydro unit
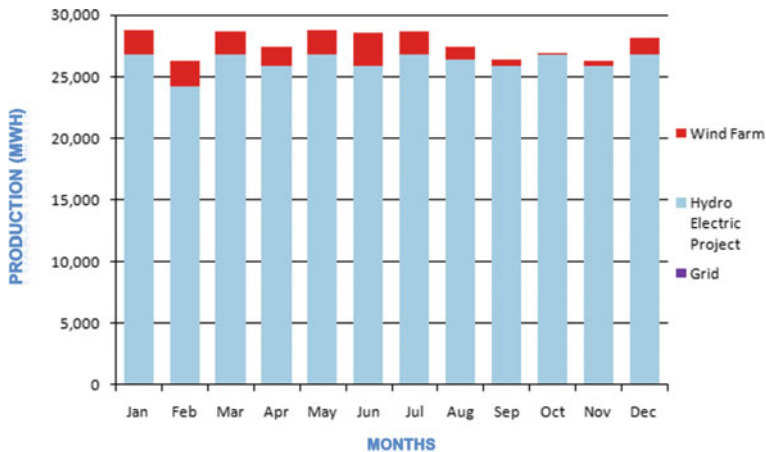
Fig. 7 The total electricity production from the proposed system

References

1. Gielen D, Boshell F, Saygin D, Bazilian MD, Wagner N, Gorini R (2019) The role of renewable energy in the global energy transformation. Energ Strat Rev 24:38–50
2. Gupta J, Vegelin C (2016) Sustainable development goals and inclusive development. Int Environ Agreement Politics Law Econ 16:433–448
3. Energy and the environment explained. https://www.eia.gov/energyexplained/energy-and-the-environment/. Last accessed 2021/07/05
4. Aghahosseini A, Bogdanov D, Breyer C (2020) Towards sustainable development in the MENA region: analysing the feasibility of a 100% renewable electricity system in 2030. Energ Strat Rev 28:100466
5. Karim MK (2018) Exploring the impact of climate change on the outbreak of early twenty-first-century violence in the Middle East and North Africa and the potential of permaculture as an effective adaptation. Weather Clim Soc 10:179–186

6. Nandi C, Bhattacharjee S, Chakraborty S (2019) Climate change and energy dynamics with solutions: a case study in Egypt. In: Qudrat-Ullah H, Kayal A (eds) Climate change and energy dynamics in the Middle East. Understanding complex systems. Springer, Berlin, pp 225–257

7. Timmerberg S, Sanna A, Kaltschmitt M, Finkbeiner M (2019) Renewable electricity targets in selected MENA countries—assessment of available resources, generation costs and GHG emissions. Energ Rep 5:1470–1487

8. Bhattacharjee S, Nandi C (2019) Implementation of industrial internet of things in the renewable energy sector. In: Mahmood Z (ed) The Internet of Things in the industrial sector, computer communications and networks. Springer, Berlin, pp 223–259

9. Abuelnuor A, Abuelnuor A, Ahmed K, Saqr KM, Nogoud YAM, Babiker MEAM (2020) Exergy analysis of large and impounded hydropower plants: case study El Roseires Dam (280 MW). Environ Prog Sustain Energ 39:13362

10. Elkadeem MR, Wang S, Sharshir SW, Atia EG (2019) Feasibility analysis and techno-economic design of grid-isolated hybrid renewable energy system for electrification of agriculture and irrigation area: a case study in Dongola, Sudan. Energ Convers Manage 196:1453–1478

11. Mulat GA, Moges SA, Moges MA (2018) Evaluation of multi-storage development in the upper Blue Nile River (Ethiopia): regional perspective. J Hydrol Reg Stud 16:1–14

12. NASA Power website. https://power.larc.nasa.gov/. Last accessed 2021/06/01

13. Nandi C, Bhattacharjee S, Reang S (2018) An optimization case study of hybrid energy system based charging station for electric vehicle on Mettur, Tamil Nadu. Int J Adv Sci Res Manage 3:225–231

14. Rabah AA, Nimer HB, Doud KR, Ahmed QA (2016) Modelling of Sudan's energy supply, transformation, and demand. J Energ Hindawi Publ Corp 5082678

15. Bhattacharjee S, Das U, Chowdhury M, Nandi C (2020) Role of hybrid energy system in reducing effects of climate change. In: Qudrat-Ullah H, Asif M (eds) Dynamics of energy, environment and economy, Lecture notes in energy, vol 77. Springer, Switzerland, pp 115–138

16. Lange MA (2019) Impacts of climate change on the Eastern Mediterranean and the Middle East and North Africa region and the water-energy nexus. Atmosphere 10(8):455

17. Rignall K (2019) Living climate change in the Middle East and North Africa. Int J Middle East Stud 51:629–632

18. Bhattacharjee S, Batool S, Nandi C, Pakdeetrakulwong U (2017) Investigating electric vehicle (EV) charging station locations for Agartala, India. In: 2nd international conference of multidisciplinary approaches on UN sustainable development goals, Bangkok

19. Huang XJ, Bao NS (2016) Modeling and simulation analysis of wind—hydro hybrid power plant. In: 2nd annual international conference on energy, environmental and sustainable ecosystem development; advances in engineering research, Springer Nature, China

20. Bhattacharjee S, Nandi C (2019) Design of a voting based smart energy management system of the renewable based hybrid energy system for a small community. Energy 214:118977

Arduino Based Automatic Sanitizer Dispenser Controlled Door

Harsh Vardhan and Kirti Pal

Abstract The newly discovered infectious disease COVID-19 infected many people. The coronavirus causes respiratory problems and also gets affected in many parts of the human body. This virus is transmitted from one body to another body through the air or by touch. The only way to stop the transmission is to use a mask on the face and washing or sanitizing hands frequently. Sanitizers are liquid, gel, or foam which is designed to eliminate germs on skin or any other object. In daily lives also sanitization is necessary to prevent various germs which can make you ill. One of the main modes of contact with germs is our hands because in our daily lives we touch many infected surfaces and objects unknowingly hence to prevent any type of illness due to those germs, hand sanitization is necessary, especially for a person working in a closed and congested environment like offices, canteens, restaurants, schools, etc. This paper aims to design a low-cost Arduino-based automatic sanitizer dispenser-controlled door and it will be of great help in public places where people don't follow hand hygiene properly. This automatic sanitizer system will be placed at the entry point of the main gate and it will only allow entry from that gate if and only if the person goes through the sanitization process first.

Keywords COVID-19 · Sanitizer · Microcontroller · IR sensor · Ultrasonic sensor · Relay module · Servo motor

1 Introduction

The main cause of spreading corona virus or any other infectious germs from person or from any contaminated surface is the hand [1–3]. There is a greater chance of infection for people who are using public facilities and those who are living or working in a close environment such as banks, colleges, canteens, public toilets, hospitals etc. [4]. As there are chances of frequent contacts with hands and various

H. Vardhan (✉) · K. Pal
Department of Electrical Engineering, School of Engineering, Gautam Buddha University, Greater Noida, UP, India
e-mail: vardhan1204@gmail.com

surfaces and objects, therefore chances of cross contamination increases significantly. In general also hand hygiene is of very much importance for human health and if not followed properly there are chances of spread of infectious disease. In [5] the author suggested that washing hands or cleansing hands is one of the most basic and simplest ways of maintaining hand hygiene.

Hand sanitizers are mainly made up from materials such as alcohol, polyacrylic acid, glycerin, propylene gycol or plant extracts [6, 7]. Over recent years, there has been an increase in the use of alcohol based hand sanitizers. The author [8] illustrates the main advantages of alcohol based sanitizer that how they eliminate more germs easily and quickly with respect to traditional hand washing with soaps. Many authors [9–11] suggested that alcohol based sanitizers are effective against corona virus. The government and many NGOs creating awareness about proper hand hygiene and its practices because still there are so many people in poor and developing countries who are not aware of hand hygiene and there is also a proportion of people who don't want to wash hands or sanitize hands when required also like before eating food or after using restroom etc.

Covid-19 is a highly infectious virus among humans, apart from vaccines only with proper sanitization and isolation it can be prevented [12]. The pandemic situation created by Covid-19 can be reduced by the use of masks and sanitizers. These two things are essential for everyone and it can be seen that with proper sanitization and usage of masks the spreading of infection can be slowed down. But there are still a proportion of people who are not following proper preventive measures like sanitizing before entering malls, college hostels, banks, offices, etc. [13, 14]. There is a lack of compliance among personnel who interact with patients in the healthcare sector also which eventually increases healthcare-associated infections. Given these issues, in this paper low-cost automatic dispenser sanitizer is designed for the door, so that no one can enter any premises without sanitization.

1.1 Objective of the Proposed Hardware Model

To prevent entry of any person without sanitization in any premises is the main objective of this proposed model.

To overcome this problem of people entering any premises without sanitization, in this paper hardware model is designed and implemented to sanitize any object or person passing through the main gate. Also as it is an automatic sanitizer dispenser so chances of cross contamination also reduces.

To program Arduino to control IR sensor, ultrasonic sensor and relay operation.

To perform several testing for checking the effectiveness of the proposed model.

2 Proposed Hardware Model Description

In this project, an Ultrasonic sensor is used to detect the presence of a hand. An ultrasonic sensor detect hand at a certain distance then send a signal to relay to trip as the directions set by the Arduino program. An external power supply and submersible water pump is connected to the relay. The desired voltage for the model is maintained by the external power supply. The water pump is switched 'ON' and the sanitizer is pumped from the container to your hands through a tube.

IR tracking sensor sense wet or dry hands. If the hands are dry and placed in front of the sensor the door will not open and the LCD display show a message "Wash Your Hand". If the hands are wet and placed in front of the sensor, it sends a LOW signal to the servo motor to rotate 90° so that the door will open. As the time is set by Arduino the door will automatically close after a fixed time.

This system consists of two parts, Hardware and Software.

Hardware part includes:

- Arduino Uno
- IR sensor
- Ultrasonic Sensor
- Servo motor
- Submersible water pump
- 16*2 LCD display
- Relay Module
- Breadboard
- Jumper wires.

Software part includes:

- Arduino IDE

Arduino UNO is based on an ATmega328P microcontroller and operates at 5 V DC supply with a clock speed of 16 MHz. Ultrasonic sensor module provides 2–400 cm measurement function and operates at 5 V DC supply. The module has ultrasonic transmitters, receiver and a control unit. Its ranging accuracy is up to 3 mm. Infrared sensor is a combination of IR LED and IR photodiode which is used to detect the presence of some object in the range of 20 cm. IR sensor operates at 5 V DC supply. Relay module is an electromagnetic relay which can be controlled through a microcontroller, it operates at a supply voltage of 3.75–6 V DC supply with a maximum contact potential of 250 V AC and 30 V DC. Mini servo motor is used for rotation purposes and it can rotate from 0° to 180° with a torque of 2.5 kg/cm, operating on 5 V DC supply.

The block diagram in Fig. 1 shows the different components used in the Automatic sanitizer dispenser controlled door using Arduino. Five volt regulated power supply is required for Arduino Uno and it is connected through ultrasonic sensor whose function is to detect hands or any objects near to door.
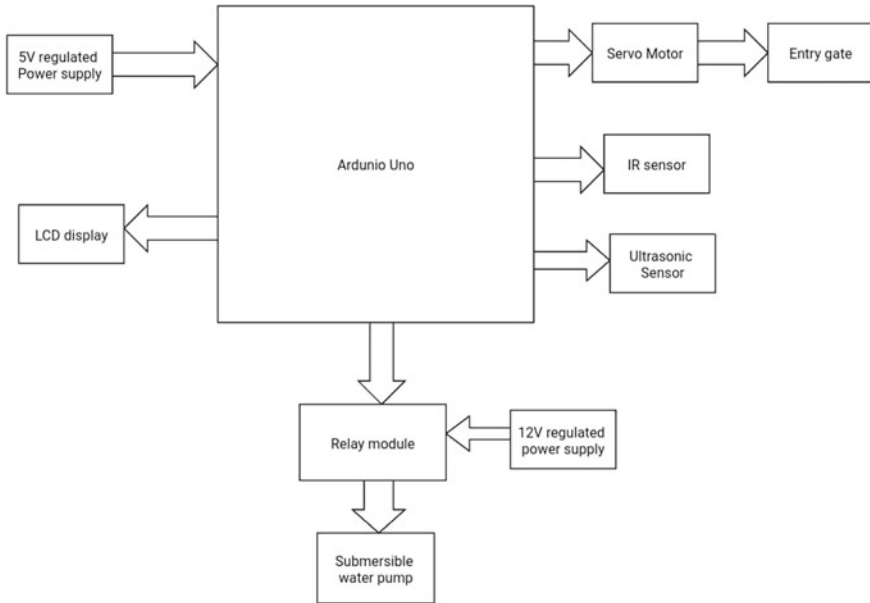
Fig. 1 Block diagram of proposed model

Relay module gets power from a 12 V regulated power supply and it is connected with a submersible water pump. When the ultrasonic sensor sense hands it gives a signal to arduino then in turn it provides a signal to relay and relay will give a signal to submersible water pump to spray the sanitizer. An IR sensor is also connected with arduino uno which will sense wet or dry hands. When the hands are wet/dry it sends signal to servo motor which will open/close entry gate/door. Also, an LCD block is also connected with arduino to display "Wash Your Hand" or "You May Go In".

3 Circuit Designing

Circuit diagram of the proposed model is shown in Fig. 2 which is implemented in hardware and it consists of an Arduino Uno as a microcontroller which has 28 pins out of which 14 are digital pins and 6 are analog pins, it has a flash memory of 32 kB and it operates at 5 V supply. Also, an HC-SR04 Ultrasonic sensor which has 4 pins (Vcc, echo, trig, ground) is used and echo and trig pin are connected with the digital PWM pin of arduino board and when trig pin is made high from arduino it initializes to send an ultrasonic wave for 100 microseconds and similarly echo pin will get high until the sent wave is received, during this operation arduino will be calculating the distance and comparing it with the preset level. If the calculated distance is equal to
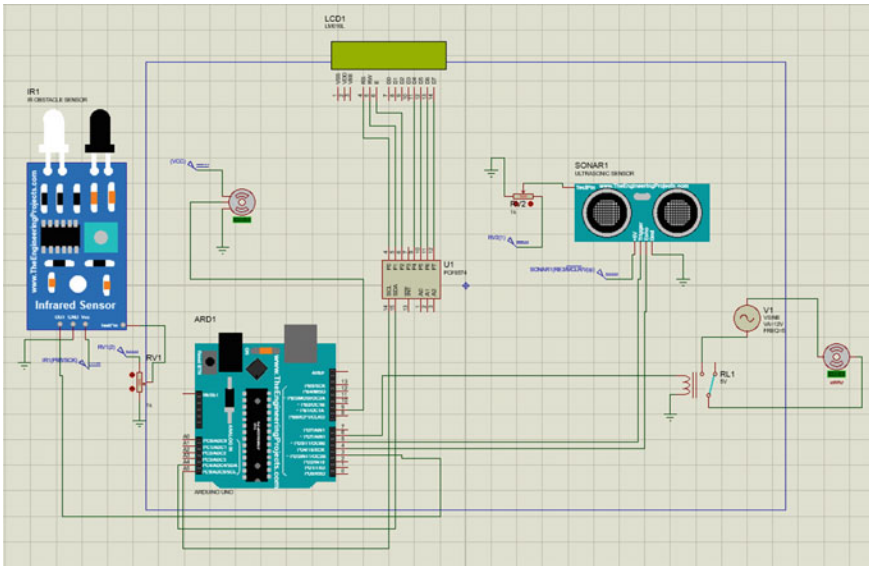
Fig. 2 The circuit diagram of the proposed model

or less than the preset level then arduino will send a PWM signal to the relay module, which is also connected to the arduino digital PWM pin, and have 3 pins (Vcc, input, ground) on one side and on other side it has NO (normally open), NC (normally closed) and COM (common) terminals and a water pump is connected with NO and COM terminal of the relay with a 12 V power supply and relay will operate after a signal is received from arduino. An IR (infrared) sensor which has 3 pins (Vcc, OUT, Ground) is also connected to arduino and will send a LOW signal to arduino when a person is detected. For opening and closing of the door a Servo motor is used which has 3 input pins (Vcc, PWM, ground) and it is also connected to arduino and operates when a PWM signal is obtained from arduino. A 16*2 LCD display with I2C interface is used which has 4 pins (Vcc, SDA, SCL, Ground) and is connected to the analog pin of arduino board. I2C interface is used because it provides easy communication without data loss. Finally for providing an operating voltage of 5 V to arduino and various sensors we used a 5 V constant DC supply.

4 Working and Implementation

The flow chart in Fig. 3 is demonstrating the steps for code that have been put in Arduino Uno using Arduino IDE application which supports code in C/C++

language. Firstly the system is initialized by defining the various hardware components connected with the Arduino UNO and also by initializing various libraries which will be used for working of components like LCD etc.

The initialization will begin with initializing the LCD and displaying 'Wash your Hands' through it and also make sure that backlit is on for LCD operation so that

Fig. 3 The flow chart of working of proposed model
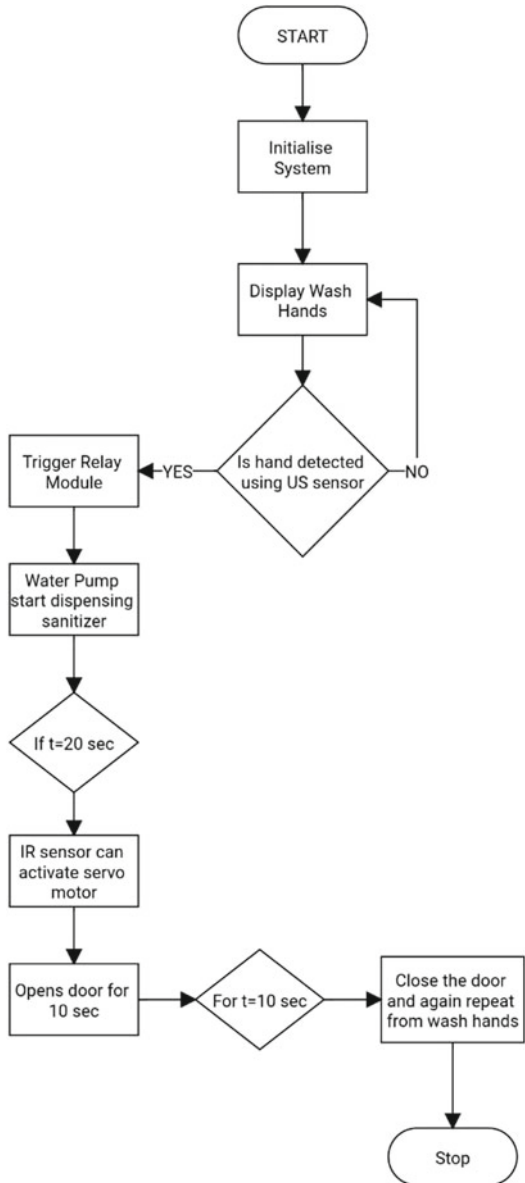
visibility is good. After this decision loop will decide if hands are detected or not with the help of an ultrasonic sensor. Logic will be like if hands are detected then exit the loop for next operation otherwise continue to repeat the loop which will result in the LCD showing 'Wash your hands'.

Now if hands are detected then it triggers the relay module which is controlling the operation of the submersible water pump. During the operation of the water pump, it initializes another nested-decision loop which will count for 20 s and will only proceed further if water pump dispenses sanitizer for 20 s. If the time dependent nested loop operation is achieved then IR sensor will send a LOW signal to arduino, then arduino will initialize the servo motor such that it will rotate 90°. After this again initialized a nested-decision loop according to which after 10 s arduino will send servo a signal to return to 0°.

The ultrasonic sensor will detect the presence of a hand and after that relay module will be triggered which will operate the water pump that will pour sanitizer on the hand. The complete model is designed as shown in Fig. 4a and tested many times. After sanitizing the hand, LCD will display that 'You may now go in' as shown in Fig. 4c. After that hands are sensed by IR sensor which will operate the servo motor and the gate will open for 10 s and will automatically close after that. The main advantage of the proposed model is low cost, low maintenance with efficient working. It is mainly designed to prevent the spread of corona virus by sanitizing every person or object entering in premises. It is non contactable, user friendly and easy to install on the wall or at door.

This system can be applied at any public entrance point or in places where hand hygiene is of utmost importance such as hospitals, banks, offices, home, shopping malls, colleges, canteens, public toilets etc.

5   Conclusion

The designed model is a must to sanitize the system hence it will surely help in implementing hand hygiene without any problem. It will also reduce the chances of cross contamination as it is truly touch less for any person or object entering to gate. As it is of small size (comparable with the size of switch board), it can be easily installed and as it is of low cost also it is very much affordable for every section of society. As we know that many times doctors and researchers pointed out that excess use of sanitizer have some adverse effect also so this system being automatic and controlled by a microcontroller can provide an optimal dose of sanitizer to a person without any wastage and in compliance with standards. One thing to keep in mind during the implementation of this system is that if alcohol based sanitizer is used then it must be kept in a closed container otherwise alcohol will get evaporated from the solution. As now a days concept of smart cities is being implemented so this system will also add modern appeal to the places where they are installed. It can also be improved for COVID-19 applications by integrating this system with computer vision which can be used to detect masks on people's faces automatically
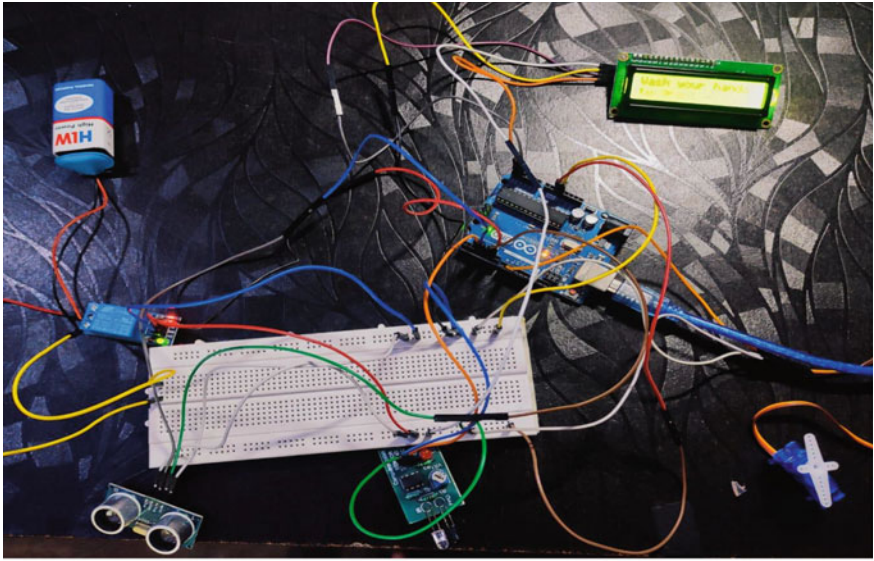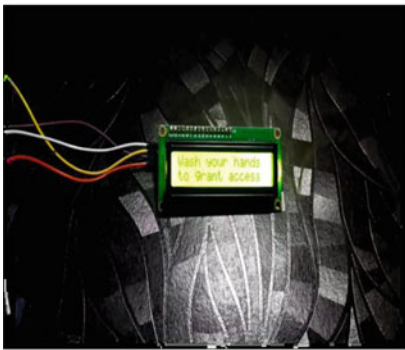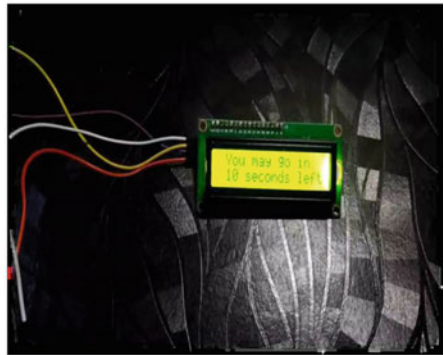
Fig. 4 Automatic sanitizer dispenser controlled door using arduino

and allowing them entry only if they are wearing masks and have gone through the sanitization process. It can be concluded here that the system has been successfully implemented and the objective is achieved.

References

1. Ansari SA, Springthorpe VS, Sattar SA, Rivard S, Rahman M (1991) Potential role of hands in the spread of respiratory viral infections: studies with human parainfluenza virus 3 and rhinovirus 14. J Clin Microbiol 29(10):2115–2119

2. Khan Z, Muhammad K, Ahmed A, Rahman H (2020) Coronavirus outbreaks: prevention and management recommendations. In: Drugs and therapy perspectives: for rational drug selection and use, pp 1–3. Advance online publication. https://doi.org/10.1007/s40267-020-00717-x
3. Guo YR, Cao QD, Hong ZS, Tan YY, Chen SD, Jin HJ, Yan Y et al (2020) The origin, transmission and clinical therapies on coronavirus disease 2019 (COVID-19) outbreak–an update on the status. Military Med Res 7(1):1–10
4. World Health Organization (2020) Surveillance case definitions for human infection with novel coronavirus (nCoV), interim guidance, 15 January 2020 (No. WHO/2019-nCoV/Surveillance/2020.2). World Health Organization
5. Bloomfield SF, Aiello AE, Cookson B, O'Boyle C, Larson EL (2007) The effectiveness of hand hygiene procedures in reducing the risks of infections in home and community settings including handwashing and alcohol-based hand sanitizers. Am J Infect Control 35(10):S27–S64
6. Akshay S (2020) Review on automatic sanitizer dispensing machine. Int J Eng Res 9. https://doi.org/10.17577/IJERTV9IS070307
7. Golin AP, Choi D, Ghahary A (2020) Hand sanitizers: a review of ingredients, mechanisms of action, modes of delivery, and efficacy against coronaviruses. Am J Infect Control 48(9):1062–1067
8. Boyce JM, Pittet D (2002) Guideline for hand hygiene in health-care settings: recommendations of the Healthcare Infection Control Practices Advisory Committee and the HICPAC/SHEA/APIC/IDSA Hand Hygiene Task Force. Infect Control Hosp Epidemiol 23(S12):S3–S40
9. Hayat A, Munnawar F (2016) Antibacterial effectiveness of commercially available hand sanitizers. Int J Biol Biotech 13(3):427–431
10. Ikegbunam MN, Metuh RC, Anagu LO, Awah NS (2013) Antimicrobial activity of some cleaning products against selected bacteria. Int Res J Pharm Appl Sci 3:133–135
11. Wanarti P, Nurhayati N, Yundra E, Rahmadian R, Widodo A, Dermawan MA (2020, November) Automatic hand sanitizer container to prevent the spread of corona virus disease. In: International joint conference on science and engineering (IJCSE 2020). Atlantis Press, pp 60–64
12. Wang C, Horby PW, Hayden FG, Gao GF (2020) A novel coronavirus outbreak of global health concern. The Lancet 395(10223):470–473
13. Klevens RM, Edwards JR, Richards CL Jr, Horan TC, Gaynes RP, Pollock DA, Cardo DM (2007) Estimating health care-associated infections and deaths in US hospitals, 2002. Public Health Rep 122(2):160–166
14. Sickbert-Bennett EE, DiBiase LM, Willis TMS, Wolak ES, Weber DJ, Rutala WA (2016) Reduction of healthcare-associated infections by exceeding high compliance with hand hygiene practices. Emerg Infect Dis 22(9):1628

VSC for DG Integration and Harmonics Reduction

Archana Sharma, Anshul Kumar Mishra, Aseem Chandel, and Radhe Shyam Dwivedi

Abstract This paper presents an algorithm for optimum utilization of the grid connected Voltage Source Converter (VSC) for power quality improvement and the integration of Distributed Generation (DG) sources. Conventionally, VSC is used as an interfacing device for DG with grid, and a separate VSC is used for intensification of power quality issues. This paper suggests the use of the same VSC for DG integration and for power quality enhancement also. The targets of the application is to: (1) inject available active power from DG to power grid, (2) harmonic mitigation of load side grid current, (3) keep grid current three phase balanced in case of fault at the load side, (4) operate system safely in condition of frequency deviation. The proposed algorithm shows very fast and robust response which is due to its less complex circuitry. Furthermore, the use of phase-locked loop (PLL) is eliminated with increase in the speed of operation of the system. Simulation of the proposed work considering most of the power system operating conditions is done to present the effectiveness of the work.

Keywords Distributed generation · Harmonics · Power quality · Voltage source converter

A. Sharma (✉)
Department of Electrical Engineering, Rajkiya Engineering College Bijnor, Bijnor, UP 246725, India
e-mail: archana.recb@gmail.com

A. K. Mishra · A. Chandel
Department of Electrical Engineering, Rajkiya Engineering College Mainpuri, Mainpuri, UP 205001, India

R. S. Dwivedi
Department of Applied Sciences and Humanities, Rajkiya Engineering College, Azamgarh, UP 276201, India

1 Introduction

DG refers to locally generated power consumed by the individual customers, which sometimes transfers to other customers (if available in excess) through the existing power grid. DG is not limited to only renewable energy generation; it includes micro-turbines which uses fuels for local electricity generation and many more [1, 2]. The integration of the DG to the grid requires the use of a power electronics converter. The main purpose of converters in DG integration is to make DG power compatible with the grid power. One more very often use of power electronic converter is for filtering the active power to intensify the quality of power. The intensification majorly includes grid current harmonic elimination, grid power factor correction, load balancing and fault correction.

Many control algorithms have been reported for VSC. Some of the algorithms are based on conventional approaches like Instantaneous Reactive Power Theory (IRP), Synchronous Reference Frame Theory (SRF) [3], power balance theory, etc. [4]. Other types of algorithms are adaptive algorithms in which the extraction of reactive and active power components of load current is done by the equation of weight update [5, 6]. Every year, a new addition in the adaptive control algorithm is seen in the literature with various features that help in working in a smart grid environment [7–10].

Although the control algorithms are changing but they should comply with the grid codes available for DG integration to the grid [11]. The technical issues that arise while integrating the DG to the grid should also be studied [12–15].

In this work, the basic control algorithm is modified, so that it can draw both active power from the DG and reactive power from the capacitor of the VSC. The DG is maintaining the frequency deviation of the electrical source by providing the active power deviation of the source, while the reactive power demand, as well as the anti-harmonics, are supplied by the DC capacitor of the VSC. The capacity of the DG depends on the magnitude of frequency deviation and the capacity of the DC capacitor is required as the reactive power demand of the load.

2 Power System Distribution Network

The system is composed of a DG unit connected to the VSC through a DC link capacitor which is at the end connected to the power grid as shown in Fig. 1. For driving the voltage source inverter, a control algorithm is used. The control algorithm takes the parameters of voltage and current from the source and load as the input which is processed to produce an output of pulses for VSC. The VSC works in accordance with the generated pulses to inject the reactive power and anti-harmonics to the load current at PCC.
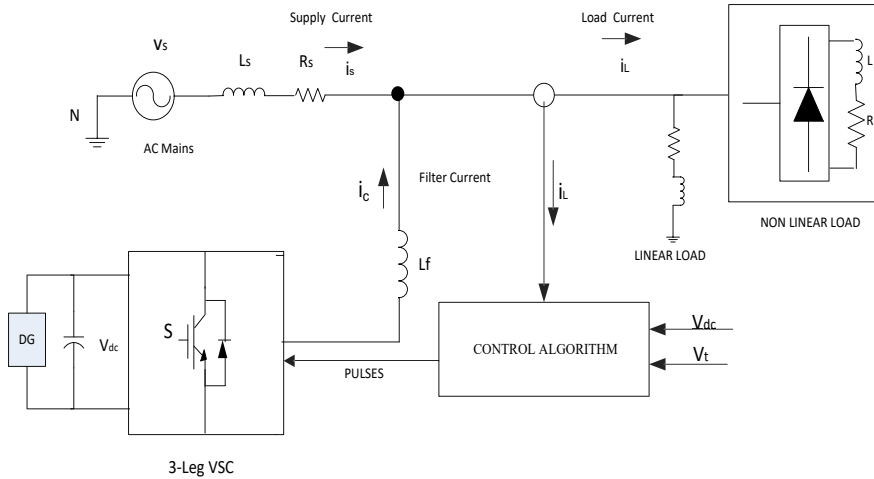
Fig. 1 Simplified diagram of DG integration to power grid

2.1 DC Link Voltage for Power Control

The infrequent nature of the renewable source used as a DG produces difficulties in directly adding them to the power grid. In this work, the DG is connected to a capacitor which absorbs the deviations of the renewable power sources. Figure 2 shows the network to transfer power from DG to grid. There are two current components, one is the injected current from DG to grid (I_{DG_1}) as mentioned in Eq. (1) and another (I_{DG_2}) as mentioned in Eq. (2) is flowing to other side of the dc link.

$$I_{DG_1} = \frac{P_{DG}}{V_{dc}} \tag{1}$$

where P_{DG} is the generated DG power and V_{dc} is dc link voltage.

$$I_{DG_2} = \frac{P_{inv}}{V_{dc}} \tag{2}$$

where P_{inv} is power available at grid interfacing unit.

Fig. 2 DC link diagram
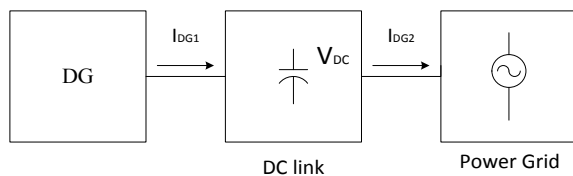
The control algorithm is designed with the concept that the DG power is supplied to the load if the requirement of the load is more than that is generated by the utility; on the other hand, if the DG power is in surplus to the load, the excess power is supplied to the grid. In both the cases, the reactive power generated by the VSC is supplied to the load.

2.2 Control Algorithm Design for Voltage Source Converter

Power balance theory is a simple algorithm designed by some basic components like multipliers, adders, filters, etc. This simple design of the algorithm makes it to work with a small delay. Power balance theory based control algorithm requires the voltage at the PCC (v_{soa}, v_{sob} and v_{soc}), source current (i_{s_a}, i_{s_b} and i_{s_c}), load current (i_{l_a}, i_{l_b} and i_{l_c}) and dc link voltage (V_{dc}) as input.

Firstly, the computation of in-phase unit voltage templates is done by calculating the amplitude of three phase terminal phase voltages (v_{soa}, v_{sob} and v_{soc}) at PCC as (3)

$$V_m = \text{sqrt}\left(\left\{(2/3)\left(v_{soa}^2 + v_{sob}^2 + v_{soc}^2\right)\right\}\right) \tag{3}$$

The computation of in-phase unit voltage templates as (4)

$$u_{p_a} = \frac{v_{soa}}{V_m}, u_{p_b} = \frac{v_{sob}}{V_m}, u_{p_c} = \frac{v_{soc}}{V_m} \tag{4}$$

Next, instantaneous active power of the load is calculated as Eq. (5):

$$p_L = V_t\left(u_{p_a}i_{l_a} + u_{p_b}i_{l_b} + u_{p_c}i_{l_c}\right) \tag{5}$$

This instantaneous load power contains two components, one is an average component and other is a double frequency component (6).

$$p_l = \overline{p} + \tilde{p} \tag{6}$$

DC component ($\overline{p}$) is filtered by a low pass filter. This part is supplied by DG in case if it is not greater than the power injecting capacity of DG. Double frequency component ($\tilde{p}$) is supplied by voltage source converter, thus harmonics will not appear at grid side as shown in Fig. 3. The active component of grid current has two components. One is active power demand of load current (7) and other is DC bus regulator current, which determines how much power is exchanged by DG and load (8).

$$I_{lp}^* = \frac{2}{3}\overline{p}/V_m \tag{7}$$
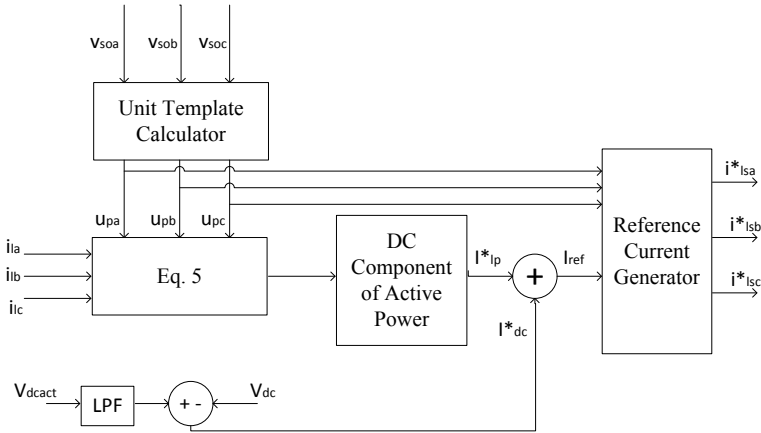
Fig. 3 Simplified diagram of the control algorithm

$$I_{dc}^* = K_p V_{dce} + K_d \int V_{dce} dt \tag{8}$$

where, $V_{dce} = V_{dc} - V_{dcact}$ = error in DC bus voltage. V_{dc} is reference bus voltage and V_{dcact} is actual bus voltage.

The active power component of reference current,

$$I_{ref} = I_{lp}^* + I_{dc}^* \tag{9}$$

3 Results and Discussions

The results show the behavior of the proposed work under power system operating conditions. A voltage source converter is used to interface DG and to the power grid. The operating conditions included for system working verification are a sudden change in load power, single phase and three phase fault conditions at the load side and variation in frequency in a predefined range. DG power output can be varied to some amount as the excess power generated from DG has to supply to the grid. But the limitation of distribution voltage limits the power variation to some defined limit. Faults considered in this work are single line and three phase faults. Single line fault is creating unbalance in the system and three phase fault completely disconnects the system. At this condition probability of grid current distortion is very high, but the algorithm used is able to make grid current balance and harmonics free. Frequency variation in the grid system is only some percent, in the case of frequency variation; the proposed system is able to work properly. Figure 4 shows the performance of the system when most of the operating conditions are chosen.

The figure presents grid voltages (v_{soa}, v_{sob} and v_{soc}), grid currents (i_{s_a}, i_{s_b} and i_{s_c}), load currents (i_{l_a}, i_{l_b} and i_{l_c}), inverter current (i_{inv_a}, i_{inv_b} and i_{inv_c}) and dc link voltage (V_{dc}). As shown in the figure, DG is connected to grid at $t = 0.2$ s. Before $t = 0.2$ s, load power is supplied by the grid and the non-linear nature of load current makes grid current non-sinusoidal, which contains different harmonics components. After connecting DG to the grid, DG supplies load power as well as extra power to grid. Supply of load power from DG, makes grid current sinusoidal again. This figure is briefly explained in the later part of this paper (Table 1).

The compatibility of active and reactive power between grid (P_{grid}, Q_{grid}), DG (P_{inv}, Q_{inv}) and load (P_{load}, Q_{load}) is presented in Fig. 5. This figure shows the variation in power exchange between grid, load and inverter at different conditions.
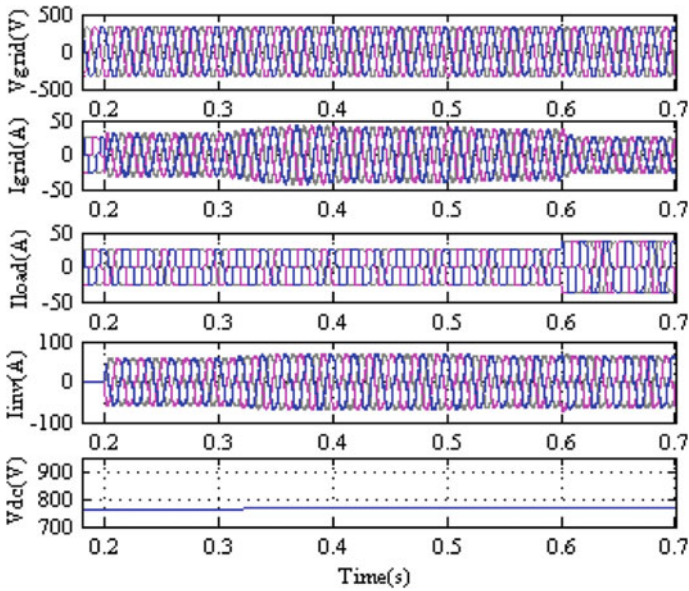
Fig. 4 Performance of the proposed concept: **a** three phase PCC voltages, **b** three phase grid currents, **c** three phase load currents, **d** current from VSC, **e** DC link voltage

**Table 1** Power system network parameters

Parameter	Magnitude
Source voltage	415 V
Frequency deviation	50 ± 0.5 Hz
X/R ratio	15
DC bus voltage	850 V
Interfacing inductance	2 mH
DG power	35 kW, 18 kVA
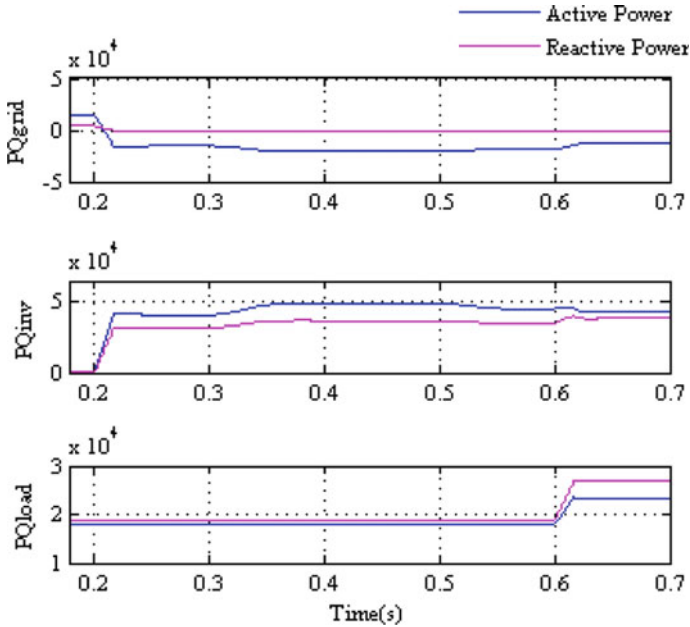
Fig. 5 Performance of the proposed concept: **a** PQ-grid, **b** PQ-inverter, **c** PQ-load

3.1 Change in DG Output

See Fig. 6.

3.2 Variation in Load

System behavior for load change is shown in Fig. 7. At $t = 0.6$ s, load changes to some higher value. This value of load change is less than the total capacity of DG power. DG supplies the load change, but the source current decreases due to a decrease in the amount of power supplied by DG as shown in Fig. 5.

3.3 In Condition of Fault

Fault in the system can cause both unbalance and instability of the system. To check the performance of the system both single line and three phase faults are considered in the system. At $t = 0.8$ s, a single line fault encountered the system as shown in
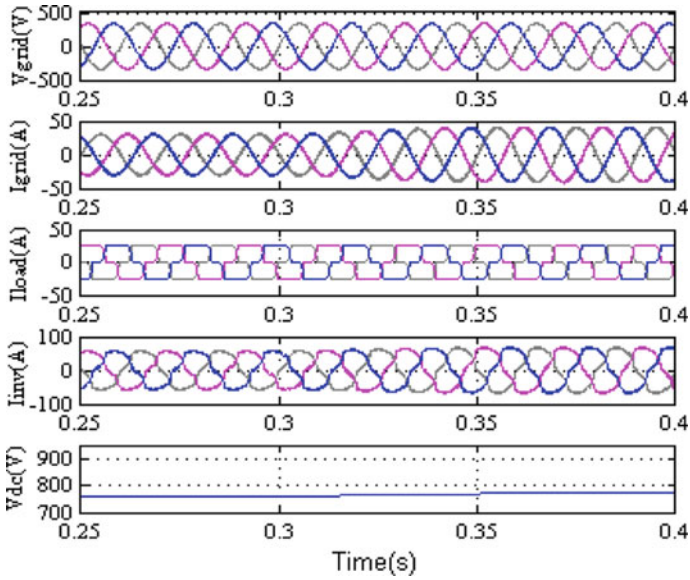
Fig. 6 Response under DG output variation: **a** three phase PCC voltages, **b** three phase grid currents, **c** three phase load currents, **d** current from VSC, **e** DC link voltage
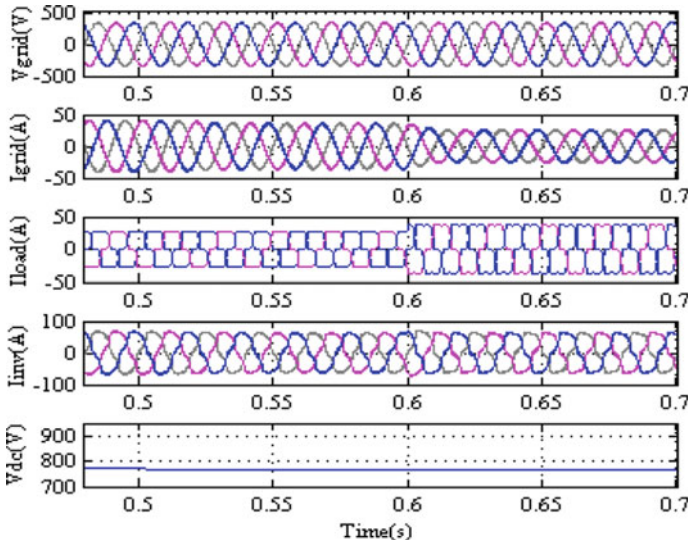
Fig. 7 Response under load variation: **a** three phase PCC voltages, **b** three phase grid currents, **c** three phase load currents, **d** current from VSC, **e** DC link voltage
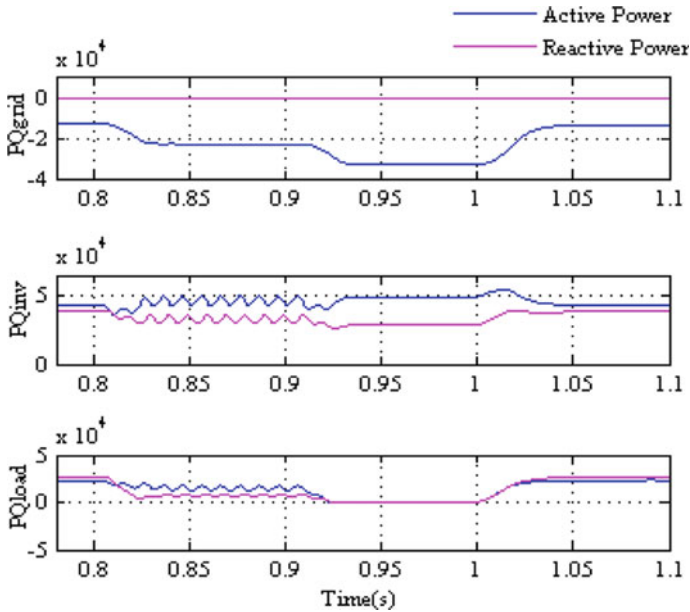
Fig. 8 Complete response under fault: **a** PQ-grid, **b** PQ-inverter, **c** PQ-load

Figs. 8 and 9, this fault has a tendency to make the system unbalanced. DG power supply makes the system balanced under the fault.

At $t = 0.9$ s, three phase fault occur in the system, this makes load current zero and power generated from DG is supplied to the grid. At $t = 1$ s, fault is cleared and system reached its initial condition back. This shows that the system can take momentarily fault conditions properly.

3.4 Frequency Deviation

Frequency deviation is a rare phenomenon because of many regulating devices used to correct frequency, but severity of frequency deviation is very high. To make system able to momentarily work in condition of frequency deviation, system performance is checked for a deviation of 2 Hz from its nominal value. All the conditions remains same as earlier, change in frequency does not show any major difference in system performance (Fig. 10).
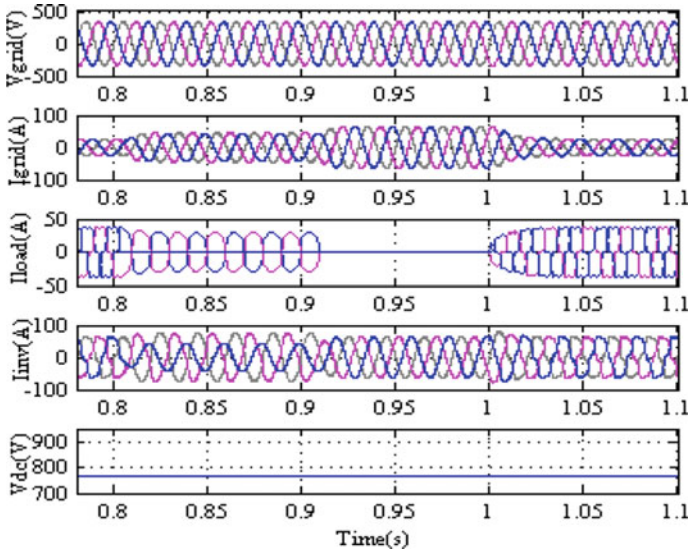
Fig. 9 Performance during fault condition: **a** three phase PCC voltages, **b** three phase grid currents, **c** three phase load currents, **d** current from VSC, **e** DC link voltage
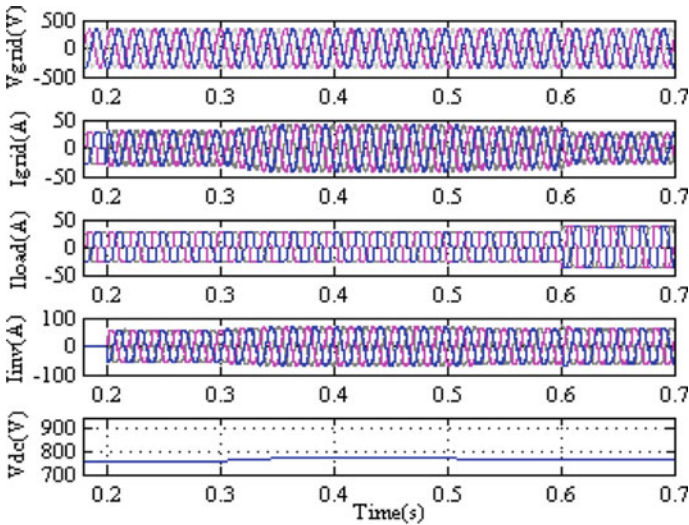
Fig. 10 Response under frequency variation: **a** grid voltages, **b** grid currents, **c** load currents, **d** inverter currents, **e** dc link voltage

3.5 *Total Harmonic Distortion (THD)*

Harmonic percentage in various parameters of the system is shown in Fig. 11. This can be shown easily that harmonic distortion of grid current is 1.68%, which is very less compared to load current of 21.97%. Grid voltage THD is only 0.21%.

Fig. 11 FFT analysis of (1) grid current, (2) load current and (3) grid voltage
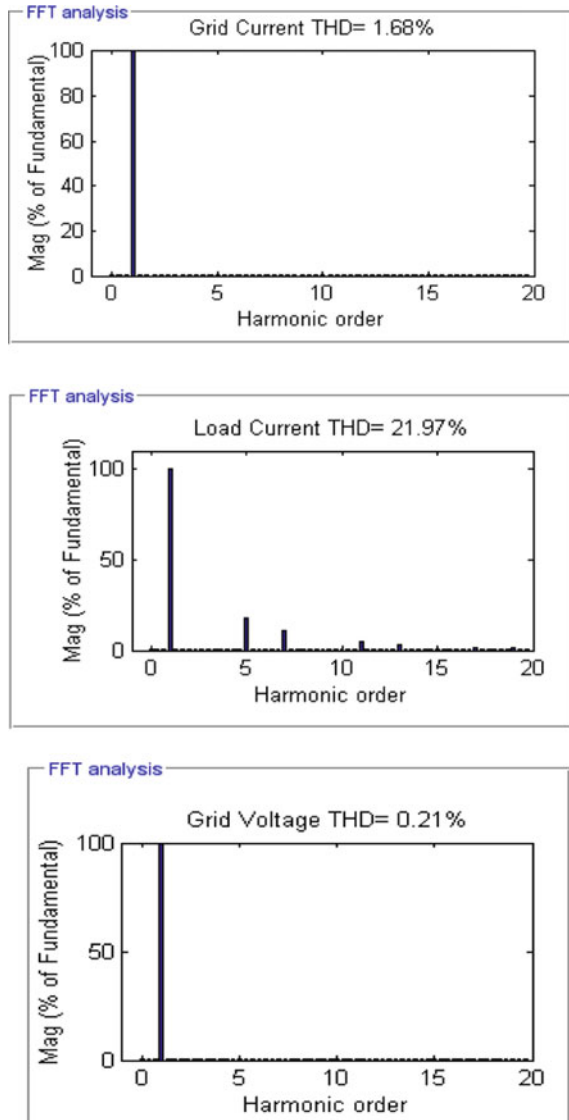
4 Conclusions

More numbers of VSCs connected to the power grid can cause instability in the power grid. The integration of DG to the grid requires the use of VSC to make the DG power compatible to the grid power, on the other hand, the VSC is used to mitigate the power quality problems of the distribution side network. In this work, the same VSC is used for integration of DG to power grid and to mitigate the power quality issues of the distribution side. The control algorithm has shown satisfactory performance in the harmonic mitigation, reactive compensation, load balancing and frequency deviation. Various results of the algorithm is shown to justify the behavior of the VSC under various conditions.

References

1. Wang F, Duarte JL, Hendrix MAM, Ribeiro PF (2011) Modeling and analysis of grid harmonic distortion impact of aggregated DG inverters. IEEE Trans Power Electron 26(3):786–797
2. Po-Hsu H, El Moursi MS, Weidong X, Kirtley JL (2014) Fault ride-through configuration and transient management scheme for self-excited induction generator-based wind turbine. IEEE Trans Sustain Energ 5(1):148–158
3. Divan DM, Bhattacharya S, Banerjee B (1991) Synchronous frame harmonic isolator using active series filter. In: Proceedings of European conference on power electronics, pp 3030–3035
4. Asiminoaei L, Blaabjerg F, Hansen S (2007) Detection is key—harmonic detection methods for active power filter applications. IEEE Ind Appl Mag 13(4):22–33
5. Rodríguez P, Luna A, Candela I, Mujal R, Teodorescu R, Blaabjerg F (2011) Multiresonant frequency-locked loop for grid synchronization of power converters under distorted grid conditions. IEEE Trans Ind Electron 58(1):127–138
6. Kumar P, Mahajan A (2009) Soft computing techniques for the control of an active power filter. IEEE Trans Power Del 24(1):452–461
7. Abdeslam DO, Wira P, Merckle J, Flieller D, Chapuis Y-A (2007) A unified artificial neural network architecture for active power filters. IEEE Trans Ind Electron 54(1):61–76
8. Awad H, Svensson J, Bollen MJ (2005) Tuning software phase-locked loop for series-connected converters. IEEE Trans Power Del 20(1):300–308
9. da Silva CH, Pereira RR, da Silva LEB, Lambert-Torres G, Bose BK, Ahn SU (2010) A digital PLL scheme for three-phase system using modified synchronous reference frame. IEEE Trans Ind Electron 57(11):3814–3821
10. Singh B, Arya SR, Chandra A, Haddad KA (2014) Implementation of adaptive filter in distribution static compensator. IEEE Trans Ind Electron 50(5):3026–3036
11. Preda T, Uhlen K, Nordgård DE (2012) An overview of the present grid codes for integration of distributed generation. In: CIRED 2012 workshop: integration of renewables into the distribution grid
12. Kumar DS, Savier JS (2017) Impact analysis of distributed generation integration on distribution network considering smart grid scenario. I: 2017 IEEE region 10 symposium (TENSYMP), pp 1–5
13. Kazmi SAA, Hasan SF, Shin D (2015) Analyzing the integration of Distributed Generation into smart grids. In: 2015 IEEE 10th conference on industrial electronics and applications (ICIEA), pp 762–766
14. Coster EJ, Myrzik JMA, Kling WL (2009) Effect of grid disturbances on fault-ride-through behaviour of MV-connected DG-units, in especially CHP-plants. In: 2009 CIGRE/IEEE PES

joint symposium integration of wide-scale renewable resources into the power delivery system, pp 1–11
15. Pouresmaeil E, Miguel-Espinar C, Massot-Campos M, Montesinos-Miracle D, Gomis-Bellmunt O (2013) A control technique for integration of DG units to the electrical networks. IEEE Trans Industr Electron 60(7):2881–2893

Comparison of Charging Techniques for Electric Vehicle Battery Charging

Allamsetty Hema Chander, Madisa V. G. Varaprasad, and Phani Teja Bankupalli

Abstract The objective of reducing the pollution levels widely promotes the usage of electric vehicles (EVs) throughout the globe. Government of India also works in this regard with the motto of having 100% electric vehicle mobility by the year 2030. However, unlike many other nations, India is still developing the charging stations, which is the major limitation for the usage of EVs in India. Moreover, the charging stations available, take a long time to charge the battery. To compete with its counterparts like conventional fuel stations, the time taken for charging should drastically be reduced. Most of the fast charging techniques proposed in the state of the art have a major limitation of degrading the battery performance. In this regard, this work investigates the performance of the widely employed fast charging technique when implemented to the conventional buck converter. Further, a comparison of the technique with conventional charging techniques is also presented.

1 Introduction

The increased concern about the environment and rapid growth in the price of crude oil has resulted in increased research on the alternatives to conventional automobile vehicles. The research resulted in the development of EV technology, a clean mode of transportation [1]. The key features like environment friendly, less maintenance and low energy consumption made EVs emerge as a new era in the mode of transportation. Most of the EVs are powered by battery alone and hence are limited in

A. H. Chander (✉)
National Institute of Technology Puducherry, Karaikal, India
e-mail: ahemachander01@gmail.com

M. V. G. Varaprasad
Vignan's Institute of Information Technology, Visakhapatnam, India

P. T. Bankupalli
SRM Institute of Science and Technology, Chennai, India

range. Moreover, the availability of charging stations and the time taken to charge the battery are the major limitations [2]. The battery technology in the recent times is the Lithium ion technology. The advantage of the Li-ion batteries is the long life, high energy density, higher number of charge-discharge cycles and durability [3, 4], compared to its counterpart, the conventional lead acid batteries.

The time taken to charge the battery is the major limitation for the development of the charging stations and limited EV usage in most of the developing countries like India. The conventional methods of charging the battery include constant voltage (CV) charging method and constant current (CC) charging method [5]. Both the methods are widely employed and have their own pros and cons. The CV method charges the battery without the degradation of battery performance, however, takes a very long time to completely charge the battery. On the other hand, CC method charges the battery in a less time comparatively; however, due to high currents near the upper cut off value of the voltage, the chance of performance degradation is high and is also risky. Hence, it is a general practise to use CV method more often and CC method with more precautions taken. However, in order to reduce the risk of high currents, most of EVs used CV method, in which charging time is too high approximately 7–8 h.

In this regard, there has been increased research on the charging techniques of the battery in the recent era. Based on the research, various safe and precise fast charging techniques have been developed and reported in the literature. One of the most popular and widely employed techniques is the CC-CV method [6]. The CC-CV method, even though is popular, very few literature reports the comparison of the performance with respect to the conventional CV method. In this regard, this paper aims to investigate the performance of the two methods and highlight the advantages of the CC-CV method quantitatively. Further, the CC-CV method has been implemented using a power electronic converter to charge the battery. The rest of the paper is organized as follows: Sect. 2 briefs the CC-CV method. Section 3 deals with the implementation of the CC-CV method for charging the battery followed by a comparison with CV method. Finally, Sect. 4 summarizes the paper.

2 CC-CV Method

As mentioned, one of the most widely adopted fast charging techniques is the CC-CV method. In this section, the charging method to charge Li-ion cells has been briefed. The battery initially is made to charge at a constant rate of current, generally in the range 0.5–1 C specified by the manufacturer. In general, the battery is available as a battery pack, with cells connected in a series-parallel combination. During charging, the cell equalization technique is generally preferred [6, 7]. With the assumption of balanced cells, the battery is charged through CC method till the voltage reaches 4.2 Ns, where, N represents the number of series connected cells and 4.2, the maximum voltage for a Li-ion cell. Further, the charging continues in CV method so as to limit the stress on cells due to over voltage. This helps in improvement of the performance

of the battery. Moreover, the usage of CC-CV technique reduces the charging time drastically, up to 60–120 min from 7 to 8 h. However, safety precautions are to be taken for limiting the temperature to avoid excessive cell heating. As a case study, the working of CC-CV method is discussed for a 24 V battery. The maximum chargeable and minimum dischargeable voltages for 24 V battery is say 28 V and 15 V respectively. In this method of charging, the battery is charged with a preset value of current generally, in the range of 0.5–1 C. The process is continued till the battery reaches the maximum voltage. At this instant, the battery is charged by applying a constant voltage. The same has been illustrated in Fig. 1. The first stage is the initial pre-charging stage; the second stage is the intermediate CC stage followed by the CV charging stage at the end.

In the first stage, the current is slowly increased in steps until the battery voltage slowly rises to the constant current threshold value which protects the battery from damaging. In the second stage, the battery is charged with a high value of constant current. Once the battery reaches the maximum voltage, the battery is charged with the constant voltage which is the last stage for avoiding the overcharge and thereby protecting the battery. The charging time of the battery in the standard CC/CV method is given by [8]

$$\text{Charging Time} = 1.3 * \frac{\text{Battery capacity(Ah)}}{\text{Charging Current during CC}} \tag{1}$$

In most of the cases, the mode transition is done based on the state of charge (SoC) of the battery [9]. Initially, the battery is charged with the constant current up to a predefined SoC level (mostly 80%). When the battery reaches 80% SoC level
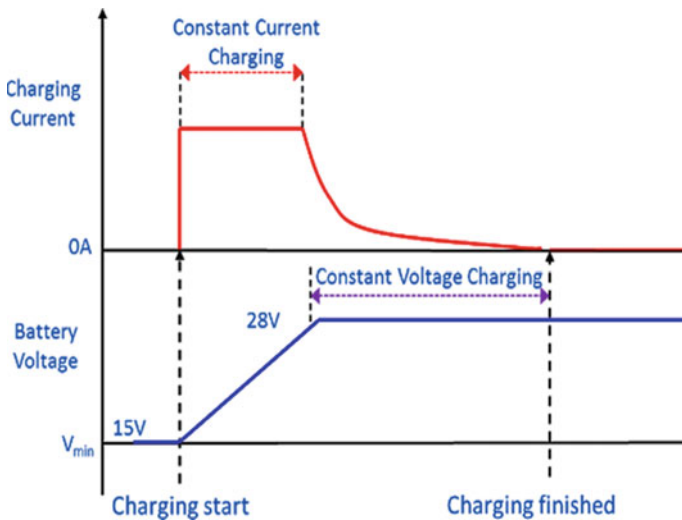
Fig. 1 Stages in CC-CV charging method

Fig. 2 Flowchart of CC-CV charging method
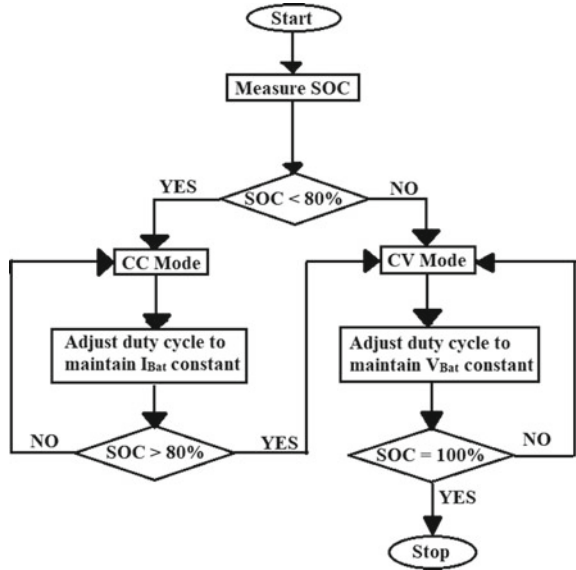
the transition in the charging mode occurs from constant current mode to constant voltage mode. The flow chart in Fig. 2 depicts the CC-CV technique. The SoC of the battery can be estimated in terms of open circuit voltage.

3 Implementation of CC-CV Method

In this work, the CC-CV method is implemented using a buck converter for charging the Li-ion battery [10]. The block diagram of the implemented system is depicted in Fig. 3.
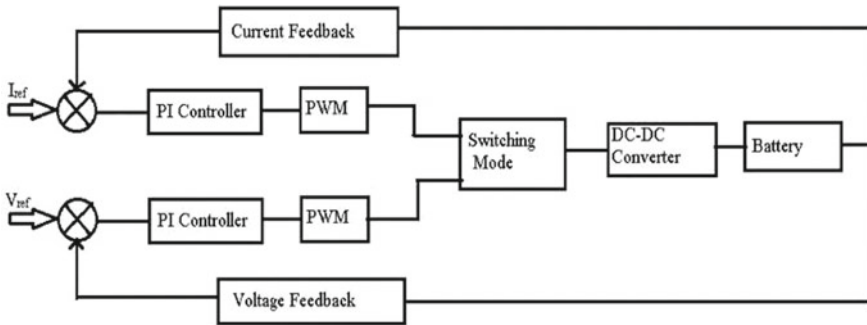
Fig. 3 Control loop block diagram for the CC-CV charging scheme

The output voltage and current are sensed from which the SoC can be estimated. In CC mode, the PI controller in the current loop adjusts the duty cycle of the buck converter to maintain the constant current throughout this mode. The controller adjusts the duty cycle to maintain the constant current irrespective of the change in input voltage. Similarly, in CV mode the PI controller in the voltage loop adjusts the duty cycle of the converter to maintain a constant voltage. The transition of the mode of charging occurs depending on the SoC or open circuit voltage of the battery. When SOC becomes 100% or the open circuit voltage reaches the maximum value, the battery is considered as completely charged.

The CC-CV method has been implemented in MATLAB/Simulink environment using a buck converter for charging a 24 V, 13 Ah Li-ion battery. The maximum chargeable voltage has been considered to be 26.5 V. A constant current of 10 A has been considered to charge the battery in CC mode. The input voltage considered is 48 V. The initial SoC has been taken as 80% (Fig. 4).

To observe the superiority of the CC-CV method compared to its counterpart, CV method, a 24 V, 13 Ah battery with initial SoC of 38% has been considered and charged up to 1000 s (17 min approximately). The maximum chargeable voltage of 26.5 V has been considered, which is the voltage applied to the battery in CV mode. A constant current of 10 A has been considered to charge the battery in CC mode. The SoC of both the charging methods have been compared and depicted in Fig. 5. It can be observed that, using CV method, the SoC of the battery has been increased from 38 to 41%, i.e. the increase in SoC is approximately 7.3%. On the other hand, with CC-CV method, the SoC has been increased from 38 to 60%, i.e., an approximate raise of 36.6% has been noticed. Thus, it can be concluded that for the battery considered, the CC-CV method charges the battery 5 times faster than the CV method.
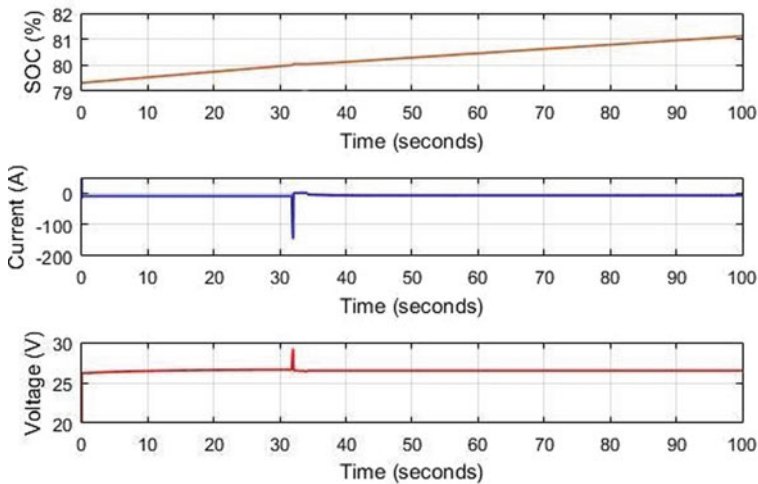
Fig. 4 Mode transition from CC to CV
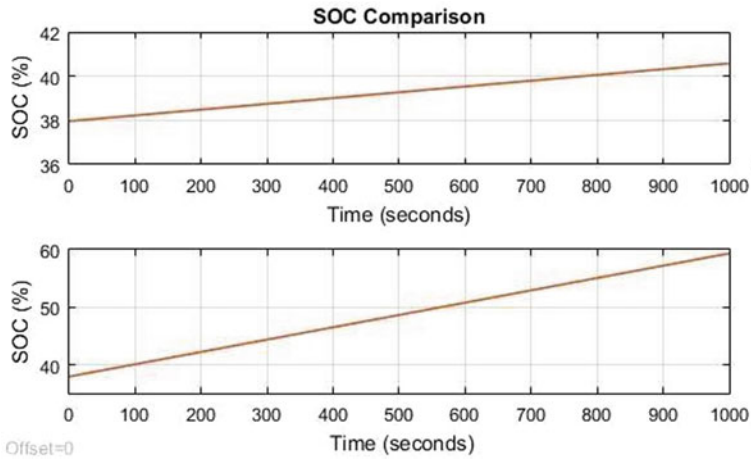
Fig. 5 SoC comparisons of CV and CC-CV methods

The parameters of the battery have been compared for both methods. The battery parameters in CV method are depicted in Fig. 6. As discussed, it can be observed that, the SoC has been increased from 38 to 41% with a charging current of 2 A.

Similarly, the battery parameters using CC-CV method are illustrated in Fig. 7. The SoC has been increased from 38 to 60% as discussed with a constant charging current of 10 A.

The buck converter parameters in CC-CV mode are depicted in Fig. 8. As observed, the input voltage is 48 V and the input current is 10 A. The output of the buck converter, since connected to the battery, it can be observed that, the output
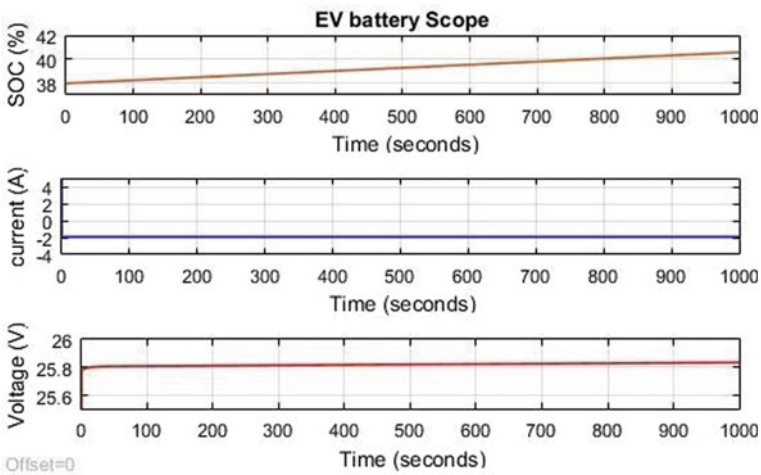
Fig. 6 Battery parameters in CV charging method
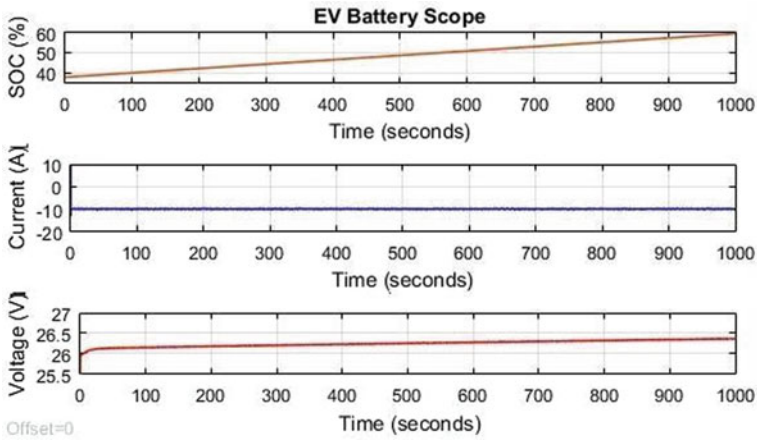
Fig. 7 SOC, voltage and current of the battery for CC-CV charging method
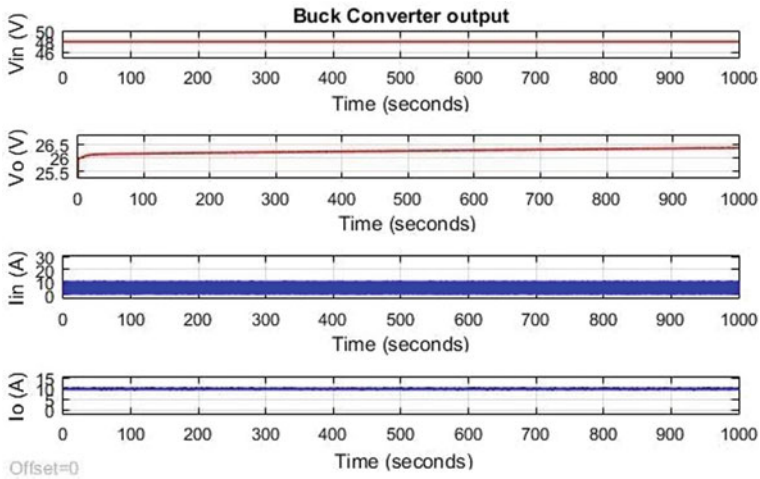
Fig. 8 Output waveforms of voltage and current of buck converter using CC-CV technique

voltage (V_o) slowly increases and the output current (I_o) is maintained at a constant 10 A.

4 Conclusion

In this paper, the CC-CV charging method for charging the battery of EV has been discussed. The method has been implemented for a 24 V, 13 Ah, Li-ion battery using

a buck converter. Further, the superiority in charging time compared to CV method has been investigated. It has been observed that, the CC-CV charging method charges the battery five times faster than the CV method. Moreover, the results also show a proper dynamic behaviour of the battery voltage, current and the SOC confirming that the chances of performance degradation is quite low. The CC-CV method due to reduced charging time without performance degradation of the battery is best suited for the establishment of the fast charging stations to promote EVs in developing countries.

References

1. Larminie J, Lowry J (2012) Electric vehicle technology explained. Wiley
2. Hussein AA-H, Batarseh I (2011) A review of charging algorithms for nickel and lithium battery chargers. IEEE Trans Veh Technol 60(3):830–838
3. Khaligh A, Li Z (2010) Battery, ultracapacitor, fuel cell, and hybrid energy storage systems for electric, hybrid electric, fuel cell, and plug-in hybrid electric vehicles: state of the art. IEEE Trans Veh Technol 59(6):2806–2814
4. Dhameja S (2001) Electric vehicle battery systems. Elsevier
5. Kang T, Chae B, Suh Y (2013) Control algorithm of bi-directional power flow rapid charging system for electric vehicle using Li-Ion polymer battery. In: 2013 IEEE ECCE Asia Downunder. IEEE, pp 499–505
6. Cope RC, Podrazhansky Y (1999) The art of battery charging. In: Proceedings of the conference on fourteenth annual battery conference on applications and advances (Cat. No. 99TH8371). IEEE, pp 233–235
7. Jiang W, Fahimi B (2009) Active current sharing and source management in fuel cell–battery hybrid power system. IEEE Trans Ind Electron 57(2):752–761
8. Rachid A, El Fadil H, Giri F (2018) Dual stage CC-CV charge method for controlling dc-dc power converter in BEV charger. In: 2018 19th IEEE mediterranean electrotechnical conference (MELECON). IEEE, pp 74–79
9. Omar N, Daowd M, van den Bossche P, Hegazy O, Smekens J, Coosemans T, van Mierlo J (2012) Rechargeable energy storage systems for plug-in hybrid electric vehicles—assessment of electrical characteristics. Energies 5(8):2952–2988
10. Kazimierczuk MK (2015) Pulse-width modulated DC-DC power converters. Wiley

Design and Implementation of an Unidirectional Isolated DC-DC Converter for Fuel Cell Applications

Phani Teja Bankupalli, Madisa V. G. Varaprasad, and Allamsetty Hema Chander

Abstract The drastic increase in demand for non-conventional energy sources for grid or standalone applications has led to a focus on the design of power electronics converters. Isolated DC/DC converter converters are emerging as very good interfacing elements for electrical applications including high voltage range requirements. Flexibility to vary voltage gain using a coupled transformer, electrical isolation between input and output, high power transfer capability and improved power quality have been the significant aspects for adopting isolated DC/DC converter converters for various power applications. High current demand for high voltage gain requires the integration of promising sources like fuel cells. High efficiency, portable size, high energy density and low temperature operation make the usage of fuel cells a dominating factor. The combination of fuel cells with an isolated DC/DC converter is a promising alternative to conventional systems involving PV and non isolated converters. The power electronic converters are controlled by fast switching semiconductor components. Conventional control uses hard switching technique in which the semiconductor switch is subjected to turn ON/OFF at a finite current or voltage level. This process increases the switching loss and reduces the overall efficiency of the converter. However, soft switching technique includes zero voltage and/or zero current switching is an advanced switching method which reduces the loss and improves efficiency. Thus the present work aims at design and implementation of a fuel cell fed isolated DC/DC converter with soft switching technique. As compared to conventional switching, the efficiency using the proposed system is improved and justified using MATLAB simulations.

Keywords Isolated DC/DC converter · Fuel cell · Soft switching technique

P. T. Bankupalli (✉)
SRM Institute of Science and Technology, Kattankulthur, India
e-mail: phanib@srmist.edu.in

M. V. G. Varaprasad
Vignan's Institute of Information Technology, Visakhapatnam, India

A. H. Chander
National Institute of Technology, Puducherry, India

1 Introduction

These days power is generated by burning of fossil fuels and as the demand increases the green-house gas emissions also increases. Increase in the usage of eco-friendly fuel cells which does not produce any emission is observed in modern days [1]. For proper operation of the above renewable sources, DC/DC converters are very helpful in improving the efficiency and reduction of size. When the DC/DC converter provides a constant voltage which is stable many other required subsidiary systems are reduced which results in reduced cost and reduced size [2]. Polymer electrolyte membrane type (PEM) type fuel cells are very advantageous in context to other energy sources, they have a normal operational range of temperature, they utilize hydrogen fuel and give nil harmful waste products, moreover, their by-products are just water which can easily be reused after processing and also heat which can be put to use to again to generate energy. These systems cannot be integrated with the grid using non isolated converters because of low voltage gain and large leakage current [3].

Whereas isolated converters provide insulation between the source and the device, also increases the voltage gain and reduces the leakage current with providing a safe environment to operate [3]. Switches present on the secondary side are the reason for the large loss of power when the conventional converters are used for sources which have low voltage and high current value. A power converter which undergoes soft-switching will be more efficient for sources with low voltage and high current if the switches are on the primary side [4]. Pulse width modulated DC/DC converters are suitable for applications which require high power [5]. The efficiency of a non-isolated system for photovoltaic uses was found to be 3–4% less than the efficiency of an Isolated DC/DC converter, hence isolated DC/DC converter is much more efficient for such applications [6].

In conventional unidirectional topology in the circuit using conventional switching devices, the potency is good but the transformer is not utilized fully, if we make use of a diode rectifier circuit the potency can be increased [7]. There are many types of soft switching techniques which can be used i.e. zero current switching, zero voltage switching, zero current zero voltage switching [8]. The soft switching strategy which is to be implemented in the DC/DC converter device will lead to a reduction in switching losses and will in turn improve efficiency [9].

The output voltage of the fuel cell is very low in a range less than 1 V so a converter is needed to increase the voltage and as there is ripple present in the output, to reduce the ripple a filter needs to be designed. Interleaved converters are very heavy and large in size so they cannot be used for mobile applications or applications which need light weight devices [10]. Galvanic isolation is a very good merit of isolated DC/DC converters which makes them suitable for application in medium voltage direct current grid applications in which if a fault is to be removed there is insulation between the two sides [11].

Small variety of parts, Low device and component stresses with biface power flow, the most important disadvantage is that the sensible realization of a three-phase

symmetrical electrical device with identical leakage inductances in every section [12]. Commercially on the market IGBT modules don't seem to be appropriate for high-density high frequency applications [13]. The most blessings of the device are high-operation frequency and nil value of the switching losses however it needs a lot of power and magnetic devices that increase the scale and price [14].

Soft switching during a wide load power varies with no further auxiliary circuits and elimination of freewheeling current-mode however it's the high price of parts [15]. With the use of the voltage multiplying device, high voltage gain at the output is obtained and therefore the voltage stresses that occur on the devices of the hybrid rectifier are created to be 1/2 the voltage at the output. Moreover, conversion in a single stage, a large selection range of Zero Voltage switching and large potency should be accomplished within the planned device [3].

High switching frequency converters are very widely used nowadays due to their compact size, less magnitudinal value of components used as well as reduced price due to former. Quasi resonant technique of soft switching is very helpful in reducing distortion due to other components in the converter. There is also a disadvantage of this type of switching and it is that it requires a high value snubber circuit, which eventually increases the cost [16]. But there are many techniques to remove the need of a snubber circuit which make use of this switching efficient. The conventional circuits which make use of various types of soft switching techniques are very costly as they have a very large number of components required [17]. These converters cannot be used in areas where the value of power is low because they result in less power density. Generally to decrease power loss operation, a converter is preferred at a high frequency of switching which in turn increases the electromagnetic interference, to remove these increased losses soft switching is employed. There are two types of soft switching techniques when it comes to frequency, constant frequency and variable frequency [18]. Constant switching frequency techniques require a lot of extra components and switches thereby increasing the cost of the converter and complexity also [18]. Variable switching frequency (like Quasi resonant switching) converters can function with a single switch and provide better efficiency than its counterpart and also reduces the cost and complexity of the converter because of the low component count.

As discussed earlier, isolated converters have the flexibility of improved voltage gain at the output due to the presence of high frequency transformer. Achieving high voltage at the output demands a high input current from the source. Since fuel cell is attributed with high current density characteristics, it is best suited for integration with high gain isolated converters. However, high current operation increases the power loss in the converter and results in a reduction in the overall efficiency of the system. Majority of the existing work with fuel cell integrated isolated converter with high current carrying capability has aimed at improved voltage regulation at DC bus. However, reported works have not concentrated on the integration of novel switching methodologies for improved converter efficiency. In this regard, the present work adopts a soft switching strategy interfacing with the isolated converter aiming at improving the efficiency. Also, this paper quantifies the power loss minimization in the switch of the integrated fuel cell system.

2   Fuel Cell

Fuel cells are electrochemical devices that produce electricity from the energy present in chemical form in fuels, producing electricity with high potency as well as extremely tiny result on surroundings. As a result of the manufacturing process, the work and the heat energy which occurs in other power production strategies are not used, fuel cells are not put in limitation by restrictions of thermodynamics of the heat of engines like the carnot efficiency. The fuel cells doesn't undergo any burning, and therefore they are eco-friendly and do not leave out any products which are of no use. As in batteries, we do not need to replenish the electrolytes inside but here in fuel cells, fuel has to be given unceasingly to make power constantly. Fuel cells are very likely electrolyzers. In fact, some fuel cells can operate in opposite conditions, which is like a revered cell in which the energy can be kept. although fuel cells might theoretically, make use of a good type of oxidizing agent and fuel, these days commonly those fuel cells are used which have common fuels or reducer as gas, and the oxidizing agent is air. The fuel cells are composed of different number of components.

Unit cells, these are the components where the chemical reactions happen. Stacks in which the conjugation of cells are done by making an electrical connection between them to get units which have the required output power. Balance of plant that includes elements which offer management of thermal processes, conditioning of power and sometimes a fuel controller. The basic structures of fuel cells are unit cells. The chemical energy is changed into electrical energy by these devices. The fundamental body of a cell is made up of an electrolytic solution part connected with a cathode and an anode on either facet. Fuel cell characteristics used in the present work (Figs. 1 and 2).

Simulation Results and Analysis—(curve 1—input voltage to inverter part, curve 2—output voltage of inverter part and curve—3 output voltage of transformer part) (Fig. 3).
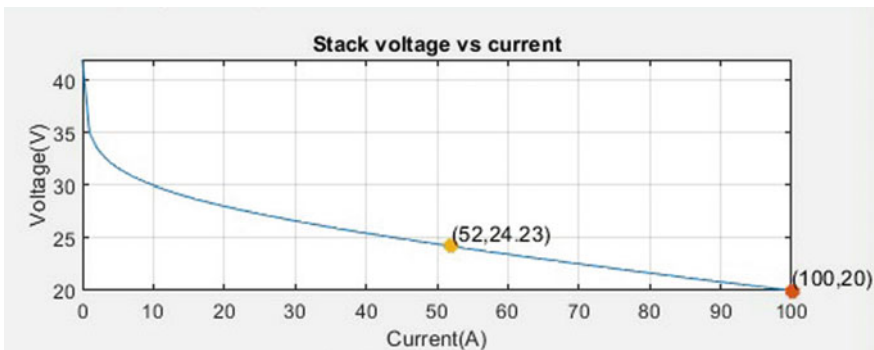
Fig. 1 Stack voltage versus current characteristics
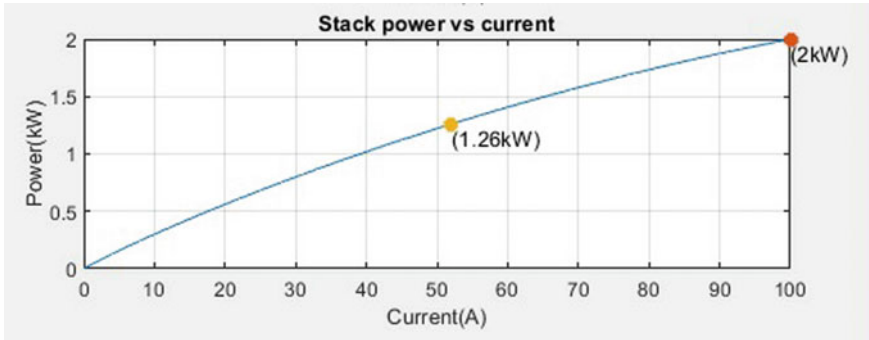
Fig. 2 Stack power versus current characteristics
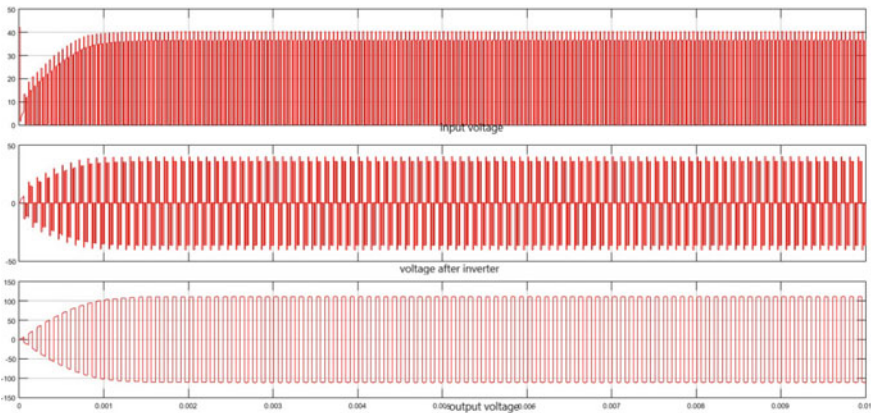
Fig. 3 Simulation results with PEMFC as source

3 Soft Switching Strategy

The soft switching strategy is being implemented in this project because there is a need to improve the efficiency of the power converters and this can be done by reducing the switching losses by the use of this strategy. Other merits of soft switching include a huge increase in the power density since there is a reduction in the weight and size of the magnetic components used because of the higher operating frequency, thereby reducing the cost. There is also a reduction in EMI loss and there is no harmonic distortion and so no extra shielding is required. Soft switching has a wide range of operations rather than its hard switching counterpart. Moreover, hard switching is not an isolated converters operation as it is generally used for high power applications and due to which hard switching causes a much more significant loss than its counterpart strategy.

In this project as the operation is being carried out at high frequency along with high power, at high frequency the switching losses of hard switching are very large so it is not suitable to use hard switching at such magnitude of frequency. The various types of soft switching resonant strategies include the zero voltage switching and the zero current switching strategy. They can be further classified according to the resonant tank being used such as the quasi resonant converters, multi-resonant converters and resonant transition converters. Soft switching is classified into two types which are zero current switching and zero voltage switching. A combination of these two types of switching makes a third kind of switching known as zero voltage zero current switching.

Quasi resonant switching scheme is being implemented in our model. This switching scheme uses resonant techniques for operation. In comparison with traditional (continuous and discontinuous) modes of operation, there is a reduction in turn-on losses at the switch which results in a reduction in temperature, meaning there is an increase in efficiency. The only major disadvantage is that operations with lighter loads cause relatively high loss. Resonant frequency helps in determining the time between the initial turn-off and the first trough. Time between turn-off and turn-on is set by the controller. The time is smaller for lighter loads as less energy is required, resulting in a shorter on-time, as well as output conduction time. Hence lighter loads mean higher switching losses.

Two main types quasi resonant switching are the half wave quasi resonant switching and the full wave quasi resonant switching. For half wave type of quasi resonant switching, conversion ratios are heavily dependent on load currents and the resonant voltages have only one direction. In the full wave quasi resonant switching conversion ratios are independent of load currents. However, there is a reduction in efficiency at lighter loads because of large circulating currents and the resonant voltages are bidirectional. In the thesis quasi resonant zero voltage switching will be carried out for a single MOSFET switch because to implement the same in all the switches will require a larger algorithm with the same approach. Hard switching will be carried out for a single switch and the efficiency analysis will be done for both the techniques (Fig. 4).

4   Simulation Output

It is observed that the output of the load voltage and load current obtained by using the soft switching strategy is much smoother than the former output obtained by using conventional switching. It is also observed that the proposed combination of quasi resonant switching for fuel cell fed isolated DC/DC converter has smooth switching action from the following response (Figs. 5 and 6).
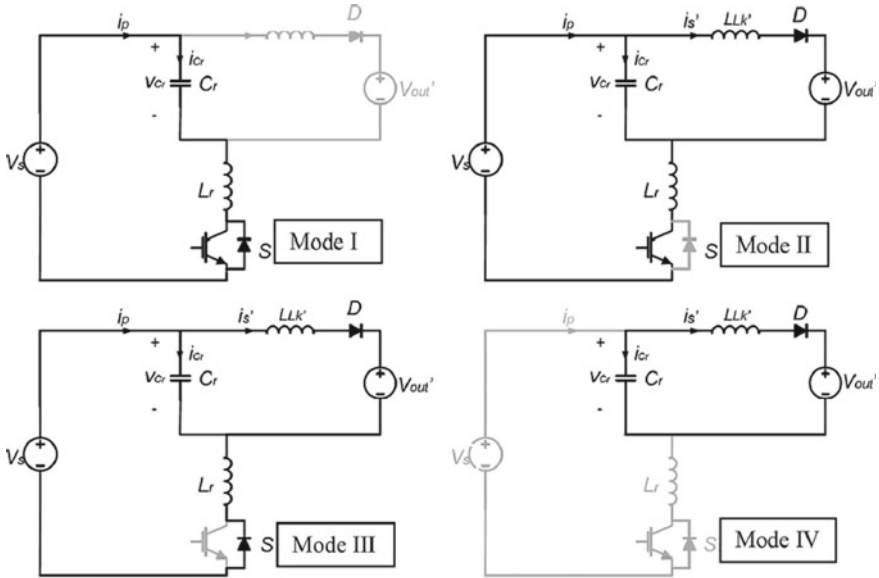
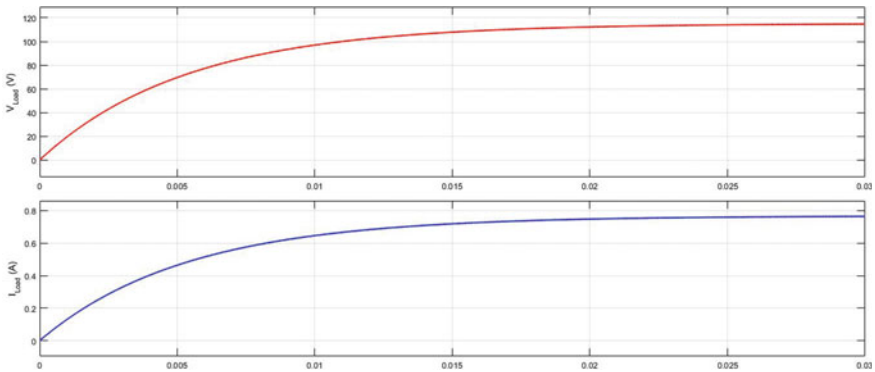**Fig. 4** Modes of operation of single switched converter

Fig. 5 Simulation results (load)

5 Loss Analysis Using a Case Study

To verify the effectiveness of the proposed soft switching strategy for fuel cell isolated DC/DC converter, a case study has been carried out considering the loss analysis for a particular MOSFET. The power loss occurring at any switching device can be calculated by considering two major losses.

(a) Conduction losses (P_c)
(b) Switching losses (P_{sw})
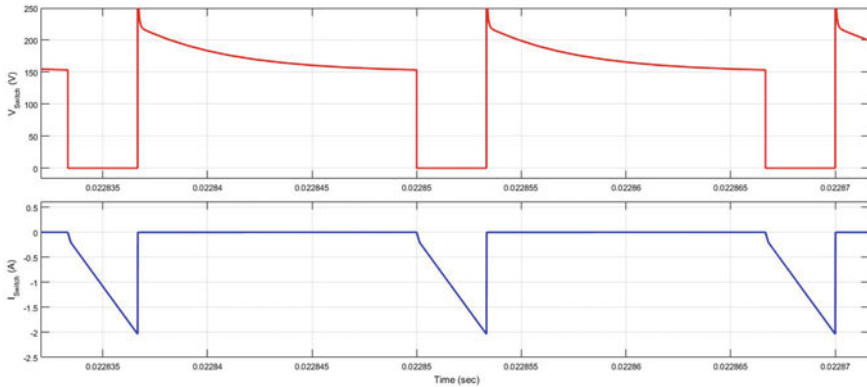
Fig. 6 Switch voltage and current waveforms

(c) Blocking (leakage) losses (P_b), normally being neglected.

The switching loss of a semiconductor device is given by (Fig. 7)

$$P_{sw} = (E_{on} + E_{off})f_s$$

where, E_{on}, E_{off} and f_s are denoted by switching energy loss during ON state, OFF state and switching frequency respectively. For the present case study, a particular MOSFET APT20M20B2LL (Mouser electronics) whose rating is 200 V, 100 A is considered due to its relevance with the present converter rating. On inspecting the data sheet, the energy dissipation during ON and OFF states for the switch at 50 A current (RMS) is observed to be 400 uJ and 280 uJ respectively. Hence, using the above equation considering 10 kHz switching frequency, the switching loss difference between conventional switching and soft switching is observed to be 6.8 W for a single switch. In other words, the soft switching strategy allows improving the efficiency of the present converter by reducing the switching loss of 6.8 W.

6 Conclusion

It is widely known that the major parts of losses in converter circuits are conduction and switching losses. Due to the inherent property of high voltage gain of the converter, the current demand from the source is higher resulting in higher conduction losses. However, there is a scope for reducing the switching losses to improve the overall efficiency of the converter. This paper deals with the implementation of a soft switching methodology for an integrated fuel cell isolated power converter system. The soft switching method consists of a quasi resonant switching using an additional inductor and capacitor combination. The inductor and capacitor have been operated in a resonant condition providing zero voltage and zero current switching, thereby

Fig. 7 Switching energy with drain to source current (data sheet of APT20M20B2LL)
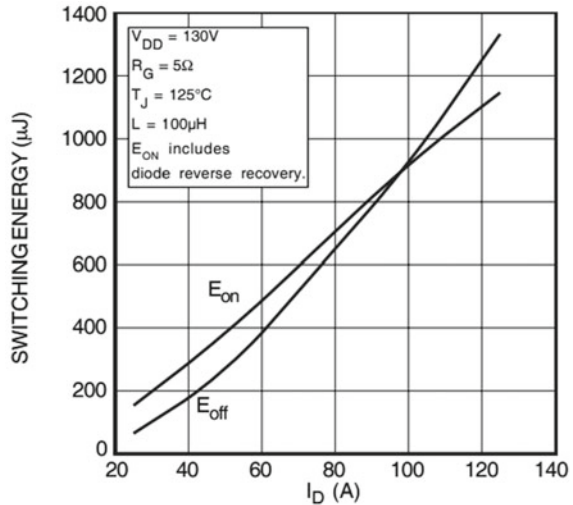
resulting in reduced switching losses. To validate the effectiveness of the proposed work, an investigation has been carried out in terms of a power loss measurement across a single switch. The minimization in power loss at a single switch (MOSFET) is 6.8 W while carrying out the simulations at 1 kW power level.

References

1. Bankupalli PT, Ghosh S, Kumar L, Samanta S, Jain S (2020) Operational adaptability of PEM fuel cell for optimal voltage regulation with maximum power extraction. IEEE Trans Energ Convers 35(1):203–212
2. Bankupalli PT, Ghosh S, Kumar L, Samanta S (2018) Fractional order modeling and two loop control of PEM fuel cell for voltage regulation considering both source and load perturbations. Int J Hydrogen Energ 43(12):6294–6309
3. Pal A, Basu K (2019) A unidirectional single-stage three-phase soft-switched isolated DC–AC converter. IEEE Trans Power Electron 34(2):1142–1158. https://doi.org/10.1109/TPEL.2018.2833747
4. Fathy K, Morimoto K, Doi T, Ogiwara H, Lee HW, Nakaoka M (2006) A divided voltage half-bridge high frequency soft-switching PWM DC-DC converter with high and low side DC rail active edge resonant snubbers. In: 2006 CES/IEEE 5th international power electronics and motion control conference, pp 1–5. https://doi.org/10.1109/IPEMC.2006.4778201
5. Etoh T et al (2005) New auxiliary active lossless snubber-assisted full bridge soft switching PWM high frequency inverter-fed DC-DC power converter. In: 2005 international conference on electrical machines and systems, vol 2, pp 1090–1094. https://doi.org/10.1109/ICEMS.2005.202715
6. Alassi A, Al-Aswad A, Gastli A, Brahim LB, Massoud A (2017) Assessment of isolated and non-isolated DC-DC converters for medium-voltage PV applications. In: 2017 9th IEEE-GCC conference and exhibition (GCCCE), pp 1–6. https://doi.org/10.1109/IEEEGCC.2017.8448079

7. Tuan CA, Naoki H, Takeshita T (2019) Unidirectional isolated high-frequency-link DC-DC converter using soft-switching technique. In: 2019 IEEE 4th international future energy electronics conference (IFEEC), pp 1–7. https://doi.org/10.1109/IFEEC47410.2019.9015117

8. Mishima T, Nakaoka M (2010) A new family of soft switching PWM non-isolated DC-DC converters with Active auxiliary Edge-Resonant Cell. In: The 2010 international power electronics conference—ECCE ASIA, pp 2804–2809.https://doi.org/10.1109/IPEC.2010.5543740

9. Huang, Mazumder SK (2009) A soft-switching scheme for an isolated DC/DC converter with pulsating DC output for a three-phase high-frequency-link PWM converter. IEEE Trans Power Electron 24(10):2276–2288. https://doi.org/10.1109/TPEL.2009.2022755

10. Ravi D, Letha SS, Samuel P, Reddy BM (2018) An overview of various DC-DC converter techniques used for fuel cell based applications. In: 2018 international conference on power energy, environment and intelligent control (PEEIC), pp 16–21. https://doi.org/10.1109/PEEIC.2018.8665465

11. Alhurayyis I, Elkhateb A, John Morrow D Isolated and non-isolated DC-to-DC converters for medium voltage DC networks: a review. IEEE J Emerg Sel Topics Power Electron. https://doi.org/10.1109/JESTPE.2020.3028057

12. De Doncker RW, Divan DM, Kheraluwala MH (1988) A three-phase soft-switched high power density DC/DC converter for high power applications. In: Conference record of the 1988 IEEE industry applications society annual meeting, vol 1, pp 796–805. https://doi.org/10.1109/IAS.1988.25153

13. Kheraluwala MN, Gascoigne RW, Divan DM, Baumann ED (1992) Performance characterization of a high-power dual active bridge DC-to-DC converter. IEEE Trans Ind Appl 28(6):1294–1301. https://doi.org/10.1109/28.175280

14. Zhao B, Song Q, Liu W, Sun Y (2014) Overview of dual-active-bridge isolated bidirectional DC–DC converter for high-frequency-link power-conversion system. IEEE Trans Power Electron 29(8):4091–4106. https://doi.org/10.1109/TPEL.2013.2289913

15. Awwad AE, Badawi N, Dieckerhoff S (2016) Efficiency analysis of a high frequency PS-ZVS isolated unidirectional full-bridge DC-DC converter based on SiC MOSFETs. In: 2016 18th European conference on power electronics and applications (EPE'16 ECCE Europe), pp 1–10. https://doi.org/10.1109/EPE.2016.7695601

16. Xu S, Wang C, Qian Q, Zhu J, Sun W, Li H (2019) A single-switched high-switching-frequency quasi-resonant flyback converter with zero-current-switching and valley-switching. In: 2019 IEEE applied power electronics conference and exposition (APEC), pp 2123–2127.https://doi.org/10.1109/APEC.2019.8721815

17. Kwon J, Choi W, Kwon B (2009) Single-switch quasi-resonant converter. IEEE Trans Industr Electron 56(4):1158–1163. https://doi.org/10.1109/TIE.2008.2006239

18. Emrani A, Adib E, Farzanehfard H (2012) Single-switch soft-switched isolated DC–DC converter. IEEE Trans Power Electron 27(4):1952–1957. https://doi.org/10.1109/TPEL.2011.2170857

Performance Investigation of Cycloconverter Fed High Power AC Drives

Boga Jyothi, Sudheer Vinnakoti, Madisa V. G. Varaprasad, B. Arundhati, and Vijayakumar Gali

Abstract Induction Motor is a constant speed drive. There is a requirement to vary the speed as per the application. The speed depends upon the frequency as well as the number of poles, but it is quite difficult to change the structure of the whole machine. This paper describes about the speed control using a cycloconverter. Cycloconverters are used for the conversion of fixed AC to variable AC, by changing the frequency. The frequencies are reduced to F/3, F/4 and F/5. The corresponding gate pulses are triggered by the pulse generator. As the frequency varies, speed regulates in the machine.

Keywords Cycloconverter · Induction motor · Thyristor · Variable frequency

1 Introduction

In a cycloconverter, the AC power at one frequency is converted to an AC power at another frequency without any intermediate DC link. This technique of conversion was first known in Germany in the 1930s when Mercury-Arc rectifiers were used to convert power from 50 to 16 Hz for the transfer of goods by locomotives.

B. Jyothi (✉) · M. V. G. Varaprasad · B. Arundhati
Vignan's Institute of Information Technology, Visakhapatnam, Andhra Pradesh, India
e-mail: jyothi_chinni2002@yahoo.com

M. V. G. Varaprasad
e-mail: mvgvaraprasad1@gmail.com

B. Jyothi
KLEF, Vijayawada, AP, India

S. Vinnakoti
RAGHU Engineering College, Visakhapatnam, India
e-mail: sudheeer.218@gmail.com

V. Gali
Poornima University, Jaipur, India

757

After the development of semiconductor devices, the first application of cycloconverter was in the variable speed constant frequency supply systems [1–5]. The next important application was variable-frequency induction motor drives. It works on the phenomenon of Volts/Hertz and they must have a constant proportion for varying the motor speed.

The control circuits were pretty much complicated that the applications of cycloconverter were limited mainly to large-scale domains. Developments in dual in-line packages such as microprocessors took over the control attractively, the complicated control circuit hardware was then replaced by the microprocessor software which reduced manufacturing cost, increased reliability and improved maintenance.

2 Operational Features

The cycloconverter consists of phase-controlled rectifiers connected in inverted mode. Three such pairs are necessary to drive a 3-Phase load. The pulse number affects the harmonic content output waveforms. The output of this device is modulated to get AC power at a frequency generally lower than the source frequency (step-down). An AC voltage controller (TRIAC) can also be used.

The triggering pulses are being generated by the pulse generator [5–7, 10, 11]. The frequency varies like 16.66, 12.5, and 10 Hz. The AC motor characteristics require the applied voltage to be proportionally adjusted whenever the frequency is changed to deliver the rated torque, this method is also called Volts/Hertz method. If there is any disproportion of Volts/Hertz, then the efficiency decreases, which makes it unreliable.

The circuit is shown in Fig. 1. It consists of 8 switches $(T_1, T_2, T_3, T_4, T_5, T_6, T_7,$ and $T_8)$ in inversion mode. There are two bridges named P and N respectively. The two bridges are connected in series, in other words, they are cascaded. At the output side of both the bridges a load is connected (Induction Motor). P and N bridges are biased with 230 V, 50 Hz single-phase AC supply.

The mode of operation is illustrated below for frequency F/4:

Mode 1
In this mode, thyristors T_1 and T_2 are forward biased and corresponding gate triggering is done. The current from the source flows through T_1 to load and to T_2 as shown in Fig. 2. The red line depicts the path of current flowing. As said earlier, it is in the rectification mode the corresponding output voltage is appeared at the load and the power is positive.

Mode 2
In this mode, thyristors T_3 and T_4 are forward biased and corresponding gate triggering is done. As the supply alternates, the current from the source flows through thyristor T_3 to load and to T_4 as shown in Fig. 3. The red line depicts the flow of
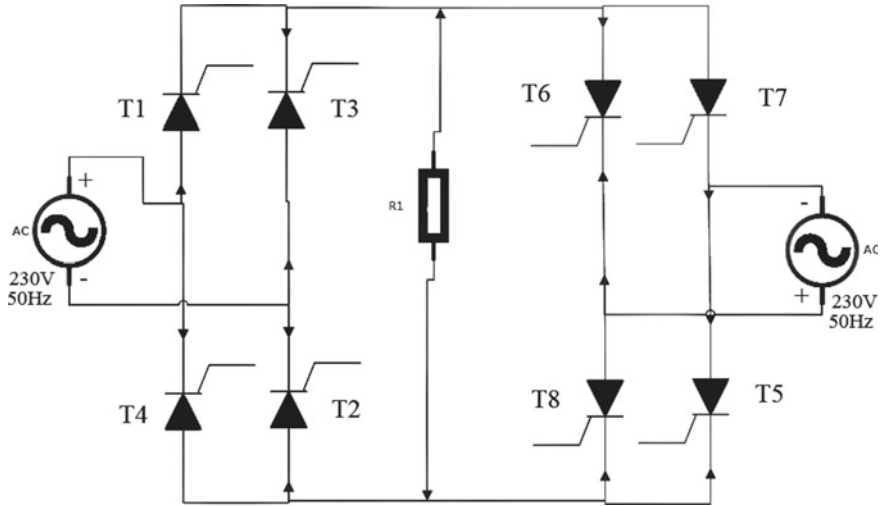
Fig. 1 Circuit diagram
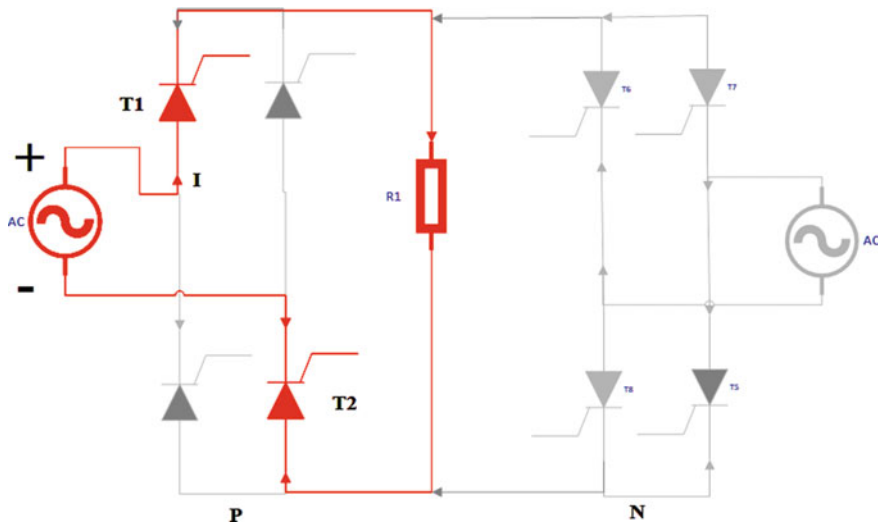
Fig. 2 Mode 1

current to load. The corresponding output voltage is appeared at the load and the power is positive.

Mode 3

In this mode, thyristors T_8 and T_7 are forward biased and corresponding gate triggering is done. The current from the source flows through thyristors T_8 to load and
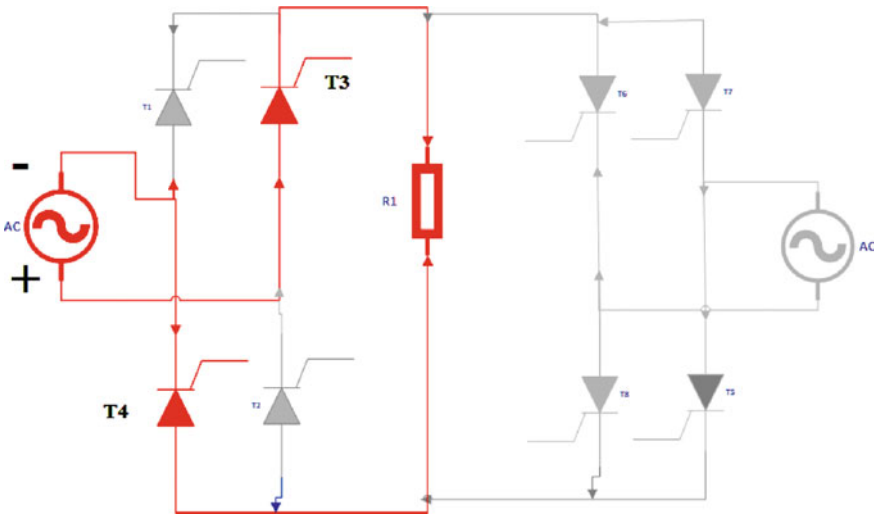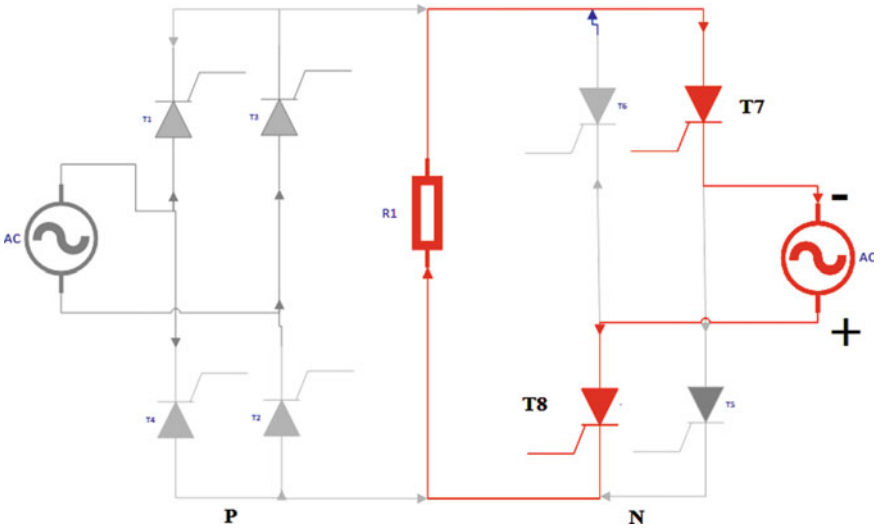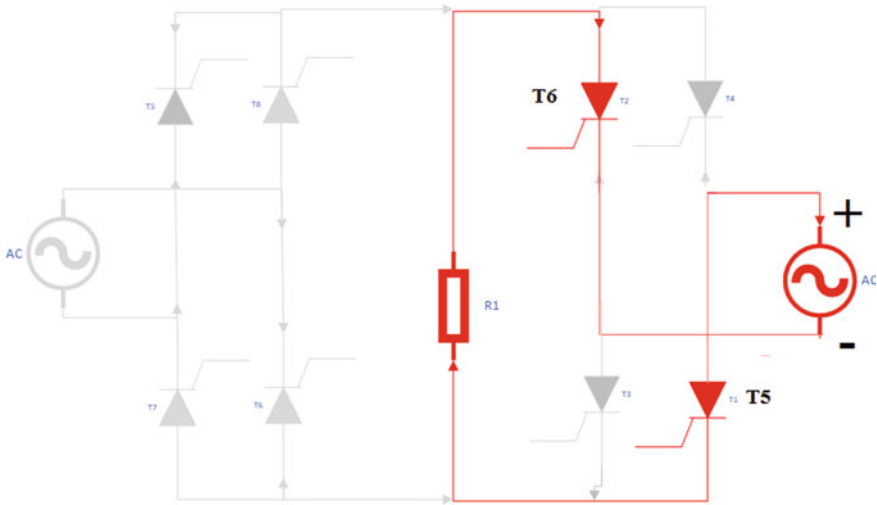
Fig. 3 Mode 2

to T_7 as shown in Fig. 4. The red line depicts the flow of current to load. As said earlier, it is in inversion mode the corresponding output voltage is appeared at the load and the power is negative.

Fig. 4 Mode 3

Fig. 5 Mode 4

Mode 4

In this mode, thyristors T_5 and T_6 are forward biased and corresponding gate triggering is done. As the supply is alternated the current from the source flows through thyristor T_5 to load and to T_6 as shown in Fig. 5. The red line depicts the flow of current to load. The corresponding voltage is appeared at the load and the power is negative.

The above illustration completely shows about the operation of the cycloconverter. The triggering pulses of thyristors are calculated theoretically for different frequencies. For the positive cycle, P type converter is responsible, at the same time N type converter is responsible for the negative waveform. Figure 6 shows the output waveform (F/4) with reference to the output RMS voltage is calculated. The average voltage is zero, and current varies with respect to load.

RMS Voltage Calculation

Formula for RMS Voltage:

$$V_s = \sqrt{\frac{1}{T} \times \int_{\alpha}^{\pi} (V_m \, \text{Sin}(\omega T))^2 \text{d}(\omega T)} \tag{1}$$

$$V_m = \sqrt{2} \times V_{\text{supply}} \tag{2}$$

$$\textbf{Firing angle}: \alpha = 0 \tag{3}$$

Voltage (volts)

y- Axis: 50 V

x- Axis: 0.01s

t (sec)

Time offset: 0
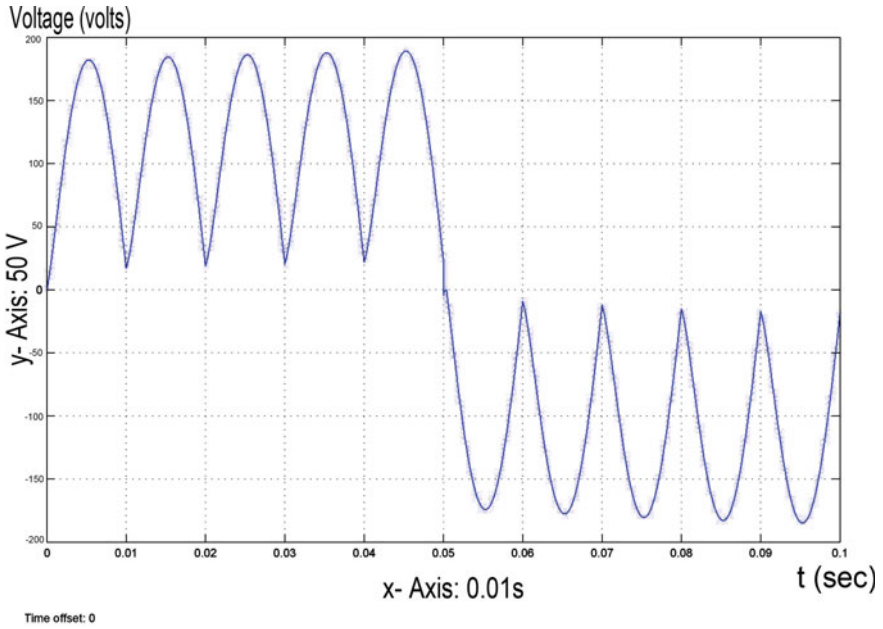
Fig. 6 Output waveform (F/5)

$$V_s = \sqrt{\frac{1}{4\pi} \times \int_0^\pi (V_s \, \text{Sin}(\omega T))^2 \text{d}(\omega T)} \qquad (4)$$

$$V_s = \sqrt{V_{\text{sup}}^2 \left[\frac{1 - \cos 2(\omega T)}{8\pi} \right] \text{d}(\omega T)} \qquad (5)$$

$$V_s = \sqrt{\frac{V_{\text{sup}}^2}{8\pi} \left[\pi - \frac{\sin 2\pi}{2} \right]} \qquad (6)$$

$$V_s = \sqrt{\frac{V_{\text{sup}}^2}{8\pi} [3.03]} \qquad (7)$$

$$V_s = V_{\text{sup}} \sqrt{\frac{3.03}{8\pi}} \qquad (8)$$

$$V_s = 230 \sqrt{\frac{3.03}{8\pi}} \qquad (9)$$

RMS Voltage, $V_s = 79.6$V (At frequency F/4).

3 Modeling of Induction Motor

The Single-phase induction motors have a wide variety of applications that include both industrial as well as domestic purposes. Basically, the induction motor is made up of two parts, a rotating part called the rotor and a stationary part called the stator. A single-phase power system is used for domestic purposes, commercial purposes and to some extent industrial purposes rather than a three-phase system. This makes single-phase system economically viable in such a setting. The single-phase motors are simple in construction, economical, reliable and easy to repair and maintain. As a result of these advantages, the single-phase induction motor finds its application in centrifugal pump, blowers, vacuum cleaner, washing machine, fans, small toys, etc. [9].

The induction machine is essentially a constant speed machine when operating from the main supply. The difficulty in varying its speed using a cost-effective means is one of its major drawbacks.

The rotor speed of induction motor is given by:

$$\text{Synchronous speed, } N_s = (120F)/P$$
$$\text{Slip, } s = (N_s - N_r)/N_s$$

N_s Synchronous speed
N_r Rotor speed
F Frequency
P Number of poles

The simulation is been carried out by using cycloconverter and split-phase asynchronous motor. A Switch might be anything such as a diode, MOSFET, etc. This diode is used followed by an ideal switch. An Ideal switch operates only when the gate signal is been given.

As said earlier, both the bridges should not be conducted at the same time. To make this happen a logic gate is used (NOT Gate). Both the bridges are biased with the 230 V, 50 Hz AC Supply. If there is any malfunction of the switch that leads to distortion or notch. To avoid that an R-C Low pass filter is connected [9, 10].

A split-phase asynchronous motor is connected at the output side. This motor mainly consists of two windings, main winding and auxiliary winding. Both have a phase difference of 90°. The motor has three terminals $M+$, $M-$ and T_m.

$M+$ Motor Positive Terminal
$M-$ Motor Negative Terminal
T_m Maximum Torque.

Give T_m value $\leq +1$ (preferably), because from the torque-slip characteristics of induction motor the starting torque is zero also, as T_m is low the RPM increases.

4   Simulation

The above Simulink model is designed and the above circuit has two bridges *P* and
N. Each bridge consists of 4 switches and is been biased by an AC Voltage Source.
The magnitude and frequency are adjusted to 230 V and 50 Hz respectively. Both the
bridges have been configured in such a way that, the output frequencies (F/3, F/4,
F/5) are obtained. The simulation time is 0.1 s. A Single-phase asynchronous motor
is connected at the output of bridges. The rotor speed of the motor is been measured
by bus selector and with aiding of corresponding gain. This wholesome shows the
speed in RPM. The observation is been done with the measuring equipment [11]
(Fig. 7).

- The output frequency is F/3.

Figure 8 shows the output frequency for F/3. It can be seen that it has 3 positive
cycles and 3 negative cycles. The frequency is been reduced to 16.66 Hz (approx).

- The output frequency is F/4.

Figure 9 shows the output frequency for F/4. It can be seen that it has 4 positive
cycles and 4 negative cycles. The frequency is been reduced to 12.55 Hz (approx).

- The output frequency is F/5.

Figure 10 shows the output frequency for F/5. It can be seen that it has 5 positive
cycles and 5 negative cycles. The frequency is been reduced to 10 Hz.

   The output waveform depicts the frequency variations at the output (Figs. 8, 9
and 10) with these variations the motor rotates correspondingly, as shown Table 1.
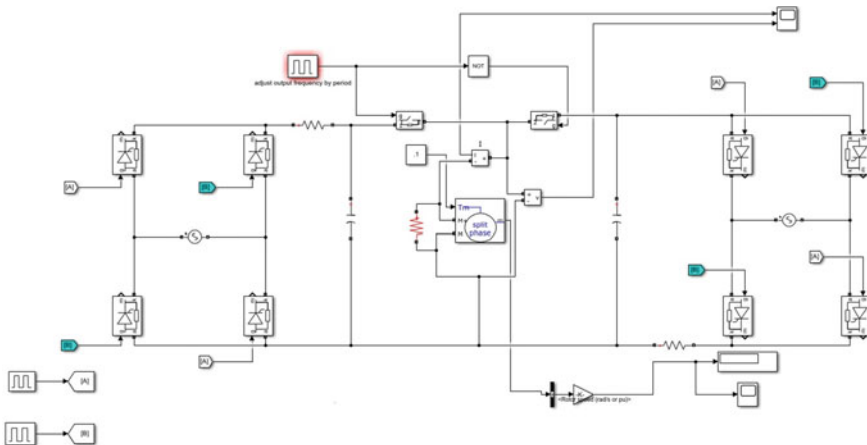
Fig. 7 Simulation circuit
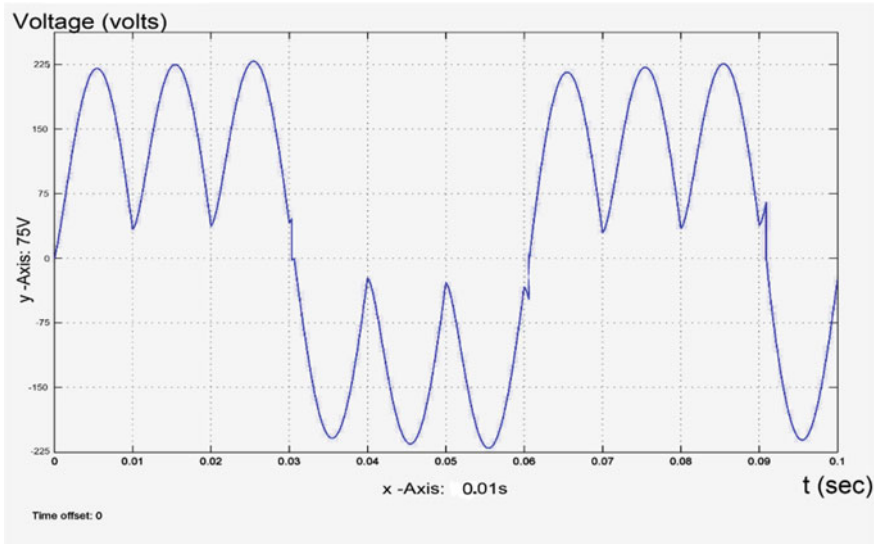
Fig. 8 Output waveform (F/3)
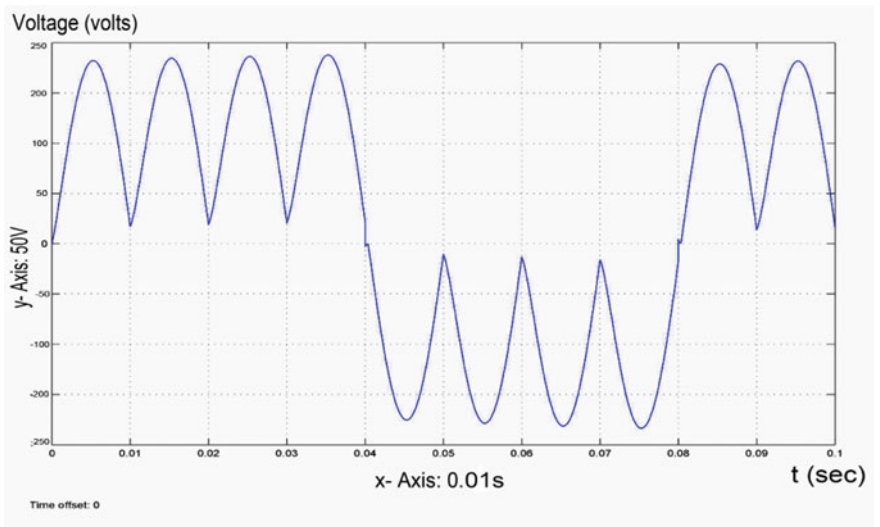
Fig. 9 Output waveform (F/4)

The output waveforms clearly show that the frequency is 1/3, 1/4 and 1/5 times the supply frequency. As it is discussed earlier, with the change in frequency N_s changes. When N_s changes corresponding slip changes. When slip changes the rotor speed changes the motor speed regulates accordingly. There might be some circulating
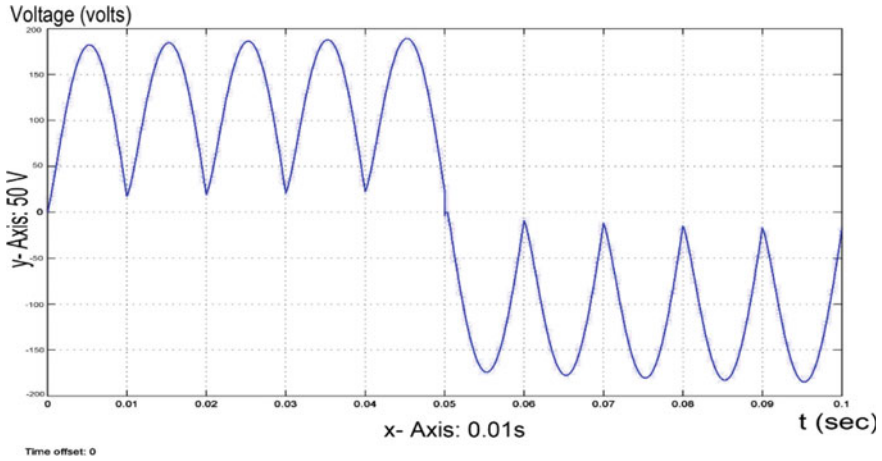
Fig. 10 Output waveform (F/5)

Table 1 Motor speeds at different frequencies

Frequency (Hz)	Speed (RPM)
F/3	44.6
F/4	37.7
F/5	29.68

currents flowing in the circuit, henceforth notch is obtained in the waveform. To limit a high rated filter is used [12].

The main objective of this paper is that the output frequency value is much lowered than the supply frequency. To operate the motor in less than the rated speed, this is the optimum and efficient solution.

5 Hardware Implementation

Figure 11 clearly illustrates the block diagram. According to the control strategy used in simulation, same principle is implemented by the following equipment:

1. 8051 Microcontroller
2. BT136 (TRIAC)
3. MOC3020
4. MCT2E
5. LM7805
6. Transformer (230 V//12 V)
7. Diodes
8. Keypad (3*4)
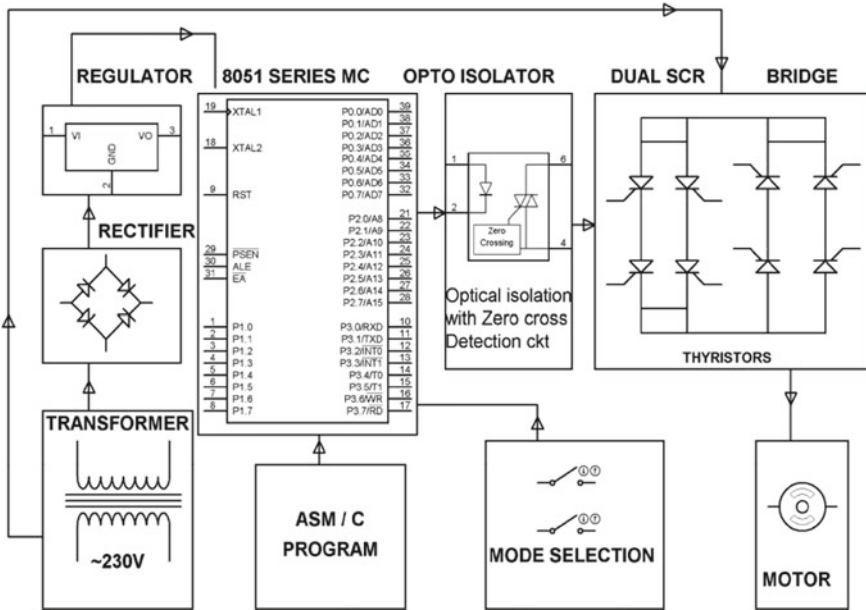
Fig. 11 Descriptive block diagram

9. LCD (16*2)
10. Induction Motor
11. Capacitors and Resistors (Filtering)

- Power Supply Unit

This unit is responsible for providing 5 V pure DC supply to 8051 microcontroller. The input 230 V, 50 Hz AC supply is given to the primary winding of the transformer and stepped down to 12 V. This 12 V is converted into DC by a rectifier (diode). For attaining a ripple free DC, a capacitor is connected in parallel. This 12 V DC is given to LM7805 voltage regulator, which converts 12–5 V pure DC which directly gets connected to the V_{cc} terminal of 8051.

- Control Unit

This unit comprises of 8051 microcontroller and opto-coupler. The program developed is in embedded C-Language and dumped in the ROM of 8051. Depending upon the input provided by the keypad, the microcontroller calculates the triggering pulses and feeds the switching circuit through opto-coupler. The opto-coupler plays a crucial role in isolating the 8051 microcontroller from the load side variations and distortions.

- Switching Unit
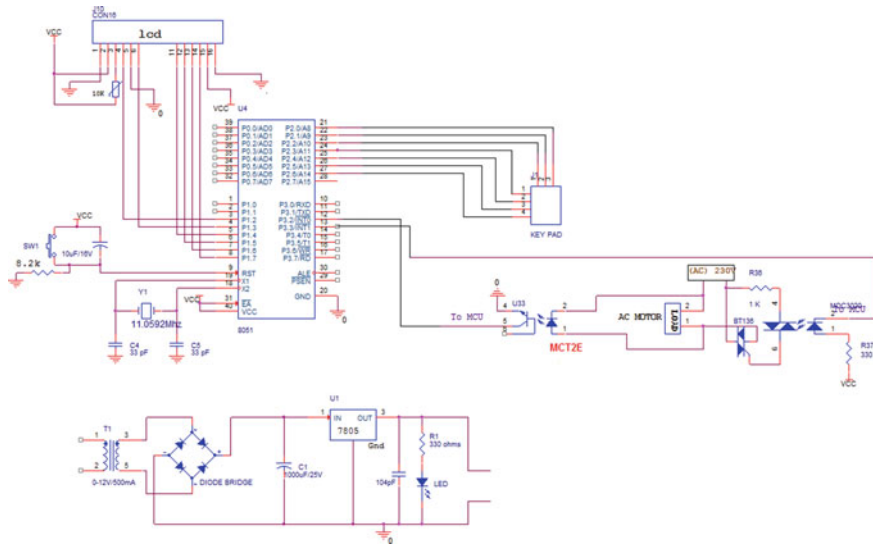
Fig. 12 Schematic block diagram

This unit consists of TRIAC i.e., two anti-parallel thyristors with each connected by the opto-coupler. The triggering pulses are calculated by the 8051 microcontroller, based upon the program dumped in it. The converter is in blocking mode, as one converter should operate at a time. This causes alternating supply with which motor rotates.

Figure 13 shows the pin diagram of opto-coupler, it has an IR LED and a transistor. Every time when the LED gets biased the transistor enters into a conduction state. The emitter terminal (Pin 4) and LED cathode (Pin 2) are grounded. The Anode terminal is connected to the interrupt pins of 8051.

8051 microcontroller mainly has 4 ports, except port 3 each and every port can be used for input and output operations. Figure 12 shows that port 1 is designated for LCD and port 2 is designated for keypad. EA pin of 8051 is connected to 5 V in order to enable the internal interrupts. The interrupts in 8501 (INT0 and INT1) is connected to switches through an opto-coupler. The RST pin is connected to a push button to develop hardware interrupt, which stands to the highest priority. These operations are displayed in LCD, which makes the whole operation easy (Fig. 14).

The following Table 2 shows the speed variation to different frequencies:

6 Conclusion

The cycloconverter circuit is simulated and practically tested. From the above simulated circuit and as well as the hardware implementation the improvements in its

Fig. 13 Opto-coupler pin diagram
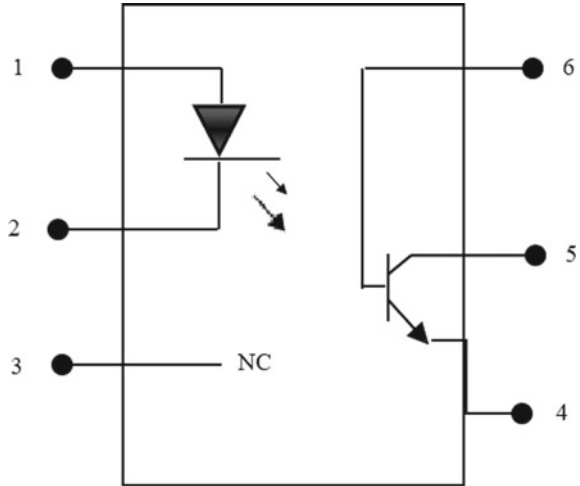
Fig. 14 Hardware prototype
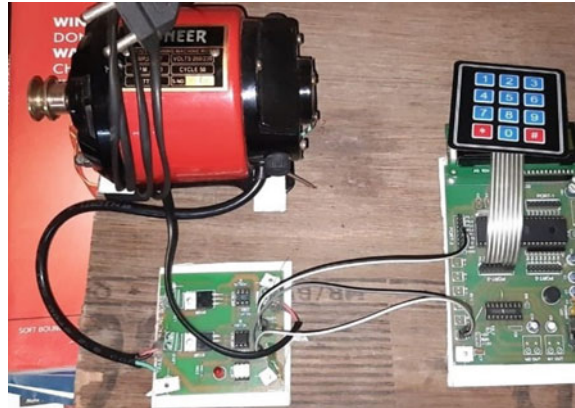
Table 2 Motor speeds at different frequencies

S. No.	Frequency (Hz)	Speed (RPM)
1	50	6000
2	12.5	1534
3	10	736

performance means a great saving in electrical consumption. Considering the use of this method in ship propulsions to manoeuvre it perfectly and in roller mills to churn the grains smoothly. For domestic use, a household mixer is the best example, for making all the eatable stuff. It also has other dimensions and a wide variety of applications. The single-phase cycloconverter is used to control the speed of single-phase induction motor by supplying desired variable frequency and also the frequency

change is the expanding mean of power conversion. For the dynamic control of speed and with a minimal amount of losses, this process is pretty much economical. Thus increases the motor life as there will be less wear and tear. This single-phase cycloconverter circuit can be extended further for three-phase application (Scherbius Drives).

References

1. Rocha R, de Siqueira Martins L, de Melo JCD (2005) A speed control for variable-speed single-phase induction motor drives. In: Proceedings of the IEEE international symposium on industrial electronics, ISIE, Dubrovnik, Croatia, pp 43–48
2. Hamad SH, Bashi SM, Aris I, Marlah NF (2004) Speed drive of single-phase induction motor. In: National power and energy conference
3. Sugimura H, Saha B, Mun SP, Hiraki E, Omori H, Nakaoka M (2007) Direct high frequency soft switching PWM cyclo-converter-fed AC-DC converter without DC link for consumer magnetron drive. In: 7th international conference on power electronics, Daegu, Korea (South), pp 1185–1190
4. Roy RB, Amin R (2012)Design and construction of single phase cycloconverter. Int J Rec Technol Eng (IJRTE) 1(3):2277–3872
5. (2016) Cycloconverter for speed control applications in a single phase induction motor. Effurun
6. Performance and simulation of a 1-ph to 2-ph cycloconverter driving an induction motor. Accepted for publication in JEE Proc. B and Doi, K., JEEE Trans. IA. vol 24 (1988)
7. Adli M, Mecke R, Palis F (1993) A new control strategy of quasi-cycloconverter fed induction motor drive. In: 1993 fifth European conference on power electronics and applications, vol 4. Brighton, UK, pp 82–87
8. Wu B, Pontt J, Rodriguez J, Bernet S, Kouro S (2008) Current-source converter and cycloconverter topologies for industrial medium-voltage drives. IEEE Trans Ind Electron 55(7):2786–2797
9. Stemmler H (1994) High-power industrial drives. Proc IEEE 82(8):1266–1286
10. Maamoun A (2003) Development of cycloconverters. In: CCECE 2003—Canadian conference on electrical and computer engineering. Toward a caring and humane technology (Cat. No.03CH37436), vol 1, pp 521–524
11. Pandey S, Dalvi H (2011) Simulation of cycloconverter based induction motor. Int J Adv Eng Technol
12. Arundhati B, Varaprasad MVG, Ravi Sankar RS (2020) Adaptive control of permanent magnet linear synchronous motor using non linear Kalman filtering techniques. Solid State Technol 63(6):11310–11321

A Unique Three Phase Multi-level Inverter for Low and Medium Power Applications in Photo-Voltaic System

Venkata Lakshmi Vasamsetti ⬡**, Madisa V. G. Varaprasad** ⬡**,
and Swathi Yarnagula** ⬡

Abstract This paper propounds a new approach for 1-Ø and 3-Ø MLI (multi-level inverters) to lower the count of components utilized. The suggested methodology utilizes a single DC source which can be either an energy storage device or AC-coupled renewable resource, along with power capacitors, diodes, and less number of active switches per phase, making it ideal for applications with low and medium voltage applications. By expanding the generalized circuit configuration, it is possible to obtain N stages of output voltages. The methodology utilized is unipolar staircase sinusoidal pulse width modulation to give rise to the corresponding gating pulses to the respective switches, making it suitable for operating at low switching frequencies, with decreased switching losses and optimal harmonic distortion. The efficacy of the proposed method is validated by simulating 5-, 13-, and 25-level output voltages with a total harmonic distortion of 17.6%, 6.40%, and 3.26%, respectively in MATLAB/Simulink.

Keywords Multi-level inverter · Pulse width modulated inverters · Photovoltaic systems

1 Introduction

In the present day, the role of multi-level inverters (MLIs) has been expanded, due to their capability of being reliable, and high qualitative voltage levels are achieved at the output terminals of the converters, making the dc systems suitable to relate with the AC systems. They have a wide range of applications with good potential for further technology and rapidly developing the area of power electronics. For decades, multi-level inverters are in focus because of their reduced voltage stress on the switches, high-quality output response, and their capability of operating in high and low voltage/power levels. Multi-level inverters can widely be used in wind farms, HVDC transmission, microgrids, photovoltaic systems, electric vehicles, and

V. L. Vasamsetti (✉) · M. V. G. Varaprasad · S. Yarnagula
Vignan's Institute of InformationTechnology (JNTUK), Visakhapatnam, India
e-mail: lakshmi.vasamsetti270@gmail.com

driver systems. The multi-level inverters have a high resolution at the output with shoot-up in the no. of output stages. The traditional MLIs are classified as Neutral Point Clamped (NPC) MLI [1], Flying Capacitor (FC) MLI [2], and Cascade H-bridge MLI.(CHB) [3]. Some other reviewing methodologies are presented in [4–7]. The primary disadvantage of FC and NPC is the use of high capacitor count and unbalanced DC links to bring about the desired voltage levels. The drawback also involves the use of a huge number of active switches, which, in turn, incorporates more stress on the switches. In view of this study, the emphasis was on the reduction of switch count in MLIs by utilizing CHB inverter. The design and the nature of multi-level inverters rely on the semiconductor switch count, the number of DC links, THD, modularity, output voltage levels, maximum voltage level, total standing voltage (TSV), and switch stress. Utilizes a DC source for generating a single level with the help of two switches, making a module [8]. Since only positive levels are generated, it needs an additional circuit to generate the negative pulses. In [9], to create both positive and negative half cycles, an H-bridge circuit is added, but at an additional expense of an increased number of active switches.

For a decade, researches are focusing on MLIs with a diminished count in the switches in the active state. In [10] the author proposed a methodology with reduced number of active switches, but the count of DC sources are getting increased. In [11, 12], the authors presented a methodology with moderate no. of active switch count, unless the TSV (total standing voltage) and the number of DC source links are higher. The topology presented by the author in [13] suppressed the problem of no. of active switches, but the total no. of DC voltage source requirement is higher.

Furthermore, in [14–16], by cascading the reference modules, the authors provided multi-level converter topologies. Nevertheless, the MLI topology has been stated with various sources of input DC voltage in [17–21], Where the proposed methodologies are able to decrease the no. of switches and DC voltage source count, but the topologies deteriorate from significant conduction losses and higher values of (TSV). In [22, 23], switched capacitor MLI topologies are presented, which have the capability of balancing the charging of the capacitor. The main throwback of this methodology is that for a similar number of active switches, apart from the high rise in TSV their is a shoot through in the cost of the equipment.

In order to solve the issues listed above in multi-level inverters; this paper tends to present a new 3-Ø MLI topology that is capable of minimizing the count of active switches and circuit elements in low and medium power applications. The proposed methodology makes use of a single DC source which can be an eco-friendly energy resource and is being divided into several DC links addressed by DC link capacitors to solve the need for independent DC sources by fulfilling both storing and supplying the energy demand if necessary. The propound methodology has the capability of putting down the number of active switches, lowering the voltage stress on switches. The TSV of the proposed methodology is low which in fact reduces the overall cost of the equipment compared to the existing methodologies discussed. The circuit configuration presented can generate preferred no. of voltage response levels at the output without involving complexity. In comparison to other topologies, this is an additional benefit of the suggested framework.

The structure of this paper is as follows. Section 2 acknowledges the description of the entire system's generalized configuration considered and its methodology, along with the discharging and charging process of the capacitor, and the control methodology along with mathematical formulation. Section 3 presents the classification of losses and their mathematical equations. Section 4 presents the simulation results and their discussion. And Sect. 4 presents the comparison of the suggested methodology to the existing topologies. Finally, the conclusion of the proposed methodology is presented in Sect. 6.

2 Proposed Methodology for Three Phase Multi-level Inverter

2.1 Generalized Model Configuration

The model configuration of the 3-Ø circuit is exhibited in Fig. 1. Each of the phases of the proposed circuitry constitutes a DC source, DC bus capacitors, and power electronic switches such as MOSFETs and power diodes. A battery or an energy storage device can be utilized as a DC source (V_{dc}), which is split into a no. of reduced voltage levels equal to $1/p$ times to V_{dc}. Where p denotes no. of capacitors connected in series. The discharge path for the capacitors is provided through the power diodes to the load, and the power MOSFETs provide the path for discharging the current of the capacitors by applying the corresponding trigger signals to the switches, in accordance with the switching logic designed. The circuit configuration in each phase exempting the H-bridge provides only a positive multi-level output voltage cycle. Hence, H-bridge is included at the lower part of the circuit to obtain a negative half cycle in response to multi-level output voltage, which eventually decreases the usage of power switches.

The count of components needed per phase for an inverter of $(2p + 1)$ level output is mathematically expressed as follows:

$$N_{source} = 1 \tag{1}$$

$$N_{capacitor} = p \tag{2}$$

$$N_{diode} = p - 1 \tag{3}$$

$$N_{switch} = p + 4 \tag{4}$$

where $p = 1, 2, 3 \ldots$
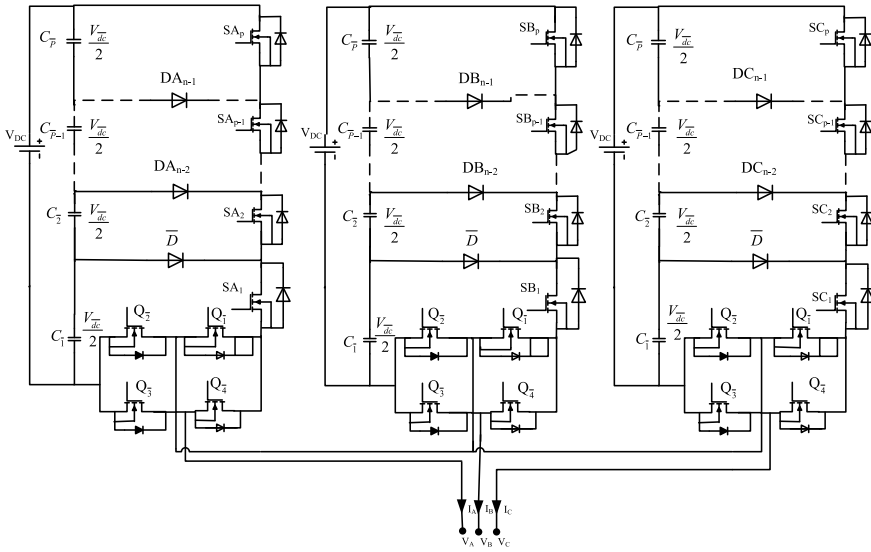
Fig. 1 Generalized layout of the propound 3-Ø MLI circuit configuration

The TSV of the configuration is the summation of the voltage stress acting on the power switches. The TSV [24] of a phase in a $(2p + 1)$ leveled inverter of the proposed method is calculated as

$$TSV = (2p + 1)V_{dc} \tag{5}$$

The detailed layout of the generalized circuit is shown in Fig. 1.

2.2 Modulation Strategy

The level shifted multi-carrier dependent unipolar staircase SPWM technique [25] is used to obtain the gating signals for the propound topology. However, the lower order odd harmonics are minimized with the use of unipolar staircase Pulse Width Modulation (PWM) approach, and the output voltage waveform tends to be accurate resulting in a reduction of total harmonic distortion. By correlating the reference sine wave of the respective phases, with the level shifted carrier signals, gating signals are produced for the corresponding switches. For a $(2p + 1)$ stage 3-Ø inverter, $3p$ number of switches are required where p represents the count of carrier signals required to generate the corresponding gating signals for the respective switches (Fig. 2). If the peak magnitude of the reference is denoted as $A_{ref,}$ and A_c represents the carrier signals, then the peak magnitude of individual p carrier signals is followed by
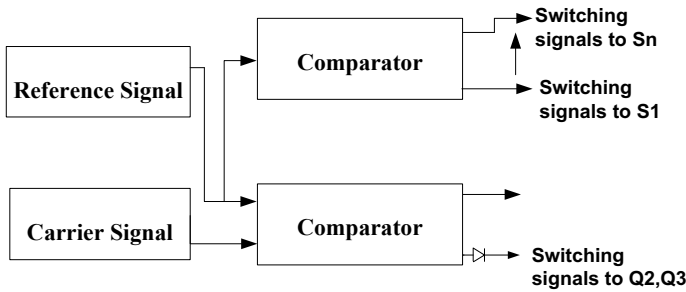
Fig. 2 Generalized block diagram for generating the switching signals to the switches

$$A_c = A_{\text{ref}}/2p \qquad (6)$$

2.3 Operating Principle

With the aid of a 1-Ø 5-stage unit, the operating design of the suggested 3-Ø inverter is described. The mechanism of three phases being analogous to single phase unit, A 1-Ø, 5-level inverter circuit unit is considered in order to analyze the operating process of other phases. The 5-level unit comprises of a diode, six switches, and two capacitors. The DC input voltage is split evenly between the two DC power link capacitors. The five-stage output voltage is obtained with five different operating modes explained as follows:

Mode0: In this mode of operation capacitors $C1$ and $C2$ gets fully charged since there is no path for the capacitors to get discharged. Hence output voltage $V_0 = 0$ V. Figure 3a shows the operation of mode0 (Table 1).

Mode1: In this mode, along with $Q1$ and $Q4$, switch $S1$ is in the ON state and switches $S2$, $Q2$, and $Q3$ are in the OFF state. The discharging path of capacitor $C1$ is via the path provided by the switch $S1$, $Q1$, $Q4$, and the diode $D1$ to the load. Thus, the voltage across the load is equal to the voltage across the capacitor and is given by $V_0 = V_{\text{dc}}/2$. The current conduction path of the capacitor in this mode of operation as shown in Fig. 3b.

Mode2: In this operating mode, switches $S1$, $Q1$, $S2$, and $Q4$ are triggered ON. And the switches $Q2$ and $Q3$ are kept OFF. When $S2$ is ON, the diode is reversed biased and capacitors $C1$ and $C2$ get discharged through the load via the path provided by the switches $S1$, $S2$, $Q1$, and $Q4$, and the entire DC voltage is reflected at the load and is given as $V_0 = V_{\text{dc}}$. The operation of mode 2 is shown in Fig. 3c.

Mode3: The working of mode3 is similar to the operation of mode1. In this state of operation, switches $Q2$, $S1$, and $Q3$ are ON and $S2$, $Q1$, and $Q4$ are triggered OFF.

a) mode 0

b) mode 1

c) mode2

d) mode 3
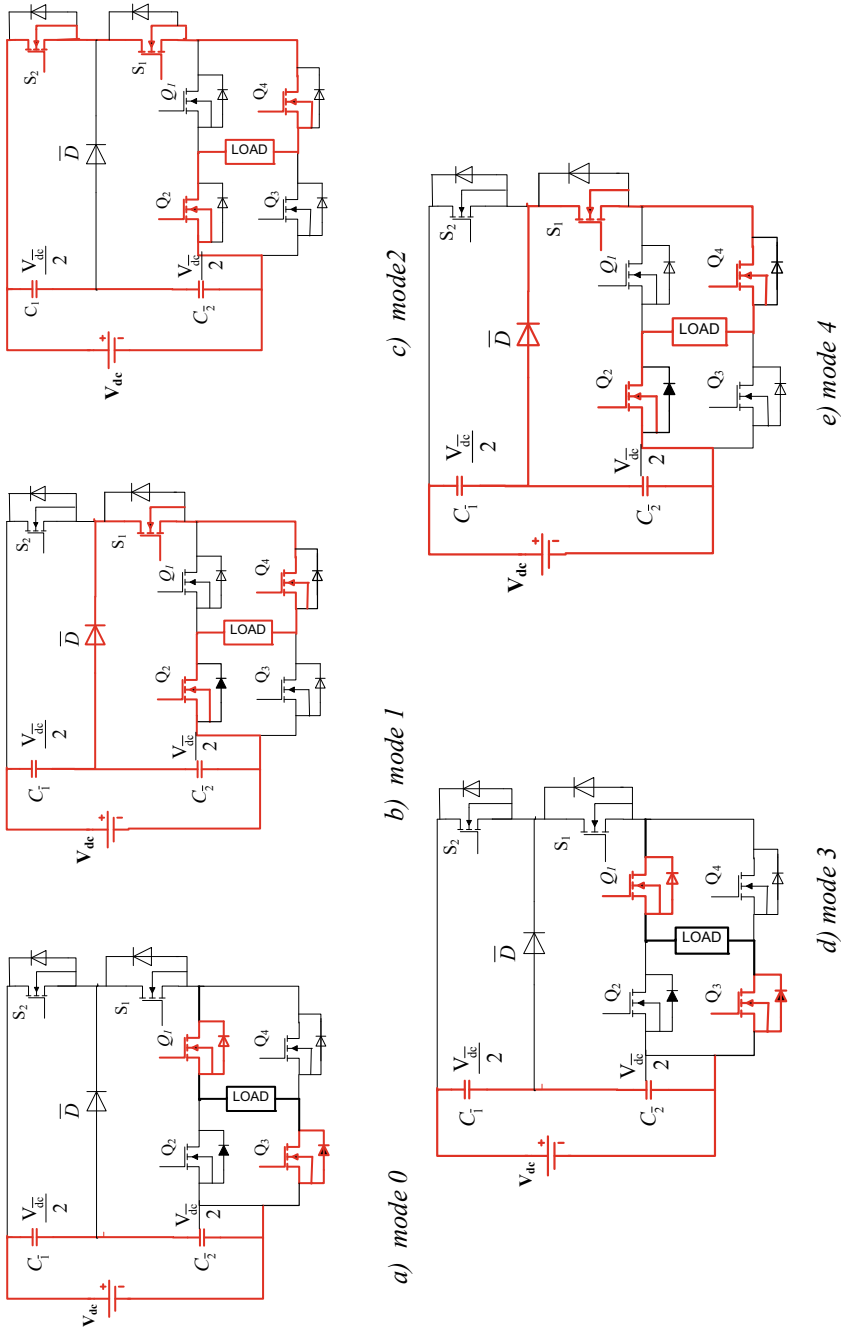
e) mode 4

Fig. 3 Various modes of operation of the proposed five-level 1-Ø inverter circuit

Table 1 Switching states and their corresponding output voltages

Output voltage	modes	Switching states (1=ON, 0=OFF)					
		S1	S2	Q1	Q2	Q3	Q4
V_{dc}	M-2	1	1	1	0	0	1
$V_{dc}/2$	M-1	1	0	1	0	0	1
0	M-0	0	0	1	0	0	1
$-V_{dc}/2$	M-3	1	0	0	1	1	0
V_{dc}	M-4	1	1	0	1	1	0

The diode $D1$, switches $S1$, $Q2$, and $Q3$ provide a loop for the capacitive current to discharge through the load but in the reverse direction with respect to mode1, hence the load voltage is given by $V_0 = -V_{dc}/2$. Figure 3d shows the operation of mode3.

Mode4: This mode is similar to mode0, in which all the switches $S1$, $S2$, $Q2$, and $Q3$ were in OFF condition, and $Q1$ and $Q4$ are in ON state. The discharging path for the capacitors $C1$ and $C2$ is provided by $S1$, $S2$, $Q2$, and $Q3$ through the load but in the reverse direction. Hence, the output response is $V_2 = -V_{DC}/2$ and the loop for the flow of current is shown in Fig. 3e.

2.4 Charging–Discharging Process of Capacitor and Calculation of Capacitance

It is possible to express the voltage at each capacitor as

$$V_C = V_{dc}/p \tag{7}$$

where p represents the capacitors count for the required output voltage level of a phase. Considering a proposed 1-Ø five-level inverter unit, the charging and discharging path for the capacitors is represented as shown in Fig. 3. Initially, the charging periods of $C1$ and $C2$ are t_0. With the triggering of switch $S1$ ON, $C1$ starts discharging, and the period of discharging of $C1$ is given by $t_{C1} = t_1 - t_0$.

When switch $S2$ starts conducting, both $C1$ and $C2$ discharge through the load via the switch $S2$, because the diode $D1$ gets reverse biased because of unequal polarity at the anode and cathode terminals of the diode. The discharging period of $C1$ and $C2$ is given as $t_{C1} + t_{C2} = t_2 - t_1$. $C2$ stops discharging when $S2$ is turned OFF and $C1$ discharges via switch $S1$. The discharging period of $C1$ is given as tc1 $= t_3 - t_2$. Again, the charging of capacitors $C1$ and $C2$ takes place and is given as $t_3 - t_4$. The same is repeated with the negative half cycle. Hence, for each capacitor, the maximum discharging value is given by [25] (Figs. 4 and 5)
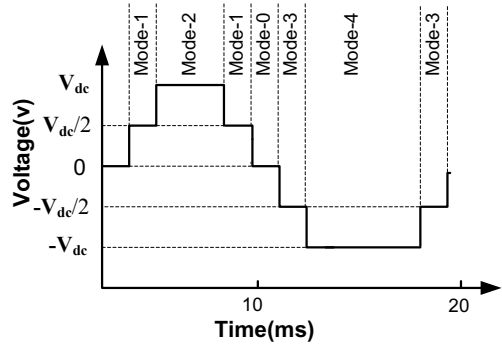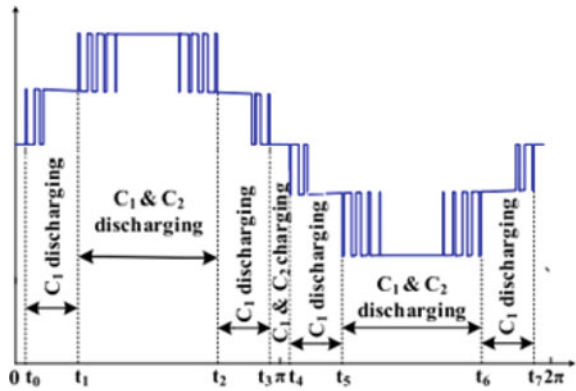
Fig. 4 Modes of operation

Fig. 5 Modes of charging and discharging time intervals of the capacitor

$$\Delta Q_{\mathrm{c}} = \int_{t_{\mathrm{a}}}^{t_{\mathrm{b}}} I_{\mathrm{load}} \mathrm{Sin}(2\pi f_{\mathrm{ref}} t) \mathrm{d}t \tag{8}$$

where I_{load} = maximum load current

t_{a}, t_{b} = discharging interval of the capacitor

The time intervals from t_0 to t_3 and t_4 to t_7 are calculated as follows:

$$t_0 = \frac{\sin^{-1}\left(\frac{A_{\mathrm{c}}}{A_{\mathrm{ref}}}\right)}{2\pi f_{\mathrm{ref}}} \tag{9}$$

$$t_1 = \frac{\sin^{-1}\left(\frac{2A_{\mathrm{c}}}{A_{\mathrm{ref}}}\right)}{2\pi f_{\mathrm{ref}}} \tag{10}$$

$$t_4 = \pi + t_0 \tag{11}$$

$$t_5 = \pi + t_1 \tag{12}$$

$$t_5 = \pi + t_2 \tag{13}$$

$$t_2 = \frac{\pi - \sin^{-1}\left(\frac{2A_c}{A_{ref}}\right)}{2\pi f_{ref}} \tag{14}$$

$$t_3 = \frac{\pi - \sin^{-1}\left(\frac{2A_c}{A_{ref}}\right)}{2\pi f_{ref}} \tag{15}$$

$$t_6 = \pi + t_3 \tag{16}$$

where A_{ref} represents the amplitude and f_{ref} denotes the frequency of the reference waveform, A_c indicates the magnitude of the carrier waveform, and K is assumed as the peak ripple ratio of capacitor voltage; the capacitance value of each phase is calculated such as to avoid immense voltage drop during discharging times of the capacitor. C_i is the capacitance value for each phase and is given as [26]

$$C_i \geq \frac{\Delta Q c_i}{k V_{dc}} \tag{17}$$

3 Calculation of Losses

For a NPC (neutral point clamped) inverter, two major losses are essentially regarded as, switching losses (P_{sw}) and conduction losses (P_{con}). These losses in the suggested topology are calculated by considering resistive load at the output terminals.

3.1 Switching Losses (Psw)

The switching losses occur due to delays in switching that involve the semiconductor devices. The switching losses constitute two transition states, i.e., ON state and OFF state, whichdefine the time periods for the complete t-ON and t-OFF of the switch, respectively. The voltage and currents have substantial values during these transition states and cause significant power losses. The turn-on (P_{sw-ON}) and turnoff (P_{sw-OFF}) power losses are calculated as follows [27]:

$$P_{\text{switch-ON, k}} = f_s \int_0^{t_{\text{no}}} V_{\text{off-state}}, K(t).i(t)\mathrm{d}t \tag{18}$$

$$P_{\text{switch-OFF, k}} = f_s \int_0^{t_{\text{off}}} V_{\text{off-state}}, K(t).i(t)\mathrm{d}t \tag{19}$$

3.2 Conduction Losses (Pcon)

The internal resistance, i.e., the parasitic impedance of the switches and the diodes involved in the circuit elements causes conduction power losses in the switch ($P_{\text{con-SW}}$), and conduction power losses in the diode ($P_{\text{con-D}}$) are calculated as follows: [1]

$$P_{\text{con\_sw}} = V_{\text{sw\_on}}.I_{\text{sw\_avg}} + R_{\text{sw\_on}}.I^2_{\text{sw\_avg}} \tag{20}$$

$$P_{\text{con\_D}} = V_{\text{D\_on}}.I_{\text{D\_avg}} + R_{\text{D\_on}}.I^2_{\text{D\_rms}} \tag{21}$$

4 Performance Analysis of the System

The simulated results of the single phase and 3-Ø 5-level, 13-level, and 25-level line voltages, line currents, and the THD are presented in this section. The necessary description for the corresponding figures is explained as follows. The suggested methodology is validated by carrying out the simulation in MATLAB/Simulink with the specifications shown in Table 2.

Table 2 Parameters and their ratings

Parameters	Values/rating
Input DC voltage	100 V
Number of levels of output	5
Frequency	50 Hz
Electrolytic capacitor	4700 μF
Type of load (resistive)	10 Ω
Diodes	40 V, 3 A

Fig. 6 Frequency response
of proposed 5-level inverter
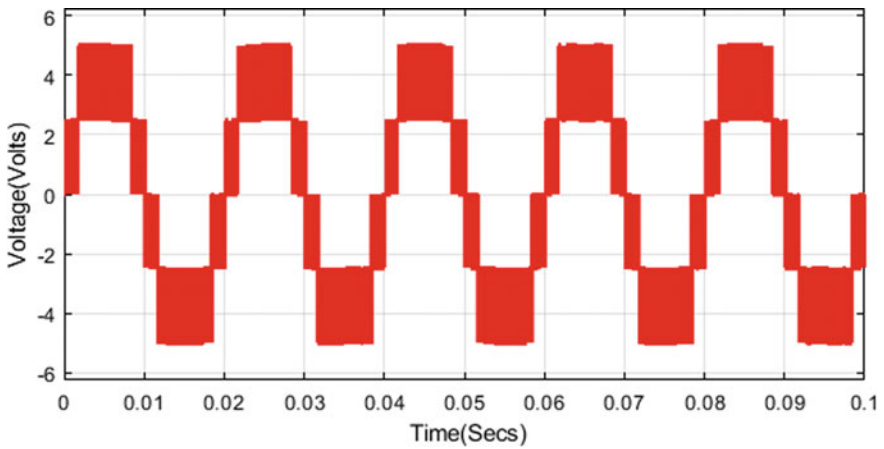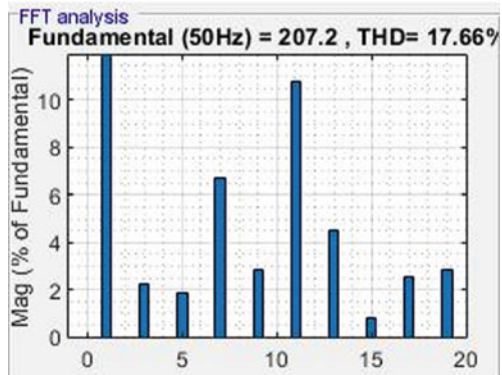
Fig. 7 Current response of proposed 5-level inverter

4.1 Proposed 5-Level Multi-level Inverter Topology

The 5-level inverter topology constitutes a single DC source, 6 active switches, 2
power capacitors, and a single diode, and the simulated response of current and
voltage at the output terminals are shown in Figs. 7 and 8, respectively, and THD of
17.6% is obtained as shown in Fig. 6.

4.2 11-Level Proposed Multi-level Inverter

See Figs. 9, 10, 11 and 12.
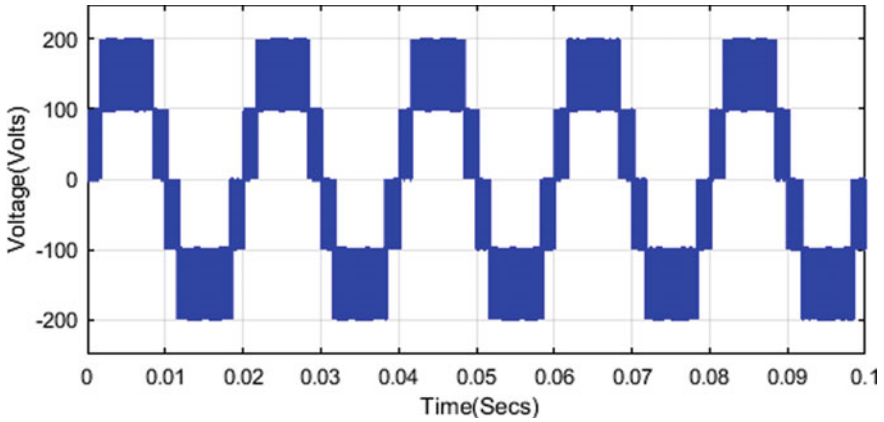
Fig. 8 Voltage spectrum of 5-level inverter
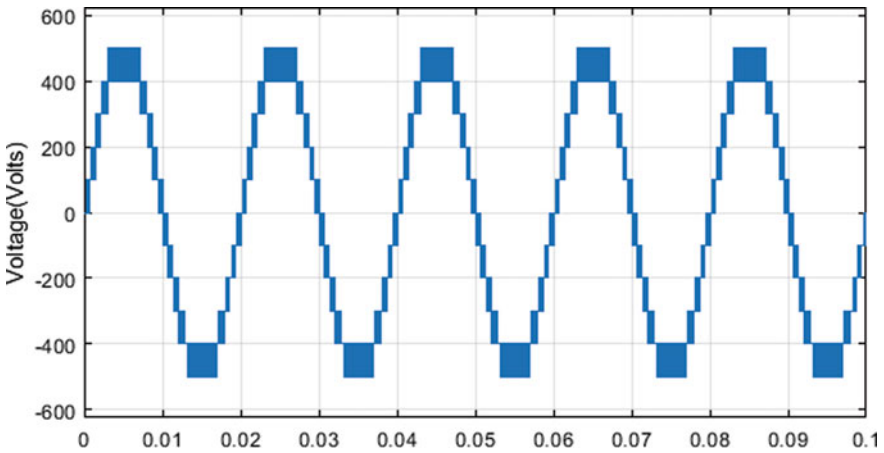
Fig. 9 Voltage spectrum of 1-Ø,11-level inverter

4.3   13-Level Proposed Multi-level Inverter

The proposed 3-Ø, 13-level inverter requires a single DC voltage source (which is basically a renewable energy resource or a battery), 15 power diodes, 18 bus capacitors (DC), and 30 switches. The corresponding voltage and current waveforms of 1-Ø, 13-level inverter are shown in Figs. 13 and 14, respectively. Figures 15 and 16 show the response of voltage and current at the output of the proposed 3-Ø, 13-level inverter. The THD analysis is presented in Fig. 17 and measured as 6.40% without any filter.
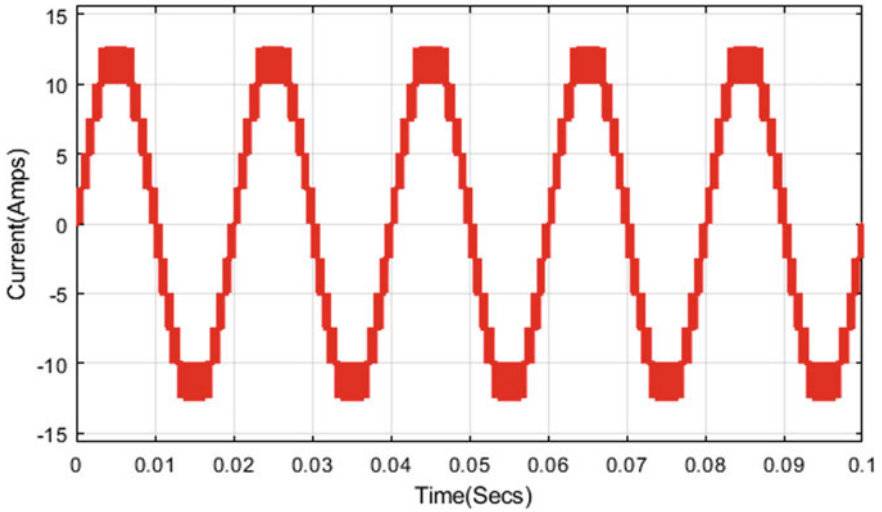
Fig. 10 Current spectrum of 1-Ø, 11-level inverter
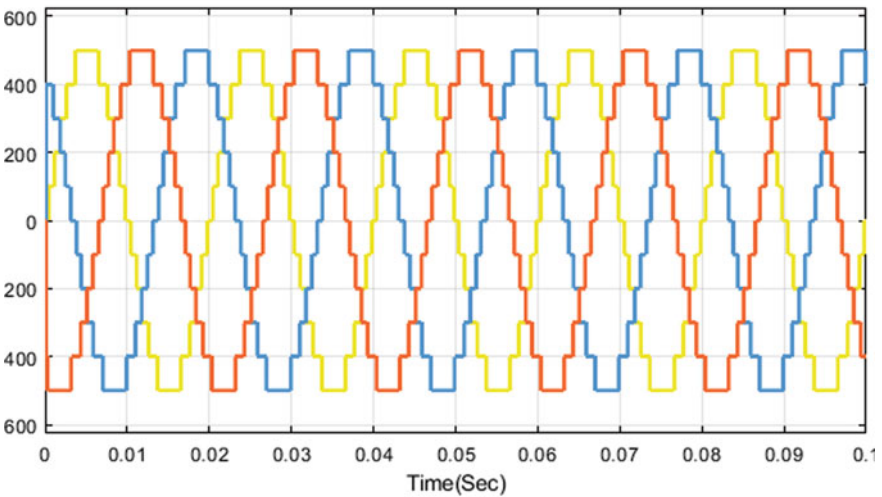
Fig. 11 Voltage spectrum of 11-level, 3-Ø inverter

4.4 1-Ø, 25-Level Proposed Multi-level Inverter

The 25-level 3-Ø proposed multi-level inverter consists of 48 switches, 36 capacitors, a DC source, and 33 diodes. The corresponding response of voltage and currents at the output of 1-Ø inverter are shown in Figs. 18 and 19, respectively. The output current and output voltage of a 3-Ø, 25-level inverter is shown in Figs. 20 and 21,
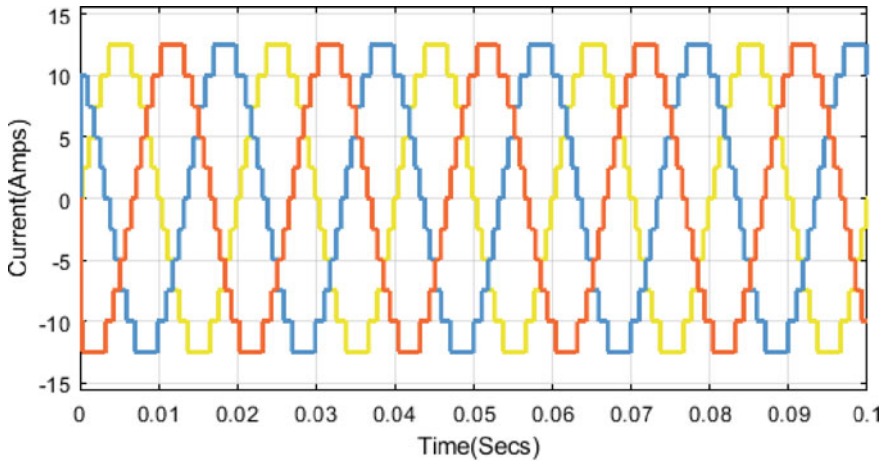
Fig. 12 Current spectrum of 11-level, 3-Ø inverter
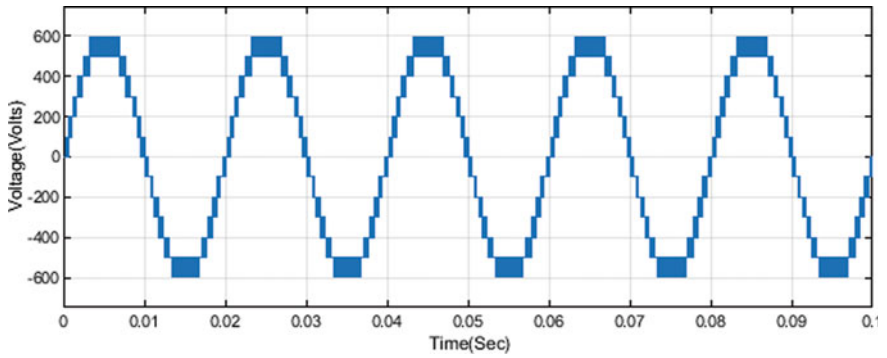
Fig. 13 Voltage response of 1-Ø, 13-level inverter
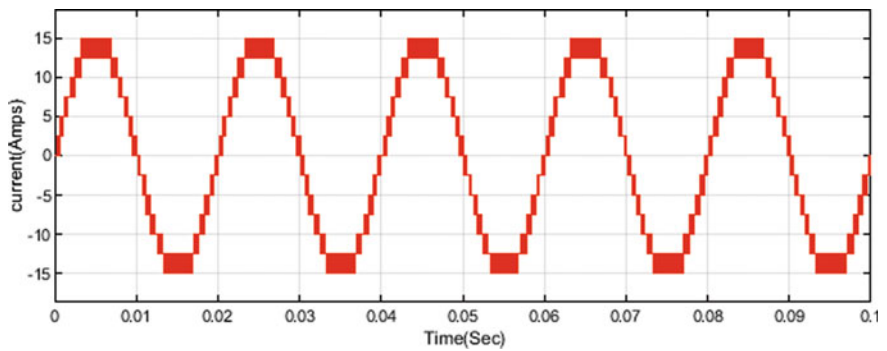
Fig. 14 Current response of 1-Ø,13-level inverter
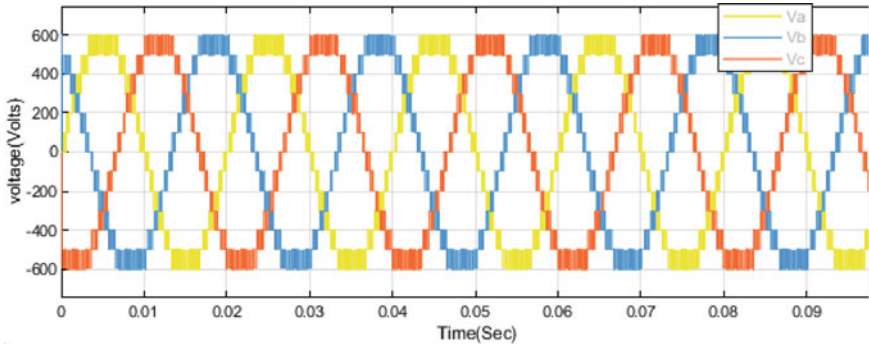
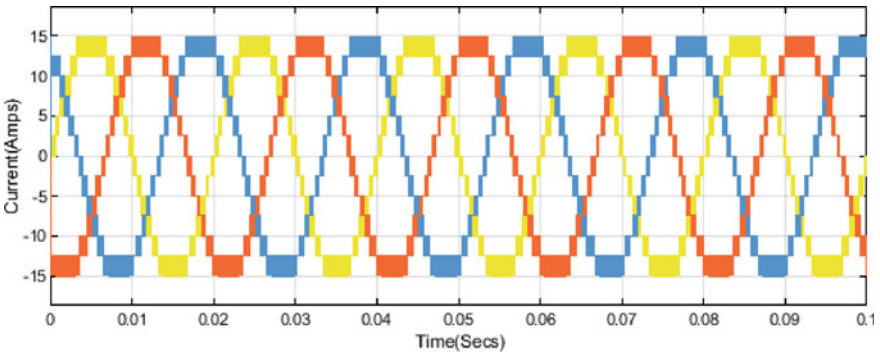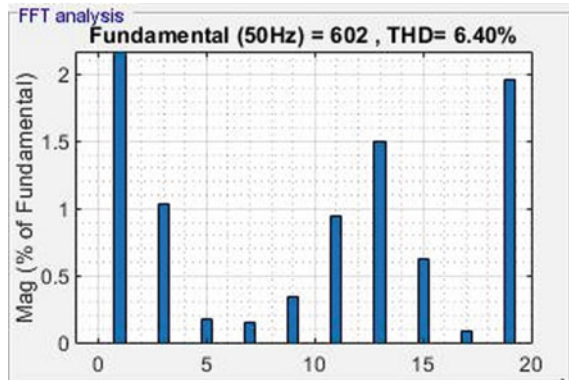**Fig. 15** Voltage response of 3-Ø,13-level inverter

Fig. 16 Current response of 3-Ø,13-level inverter
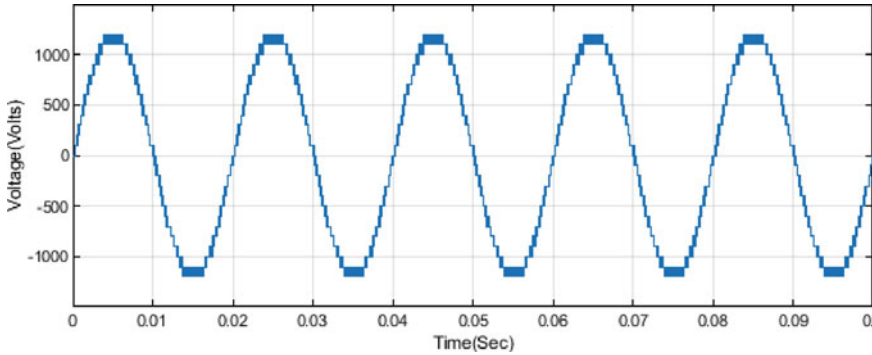
Fig. 17 Frequency spectrum of 13-level output voltage

Fig. 18 Output response of 1-Ø,25-level inverter
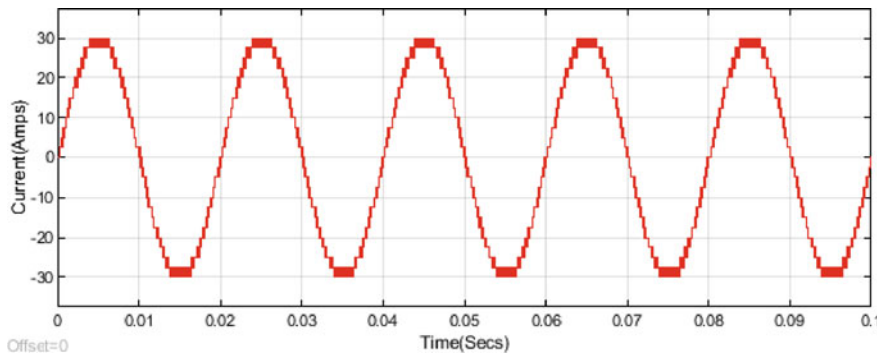

Fig. 19 Current response of 1-Ø,25-level inverter

respectively, and the harmonic analysis is carried out and is measured as 3.26% shown in Fig. 22.

5   Comparison with the Existing Topologies

The proposed methodology is compared with the already existing methodologies, and the effectiveness is analyzed in terms of the count of switches in active, diodes, capacitors, and in terms of losses. The following table shows the contrast between already existing inverter topologies with the proposed methodology (Table 3).

From the equations listed in Table 2, a graph is plotted between the components count versus no. of levels and is shown in Figs. 23, 24, 25 and 26 and depicts that the analyzed methodology utilizes reduced no. of active switches and a medium range of diodes, making the size compact, making it lighter and reducing the cost of the equipment when compared with the existing topologies.
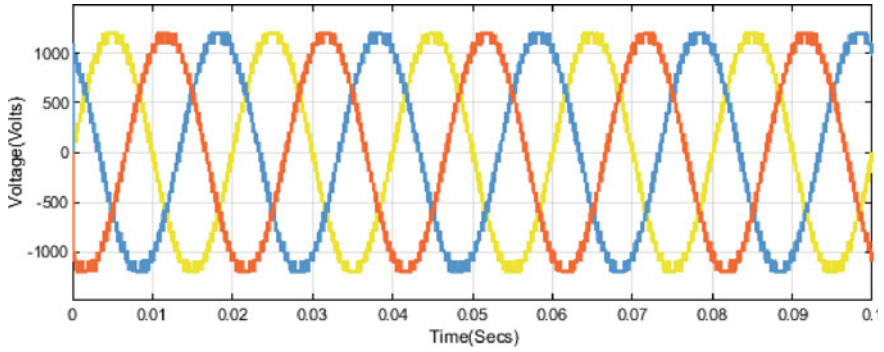
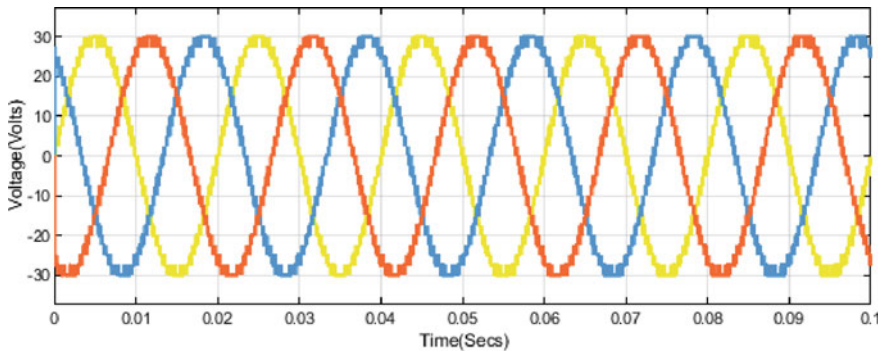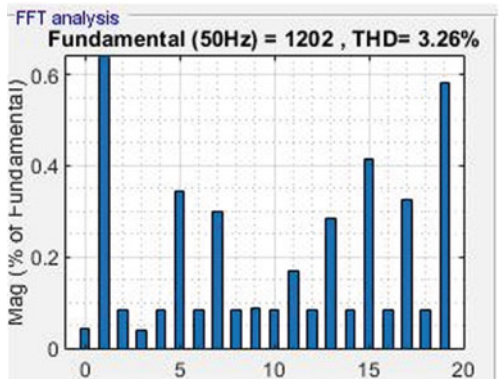**Fig. 20** Three phase 25-level inverter Output voltage

**Fig. 21** Three phase 25-level inverter output current

**Fig. 22** Frequency spectrum of 25-stage output voltage

Table 3 Comparison of proposed methodology with the existing topology

| Parameter	[1] 1981	[28] 2012	[29] 2016	[29] 2016	[22] 2017	[21] 2018	Proposed
No. of levels	$2P+1$	$2P+1$	$2P+1$	$12P+1$	$2P+1$	$2P+1$	$2P+1$
No. of active switches	$4P$	$2P+4$	$3P+1$	$10P$	$5P-1$	$14P$	$P+4$
No. of capacitor	$2P$	P	$P-1$	$4P$	$P-1$	$2P$	P
No. of Diode	$4P-2$	$2P+4$	0	$10P$	0	$14P$	$P-1$
TSV(*V_{dc})	$4P$	$2P+4$	$0.5P^2+5P$	$20P$	$5P-1$	$32P$	$P+4$

Fig. 23 Number of switches involved versus number of levels
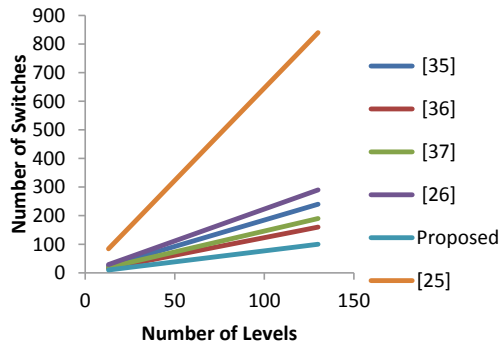
Fig. 24 Number of levels versus number of capacitors
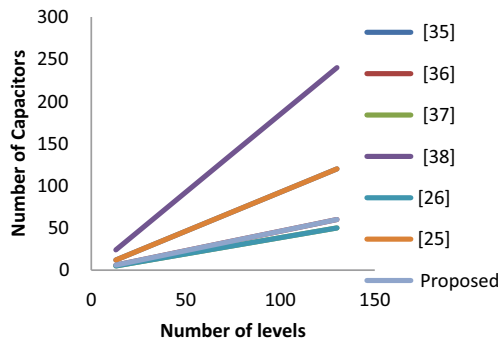
6 Conclusion

A new 3-Ø multi-level inverter is propounded in this paper, which utilizes a DC voltage source and reduced count of diodes, switches, and a moderate range of capacitors so as to generate desired voltage level when compared with the already existing methodologies. The description regarding the number of components, mathematical formulation, and operation of the proposed is presented with relevant circuit

Fig. 25 Number of levels
versus number of diodes
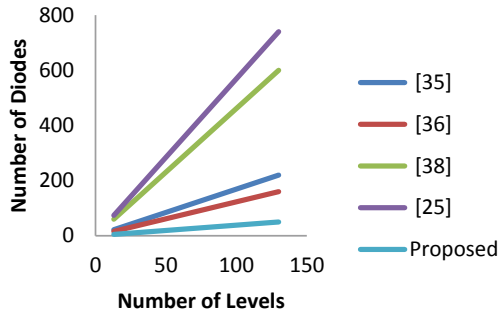
Fig. 26 TSV versus
Number of levels
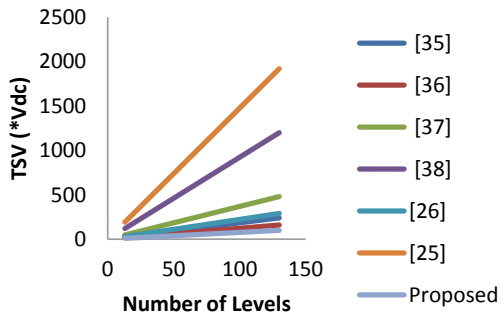
diagrams and waveforms for a single leg. The efficacy of the methodology is observed by carrying out the simulation in MATLAB/Simulink. Considering the above aspects, the proposed methodology has the following advantages: (a) less switch count, (b) reduced number of capacitors count, (c) produces less losses, hence improving the efficiency, and (d) The THD is less, hence reducing the voltage and current ratings results in reducing the price of the equipment. The proposed methodology is light weighted and compact in size fulfilling the huge demands in the renewable energy resource domain, particularly in low and medium power applications.

References

1. Nabae A, Takahashi I, Akagi H (1981) A new neutral-point-clamped PWM inverter. IEEE Trans Ind Appl IA-17(5):518–523
2. Meynard TA, Foch H (1992) Multi-level choppers for high voltage applications. Proc Eur Conf Power Electron Appl 2:45–50
3. Peng FZ, Lai J-S, McKeever JW, Van Coevering J (1996) A multilevel voltage source inverter with separate DC sources for static var generation. IEEE Trans Ind Appl 32(5):1130–1138
4. Zare, F (2008) Power electronics education electronic-book. School of Engineering Systems, Queensland University of Technology, Brisbane, Qld
5. Gupta KK, Ranjan A, Bhatnagar P, Sahu LK, Jain S (2016) Multilevel inverter topologies with reduced device count: a review. IEEE Trans Power Electron 31(1):135–151

6. Debnath S, Qin J, Bahrani B, Saeedifard M, Barbosa P (2015) Operation, control, and applications of the modular multilevel converter: a review. IEEE Trans Power Electron 30(1):37–53

7. Venkataramanaiah J, Suresh Y, Panda AK (2017) A review on symmetric, asymmetric, hybrid and single DC sources based multilevel inverter topologies. Renew Sustain Energ Rev 76:788–812

8. Babaei E, Hosseini SH (2009) New cascaded multilevel inverter topology with minimum number of switches. Elsevier J Energ Convers Manage 50(11):2761–2767

9. Babaei E, Kangarlu MF, Sabahi M (2014) Extended multilevel converters: an attempt to reduce the number of independent DC voltage sources in cascaded multilevel converters. IET Power Electron 7(1):157–166

10. Karasani RR, Borghate VB, Meshram PM, Suryawanshi HM, Sabyasachi S (2017) A three-phase hybrid cascaded modular multilevel inverter for renewable energy environment. IEEE Trans Power Electron 32(2):1070–1087

11. Babaei E, Laali S, Bayat Z (2015) A single-phase cascaded multilevel inverter based on a new basic unit with reduced number of power switches. IEEE Trans Ind Electron 62(2):922–929

12. Babaei E, Laali S (2015) Optimum structures of proposed new cascaded multilevel inverter with reduced number of components. IEEE Trans Ind Electron 62(11):6887–6895

13. Siddique MD, Mekhilef S, Shah NM, Memon MA (2019) Optimal design of a new cascaded multilevel inverter topology with reduced switch count. IEEE Access 7:24498–24510

14. Jahan HK, Zare K, Abapour M (2018) Verification of a low component nine-level cascaded-transformer multilevel inverter in grid-tied mode. IEEE J Emerg Sel Top Power Electron 6(1):429–440

15. Hasan MM, Abu-Siada A, Dahidah MSA (2018) A three-phase symmetrical DC-link multilevel inverter with reduced number of DC sources. IEEE Trans Power Electron 33(10):8331–8340

16. Lee SS, Sidorov M, Idris NRN, Heng YE (2018) A symmetrical cascaded compact-module multilevel inverter (CCM-MLI) with pulsewidth modulation. IEEE Trans Ind Electron 65(6):4631–4639

17. Wu H, Zhu L, Yang F, Mu T, Ge H (2017) Dual-DC-port asymmetrical multilevel inverters with reduced conversion stages and enhanced conversion efficiency. IEEE Trans Ind Electron 64(3):2081–2091

18. Chattopadhyay SK, Chakraborty C (2017) A new asymmetric multilevel inverter topology suitable for solar PV applications with varying irradiance. IEEE Trans Sustain Energ 8(4):1496–1506

19. Norambuena M, Kouro S, Dieckerhoff S, Rodriguez J (2018) Reduced multilevel converter: a novel multilevel converter with a reduced number of active switches. IEEE Trans Ind Electron 65(5):3636–3645

20. Samadaei E, Sheikholeslami A, Gholamian SA, Adabi J (2018) A square T-type (ST-type) module for asymmetrical multilevel inverters. IEEE Trans Power Electron 33(2):987–996

21. Samadaei E, Kaviani M, Bertilsson K (2019) A 13-levels module (K-type) with two DC sources for multilevel inverters. IEEE Trans Ind Electron 66(7):5186–5196

22. Taghvaie A, Adabi J, Rezanejad M (2018) A self-balanced step-up multilevel inverter based on switched-capacitor structure. IEEE Trans Power Electron 33(1):199–209

23. Saeedian M, Adabi ME, Hosseini SM, Adabi J, Pouresmaeil E (2019) A novel step-up single source multilevel inverter: topology, operating principle, and modulation. IEEE Trans Power Electron 34(4):3269–3282

24. Ebrahimi J, Babaei E, Gharehpetian GB (2012) A new multilevel converter topology with reduced number of power electronic components. IEEE Trans Ind Electron 59(2):655–667

25. Hinago Y, Koizumi H (2010) A single-phase multilevel inverter using switched series/parallel DC voltage sources. IEEE Trans Ind Electron 57(8):2643–2650

26. Babaei E, Gowgani SS (2014) Hybrid multilevel inverter using switched capacitor units. IEEE Trans Ind Electron 61(9):4614–4621

27. Ioinovici A (2013) Power electronics and energy conversion systems: fundamentals and hard-switching converters, vol 1. Wiley, Hoboken, NJ, USA

28. Najafi E, Yatim AHM (2012) Design and implementation of a new multilevel inverter topology. IEEE Trans Ind Electron 59(11):4148–4154
29. Samadaei E, Gholamian SA, Sheikholeslami A, Adabi J (2016) An envelope type (E-type) module: asymmetric multilevel inverters with reduced components. IEEE Trans Ind Electron 63(11):7148–7156

Grid Connected PV Fed EV Charging Station for College Campus with an Energy Storage System

V. P. Sathyajith and C. Ismayil

Abstract This paper describes a solar-powered electric vehicle (EV) charging station that works with a battery energy storage system and a single phase grid. This article focuses primarily on EV charging stations located in parking lots on college campuses, schools, or workplaces. As PV power is not constant, a battery energy storage system is used as a backup. If the PV produces more power than the vehicle load demands, the excess power is stored in the BESS, and when the PV power drops below a certain threshold, the stored energy in the battery is used as a backup source. If a single-phase grid is connected to the system, excess power can be sent to the grid and considered a source of money. Alternatively, if PV power is low and the battery has a low charge capacity, grid power can be used to charge the vehicles. This work discusses the mutual sharing of power between these sources in various cases. In all the operating conditions, the THD of grid current founds to be within the IEEE standard limit. A Modified Incremental Conductance MPPT technique is used to extract the maximum PV power. The system is designed to charge three vehicles simultaneously in a multi-port dc-link and is simulated using Matlab under three different conditions. The performance of the charging system is validated with simulation results.

Keywords Constant current constant voltage charging (CCCV) · Electric vehicle charging station · Energy storage system (ESS) · Photo voltaic (PV)

1 Introduction

In the current scenario, electric vehicles are the best mode of transportation because fuel prices are rising and petroleum products are becoming scarce. Although electric vehicles are not widely used today, studies show that by the end of 2025, the trans-

V. P. Sathyajith · C. Ismayil (✉)
Department of Electrical and Electronics, Government College of Engineering Kannur, Kannur, Kerala, India
e-mail: ismayilc@gmail.com

portation system will be entirely comprised of electric vehicles. The Indian government has set objectives to accelerate the adoption of electric vehicles (EVs). Electric vehicles have an advantage over conventional vehicles because they emit less pollution. After all, no fuel is used. The engine of EV operates on a closed circuit, so EVs do not emit any of the gases causing global warming. And by comparing the maintenance, the combustion engine has many parts which can cause damages whereas an electric vehicle has less than 20 parts. This means EVs are likely to have lower long-term maintenance costs than other vehicles. As the demand for EVs increases the population of electric vehicle charging stations are also increases. Charging stations at every point of cities are needed for the effective use of electric vehicles. Renewable energy sources (RES) can be used for an EV charging station as it has no emission content compared to conventional energy generation. The environment has an impact on renewable energy output. An energy storage system is required to ensure system stability and efficient management of renewable energy [1, 2]. An Energy Storage System consists of a battery that stores energy and a bidirectional DC–DC converter that transfers energy in both directions between the battery and the renewable energy source. Energy storage with batteries is best suited for renewable energy sources such as solar, wind, and so on [3, 4]. A charging station powered by Renewable Energy Sources (RES) is more appealing than conventional energy generation because RES are free, pollution-free, and emit less. Since petroleum fuels are depleting and prices are rising, RES power charging stations on college campuses, school offices, and workplaces are an appealing concept. Because it primarily focuses on charging EVs during school, college, or workplace hours, this charging configuration has the advantage of not requiring any quick charging or rushes [5, 6]. Customers can thus plug in their vehicles in the parking lot, go about their business, and unplug whenever they want. People are more likely to choose electric vehicles if convenient charging stations are installed in parking lots. If this system is linked to the utility grid, it will be possible to provide continuous charging even if PV and energy storage are insufficient. In low-load demand situations, extra power can be sent into the utility grid and considered an economic advantage.

As a result, in this paper, a single-phase grid-connected, PV-powered electric vehicle charging station with an energy storage system is implemented to charge vehicles on a college campus during working hours. The system has several advantages, including the following: (1) The PV array is controlled by a modified INC algorithm to extract the maximum power. (2) Depending on the energy requirements of the loads, the bidirectional converter operates in buck and boost modes to charge and discharge the station battery. (3) The dc-link voltage is maintained constant under all operating conditions. (4) The total harmonic distortion of grid current sending and receiving from the grid is always less than 5% under all operating conditions.

2 System Configuration

The overall system has a solar array with a boost DC–DC converter, Energy storage system battery with a bidirectional converter, buck converters as charging circuits of EV battery, and a single-phase grid integrated to it using a bidirectional AC/DC converter as shown in the Fig. 1. Ev batteries are charged from the DC bus is controlled by a constant current constant voltage control depend on the state of charge of the EV battery. The bidirectional converter was employed for charging and discharging the BESS is controlled by a PI controller, which determines whether to operates in buck or boost mode for the power flow in both directions. For power flow from grid to system and system to the grid, a DQ frame current control is employed in grid side AC/DC converters.
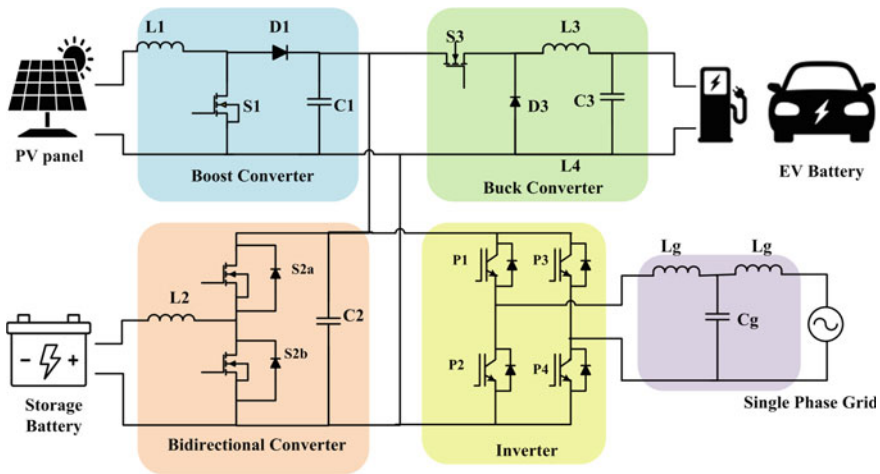

Fig. 1 Schematic diagram of the system

2.1 Solar Array and Storage Battery

(i) The solar array is designed to charge three EV batteries, the EV batteries considered are lithium–ion batteries with 240 V, 40 Ah capacity.

The following is the mathematical relationship used for designing solar arrays and storage batteries. Power required by three EV's to charge for 8 h is calculated using Eqs. 1 and 2 and found that a minimum of 3.6 kW power is required to charge three vehicles.

$$E_{EV} = \text{Battery Voltage} \times \text{Capacity} \times 3 \tag{1}$$

$$P_{EV} = \frac{E_{EV}}{8} \qquad (2)$$

So considering extra charges to charge BESS and to supply grids PV panel with 6 kW chosen. PV model of 1 soltech 1STH-250-WH array with one array power of 250 W is selected with Number of Parallel Strings as 2 and number of Series Connected modules per string as 8 to get selected PV output power.

(ii) The storage battery is designed on the consideration that a maximum of 2 h battery has to power the loads considering PV fail conditions. The Depth of Discharge (DoD) of battery is assumed as 50%, its efficiency as 80%, and the converter efficiency as 90%, Energy supplied by the battery is given as

$$E_{bat} = \frac{P_{EV} \times 2}{0.9 \times 0.9 \times 0.8} \qquad (3)$$

Considering a 240 V battery, then the battery's Ah rating is calculated using Eq. 4.

$$\text{Battery Ah} = \frac{E_{bat}}{240 \times \text{DoD}} \qquad (4)$$

hence 240 V, 100 Ah lithium–ion battery is chosen as station battery in this system.

3 Control Configuration of PV Fed EVCS

This section discusses various controlling techniques used to control the operation of converters in this system. The MPPT method generates the boost converter duty ratio by employing a modified incremental conductance method. This work employs PID control for the bidirectional converter, constant current constant voltage charging control for the buck charging circuit, and D–Q frame current control for the grid-tied inverter.

3.1 Modified Incremental Conductance Method

The maximum solar power is tracked using a modified incremental conductance algorithm. This algorithm operates by calculating the change in output power over a fixed period and calculating duty ratios from this. The flow chart of Modified INC is depicted in Fig. 2. As an improvement from the incremental conductance algorithm here uses two-loop conditions for calculations [7]. In the case where solar irradiation increases, voltage, and current will increases, and the values $\Delta V/\Delta P$ and $\Delta I/\Delta P$ both become positive. So the algorithm will reduce the duty ratio. And when irradiation reduces the voltage and power falls, but the ratio between $\Delta V/\Delta P$
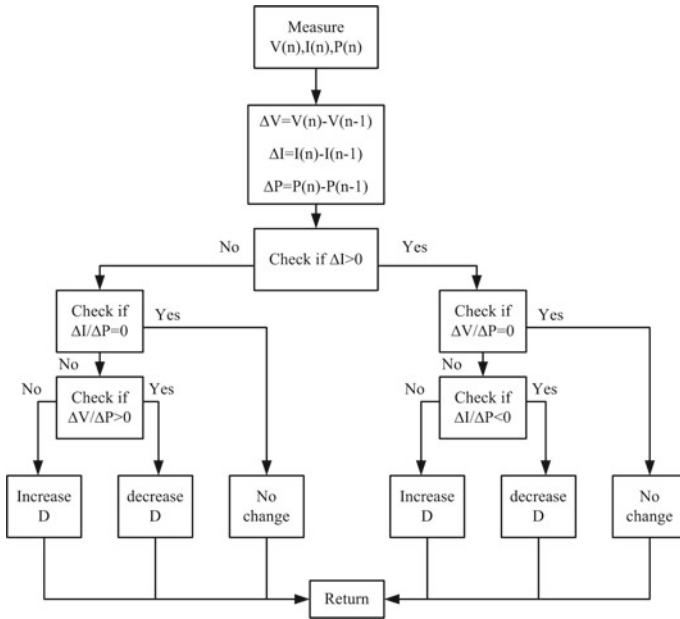
Fig. 2 Flow chart of modified INC MPPT

is positive, so the command is to increasing the duty ratio, which is improper in this case. As a result, the second loop is used for the conditions of reducing irradiation. As a result, the second loop is used, and it uses the first loop to determine the duty ratio when radiation rises. In Modified INC the control can calculate maximum points more quickly, and duty produces are more precise.

3.2   PI Controller for Bidirectional Converter

The bidirectional converter has two objectives: to operate in buck or boost mode depending on the charging and discharging of the storage battery, and to maintain a constant DC-link voltage. The converter can control the transition between operating quadrants to ensure that it is as smooth as possible. To create a control for both the boost and buck modes, the proportional-integral (PI) control was used. By sensing the dc-link voltage and battery current, the control made switching between operating modes easier.

3.3 CC–CV Control of Battery Charging

Constant current–constant voltage (CC–CV) charging is a hybrid of CC and CV charging. The charger limits the amount of current to a reference level until the battery reaches a predetermined SoC value. The charging current decreases as the battery is fully charged. This system, which is widely used in EV charging, enables fast charging while avoiding the risk of overcharging. The battery is charged at a constant current rate until it reaches the SoC level of 90%, at which point constant voltage charging is included [8]. The battery is normally charged at a constant current and if the battery reaches an SoC greater than 90%, it enters the CV mode of charging, where the change in duty keeps the battery voltage constant.

3.4 DQ Frame Current Control for Single Phase Grid

The single-phase inverter under consideration in this paper is made up of an IGBT-based H-bridge and an LCL output filter. DQ frame control is used to control grid-connected inverters in this case. The sensed grid voltage and current are transformed to the α–β frame and then to the d–q frame. Current controller with PID uses the d–q frame values of current and voltages. This d–q quantity finally transformed to α–β to generate the switching pulses of the inverter [9, 10].

3.5 Control Coordination Between Converters

The bidirectional converter and inverter are controlled based on the difference between PV power and total load power (including EV batteries and DC load). If the PV power exceeds the load power, the bidirectional converter's buck side switch is activated. Inverters are given a positive reference current, so they provide excess power to the grid [11]. If the PV power is less than the load power, the storage battery's SoC is examined. If the SoC is greater than 10%, the storage battery is allowed to discharge and provide power to the load. In this case, the bidirectional converter's boost switch is activated. And if the SoC is less than 10%, the storage battery is not allowed to discharge, forcing the grid to provide power; at this point, a negative reference current with a larger magnitude is provided for inverter control. Because they are always on, the boost and buck converters have no mutual control relationship.
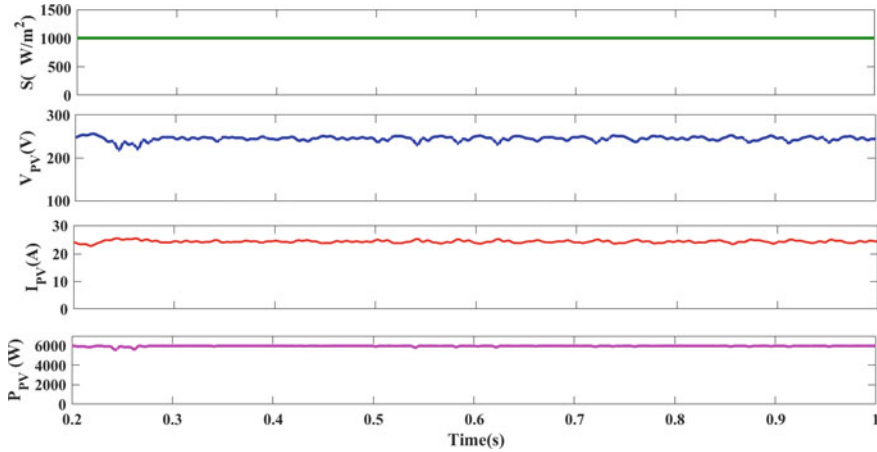
**Fig. 3** PV waveforms at irradiation of $1000\,\text{W/m}^2$

4 Results and Discussion

The system is designed for a maximum PV power of 6 kW; the PV array's MPP voltage and current are 245 V and 24 A, respectively. A 240 V, 40 Ah lithium–ion battery is used as an EV battery, and a 240 V, 100 Ah battery is used as a storage battery. The system's performance is validated in three different scenarios. (1) PV powering mode: where PV generates enough power to power the load and the rest is used to charge storage batteries and supply power to the grid. This condition is simulated by keeping the solar irradiation constant at $1000\,\text{W/m}^2$. (2) Battery supporting mode: this mode displays the storage battery's assistance in meeting load demand when PV power is low. The battery provides the required extra power by discharging stored energy. For simulation analysis, the irradiation is gradually reduced from 1000 to $300\,\text{W/m}^2$ to demonstrate a low PV production value, and the results are analyzed. (3) Grid powering mode: when PV and storage batteries do not have enough power to supply the load, the grid feeds the loads by injecting the necessary power. For simulation purposes, the irradiation is reduced from 1000 to $10\,\text{W/m}^2$, and the State of Charge of the station battery is set to a low value (9%). This section examines the results obtained from these three conditions. To demonstrate power balance, PV power (P_{PV}) is taken as positive, while rest powers such as vehicle power (P_{EV}), grid power (P_{grid}), storage system power (P_{ESS}), and load power (P_{load}) are taken as negative because they receive power.

The PV voltage, current, and power are shown in Fig. 3 at $1000\,\text{W/m}^2$. As a result, maximum voltage and current are obtained as MPP values, and the designed power is obtained under this condition. Figure 4 depicts the performance of the storage battery and grid in PV powering mode. Because the PV power is surplus at this time, the station battery is charging, as evidenced by the negative charging current and increasing SOC curve. It is also injecting power into the grid because the grid current
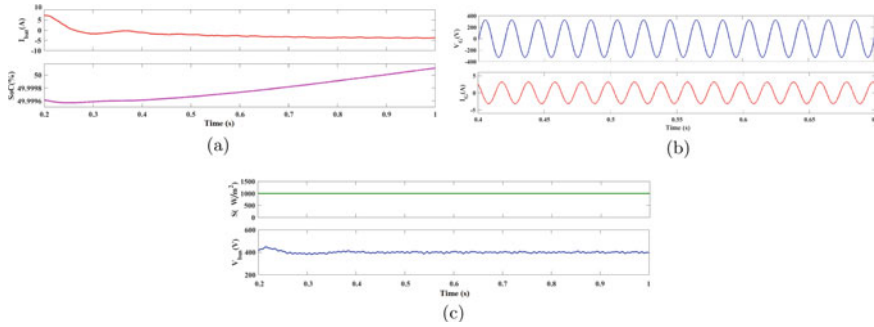
Fig. 4 Performances in PV powering mode. **a** Storage battery current and SoC. **b** Grid voltage and grid current, **c** DC-link voltage
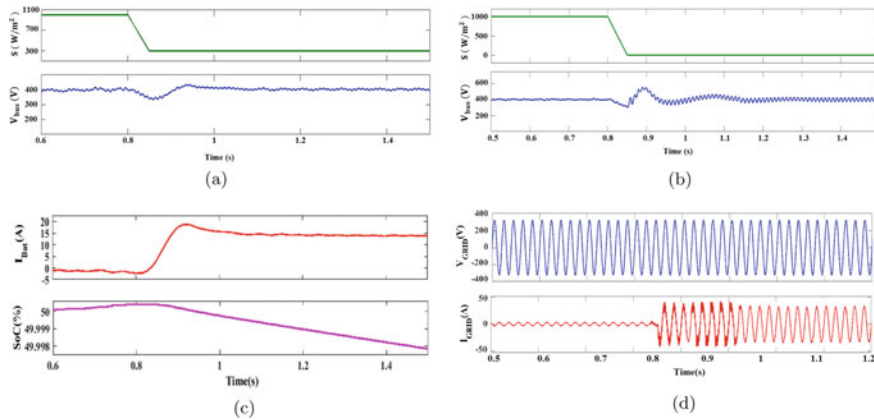

Fig. 5 Dynamic performance of system **a** DC-link voltage in battery supporting mode, **b** DC-link voltage in grid powering mode, **c** storage battery in battery supporting mode, **d** grid voltage and current in grid powering mode

and voltage are out of phase. From Fig. 4c the dc-link voltage seems to be maintained at a constant voltage of 400 V. The battery supporting mode is simulated by changing the irradiation from 1000 to 300 W/m^2, as shown in Fig. 5a, and the dc-link voltage remains constant at 400 V despite the irradiation change. Figure 5b shows that the charging current shifts from a negative to a positive value, and the soc curve appears to be decreasing as the point of irradiation changes. This demonstrates that the battery is injecting the necessary power for loads when PV power is low. Similarly, the irradiation is reduced from 1000 to 10 W/m^2 to demonstrate the performance when using grid power. Figure 5c depicts the irradiation change and shows that, even after the irradiation change, the dc-link voltage remains constant at 400 V. The grid current increases from the point of irradiation change on wards, as shown in Fig. 5d. The initial grid current is out of phase with the voltage and is regarded as negative power; however, after the irradiation change, the grid current is in phase with the voltage,
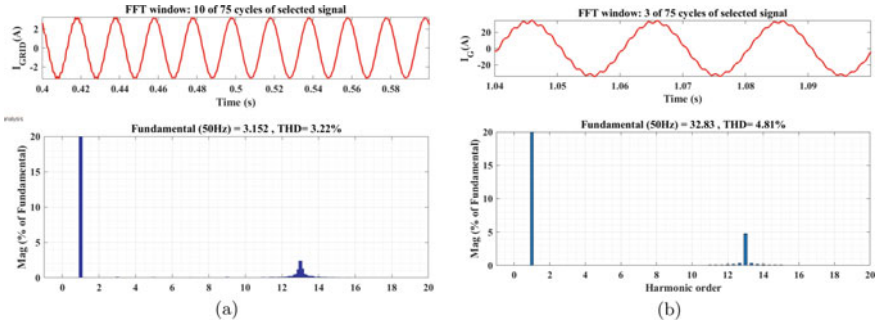
Fig. 6 THD analysis of grid current **a** when PV injecting current to grid and **b** when grid inject current to system
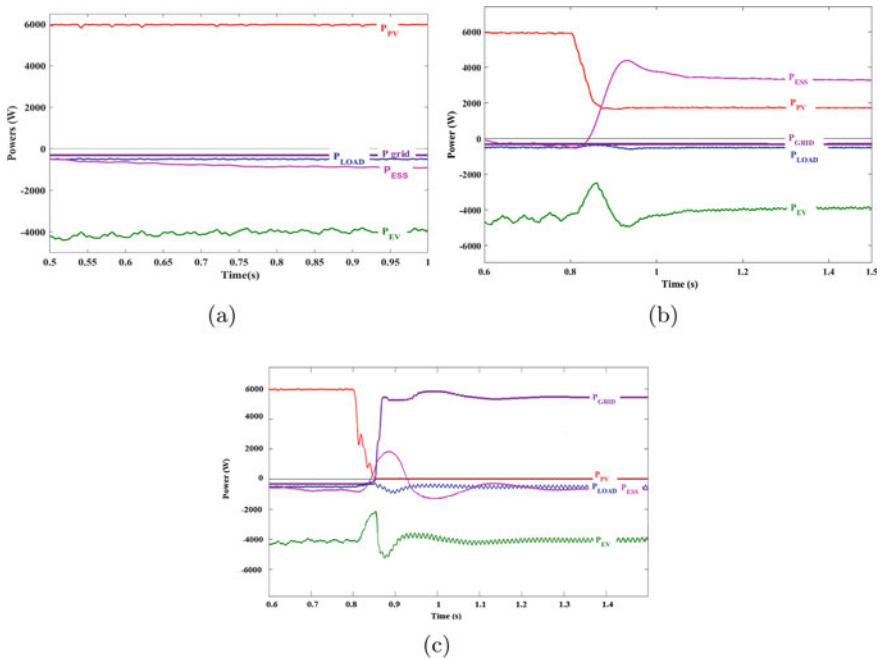
Fig. 7 Power-sharing between source and loads in system **a** PV powering mode, **b** battery supporting mode, **c** grid powering mode

and the grid power is regarded as positive. This demonstrates that when PV power and storage battery capacity are low, the grid injects the necessary power for loads. The total harmonic distortion of grid current is shown in Fig. 6 in both scenarios, namely (a) when PV injects power into the grid and (b) when the grid injects current into the system. THD is extremely low in both cases, at less than 5%, well below the IEEE 519 standard limit.

The power-sharing relationship between PV, Storage battery, Grid, and loads like EV battery and DC load is depicted in Fig. 7. PV power is the only positive power and the others are negative in Fig. 7a, suggesting that PV is the only active source and the others are loads. The system's first mode of functioning is therefore confirmed.

The battery supporting mode is shown in Fig. 7b, when the PV power is low, the battery power changes from negative to positive, indicating that the battery supply power is active at that moment (positive power means power is supplying, while negative power shows power is accepting). As a result, battery support at the PV low output power stage is validated. Similarly, in Fig. 7c, which depicts power-sharing in grid powering mode, it is observed that when PV power is very low, grid power appears to change from negative to positive while battery power remains the same, indicating that the battery cannot discharge or support due to its low capacity. Power-sharing between PV sources, storage batteries, and the grid is validated in all three scenarios. In all cases, the EV battery power appears to be constant, indicating that vehicle charging is not disrupted in any way.

5 Conclusion

A grid-connected PV-fed electric vehicle charging station with an energy storage system is simulated in order to charge three electric vehicle batteries from the dc bus. The simulation is carried out for various transmission conditions of power between PV, ESS, and the grid. In all of the scenarios investigated, the overall power-sharing between sources and loads was satisfactory. When PV power is low, the energy storage system is seen to keep vehicle charged continuously. The utility grid is connected into the system allows bidirectional power transmission, and the grid has been shown to support the charging system even when the PV and ESS systems were not operating at full capacity. The fact that grid current has a very low THD value in all conditions makes the system more reliable. The operation of a bidirectional converter is found to be satisfactory because the charging and discharge of ESS occur at an appropriate time and also maintains a DC bus voltage.

References

1. Lee H-S, Yun J-J (2019) High-efficiency bidirectional buck-boost converter for photo voltaic and energy storage systems in a smart grid. IEEE Trans Power Electron 34:4316–4328
2. Savio DA, Juliet VA, Chokkalingam B, Padmanaban S, Holm-Nielsen JB, Blaabjerg F (2019) Photo voltaic integrated hybrid micro grid structured electric vehicle charging station and its energy management approach. Energies 12(1)
3. Elsayad N, Moradisizkoohi H, Mohammed OA (2019) Design and implementation of a new transformer less bidirectional dc-dc converter with wide conversion ratios. IEEE Trans Ind Electron 66:7067–7077

4. Singh B, Verma A, Chandra A, Al-Haddad K (2020) Implementation of solar pv-battery and diesel generator based electric vehicle charging station. IEEE Trans Ind Appl 56:4007–4016
5. Hasanpour S, Baghramian A, Mojallali H (2020) Analysis and modeling of a new coupled inductor buck boost dc-dc converter for renewable energy applications. IEEE Trans Power Electron 35:8088–8101
6. Biya TS, Sindhu MR (2019) Design and power management of solar powered electricvehicle charging station with energy storage system. In: 3rd International conference on electronics, communication and aerospace technology (ICECA), Coimbatore, India, pp 815–820
7. Adhikari N, Singh B, Vyas AL (2011) Performance evaluation of a low power solar-PV energy system with SEPIC converter. In: IEEE Ninth international conference on power electronics and drive systems, Singapore, pp 763–769
8. Preetha Yesheswini B, Jai Iswarya S, Amani B, Prakash PSMR (2020) Solar pv charging station for electric vehicles. In: International conference for emerging technology (INCET), Belgaum, India, pp 1–7
9. Arab N, Kedjar B, Al-Haddad K (2016) D-Q frame optimal control of single phase grid connected inverter with LCL filter. In: IEEE Electrical power and energy conference (EPEC), Ottawa, ON, Canada, pp 1–6
10. Tang Y, Burgos R, Li C, Boroyevich D (2017) Stability assessment of utility PV integration to the distributed systems based on D-Q frame impedances and GNC. In: IEEE 18th Workshop on control and modeling for power electronics (COMPEL), Stanford, CA, USA, pp 1–6
11. Ma C-T (2019) System planning of grid-connected electric vehicle charging stations and key technologies: a review. Energies 12(21)

Human Arm Motion Capture Using IMU Sensors

Aniruddha Bhattacharjee and **Chanakya Bhatt**

Abstract The human arm is a system which is constrained and yet can produce an orientation of each of its segments in order for the end effector, in this case, the hand, to be moved to any coordinate inside its sphere of operation. Different segments or parts of the arm (upper arm, forearm and hand) can enable a fixed set of rotational motions about certain axis with a constrained space for movement to achieve movement in three dimensions. This behaviour falls somewhere between a parallel robot and a six degrees of freedom robotic manipulator. Thus, determining the orientation of the individual segments can help determine the position of the hand due to the rigid coupling witnessed between the different segments in the form of joints as well as the fact concerning the cascaded movement of segments in response to change in orientation of one of the segments. This paper lays down a concept which uses quaternions representing rotation to calculate the orientation and determine the three-dimensional position of the hand. The kinematic quantities required to calculate orientation is obtained from Inertial Measurement Units (IMUs) deployed on each segment of the arm to fetch the relevant kinematic data associated with the respective arm segment.

Keywords Motion capture · Orientation tracking · Inertial Measurement Units

1 Introduction

Systems which involve tracking human arm motion or orientation generally involve either an array of sensors deployed on the body and arm itself, or may involve a set-up which uses computer vision techniques and image processing software to track the individual components of the arm (refer [1]). The latter can be realized by designing a software which can track certain coloured objects scattered on the arm, tracking which would yield measurements which can then be used to track the orientation of

A. Bhattacharjee · C. Bhatt (✉)
Institute of Technology, Nirma University, Ahmedabad, Gujarat 382481, India
e-mail: chanakya.bhatt@nirmauni.ac.in
URL: http://www.nirmauni.ac.in

the arm segments itself. A combination of camera can act as the primary input sensors in this method. Apart from this technique, the image processing software might simply track the different segments of the arm itself. Computer vision techniques offer an accurate way to map motion, but it comes at a cost of increased computational complexity and hardware, thus being slightly difficult to accommodate in scenarios involving low-power applications or wearable technology. On the other hand, techniques involving sensors deployed on the arm segments can comprise a simple embedded system. Such techniques employ different types of sensors such as strain sensors [2] and rotary encoders [3] to measure angular displacement or any other sensor which can directly or indirectly provide data which can be used to determine the orientation of the segment it is attached to. One such technique [4] involves strain sensors for measuring the relative rotation or bending of an arm segment relative to another, at the joints, thus mapping the orientation of each segment. Using strain sensors or rotary encoders at the joints to capture angular displacement of the arm segments involves deploying these sensors on specifically designed substrates or placing them along the portion of the arm which see a lot of movement. Thus, these techniques bring in some level of discomfort for the wearer since the free movement of the arm is hindered due to the presence of sensors at the joints. In addition to this, only the relative angular distance between two segments can be determined from this method, limiting the accuracy of the captured motion of the arm.

Another class of sensors, Inertial Measurement Units or IMUs consist of an array of sensors such as accelerometer, gyroscope and magnetometer, which can provide kinematic data such as angular velocity, acceleration and magnetic heading of the object the IMU sensors are placed on. IMUs involve the least mechanical or computational complexity that is generally witnessed in the other techniques discussed above. This paper lays down a procedure to capture the motion of a human arm using Inertial Measurement Units or IMUs. Inertial Measurement Units (IMUs) [5] are sensors or units comprising accelerometer, gyroscope or magnetometer, sensors capable of measuring the kinematic quantities and forces experienced by an object. The IMU sensor referred to in this paper comprises a unit housing a gyroscope and an accelerometer in it. Since the semiconductor revolution, sensors such as these have been able to be designed and made into semiconductor Micro Electro-Mechanical Systems (MEMS)-based electronic sensor. A typical example of the sensor used is shown (see Fig. 1).

2   Forming Rotation Quaternions from Sensor Data

The IMU [5] used for tracking motion comprise an accelerometer and gyroscope sensor, thus giving the acceleration and angular rotation rate of the different arm segments. From each of these sensors, one rotation quaternion is calculated, quantifying the change in orientation of a predetermined unit vector (which can consequently be written as a vector quaternion), called the object vector q_o^{IMU}. Keeping one of the coefficients nonzero while the others being zero can align this object vector along the

Fig. 1 A sensor breakout board housing the InvenSense MPU6050 accelerometer-gyroscope sensor [6]. This package is aimed at interfacing with a microcontroller at the prototyping stage. The sensor uses the I²C digital communication protocol (refer [7]) to transmit data to the microcontroller
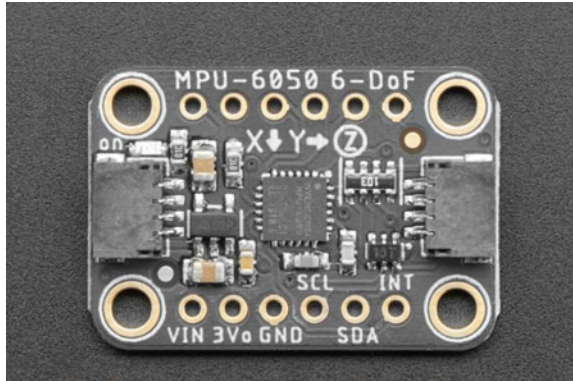

required 'up', 'down' or 'right/left' direction, depicting either the axis of the arm segment or the normal vector to the IMU, depending on the direction. Quaternions [8] are four dimensional mathematical entities which can be very effectively used to describe rotations happening in the three dimensions. A quaternion has a scalar part and three imaginary or directional parts. A three-dimensional vector can be represented as a quaternion with the scalar part being zero. For a vector $\boldsymbol{v} = v_x\hat{i} + v_y\hat{j} + v_z\hat{k}$, a quaternion representing $\boldsymbol{v}$ would be $q_v = 0 + \boldsymbol{v} = v_x\hat{i} + v_y\hat{j} + v_z\hat{k}$. A point in three-dimensional space can be represented in a similar way, by taking the scalar part of the quaternion as $zero$ and assigning the x, y, z components (rectangular representation) to the respective $\hat{i}$, $\hat{j}$, $\hat{k}$ parts of a quaternion. Rotations, while using quaternions, can be described in the form of axis-angle representation [9]. Any object being rotated in three dimensions, its rotations can be characterized as a rotation through an angle about some axis. Thus if an object is rotating in three-dimensional space, about an axis represented by vector quaternion q_v and being rotated through an angle θ about q_v, the entire rotation can be built into a rotation quaternion q_{rot} which is given by Eq. 1.

$$q_{\text{rot}}(\theta, q_v) = \cos(\theta/2) + \sin(\theta/2)q_{v_x}\hat{i} + \sin(\theta/2)q_{v_y}\hat{j} + \sin(\theta/2)q_{v_z}\hat{k} \quad (1)$$

If IMU sensors are deployed on every segment of a human arm, calculating the rotation quaternion associated with each IMU enables the determination of the orientation of each arm segment (see Fig. 2).

2.1 Gyroscope Rotation Quaternion

Data from the gyroscope involves the angular velocity along three-orthogonal axes which the sensor experiences while its rotating. Integrating angular rates gives the angle covered in that rotation and accumulating this sweep in angle gives the total
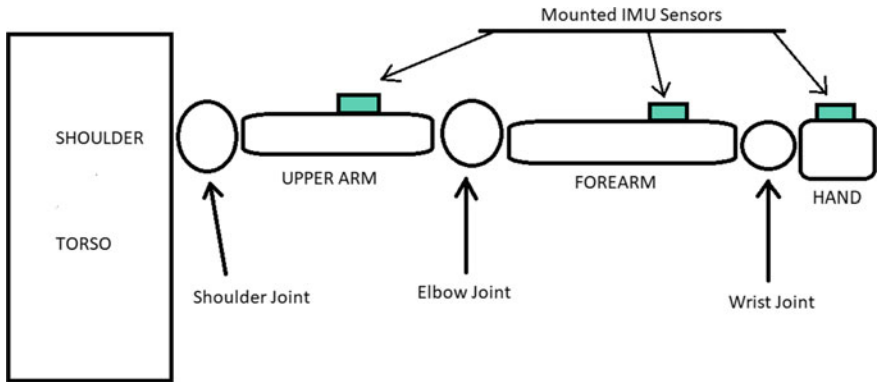
Fig. 2 Set-up to capture human arm motion. Deploying IMU sensors on each segment of the human arm to determine orientation of each segment and calculate the position of each joint in three-dimensional space

angle covered. If the sampling interval of the gyroscope sensor is Δt, the rotation quaternion associated with the gyroscope would include the change in angular distance happening in the sampling interval. The gyroscope data consisting of angular velocities about three-orthogonal axes, x, y, z at time t can be represented as a vector as

$$\boldsymbol{\omega} = 0 + \omega_x \hat{i} + \omega_y \hat{j} + \omega_z \hat{k} \tag{2}$$

Normalizing the vector $\boldsymbol{\omega}$ would yield the unit vector about which the rotation is taking place. Multiplying the norm of $\boldsymbol{\omega}$ with Δt would yield the angle of rotation about the unit vector formed from $\boldsymbol{\omega}$. Thus, with an axis and angle extracted from the gyroscope data quaternion, a gyroscope rotation quaternion can be formed as shown in Eq. 3.

$$q_\Delta = q_{\text{rot}} \left(\Delta t * ||\boldsymbol{\omega}||, \frac{\boldsymbol{\omega}}{||\boldsymbol{\omega}||} \right) \tag{3}$$

This is the rotation that the IMU has experienced between the last gyroscope sample and the current gyroscope sample. Thus, in order to update the orientation of the IMU from the previous time step, the gyroscope rotation quaternion q_Δ is multiplied with the quaternion representing accumulated rotation of the IMU, calculated in the previous time steps. In this way, subsequent rotation of the IMU would be chained, thus accumulating rotation over time, as the IMU rotates. If q_{IMU}^t represents the best estimate of the IMU rotation quaternion, using the gyroscope, this rotation quaternion can be updated by a quaternion multiplication shown in Eq. 4.

$$q_{\text{IMU}}^{t+1} = q_{\text{IMU}}^t * q_\Delta \tag{4}$$

2.2 Quaternion-Based Tilt Estimation Using Accelerometer

The accelerometer provides acceleration along three-orthogonal axes. The accelerometer senses the pseudo forces acting on the IMU under the presence of some force, thus detecting the acceleration experienced by the IMU along three axes. On the surface of the Earth, while at rest and under negligible motion, the accelerometer experiences Earth's acceleration due to gravity or g, a line of force pointing straight down towards the centre of Earth. If the IMU is placed such that the marked vertical axis of the IMU is anti-parallel to the gravitational line of force, then the accelerometer will read a positive g m/s^2 on the vertical axis. The other two axes, both being perpendicular to the vertical axis and hence also to the gravitational lines of force, would experience zero acceleration (the IMU being stationary). But if the IMU is tilted, the marked axes of the IMU might not be aligned in such a way that the vertical axis of the IMU be anti-parallel or parallel to gravitational lines of force. This leads to a scenario where all the three axes of the IMU might experience some component of gravity. Tilt estimation using accelerometer leverages this scenario, wherein the orientation of the IMU can be determined by using the components of g along all the axes of the accelerometer. The acceleration experienced by the IMU in its own frame of reference may be different from the what an entity in the Earth's frame of reference might experience. If the IMU is tilted or has undergone rotation about some axis parallel to the Earth's surface, it experiences some acceleration on its axes, due to g being at some angle to each individual axis. But from outside the IMU's frame of reference, the IMU is still stationary. If a rotation quaternion q_R, describing the IMU's previous rotations that have led to its current orientation, then using that rotation quaternion, the accelerometer data can be rotated to outside the IMU's frame of reference. Let the accelerometer data be represented as a vector quaternion

$$q_a^{\text{IMU}} = 0 + a_x \hat{i} + a_y \hat{j} + a_z \hat{k} \tag{5}$$

Now, this vector quaternion can be rotated to world frame of reference using the known rotation quaternion q_R using the quaternion transformation equation-

$$q_a^{\text{world}} = q_R * q_a * (q_R)^{-1} \tag{6}$$

The q_R rotation quaternion could be the gyroscope rotation quaternion q_{IMU}^{t+1}, since the gyroscope is keeping track of the orientation of the IMU by integrating the angular velocities about the three axes. Therefore, the gyroscope rotation quaternion will be used for this purpose.

3 Sensor Fusion: The Complementary Filter

The vector quaternion obtained in Eq. 6 exists outside the IMU's frame of reference, hence, being rotated to an orientation where the vertical axis of the IMU is again anti-parallel to the gravitational lines of force, the vector quaternion q_a^{world} must align with the vertical axis of the IMU (as if the IMU never tilted). But, some errors creep into q_a^{world}, deviating it from its actual value. This is due to the fact that the updated gyroscope rotation quaternion, obtained in Eq. 4, contains error due to drift. This leads to a scenario where the accelerometer quaternion is not properly aligned with the vertical axis of the IMU. This error in the rotation can be modelled as a quaternion transformation equation. Let the vertical axis of the IMU be represented by $q_{\text{up}}^{\text{world}}$. This refers to the 'up' direction in Earth's frame of reference. 'Up', here, is defined as the direction at which one would find gravitational lines of force pointing straight down, towards the centre of the Earth (Fig. 3).

$$q_{\text{up}}^{\text{world}} = q_\epsilon * q_a^{\text{world}} * (q_\epsilon)^{-1} \tag{7}$$

Equation 7 models the deviation between the actual 'up' direction and the direction of the accelerometer quaternion in world frame of reference. q_ϵ is the error rotation quaternion which is responsible for the non-alignment of q_a^{world} and $q_{\text{up}}^{\text{world}}$ or the IMU vertical axis.

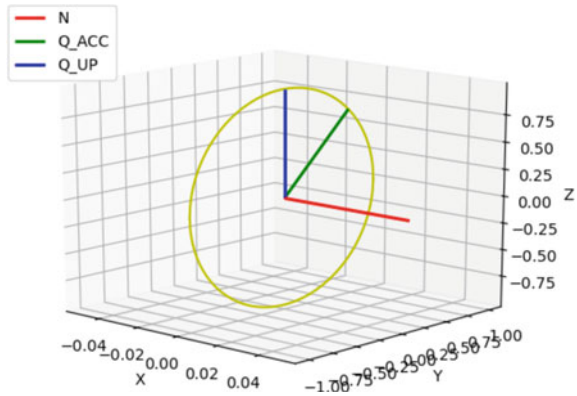## 3.1 Compensating the Error Rotation Quaternion

In order to reconcile the accelerometer quaternion in Earth's frame of reference with $q_{\text{up}}^{\text{world}}$, a tilt correction quaternion is calculated, which results in a rotation in the opposite sense. If q_ϵ rotates q_a^{world} away from $q_{\text{up}}^{\text{world}}$ by angle Φ about an axis $\boldsymbol{n}$, then the tilt correction quaternion, represented by $q_{\epsilon c}$, would rotate it by an angle $-\Phi$ about $\boldsymbol{n}$ or it can be interpreted as a being rotated by angle Φ about an axis $-\boldsymbol{n}$. Thus, the correction of q_a^{world} can be modelled as-

Fig. 3 IMU normal vector. Here, the maroon plane represents the IMU sensor, and the normal to this surface is the blue arrow depicting the IMU normal vector. (Visual rendered using Python programming language module: Matplotlib [10])
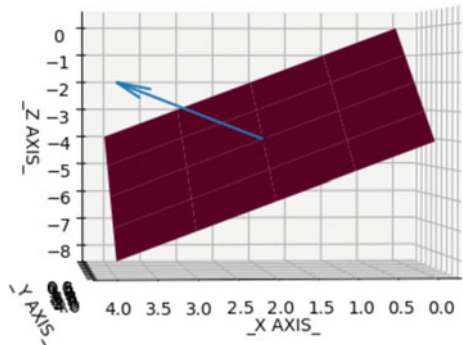
Fig. 4 Visualizing the cross-product between A^{world} (green line) and v_{up} (blue line). The result, $\hat{n}$, is the red line. (Visual rendered using Python programming language module: Matplotlib [10])

$$q_{\text{up}}^{\text{world}} = q_{\epsilon c} * q_a^{\text{world}} * (q_{\epsilon c})^{-1} \tag{8}$$

Compensating the error rotation quaternion involves determining the tilt correction quaternion $q_{\epsilon c}$ which satisfies Eq. 8. An intuitive way to determine $q_{\epsilon c}$ is to picture the situation in a three-dimensional environment (see Fig. 4). Since $q_{\text{up}}^{\text{world}}$ is vector quaternion representing a direction anti-parallel to gravity, it is essentially a vector pointing in the direction of positive Z-axis. The accelerometer quaternion in Earth's frame of reference q_a^{world} forms an angle with $q_{\text{up}}^{\text{world}}$. Let $\boldsymbol{v}_{\textbf{up}}^{\textbf{world}}$ be the vector form of $q_{\text{up}}^{\text{world}}$ with its components representing a unit vector pointing towards positive Z-axis.

$$\boldsymbol{v}_{\text{up}}^{\text{world}} = 0\hat{i} + 0\hat{j} + 1\hat{k} \tag{9}$$

$$\boldsymbol{A}^{\text{world}} = (q_a^{\text{world}})_x \hat{i} + (q_a^{\text{world}})_y \hat{j} + (q_a^{\text{world}})_z \hat{k} \tag{10}$$

The accelerometer values in Earth's frame of reference, which are the imaginary components of quaternion q_a^{world} is also represented as a vector A^{world}, given in Eq. 10.

The vector A^{world} can be normalized, as shown in Eq. 11, since its orientation is what matters here the most and would also provide a simplification in the computation of the vector cross-product of A^{world} and $v_{\text{up}}^{\text{world}}$.

$$\hat{A}^{\text{world}} = \frac{(q_a^{\text{world}})_x}{||q_a^{\text{world}}||}\hat{i} + \frac{(q_a^{\text{world}})_y}{||q_a^{\text{world}}||}\hat{j} + \frac{(q_a^{\text{world}})_z}{||q_a^{\text{world}}||}\hat{k} \tag{11}$$

$$\hat{n} = \hat{A}^{\text{world}} \times \boldsymbol{v}_{\text{up}}^{\text{world}} \tag{12}$$

Axis of Rotation: Taking the cross-product of $\hat{A}^{\text{world}}$ with $\boldsymbol{v}_{\text{up}}^{\text{world}}$ as shown in Eq. 12, yields the axis of rotation of the accelerometer quaternion (or the IMU itself) (see Fig. 4). This axis rotation is the unit vector $\hat{n}$.

Angle of Rotation: The rotation angle Φ, which is the angle between $\hat{A}^{\text{world}}$ and $\boldsymbol{v}_{up}^{\text{world}}$ can be determined by using the vector dot product, as shown in equations

$$\cos(\Phi) = \frac{\hat{A}^{\text{world}} \cdot \boldsymbol{v}_{\text{up}}^{\text{world}}}{||q_a^{\text{world}}|| \cdot ||\boldsymbol{v}_{\text{up}}^{\text{world}}||} \tag{13}$$

$$\Phi = \cos^{-1}\left(\frac{(q_a^{\text{world}})_z}{||q_a^{\text{world}}||}\right) \tag{14}$$

Simplifying Eq. 13, angle Φ can be obtained using Eq. 14. Thus, an axis and an angle have been obtained. Therefore, the tilt correction rotation quaternion can be formed with $\hat{n}$ and Φ as shown in Eq. 15.

$$q_{\epsilon c} = q_{\text{rot}}(\Phi, \hat{n}) \tag{15}$$

3.2 Deploying the Complementary Filter on $q_{\epsilon c}$

The complementary filter works as a linear interpolation between two quantities. The filter coefficient (α) determines how much the final estimate skews towards one of the quantities. If two quantities, 'Q_1' and 'Q_2' are estimates (determined from different sources) of a certain value 'V', then using the complementary filter, a better estimate can be determined using Eq. 16.

$$V = \alpha * Q_1 + (1 - \alpha) * Q_2 \tag{16}$$

$$0 \leq \alpha \leq 1 \tag{17}$$

This filter can deployed here between the tilt correction rotation quaternion $q_{\epsilon c}$ and the gyroscope rotation quaternion obtained in Eq. 4. The complementary filter is deployed by assigning a weight α to angle Φ in Eq. 15, and then multiplying $q_{\epsilon c}$ with q_{IMU}^{t+1}. This operation is shown in Eq. 18. The value 'α' should satisfy the inequality given by Eq. 17. The choice of selecting a particular value for the complementary filter weight 'α' does not follow a strict rule but is left to the engineer to decide on a suitable value. Usually, while deciding a value for α, more weight is given to the input which is closer to the actual value of the quantity in question. In such cases, experimental complementary filter estimates maybe compared with known values for a particular set-up.

$$q_{\text{CF}} = q_{\text{rot}}((1 - \alpha) * \Phi, \hat{n}) * q_{\text{IMU}}^{t+1} \tag{18}$$
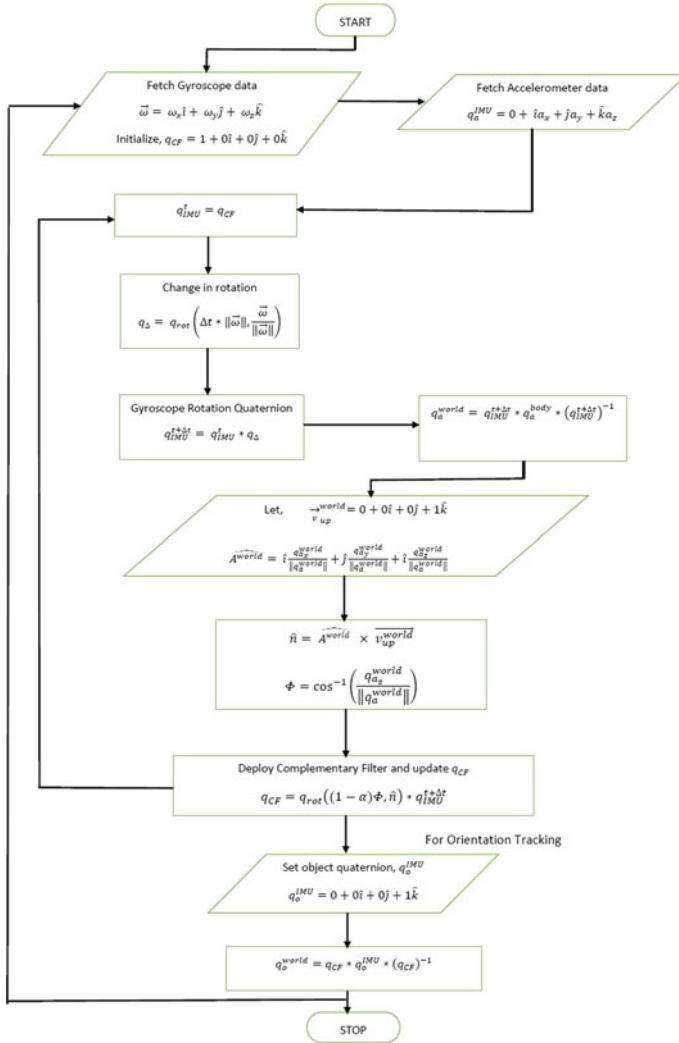
Fig. 5 Flow chart: calculating the IMU rotation quaternion for object orientation tracking

In order provide feedback and make the flow of determining orientation closed loop, the gyroscope rotation quaternion in Eq. 4 can be updated using the complementary filter rotation quaternion from the previous time step.

4   Orientation and Motion Tracking of Arm Segment End Point

Since the rotation quaternions describing the IMU's rotation or tilt has been determined, the coordinates of any point in the IMU's frame of reference can be determined after every rotation that the IMU undergoes. Any point in the three-dimensional space can be represented as a vector quaternion and using the transformation equation, that point could be rotated to the new coordinates using the rotation quaternion. Thus, for an object mounted with an IMU, any point on the object can be mapped to its new location by transforming that point using the rotation quaternion of the IMU calculated previously (Fig. 5).

4.1   Tracking Orientation Using Object Vectors

Consider a point or axis fixed to the IMU. A vector quaternion can be formed out of that point. If its an axis (like the transverse or lateral axis of an object), a unit vector in its direction could be considered as an imaginary marker for that object, with the marker located at the coordinates formed by the components of its unit vector. Let the set of three coordinates of the object marker or point be represented by the vector quaternion q_o^{IMU}. This quaternion is present in the IMU sensor's frame of reference. Rotating it using the rotation quaternion calculated in Eq. 18, the vector quaternion q_o^{IMU} would be then oriented to its new position q_o^{world}, the transformation being carried at as shown in Eq. 19.

$$q_o^{\text{world}} = q_{\text{CF}} * q_o^{\text{IMU}} * (q_{\text{CF}})^{-1} \tag{19}$$

Normalizing q_o^{IMU} or q_o^{world} turns out to be quite intuitive since only the direction is preserved while transformation, which is the purpose of orientation tracking. Hence, even if a point or marker is selected such that its position reflects its distance from the centre of mass of the IMU (or the object its attached to), ultimately only its direction would be used for orientation tracking, that is, a unit vector directed towards the marker. This system can be used to track an object's orientation by assigning the normal vector of the IMU to q_o^{IMU}. This is depicted in Fig. 6, where the blue quiver arrows represent the IMU normal vector (unit vector normal to the surface of the IMU) being constantly made to rotate, thus visualizing the orientation of the IMU.

4.2   Tracking Arm Segment End Point Trajectory

An arm segment is an element, stretching between one or two joint or points of rotation. If the shoulder ball and socket joint is considered as the origin of a three-dimensional Cartesian space, then the upper arm could be imagined as a line segment with one end at the origin, and the other at a scaled distance away from the origin.

Fig. 6 IMU normal vector
represented as blue arrows,
originating at the IMU's
centre of mass (red dot).
(Visual rendered using
Python programming
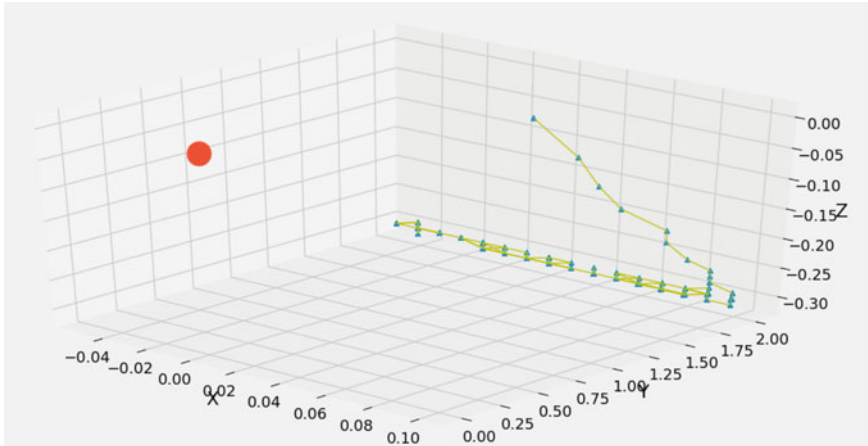language module: Matplotlib
[10])
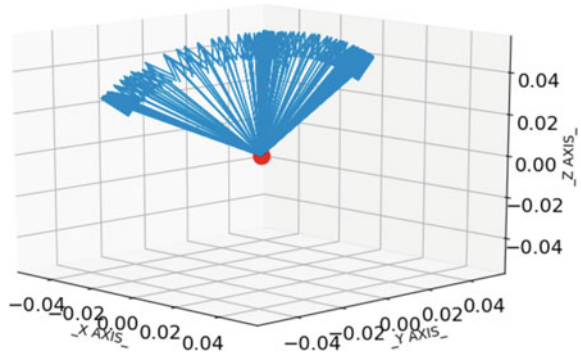
Fig. 7 Visualization of the
vector quaternion q_o^{IMU}. The
red square represents the
position of the IMU and the
yellow dot representing the
end point of an arm segment
(for the upper arm, it could
be the elbow). Thus, the
vector joining these two
points would be rotated by
the IMU rotation quaternion,
rotating the end point,
tracking the elbow joint.
(Visual rendered using
Python programming
language and open source
python module: Matplotlib
[10])
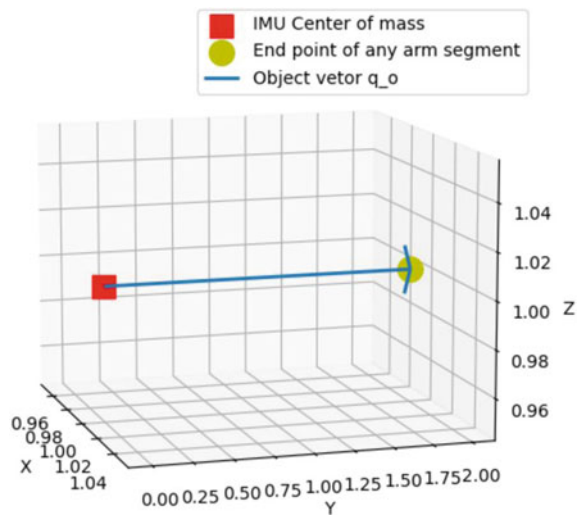
Thus, the upper arm would be capable of rotating in spherical space, with the radius being equal to the length of the upper arm. The end which is free to rotate is actually the elbow joint, connecting the upper arm to the forearm. Now, taking the position of the shoulder joint as the initial point, if q_o^{world} is taken such that it points in the direction connecting the shoulder joint to the elbow joint in a straight line, with the coordinates of q_o^{IMU} set at the elbow joint, reflecting its distance from the shoulder joint, rotating this vector quaternion would actually orient the entire vector connecting the shoulder joint with the elbow joint (see Fig. 7).

This is essentially rotating a line segment in three dimensions, beginning at the origin and rotating the other end (the elbow joint) on the surface of a sphere. Thus, assigning a suitable point to q_o^{IMU} and transforming it using the IMU rotation quaternion q_{CF} would actually orient and locate the end point of an arm segment. This can be done for the upper arm, forearm and the hand. In the end, each segment's orientation can be found using Eq. 19, and the same equation can be used for track-

Fig. 8 Tracking the end point of a segment. (The red dot represents the point or joint relative to which the other extremity of the segment (represented by blue-triangles) is moving). (Visual rendered using Python programming language module: Matplotlib [10])

ing the end point trajectory in three-dimensional space. Such tracking is depicted in Fig. 8, wherein the end point, i.e. q_o^{IMU}, is being plotted while the other end of the arm segment is represented by the fixed red dot.

5   Conclusion

The fact that the human arm is a system where the orientation of the individual segments is coupled with the translational and rotational motion of the respective segments plays a crucial role in using rotation quaternions (used for orientation tracking) to actually track a point associated with an arm segment. This coupling actually provides a faster and less computationally intensive approach to determine the orientation and tracking the motion of the human arm since only the calculation related to finding orientation of the different segments is required. This lightweight technique can find applications in areas such as gesture controlled systems and robotics and can be easily deployed on embedded devices.

References

1. Alper Y, Omar J, Mubarak S (2006) Object tracking: a survey. ACM Comput Surv 38(4). ISSN: 0360-0300
2. Wikipedia Contributors (2021) Strain gauge. Wikipedia, The Free Encyclopedia. https://en.wikipedia.org/w/index.php?title=Strain_gauge&oldid=1034024779. Last accessed 11 Aug

2021

3. Wikipedia Contributors (2021) Rotary encoder. Wikipedia, The Free Encyclopedia. https://en.wikipedia.org/w/index.php?title=Rotary_encoder&oldid=1026747750. Last accessed 11 Aug 2021

4. Mechael SS, Wu Y, Chen Y, Carmichael TB (2021) Ready-to-wear strain sensing gloves for human motion sensing. iScience 24(6). ISSN 2589-0042

5. Wikipedia Contributors (2021) Inertial measurement unit. Wikipedia, The Free Encyclopedia. https://en.wikipedia.org/w/index.php?title=Inertial_measurement_unit&oldid=1025660823. Last accessed 20 May 2021

6. InvenSense, MPU-6000 and MPU-6050 product specification, revision 3.4. https://invensense.tdk.com/wp-content/uploads/2015/02/MPU-6000-Datasheet1.pdf. Last accessed 29 May 2021

7. Valdez J, Becker J (2015) Understanding the I^{2}C bus. Texas instruments application report. https://www.ti.com/lit/an/slva704/slva704.pdf. Last accessed 29 May 2021

8. Weisstein EW (2021) Quaternion. From MathWorld—a Wolfram web resource. https://mathworld.wolfram.com/Quaternion.html. Last accessed 20 May 2021

9. Wikipedia Contributors (2021) Quaternions and spatial rotation. Wikipedia, The Free Encyclopedia. https://en.wikipedia.org/w/index.php?title=Quaternions_and_spatial_rotation&oldid=1031919218. Last accessed 20 May 20 2021

10. Hunter JD (2007) Matplotlib: a 2D graphics environment. Comput Sci Eng 9(3):90–95. https://doi.org/10.5281/zenodo.3695547

Boost Derived Multi Level Hybrid Converters in Micro Grid

Bankuru Sonia ⓘ, **V. Venkata Lakshmi** ⓘ, **and Madisa V. G. Varas Prasad** ⓘ

Abstract In the modern scenario, the importance of the multilevel inverter has been extended to different applications of power conversion methods. Multilevel inverter provides the resourceful use of non-conventional energy sources, and output power from the non-conventional energy Sources direct current in nature and is to be converted to alternating current to meet the domestic and industrial loads. The proposed methodology is to provide supply to the concurrent direct and alternating current loads from one dc input supply with the help of hybrid converter topologies. The projected converter is named as boost derived multilevel hybrid converter (BDMHC), which is derived from the conventional boost converter. The proposed converter is constructed with H-bridge symmetrical multilevel inverter with the help of three different boost converters topologies. The response of the proposed converter is validated for resistive loads. The proposed boost derived multilevel hybrid converter shows good cross-regulation properties to vibrant load variations. To analyze the proposed converter, state-space mathematical expressions have been developed and evaluated through MATLAB/Simulink.

Keywords Hybrid converter · Multilevel inverter · Microgrid

1 Introduction

In current developed electrical systems are including both alternating and direct loads and they are effectively incorporating with all types of energy sources [1–4] like renewable and non-renewable sources with the help of power electronic converters. Figure 1. illustrates the conventional power converter in which dc and ac loads are
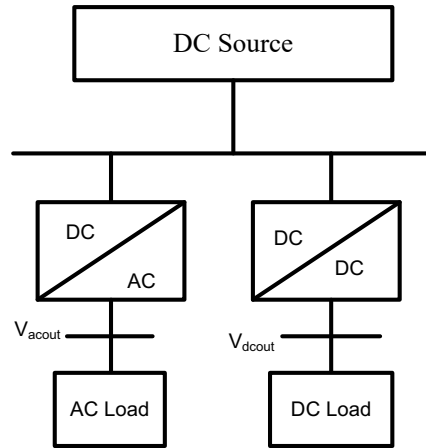
B. Sonia (✉) · V. Venkata Lakshmi · M. V. G. Varas Prasad
Vignan's Institute of InformationTechnology (A), Visakhapatnam, India

V. Venkata Lakshmi
e-mail: lakshmi.vasamsetti270@gmail.com

M. V. G. Varas Prasad
e-mail: mvgvaraprasad1@gmail.com

Fig. 1 Conventional converter

supplied from one dc source, i.e. in which two different converters, an inverter for DC-AC conversion and a chopper for DC-DC conversion, are used. Figure 2. represents the proposed multilevel hybrid converter by using this dc and ac loads supplied from one source with a single converter. With this proposed method, converter reliability increases resulting in inherent shoot-through protection capability. Here, DC Input is supplied from the renewable energy sources such as solar, wind, etc. with low voltage and power rating, to increase the voltage level to higher value boost converter is needed for dc loads and to feed the ac loads voltage source inverter is necessary. A power circuit that can feed both ac and dc loads simultaneously is called a boost derived multilevel hybrid converter. The conventional converter consists of a single control switch for conversion, which is replaced by a bidirectional single-phase bridge network in BDMHC. Because of the single-phase bridge network, both DC and AC outputs are controlled by the same switches. Therefore, the proposed converter decreases the switches count compared to the conventional converter.

Figure 3 represents the conventional converter and voltage source inverter in parallel connection and Fig. 4 describes the cascade connection of conventional converter and voltage source inverter, producing dc output V_{dcout} and ac output V_{acout}. Based on the application, different topologies of higher gains are used to reach step-up operation [5, 6]. Developed expressions for this model are validated through MATLAB/Simulink.

2　Proposed Methodology

Single stage topology is not sufficient to meet increasing ratings of power applications, in order to meet high and medium power requirements combinations of (parallel/cascade) two or more stages are used, which is termed a multilevel inverter. The advantage of a multilevel inverter is generating pure sinusoidal waveform with
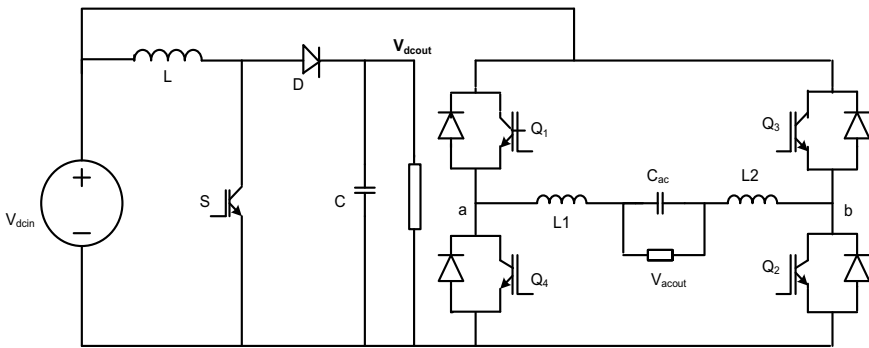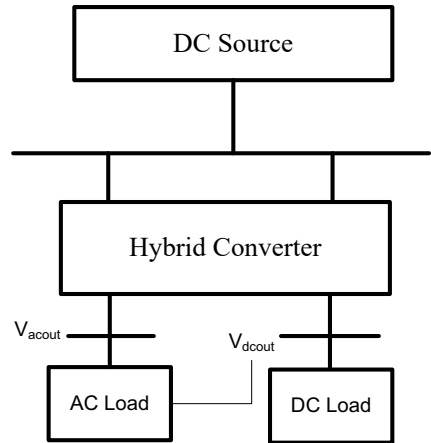
Fig. 2 Hybrid converter

Fig. 3 Parallel connection of conventional converter and voltage source inverter
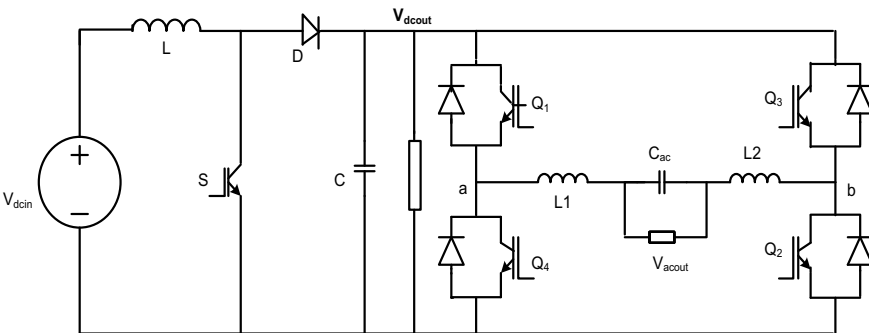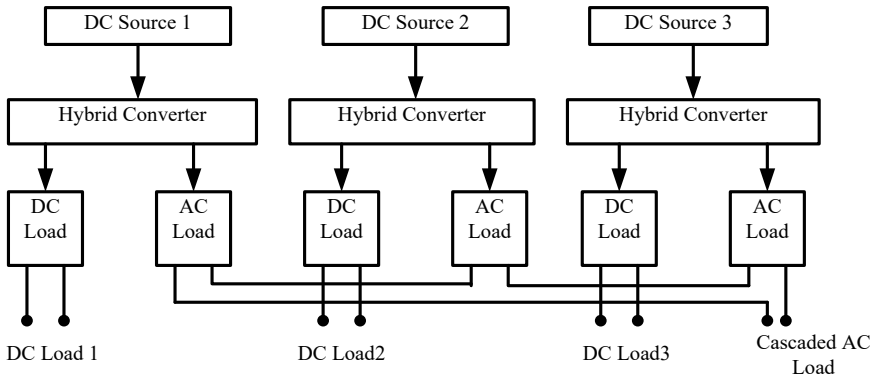

Fig. 4 Cascade connection of conventional converter and voltage source inverter

Fig. 5 Circuit diagram of BDMHC

less harmonic distortion and also decreases the electromagnetic interference [7]. There are many multilevel configurations described in [8, 9], in which cascaded H-bridge multilevel inverter has huge applications in EV, photovoltaic systems and motor drive.

Generally, conventional boost converters consist of opposed switch pairs, in which one is used to control the duty ratio and another switch is implemented using diode. The hybrid converter is constructed by using an inverter bridge circuit ($1 - \phi$ or $3 - \phi$) which replaces the control switch. The generalized circuit illustration and working are described in [10]. The proposed methodology is shown in Fig. 5, in which three single BDHCs are cascaded to get a high power level and seven-level symmetrical multilevel inverter with three boost converters.

Figures 6 and 7. illustrates the operation of Boost derived multilevel hybrid converter consisting of three input DC sources (V_{dci1}, V_{dci2} and V_{dci3}), three bridge circuits to get the three boosting output of DC (V_{dco1}, V_{dco2} and V_{dco3}), and a seven-level MLI ac output (V_{aco}). Every bridge circuit consists of four switches (IGBT) and they perform boosting and inverting operations depending on applications. L_1, L_2 and L_3, C_1, C_2 and C_3, diodes (D_1 to D_3) and Resistors R_{dc1}, R_{dc2}, R_{dc3} engage in boosting operation, and the output resistor Raco is used for inverting operation.

2.1 Output Voltage of BDMHC

Output expressions for DC input and DC output voltage relation of a single BDHC [11– 16] are described in Eqs. (1) and (2).

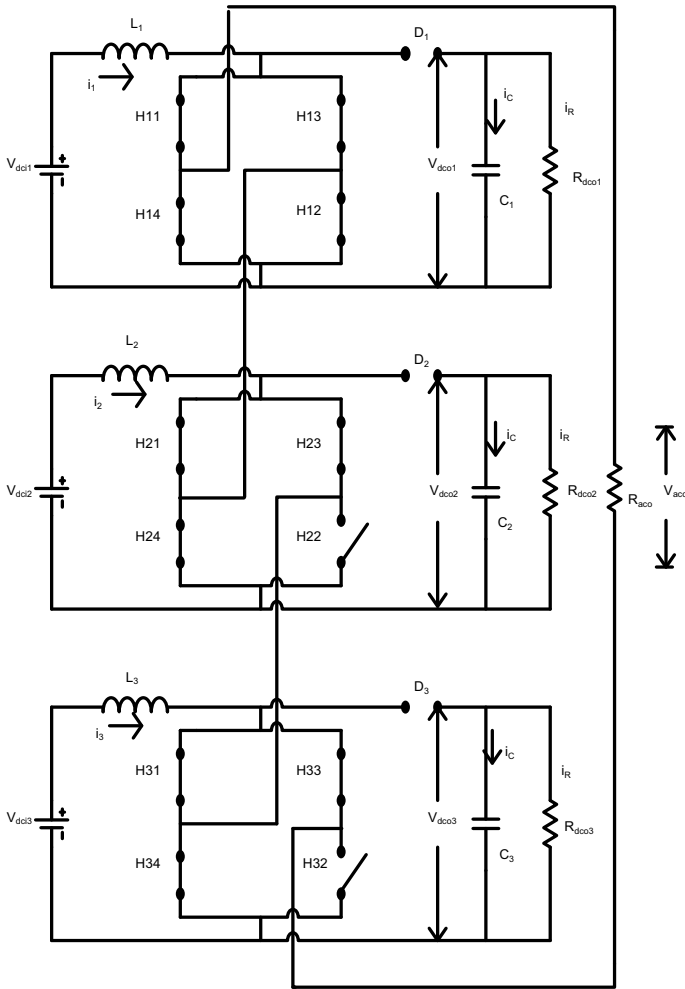$$\frac{V_{\text{dco1}}}{V_{\text{dco2}}} = \frac{1}{1 - \delta} \tag{1}$$

Fig. 6 Boosting mode shoots through interval

$$\frac{V_{\text{dco}}}{V_{\text{dci}}} = \frac{m_a}{1 - \delta} \tag{2}$$

The DC voltage response of boost derived hybrid converter is controlled with the duty ratio of the converter represented by δ like a conventional boost converter [9] and the AC voltage response is controlled by using the modulation index m_a ($0 \leq m_a \leq 1$) of the hybrid converter. The AC output value can increase by rising m_a for a fixed value of duty ratio δ. Hence, boosting and inverting operations are done through the same set of switches. The total output voltage in multilevel inverter [12] is the addition of individual inverter outputs.
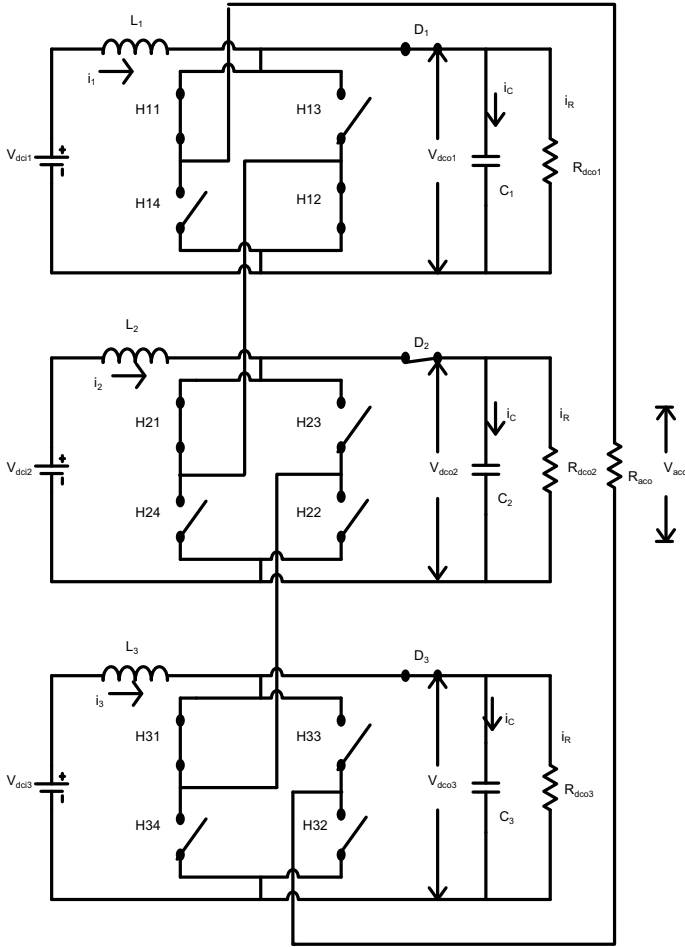
Fig. 7 Inverting mode and boosting power interval

The total no. of voltage levels in cascades mode of operation, [13– 17] ac Output is given by $m = 2\,s + 1$, here s represents no. of DC input sources. The AC response (voltage) expression for the seven-level multilevel inverter is described in Eq. (4).

$$m_a + 1 \leq \delta \tag{3}$$

$$V_{aco} = V_{dco1} + V_{dco2} + V_{dco3} \tag{4}$$

By substituting the Eq. (2) in the output expression (4)

$$V_{aco} = V_{dci1}\frac{m_a}{1-\delta} + V_{dci2}\frac{m_a}{1-\delta} + V_{dci3}\frac{m_a}{1-\delta} \tag{5}$$

Table 1 Switching sequence table

Status	$H11$	$H12$	$H13$	$H14$	$H21$	$H22$	$H23$	$H24$	$H31$	$H32$	$H33$	$H34$	V_{aco}(peak)
Positive half cycle	X	X	B	B	X	X	B	B	X	X	B	B	0
	Y	Y	B	B	Y	X	B	B	Y	X	B	B	61.25
	Y	Y	B	B	Y	Y	B	B	Y	X	B	B	122.5
	Y	Y	B	B	Y	Y	B	B	Y	Y	B	B	184.0
Negative half cycle	B	B	X	X	B	B	X	X	B	B	X	X	0
	B	B	Y	Y	B	B	Y	X	B	B	Y	X	−61.25
	B	B	Y	Y	B	B	Y	Y	B	B	Y	X	−122.5
	B	B	Y	Y	B	B	Y	Y	B	B	Y	Y	−184.0
	X	X	B	B	X	X	B	B	X	X	B	B	0

The generalized expression for n-level BDMHC, AC output voltage expression is

$$V_{aco} = \sum_{n=1}^{n} V_{dcin} \frac{m_a}{1 - \delta} \qquad (6)$$

Each bridge converter operation is depending upon the sequence of the switching given in Table 1.

Here, $X = 0$ indicates the off period, $Y = 1$ indicates the on period and B indicates the boost period. Triggering pulses are developed by analyzing the sine waveform with the 3 dc signals V_{r1}, V_{r2}, and V_{r3} of constant magnitude as illustrated in Fig. 8. To obtain the ac output response, the V_{tri} is compared with V_d, then the dc signal is generated to control the boosting period of the boost derived multilevel hybrid converter. In this, triggering signals for inverter operation and boosting purpose are developed individually then they are added logically. Figure 8 represents a generation of gate pulses of Y_{11}–Y_{14}, Y_{21}–Y_{24} and Y_{31}–Y_{34} [18].

2.2 Production of Gate Signals

The signals which are required to trigger the switches are developed by comparing base DC signals (V_{r1}, V_{r2} and V_{r3}) with carrier signals of triangular form, then generated signals for triggering purposes are given to the switches, respectively.

2.2.1 1st Level of Working (Period ($\pi - 2\alpha 1$))

The IGBTs $H11$, $H12$, $H21$ and $H31$ are closed for inverting period and $H13$, $H14$, $H23$, $H24$, $H33$, $H34$ are closed during boosting period in Level-1operation which is shown in figure. Closing Position of IGBT is represented with δ and the
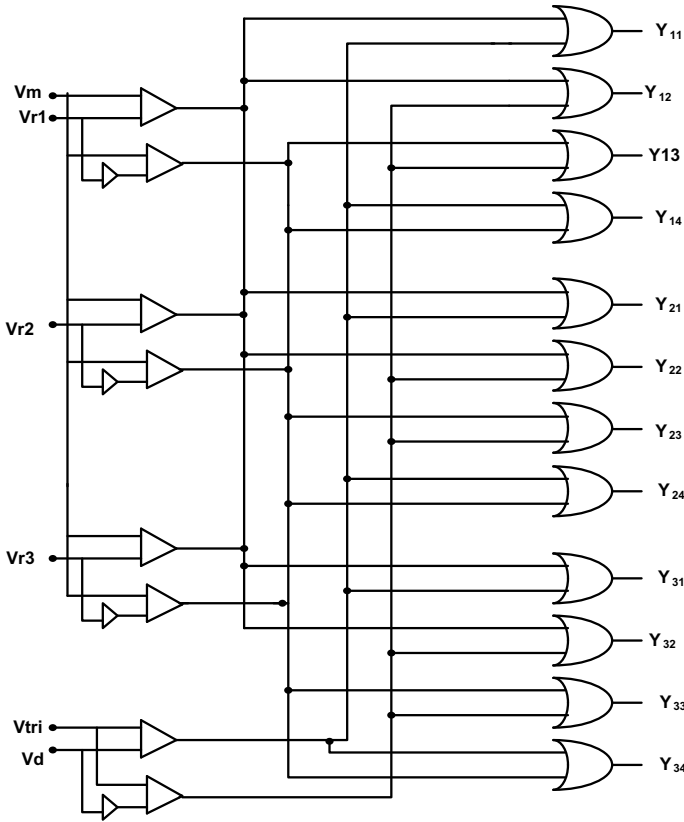
Fig. 8 Circuit diagram for gate signals

open position of IGBT is denoted by $(1 - \delta)$, for boosting operation. 1st Level of operation is described with state-space equations and Eq. (7) and (8) represent Converter operation at various stages.

Shoot through interval (δ) level of boosting.

$$L_1 \frac{di_1(t)}{dt} = V_{dci1}$$

$$L_2 \frac{di_2(t)}{dt} = V_{dci2}$$

$$L_3 \frac{di3(t)}{dt} = V_{dci3}$$

and

$$C_1 \frac{dV_{dco1}}{dt} = \frac{V_{dco1}}{R_{dc1}}$$

$$C_2 \frac{dV_{dco2}}{dt} = \frac{V_{dco2}}{R_{dc2}}$$

$$C_3 \frac{dV_{dco3}}{dt} = \frac{V_{dco3}}{R_{dc3}} \tag{7}$$

Power interval $(1 - \delta)$ of boosting expressions

$$L_1 \frac{di_1(t)}{dt} = V_{dci1} - V_{dco1}$$

$$L_2 \frac{di_2(t)}{dt} = V_{dci2} - V_{dco2}$$

$$L_3 \frac{di_3(t)}{dt} = V_{dci3} - V_{dco3}$$

and

$$C_1 \frac{dV_{dco1}}{dt} = i_1 - \frac{V_{dco1}}{R_{dc1}}$$

$$C_2 \frac{dV_{dco2}}{dt} = i_2 - \frac{V_{dco2}}{R_{dc2}}$$

$$C_3 \frac{dV_{dco3}}{dt} = i_3 - \frac{V_{dco3}}{R_{dc3}} \tag{8}$$

The currents i_1, i_2 and i_3 flowing through L_1, L_2 and L_3, respectively. Response of BDMHC voltages are V_{dco1}, V_{dco2} and V_{dco3} and ac output current flowing through the resistor R is i_{aco}. The operation inverter is described with Eq. (9)

$$L_1 \frac{di_{ac}}{dt} = V_{dci1} - R_{aco} i_{aco} \tag{9}$$

2.2.2 2nd Level of Working (Period $(\Pi - 2\alpha 2)$)

Switches $H11$, $H12$, $H21$, $H22$ and $H31$ are closed and $H13$, $H14$, $H23$, $H22$, and $H31$ are in boosting, in 2nd level and 1st level of converter expressions (7) and (8) are the same whereas inverter expressions for 2nd level is described in the Eq. (10)

$$(L_1 + L_2) \frac{di_{ac}}{dt} = (V_{dci1} + V_{dci2}) - R_{aco} i_{aco} \tag{10}$$

2.2.3 3rd Level of Working (Period (π-2α3))

Switches $H11$, $H12$, $H21$, $H22$, $H31$ and $H32$ are closed and $H13$, $H14$, $H23$, $H24$, $H33$, and $H34$ are in boosting, 3rd level and 1st level of converter expressions (7) and (8) are the same but inverter expressions for 3rd level is described in the Eq. (11).

$$(L_1 + L_2 + L_3)\frac{di_{ac}}{dt} = (V_{dci1} + V_{dci2} + V_{dci3}) - R_{aco}i_{aco} \tag{11}$$

3 State Space Modeling

To calculate the steady state response of voltages and currents [19–21], state-space averaging method is used. A generalized expression for state-space model [23,24] is described in Eq. (12) and (13). Multi level inverter output expressions (7–9) can be arranged lie state-space equations. Where state variables are the current flowing through the inductor and voltage across the capacitor.

$$\overset{\bullet}{X} = AX + BU \tag{12}$$

$$Y = CX + DU \tag{13}$$

here X represents the state vector–matrix is described in Eq. (14)

$$X = \left(\frac{di_1}{dt} \frac{di_2}{dt} \frac{di_3}{dt} \frac{dV_{dco1}}{dt} \frac{dV_{dco2}}{dt} \frac{dV_{dco3}}{dt} \frac{di_{ac}}{dt} \right)^T \tag{14}$$

here, U represents input vector and Y represents output states, as described in Eq. (15)

$$U = (V_{dci1} \, V_{dci2} \, V_{dci3})^T$$

and

$$Y = (V_{dco1} \, V_{dco2} \, V_{dco3} i_{aco}) \tag{15}$$

The avg state eq is given in the Eq. (16) and (17)

$$A = \delta x_1 + (1 - \delta)x_2 \tag{16}$$

$$B = \delta y_1 + (1 - \delta)y_2 \tag{17}$$

Table 2 Inputs and specifications

Inputs	Specifications	Inputs	Specifications
V_{dci1}, V_{dci2} and V_{dci3}	30 V	R_{aco}	200 Ω
$L1, L2$ and $L3$	5 mh	Switching frequency	10×10^3 Hz
C_1	1 mF	Duty cycle	50%
R_{dc1}, R_{dc2} and R_{dc3}	20 Ω	m_a	0.4

x_1, x_2, y_1 and y_2 are constants which are used level 1 shoot-through and power interval state and input matrices, derived from the Eqs. (7–9) and which are substituted in the Eq. (12). Now, the derived level 1 state matrix is described in Eq. (18)

$$X = (i_1 i_2 i_3 V_{dco1} V_{dco2} V_{dco3})^T \qquad (18)$$

$$L_1 \frac{di_{ac}}{dt} = V_{dci} - R_{ac} i_{aco} \qquad (19)$$

4 Results and Discussion

The specifications considered for the simulation of boost derived multilevel hybrid converter is represented in Table 2. The response at the output voltage of AC load terminals is shown in Fig. 9. And the DC voltage at the dc load terminals is shown in Fig. 10 (Table 3).

5 Conclusion

The proposed boost derived multilevel hybrid converter is able to supply the ac and dc outputs concurrently for medium and high power domestic requirements. The proposed converter state-space mathematical expressions have been derived and evaluated through MATLAB/Simulink and the results are accurate and forecast the vibrant performance of the converter.
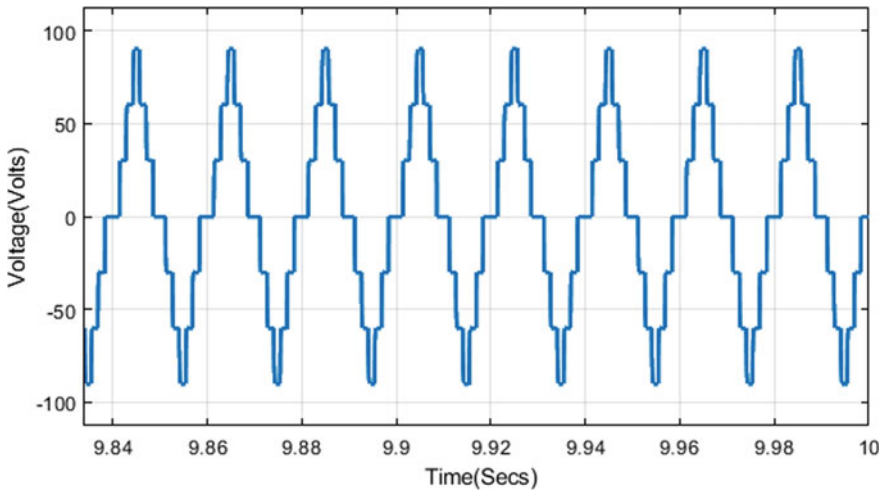
Fig. 9 Multilevel AC output voltage of BDMHC
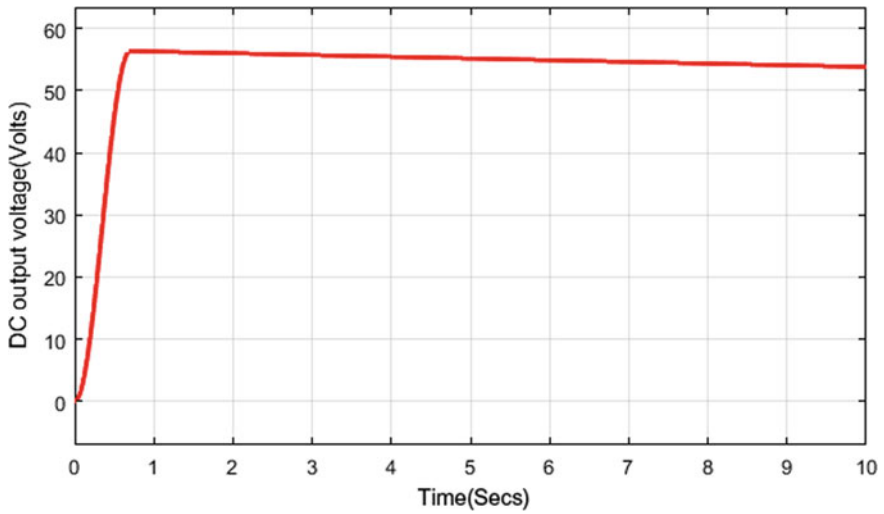
Fig. 10 DC output voltage of BDMHC

Table 3 Theoretical and practical output comparison

Output values	Theoretical value	Simulated value
$V_{dco1}, V_{dco2}, V_{dco3}$	61.25 V	55.5 V
V_{aco}	90 V	91.5 V
i_{dc}	3.075 A	3.3 A
i_{ac0}	4.5 mA	4.72 mA

References

1. A Dianov N-S Kim Y-K Kim 2015 Foture drives of home appliances: Elimination of the electrolytic DC-link capacitor in electrical drives for home appliances IEEE Trans Ind Elec Magazine 9 3 10 18
2. W-C Lee D-S Hyun T-K Lee 2000 Lee: a novel control method for three-phase PWM rectifiers using a single current sensor IEEE Trans Power Electron 15 5 861 870
3. Chen YM, Chen YL, Chen CW (2011) Progressive smooth transition for four-switch buck-boost converter in photovoltaic applications. In: Proceeding IEEE energy conversion congress and exposition, pp 3620–3625
4. Zhoing Q, Hornik T (2012) Control of power inverters in renewable energy and smart grid integration. Chap. 3. Wiley-IEEE Press
5. F Blaabjerg Z Chen SB Kjaer 2004 Power electronics as an efficient interface in dispersed power generation systems IEEE Trans Power Electron 19–5 1184 1194
6. O Ray S Mishra 2014 Boost-Derived hybrid converter with simultaneous DC and AC outputs IEEE Trans Ind Appl 50 2 1082 1093
7. Du Z, Tolbert LM, et al (2009) Fundamental frequency switching strategies of a seven-level hybrid cascaded H-bridge multilevel inverter. IEEE Trans power electronics 24–1
8. I Colak E Kabalci 2011 Review of multilevel voltage source invertertopologies and control schemes Energy Conver Manag 52 1114 1128
9. Xian B, Ljun Hang L, Mei J, Riley C et al (2014) Modular cascaded H-bridge multilevel PV inverter with distributed MPPT for grid-connected applications. IEEE Trans Ind Appl 101–109
10. EE Carbajal-Gutierrez JA Morales-Saldana J Leyva-Ramos 2005 Modelling of single switch quadratic buck converter IEEE Trans Aerosp Electron Syst 41–4 1451 1457
11. Boroyevich D, Cvetkovic I, Dong D, Burgos R, Wang F, Lee F (2010) Future electronic power distribution systems—a contemplative view. In: Proceeding 12th international conference OPTIM electrical electronic equipment. Brasov, Romania, pp 1369–1380
12. F Blaabjerg Z Chen SB Kjaer 2004 Power electronics as efficient interface in dispersed power generation systems IEEE Trans Power Electron 19 5 1184 1194
13. Ray O, Mishra S, Joshi A, Pradeep V, Tiwari A (2012) Implementation and control of a bidirectional high-gain transformer-less standalone inverter. In: Proceeding IEEE energy conversation congress expo. Raleigh, NC, USA, pp 3233–3240
14. Peng FZ (2003) Z-source inverter. IEEE Trans Ind Appl 39(2):504–510
15. CJ Gajanayake FL Luo HB Gooi PL So LK Siow 2010 Extended-boost Z-source inverters IEEE Trans Power Electron 25 10 2642 2652
16. Upadhyay S, Adda R, Mishra S, Joshi A (2011) Derivation and characterization of the switched-boost inverter. In: Proceeding 14th European conference power electronic application—EPE. Birmingham, U.K., pp 1–10
17. S Mishra R Adda A Joshi 2012 Inverse Watkins-Johnson topology-based inverter IEEE Trans Power Electron 27 3 1066 1070
18. Mishra S, Adda R, Joshi A (2011) Switched-boost inverter based on inverse Watkins-Johnson topology. In: Proceeding IEEE ECCE. Phoenix, AZ, USA, pp 4208–4211
19. Adda R, Mishra S, Joshi A (2011) A PWM control strategy for switched boost inverter. In: Proceeding IEEE ECCE, Phoenix. AZ, USA, pp 991–996
20. FZ Peng M Shen Z Qian 2005 Maximum boost control of the Z-source inverter IEEE Trans Power Electron 20 4 833 838
21. M Shen J Wang A Joseph FZ Peng LM Tolbert DJ Adams 2006 Constant boost control of the Z-source inverter to minimize current ripple and voltage stress IEEE Trans Ind Appl 42 3 770 778
22. Tymerski R, Vorperian V (1986) Generation, classification, and analysis of switched-mode dc-to-dc converters by the use of switched-inductor-cells. In: Proceeding international telecommunication energy conference, pp 181–195

23. Varaprasad MVG, Arundhati B, Hema Chander A, Phani Teja B (2021) Design and implementation of a modified H-bridge multilevel inverter with reduced component count. In: Machine intelligence and soft computing. advances in intelligent systems and computing. Springer Publisher, vol 1280, pp 321–334
24. Arundhati B, Varaprasad MVG, Vijayakumar G (2021) Novel topology for 9-level HBridge multilevel inverter with optimum switches. In: Machine intelligence and soft computing. Advances in intelligent systems and computing. Springer Publisher, vol 1280, pp 419–433